

Short Papers from the 11th International Trondheim CCS Conference



Trondheim CCS Conference

CO₂ Capture, Transport and Storage

TCCS-11

The 11th Trondheim Conference on
Carbon Capture, Transport and Storage



www.tccs.no

Organized by: NCCS – Norwegian CCS Research Centre, under the auspices of NTNU and SINTEF

SINTEF Proceedings

Editors:

Nils A. Røkke (SINTEF) and Hanna K. Knuutila (NTNU)

TCCS-11
CO₂ Capture, Transport and Storage
Trondheim 22nd–23rd June 2021

Short Papers from the 11th International Trondheim CCS Conference

SINTEF Academic Press

SINTEF Proceedings 7

Editors: Nils A. Røkke (SINTEF) and Hanna K. Knuutila (NTNU)

TCCS-11

CO₂ Capture, Transport and Storage. Trondheim 22nd–23rd June 2021

Short Papers from the 11th International Trondheim CCS Conference

Keywords:

CCS – Carbon Capture, Transport and Storage, CO₂ Capture, CO₂ Transport, CO₂ Storage, CO₂ Utilization, Pre-combustion capture, Post-combustion capture, Oxy-fuel capture, CCS and hydrogen, CO₂ positive solutions, International R&D activities, Whole system issues, Novel CCS technologies, Public Acceptance, Communication, Policy, Business models

Cover illustration: SINTEF Energy

ISSN 2387-4295 (online)

ISBN 978-82-536-1714-5 (pdf)



© 2021 The Authors. Published by SINTEF Academic Press.

SINTEF has the right to publish the conference contributions in this publication.

This is an open access publication under the CC BY license

<https://creativecommons.org/licenses/by/4.0/>

SINTEF Academic Press

Address: Børrestuveien 3

PO Box 124 Blindern

N-0314 OSLO

Tel: +47 40 00 51 00

www.sintef.no/community

www.sintefbok.no

SINTEF Proceedings

SINTEF Proceedings is a serial publication for peer-reviewed conference proceedings on a variety of scientific topics.

The processes of peer-reviewing of papers published in SINTEF Proceedings are administered by the conference organizers and proceedings editors. Detailed procedures will vary according to custom and practice in each scientific community.

Preface

These proceedings contain the short papers from the 11th International Trondheim CCS Conference (TCCS-11), which was organised as a virtual event owing to the pandemic on June 22nd – 23rd, 2021.

The bi-annual Trondheim CCS Conference is one of the leading scientific CCS technology conferences. Since its inception in 2003, the conference has become a globally important meeting place for CCS experts. In summer 2021, around 350 people joined the conference to listen to world-leading keynote speakers, scientific presentations and panel discussions.

The authors submitted short papers (4-8 pages) as an abstract to the conference. These short papers are presented in these proceedings after peer review by two experts.

The organizing committee would like to thank

- The numerous reviewers helping us with the extensive review process of all the submitted short papers,
- The authors presenting their work during the conference and
- The conference sponsors for their support, making this conference possible.

Nils A. Røkke and Hanna K. Knuutila

Conference sponsors



Contents

TOMAKOMAI CCS DEMONSTRATION PROJECT - ACHIEVEMENTS AND FUTURE OUTLOOK ...10 Yoshihiro Sawada, Jiro Tanaka, Daiji Tanase, Takashi Sasaki and Chiyoko Suzuki	
ESTIMATION OF THICKNESS AND LAYERING OF JOHANSEN AND COOK SANDSTONES AT THE POTENTIAL CO ₂ STORAGE SITE AURORA19 Eyvind Aker, Heidi Kjønberg, Manzar Fawad and Nazmul Haque Mondol	
ANALYSIS OF SURFACE MOVEMENT THROUGH CONCEPTUAL AND COUPLED FLOW-GEOMECHANICS MODELS AN EXAMPLE OF SURFACE MONITORING ASSESSMENT FOR CCS PROJECT27 Sarah Bouquet, Jeremy Frey, Iryna Malinouskaya, Antoine Soulat, Audrey Estublier, André Fourné and SENSE Consortium	
EVALUATION OF RESULTS FROM SDR CAMPAIGNS AND PILOT DATA35 Solrun Johanne Vevelstad, Andreas Grimstvedt, Geir Haugen, Merete Wiig and Kai Vernstad	
EXPERIMENTAL STUDY OF CO ₂ TWO-PHASE FLOW REGIME IN A LARGE DIAMETER PIPE.....40 Hilde Andersen, Hedda E.S. Svendsen, Stine Solum, Zhilin Yang, Leyla Teberikler, Svein Solvang and Loek Vreenegoor	
CO-ADSORPTION AND PURE-COMPONENT ISOTHERM MEASUREMENTS ON DIRECT AIR CAPTURE ADSORBENTS USING THE DVS VACUUM45 John P Young, Vladimir Martis, Susana Garcia and Mijndert van der Spek	
THE ROLE OF BECCS TO DELIVER NEGATIVE CO ₂ EMISSIONS IN EUROPE51 Lorenzo Rosa, Daniel Sanchez and Marco Mazzotti	
THE INFLUENCE OF AQUIFER GEOCHEMISTRY ON SALT PRECIPITATION DURING CO ₂ INJECTION: INSIGHTS FROM 1D SIMULATIONS USING THE RAND ALGORITHM55 Fernando de A. Medeiros, Erling H. Stenby and Wei Yan	
INDUSTRIAL CO ₂ CAPTURE PROJECTS: STATUS, LESSONS LEARNED AND NEEDS FOR PROGRESSING TOWARDS FULL-SCALE IMPLEMENTATION63 Adriana Reyes-Lúa and Kristin Jordal	
CARBONATE LOOPING FOR INTERMEDIATE TEMPERATURE CO ₂ CAPTURE: EVALUATING THE SORPTION EFFICIENCY OF MINERAL-BASED MGO PROMOTED WITH CaCO ₃ AND ALKALI NITRATES77 Theodoros Papalás, Andy N. Antzaras and Angeliki A. Lemonidou	
CO ₂ CKTAILS IN A PIPELINE': THE PHASE BEHAVIOUR OF CO ₂ WITH >20 IMPURITIES85 Eduardo Luna-Ortiz	
INTRODUCTION OF POTASSIUM IODIDE AS AN INHIBITOR FOR OXIDATIVE DEGRADATION OF AMINES91 Vanja Buvik, Silje Thorstad, Ricardo R. Wanderley and Hanna K. Knuutila	
MODIFIED DOLOMITE-BASED PELLETS FOR HIGH TEMPERATURE POST-COMBUSTION CO ₂ CAPTURE96 Ainara Moral, Anne Charlotte Wold, Kumar Ranjan Rout and De Chen	
GENERALIZED GEERTSMA SOLUTION FOR ISOTROPIC LAYERED MEDIUM 103 Joonsang Park, Ola Eiken, Tore I. Bjørnarå and Bahman Bohloli	
ANALYSIS OF PRESSURE AND TEMPERATURE DYNAMICS DURING DEPRESSURIZATION OF A PIPE FILLED WITH A CO ₂ -HE OR CO ₂ -N ₂ MIXTURE..... 107 Svend T. Munkejord, Han Deng, Anders Austegard, Morten Hammer, Ailo Aasen and Hans L. Skarsvåg	

CONVECTIVE DISSOLUTION IN FIELD SCALE CO ₂ STORAGE SIMULATIONS USING THE OPM FLOW SIMULATOR	113
Tor Harald Sandve, Sarah E. Gasda, Atgeirr Rasmussen and Alf Birger Rustad	
INTEGRATING CO ₂ -ABSORPTION TO A BATCH-WISE PRODUCTION PROCESS – A CASE STUDY ON A SMELTER PLANT IN NORTHERN SWEDEN	120
Elin Fahrman, Fredrik Normann, Simon Harvey and Åsa Eliasson	
PROBABILISTIC ANALYSIS OF DRAUPNE SHALE CAPROCK RELIABILITY OF THE ALPHA PROSPECT - A POTENTIAL CO ₂ STORAGE SITE IN THE SMEAHEIA AREA, NORTHERN NORTH SEA	127
Md Jamilur Rahman, Jung Chan Choi, Manzar Fawad and Nazmul Haque Mondol	
ELEGANCY – ENABLING A LOW-CARBON ECONOMY VIA HYDROGEN AND CCS.....	135
Svend T. Munkejord, Marco Mazzotti, Mijndert van der Spek, Catherine Banet, Nilay Shah, Nixon Sunny, Gunhild A. Reigstad, Gianfranco Guidati, Hans L. Skarsvåg, Roland Span, Jaap Vente, J.P. Martin Trusler and Nils A. Røkke	
THERMODYNAMIC PROPERTIES OF THE BINARY MIXTURE OF MONOETHANOLAMINE AND CARBON DIOXIDE.....	143
Tobias Neumann, Ida M. Bernhardsen, Hanna K. Knuutila, Jana P. Jakobsen and Roland Span	
ARTIFICIAL INTELLIGENCE FOR WELL INTEGRITY MONITORING BASED ON EM DATA.....	152
Seyed Ehsan Hosseini, Simone Zonetti, Anouar Romdhane, Bastien Dupuy and Børge Arntsen	
A WORKFLOW FOR REGIONAL EXPLORATION OF CO ₂ STORAGE SITES IN SALINE AQUIFERS	157
Christopher Lloyd, Mads Huuse, Bonita J. Barrett and Andrew M. W. Newton	
NEGATIVE GREENHOUSE GAS EMISSIONS IN FRANCE BY 2050: TECHNO-ECONOMIC POTENTIAL ASSESSMENT	165
Ancuta Isbasoiu and Paula Coussy	
CHALLENGES AND OPPORTUNITIES OF ACHIEVING EUROPEAN CO ₂ TRANSPORTATION AND STORAGE SPECIFICATIONS FOR CARBON CAPTURE IN THE IRON AND STEEL INDUSTRY	174
R.T.J. Porter, J. Barnett, P. Cobden, E. De Coninck, H. Mahgerefteh, G. Manzolini, S. Martynov, F. Ruggeri and V. Spallina	
ON THE DISTINCTIVENESS OF NOBLE GASES IN INJECTED CO ₂ FROM BACKGROUND FLUIDS	182
Ulrich W. Weber, Niko Kampman and Anja Sundal	
IS CARBON CAPTURE A VIABLE SOLUTION TO DECARBONISE THE SHIPPING INDUSTRY?	184
Carolina Font-Palma	
MONITORING OF CO ₂ WELL PLUG INTEGRITY. ELECTRICAL RESPONSE OF CEMENT/CNF SENSOR TO MECHANICAL LOAD, WATER SATURATION AND CARBONATION	193
Kamila Gawel, Sigurd Wenner, Ali Taghipour, Dawid Szewczyk, Laura Edvardsen, Anette Brocks Hagen, Anna Stroisz, Bartłomiej Gawel, Ruben Bjørge, Amir Ghaderi, Pierre Cerasi and Malin Torsæter	
INTEGRATION OF INDUSTRIAL CO ₂ CAPTURE WITH DISTRICT HEATING NETWORKS: A REFINERY CASE STUDY	197
Åsa Eliasson, Elin Fahrman, Maximilian Biermann, Fredrik Normann and Simon Harvey	
INFLOW PERFORMANCE OF COLD CO ₂ INJECTION IN DEPLETED GAS FIELDS	202
E. Peters, D. Loeve, S. Hurter and F. Neele	

EXPERIMENTAL ASSESSMENT OF THE ENVIRONMENTAL IMPACT OF ETHANOLAMINE	207
Vanja Buvik, Richard Strimbeck and Hanna K. Knuutila	
MODELLING AND EVALUATING CARBAMATE POLYMERIZATION OF MONOETHANOLAMINE IN POST-COMBUSTION CARBON CAPTURE	212
Lucas Braakhuis and Hanna K. Knuutila	
ELECTROCHEMICALLY ENHANCED DEPOSITION OF MINERALS FROM SYNTHETIC RESERVOIR BRINE	218
Laura Edvardsen, Benjamin Udo Emmel, Mohammad Hossain Bhuiyan, Sigurd Wenner, Kamila Gawel and Malin Torsæter	
RATE BASED MODEL AND TECHNO-ECONOMIC ASSESSMENT OF A POST-COMBUSTION CO ₂ CAPTURE UNIT OPERATING WITH POTASSIUM LYSINATE FOR NGCC DECARBONISATION	224
Antonio Conversano and Manuele Gatti	
MATERIAL INTEGRITY ASPECTS OF CCS: AN OVERVIEW FOR CO ₂ TRANSPORT AND STORAGE	231
Cécile Millet, Dwaipayan Mallick, Guillaume Néel, Leila Faramarzi and Ali Meschi Amoli	
DESCRIPTION OF THE WORK AND PRELIMINARY RESULTS OF THE AC2OCEM PROJECT IN FACILITATING CARBON CAPTURE TECHNOLOGY IN THE CEMENT INDUSTRY USING OXYFUEL COMBUSTION	237
Cynthia Kroumian, Kristina Fleiger, Ines Veckenstedt, Mari Voldsund, Otávio Cavalett, Simon Roussanaly, Joerg Maier, Volker Hoenig, Konstantina Peloriadi and Günter Scheffknecht	
DESIGN AND MULTI-OBJECTIVE OPTIMIZATION OF CO ₂ VALUE CHAINS FOR A NET-NEGATIVE WASTE TO ENERGY SECTOR: A SWISS CASE STUDY	245
Paolo Gabrielli, Viola Becattini, Alberto Acquilino, Cristina Antonini, Jordi Campos Schweitzer, Giovanni Sansavini and Marco Mazzotti	
THE ROLE OF CARBON CAPTURE, STORAGE AND UTILIZATION TO ENABLE A NET-ZERO-CO ₂ -EMISSIONS AVIATION SECTOR	250
Viola Becattini, Paolo Gabrielli and Marco Mazzotti	
FROM PRE-SCREENING TO MONITORING OF PLUGGED AND ABANDONED MARINE EXPLORATION WELLS - ENABLING REUSE OF RESERVOIRS FOR CO ₂ STORAGE THROUGH GEOPHYSICAL MONITORING	254
Benjamin Emmel, Simone Zonetti, Anouar Romdhane, Bastien Dupuy and Malin Torsæter	
EFFECT OF CAPROCK RELATIVE PERMEABILITY ON CO ₂ FLOW THROUGH IT	259
Iman Rahimzadeh Kivi, Victor Vilarrasa and Roman Makhnenko	
EXPERIMENTAL INVESTIGATION OF THE INFLUENCE OF INJECTION PRESSURE AND CLAY SMEAR ON FAULT REACTIVATION FOR CO ₂ STORAGE	265
Luke Griffiths, Joonsang Park, Pierre Cerasi, Laura Edvardsen and Andreas Wüstefeld	
FROM NATIONAL TO INTERNATIONAL FOCUS – RESULTS AND IMPACTS FROM THE NORWEGIAN NATIONAL RD&D PROGRAMME FOR CCS (CLIMIT)	272
Aage Stangeland, Åse Slagtern, Ragnhild Rønneberg, Lars Ingolf Eide and Ingrid Sørum Melaaen	
CO ₂ -ENHANCED GEOTHERMAL SYSTEMS FOR CLIMATE NEUTRAL ENERGY SUPPLY	277
Anna Sowiżdżał, Paweł Gładysz, Trond Andresen, Maciej Miecznik, Bjørn S. Frengstad, Marcin Liszka, Anna Chmielowska, Marcel Gawron, Sigurd W. Løvseth, Leszek Pająk, Lars A. Stenvik and Barbara Tomaszewska	
NUMERICAL STUDIES OF CO ₂ LEAKAGE REMEDIATION BY MICP-BASED PLUGGING TECHNOLOGY	284
D. Landa-Marbán, K. Kumar, S. Tveit and S.E. Gasda	

RAPID OPTIMISATION OF THE NEW SLEIPNER BENCHMARK MODEL	291
Francesca Watson, Odd Andersen and Halvor Møll Nilsen	
HOW FAULT INTERPRETATION METHOD MAY INFLUENCE THE ASSESSMENT OF A FAULT-BOUND CO ₂ STORAGE SITE	297
E.A.H.Michie, A. Braathen and B. Alaei	
A PRELIMINARY ASSESSMENT OF RIO BONITO FORMATION (PARANÁ BASIN, BRAZIL) SUITABILITY FOR CO ₂ STORAGE	304
Nathália Weber, Saulo B. de Oliveira, Julio Romano Meneghini and Colombo Celso Gaeta Tassinari	
USING THE URBAN STOCK AS A CARBON SINK: A CASE STUDY FROM THE GERMAN FEDERAL STATE OF NORTH RHINE – WESTPHALIA	310
Ali Abdelshafy and Grit Walther	
CO ₂ -SPICER – CZECH-NORWEGIAN PROJECT TO PREPARE A CO ₂ STORAGE PILOT IN A CARBONATE RESERVOIR	318
Vit Hladik, Robert Prochac, Vladimir Opletal, Milan Pagac, Petr Jirman, Roman Berenblyum, Anton Shchipanov, Eric Ford and Anders Neramoen	
ESTIMATION OF MUTUAL SOLUBILITY OF CO ₂ -H ₂ O IN SALINE AQUIFER SYSTEMS USING EPC-SAFT EQUATION OF STATE	323
Mohammad Masoudi, Anja Sundal and Helge Hellevang	
A MODEL TO ESTIMATE CO ₂ LEAKAGE AND IDENTIFY CO ₂ HYDRATE STABLE CONDITIONS FOR OFFSHORE CCS	328
Hariharan Ramachandran	
SYNTHESIS PROPERTIES OF FECO ₃ : UNDERSTANDING THE UNDERGROUND REACTIVE ROCK	336
Randi Neerup, Isaac A. Løge and Philip L. Fosbøl	
POST-COMBUSTION CO ₂ CAPTURE: A COMPARISON BETWEEN COMMERCIALY READY TECHNOLOGIES	340
Stefano E. Zanco, Jose-Francisco Pérez-Calvo, Viola Becattini and Marco Mazzotti	
EFFECTIVE PERMEABILITY OF DEFORMATION BANDS IN FAULT DAMAGE ZONES – CAN DEFORMATION BANDS REDUCE THE RISK OF FAULT LEAKAGE?	347
Runar L. Berge, Sarah E. Gasda, Eirik Keilegaveln and Tor H. Sandve	
RESULTS FROM CESAR-1 TESTING WITH COMBINED HEAT AND POWER (CHP) FLUE GAS AT THE CO ₂ TECHNOLOGY CENTRE MONGSTAD	355
Scott A. Hume, Muhammad I. Shah, Gerard Lombardo and Eirik Romslo Kleppe	
SCREENING MICROORGANISMS FOR REMEDIATION OF WELLS VIA CARBONATE PRECIPITATION	362
Megan J. Barnett, Simon P. Gregory and Audrey Ougier-Simonin	
UPSCALED GEOCELLULAR FLOW MODEL OF POTENTIAL ACROSS- AND ALONG-FAULT LEAKAGE USING SHALE GOUGE RATIO	366
T.I. Bjørnarå, E.M. Haines and E. Skurtveit	
TECHNO-ECONOMIC PERFORMANCE OF DORA WITH MEA AND CESAR1	374
Tanya Srivastava, Roberta V. Figueiredo, Tarjei Skaar, Niels Warning, Paul Gravesteijn, Juliana Monteiro, Peter van Os and Earl Goetheer	

SOLVENT RECLAIMING AT A POST COMBUSTION CO ₂ CAPTURE PLANT AT TWENCE (WTE FACILITY).....	380
Tanya Srivastava, Juliana Monteiro, Arjen Huizinga, Jill Jansen, Paul Gravesteijn, Ronald de Vries, Mathijs Vos, Kirsten Telgenkamp and Peter van Os	
SIMULATIONS OF SUBSEA CO ₂ LEAKAGE SCENARIOS.....	384
Anusha L Dissanayake, Tor Nordam and Jonas Gros	
TECHNO-ECONOMIC ASSESSMENT OF FLUIDIZED BED CALCIUM LOOPING FOR THERMOCHEMICAL ENERGY STORAGE WITH CO ₂ CAPTURE	390
Guillermo Martinez Castilla, Diana Carolina Guío-Pérez, Stavros Papadokonstantakis, David Pallarès and Filip Johnsson	
EFFICIENCY OF CO ₂ FOAM MOBILITY CONTROL WITH HETEROGENEOUS RESERVOIR PROPERTIES	398
Alv-Arne Grimstad and Øystein Strengehagen Klemetsdal	
AEROSOL EMISSION AT A POST COMBUSTION CO ₂ CAPTURE PLANT AT TWENCE (WTE FACILITY).....	404
Juliana Monteiro, Tanya Srivastava, Jasper Ros, Arjen Huizinga, Paul Gravesteijn, Peter van Os, Ronald de Vries, Mathijs Vos, Kirsten Telgenkamp, Susanna Sprauten Uhre, Hallvard Fjøsne Svendsen and Hanna K Knuutila	
THE COSTS OF CO ₂ CARBONATION IN THE CEMENT INDUSTRY	410
Till Strunge	
PVT AND FLOW BEHAVIOR OF IMPURE CO ₂ IN AQUIFERS.....	415
O. Sævareid, S.E. Gasda and T.S. Mykkeltvedt	
ENERGY-INTENSIVE INDUSTRY AS A PRACTICAL AND COST-EFFECTIVE VECTOR FOR BLUE HYDROGEN EXPORTS – A NORWEGIAN CASE STUDY	420
Schalk Cloete and Jan Hendrik Cloete	
ROUTING DEPLOYMENT OF CC(U)S IN THE BALTIC SEA REGION	428
Monika Ivandic, Alla Shogenova, Farid Karimi, Adam Wójcicki and Kazbulat Shogenov	
REGULATION OF CCS STORAGE SITES IN NORWAY AND COMPLIANCE WITH EEA LAW	435
Viktor Weber	
A NEW FACILITY ON ACCURATE VISCOSITY AND DENSITY MEASUREMENTS	443
Bahareh Khosravi, Sigurd W. Løvseth, Anders Austegard, Caroline Einen, H. G.Jacob Stang, Ingrid Snustad, Jana P. Jakobsen and Håvard Rekstad	
MOLECULAR TO PROCESS SCALE: A REVIEW OF HOLISTIC DIRECT AIR CAPTURE CONTACTOR DESIGN	450
Quirin Grossmann, Valentina Stampi-Bombelli and Marco Mazzotti	
CSEM FOR CO ₂ STORAGE – FEASIBILITY STUDY AT SMEAHEIA TO OPTIMISE ACQUISITION	455
Romina Gehrman, Anouar Romdhane, Joonsang Park and Peder Eliasson	
THE EFFECT OF NEW USER SECTORS ON THE CCS INNOVATION SYSTEM.....	462
Jørgen Finstad, Allan Dahl Andersen and Jakoba Sraml Gonzalez	
HEAT OF ABSORPTION OF CO ₂ IN NOVEL ENERGY REDUCING SOLVENTS FOR BIOGAS UPGRADING	470
Sai Hema Bhavya Vinjarapu, Teresa Regueira Muniz and Philip Loldrup Fosbøl	

ENABLING CCS VIA FISCAL METERING	474
Sigurd W. Løvseth, Yessica Arellano, Han Deng, Francesco Finotti, Edward Jukes and Gérard Bottino	
CCS PUBLIC PERCEPTION LEARNINGS APPLIED TO BRAZIL.....	482
Karen Louise Mascarenhas and Julio Romano Meneghini	
IMPACT OF UNCERTAINTY OF PHYSICAL PROPERTIES ON CO ₂ ABSORPTION DESIGN	489
Lars Erik Øi and Sumudu Karunaratne	
CO ₂ IMPACT ON FeCO ₃ CORROSION PRODUCT	495
Randi Neerup, Isaac A. Løge, Caroline G. Rudbeck and Philip L. Fosbøl	
CO ₂ CAPTURE WITH STRUCTURED SORBENTS CONTAINING MULTIWALLED CARBON NANO TUBES AND POLYETHYLENIMINE (PEI).....	499
Shreenath Krishnamurthy, Richard Blom, Kari Anne Andreassen, Carlos Grande, Vesna Middelkoop, Marleen Rombouts and Adolfo Benedito Borrás	
A MULTISCALE APPROACH FOR EVALUATING UTSA-16 ADSORBENT FOR POST COMBUSTION CARBON CAPTURE	504
Shreenath Krishnamurthy, Enzo Mangano, Maria-Chiara Ferrari, Richard Blom, Carlos Grande, Daniel Friedrich, Lev Sarkisov and Stefano Brandani	
PHASE EQUILIBRIUM MEASUREMENTS OF AMMONIA BASED CO ₂ CAPTURE SOLVENTS WITH FTIR FOR GAS PHASE ANALYSIS	510
Inna Kim, Actor Chikukwa, Hanne Kvamsdal, Karl Anders Hoff, Thor Mejdell and Geir Haugen	
PROCESS INTEGRATION OF INDIRECTLY HEATED CARBONATE LOOPING IN LIME PLANT FOR ENHANCED CO ₂ CAPTURE	515
Peloriadi Konstantina, Atsonios Konstantinos, Nikolopoulos Aristeidis, Intzes Konstantinos, Dimitriadis Giorgos and Nikolopoulos Nikos	
HIGH LEVEL ANALYSIS OF CO ₂ CAPTURE IN THE WASTE-TO-ENERGY SECTOR.....	523
J.A. Ros, J.G.M-S. Monteiro and E.L.V. Goetheer	
HIGH LEVEL ANALYSIS OF CO ₂ CAPTURE ON LNG FUELLED SHIPS.....	526
J.A. Ros, J.G.M-S. Monteiro and E.L.V. Goetheer	
CO ₂ CAPTURE FROM LIME AND CEMENT PLANTS USING AN INDIRECTLY HEATED CARBONATE LOOPING PROCESS – THE ANICA PROJECT	529
Jochen Ströhle, Carina Hofmann, Martin Greco-Coppi and Bernd Epple	
HEURISTIC METHODS FOR PIPELINE NETWORK DESIGN.....	536
Christopher Yeates, Cornelia Schmidt-Hattenberger and David Bruhn	
IMPACT OF INNOVATIONS FROM THE NORWEGIAN CCS RESEARCH CENTRE (NCCS).....	541
Grethe Tangen, Inna Kim, Amy Brunsvold, Mona J. Mølnvik, Solrun J. Vevelstad, Elin Skurtveit, Simon Roussanly, Svend T. Munkejord, Pierre Cerasi and Peder Eliasson	
FAST WATER-LEAN SOLVENT SCREENING USING FTIR SPECTROSCOPY: IN-SITU (IN-LINE) MONITORING USING AN ATR REACTION CELL INTEGRATED WITH ON-LINE MONITORING ATTACHED TO A LIQUID-FLOWCELL.....	547
Jayangi D. Wagaarachchige, Zulkifli Idris, Maths Halstensen and Klaus-J. Jens	
CCS IN THE EUROPEAN ENERGY TRANSITION TO CLIMATE NEUTRALITY	553
G. A. Reigstad, J. Straus, O. Wolfgang, J. A. Ouassou, G.S. Seck, E. Hache and M. Villavicencio	

TOMAKOMAI CCS DEMONSTRATION PROJECT - ACHIEVEMENTS AND FUTURE OUTLOOK

Yoshihiro Sawada^{1*}, Jiro Tanaka¹, Daiji Tanase¹, Takashi Sasaki¹, Chiyoko Suzuki¹

¹ Japan CCS Co., Ltd., SAPIA Tower 21F, 1-7-12, Marunouchi, Chiyoda-ku, Tokyo 100-0005 Japan

* Corresponding author e-mail: yoshihiro.sawada@japanccs.com

Abstract

The Tomakomai CCS Demonstration Project is being conducted over a nine-year period from JFY* 2012 to 2020. The original plan comprised a four years construction, three years CO₂ injection and two years post-injection monitoring period, aiming to establish CCS technology for practical use by around 2020.

The main objectives and tasks of the project were; 1) demonstrate a full-chain CCS system from capture to storage, 2) demonstrate that the CCS system is safe and reliable, 3) remove concerns about earthquakes by the data collected (As Japan is an earthquake-prone country, removing concerns regarding earthquakes by establishing that natural earthquakes will not affect the CO₂ stored, and conversely that the CO₂ injection will not induce perceptible tremors is vital), 4) enhance the understanding of CCS through information disclosure and public engagement activities and, 5) acquire operational technology as well as strive towards practical implementation.

The project achieved the following results. 1) The operation of a full chain CCS system from capture to storage was conducted successfully, and the target of 300,000 tonnes of CO₂ injection was achieved in November 2019. 2) No micro-seismicity or natural earthquakes attributable to CO₂ injection were detected in the vicinity of the injection area. 3) The time-lapse monitor seismic surveys showed clear anomalies reflecting the evolution of the CO₂ plume. 4) No abnormalities suggesting seepage of injected CO₂ into the ocean have been detected in the marine environmental survey. 5) 2018 Hokkaido Eastern Iwate Earthquake of moment magnitude (Mw) 6.6 did not affect the CO₂ stored. 6) The public outreach program has been largely successful, with no major opposition to the project. Information disclosure and diligent efforts to secure the understanding of local stakeholders were of utmost importance.

As a future step, the Japanese government plans to implement a CCU demonstration project making efficient use of the Tomakomai facilities and CO₂ ship transportation. JCCS is presently supporting a feasibility study being conducted by the Ministry of Economy, Trade and Industry (METI) and the New Energy and Industrial Technology Development Organization (NEDO). (*JFY denotes April of calendar year to following March)

Keywords: CCS; demonstration; two-stage absorption; micro-seismicity, earthquake; public outreach

1. Introduction

The Tomakomai CCS Demonstration Project, Japan's first full-chain CCS demonstration project is being conducted by Japan CCS Co., Ltd. (JCCS) in Tomakomai City, Hokkaido Prefecture, Japan. The project has been conducted over a nine-year period from JFY 2012 to 2020. The project was commissioned to JCCS by METI between JFY2012 and 2017, and from JFY2018 by NEDO with subsidies from METI.

JCCS was founded in May 2008 when a group of major companies with expertise in CCS-related fields, including electric power, petroleum, oil development, and plant engineering, joined forces to answer the Japanese government's call for development of CCS technology. The project schedule is shown in Fig.2 respectively.

Prior to the selection of Tomakomai as the demonstration project site, site surveys and a site selection process were conducted from JFY 2008 to 2011. At first, there were 115 candidate locations. After an evaluation of existing data and site surveys, Tomakomai was finally selected due to technical reasons including the confirmation of a good reservoir and overlying cap rock, and that no active faults were found at the Tomakomai site. In addition, the local community, in particular the Tomakomai city mayor supported the project. The support by the city mayor was decisive. Furthermore, the Tomakomai CCS site was located in an oil exploration area, and one of the leading shareholders of JCCS had acquired a lot of geological data. The abundance of existing geological data made it possible to characterize the CCS site within a limited period.

The original project schedule comprised a four-year construction, three-year CO₂ injection and two-year post-

injection monitoring period, aiming to establish CCS technology for practical use by around 2020.

The main objectives and tasks of the project are as follows:

- Demonstrate a full-chain CCS system from capture to storage
- Demonstrate that the CCS system is safe and reliable
- Remove concerns about earthquakes by the data collected;
 - No influence by natural earthquakes on CO₂ stored
 - No perceptible earth tremors induced by CO₂ injection
- Disclose project information and data and enhance understanding of CCS by local residents
- Acquire operational technology as well as strive towards practical implementation.

As Japan is an earthquake-prone country, removing concerns regarding earthquakes is vital.

The actual CO₂ injection period was three years and eight months. The target of 300,000 tonnes of CO₂ injection was achieved in November 2019. Monitoring operations are being continued (Fig.1).

This paper presents the main results and the lessons learned from the project.

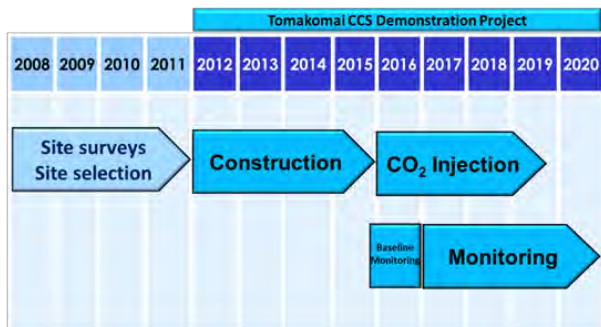


Figure 1: Project schedule

2. Overview of the Tomakomai Project

The project scheme and a bird's eye view of the facilities are shown in Fig.2 and Fig.3 respectively. The CO₂ source is an HPU (hydrogen production unit) of an oil refinery neighbouring the capture facility. At the HPU, hydrogen is produced by a PSA (pressure swing adsorption) process and a portion of the CO₂-rich PSA off gas is sent to the CO₂ capture facility by a pipeline 1.4km in length. At the capture facility, gas phase CO₂ of 99% or higher purity is recovered from the off gas by an activated amine scrubbing process with a maximum capacity of 25.3 tonnes per hour (~200,000tonnes/year), and is sent to the injection facility.

At the injection facility, the gas phase CO₂ is compressed and injected into two offshore reservoirs deep below the seabed of the Tomakomai port area, namely, the sandstone layer of the Lower Quaternary Moebetsu

formation at 1,000 to 1,200 m in depth and approximately 3 km off the coastline, and the volcanic and volcanoclastic Miocene Takinoue formation at 2,400 to 3,000 m in depth and approximately 4km offshore.

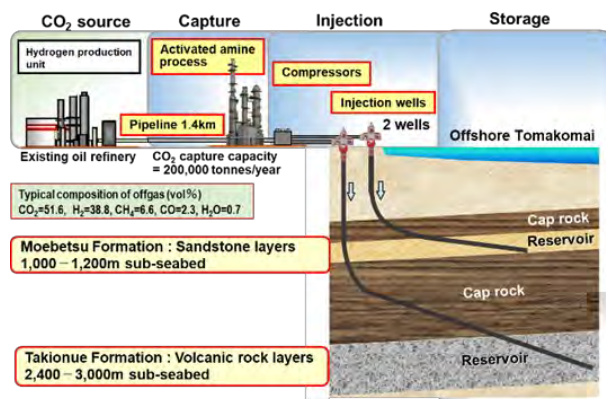


Figure 2: Project scheme

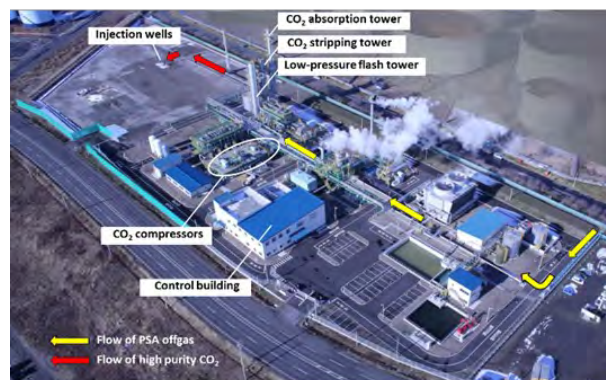


Figure 3: Bird's eye view of facilities

3. Key Results of Tomakomai Project

3.1 CO₂ capture

The CO₂ capture process used in the Tomakomai project is a commercially proven amine scrubbing process (OASE® by BASF), and the capture facility is comprised of a two-stage CO₂ absorption tower, a CO₂ stripping tower and a Low-Pressure Flash Tower (LPFT), as shown in Fig. 4. The maximum CO₂ capture rate is 25.3 tonnes per hour.

The PSA off gas enters the lower stage of the two-stage CO₂ absorption tower, where CO₂ is absorbed by an amine solution pouring from the upper part of the tower, thereby generating a CO₂ rich amine. The CO₂ rich amine is sent to the LPFT, where 60-70% of CO₂ is stripped by the effect of depressurization and the heat of CO₂ flow from the CO₂ stripping tower, and a CO₂ semi-lean amine is generated. The greater part of the semi-lean amine is recycled to the upper part of the lower stage of the CO₂ absorption tower, and the remainder is sent to the CO₂ stripping tower. In the CO₂ stripping tower, the semi-lean amine is heated by an amine reboiler, where the CO₂ is stripped and sent to the LPFT. The regenerated CO₂ lean amine is recycled to the upper stage of the CO₂ absorption tower. Finally, CO₂ of 99% or higher purity is captured at the top of the LPFT.

The two-stage absorption system results in a significant reduction of the amine reboiler duty in the CO₂ stripping tower as only a small amount of semi-lean needs to be sent to the CO₂ stripping tower. The reboiler duty was measured as approximately 0.9 GJ/t-CO₂ or less for the typical composition of PSA off gas as shown in Table 1, which is a significantly low energy consumption.

The gross capture energy including the boiler efficiency and pump electricity was about 1.2 GJ/t-CO₂.

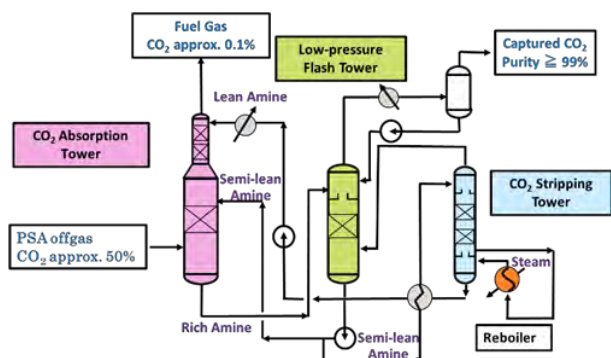


Figure 4: Two-stage absorption process

Table 1: Reboiler duty

	FY2016	FY2017	FY2019
CO ₂ recovery (t/h)	25.3	24.3	26.4
Reboiler duty (GJ/t-CO ₂)	0.923	0.882	0.915

3.2 CO₂ injection and monitoring

3.2.1 Reservoirs and injection wells

A schematic geological section is shown in Fig.5 with profiles of the injection wells. For CO₂ storage, the Tomakomai project targets two independent reservoirs of different depths and different lithofacies.

The shallow reservoir is a sandstone layer of the Moebetsu formation (hereinafter “the Moebetsu formation”), located at a depth of 1,000 m to 1,200 m below the seabed. This reservoir is a Lower Quaternary saline aquifer and is approximately 200 m thick with an average porosity of 22%.

The deep reservoir is the T1 Member of the Takinoue formation (hereinafter “the Takinoue formation”), located at a depth of 2,400 m to 3,000 m below the seabed. This reservoir is a Miocene saline aquifer composed of volcanic and volcanoclastic rocks and is approximately 600 m thick with an average porosity of 13%.

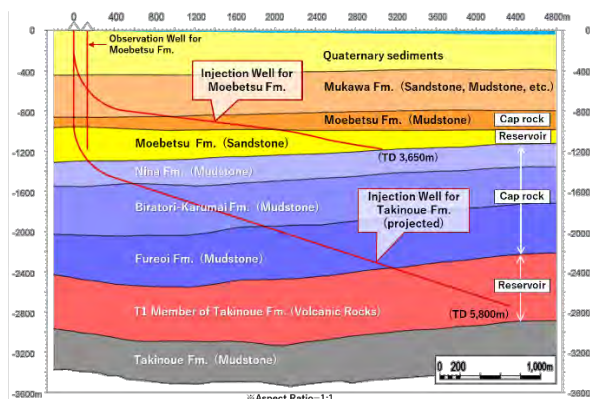


Figure 5: Schematic geological section

The injection well for the Moebetsu formation is an extended reach drilling (ERD) well with a maximum inclination of 83 degrees and a horizontal reach of approximately 3km (Fig. A). The injection interval of the injection well for the Moebetsu formation is approximately 1.2 km in length. The injection well for the Takinoue formation has a maximum inclination of 72 degrees with a horizontal reach of approximately 4.3 km. The injection interval of the injection well for the Takinoue formation is approximately 1.1 km in length. The onshore to offshore injection scheme saved drilling cost and avoided disturbing the harbor operations and fishing activities.

3.2.2 Monitoring System

In order to confirm that CO₂ is injected and stored safely and stably, it is necessary to monitor the behavior of the injected CO₂ in the reservoirs. As Japan is highly susceptible to earthquakes, it is also necessary to allocate systems to monitor and verify that there is no relationship between the CO₂ storage and seismicity. The schematic diagram of the monitoring system, the layout of the monitoring facilities and the monitoring items are shown in Fig.6, Fig.7 and Table 2 respectively.

At the two injection wells, downhole temperatures and pressures are continuously monitored. Temperature and pressure sensors and downhole seismometers are installed in the three observation wells. An ocean bottom cable (OBC) 3.6 km long permanently buried below the seabed with 72 seismometers is deployed directly above the storage area of the reservoirs. Four ocean bottom seismometers (OBSs) are placed above and surrounding the CO₂ storage areas. Additionally, one onshore seismic station is set up in the northwestern part of Tomakomai City.

3.2.3 Marine Environmental Survey

In Japan sub-seabed CO₂ storage is governed by the Act for the Prevention of Marine Pollution and Maritime Disaster, reflecting the London Protocol, and administered by Ministry of the Environment (MOE). On February 22, 2016, METI submitted a permit application for offshore CO₂ storage at Tomakomai area to MOE attaching a prescribed monitoring plan that provided for the conduct of seasonal marine environmental surveys consisting of chemical measurements of seawater and sea

bottom sediments, as well as plankton and benthos observation at twelve

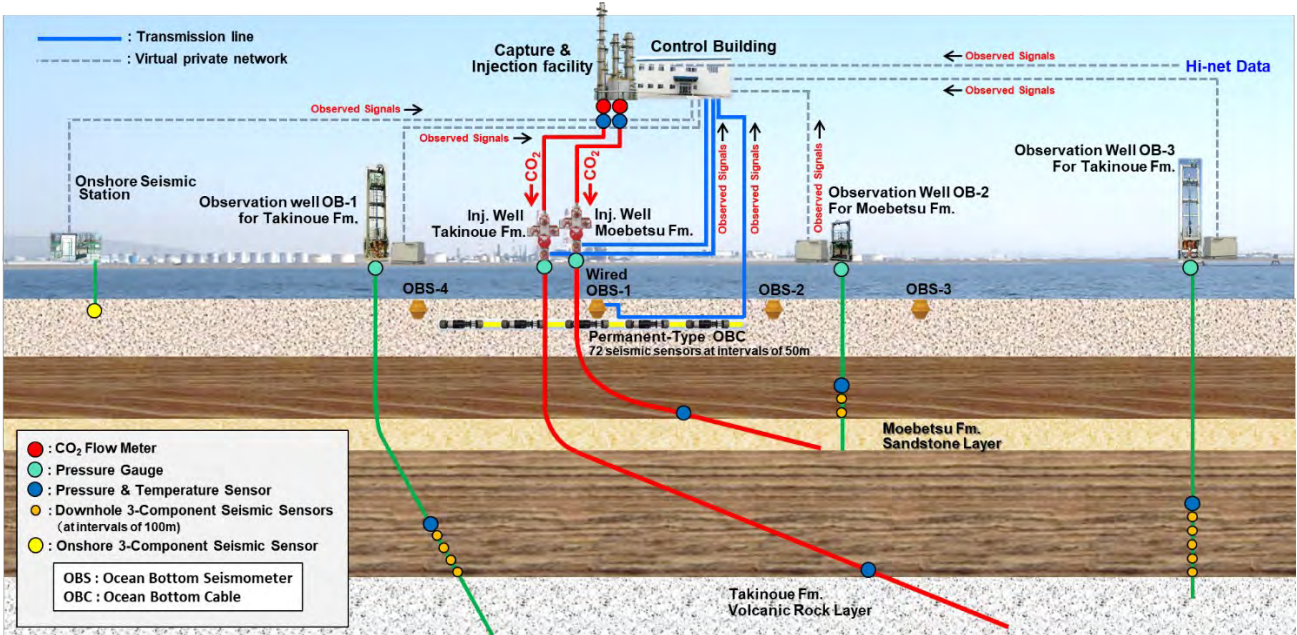


Figure 6: Schematic diagram of monitoring system

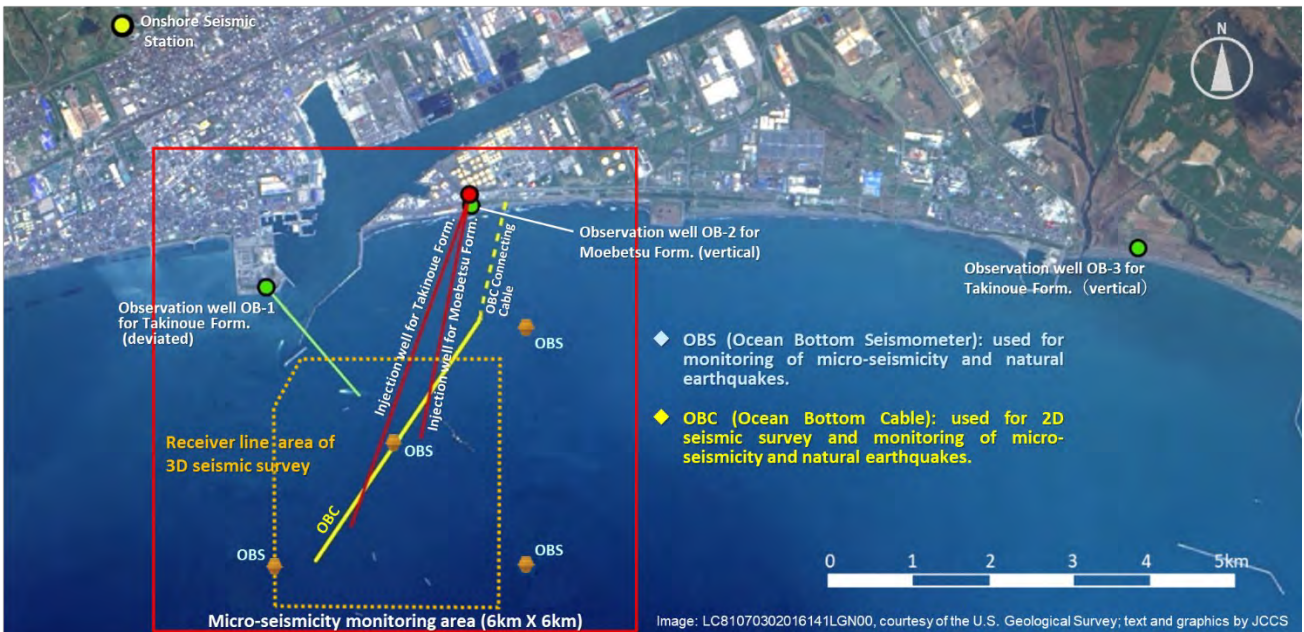


Figure 7: Layout of monitoring facilities

Table 2: Monitoring items

Equipment/Work	Monitored Items
Injection facilities	Temperature, pressure, CO ₂ injection rate
Injection wells	Downhole: temperature, pressure Wellhead: pressure
Observation wells	Downhole: temperature, pressure, seismicity
Ocean Bottom Cable (OBC)	Seismicity, receiver for 2D seismic survey
Ocean Bottom Seismometers (OBS)	Seismicity
Onshore seismometer	Seismicity
2D seismic survey	Distribution of CO ₂ in reservoir
3D seismic survey	

2D seismic survey plus mini-3D survey

Marine environmental survey Marine data (physical, chemical properties, biological habitat, etc.)

survey points above and surrounding the injection areas during and after CO₂ injection, as shown in Fig. 8.

In the February 2016 monitoring plan, the marine environmental survey consists of four phases: “regular survey (regular seasonal marine environmental survey)”, “additional survey” of regular survey, “precautionary survey”, and “contingency survey”, in which a threshold line based on the relationship between partial pressure of CO₂ (pCO₂) and dissolved oxygen (DO) of sea water was used as the criterion for transition of survey phases. The initial threshold line was established based on data

obtained in seasonal baseline surveys conducted between August 2013 and May 2014 in accordance with the requirement of MOE.

In case of exceedance of the threshold line, an “additional survey” of chemical re-measurements of sea water was to be conducted at the point(s) of the exceedance. In case of exceedance of the threshold line in the additional survey, CO₂ injection was to be suspended, and the survey phase would proceed from the “regular survey” to a “precautionary survey” consisting of re-re-measurements of sea water at the point(s) of the exceedance. In case of exceedance of the threshold line in the precautionary survey, a “contingency survey” of re-re-re-measurements of sea water was to be conducted.

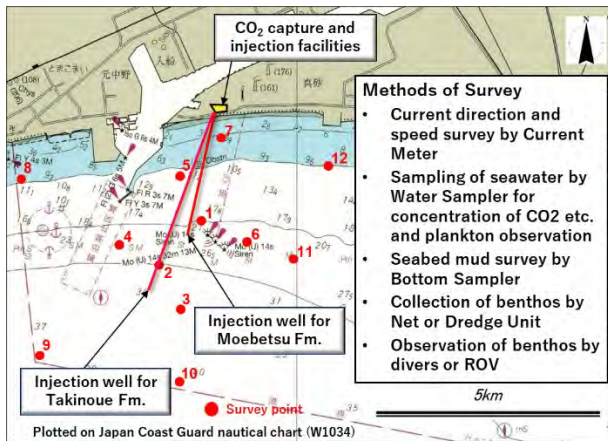


Figure 8: Marine Environmental Survey

3.2.4 Injection Results

The injection record of the Moebetsu formation is shown in Fig.9. As for the injection well for the Moebetsu formation, the maximum operational limit of downhole pressure during CO₂ injection was set as 12.6 MPaG, which is 90% of the leakoff pressure of the cap rock obtained from an extended leakoff test conducted during the drilling of the injection well. During periods of injection, the downhole pressure rose only slightly from an initial pressure of 9.3 MPaG to a maximum pressure of 10.0 MPaG implying that the injectivity of the Moebetsu formation was very high.

On the other hand, the Takinoue Formation, a volcanic and volcanoclastic rocks layer, indicated very low injectivity at the injection well. An exploration well drilled near the injection well found the formation to be composed of lava and tuff breccia, and good injectivity was confirmed by water injection tests. However, when the injection well was drilled, the reservoir around the well was found to be dense tuffaceous rock and the injectivity was confirmed to be very low. Test injections into the Takinoue Formation were conducted from February 6 to February 23, 2018, and from July 31 to September 1, 2018. As the injectivity of the Takinoue formation was much lower than expected, the cumulative injection of CO₂ ended in 98 tonnes.

The spatial lithological variation of volcanic and volcanoclastic rocks is in general very large, and we learned that it was very difficult to predict their heterogeneity in advance.

The target of 300,000 tonnes of CO₂ injection was achieved in November 2019. Monitoring operations are being continued.

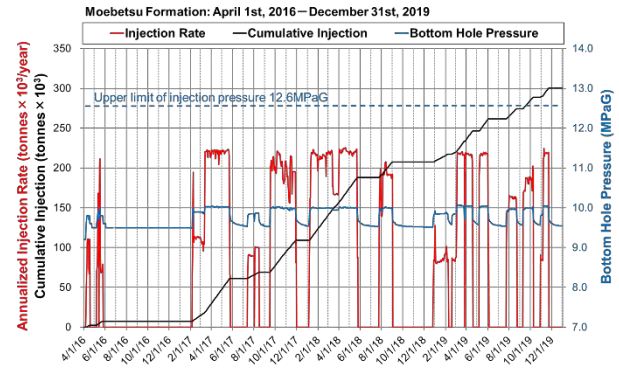


Figure 9: CO₂ injection record of Moebetsu Formation

3.2.5 Monitoring Results

The seismicity monitoring results in the monitoring area for micro seismicity are shown in Fig. 10 and 11 respectively. The detectability is Mw (moment magnitude) > -0.5. Before the start-up of CO₂ injection, a total of nine events were detected, whereas a total of three events were detected during injection, and one event was detected after injection. As shown in Fig.10, all the events have occurred in the same area with a depth of approximately 6 to 8 km and in the Cretaceous basement igneous rocks. No micro-seismicity or natural earthquakes attributable to CO₂ injection have been detected in the vicinity of injection area between start-up of injection and October 3, 2020.

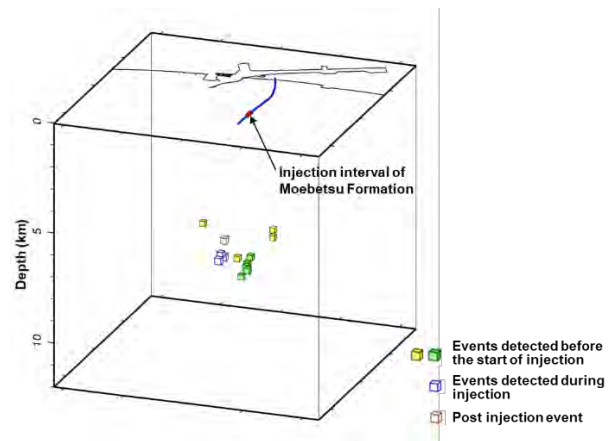


Figure 10: Micro-seismic events detected (1)

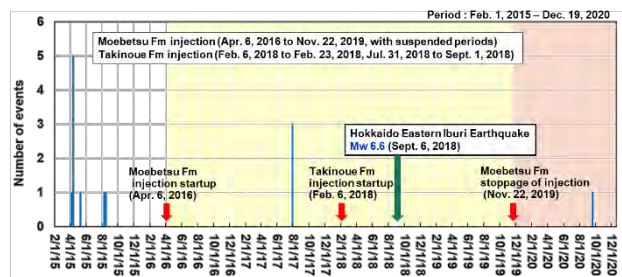


Figure 11: Micro-seismic events detected (2)

We have conducted seismic surveys two times before injection, three times during injection and two times after termination of injection. The time-lapse monitor seismic

surveys at cumulative CO₂ injection of approximately 65,000, 207,000 and 300,000 tonnes into the Moebetsu Formation have detected amplitude anomalies. Growth of the anomaly is observed in the seismic data acquired at 65,000 tonnes and 300,000 tonnes injection, indicating the evolution of the CO₂ plume (Fig. 12).

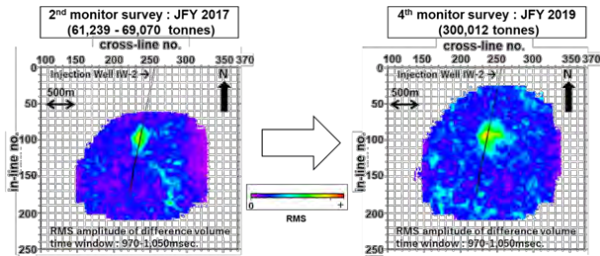


Figure 12: Comparison of 2nd and 4th monitor surveys

3.2.6 Marine environmental survey results

In June 2016, the spring regular survey was conducted, and the initial threshold line shown in Fig.13 was exceeded at several survey points. In July, in accordance with the monitoring plan, re-measurements of sea water were conducted as an “additional survey”, and again resulted in exceedances of the threshold. The prescribed “precautionary survey” was further conducted, and again resulted in exceedances of the threshold. A “contingency survey” of re-re-measurements of sea water was conducted from August to September, but resulted in no exceedances of the threshold.

In October 2016, METI reported all the results to MOE. After assessment of the results, MOE judged that the exceedances of the threshold were not caused by CO₂ leakage, and instructed METI to revise the monitoring plan by adding the implementation of new investigation items such as towed pH sensor survey and side-scan sonar bubble detection to the “additional survey” before proceeding to the “precautionary survey”.

A supplemental permit application with the revised monitoring plan was accepted by the MOE on February 1, 2017, and CO₂ injection was resumed on February 5, 2017, after a six-month suspension.

Subsequently, in the regular seasonal marine environmental surveys, “additional surveys” were conducted on two occasions following exceedances of the threshold line. Each time, no anomalies of pH, bubbles from the seabed or re-exceedance of the threshold were detected. All the results were reported by METI to MOE, and METI received official statements from MOE on each occasion that seepage or threats of seepage of injected CO₂ into the ocean were not detected. Another exceedance of the threshold was detected in August 2020 at 5 survey points, and an “additional survey” was completed by November 2020, resulting in no anomaly.

As for chemical measurement of sea bottom sediments, and plankton and benthos observation, no abnormalities have been detected.

Under the Act for the Prevention of Marine Pollution and Maritime Disaster, METI must obtain permission from the MOE every five years forever, as long as this 300,000

tonnes of CO₂ remains in the reservoir. Preparations of the permit application for the next five years from JFY 2021 to 2015 are underway.

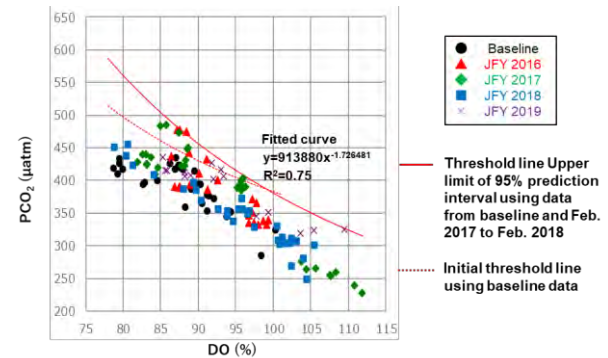


Figure 13: Results of marine environmental survey

3.3 Public Outreach

3.3.1 Public outreach activities

As the project is being conducted close to the center of Tomakomai, a large industrial city with a population of approximately 170,000, extensive public outreach is being carried out. A survey conducted in 2011 for the residents of Tomakomai found that their main concerns were information disclosure, safety of CO₂ storage, and dissemination to the young generation, which were reflected in our public outreach activities.

We concentrated our efforts on securing the trust of the local community through sustained communication as well as risk communication on such topics as CO₂ leakage and induced seismicity.

Our public outreach activities have comprised forums for local residents (Fig.14), panel exhibitions, exhibits at environmental conferences, site tours (Fig.15), lectures, and experiment classes for schoolchildren. We have also maintained an information disclosure system in the city hall of Tomakomai.

As a result of these activities, we have maintained a good relationship with the local community. We would like to stress the importance of information disclosure and diligent efforts to secure the understanding of local stakeholders.

A key factor was the strong support of the city mayor and the local government, which formed the Tomakomai CCS Promotion Association in April 2010, during the site selection process to attract the CCS demonstration project to Tomakomai City. The association has been chaired by the mayor of Tomakomai and comprises all the major local industries including the fishery cooperatives.



Figure 14: CCS Forum for Citizens



Figure 15: Site Tour

3.3.2 Experience of Major Earthquake

Our activities and public acceptance of CCS in Japan were subjected to a serious trial by the occurrence of a major earthquake in September 2018. The moment magnitude (M_w) was 6.6 (Japan Meteorological Agency Magnitude 6.7), which is quite large even in Japan. The epicenter was 30km from the injection area, at a depth of 37km (Fig.16), and caused massive destruction in a nearby village. A maximum acceleration of 158gal was recorded at the demonstration site, but no damage was incurred by the facilities.

The diagram in Fig.17 shows the conditions in the Moebetsu formation injection well before and after the earthquake. We had been injecting from July, which is indicated by a rise in the bottomhole temperature and pressure. Five days prior to the earthquake, the supply of CO₂ from the refinery stopped due to technical reasons, causing a suspension of injection, and the temperature and pressure in the well were in decline. It was during this decline that the earthquake struck. It caused a black out, and our data acquisition system lost power, causing a break in the data.

However, when we regained power three days later the continuation of the decline in the well temperature and pressure can be observed, clearly indicating that the conditions in the reservoir were unaffected by the earthquake.

JCCS convened an expert review meeting one month after the earthquake. A comprehensive review was conducted, and the unanimous conclusion was that no leakage of CO₂ had been caused by the earthquake, and that there was no data suggesting a connection between the CO₂ storage and the earthquake. As part of this discussion, the stress change caused by the CO₂ injection at the hypocenter of the earthquake was calculated and found to be about 1/1000th of the pressure change exerted on the earth's crust by tidal forces, and was therefore negligible.

The technical data including the data shown in Fig.17 was posted on our website 6 days after the earthquake [1]. After convening the expert review meeting, a detailed report was posted on our website.

Major earthquakes are typically not one-time occurrences but are followed by numerous aftershocks. The largest aftershock of the Eastern Iburu Earthquake to date occurred on February 21, 2019, recording a moment magnitude (M_w) of 5.6 (Japan Meteorological Agency Magnitude 5.8). Once again, we posted our data on our website 5 days later, explaining that there was no indication of CO₂ leakage, and no data suggesting a connection between the injection area and hypocenter.

In our response, we have made an effort to respond as quickly as possible, and to include technical data with our explanation. We believe this is important, as a large amount of false news is distributed over social media after an earthquake, and there is a risk that the project may be misunderstood.

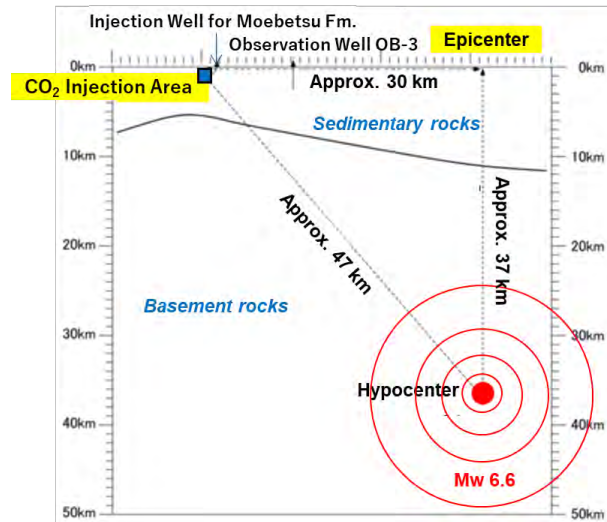
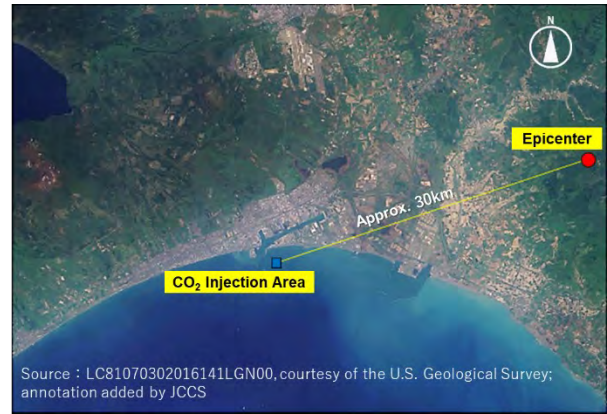


Figure 16: Location of 2018 Hokkaido Eastern Iburu Earthquake

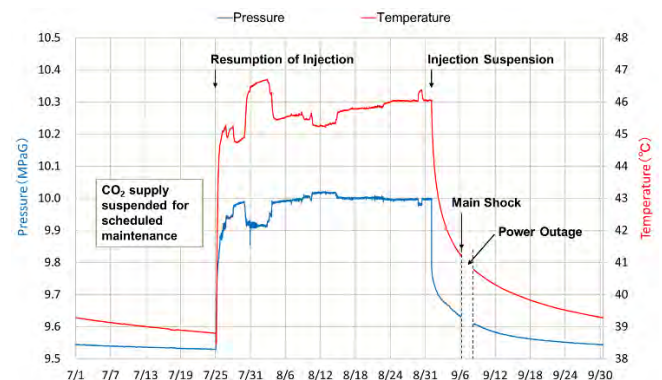


Figure 17: Change in the pressure and temperature of the Moebetsu Formation injection well.

3.4 Cost

Based on the data acquired in the Tomakomai Project, a cost estimate of a 1 million tonnes/yr commercial model was conducted in two steps as follows:

In step 1, based on the Tomakomai facilities, the capacity of which is 200 thousand tonnes/yr, the cost of a 200 thousand tonnes/yr commercial model was estimated under the following conditions.

- As the Tomakomai project was a demonstration project with facilities for testing purposes, a commercial model which excluded these facilities was considered. For example, the injection well and

observation wells for the Takinoue formation were excluded, as well as the ocean bottom cable.

- CO₂ source gas was assumed to be separated from the PSA upstream as this provides a CO₂ source gas at a high pressure favorable for CO₂ capture, and that the off gas is returned to the PSA upstream.
- Control building and operator labor costs were assumed to be provided by refinery and not included.
- Fuel gas and electricity costs were based on commercial prices.
- The depreciation period is 25 years. etc.

In step 2, the 200 thousand tonnes/yr commercial model was scaled-up to a 1 million tonnes/yr commercial model and the cost was estimated under the following conditions.

- The CO₂ capture facilities increases from one line of 200 thousand tonnes/yr to two lines of 500 thousand tonnes/yr.
- The number of the injection wells increases from one well to two wells. etc.

The captured CCS cost of the 200 thousand tonnes/yr commercial model was approximately 103 USD/t-CO₂ and the avoided cost was approximately 123 USD/t-CO₂ (1 USD = 108 JPY). The captured CCS cost of the 1 million tonnes/yr commercial model was approximately 57 USD/t-CO₂ and the avoided cost was approx. 67 USD/t-CO₂. (Table 3)

Unit costs are typically not linearly proportional to facility capacity, and the rate of increase in unit costs is less than the rate of increase in facility capacity. The cost estimation indicates that economy of scale plays an important role in reducing costs.

The percentages of each component of the 1 million tonnes/yr commercial model are shown in Fig.18. The percentages for each component in decreasing order are; capture OPEX, injection OPEX, capture CAPEX and injection CAPEX, where capture includes compression costs and injection includes monitoring costs. As we assumed commercial prices for fuel gas and electricity, the percentage of capture OPEX was high. The CCS costs can be reduced in case the operator is able to internally obtain fuel and generate electricity. Injection OPEX is the second largest cost component. In order to reduce this cost, monitoring items need to be minimized.

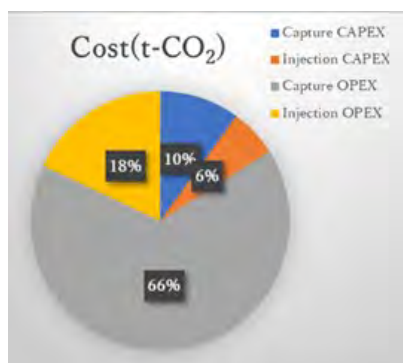


Figure 18: Percentage of CCS cost component (1million tonnes/yr commercial model)

Table 3: CCS Cost

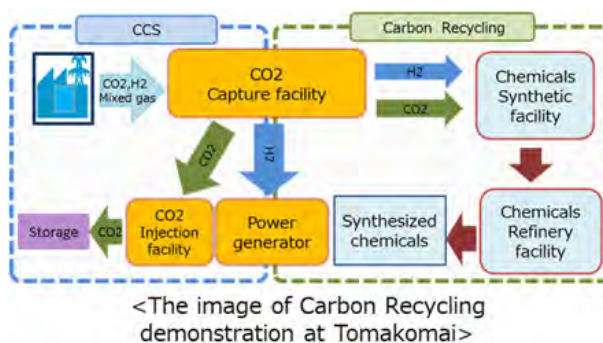
1 USD = 108 JPY

200 thousand tonnes/yr commercial model		1 million tonnes/yr commercial model	
Captured cost	Avoided cost	Captured cost	Avoided cost
103 USD/t-CO ₂	123 USD/t-CO ₂	57 USD/t-CO ₂	67 USD/t-CO ₂

3.5 Future Plans for the Tomakomai Site

3.5.1 Carbon recycling

The Japan-Asia CCUS Forum 2020 was held on October 6, 2020. At the forum, METI and NEDO announced that they will promote carbon recycling, which utilizes CO₂ as a resource by converting it into synthesized chemicals, and that they will conduct a CCU (carbon capture and utilization) demonstration project at the Tomakomai site, making efficient use of the facilities (Fig.19). To this end, JCCS is supporting a feasibility study being conducted by METI and NEDO.



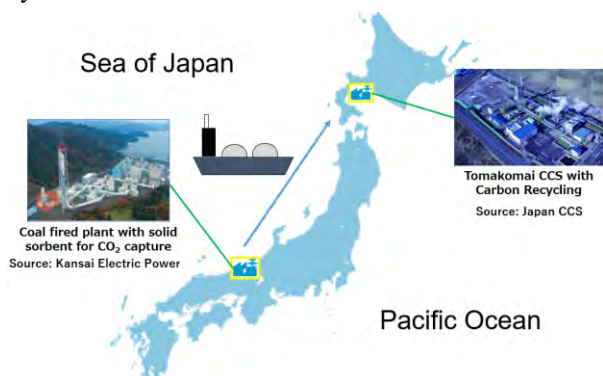
Source: METI [2]

Figure 19: Carbon recycling plan at Tomakomai

3.5.2 CO₂ ship transportation [3]

According to existing literature and data, Japan's offshore areas have the potential to store about 150 to 240 billion tonnes of CO₂. A notable point is that while industrial areas that emit a large amount of CO₂ are located mainly in the coastal areas on the Pacific Ocean side, areas suitable for storage are mainly located on the Sea of Japan side. Due to the distances between the source and storage locations, long-distance transportation by ship is believed to be more feasible than land transportation by such means as pipelines. In order to verify this, the Japanese government is currently planning to demonstrate long-distance transportation of CO₂ captured and liquefied at the coal-fired power plant in Maizuru City on the coast of the Sea of Japan to Tomakomai (Fig.20). The transport of liquefied CO₂ at low temperature and low pressure by ship has not yet

been demonstrated in the world, and Japan is aiming to be the first country to start the demonstration in 2024. JCCS is taking part in a feasibility study being conducted by METI and NEDO.



Source: Source: METI [2], partly modified by JCCS
Figure 20: CO₂ ship transportation

4. Conclusions

The main objectives and tasks of the project were; 1) demonstrate a full-chain CCS system from capture to storage, 2) demonstrate that the CCS system is safe and reliable, 3) remove concerns about earthquakes by the data collected (As Japan is an earthquake-prone country, removing concerns regarding earthquakes by establishing that natural earthquakes will not affect the CO₂ stored, and conversely that the CO₂ injection will not induce perceptible tremors is vital), 4) widely disclose information on this project through information disclosure and public engagement activities and enhance the understanding of CCS, 5) acquire operational technology as well as strive towards practical implementation.

The project achieved the following results. 1) The operation of a full chain CCS system from capture to storage was conducted successfully, and the target of

300,000 tonnes of CO₂ injection was achieved in November 2019. 2) No micro-seismicity or natural earthquakes attributable to CO₂ injection were detected in the vicinity of the injection area. 3) The time-lapse monitor seismic surveys showed clear anomalies reflecting the evolution of the CO₂ plume. 4) No abnormalities suggesting seepage of injected CO₂ into the ocean have been detected in the marine environmental survey. 5) The magnitude 6.6 2018 Hokkaido Eastern Ibari Earthquake did not affect the CO₂ stored. 6) The public outreach program has been largely successful, with no major opposition to the project. Information disclosure and diligent efforts to secure the understanding of local stakeholders were of utmost importance.

As a future step, the Japanese government plans to implement a CCU demonstration project making efficient use of the Tomakomai facilities and a project to demonstrate CO₂ ship transportation. JCCS is presently supporting feasibility studies being conducted by METI and NEDO.

Acknowledgements

The authors would like to express special thanks to METI and NEDO for their kind permission to disclose information on the Tomakomai CCS Demonstration Project.

References

- [1] JCCS website
https://www.japanccs.com/wp/wp-content/uploads/2018/09/201809_180912_oshirase.pdf
- [2] Yukihiro Kawaguchi, METI, CCUS in Japan – Present and Future. Japan-Asia CCUS Forum 2020 ;2020
https://www.japanccs.com/en/news/201006_ccus-forum-2020/
- [3] METI website (in Japanese)
https://www.enecho.meti.go.jp/about/special/johoteikyo/ccs_tomakomai_2.html?ui_medium=tw_enechosp

ESTIMATION OF THICKNESS AND LAYERING OF JOHANSEN AND COOK SANDSTONES AT THE POTENTIAL CO₂ STORAGE SITE AURORA

Eyvind Aker^{1*}, Heidi Kjønsgberg¹, Manzar Fawad², Nazmul Haque Mondol^{2,3}

¹ Norwegian Computing Center, Oslo, Norway

² Institute of Geology, University of Oslo, Oslo, Norway

³ Norwegian Geotechnical Institute, Oslo, Norway

* Corresponding author e-mail: eyvind.aker@nr.no

Abstract

We have estimated the reservoir sand thickness and internal layering in the Aurora area, a planned geological CO₂ storage site in the northern North Sea. The results are obtained by stochastic Markov chain Monte Carlo (MCMC) simulations on probabilistic lithology and fluid distributions in the subsurface. The probabilistic distributions are obtained by inverting the seismic data in a Bayesian framework. The inversion is using angle-dependent pre-stack seismic data and the linearized seismic forward model of Aki and Richards to estimate the posterior probabilities of lithology and fluid classes (facies) in the subsurface. The facies are defined from well log data by identifying depth intervals with distinct elastic responses to seismic waves. The inversion methodology and the MCMC simulations are developed and implemented by the Norwegian Computing Center.

The planned CO₂ storage reservoir comprises the Johansen and Cook sandstones belonging to the Early Jurassic Dunlin Group. The injection site (well 31/5-7) is located south and west of the Troll field in the northern North Sea and is currently being developed by Equinor in partnership with Total and Shell as part of the Northern Light project.

The seismic inversion is mapping structural details like faults and internal layering of the sandstones, and the MCMC simulations estimate the probability of sand thickness and expected layering. Results show that the Johansen Formation sandstone has a tendency of layering towards the west and largest thickness to the east in the inversion area. The sandstone in the Cook Formation is generally thinner, and probability maps indicate that it pinches out to the east. Cumulative thickness distributions provide low (P90), median (P50), and high (P10) thickness maps of both Johansen and Cook Formation sandstones. The presented methodology defines a functional workflow for quantifying the thickness uncertainty and possibly internal layering of the reservoir sands. Such results may provide important input for future field development strategies and CO₂ migration predictions.

Keywords: CO₂ storage, Aurora, Cook and Johansen Formation, Seismic inversion, Bayesian probability, Markov chain Monte Carlo simulations

1. Introduction

In hydrocarbon exploration, seismic data is used for mapping potential hydrocarbon accumulations below the seabed, with subsequent drilling of wildcat and appraisal wells to prove the reserves. Similar operations are expected in the exploration phase of a CO₂ storage project. However, we may expect fewer wells and less adequate seismic data coverage than what is typical in a hydrocarbon project since the economic viability of injecting CO₂ is lower than corresponding oil and gas production. Less data would often lead to higher uncertainty about the storage reservoir properties. Therefore, methodologies that can lower and quantify the uncertainty from data would be valuable.

Seismic inversion is the process of transforming seismic reflection data to quantitative knowledge of the subsurface, often represented by rock properties. The inversion is routinely being performed by geophysicists gathering knowledge of hydrocarbon reservoirs in the exploration and production phase. In recent years, inversion methodologies for probabilistic lithology and

fluid predictions have been developed, e.g. [1-6]. These techniques are using a Bayesian statistical framework suitable for lowering the uncertainty of an initial belief by observing (relevant) data. More specifically, the Bayesian seismic inversion methods seek to estimate a posterior probability model of different facies in the subsurface, based on a prior probability model and the seismic data. The facies can be defined as bodies of rock and fluid with varying distributions of elastic properties. For better facies predictions, the Bayesian methods utilize angle-dependent information and the inversion engine's forward model is often based on the Aki and Richards approximation [7] of the seismic amplitude variations with offset (AVO).

The layered structure of geological formations makes them suitable for modeling in terms of Markov chains [8], where the properties in one location depend only on the properties in the neighbor locations. Vertical continuities and transitions between facies layers can be described by transition probabilities that encompass a Markov chain model. Strict ordering of facies based on

for example geologic knowledge of the deposition can be accounted for. Various models like single trace [1], extensions to 3D [9-10], and more general Markov random field models [11-12] have been investigated in recent years.

We use a Bayesian-based AVO inversion process that is developed by the Norwegian Computing Center to invert a 3D seismic cube within the Aurora area. The inversion model estimates the probability of different facies combinations within a short window centered around every sample point [6]. The probabilities are used to construct a 1D Markov model to estimate the marginal probabilities of each facies class in every sample and to simulate realizations of the subsurface using Markov chain Monte Carlo simulations. From the realizations, we estimate distributions of thicknesses and probability of the presence of Johansen and Cook sandstones for every trace in the inversion area. The results are presented in probability cubes, maps of thickness estimates, and the accumulated probability of presence. The latter is interpreted as the expected number of internal layers of the sands. All results are shown for both Johansen and Cook sandstones.

2. Geological setting

The northern North Sea has undergone two main rifting events, which took place during Permo-Triassic and the Late Jurassic to Mid-Cretaceous times [13-14]. A wide basin with deep-rooted faults and thick syn-depositional wedges established below the Horda Platform during the first rifting event. The major rifting and tilting shifted westward (i.e., Lomre Terrace) during Late Jurassic to Mid Cretaceous event [15]. A weak stretching continued with the reactivation of major Permo-Triassic faults on the Horda Platform. The large normal faults with predominant N, NE and NW orientations mainly controlled the basins with several kilometres of throw-bound half grabens (15-50 km in width) and are the rifted area's fundamental morphological elements (Figure 1).

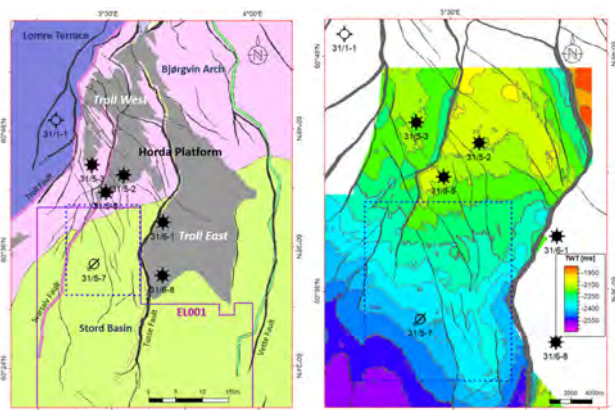


Figure 1: Inversion area (blue dotted rectangle) with the location of injection (31/5-7) and exploration wells. Well 31/5-7 was drilled within the exploitation license (EL001) for CO₂ storage (left). The colored map is a two-way time (TWT) surface of the top Johansen Formation (right).

A general stratigraphic section of the area is shown in Figure 2. The potential CO₂ storage reservoir comprises brine-filled sandstones in Johansen and Cook Formations belonging to the early Jurassic Dunlin Group. The Johansen Formation consists of sandstones with thin calcite cemented streaks [18]. The lower part is medium- to fine-grained, micaceous, well-sorted sandstone, which grades downwards into light grey silty micaceous claystone. The uppermost part is composed of medium- to fine-grained, micaceous sandstones, which are moderately sorted, silty, and argillaceous [19]. The Cook Formation consists of very fine to fine-grained, subangular to subrounded, well-sorted, hard to friable sandstones [18]. Mica, glauconite, carbonaceous material, and calcareous cement are present. Shales and siltstones separate the Johansen and Cook Formations, but they can be treated as one reservoir due to fault juxtaposition.

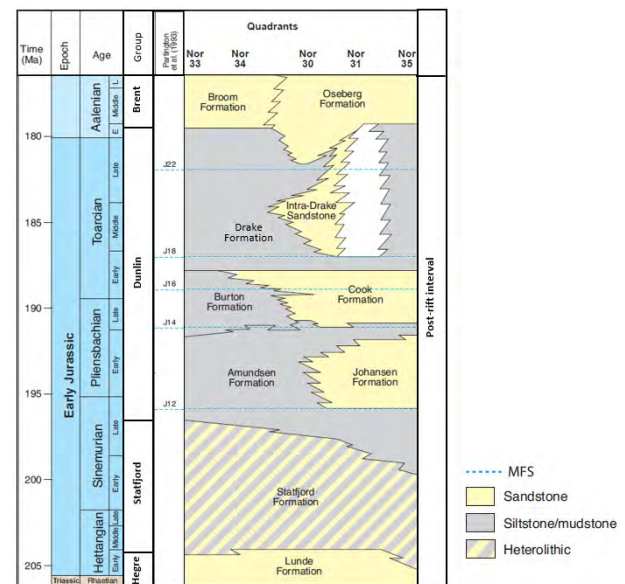


Figure 2: A generalized Early Jurassic stratigraphic succession of the study area (modified from [16]). MFS is the maximum flooding surface, according to [17].

The storage reservoirs and overlying caprocks were deposited after the Permo-Triassic rifting. The reservoir sandstones of Johansen Formation are prograding and retrograding deltaic in nature deposited during a lowstand [20]. The Amundsen Formation mudstones, which interfinger the Johansen Formation, consist of light to dark grey, non-calcareous siltstones and shales, in part carbonaceous and pyritic. The reservoir sandstone of Cook Formation is represented by prograding shelf sand on the Horda Platform and along its western margin [19]. The primary seal, i.e., Drake Formation, overlies the Cook Formation sandstone in most of the area; however, it directly overlies the Johansen Formation where the Cook and Amundsen Formations pinch out. The Drake Formation consists of medium grey, slightly sandy, calcareous, and silty claystone. The upper section is dark grey to black, fissile, micaceous shale containing calcareous nodules. Some fine to coarse sandstones are present in the formation within the study area [19].

3. Data

3.1 Geophysical data

We extracted small partial-stack cubes from the original GN10M1 seismic survey for inversion (Figure 1). The 3D seismic data is mostly of good quality, having been acquired reasonably recently in 2010. The partial stack cubes comprised angles 0-10°, 10-20°, 20-30°, and 30-40°. The inline and crossline intervals were 25 m and 12.5 m, respectively, whereas the vertical sampling rate was 4 ms. Statistical wavelets from all the five partial stacks were extracted using the entire volumes keeping the wavelet length of 200 ms. Wells 31/5-2 and 31/5-7 were correlated with the post-stack (GN10M1) seismic using sonic and checkshot data. A peak in the seismic trace represented a hard event. The interpretation of horizons was carried out based on the interface characteristics, i.e., hard or soft event, by selecting peak or trough accordingly. The horizon interpretation was initially carried out using the wells as control points, and then the 3D seeded autotracking was employed to fill the gaps. A relatively small cube surrounding the injection well is chosen for the inversion to save computational time and to get fast-track results. The injected CO₂ is expected to migrate towards north to the Troll West field and follow the updip layers of the reservoir sandstones.

3.2 Well data

The well database comprises seven exploration wells, as displayed in the map of Figure 1. Well 31/5-7 that is inside the inversion area was completed in early 2020 and is proposed as the CO₂ injection well of the Aurora license. Wells 31/1-1, 31/5-7, 31/5-2, and 31/6-1 penetrate the Johansen Formation and have been used to define the elastic properties of the facies in the inversion (see section 5). Gamma ray log, P- and S-wave velocity (V_p and V_s) and density (ρ) logs were obtained from the Norwegian National Data Repository for Petroleum Data (DISKOS), and formation well tops were downloaded from the Norwegian Petroleum Directorate fact-pages [19].

4. Methodology

We use the Bayesian AVO inversion methodology that is developed by the Norwegian Computing Center [6]. The method is inverting angle-dependent pre-stack seismic data to facies classes in a Bayesian framework. It estimates the posterior probabilities of the facies from a prior probability model and a data likelihood model quantifying how probable it is to observe the seismic data given combinations of facies in the subsurface.

In the following, facies should be thought of as a body of rock and fluid that causes a seismic response in the data and is characterized by a certain distribution of elastic properties. The distribution is represented by the mean and covariance of V_p , V_s , and ρ .

Let the seismic angle gather at a specific lateral location be denoted as \mathbf{d} , corresponding to an assumed response of a vertical column (trace) of facies \mathbf{f} in the subsurface.

Then Bayes' rule states that the posterior probability distribution of facies given the seismic data, $p(\mathbf{f}|\mathbf{d})$, is expressed by

$$p(\mathbf{f}|\mathbf{d}) = \frac{p(\mathbf{d}|\mathbf{f})p(\mathbf{f})}{p(\mathbf{d})}$$

Here $p(\mathbf{d}|\mathbf{f})$ is the data likelihood model, $p(\mathbf{f})$ is the prior probability model for facies distribution, and $p(\mathbf{d})$ is the probability distribution of observing the data.

In practice, we do not compute the full distribution of $p(\mathbf{d}|\mathbf{f})$ because the number of different facies combinations along the trace is far too high to be manageable. Instead, we assume that $p(\mathbf{d}|\mathbf{f})$ can be approximated in a neighborhood around each location and define the neighborhood to be a short vertical window of typically three to five samples. If for example, three different facies can exist at a specific location in the trace, then a five-sample length window centered around the location will result in $3^5 = 243$ different facies combinations. Hence, the problem is reduced to compare the expected seismic of these 243 different combinations (windows) with the recorded data. When there is a good match, the likelihood of the seismic data becomes high and vice versa.

By sliding the windows downwards along the trace, an approximate posterior probability of each window, $p_*(\mathbf{f}_w|\mathbf{d})$ is computed at every sample. The procedure is repeated for every lateral trace location in the seismic cube. The prior model $p(\mathbf{f}_w)$ as well as the approximate likelihood $p_*(\mathbf{d}|\mathbf{f}_w)$ utilize vertical Markov chains to account for spatial continuity and transitions among facies. See [6] for further details on how to compute $p_*(\mathbf{f}_w|\mathbf{d})$ and the resulting approximate marginal posterior probability for facies in every sample.

The expected seismic of the windows is computed by using the seismic forward model defined in [21]. It is a convolutional model based on the linearized approximation of the Aki and Richards equations [7] with added frequency-dependent Gaussian noise.

Note that the facies combinations of the windows entail the inversion to specifically look for reflections caused by facies transitions or thin layers. Layer thicknesses down to one sample are checked, despite being thinner than the seismic tuning thickness.

4.1 Creation of the posterior Markov chain

To extract additional outputs from the inversion like expected thickness and probability of the presence of individual facies, we create a posterior Markov model. It is constructed by taking the approximate window posterior probabilities $p_*(\mathbf{f}_w|\mathbf{d})$ and compute the posterior transition probabilities between facies at every sample along the trace. The vertical resolution of the Markov model is the seismic sample rate, and the calculations are repeated for every lateral location.

For facies that can disappear and re-enter further down the trace, we must sample from the posterior Markov model to get informative results. The sampling is performed by using Markov chain Monte Carlo simulations, and the number of simulations is typically

several 1000s depending on the complexity of the model. From the simulations, we can estimate distributions of thickness and probability of presence for individual facies. The latter is summed in the vertical direction and can be interpreted as the expected number of distinct layers. From the thickness distributions, we estimate the cumulative thickness generating low (P90), median (P50), and high (P10) thickness maps.

5. Litho-fluid classification

The different facies are classified by using the gamma ray log as an indicator for shale/sand content, well tops as an indicator for zonation between different depositional settings, and elastic logs (V_p , V_s , and ρ) for identifying depth intervals of distinct seismic responses.

Figures 3 and 4 show the facies classification obtained from the well logs of 31/1-1 and 31/5-7, focusing on the sands and shales in and around the Johansen and Cook Formations. The plotted depth is the measured depth with reference to the drill deck (Kelly bushing), and the horizontal dashed lines are the interpreted formation tops. The top names are shown in the yellow column. The log tracks from left to right is displaying ρ in units of g/cm³, gamma-ray (GR) in unit API, acoustic impedance (AI) in unit of km/s·g/cm³ and V_p/V_s (unitless). The last column shows the facies' classification in different colors, where white is unclassified/not used.

The well log data can be classified into six facies. The facies “Johansen sandstone” and “Cook sandstone” comprise the sandy parts of the Johansen and Cook Formations. “Dunlin shale” represents the shalier sediments in the Dunlin group, while “Drake shale” seems to only appear in the Drake Formation with a slightly higher V_p/V_s (see Figure 4). In the Statfjord Formation, there are intervals with higher V_p/V_s ratio than “Dunlin shale” and higher AI than “Drake shale”. These intervals constitute the “Statfjord” facies. The AI logs in Figures 3 and 4 contain characteristic spikes that could be caused by thin layers of hard calcareous cemented shale and/or sandstone. They form the basis for the “Stringer” facies class.

The distribution of elastic properties of the six facies is inferred from the recorded V_p , V_s , and ρ of the classified points in Figures 3 and 4. The result is displayed in Figure 5 cross-plotting V_p/V_s versus AI. The variance of the distributions is manually lowered to compensate for the upscaling effect from well logs to seismic data. Moreover, the distributions define the probability distributions of elastic properties in the forward model of the inversion. Since both Johansen and Cook Formations are brine-saturated, it is not necessary to consider fluid effects (like oil and gas) on the elastic properties.

The recorded V_p and ρ in wells 31/5-2 and 31/6-1 overlap reasonably well with the facies classification in Figure 4 and the resulting elastic distributions in Figure 5. Thus, we assume that the estimated distributions can characterize the rock in the entire inversion area. Note that V_s was only recorded in wells 31/1-1 and 31/5-7; therefore, lateral variability of those values is uncertain.

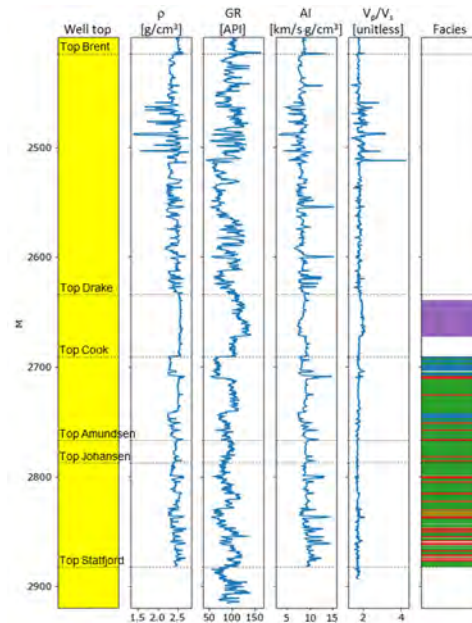


Figure 3: Facies classification in well 31/1-1.

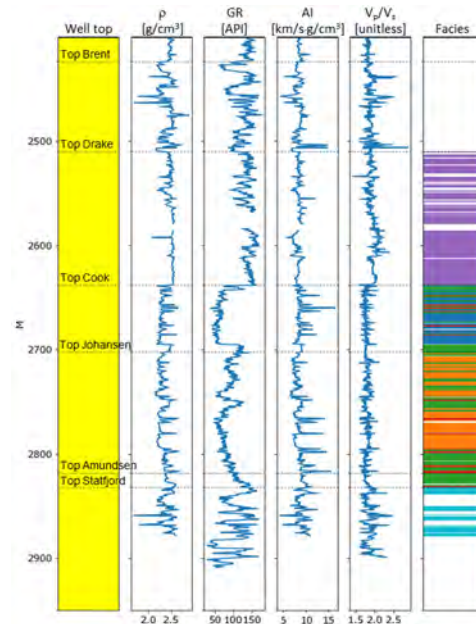


Figure 4: Facies classification in well 31/5-7.

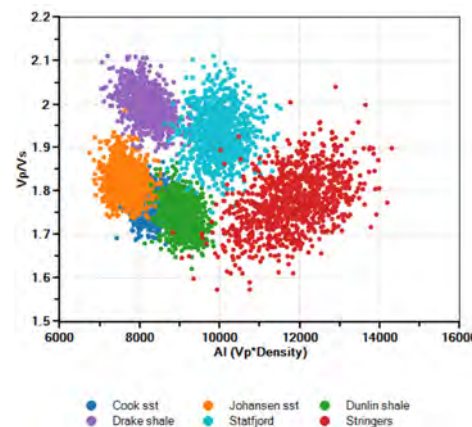


Figure 5: Elastic distributions of the facies.

6. Inversion

6.1 Prior probability model

The facies' prior probability model is constructed by a Markov chain, and the resulting model along a single trace is shown in Figure 6. The model comprises of the interpreted horizons Drake 2, Cook 4, Johansen 4, and Statfjord dividing the inversion interval into five zones from top to bottom. An initial uncertainty of +/- 10 ms is applied to the depth (time) of the interpreted horizons.

The prior probabilities of the facies and their expected thicknesses within each zone are defined from our initial belief and are based on the interpretation of well log data and the geological background knowledge. The prior input values are listed in Table 1, where the thickness values define the probability of staying in a facies class. We let the probability for transitions between different facies be evenly distributed within each zone.

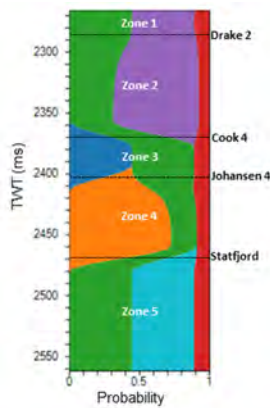


Figure 6: Prior probability model along a single trace.

The inversion interval is 300 ms and starts 20 ms above Drake 2 (zone 1) and stops in Statfjord (zone 5). The total number of traces in the inversion area is 755,970, and the number of facies combinations in the window is 648 with a window length of three samples. We do not assume any

apriori ordering of the facies within a zone and allow vertical transitions between all facies with non-zero probability. The computation time of the inversion was about 40 minutes on a Windows computer with 24-core 3.0 GHz processor and 128 GB ram.

Elastic properties of the inverted result are inferred from the marginal posterior probability of facies and their corresponding elastic distribution mean values. The result is compared with the elastic logs at 31/5-7, giving a reasonable match and the inversion model seems to confirm the observations in the well.

Zone	Cook sst	Johan-sen sst	Dunlin shale	Drake shale	Stat-fjord	Stringers
1	0	0	0.45 / 20 ms	0.45 / 20 ms	0	0.1 / 5 ms
2	0	0	0.45 / 20 ms	0.45 / 40 ms	0	0.1 / 5 ms
3	0.45 / 20 ms	0	0.45 / 20 ms	0	0	0.1 / 5 ms
4	0	0.45 / 40 ms	0.45 / 10 ms	0	0	0.1 / 5 ms
5	0	0	0.45 / 20 ms	0	0.45 / 20 ms	0.1 / 5 ms

Table 1: Prior probabilities of each facies. Prior thickness is given in time (ms) for facies with non-zero prior probabilities. Listed probabilities refer to values at the top of each zone.

6.2 Posterior results

Figure 7 shows the posterior probability of Johansen sandstone within the Johansen Formation along cross-sections A-A' and B-B' intersecting well 31/5-7 (Figure 8). The posterior probability of sand appears high (close to 1) immediately below top Johansen 4 in both cross-sections. A solid thick interval with probability close to 1 from top to bottom of the Johansen formation is observed east of the well in section A-A'. The probability tends to drop or split between a lower and an upper peak west and south of the well in cross-sections A-A' and B-B', respectively.

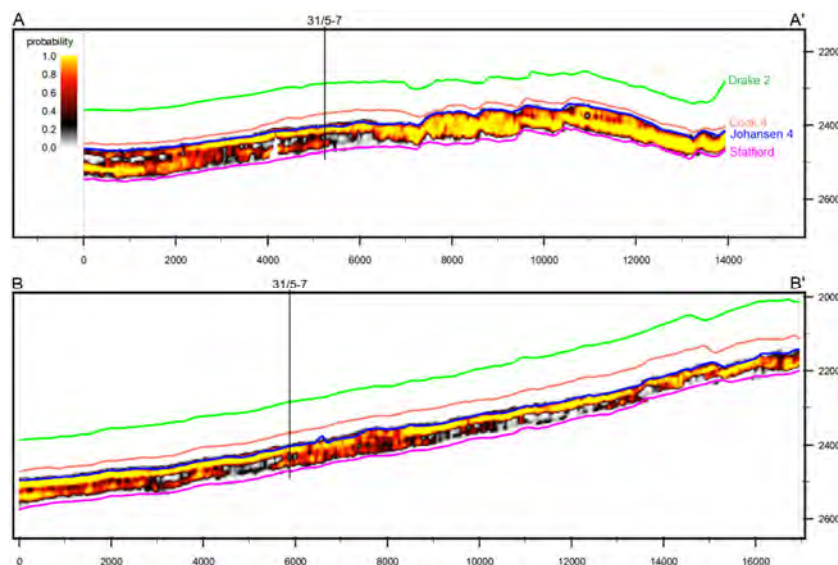


Figure 7: Posterior probability of Johansen sandstone along cross-sections A-A' and B-B' (see Figure 8). Solid colored lines correspond to the interpreted horizons.

The thickness distribution of the Johansen sandstone is estimated from MCMC simulations using the posterior Markov model. Five thousand realizations were simulated, and the resulting expected (mean) thickness is shown in Figure 8. The colors in the map span from 0 to 60 ms thickness. The thickness (in meters) is approximately double these numbers according to the time to depth conversion of well 31/5-7.

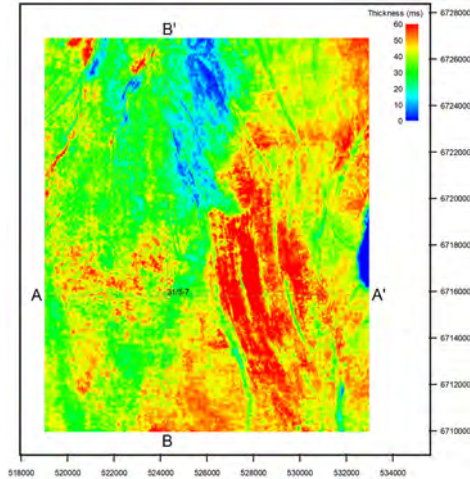


Figure 8: Expected thickness of the Johansen sandstone with well 31/5-7 and cross-sections overlaid.

The Johansen sandstone seems to be generally thickest to the east with a maximum expected thickness above 60 ms. Towards west and north, the thickness is lower and about 30 ms at the well 31/5-7. Notice the NNW-SSE sinusoidal shaped features of lower thickness to the east. They correspond to faults in the area, and the largest ones are also seen as four characteristic steps in the posterior probability in Figure 7 at around 7500, 8500, 9500, and 10500 meters in cross-section A-A'. Similar features were reported in [22].

The Johansen sandstone can disappear and reappear further down in the Johansen Formation, and the

posterior probability in Figure 7 indicates that the sand may have some internal layering. To quantify the degree of layering, we let the vertical sum of probability of presence correspond to the expected number of layers. The result is plotted in Figure 9 for the Johansen sandstone. Zero means that the Johansen sandstone is not present. The figure shows that there is a tendency for the sand to split into more than one layer as we move towards the west. There is also a small region towards the north where the probability of presence is very low and close to zero. The observed layering is confirmed by horizon interpretation from the seismic data identifying an internal horizon inside the Johansen formation.

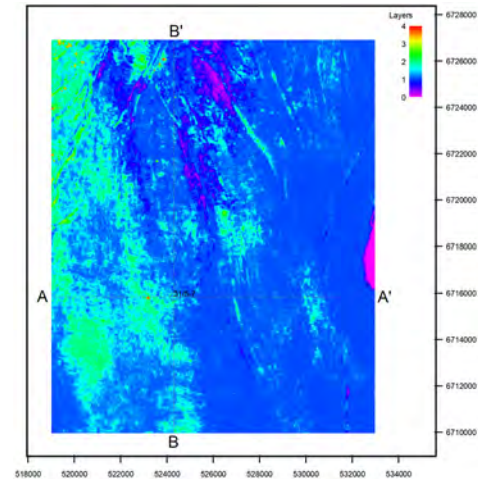


Figure 9: Expected number of layers of Johansen sandstone.

Figure 10 shows the cross-sections A-A' and B-B' for the posterior probability of Cook sandstone in the Cook Formation. The estimated probability of Cook sandstone is generally lower than the corresponding probability of Johansen sandstone (Figure 7). This is presumably because the elastic distribution of Cook sandstone is partly overlapped by Dunlin shale (see Figure 5), making them elastically more similar than the Johansen sandstone and more difficult for the inversion to resolve.

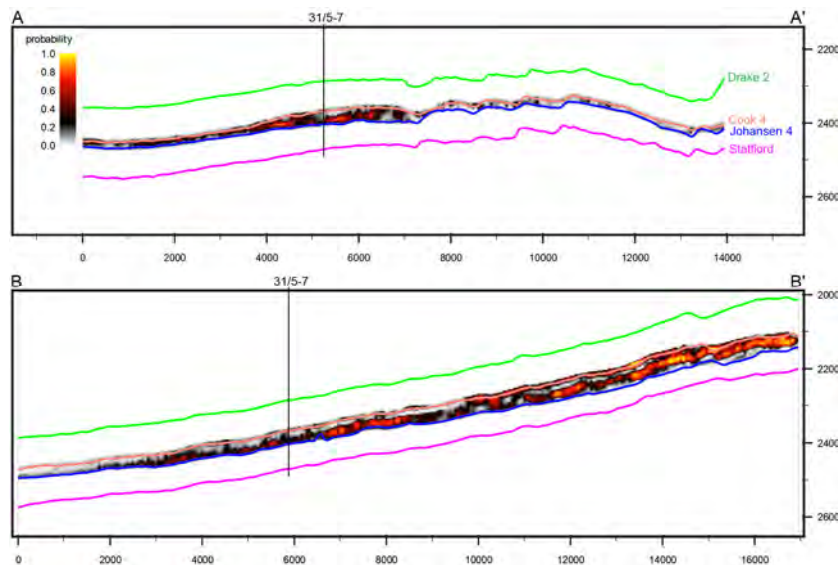


Figure 10: Posterior probability of Cook sandstone along sections A-A' and B-B'. Solid colored lines correspond to interpreted horizons.

In cross-section A-A' towards the east, the posterior probability of Cook sandstone becomes close to zero, which could indicate that it pinches out or that it is thinner than the seismic tuning thickness. Corresponding MCMC simulations giving the expected number of layers of the Cook sandstone is plotted in Figure 11. It clearly shows that the Cook sandstone diminish eastwards from well 31/5-7.

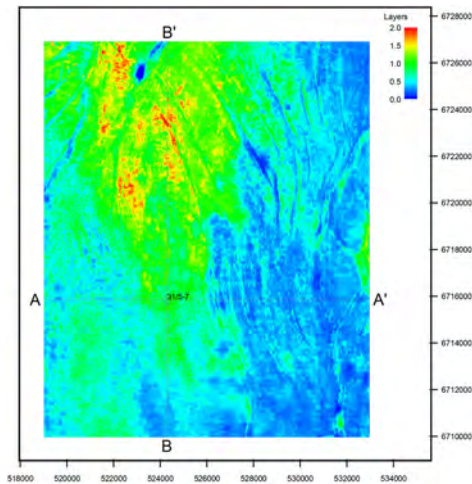


Figure 11: Expected number of layers of Cook sandstone.

6.3 P90, P50, and P10 thickness maps

From the cumulative thickness distributions of the MCMC simulations, we can make low, median, and high thickness estimates of the Cook and Johansen sandstones. Figures 12 and 13 show the P90 (low), P50 (median), and P10 (high) in the inversion area for Johansen and Cook sandstones, respectively. Here P90 means that 90% of the realizations are thicker than the estimate, and P10 means the 10% thickest realizations. Since the distributions are not symmetric around the mean value, the median thickness in Figure 12b) is slightly different from the expected (mean) thickness in Figure 8.

From the thickness maps, we observed that the Cook sandstone is thickest towards north and west in the inversion area with a median thickness of about 30 ms. The thickness of the Johansen sandstone is higher, with peaks at about 80 ms east of the well 31/5-7. It is interesting to observe the NNE to SSW boundary between thicker and thinner sands in Figure 12a).

Future work should focus on investigating the robustness of the inversion with respect to variability in the prior model. The classification into facies that was suggested in Figures 4 and 5 should be refined by more detailed rock physics analysis. Hopefully, it could give a better distinction between the Cook sandstone and the Dunlin shale and improve the classification in the Statfjord formation. Finally, the result of the inversion should be confirmed by the geological interpretation of well 31/5-7.

7. Conclusions

We have inverted the seismic data around the prosed CO₂ injection well 31/5-7 of the Aurora prospect. The inversion was done using the probabilistic inversion

methodology developed at the Norwegian Computing Center. The inversion estimates the probability for Cook and Johansen sandstones encased in the Early Jurassic Dunlin group's shale. MCMC simulations on the inverted result provide estimates of sand thicknesses and expected layering.

The Johansen sandstone is abundant in the inversion area and thickest to the east, with an estimated total thickness above 60 ms. Towards north and west, the sandstone is thinner and seems to split into an upper and lower unit with potentially a thin shale layer in between.

The Cook sandstone is generally much thinner than the Johansen sandstone, and it pinches out towards the east. The estimation of the expected number of layers, that is, the vertical sum of probability of presence may be used to identify the boundary where it pinches out.

The presented methodology defines a functional workflow for quantifying the probability of presence and thickness uncertainty of the reservoir sands. Such results are useful input for future CO₂ injection strategies and migration predictions.

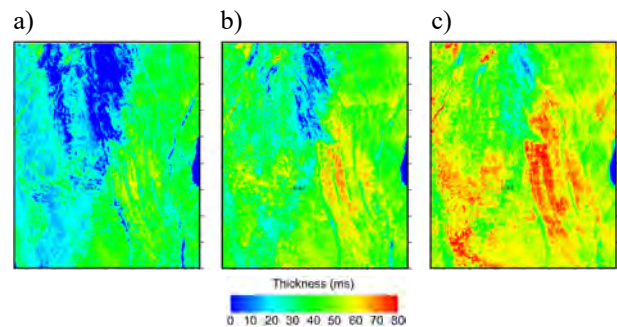


Figure 12: Thickness estimates of Johansen sandstone corresponding to a) P90, b) P50, and c) P10.

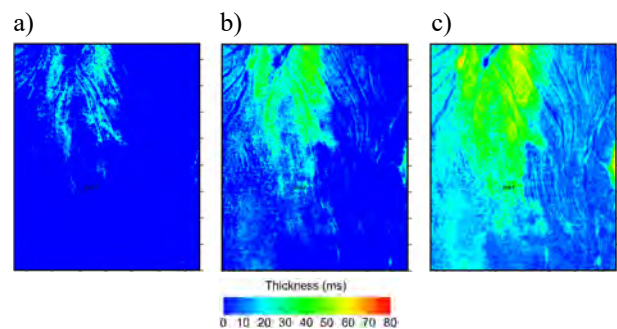


Figure 13: Thickness estimates of Cook sandstone corresponding to a) P90, b) P50, and c) P10.

Acknowledgments

We thank Gassnova for permission to use the seismic data and the Norwegian Petroleum Directorate for providing access to well data through the Norwegian National Data Repository for Petroleum data (DISKOS). We also thank the sponsors of the GIG consortium, AkerBP, ConocoPhillips, Equinor, Lundin, Total, Vår Energi, and Wintershall Dea, for financing the development of the algorithm used in this paper. Finally, we thank D. Barker at the Norwegian Computing Center for assistance when generating thickness histograms and

J. Rahman at UiO for seismic interpretation of the key horizons.

This work has been funded by the Norwegian Computing Center and The Norwegian Research Council through the CLIMIT program, project no. 280472 (OASIS) with financial support from Equinor and Total.

References

- [1] Larsen, A. L., Ulvmoen, M., Omre, H., Buland, A. (2006). Bayesian lithology/fluid prediction and simulation on the basis of a Markov-chain prior model, *Geophysics*, **71**, R69–R78.
- [2] Grana, D., & Rossa, E. D. (2010). Probabilistic petrophysical-properties estimation integrating statistical rock physics with seismic inversion, *Geophysics*, **75**, O21–O37.
- [3] Kemper, M., & Gunning, J. (2014). Joint impedance and facies inversion—Seismic inversion redefined, *First Break*, **32**, 89–95.
- [4] Connolly, P., & Hughes, M. (2016). Stochastic inversion by matching to large numbers of pseudo-wells, *Geophysics*, **81**, M7–M22.
- [5] Nawaz, M.A., & Curtis, A. (2018). Variational Bayesian inversion (VBI) of quasi-localized seismic attributes for the spatial distribution of geological facies, *Geophysics. J. Int.*, **214**, 845–875.
- [6] Kolbjørnsen, O., Buland, A., Hauge, R., Røe, R., Ndingwan, A.O., Aker, E. (2020). Bayesian seismic inversion for stratigraphic horizon, lithology, and fluid prediction, *Geophysics*, **85**, R207-R221.
- [7] Aki, K., & Richards, P.G. (1980). *Quantitative seismology*, W. H. Freeman and Co.
- [8] Krumbein, W.C., & Dacey, M.F. (1969). Markov chains and embedded Markov chains in geology: *Mathematical Geology*, **1**, 79–96.
- [9] Ulvmoen, M., & Omre, H. (2010). Improved resolution in Bayesian lithology/fluid inversion from prestack seismic data and well observations – Part 1: Methodology: *Geophysics*, **75**, R21–R35.
- [10] Ulvmoen, M., Omre, H., Buland, A. (2010). Improved resolution in Bayesian lithology/fluid inversion from prestack seismic data and well observations – Part 2: Real case study: *Geophysics*, **75**, B73–B82.
- [11] Rimstad, K. & Omre, H. (2010). Impact of rock-physics depth trends and Markov random fields on hierarchical Bayesian lithology/fluid prediction: *Geophysics*, **75**, R93–R108.
- [12] Gunning, J. & Sams, M. (2018) Joint facies and rock properties Bayesian amplitude-versus-offset inversion using Markov random fields: *Geophysical Prospecting*, **66**, 904–919.
- [13] Steel, R., Ryseth, A. (1990). The Triassic – Early Jurassic succession in the northern North Sea: megasequence stratigraphy and intra-Triassic tectonics. *Geological Society, London, Special Publications* **55**, 139–168.
- [14] Steel, R.J. (1993). Triassic – Jurassic megasequence stratigraphy in the Northern North Sea: rift to post-rift evolution, in: *Geological Society, London, Petroleum Geology Conference Series. Geological Society of London*, 299–315.
- [15] Stewart, D.J., Schwander, M., Bolle, L. (1995). Jurassic depositional systems of the Horda Platform, Norwegian North Sea: Practical consequences of applying sequence stratigraphic models. *Norwegian Petroleum Society Special Publications*, 291–323.
- [16] Husmo, T., Hamar, G.P., Høiland, O., Johannesen, E.P., Rømuld, A., Spencer, A.M., Titterton, R. (2003). Lower and Middle Jurassic. In: Evans, D., Graham, C., Armour, A., Bathurst, P. (Eds.), *The Millennium Atlas: Petroleum Geology of the Central and Northern North Sea*. The Geological Society, London, UK, 129-155.
- [17] Partington, M.A., Copestake, P., Mitchener, B.C., Underhill, J.R. (1993). Biostratigraphic calibration of genetic stratigraphic sequences in the Jurassic-lowermost Cretaceous (Hettangian to Ryazanian) of the North Sea and adjacent areas. In: Parker, J.R. (Ed.), *Petroleum Geology of Northwest Europe: Proceedings 4th Conference London (1992)*. Geological Society of London, UK, 371-386.
- [18] Vollset, J. & Doré, A. G. (eds.) 1984: A revised Triassic and Jurassic lithostratigraphic nomenclature for the Norwegian North Sea. *NPD-Bulletin No. 3*.
- [19] Norwegian Petroleum Directorate Fact-pages (2021), URL <https://factpages.npd.no/> (accessed 11.01.21).
- [20] Sundal, A., Nystuen, J.P., Dypvik, H., Miri, R., Aagaard, P. (2013). Effects of geological heterogeneity on CO₂ distribution and migration—a case study from the Johansen Formation, Norway. *Energy Procedia* **37**, 5046–5054.
- [21] Buland, A., & Omre, H. (2003). Bayesian linearized AVO inversion, *Geophysics*, **68**, 185–198.
- [22] Sundal, A., Nystuen, J.P., Rørvik, K-L., Dypvik, H., Aagaard, P. (2016). The Lower Jurassic Johansen Formation, northern North Sea – Depositional model and reservoir characterization for CO₂ storage, *Marine and Petrol. Geol.* **77**, 1376-1401.

ANALYSIS OF SURFACE MOVEMENT THROUGH CONCEPTUAL AND COUPLED FLOW-GEOMECHANICS MODELS AN EXAMPLE OF SURFACE MONITORING ASSESSMENT FOR CCS PROJECT

**Sarah Bouquet^{1*}, Jeremy Frey¹, Iryna Malinouskaya¹, Antoine Soulat¹, Audrey Estublier¹, André Fournio¹,
SENSE Consortium**

¹ IFP Energies Nouvelles, 1 et 4 avenue de Bois-Préau, 92852 Rueil-Malmaison, France

* Corresponding author e-mail: sarah.bouquet@ifpen.fr

Abstract

Monitoring of geological CO₂ storage sites is crucial for the widespread deployment of this technology to be accepted as a reliable method of reducing CO₂ emissions worldwide. The SENSE project aims to develop reliable, continuous and cost-effective monitoring based on ground motion detection combined with modelling and geomechanical inversion, using new technological developments, data processing optimization and interpretation algorithms. In this context, we present a methodology based on coupled flow/geomechanical simulations which, from the uncertainty on the subsurface properties and uncertainties on the measurements, can reproduce the measurements from different surface monitoring tools. By carrying out an uncertainty study on simulations results and taking into account the advantages and disadvantages of each of these tools, a monitoring strategy can be designed such that the tools will record potential displacements at the most sensitive periods and locations, taking into account their respective accuracies. If surface displacements are measurable and sufficiently sensitive to subsurface properties then this kind of monitoring will help to better constrain subsurface properties and possibly subsurface behavior such as plume migration, pressure propagation, and storage capacity. This methodology is applied to conceptual models in order to identify which conditions induce different surface displacements and thus may require specific surface monitoring strategy.

Keywords: *Surface displacement – Coupled flow-geomechanical simulation – CO₂ storage integrity – Cost-effective monitoring – conceptual models – subsurface uncertainties*

1. Introduction

For carbon dioxide capture and storage (CCS) to have a significant impact on climate objectives, significant quantities of CO₂, on the order of several gigatonnes per year, must be captured and stored. This means that the volume and number of injection sites must be rapidly increased, from today's isolated demonstrations pilots to large-scale storage sites. Monitoring of CO₂ geological storage sites is crucial to gain acceptance of the process as a reliable method of reducing CO₂ emissions, as well as to verify the behavior of the sites and to enable the closure of the storage sites in the long term. The SENSE project aims to develop reliable and cost-effective monitoring based on the combination of ground motion measurements with geomechanical modelling and inversion. The objective of this project is to demonstrate how surface displacements can be used in a monitoring program aimed at verifying the long-term integrity of a CO₂ geological storage site.

From numerical simulations of CO₂ injection for synthetic case studies, the objectives of this paper are :

- To identify whether surface displacements are likely to be "visible" by monitoring tools and for which resolution
- To identify which conditions impact surface displacements,
- Analyze the usefulness of various surface monitoring techniques (based on satellites, tiltmeters, GPS, etc.) and their ability to provide concrete information on subsurface behavior.

To achieve these objectives, numerical models coupling flow and geomechanics are developed for different key scenarios. For each specific surface displacement, the potential for surface monitoring in time and space can be evaluated.

For the identification of conditions inducing variations in surface displacements, we rely on the definition of different scenarios, representative of real potential storage sites. Thus, for each of these scenarios, a statistical analysis of the system responses is performed as a function of the a priori uncertain subsurface properties. If differences in observed surface displacements can be related to some model parameters (e.g. subsurface properties), then the measured surface displacements could help to characterize such subsurface properties.

2. Methods

2.1 Definition of conceptual models

Different structural models can be considered as potential structures for CO₂ storage. Here, an anticlinal structure without faults is modeled.

Several scenarios are considered to represent different types of sedimentary formations and therefore corresponding to different subsurface properties. These scenarios are defined to generate realistic intervals of

uncertainty of the properties. This paper deals with a "carbonate" scenario based on data from the Brindisi carbonate formations [1] and those of the Michigan Basin (MRCSP Michigan Basin, [2]).

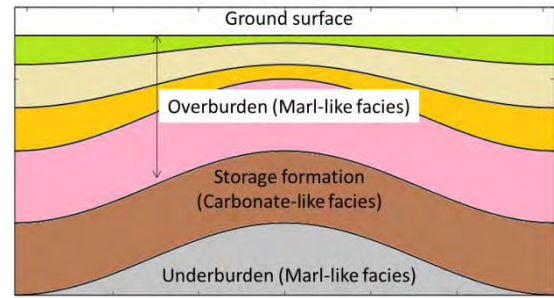


Figure 1 : Schematic representation of the geology of the "Carbonate", anticline model

Other scenarios based on sandstone formations data have also been defined but are beyond the scope of this paper.

Pressure and temperature conditions, salinity, storage depth and thickness, petrophysical properties, mechanical properties of the storage formation and of the overlying and underlying formations are defined from the collected data. Of these properties, nine are considered critical and uncertain in these scenarios. These include the porosity, permeability, Young's modulus and Poisson's ratio properties of the storage formation and overburden (caprock), as well as the capillary CO₂ entry pressure of the caprock. These uncertain parameters are defined through uncertainty intervals determined from the collected information. The a priori distribution of the parameter values corresponds to a uniform law on the defined uncertainty interval. Table 1 gives the range of values for those uncertain parameters for the "Carbonate" case.

Table 1: Uncertain parameters and related ranges of values for the "Carbonate" case.

Variables	Minimum	Maximum
Carbonate Porosity [-] (Φ)	0.15	0.25
Carbonate Permeability [mD] (K)	15	150
Carbonate Young Modulus [bar] (E)	250000	450000
Carbonate Poisson coefficient [-] (η)	0.15	0.25
Marl Porosity [-]	0.05	0.4
Marl Permeability [mD]	2e-3	6.e-2
Marl Entry Capillary Pressure [bar]	5	60
Marl Young Modulus [bar]	60000	550000
Marl Poisson coefficient [-]	0.15	0.35

2.1 Definition of surface monitoring tools and related limitations

Among the tools proposed for surface monitoring, two kind of tools are considered. For local measurements, and allowing fine temporal sampling, tools such as tiltmeters, GNSS, i.e. Geolocation and Navigation by Satellite System can be used. For covering large areas

but with a more limited resolution in displacement and time, scanning systems like InSAR can be used [3,4]. InSAR data can provide, after processing, displacement maps covering at least the entire storage area, at low cost and with low hardware constraints. However, the usefulness of these data may be limited by their spatial and temporal resolution, the duration of data processing and their sensitivity to land cover (e.g. vegetation). Typical limitation of displacement detection by InSAR will be 1 mm/yr. This may be improved with corner-reflectors installation in the area of interest.

Point measurements from tiltmeters provide spatially and temporally accurate but local, expensive information, with measurement accuracy (e.g. 5 to 50 nanorads) which can be affected by weather conditions and necessarily require the installation of surface tools. From the uncertainty on the subsurface properties and the uncertainties on the measurements, predictive models (coupled flow-geomechanics simulations) can reproduce the expected measurements obtained with the different tools. By carrying out a sensitivity study and taking into account the advantages and disadvantages of each of those tools (including their respective accuracies), a design can be defined such that the tools will record potential displacements at the most sensitive periods and locations.

2.2 Coupled flow-geomechanics simulations

A coupled hydro-mechanical calculation was applied for estimating mechanical deformations during and after the injection process. It is based on a sequential coupling between the IFPEN Puma reservoir simulator [1], and the finite element code Code_Aster [2]. The simulation is divided into temporal sequences called "periods". Pressure results from the reservoir simulation are imposed as loading to Code_Aster in order to compute the corresponding displacements field. It should be noted that the flow and mechanical equations are solved independently and the mechanical behaviour is limited to linear elasticity.

A "one-way" coupling scheme was used as described on Figure 3.

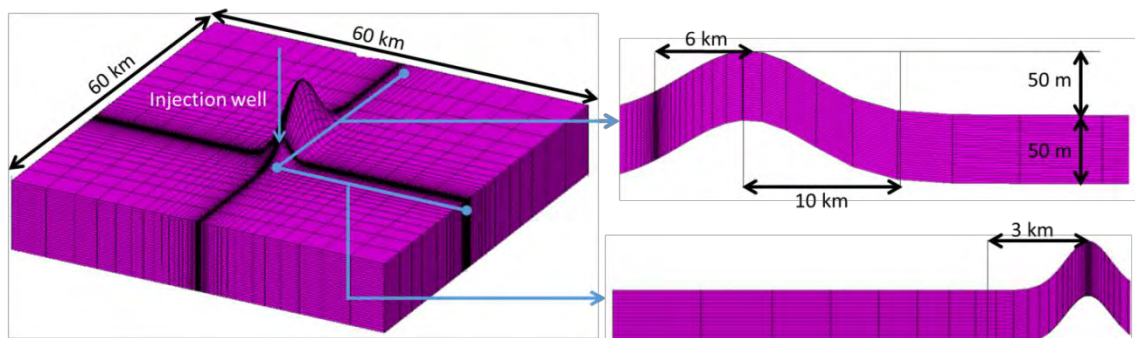


Figure 3: 3D model of the anticline structure and injection zone. Only storage formation (50 m thickness) is represented here. The coupled simulations are performed with 3D model from the surface to few meters of underburden (below the storage formation).

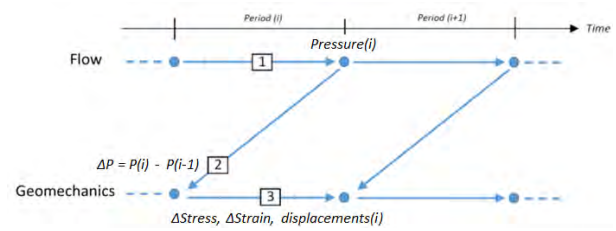


Figure 2: Schematic representation of the "one-way" coupling between flow and geomechanics simulations.

2.3 Statistical analysis methodology

The statistical analysis includes a sensitivity analysis and an uncertainty analysis on surface displacements. Uncertainty analysis consists of evaluating the uncertainty in the predictions of displacements given the a priori distribution of uncertain parameters (e.g. statistics of surface displacement maps). Sensitivity analysis is used to quantify the influence of model parameters on the model-simulated outputs of interest (e.g. Sobol index [5]). These analyses require a large sampling of combinations of parameters and outputs, too costly in computational time to be carried out from coupled flow/geomechanical simulations only.

The strategy used here consists first of defining the uncertain parameters and their uncertainty intervals (as described in paragraph 2.1.). Then a design of m experiments for the coupled simulation is built. This will be used as a learning sample for surrogate models. Surrogate models (or metamodels) are mathematical approximations of the responses of interest in studied parameters space, built based on simulated data [6].

3. Results

A single injector well is modeled, injecting CO₂ on the flank of the anticline, so as to facilitate the dissolution of CO₂ in the water during its migration to the top of the fold. CO₂ injection is controlled by a maximum pressure increase of 50 bar at the bottom of the well. The maximum injection rate is 1,500,000 m³/day under surface conditions, or approximately 2800 t/day.

The extension of the model is about 60×60 km. The anticlinal structure is located in the center of the grid, the well is 6 km from the top of the fold (figure 2). The injection site is "onshore", the top of the storage formation is at a depth of about 1600 m, its thickness is 50 m. The pressure and temperature conditions are 160

bar and 40°C, respectively. The salinity of the aquifer is 35,000 mg/L.

From the uncertainty intervals on the 9 parameters of interest (defined in Table 1), an LHS (Latin Hypercube Sampling, [7]) design of 115 simulations was built.

3.1 Storage capacity results

The storage capacity results for these 115 models, with the injection constraints described above, are shown in Figure 4; the evolution of the well pressure is shown in Figure 5. The differences in terms of injected volume (and therefore storage capacity) are mainly due to variations in formation properties from one case to another, knowing that the injected volume is constrained by a maximum bottom-hole pressure. According to the sensitivity study (with uncertain parameters as defined in Table 1), variations in the injected volume depend mainly on the permeability of the storage formation.

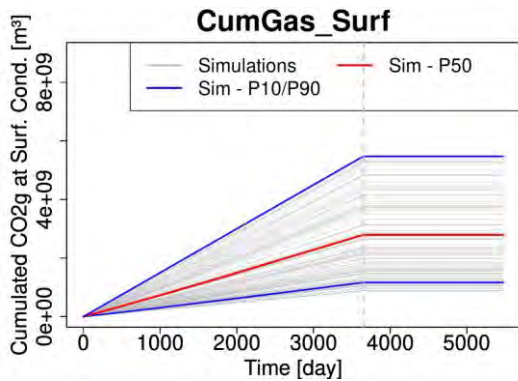


Figure 4: Cumulative volume of injected gas for each of the 115 simulations (in gray). In blue and red, the percentiles computed from these 115 simulations

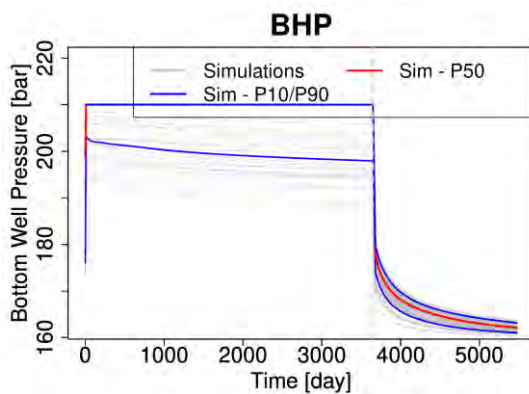


Figure 5: Bottom-Hole Pressure for each of the 115 simulations (in gray). In blue and red, the percentiles computed from these 115 simulations

3.2 Example of results from a given realization

The observation of results obtained from a particular example allows a better understanding of the physical mechanisms at work and links migration of the injected CO₂, pressure evolution in subsurface (Figure 6 and Figure 7), and the resulting surface displacement (Figure 8 - from the definition of our coupling, the surface displacement comes directly from the pressure variation observed in-situ).

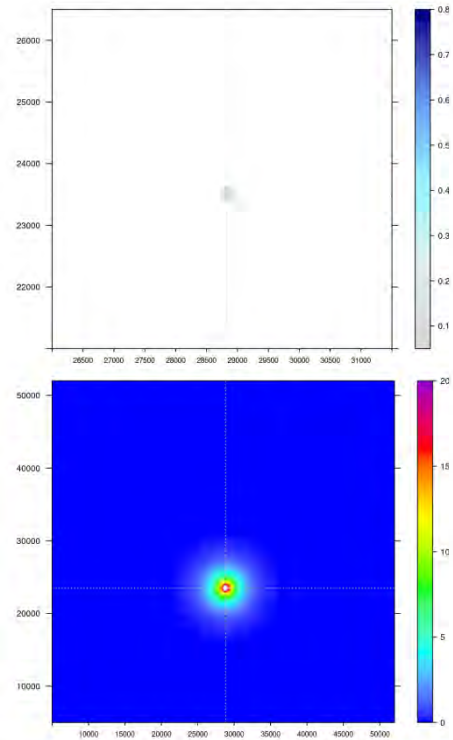


Figure 6: After 1 year of injection, (top) gas saturation at the and (bottom) pressure perturbations (i.e difference of pressure between the initial and current state, in bar) at the top of the storage formation for one realization. Spatial scales are different between gas saturation and pressure perturbations.

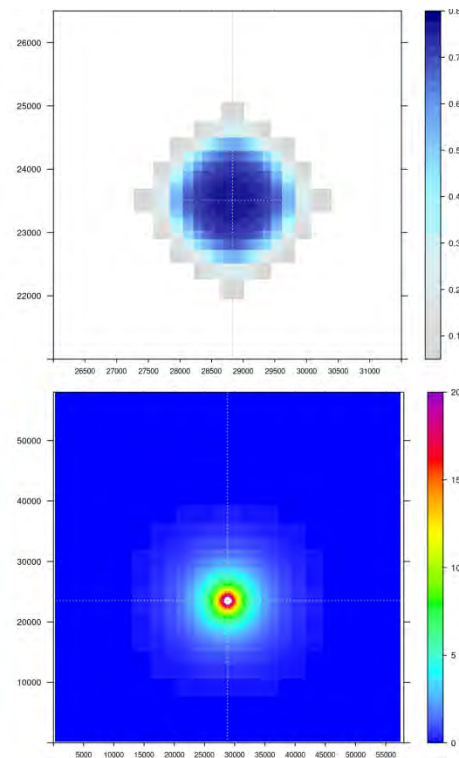


Figure 7: After 10 years of injection, (top) gas saturation and (bottom) pressure perturbations (i.e difference of pressure between the initial and current state, in bar) at the top of the storage formation for one realization. Spatial scales are different between gas saturation and pressure perturbations.

Thus, the largest pressure increases are located in the near-well, as are the highest vertical displacements at the surface. Furthermore, the shape and extent of the displacement also provides information on the properties of the deposit (here, its circular and uniform appearance reflects a low-slope structure made up of homogeneous materials). It should be noted that the propagation front of the pressure perturbation moves further than the saturation front at a given time.

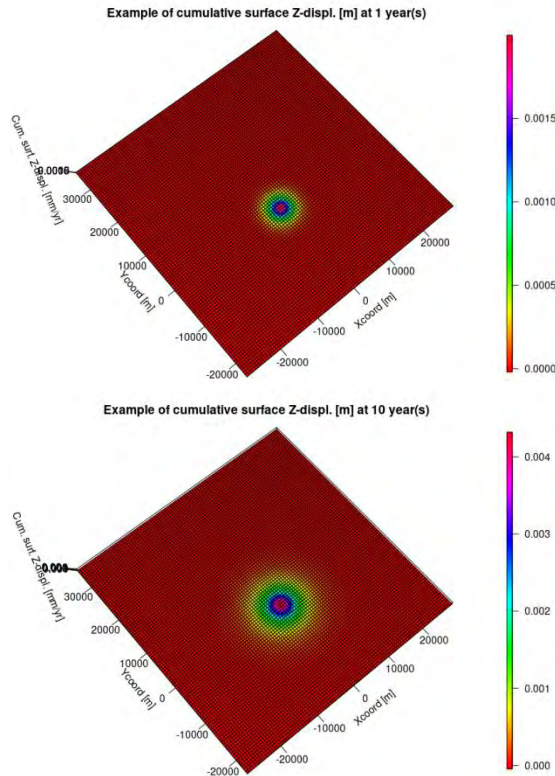


Figure 8: Maps of vertical displacements observed at the surface, cumulated (units in meters) (top) after 1 year of injection (bottom) after 10 years of injection for one realization.

3.3 Velocity of Displacement results and InSAR data

The surface displacements are analyzed here in terms of displacement velocities (mm/year) within the framework of InSAR measurements. The limit of detection of displacement velocities using InSAR methods is considered to be 1 mm/year, with +/- 1 mm/year accuracy.

Figure 9 and Figure 10 show statistical maps of surface displacement velocities after about half a year, and after 5 years of CO₂ injection respectively. If the displacement velocities are easily detectable at least until half a year of injection (minimum and maximum are above the detection limit), they are no longer detectable after 5 years with velocities below the InSAR detection threshold.

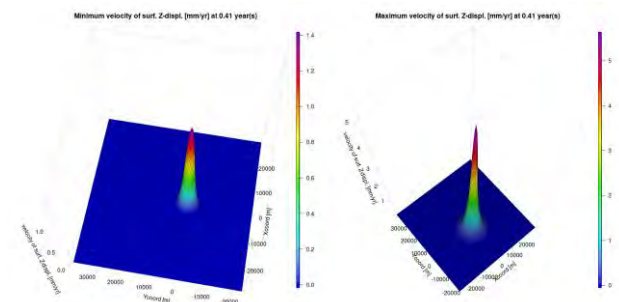


Figure 9: Minimum (left) and maximum (right) surface displacement velocities after about half a year of injection, based on 115 simulations.

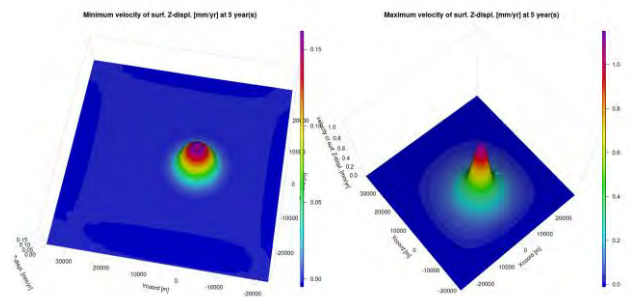


Figure 10: Minimum (left) and maximum (right) surface displacement velocities after five years of injection, based on 115 simulations.

For all simulations, the fastest vertical displacements velocities at the surface occur near the well. From the results of vertical displacements velocities over the well (Figure 11), one can distinguish the limits of the InSAR tool over time for this scenario. In the short term and up to about 2 years of injection, the InSAR data will detect displacements velocities. Beyond and until the end of the injection, the displacements velocities will not be measurable by InSAR anymore. On the other hand, post-injection displacements velocities could be detected by InSAR (see results post-injection, after 10 years in Figure 11).

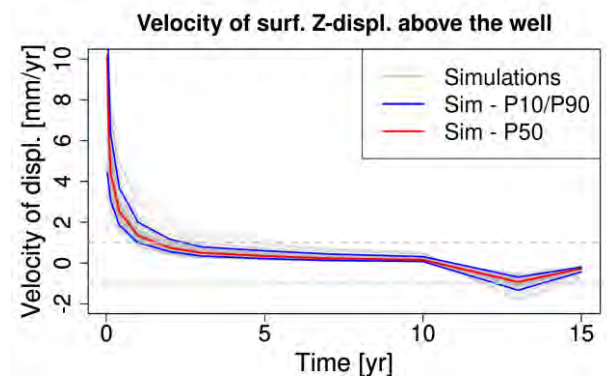


Figure 11: Simulations results of surface displacement velocities above the well function of time. In red, the median, in blue P10 and P90 percentiles of the 115 simulations (in grey).

Moreover, as results are X-symmetrical, one can simply analyze the results along the Y-axis. The statistical analysis performed on the metamodels from the 115 simulations (Figure 12) confirms that most of the

displacements occur at the beginning of the injection: from the start of injection to about 2 years of injection (in more than 50% of the cases the displacements will not even be detectable at the wells after 2 years of injection). From the two-year injection period onwards, displacements velocities are no longer detectable via InSAR (less than 1 mm/year). It is also noted that these detectable displacements velocities will only be detectable over distances of less than 5 km around the well (in 90% of the cases at about half a year of injection), and given the limit of precision, the constraint brought by these data will be limited since the standard deviation is lower than the precision of the tool. InSAR measurements would only be of interest here if a high precision (1 mm/year) is required, over short periods (at the beginning of injection), and over a limited area around the well.

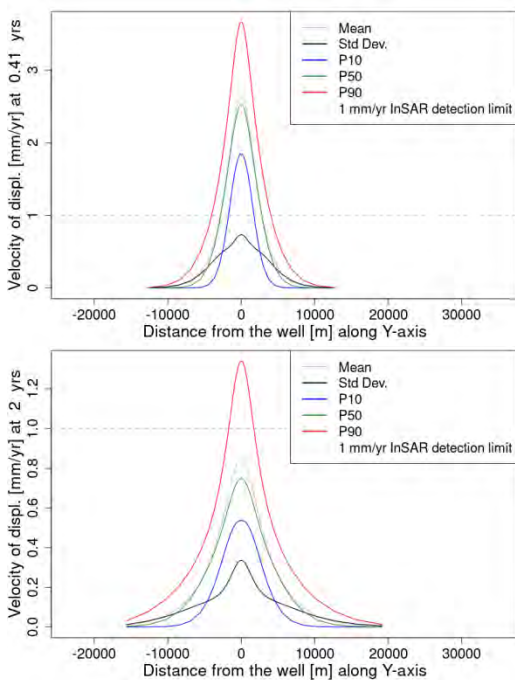


Figure 12: Uncertainties on the surface displacement velocities for the model studied (mean, standard deviation, median, quantiles 10% and 90%) related to the uncertainties on the subsurface properties. Statistical calculations performed from a Monte-Carlo sampling on metamodels built from the training sample. The detection threshold of the measurement is estimated at 1 mm/year. Beyond the two-year injection period, most of displacements are no longer detectable via InSAR.

The Shannon entropy [8, 9] calculation is carried out by classifying the displacements velocities values into five categories, in particular :

- Values below the detection threshold, i.e. of -1 to 1mm/year;
- Values from 1 to 3 mm/year, which, given the accuracy of the tool, globally represents a single type of measured value;
- Values from -1 to -3 mm/year;
- Values above 3 mm/year;
- Values under -3 mm/year.

The results obtained after one year of injection (Figure 13) make it possible to distinguish the zones of uncertainty where InSAR measurements could be useful.

The entropy is zero when the probability of obtaining a category of measurements is 1, i.e. when whatever the model parameters, the same category of measurement will always be obtained. For example, at one year of injection, there is a zero probability of obtaining displacements velocities above the detection threshold beyond 4 km distance from the well. Thus, there is no need to process InSAR measurements beyond 4 km from the well.

Entropy also drops when the probability of having a measurement between 1-3 mm/year is high, i.e. it becomes unlikely to obtain values outside this interval. The areas with high uncertainties, where the measurements could be most informative, correspond to the highest entropies (here, greater than 0.5).

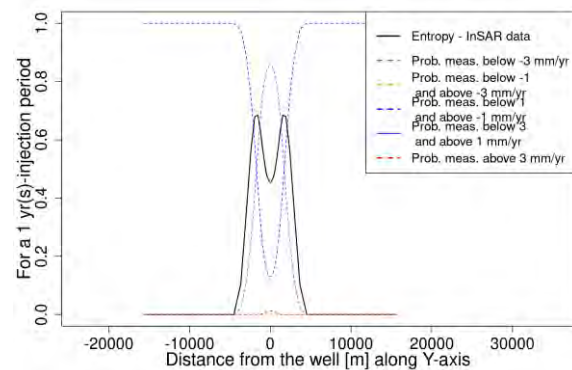


Figure 13: Shannon entropy for five categories of InSAR surface displacement velocity measurements after one year of injection. The measurement error is estimated at +/- 1mm/year.

Finally, here, surface monitoring by InSAR would be restricted to the short term at the beginning of injection or post-injection (e.g. one to two years after the start of injection) and over a 4 by 4 km zone around the well for this scenario. Given the small variations, it will be necessary to ensure the accuracy of the tool and to consider placing reflectors (which will improve the accuracy) in the areas of high uncertainties.

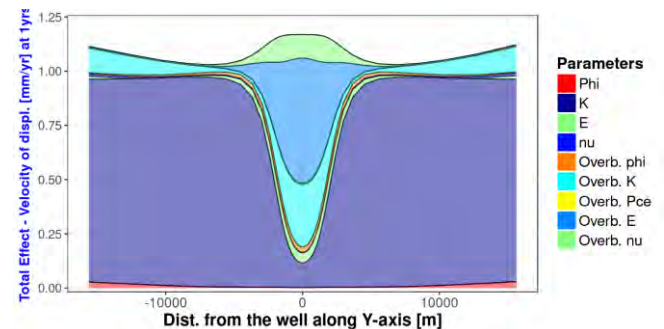


Figure 14: Total Sobol Indices calculated between uncertain parameters and surface displacements velocities variations after one year of injection.

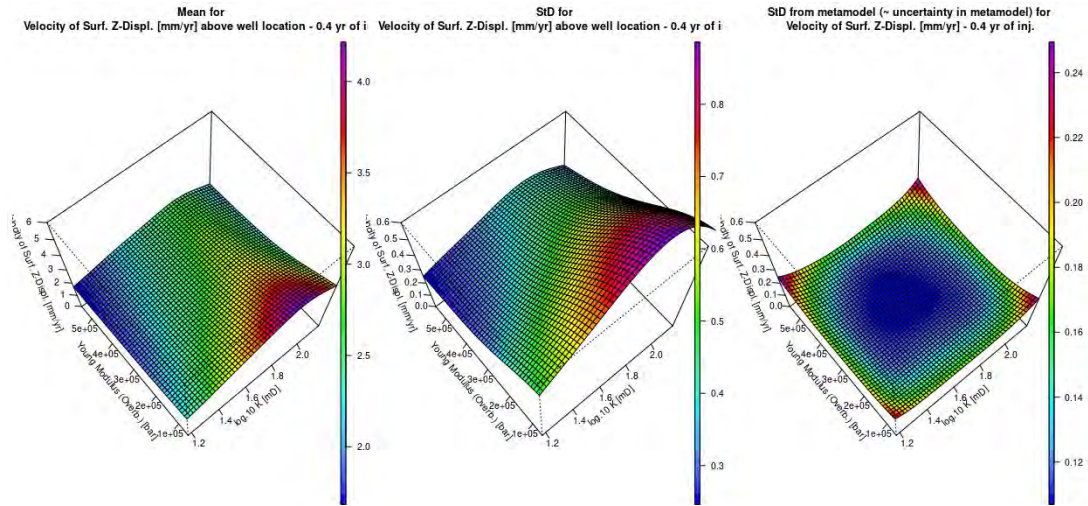


Figure 15: From metamodel: velocity of displacement above the well as a function of the Young's modulus value of the cover and the permeability of the storage formation, averaged with respect to the variations induced by the other parameters (left), the standard deviation associated with the variation of the other parameters (middle) and the uncertainty associated with the metamodel (right) used to evaluate these projections.

The results of the sensitivity analysis performed on the displacement velocities with respect to the model parameters (Figure 14) suggest a spatial and temporal variation of this sensitivity with a high sensitivity to the permeability value of the storage formation over the entire model and a significant sensitivity to the overburden parameters (mostly Young's modulus) near the well. Notice that the prior interval of the caprock Young's modulus is far larger than the one from the storage formation (6-55 GPa vs. 25-45 GPa). This would partly explain why the response is more sensitive to the caprock Young modulus variations than the one from the storage formation. This also reflects the highest uncertainty that we often have in overburden properties compared to storage formation properties.

Thus, precise near-well displacement measurements would contribute over time to constrain mainly the model values of permeability and Young's modulus in the cap rock.

If we project the predictions of vertical displacement velocities over the well as a function of these two parameters, we see that this measurement could significantly constrain the values of this pair of parameters at short-term (Figure 15). Most of the variations would be explained by these two parameters (between 2 and 4 mm/year) while the other parameters induce an average variation of an order of magnitude lower (between 0.3 and 0.8 mm/year).

3.4 Tilts variations and tiltmeters relevancy

Tiltmeter measurements are estimated by transforming the results into simulation displacements. Tilts are expressed in nanorad.

Due to its higher accuracy, the tiltmeter is both more sensitive in time and space to surface displacements induced by CO₂ injection, compared to InSAR data.

We obtain tilts variations of the order of a hundred nanorads at 1 year and of the order of ten nanorads at 5 years over distances of a few kilometers around the well (Figure 16). Consequently, if the precision of the

tiltmeters is ensured at a minimum at about 10 nanorads, tiltmeters located few kilometers from the well would make it possible to follow the injection of CO₂ over time.

It is noted that near the well the tilts are null because the displacement is mostly vertical (no dip), so the tiltmeters should preferably be placed where vertical and horizontal displacements are expected.

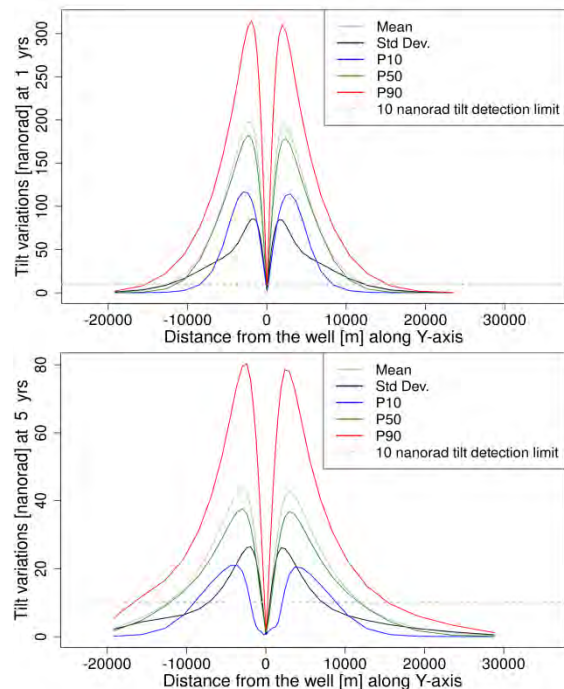


Figure 16: Uncertainties on the tilts measurements for the model studied (mean, standard deviation, median, quantiles 10% and 90%) relative to the uncertainties on the subsurface properties. Statistical calculations performed from a Monte-Carlo sampling on the metamodels built from the training sample. The detection threshold of the measurement is assumed at 10 nanorads.

For tiltmeters, the aim is to define a number of locations that would be informative, *i.e.* above the threshold of

accuracy over time, and that would reduce the uncertainty in the model.

According to the entropy calculation (Figure 17), based on the definition of categories by precision limit, the uncertainties on the measurement of tilts are high on both sides of the well: between 800 and 2.5 km at one year and between 1 and 3 km at 5 years.

Considering the small variations in tilts away from the well with time, it would be recommended to place tiltmeter(s) about 1.5 km from the well for short- and long-term monitoring.

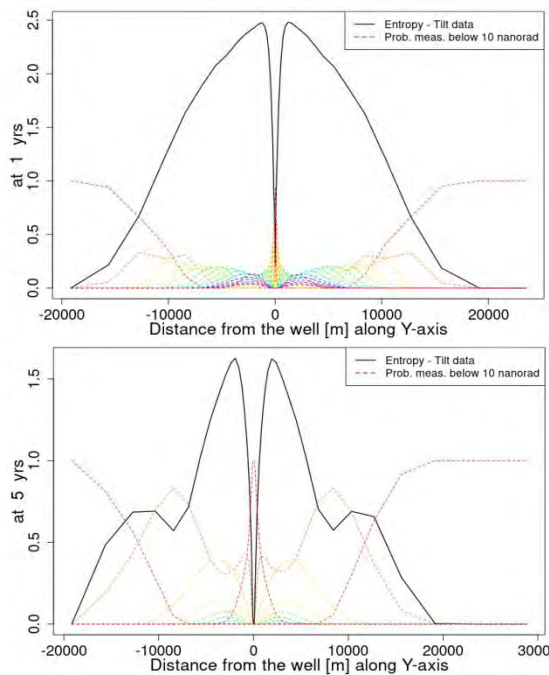


Figure 17: Shannon entropy for categorical tiltmeter data : the measurement error is assumed at +/- 10 nanorad, categories are defined from 10 nanorads up to 300 nanorads with an interval of 20 nanorads.

4. Conclusions

A methodology is proposed to define if these tools are relevant for CCS monitoring in specific conditions. This approach is based on coupled flow/geomechanical simulations reproduce the measurements from surface monitoring tools while taking into account the uncertainties on the subsurface properties. This is performed by carrying out an uncertainty study on simulations results and taking into account the advantages and disadvantages of each of those tools. Finally, a design can be defined such that the tools will record potential displacements at the most sensitive periods and locations, taking into account their respective accuracies. Measurable surface displacements could help to better constrain subsurface properties and behaviors such as plume migration, pressure propagation, and longer-term storage capacity. This methodology is applied here to a specific conceptual model but will be applied to other representative conceptual models (in particular models with fault zones) as well as models derived from actual storage sites in order to identify which conditions induce different surface displacements and thus may

require specific surface monitoring strategy. An iterative coupling scheme would be considered for real cases to improve the accuracy of surface displacement estimation via simulations.

Acknowledgements

SENSE (Assuring integrity of CO₂ storage sites through ground surface monitoring) project No. 299664, has been subsidized through ACT (EC Project no. 691712) by Gassnova, Norway, United Kingdom Department for Business, Energy and Industrial Strategy, Forschungszentrum Jülich GMBH, Projektträger Jülich, Germany, The French Agency for the Environment and Energy Management, The United States Department of Energy and State Research Agency, Spain.

References

- [1] Baroni, A., Estublier, A., Vincké, O., Delprat-Jannaud, F., Nauroy, J-F., (2015). Dynamic Fluid Flow and Geomechanical Coupling to Assess the CO₂ Storage Integrity in Faulted Structures. *Oil & Gas Science and Technology* - 70 (4), pp.729-751.
- [2] Michael, K., Golab, A., Shulakova, V., Ennis-King, J., Allinson, G., Sharma, S., Aiken, T (2010). Geological storage of CO₂ in saline aquifers-A review of the experience from existing storage operations, *International Journal of Greenhouse Gas Control*, 4 (4), pp. 659-667. doi: 10.1016/j.ijggc.2009.12.011
- [3] McColpin, G. (2009). Surface Deformation Monitoring As a Cost Effective MMV Method. *Energy Procedia* 1(1):2079-2086. DOI: 10.1016/j.egypro.2009.01.271
- [4] Vasco, D., Ferretti, A., Rucci, A., Samsonov, S., & White, D. (2019). Monitoring the Deformation Associated with the Geological Storage of CO₂. In T. Davis, M. Landrø, & M. Wilson (Eds.), *Geophysics and Geosequestration* (pp. 93-114). Cambridge University Press. DOI 10.1017/9781316480724.007
- [5] Sobol, I.M, (1993). Sensitivity analysis for non-linear mathematical models, *Mathematical modelling and computational experiment* (translated from Russian: I.M. Sobol', sensitivity estimates for nonlinear mathematical models. *Matematicheskoe Modelirovanie* 2 (1990), 112–118 407–414).
- [6] Feraille, M., Marrel, A. (2012). Prediction under Uncertainty on a Mature Field. *Oil & Gas Science and Technology – Rev. IFP Energies Nouvelles*, Vol 67, No. 2, pp. 193-206. DOI: <https://doi.org/10.2516/ogst/2011172>
- [7] McKay, M.D., Beckman, R., Conover, W. (1979). A Comparison of Three Methods for Selecting Values of Input Variables in the Analysis of Output from a Computer Code. In *Technometrics*, Vol. 21, No. 2, pp. 239-245. <https://doi.org/10.1080/00401706.1979.10489755>
- [8] Leibovici D.G. (2009) Defining Spatial Entropy from Multivariate Distributions of Co-occurrences. In: Hornsby K.S., Claramunt C., Denis M., Ligozat G. (eds) *Spatial Information Theory. COSIT 2009. Lecture Notes in Computer Science*, vol 5756. Springer, Berlin, Heidelberg. https://doi.org/10.1007/978-3-642-03832-7_24
- [9] Schweizer, D., Blum, P., Butscher, C. (2017). Data assimilation and uncertainty assessment in 3D geological modeling. *Solid Earth Discussions*, 1-23.

EVALUATION OF RESULTS FROM SDR CAMPAIGNS AND PILOT DATA

Solrun Johanne Vevelstad^{*}, Andreas Grimstvedt, Geir Haugen, Merete Wiig and Kai Vernstad

SINTEF, Trondheim, Norway

* Solrun.J.Vevelstad@sintef.no

Abstract

For ethanolamine (MEA) many degradation products have been identified and quantified, and the formation of these compounds at different process conditions should be verified. This short paper shows that lab scale experiments, especially cycled degradation rigs, are capable of mimicking formation of the major degradation compounds found in larger pilot campaigns. A larger build-up of HEEDA in the cycled degradation experiment, compared to pilot samples, was observed. Observations like this could play a role to understand why deviations between lab scale and pilot plant or pilot plants occurs.

Keywords: CO₂ capture, amine solvents, degradation products, comparison lab and pilot data

1. Introduction

In post-combustion CO₂ capture with chemical absorbents, the absorbent chemically binds to the CO₂ and then it is cycled to the desorber where the reaction is reversed. In addition to the main reaction, other unwanted reactions also take place leading to products that often are called degradation compounds. Formation of these compounds are not necessarily reversible, and their formation could lead to operational problems as foaming, fouling and corrosion. Furthermore, the formation of these compounds reduces the CO₂ capacity of the solvent and may also produce compounds that are of environmental or health concern. Studying the chemical stability of the solvent at various process conditions is therefore a necessity in screening programs for new solvents [1]. Low chemical stability, formation of volatile compounds that could have an HSE impact are risks that need to be evaluated for different solvent systems. Further, chemical stability also includes evaluation of a solvent corrosivity since they are closely related, and these properties are potential showstoppers for a given solvent technology. However, there are several existing and future mitigation technologies to for example reduce emission levels and improve chemical stability.

Ethanolamine (MEA) is the most studied amine when it comes to identification and quantification of degradation compounds. This involve advanced analytical techniques which are not available on site [2]. Mechanisms of several of the major degradation compounds for MEA have been suggested and a summary of this could be found by Gouedard [3]. For some of the degradation compounds several pathways have been suggested and it is likely that more than one reaction can take place in the capture plant. Due to variation in operational conditions in a plant, as well as differences related to flue gas impurities and other additives or mitigation technologies introduced, comparison is never easy.

Amines in the CO₂ capture process reacts to other amines (non-volatile or volatile, polyamine, alkylamine), ammonia, aldehydes, acids (organic and inorganic, as well as amino acids), ring structures (oxazolidinone, oxazoline, piperazinone, imidazole, pyrazine, pyridine), nitramines, nitrosamine (formed from secondary amine), amide. Even if many degradation compounds are formed, several of them are only present in amounts lower than 100 mg/kg. The parent amine molecular structure is a requirement to predict which compounds are formed and to evaluate if actions must be taken for mitigation regarding safe working conditions and emissions. Various analytical instruments are required to fully map the degradation products, since no single instrument can detect all the compounds. An overview of different analytical techniques used for different compounds could be found in Cuccia et al. [4] while exploration of degradation chemistry using advanced chemical analysis is described by Grimstvedt et al. [2].

The aim of this work is to share light on several of the major and important degradation compounds formed in MEA solvent and how different process conditions influence them. Here this is based on observations from bench scale experiments mimicking the capture process (solvent degradation rig - SDR) and available pilot data e.g., from Technology Centre Mongstad (TCM).

2. Experimental set-up

SINTEF's solvent degradation rig (SDR) is an advanced laboratory test rig for studies of solvent degradation at process conditions. The total solvent inventory is about 5 liters. The solvent is cycling in a combined absorber and desorber setup where the temperature of the absorber and desorber is set at different levels (absorber: 25 - 80°C, desorber: 110-150 °C). The flue gas is a synthetic mixture of different gases (e.g., N₂, CO₂, O₂, NO_x, SO_x) where the composition could be varied. Compared with separate setups for oxidative or thermal degradation, the SDR enables studies of the combined effect of different

degradation mechanisms occurring in a real-life process. More details around the rig are given by Einbu et. al 2012 [5]. Three different MEA campaigns have been conducted, and the duration and conditions have varied for all of them as shown in Figure 1. The factors that have been varied are the oxygen concentration (12 or 18 vol%), reboiler temperature (120 or 140 °C) and NOx concentration (5 or 50 ppmv for campaign in 2012 and 2016 and 10 or 100 ppmv in 2020) [5, 6]. For the last campaign (2020) the MEA concentration was increased to 40wt% (30wt% used in the earlier campaigns) and absorber sump stripping using N₂ was also tried for two periods (week 5 and week 8). The impact of NOx is mostly related to possible nitrosamine formation.

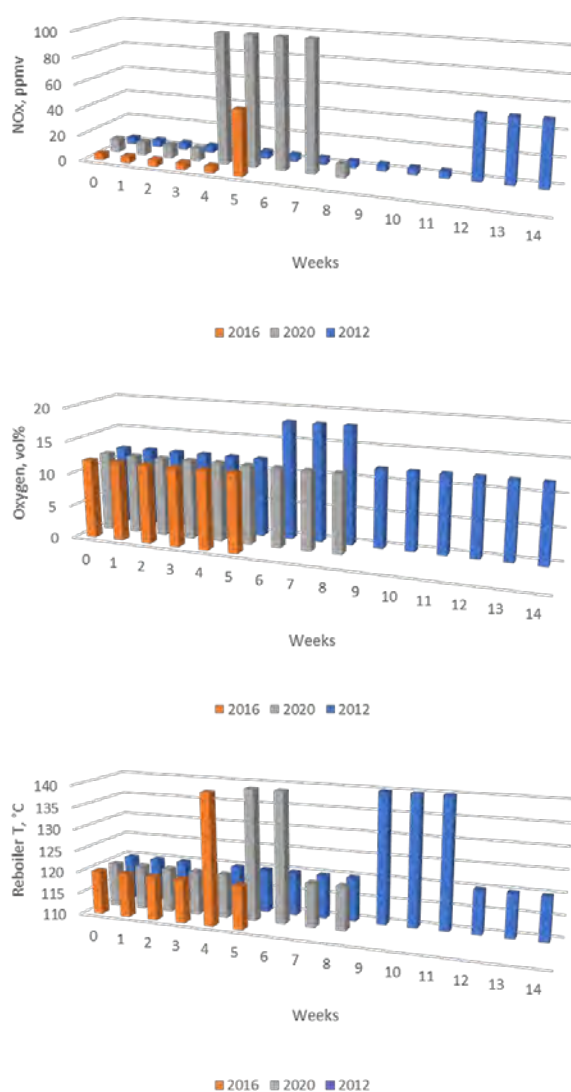


Figure 1: NOx (ppmv), reboiler temperature (°C) and oxygen (vol%) variations for the different campaigns.

LC-MS (Liquid Chromatography – Mass Spectrometry) is our preferred method for analyses of degradation compounds. Analysis of the degraded samples were carried out on a LC-MS/MS system, a 6490 triple quadrupole mass spectrometer that is coupled with a

1290 Infinity LC chromatograph and an Infinity autosampler 1290 Series G4226A from the supplier Agilent Technologies. The analytical column for degradation compounds described in Figure 3 was Discovery® HS F5 HPLC Column from Sigma-Aldrich.

General abbreviations and short name for chemical compounds used are given in Table 1.

Table 1: Abbreviations and short name for chemical compounds.

Abb		CAS
CO ₂	Carbon dioxide	124-38-9
O ₂	Oxygen	7782-44-7
N ₂	Nitrogen	7727-37-9
NO _x	Nitrogen oxide	
SO _x	Sulfur oxide	
MEA	Ethanolamine	141-43-5
FeSO ₄ *7H ₂ O	Ferrous sulfate heptahydrate	7782-63-0
HEA	N-(2-hydroxyethyl)-acetamide	142-26-7
HEF	N-(2-hydroxyethyl)-formamide	693-06-1
HEGly	N-(2-hydroxyethyl)-glycine	5835-28-9
HEI	1H-imidazole-1-ethanol	1615-14-1
HEPO	4-(2-hydroxyethyl)-2-piperazinone	23936-04-1
OZD	2-oxazolidinone	497-25-6
HEEDA	2-[(2-aminoethyl)amino]-ethanol	111-41-1
HEHEAA	N-(2-hydroxyethyl)-2-[(2-hydroxyethyl)amino]-acetamide	144236-39-5
MEA-urea	N,N'-bis(2-hydroxyethyl)-urea	15438-70-7

3. Results

3.1 Principal component analysis for bench scale degradation experiments and pilot data

Chemical stability of the different solvents has been studied under various process conditions mimicking different parts of the capture process [7-14]. The different studies also have variations in laboratory set-ups, process conditions as well as chemical components. A principal component analysis (PCA) was conducted to investigate how these bench scale degradation experiments, either separate oxidative degradation studies or cycled studies, compares with respect to the degradation profile (concentrations of several degradation compounds) against pilot scale. In PCA the original variables are reduced to a few new variables (principal components) in directions that explain the main variation in the data set. Mathematically this is done by determine the eigenvalues and eigenvectors of the covariance matrix where the vectors with highest eigenvalues are chosen. The value for each sample in this new coordinate system is called the score, which describe the data structure in terms of sample patterns, and more generally show sample differences or similarities. In this case a range normalization of the data prior to the PCA was done.

The obtained score plot for principal component 1 versus principal component 2 is shown in Figure 2 and shows that the SDR campaigns have similar trends as the Pilot campaigns. For the oxidative experiments, the experiments with low oxygen (6%O₂) and high temperature (75°C) show a trend that is close to the SDR and Pilot campaigns.

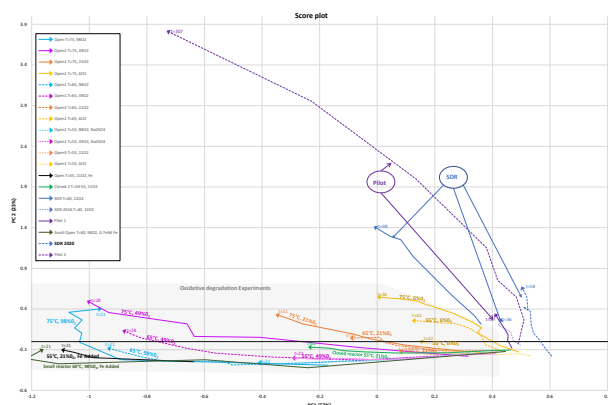


Figure 2: PCA score plot comparing lab-scale experiment with SDR and pilot data for following degradation compounds: HEGly, HEF, BHEOX, HEA, HEPO, OZD and HEI. Duration of experiments (t) is in the unit of days.

3.2 SDR comparison

As mentioned earlier, three MEA campaigns have been conducted since 2011 with the solvent degradation rig. Different process conditions have been varied in the campaigns to study the different conditions influence on the formation and destruction (decomposition or as middle product) of degradation compounds. The operational hours of the campaigns have varied from 860 to 2352 hours. Since the first campaign, more degradation compounds have been identified and quantified for MEA. A thorough mapping of degradation compounds from different amine structures requires a combination of advanced analytical instrumentation as well as understanding related to amine structure and their destruction mechanisms.

For MEA, mechanisms have been suggested for several of the degradation compounds, and some of these are transferable to other amines if one consider the structure of the parent amine. Lepaumier et al. have suggested more generalized mechanisms for both alkanolamines and polyamines [11, 12, 15] while Gouedard has summarized mechanisms related to MEA degradation compounds in her thesis [3].

Figure 3 shows the development of eight degradation compounds (2 of them were not available in 2012) for the three campaigns. These compounds are also quantified in the MEA campaign at Mongstad described by Morken et al. 2017 [16]. However, the SDR campaigns in 2016 and 2020 also quantified additional compounds. More details regarding these degradation compounds for the 2016 campaign are available in Vevelstad et al. [6]. Since there are no pilot data to compare with, these compounds will not be discussed in this short paper. However, it is worth noticing that one of these compounds, MEA-urea, was a

major contributor to the degradation in the SDR rig. It is likely that MEA-urea also is present in MEA pilot samples, but this must be verified by chemical analysis. There is currently no standard analytical method for analysis of degradation compounds in MEA, thus there exists a large variation in degradation compounds reported from the different pilot campaigns [17].

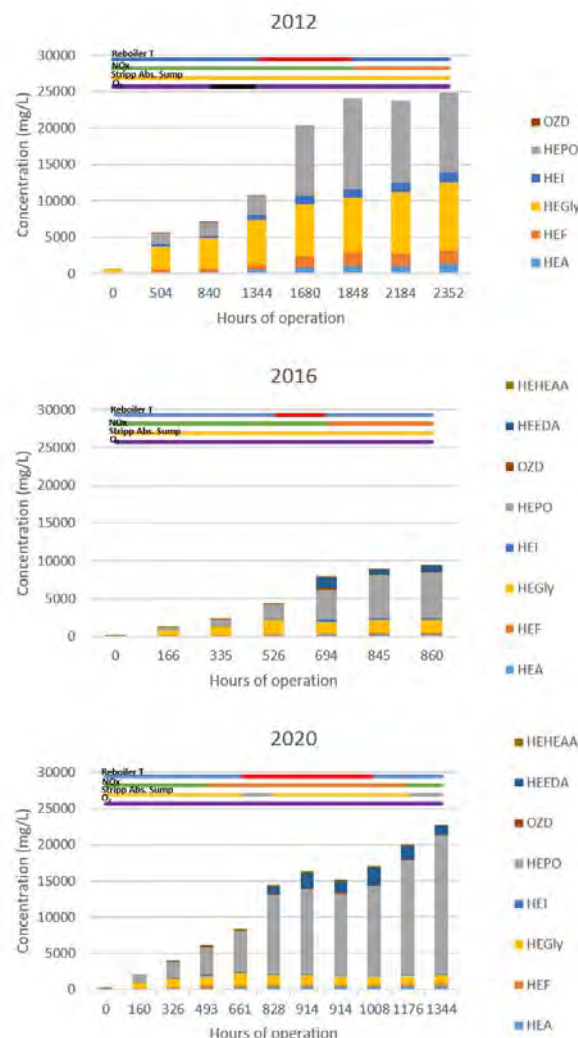


Figure 3: Development of eight degradation compounds (concentration mg/L) as a function of time (hours of operation) in the different SDR campaigns (standard conditions; reboiler temperature 120 °C (blue), NO_x 5 or 10 ppm (green), no stripping absorber sump (yellow) & oxygen concentration 12% (purple)).

As shown in Figure 3, the major degradation compounds amongst these eight compounds are HEPO and HEGly. Similar observations were also found in pilot samples from MEA campaigns at Tiller [8], Esbjerg [8] and Technology Centre Mongstad (TCM) [16, 18]. HEA, HEI and HEF are also important degradation compounds in pilot samples. In general, the same major degradation compounds are identified both in the MEA campaigns in the SDR and in TCM (comparing the degradation components compared at both places). Although, some deviations can be observed for compounds at trace levels

(concentrations close to lower limit of quantification - LOQ).

An interesting observation is the process conditions in the SDR rig seem to favor more build-up of HEEDA compared to the campaign at TCM. HEEDA is a diamine, which has been suggested to be an intermediate in the reaction toward several imidazolidinone and piperazinone [3], where the imidazolidinone pathway is more familiar. HEEDA's role as known intermediate has often been used to explain the low concentration observed in pilot samples and in thermal degradation experiments. Recently several formation reactions of HEEDA have been suggested [3, 19], and reactions with nitrite has an important role for one of these. In the TCM campaign, nitrite was not observed above the LOQ (10 mg/L) [16]. Unfortunately, data for nitrite were not available for the different SDR campaigns and a hypothesis regarding nitrite and HEEDA could therefore not be verified. It has also been postulated that fly ash could inhibit nitrite-induced MEA degradation [19]. Further investigation should include analysis of other degradation compounds that are expected to be formed in higher amounts in the presence of nitrite, such as MEA-urea.

It is difficult to support degradation mechanism pathways suggested for different compounds due to variation in which components that are quantified in different pilot samples. Therefore, lab experiments combined with pilot data with focus on mapping and quantification of large set of degradation compounds, even for MEA as a solvent, are still important to explain the degradation loss of MEA, and to give input to solvent management strategies to maintain a fresh and healthy solvent.

4. Summary

Lab scale experiments, especially cycled degradation rigs, are capable of mimicking formation of the major degradation compounds in pilot campaigns. For some smaller compounds, some deviations between cycled degradation experiment and pilot data, e.g., HEEDA, could be observed, however more information is required to fully understand these observations. Such observations could however play a role to understand why deviations between lab scale and pilot plant or between pilot plants occurs.

Acknowledgements

This publication has been produced with support from the NCCS Centre, performed under the Norwegian research program Centres for Environment-friendly Energy Research (FME). The authors acknowledge the following partners for their contributions: Aker Solutions, Ansaldo Energia, Baker Hughes, CoorsTek Membrane Sciences, EMGS, Equinor, Gassco, Krohne, Larvik Shipping, Lundin, Norcem, Norwegian Oil and Gas, Quad Geometrics, Total, Vår Energi, and the Research Council of Norway (257579/E20).

References

- Hoff, K.A., et al., *Solvent development in post combustion CO₂ capture-selection criteria and optimization of solvent performance, cost and environmental impact*. Energy Procedia, 2013. **37**: p. 292-299.
- Grimstvedt, A., et al., *Exploration of Degradation Chemistry by Advanced Analytical Methodology*. Energy Procedia, 2017. **114**: p. 1785-1793.
- Gouedard, C., *Novel degradation products of ethanolamine (MEA) in CO₂ capture conditions: identification, mechanisms proposal and transportation to other amines*. 2014, Universite Pierre et Marie Curie.
- Cuccia, L., et al., *Analytical methods for the monitoring of post-combustion CO₂ capture process using amine solvents: A review*. International Journal of Greenhouse Gas Control, 2018. **72**: p. 138-151.
- Einbu, A., et al., *A new test rig for studies of degradation of CO₂ absorption solvents at process conditions; comparison of test rig results and pilot data of degradation of MEA*. Energy Procedia, 2013. **37**(0): p. 717-726.
- Vevelstad, S.J., et al., *Comparison of different Solvents from the Solvent Degradation Rig with Real Samples*. Energy Procedia, 2017. **114**: p. 2061-2077.
- Closmann, F. and G.T. Rochelle, *Degradation of aqueous methyl-diethanolamine by temperature and oxygen cycling*. Energy Procedia, 2011. **4**: p. 23-28.
- da Silva, E.F., et al., *Understanding 2-Ethanolamine Degradation in Postcombustion CO₂ Capture*. Ind. Eng. Chem. Res., 2012. **51**(41): p. 13329-13338.
- Davis, J. and G. Rochelle, *Thermal degradation of monoethanolamine at stripper conditions*. Energy Procedia, 2009. **1**(1): p. 327-333.
- Goff, G.S., *Oxidative Degradation of Aqueous Monoethanolamine in CO₂ Capture Processes: Iron and Copper Catalysis, Inhibition, and O₂ Mass Transfer*, in *Chemical Engineering*. 2005, University of Texas: Austin. p. 283.
- Lepaumier, H., D. Picq, and P.-L. Carrette, *New Amines for CO₂ Capture. I. Mechanisms of Amine Degradation in the Presence of CO₂*. Industrial & Engineering Chemistry Research, 2009. **48**(20): p. 9061-9067.
- Lepaumier, H., D. Picq, and P.-L. Carrette, *New Amines for CO₂ Capture. II. Oxidative Degradation Mechanisms*. Industrial & Engineering Chemistry Research, 2009. **48**(20): p. 9068-9075.
- Vevelstad, S.J., et al., *Extensive dataset for oxidative degradation of ethanolamine at 55–75 °C and oxygen concentrations from 6 to 98%*. International Journal of Greenhouse Gas Control, 2016. **50**: p. 158-178.
- Voice, A.K., F. Closmann, and G.T. Rochelle, *Oxidative Degradation of Amines With High-Temperature Cycling*. Energy Procedia, 2013. **37**: p. 2118-2132.
- Lepaumier, H., et al., *New Amines for CO₂ Capture. III. Effect of Alkyl Chain Length between Amine Functions on Polyamines Degradation*. Industrial & Engineering Chemistry Research, 2010. **49**(10): p. 4553-4560.
- Morken, A.K., et al., *Degradation and Emission Results of Amine Plant Operations from MEA Testing at the CO₂ Technology Centre Mongstad*. Energy Procedia, 2017. **114**: p. 1245-1262.
- Buvik, V., et al., *A review of degradation and emissions in post-combustion CO₂ capture pilot*

- plants*. International Journal of Greenhouse Gas Control, 2021. **106**: p. 103246.
18. Morken, A.K., et al., *Emission Results of Amine Plant Operations from MEA Testing at the CO₂ Technology Centre Mongstad*. Energy Procedia, 2014. **63**(Copyright (C) 2015 American Chemical Society (ACS). All Rights Reserved.): p. 6023-6038.
19. Huang, Q., et al., *Impact of Flue Gas Contaminants on Monoethanolamine Thermal Degradation*. Ind. Eng. Chem. Res., 2014. **53**(2): p. 553-563.

EXPERIMENTAL STUDY OF CO₂ TWO-PHASE FLOW REGIME IN A LARGE DIAMETER PIPE

Hilde Andersen¹, Hedda E.S. Svendsen¹, Stine Solum¹, Zhilin Yang^{2*}, Leyla Teberikler³, Svein Solvang⁴, Loek Vreenegoor⁵

¹ Equinor, Porsgrunn, Norway

² Equinor, Trondheim, Norway

³ Total E&P Norge, Stavanger, Norway

⁴ Gassco, Haugesund, Norway

⁵ Shell, Amsterdam, Netherlands

* Corresponding author e-mail: zhy@equinor.com

Abstract

An experimental study was carried out on two-phase CO₂ flow in Equinor's multiphase flow rig in Porsgrunn, Norway. This facility was recently upgraded for CO₂ applications. This paper presents the experimental results on two-phase regimes of CO₂ flow in a pipe close to horizontal inclinations. One of the main discoveries from this work is that hydrodynamic slug flow is not observed. The flow regime information will be used as an input to the model development of flow assurance tools for CO₂ applications.

Keywords: CO₂ two-phase flow, Flow regimes, X-ray measurement

1. Introduction

Long distance transport in pipelines is found to be an effective part of the solution for storage of CO₂, for instance Snøhvit CO₂ pipeline operated by Equinor Energy AS since 2008. Operation of CO₂ transport systems has currently been restricted to single phase (gaseous or liquid) flow in the flowline. Such restrictions limit the selection of the storage site (may exclude low pressure reservoirs), and sometimes require complex system design as well as operational procedures.

To allow two-phase flow in transport and injection systems can facilitate and reduce the cost for storage in low pressure reservoirs. The existing commercial flow assurance softwares were developed based on laboratory studies and tuned against operational data of oil and gas transport lines and production systems. It is believed that many physical models in these softwares are still applicable for some flow scenarios of CO₂ transport and injection systems. However, due to large differences in thermodynamics and physical properties between CO₂ and oil & gas fluids, some flow models as well as some aspects of numerical methods in the existing software need to be tested against dedicated experimental data and the available field operational data.

In this context, a research program ECOTS JIP (Extending CO₂ Transport Solution) was established in 2020. The main objectives of this program are:

- Enabling Equinor's multiphase phase flow rig in Porsgrunn for CO₂ applications
- Experimental study of CO₂ flow with various flow conditions.

In previous studies [1,2], extensive experimental study of various two-phase flow phenomena was carried out at IFE's CO₂ flow loop in Norway. The results from these studies provide first-hand information of CO₂ flow behaviour in conditions relevant for CO₂ transport and injection system. IFE's CO₂ rig has a test section with internal pipe diameter of 44 mm and a length of 13 m. The experimental results from a larger scale facility are essential to validate the scaling behaviour of the flow model. Equinor's multiphase flow rig in Porsgrunn has been used extensively for validation of multiphase flow models for oil and gas applications. It is found that this facility is the largest in the world that has both temperature and process controls critical for CO₂ fluid systems.

In this work, the experimental results from ECOTS JIP on the two-phase flow regimes will be presented. The flow regimes of two-phase flow are critical input to the concept development of the flow models.

2. Experimental facility

Equinor's multiphase flow rig is a closed loop designed for three-phase flow tests with crude oil and natural gas fluid system. It has been in operation since 1996.

In 2020, this rig was upgraded to handle CO₂ fluid. Process safety and HSE related issues had a large focus in the upgrade.

Figure 1 shows the schematic of the flow loop in Porsgrunn. The flow loop consists of a main separator, gas compressor, liquid pump, heat exchanger for both liquid and gas phase and test section. The main separator ensures accurate phase flow rate control. The CO₂ fluid

in the main separator is maintained at saturated condition with CO₂ vapor filled in the upper part of the separator, and liquid CO₂ at bottom. CO₂ vapor needs to be cooled downstream the compressor so that similar vapor and liquid temperatures are achieved at their merging location. This minimizes the mass transfer between vapor and liquid.

The flow loop has a 200 m long test section, in which a section of 80 meter is inclinable within the range of -5 to 10 degrees. Pipe internal diameter is 0.0779m. The pipe material is duplex steel, and the whole loop is insulated. The rig has the following operational window for CO₂ flow tests

- Maximum liquid rate: 40 m³/h
- Maximum vapor rate: 100 m³/h;
- Pressure: 45-65 bar
- Temperature: 10 -26 °C

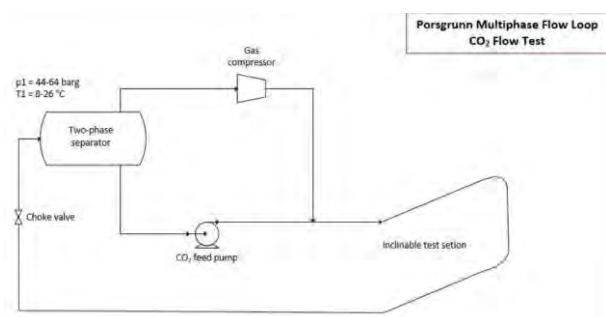


Figure 1: Sketch of Equinor's multiphase flow rig in Porsgrunn

This facility is equipped with advanced instrumentations as follows:

- Coriolis meter for both vapor and liquid mass flow rate measurement
- 5 absolute pressure sensors
- 11 thermal-couples for temperature measurement at different locations
- 6 differential pressure transducers
- 7 narrow-beam Gammas
- 1 X-ray
- Two pipe sections with transparent materials (sight glass) for video recording.

The narrow beam Gamma is mounted at the centre-line of the pipe in a vertical direction. It measures the average fluid density along the beam diameter. This average density can be converted into liquid holdup if an ideal stratified flow is observed. The transient measurement with sampling rate of up to 20 Hz provides the information of vapor-liquid flow geometry, a large variation of narrow beam measurement indicates either stratified flow with large wave interface or gas-liquid slug flow.

The X-ray system is a mono camera system, measuring liquid holdup and fluid distribution in two- or three-phase flow. A principle sketch of the system used in the flow loop is shown in Figure 2. The camera can obtain up to

190 images per second with resolution of 75 μm. This X-ray system has been in operation for oil and gas application since 2015.

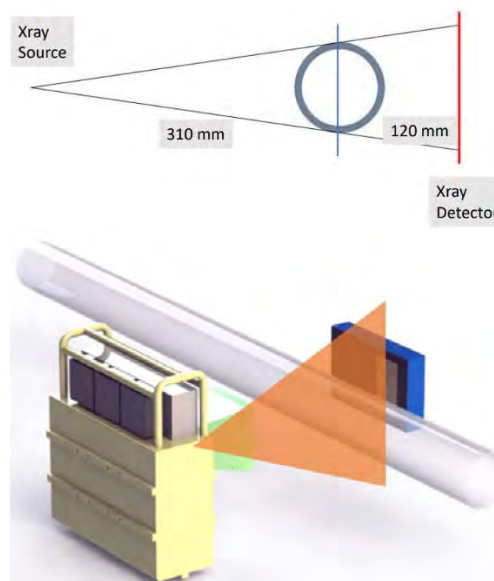


Figure 2 Schematic of the X-ray mono camera system. Upper: source-camera configuration. Bottom: 3D layout.

3. Experimental observations

The experiments of two-phase CO₂ fluid were carried out under steady-state conditions. Pure CO₂ fluid was used in the experiments. Under a defined pressure in the main separator, all instruments should show stable parameter values during a period of 10 minutes. These parameters are: vapor and liquid mass flowrate, temperature at different locations, pressure and differential pressure sensors, readings from Gammas and X-ray. During the experiments, the choke valves downstream the gas compressor and liquid pumps were used to control the mass flowrate of each phase, and the cooling of vapor phase downstream the compressor was imposed to ensure the desired temperature for vapor phase achieved.

The experiments were carried out with following conditions:

- System pressure: 45, 50 and 60 bar, with corresponding temperatures: 10, 15 and 22 °C.
- Liquid superficial velocity (U_{sl}): 0.1, 0.2, 0.3, 0.4 0.5, 1, 1.5 and 2.0 m/s.
- Vapor superficial velocity (U_{sg}): 0.1, 0.2, 0.25, 0.3, 0.4, 0.5, 0.75, 1.0, 1.5, 2.0, 3.0 and 4.0 m/s.
- The test section inclinations are: -5, -1, 0, 1, 5 and 10 degrees.

The information from three different measurements were used to identify the flow regime:

- Direct observation via transparent windows, video was recorded for most of the cases.

- Transient measurement from narrow beam-Gamma, which gives mixture density at the pipe centreline.
- X-ray measurement of the liquid holdup profile (distribution) across pipe

Figure 3 shows typical flow geometries from the video recorded through transparent window. Under the flow condition with low U_{sg} and U_{sl} , a clear stratified gas-liquid flow is observed with and without presence of vapor bubbles at the gas-liquid interface, depending on the mixture flowrate. A smooth vapor-liquid interface without bubble generation is observed with very low mixture velocity. Increase in mixture flow rate leads to increased mixing intensity, and generation of more bubbles. In these pictures, secondary flow is observed along the pipe wall, this is simply due to that fact that the diameter of transparent window is slightly smaller than the main pipe (0.065 m vs. 0.0779m ID).

Both Gamma and X-ray measurements show very stable liquid holdup behaviour with time. The X-ray measurements provide the holdup profile along the pipe cross-section (horizontally from bottom to top of the pipe). Figure 4 and Figure 6 show the X-ray measurement for two series of tests with $U_{sl} = 0.5$ m/s and $U_{sl} = 2.0$ m/s, respectively. These two series of tests have the same system pressure (60 bar) and pipe inclination (1 degree upward flow). These two series represent two extreme situations: gas dominated and liquid dominated flow. The time series measurement shown in these figures have 30 seconds. The red colour represents liquid dominant measurement, and the blue colour indicates gas/vapour dominant measurement. The time-averaged distribution of liquid holdup gives quantitative representation of phase distribution in a pipe as shown in Figure 5 and Figure 7.

The measurements give the following observations on the flow regime:

- The volume fraction of phases segregated with relatively smooth interfaces. The slug type of the flow geometry is not identified in any of the tests carried out. This is also consistent with the experimental observations from IFE'e test loop [2], which has smaller a pipe diameter (44 mm ID).
- For the cases with relatively low mixture flow rate, stratified gas-liquid flow regime is observed. Bubbles are generated at the interface. Increase in mixture flowrate and system pressure leads to more bubble generation. If liquid flowrate is significantly higher than the gas flowrate, a pure liquid layer is observed at the bottom part of the pipe, the top part of the pipe is filled with the strong mixing flow layer (bubble flow layer). This bubbly flow layer has low liquid volume fraction. The interface at these two layers exhibits wavy structure, indicating strong mixing intensity. Smooth interface is observed only for very low mixture velocity situations.

- With high mixture flowrate, the gas-liquid is well mixed with very small bubbles.
- High system pressure gives a large gas-liquid density ratio, this leads to more bubble generation.
- For liquid dominated flow condition, there is a trend of liquid layer, and the dispersion process begins at the upper part of the flow.
- For vapor dominated flow condition, there is a trend of vapor layer, and the dispersion process occurs at the bottom part of the flow.



(a) Low U_{sg} & low U_{sl} (b) Low U_{sg} & moderate U_{sl}



(c) High U_{mix} (d) Moderate U_{sg} & low U_{sl}

Figure 3 Flow geometry observed from transparent window (sight glass)

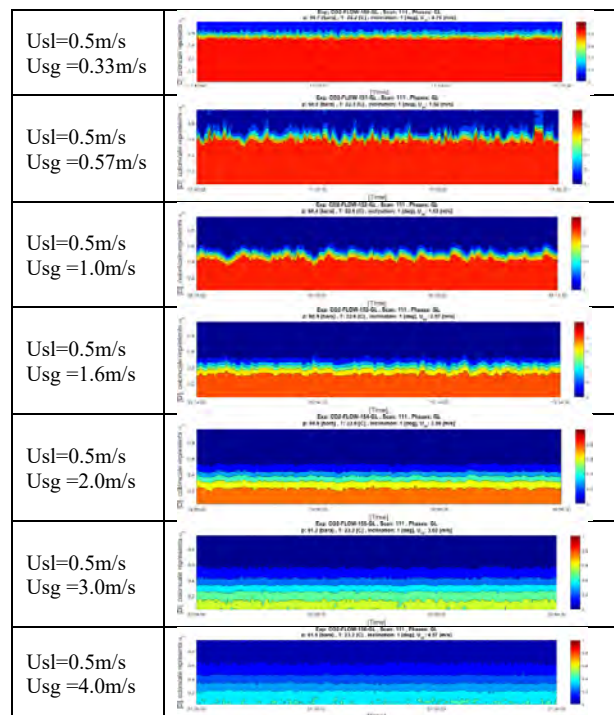


Figure 4 X-ray measurement of liquid holdup profile across the pipe, color scale gives the liquid holdup. Test conditions are 1 degree upward pipe and $P = 60$ bar

The following flow regimes are summarised from the experimental observations:

- Stratified flow with bubbles generated at the interface (ST) (Figure 3a)
- Stratified flow with bubble & churn flow at the top layer and liquid layer at the bottom (ST/Ch)(Figure 3b)
- Bubbly flow (BB)(Figure 3c)
- Stratified flow with gas layer at the top and bubbly flow at the bottom (ST/BB)(Figure 3d).

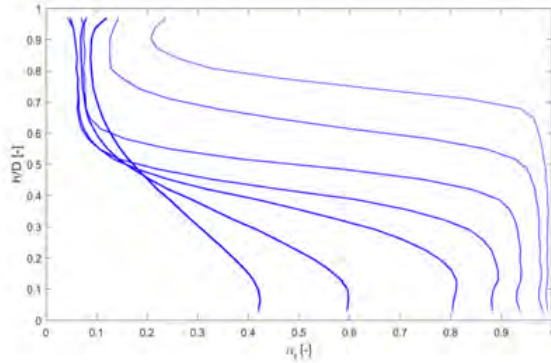


Figure 5 Time-averaged liquid holdup profile from X-ray for the tests with $U_{sl} = 0.5$ m/s, U_{sg} varies from 0.3 to 4.0 m/s, 1 degree upward pipe and $P = 60$ bar.

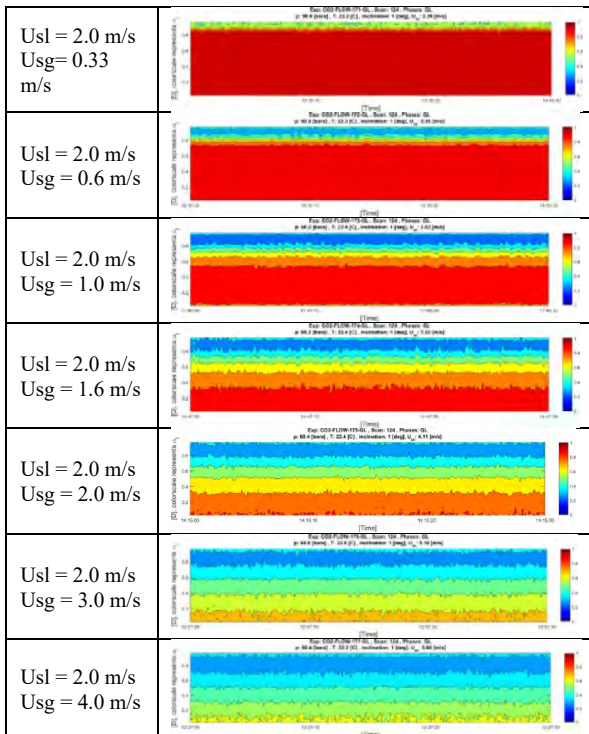


Figure 6 X-ray measurement of liquid holdup profile across the pipe, color scale gives the liquid holdup. Test conditions are 1 degree upward pipe and $P = 60$ bar

The two-phase flow regimes can also be illustrated in a flow regime map in terms of vapor-liquid superficial velocity. Figure 8 shows the flow regime map for the flow condition of 60 bar and 1 degree upward inclination. Similar flow regime maps were observed for other flow conditions in the test program. The pipe inclinations

(within the range of -5 and 10 degrees) have little impact the flow regime boundary.

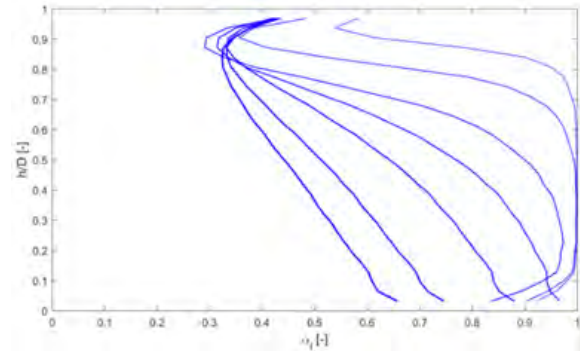


Figure 7 Time-averaged liquid holdup profile from X-ray for the tests with $U_{sl} = 2.0$ m/s, U_{sg} varies from 0.3 to 4.0 m/s, 1 degree upward pipe and $P = 60$ bar.

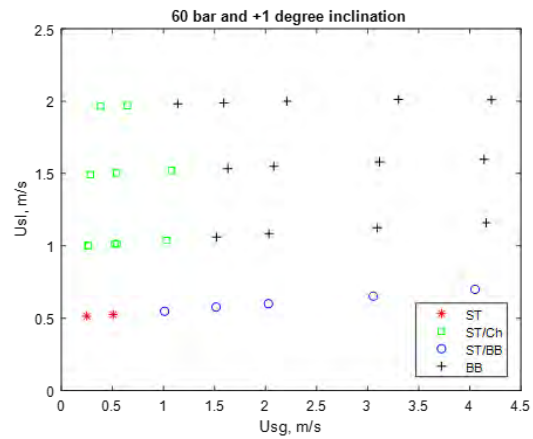


Figure 8 Flow regime map for the flow with 1 degree upward inclination and $P = 60$ bar.

4. Summary

The multiphase flow rig in Porsgrunn has been upgraded to carry out two-phase flow studies of pure CO₂. This is currently the largest test facility in terms of pipe diameter and pipe length for CO₂ applications in the world. The facility is a closed system with both temperature and pressure control, and is equipped with advanced instrumentation for accurate measurement of various physical parameters.

This paper presents the experimental observations of two-phase CO₂ flow regimes in a near horizontal pipe configuration. Both direct observation via class window and X-ray measurement shows that the flow regimes observed are: stratified flow with and without bubble generation at vapor-liquid interface, stratified flow with liquid layer at bottom and bubbly flow at top, stratified flow with gas layer at top and bubbly flow at bottom, and dispersed bubbly flow. The hydrodynamic slug flow which is one of the typical flow regimes for oil and gas flow system is not observed. This may be due to relatively small gas-liquid density ratio and very small surface tension of CO₂ fluid system.

Acknowledgements

This study is financed partially by Gassnova's CLIMIT Demo program through the 'ECOTS' project nr. 620054.

References

- [1] Yang, Z.L. et al, Flow assurance from oil & gas to CO₂ transport and injection, TCCS-10, Trondheim, 2019.
- [2] Yang, Z.L., et al. Improved understanding of flow assurance for CO₂ transport and injection. 15th International Conference on Greenhouse Gas Control Technologies, GHGT-15. March 15-18, 2021 Abu Dhabi, UAE.

CO-ADSORPTION AND PURE-COMPONENT ISOTHERM MEASUREMENTS ON DIRECT AIR CAPTURE ADSORBENTS USING THE DVS VACUUM

John P Young^{1*}, Vladimir Martis², Susana Garcia¹, Mijndert van der Spek¹

¹Research Centre for Carbon Solutions, Heriot-Watt University, Edinburgh, EH14 4AS, United Kingdom

²Surface Measurement Systems, Unit 5, Wharfside, Rosemont Road, London, HA0 4PE, United Kingdom

* Corresponding author e-mail: jpy1@hw.ac.uk

Abstract

Temperature vacuum swing adsorption processes that employ amine-functionalised adsorbents are a promising technology to enable carbon dioxide removal directly from the atmosphere. These adsorbents capture carbon dioxide selectively over nitrogen from the air. They also capture significant amounts of water. The co-adsorption of carbon dioxide and water is still poorly understood due to the difficulty of measuring this effect. To date, water adsorption and co-adsorption measurements were time-consuming as breakthrough or equilibrium adsorption experiments were required for each point on an isotherm. Additionally, data required for the accurate modelling of the process includes pure-component water and carbon dioxide isotherms at a range of temperatures and co-adsorption isotherms at a range of temperatures and relative humidities. Attempting to model direct air capture (DAC) processes without this complete set of data might lead to a limited understanding of the process. As a result, process design may be sub-optimal, and the chosen operating conditions might be inefficient. Here we demonstrate how co-adsorption isotherms and pure-component isotherms can be measured swiftly on an amine-functionalised adsorbent using the Dynamic Vapour Sorption (DVS) Vacuum instrument. We also show how the obtained data can be used to perform first-order kinetic analysis. In this study, Lewatit VP OC 1065® is chosen as an example of an amine-functionalised adsorbent, as it is believed to be similar to the sorbents used by some commercial DAC companies.

Keywords: Direct air capture, adsorption, DVS Vacuum

1. Introduction

Climate change is the most pressing issue of our time. Humanity is currently in a race to restrict the warming of earth to 1.5 °C to avoid catastrophic effects on both the natural world and the human population. In the likely scenario that this target is missed, net negative emissions will be required to bring the temperature back down to the desired range. [1] Carbon dioxide removal (CDR) on a vast scale will be required to implement net negative emissions. One technology that can be utilised to this end is direct air capture (DAC) coupled with long term carbon dioxide storage. Realmonde et al. showed, using bottom-up energy systems modelling, that a carbon tax of just \$50 per tonne of CO₂ will be needed by 2030 in order to meet the 1.5°C scenario when DAC is available as a technology. [2] Without DAC, this figure goes up to \$2119 per tonne of CO₂ by 2030, and the scenario is completely infeasible without any CDR. The study also does the same analysis using a different model, with a top-down macroeconomic emphasis, and come to a required carbon tax of \$151 per tonne of CO₂ with DAC and \$446 per tonne of CO₂ without DAC by 2030 to meet the 1.5°C scenario.

Currently, the most mature technology for DAC is temperature vacuum swing adsorption (TVSA) using amine-functionalised adsorbents. Examples of companies currently implementing this are Climeworks, Global Thermostat, and Oy Hydrocell. [3]–[5] Despite the significant advancements made by industry, the

academic community still has some significant contributions to make to DAC. The co-adsorption of water and carbon dioxide onto amine-functionalised adsorbents is still poorly understood. It is understood that there is some enhancement of carbon dioxide adsorption under wet conditions. [6]–[10] However, mechanistic mathematical adsorption isotherm descriptions are required to accurately model and optimise the TVSA processes employing these materials. Gathering equilibrium co-adsorption data has been time-consuming to date. Some effort was made by Veneman et al. to gather co-adsorption data using breakthrough experiments on a commercially available amine-functionalised adsorbent, Lewatit VP OC 1065®. [7] Nevertheless, only 12 data points were collected at different relative humidities and temperatures, whilst CO₂ partial pressure was kept constant. Presumably, this was due to the time-intensive nature of breakthrough experiments. An extensive range of temperatures, CO₂ partial pressures, and relative humidities are required to build and fit an accurate co-adsorption isotherm model. Furthermore, there are questions about the accuracy of measured breakthrough data. There are a few different operating variables to control in breakthrough experiments, and the reactor outlet concentration must be measured precisely. These factors all add to the potential for experimental error. Veneman et al. also use breakthroughs to measure water adsorption isotherms, but the less time-consuming thermogravimetric analysis (TGA) is used for CO₂ isotherms. A volumetric method

combined with gas chromatography was used by Didas et al. for measuring co-adsorption isotherms on an amine-functionalised silica. [11] Aside from amine-functionalised adsorbents, Wilkins and Rajendran also used breakthrough experiments to measure the competitive adsorption of CO₂ and N₂ on zeolite 13X. [12] Meanwhile, Hefti et al. combined gravimetric experiments with gas chromatography to measure the same competitive adsorption on zeolites 13X and ZSM-5. [13]

A piece of equipment that may be quicker and more effective at measuring pure CO₂ adsorption, pure H₂O adsorption, and co-adsorption is the DVS Vacuum. [14] This has previously been used by Su et al. to measure CO₂ and H₂O isotherms on an amine-functionalised Mg-MOF-74. [15] The DVS Vacuum uses a microbalance to measure the weight change of a sample subjected to various conditions. The temperature, pressure, and composition in the sorption chamber can be controlled very accurately.

This study sets out to show how co-adsorption isotherms and water adsorption isotherms on a commercially available amine-functionalised adsorbent, in the form of Lewatit VP OC 1065®, can be measured using the DVS Vacuum. Beyond this study, this methodology can be extended to other adsorbents, given that certain assumptions hold. These will be discussed in the Experimental method and analysis section. In future work, the data collected here will be used to develop a mechanistic mathematical water-CO₂ co-adsorption isotherm model that can be extended to any amine-functionalised adsorbent. It is hoped that this will lead to more accurate modelling of DAC processes, and therefore improved optimisation and enhanced efficiency.

2. Experimental method and analysis

The material investigated, Lewatit® VP OC 1065, was obtained from Sigma-Aldrich. It is a divinylbenzene (DVB) crosslinked polymer functionalised with primary amine groups with an average pore diameter of 25 nm, a bead size of 0.315 – 1.25 mm, pore volume of 0.27 cm³ g⁻¹, surface area of 50 m² g⁻¹, and bulk density of 630 – 710 g l⁻¹. [14] Meanwhile, the heat capacity is reported as 1.58 kJ kg⁻¹ K⁻¹. [23]

Figure 1 shows a schematic of the DVS Vacuum. In the experiments presented in this work, the gas and vapour used are CO₂ and water. A turbomolecular pump enables the pressure in the chamber to reach as low as 10⁻⁶ mbar. This ensures very thorough outgassing of the sample prior to adsorption. The vacuum pump, coupled with various control valves, allows very accurate control of the sorption chamber pressure during adsorption and desorption measurements. The temperature in the sorption chamber can range from room temperature up to 400°C whilst the whole system, apart from the gas storage and vacuum pumps, is inside an incubator (temperature-controlled enclosure) operating in the temperature range from 20 up to 70°C. The incubator temperature sets the maximum limit of the solvent's partial pressure in the sorption chamber as the saturation pressure at this temperature. The set partial pressure of

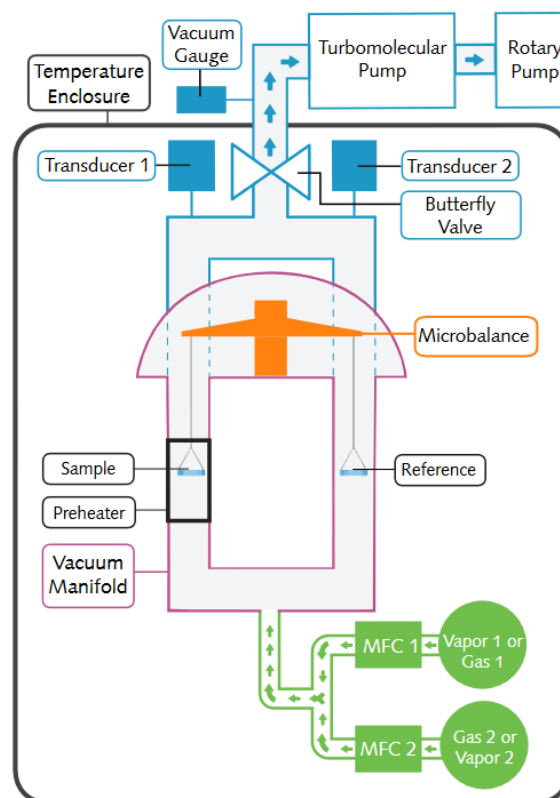


Figure 1: A simple schematic of the DVS Vacuum.

water is introduced under vacuum without the interference of a carrier gas at the set experimental temperature. Such measurements will provide true water adsorption isotherms eliminating the impact of water adsorption on the structure. The sample's weight is measured directly and continuously using Surface Measurement Systems' UltraBalance with a resolution of 0.1 µg. The whole system is controlled via the control software, allowing the user to create and modify experimental methods easily. The method can be set to measure a whole isotherm, including a desorption branch in one experiment. It also allows the collection of multiple adsorption/desorption isotherms with in-situ outgassing between cycles in a single experiment. The sorption measurements can be done in a fixed time mode or mass equilibrium mode where the mass equilibrium criterion is set as the change in mass per minute (dm/dt). The control software automatically calculates and checks the dm/dt criterion against the set dm/dt value. When the sample's mass has reached equilibrium at a certain partial pressure of the gas or vapour, the control software automatically moves on to the next partial pressure step in the method. Due to this highly automated system, the labour time required to measure an isotherm is very low, whilst the actual time the equipment takes to measure an isotherm is dependent on the sample itself, the adsorbate, and the experimental conditions defined in the method.

The DVS Vacuum can be operated in a "dynamic", "semi-static", or "static" mode. In dynamic mode, the downstream and upstream sorbate flow is controlled, while changes in sample mass are continuously monitored. In a typical experiment, vapour or gas flows at a constant rate over a sample while the total system

pressure is kept constant. Meanwhile, in static mode, the upstream and downstream control valves are closed upon the injection of a sorbate in the chamber (similar to manometric systems). At the same time, changes in sample mass are continuously monitored using the UltraBalance. There are two options for static mode: semi-static and true static. The difference between these two options is that in semi-static mode, more sorbate molecules are added to the chamber when the pressure inside the vacuum chamber decreases below the set pressure due to sorption of molecules by the sample. On the other hand, in true static mode, when the partial pressure drops below the set pressure, more molecules are not injected into the chamber and the sample is simply left to equilibrate.

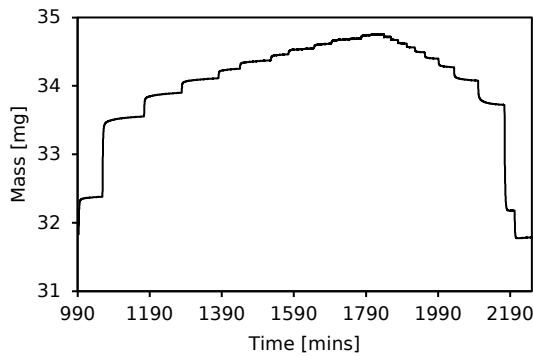


Figure 2: Mass vs time graph obtained from a CO₂ isotherm experiment at 75°C that measures both the adsorption and desorption branches.

In a typical experiment with Lewatit VP OC 1065®, around 50 mg of the sample mass is loaded into the metal pan that hangs from the microbalance. The first step in the method used here involves heating the sample to 100 °C under the highest achievable vacuum for 12 hours. This ensures thorough degassing of the sample with the removal of any H₂O, CO₂, or N₂. Then a cooling step is implemented to bring the sample back down to the temperature of interest while maintaining the same level of vacuum. Next, the sorbate pressure in the sorption chamber is increased stepwise as per the method, and the sample mass in the chamber is allowed to equilibrate at each step. The desorption branch is performed in a similar manner, that is, the pressure is decreased stepwise with the sample mass equilibrating at each step. Figure 2 depicts typical sorption raw data showing changes in the sample mass during adsorption and desorption as a function of time. Pure H₂O sorption experiments were done in dynamic mode whilst pure CO₂ experiments were done in semi-static mode, with pressures ranging up to 1 bar. Dynamic mode was chosen for water sorption experiments to maintain the purity of water vapour in the sorption chamber. Any gases dissolved in the liquid water flask or desorbed molecules would quickly be flushed away from the sample. It also allows better control of pressure at extremely low values. Semi-static mode is used for CO₂ experiments, as the gas source is expected to be high purity, and it will eliminate any effect flow may have on the measurements. It also protects the vacuum pumps from corrosion and uses much less gas.

Veneman et al. showed that the presence of CO₂ does not affect H₂O adsorption on Lewatit VP OC 1065®. [7] Other literature also shows that this assumption holds for other types of amine-functionalised adsorbents, such as silica and cellulose. [6], [11] If this was not previously known, other experiments such as breakthroughs would be required to confirm this, as it is a hard constraint on this method. Thompson and Zones have previously used this assumption to measure competitive adsorption on a zeolite with the DVS Vacuum. [16] Using this assumption, that CO₂ does not affect H₂O adsorption, we can measure CO₂ co-adsorption isotherms under wet conditions. This is done in semi-static mode, so the amount of CO₂ and H₂O in the chamber is known. The first pressure increase in the co-adsorption isotherm measurement is a pure water step. The pressure is equilibrated at the relative humidity of interest. Here we need to carefully ensure the mass of the sample has fully equilibrated. We have made the assumption that this amount of water adsorbed is now constant for the rest of the experiment, as is the chamber's relative humidity. Each subsequent pressure addition of pure CO₂ allows an isotherm to be built.

For pure-component isotherms, the saturation loading, q_i^* [mol kg⁻¹], at the end of step n is calculated according to Equation 1.

$$q_i^* = \frac{m_n - m_0}{m_0 M_{w,i}} \quad 1.$$

Where m_n [kg] is the mass of the sample at the end of step n , m_0 [kg] is the mass of the sample at the end of the degassing step, and $M_{w,i}$ [kg mol⁻¹] is the molecular weight of adsorbate i .

For co-adsorption CO₂ isotherms, the loading of H₂O is calculated from Equation 2.

$$q_{H_2O}^* = \frac{m_1 - m_0}{m_0 M_{w,H_2O}} \quad 2.$$

Where m_1 [kg] is the mass of the sample at the end of the water adsorption step. The CO₂ loading at the end of step n in the co-adsorption experiments is calculated according to Equation 3.

$$q_{CO_2}^* = \frac{m_n - m_1}{m_0 M_{w,CO_2}} \quad 3.$$

The same raw data from the DVS, shown in Figure 2, can also be used to do some kinetic analysis. Equation 4, shows a common kinetic model called the linear driving force (LDF) model. [17] This is the most popular choice for process modelling due to its simplicity and effectiveness at predicting breakthrough.

$$\frac{dq_i}{dt} = k_{LDF}(q_i^* - q_i) \quad 4.$$

Here k_{LDF} [s⁻¹] is the LDF constant, t [s] is time, and q_i [mol kg⁻¹] is the loading at any given time in the step. The model can be fit to each pressure step in order to obtain the LDF constant for that pressure and temperature.

The Toth model is also used to fit pure-component CO₂ isotherm data and this presented in equations is presented in Equations 5-8 below: [18]

$$q_{CO_2}^* = \frac{n_{\infty}(T)b(T)p_{CO_2}}{\left(1 + (b(T)p_{CO_2})^{t(T)}\right)^{\frac{1}{t(T)}}} \quad 5.$$

Where, n_{∞} [mol kg⁻¹] is the loading of CO₂ that is approached at an infinite pressure, b [Pa⁻¹] is the affinity of CO₂ to the adsorbent, p_{CO_2} [Pa] is the partial pressure of CO₂, and t [-] is an exponential factor.

$$n_{\infty}(T) = n_{\infty,0} \exp\left(\chi\left(1 - \frac{T}{T_0}\right)\right) \quad 6.$$

Where $n_{\infty,0}$ [mol kg⁻¹] is n_{∞} at the reference temperature T_0 [K], T [K] is the temperature, and χ [-] is a factor used to describe the temperature dependency.

$$b(T) = b_0 \exp\left(\frac{-\Delta H_0}{RT_0}\left(\frac{T_0}{T} - 1\right)\right) \quad 7.$$

Where b_0 [Pa] is b at the reference temperature, ΔH_0 [J mol⁻¹] is the isosteric heat of adsorption, and R [J mol⁻¹ K⁻¹] is the universal gas constant.

$$t(T) = t_0 + \alpha\left(1 - \frac{T_0}{T}\right) \quad 8.$$

Where t_0 [-] is t at the reference temperature, and α [-] is a factor used to describe the temperature dependency.

3. Results and discussion

3.1 Water adsorption

Water isotherms were measured at three different temperatures, including both adsorption and desorption branches for three different temperatures.

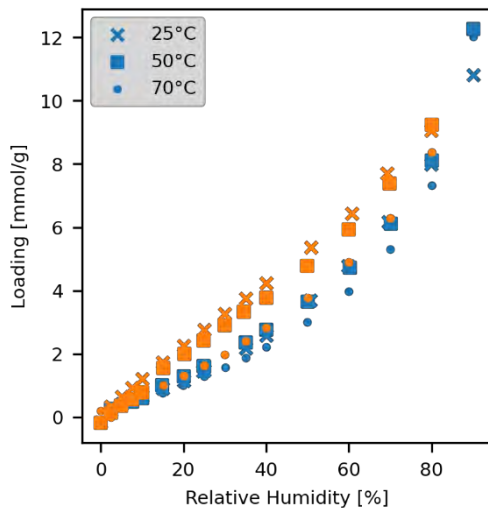


Figure 3: Lewatit VP OC 1065® H₂O isotherms showing both adsorption (blue) and desorption (orange) branches for three different temperatures.

Figure 3 shows H₂O isotherms, which are type III, indicating multilayer adsorption clustering around favourable sites. This is consistent with the expectation that water would form hydrogen bonds with the amine groups on the adsorbent, and then subsequently more water would form hydrogen bonds onto this first layer. The hysteresis exhibited is type H3, which describes macropore adsorbents with pores partially filled by

condensate. [19] This again is consistent with what we would expect from this adsorbent.

In Figure 3 there are 45 adsorption points, which would require 45 individual breakthrough experiments if we were to measure these isotherms in a breakthrough set up. Meanwhile, it would not be possible to measure the desorption branch completely. On the other hand, in the DVS Vacuum, these measurements take just three experiments, each lasting between half a week and a week, meaning a full set of water isotherms was measured in the space of three weeks at most.

3.2 Carbon dioxide pure component adsorption and co-adsorption

Pure-component carbon dioxide isotherms were measured at two temperatures and then fit to the Toth model in order to present them as solid lines, so the co-adsorption isotherms can be compared point-for-point. [18] The parameters shown from this fitting process are found in Table 1. The R² value for this was 0.99.

Table 1: Parameters found for the pure-component CO₂ isotherm fit to the Toth equation.

Parameter	Value	Unit
T_0	298.15	K
$n_{\infty,0}$	6.80	mol kg ⁻¹
χ	0.424	-
b_0	21.2	Pa ⁻¹
$-\Delta H_0$	134000	kJ mol ⁻¹
t_0	0.149	-
α	0.401	-

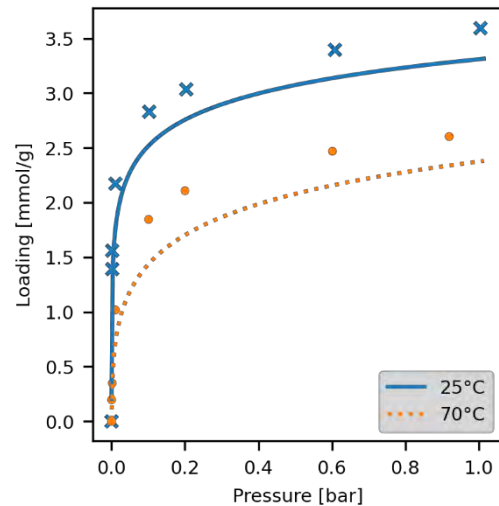


Figure 4: Lewatit VP OC 1065® Pure CO₂ isotherms calculated from the Toth model are shown as lines, whilst the markers are experimental CO₂ isotherms subjected to a relative humidity of 30%. The blue crosses refer to the co-adsorption isotherm at 25°C, whilst the orange dots refer to the co-adsorption isotherm at 70°C.

Figure 4 shows pure CO₂ isotherms compared to CO₂ co-adsorption isotherms at 30% relative humidity for two different temperatures, 25°C and 70°C. The isotherms are type I as expected by a chemisorbent material. It is seen

that the presence of 30% humidity enhances the amount of CO₂ adsorbed as literature has previously suggested for amine-functionalised adsorbents. [6]–[10] Gebald et al. previously presented 4 points of a CO₂ co-adsorption isotherm at two different temperatures under a constant partial pressure of water, resulting in relative humidities of 21% and 92%, for amine-functionalised cellulose. [6] Meanwhile, Didas et al. presented 3–4 points of a co-adsorption isotherm at one temperature for three different amine-functionalised silicas with varying amine coverage. [11] To the authors' knowledge, this is the closest any previous literature has come to presenting a full co-adsorption isotherm, like in this study, on an amine-functionalised adsorbent. One drawback is that the assumption that CO₂ does not affect water adsorption must hold for this method to give valid results. This is something that may not be true for other types of adsorbents. Indeed, preliminary breakthrough experiments may be needed to verify the assumption or establish a different method to use in the DVS Vacuum.

3.3 Kinetic analysis of water adsorption

LDF constants, which are mathematically similar to first-order rate constants in the area of chemical kinetics, were fitted to raw data for water adsorption isotherm measurements.

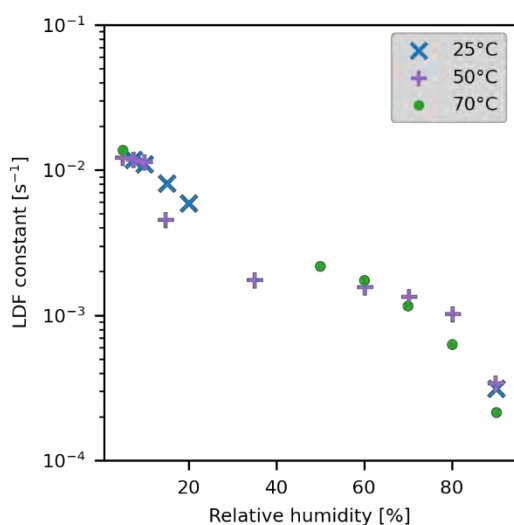


Figure 5: LDF constants for water adsorption fitted to raw data used for building the isotherms. Sometimes, it is hard to find a suitable model fit, and in these cases, the points have been removed from this graph. The tolerance for this removal is an R² value of less than 0.9.

Figure 5 shows LDF constants of water adsorption, plotted against relative humidity for three different temperatures. No clear trend with temperature is observed when plotted against relative humidity. The authors propose that this is because converting pressure to relative humidity already takes temperature into account. However, there is a clear decreasing trend between the LDF constants and relative humidity: the kinetic rate deteriorates with approximately two orders of magnitude when moving from 0 to 90% RH. This is important for modelling purposes and cycle design, as the prospective plant's environmental circumstances may

have a considerable influence on the rate-based adsorption of water, and therefore on energy performance. Some individual points in Figure 5 deviate from the trend, potentially due to some experimental error, and fitting errors caused by imperfections in the mass change over time graph like the one presented in Figure 2.

More work does need to be done to assess whether these LDF constants also hold when scaling up from a gravimetric to a breakthrough set-up. This is key since real processes involve fixed-bed columns like those used in a breakthrough set-up. There may be additional or fewer mass transfer barriers in a fixed-bed column, for example, film resistance. At the same time, it has previously been shown by Casas et al. that the values of the LDF constants do not have an enormous effect on breakthrough modelling results, so the values from a gravimetric set-up may be a sufficient approximation if a breakthrough experiment is unavailable. [20]

4. Conclusion and future work

Water and co-adsorption isotherms have been measured on Lewatit VP OC 1065®. The DVS Vacuum enables the efficient measurement of co-adsorption isotherms under the condition that one of the component's adsorption is unaffected by the other. It is also very effective for measuring water adsorption isotherms in comparison to using a breakthrough set-up. The enhancing effect of water on CO₂ adsorption for amine-functionalised adsorbents has been confirmed, and the most complete CO₂ co-adsorption isotherms on these adsorbents yet have been measured. The same raw data that was used to measure the isotherms was also used to perform kinetic analysis, and LDF constants were calculated for water adsorption. A decreasing trend with relative humidity was observed for these values. Further assessment is required to check how these values predict mass transfer in breakthrough columns.

In future work, we will complete a full assessment of equilibrium adsorption on Lewatit VP OC 1065® to model the pure component isotherms and co-adsorption isotherms using mechanistic descriptions. Next, breakthrough experiments will be used to study the dynamics of pure-component and co-adsorption. We hope this will lead to the establishment of Lewatit VP OC 1065® as a benchmark DAC sorbent since it is one of the few commercially available, amine-functionalised adsorbents.

Acknowledgements

None

References

- [1] V. Masson-Delmotte *et al.*, “Global warming of 1.5°C. An IPCC Special Report on the impacts of global warming of 1.5°C above pre-industrial levels and related global greenhouse gas emission pathways, in the context of strengthening the global response to the threat of climate change,” 2018.
- [2] G. Realmonte *et al.*, “An inter-model assessment of the role of direct air capture in deep mitigation pathways,” *Nat. Commun.*, vol. 10, no. 1, pp. 1–12, 2019.
- [3] “Climeworks 2009-2020.” .
- [4] E. Ping, M. Sakwa-novak, and P. Eisenberger, “Global Thermostat Low Cost Direct Air Capture Technology Summary of Global Thermostat (GT) Technology,” *Int. Conf. Negat. CO₂ Emiss. May 22-24, 2018, Göteborg, Sweden*, pp. 1–9, 2018.
- [5] “Oy Hydrocell 1993-2020.” .
- [6] C. Gebald, J. A. Wurzbacher, A. Borgschulte, T. Zimmermann, and A. Steinfeld, “Single-component and binary CO₂ and H₂O adsorption of amine-functionalized cellulose,” *Environ. Sci. Technol.*, vol. 48, no. 4, pp. 2497–2504, 2014.
- [7] R. Veneman, N. Frigka, W. Zhao, Z. Li, S. Kersten, and W. Brilman, “Adsorption of H₂O and CO₂ on supported amine sorbents,” *Int. J. Greenh. Gas Control*, vol. 41, pp. 268–275, 2015.
- [8] N. R. Stuckert and R. T. Yang, “CO₂ capture from the atmosphere and simultaneous concentration using zeolites and amine-grafted SBA-15,” *Environ. Sci. Technol.*, vol. 45, no. 23, pp. 10257–10264, 2011.
- [9] Y. Kuwahara *et al.*, “Dramatic enhancement of CO₂ uptake by poly(ethyleneimine) using zirconosilicate supports,” *J. Am. Chem. Soc.*, vol. 134, no. 26, pp. 10757–10760, 2012.
- [10] J. Yu and S. S. C. Chuang, “The structure of adsorbed species on immobilized amines in CO₂ capture: An in situ IR study,” *Energy and Fuels*, vol. 30, no. 9, pp. 7579–7587, 2016.
- [11] S. A. Didas, M. A. Sakwa-Novak, G. S. Foo, C. Sievers, and C. W. Jones, “Effect of amine surface coverage on the Co-adsorption of CO₂ and water: Spectral deconvolution of adsorbed species,” *J. Phys. Chem. Lett.*, vol. 5, no. 23, pp. 4194–4200, 2014.
- [12] N. S. Wilkins and A. Rajendran, “Measurement of competitive CO₂ and N₂ adsorption on Zeolite 13X for post-combustion CO₂ capture,” *Adsorption*, vol. 25, no. 2, pp. 115–133, 2019.
- [13] M. Hefti, D. Marx, L. Joss, and M. Mazzotti, “Adsorption equilibrium of binary mixtures of carbon dioxide and nitrogen on zeolites ZSM-5 and 13X,” *Microporous Mesoporous Mater.*, vol. 215, pp. 215–228, 2015.
- [14] Surface Measurement Systems, “DVS Vacuum Dynamic Vacuum Vapor & Gas Gravimetric Sorption Analyzer.” 2020.
- [15] X. Su, L. Bromberg, V. Martis, F. Simeon, A. Huq, and T. A. Hatton, “Postsynthetic Functionalization of Mg-MOF-74 with Tetraethylenepentamine: Structural Characterization and Enhanced CO₂ Adsorption,” *ACS Appl. Mater. Interfaces*, vol. 9, no. 12, pp. 11299–11306, 2017.
- [16] J. A. Thompson and S. I. Zones, “Binary- And Pure-Component Adsorption of CO₂, H₂O, and C₆H₁₄ on SSZ-13,” *Ind. Eng. Chem. Res.*, vol. 59, no. 40, pp. 18151–18159, 2020.
- [17] E. Glueckauf, “Theory of chromatography. Part 10.—Formulæ for diffusion into spheres and their application to chromatography,” *Trans. Faraday Soc.*, vol. 51, pp. 1540–1551, 1955.
- [18] J. Toth, “State equations of the solid gas interface layer,” *Acta Chim. Acad. Sci. Hungaricae*, vol. 69, pp. 311–317, 1971.
- [19] M. Thommes *et al.*, “Physisorption of gases, with special reference to the evaluation of surface area and pore size distribution (IUPAC Technical Report),” *Pure Appl. Chem.*, vol. 87, no. 9–10, pp. 1051–1069, 2015.
- [20] N. Casas, J. Schell, R. Pini, and M. Mazzotti, “Fixed bed adsorption of CO₂/H₂ mixtures on activated carbon: Experiments and modeling,” *Adsorption*, vol. 18, no. 2, pp. 143–161, 2012.

THE ROLE OF BECCS TO DELIVER NEGATIVE CO₂ EMISSIONS IN EUROPE

Lorenzo Rosa^{1*}, Daniel Sanchez², Marco Mazzotti¹

¹ Institute of Energy and Process Engineering, ETH Zurich, 8092 Zurich, Switzerland

² Department of Environmental Science, Policy, and Management, University of California, Berkeley, United States of America

* Corresponding author e-mail: lorosa@ethz.ch

Abstract

Bio-Energy with Carbon Capture and Storage (BECCS) is a key climate mitigation technology, which involves the capture and permanent sequestration of biogenic carbon dioxide (CO₂). To reach net-zero-CO₂-emissions by 2050, it is forecasted that many million tons of CO₂ will have to be sequestered through BECCS in Europe. There are different industrial processes that utilize biomass for bio-energy production, namely, pulp and paper mills, biogas facilities, incinerators, and biomass-fired power plants. Moreover, crop residues, organic food waste, and livestock manure could be utilized to transform biomass from a poor energy carrier to an efficient carbon drawdown carrier through BECCS. Here, we quantify the techno-environmental potential for biogenic carbon dioxide removal considering prospective BECCS opportunities that do not require purpose-grown bio-energy plantations. Combining process engineering with a bottom-up assessment, we find that there are 200 million tons CO₂ yr⁻¹ that could be deployed for biogenic carbon dioxide removal through BECCS in Europe. We find that this biogenic CDR potential is equivalent to 5% of 2018 total European greenhouse gas emissions. We find that 62 million tons of biogenic CO₂ yr⁻¹ are located within a distance of 300 km to prospective CO₂ storage sites, and therefore do not require long-distance CO₂ source-sink transport networks. We then determine to what extent the adoption of BECCS would allow to mitigate hard-to-abate emissions. We show that most European countries will not be able to reach climate-neutrality with domestic BECCS endowments and will likely need to resort to other CDR strategies and outsource biomass from other countries. Country-specific BECCS potential are still unknown and the proposed research has the potential to help decision makers to design suitable and appropriate climate policies. Because policy makers are investigating pathways to reach net-zero targets by 2050, the results of this proposed work could help to estimate the role that BECCS could have to reach net-zero targets by 2050.

Keywords: BECCS; Net-zero Emissions; Negative Emission Technologies.

1. Introduction

Atmospheric carbon dioxide removal (CDR) will likely play a critical role in climate mitigation and in reaching net-zero carbon emissions worldwide¹⁻⁸. CDR schemes, or negative emissions technologies (NET), are strategies whereby CO₂ is captured and removed from the atmosphere⁹⁻¹⁶. CDR strategies are receiving an increasing interest not only from the scientific community, but also from the international political community and the corporate world. For example, CDR is being considered by European countries to mitigate hard-to-abate carbon emissions and to reach net-zero-CO₂-emissions by 2050. Scenarios for CDR deployment consistent with climate goals involve gigatonne-scale deployment of Bio-Energy with Carbon Capture and Storage (BECCS) within the next decades^{17,18}. BECCS involves the capture and permanent sequestration of biogenic CO₂ produced during energy conversion from biomass^{13,14} and is widely considered due to its near-term feasibility, scalability, and ability to produce reliable bio-energy^{14,15}.

Creating vast bioenergy plantations could jeopardize food production, exacerbate water scarcity and have negative impacts on biodiversity and rural livelihood¹⁹⁻²². Technology developers and policymakers should ensure that BECCS operations reliably sequester CO₂ emissions and minimize unnecessary environmental impacts. There are different industrial processes that could avoid new bioenergy plantations and provide opportunities for CDR through BECCS, namely, pulp and paper mills, incinerators, wastewater treatment facilities, and biomass co-fired power plants²³⁻²⁹. Biogenic CDR could also be performed during biogas production from crop residues and household organic food waste^{24,25,30}. Moreover, biogenic CDR could be deployed by retrofitting biogas facilities currently treating livestock manure^{24, 30}.

2. Methods

In this study, we combine process engineering, with a bottom-up assessment to determine the techno-environmental potential of biogenic CDR in Europe considering prominent BECCS schemes. Specifically, we assessed the techno-environmental potential for

biogenic CDR (10⁶ tons CO₂ yr⁻¹) at 1 km resolution for 30 European countries (European Union countries, Switzerland, the United Kingdom, and Norway) considering different BECCS schemes (Figure 1).

For each BECCS scheme, biogenic CDR was assessed considering already existing point sources and distributed potential sources of biogenic CO₂.

We then designed BECCS supply chains for seven prominent sources for biogenic CDR considering bio-energy sources that would not require additional pressures on land and water resources through purpose grown bio-energy plantations. Using a bottom-up assessment, biogenic CDR was assessed considering already existing point sources and distributed potential sources of biogenic CO₂. For already existing point sources we considered: 1) pulp and paper mills; 2) waste-to-energy plants (or incinerators); 3) biomass co-fired power stations (or bio-power); and 4) urban wastewater treatment plants. For distributed potential sources we designed three BECCS schemes that could be potentially deployed to produce methane from 5) current crop residues and 6) currently collected household organic food waste; and produce methane from 7) collectible livestock manure.

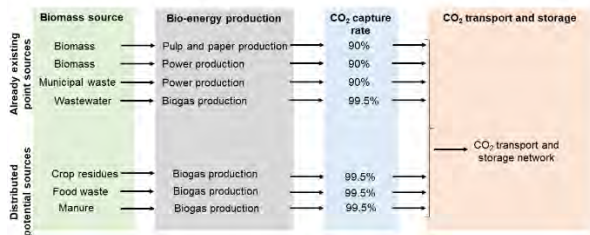


Figure 1: BECCS technology chains for seven prominent sources for biogenic CDR.

3. Results

Full results of this study are available at Rosa et al., 2021³¹. We find that there are 201 Mtons of biogenic CO₂ that could be deployed for CDR in Europe (Figure 2). We estimate that 65% of biogenic CDR potential is from existing point sources (pulp and paper mills, incinerators, bio-power plants, and wastewater treatment facilities), and 35% is from potential BECCS distributed sources (crop residues, food waste, and livestock manure). With 62 Mtons CO₂ yr⁻¹, pulp and paper facilities have the greatest potential for biogenic CDR from existing point sources, followed by waste-to-energy facilities (36 Mtons CO₂ yr⁻¹), biomass co-fired plants (31 Mtons CO₂ yr⁻¹), and wastewater treatment plants (1 Mtons CO₂ yr⁻¹) (Figure 3). Considering distributed potential biogenic BECCS sources, crop residues have the greatest potential for biogenic CDR (36 Mtons CO₂ yr⁻¹), followed by livestock manure (19 Mtons CO₂ yr⁻¹), and household organic food waste (18 Mtons CO₂ yr⁻¹) (Figure 2). Sweden, with 31 Mtons CO₂ per year, has the largest biogenic CDR potential among European countries, followed by Germany (28 Mtons CO₂ per year), the United Kingdom (24 Mtons CO₂ per year), Finland (23 Mtons CO₂ per year), and France (22 Mtons CO₂ per year).

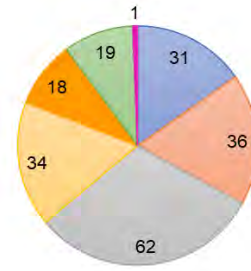


Figure 2: BECCS-specific biogenic CDR potentials in Europe (10⁶ tons CO₂ per year).

Assuming that 5% of 2018 emissions will need to be removed through CDR, we find that Europe has sufficient domestic BECCS potential to mitigate hard-to-abate emissions. However, under a low emissions reduction scenario (or 30% CDR), we find that Europe could only meet 16% of the CDR necessary to reach net-zero emissions with domestic BECCS resources. Some countries are better positioned to reach net-zero emissions with domestic BECCS endowments than others (Figure 3). In fact, we find that Sweden, Estonia, and Finland will be able to mitigate 5% and 30% of their emissions with domestic BECCS resources (Figure 3). Because of their large endowments, Switzerland, Portugal, and Austria could mitigate 5% of their 2018 emissions by sequestering biogenic CO₂ from already existing point sources (Figure 5b). By deploying full biogenic CDR from BECCS endowments, Germany, the United Kingdom, France, and Spain will be able to mitigate 5% of their emissions.

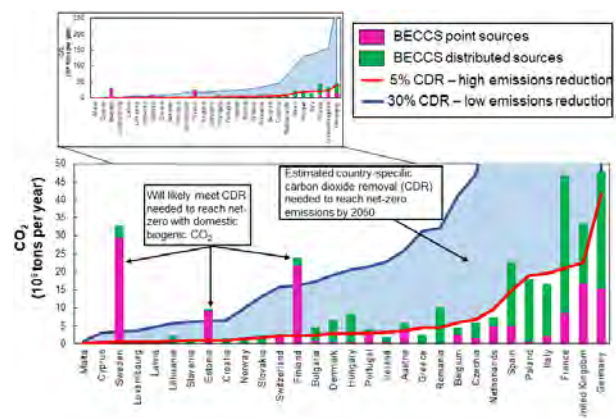


Figure 3. Comparison between domestic BECCS endowments and country-specific CDR quotas needed to reach net-zero emissions by 2050. Country-specific CDR quotas are assessed assuming that 5% to 30% of current total greenhouse gas emissions will need to be balanced with CDR to reach net-zero emissions by 2050.

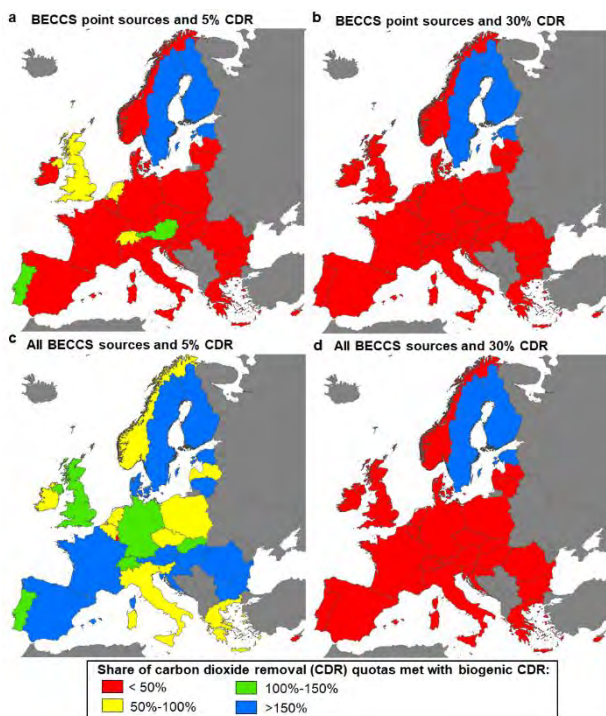


Figure 4. Map showing the share of CDR quotas that could be potentially met with domestic BECCS endowments. We considered four scenarios considering a combination among low emissions reduction (30% CDR), high emissions reduction (5% CDR), low BECCS adoption from biogenic point sources only, and high BECCS adoption from full deployment of domestic BECCS endowments.

By investigating BECCS potentials, this work may guide to identify the role of BECCS to deliver negative emissions through biogenic carbon dioxide removal in Europe.

References

- [1] Fuss, S., et al., 2018. Negative emissions—Part 2: Costs, potentials and side effects. *Environmental Research Letters*, 13(6), p.063002.
- [2] Peters, G.P. and Geden, O., 2017. Catalysing a political shift from low to negative carbon. *Nature Climate Change*, 7(9), pp.619-621.
- [3] Solano Rodriguez, B., Drummond, P. and Ekins, P., 2017. Decarbonizing the EU energy system by 2050: an important role for BECCS. *Climate Policy*, 17(sup1), pp.S93-S110.
- [4] Minx, J.C., Lamb, W.F., Callaghan, M.W., Fuss, S., Hilaire, J., Creutzig, F., Amann, T., Beringer, T., de Oliveira Garcia, W., Hartmann, J. and Khanna, T., 2018. Negative emissions—Part 1: Research landscape and synthesis. *Environmental Research Letters*, 13(6), p.063001.
- [5] Luderer, G., Vrontisi, Z., Bertram, C., Edelenbosch, O.Y., Pietzcker, R.C., Rogelj, J., De Boer, H.S., Drouet, L., Emmerling, J., Fricko, O. and Fujimori, S., 2018. Residual fossil CO₂ emissions in 1.5–2 C pathways. *Nature Climate Change*, 8(7), pp.626-633.
- [6] Rogelj, J. et al. in *Global Warming of 1.5 °C* (eds Masson-Delmotte, V. et al.) 93–174 (IPCC, 2019).
- [7] Realmonte, G., Drouet, L., Gambhir, A., Glynn, J., Hawkes, A., Köberle, A.C. and Tavoni, M., 2019. An inter-model assessment of the role of direct air capture in deep mitigation pathways. *Nature communications*, 10(1), pp.1-12.
- [8] Schreyer, F., Luderer, G., Rodrigues, R., Pietzcker, R.C., Baumstark, L., Sugiyama, M., Brecha, R.J. and Ueckerdt, F., 2020. Common but differentiated leadership: strategies and challenges for carbon neutrality by 2050 across industrialized economies. *Environmental Research Letters*, 15(11), p.114016.
- [9] Minx, J.C., et al., 2018. Negative emissions—Part 1: Research landscape and synthesis. *Environmental Research Letters*, 13(6), p.063001.
- [10] Kemper, J., 2015. Biomass and carbon dioxide capture and storage: A review. *International Journal of Greenhouse Gas Control*, 40, pp.401-430.
- [11] Sanchez, D.L., Johnson, N., McCoy, S.T., Turner, P.A. and Mach, K.J., 2018. Near-term deployment of carbon capture and sequestration from biorefineries in the United States. *Proceedings of the National Academy of Sciences*, 115(19), pp.4875-4880.
- [12] Bui, M., et al., 2018. Carbon capture and storage (CCS): the way forward. *Energy & Environmental Science*, 11(5), pp.1062-1176.
- [13] Hepburn, C., Adlen, E., Beddington, J., Carter, E.A., Fuss, S., Mac Dowell, N., Minx, J.C., Smith, P. and Williams, C.K., 2019. The technological and economic prospects for CO₂ utilization and removal. *Nature*, 575(7781), pp.87-97.
- [14] Sanchez, D.L., Nelson, J.H., Johnston, J., Mileva, A. and Kammen, D.M., 2015. Biomass enables the transition to a carbon-negative power system across western North America. *Nature Climate Change*, 5(3), pp.230-234.
- [15] Fajardy, M. and Mac Dowell, N., 2017. Can BECCS deliver sustainable and resource efficient negative emissions?. *Energy & Environmental Science*, 10(6), pp.1389-1426.
- [16] Fajardy, M., Chiquier, S. and Mac Dowell, N., 2018. Investigating the BECCS resource nexus: delivering sustainable negative emissions. *Energy & Environmental Science*, 11(12), pp.3408-3430.
- [17] IPCC *Special Report on Global Warming of 1.5 °C* (eds Masson-Delmotte, V. et al.) (WMO, 2018).
- [18] Van Vuuren, D.P., et al., 2018. Alternative pathways to the 1.5 C target reduce the need for negative emission technologies. *Nature climate change*, 8(5), pp.391-397.
- [19] Rosa, L., Reimer, J.A., Went, M.S. and D'Odorico, P., 2020. Hydrological limits to carbon capture and storage. *Nature Sustainability*, pp.1-9.
- [20] Rosa, L., Sanchez D., Realmonte G., Baldocchi D., and D'Odorico, P., 2021. The global water footprint of large-scale deployment of carbon capture and storage technologies under stringent climate policy. *Renewable and Sustainable Energy Reviews*. 138-110511.
- [21] Smith, P., et al., 2016. Biophysical and economic limits to negative CO₂ emissions. *Nature climate change*, 6(1), pp.42-50.
- [22] Heck, V., Gerten, D., Lucht, W. and Popp, A., 2018. Biomass-based negative emissions difficult to reconcile with planetary boundaries. *Nature climate change*, 8(2), pp.151-155.
- [23] Sanchez, D.L. and Kammen, D.M., 2016. A commercialization strategy for carbon-negative energy. *Nature Energy*, 1(1), pp.1-4.

- [24] Baker, S.E., Peridas, G., Stolaroff, J.K., Goldstein, H.M., Pang, S.H., Lucci, F.R., Li, W., Slessarev, E.W., Pett-Ridge, J., Ryerson, F.R. and Aines, R.D., 2019. *Getting to neutral: options for negative carbon emissions in California* (No. LLNL-TR-796100). Lawrence Livermore National Lab.(LLNL), Livermore, CA (United States). Available at: https://www-gs.llnl.gov/content/assets/docs/energy/Getting_to_Neutra1.pdf
- [25] Sandalow D, Aines R, Friedmann J, McCormick C, Sanchez D, 2020. Biomass carbon removal and storage (BiCRS) roadmap. ICEF. Available at: <https://www.icef-forum.org/roadmap/>
- [26] Onarheim, K., Santos, S., Kangas, P. and Hankalin, V., 2017. Performance and costs of CCS in the pulp and paper industry part 1: Performance of amine-based post-combustion CO₂ capture. *International Journal of Greenhouse Gas Control*, 59, pp.58-73.
- [27] Sagues, W.J., Jameel, H., Sanchez, D.L. and Park, S., 2020. Prospects for bioenergy with carbon capture & storage (BECCS) in the United States pulp and paper industry. *Energy & Environmental Science*, 13(8), pp.2243-2261.
- [28] Pour, N., Webley, P.A. and Cook, P.J., 2018. Potential for using municipal solid waste as a resource for bioenergy with carbon capture and storage (BECCS). *International Journal of Greenhouse Gas Control*, 68, pp.1-15.
- [29] Bui, M., Fajardy, M. and Mac Dowell, N., 2018. Bioenergy with carbon capture and storage (BECCS): Opportunities for performance improvement. *Fuel*, 213, pp.164-175.
- [30] Li, Y., Zhang, R., Liu, G., Chen, C., He, Y. and Liu, X., 2013. Comparison of methane production potential, biodegradability, and kinetics of different organic substrates. *Bioresource technology*, 149, pp.565-569.
- [31] Rosa, L., Sanchez, D. and Mazzotti, M., 2021. Assessment of carbon dioxide removal potential via BECCS in a carbon-neutral Europe. *Energy & Environmental Science*. <https://doi.org/10.1039/D1EE00642H>

THE INFLUENCE OF AQUIFER GEOCHEMISTRY ON SALT PRECIPITATION DURING CO₂ INJECTION: INSIGHTS FROM 1D SIMULATIONS USING THE RAND ALGORITHM

Fernando de A. Medeiros¹, Erling H. Stenby¹, Wei Yan^{1*}

¹ Center for Energy and Resources Engineering, Department of Chemistry, Technical University of Denmark, 2800 Kongens Lyngby, Denmark

* Corresponding author e-mail: weya@kemi.dtu.dk

Abstract

CO₂ storage in saline aquifers is deemed as a feasible way to control the atmospheric levels of greenhouse gases. When CO₂ is injected in saline aquifers, several phenomena take place, such as multiphase fluid flow, adsorption and chemical reactions, which can in turn produce mineral phases that might risk the whole process. Thus, mathematical modelling of CO₂ storage in saline aquifers is a very complex task. In this work, we resort to the RAND algorithm for chemical and phase equilibrium (CPE), coupled with 1D material balance equations for multiphase fluid flow in porous media, to simulate the injection of CO₂ in saline aquifers. Two types of aquifers were studied: one with NaCl and water; and another one involving a more complex brine containing Na⁺, Mg²⁺, K⁺, Cl⁻, SO₄²⁻. We focused the analysis on salt precipitation, a phenomenon that takes place when dry CO₂ is injected into an aquifer. From the 1D-simulation and from phase equilibrium diagrams, we produced insights on the thermodynamic conditions that allow for salt precipitation, the typical flow patterns observed, and the precipitation of multiple salts. The analysis performed is intended as a systematic evaluation of the interplay between geochemistry and fluid flow, with a special focus on salt clogging. Furthermore, we have shown the applicability of the RAND algorithm to challenging conditions involving fluid flow and several reactions and mineral phases.

Keywords: Salt Precipitation, CO₂ storage, Saline Aquifers, Two-phase flow, Geochemistry

1. Introduction

The underground storage (UGS) of CO₂ is an important means to control the atmospheric level of greenhouse effect gases [1]. One of the steps in the development of safe and efficient CO₂ UGS processes is the mathematical modeling of CO₂ injection into geological formations [2, 3, 4], such as saline aquifers, where CO₂ should remain trapped for long periods.

However, many phenomena take place when CO₂ mixes with brines and interact with minerals present in the geological formations [2], significantly increasing the complexity of the CO₂ UGS simulations. Among these phenomena, chemical and phase equilibria (CPE) play a central role, and, because of that, many geochemical simulators capable of performing CPE calculations exist in literature [5, 6, 7, 8]. Among those, there is the class of RAND algorithms. This type of method is a non-stoichiometric CPE algorithm, originally developed for problems at constant temperature and pressure [9, 10, 11]. We have recently applied a version of this algorithm (the modified RAND [12]) to problems involving CO₂, brine and minerals [13, 14]. Furthermore, we have coupled it with other algorithms to simulate conditions beyond thermodynamic equilibrium [15].

In this work, we coupled the RAND method with an algorithm for the 1D-simulation of two-phase flow in porous media, via the implicit solving of mass balance equations [16], and we performed simulations of CO₂ injection into saline aquifers containing brines. We

studied two types of systems. First we studied a ternary system (NaCl, CO₂, H₂O), then we analyzed a complex brine (Na⁺, Mg²⁺, K⁺, Cl⁻, SO₄²⁻). By doing so, we tested the robustness of the RAND algorithm and, from the results issued, we obtained insights on the evolution of the 1D reservoir under continuous CO₂ injection.

The analyses performed here were especially focused on the salt clogging problem. Salt clogging is generally considered a nuisance typical of CO₂ injection in saline aquifers [17]. Several phenomena may play a role in salt clogging (capillary effects, perpendicular flow, etc.). Its driving force, however, is related to geochemistry: the drying of the aquifer brine by constant mixing with a CO₂-rich stream. Salt clogging can lead to reductions in injectivity and ultimately render the whole storage procedure inefficient [17, 18]. Several simulation works capable of capturing salt precipitation or focusing on understanding the phenomenon are present in literature. They vary from analytical solutions to two-phase flow equations [19] to simulations involving multiple dimensions, capillary effects [20]. Here, we focus the analysis on the thermodynamic conditions that allow for salt clogging to occur, and we investigate the interplay between geochemistry and the 1D flow pattern observed.

2. Methodology

2.1 The modified RAND Algorithm

The modified RAND algorithm is a non-stoichiometric chemical and phase equilibrium algorithm first described

by Paterson et al. [12]. It has been previously tested with various systems (hydrocarbons [12, 21], CO₂ and minerals [13, 14], and petrochemicals [22]), and it has also been extended to equilibrium specifications other than T and P [23, 24, 25].

In this work, the RAND method for closed systems at fixed T and P was used as the phase equilibrium core of an implicit algorithm to solve the multiphase material balance equations in porous media. Figure 1 shows a schematic representation of the problem. The reservoir is divided into a finite number of cells and CPE calculations are performed in each one of them. As a consequence of this coupling, the precipitation reactions and the mixing between brine and CO₂ are considered equilibrated, i.e. instantaneous w.r.t the time scale of the simulation.

Furthermore, the RAND algorithm was utilized to generate the phase diagrams presented here (Figure 2, 14, and similar ones). A methodology similar to the reaction path analysis was used in those cases [15, 26], which consists in a stepwise addition of a given mineral. Then, a phase equilibrium calculation is performed at the new conditions to observe how the system responds to the mineral addition.

2.2 The 1D Simulation Algorithm

Multiphase flow into a 1D reservoir is described in this work by the following equation:

$$\phi \frac{\partial}{\partial t} \left(\sum_{j=1}^{N_F} x_{ij} \rho_j s_j \right) + \frac{\partial}{\partial x} \left(\nu \sum_{j=1}^{N_F} x_{ij} \rho_j f_j \right) = 0 \quad (1)$$

in which ϕ represents the porosity of the reservoir, x_{ij} represents the molar fraction of component i in phase j , ν represents the velocity of the fluid flow, ρ_j is the density of phase j , s_j is the saturation of phase j and f_j is the fractional flow function value of phase j . This equation is valid for all N_C components, and the summations in phase run until they reach the total number of fluid phases N_F . This equation can be made dimensionless by the introduction of dimensionless time (τ , measured in pore volumes injected, p.v.i.); dimensionless distance (χ) and dimensionless velocity (ν_D). It becomes:

$$\frac{\partial G_i}{\partial \tau} + \frac{\partial F_i}{\partial \chi} = 0 \quad (2)$$

with

$$G_i = \sum_{j=1}^{N_F} x_{ij} \rho_j s_j; \quad F_i = \nu_D \sum_{j=1}^{N_F} x_{ij} \rho_j f_j \quad (3)$$

Equation (1) is obtained after the assumption of Darcy flow and the same value of pressure for all fluid phases. The solution of Equation (2) is self-similar, i.e., the solution for both τ and χ can be obtained from a single variable, the so-called similarity variable $\zeta = \chi/\tau$. The fractional flow function f_j is obtained as

$$f_j = \frac{k_{r,j}/\mu_j}{\sum_{j=1}^{N_F} k_{r,j}/\mu_j} \quad (4)$$

with constant viscosities and relative permeabilities of a fluid phase j ($k_{r,j}$) calculated as in Yan et al. [16]. This equation is solved using the implicit algorithm described by Yan et al. [16]. In this algorithm, the fluid flow equation is solved separately from the CPE part. The effect of salt precipitation in our analysis is accounted for only in the porosity of a cell. The values of porosity reduction (ϕ/ϕ_0) presented here were calculated as a function of the volume of each solid phase k (V_k) and the volume of the cell (V_{cell}):

$$\frac{\phi}{\phi_0} = V_{cell} - \frac{\sum_{k=1}^{N_S} V_k}{V_{cell}} \quad (5)$$

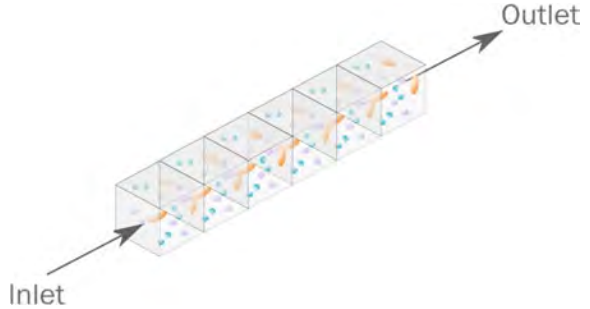


Figure 1: Schematic representation of the 1D simulation. The reservoir is split into different cells where the CPE calculations are performed. Flow from one cell to the other is taken into account by Equation 1.

Table 1: Simulation parameters.

Reservoir and Fluid Properties	Value
Residual saturation (brine)	0
Residual saturation (CO ₂ -rich fluid)	0
Viscosity brine / (Pa.s)	5×10^{-4}
Viscosity CO ₂ -rich fluid / (Pa.s)	1×10^{-4}
Temperature / K	328.15
Pressure / MPa	17.9
Numerical Scheme Properties	Value
Number of cells	300
Number of time steps	3000
Number of moles injected per time step	0.1
Total mole number in the initial cell	1

3. Results

3.1 Benchmark Simulation (NaCl + CO₂ + H₂O)

In the first set of results, we analyze the CO₂ addition to a reservoir containing NaCl and water. This simulation works as a benchmark for the rest of this study, as it establishes the main parameters and features of the 1D simulation. The results for the ternary system have three parts. First, we present the ternary diagram of the NaCl + CO₂ + H₂O system at the conditions of temperature and pressure used in the 1D simulations. From this initial analysis, we can identify all the possible thermodynamic states of the brine and the CO₂-rich fluid phase, and they can be interpreted as the underlying set of possible thermodynamic states in which the 1D simulation unfolds.

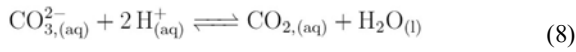
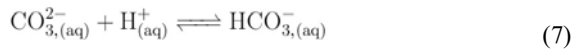
Second, we set an initial brine molality and the composition of the injected CO₂-rich fluid, and we show

how the fluid properties are distributed along the 1D-reservoir w.r.t. dimensionless time and space.

Third and finally, we analyze the interplay between the results observed in the first part and in the second part, i.e., the relation between the thermodynamic behavior of the system and the general aspect of fluid flow in the reservoir. By doing so, we were able to identify several typical zones in the 1D simulation.

3.1.1. The Ternary Diagram

The first system studied can be considered a ternary one (NaCl + CO₂ + H₂O), even though several reactions take place. The following reactions were considered in the aqueous phase:



The following interfacial reaction accounts for NaCl precipitation as a solid (halite):



The parameters used to model the reactions were taken from PHREEQC's Pitzer database [5]. The CO₂-rich fluid phase was modeled by the PR equation of state [27] with binary interaction parameters set to zero. The Pitzer model [28], implemented as in Felmy and Weary [29], with interaction parameters from PHREEQC [5], was used for the brine. The density of the CO₂-rich fluid was obtained via PR-EoS, and the density of the brine was calculated using the approach of Apello et al. [30].

The application of the Gibbs phase rule to the system shows that the number of degrees of freedom (F) is a function of the number of components (N_C), number of phases (N_P), number of equilibrated reactions (N_R), number of phases containing ions (EL)

$$F = N_C - N_R - EL - N_P + 2 = 6 - N_P \quad (10)$$

However, Na⁺ and Cl⁻ can only be added together as a single component and disappear from the brine as halite following the same stoichiometry. This has essentially added a constraint on the ratio between Na⁺ and Cl⁻, reducing F by 1, leading to a final value of $5 - N_P$. This means that if 3 phases are present at a fixed set of T and

P , the system is completely determined. Furthermore, if 2 phases are present, there is only one degree of freedom left. In the single phase case, two extra intensive variables have to be specified to determine the state of the system. Thus, despite the large number of species present, this system can be virtually considered as a ternary one, as if no reaction or aqueous speciation was taken into account.

Figure 2 (a) shows the brine thermodynamic condition as a function of the molality (per kilogram of water) of NaCl and the total molality of carbonic species. The color scheme represents the tangent plane distance (tpd) [31] of halite (solid NaCl), and the dotted line represents its equilibrium with the brine. The tangent plane distance of a phase is a measure of its saturation. Below the dotted line (blue region), halite is undersaturated (positive tpd), and more NaCl has to be added to the brine before it reaches equilibrium. Above the dotted line (red region), halite is supersaturated (negative tpd), and it naturally precipitates from brines in these conditions. The solid black line represents the solubility of CO₂ in the brine. If the brine has a total CO₂ molality higher than the black line at a given molality of NaCl, it will eventually split into two phases, being the composition of the new CO₂-rich fluid phase given by Figure 2 (b). This figure represents the molar fraction of water (x-axis) in the CO₂-rich fluid phase, which consists only of H₂O and CO₂, in equilibrium with a brine of a certain molality of NaCl (y-axis). This means that a brine – Figure 2(a) – at the black line is in equilibrium with a fluid phase – Figure 2(b) – both at the same molality of NaCl. Furthermore, the interception between the dotted and the black line in Figure 2 (a) represents a ternary invariable point (at fixed T and P) containing NaCl, a brine and a CO₂-rich fluid, these two having their compositions established by Figure 2 (a) and (b), respectively.

3.1.2. Profiles along the Reservoir

We simulated the injection of a CO₂-rich fluid containing 0.001 of water (mole fraction) into an aquifer containing a brine of 2 molal NaCl (total 4 molal of dissolved Na⁺ and Cl⁻ in water). The saturation and molality profiles at 0.576 p.v.i. are displayed in Figure 3.

3.1.3. Interplay between Simulation Zones and Thermodynamics

Figure 4 was obtained from the analysis of the saturation and molality profiles observed in all simulated values of p.v.i. for the whole reservoir. The x-axis of Figure 3

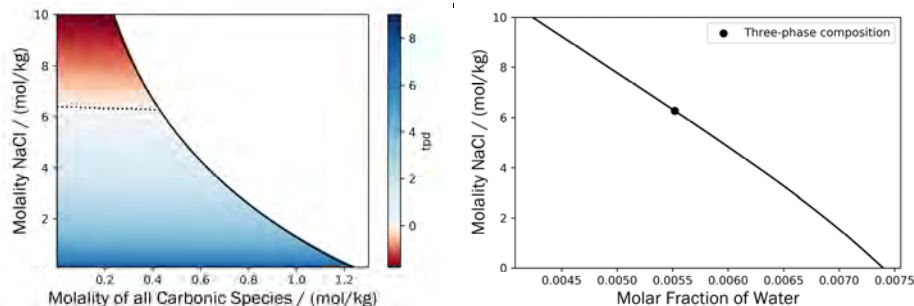


Figure 2: (a) Ternary phase diagram of the NaCl + CO₂ + H₂O system at 328.15 K and 176.659 atm; (b) composition of the CO₂-rich fluid in equilibrium with the brine depicted in (a).

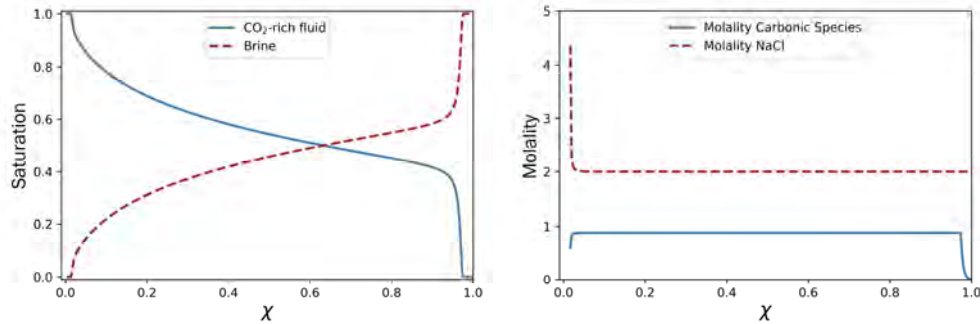


Figure 3: Saturation (a) and molality (b) profiles at 0.576 p.v.i.

(dimensionless distance) corresponds to the y-axis of Figure 4, and the x-axis of Figure 4 is the juxtaposition of the different time steps of the simulation (i.e. different values of p.v.i.). From Figure 4, we see that the simulation can be divided into five different zones. Zone A has just one phase and it corresponds to the unswept brine, i.e., the change in brine composition is not observable to the machine precision level. This zone should not appear in the analytical solution. Zone B corresponds to a one phase region containing a brine that has already undergone a composition change, but it is still not saturated in CO₂. This zone is characterized by a steep increase in CO₂ molality (Figure 3(b) close to $\chi=1$). Zone C corresponds to the two-phase region containing both brine and the CO₂-rich fluid. In this zone, the saturation of the brine reduces, and we see a similar development to Figure 3 from close to $\chi=1$ to close to $\chi=0$. Zone D is very narrow and corresponds to a three-phase region. In this zone, precipitation of solid NaCl has already taken place and the brine drying is in its late stages. Since the equilibrium assumption is used in the simulation, this three-phase zone is very narrow and corresponds to just a single cell for a given time step, and it only moves forward in χ once the brine has evaporated completely. Finally, we have Zone E, which is the dry-out zone, containing halite and CO₂-rich fluid. This zone is characterized by a marked porosity reduction (around 0.4% at 3.46 p.v.i., Figure 5). Since the two phases present do not interact, no further changes w.r.t. the system variables occur in Zone E. The boundaries of the zones correspond to different fronts, whose velocities can be determined from Figure 4, as $\xi_F = \chi_F / \tau_F$. Hence, the state of a cell at a certain time (τ) and position (χ) can be inferred by comparison of dimensionless variable of the cell ($\xi = \chi / \tau$) to the front velocities.

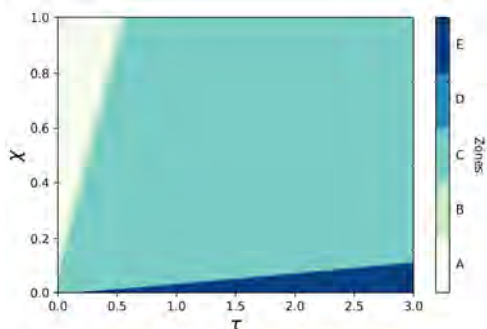


Figure 4: Different zones of the benchmark simulation w.r.t. space (χ) and time (τ).

The simulation can be better understood if we plot the different zones from Figure 4 in the ternary diagram. In Figure 6, one can see the thermodynamic state of every simulation cell over the ternary diagram from Figure 2 (a). Zone A corresponds to a dot in the y-axis marking the initial brine molality of 2 molal NaCl. As the fluid flow brings carbon-containing species to the brine, the thermodynamic state of the system moves almost as a straight line until it reaches the solubility limit of CO₂ (full black line).

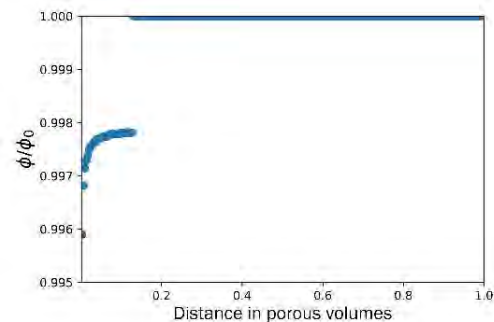


Figure 5: Porosity decrease w.r.t. to reservoir distance χ at 3.46 p.v.i. (benchmark simulation).

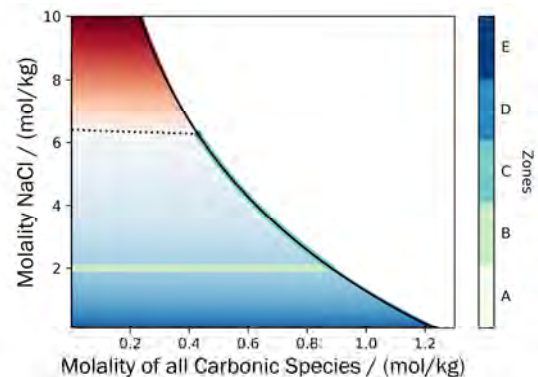


Figure 6: Thermodynamic path of the different zones of the benchmark simulation.

The pale green straight line connecting those two limits corresponds to the thermodynamic states within Zone B. As soon as the system reaches the solubility line of CO₂, it enters Zone C, which moves along the solubility line, until it reaches equilibrium with halite (the dotted line) and originates Zone D, containing three phases. Finally, Zone E cannot be represented in this plot, since the brine is no longer present. Figure 6 shows that some

characteristics of the 1D simulation can be inferred from a simple ternary diagram, including the thermodynamic path of the 1D simulation and the thermodynamic state of each cell at a certain pair of χ and τ .

3.2 Sensitivity Analysis: Injected Fluid Composition

Based on the analysis in Section 3.1, we proceed to analyze how the composition of the injected fluid affects the general behavior of the simulation. We selected three values of water composition in the CO₂-rich injected fluid (0.006, 0.007 and 0.01 in molar fraction) and compared their results to the benchmark one from section 3.1 (0.001). None of the three new simulations generated the same five zones as in the benchmark one. They produced only three zones, without any NaCl precipitation. No obvious changes were observed w.r.t. the front velocities.

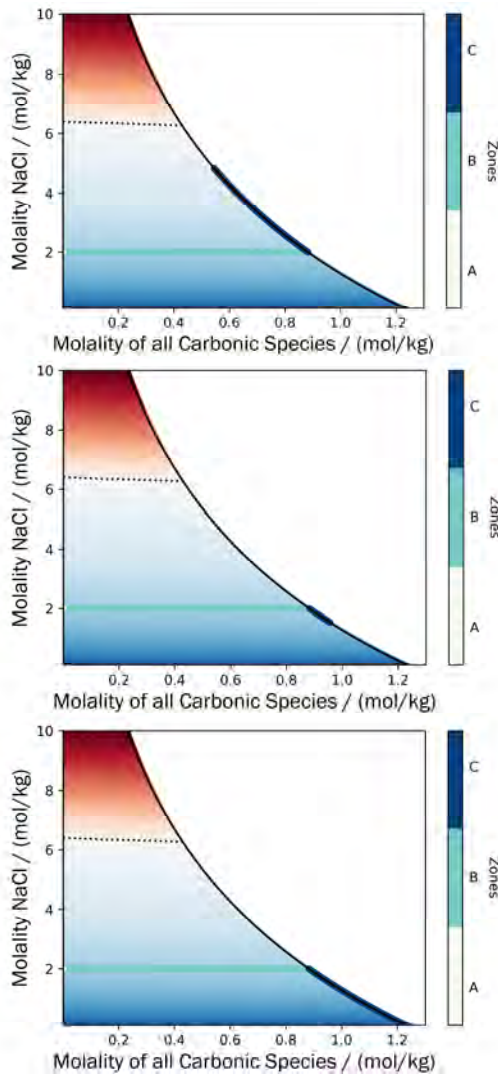


Figure 7: Thermodynamic path of the simulations with different compositions of the injected fluid: (a) 0.006 mole fraction of water; (b) 0.007 mole fraction of water; and (c) 0.01 mole fraction of water.

A better understanding of this behavior is obtained by analyzing the thermodynamic path (Figure 7). The CO₂-rich fluid composition plays a major role in the drying of the brine. The composition of 0.006 leads to brine concentration, which is not strong enough to ever reach salt precipitation – Figure 7 (a). The injection of compositions of 0.007 and 0.01 dilute the brine, the former stopping at a certain value of NaCl molality (Figure 7 (b)) and the latter washing out completely any solute in the brine (Figure 7 (c)).

The different thermodynamic paths can be explained by the composition of the CO₂-rich phase in equilibrium with the brine. Figure 8 shows four different ranges of wetness for the injected CO₂-rich phase at fixed T and P for an initial brine composition of 2 molal. Range W corresponds to the range of compositions that lead to salt clogging. They include all compositions dryer than the three-phase equilibrium composition (blue dot). Range X corresponds to a range of wetness that concentrates the brine, but stops until the brine reaches its equilibrium molality w.r.t. the injected fluid. This range encompasses compositions between the three-phase equilibrium one (blue dot) and the two-phase equilibrium at the molality of the initial brine (yellow dot). Range Y corresponds to a humid injection fluid, which dilutes the brine, until the brine reaches a molality in equilibrium with the injected fluid. The range is bounded by the two-phase equilibrium composition at the initial brine molality (yellow dot) and the CO₂ composition when in equilibrium with pure water (orange dot). Range Z represents a CO₂ stream which is supersaturated with water and washes out completely all solutes in the brine. All compositions higher than the composition of the CO₂-rich fluid in equilibrium with pure water belong to this range, i.e. CO₂ supersaturated with water. The saturation profiles at late stages of the simulation displayed in Figure 9 can give us an idea of how the fluid flow responds to the change in composition of the injected fluid. The composition of 0.001 (range W) leads to a sharp saturation front that reaches 1. The composition of 0.006 (range X) will eventually lead to the complete vanishing of the brine ($s_g=1$), but there is no sharp front or salt precipitation. The steep increase in saturation might be attributed to the reducing CO₂ solubility as the brine gets more concentrated in NaCl. The composition of 0.007 also eventually leads to the vanishing of the brine, without any salt precipitation. One can also see a slight tendency of decrease in the CO₂-rich fluid saturation, probably due to the increase in CO₂ solubility as the brine is diluted. Finally, the composition of 0.01 (range Z) does not lead to the vanishing of the brine. Rather, it tends to a saturation plateau around $s_g=0.94$. This is because the injected fluid is already saturated in water and an aqueous phase naturally appears. It follows from the analysis that the injected fluid composition that leads to salt precipitation is a function of the geochemistry of the system (i.e., T , P and initial brine composition), and the saturation profiles observed are a function of the possible thermodynamic states of the system.

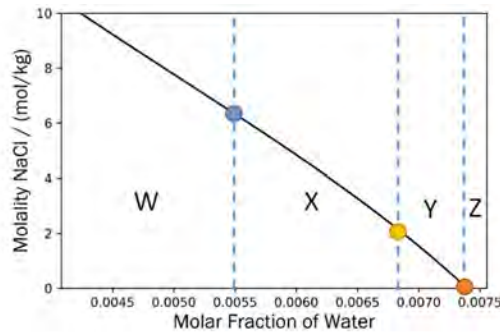


Figure 8: Different water fraction regions in the injection fluid for a brine at 2 molal NaCl.

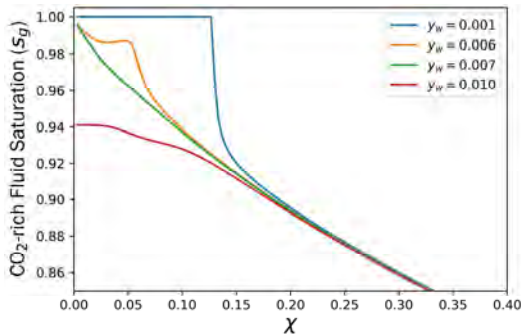


Figure 9: Typical saturation profiles according to the composition of the injected fluid.

3.3 Sensitivity Analysis: Initial Brine Molality

The initial molality of an aquifer brine has been regarded as one of the most important parameters in the salt clogging phenomenon [17]. Here, we have performed a sensitivity analysis by selecting two different initial brine molalities (4 and 6 molal of NaCl) and we compared it to the benchmark one (2 molal).

No major changes were observed in the overall results of the simulation. The same five zones (A, B, C, D and E) are present, with some minimal changes to their front velocities. The variable that was most influenced by the change in molality was porosity. Higher values of molality result in larger porosity reductions, as seen in Figure 10, in comparison to the benchmark one (Figure 5). The molalities of 2, 4 and 6 led to maximum porosity reductions of around 0.4%, 0.8%, 1.4%, respectively. Even though the porosity changes are not large, it has

been shown that even minor changes in porosity can lead to important reductions in permeability [17, 18], which the simulations we have performed here were not capable of capturing. In addition, the simulations were performed at residual saturations of 0 for both the brine and the CO₂-rich fluid and, therefore, the reduction might be more drastic in real cases.

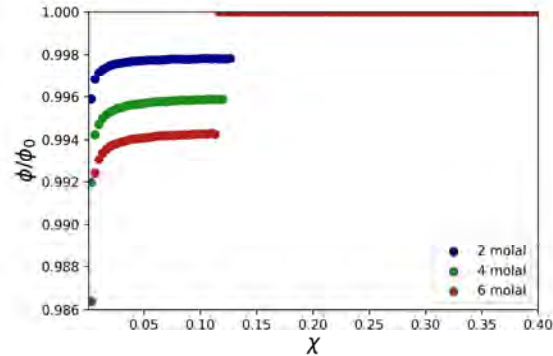


Figure 10: Porosity decrease w.r.t. to reservoir distance χ at 3.46, 3.40 and 3.31 p.v.i. for initial brine molality of 2, 4 and 6 molal of NaCl, respectively.

3.4 Analysis of a Complex Brine

In this part, we apply the methodology we have discussed for the NaCl + CO₂ + H₂O system to a more complex brine containing the following mole ratio of elements: 0.4 Na⁺, 0.002 K⁺, 0.02 Mg²⁺, 0.44196 Cl⁻ and 0.00002 SO₄²⁻. All parameters needed were taken from the Pitzer database from PHREEQC [5]. Many solids can precipitate from it. The construction procedure of the pseudo-ternary phase diagram (Section 3.4.1) allowed for the precipitation of all available minerals in PHREEQC that involve the five ionic species mentioned. After the identification of the ones that actually precipitated, the list of possible minerals was shortened to four: halite, carnallite, bischoffite and kieserite.

3.4.1. The Pseudo-Ternary Diagram

As in the previous case, we performed here a reaction path analysis [13, 26], using the RAND algorithm. The complex brine has several anions and cations, but the system can still be represented in a ternary manner, as

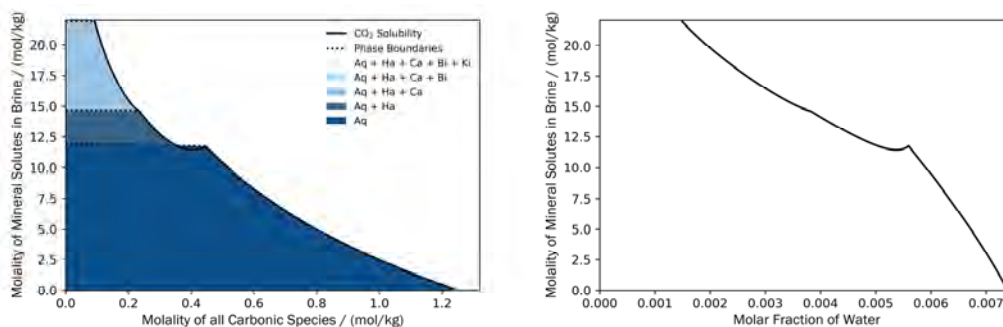


Figure 11: (a) Pseudo-ternary phase diagram of the complex brine; (b) Composition of the CO₂-rich fluid in equilibrium with the brine from (a).

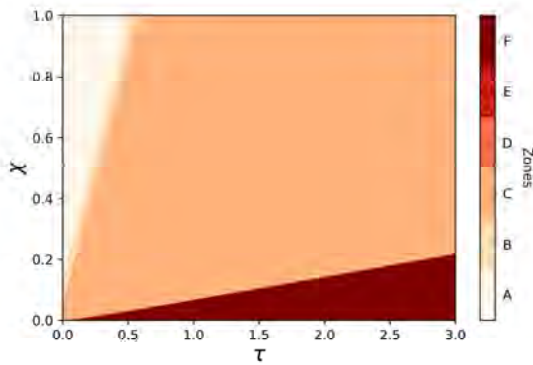


Figure 12: Different zones of the real brine simulation w.r.t. space (χ) and time (τ) (analogous to Figure 4).

only the amount of carbonic species and water changes due to CO₂ injection and drying. However, now, several different minerals can precipitate and they follow a certain order of appearance w.r.t. to the drying of the brine. The mineral composition of the whole system (solid phases included) does not change, but once precipitation of a given salt starts, the mineral proportions in the brine change. In Figure 11 (a) we see the pseudo-ternary diagram of the complex brine. There is a region at lower molalities in which only an aqueous phase (Aq) is present. As the molality increases, the system crosses the first phase boundary (dotted line) and halite (Ha) precipitates. From this point onwards, the mineral proportions in the brine no longer correspond to the global one. As water is further removed, carnallite (Ca) precipitates, followed by Bischoffite (Bi) and Kieserite (Ki), ending in a very small 5-phase region. The solid black line represents the solubility of CO₂ in the brine phase. Figures 11 (b) shows the water molar fraction of the CO₂-rich fluid (x -axis) in equilibrium with a mineral system of molality given by the y -axis.

3.4.2. The Flow Variables and the Different Zones in a Complex Brine

The 1D simulation results are presented in Figure 12. In the NaCl example, 5 zones were present. Here, 6 zones were observed. Zone A, B and C have the same meaning as before, i.e., unswept brine, zone of molality increase in CO₂ in the single phase, and two-phase flow, respectively. Zone D represents the precipitation of halite and it is immediately followed by Zone E, which is a four-phase zone (brine, CO₂-rich fluid, halite and carnallite). Since the amounts of bischoffite and kieserite are very small, no precipitation front for those two phases was observed. They only appeared in the dry-out zone (Zone F), which here consists of the CO₂-rich fluid, halite, carnallite, bischoffite and kieserite. Regarding the front velocities of the different zones, we see no major changes w.r.t. to Zone A, B and C, when compared to the NaCl benchmark case (Figure 4). Halite precipitation front, however, is faster here than it was before ($2/30 > 1/30$), even though the molality of total solutes in water was the same at the beginning of the simulation (4 molal of dissolved ions), and this is probably due to a decrease in halite solubility in the presence of other solutes (salting

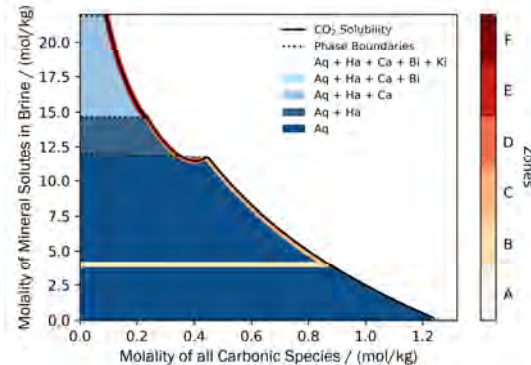


Figure 13: Thermodynamic path of the different zones of the real brine simulation (analogous to Figure 6).

out effect). From Figure 11 (a), we see that halite starts precipitating at around 12 molal of total dissolved ionic species (6 molal of NaCl, i.e., 6 molal of Na⁺ and 6 molal of Cl⁻), whereas in the real brine it starts around 11 molal.

The plotting of the simulation zones on top of the pseudo-ternary diagram (Figure 13) reveals the regions that are hard to see in Figure 12. Zone A is again a dot in the y -axis marking the initial brine molality. As CO₂ is added to the brine, a straight line appears until the system achieves CO₂ solubility (Zone B). The system moves along the solubility line until halite precipitates (Zone C). After halite precipitation, there is a major change in the solubility curve and the system enters Zone D. Zone D goes on until carnallite precipitates, at the beginning of Zone E. Zone F is not plotted in the diagram, as the brine has evaporated completely.

The porosity profile at 3.55 pvi reveals an increase in porosity reduction when compared to the benchmark simulation (Figure 14). There are two main causes for this. One is that more halite (the major constituent of the complex brine) precipitates as its solubility is reduced and the other one is the higher molar volumes of the other mineral phases, especially carnallite, the second most abundant mineral. In addition, the plot presents several numerical fluctuations. This is probably because the trace amounts of kieserite and bischoffite are close to machine precision.

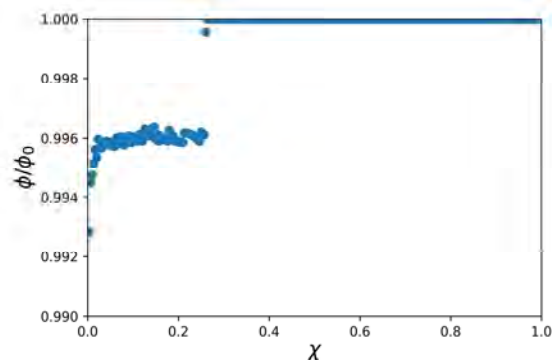


Figure 14: Porosity decrease w.r.t. reservoir distance (χ) at 3.55 p.v.i. (complex brine).

4. Conclusions

In this work, we have successfully coupled the RAND CPE algorithm with an implicit solver for the 1D material balance equations governing the two-phase flow in porous media (Equation 1) and from those simulations, we obtained insights on the relation between geochemistry and fluid flow in a saline aquifer.

The results show that the core equilibrium algorithm is robust and suitable for compositional simulation. It was tested under challenging conditions, with many phases present, both solid and fluid. The algorithm also succeeded in calculating the precipitation of minerals present at very small amounts in the brine and the results are sound from a geochemical perspective.

The results for the NaCl + CO₂ + H₂O and for the complex brine provide a systematic approach to assess salt clogging conditions in different formation waters. From this simple analysis, we can infer the composition of the injected fluid that lead to precipitation, the most important features of fluid flow, the different mineral phases that can appear, and the relation between fluid flow and geochemistry.

Acknowledgment

The study was carried out under “modelling of CO₂ induced near wellbore precipitation phenomena” funded by Energy Cluster Denmark.

References

- [1] IPCC Special Report on Carbon Dioxide Capture and Storage, Technical Report, IPCC, 2005.
- [2] X. Jiang, A review of physical modelling and numerical simulation of long-term geological storage of CO₂, Applied Energy 88 (2011) 3557–3566.
- [3] A. N. J. Bear, J. Bensabat, Geological Storage of CO₂ in Deep Saline Formations, volume 29, 2017.
- [4] P. Liu, T. Zhang, S. Sun, A tutorial review of reactive transport modeling and risk assessment for geologic CO₂ sequestration, Computers and Geosciences 127 (2019) 1–11.
- [5] D. L. Parkhurst, C. A. J. Appelo, Description of input and examples for PHREEQC version 3: a computer program for speciation, batch-reaction, one-dimensional transport, and inverse geochemical calculations, Technical Report, Reston, VA, 2013.
- [6] T. J. Wolery, EQ3/6, a Software Package for Geochemical Modeling of Aqueous Systems, Technical Report, Lawrence Livermore National Lab., Livermore, CA, 1992.
- [7] D. A. Kulik, T. Wagner, S. V. Dmytrieva, G. Kosakowski, F. F. Hingerl, K. V. Chudnenko, U. R. Berner, GEM-Selektor geochemical modeling package: Revised algorithm and GEMS3K numerical kernel forcoupled simulation codes, Computational Geosciences 17 (2013) 1–24.
- [8] T. Xu, N. Spycher, E. Sonnenthal, TOUGHREACT User's Guide: A Simulation Program for Non-isothermal Multiphase Reactive Transport in Variably Saturated Geologic Media, version 2.0, Technical Report October, Earth Sciences Division, Lawrence Berkeley National Laboratory, Berkeley, CA, 2004.
- [9] S. R. Brinkley, Calculation of the equilibrium composition of systems of many constituents, The Journal of Chemical Physics 15 (1947) 107–110.
- [10] W. B. White, S. M. Johnson, G. B. Dantzig, Chemical equilibrium in complex mixtures, The Journal of Chemical Physics 28 (1958) 751–755.
- [11] H. Greiner, An efficient implementation of Newton's method for complex nonideal chemical equilibria, Computers and Chemical Engineering 15 (1991) 115–123.
- [12] D. Paterson, M. L. Michelsen, E. H. Stenby, W. Yan, New formulations for isothermal multiphase flash, Society of Petroleum Engineers - SPE Reservoir Simulation Conference 2017 (2017) 1947–1964.
- [13] F. d. A. Medeiros, E. H. Stenby, W. Yan, RAND-Based Geochemical Equilibrium Algorithms with Applications to Underground Geological Storage of CO₂, submitted to Advances in Water Resources (2021).
- [14] C. Tsanas, E. H. Stenby, W. Yan, Calculation of multi-phase chemical equilibrium in electrolyte solutions with non-stoichiometric methods, Fluid Phase Equilibria 482 (2019) 81–98.
- [15] F. d. A. Medeiros, W. Yan, E. Stenby, Modified RAND Algorithms for Multiphase Geochemical Reactions, in: ECMOR XVII, European Association of Geoscientists & Engineers, 2020, pp. 1–15.
- [16] W. Yan, M. L. Michelsen, E. H. Stenby, Calculation of minimum miscibility pressure using fast slimtube simulation, Proceedings - SPE Symposium on Improved Oil Recovery 1 (2012) 386–401.
- [17] R. Miri, H. Hellevang, Salt precipitation during CO₂ storage - A review, International Journal of Greenhouse Gas Control 51 (2016) 136–147.
- [18] Y. S. Jun, D. E. Giammar, C. J. Werth, Impacts of geochemical reactions on geologic carbon sequestration, Environmental Science and Technology 47 (2013) 3–8.
- [19] M. Noh, L. W. Lake, S. L. Bryant, A. Araque-Martinez, Implications of coupling fractional flow and geochemistry for CO₂ injection in aquifers, SPE Reservoir Evaluation and Engineering 10 (2007) 406–414.
- [20] L. André, Y. Peysson, M. Azaroual, Well injectivity during CO₂ storage operations in deep saline aquifers - Part 2: Numerical simulations of drying, salt deposit mechanisms and role of capillary forces, International Journal of Greenhouse Gas Control 22 (2014) 301–312.
- [21] D. Paterson, W. Yan, M. L. Michelsen, E. H. Stenby, Multiphase isenthalpic flash: General approach and its adaptation to thermal recovery of heavy oil, AIChE Journal 65 (2019) 281–293.
- [22] C. Tsanas, E. H. Stenby, W. Yan, Calculation of Multiphase Chemical Equilibrium by the Modified RAND Method, Industrial and Engineering Chemistry Research 56 (2017) 11983–11995.
- [23] D. Paterson, Flash Computation and EoS Modelling for Compositional Thermal Simulation of Flow in Porous Media, Springer Theses, Springer International Publishing, 2019.
- [24] D. Paterson, M. L. Michelsen, W. Yan, E. H. Stenby, Extension of modified RAND to multiphase flash specifications based on state functions other than (T,P), Fluid Phase Equilibria 458 (2018) 288–299.
- [25] F. d. A. Medeiros, E. H. Stenby, W. Yan, State function-based flash specifications for open systems in the absence or presence of chemical reactions, AIChE Journal 67 (2021).
- [26] L. Marini, Geological Sequestration of Carbon Dioxide: Thermodynamics, Kinetics, and Reaction Path Modeling, 1st ed., Elsevier, 2007.
- [27] D.-Y. Peng, D. B. Robinson, A New Two-Constant Equation of State, Industrial & Engineering Chemistry Fundamentals 15 (1976) 59–64.
- [28] K. S. Pitzer, Thermodynamics of Electrolytes. I. Theoretical Basis and General Equations, The Journal of Physical Chemistry 77 (1973) 268–277.
- [29] A. R. Felmy, J. H. Weare, The prediction of borate mineral equilibria in natural waters: Application to Searles Lake, California, Geochimica et Cosmochimica Acta 50 (1986) 2771–2783.
- [30] C. A. Appelo, D. L. Parkhurst, V. E. Post, Equations for calculating hydrogeochemical reactions of minerals and gases such as CO₂ at high pressures and temperatures, Geochimica et Cosmochimica Acta 125 (2014) 49–67.
- [31] Michelsen, M. L., The isothermal flash problem. Part I. Stability, Fluid Phase Equilibria, 9 (1982) 1–19.

POTENTIAL IMPACT OF THE PREEM CCS PROJECT

Adriana Reyes-Lúa^{1*}, Stefania Osk Gardarsdottir¹, Max Biermann², Karin Lundqvist³, Simon Harvey²

¹ SINTEF Energy Research, Trondheim, Norway

² Chalmers University of Technology, Division of Energy Technology, Gothenburg, Sweden

³ Preem AB, Box 48084, 418 23 Gothenburg, Sweden

* Corresponding author e-mail: adriana.r.lua@sintef.no

Abstract

The ongoing Preem CCS project investigates opportunities for CO₂ capture from the Preem refineries in Lysekil and Gothenburg, Sweden, with focus on the Lysekil refinery. The consortium members of this Norwegian-Swedish collaboration are Preem AB, Chalmers University of Technology, SINTEF Energy Research, Equinor Energy and Aker Carbon Capture. In this paper, we present the alternative carbon capture and storage (CCS) value chains that are being studied, together with the potential amounts of direct CO₂ emissions from production that can be captured in each case. We also discuss potential cost reduction factors for CO₂ capture at the Preem refineries, such as heat integration within the refinery and economies of scale, which may also be of relevance for reduction of capture costs for other Northern Lights partners. The implementation of CO₂ capture in the Preem refineries will be an important step not only for Preem but also for Sweden to reach their climate neutrality goals.

Keywords: Preem, CCS, value chain analysis, Northern Lights, Longship

1. Introduction

The target for Sweden to reach net-zero emissions by 2045 at the latest [1], [2] is highly likely to require deployment of carbon capture and storage (CCS), especially in the process industry. The proximity to Norway, with its plans to realize a full-scale CCS chain by 2024 [3], [4], presents opportunities to implement CCS from Swedish emission sources despite the lack of established large-scale CO₂ storage capacity in Sweden.

The vision of Preem AB (Publ) – or Preem – is: To lead the transition towards a sustainable society. Preem is the largest oil refiner in the Nordic region, and one of the largest emitters of fossil CO₂ in Sweden, with emissions from production in the order of 2 Mt/y from the refineries in Lysekil and Gothenburg. Preem has a climate neutrality goal for 2045 [5], and values CCS as an important building block for achieving this vision. The geographical location of Preem's operations on the Swedish west coast imply that the company is a potential early mover among possible international CO₂ suppliers to the planned Norwegian CO₂ transport and storage infrastructure.

The Preem CCS project investigates opportunities for CO₂ capture from the Preem refineries in Lysekil and Gothenburg in Sweden, and subsequent transport of the captured CO₂ for permanent storage beneath the seabed on the Norwegian Continental Shelf, within the Northern Lights project, as shown in Figure 1. The consortium members are Preem AB and Chalmers University of Technology, in Sweden, and SINTEF Energy Research, Equinor Energy and Aker Carbon Capture, in Norway.



Figure 1: Location of the Lysekil and Gothenburg refineries, the onshore terminal at Naturgassparken in Øygarden and final sub-sea storage in the Norwegian Continental Shelf. The Preem CCS project considers ship transportation of liquefied CO₂.

Preem CCS activities include:

- Investigation of heat integration opportunities in the Lysekil refinery and design of compact heat exchangers for residual heat utilization.
- Simulation of the CO₂ capture and conditioning process for different scenarios.
- Identification and analysis of possible CCS value chain alternatives integrated into the Norwegian full-scale CCS project.

- On-site demonstration of CO₂ capture from the hydrogen production unit in the Lysekil refinery [6], [7].
- Identification of actions to overcome regulatory barriers for transborder ship transport and storage of CO₂.
- Establishing a roadmap for CO₂ emission reduction pathways at Preem in the context of Swedish national targets (net zero-carbon emissions in 2045) [1], [2].

This paper focuses on the first three points mentioned above, specifically on the CCS value chain scenarios and the role of heat integration as well the potential impact of realizing CO₂ capture from the Preem refineries.

1.1 Structure of the paper

This paper is structured as follows. In Section 2, we present a generalized CCS value chain, the CO₂ capture possibilities in the Preem refineries and an overview of the scenarios studied within the Preem CCS project. In Section 3, we put into perspective the potential impact of Preem CCS within Sweden and in the Northern Lights project by comparing the potential CO₂ capture from the Preem refineries to the Longship project, which will implement CO₂ capture from the Norcem cement plant in Brevik and (probably) from the Fortum Oslo Varme (FOV) waste-to-energy plant. Section 4 presents some final comments.

2. CO₂ capture possibilities at Preem refineries

2.1 Emissions baseline

The CO₂ emissions baseline will be used to estimate the potential reduction in direct CO₂ emissions from production that could result from further development based on this project. In 2019 there was a planned 67-day shutdown at the Lysekil refinery [5], and therefore the emissions in 2019 were lower than in a typical year. For this reason, to establish the emissions baseline we consider CO₂ emissions data from all stacks at Lysekil in 2018, which were 1.702 Mt CO₂. Considering direct CO₂ emissions from production, the refinery in Gothenburg emitted 570 kt CO₂ in 2019 and 536 kt CO₂ in 2018 [5]. Considering 2019 data for the refinery in Gothenburg and 2018 for the refinery in Lysekil, the total emissions baseline for the two refineries is 2.272 Mt CO₂/y.

2.2 The Preem CCS value chain

The different CCS value chains evaluated within the Preem CCS project consider CO₂ capture from the Preem refineries in Sweden. The study considers CO₂ capture from the flue gases using an amine absorption process. Two different solvents are considered for modeling the CO₂ capture process: monoethanolamine (MEA) and a blend of piperazine/amino-methyl-propanol (PZ/AMP), suggested as a new benchmark solvent by IEAGHG/CSIRO [8], [9]. Captured CO₂ is then compressed and liquefied, conditioning it for ship transport to the Northern Lights facilities at

Naturgassparken, for permanent sub-sea storage in the Norwegian Continental Shelf. Moreover, the effect on costs of selecting 15 bar or a reduced, 7 bar, transport pressure is also investigated [10]. Figure 2 depicts the main building blocks for the CCS value chains to be analyzed within Preem CCS. Note that the CO₂ capture process is assumed to predominantly utilize heat recovered from the refinery and a heat integration study is being performed within the project.

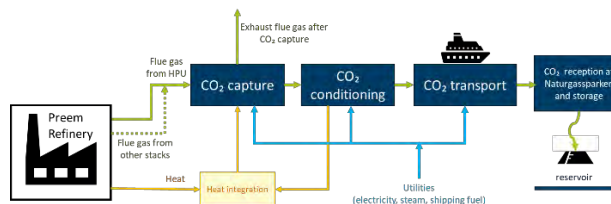


Figure 2: Generic block structure of the proposed CCS value chains evaluated in the Preem CCS project.

2.3 CO₂ capture scenarios

For the CCS chain analysis, several scenarios are evaluated, considering CO₂ capture from both single and multiple sources at the refinery in Lysekil as well as the refinery in Gothenburg. Ship-based transport solutions at 7 and 15 bar, linking up to the Northern Lights CO₂ storage infrastructure, are also considered within Preem CCS.

Table 1 summarizes the potential CO₂ capture with the different CCS scenarios to be analyzed within Preem CCS, considering a capture rate of 90%.

Table 1: Value chains studied within the Preem CCS project

Case	CO ₂ source	Captured CO ₂ [Mt CO ₂ /y]
A	HPU flue gas in Lysekil	~0.48
B	HPU and low-sulfur stacks in Lysekil	~0.81
C	HPU and all major stacks in Lysekil	~1.44
D	Lysekil HPU and Gothenburg	~0.78

The refinery in Lysekil is the focus of Preem CCS. Case A considers capturing CO₂ from the flue gas from the HPU (Hydrogen Production Unit) in Lysekil. This stack has the highest CO₂ concentration among all stacks in this site and the highest contribution to CO₂ emissions at the refinery. Therefore, Case A is considered the base case. Cases B and C consider capturing CO₂ emissions from other stacks in addition to the flue gas from the HPU. Case B considers capture from the HPU and another low-sulfur stacks. Case C includes the four major stacks and, potentially, up to 1.44 Mt/y could be captured in this case. Some of these stacks have varying sulfur content, which will affect the flue gas treatment requirements to avoid solvent degradation in the CO₂ capture plant [11]. This will impact the total cost [12] and footprint of the capture plant. In cases B and C, different clustering alternatives or configurations for the CO₂ capture facilities within the

Lysekil refinery (e.g. independent vs common equipment) will be considered in order to minimize the cost of capture maximizing captured CO₂. Case D considers capturing CO₂ from the HPU flue gas in Lysekil (as in Case A) and CO₂ from the gas in Gothenburg, which accounts for additional ~300 kt CO₂/y. The focus of Case D will be to estimate the effect of transportation costs on this type of cluster, with sites connected by ship. This case will provide insights for further development and optimization of shared CO₂ transport infrastructure.

2.4 Heat integration as an enabler for the Preem CCS project

The existence of residual heat within a facility, and its use for CO₂ capture, compared to the alternative of producing the heat with additional primary energy input has an important impact on the operating costs of the CO₂ capture facility. Therefore, energy efficiency and available or low-cost residual heat for the post-combustion absorption process have been identified as a key cost driver for carbon capture [13]. In other words, the cost of the heat used in the CO₂ capture process is critical for the overall feasibility and potential economic performance of CO₂ capture projects. It will also have an important effect on CO₂ avoidance costs [12]. This has been clearly highlighted in the economical and feasibility evaluations of the projects considered within Longship, the Norwegian full-scale project, which is described in Section 3 [13], [14]. In addition, the choice of heat supplying technologies, together with the overall amount of CO₂ capture, will impact the energy efficiency of the refinery and the CO₂ intensity (scope 1 and 2 emissions) of the refinery products.

For the reasons described above, analyzing the possibility to utilize residual heat and the development of a heat supply cost model are central activities within the Preem CCS project. The heat supply model will be used to investigate the choice of heat supplying technologies in the context of current or future energy and emission price regimes and identify the mix of technologies that supplies most heat at lowest cost and lowest emission impact, satisfying heat requirements of the CO₂ capture plant whilst considering variations of available heat over time. The design of heat collection networks, similar to previous works [15], [16], must be conducted within the context of such energy and emission price regimes and compared to alternative heating options. Biermann et al [17] have identified three potential classes of heat supply:

1. Existing sources of residual heat/steam,
2. unused capacity in boilers/equipment for heat/steam production,
3. new installation of heat supply capacity.

The role of unused capacity was not investigated in previous work by Biermann et al [17] but is being studied by investigating the interplay between switchable drives (electricity/steam) for pumps and compressors and heat recovery steam generators at the Preem refinery in Lysekil.

3. Potential impact of Preem CCS

3.1 Preem CCS within Northern Lights

The Northern Lights infrastructure is a natural option for offloading CO₂ from Preem's refineries, and a Memorandum of Understanding (MoU) has been signed between these two entities [22].

3.1.1. The Northern Lights and Longship projects

The Northern Lights project is part of the Norwegian full-scale carbon capture and storage (CCS) demonstration project and is the world's first large scale "open-source" infrastructure for receiving and storing CO₂ from multiple sources and industries. Equinor is executing the project, while Norske Shell and Total E&P Norge are equal partners [23], [24].

As shown in Figure 3, the Northern Lights project comprises transportation, reception, and permanent storage of CO₂ in a reservoir under the North Sea. The receiving terminal will be located at the premises of CCB Kollsnes AS, in the Naturgassparken industrial area in the municipality of Øygarden (Western Norway). This onshore plant will temporarily store liquid CO₂, which will be pumped from the storage vessels through a pipeline to an offshore injection well. Permanent storage is located approximately 2500 m below the seabed, south of the Troll field. The plant will be operated from Equinor's facilities at the Sture terminal in Øygarden, and the subsea facilities from the Oseberg A platform in the North Sea [23], [25]. The facilities are scheduled to be operational in 2024 [24].

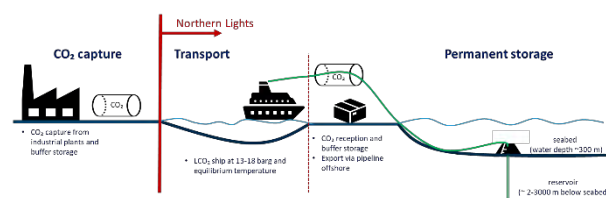


Figure 3 Northern Lights project as part of the Norwegian CCS demonstration project (adapted from [24]).

In late 2020, the Norwegian government made a positive investment decision for Northern Lights and Norcem's cement factory in Brevik, Norway, which plans to have a flat capture profile of 400 kt CO₂/y. In addition, Fortum Oslo Varme (FOV), a waste-to-energy plant with the potential to capture additional 400 kt CO₂/y, may get partial funding if the project secures sufficient own funding as well as funding from the EU or other sources. The full-scale project has been named "Longship" [26]. It should be noted that the Norcem Brevik capture costs are lower than Fortum Oslo Varme, mainly due to the low cost residual heat available from the cement process [13], [14].

Northern Lights is planned to be developed in two phases, with storage capacities of up to 1.5 and 5 Mt/y, respectively [23]. Different expansion scenarios, for up to 100 Mt/y have been explored [22]. Given the planned storage capacity and the capture profiles of the Longship project, Northern Lights has the flexibility to receive and

store additional 0.7 Mt/y CO₂ from third parties¹, such as Preem, also in the first phase [23]. The access for third parties has in fact been prioritized during the design of the Northern Lights project [13].

3.1.2. Potential impact of Preem CCS within the Northern Lights project

Capture cases analyzed within the Preem CCS project are described in Table 1 in Section 2. Figure 4 compares the CO₂ that could potentially be captured in the alternative Preem CCS cases with the CO₂ to be captured in Norcem Brevik and FOV, the facilities considered in the Longship project. All cases evaluated within the Preem CCS project consider a larger amount of CO₂ captured than the CO₂ captured (individually) at the facilities included in the Longship project.

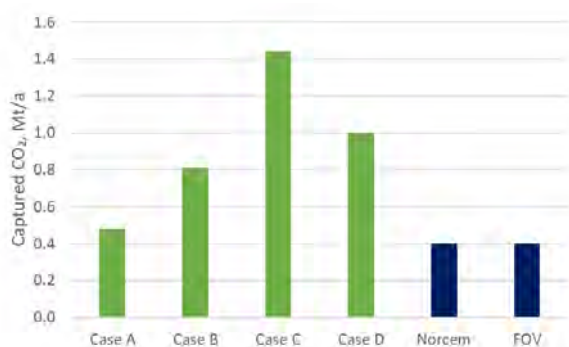


Figure 4: Potential captured CO₂ corresponding to the Preem CCS project cases (Table 1) compared to CO₂ to be captured in the Norcem and FOV projects (Longship project).

Case A, capturing ~480 kt CO₂ /y, which corresponds to ~90% of the CO₂ in the flue gas from the HPU at the Lysekil refinery, is the case with the lowest amount of captured CO₂ among all the possible alternatives considered within the Preem CCS project. This amount of CO₂ is nonetheless higher than the expected 400 kt CO₂/y to be captured at the facilities in the Longship project. Cases B and D correspond approximately to the combined CO₂ captured of the two Longship facilities. Note that if these cases are realized, the excess capacity of the first phase of the Northern Lights project would be exceeded, assuming that the FOV project is implemented. Case C, capturing from all major refinery stacks, has the potential to capture more than 90% of the first phase of the Northern Lights project, which implies that it would need to be implemented in the second phase of the Northern Lights project. Therefore, Preem could potentially be the anchor supplier that could trigger the expansion to 5 Mt/y storage capacity of the Northern Lights project [22].

3.2 The impact of scale

In Section 2 we discussed heat integration for cost reduction as an enabler for the implementation of the results from Preem CCS project. Another important enabler is the scale of the captured CO₂. Roussanaly et al.

[12] illustrated that CO₂ transport and storage costs can sharply decrease with higher CO₂ flow rates due to economies of scale considering different scenarios such as transport distances, both via pipeline and shipping, and storage sites.

The specific costs of the Norwegian full-scale project are relatively high compared with estimated costs for future developed full-scale capture sites and value chains. This is due to an overcapacity and costs are expected to be brought down by several factors. The cost per ton of CO₂ is expected to decrease significantly when the value chain capacity is fully utilized from 0.8 to 5 Mt CO₂ per year. Therefore, utilizing third party volumes is regarded as a key driver for more affordable CCS for all Northern Light partners [13]. As quantities of CO₂ to be captured from the Preem refineries are higher than the CO₂ captured from the facilities in the Longship project, cost per ton for Preem's CO₂ is expected to be lower than the initial cost for the Longship project. This will also reduce the average unitary costs, which might be especially beneficial for small emitters [12], which may also use the Northern Lights facilities.

It should also be noted that in Cases A and D, CO₂ would be captured (at least partly) from flue gas from HPUs and the cost of capture from processes for hydrogen production from fossil methane is expected to be lower than the cost of capture from cement and waste to energy plants [13], further contributing to reducing the cost per ton for Preem's CO₂.

3.3 Impact of Preem CCS for achieving Sweden's sustainability goals

In 2017, Sweden announced the goal of reaching net zero emissions by 2045 at the latest and passed a new Climate Act legally binding this commitment [2], [18]. This target responds directly to the United Nations' sustainable development goal (SDG) 13, which is to "take urgent action to combat climate change and its impacts" [1].

In 2018, the total CO₂ emissions in Sweden were ~41.8 Mt [19], [20], of which ~16.4 Mt corresponded to the industrial sector [21]. As described in Section 2, Preem's CO₂ emissions from production are in the order of 2 Mt/y. Figure 5 illustrates the industrial CO₂ emissions in Sweden and Preem's contribution.

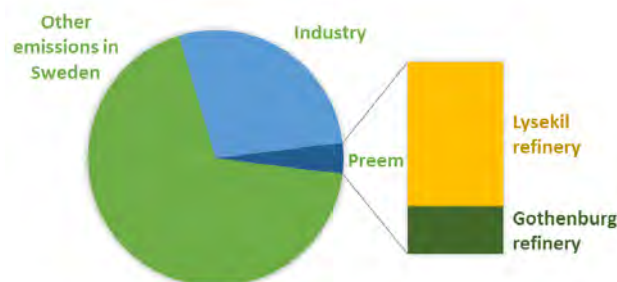


Figure 5: Contribution of Preem's CO₂ emissions to total fossil emissions in Sweden in 2018.

¹ This value considers that the FOV project will be financed.

Reducing these will be a major enabler to reach Sweden's sustainability goals. It should be noted that the CO₂ captured will depend on which case, among those described in Table 1, is implemented. Preem is pursuing an increase in advanced biofuels production, in both their refineries in Lysekil and Gothenburg. This will bring an increased possibility for Bio-CCS with *negative* CO₂ emissions as more renewable feedstock is used at the two refinery sites, which will enable reaching Preem's climate neutrality goal for 2045 [5]. This will also contribute to reaching Sweden's goal for net zero emissions by 2045.

4. Final comments

The Preem CCS study and subsequent implementation of CO₂ capture from Preem's refineries differs from the Longship project in the following aspects:

- a) The possibility of CO₂ capture from different stacks, each from different processes and with different compositions and CO₂ content. This enables analyzing and comparing different clustering configurations of the CO₂ capture facilities.
- b) The cost of heat is known to be critical for the overall feasibility of CO₂ capture [13], [14]. Preem CCS will quantify the effect of heat integration in a refinery environment, which will bring valuable insights for similar projects.
- c) From the transport point of view, Preem CCS will bring quantitative insights with respect to the 7 and 15 bar options, as well as the convenience of joint transport of CO₂ from different locations (Lysekil and Gothenburg). In addition, the implementation of the project will bring experience with respect to cross-border transport of captured CO₂ from Sweden to Norway.

Therefore, Preem CCS brings additional insights compared to other projects considered within Northern Lights, and thus can be considered as a first of a kind project and the lessons learned from Preem CCS and the full-scale implementation of CO₂ capture in the Preem refineries will enable future CCS projects.

The outcome of the Preem CCS project will be to establish a roadmap for CO₂ emission reduction pathways at Preem's two refineries in Sweden in the context of national emission reduction commitments, considering the strategic implementation of CO₂ capture in relation to possible future development pathways at the refinery.

Acknowledgements

The *Preem CCS* project is funded by the Norwegian CLIMIT-Demo programme via Gassnova, by the Swedish Energy Agency and by the participating industry and research partners (Preem, Aker Carbon Capture, SINTEF Energy Research, Chalmers University of Technology and Equinor).

The authors acknowledge Sandra Karlsson (Preem AB) as well as Simon Roussanaly and Rahul Anantharaman (SINTEF Energy Research) for their input for the definition of the value chain cases described in Section 2. The authors also acknowledge Berit F. Fostås (Equinor Energy) and Oddvar Gorset (Aker Carbon Capture) for reading the manuscript.

References

- [1] UN, 'Sweden's goal – becoming the world's first fossil-free welfare state', *Sustainable development goals*, 2017. [Online]. Available: <https://sustainabledevelopment.un.org/partnership/?p=33918>.
- [2] Ministry of the Environment, 'The climate policy framework', *Government Offices of Sweden*, 2017. [Online]. Available: <https://www.government.se/articles/2017/06/the-climate-policy-framework/>.
- [3] Regjeringen (Norwegian Government), 'The Government launches "Longship" for carbon capture and storage in Norway', 2020. [Online]. Available: <https://www.regjeringen.no/en/aktuelt/the-government-launches-longship-for-carbon-capture-and-storage-in-norway/id2765288/>.
- [4] Norwegian Ministry of Petroleum and Energy, 'Longship – Carbon capture and storage', *Meld. St. 33 (2019–2020) Report to the Storting (white paper)*, 2020. [Online]. Available: <https://www.regjeringen.no/contentassets/943cb244091d4b2fb3782f395d69b05b/en-gb/pdfs/stm201920200033000engpdfs.pdf>.
- [5] Preem, 'Preem Progress Book - Sustainability Report 2019', *The target is set: Climate neutral by 2045*, 2019. [Online]. Available: https://www.preem.com/globalassets/om-preem/hallbarhet/hallbarhetsredovisning/preem_sustainability_report_2019_eng.pdf. [Accessed: 14-Sep-2020].
- [6] Aker Solutions (Aker Carbon Capture), 'Aker Solutions Starts CCS Test Program at Preem Refinery in Sweden', 2020. [Online]. Available: <https://www.akersolutions.com/news/news-archive/2020/aker-solutions-starts-ccs-test-program-at-preem-refinery-in-sweden/>. [Accessed: 09-Feb-2021].
- [7] Gassnova, 'Milestone for Swedish-Norwegian CCS project', 2020. [Online]. Available: <https://gassnova.no/en/news/milestone-for-swedish-norwegian-ccs-project>. [Accessed: 09-Feb-2021].
- [8] A. Cousins, P. Feron, J. Hayward, K. Jiang, and R. Zhai, 'Further Assessment of Emerging CO₂ Capture Technologies for the Power Sector and their Potential to Reduce Costs', 2019.
- [9] P. H. M. Feron, A. Cousins, K. Jiang, R. Zhai, and M. Garcia, 'An update of the benchmark post-combustion CO₂-capture technology', *Fuel*, vol. 273, p. 117776, Aug. 2020.
- [10] H. Deng, S. Roussanaly, and G. Skaugen, 'Techno-economic analyses of CO₂ liquefaction: Impact of product pressure and impurities', *Int. J. Refrig.*, vol. 103, pp. 301–315, Jul. 2019.
- [11] N. E. Flø *et al.*, 'Results from MEA Degradation and Reclaiming Processes at the CO₂ Technology Centre Mongstad', *Energy Procedia*, vol. 114, pp. 1307–

- 1324, Jul. 2017.
- [12] S. Roussanaly *et al.*, ‘Towards improved cost evaluation of Carbon Capture and Storage from industry’, *Int. J. Greenh. Gas Control*, 2021.
- [13] Gassnova SF, ‘Potential for reduced costs for carbon capture, transport and storage value chains (CCS)’, *Report No.: 2019-1092, Rev. 2*, 2019. [Online]. Available: <https://ccsnorway.com/wp-content/uploads/sites/6/2020/10/Potential-for-reduced-cost-for-carbon-capture-2019.pdf>.
- [14] Atkins and Oslo Economics, ‘Kvalitetssikring (KS2) av tiltak for demonstrasjon av fullskala CO₂-håndtering’, 2020.
- [15] V. Andersson, P.-Å. Franck, and T. Berntsson, ‘Industrial excess heat driven post-combustion CCS: The effect of stripper temperature level’, *Int. J. Greenh. Gas Control*, vol. 21, pp. 1–10, Feb. 2014.
- [16] V. Andersson, P.-Å. Franck, and T. Berntsson, ‘Techno-economic analysis of excess heat driven post-combustion CCS at an oil refinery’, *Int. J. Greenh. Gas Control*, vol. 45, pp. 130–138, Feb. 2016.
- [17] M. Biermann, H. Ali, M. Sundqvist, M. Larsson, F. Normann, and F. Johnsson, ‘Excess heat-driven carbon capture at an integrated steel mill – Considerations for capture cost optimization’, *Int. J. Greenh. Gas Control*, vol. 91, p. 102833, Dec. 2019.
- [18] United Nations Climate Change, ‘Sweden Plans to Be Carbon Neutral by 2045’, 2017. [Online]. Available: <https://unfccc.int/news/sweden-plans-to-be-carbon-neutral-by-2045#:~:text=Sweden passed legislation last week,years earlier than previously planned>.
- [19] G. Andrew, R., Andrews, O., Arora, V., Bakker, D., Barbero, L., Becker, M., Betts, R., Boden, T., Bopp, L., Canadell, J., Chevallier, F., Chini, L., Ciais, P., Cosca, C., Cross, J., Currie, K., Friedlingstein, P., Gasser, T., Harris, I., Hauck, J., Haverd, V., ‘National Carbon Emissions 2020’, *GCP, 2020*. [Online]. Available: <https://hdl.handle.net/11676/xUUehljs1oTazlGlmigAhvfe>.
- [20] P. Friedlingstein *et al.*, ‘Global Carbon Budget 2020’, *Earth Syst. Sci. Data*, vol. 12, no. 4, pp. 3269–3340, Dec. 2020.
- [21] Statistics Sweden (SCB), ‘Total emissions and removals of greenhouse gases by greenhouse gas and sector. Year 1990 - 2019’, *Greenhouse gas emissions and removals*, 2020. [Online]. Available: www.statistikdatabasen.scb.se/pxweb/en/ssd/START_MI_MI0107/TotaltUtslappN/.
- [22] Equinor ASA, ‘Northern Lights Contribution to Benefit Realisation’, 2019. [Online]. Available: <https://ccsnorway.com/wp-content/uploads/sites/6/2020/07/Northern-Lights-Contribution-to-Benefit-Realisation-sladdet-versjon-1.pdf>.
- [23] Equinor, ‘Northern Lights Project Concept report-DG2 report’, RE-PM673-00001, 2018.
- [24] ‘Northern Lights Project’, 2020. [Online]. Available: <https://northernlightsccs.com/en>. [Accessed: 14-Sep-2020].
- [25] Equinor ASA, ‘Northern Lights CCS-Part of The Full-Scale CCS Project in Norway’, 2020. [Online]. Available: www.equinor.com/en/what-we-do/northern-lights.html. [Accessed: 15-Sep-2020].
- [26] Regjeringen (Norwegian Government), ‘The Government launches “Longship” for carbon capture and storage in Norway’, 2020. [Online]. Available: www.regjeringen.no/en/aktuelt/the-government-launches-longship-for-carbon-capture-and-storage-in-norway/id2765288/. [Accessed: 21-Sep-2020].

INDUSTRIAL CO₂ CAPTURE PROJECTS: STATUS, LESSONS LEARNED AND NEEDS FOR PROGRESSING TOWARDS FULL-SCALE IMPLEMENTATION

Adriana Reyes-Lúa^{1*}, Kristin Jordal¹

¹SINTEF Energy Research, Trondheim, Norway

* Corresponding author e-mail: adriana.r.lua@sintef.no

Abstract

Existing CO₂ capture projects are accumulating experience of adapting generalized results to individual projects, which will be extremely valuable for accelerating emerging CCS projects. Through knowledge-sharing, the CCUS Projects Network (CCUS PN) aims to speed up delivery of these technologies, which the European Commission recognizes as crucial to achieve the 2030 and 2050 climate targets. In this paper, we summarize learnings accumulated so far from industrial CO₂ capture projects across Europe, including CO₂ capture technology selection as well as CO₂ capture project development and implementation. CO₂ capture technologies are reaching maturity and defining the regulatory framework and providing tools for building a business case is becoming increasingly relevant for enabling full-scale implementation.

Keywords: CCS, CO₂ capture, dissemination, regulations, full-scale implementation

1. Introduction

The Intergovernmental Panel on Climate Change (IPCC) Special Report on Global Warming of 1.5 °C [1] has pointed out the need of reaching net-zero emissions by 2050. Three out of four of the presented mitigation pathways require major use of carbon capture and storage (CCS), including bioenergy with carbon capture and storage (BECCS), to limit global rise to 1.5 °C. In an European context, *A Clean Planet for All*, COM (2018) 733 [2], is the European strategic vision for a prosperous, modern, competitive and climate neutral economy which states that CCS deployment is necessary for tackling CO₂ emissions that cannot be cut through other means such as energy efficiency and renewable energy production. The European Green Deal and Climate Law are converting the political commitment to climate neutrality into a legal obligation and have led to the development of additional EU policy supportive of CCS. By 2030, Europe plans to cut emissions by at least 55% below 1990 levels, aiming to become the world's first climate-neutral continent by 2050 [3].

The CCUS Projects Network (CCUS PN) [4] is supported by the European Commission and represents and supports major industrial projects underway across Europe in the field of CCS and carbon capture and utilization (CCU). By sharing knowledge and learning from each other, the aim is that the CCUS PN members will drive forward the delivery and deployment of CCS and CCU, enabling Europe's member states to reduce CO₂ emissions from industry, electricity, transport, and heat. The CCUS PN is organized in three thematic working groups: Policy, regulation and public perception, CO₂ capture and utilization, and CO₂ transport and storage networks.

1.1 Methodology

This paper reflects input gathered from members of the CCUS PN by the CO₂ capture and utilization thematic working group. CCUS PN members focusing only on transportation and/or storage have not participated in this study. The paper summarizes lessons learned from CO₂ capture technology selection and capture project implementation, as well as from HSE (health, safety and environment) and regulatory work related to CO₂ capture. The paper also reflects input from the CCUS PN members on needs perceived as important for the realization of CO₂ capture at industrial scale. It should be highlighted that these projects are at different stages, which was reflected in the inputs received from the different projects. Contributing projects are listed in Table 1, but their inputs have been anonymized in the paper.

Table 1: Contributing CCUS Projects Network members in this paper.

Project name	Country
Acorn	United Kingdom
Fortum Oslo Varme (FOV)	Norway
Everest (Tata Steel)	Netherlands
LEILAC	Belgium and Germany
CarbFix	Iceland
Drax Bioenergy & CCS	United Kingdom
KVA Linth	Switzerland
Norcem	Norway

In addition, reports from first of a kind (FOK) projects worldwide (e.g. [5], [6],[7] [8], [9]) and the recently published report on lessons learned from the Norwegian Longship project [10] have been used as references. It has been noted that learnings can be, but are not always, common for several projects. This depends, e.g., on the

nature of the CO₂ sources, location and current maturity of the projects.

1.2 Structure of the paper

Figure 1 shows how the information is organized in this paper. Section 2 gives a high-level outlook of the status or large-scale CCUS projects, some of which are among the CCUS PN members. A summary of the CO₂ capture technologies currently relevant at industrial scale is also included in Section 2. Section 3 presents the lessons learned *so far* from the CCUS PN members, including the factors that have influenced the evaluation and selection of the CO₂ capture technology as well as the activities and lessons learned during project development and implementation. Section 3 also describes aspects that are considered for the whole project lifetime, from the selection of the CO₂ capture technology to the piloting, implementation, and operational phases. In Section 4, the paper summarizes the crucial needs and barriers identified in this work for the realization of CO₂ capture projects. Finally, Section 5 gives an outlook for the realization of industrial CO₂ capture projects.

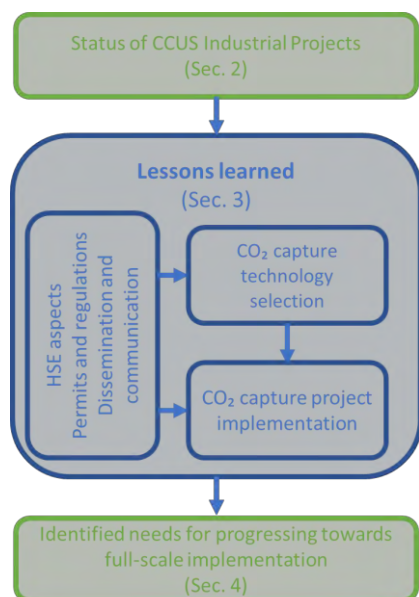


Figure 1: Organization of the paper.

2. Status of large-scale CO₂ capture projects and technologies

According to the Global CCS Institute (GCCSI), 26 commercial CO₂ capture facilities (≥400 kt per year) are currently operating worldwide, capturing 40 Mt of CO₂ every year, with most projects in North America, with 38 commercial facilities in operation or advanced development [11]. The CO₂ capture facility at Boundary Dam coal-fired power plant in Canada was the world's first fully integrated and full-chain industrial-scale CO₂ capture and storage facility, with CO₂ capture retrofitted to a coal-fired power plant [7]. Currently, the Gorgon Carbon Dioxide Injection facility on Barrow Island,

Western Australia, is the largest dedicated geological storage operation in the world with a capacity of up to 4 Mt CO₂ per year [11][12].

2.1 Large scale CCUS projects in Europe

In 1996, Sleipner, in Norway, was the first site where CO₂ was injected into a dedicated storage site (opposed to Enhanced Oil Recovery, EOR) and the first industrial-scale CCS project worldwide. Currently, Sleipner (storing 1 Mt per year) and Snøhvit (storing 0.7 Mt per year), also in Norway, are the only industrial-scale operating CCS projects in Europe, and still among the few worldwide facilities with dedicated geological storage [11]. In both facilities, CO₂ is separated from natural gas and injected back into formations for storage.

Several other CO₂ capture projects are currently being developed across Europe, some of them are focusing on capture only, and others are developed in the context of a full-chain CCS project. According to the GCCSI [11], besides Sleipner and Snøhvit, there are 11 commercial facilities in construction, or at various stages of development, which are targeting operation before 2030 in Europe, specifically in the United Kingdom, Ireland, the Netherlands and Norway, where the government has shown support for realizing CCS projects. In late 2020, the Norwegian government granted funding for 73% of the Norcem Brevik project through the Norwegian Longship project [13]–[16]. In 2020 the British government announced funding for CO₂ capture clusters in the UK [17]. Some of these CCS projects in development are part of the CCUS PN, namely Fortum Oslo Varme, Norcem Brevik, Drax Bioenergy & CCS, Ervia and Acorn [4] and have provided input reflected in this paper (see Table 1). There are also projects and CCS initiatives (e.g. [18], [19]) not included in the aforementioned report with a large potential for CO₂ capture that may also be realized before 2030. Some relevant emerging projects in Europe were not included in the GCCSI report because the expected captured CO₂ is less than 400 kt per year.



Figure 2: Existing onshore infrastructure will bring CO₂ captured in the Grangemouth cluster to the St Fergus Terminal (pictured¹) in the Acorn project in Scotland, UK.

¹ Picture taken from www.geograph.org.uk/photo/1695742
Licensed under the Creative Commons License.

2.2 CO₂ capture technologies

Here we briefly introduce CO₂ capture technologies currently relevant for or developing towards commercial-scale applications. The described technologies should reflect relevant options for large-scale applications. Examples of emerging technologies not *currently* relevant for large-scale applications are electrochemical separation, microbial and microalgae, and direct air capture (DAC) [20].

Post-combustion CO₂ capture with amine solvents (liquid absorption) is currently the most mature CO₂ capture technology, and it has been demonstrated at full scale [21], reaching a Technology Readiness Level (TRL) 9. In this technology, CO₂ is removed from the flue gases when it reacts in a vessel with a (generally amine-based) solvent to form an intermediate compound, which is fed to a second vessel, where the solvent is regenerated with heat, producing the original solvent and a high-purity CO₂ stream. It can be implemented as a retrofit option.

With *solid sorbents* the CO₂ adsorbs into the surface of highly porous solids. Once the solid is saturated, the solid adsorbent can be regenerated via temperature (TSA), pressure (PSA) or electrical swings [20]. Vacuum-swing adsorption (VSA), is the CO₂ capture technology implemented in the Air Products Steam Methane Reformer facility for hydrogen production at the Valero Port Arthur Refinery in Texas (1 Mt CO₂ per year) [9].

Membranes are thin barriers over which one species is more mobile than others which allows the specific separation of species in a gas mixture. CO₂ selective membranes typically produce a CO₂ enriched stream at low pressure and a CO₂ depleted stream at high pressure [22]. Membranes are used in the FPSO vessels in the Petrobras Santos Basin in Brazil (4.6 Mt CO₂ per year) to separate CO₂ from natural gas; but in general, membranes have a TRL of 6, and the process itself has a lower TRL [20]. American membrane producer MTR report on their website about a plan for construction, installation and operation of a large scale membrane pilot system [23].

In *oxyfuel processes*, nitrogen is removed from air via an air separation process (typically cryogenic), producing nearly pure oxygen, which is used to burn the fuel and produce power or heat. With this scheme, the produced flue gas mainly contains CO₂ and water (steam), which can be separated via cooling and a CO₂ compression and purification unit. Oxycoal power plant technologies are reported to be under trials to establish TRL 8 during the period from 2016 to 2020 [24]. Oxyfuel cement production is being investigated [25], [26]. *Chemical looping combustion* is a type of oxy-fuel process without the need of an air separation unit [27]. Here, a metal-metal oxide system is used to transport oxygen from the air to the fuel, avoiding direct contact, also producing almost pure contains CO₂ and water (steam). There are research projects to push this technology to TRL 7 [28].

In *post-combustion calcium looping* the flue gas enters a carbonator with CaO, which captures the CO₂, reacting into CaCO₃, which is circulated to the calciner, where it is regenerated at a high temperature, releasing raw CO₂

for conditioning (and turning CaCO₃ back to CaO) [29]. This technology is more likely to be applied as a retrofit.

In *low-temperature separation* processes the CO₂ is cooled such that CO₂ forms a liquid or a solid that can be separated. This technology is suitable as a standalone for some applications where a high CO₂ concentration is available in a stream, such as H₂ production with CO₂ capture or in combination with membranes or adsorption (PSA). A commercial application of the technology is the AirLiquide CryoCap technology [30].

There are also *industry specific technologies*, such as *Hlsarna*, developed by Tata Steel and Rio Tinto for the production of pure liquid iron and CO₂ [31], [32]. Another industry specific technology is the direct separation process [36] developed by the *LEILAC* project to capture unavoidable CO₂ process emissions in the cement and lime industries, also producing highly concentrated CO₂.

3. Lessons learned

This section outlines the main lessons learned so far by the CCUS PN members while developing CO₂ capture projects. We first describe the lessons learned regarding aspects that are relevant throughout the complete project lifetime. We then go through the lessons learned with respect to CO₂ capture technology selection and project implementation, which is the current phase for most of the CCUS PN members.

3.1 Factors relevant for the complete project lifetime

Aspects such as the regulatory framework or the communication strategy shape the project from the beginning, influencing the selection of the technology. These aspects are also present during the implementation of the project and impact the operational and decommissioning phases of the project.

3.1.1. Permits and regulations

A favorable policy and regulatory framework is crucial for the large-scale deployment of CCS projects. Project developers, vendors and contractors as well as authorities are only starting to accumulate experience regarding CO₂ capture projects. Identifying and contacting the relevant authorities for permitting regarding air, water, noise, and environment should be one of the first actions when developing any industrial project. The regulatory environment is continuously evolving, as discussed further in this paper. This situation can make it challenging to contact vendors and get bids when regulations are not fully in place. Therefore, regulation agencies, project developers and vendors should work together to find a balance that protects the environment without unnecessarily curtailing or stopping CCUS markets.

3.1.2. Health, Safety and Environment (HSE)

From experience in other industries, unplanned HSE events such as leakages or accidents are highly publicized and may damage a whole industry. A HSE responsible of coordinating and documenting all HSE activities should be part of the core team in an industrial capture project

[10]. Documentation can be done through a Management Study Report, which includes a scope of responsibilities, as well as a health and safety plan, and an environmental plan. These documents are not static and should be continuously refined and updated.

Industrial HSE standards and practices have proven useful on pilot plants and industrial-scale projects, although specific limits for CO₂ management still need to be defined. Capture projects may be directly connected to large-scale intermediate storage and transportation of CO₂ to a port or to a storage site, which may become a concern for third parties.

Measurement, monitoring and verification (MMV) or monitoring, verification and accounting (MVA) plans are important for stakeholder acceptance and to ensure that the CO₂ capture and transport facilities, as well as the storage site perform as expected [33] [9].

In this regard, tools for estimating emissions and modelling leakages, including amine emission to the air or large CO₂ leakages, as well as property databases specific for CO₂, solvents and solvent degradation by-products should be further developed.

3.1.3. Dissemination and communication

Industries implementing CO₂ capture projects are aware that results-sharing and public acceptance are not only beneficial but fundamental. As shown in Figure 3, besides the internal communication, plans and results can typically be shared with different stakeholders, such as government, academia, the general public, or other industrial CO₂ capture projects.



Figure 3: Stakeholders with whom results and plans typically can be shared.

In general, CCUS PN members have positive experiences engaging with stakeholders and have used every opportunity to share knowledge. Most projects are being deployed in existing industrial facilities, and the local public is aware of the benefits that a CO₂ capture project could bring to the region. In advanced projects, such as Boundary Dam in Canada, the public commitment to directly address stakeholder concerns regarding the level

of investment and a central vision to reach a CO₂ capture goal was a successful tactic to overcome difficulties [34].

A majority of the existing CO₂ capture projects have been at least partially funded by national or EU government schemes. Therefore, dissemination is typically an important activity within these projects, and they are obliged to provide open access key knowledge deliverables to government representatives.

Knowledge sharing among CO₂ capture projects, as well as partnership-based cooperation among plant operators and industrial associations, can be decisive to bring forward emerging CO₂ capture projects, for example, by having accessible cost information regarding comparable projects. Currently, several CO₂ capture projects include running a pilot plant onsite before the investment decision of constructing the industrial-scale CO₂ capture plant. Accumulated piloting and industrial operation experience, including HSE, can reduce or eliminate the need for on-site pilot periods, reducing project implementation costs and accelerating deployment. First-of-a-kind (FOAK) projects, such as the one in the Boundary-Dam power station in Canada, have shared that the learning curve for operation has been a factor for a challenging undertaking [34]. Therefore, best practices guidance and knowledge sharing among projects for safe operation, solvent degradation reduction, and pollution prevention will certainly pave the way for the deployment of CO₂ capture.

An important aspect that should be considered is that results sharing should be timely and, depending on the project stage, within reasonable agreements that do not affect tender processes or interfere with intellectual property (IP) rights, not only of the project owner, but also of the technology providers.

3.2 CO₂ capture technology selection: main decision factors

The selection of CO₂ capture technology is a major decision typically taken during the concept phase [10]. Companies implementing CO₂ capture that have solid industrial experience can build on their existing project-developing knowledge and skills. Figure 4 depicts important factors influencing technology selection. Technical aspects, cost, and compliance with regulations are natural decision factors when evaluating candidate technologies.

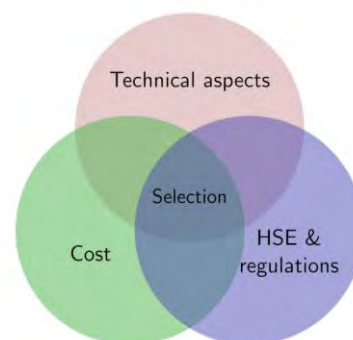


Figure 4: Decision factors affecting CO₂ capture technology selection.

3.2.1. Evaluation of capture technology

It is important to note that the choice of technology will be influenced not only by technology maturity but by factors such as the source of CO₂, flue gas composition (CO₂ concentration), temperature, pressure, flowrate, and type of industrial CO₂-emitting facility being considered for capture, where the availability of waste heat is an important parameter.

The selected technology should have the ability to capture CO₂ when considering a specific set of flue gas characteristics, such as CO₂ concentration and impurities, as well as flue gas pressure and temperature. The technology should be able to achieve the required CO₂ capture rate and required CO₂ purity, which will depend on the downstream (transport/storage/use) requirements for the captured CO₂.

As most of the presently existing projects are FOAK projects, technology readiness, maturity, references, and previous operating and project experience have been key factors in this first screening, reducing risk and uncertainty [10]. Piloting has been used to provide confidence in the selected technology as well as operating experience.

3.2.2. Capture cost

Expected capital (CAPEX) and operating (OPEX) costs are key factors when evaluating and selecting the CO₂ capture technology. Capture cost is influenced by technical aspects of the CO₂ capture technology and design decisions, such as energy requirements, integration, and the price of consumables (solvents, sorbents). The selected technology should be not only efficient but also simple to integrate and to operate without jeopardizing the industrial production. Uncertainties in this regard are mitigated with higher TRL technologies, which are being chosen in the projects currently being developed and close to implementation.

Energy requirement is one of the most important performance parameters for CO₂ capture technologies. Thus, efficient heat integration is a key aspect to reduce operating costs. For example, in the Longship project, efficient heat integration made it possible to reduce the energy input to the chain with 42% in the Fortum Oslo Varme (waste to energy) case and with 74% in the Norcem (cement) case [10]. Besides heat integration, other integration and optimization opportunities are on electricity (e.g. for CO₂ compression), water (both usage and treatment) and pre-conditioning of flue gas coming from different stacks within the same industrial facility.

3.3 CO₂ capture technology implementation: selecting suppliers and partners

CO₂ capture projects that are close to implementation today are in general retrofit projects. In some cases, these are not the only ongoing retrofit or modernization projects at the industrial sites. Therefore, design and construction of CO₂ capture and conditioning facilities should be put in a context of modernization plans of the overall industrial site. This will impact, for example, the

availability of utilities or the design basis for the CO₂ capture plant.

CCUS PN members have observed that appropriate project planning arrangements and revision of relevant internal protocols should be started early as possible. As some aspects of the project such as legislation or some technological aspects may not be defined at the beginning of the project, collaboration and flexibility are key for both team interactions and project management. For example, key success factors of projects such as the CO₂ capture plant in the Valero refinery in Texas were related to coordination and partnership between the technical team, site host, consultants and contractors [9].

Based on publicly available pilot results (e.g. [35]) or shared knowledge among CO₂ capture projects, some projects have initiated a tender process around a type of capture technology, without an on-site piloting phase. Projects reaching the contract phase have found it highly beneficial to develop a contract strategy that ensures competition for the detailed engineering and construction of the major parts of the system.

A technology provider should be able to issue and back up performance guarantees [10], for example, in terms of CO₂ capture rates, operability, and ability to comply with regulations. In this regard, CO₂ capture projects that are implementing amine-based capture technologies are also considering the long-term availability of the required solvent and possible future dependence on suppliers. Thus, reliable, well-established vendors that have developed mature technologies are preferred, as this relationship will most likely be a long-term one.

CO₂ capture projects often involve both CO₂ capture and conditioning (e.g. liquefaction), and the vendors are not necessarily the same. Therefore, industries implementing capture projects for ship transport need to find competent partners for the construction of CO₂ liquefaction and storage facilities.

More advanced projects, which currently are FOAK projects, have shared that it has been challenging to keep the cost level from the Front-End Engineering Design (FEED) study. Thus, contractual and commercial requirements, as well as assumptions and uncertainties, should be clarified with shortlisted technology suppliers. It is expected that cost estimates will become more accurate as more CCUS projects are implemented and experiences are gained.

4. Identified needs for full-scale implementation

To reach industrial-scale operation, CCS projects must be developed along several axes, including securing funding for construction and operation. Timing with respect to access to funding, implementation of necessary regulations and access to transport and storage infrastructure is important, as well as good models for risk sharing. Furthermore, it is generally observed that political support and implementation plans are necessary on all levels: regional (e.g. EU), national, and local [36].

4.1 Building the business case

Technology improvements will be important cost-reduction factors for new projects. Capital expenses may be reduced for current technologies through stepwise learning from one project to the next. Reductions in operating costs can be achieved, for example, by identifying better heat integration solutions.

Supporting policy and regulatory frameworks as well as financing instruments are a pre-requisite for building the business case for new capture projects. Currently, the EU Emissions Trading System (ETS) [37] contributes to a business case, since emission allowances can be traded rather than surrendered at the end of each year if CO₂ has been captured, transported and stored in compliance with the Monitoring and Reporting Regulation (MRR) [38]. However, the current EU ETS scheme only covers CO₂ captured from *fossil* emission sources, and therefore incentives for investing in BioCCS could help trigger CO₂ removal (negative emissions). Early movers in CO₂ capture implementation can to some extent be supported from additional sources such as the Innovation Fund [39], and there are also examples of government support for realizing early CCS projects, such as in the Norwegian Longship project that was launched in September 2020 [13]–[15] with the budget approved by the Norwegian Parliament on December 14, 2020 [16], or the recent announcement of the British government to fund CO₂ capture clusters in the UK [17]. Further and future steps and additional mechanisms, such as contracts for difference, tax or emissions credits or appropriate carbon taxes [11], can also be envisaged to accelerate CCS implementation.

4.1.1. Risks sharing

There are many risks for early industrial movers in CO₂ capture. The risk of failing should be shared, which could be addressed through strategic partnerships. Governments (local, EU) can contribute to the risk-taking capacity. For example, in the Longship project, risks are shared between the Norwegian state, Northern Lights and the industries (Norcem and FOV) [15]. FOAK projects require more time for commissioning and start-up than conventional projects [8]. Projects may need recognition from investors that they will not yield normal returns. As such, the financial world and government have an opportunity to take responsibility in sharing the risk for CCS.

4.2 Access to CO₂ transport and storage infrastructure

The widespread development of CO₂ infrastructure (primarily pipeline and ship, but also in some cases train or truck) will be a key enabling step for CO₂ capture implementation. Access, tariffs, and liabilities must be appropriate for all users and not inhibit the fast and widespread uptake of carbon capture across Europe and the globe.

Industry coordination and mobilization of industry-wise resources can support the development of new projects [36]. Development and implementation of capture in industrial clusters as the one depicted in Figure 5, with a

joint backbone infrastructure can be seen as an enabler. This may require dedicated development of, for example, loading and offloading systems for truck or train transport. In some cases (e.g. Acorn [40]), existing infrastructure developed for other uses may be used. Available CO₂ transport and storage capacity needs to be sufficient for CO₂ captured from industrial sites. Joint transportation and storage facilities reduce costs [33][41]. This means that transport and storage projects that oversize their capacity, such as Northern Lights in Norway [42], are a prerequisite for the development of industrial CO₂ capture projects, which will eventually lead to reduced costs.

Implementation plans for capture projects must be developed to match with the timing of infrastructure implementation and an appropriate regulatory framework. The major hurdle for cross-boundary ship transport of CO₂ was resolved in 2019 with the provisional application of the 2009 amendment to article 6 of the London Protocol [43].

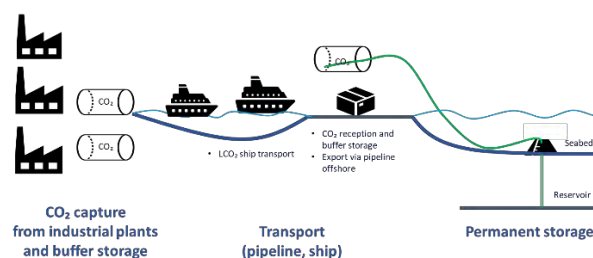


Figure 5 Example of shared infrastructure scheme (inspired by the Northern Lights [44] project).

4.3 R&I needs for improving CO₂ capture

Beyond the needs of current projects there is a need for improving knowledge and generating innovations in the field of CO₂ capture, for realizing future CCS projects with reduced costs and risks. Currently, amine-based CO₂ capture is the most mature alternative and has been successfully tested or implemented in different facilities. However, other technologies or technology synergies may be more convenient for some industries or applications. Some identified R&I needs are:

- Capture technologies and technology integration that significantly reduce capital and operating expenses.
- Improving models for CO₂ dispersion and large-scale leakages, as well as for dispersion and deposition of nitrosamines and nitramines, which are tools for HSE and risk analyses.
- Defining best available technologies (BAT) for pollution prevention, as well as reliable and standardized measurements and methods appropriate for the different technologies and processes to facilitate operation, reporting and compliance with regulations. This goes hand in hand with increasing knowledge with respect to measurement techniques and instrumentation for monitoring flow and CO₂ concentration in the different streams.

5. Final remarks

Knowledge sharing with all stakeholders brings benefits such as accelerating emerging projects and increasing public acceptance. Improving CO₂ capture through cost cuts and reduced energy penalty is a vast field of RD&I. The existing and emerging technologies for CO₂ capture are a necessary element for realizing CCS as a means to reduce anthropogenic CO₂ emissions and combat global warming, but not sufficient in itself – CO₂ transport and storage must obviously also be implemented for realizing CCS.

Additionally, for realizing CO₂ capture and storage, business models and financial viability as well as the necessary legal and regulatory frameworks must be in place. A favorable policy and regulatory framework is essential for the large-scale deployment of CCS projects, as well as good collaboration between project owners and governments for permitting, which should be started early in the project.

Timing is critical: it is difficult for a company to make a final investment decision if the business case is pending, the regulatory framework is uncertain or complementary CO₂ transport and storage infrastructure may be unavailable or insufficient.

Acknowledgements

The CCUS Projects Network is financed by the European Commission under service contract No ENER/C2/2017-65/SI2.793333. This paper reflects only the authors' view and the Commission is not responsible for any use that may be made of the information it contains.

The authors acknowledge the input received from the CCUS PN members mentioned in Table 1, represented by: Jørgen Thomassen, Charlotte Hartley, William Hazell, Carl van der Horst, Daniel Rennie, Kári Helgason, Carl Clayton, Stefan Ringmann and Per Brevik. We also acknowledge the input from Jessica Yearwood, Liliana Guevara Opinska and Hans Bolscher.

References

- [1] J. Rogelj *et al.*, “‘Mitigation Pathways Compatible with 1.5°C in the Context of Sustainable Development’ in Global Warming of 1.5°C. An IPCC Special Report on the impacts of global warming of 1.5°C above pre-industrial levels and related global greenhouse gas emission pathway”, 2018.
- [2] European Commission, ‘A Clean Planet for All. A European strategic long-term vision for a prosperous, modern, competitive and climate neutral economy’, COM(2018) 773, 2018.
- [3] European Commission, ‘EU climate action and the European Green Deal’, 2020. [Online]. Available: https://ec.europa.eu/clima/policies/eu-climate-action_en.
- [4] ‘CCUS Projects Network’, 2021. [Online]. Available: www.ccusnetwork.eu/.
- [5] International CCS Knowledge Centre, ‘Boundary Dam CCS Project’, 2019. [Online]. Available: <https://ccsknowledge.com/bd3-ccs-facility>. [Accessed: 11-Nov-2019].
- [6] IEAGHG, ‘Integrated Carbon Capture and Storage

- Project at SaskPower’s Boundary Dam Power Station’, 2015.
- [7] IEAGHG, ‘The road to deploying Carbon Capture + Storage at SaksPower’, *Integrated Carbon Capture and Storage Project at SaskPower’s Boundary Dam Power Station*, 2015. [Online]. Available: https://ccsknowledge.com/pub/documents/publication/s/saskpower-boundry-dam/Deploying_Carbon_Capture.pdf. [Accessed: 21-Nov-2019].
- [8] N. Shimokata, ‘Petra Nova CCUS Project in USA’, 2018.
- [9] IEAGHG, ‘The Carbon Capture Project at Air Products’ Port Arthur Hydrogen Production Facility’, 2018.
- [10] Gassnova SF, ‘Developing Longship- Key Lessons Learned’, 2020. [Online]. Available: <https://gassnova.no/wp-content/uploads/2020/11/Gassnova-Developing-Longship-FINAL-1.pdf>.
- [11] Global CCS Institute, ‘Global Status of CCS 2020’, 2020. [Online]. Available: <https://www.globalccsinstitute.com/resources/global-status-report/>.
- [12] Global CCS Institute, ‘World’s 19th large-scale CCS project begins operation in Australia’. [Online]. Available: <https://www.globalccsinstitute.com/news-media/latest-news/worlds-19th-large-scale-ccs-project-begins-operation-in-australia/>.
- [13] Gassnova SF, ‘CCS Norway’, 2020. [Online]. Available: <https://ccsnorway.com/>. [Accessed: 12-Apr-2020].
- [14] Regjeringen (Norwegian Government), ‘The Government launches “Longship” for carbon capture and storage in Norway’, 2020. [Online]. Available: <https://www.regjeringen.no/en/aktuelt/the-government-launches-longship-for-carbon-capture-and-storage-in-norway/id2765288/>.
- [15] Norwegian Ministry of Petroleum and Energy, ‘Longship – Carbon capture and storage’, *Meld. St. 33 (2019–2020) Report to the Storting (white paper)*, 2020. [Online]. Available: <https://www.regjeringen.no/contentassets/943cb244091d4b2fb3782f395d69b05b/engb/pdfs/stm201920200033000engpdfs.pdf>.
- [16] Regjeringen (Norwegian Government), ‘Funding for Longship and Northern Lights approved’, 2020. [Online]. Available: <https://www.regjeringen.no/en/aktuelt/funding-for-longship-and-northern-lights-approved/id2791729/>.
- [17] Prime Minister’s Office (UK), ‘PM outlines his Ten Point Plan for a Green Industrial Revolution for 250,000 jobs’, *Climate change and energy - Press release*, 2020. [Online]. Available: <https://www.gov.uk/government/news/pm-outlines-his-ten-point-plan-for-a-green-industrial-revolution-for-250000-jobs>.
- [18] Preem, ‘Preem Progress Book - Sustainability Report 2019’, *The target is set: Climate neutral by 2045*, 2019. [Online]. Available: https://www.preem.com/globalassets/om-preem/hallbarhet/hallbarhetsredovisning/preem_sustainability_report_2019_eng.pdf. [Accessed: 14-Sep-2020].
- [19] Port of Gothenburg, ‘Cinfracap’, 2020. [Online]. Available: <https://www.portofgothenburg.com/about-the-port/the-port-is-growing/cinfracap/>. [Accessed: 14-Sep-2020].

- [20] A. Cousins, P. Feron, J. Hayward, K. Jiang, and R. Zhai, 'Further Assessment of Emerging CO₂ Capture Technologies for the Power Sector and their Potential to Reduce Costs', 2019.
- [21] E. I. Koytsoumpa, C. Bergins, and E. Kakaras, 'The CO₂ economy: Review of CO₂ capture and reuse technologies', *J. Supercrit. Fluids*, vol. 132, pp. 3–16, Feb. 2018.
- [22] M. Voldsund, K. Jordal, and R. Anantharaman, 'Hydrogen production with CO₂ capture', *Int. J. Hydrogen Energy*, vol. 41, no. 9, pp. 4969–4992, Mar. 2016.
- [23] Membrane Technology Research, 'Large Pilot Testing of the MTR Membrane Post-Combustion CO₂ Capture Process', 2020. [Online]. Available: www.mtrinc.com/news/large-pilot-testing-of-the-mtr-membrane-post-combustion-co-2-capture-process/. [Accessed: 12-Feb-2020].
- [24] M. A. Nemitallah *et al.*, 'Oxy-fuel combustion technology: current status, applications, and trends', *Int. J. Energy Res.*, vol. 41, no. 12, pp. 1670–1708, Oct. 2017.
- [25] ACT, 'AC²OCem', *Accelerating Carbon Capture using Oxyfuel Technology in Cement Production*, 2020. [Online]. Available: <http://www.eu-projects.de/ac2ocem/ACOCem/tabid/1009/Default.aspx>. [Accessed: 12-Feb-2021].
- [26] M. Voldsund *et al.*, 'Comparison of Technologies for CO₂ Capture from Cement Production—Part 1: Technical Evaluation', *Energies*, vol. 12, no. 3, p. 559, Feb. 2019.
- [27] Ø. Langørgen, 'Chemical Looping Combustion 150 kW pilot unit at SINTEF'. [Online]. Available: www.sintef.no/en/all-laboratories/eccsel-norway-ccs-ri/chemical-looping-combustion-150-kw-pilot-unit-at-sintef/. [Accessed: 26-Nov-2019].
- [28] 'CHEERS Project', *Chinese-European Emission-Reducing Solutions*, 2019. [Online]. Available: <http://cheers-clc.eu/>. [Accessed: 15-Nov-2019].
- [29] D. Berstad, R. Anantharaman, and K. Jordal, 'Post-combustion CO₂ capture from a natural gas combined cycle by CaO/CaCO₃ looping', *Int. J. Greenh. Gas Control*, vol. 11, pp. 25–33, Nov. 2012.
- [30] 'AirLiquide'. [Online]. Available: www.airliquide.com/magazine/cryocap-co2-cold-capture-system-unlike-any-other-in-the-world. [Accessed: 15-Nov-2019].
- [31] Tata Steel, 'Hisarna'. [Online]. Available: www.tatasteeleurope.com/en/innovation/hisarna. [Accessed: 21-Nov-2019].
- [32] Tata Steel, 'Hisarna: game changer in the steel industry', *Hisarna factsheet*, 2017. [Online]. Available: [www.tatasteeleurope.com/static_files/Downloads/Corporate/About us/hisarna factsheet.pdf](http://www.tatasteeleurope.com/static_files/Downloads/Corporate/About%20us/hisarna%20factsheet.pdf). [Accessed: 21-Nov-2019].
- [33] IEAGHG, 'The Shell Quest Carbon Capture and Storage project', 2019.
- [34] C. Preston, C. Bruce, and M. Monea, 'An Update on the Integrated CCS Project at SaskPower's Boundary Dam Power Station', in *14th Greenhouse Gas Control Technologies Conference (GHGT-14)*, 2018.
- [35] TCM, 'Vitenskaplige artikler', *Catching for future*. [Online]. Available: <https://catchingourfuture.no/#artikler>. [Accessed: 13-Nov-2019].
- [36] J. Burnham, O. Debande, O. Jones, J. M. C. Mihai, and I. Temperton, 'Report on Innovative Financial Instruments for the Implementation of the SET Plan, First-Of-A-Kind projects', 2013.
- [37] European Commission, 'EU Emissions Trading System (EU ETS)', 2020. [Online]. Available: https://ec.europa.eu/clima/policies/ets_en. [Accessed: 12-Apr-2020].
- [38] European Commission, 'Monitoring, reporting and verification of EU ETS emissions', 2020. [Online]. Available: https://ec.europa.eu/clima/policies/ets/monitoring_en. [Accessed: 12-Apr-2020].
- [39] European Commission, 'Innovation Fund', 2020. [Online]. Available: https://ec.europa.eu/clima/policies/innovation-fund_en. [Accessed: 12-Apr-2020].
- [40] PaleBlueDot, 'Project overview', *Acorn CCS & Acorn Hydrogen*. [Online]. Available: <https://paleblu.com/acorn/>. [Accessed: 20-Nov-2019].
- [41] S. Roussanaly *et al.*, 'Towards improved cost evaluation of Carbon Capture and Storage from industry', *Int. J. Greenh. Gas Control*, 2021.
- [42] Equinor ASA, 'Northern Lights Contribution to Benefit Realisation', 2019. [Online]. Available: <https://ccsnorway.com/wp-content/uploads/sites/6/2020/07/Northern-Lights-Contribution-to-Benefit-Realisation-sladdet-versjon-1.pdf>.
- [43] International Maritime Organization, '41st Consultative Meeting of Contracting Parties to the London Convention and the 14th Meeting of Contracting Parties to the London Protocol (LC 41/LP 14) 7-11 October 2019', *Carbon Capture and Sequestration*, 2020. [Online]. Available: <https://www.imo.org/en/MediaCentre/MeetingSummaries/Pages/LC-41-LP-14-.aspx>.
- [44] 'Northern Lights Project', 2020. [Online]. Available: <https://northernlightscs.com/en>. [Accessed: 14-Sep-2020].

CARBONATE LOOPING FOR INTERMEDIATE TEMPERATURE CO₂ CAPTURE: EVALUATING THE SORPTION EFFICIENCY OF MINERAL-BASED MGO PROMOTED WITH CaCO₃ AND ALKALI NITRATES

Theodoros Papalas¹, Andy N. Antzaras¹, Angeliki A. Lemonidou^{1*}

¹Department of Chemical Engineering, Aristotle University of Thessaloniki, University Campus, 54124, Greece

* Corresponding author e-mail: alemonidou@cheng.auth.gr

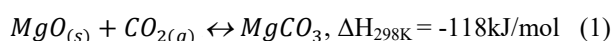
Abstract

This work focused on enhancing the CO₂ capture kinetics of magnesite-derived MgO via alkali nitrate and mineral CaCO₃ promoters for its application in the Carbonate Looping technology at intermediate temperatures ($\leq 400^\circ\text{C}$). Alkali salts had a prominent role by shifting into molten state to offer a favorable carbonation pathway and allow a significantly higher CO₂ uptake than non-promoted MgO, while their synergy with CaCO₃ bestowed even better sorption activity. MgCO₃ and CaMg(CO₃)₂ were detected as the main carbonate products, with the latter exhibiting faster formation rate. The sorbent with CaCO₃ and alkali salts to MgO molar ratios of 0.05 and 0.20 respectively attained an uptake of 7.2 moles CO₂/kg of sorbent when exposed to a 30%CO₂ flow at 300°C with only 6% activity loss after 50 carbonation cycles, proving the applicability of the materials. Despite the cyclic sorption activity loss due to sintering and dewetting, alkali salts redistribution enabled a stable performance under proper conditions.

Keywords: Carbonate looping, CO₂ capture, MgO-based sorbent, molten salt promoter, In-situ XRD

1. Introduction

Global CO₂ emissions have been accelerating by the rampant exploitation of fossil energy sources, as demonstrated by their 2.6% annual increase between 2000 and 2014 [1]. The tremendous impact of the industrial sector on climate led to the development of Carbon Capture, Utilization and Storage (CCUS) technologies, which can reduce the contribution of the industry on the environmental disruption. Carbonate looping embodies an auspicious CCUS process, which employs a solid metal oxide to selectively adsorb CO₂ of industrial flue gases via an exothermic carbonation, followed by its endothermic calcination at a subsequent stage in a separate reactor to deliver a high-purity CO₂ stream ready for sequestration [2]. CaO comprises a widely-studied sorbent, since its fast sorption kinetics in the temperature range of 600-750°C have enabled its application for post-combustion CO₂ capture [2],[3] or the intensification of steam methane reforming process for high-purity H₂ generation [4]. Nevertheless, the elevated temperatures of its calcination ($\geq 900^\circ\text{C}$) have shifted attention towards alternative sorbents with lower energy requirements [5]. MgO is an example of such material, which captures CO₂ (Eq. (1)) at intermediate temperatures ($\leq 400^\circ\text{C}$), while other benefits include its theoretical sorption uptake ($\sim 25\text{mol CO}_2/\text{kg MgO}$) and abundance in nature [6].



Nonetheless, the advantages of MgO are eclipsed by its intrinsically high lattice energy and facile formation of rigid carbonate layers while in contact with CO₂, which both lead to slow CO₂ sorption kinetics. The blockage of MgO sites can be evaded by using proper MgO

precursors or promoters that secure a CO₂ sorbent with enhanced surface area. [6] But, this approach does not address the MgO lattice energy. As a solution to this problem, Zhang et al. [7] studied the addition of alkali nitrate promoters, which act as phase-transfer catalysts for MgO carbonation. These salts shift to a molten state in the temperature conditions where sorption occurs and dissolve both MgO and CO₂, thereby supporting their reaction and the generation of MgCO₃ nuclei. Through the years, the application of binary or ternary mixtures of alkali nitrates/nitrites was found to enhance solubility of reactants or cyclic stability and ensure a better CO₂ sorption activity. Harada et al. [8] firstly demonstrated a better sorption activity of MgO promoted with Li, Na and K nitrates with a molar ratio 30/18/52 compared to other works in the literature. Besides alkali nitrates, metal carbonates can also improve CO₂ uptake, by forming a kinetically more favoured mixed phase with MgO and CO₂ than MgCO₃. [9] Even if they remain unreacted, these compounds can also serve as carbonate seeds that facilitate the formation of MgCO₃ nuclei. [10]

The current infancy of carbonate looping with MgO has intensified research efforts on developing sorbents with high CO₂ uptake using various chemical reactants as MgO precursors or nitrate and carbonate promoters. Preparation methods also intend to improve the stability of MgO materials, since their sorption activity tends to gradually decrease over cycles. Nevertheless, the wide variety of chemical commodities and complex synthesis routes foster doubts on the economic feasibility of the process. Moreover, despite the existence of studies on the sorption mechanism and the reasons for the activity loss of these materials, [6] a thorough investigation is still required to demonstrate the influence of various

parameters, such as the promoter content or the feed stream composition and temperature during sorption or desorption stages on the performance of sorbents.

Towards the direction of low-cost sorbents, this research focused on fabricating MgO-based materials derived from mineral magnesite and promoted with limestone and a mixture of Li, Na and K nitrates. Physicochemical properties were assessed via XRD, BET and SEM, while advanced *in-situ* XRD was used to examine the sorption mechanism. The applicability of sorbents was eventually proven by evaluating their sorption activity under continuous carbonation cycles via TGA, while employing various operating conditions.

2. Experimental

2.1. Sorbent preparation

MgO precursor comprised a calcined mineral magnesite (denoted as Mg) supplied from Grecian Magnesite S.A, while mineral limestone (denoted as LM) provided by A.G.E.T. Heracles was employed as Ca precursor after being subjected to calcination at 900°C for 2h under air to decompose to CaO. Table 1 presents the composition of minerals, which was defined by X-Ray Fluorescence analysis. For the alkali nitrates, chemical commodities of Merck, namely lithium nitrate (LiNO₃, ≥99.0%), sodium nitrate (NaNO₃, ≥99.5%) and potassium nitrate (KNO₃, ≥99.0%) were used. Acetic acid from Panreac Quimica SA was also applied (CH₃COOH, ≥99.7%).

Table 1: X-Ray Fluorescence analysis results.

%	MgO	CaO	Al ₂ O ₃	SiO ₂	Others	LOI
Mg	91.76	1.31	0.13	0.52	0.12	6.16
LM	0.45	56.80	0.04	0.06	0.02	42.63

Sorbents were crafted with a facile preparation protocol, starting with wet mixing of calcined magnesite and limestone in a solution of 12%_{v/v} acetic acid by applying a molar ratio of CH₃COOH/(Ca+Mg) of 3/1. The solution was stirred for 0.5h at 25°C, followed by solvent removal in a rotary evaporator at 80-85°C under reduced pressure and drying at 120°C for 12h. The obtained material was calcined at 450°C for 4h in air and then at 600°C for another 1 h in air with 5% CO₂ to obtain a MgO-CaCO₃ material. The applied CO₂ partial pressure intended to avoid decomposition of CaCO₃. The MgO-CaCO₃ material was immersed in an aqueous mixture of LiNO₃/NaNO₃/KNO₃ (with a molar ratio of 30/18/52). The obtained suspension was stirred for 1h, dried at 120°C for 12h and calcined at 450°C for 4h in air to obtain the final sorbent.

A parametric evaluation of the composition of sorbents was performed, including the molar ratios of alkali (Li+Na+K) salts to MgO (0.05, 0.10, 0.15, 0.20, 0.25) and CaCO₃ to MgO (0.05, 0.10, 0.20, 0.25). Materials were abbreviated as MgCa_XA_Y, with X and Y reflecting the aforementioned ratios. Two additional sorbents were prepared by skipping alkali salts or limestone addition and were denoted as MgCa_{0.05} and MgA_{0.10} respectively.

2.2. Characterization

Crystal structure of sorbents was examined via X-ray diffraction (XRD) with a BRUKER D8 ADVANCE apparatus with a CuKα radiation wavelength λ of 0.15406 nm. XRD spectra between 20 and 80° were recorded with a step of 0.02° and a scanning rate of 0.2s/point. MgO crystal size (d_{MgO}) was retrieved with the Scherrer equation (Eq. (2)) via the full width of half the maximum (β) of the peak with 2θ equal to ~42.7°. N₂ adsorption analysis at 77K defined the surface area (S_{BET}) and pore volume (V_p) via the multipoint BET method in a Autosorb-1 Quantachrome flow apparatus after dehydrating sorbents overnight at 250°C. Lastly, Scanning Electron Microscopy (SEM) was employed to examine the morphology of sorbents with a JEOL JSM-IT500 microscope.

$$d_{MgO} = \lambda / \beta \cos \theta \quad (2)$$

2.2.1. Structure alterations assessment via *in-situ* XRD

Advanced *in-situ* XRD analysis was used to understand the structural modifications during carbonation cycles. Experiments were conducted through a BRUKER D8 ADVANCE diffractometer, coupled with a XRK-900 Anton-Paar cell, allowing operation at temperatures ranging from 25 to 900°C. Initially, the samples were treated for 10min at 450°C to release CO₂ and/or H₂O that were physisorbed from the atmosphere. The temperature was reduced to 325°C with a 40°C/min rate and the feedstock was altered to 100%CO₂ and maintained for 30min to perform the sorption step. Carbonation was succeeded by the temperature increase to 450°C under pure N₂ with a rate of 25°C/min, where the desorption step was carried out for 10min. The reactor cell was cooled down to 325°C to repeat sorption and the material underwent a total 20 sorption/desorption cycles. XRD spectra were recorded during sorption and desorption steps with a 2θ range of 28-45°, a step of 0.02° and a scanning rate of 0.2s/point. The chosen 2θ range enabled the supervision of changes of the main MgO and MgCO₃ peaks. Scherrer equation was used after each desorption to monitor the MgO size.

2.3. Evaluation of sorption performance

CO₂ sorption activity and stability were tested under continuous sorption/desorption cycles performed in a TGA apparatus (TG 209 F3 Tarsus, Netzsch). A sample of 10-15mg of each sorbent was placed in an Al-based crucible and subjected into a temperature and flow alteration program, by concurrently recording the mass changes over time. Sorbents were initially treated with a pure N₂ flow for 10min at 450°C to remove physisorbed CO₂ and/or humidity. Temperature was then reduced with a rate of 50°C/min and the gas feedstock was switched to a CO₂ containing stream to conduct carbonation for 30 min. Various temperatures (300 and 325°C) and gas feedstocks (100%CO₂ and 30% CO₂/N₂) were tested. Sorption was followed by heating to 450°C with 10°C/min rate to carry out desorption with pure N₂ or CO₂ flow. Cooling down was applied to repeat the carbonation stage and assess the stability over cycles.

3. Results

3.1. Characterization

The obtained XRD spectra (Figure 1) clarified that the applied preparation protocol delivered sorbents with MgO as their main crystal phase. CaCO₃ peaks were also detected, proving that the calcination step after the organic acid treatment provoked the decomposition of the acetate compounds at their desired forms, without forming CaO. Alkali metals retained their nitrate forms, with the main peak of NaNO₃ overlapping with CaCO₃ and KNO₃ emerging in rhombohedral and orthorhombic crystal forms (existence of both structures was proven with Rietveld analysis). Increasing the loading of either CaCO₃ or alkali salts caused the augmentation of the intensities of their characteristic peaks. Regarding LiNO₃, even though it was not identified, its inclusion as part of a ternary mixture of salts rejects the proposition that it possibly disintegrated in other composites while calcining at 450°C during preparation. Thus, LiNO₃ either belongs to the amorphous phase of sorbent or it is composed of uniformly dispersed small crystallites. [9]

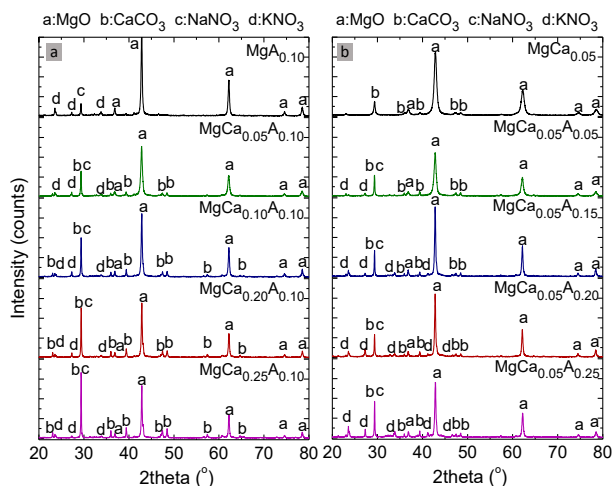


Figure 1: XRD spectra of sorbents with various (a) CaCO₃ and (b) alkali salt loadings.

Textural properties of prepared sorbents are summarized in Table 2. The calcined magnesite (Mg) was composed of a wide pore network, which was ideal for alkali nitrates to deposit and cause a notable reduction of both surface area and pore volume (MgA_{0.10}). The deposition occurred during the final calcination step while preparing the sorbents, where alkali salts shifted to their molten state, spread into the pores and eventually solidified after cooling down to ambient conditions. The change of physicochemical characteristics was milder with the addition only of CaCO₃ (MgCa_{0.05}), due to the ability of Ca²⁺ ions to incorporate in the MgO lattice and prevent a larger surface area reduction. [10] This effect enabled materials with both alkali nitrate and CaCO₃ promoters (MgCa_{0.05}A_{0.10}) to demonstrate better textural properties than the material only with alkali nitrates (MgA_{0.10}). Higher alkali salt contents led to higher

occupation of pores and further decrease of the surface area. Moreover, the larger ionic radius of Ca²⁺ compared to Mg²⁺ allowed a limited amount of former ions to enter the MgO lattice. Thus high CaCO₃ loadings provoked the generation of CaCO₃ crystallites which were deposited in the pores of MgO and reduced its available surface area. The inclusion of Ca²⁺ in the MgO lattice was also beneficial for the crystallite size, which was smaller in materials with both promoters than single alkali salts. However, a gradual growth of crystal size was observed while increasing either promoter amount.

Table 2: BET surface area (S_{BET}), pore volume (V_p) and MgO crystallite size (d_{MgO}) of sorbents.

Sorbent	S _{BET} (m ² /g)	V _p (cm ³ /g)	d _{MgO} (nm)
Mg	110.2	0.35	22.3
MgCa _{0.05}	52.3	0.27	18.4
MgA _{0.10}	19.4	0.13	32.8
MgCa _{0.05} A _{0.10}	22.7	0.23	25.8
MgCa _{0.10} A _{0.10}	17.5	0.15	26.9
MgCa _{0.20} A _{0.10}	13.5	0.14	29.0
MgCa _{0.25} A _{0.10}	11.0	0.10	30.5
MgCa _{0.05} A _{0.05}	60.6	0.65	23.4
MgCa _{0.05} A _{0.15}	14.7	0.12	27.2
MgCa _{0.05} A _{0.20}	10.1	0.08	27.5
MgCa _{0.05} A _{0.25}	7.3	0.04	29.8

Regarding the nature of the pore network defined by the N₂ adsorption analysis, sorbents with both CaCO₃ and alkali nitrate promoters presented type IV adsorption isotherms (Figure 2) with a H₃ hysteresis loop at high partial pressures (P/P₀ ≥ 0.8). This adsorption behavior is found in sheet-like materials with slit-like mesopores, while the hysteresis loop disclosed the presence of capillary condensation. Higher promoter loadings reduced the volume of adsorbed N₂, which is evidence of their deposition to the pores of the sorbent.

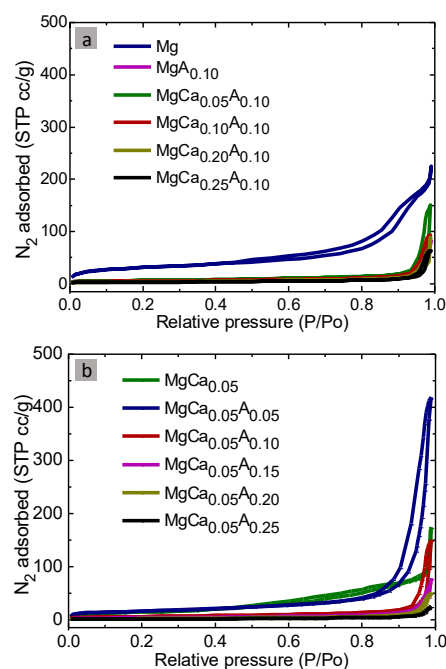


Figure 2: N₂ adsorption isotherms of sorbents with different (a) CaCO₃ and (b) alkali salt contents.

The hysteresis loop was different in the parent materials Mg and MgCa_{0.05}, since it was more representative for pores of irregular size or micropores. This proves that the immersion of MgO-CaCO₃ in the solution of alkali nitrates during sorbent preparation is a fundamental step to define the textural and morphological characteristics of the final sorbents. This was also proven by employing SEM analysis (Figure 3). Mg and MgCa_{0.05} consisted of small grains resembling spheres, while the sorbents promoted with alkali nitrates displayed a flower-like morphology. During the alkali salt deposition, MgO was hydrated to Mg(OH)₂, which consisted of flake grains. Magnesium reverted back to its oxide form during calcination by retaining the flake grains, which agglomerated via an Ostwald ripening process [9]. Eventually, sorbents with both CaCO₃ and alkali salts had a morphology similar to MgCa_{0.05}A_{0.10} (Figure 3d) despite the loading of each promoter.

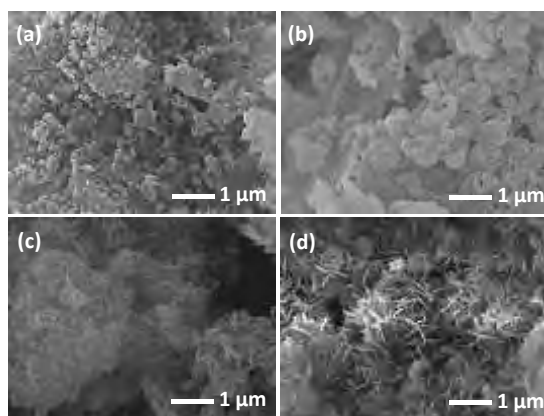


Figure 3: SEM analysis of (a) Mg, (b) MgCa_{0.05}, (c) MgA_{0.10} and (d) MgCa_{0.05}A_{0.10}.

3.2 Evaluation of sorption performance

3.2.1. Role of each promoter on sorption mechanism

The mass alterations of calcined magnesite (Mg), or materials with either one (MgCa_{0.05}, MgA_{0.10}) or both promoters (MgCa_{0.05}A_{0.10}) were examined via TGA while heating to 450°C under a 100%CO₂ flow as an initial step of evaluating the effect of each promoter in the sorption activity (Figure 4a). It was observed that only MgA_{0.10} and MgCa_{0.05}A_{0.10} demonstrated notable weight increase at temperatures above 200°C due to the attained CO₂ uptake. The weight of both sorbents followed a sigmoidal curve, since the increase rate was initially slow and gradually enhanced. Temperatures higher than ~375°C eventually caused the desorption of the captured CO₂ and the weight reduction to its initial value. On the other hand, Mg and MgCa_{0.05} remained inert during the whole experiment. These results establish alkali nitrates as essential promoters to enhance the CO₂ capture kinetics. This is in accordance to their role as phase-transfer catalysts that shift to a molten state, dissolving MgO and CO₂ and facilitating their reaction, [7] while the sigmoidal curve made clear that the generation of carbonate products follows a nuclei formation and growth mechanism. [10]

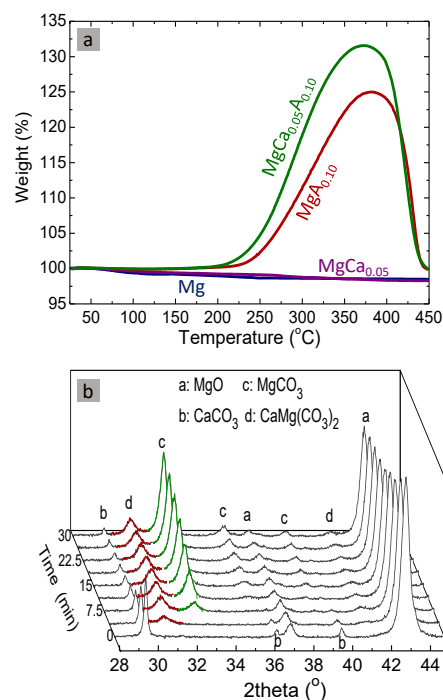


Figure 4: (a) Weight vs temperature of Mg, MgCa_{0.05}, MgA_{0.10} and MgCa_{0.05}A_{0.10} while heating to 450°C and (b) *in-situ* XRD of MgCa_{0.05}A_{0.10} during carbonation at 325°C with 100%CO₂.

The addition only of the CaCO₃ promoter did not have a beneficial effect, while it seems that its synergy with alkali nitrates allowed for a more efficient sorption activity compared to the addition only of molten salts. *In-situ* XRD was employed to understand the role of CaCO₃ by carrying out a sorption step for 30min under a 100%CO₂ stream (Figure 4b). It was found that carbonation proceeded via the formation of both MgCO₃ and CaMg(CO₃)₂, which proves that CaCO₃ also dissolved in the molten phase and enabled the generation of the mixed carbonate phase. Furthermore, the reflection peak of CaMg(CO₃)₂ emerged faster than MgCO₃, which was expected due to the lower equilibrium CO₂ partial pressure for the formation of mixed carbonates at a specific temperature. [9] The formation kinetics of each carbonate are controlled by a driving force term, which is calculated as the difference between the applied CO₂ partial pressure and the equilibrium CO₂ partial pressure ($P_{\text{CO}_2} - P_{\text{CO}_2,\text{eq}}$). Since $P_{\text{CO}_2,\text{eq}}$ is lower for CaMg(CO₃)₂, its formation is kinetically more favored than MgCO₃. This explains the faster appearance of CaMg(CO₃)₂ at 325°C.

Regarding the beneficial effect of CaCO₃, it can be seen that except from a higher sorption capacity (Figure 4a), CO₂ uptake of MgCa_{0.05}A_{0.10} began at relatively lower temperatures (~200°C) compared to MgA_{0.10} (~220°C). Even though the formation of CaMg(CO₃)₂ nuclei would justify the faster CO₂ sorption kinetics at 325°C, carbonation of the samples at 275°C with *in-situ* XRD (not shown for brevity) revealed that CO₂ capture occurs only via the MgCO₃ formation. The absence of CaMg(CO₃)₂ was possibly due to its slow formation kinetics and inadequate CaCO₃ solubility in the molten

alkali nitrates, with both elements having the potential of improving only with the application of higher temperatures [8]. This implies that CaMg(CO₃)₂ is not available at ~200°C, where the weight increase started in TGA. Thus, the enhanced sorption of MgCa_{0.05}A_{0.10} was associated with the ability of CaCO₃ to act as a carbonate seed that facilitates the formation of the first MgCO₃ nuclei. [10] Approaching higher temperatures enabled also the CaMg(CO₃)₂ generation and retained the CO₂ capture of MgCa_{0.05}A_{0.10} faster than MgA_{0.10}.

3.2.2. Effect of promoters loading on sorption activity

Sorbents with different CaCO₃ and alkali salt loadings were subjected to a carbonation cycle in order to assess the impact of each promoter. Figure 5 displays the weight alterations of the sorbents as a function of time. Regarding CaCO₃, all sorbents exhibited similar weight increase during the first ~2.5min, implying that sorbents with higher CaCO₃ loadings attained higher conversion of MgO. This is ascribed to the fast and more apparent formation of CaMg(CO₃)₂. However, the MgCa_{0.20}A_{0.10} and MgCa_{0.25}A_{0.10} materials displayed lower BET surface area (Table 2) and thus the formed carbonates limited the CO₂ diffusion and blocked the MgO sites more easily. This resulted in a lower mass increase rate after ~2.5min of sorption compared to MgCa_{0.05}A_{0.10} and MgCa_{0.10}A_{0.10}, while the similar uptake of the latter sorbents inferred that the harmful effect of CaCO₃ is evident only after surpassing a specific amount.

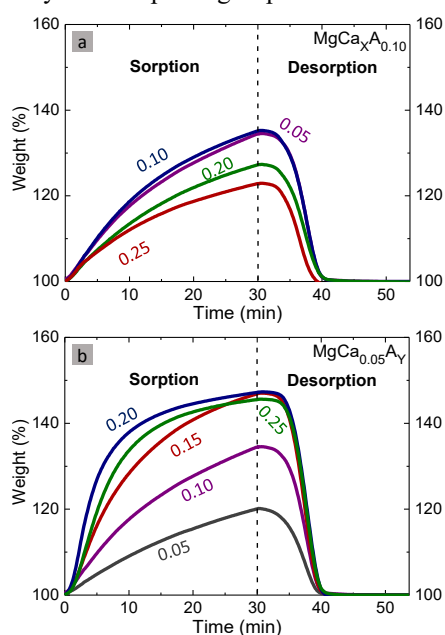


Figure 5: Weight vs time of sorbents with varying (a) CaCO₃ and (b) alkali salt loadings (sorption: 325°C, 100%CO₂, 30min; desorption: 450°C, 100%N₂, 10min).

Concerning the influence of the molten promoter loading, even though the higher alkali nitrate amounts reduced the surface area of the sorbents in the same way as CaCO₃, they generally provoked an enhancement of the sorption kinetics. This effect was widely evident while increasing the molar ratio of alkali salts to MgO

up to 0.15, proving that the lower alkali nitrate amounts did not attain an adequate coating and thus exploitation of the MgO surface. Raising the molar ratio to 0.20 did not alter the sorption capacity attained after the 30min of reaction, but instead profoundly improved the CO₂ capture rate in the first minutes of sorption. Nuclei carbonates were formed and grown rapidly in the first 10min and the material secured most of its maximum permitted uptake. The slower weight increase in the remaining time (t>10min) was attributed to the hindered CO₂ diffusion through the carbonate products. [8]

Further increase of alkali salts content (MgCa_{0.05}A_{0.25}) led to the formation of thick molten salt layers which impeded the efficient contact between MgO and CO₂ and thus decreased the CO₂ capture rate in the initial minutes of carbonation. [12] Regarding the relation of the performance of molten salt promoted sorbents with surface area, it is clear that the two parameters do not have a direct connection with each other. [8] However, it was seen that the surface area decreased drastically with the increase of the alkali salt to MgO ratio from 0.05 to 0.15, while further increase of the latter resulted in milder reduction of the surface (Table 2). A similar behavior was demonstrated from the CO₂ uptake after 30min of reaction. Hence, BET surface functions mostly as an indicator of the maximum alkali salt loading allowed to prevent the deterioration of CO₂ capture.

3.2.3. Effect of operating conditions on sorption activity

Based on the aforementioned results, MgCa_{0.05}A_{0.20} was considered a promising sorbent due to its high sorption rate and thus it was tested under 50 continuous sorption/desorption cycles under different temperature or gas feedstock composition conditions for the sorption stage. MgCa_{0.05}A_{0.10} was also tested under the same conditions to clarify the role of molten promoters (Figure 6).

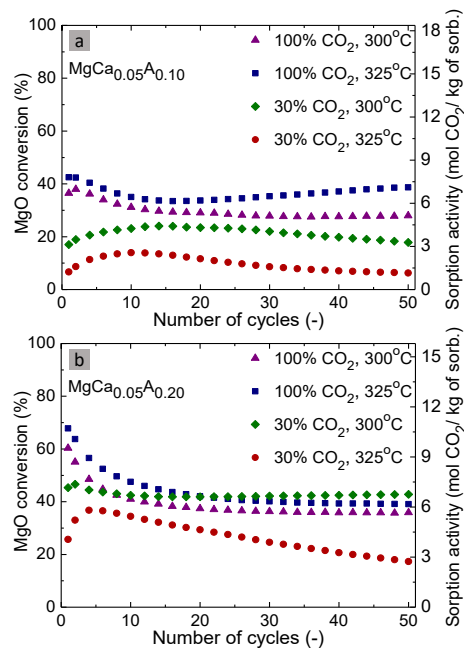


Figure 6: Sorption activity of (a) MgCa_{0.05}A_{0.10} and (b) MgCa_{0.05}A_{0.20} while applying various sorption conditions (sorption: 30min; desorption: 450°C, 100%N₂, 10min).

It was evident that the CO₂ uptake activity of both materials deteriorated during cyclic operation with sorption tested at either 325 or 300°C with 100%CO₂. Liquid phase sintering was identified as one of the main reasons for this performance, which is related to the gradual disappearance of pores and densification of solid grains during their exposure at high temperatures. This is related to the MgCO₃ phase, which has a low Tammann temperature (180°C) and thus is prone to sintering. The spreading of molten alkali nitrates into the pores intensify this phenomenon by pulling solid grains together via a capillary force, which is reinforced due to the solution of solid reactants in the molten salts. [13] The MgCa_{0.05}A_{0.20} sorbent exhibited higher loss of activity than MgCa_{0.05}A_{0.10} when tested with 100%CO₂, which was expected since the higher alkali salt content of the former could lead to accelerated densification, according to the theory of liquid phase sintering.

The existence of sintering was verified by evaluating MgCa_{0.05}A_{0.10} over 20 carbonation cycles in *in-situ* XRD (Figure 7). It was proven that the crystallite size of MgO displayed a constant augmentation during cyclic operation. Besides the crystal size, the $I_{\text{MgCO}_3}/I_{\text{MgO}}$ ratio achieved at the end of the sorption step of each cycle was also assessed as a means of testing the MgO conversion attained with *in-situ* XRD analysis. It was found that the ratio presented an initial reduction followed by a tendency of stabilization, while similar behavior was also exhibited in TGA (Figure 6). Hence, except from sintering, there is another counteracting phenomenon which may have a beneficial role in the stability of sorbents, as discussed more thoroughly later.

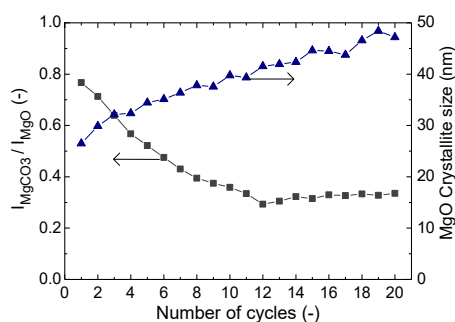


Figure 7: $I_{\text{MgCO}_3}/I_{\text{MgO}}$ ratio after sorption step and MgO crystal size after desorption step of MgCa_{0.05}A_{0.10} for each cycle.

The reduction of CO₂ concentration of gas feedstock from 100% to 30% by retaining 325°C as default temperature had an expected detrimental effect on the performance of sorbents due to the weakening of the carbonation kinetic driving force ($P_{\text{CO}_2} - P_{\text{CO}_2,\text{eq}}$). Self-reactivation was witnessed in the first carbonation cycles due to alkali salt and solid grain rearrangement during the formation and decomposition of carbonates. [14]. These transformations portend the densification of grains caused by the liquid phase sintering [13] and thus the maintenance of their effect for a number of cycles with the reduced CO₂ concentration (30%) implies that sintering progresses with a slower rate than with the 100%CO₂ flow. This was supported by employing SEM

analysis on spent sorbents (available for MgCa_{0.05}A_{0.20} at Figure 8) after their evaluation under the two different sorption conditions. The initial flower-like structure (Figure 3d) was replaced with agglomerated grains with no visible small pores when sorption was tested with the 100% CO₂ flow (Figures 8a). However, sintering was less severe with 30%CO₂, with SEM analysis revealing a visible pore network (Figures 8b). Hence, sintering rate seems to depend on the gas feedstock composition and thus the MgO conversion.

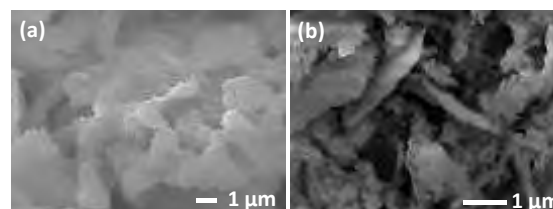


Figure 8: SEM analysis of spent MgCa_{0.05}A_{0.20} with sorption tested with (a) 100%CO₂ or (b) 30%CO₂.

Even though the effect of sintering was not severe, the sorbents displayed a higher loss of activity during cyclic operation when carbonation was executed at 325°C with the 30%CO₂/N₂ flow. During the continuous loop of magnesium between oxide and carbonate forms, the pore network undergoes consecutive shrinkages and expansions because of the different molar volumes of reactants MgO and CaCO₃ (11.2 and 36.9cm³/mol respectively) and products MgCO₃ and CaMg(CO₃)₂ (28.5 and ~42.9cm³/mol respectively). The extent of the alterations of pore network are more pronounced when a high MgO conversion is achieved. Furthermore, the formation of carbonates causes molten alkali nitrates to lose their contact with the magnesium compound due to their lower affinity with MgCO₃ compared to MgO [10] and to form aggregated clusters. [14] Even though the molten salts can re-spread and regain their contact with MgO after the CO₂ desorption step, there is a risk that part of the surface will eventually be left uncoated, leading to the gradual CO₂ uptake loss with cycles. The dewetting possibility should probably be higher with milder morphological transformations of the pore network and thus lower chance for alkali salts to re-coat efficiently the MgO surface. Since the application of the 30%CO₂/N₂ stream led to lower MgO carbonation and milder morphological transformations, it is inferred that dewetting is the main reason behind the severe loss of activity of sorbents when tested under these conditions.

The aforementioned proposition that an extended MgO carbonation can limit the dewetting possibility and enable alkali salt redistribution to bestow its beneficial effect of high CO₂ uptake agrees with the stable performance of sorbents when exposed to a 100%CO₂ flow. It was noticed that MgCa_{0.05}A_{0.10} even displayed a self-reactivation behavior in subsequent carbonation cycles (Figure 6). The comparison of textural properties between MgCa_{0.05}A_{0.10} and MgCa_{0.05}A_{0.20} showed that the former had higher BET surface (Table 2), indicating the potential existence of larger uncoated MgO surface

from alkali nitrates after their transition to molten state. Although the uncoated surface does not contribute to the uptake of the first cycles, [9] it is believed that molten salts gradually dewet the sintered MgO to spread on the originally uncoated surface and bestow higher activity and even a self-reactivation ability to MgCa_{0.05}A_{0.10}.

In an effort to improve the activity of sorbents, the carbonation temperature was reduced to 300°C, which led to a more pronounced MgO carbonation and a better overall CO₂ capture performance, especially for the MgCa_{0.05}A_{0.20} material (Figure 6). The latter attained an initial sorption capacity of 7.2 moles CO₂/kg of sorbent when exposed to a 30%CO₂ flow for 30min, while its activity reduced only by 6% after 50 carbonation cycles. This performance is promising, since the MgCa_{0.05}A_{0.20} material would attain a sufficient CO₂ sorption activity in the flue gases of a water gas shift reactor in coal integrated gasification combined cycles, where CO₂ content can reach up to 40%. The better activity when carbonation was performed at 300°C instead of 325°C with the 30%CO₂ flow was expected because of the different ways that temperature can affect the performance of molten salt promoted MgO. In terms of kinetics, low temperatures would limit the beneficial influence of the Arrhenius parameter, but would bolster the kinetic driving force ($P_{CO_2} - P_{CO_2,eq}$) due to the reduction of $P_{CO_2,eq}$. Due to the nature of the sorption mechanism, temperature also plays a role on the solubility of solid and gas reactants, while it is known that CO₂ solubility is enhanced with lower temperatures. [6] It has also been mentioned that the application of a stream with P_{CO_2} lower than 0.5bar requires the reduction of the carbonation temperature in order to achieve sufficient CO₂ trapping in the molten phase. [8] These factors contributed to the enhancement of the MgO conversion and secured an adequate salt spreading and a stable sorption activity, notably for MgCa_{0.05}A_{0.20}.

Except from a relatively low CO₂ concentration during sorption, a realistic carbonate looping operation requires calcination to be carried out under pure CO₂, in order for the gas outlet to be comprised of a pure CO₂ stream ready for sequestration and isolation. Thus, the activity of MgCa_{0.05}A_{0.10} and MgCa_{0.05}A_{0.20} was tested with calcination performed under a pure CO₂ flow (Figure 9). Both sorbents displayed inferior performance in contrast to the operation of calcination with a 100%N₂ flow. Since the temperature of calcination remained the same, the presence of CO₂ decreased the rate of desorption and increased rate for sintering. However, the MgCa_{0.05}A_{0.10} material maintained its self-reactivation ability, which limited its activity loss to 28%. MgCa_{0.05}A_{0.20} displayed a faster decrease of its sorption activity followed by a tendency of stabilization near the end of the 50 sorption/desorption cycles. The reduction rate of CO₂ uptake was slower compared to the application of the 30%CO₂/N₂ stream for carbonation (Figure 6), where dewetting was recognized as the main reason for the activity loss. MgO conversion was also high enough to ensure an alkali salt re-spreading with limited chance for dewetting. Hence, it is implied that calcination in pure CO₂ affects mainly sintering rather than the alkali salt rearrangement.

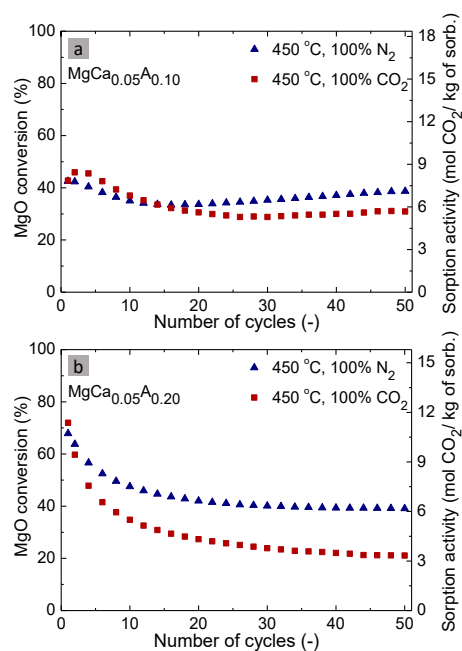


Figure 9: Sorption activity of (a) MgCa_{0.05}A_{0.10} and (b) MgCa_{0.05}A_{0.20} while applying various desorption conditions (sorption: 325°C, 100%CO₂, 30min; desorption: 10min).

3.3. Comparison with high temperature CaO sorbents

The cyclic performance of MgCa_{0.05}A_{0.20} was compared (Figure 10) with two CaO-based sorbents from previous works [2], [3]. These included a synthetic material (Ca-Zr-66) composed of 66%_{w/w} CaO/CaZrO₃, which was synthesized via a sol-gel auto-combustion method and a mineral sorbent (LM_W30Mg) prepared by wet mixing calcined limestone and magnesite with a weight ratio of 70/30. It should be noted that the different temperature applied to achieve adequate sorption with CaO (650°C) and MgO (300°C) does not enable a direct comparison between sorbents. The ΔT (350°C) signifies limited MgO carbonation kinetics and CO₂ diffusion through formed carbonates, while higher operating temperatures cannot be employed for MgO due to thermodynamic restrictions of the reaction. However, a comparison can still be accepted in terms of stability and CO₂ uptake.

CaO-based sorbents gradually lose their activity over cycles due to the severe sintering. The incorporation of synthetic CaZrO₃ promoter in Ca-Zr-66 enabled CaO to withstand sintering more efficiently than CaO promoted with mineral-derived MgO (LM_W30Mg). Despite the better performance, the high cost of synthetic materials intensifies the necessity for high-stability sorbents using low-cost precursors. This is attained in the intermediate-temperature MgCa_{0.05}A_{0.20} material, whose stability is similar to Ca-Zr-66, despite its mineral nature, and thus would lead to a higher sorption capacity compared to LM_W30Mg after the 50 carbonation cycles. However, the carbonation extent after 30min of reaction was lower than the high-temperature sorbents. This signifies that despite the enhanced sorption kinetics, future research could focus more on further exploiting the available MgO content in limited but realistic sorption durations.

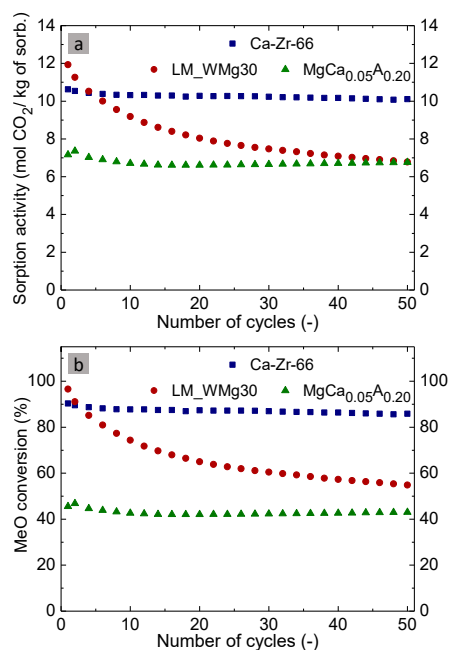


Figure 10: (a) CO₂ uptake and (b) MeO conversion of the sol-gel synthesized 66%_{w/w} CaO/CaZrO₃ (Ca-Zr-66), the mineral sorbent (LM_WMg30) derived by wet mixing calcined limestone and magnesite with a 70/30 weight ratio (Me: Ca; sorption: 650°C, 15%CO₂, 30min; desorption: 850°C, 5min, N₂) and the sorbent (MgCa_{0.05}A_{0.20}) of this study (Me: Mg; sorption: 300°C, 30%CO₂, 30min; desorption: 450°C 10min, N₂).

4. Conclusions

This study focused on the preparation of low-cost MgO sorbents based on mineral magnesite and reinforced with adequate CO₂ capture kinetics via limestone and Li, Na and K nitrates. Alkali nitrates successfully upgraded the sorption kinetics of magnesite via their transition into a molten state and the provision of an alternative pathway for MgO carbonation. CaCO₃ either acted as a carbonate seed to facilitate the generation of the first MgCO₃ nuclei or it reacted with MgO and CO₂ to form CaMg(CO₃)₂. The beneficial effects of CaCO₃ were apparent principally with the application of a low molar ratio of CaCO₃ to MgO of 0.05 in order to avoid the hindering of the CO₂ diffusion through the formed carbonates. The alkali salts to MgO ratio was another important parameter, since an increase up to 0.20 was profitable in terms of enhanced sorption kinetics, while higher ratios disabled the effective contact of CO₂ and MgO. The sorbent with the aforementioned composition attained an uptake of 7.2 moles CO₂/kg of sorbent when carbonation was performed with 30%CO₂ for 30min at 300°C and a negligible activity loss after 50 carbonation cycles. Sorbents were found prone to sintering which reduced their cyclic activity. Alkali salt rearrangement was also denounced for activity changes, which had a detrimental effect by dewetting the surface with limited MgO carbonation. However, high MgO conversions attained a beneficial salt rearrangement and enhanced stability under realistic operating conditions. This work highlighted mineral MgO as a low-cost CO₂ sorbent for carbonate looping in relatively mild temperature conditions.

Acknowledgements

This research has been co-financed by the European Regional Development Fund of the European Union and Greek national funds through the Operational Program Competitiveness, Entrepreneurship and Innovation, under the call RESEARCH - CREATE - INNOVATE (project code:T1EDK-01532).

References

- [1] Dowell, N. M., Fennel, P. S., Shah, N. & Maitland, G. C. (2017). The role of CO₂ capture and utilization in mitigating climate change, *Nat. Clim. Change*, 7, 243-249.
- [2] Antzara, A., Heracleous, E. & Lemonidou, A. A. (2016). Improving the stability of synthetic CaO-based CO₂ sorbents by structural promoters, *Appl. Energy*, 156, 331-343.
- [3] Papalas, T., Antzaras, A. N. & Lemonidou, A. A. (2020). Evaluation of Calcium-Based Sorbents Derived from Natural Ores and Industrial Wastes for High-Temperature CO₂ Capture, *Ind. Eng. Chem. Res.*, 59, 9926-9938.
- [4] Papalas, T., Antzaras, A.N., & Lemonidou, A. A. (2020). Intensified steam methane reforming coupled with Ca-Ni looping in a dual fluidized bed reactor system: A conceptual design, *Chem. Eng. J.*, 382, 122993.
- [5] Dal Pozzo, A., Armutlulu, A., Rekhina, M., Abdala, P. M. & Müller, C. R. (2019). CO₂ uptake and Cyclic Stability of MgO-Based CO₂ Sorbents Promoted with Alkali Metal Nitrates and Their Eutectic Mixtures, *ACS Appl. Energy Mater.*, 2(2), 1295-1307.
- [6] Hu, Y., Guo, Y., Sun, J., Li, H. & Liu, W. (2019). Progress in MgO sorbents for cyclic CO₂ capture: a comprehensive review, *J. Mater. Chem. A*, 7, 20103-20120.
- [7] Zhang, K., Li, X. S., Li, W.-Z., Rohatgi, A., Duan, Y., Singh, P., Li, L. & King, D. L. (2014). Phase Transfer-Catalyzed Fast CO₂ Absorption by MgO-Based Adsorbents with High Cycling Capacity, *Adv. Mater. Interfaces*, 1(3), 1400030.
- [8] Harada, T., Simeon, F., Hamad, E. Z. & Hatton, T. A., (2015). Alkali Metal Nitrate-Promoted High-Capacity MgO Adsorbents for Regenerable CO₂ Capture at Moderate Temperatures, *Chem. Mater.*, 27(6), 1943-1949.
- [9] Cui, H., Zhang, Q., Hu, Y., Peng, C., Fang, X., Cheng, Z., Galvita, V. V. & Zhou, Z. (2018). Ultrafast and Stable CO₂ Capture Using Alkali Metal Salt-Promoted MgO-CaCO₃ Sorbents, *ACS Appl. Mater. Interfaces*, 10, 20611-20620.
- [10] Jo, S.-I., An, Y.-I., Kim, K.-Y., Choi, S.-Y., Kwak, J.-S., Oh, K.-R. & Kwon, Y.-U. (2017). Mechanisms of absorption and desorption of CO₂ by molten NaNO₃-promoted MgO, *Phys. Chem. Chem. Phys.*, 19, 6224-6232.
- [11] Jin, S., Ho, K. & Lee, C.-H. (2018). Facile synthesis of hierarchically porous MgO sorbent doped with CaCO₃ for fast CO₂ capture in rapid intermediate temperature swing sorption, *Chem Eng. J.*, 334, 1605-1613.
- [12] Wang, J, Li, M., Lu, P., Ning, P. & Wang Q. (2020), Kinetic study of CO₂ capture on ternary nitrates modified MgO with different precursor and morphology, *Chem Eng. J.*, 392, 123752.
- [13] German, R. M., Suri, P. & Park S. J., (2009), Review: liquid phase sintering, *J. Mater. Sci.* 44, 1-39.
- [14] Lee, H., Triviño, M. L. T., Hwang, S., Kwon, S. H., Lee, S. G., Moon, J. H., Yoo, J. & Seo, J. G. (2018), In Situ Observation of Carbon Dioxide Capture on Pseudo-Liquid Eutectic Mixture-Promoted Magnesium Oxide, *ACS Appl. Mater. Interfaces*, 10(3), 2414-2422.

‘CO₂CKTAILS IN A PIPELINE’: THE PHASE BEHAVIOUR OF CO₂ WITH >20 IMPURITIES

Eduardo Luna-Ortiz¹*

¹ Pace Flow Assurance, London, UK

* Corresponding author e-mail: eduardo@paceflowassurance.co.uk

Abstract

CO₂ in transportation pipelines will contain several impurities due to the wide range of potential emitters. Depending on the physical and chemical nature of the impurities, these will induce diverse phase equilibria. This will be the case even if the impurities are at the ppm level. Certain impurities can induce undesirable liquid phases when the system operates in low pressure single gas phase mode. These liquid phases can appear at normal operating temperatures and can lead to corrosion mechanisms. Thus, there is a need to accurately predict the thermodynamic behaviour of the multicomponent mixture that will be transported in a CCS network. In this work, we investigate the phase behaviour of a CO₂ multicomponent mixture. While the aim is to qualitatively identify the potential number of phases that could form, we focus on the potential issue of liquid dropout at low pressure conditions during gas phase operation.

Keywords: Phase behaviour, Thermodynamics, EoS, CPA, CO₂ transport, Impurities

1. Introduction

Rarely, anthropogenic CO₂ to be transported for geological storage is 100% pure. In most cases, exported CO₂ from capture sites will contain a number of impurities (often at the ppm level but as high as 5% mol of non-condensable gases). This is not only beneficial to the project economics [1] but also reduces energy penalties and associated emissions due to further purification.

Several CO₂ specifications have been developed over the years. In [2], a review of various specifications can be found. The development of these specifications takes into consideration health and safety regulations, industry standards, country legislations and the integrity/flow assurance of the full-chain. Although these specifications serve as guidance and provide a common basis for the design of the components of the CCS system, each project/development will develop its own specification that is appropriate for its own characteristics. Nonetheless, we argue that the limit of impurities should be set, primarily, as to preserve the integrity of the transport/storage system: it should not be transported what cannot be stored.

Moreover, in order to maximise economies of scale and meet decarbonisation targets, CCS systems are being developed in (industrial) clusters (i.e. Hynet, Porthos, Acorn, just to name a few) where emitters of diverse industries (cement, fertilizer, steel, refinery, power, H₂ production, etc.) will be exporting its captured emissions to a common transport infrastructure (existing or purpose-built) for storage in depleted reservoirs, e.g. [3],[4],[5]. Here, the typical operating philosophy is to operate the transport pipeline at low pressure (in gas phase) and then, at some point as pressure builds up in the reservoir, transition to high pressure operation (liquid phase). Usually, the operator of the transport/storage

system will set the fluid specification to which all the emitters will have to meet. The emitter will then need to design its purification and conditioning system accordingly. Often, the transport operator will need to balance the diverse nature of the capture technologies as well as the costs for purification and the costs of design for undesirable species in the pipeline.

While the impurities content is controlled and measured, each emitter will be discharging its CO₂ at different compositions and the operator will be accepting it if it meets the specification. Therefore, the final composition to be transported and injected will contain, potentially, all the possible compounds associated to each capture and purification technology (i.e., solvents or other chemicals) or other compounds used in each individual industrial process. Thus, it is realistic to expect that more than 20 species of diverse chemical nature will be present in the mixture: a chemical cocktail. Additionally, temporal variations in the feed rate of the various emitters will result in variations of composition along the pipeline. These variations may have a (temporal) impact in the transport, injection, and storage of CO₂ [6].

In this work, we investigate the phase behaviour of a CO₂ mixture with more than 20 impurities. While the aim is to qualitatively identify the potential number of phases that could form, we focus on the potential issue of liquid dropout at low pressure conditions during gas phase operation.

2. Impact of Impurities in CO₂ streams

The effect of impurities in CO₂ streams, in general, is well documented, e.g., [7],[8],[9],[10],[11]. Their presence can lead to flow assurance, corrosion, integrity, safety, processing, economic and geological storage issues.

Understanding the thermo-physical and transport properties of the mixture is fundamental for the design and operation of all stages of CCS systems. It is often assumed that impurities less than 1000 ppm(v) do not “significantly” affect the properties of the fluid. Indeed, this might be the case (and assumption) in the design of pipeline transportation systems. However, it is noted that certain low molecular weight or light gases will have a particular strong impact in the physical properties (and, in consequence in the design and operation of CCS transport systems) even in small quantities (such as hydrogen, see e.g., [12],[13]).

The effect on impurities could be classified in two groups. The first group relates to the impurities related to the operation of the transport system at high pressure (liquid/supercritical). Here, the key impact is that some impurities open-up the two-phase region, in the pressure-temperature plane, leading to an increase of required operating pressure to ensure single phase flow. The second key group is related to the effect of the solubility of water (or other heavy components such as TEG) in the presence of impurities in CO₂. In order to avoid water (or any liquid) dropout, it is crucial to determine dew point of any liquid phase. In addition, it is important to determine the speciation in the liquid phases as particular impurities will increase (or decrease) corrosion risk.

2.1 Thermodynamic modelling of CO₂ mixtures

Several comprehensive reviews of thermodynamic models and their performance for CCS transport systems are available elsewhere and the reader is referred to them (e.g. [14],[15],[16],[17]). However, all these works address fluid equilibria of CO₂ mixtures with few light impurities. There is some thermodynamic modelling and validation for CO₂ with water and the effect of various gases (e.g. [18]), solubility of CO₂ in water with glycols or some amines (e.g., [19],[20]) or some ternary/quaternary/quinary mixtures of CO₂ with light/sour gases, water and TEG or amines (e.g., [21],[22]).

There is not a single universal Equation of State for use with CO₂ with all potential impurities (from non-condensable gases, polar components such as glycols, solvents such as amines or associating fluid such as methanol). While GERG-2008 (or EOS-CG/TREND) could be used for relatively simple CO₂ mixtures with some other gases and water, the EoS cannot support other component such as TEG or alcohols. In this scenario, cubic EoS with appropriate mixing rules (i.e., Huron-Vidal) or extensions to account for associating and solvation effects (for example, most notably Cubic-Plus-Association – CPA) seems more adequate. Other approaches that could be used up to certain extent are SAFT-based EoS.

Thus, the conventional approach to model CO₂ mixtures with a large set of components is to apply some empirical model reduction (mostly empirical) as to suit the final use (flow assurance, corrosion, reservoir, etc.) and use the most appropriate EoS. It is not a common practice to perform the thermodynamic modelling of the full set of CO₂ with impurities. In this work, we attempt to

investigate the phase behaviour of a CO₂ mixture with a large set of impurities.

3. Methodology and Basis

3.1 Equation of State (EoS)

All the computational experiments have been performed using Cubic-Plus-Association (CPA-Infochem) implemented in Multiflash v.7.1. In general, CPA covers well mixtures of CO₂ with non-condensable gases as well as other sour/acid gases. In addition, it can cover polar/associating effects induced by alcohols, glycols, and amines.

3.2 Unavailable Components in Multiflash Database

There are three components (α -aminoisobutyric acid, dimethyl sulphide – DMS, and potassium carbonate – K₂CO₃) that are not available in the Multiflash component library. These components were created using Symmetry Process Simulator and then exported into Multiflash.

3.3 Binary Interaction Parameters (BIPs)

The CPA EoS in Multiflash has already a large set of default BIPs that have been optimised against experimental data and these have been used (i.e., CO₂-water, CO₂-TEG, TEG-Water, MeOH-Water, MeOH-CO₂ to name few). All the default BIPs have been assumed. Additional BIPs have been added or modified as per Table 1. The default cross-association BIPs in Multiflash have been used.

Table 1: Non-zero BIPs added or modified in CPA EoS.

Pair	Value	Source
CO ₂ -Ar	0.18	[17]
CO ₂ -H ₂ S	0.106	
CO ₂ -O ₂	0.116	
CO ₂ -SO ₂	0.048	
CO ₂ -CO	-0.071	[23]
Water-Piperazine	-0.248	[24]

4. Phase Behaviour of CO₂ mixtures

Table 2 and Table 3 show the compositions of the two fluids considered in this work. Figure 1 and Figure 2 depict the corresponding phase diagrams of each CO₂-rich cocktail. Both compositions have the same impurities and amounts except that Cocktail 2 is TEG-free.

There are a few interesting features. Firstly, in Cocktail 1, it is seen that even a small addition of TEG is sufficient to induce liquid dropout at high temperatures (circa 70°C). A second liquid phase (MDEA-rich) is induced at lower temperatures (near critical temperature). In order to avoid any liquid dropout, at low pressures (or gas phase), the system would need to operate at temperatures higher than 70°C. Alternatively, the fluid would need to be TEG-free and, in this case, the operating temperature would need to be circa 30°C for liquid to appear (see Cocktail 2). In this scenario, there is not a ‘free’ liquid

dropout but two-phase equilibrium between liquid CO₂ dissolved in the MDEA phase in equilibrium with gaseous CO₂. For Cocktail 2, a ‘free’ liquid phase can appear at temperatures lower than -20°C.

A realistic operating condition of a low pressure pipeline at subsea ambient condition (i.e., 25 bar and 5°C) will likely see liquid dropout. However, the liquid fractions are expected to be significantly low (0.0005-0.0006% mol, see Figure 3). At relatively high velocities, the liquid may be transported in a mist/bubbly flow regime. Nevertheless, in the low points of the pipeline and, particularly at low flow conditions, this liquid could accumulate and lead to, for example, corrosion mechanisms. These liquid pools should be managed by pigging campaigns. The frequency will be dictated by how fast the liquid holdup will be built in the system.

O ₂	0.00000786533
H ₂ S	0.00000071254
SO ₂	0.00000235812
NO	0.00000011062
NO ₂	0.00000011062
EtOH	0.00000517203
HCN	0.00000071254
COS	0.00000041221
DMS	0.00000013459
α-aminoisobutyric acid	0.00000002886
K ₂ CO ₃	0.00000002886
Piperazine	0.00000112468
MDEA	0.00000241768
TEG	0.0

Table 2: Composition of Cocktail 1.

Component	Mol fraction
Water	0.00003434850
MeOH	0.00030863633
CO ₂	0.98948056152
H ₂	0.00231148724
Acetaldehyde	0.00000513430
Benzene	0.00000041221
CH ₄	0.00175477129
Ethane	0.00000772394
Propane	0.00000903478
Butane	0.00000382301
CO	0.00056379386
Ar	0.00000201998
N ₂	0.00549450240
O ₂	0.00000786533
H ₂ S	0.00000071254
SO ₂	0.00000235812
NO	0.00000011062
NO ₂	0.00000011062
EtOH	0.00000517203
HCN	0.00000071254
COS	0.00000041221
DMS	0.00000013459
α-aminoisobutyric acid	0.00000002886
K ₂ CO ₃	0.00000002886
Piperazine	0.00000112468
MDEA	0.00000241768
TEG	0.00000256197

Table 3: Composition of Cocktail 2.

Component	Mol fraction
Water	0.00003434850
MeOH	0.00030863633
CO ₂	0.98948312349
H ₂	0.00231148724
Acetaldehyde	0.00000513430
Benzene	0.00000041221
CH ₄	0.00175477129
Ethane	0.00000772394
Propane	0.00000903478
Butane	0.00000382301
CO	0.00056379386
Ar	0.00000201998
N ₂	0.00549450240

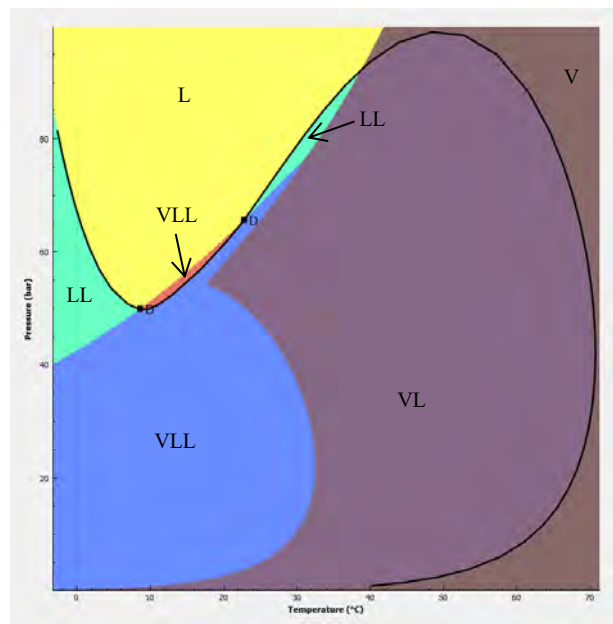


Figure 1: Phase Diagram for Cocktail 1.

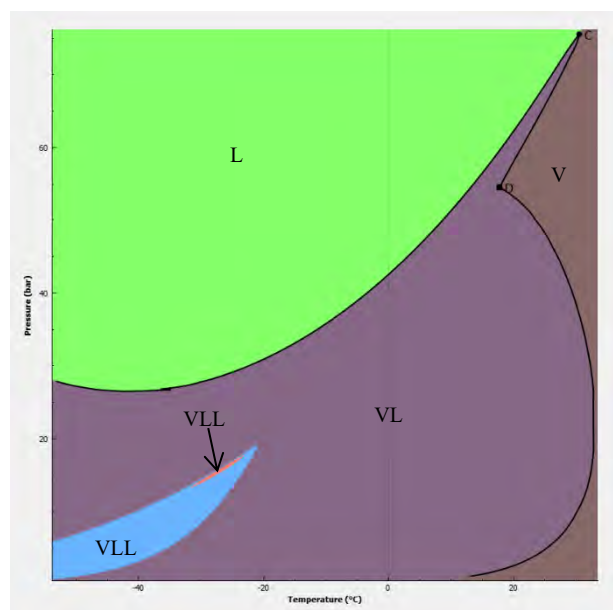


Figure 2: Phase Diagram for Cocktail 2. Note that solid phases (CO₂ and H₂O) are not shown (captured) by the thermodynamic model.

One could ask if the model is suitable to handle the solubility of CO₂ in TEG/water mixtures given the very low concentration of TEG. This is an important issue as if any liquid dropout is to be avoided (assuming low pressure operation), the TEG specification would need to be excessively low, thereby imposing severe constraints to the CO₂ emitters. Firstly, we assess the performance of the CPA EoS versus experimental data of a binary CO₂-TEG mixture. Figure 4 shows a (limited) comparison of the solubility of CO₂ in TEG. The experimental data has been taken from [25]. It is seen that there is good match at the relatively low pressures (which are the operating conditions of interest). This provides a good level of confidence in the thermodynamic model.

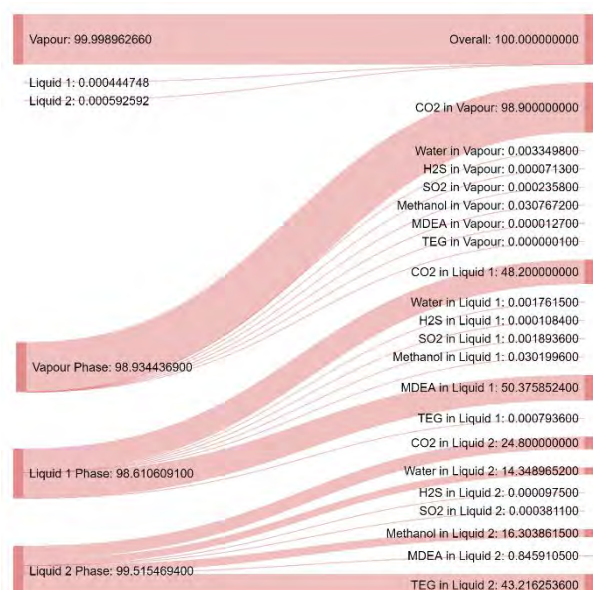


Figure 3: Phase and Component splitting of selected species at 25 bar and 5 °C in Cocktail 1. Amounts are given in mol %. Distribution of rest of components is not shown.

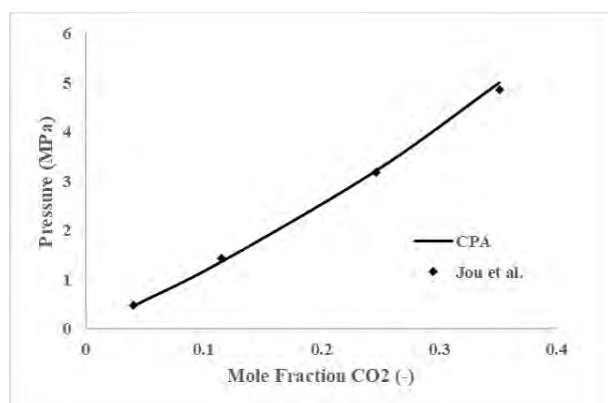


Figure 4: Comparison of CPA estimations and experimental data of CO₂ solubility in TEG at 298.15 K.

The comparisons performed in this work are of limited scope, one should also investigate the solubility of CO₂ in multicomponent systems, particularly in the presence of water, methanol, and amines (at very low

concentrations). These comparisons were not part of this study.

4. Discussion and Conclusions

It is reasonable to expect liquid dropout from impure gas CO₂ even with very small amounts of components such as water, TEG, amines, etc. At certain conditions, this liquid could be problematic inducing corrosion, erosion, or accumulation (holdup) in the pipeline. Thus, it is important to be able to determine the operating conditions and/or concentrations at which the liquid could dropout from the bulk.

It has been observed that a CO₂-rich fluid with low TEG content can induce liquid dropout at relatively high temperatures. It follows that for typical low pressure operating conditions and ambient condition, liquid dropout is a real possibility. The relative amount of liquid is very low and at high flowrate, the liquid may be transported in a misty/bubbly flow regime. Liquid accumulation (over a long period of time) at low flowrates should be managed with, for example, pig runs.

If there is a drive to avoid liquid dropout, in any foreseeable scenario, then a more onerous specification would be required. For example, the composition of Cocktail 3 (Table 4) will meet that requirement. Figure 5 shows the corresponding “exotic” phase diagram. It is seen that for low operating pressures there is no liquid dropout expected at temperatures above circa 5 °C (typical seabed ambient temperature). However, in case a depressurization scenario, it is possible that the system will experience liquid condensation, albeit temporal as it will vaporize back once system settles to ambient temperature. It is also noted that such diminute amounts could be problematic (and expensive) to technically achieve, detect and measure.

Table 4: Composition of Cocktail 3.

Component	Mol fraction
Water	0.0000070000
MeOH	0.0006100000
CO ₂	0.9892141038
H ₂	0.0023108790
Acetaldehyde	0.0000051330
Benzene	0.0000004121
CH ₄	0.0017543090
Ethane	0.0000077219
Propane	0.0000090324
Butane	0.0000038220
CO	0.0005636450
Ar	0.0000020195
N ₂	0.0054930560
O ₂	0.0000078633
H ₂ S	0.0000007124
SO ₂	0.0000023575
NO	0.0000001106
NO ₂	0.0000001106
EtOH	0.0000051707
HCN	0.0000007124
COS	0.0000004121
DMS	0.0000001346
α -aminoisobutyric acid	0.0000000289
K ₂ CO ₃	0.0000000289
Piperazine	0.0000011244
MDEA	0.0000000989

TEG	0.0000000014
-----	--------------

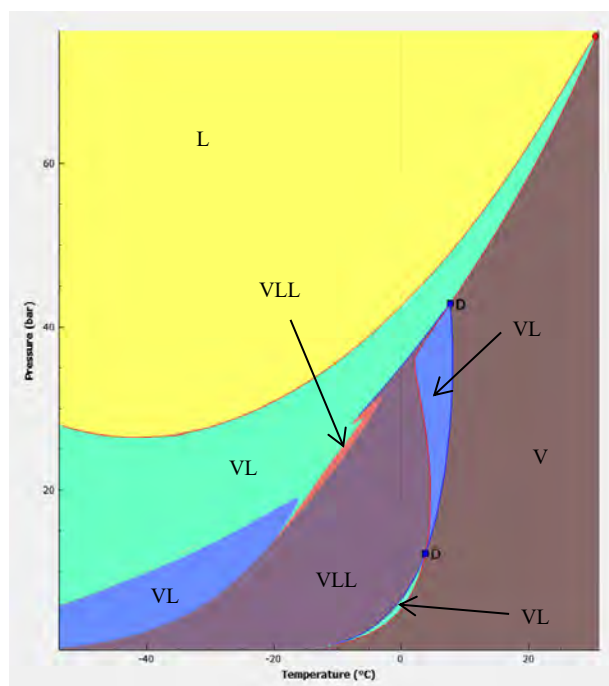


Figure 5: Phase Diagram for Cocktail 3.

The thermodynamic model used in this work is CPA (Infochem). The model has shown excellent prediction capabilities, in particular, for phase behaviour of polar and associating components. While there is a good degree of confidence in the model at high TEG concentrations, at low TEG concentrations there is some uncertainty that should be addressed (although we have shown good capability predictions). In addition, the CPA model does not have BIP for binary pairs with MDEA (although this does not seem to have a great impact, at least with the fluids considered in this work). It is also noted that the CPA model does not include association parameters between CO₂ and TEG to describe cross-association and solvation effects. This potentially has the largest effect and should be investigated in future work.

While there is wealth of data for many binary CO₂ mixtures of interest, there is lack of experimentation for truly multicomponent CO₂ mixtures. In order to reduce uncertainty, each transport operator would need to commission experimental campaigns to validate EoS models (with a large number of impurities) such the one presented in this work. Indeed, these experiments may be complicated and expensive to carry out. Joint-Industry Partnerships and collaborations (knowledge sharing) will be fundamental. We are currently working in the formation of one.

References

[1] Kolster et al. (2017). The role of CO₂ purification and transport networks in carbon capture and storage cost reduction, *Intl. J. Greenh. Gas Cont.*, 58, 127-141.

- [2] Murugan et al. (2020). Performing Quality Assurance of Carbon Dioxide for Carbon Capture and Storage, *C*, 6(4),76.
- [3] Brunsvold et al. (2011). Case studies on CO₂ transport infrastructure: optimization of pipeline network, effect of ownership, and political incentives, *Energy Proc.*, 4, 3024-3031.
- [4] Chandel et al. (2010). Potential economies of scale in CO₂ transport through use of a trunk pipeline, *Energy Convers. Manage.*, 51(12), 2825-2834.
- [5] Brownsort et al. (2016). Reducing costs of carbon capture storage by shared reuse of existing pipeline—Case study of a CO₂ capture cluster for industry and power in Scotland, *Intl. J. Greenh. Gas Cont.*, 52, 130-138.
- [6] Kahlke et al. (2020) Potential Dynamics of CO₂ Stream Composition and Mass Flow Rates in CCS Clusters, *Processes*, 8(9), 1188.
- [7] Peletri et al. (2019). Process simulation of impurity impacts on CO₂ fluids flowing in pipelines, *J. Clean. Prod.*, 118145.
- [8] Blanco et al. (2013). Influence of methane in CO₂ transport and storage for CCS technology, *Environ. Sci. Technol.*, 46(23), 13016-13023.
- [9] Chen et al. (2018). Effects of impurities on CO₂ sequestration in saline aquifers: Perspective of interfacial tension and wettability, *Ind. Eng. Chem. Res.*, 57(1), 371-379.
- [10] Skaugen et al. (2016). Techno-economic evaluation of the effects of impurities on conditioning and transport of CO₂ by pipeline, *Intl. J. Greenh. Gas Con.*, 54(2), 627-639.
- [11] Verma et al. (2011). Effect of contaminant on the thermodynamic properties of CO₂-rich fluids and ramifications in the design of surface and injection facilities for geological CO₂ sequestration, *Energy Proc.*, 4, 2340-2347.
- [12] Al-Siyabi I (2013). Effect of Impurities on CO₂ Stream Properties. PhD Thesis. Heriot-Watt University
- [13] Wettenhall et al. (2014). The Effect of CO₂ Purity on the Development of Pipeline Networks for Carbon Capture and Storage Schemes. *Intl J Greenh Gas Con.* 30,197-211
- [14] Munkejord et al. (2016). CO₂ transport: Data and models – A review. *Appl. Energy*, 169, 499-523.
- [15] Diamantonis et al. (2013). Evaluation of Cubic, SAFT, and PC-SAFT Equations of State for the Vapor-Liquid Equilibrium Modeling of CO₂ mixtures with other gases, *Ind. Eng. Chem. Res.*, 52, 3933-3924.
- [16] Diamantonis et al. (2013). Thermodynamic and transport property models for carbon capture and sequestration (CCS) processes with emphasis on CO₂ transport, *Chem. Eng. Res. Des.*, 91, 1793-1806.
- [17] Li et al. (2009). Evaluating cubic equations of state for calculation of vapor-liquid equilibrium of CO₂ and CO₂-mixtures for CO₂ capture and storage processes, *Appl. Energy*, 86, 826-836.
- [18] Rowland et al. (2018). Reliable prediction of aqueous dew points in CO₂ pipelines and new approaches for control during shut-in. *Intl. J. Greenh. Gas Cont.*, 70, 97-104.
- [19] Wise and Chapoy (2016). Carbon dioxide solubility in Triethylene Glycol and aqueous solutions, *Fluid Phase Equil.*, 419, 39-49.
- [20] Skylogianni et al. (2020). Carbon dioxide solubility in mixtures of methyldiethanolamine with monoethylene glycol, monoethylene glycol–water, water and triethylene glycol, *J. Chem. Thermodyn.*, 151, 106176.
- [21] Afsharpour and Haghtalab (2019). Implementation of electrolyte CPA EoS to model solubility of CO₂ and CO

- + H₂S mixtures in aqueous MDEA solutions, *Chin. J. Chem. Eng.*, 27, 1912-1920.
- [22] Dawass et al. (2021). Solubility of Carbon Dioxide, Hydrogen Sulfide, Methane, and Nitrogen in Monoethylene Glycol; Experiments and Molecular Simulation, *J. Chem. Eng. Data*, 66(1), 524-534.
- [23] Gomez Perez et al. (2017). Comparative study of vapour-liquid equilibrium and density modelling of mixtures related to carbon capture and storage with the SRK, PR, PC-SAFT and SAFT-VR Mie equations of state for industrial uses, *Fluid Phase Equil.*, 440, 19-35.
- [24] Mota et al. (2010) Water solubility of drug-like molecules with the cubic-plus-association equation of state, *Fluid Phase Equil.*, 298, 75-82.
- [25] Jou et al. (1987). Vapor-Liquid equilibria for acid gases and lower alkanes in triethylene glycol, *Fluid Phase Equil.*, 36, 121-140.

INTRODUCTION OF POTASSIUM IODIDE AS AN INHIBITOR FOR OXIDATIVE DEGRADATION OF AMINES

Vanja Buvik, Silje Thorstad, Ricardo R. Wanderley and Hanna K. Knuutila*

Department of Chemical Engineering, NTNU, NO-7491 Trondheim, Norway

* Corresponding author e-mail: hanna.knuutila@ntnu.no

Abstract

Oxidative degradation of amines for CO₂ capture is a challenge that has yet to be overcome. This work presents the potential of using potassium iodide as a stable inhibitor, potentially without the need for replenishment in the capture process. The experimental results prove that the addition of only 1wt% potassium iodide to a 30 wt% ethanolamine (aq.) solution significantly reduces amine loss at absorber conditions, even if the amine solution already is degraded. 3-Aminopropanol seems to be equally stabilized under oxidative conditions as ethanolamine. Thermal stability and corrosivity as well as viscosity, density and vapour liquid equilibrium properties seem unaltered by the addition of a small amount of salt. The results presented here show why potassium iodide should further be evaluated as an inhibitor for oxidative degradation of amines.

Keywords: amine scrubbing, stability, inhibition

1. Introduction

Amine scrubbing is a popular choice for carbon capture and storage (CCS) as it is one of the most mature technologies for CO₂ capture and delivers storage quality carbon dioxide (CO₂) streams (<99%). A challenge faced within the technology is amine degradation, giving rise to cost issues such as solvent replacement, corrosion of equipment, interruption of operation and increased potential of emissions due to formation of volatile degradation compounds. With the currently existing knowledge about degradation, this issue is fortunately not a showstopper in the process but finding a means of stopping it will increase the amine solvent's lifetime and decrease the overall cost the capture process.

Degradation reactions inside a CO₂ capture facility are usually divided into those induced by oxidation reactions in the absorber column and those induced by the high temperatures in the reboiler and the desorber column. The conditions in the system are complex, with the presence of multiple gas species, including flue gas contaminants, as well as taking place inside metal equipment, potentially supplying catalytic surfaces and sources of corrosion products that dissolve into the liquid amine.

Ethanolamine (MEA) is one of the most widely studied amines for CO₂ capture, with an abundance of degradation products identified and many degradation mechanisms suggested.¹⁻³ Of the degradation compounds observed in pilot scale tests using ethanolamine, products of oxidative degradation tend to be found in higher abundance than thermal degradation products.⁴ Many of the oxidative degradation compounds are acidic and therefore known to give rise to corrosion⁵, providing corrosion products to the solution that in turn catalyse the degradation reactions⁶.

Oxidative degradation inhibitors have been widely studied and commercially available solvent blends.⁶⁻¹⁰ A downside to many studied degradation and corrosion inhibitors is their single-use nature, making replenishment of the inhibitor necessary, as well as removal of used inhibitor.¹¹ Other disadvantages associated with additives to the solvent are foaming or cross-reactions between solvent molecules and the inhibitor molecules.^{12, 13} In Buvik et al. 2021¹⁴ we first introduced potassium iodide (KI) as an for oxidative degradation of MEA. Sodium chloride was also considered as a degradation inhibitor in that work but deemed too inefficient to successfully be implemented in commercial CCS plants. KI is however still being thoroughly studied and will be tested under different conditions and with different amines and blends in the upcoming months.

At TCCS-11 we want to present experimental results indicating that KI could be of use as an oxidation inhibitor for industrial CO₂ capture including the results given here and in Buvik et al. 2021¹⁴, as well as further experimental testing of the inhibitor with other amine solvents.

2. Materials and methods

2.1. Chemicals

Ethanolamine (MEA, CAS: 141-43-5, purity ≥99.0%), 3-aminopropanol (AP, CAS: 156-87-6, 99%), ferrous sulfate heptahydrate (FeSO₄·7H₂O, CAS: 7782-63-0, purity ≥ 99.0%) and potassium iodide (KI, CAS: 7681-11-0, purity ≥ 99.0%) were purchased from Merck Life Science/Sigma Aldrich Norway. Oxygen (O₂, N5.0), carbon dioxide (CO₂, N5.0) and synthetic air (79% N₂, 21% O₂) were purchased from AGA, and deionized water was obtained from a local water purification system at NTNU.

2.2. Oxidative degradation experiments

Oxidative degradation experiments were done at simulated absorber conditions in open, water bath-heated, double-jacketed glass reactors (approximately 250 mL) as shown in Figure 1. The temperature of the reactors was maintained at 60 °C and the water bath-cooled Graham condensers at 5 °C. Each reactor was filled with 200 mL of the 30 wt% (aq.) amine solution, which was pre-loaded to 0.4 mol of CO₂ per mol amine and contained 0.5 mM iron sulfate (FeSO₄·7H₂O). Also, solutions of pre-used 30wt% MEA (aq.) were prepared from two pilot campaigns where degradation of the amine had been observed, these are denominated Pilot A and B, for the sake of simplicity. Pre-degraded MEA solutions were corrected to contain 30wt% MEA (assuming all alkalinity of pre-degraded solution being present as MEA) and 0.4 mol CO₂ per mol MEA, as well as added 0.5 mM FeSO₄. These were run with and without the addition of 2wt% KI under the same conditions as fresh MEA.

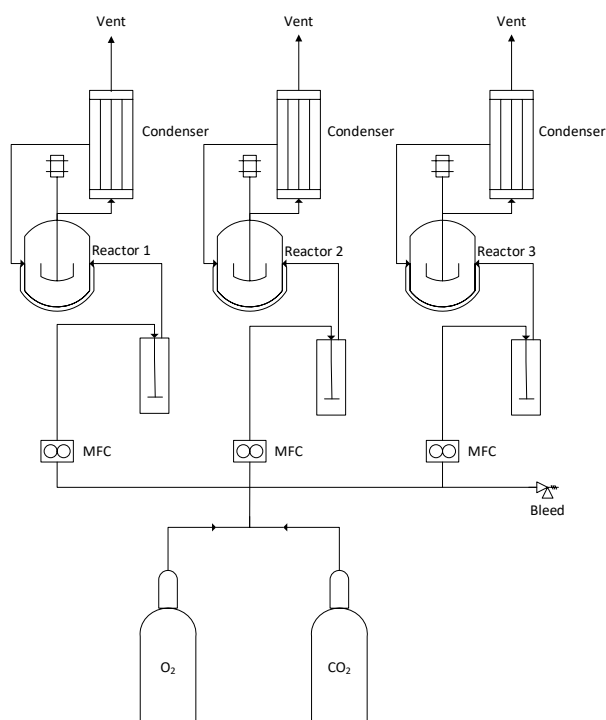


Figure 1: Schematic of oxidative degradation setup.

A mixture of O₂ and CO₂ gas was sparged through the solutions from Alicat mass flow controllers (MFC) and through Pyrex® glass gas distribution tubes (porosity grade 1), under constant magnetic stirring for the total experimental time of three weeks. Gas wash bottles were used between the mass flow controllers and the gas distribution tubes in case of power outage. Sampling from the liquid phase was performed through a septum on top of each reactor. Each experiment was run in three identical parallels, and the data presented in this work is given as the average of the three, with the standard deviation of the sample average given as the uncertainty. Uncertainty within each analytical method is given in the description of each method and comes in addition to the standard deviation of the sample average.

2.3. Thermal degradation experiments

Thermal degradation experiments were performed following Eide-Haugmo et al. (2011)¹⁵ in 316 stainless steel cylinders with diameters of 0.5 inch and volumes of 11 mL. Each cylinder was equipped with Swagelok® end caps. The cylinders were filled with 8 mL of the solution, pre-loaded to 0.4 mol CO₂ per mol MEA, and kept at 135 °C for up to five weeks. For each sampling two metal cylinders per experiment were sacrificed and their contents analysed, meaning that every experiment consisted of 10 cylinders (2 identical samples per week).

2.4. Analytical methods

More thorough descriptions of all analytical procedures can be found in Buvik et al. 2021¹⁶.

Titration with sulfuric acid was used to measure the concentration of amine in the solutions, according to Ma'mun et al. (2006)¹⁷. This procedure has an uncertainty of $\leq 2\%$. For all samples, the amine concentration is back calculated to the solution without CO₂ and corrected for evaporation of water and degradation products, assuming a linear loss throughout the experiment, as the total mass of the solution is only known for the start and end solutions.

A Shimadzu TOC-L_{CPH} analyzer equipped with an auto sample injector (ASI) was used for the quantification of CO₂ loading as total inorganic carbon (TIC).

Inductively coupled plasma mass spectrometry (ICP-MS) analyses were performed on a High Resolution Inductive coupled plasma ELEMENT 2 from Thermo Electronics. The results were verified against certified reference material and the relative standard deviation for three scans of a sample varies from sample to sample.

Anion exchange ion chromatography (IC) was used to quantify the iodide concentration in the oxidative degradation experiment with 30 wt% MEA and 1.0 wt% KI. This was performed on a Thermo Scientific™ ion chromatographic system.

3. Results and discussion

3.1. Stability of 30wt% MEA (aq.) with and without salt addition

As can be seen in Figure 2, 30 wt% MEA (aq.) linearly loses alkalinity, resulting in a loss of as much as $60 \pm 4\%$ after three weeks. Upon addition of 2.0 wt% KI, this loss is reduced to $4 \pm 1\%$. KI was therefore further considered for use as an oxidative degradation inhibitor for industrial CO₂ capture. In Buvik et al. 2021¹⁶ we also studied sodium chloride as a potential stable salt for degradation inhibition, but its effect ($24 \pm 3\%$ loss in alkalinity after 21 days) was deemed insufficient for commercial applications and will therefore not be described in detail in this short paper.

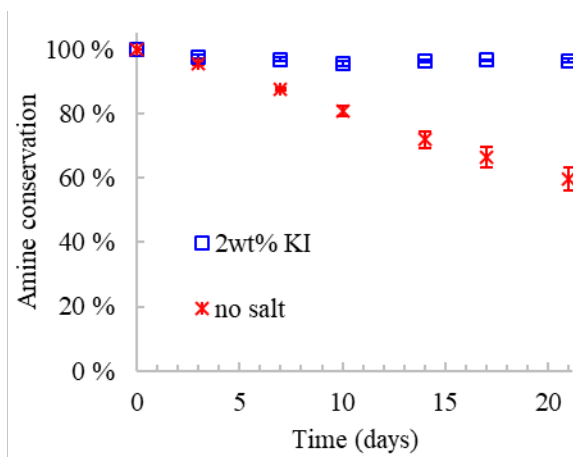


Figure 2: Loss of alkalinity of MEA with and without the addition of KI over the course of the 21 days at 60 °C, 0.5 mM of Fe²⁺ added and 60 mL min⁻¹ O₂ (98%) and CO₂ (2%) added per 200 mL liquid.

Under these experimental conditions the addition of KI inhibitor is not just positive for the amines oxidative stability in fresh MEA solutions, but also when added into already degraded solutions, as shown in Figure 3.

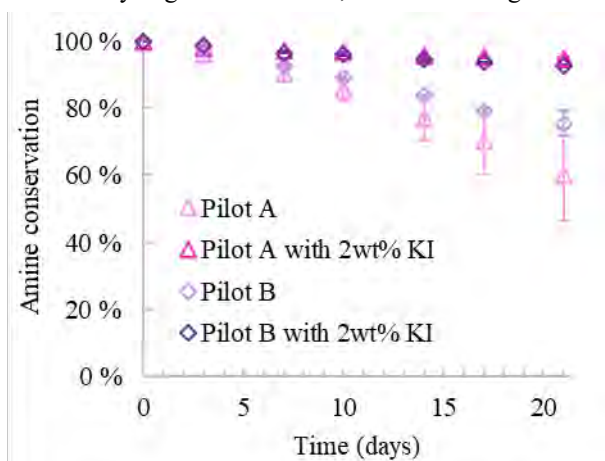


Figure 3: The oxidative stability of pre-used 30wt% MEA (aq.) from two pilot scale campaigns, with and without addition of the KI inhibitor.

3.2. The effect of KI concentration on 30wt% MEA (aq.) stability

To assess the concentration of KI necessary to stabilize 30 wt% MEA (aq.), two additional sets of experiments were run with 1.0 and 0.2 wt% KI addition to the solvent. As Figure 4 shows, the addition of only 1.0 wt% KI is as effective as 2.0 wt%, but when reducing the concentration to 0.2 wt% the effect is drastically reduced. In the case of 1.0 wt% the experiments were run for additional three weeks, to investigate whether the degradation inhibition effect decreases with time. The degradation inhibition did not decrease throughout the six weeks under highly oxidative conditions for the 1.0 wt% KI case, where the loss of alkalinity was only $4 \pm 1\%$ at the end. The 0.2 wt% KI solution had lost $25 \pm 2\%$ alkalinity after three weeks. This indicates that the minimum concentration of KI needed for inhibiting degradation of MEA is ≤ 1.0 wt% and > 0.2 wt%.

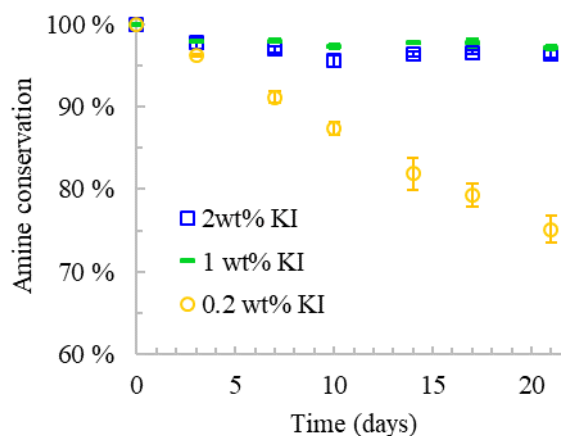


Figure 4: The effect of addition of different concentrations of KI in 30wt% MEA (aq.) under oxidative conditions of 60 °C, with 0.5 mM of Fe²⁺ added and 60 mL min⁻¹ O₂ (98%) and CO₂ (2%) added per 200 mL liquid.

Anion chromatographic testing of the concentration in the solution before and after the experiment the 2.0 wt% KI case, showed no difference in the iodide concentration. This, and the linear rate of loss of alkalinity in the 0.2 wt% KI case, suggest that the inhibition effect is not caused by a single-reaction of the iodide with oxygen or that it acts as a scavenger that is used by the oxidant, rather that the stabilization originates from other physical effects. This eliminates the need for inhibitor replenishment in the CO₂ capture process, which is a highly desirable property of the system. It is still unsure whether the iodide oxidized and then is reduced and that this could be the cause of the unchanging iodide concentration and continuous inhibition.¹⁸ Foaming was not observed with any of the 30 wt% MEA (aq.) systems, with or without added KI or NaCl.

3.3. The effect of KI on 30wt% AP (aq.) stability

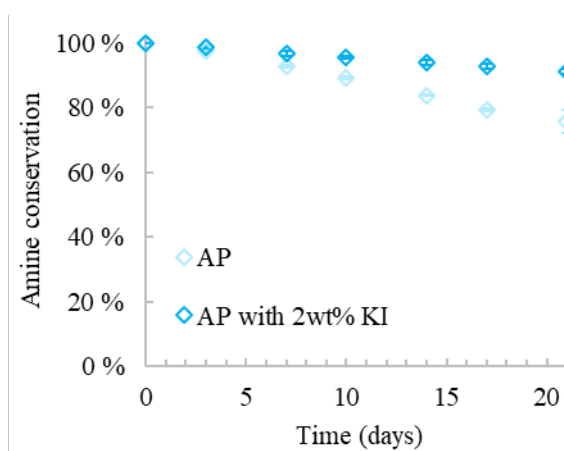


Figure 5: Oxidative stability of 30wt% AP (aq.), with and without the addition of 2wt% KI inhibitor.

Also aqueous aminopropanol (AP) is stabilized under oxidative conditions in the presence of the KI inhibitor, as seen in Figure 5, giving reason to suspect that the inhibition effect is independent of the amine in use.

3.4. Effect of KI addition on other properties of the 30 wt% MEA (aq.) solution

Thermal and oxidative degradation mechanisms are independent of one another, so to assure that the addition of salt does not decrease the thermal stability of the amine solution, a set of thermal degradation experiments were performed. The amine loss, given as loss of alkalinity, is shown in Figure 6. It is evident that the addition of KI neither has a positive nor negative effect on the 30 wt% MEA (aq.) seeing as oxidative degradation being the dominating degradation pathway in large scale CO₂ capture by amine scrubbing, the fact the thermal degradation is not inhibited is acceptable.

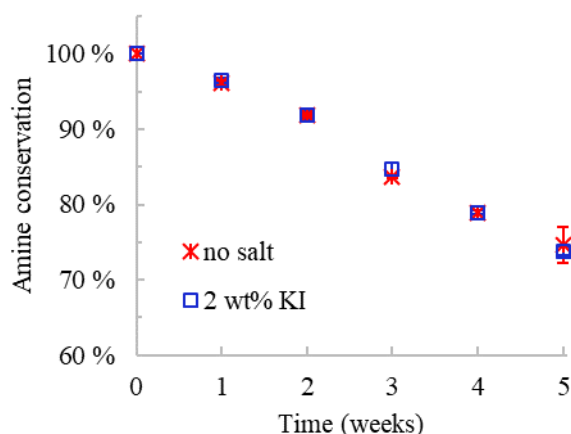


Figure 6: Thermal degradation of 30 wt% MEA (aq.) with and without addition of KI, at 135 °C in 316 cylinders. Data from Buvik et al. (2021)¹⁴.

The end samples, those degraded at 135 °C for 5 weeks, were analysed by ICP-MS to determine the content of dissolved metals from the 316 stainless-steel cylinders. the addition of 2 wt% KI to 30 wt% MEA (aq.) does not seem to increase the amount of dissolved metals in the solution, on the contrary, the concentration of nickel is lower in the solution containing KI than in that without, as can be seen in Figure 7. This indicates that KI does in fact not increase the corrosivity of the MEA solution.

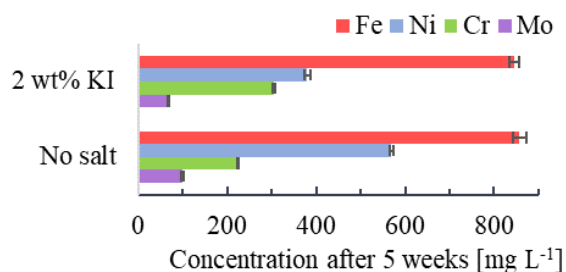


Figure 7: Concentration of metals in the thermally degraded (in closed 316SS cylinders at 135 °C) solutions of 30 wt% MEA (aq.) with and without KI. Data from Buvik et al. (2021)¹⁴.

Furthermore, the viscosity, density and the vapour liquid equilibrium (VLE) properties of MEA with and without 2 wt% KI were studied. None of these properties showed any significant deviations between the two solutions.

3.5. Finalizing remarks and planned work

The inhibition effect seen by KI in MEA seems independent of the presence of degradation products in the solvent. The stabilization of AP shows that KI does not only stabilize MEA and gives reason to expect a similarly positive effect on more amines. The mechanism of inhibition given by KI is still unclear, but it can be expected that an analogous process as suggested in the patent of Sjoström et al. from 2020¹⁹ takes place also in this scenario. This includes direct oxidation of iodide to iodine in contact with the oxidizing species in the solution, then a reversed reaction by contact with slightly reducing agents also present. We have, in agreement with Sjoström et al. not observed that iodide is consumed throughout the process, further supporting this hypothesis.

It can be assumed removing heat stable salts (HSS) from the solvent in the reclaimer will also remove the KI inhibitor. MEA is, however, lost at only a fraction of the rate with inhibitor compared to without. This would mean that the need for reclaiming to keep HSS concentrations in the solvent low enough would also reduce. Despite KI being relatively costly, the lower loss of solvent and lower reclaiming frequency could make up the cost of inhibitor replenishment. Anyhow, the possibility of recovering the salt from the reclamation waste should be evaluated.

The experimental setup, supplying a constant bubbling flow of 98% O₂, as well as continuous agitation by magnetic stirring may not be directly translatable to the conditions in a CO₂ capture facility. It can be argued that the degradation mechanisms must differ a lot to those that are likely to occur under industrial conditions, but these experiments do provide an extremely harsh oxidative environment, under which compounds sensitive to oxidation will degrade. We argue that the performed experiments indeed are a valuable primary tool to assess the stability of an amine before performing cyclic absorption/desorption testing with temperature swing. Testing at cyclic conditions will be the next step in the inhibitor development.

Acknowledgements

This publication has been produced with support from the NCCS Centre, performed under the Norwegian research program Centres for Environment-friendly Energy Research (FME). The authors acknowledge the following partners for their contributions: Aker Solutions, ANSALDO Energia, CoorsTek Membrane Sciences, EMGS, Equinor, Gassco, KROHNE, Larvik Shipping, Norcem, Norwegian Oil and Gas, Quad Geometrics, Shell, TOTAL, and the Research Council of Norway (257579/E20).

The authors would like to acknowledge Dr. Syverin Lierhagen at the Department of chemistry at NTNU for running the ICP-MS analyses.

References

1. Vevelstad, S. J.; Johansen, M. T.; Knuutila, H.; Svendsen, H. F., Extensive dataset for oxidative degradation of ethanolamine at 55–75 °C and oxygen concentrations from 6 to

- 98%. *International Journal of Greenhouse Gas Control* **2016**, 50, 158-178.
2. Chi, S.; Rochelle, G. T., Oxidative Degradation of Monoethanolamine. *Industrial & Engineering Chemistry Research* **2002**, 41 (17), 4178-4186.
 3. Bello, A.; Idem, R. O., Pathways for the formation of products of the oxidative degradation of CO₂-loaded concentrated aqueous monoethanolamine solutions during CO₂ absorption from flue gases. *Industrial & engineering chemistry research* **2005**, 44 (4), 945-969.
 4. Buvik, V.; Høisæter, K. K.; Vevelstad, S. J.; Knuutila, H. K., A review of degradation and emissions in post-combustion CO₂ capture pilot plants. *Accepted: International Journal of Greenhouse Gas Control* **2021**.
 5. Fytianos, G.; Grimstvedt, A. M.; Knuutila, H.; Svendsen, H. F., Effect of MEA's degradation products on corrosion at CO₂ capture plants. **2014**.
 6. Sexton, A. J.; Rochelle, G. T., Catalysts and inhibitors for oxidative degradation of monoethanolamine. *International Journal of Greenhouse Gas Control* **2009**, 3 (6), 704-711.
 7. Voice, A. K.; Closmann, F.; Rochelle, G. T., Oxidative Degradation of Amines With High-Temperature Cycling. *Energy Procedia* **2013**, 37, 2118-2132.
 8. Voice, A. K.; Rochelle, G. T., Oxidation of amines at absorber conditions for CO₂ capture from flue gas. *Energy Procedia* **2011**, 4, 171-178.
 9. Fytianos, G.; Vevelstad, S. J.; Knuutila, H. K., Degradation and corrosion inhibitors for MEA-based CO₂ capture plants. *International Journal of Greenhouse Gas Control* **2016**, 50, 240-247.
 10. Goff, G. S.; Rochelle, G. T., Oxidation inhibitors for copper and iron catalyzed degradation of monoethanolamine in CO₂ capture processes. *Industrial & engineering chemistry research* **2006**, 45 (8), 2513-2521.
 11. Léonard, G.; Voice, A.; Toye, D.; Heyen, G., Influence of dissolved metals and oxidative degradation inhibitors on the oxidative and thermal degradation of monoethanolamine in postcombustion CO₂ capture. *Industrial & Engineering Chemistry Research* **2014**, 53 (47), 18121-18129.
 12. Thitakamol, B.; Veawab, A., Foaming behavior in CO₂ absorption process using aqueous solutions of single and blended alkanolamines. *Industrial & engineering chemistry research* **2008**, 47 (1), 216-225.
 13. Chen, X.; Freeman, S. A.; Rochelle, G. T., Foaming of aqueous piperazine and monoethanolamine for CO₂ capture. *International Journal of Greenhouse Gas Control* **2011**, 5 (2), 381-386.
 14. Buvik, V.; Wanderley, R. R.; Knuutila, H. K., Addition of potassium iodide reduces oxidative degradation of monoethanolamine (MEA). *Chemical Engineering Science: X* **2021**.
 15. Eide-Haugmo, I., Environmental impacts and aspects of absorbents used for CO₂ capture. **2011**.
 16. Buvik, V.; Wanderley, R. R.; Knuutila, H. K., Addition of potassium iodide reduces oxidative degradation of monoethanolamine. *Under review: Chemical Engineering Science: X* **2021**.
 17. Ma'mun, S.; Jakobsen, J. P.; Svendsen, H. F.; Juliussen, O., Experimental and modeling study of the solubility of carbon dioxide in aqueous 30 mass% 2-((2-aminoethyl) amino) ethanol solution. *Industrial & engineering chemistry research* **2006**, 45 (8), 2505-2512.
 18. Sjostrom, S.; Baldrey, K. E.; Senior, C. Control of wet scrubber oxidation inhibitor and byproduct recovery. 25.12.2018, 2018.
 19. Sjostrom, S.; Baldrey, K. E.; Senior, C. Control of Wet Scrubber Oxidation Inhibitor and Byproduct Recovery. 2020.

MODIFIED DOLOMITE-BASED PELLETS FOR HIGH TEMPERATURE POST-COMBUSTION CO₂ CAPTURE

Ainara Moral^{1*}, Anne Charlotte Wold¹, Kumar Ranjan Rout^{1,2}, De Chen¹

¹ Department of Chemical Engineering, Norwegian University of Science and Technology (NTNU), Sem Sælands vei 4, N-7491 Trondheim, Norway

² SINTEF Industry, Norway

* Corresponding author e-mail: ainara.moral.larrasoana@ntnu.no

Abstract

In this study, synthetic dolomite-based pellets were prepared by means of one-pot method. Zr and Ce were used as modifier and aluminate cement was employed as binder. The addition of the promoters by two different routes (1-step or 2-step) was analyzed. The pellets were exposed to several carbonation-calcination cycles in a thermogravimetric analyzer at low CO₂ concentration (5 vol.%) and wet conditions (8 vol.% steam) at 600 °C. The calcination was carried in harsh conditions to mimic the realistic process (950 °C, 77 vol.% CO₂). The Zr-modified and synthesized by 2-step one-pot method was presented as the most promising among all the sorbents with an initial capturing capacity of 16.9 % in cycle 2 to 14.4 % after cycle 40. It was proved that both, sintering and pore blockage are fairly well prevented. Different characterization techniques were employed, including N₂ adsorption-desorption at 77 K, X-ray diffraction (XRD) and scanning electron microscopy combined with energy-dispersive spectroscopy (SEM-EDS).

Keywords: Calcium-Looping; dolomite; cement; zirconium

1. Introduction

Carbon capture and storage (CCS) was identified by the International Energy Agency (IEA) as a crucial technology to reach the mitigations requirements targeted by United Nations in the Paris agreement in 2015 [1], where the target of keeping temperature increase below 2 °C (above pre-industrial levels) was agreed. As a result, approximately 48 % of the CO₂ emission reduction will come from power plants [2]. Within the CCS technologies, post-combustion CO₂ capture has raised among the best processes to be implemented in the existing power plants. Currently, the most mature technology employed industrially is the Monoethanolamin Absorption (MEA). However, several problems associated such as, low total efficiency as a result of the extraction of steam in the solvent regeneration [3], solvent degradation [4] or corrosion [5] and the high cost [6] makes necessary to find new technologies.

A promising alternative is the calcium-looping (CaL), consisting of a first carbonation step with calcium oxide-based sorbent, following by the regeneration of the sorbent at high temperature in a calciner. The interest on this process has increased due to its potential to achieve a lower energy penalty than the one reached in the MEA. The application of this technology have been investigated in cement [7], coal-fire [8] and Natural Gas Combined Cycle (NGCC) power plants [9].

Several studies have been done to evaluate the performance of the CO₂ capture by CaL on the NGCC power plants [9–14]. A significant challenge associated with the combination of the processes are the higher

energy requirement due to lower CO₂ concentration in the flue gas (4 vol.%) and consequently, lower temperature (600 °C) in the carbonator comparing to the coal fire plants (650 °C and 15 vol.%). On the other hand, steam will be a subproduct in combustion flue gas (5-10 vol.%) [15], which will influence the capturing efficiency. Furthermore, the process requirement of harsh calcination conditions (>80 vol.% CO₂, T>900 °C) must be taken into account in the sorbent evaluation [16].

Environmental and economic factors regarding the nature of sorbents hinders the development of the CaL. Therefore, the necessity of cost efficient environmentally friendly sorbent is significant for the overall cost. The use of calcium sorbents based on natural resources [17], mainly limestone (CaCO₃) and dolomite (CaCO₃.MgCO₃) might solve this problems. However, they suffer a rapid decrease in CO₂ sorption capacity with an increasing number of carbonation/calcination cycles mainly due to sintering and pore collapse. Dolomite presents a significantly lower capacity than limestone, however, its lower decomposition temperature and higher resistance to sintering, due to the action of MgO as a thermally stable support mitigating the capacity loss [18], makes it a promising raw material.

Large efforts have been carried out for enhancing the natural sorbents uptake capacity and stability [19]. An interesting approach in material development is the incorporation of inert supporting materials with high melting points. In this respect, Zr modified sorbents have been extensively investigated showing a notable stability over several cycles, attributed to the formation of the thermally resistant CaZrO₃ when CaO reacts with ZrO₂

[20–24]. On the other hand, the possibility of using CeO₂ as modifier have been less investigated although its stabilizer effect by creating a physical barrier has been trusted. It has been suggested that the release of O²⁻ from the surface of CeO₂ can facilitate the reaction of CaO with CO₂ [25]. Aluminate cement has been previously reported as a good and inexpensive support for pelletization [26–30], owing to the formation of calcium-aluminum oxides (specially mayenite) from the solid reaction of Al₂O₃ and CaO that results in the formation of a solid and inert framework which prevents the sintering and acts as mechanical stabilizer.

Beside the composition, the preparation method have a big impact on the sorbent properties. In the literature several methods have been proposed. Unfortunately, most of them having disadvantages associated with expensive and challenging preparation methods and consequently, making difficult the scale up of the synthesis [31].

In this work, a one pot method has been proposed in order to produce active and stable dolomite based modified pellets for CaL. The addition of two dopants has been investigated, including Zr and Ce. Finally, the optimization of the synthesis has been investigated by the analyzes of two simple routes using the one pot method.

2. Experimental procedure

2.1. Materials

Dolomite (AGRI Hagekalk supplied by Franzefoss Miljøkalk) was employed as CaO source, aluminate cement (Cement FONDU, Al₂O₃>37%, CaO <39.8%, SiO₂<6 %, <18.5%) as binder and two different additives were used as modifiers including zirconyl nitrate solution (35 wt. % in dilute nitric acid) and Cerium(III) nitrate hexahydrate as Zr and Ce precursors respectively.

2.2. Sorbent preparation

Dolomite based pellets were prepared by means of one pot method. Two different routes, depending on how the addition of the raw materials was done, were studied. In the first route, calcined and milled dolomite (800 °C for 6 h, dp<90 μm) was impregnated by means of incipient wetness impregnation with the precursor solution (Zr or Ce). Subsequently, the dry impregnated solid and the dry cement were milled together until a homogeneous solid mixed was obtained. Finally, water was sprayed slowly with a continuous stirring until the pellets were formed (2S method). Conversely, in the second route, the calcined and milled dolomite and dry cement were previously mixed until a homogeneous solution was gotten. The solid mixture was impregnated by wetness impregnation and finally, water was sprayed until the pellet were formed (1S method). The obtained pellets were aged for 4-7 days until a hard solid was formed. Finally, the calcination of the pellets was done at 950 °C for 6 hours.

2.3. Cycling stability

The capture capacity of the sorbents along carbonation-calcination cycles was measured in a common

thermogravimetric analyzer (Linseis Thermal Analysis STA PT1600). A small quantity (10-15 mg) of sorbent was placed in a sample holder. The sample was initially heated up until 900 °C in air/Ar atmosphere (200 cm³/min) in order to remove possible humidity and CO₂ adsorbed. The carbonation reaction was carried out at CO₂ partial pressure of 5 vol.% CO₂ and 8 vol.% H₂O (air/Ar balance) at a temperature of 600 °C for 30 minutes. Subsequently, the temperature was increased until 800 °C in 5 vol.% CO₂ (air/Ar balance). Finally, the atmosphere was changed to 77 vol.% CO₂ and the temperature was increased until 950 °C, where it was kept for 5 minutes, simulating the real calcination conditions.

The capture capacity was calculated assuming the weight change showed in TGA analyzed was due to the carbonation or calcination of the sorbent.

2.4. Characterization

Fresh and spent sorbents were characterized by different techniques including, N₂ adsorption-desorption at 77 K, X-ray diffraction (XRD) and emission scanning electron microscopy combined with energy-dispersive spectroscopy (SEM-EDS).

N₂ adsorption-desorption isotherms were measured in a Micrometrics TriStar 3020 automatic volumetric analyzer at 77 K, with previous preconditioning of the samples at 300 °C for 2 h and vacuum. The surface area of the different samples was determined using the Brunauer-Emmett-Teller (BET) method, and the pore size distribution was calculated using the Barrett-Joyner-Halenda (BJH) method.

XRD experiments were performed at ambient temperature on a D8-Focus diffractometer equipped with the Cu K α radiation ($\lambda = 0.15418$ nm) X-ray source. XRD patterns were examined with 2θ values ranging from 5° to 75° with a step of 0.02 ° and a signal accumulation period of 1 s per step.

Lastly, the morphological analysis was completed using field emission scanning electron microscopy (SEM), (FEI APREO) coupled with an EDS detector (Oxford).

3. Results and discussion

3.1. Sorbents

Table 1 summarizes the synthesized materials, including, sample, employed route (1- or 2-step) as well as the content (% wt) of the different modifiers, including Zr, Ce and Al (from cement, assuming that aluminate cement consists of CaO and Al₂O₃). Additionally, calcined and milled dolomite (800 °C for 6 h, dp< 90 μm) was used as reference to compare the performance of the synthetic sorbents tested in a size range of 500-850 μm.

Table 1: Summary of the different prepared sorbent

Sample	Meth.	Zr (wt. %)	Ce (wt. %)	Al (wt. %)
1S(5.5Zr,10Al)	1-step	5.5	-	10
2S(5.5Zr,10Al)	2-step	5.5	-	10
2S(5.5Ce,10Al)	2-step	-	5.5	10
1S(15Al)	1-step	-	-	15

3.2. Cycling stability

Capturing capacity (%) over cycles under experimental conditions described in 2.3 is represented in Figure 1. As expected, calcined dolomite presented a pronounced fast loss in capacity from 38.4 % of initial capturing capacity to 19 % after only 15 cycles and to 13 % after 40 cycles and which expected to decrease until a very low residual values around 10 % [18]. Conversely, a strong improvement on the stability was observed in the synthetic sorbents. The 2S sorbents prepared with both modifiers, Ce and Zr, presented a similar initial capacity (~19 %). Nevertheless, its performance throughout cycles varied significantly. The sorbent containing Cerium exhibited a minor initial increase in the capturing capacity from cycle 1 to cycle 2. However, it gradually decreased from 21.6 % in cycle 2 to 16.5 % of capture capacity in cycle 15. By contrast, the homologous sorbent modified with Zr 2S(5.5Zr,10Al) presented a slightly initial decrease in capacity to later show relatively stable behavior (from 16.9 % in cycle 2 to 15.5 % in cycle 15 and 14.4 % in cycle 40). On the other hand, comparing both Zr-modified sorbents with same composition but prepared by the different routes (1S and 2S) a noticeable difference, especially in terms of activity, was observed. Around 2 % lower capacity was found for 1S(5.5Zr,10Al) than for 2S(5.5Zr,10Al) and a slightly higher capacity lost (22.0 % and 15.1 % from 2-40 respectively) over 40 carbonation-regeneration cycles tested. This is surprising considering that the CaO from cement is inactive in the carbonation [26], hence, it was expected to observe more active CaO sites and therefore, higher capture capacity, in the 1S(5.5Zr,10Al) sorbent compared to the sorbent made by 2S route, where all the Zr was directly impregnated in the active CaO sites to form CaZrO₃.

Finally, the sorbent supported on cement (1S(15Al)) presented an initial capacity of 14.5 % and a loss in capacity of 17.4 % through 15 cycles (2-15). This would prove that the addition can be also beneficial for the stability of the sorbent. However, the combination of Zr and cement appears as the most beneficial combination in order to obtain a sorbent with relatively good activity and stability. Furthermore, the synthesis realized by 2-step has been found as the best route.

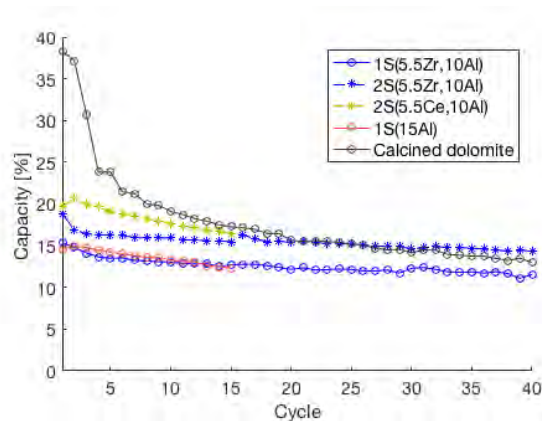


Figure 1. Capturing capacity (%) as a function of carbonation-calcination cycles for calcined dolomite, 1S(5.5Zr,10Al), 2S(5.5Zr,10Al), 2S(5.5Ce,10Al) and 1S(15Al) (Carb: F_T=400 mL/min, 5 % CO₂, 8 % H₂O, T_{carb}= 600 °C, t=30 min; Calc: 77 % CO₂ (N₂/Ar), T_{calc}= 950 °C, t=5 min)

3.3. Characterization

The chemical composition was assessed by XRD. The patterns of the synthetic pellets, calcined dolomite and dry cement are depicted in Figure 1.

The crystallographic phases corresponding to CaO and MgO were mainly detected in calcined dolomite, however, small signals corresponding to Ca(OH)₂ and CaCO₃ were also distinguished, possibly due to water and CO₂ adsorbed during the cooling down post-calcination. The diffractogram of dry cement revealed the presence of different calcium aluminates phases, including mainly CaAl₂O₄, and Ca₃Al₂O₆. Furthermore, two more phases were identified in the cement diffractogram, Fe₂O₃ and SiO₂, as it was indicated in the specifications of FONDU cement. As expected, the formation of mayenite was observed in all prepared sorbents, as it has been reported by several authors when aluminate cement is used as binder [26–30], indicating the solid state reaction between CaO and Al₂O₃ oxides forming the inert framework.

For the sorbents modified with Zr, the presence of CaZrO₃ was confirmed verifying the reaction of ZrO₂ with CaO [32], which improves the durability of the sorbents by means of the action of CaZrO₃ as a barrier against sintering. Oppositely, when Ce was used as modifier, CeO₂ was recognized, indicating the absence of reaction of CaO with the modifier [25]. Furthermore, comparing the Ce and Zr modified sorbents, the last one presented a more intense mayenite (Ca₁₂Al₁₄O₃₃) peaks, which can indicate a stronger formation of the inert solid framework preventing better the sintering, than in the Ce-modified sorbent, where a more pronounced deactivation was observed. There were not major differences between the patterns of fresh and spent samples, nor comparing the sorbents prepared by 2 different methods (1- or 2- step).

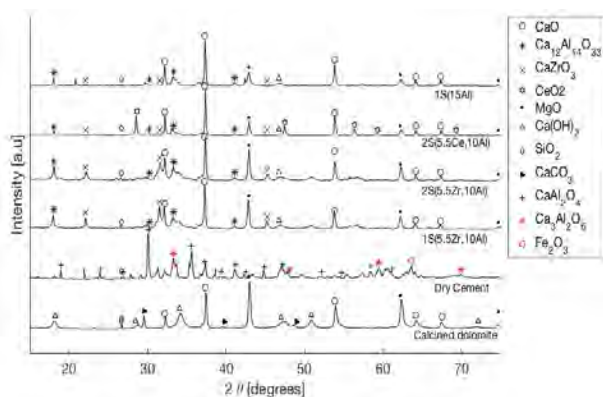


Figure 2: XRD patterns of calcined dolomite, cement, and modified sorbents (1S(5.5Zr,10Al), 2S(5.5Zr,10Al), 2S(5.5Ce,10Al) and 1S(15Al))

On the other, Table 2 shows the CaO crystal sizes calculated by Scherrer equation [33] and BET surface of all the sorbents. Calcined dolomite presented the smallest CaO crystal size (40.4 nm) comparing to the modified sorbents (46.5-54 nm). However, it suffered a pronounced increase of CaO crystal size in only 15 cycles (47.6 nm), demonstrating that sintering is the main deactivation mechanism, as was also previously reported [18]. Among the synthesized sorbents, 2S(5.5Ce,10Al) presented the highest CaO crystal size (54.0 nm), possibly due to a slightly higher sintering during the pre-calcinations step. However, it appears that this difference does not have considerable impact in the initial capturing capacity as was previously seen (Figure 1). Hence, the CaO crystal sizes in this range, does not result in any significative effect in the capture capacity. Furthermore, the spent samples were analyzed (not shown), not showing a noticeable difference regarding CaO crystal sizes observed, nor to the crystal phases found, indicating that sintering was well prevented in the modified sorbents.

Table 2: CaO crystal sizes (nm) and BET surface area (m²/g) for calcined dolomite and modified sorbents (1S(5.5Zr,10Al), 2S(5.5Zr,10Al), 2S(5.5Ce,10Al) and 1S(15Al))

Sample	CaO Crystal Size (nm)	S _{BET} (m ² /g)
Calcined Dolomite	40.4	21.0
1Sa(5.5Zr,10Al)	46.5	8.8
2Sa(5.5Zr,10Al)	49.0	10.6
2S(5.5Ce,10Al)	54.0	7.2
1S(15Al)	49.6	11.4

It is known that sorbents porosity plays an important role in the gas–solid reaction, since the diffusion inside particles has a strong dependency on the pore structure [34]. The BET surface areas of dolomite and modified sorbents are summarized in Table 2. It was clearly seen that calcined dolomite presented higher surface area

(21.0 m²/g) comparing to synthetic sorbents (7.2-11.4 m²/g). This can be attributed to the lower sintering suffered during lower degree of pre-calcination as well as related to the addition of dopants and cement [35,36]. Regarding to Zr and Ce-doped sorbents, a clear relation between the capturing capacity and surface area was observed, being 2S(5.5Zr,10Al) the sorbent with higher surface area (10.6 m²/g), the one which presented higher activity in the CO₂ capture. However, this trend was not followed by the sorbent 1S(15Al), which with the highest surface does not appear as the most active.

Nevertheless, not only the surface areas have an important effect in the sorbent performance, but also changes in the pore distribution can significantly affect to the stability. Indeed, Chen et al. [37] reported that the pore size distribution has a more critical role than the surface area and the pore volume. Hence, the pore size distribution of calcined dolomite and Zr modified sorbents are represented in Figure 3. Both calcined dolomite and the Zr-doped sorbents presented a bimodal distribution, with peaks in the small range of mesopores (3-4 nm) as well as in the big mesopores and macropores range (20-150 nm). A similar tendency was also reported by other authors [30,38].

More mesopores with small size (3-4 nm) were identified in calcined dolomite than in the modified pellets. In the large pore sizes, there were no significant differences between the three samples, however, a decrease of the mesopores was seen in the Zr doped sorbents comparing to calcine dolomite. Although larger mesopores were detected in the Zr modified sorbent, the bimodal distribution was maintained. The larger mesopores of calcined dolomite corresponds also with its higher surface area and hence, higher initial activity.

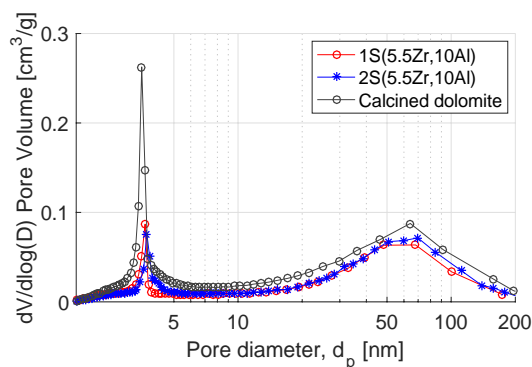


Figure 3: Pore diameter distribution of 1S(5.5Zr,10Al), 2S(5.5Zr,10Al) and calcined dolomite

It has been demonstrated that the smaller pores contribute more in the reaction-controlled regime, while the bigger pores in the diffusional regime [34]. This reveals the importance of maintaining small micropores throughout calcination-regeneration cycles in order to have an active and stable sorbent where fast kinetic and short times of carbonation are required (around 5 min) as in the CaL process. The evolution of pore volume distribution of 1S(5.5Zr, 10Al) during cycles (fresh, cycle 3 and 20) was analyzed in Figure 4. While the small sizes were closer to 3 nm in the fresh samples, they turned a bit bigger (around 5 nm) in the spent samples. Furthermore, the larger maximum pores shift from a peak at about 50 nm

to a peak around 100 nm. The changes in the sorbents surface area and pore-structure during cycles can indicate that a small degree of pore collapse occurs during carbonation-regeneration cycles. It is important to notice that the pores kept their bimodal distribution, with small mesopores. It was also identified a small decrease in the surface area from 8.8 m²/g in the fresh sample to 8.4 and 7.6 m²/g for the sample exposed to 3 and 20 cycle respectively, which indicates that even than a redistribution of the pores can arise, they are able to keep relatively good porous structure and surface area throughout the calcination-regeneration cycles. However, an interesting technique for the improvement can be the additions of pore generators during the synthesis as has been demonstrated [39,40].

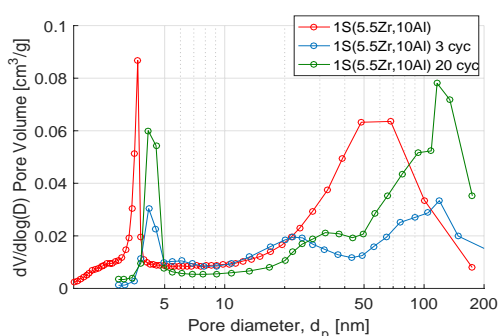


Figure 4: Pore volume distribution of 1Sa(5.5Zr,10Al), including fresh and spent sorbent after 3 and 20 carbonation-regeneration cycles

In order to gain further insight concerning the surface morphology, SEM-EDS analysis was done. Figures 5 and 6 show a selection of images from fresh and spent samples (after 40 carbonation/calcination cycles) for 1S(15Al), 1S(5.5Zr,10Al) and 2S(5.5Zr,10Al).

The images taken for fresh samples showed a great similarity with the ones found in the literature [29,39], especially for the image taken to 1S(15Al) where the calcium aluminate framework was clearly detected (Figure 5), forming stable cross-linked framework where possibly, the CaO grains are surrounded in the framework.

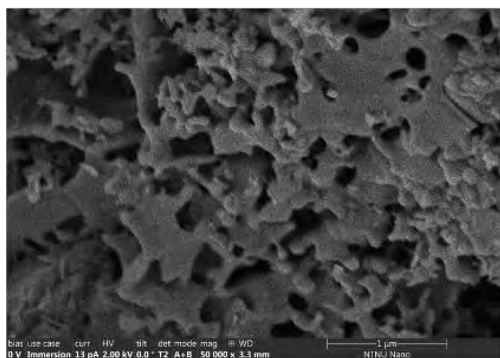


Figure 5: SEM images of 1S(15Al)

On the other hand, in the Zr-modified sorbents more compact structure was detected in 1S(5.5Zr,10Al) (Figure 6) comparing to 2S(5.5Zr,10Al) (Figure 7). This is in agreement with the slightly lower BET surface

observed for 1S(5.5Zr,10Al) (Table 2). Hence, this can be a cause of the lower capture capacity obtained for 1S(5.5Zr,10Al) than for 2S(5.5Zr,10Al) as was pointed by Wei et al. [34]. Conversely, the sorbents prepared by 2S route presented an intermediate structure, where the calcium aluminate framework was detected forming a more opened structure. Simultaneously, the CaZrO₃ particle effect also was clearly seen forming a rougher structure which can be the responsible for the prevention of sintering [24].

In agreement with the XRD and the N₂ adsorption-desorption measurements, the images demonstrated that not major differences between the fresh and spent sorbents were observed, especially in the sorbents modified with Zr and prepared by 2-step route (2S(5.5,10Al)) where the surface morphology seems appropriate to reach an acceptable capture capacity and maintained it through several carbonation-regeneration cycles.

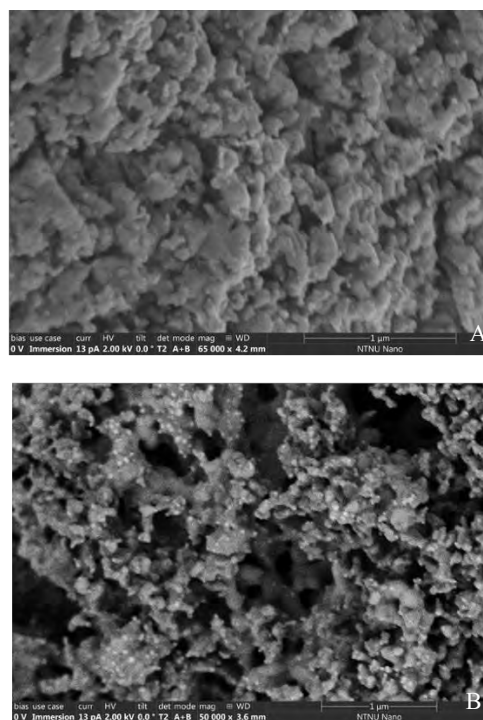


Figure 6: SEM images of 1S(5.5Zr,10Al) (fresh (A) and spent after 40 carbonation-calcination(B))

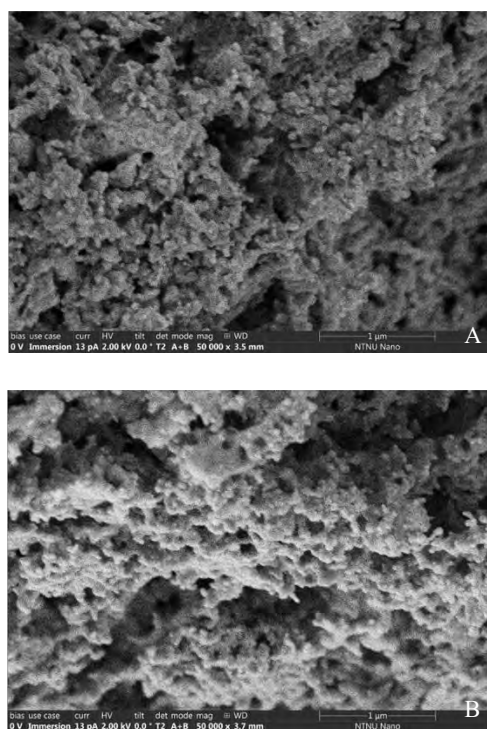


Figure 7: SEM images of 2S(5.5Zr,10Al) (fresh (A) and spent sorbent after 40 carbonation-calcination (B))

Finally, the distribution of the compounds was analyzed by the EDS mapping (Figure 8 and 9). It is known the importance of having a well dispersed CaZrO₃ particles in order to reach a good activity and stability [41]. In the images, the elemental mapping of Ca, Al, Zr, Mg and O are represented. As expected, Ca is well dispersed in both sorbents. On the other hand, Mg and Al zones can be distinguished, which belongs to the areas rich on dolomite and cement respectively. These areas are clearly more divided in the sorbent synthesized by 1-step than 2-step route, indicating a worse homogeneous distribution of materials. Furthermore, the Zr is clearly not well dispersed also in this sorbent 1S(5.5Zr,10Al). This could explain the worse capture capacity shown by 1S(5.5Zr,10Al) comparing to 2S(5.5Zr,10Al). The sorbent synthesized by 2-step clearly present a better homogeneity and Zr dispersion. Hence, the higher capacity and slightly better stability of 2S(5.5Zr,10Al) can be attributed to the slightly higher surface area obtained, probably due to the better homogeneity as well as to the better Zr dispersion.

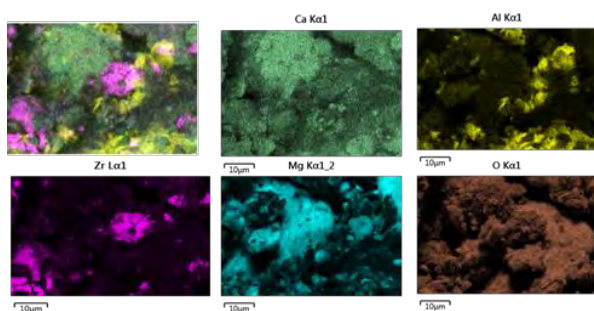


Figure 8: Elemental mapping of 1S(5.5Zr,10Al)

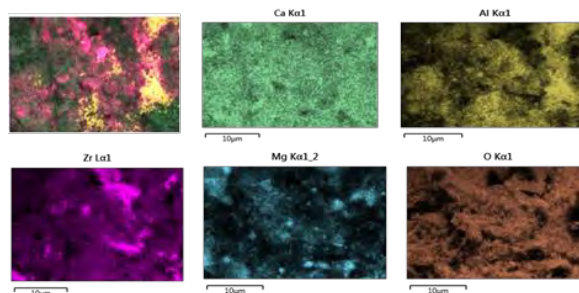


Figure 9: Elemental mapping of 2S(5.5Zr,10Al)

4. Conclusions

The results obtained in this work are shown as really promising. It has been observed that Zr is an interesting modifier comparing with Ce. The relatively high stability observed, for Zr modified sorbents, especially for 2S(5.5Zr,10Al) sorbent, is attributed mainly to two aspects. Firstly, to the formation of a mayenite framework which stabilize and, at the same time acts as a good binder. And secondly, to the formation of a relatively well dispersed CaZrO₃, which creates a barrier between CaO particles preventing the sintering and pore blockage. Regarding the two different synthesis routes employed (1-step and 2-step), the sorbent prepared by 2S route appears as the most active, mainly because of a more optimal dispersion of the Zr in the sorbent.

On the other hand, pellets were synthesized through manual pelletization in this work, but likewise, the method could be used to make mechanically strong sorbent by means of granulation-pelletization method, something that is already being investigated with promising results as well. Further exploration must be done including more realistic conditions to mimic the real process, including short carbonation times, higher carbonation/regeneration ramps and long-term experiments. Lastly, the simplicity of the synthesis procedure permits an easy scaling up.

5. References

- [1] United Nations, United Nations Framew. Conv. Clim. Chang. (2015) 27–52.
- [2] I.E. Agency, (2017).
- [3] F. Winter, R.A. Agarwal, J. Hrdlicka, S. Varjani, (2019) 1–3.
- [4] N.E. Flø, L. Faramarzi, T. De Cazenove, O.A. Hvidsten, A.K. Morken, E.S. Hamborg, K. Vernstad, G. Watson, S. Pedersen, T. Cents, B.F. Fostås, M.I. Shah, G. Lombardo, E. Gjernes, Energy Procedia 114 (2017) 1307–1324.
- [5] J. Kittel, R. Idem, D. Gelowitz, P. Tontiwachwuthikul, G. Parrain, A. Bonneau, Energy Procedia 1 (2009) 791–797.
- [6] P. Folger, Geol. Carbon Dioxide Storage (2012) 17–52.
- [7] K. Atsonios, P. Grammelis, S.K. Antiohos, N. Nikolopoulos, E. Kakaras, Fuel 153 (2015) 210–223.
- [8] D.P. Hanak, C. Biliyok, V. Manovic, Energy Environ. Sci. 9 (2016) 971–983.

- [9] D. Berstad, R. Anantharaman, K. Jordal, *Int. J. Greenh. Gas Control* 11 (2012) 25–33.
- [10] C.C. Cormos, *Appl. Therm. Eng.* 82 (2015) 120–128.
- [11] A. Perejón, L.M. Romeo, Y. Lara, P. Lisbona, A. Martínez, J.M. Valverde, *Appl. Energy* 162 (2016) 787–807.
- [12] D. Berstad, R. Anantharaman, R. Blom, K. Jordal, B. Arstad, *Int. J. Greenh. Gas Control* 24 (2014) 43–53.
- [13] A.S.R. Subramanian, K. Jordal, R. Anantharaman, B.A.L. Hagen, S. Roussanaly, *Energy Procedia* 114 (2017) 2631–2641.
- [14] J.M.G. Amann, C. Bouallou, *Energy Procedia* 1 (2009) 909–916.
- [15] F. Donat, N.H. Florin, E.J. Anthony, P.S. Fennell, *Environ. Sci. Technol.* 46 (2012) 1262–1269.
- [16] C. Luo, Y. Zheng, N. Ding, Q. Wu, G. Bian, C. Zheng, *Ind. Eng. Chem. Res.* 49 (2010) 11778–11784.
- [17] J. Chen, L. Duan, Z. Sun, *Energy & Fuels* (2020).
- [18] J.M. Valverde, P.E. Sanchez-Jimenez, L.A. Perez-Maqueda, *Appl. Energy* 138 (2015) 202–215.
- [19] J.M. Valverde, *J. Mater. Chem. A* 1 (2013) 447–468.
- [20] H.J. Yoon, K.B. Lee, *Chem. Eng. J.* 355 (2019) 850–857.
- [21] H. R. Radfarnia, M. C. Iliuta, *Ind. & Eng. Chem. Res.* 51 (2012) 10390–10398.
- [22] A. Antzara, E. Heracleous, A.A. Lemonidou, *Energy Procedia* 63 (2014) 2160–2169.
- [23] R. Koirala, G.K. Reddy, J.Y. Lee, P.G. Smirniotis, *Sep. Sci. Technol.* 49 (2014) 47–54.
- [24] X. He, G. Ji, T. Liu, M. Zhao, *Energy and Fuels* 33 (2019) 9996–10003.
- [25] I. Yanase, T. Maeda, H. Kobayashi, *Chem. Eng. J.* 327 (2017) 548–554.
- [26] V. Manovic, E.J. Anthony, *Energy and Fuels* 23 (2009) 4797–4804.
- [27] V. Manovic, E. J. Anthony, *Environ. Sci. & Technol.* 43 (2009) 7117–7122.
- [28] M. Erans, T. Beisheim, V. Manovic, M. Jeremias, K. Patchigolla, H. Dieter, L. Duan, E.J. Anthony, *Faraday Discuss.* 192 (2016) 97–111.
- [29] L. Duan, Z. Yu, M. Erans, Y. Li, V. Manovic, E. J. Anthony, *Ind. & Eng. Chem. Res.* 55 (2016) 9476–9484.
- [30] V. Manovic, E. J. Anthony, *Ind. & Eng. Chem. Res.* 48 (2009) 8906–8912.
- [31] Y. Xu, C. Luo, Y. Zheng, H. Ding, L. Zhang, *Energy & Fuels* 30 (2016) 3219–3226.
- [32] R. Koirala, K.R. Gunugunuri, S.E. Pratsinis, P.G. Smirniotis, *J. Phys. Chem. C* 115 (2011) 24804–24812.
- [33] R. Zsigmondy, P. Scherrer, *Kolloidchem. Ein Lehrb.* 277 (1912) 387–409.
- [34] S. Wei, R. Han, Y. Su, J. Gao, G. Zhao, Y. Qin, *Energy and Fuels* 33 (2019) 5398–5407.
- [35] M. Erans, V. Manovic, E.J. Anthony, *Appl. Energy* 180 (2016) 722–742.
- [36] A.H. Soleimansalim, M.H. Sedghkarder, D. Karami, N. Mahinpey, A.N. Antzara, A. Arregi, E. Heracleous, A.A. Lemonidou, *Chem. Eng. J.* 333 (2018) 5395–5402.
- [37] C. Chen, S.T. Yang, W.S. Ahn, *Mater. Lett.* 75 (2012) 140–142.
- [38] H. Chen, C. Zhao, Y. Yang, *Fuel Process. Technol.* 116 (2013) 116–122.
- [39] L. Duan, C. Su, M. Erans, Y. Li, E.J. Anthony, H. Chen, *Ind. Eng. Chem. Res.* 55 (2016) 10294–10300.
- [40] X. Tong, W. Liu, Y. Yang, J. Sun, Y. Hu, H. Chen, Q. Li, *Fuel Process. Technol.* 193 (2019) 149–158.
- [41] H. Guo, S. Wang, C. Li, Y. Zhao, Q. Sun, X. Ma, *Ind. Eng. Chem. Res.* 55 (2016) 7873–7879.

GENERALIZED GEERTSMA SOLUTION FOR ISOTROPIC LAYERED MEDIUM

Joonsang Park^{1*}, Ola Eiken², Tore I. Bjørnarå¹, Bahman Bohloli¹

¹ Norwegian Geotechnical Institute (NGI), Oslo, Norway

² Quad Geometrics, Trondheim, Norway

* Corresponding author e-mail: jp@ngi.no

Abstract

We report a generalized Geertsma solution with which we can calculate the surface deformation from a subsurface made of an arbitrary number of isotropic homogeneous layers and a thick reservoir at any depth. We validate the generalized Geertsma solution by solving simple numerical examples and comparing the results with a reference finite-element solution. Then, we apply the generalized Geertsma solution to more realistic subsurface models to study the effect of subsurface layering on surface deformation and the impact of acquisition-processing accuracy on inverted reservoir pressure. The modelling demonstrates the surface deformation (both magnitude and shape) is most influenced by the reservoir stiffness. Finally, the inversion exercise demonstrates that for the case of In Salah-inspired synthetic model, 3% noise resulting from data acquisition-processing error may introduce 15% deviation in the inverted pressure compared to the true reservoir pressure.

Keywords: surface heaving, Geertsma solution, layered subsurface, CO₂ injection

1. Introduction

Carbon capture and storage (CCS) is a promising technology that can significantly reduce the greenhouse gas emission from large-scale industrial point sources to the atmosphere. At the same time, there are several challenges to resolve. One urgent challenge is pressure control in the subsurface during CO₂ injection so that we can secure the integrity of the storage complex as well as optimize the injection rate. The Sleipner CO₂ storage is an example where there is no pressure build-up observed at the wellhead during more than 20 years of injection thanks to the good reservoir quality of the Utsira sand in the North Sea (Furre et al, 2015). On the other hand, the In Salah CO₂ storage project has experienced pressure increase to near fracture pressure in the injection well (Bohloli et al, 2018). Associated surface uplift was clearly detected with InSAR and showed how the reservoir pressure build-up was distributed in the subsurface, even delineating the temporal evolution of the footprint of a vertical fault near the KB502 injector (Bohloli et al, 2018, Bjørnarå et al, 2018).

Such precise surface deformation data is a direct response to the spatial and temporal distribution of pressure changes in the subsurface. Therefore, it is desired to have a good framework of interpreting and inverting the surface deformation in order to precisely map pressure changes and furthermore characterize geomechanical and hydraulic properties (Vasco et al, 2017). To achieve this, we need to have an accurate and fast engine to calculate surface deformation for a given pressure disturbance and a given subsurface model. Geertsma (1973) derived a closed-form solution that can calculate very quickly such surface deformations, assuming the subsurface is a homogeneous half-space. In addition, the Geertsma solution assumes the thickness of the pressure-disturbed

reservoir is much smaller than the depth of the reservoir. Mehrabian and Abousleiman (2015) overcame the homogeneous half-space limitation by modelling up to three layers using the same mechanical properties in the overburden and underburden. Here we generalize the framework in Mehrabian and Abousleiman (2015) so that we can handle: 1) arbitrary number of isotropic homogeneous layers, and 2) thick reservoir at any depth (Figure 1). We also seek to correct a few critical typographical errors in Mehrabian and Abousleiman (2015). Then, we validate the generalized Geertsma solution for the isotropic layered half space (ISO-GGS or just GGS) by solving simple numerical examples and by comparing with a reference finite-element-based solution. Finally, we apply the generalized Geertsma solution to more realistic subsurface models (inspired by an In Salah model) to study: 1) the effect of layered models on predicted surface deformation, and 2) the impact of acquisition-processing errors of surface deformation on reservoir pressure inverted with the help of such models.

2. Generalized Geertsma solution (GGS) for isotropic layered subsurface

Mehrabian and Abousleiman (2015) present a mathematical framework and derive a fully closed-form analytical solutions for stress tensor and deformation vector outside and inside an isotropic homogeneous reservoir layer embedded within another isotropic homogeneous half-space of dissimilar mechanical properties. In the closed-form solution, the reservoir layer should be quite thin compared to the reservoir depth and is subjected to axisymmetric constant pore pressure disturbance with finite radius. Although the final result plots are accurately given in Mehrabian and Abousleiman (2015), it is found during the current study

that there are critical typos in the description of the mathematical framework. The errors are discovered and corrected by following the linear elasticity framework in Park and Kaynia (2018). The kernels in Eqs 7-8 and 12-13 in Mehrabian and Abousleiman (2015) should have been written:

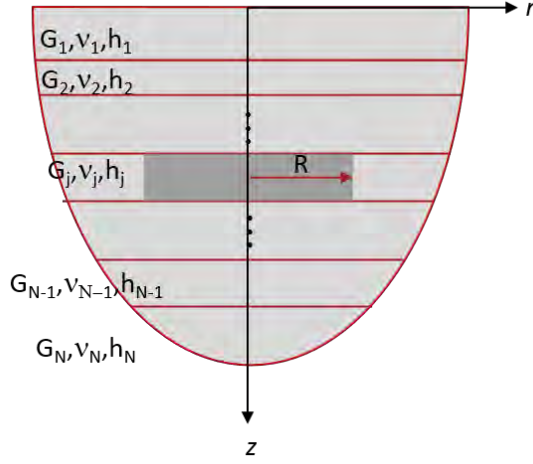


Figure 1: Isotropic subsurface model consisting of N layers and subjected to fluid-induced pore pressure (shaded) of radius R in a j -th layer. Note G , ν and h are shear modulus, Poisson's ratio and thickness of each layer. Axi-symmetric coordinates (r, z) are used.

$$U_1 = \frac{c_m P}{k} + az(Ae^{kz} - Be^{-kz}) + Ce^{kz} + De^{-kz}$$

$$U_3 = \left(\frac{a+1}{k} - az\right)Ae^{kz} - \left(\frac{a+1}{k} + az\right)Be^{-kz} - Ce^{kz} + De^{-kz}$$

$$S_{rz} = 2G \left[\left(akz - \frac{1}{2}\right)Ae^{kz} + \left(akz + \frac{1}{2}\right)Be^{-kz} + kCe^{kz} - kDe^{-kz} \right]$$

$$S_{zz} = 2G \left[\left(1 - akz + \frac{\nu}{1-2\nu}\right)Ae^{kz} + \left(1 + akz + \frac{\nu}{1-2\nu}\right)Be^{-kz} - kCe^{kz} - kDe^{-kz} - c_m P \right]$$

where $a = 1/2(1 - 2\nu)$, $c_m = \alpha(1 - 2\nu)/2G\nu$; ν and G are Poisson's ratio and shear modulus; k is the wavenumber for the associated Hankel transform; z is the depth-direction coordinate; $P=R/kJ_1(kR)$ is magnitude of pore pressure disturbance in k domain with R and J_1 being the radius of the constant pore pressure disturbance and the 1st-order Bessel function; A , B , C and D are unknown coefficients to be determined based on the boundary conditions in the layered subsurface i.e. continuity conditions of horizontal-vertical displacements (U_1 and U_3) and shear-normal stresses (S_{rz} and S_{zz}) at each interface as described in Mehrabian and Abousleiman (2015). Performing the associated Hankel transformation, we can calculate the displacements and stresses at any point in a given isotropic multilayered subsurface subjected to a pore pressure change applied at any layer.

2.1 Validation

We validate the corrected expressions against a finite element method solution. We run a numerical example of

three layers and compare with the commercial code COMSOL Multiphysics™. Table 1 shows the material properties and thicknesses of the layered subsurface. We consider three models by varying the ratio (μ) of shear moduli between Layer 2 and Layers 1 & 3 as shown in Table 1. Layer 2 is subjected to a 10 MPa pore pressure disturbance of cylinder shape with radius of 500 m. The results of the vertical displacement at the top surface (subsidence) are shown in Figure 2. It can be seen that the two solutions obtained by the generalized Geertsma (ISO-GGS) and FE solutions (solid lines and circles, respectively) are in good agreement. Additionally, we can see the significant effects of multilayers (in both magnitude and shape of surface deformation) by looking at the differences between the layered models (models 1, 3) and the homogeneous model (model 2).

Table 1: Material properties for the validation models. Poisson's ratio is 0.25 for all the layers.

layer	thickness [m]	shear modulus (G) [GPa]		
		model 1	model 2	model 3
1	1300	0.5	1.0	2.0
2	200	1.0	1.0	1.0
3	∞	0.5	1.0	2.0

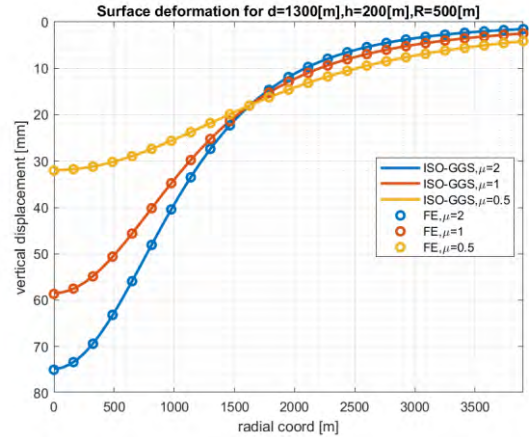


Figure 2: Comparison of the generalized Geertsma solution for isotropic subsurface (ISO-GGS, solid lines) and the finite element solution (FE, circles) for three different values for $\mu(=G_{1,3}/G_2)=0.5, 1.0$ and 2.0 . Note that the vertical axis in the plot has the positive downward convention.

3. Synthetic data study via In Salah model

3.1. Effect of layer stiffness on surface deformation

To increase our understanding of the relationship between the surface deformation and the layer stiffness, we solve a series of four numerical examples by tuning layer stiffnesses (Figure 3). The reference model is taken from Bjørnarå et al (2018) for the In Salah CO₂ storage project. The other models are made by softening the Young's moduli by 25% in either the overburden layers, the reservoir layer or the underburden, respectively. Figure 4 shows the comparison of the four models in terms of vertical displacement at the top surface.

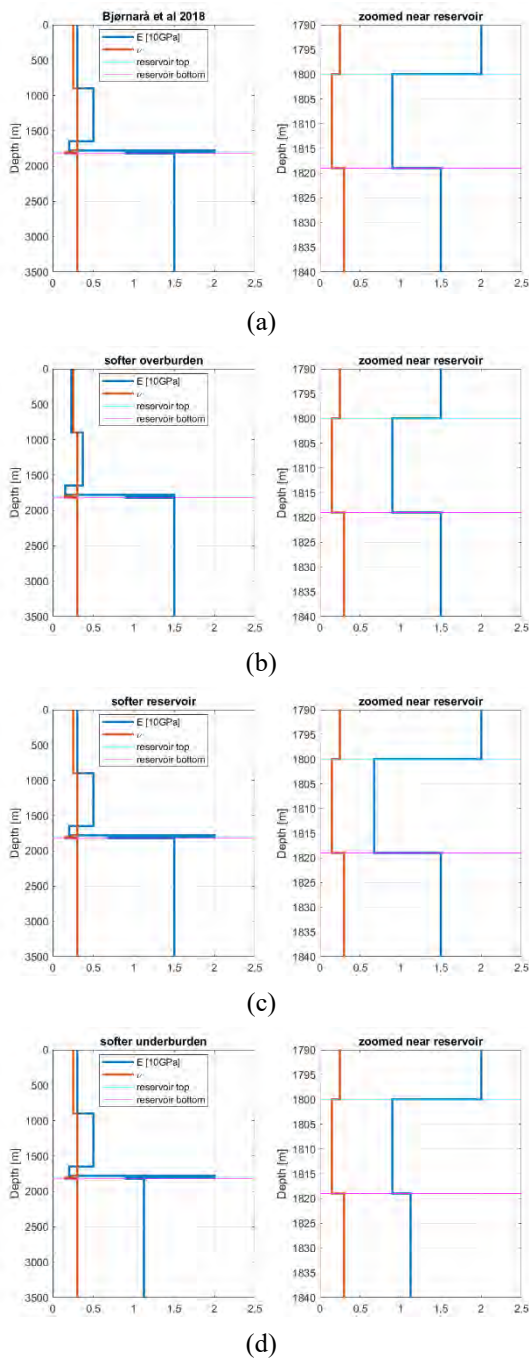


Figure 3: Four subsurface layer models taken from Bjørnå et al (2018): (a) reference model; (b) 25% softer overburden; (c) 25% softer reservoir; (d) 25% softer underburden.

Not surprisingly, the surface vertical displacement is strongly dependent on the layer stiffness. It can also be seen in this analysis that the stiffness of the reservoir (where the pore pressure disturbance is applied) has the most influence on the magnitude of vertical displacement (yellow curve in Figure 4), while the stiffness of the overburden has the least influence. The result of the softer overburden model (red curve) is very close to the reference model in both magnitude and shape. However, the softer underburden (purple curve) makes the top surface heave smaller compared to the reference model (blue curve) for $r < 2500\text{m}$, but (slightly) larger for $r > 2500\text{m}$. When the underburden becomes stiffer instead, it is expected that the surface heave becomes

larger for $r < 2500\text{m}$ and smaller for $r > 2500\text{m}$. We can see that the surface height change (in both magnitude and shape) is more sensitive to the stiffness of the underburden than the overburden. All these observations provide us with good insights on the correlation between the surface deformation and the subsurface layering, which is challenging for interpretation and inversion of the surface deformation measured by e.g. InSAR (e.g. Bohloli et al, 2018) or seabed pressure (Eiken et al, 2008).

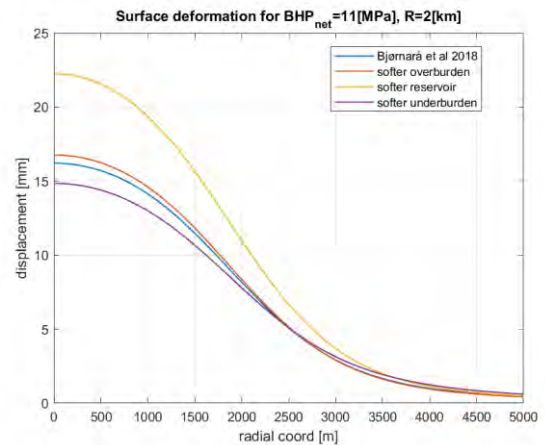


Figure 4: Comparison of top surface vertical displacements for the four subsurface models shown in Figure 3. Note that the vertical axis in the plot has the positive upward convention.

3.2. Impact of acquisition-processing accuracy on inverted reservoir pressure

High accuracy in data is generally important for characterization and monitoring of the subsurface. In particular, the surface height changes estimated from processed onshore InSAR and seabed pressure requires precision of mm-scale to be detectable, which is challenging at the field scale. In this subsection, we demonstrate the impact of the accuracy of surface deformation obtained through the acquisition-processing on the inversion result for reservoir pressure on synthetic data. We model surface uplift from the subsurface model of Figure 3a by using the generalized Geertsma solution, and assuming the reservoir pressure spatial distribution as shown in Figure 5a. To create the synthetic solution, 3% random noise is added to the calculated heave. Finally, we invert for the reservoir pressure (Figure 5b) and compare it to the synthetic reservoir pressure (Figure 5a), which was input to the forward modelling and inversion exercise. The inversion problem considered here is based on a linear superposition relationship between surface deformation and pressure change, and the detail can be found in Park et al. (2021). Figure 5c shows the difference between the synthetic and inverted reservoir pressure. The 3% noise that was added to create the synthetic solution causes absolute errors in the inverted pressure up to 1.6 MPa, which is more than 15% deviation at the locations with maximum pressure changes. Therefore, it is important to reduce the uncertainty in the surface deformation data, involving

technical improvements in both acquisition and processing of InSAR and seabed data.

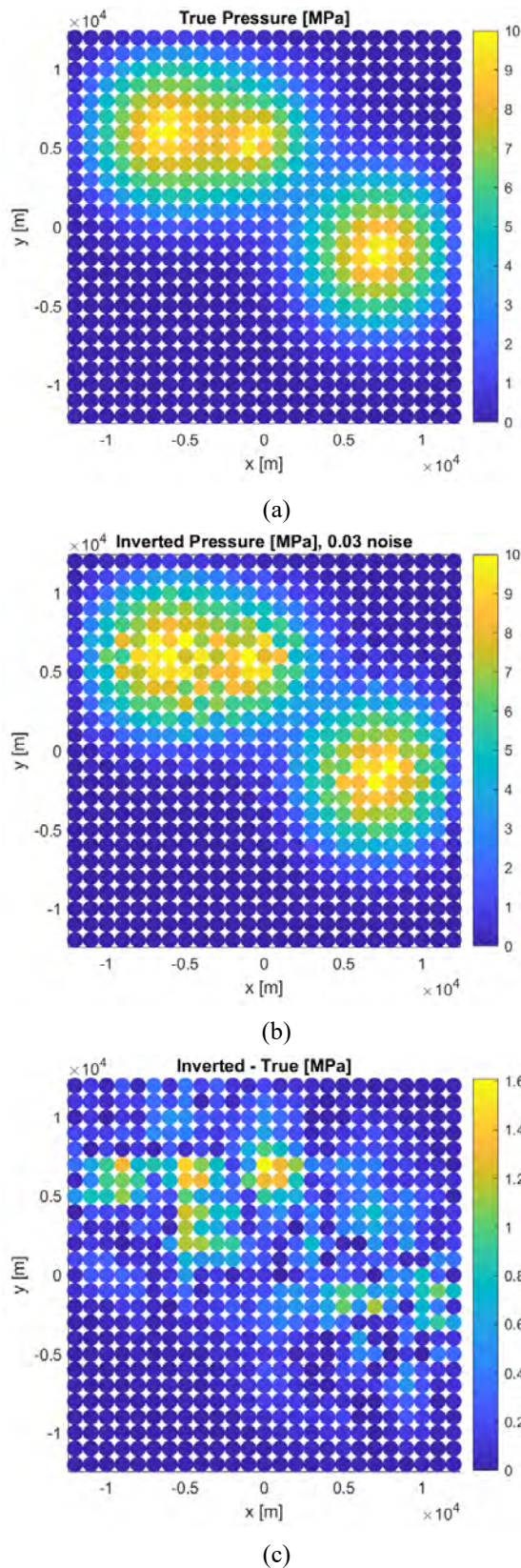


Figure 5: (a) Reservoir pressure change distribution input to the synthetic data calculation, inspired by Bjørnarå et al. (2018); note that from left to right, three pressure anomalies are related to the three injection wells of KB503, KB502 and KB501, respectively); (b) inverted reservoir pressure distribution; (c) difference between "true" and inverted reservoir pressures.

4. Summary and conclusion

In the current study, we have described the generalized Geertsma solution (GGS) that can handle arbitrary number, depth and thickness of isotropic homogeneous layers. The solution is validated by comparing the analytical solution to a numerical solution. We have applied the GGS to various subsurface models to study the effect of subsurface layering on surface deformation and the impact of acquisition-processing accuracy on inverted reservoir pressure. It is shown that, for the tested case-study inspired by the In Salah CO₂ storage project, the surface deformation is particularly dependent on the mechanical properties of the reservoir. Finally, the inversion exercise has demonstrated that 3% noise due to acquisition-processing error may introduce up to 15% error in the inverted pressure.

Acknowledgements

The study is supported jointly by 1) SENSE (Assuring integrity of CO₂ storage sites through ground surface monitoring, CLIMIT Demo Project No. 299664, ACT2-EC Project no. 691712) and 2) SHAPE (Seafloor height from aqua pressure for offshore CO₂ storage, CLIMIT Demo Project No. 620080). Equinor and Quad Geometrics are the industry partners.

References

- [1] Bohlooli, B., Bjørnarå, T.I., Park, J., Rucci, A. (2018). Can surface uplift be used as a tool for monitoring reservoir performance? A case study from In Salah, Algeria, *International Journal of Greenhouse Gas Control*, 76, 200-207.
- [2] Bjørnarå, T. I., Bohlooli, B., Park, J. (2018). Field data analysis and hydromechanical modeling of CO₂ storage at In Salah, Algeria. *International Journal of Greenhouse Gas Control*, 79, 61-72.
- [3] Eiken, O., Stenvold, T., Zumberge, M.A., Alnes H., Sasagawa G. (2008). Gravimetric monitoring of gas production from the Troll field. *Geophysics* 73(6) WA 149 - WA 154.
- [4] Furre, A.K., Kiær, A., Eiken, O. (2015). CO₂-induced seismic time shift at Sleipner, *Interpretation*, 3(3), SS23-35.
- [5] Geertsma, J. (1973). A basic theory of subsidence due to reservoir compaction: the homogeneous case. *Trans. R. Dutch Soc. Geol. Min. Eng.* 28, 43-62.
- [6] Mehrabian, A., Abousleiman, Y.N. (2015). Geertsma's subsidence solution extended to layered stratigraphy, *Journal of Petroleum Science and Engineering* 130, 68-76.
- [7] Park, J., Kaynia, A.M. (2018). Stiffness matrices for fluid and anisotropic soil layers with applications in soil dynamics, *Soil Dynamics and Earthquake Engineering*, 115, 169-182.
- [8] Park, J., Bjørnarå, T.I., Bohlooli, B. An Analytical Solution for Pressure-Induced Deformation of Anisotropic Multilayered Subsurface. *Geosciences* 2021, 11, 180. <https://doi.org/10.3390>.
- [9] Vasco, D.W., Harness, P., Pride, S., Hoversten, M. (2017). Estimating fluid-induced stress change from observed deformation, *Geophysical Journal International*, 208(3), 1623-1642.

ANALYSIS OF PRESSURE AND TEMPERATURE DYNAMICS DURING DEPRESSURIZATION OF A PIPE FILLED WITH A CO₂-HE OR CO₂-N₂ MIXTURE

Svend T. Munkejord*, Han Deng, Anders Austegard, Morten Hammer, Ailo Aasen, Hans L. Skarsvåg

SINTEF Energy Research, Trondheim, Norway

* Corresponding author e-mail: svend.t.munkejord@sintef.no

Abstract

To design and operate safe and efficient CO₂-transportation systems for CO₂ capture and storage (CCS), engineers need simulation tools properly accounting for the fluid and thermodynamics of CO₂. As the transportation systems evolve into networks, it becomes important that these tools also account for impurities in the CO₂, which may significantly affect the thermophysical properties, directly impacting system design and safety. Tube-depressurization experiments provide crucial data to develop and validate models describing transient multiphase multicomponent flow in pipes. In this work, we perform experiments in a new facility with dense and fast instrumentation for both pressure and temperature. One experiment is for CO₂ with 1.8 mol % N₂, and one has 1.92 mol % He, both starting from 12 MPa and 25 °C. In order to quantify the effect of impurities, the experiments are compared to results for pure CO₂ and analysed on the background of simulations. We employ a homogeneous equilibrium model (HEM) augmented in this work to account for the appearance of solid CO₂ in CO₂ mixtures. We observe that these moderate amounts of impurities significantly influence both pressure and temperature dynamics. In particular, the ‘pressure plateau’, a key quantity for the assessment of running-ductile fracture, increases as much as 4 MPa for CO₂-He compared to pure CO₂. A further insight is that models must account for solid CO₂ in order to capture the correct temperature development as the pressure decreases towards atmospheric conditions.

Keywords: carbon dioxide, decompression, experiment, thermodynamics, fluid dynamics

1. Introduction

In order to mitigate climate change, CO₂ emissions must be reduced, and to attain the required scale, a portfolio of technologies are needed. CO₂ capture and storage (CCS) is regarded as one of the necessary contributions (Edenhofer et al., 2014). By the mid century, therefore, several gigatonnes of CO₂ will need to be transported from the emitters to storage sites each year (IEA, 2017). Much of this transportation will be through pipeline networks. To design and operate safe and efficient transportation systems, engineers need simulation tools properly accounting for the fluid and thermodynamics of CO₂ (Aursand et al., 2013). Here, one needs to consider that the critical point (7.38 MPa, 31.0 °C), above which there is no difference between vapour and liquid, and the triple point (517 kPa, -56.6 °C), where solid CO₂ forms, are within a range that could be attained during normal operation.

Presently, CCS projects predominantly have strict limits on the allowable impurity content in the CO₂ stream to be transported (see e.g. Equinor, 2019), to the point where the impurities may not significantly affect the thermophysical properties of the CO₂ stream. However, this may be relaxed in the future in order to optimize the system. Moreover, it is envisaged that as CCS is deployed, direct source-to-sink transportation will be superseded by transportation networks with multiple sources (Moe et al., 2020). Then, even if the specifications are strict, variations in supply between the sources may yield different total compositions. Further,

off-specification delivery of CO₂ into the network may cause significant amounts of impurities to be present in the system, at least temporarily. Among other things, this could lead to a transition from single-phase to two-phase flow, with liquid slugging and operational disturbances as a result. Therefore, models supporting the design and operational procedures of CO₂-transportation systems need to be able to predict the effect of impurities in the CO₂ stream.

In general, existing flow models and tools were developed for other fluids, and may not be accurate for CO₂ and CO₂-rich mixtures. Therefore, since there are few flow data for CO₂ available in the open literature, new high-quality data are a prerequisite to further development. One principal experiment that is needed to develop CO₂-transportation systems is the depressurization of a tube. There are several reasons for this. First, such experiments are relevant for the prediction of running-ductile fracture (RDF), where a defect in the pipeline develops into a crack running along the pipeline (see e.g. Aursand et al., 2016). This kind of event is a hazard, and pipelines transporting highly pressurized compressible fluids need to be designed to avoid running-ductile fracture (RDF) for more than 1–2 pipe sections (DNV, 2012). Second, depressurization experiments can be employed to validate model predictions for a large range of pressures and temperatures along the tube. In particular, during decompression of CO₂, the temperature can attain -78 °C, a level where several materials have turned brittle.

Importantly, tube-depressurization experiments are well defined, and therefore suited for model validation and development.

Botros et al. (2017b) reported results from six tests with N₂, O₂, Ar, CO, H₂ and CH₄, respectively, as primary impurities. The observed decompression-wave velocities were compared to velocities calculated employing different equations of state (EOS), where the GERG-2008 EOS (Kunz and Wagner, 2012) was the most accurate of the ones considered. It can be seen from the results, however, that for many of the mixtures, there was a significant deviation between the calculations and the experiments. There was also a significant deviation for the so-called ‘plateau pressure’. This is the pressure at which the decompression-wave speed abruptly decreases – hence the appearance of a plateau in the plots. If the process were at equilibrium, this would correspond to the saturation pressure. One can imagine two main reasons for this discrepancy. First, it could be the failure of the EOS to predict the saturation pressure for the state and mixture in question. Second, perhaps more significantly, it could be that the process is too fast to be in equilibrium. To study this in more detail, accurate temperature observations may help, even though the temperature sensors may not be fast enough to capture the fastest variations.

Furthermore, accurate temperature observations are required in order to develop and validate in-tube heat transfer models needed for transient simulations, and the observed temperatures can also be employed to indicate main features of the flow regime, such as two-phase gas-liquid versus single-phase flow, and the occurrence of e.g. solid CO₂ (dry ice). Hence, in this work, we present both high-resolution pressure and temperature data for the decompression of CO₂-rich mixtures. We consider nitrogen (N₂) and helium (He), as representatives of ‘medium’ and ‘very light’ non-condensable impurities. He is the lightest of all elements in terms of boiling point and critical pressure.

Here we present, for the first time, a dynamic homogeneous equilibrium model (HEM), augmented to account for equilibria involving CO₂-rich mixtures and solid CO₂. This also allows us to present new phase diagrams for CO₂-rich mixtures, including predictions for solid-phase CO₂ in equilibrium with fluid phases.

The experiments were carried out in the ECCSEL Depressurization Facility (ECCSEL, 2020), part of the

European CCS Laboratory Infrastructure, that was recently put into operation (Munkejord et al., 2020a). The facility was constructed and instrumented to obtain high-resolution and synchronized pressure and temperature data. In the present work, the facility was commissioned for use with non-flammable impurities. Moreover, the experimental data collected can be downloaded in full from Zenodo (Munkejord et al., 2020b).

There is a two-way coupling between models and experiments. Evidently, experiments are needed to validate models. Equally important, models enhance the understanding of the phenomena and help the design of the experiments. In this work following, we therefore discuss the results with a view to model predictions, both with respect to fluid and thermodynamics.

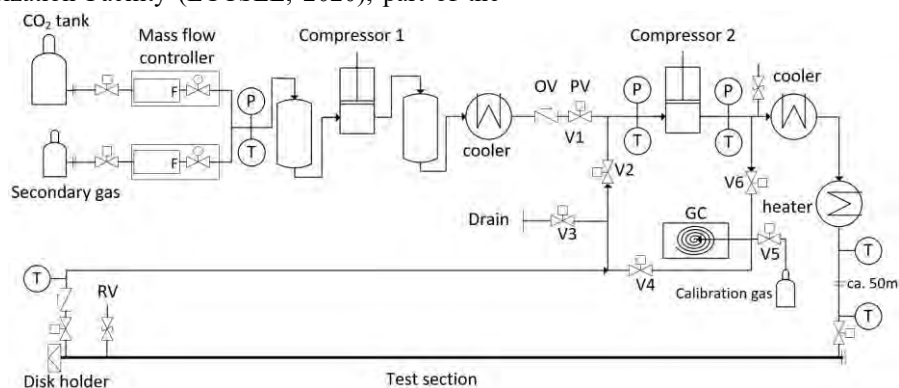
The main contributions of the present work can be summarized in this way:

- New experimental data for the depressurization of CO₂-rich mixtures in a pipe with dense and fast instrumentation for both pressure and temperature.
 - The data can be downloaded freely.
 - The data support model development and validation, and as a consequence, the deployment of CO₂-transportation systems.
- A transient HEM predicting the formation of solid CO₂ in CO₂ mixtures.
- Interaction parameters for the tc-PR EOS adapted to CO₂-He.

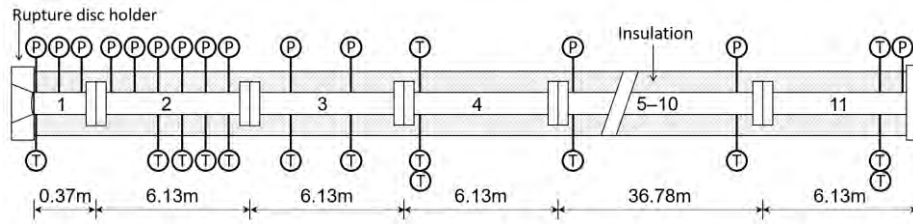
The present work has been submitted for publication in a journal. This short paper is therefore not intended to be included in the proceedings.

2. Experimental setup

Figure 1a shows a schematic view of the ECCSEL depressurization facility, which consists of a test section with a rupture disk at the open end and an auxiliary system for filling and conditioning. The auxiliary system includes gas supply with mass flow controllers, two-stage compression with cooling and heating, a circulation pipeline, and a micro gas chromatograph. The maximum operating pressure of the facility is 20 MPa, and the current design allows experiments with initial temperatures in the range 5 °C to 40 °C. A more detailed description can be found in Munkejord et al. (2020a).



(a) System (RV: relief valve; OV: one-way valve; PV: pneumatic valve)



(b) Test section (dimensions are not to scale; pipe no. 5–10 and corresponding sensors are omitted.)

Figure 1: Schematic of the ECCSEL depressurization facility.

The procedure is conducted as follows. (1) The rupture disk is installed and (2) the system is evacuated. (3) The test section is filled with a mixture of gaseous CO₂ and secondary gas heated to 40 °C. (4) The temperature is kept at 40 °C while the mixture is circulated in the test section. The test section is charged using the compressors to a pressure about 1 MPa higher than the highest two-phase pressure of the mixture in the relevant temperature region. (5) The mixture is then cooled to a few degrees below the desired temperature while the fluid is circulated and the pressure is kept constant by further charging. (6) In the final stage, the pressure is increased at a controlled rate until the disk ruptures. (7) After the test, the system is emptied.

3. Models

To describe the thermodynamic properties, we used different EOSs for the CO₂-N₂ and CO₂-He fluid mixtures. Ideally, the same EOS would be used for both mixtures, but because the most accurate EOS for CO₂-rich mixtures, EOS-CG (Gernert and Span (2016)), does not include a model for the CO₂-He binary mixture, an alternative EOS has been used for that mixture: we employ and adapt the translated and consistent Peng and Robinson (1976) equation of state (EOS) (tc-PR) by Le Guennec et al. (2016b) to data for CO₂-He. For the calculation of thermodynamic properties we employ our in-house thermodynamics library (Wilhelmsen et al., 2017).

We represent the transient compressible single-, two- or three-phase flow of CO₂-rich mixtures employing a homogeneous equilibrium model (HEM). Herein, the different phases are assumed to exist in mechanical, kinetic, thermal and chemical equilibrium at all times, i.e., the phases have the same pressure, velocity, temperature and chemical potential. This represents some physical simplifications, but it nevertheless requires a particularly robust calculation of the thermophysical properties. The model was discussed in detail by Munkejord et al. (2016).

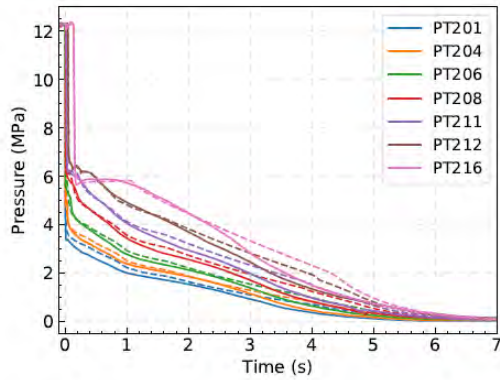
4. Results

In order to study the effect of impurities on the decompression behaviour of a CO₂ stream, we retain the conditions of Test 8 for pure CO₂, reported in Munkejord et al. (2020a). The nominal conditions are 12 MPa and 25 °C, see Table 1.

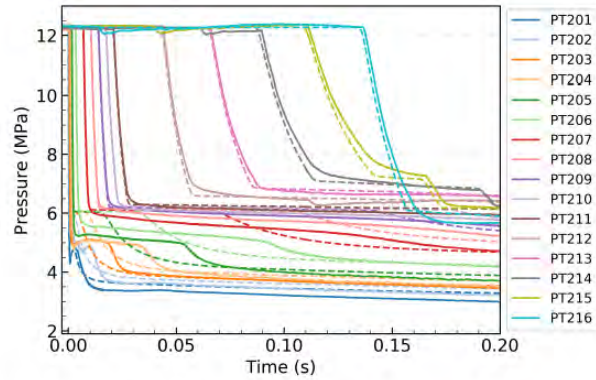
Table 1: Experimental initial conditions

Test no	Impurity	Concentration (mol %)	P (MPa)	T (°C)
8*	none	n/a	12.22	24.6
9	N ₂	1.8	12.27	25.0
12	He	1.92	12.17	24.7

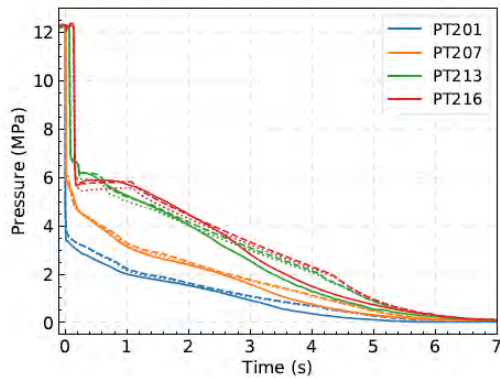
* From Munkejord et al (2020a).



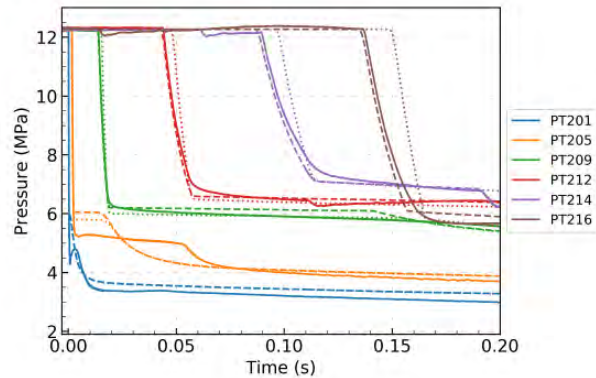
(a) Full depressurization, experiments and simulations using EOS-CG.



(b) First 0.2 s, experiments and simulations using EOS-CG.



(c) Full depressurization, experiments and comparison between simulations using EOS-CG (dashed lines) and the PR EOS (dotted lines).



(d) First 0.2 s, experiments and comparison between simulations using EOS-CG (dashed lines) and the PR EOS (dotted lines).

Figure 2: Measured (full lines) and simulated pressure, with EOS-CG (dashed lines) and with PR (dotted lines), at the sensor positions, for Test no. 9.

As an example result, we consider pressure for Test 9 for CO₂-N₂. Figure 2 displays measured and simulated pressure at the sensor positions. Simulations employing EOS-CG (dashed lines) and the PR EOS (dotted lines) are shown. The whole decompression process is shown in Figure 2a, whereas Figure 2b concentrates on the first instants where the transients are fast. As can be observed from Figure 2b, upon arrival of the first decompression wave, the pressure sensors experience an abrupt pressure reduction. At about 6 MPa at the outlet (and increasing upstream due to friction and heat transfer, see the discussion in relation to Figure 10 in Munkejord et al. (2020a)), the pressure traces level off for a shorter or longer period depending on the position, and the decompression proceeds slower. This corresponds to the onset of two-phase flow.

In Figure 2, simulation results obtained with the homogeneous equilibrium model (HEM) are plotted along with the experimental values. It can be observed that close to the outlet and during the first instants of depressurization, the HEM tends to over-estimate the pressure ‘plateau’, something which could be related to non-equilibrium effects, which will be further discussed

in the next section. Later, and further upstream, the pressure-plateau levels match relatively well, see e.g. sensor PT209 at 0.1 s (Figure 2d). Even later, see Figure 2a at about 3 s, there is an overestimation of the pressure. At this point, the outlet boundary condition and the assumption of a highly dispersed flow, which does not hold in all the pipe, play a role. All in all, however, we find that the HEM performs well, given its simplifications. Furthermore, Figure 2d illustrates that the PR EOS underestimates the speed of sound (later wave arrival times), and more so for high pressures. EOS-CG, on the other hand, gives accurate values in the single-phase region. In Figure 3 in Munkejord and Hammer (2015), we reported that the PR EOS underestimated the single-phase speed of sound for a different CO₂-rich mixture. It can also be seen from Figure 2d that in the current case, PR gives a longer duration of the pressure plateau than EOS-CG. This difference increases upstream and is due to the difference between the liquid speed of sound and the two-phase mixture speed of sound.

The difference between predictions obtained using EOS-CG and those for the PR EOS are further illustrated by

the plot in Figure 2c for the whole depressurization. It can be seen that after the initial strong transients, the difference is limited. This is because the benefit of using EOS-CG over a cubic EOS is mainly the improved density and speed-of-sound predictions. The cubic EOS, however, will predict VLE and energetic properties with satisfactory accuracy. For the initial strong transient plotted in Figure 2d, the density and speed of sound will define the rarefaction-wave velocity. For the 'slower' effects plotted in Figure 2c, when the fluid is in a two-phase state, VLE, energetic properties, heat transfer to the fluid and friction will all have an effect, through the coupling of mass, momentum and energy.

The presentation will also consider results for wave-propagation speed and for temperature, and the effect of impurities will be discussed.

5. Conclusion

The new ECCSEL Depressurization Facility has been commissioned for non-flammable impurities. We have reported and analysed two full-bore depressurization experiments of a tube, one with CO₂ with 1.8 mol % N₂ and one with 1.92 mol % He, comparing with a pure-CO₂ experiment from Munkejord et al. (2020a). In particular, both pressure and temperature data with high spatial and temporal resolution have been presented. The experiments show that the decompression behaviour of the CO₂ stream is significantly affected by impurities in this relatively moderate range. In addition, the decompression process is characterized by regimes of single-phase, two-phase (vapour-liquid and vapour-solid) and three-phase (vapour-solid-liquid) flow. As a consequence, simulation models used for considerations related to design and operation of CO₂ transport and injection systems should be able to accurately take these effects into account in order to enable safe and efficient CCS systems.

We observed an increase in the phase-transition pressure in the range of 1 MPa resulting from 1.8 mol % N₂, and almost 4 MPa resulting from 1.92 mol % He. This has consequences for systems where one for instance aims to avoid two-phase flow. For the rapid decompression relevant for the assessment of running-ductile fracture, we observed that the phase-transition pressure was significantly lower than the plateau (equilibrium) pressure. To physically model this non-equilibrium flow constitutes a challenging topic for further research.

For CO₂-N₂, the single-phase liquid decompression speed calculated using EOS-CG was in very good agreement with the experiments. For CO₂-He, on the other hand, neither the specially adapted tc-PR EOS nor the GERG-2008 EOS gave accurate results, the discrepancies being in the order of 10% for the decompression speed, depending on the pressure level.

For the early stage of depressurization, the pressure observed for pure CO₂ dropped fastest and that of CO₂-He slowest. However, after about 1.5 s, the situation was reversed, with the highest recorded pressure for pure CO₂ and the lowest for CO₂-He. This effect was reproduced by the HEM.

The impurities also affected the observed temperature dynamics. CO₂-N₂ gave a faster initial temperature drop and earlier dry-out than pure CO₂, and CO₂-He even more so.

We have implemented vapour-solid-liquid equilibrium calculations in conjunction with our HEM. Comparison with the experiments showed that in order to reproduce the correct temperature development, taking solid CO₂ into account was necessary both at the point where solid CO₂ was formed, and at downstream positions. At the closed end, failing to include solid CO₂ gave a too low calculated temperature, whereas 15 m downstream, it gave a too high temperature.

The HEM gave good temperature predictions close to the outlet, where the flow is highly dispersed, and at the closed end of the tube, where the temperature is governed mainly by the phase equilibria. In the middle of the tube, the HEM gave too early dry out, and a too high dry-out temperature. Improvements could perhaps be obtained by considering models including phase slip, as well as improved heat-transfer models.

Acknowledgements

ACT ELEGANCY, Project No 271498, has received funding from DETEC (CH), BMWi (DE), RVO (NL), Gassnova (NO), BEIS (UK), Gassco, Equinor and Total, and is cofunded by the European Commission under the Horizon 2020 programme, ACT Grant Agreement No 691712.

The construction of the ECCSEL Depressurization Facility was supported by the INFRASTRUKTUR programme of the Research Council of Norway (225868).

References

- Aursand, E., Dumoulin, S., Hammer, M., Lange, H. I., Morin, A., Munkejord, S. T., Nordhagen, H. O., Sep. 2016. Fracture propagation control in CO₂ pipelines: Validation of a coupled fluid-structure model. *Eng. Struct.* 123, 192–212. doi:10.1016/j.engstruct.2016.05.012.
- Aursand, P., Hammer, M., Munkejord, S. T., Wilhelmsen, Ø., Jul. 2013. Pipeline transport of CO₂ mixtures: Models for transient simulation. *Int. J. Greenh. Gas Con.* 15, 174–185. doi:10.1016/j.ijggc.2013.02.012.
- Botros, K. K., Geerligs, J., Rothwell, B., Robinson, T., Apr. 2017c. Measurements of decompression wave speed in simulated anthropogenic carbon dioxide mixtures containing hydrogen. *J. Press. Vess. – T. ASME* 139 (2). doi:10.1115/1.4034466.
- DNV, Aug. 2012. Submarine pipeline systems. Offshore standard DNV-OS-F-101.
- ECCSEL, 2020. Depressurization facility. https://www.eccsel.org/facilities/transport/no25_sintef_er_dep ress/. Accessed 2020-03-31.
- Edenhofer, O., Pichs-Madruga, R., Sokona, Y., Farahani, E., Kadner, S., Seyboth, K., Adler, A., Baum, I., Brunner, S., Eickemeier, P., Kriemann, B., Savolainen, J., Schlömer, S., von Stechow, C., Zwickel, T., (eds.), J. M., 2014. *Climate Change 2014: Mitigation of Climate Change*. Tech. rep., Working Group III Contribution to the Fifth Assessment Report of the Intergovernmental Panel on Climate Change, Summary for Policymakers, IPCC. URL <http://mitigation2014.org/>.

Equinor, May 2019. Northern Lights Project Concept Report. Tech. Rep. RE-PM673- 00001. Available from <https://northernlightsccs.com/assets/documents/Northern-Lights-Project-Concept-report.pdf>.

Gernert, J., Span, R., 2016. EOS-CG: A Helmholtz energy mixture model for humid gases and CCS mixtures. *J. Chem. Thermodyn.* 93, 274–293. doi:10.1016/j.jct.2015.05.015.

Hammer, M., Ervik, Å., Munkejord, S. T., 2013. Method using a density-energy state function with a reference equation of state for fluid-dynamics simulation of vapor-liquid-solid carbon dioxide. *Ind. Eng. Chem. Res.* 52 (29), 9965–9978. doi:10.1021/ie303516m.

IEA, 2017. Energy Technology Perspectives. ISBN 978-92-64-27597-3. doi:10.1787/energy_tech-2017-en.

Kunz, O., Wagner, W., October 2012. The GERG-2008 wide-range equation of state for natural gases and other mixtures: An expansion of GERG-2004. *J. Chem. Eng. Data* 57 (11), 3032–3091. doi:10.1021/je300655b.

Le Guennec, Y., Privat, R., Jaubert, J.-N., 2016b. Development of the translated-consistent tc-PR and tc-RK cubic equations of state for a safe and accurate prediction of volumetric, energetic and saturation properties of pure compounds in the sub- and super-critical domains. *Fluid Phase Equilib.* 429, 301–312. doi:10.1016/j.fluid.2016.09.003.

Moe, A. M., Dugstad, A., Benrath, D., Jukes, E., Anderson, E., Catalanotti, E., Durusut, E., Neele, F., Grunert, F., Mahgerefteh, H., Gazendam, J., Barnett, J., Hammer, M., Span, R., Brown, S., Munkejord, S. T., Weber, V., Jun. 2020. A trans-European CO₂ transportation infrastructure for CCUS: Opportunities & challenges. Report, Zero Emissions Platform, Brussels, Belgium. Available from [https://zeroemissionsplatform.eu/wp-content/uploads/A-Trans-European-CO₂-Transportation-Infrastructure-for-CCUS-Opportunities-Challenges.pdf](https://zeroemissionsplatform.eu/wp-content/uploads/A-Trans-European-CO2-Transportation-Infrastructure-for-CCUS-Opportunities-Challenges.pdf).

Munkejord, S. T., Austegard, A., Deng, H., Hammer, M., Stang, H. G. J., Løvseth, S. W., Nov. 2020a. Depressurization of CO₂ in a pipe: High-resolution pressure and temperature data and comparison with model predictions. *Energy* 211, 118560. doi:10.1016/j.energy.2020.118560.

Munkejord, S. T., Deng, H., Austegard, A., Hammer, M., Skarsvåg, H. L., Aasen, A., 2020b. Depressurization of CO₂-N₂ and CO₂-He in a pipe: Experiments and modelling of pressure and temperature dynamics – dataset. Zenodo. doi:10.5281/zenodo.3984822.

Munkejord, S. T., Hammer, M., Jun. 2015. Depressurization of CO₂-rich mixtures in pipes: Two-phase flow modelling and comparison with experiments. *Int. J. Greenh. Gas Con.* 37, 398–411. doi:10.1016/j.ijggc.2015.03.029.

Munkejord, S. T., Hammer, M., Løvseth, S. W., May 2016. CO₂ transport: Data and models – A review. *Appl. Energ.* 169, 499–523. doi:10.1016/j.apenergy.2016.01.100.

Peng, D. Y., Robinson, D. B., Feb. 1976. A new two-constant equation of state. *Ind. Eng. Chem. Fund.* 15 (1), 59–64. doi:10.1021/i160057a011.

Wilhelmsen, Ø., Aasen, A., Skaugen, G., Aursand, P., Austegard, A., Aursand, E., Gjennestad, M. A., Lund, H., Linga, G., Hammer, M., 2017. Thermodynamic modeling with equations of state: Present challenges with established methods. *Ind. Eng. Chem. Res.* 56 (13), 3503–3515. doi:10.1021/acs.iecr.7b00317.

CONVECTIVE DISSOLUTION IN FIELD SCALE CO₂ STORAGE SIMULATIONS USING THE OPM FLOW SIMULATOR

Tor Harald Sandve¹, Sarah E. Gasda¹, Atgeirr Rasmussen², Alf Birger Rustad³

¹ Norce, Bergen, Norway

² SINTEF, Oslo, Norway

³ Equinor, Trondheim, Norway

* Corresponding author e-mail: tor.harald.sandve@norce-research.no

Abstract

In this work we introduce an accurate and efficient way of including the effect of convective mixing in field scale 3D simulations. The effect of the convective mixing is included in the field scale simulations by introducing a maximum dissolution rate given by the convective mixing. This maximum dissolution rate is computed internally based on both dynamic and static properties as well as a non-dimensional input parameter. The non-dimensional input parameter upscales the effect of the convective mixing and is estimated from fine-scale simulations. Our approach differs from existing models where the maximum dissolution rate is given directly as an input parameter to the simulator and not scaled by the properties of the cell. The proposed convective dissolution rate model shows good agreement with fine-scale simulation shown in this work as well as in the literature. The model is further tested on the 3D Sleipner Benchmark model. Results on the Sleipner Benchmark model confirm the importance of including the effect of the convective dissolution in the simulation both for the injection period and during the monitoring phase as it significantly affects the pressure build-up and decay during the simulations. The proposed model is implemented in the open source OPM Flow simulator which immediately makes it available to the community for usage and adoption. This paper also gives an overview of the CO₂ storage module implemented in OPM Flow.

Keywords: CO₂ storage simulations, Open-source software, The Sleipner Benchmark, CO₂ dissolution rate. Convective mixing.

1. Introduction

Numerical simulations form an important basis for decision-making processes for CO₂ storage. Good simulation models that incorporate the relevant physics on the relevant scale is thus important. Even with the continuing advances in available computational resources, simplification and upscaling of processes is necessary for practical simulation times. The dissolution of CO₂ into brine is one such important effect that needs to be considered. The main mechanism that drives the dissolution is convective mixing. Convective mixing happens on the centimeter scale and can therefore not be included in the model directly for field-scale model. It is suggested by several authors to include this effect as an upscaled dissolution rate [1][2][3][4].

Dissolution caused by convective mixing has been successfully implemented and demonstrated in research codes based on vertical equilibrium (VE) [4]. The approach involves incorporating an upscaled CO₂ mass transfer rate to account for sub-scale convection. CO₂ dissolves dynamically into the water column below, which is facilitated by the fact that a VE model is pseudo 2D and does not require vertical discretization.

VE models are a special class of 3D simulation where gravity segregation happens faster than simulated timescale and are especially useful in models of very large spatial and long timescales. However, many field-scale assessments of CO₂ storage still necessitate a 3D simulation to enable decision making. In this paper we adapt the suggested upscaled convective dissolution models to a 3D black oil setting and include it in the OPM Flow simulator.

The OPM Flow simulator [5] is an open-source community code that supports industry standard input and output format which allows for direct incorporation into existing simulation workflows. The base simulator is black oil, but it has many extensions that for instance allows for efficient modeling of CO₂-EOR scenarios [6][7]. For details on the simulator, we refer to the technical paper [5] and the user manual [8].

The advantage of including the convective dissolution rate model in Flow is immediate access to industry standard I/O formats, and performance which allows for immediate testing on the Sleipner Benchmark model [9].

The CO₂ simulation in this work is done using the CO₂ storage module in OPM. This module builds on the CO₂-brine fluid system in Dumux [10], but is adapted to

automatic differentiation (AD) as described in [5]. With AD the derivatives are automatically computed. This allows for simple extensions and modification of the code without losing neither accuracy in the Jacobian, nor significant performance, as shown in [11]. The AD framework thus allows for modification and implementation of new PVT models etc. in the code without significant effort and programming expertise.

2. CO₂ storage simulations in Flow

Black oil simulators are commonly used in the industry to simulate CO₂ storage. They are attractive compared to more advanced compositional models due to availability, performance, and applicability into existing frameworks [12]. In black oil simulation the needed PVT properties are given as tabulated input values where brine properties correspond to oil and CO₂ to gas, using the standard black oil format. Tabulated input is very flexible but becomes cumbersome when for instance temperature effects or varying salinity etc. also needs to be considered.

A dedicated CO₂ storage module is therefore made available in the OPM Flow simulator. With the CO₂ storage option enabled Flow computes the PVT properties such as density, viscosity, and enthalpy internally as functions of pressure, temperature, and composition by using analytic correlations and models from the literature rather than by interpolation from tabulated values. These values are transformed to its black oil equivalents internally in the simulator. This thus gives us the accuracy of the compositional simulators while keeping the performance and applicability of the black oil simulator. The CO₂ storage module is enabled by adding the CO2STORE keyword to the input deck [8]. Note that a dedicated CO2STORE option is also available in the compositional Eclipse 300 simulator [13]. The internal models implemented in the CO2STORE option in OPM Flow are based on models found in the literature and does not correspond directly to the CO2STORE option implemented in Eclipse 300.

An overview of the implemented models in the 2021.04 version of Flow as used in this work now follows.

2.1 Brine-CO₂ PVT module.

The density of water is given by the simplified formula presented in [14]. The formula gives significant speedup of the simulations without any significant loss of accuracy compared to using the formula in IAPWS 95 [15]. According to the authors in [14] average deviation is around 0.005% to IAPWS 95 for the relevant pressure and temperature range. Modification of the density due to dissolved CO₂ is accounted for using the correlation presented in [16], while salinity is accounted for using the correlation given in [17]. The density of the CO₂ is given by the Span-Wagner model [18]. The viscosity of brine is given using the correlation presented in [17], while the CO₂ viscosity is given by the correlation in [19]. The effect of the dissolved CO₂ on the liquid density is small and currently neglected.

CO₂ and brine are slightly miscible. CO₂ partitions into brine instantaneously until a solubility limit is reached locally (typically 2-5% by mass).

The solubility limit of CO₂ and brine depends on temperature, pressure and salinity and is implemented according to [20], where the activity coefficients of CO₂ in brine are taken from [21]. The solubility limit gives an upper bound of the amount of CO₂ that can dissolve into the brine.

2.2 Thermal properties

No simulations with thermal effects are shown in this paper, but for completeness the thermal properties used in the CO₂ storage module is presented here. For thermal simulations, the enthalpy of the fluids needs to be computed. The CO₂ enthalpy is computed according to [18] and is represented as a table internally in the simulator. The liquid enthalpy depends on the dissolved CO₂ and salinity as well as pressure and temperature. The water enthalpy is given according to IAPWS 97 [22] and modified to account for salinity according to [23] and for CO₂ following [21].

Thermal conductivity and rock heat capacity is input parameters to the simulator and must be provided by the user. See the OPM manual for details on usage of the thermal simulator [8].

2.4 Diffusion

For field-scale simulations diffusion is a sub-grid phenomenon and is typically not explicitly represented in the equations. For simulations on the laboratory scale diffusion plays a direct role and therefore needs to be explicitly represented in the equations. The diffusion coefficients that control the diffusion depends on temperature, pressure, and salinity. The diffusion coefficient is computed internally for pure water using [24] and modified to account for salinity using [25]. The effect of the porous media on the diffusion is modeled using the relation suggested in [26]. The coefficient can also be given as an input parameter using the DIFFC keyword. The effect of diffusion is included in the fine-scale simulation in section 4.1.

3. Controlling the dissolution rate.

For field scale simulations a typical grid block size is tens or even hundreds of meters in the horizontal direction and typically a few meters in the vertical direction. The density difference between CO₂ in gas (or super critical) phase and brine leads to rapid phase segregation. The lighter CO₂ moves quickly to the top of the reservoir or to an intermediate sealing layer and then migrates along the sealing layer. For cells where a vertical equilibrium is reached only the top layer of the cell is exposed to the free CO₂ and a fully mixture of the CO₂ and brine cannot be assumed. A direct use of the solubility models presented in section 2.1 will thus over-estimate the amount of dissolved CO₂ in brine in these cells if used directly.

The dissolution process in these cells is controlled by the convective mixing. Since brine with dissolved CO₂ is slightly heavier than without, instabilities will occur at the phase boundary in form of heavier fingers of brine with dissolved CO₂ migrating downwards. These fingers happen on the centimeter scale and can therefore not be included directly in field-scale simulations. Instead, the effect of convective mixing is included through a control of the dissolution rate. The convective mixing depends on both dynamic and static properties of the reservoir but dimensional analyses in [2] suggested a scaling for the dissolution rate that allows for usage of a single parameter. The dissolution rate F in kg / (m²s) in [2] is given as

$$F = \chi c_{max} K_z \Delta \rho_c g / \mu \quad (1)$$

where χ is a non-dimensional parameter controlling the dissolution, c_{max} is the maximum concentration at the solubility limit, K_z is the vertical permeability and $\Delta \rho_c$, is the difference of the brine density at maximum amount of dissolved CO₂ and the density without dissolved CO₂. Finally, g is the gravity constant, μ the viscosity.

To use equation (1) in the OPM Flow simulator we first need to convert it to a black oil setting. In the black oil model, the amount of dissolved gas in the liquid (i.e., oil) phase is given by the solution gas/oil ratio (RS). The standard metric unit of RS is SM₃/SM₃. The solution gas/oil ratio or gas dissolution factor is related to the mass fraction as following.

$$RS \stackrel{\text{def}}{=} \frac{V_{g,ref}}{V_{o,ref}} = \frac{x_o^g \rho_{o,ref}}{1 - x_o^g \rho_{g,ref}} \quad (2)$$

Here x_o^g is the mass fraction of gas in the oil phase and $\rho_{o,ref}$, $V_{o,ref}$ and $\rho_{g,ref}$, $V_{g,ref}$ are the density and volume of the oil and gas at reference conditions, respectively.

In the black oil model, the dissolution rate (DRSDT) is defined as the maximum rate at which the solution gas-oil ratio (RS) can be increased in a grid cell per time.

To convert equation (1) into a black oil formulation we first need to replace the maximum concentration at the solubility limit used in the equation (1) with its black oil equivalent, RS_{SAT} .

$$\begin{aligned} RS_{SAT} &\stackrel{\text{def}}{=} \frac{V_{co2,max,ref}}{V_{brine,ref}} \\ &= \frac{m_{co2,max}}{V_{brine} B_{brine} \rho_{co2,ref}} \\ &= \frac{c_{max}}{B_{brine} \rho_{co2,ref}} \end{aligned} \quad (3)$$

Here $m_{co2,max}$ is the mass of CO₂ at the maximum solubility limit and B_{brine} the formation volume factor of brine.

The next step is to convert F in (1) from kg/(m²s) to change in RS (gas-oil volume ratio under reference conditions) per day. We do this by multiplying with the cell top face area (A) and a conversion factor $\tau = 86400 \text{ s/day}$, then dividing by the volume of the brine and the density of the CO₂ both at reference condition.

$$\frac{\tau FA}{V_{brine,ref} \rho_{co2,ref}} = \frac{\tau FA}{V S_{brine} \phi \rho_{co2,ref} B_{brine}} \quad (4)$$

where V is the cell volume, S_{brine} is the brine saturation, ϕ the porosity. We further assume $V \approx AD_z$ to replace A/V with the cell thickness D_z . Combining equation (3) and (4) gives the following expression for the maximum dissolution rate DRSDT (SM₃/(SM₃ day))

$$DRSDT = \chi \tau \frac{RS_{sat} K_z \Delta \rho_c g}{\mu S_{brine} D_z \phi} \quad (5)$$

According to analysis in [2], 0.04 is a reasonable value for χ for the Utsira formation. Improved estimates on χ can be computed using either numerical fine-scale simulations (see Section 4.1) or based on laboratory tests [3]. The simulation results are sensitive to the choice of χ and some range of uncertainty in the parameter is thus recommended. The χ value can further be constrained using gravimetric and/or seismic data from the field [27].

In commercial simulators like Eclipse a constant or regional value for DRSDT can be given as an input parameter. The DRSDT can be used to include the effect of convective mixing as shown for instance in [28]. Our approach differs from this in that the DRSDT value is computed internally and now depends on both static and dynamic cell properties.

To use the convective dissolution rate control given in equation in (5) in the Flow simulator a keyword DRSDTCON needs to be given with the non-dimensional χ parameter. See the OPM Flow manual for more details [8].

Note that the convective dissolution rate assumes that the cell is in vertical equilibrium an assumption that is not always fulfilled in near well regions and in heterogenous reservoirs with low vertical permeabilities. A purely convective dissolution rate thus under-estimates the dissolution in the area around the injection well where CO₂ migrates upwards due to buoyancy. We expect a hybrid approach where the dissolution is not restricted by the convective dissolution in the upcoming regions to remedy this. Efforts to define robust and accurate criteria for detecting these cells are ongoing.

4. Simulation results

In this section we present simulation results that demonstrate usage of the convective dissolution rate control in OPM Flow. All simulations are done using the CO₂ storage option (CO2STORE).

4.1 Fine-scale simulations

We start with fine-scale simulations that illustrates the dissolution process and gives estimates on the non-dimensional χ parameter given in equation (5). For this we use a column with 5-meter width and 10-meter height. Initially the column is filled with a 2-meter layer of free CO₂ on the top. A free boundary is set on the bottom to avoid pressure build-up. We discretize the domain using cells of size 0.01 m x 0.01 m. The computed dissolution rate is sensitive to the grid resolution, but we believe the given grid resolution is sufficient for the illustrative purpose of this example. Note that the given grid

resolution results in a simulation model with half a million cells.

The parameters and setup are based on the Sleipner benchmark and are given in Table 1. The capillary transmission zone plays an important role in enhancing the dissolution process [2]. In this study we compute the relative permeability and capillary pressure using the Brooks Corey model. An entry pressure of 2.5kPa and a Brooks Corey parameter of 2.8 is used as suggested in [29].

Note that diffusion plays an important role in triggering the convective mixing and is therefore included in these simulations. The diffusion coefficient for CO₂ in brine for the pressure, temperature, and salinity in using the models given in Section 2.4 is 3.0e-9 m²/s. Also, a small perturbation of the porosity (± 0.04) is added to create sufficient instabilities in the model. The dissolution rate is not sensitive to these perturbations.

A snapshot of the dissolved CO₂ in brine (RS) is shown in Figure 1 after 60 days of simulation. The figure shows the classical fingering phenomena caused by the convective mixing. Note that we stop the simulation after 60 days to avoid boundary effects due to arrival of dissolved CO₂ to the bottom of the domain.

Figure 2 shows the dissolution of CO₂ in brine through the simulation. Apart from some initial dissolution caused by the capillary transmission zone we observe how the dissolution increases linearly with time. The linear coefficient gives us the convective dissolution rate. From linear regression we estimate the linear coefficient $DRS_{DT} = 0.0064$ (SM³/(SM³ day)). With this value for DRS_{DT} and the average dynamic properties given in Table 1, Equation (5) gives us $\chi = 0.034$. This is in line with the value 0.04 reported in [2]. Inserting $\chi = 0.034$ in Equation (1) gives $F = 12.5$ kg / (m² year) which again aligns with the numerical sensitivity study reported in [1].

Improving the grid resolution and/or doing fine-scale 3D simulations could give better estimates of the χ parameter, but some uncertainty always remains due to impact of local heterogeneities etc. in the physical world.

Table 1: Input properties used for the fine-scale simulation and in the evaluation of equation (4) in Section 4.1.

Property	Value
Porosity	0.36
Permeability	2000 mD
Rock compressibility	1e-6 barsa ⁻¹
Salinity	0.7 gm-M/kg
Pressure	200 barsa
Temperature	50 °C
RS_{sat}	27.04 SM ³ /SM ³
$\Delta\rho_c$	10 kg/m ³
S_{brine}	0.8
D_z	10 m
μ	0,85 cP

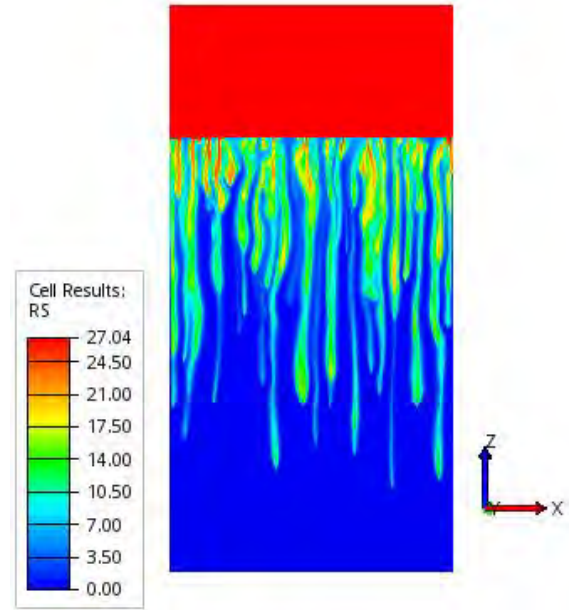


Figure 1: Dissolved CO₂ after 60 days of simulation for the fine-scale case.

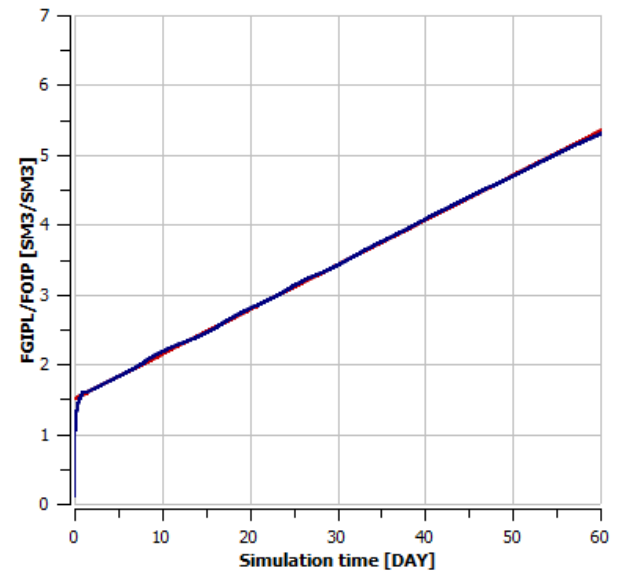


Figure 2: Estimated CO₂ dissolution (FGIPL/FOIP) from fine-scale simulations (blue) and linear function $RS = 0,0064 * \text{day} + 1.5$ (red). The 0,0064 is the convective dissolution rate while the 1.5 constant comes from the capillary transition zone.

4.2 Sleipner simulation results

The Sleipner benchmark model [9] recently released by Equinor will be the base model for demonstrating our approach. For simplicity, the mean values presented in the dataset are used for the porosity and the permeability of the layers, while all feeders are assumed to have permeability 2000mD. We use the same relative permeability and capillary pressure and salinity as in the fine-scale simulations. Initially we assume hydrostatic

pressure with 146 bar at 863 meters depth. A constant temperature gradient is imposed throughout the simulation defined by 30 C at 800 meters depths and 41 C at 1000 meters depths.

We further assume CO₂ is injecting at a constant injection rate of 1.46 million SM³ / day (1.0Mt / year) from 1st of September 1996 and until the end of 2010. After the injection is stopped the simulations continue for 200 years.

To investigate the effect of the upscaled convective mixing we use $\chi = 0.034$ and compare it with a base case without dissolution of CO₂. Figure 3 compares the total amount of CO₂ with the amount that is dissolved during the simulation period. During the injection period this shows that approximately 0.5% of the CO₂ dissolves into the brine pr year which is one third of the upper bound of 1.8% pr year estimated using gravity monitoring in [27]. As discussed in Section 3, a purely convective dissolution rate under-estimates the dissolution in the area around the injection well where CO₂ migrates upwards due to buoyancy and a lower value for the injection period is thus expected.

According to these simulations almost 60% of the CO₂ is dissolved into the brine 200 years after the injection period. Using the definition in (2) a global average RS can be computed by dividing the amount of dissolved CO₂ to the amount of oil in place which is approximately 2.0e9 SM³. This gives an average RS value of 2.2 which is still significantly lower than the theoretical limit given by RS_{sat} which is approximately 30 for the range of pressure, temperature, and salinity relevant for the Sleipner case. In other words, a significant part of the reservoir is still not reached by the injected CO₂. Figure 4 shows the development of the average reservoir pressure during the simulation period. For the case without dissolution of CO₂ the pressure reaches its maximum value (330 bar) when the injection stops and stays constant during the next 200 years. This is as expected since the model assumes closed boundaries. For the case with convective dissolution rate the pressure reaches its maximum at the same time, but the maximum value (316 bar) is 14 bar less than for the case without dissolved CO₂. The pressure then gradually decreases as more CO₂ dissolves into the brine. This is again expected since the density of brine increases as CO₂ dissolves into it. Note that the results are sensitive to the choice of χ , and the uncertainty of χ therefore should be incorporated into the simulations by for instance using an ensemble of simulations to gain confidence in the results. We also believe the dissolution rate and in particular χ to be an important history matching parameter as also claimed in for instance [27].

Snapshots of the amount of dissolved CO₂ and the CO₂ saturation are shown in Figure 5 and Figure 6, respectively. The snapshots are taken at the J-K plane going through the well at the end of the injection period and at the end of the simulations for the case with the convective dissolution rate. In all the figures we clearly see the characteristic layered structure of the Sleipner model. The CO₂ rapidly migrated to the top through the “chimneys” that acts as holes in the shale layers. What is

noticeable in Figure 5 is that most of the free CO₂ has disappeared after the 200-year period without injection. The remaining free CO₂ is gathered in a few structural traps. The top snapshot in Figure 6 shows that the dissolution process is significant also during the injection period as CO₂ slowly dissolves and migrating downwards given the characteristic fingering phenomena. After 200 years we observe how the “chimneys”, where the free CO₂ used to move upwards during the injection, now acts as sinks for the CO₂ rich brine. A significant portion of the stored CO₂ is thus securely stored in the bottom layer.

The released Sleipner model has approximately 2 million cells. For practical simulation times we have therefore used our internal cluster that allows for usage of 64 CPUs with two threads each. We observe a near ideal scaling of the simulation time for the tested range of CPUs for this model.

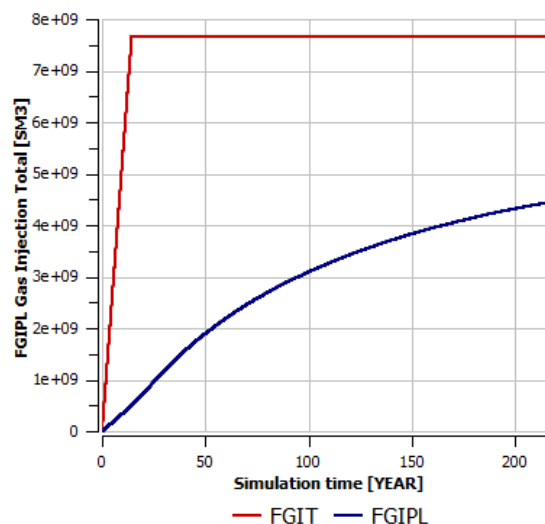


Figure 3: The amount of dissolved CO₂ in the liquid phase (FGIPL) compared to the total amount of injected gas (FGIT) for the case with the convective dissolution rate.

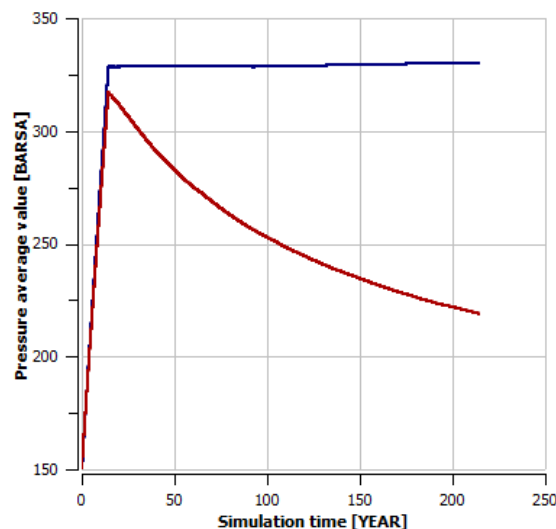


Figure 4: Field average pressure for the case without (blue) and with (red) dissolution of CO₂.

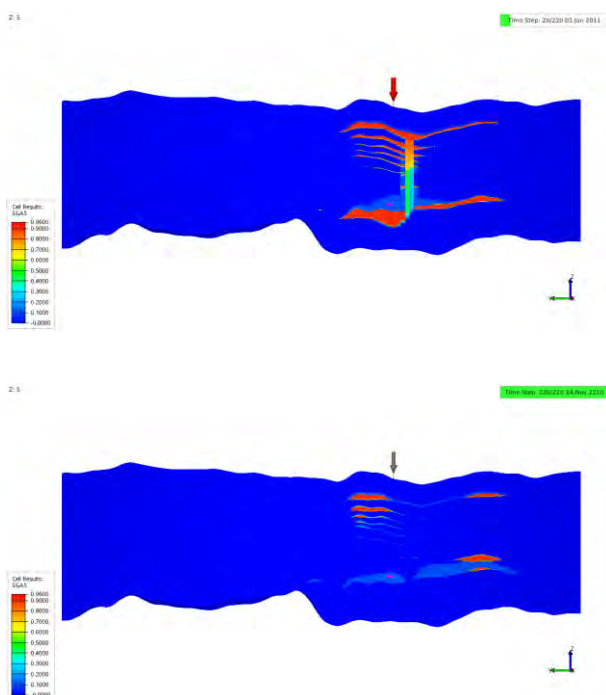


Figure 5: CO₂ saturation after the injection period (top) and after 200 years of storage (bottom).

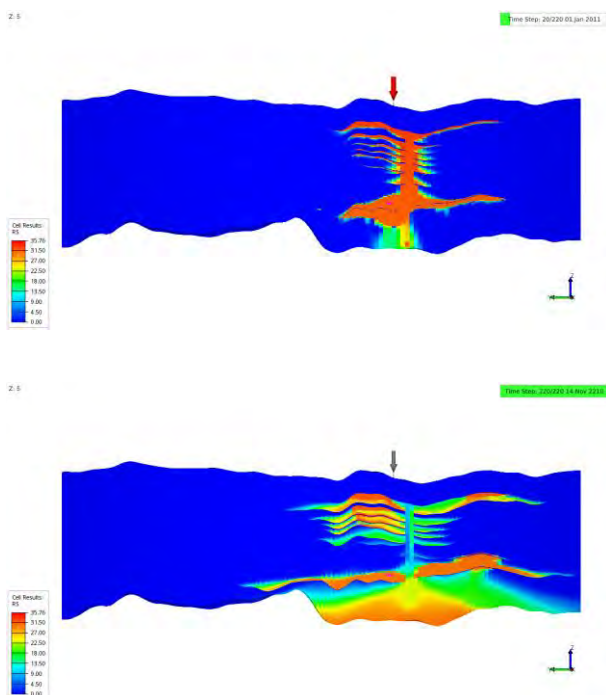


Figure 6: Dissolved CO₂ after the injection period (top) and after 200 years of storage (bottom).

5. Summary

A model for upscaling the effect of convective mixing through a convective dissolution rate control is implemented in the open-source simulator OPM Flow. The upscaled approach allows for efficient and accurate inclusion of the impact of convective mixing in field scale 3D simulations. The simulation results on the Sleipner Benchmark model agree well with the impact of

convective dissolution reported in the literature. Ongoing work on defining robust and accurate criteria for detecting cells where the convective dissolution rate is the dominant dissolution factor will further improve the accuracy and applicability of our approach.

All simulations in our work are done using the CO₂ storage module in OPM Flow. This dedicated CO₂ storage module simplifies usage of the simulator for CO₂ storage applications while maintaining the needed accuracy in the fluid properties of the CO₂-brine system. The implementation of the dissolution rate control in the OPM Flow simulator further gives immediate access to state-of-the-art parallel simulation capabilities and industry standard I/O which allows for immediate testing and usage on relevant field scale models.

Acknowledgements

The authors would like to acknowledge financial support from the CLIMIT-Demo/Gassnova project 620073.

References

- [1] Mykkeltvedt, T. S., & Nordbotten, J. M. (2012). Estimating effective rates of convective mixing from commercial-scale injection. *Environmental Earth Sciences*, 67(2), 527-535.
- [2] Elenius, M. T., Nordbotten, J. M., & Kalisch, H. (2014). Convective mixing influenced by the capillary transition zone. *Computational Geosciences*, 18(3-4), 417-431.
- [3] Taheri, A., Torsæter, O., Lindeberg, E., Hadia, N. J., & Wessel-Berg, D. (2018). Qualitative and quantitative experimental study of convective mixing process during storage of CO₂ in heterogeneous saline aquifers. *International Journal of Greenhouse Gas Control*, 71, 212-226.
- [4] Gasda, S. E., Nordbotten, J. M., & Celia, M. A. (2012). Application of simplified models to CO₂ migration and immobilization in large-scale geological systems. *International Journal of Greenhouse Gas Control*, 9, 72-84.
- [5] Rasmussen, A. F., Sandve, T. H., Bao, K., Lauser, A., Hove, J., Skaflestad, B., ... & Thune, A. (2021). The open porous media flow reservoir simulator. *Computers & Mathematics with Applications*, 81, 159-185.
- [6] Sandve, T. H., Rasmussen, A., & Rustad, A. B. (2018, October). Open reservoir simulator for CO₂ storage and CO₂-EOR. In *14th Greenhouse Gas Control Technologies Conference Melbourne* (pp. 21-26).
- [7] Sandve, T. H., & Aavatsmark, I. (2020, September). Improved Extended Blackoil Formulation for CO₂EOR Simulations. In *ECMOR XVII (Vol. 2020, No. 1, pp. 1-22)*. European Association of Geoscientists & Engineers.
- [8] The Open Porous Media Team. OPM Flow Reference Manual 2020-10. <https://opm-project.org/>
- [9] Equinor. Sleipner 2019 Benchmark Model <https://CO2datashare.org/dataset/sleipner-2019-benchmark-model> DOI:10.11582/2020.00004
- [10] Flemisch, B., Darcis, M., Erbertseder, K., Faigle, B., Lauser, A., Mosthaf, K., ... & Helmig, R. (2011). DuMux: DUNE for multi-{phase, component, scale, physics,...} flow and transport in porous media. *Advances in Water Resources*, 34(9), 1102-1112.

- [11] Lauser, A., Rasmussen, A. F., Sandve, T. H., & Nilsen, H. M. (2018, September). Local forward-mode automatic differentiation for high performance parallel pilot-level reservoir simulation. In ECMOR XVI-16th European Conference on the Mathematics of Oil Recovery (Vol. 2018, No. 1, pp. 1-12). European Association of Geoscientists & Engineers.
- [12] Hassanzadeh, H., Pooladi-Darvish, M., Elsharkawy, A. M., Keith, D. W., & Leonenko, Y. (2008). Predicting PVT data for CO₂-brine mixtures for black-oil simulation of CO₂ geological storage. *international journal of greenhouse gas control*, 2(1), 65-77.
- [13] Schlumberger, ECLIPSE Industry-Reference Reservoir Simulator – Technical Manual 2016.1.
- [14] Hu, J., Duan, Z., Zhu, C., & Chou, I. M. (2007). PVTx properties of the CO₂-H₂O and CO₂-H₂O-NaCl systems below 647 K: Assessment of experimental data and thermodynamic models. *Chemical Geology*, 238(3-4), 249-267.
- [15] Wagner, W., & Pruß, A. (2002). The IAPWS formulation 1995 for the thermodynamic properties of ordinary water substance for general and scientific use. *Journal of physical and chemical reference data*, 31(2), 387-535.
- [16] Garcia, J. E. (2001). Density of aqueous solutions of CO₂ (No. LBNL-49023). Lawrence Berkeley National Lab. (LBNL), Berkeley, CA (United States).
- [17] Batzle, M., & Wang, Z. (1992). Seismic properties of pore fluids. *Geophysics*, 57(11), 1396-1408.
- [18] Span, R., & Wagner, W. (1996). A new equation of state for carbon dioxide covering the fluid region from the triple-point temperature to 1100 K at pressures up to 800 MPa. *Journal of physical and chemical reference data*, 25(6), 1509-1596.
- [19] Feghhour, A., Wakeham, W. A., & Vesovic, V. (1998). The viscosity of carbon dioxide. *Journal of physical and chemical reference data*, 27(1), 31-44.
- [20] Spycher, N., Pruess, K., & Ennis-King, J. (2003). CO₂-H₂O mixtures in the geological sequestration of CO₂. I. Assessment and calculation of mutual solubilities from 12 to 100 C and up to 600 bar. *Geochimica et cosmochimica acta*, 67(16), 3015-3031.
- [21] Duan, Z., & Sun, R. (2003). An improved model calculating CO₂ solubility in pure water and aqueous NaCl solutions from 273 to 533 K and from 0 to 2000 bar. *Chemical geology*, 193(3-4), 257-271.
- [22] Wagner, W., & Kruse, A. (2013). Properties of Water and Steam/Zustandsgrößen von Wasser und Wasserdampf: The Industrial Standard IAPWS-IF97 for the Thermodynamic Properties and Supplementary Equations for Other Properties/Der Industrie-Standard IAPWS-IF97 für die thermodynamischen Zustandsgrößen und ergänzende Gleichungen für andere Eigenschaften. Springer-Verlag.
- [23] Daubert, T. E., Daubert, T. E., & Danner, R. P. (1989). Physical and thermodynamic properties of pure chemicals: Data compilation. Washington, DC: Taylor & Francis.
- [24] McLachlan, C. N. S., & Danckwerts, P. V. (1972). Desorption of carbon dioxide from aqueous potash solutions with and without the addition of arsenite as a catalyst. *Trans. Inst. Chem. Eng*, 50, 300-309.
- [25] Ratcliff, G. A., & Holdcroft, J. G. (1963). Diffusivities of gases in aqueous electrolyte solutions. *Trans. Inst. Chem. Eng*, 41(10), 315-319.
- [26] Millington, R. J., & Quirk, J. P. (1961). Permeability of porous solids. *Transactions of the Faraday Society*, 57, 1200-1207.
- [27] Alnes, H., Eiken, O., Nooner, S., Sasagawa, G., Stenvold, T., & Zumberge, M. (2011). Results from Sleipner gravity monitoring: Updated density and temperature distribution of the CO₂ plume. *Energy Procedia*, 4, 5504-5511.
- [28] Thibeau, S., & Dutin, A. (2011). Large scale CO₂ storage in unstructured aquifers: Modeling study of the ultimate CO₂ migration distance. *Energy Procedia*, 4, 4230-4237.
- [29] Cavanagh, A. (2013). Benchmark calibration and prediction of the Sleipner CO₂ plume from 2006 to 2012. *Energy Procedia*, 37, 3529-3545.

INTEGRATING CO₂-ABSORPTION TO A BATCH-WISE PRODUCTION PROCESS – A CASE STUDY ON A SMELTER PLANT IN NORTHERN SWEDEN

Elin Fahrman^{*}, Fredrik Normann, Simon Harvey, Åsa Eliasson

Division of Energy Technology, Chalmers University of Technology, 412 96 Gothenburg, Sweden

* Corresponding author e-mail: elin.fahrman@chalmers.se

Abstract

This work presents results from an investigation of integration of carbon capture with a batch-wise operating process conducted through a case study on a large smelter plant located in northern Sweden with annual CO₂ emissions of approximately 300 kt/a. Separate capture plants for the two major sources of emissions, Process I and Process II, were conducted using detailed, continuous flue gas property data. These two units together account for about 70% of the site's total emissions. The plants were designed for a capture rate of 90% during peak CO₂ flow. One of the objectives of the study was to investigate opportunities to operate the capture plant using excess heat sources available on site. The plant dynamics were characterized by studying the magnitude, duration, and frequency of the variations of the site steam flows, as well as the production cycle lengths of Process I and Process II. The results indicate that the present site energy system can cover 31 - 40% of the capture plant's reboiler heat demand for capture from both Process I and Process II. This coverage increases to 54% for a future scenario. Neglecting the dynamics of the existing energy system only leads to a very small difference in heat demand coverage when both Process I and Process II are integrated with the carbon capture plant (31-40% with dynamics, and 31-42% without dynamics). However, when only the emissions from Process I are captured, the potential heat demand coverage for the existing energy system varies considerably (50% heat coverage accounting for dynamics compared to 100% without). Furthermore, for the future energy system scenario, the coverage of both units is 72% when dynamics are neglected compared to 54% with dynamics. These results clearly indicate the importance of considering dynamic operating characteristics in discontinuously operating processes. The smelter plant variations are characterized by time scales that are similar to the stabilization time of the carbon capture plant. The behaviour of the capture plant can thus not be fully characterized using a steady-state model (as used in this work), but this approach nevertheless provides an initial estimation of the design configuration and the share of heat demand which can be covered by the present process site energy system.

Keywords: CCS, smelter plant, batch wise operating process

1. Introduction

As the urgency of climate change mitigation becomes more apparent, so does the necessity of implementing carbon capture and storage (CCS) technology to mitigate CO₂ emissions in energy-intensive industry[1],[2]. One of the most investigated and technically mature carbon capture techniques is absorption using amine solvents, which has also been successfully implemented in full scale, see for example the Petra Nova[3] and Boundary Dam projects[4]. Monoethanolamine (MEA) is often used as a benchmark solvent. Most studies of carbon capture have focused on continuously operating processes such as power plants, cement production and oil refining - see for example[4],[6],[7]. Even though studies on the dynamic behaviour of a post-combustion capture plant have been conducted, for example connected to a steel plant[8], literature as well as research and demonstration projects on the integration of a CO₂ absorption process to discontinuous batch-wise operating processes are limited. An in-depth understanding of process dynamics is necessary to identify the optimal design of the capture plant and a suitable control system.

This study investigates carbon capture at a smelter plant located in northern Sweden. The plant consists of several smaller plants that are operated discontinuously with batch-wise processes. The total CO₂ emissions are about 290 kton/a of which 70% originate from two process units (hereafter denoted as Process I and Process II), which both release process-related carbon emissions that are not possible or difficult to mitigate through electrification or fuel shift. The smelter plant site thus presents an important and complex process for carbon capture due to the variations in both CO₂ flow and steam generation inherent to the batch-wise operation. As the regeneration of the amine solvent requires considerable amounts of heat (3.5-4 MJ/kg CO₂)[9] it has been shown that an efficient integration into the existing plant energy system is crucial to achieve acceptable levels for the specific capture cost[6],[10].

The aim of this work is to identify the challenges, in terms of design and heat supply, related to integrating a capture plant with a discontinuously operated industrial process using a smelter plant as a case study. Furthermore, the work presents a method for

characterizing variations in heat availability and demand.

2. Methodology

An overview of the workflow is shown in Figure 1. The work is based on hourly plant operating data for one year (September to August), as well as more refined measurements of flue gas properties (minute by minute) over 48 h for Process I and 65 h for Process II. The hourly plant operational data includes production of steam through heat recovery steam generators (HRSG), steam consumption of some units, as well as temperatures and flows in the condensers producing district heat and residual heat coolers. The hourly data is used to determine the heat that is available for the carbon capture plant, as further described in Section 2.2, as well as to characterize the dynamics of the energy network. The detailed flue gas data is used to characterize the dynamics of the flue gas properties, as well as to design the capture plants using a steady-state model of an aqueous 30 wt.% MEA process originally developed by Ósk Garðarsdóttir et al. in Aspen Plus V11[11], with recent improvements described further in Section 2.4. The results of the simulations are used together with the hourly operating data of Process I and Process II to estimate the heat demand of the capture process.

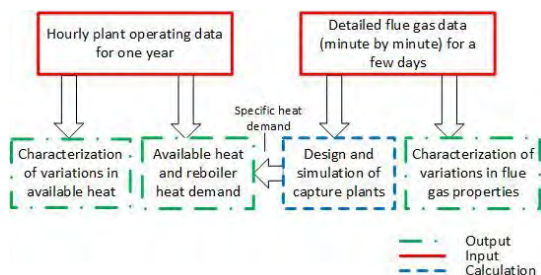


Figure 1: Overview of how the available data was utilized in this work. The red boxes show input consisting of hourly plant operational data over a year, as well as flue gas data for measurement periods of 2-3 days (minute by minute). The green boxes show the output of the work, while the blue box shows intermittent calculations (in this work simulations in Aspen Plus) utilized for several outputs.

2.1 Case study - Smelter Plant

Figure 2 shows an overview of the smelter plant process in which copper cathodes are produced from ore concentrates as well as secondary material such as waste material with high copper content. The material utilized in Process I is rich in carbon, causing about 60 kton/a of CO₂ emissions, which is about 20% of the total site emissions. The copper is refined in several steps, resulting in a number of by-products. Some of the separated material is treated in Process II through reduction with coal[12]. Process II emits about 140 kton/a of CO₂ corresponding to around 50 % of the total site emissions.

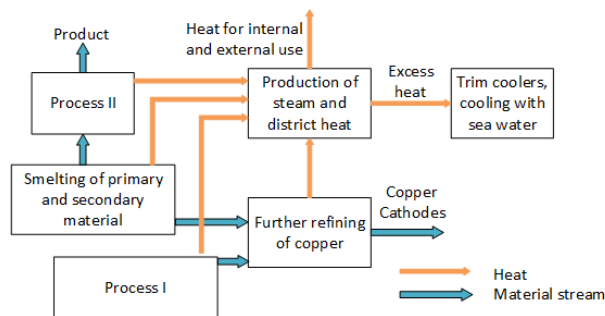


Figure 2: Simplified scheme of the processes at the case study smelter plant relevant to this work. The orange arrows indicate heat flows, while the blue arrows indicate material streams.

Both Process I and Process II are operated batch-wise, with flue gas CO₂ concentrations ranging from 0-15% in Process I, and 6-8 % in Process II. The total flue gas flow also varies during operation. For Process II the flowrate generally follows the same trends as the concentration. For Process I, the flue gas flow rate is stable during electronic waste feeding into the oven, but otherwise exhibits major fluctuations.

Steam is produced on-site in several heat recovery steam generators (HRSG), also operated batch-wise. The heat is utilized for generating steam (3-60 bar), which is used internally, e.g. to dry raw material, as well as externally for delivery of district heating or generation of electric power (primarily when heating demand is low), however, about 45 GWh/a is currently unutilized[12]. The excess heat is removed with sea water in trim coolers.

2.2 Heat supply to the capture plants

The heat considered available for carbon capture is hereafter referred to as “available heat”. Although the goal is to primarily operate the plant using heat available on site, the share of the capture plant’s heat demand to capture 90% of CO₂ which cannot be covered by the available heat is also quantified. Three scenarios with different levels of available heat were defined. Figure 3 displays the available heat over a year (Sep – Aug) in each scenario. The hourly distribution is displayed as filled areas, while the 720 hour (one month) moving average is displayed as a continuous curve. Scenario 1 considers the currently available heat, i.e. the amount of heat removed in the trim coolers. Scenario 2 also considers the steam currently utilized for electricity production in the condensing turbine and will, thus, constitute a loss of income from sales of electricity. The turbine is only operated during the summer season when the district heating demand is low. The available heat is thus equal for Scenarios 1 and 2 during a large part of the year. Scenario 3 considers the impact of planned process developments that will affect the steam demand and production on site in addition to scenario 2. The expected heat availability was determined through discussion with plant staff. As Scenario 3 is a future plant, operational data was not available. The available heat was estimated by multiplying the available heat of Scenario 2 with the expected total increase (in %) in available heat from Scenario 2 to Scenario 3.

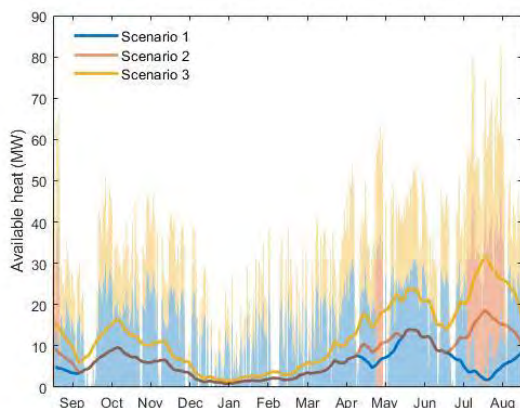


Figure 3: Available heat in Scenarios 1 (blue), 2 (red), and 3 (yellow). The filled areas display the actual heat availability for each hour during the year, while the curves show a moving average of the available heat over 720 h (one month). Note that the time period spans from September to August.

2.3 Characterisation of Process Dynamics

In order to design the capture plant and its control system, it is important to understand variations in heat availability and flue gas properties. As described in the work by Martinez Castilla et al.[8], the stabilization time of the capture plant may be several hours when subjected to changes in available heat and flue gas flow. In this work, the process dynamics for heat availability and CO₂ flow (Process I and Process II) of current operation were characterized based on magnitude, frequency and duration. The available heat data was obtained on an hourly basis. Flue gas property data measurements were available with shorter sampling intervals (minute). However, such data was only available for a shorter time period (48 h for Process I, and 65 h for Process II). Changes in flue gas property data on a minute basis were considered too frequent to be of interest to this study. Instead, the variations in the production cycles were studied.

2.4 Design and simulation

As the distance between Process I and Process II is too large to make it logistically possible to utilize a common absorber, two separate capture plants were designed. A standard configuration CO₂ absorption process was assumed, as shown in Figure 4. The capture plant was designed to capture 90% of the CO₂ in the flue gas during peak CO₂ concentration and flue gas flowrates. The reboiler duties of the two capture plants during full operation are 11.7 MW for Process I and 18.7 MW for Process II.

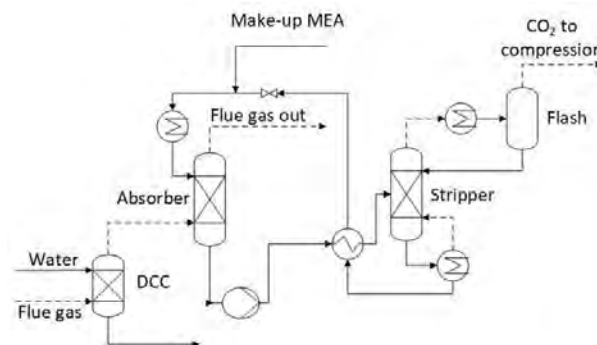


Figure 4. A simplified process schematic of a standard post-combustion CO₂ absorption process using MEA solvent. The dashed lines indicate gas phase streams, while the continuous lines indicate liquid- or mixed phase streams.

The stationary capture plant model was originally developed by Ósk Garðarsdóttir et al.[11],[12] in Aspen Plus V8.2. The model is in this work run in Aspen Plus V11, and has been updated according to the most recent recommendations by Aspen Tech for Aspen Plus MEA-absorption modelling[13]. For the gas phase, Redlich-Kwong is used for calculation of equation of state instead of PC-SAFT, for easier convergence. Recent improvements include use of a V-PLUG flow model for the stripper and absorber units. In addition, kinetic reactions have been added to the stripper, which is also modelled in rate-based mode. All columns are modelled assuming KOCH FLEXIPAC structured packing. Pressure drops have been added to the columns and the model modified to account for the pressure drop for the rich stream in the lean-rich cross heat exchanger and the elevation from the absorber to the stripper. A direct contact cooler (DCC) modelled in rate-based mode has been added.

3. Characterization of variations in available process data

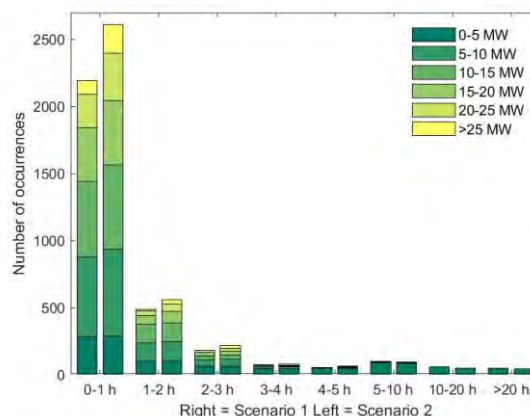


Figure 5: The number of occurrences over a year where the available heat remains within the same 5 MW interval throughout the durations of time indicated on the x-axis. The colours indicate the available heat of a certain occurrence.

Figure 5 shows the frequency of the variations in heat availability in the existing energy system on an hourly

basis for Scenarios 1 and 2. The coloured bars indicate the heat amount available for the specific occurrence. Even though the interval used is 5 MW (around 10-15% of the maximum amount of available heat depending on what Scenario is used as a reference), the change between intervals are frequent. The amount of heat available rarely remains within the same interval for more than 3 hours or above 5 MW for more than 4 hours.

Figure 6 shows the distribution of the magnitude of the variation within each hour over a year. The hourly variation is often below 1 MW. However, about 25% of the hourly variations have a magnitude of 5 MW or more.

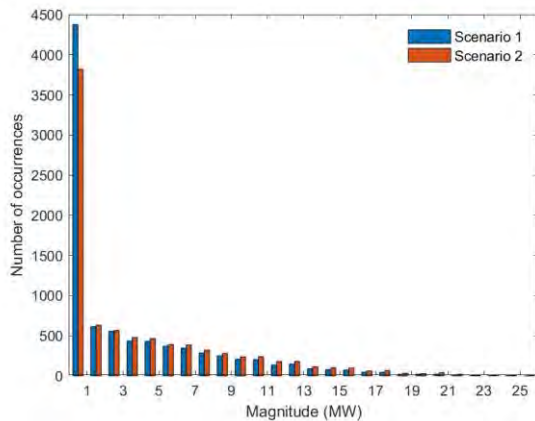


Figure 6: The distribution of the magnitude of the variations in available heat for Scenarios 1 (blue) and 2 (red) from hour to hour during a year.

Figure 7 and Figure 8 show the distribution of production cycle lengths for Processes I and II over 48 and 65 h, respectively. For Process II, the cycles range from 97 to 138 min and display a Gaussian distribution with a median of 122 min. For Process I cycles, it is difficult to discern any trend, and the cycles range from 140 min to up to 338 min, with a median of 166 hours.

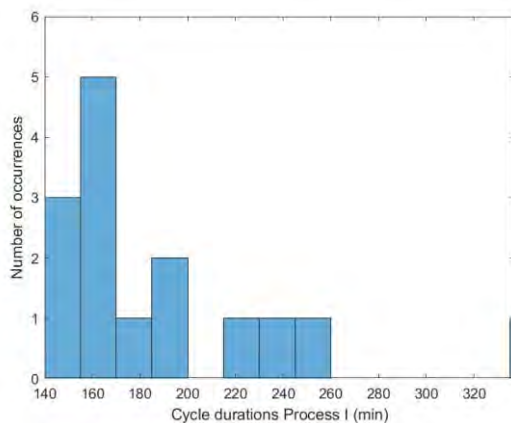


Figure 7: The distribution of the production cycle durations of Process I over 48 h.

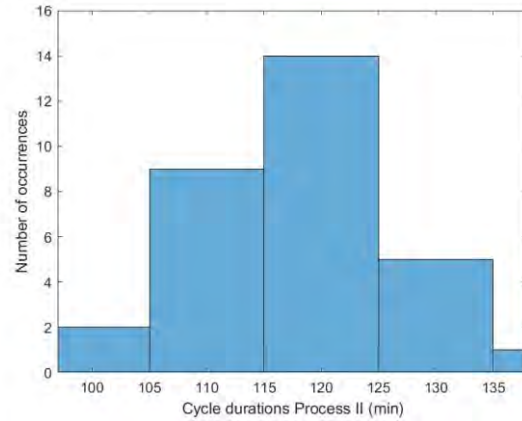


Figure 8: The distribution of the production cycle durations of Process II over 65 h.

In summary, there are significant and frequent variations in both the available heat and the CO₂ flow to the capture processes. The effect of the variations on the capture process differ depending on for example the size, piping length (residence time in the cycle) as well as the operational mode. Previous work on the dynamics of MEA absorption processes have indicated that the process has rather high inertia with stabilization times up to several hours for changes in heat availability[8], although this finding is somewhat depending on the location and sizing of solvent buffer tanks and the capture plant itself. With most significant variations in flue gas properties and available heat occurring within 3 hours in the concerned process, the capture plant will most likely not have time to stabilize. The combination of variations in CO₂ and heat availability further complicates any conclusions regarding the behaviour of the system based on the results of the steady-state model. To study effects of the dynamical behaviour of the available heat and flue gas on the capture plant, as well as to find the optimal design and control system, future work should involve dynamic modelling. The steady-state model used in this work, however, does provide a reasonable initial estimation of the heat coverage and design of the plant.

4. Results – Available heat for coverage of capture plant heat requirements

Table 1 displays the total availability of heat per year in the three scenarios. The available heat in Scenario 2 is 36% larger compared to Scenario 1. However, the additional heat is only available during summer when the steam turbine is usually in operation, as shown in Figure 3. Scenario 3 results in a 131% increase compared to Scenario 1. The estimated total heat demand during a year (September to August) are 43 and 107 GWh/a for Process I and Process II capture plants, respectively.

Table 1: Total yearly heat availability in the three scenarios. For Scenarios 2 and 3, the percental increase compared to Scenario 1 is also displayed.

	Scen. 1	Scen. 2	Scen. 3
Total availability	46.8	63.4	108.3

(GWh/a)			
Increase compared to scenario 1. (%)	-	35.5	131.4

In Figure 9, the heat load duration curves of Scenarios 1 and 2 are shown as continuous lines, while the reboiler heat demand, sorted to correspond to the heat load duration curve of Scenario 2, is shown as markers. The heat demand sorted after Scenario 1 is similar and thus not shown. Scenario 3 is not shown as it is simply a multiplication of Scenario 2. For both scenarios, heat is available to some extent for more than half the hours of the year. Scenario 2 has about 700 more hours with available heat than Scenario 1. A correlation between high demand and high availability is present in that there are few hours of zero demand when heat is available. This is expected as Process I and Process II are both heat and emission sources. There are, however, also a significant number of hours with high demand but too little or no available heat. These are hours when the steam produced in Process I and Process II HRSG is consumed internally or externally. This occurs when the demand of the district heating network is high, for example during wintertime, or when other units are not producing steam. There are also hours with a heat demand lower than the heat availability. Storage of steam in for example a steam accumulator could increase the potential utilization of this heat.

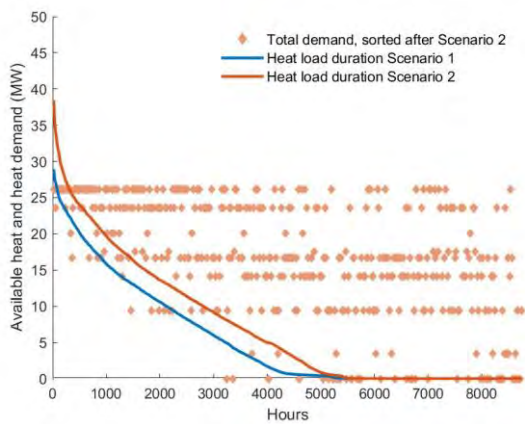


Figure 9: Heat load duration curves as continuous lines for Scenarios 1 (blue) and 2 (red). The markers indicate the heat demand for each hour sorted to correspond to the heat load duration curve of Scenario 2. The heat demand sorted after the heat load duration curves of Scenario 1 is similar. Scenario 3 is not shown, as it is simply a multiplication of Scenario 2.

Figure 10 displays the share of the reboiler heat demand covered by the heat available for carbon capture in Scenarios 1, 2 and 3 over a full year, if the available heat is utilized for capture from either Process I, Process II, or both units. Hours with zero demand are excluded, which is why the curves of Figure 10 do not reach 8760 h (one year). Table 2 gives the total coverage as well as the amount of additional heat required to cover the total demand of the capture plants to capture 90% of the CO₂ in the respective flue gases.

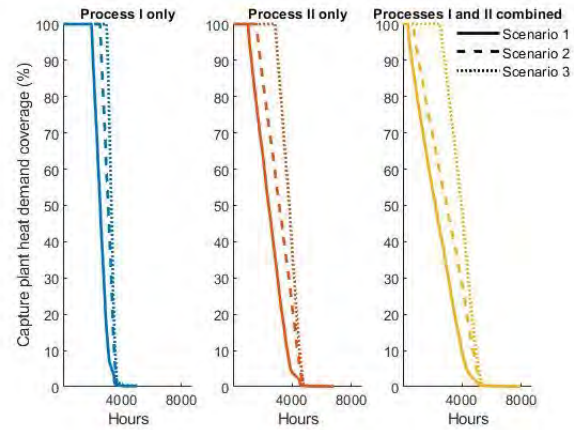


Figure 10: The share of heat demand covered by the heat available from the existing energy system in Scenarios 1 (filled line), 2 (dashed line) and 3 (dotted line) for capturing the CO₂ from Process I (blue), Process II (red) and both units combined (yellow).

Table 2: The total share of reboiler heat demand covered by the present energy system in Scenarios 1 and 2, as well as the future energy system in Scenario 3. The required heat addition to capture 90% of the total emissions from Process I and Process II is also displayed.

	Process I only	Process II only	Both units combined
Total coverage Scenario 1 (%)	51.1	36.3	30.6
Required external heat addition Scenario 1 (GWh/a)	20.9	67.9	103.6
Total coverage Scenario 2 (%)	61.2	46.3	40.3
Required external heat addition Scenario 2 (GWh/a)	16.6	57.2	89.2
Total coverage Scenario 3 (%)	65.8	56.0	53.7
Required external heat addition Scenario 3 (GWh/a)	14.6	46.9	69.2

In Table 1, the total available heat in Scenario 1 over a year is 46.8 GWh, which should theoretically be sufficient to cover the total yearly reboiler heat demand for capture from Process I (42.8 GWh). However, according to the results displayed in Table 2, only about 50% of the reboiler demand is covered when comparing the available heat and demand hour by hour. A similar result can be observed for Scenario 3, where the total reboiler heat demand coverage for capture from both units appears to be 72% when dynamics are not considered, but only 54% when dynamics are considered. It can thus be concluded that it is highly important to account for the dynamic behaviour of the available heat and the reboiler heat demand. The quantification on an hourly basis may however also be considered a “worst-case” as it assumes that no heat may be stored – as opposed to the assumption that all excess may be stored which is implicitly assumed if considering the yearly average. The true heat coverage potential of the existing energy system is thus probably

somewhere in between 50 and 100%. Additionally, the inertia of the capture plant as well as the steam network may result in a delay between the availability and demand. A detailed analysis of these factors is however beyond the scope of this study and left for future work. Furthermore, the capture plant has a cooling demand, and is therefore a heat source in itself. The heat can be recovered and utilized for example to produce district heating and could thus further increase the amount of heat that is available for the capture process, by decreasing the steam usage used to provide heat to the district heating network.

4. Conclusions

This work presented a feasibility study of the integration of carbon capture with a discontinuous batch-wise operating process, conducted through a case study of a large smelter plant in northern Sweden. The work investigated the heat integration potential for the smelting plant with carbon capture from two major emission sources, Process I and Process II. The operational dynamics of Processes I and II, as well as the available heat, were also characterized. The study concludes that there is potential for heat recovery from the smelting plant energy network to the carbon capture process. By only utilizing heat which is not currently used for other purposes (Scenario 1), 30% of the reboiler energy demand can be covered. If steam is redirected from the condensing turbine to the reboiler (Scenario 2), about 40% can be covered, and with future process developments considered (Scenario 3), about 54% can be covered. In the three Scenarios, 104, 89 and 69 GWh/a in Scenario 1, 2 and 3 respectively must be supplied by another source, requiring the addition of new steam generators to the current system.

The study also concludes that the dynamics of the plant have a significant impact on the heat recovery potential from the smelting plant to the carbon capture process. For carbon capture from Process I, 100% heat coverage appears to be possible if the yearly average is considered. However, this potential decreases to about 50% if hourly variations in the amount of available heat and reboiler heat demand are considered. Flexibility in the system through e.g. heat storage solutions is thus crucial to utilize as much heat as possible. The study also showed correlation between available heat and heat demand, in that the demand is usually high when the availability is high, pointing to the importance of studying demand and availability in relation to each other.

The frequency of changes in the amount of available heat, and the production cycle lengths are both comparable to the stabilization time of the capture plant (a few hours), and it can thus be concluded that the capture process will not have time to stabilize. The behaviour of the capture plant is therefore difficult to predict using only a steady-state simulation model.

Future work on discontinuous processes of this type could involve dynamical modelling, to gain better understanding of the behaviour of the capture plant when subjected to simultaneous changes in flue gas properties and heat supply. The heat integration study of

this work only considers currently available steam, as well as planned process developments. The heat integration study can be extended, by considering additional potential heat sources on site, as well as excess heat recovery from the capture plant and heat storage options.

Acknowledgements

This work was conducted in collaboration with Boliden. The authors take this opportunity to thank plant staff at Boliden Rönnskär and Boliden Head Office who were very helpful in providing data and answering questions. The authors also thank the research partners at the division of Energy Technology, Chalmers University of Technology and Chalmers Industriteknik (CIT), and in particular Maximilian Biermann, who has largely been responsible for the development and validation of the Aspen Plus simulation model.

References

- [1] IPCC. Global Warming of 1.5°C. IPCC special report, 2018.
- [2] IEA. The Role of CO₂ Storage. 2019.
- [3] US Energy Information Administration. Petra Nova is one of two carbon capture and sequestration power plants in the world 2017. Available from: <https://www.eia.gov/todayinenergy/detail.php?id=33552#>
- [4] Stéphane K. Start-up of World's First Commercial Post-combustion Coal Fired CCS Project: Contribution of Shell Cansolv to SaskPower Boundary Dam ICCS Project. *Energy Procedia*. 2014;63:6106-10.
- [5] Bartela Ł, Skorek-Osikowska A, Kotowicz J. Economic analysis of a supercritical coal-fired CHP plant integrated with an absorption carbon capture installation. *Energy*. 2014;64:513-23.
- [6] Andersson V, Jilvero H, Franck P-Å, Normann F, Berntsson T. Efficient Utilization of Industrial Excess Heat for Post-combustion CO₂ Capture: An Oil Refinery Sector Case Study. *Energy Procedia*. 2014;63:6548-56.
- [7] Leeson D, Mac Dowell N, Shah N, Petit C, Fennell PS. A Techno-economic analysis and systematic review of carbon capture and storage (CCS) applied to the iron and steel, cement, oil refining and pulp and paper industries, as well as other high purity sources. *Int. J. Greenh. Gas Control*. 2017;61:71-84.
- [8] Martinez Castilla G, Biermann M, Montañés RM, Normann F, Johnsson F. Integrating carbon capture into an industrial combined-heat-and-power plant: performance with hourly and seasonal load changes. *Int. J. Greenh. Gas Control*. 2019;82:192-203.
- [9] Garðarsdóttir SÓ, Normann F, Skagestad R, Johnsson F. Investment costs and CO₂ reduction potential of carbon capture from industrial plants – A Swedish case study. *Int. J. Greenh. Gas Control*. 2018;76:111-24.
- [10] Biermann M, Ali H, Sundqvist M, Larsson M, Normann F, Johnsson F. Excess heat-driven carbon capture at an integrated steel mill – Considerations for capture cost optimization. *Int. J. Greenh. Gas Control*. 2019;91:102833.
- [11] Gardarsdóttir SÓ, Normann F, Andersson K, Johnsson F. Postcombustion CO₂ Capture Using Monoethanolamine and Ammonia Solvents: The Influence of CO₂

- Concentration on Technical Performance. *Ind. Eng. Chem. Res.* 2015;54(2):681-90.
- [12] Biermann M, Normann F, Johnsson F, Skagestad R. Partial Carbon Capture by Absorption Cycle for Reduced Specific Capture Cost. *Ind. Eng. Chem. Res.* 2018;57(45):15411-22.
- [13] Aspen Tech. Rate-Based Model of the CO₂ Capture Process by MEA using Aspen Plus.
- [14] Johansson A. Energikartläggning 2018, Boliden Rönnskär, Skelleftehamn. 2018.

PROBABILISTIC ANALYSIS OF DRAUPNE SHALE CAPROCK RELIABILITY OF THE ALPHA PROSPECT- A POTENTIAL CO₂ STORAGE SITE IN THE SMEAHEIA AREA, NORTHERN NORTH SEA

Md Jamilur Rahman^{1*}, Jung Chan Choi², Manzar Fawad¹, Nazmul Haque Mondol^{1,2}

¹ University of Oslo (UiO), Oslo, Norway

² Norwegian Geotechnical Institute (NGI), Oslo, Norway

* Corresponding author e-mail: m.j.rahman@geo.uio.no

Abstract

CO₂ injection into a saline aquifer requires a viable caprock to arrest the vertical movement of the CO₂ plume. Quantitative assessment of caprock integrity is often challenging because of uncertainties involved in the model input parameters. In this study, Draupne Formation's reliability as caprock is evaluated before CO₂ injection by introducing a stochastic approach. We estimated both deterministic factors of safety and probabilistic failure values of different scenarios, and the results are compared. The probabilistic failure values are calculated using the First Order Reliability Method (FORM). Draupne formation shows a considerably low probability of failure with a high-reliability index in the initial stress condition. The sensitivity study reveals that the pore pressure and horizontal stress are the most crucial parameters and contribute two-thirds to failure probability. When the change of effective horizontal stresses in the reservoir is assumed considering the pore pressure change in the Troll field, this study shows that the field production may decrease the probability of shear failure. Moreover, the study indicates that the suggested probabilistic approach is critical in the presence of various uncertainties. However, the assumptions used in this study, especially the change in effective horizontal stresses within the reservoir, can be affected by other factors (e.g., stiffness contrast between reservoir and surroundings, geometrical effects, stress paths, etc.) and should be investigated further.

Keywords: Caprock integrity; Caprock Reliability; Probability of failure; Draupne Formation; Smeaheia

1. Introduction

Caprock assessment is a critical parameter in a CO₂ storage project because it prevents the vertical migration of fluids out of traps. The top seal commonly consists of fine-grained rocks, which have significantly small pore throat radii compared to the reservoir below and act as an impermeable layer due to exceptionally high capillary entry pressure. However, leakage occurs when the buoyancy pressure exceeds the capillary entry pressure. The capillary breakthrough is highly unlikely when the caprock consists of fine grain particles; instead, mechanical fracturing becomes the primary failure mood while the reservoir's pore pressure approaches the formation fracture strength [1]. The caprock failure risk significantly increases in the CO₂ storage project because injecting CO₂ into the saline aquifer will increase the reservoir pore pressure and affect the caprock's stress and strength. Therefore, seal strength characterization is necessary to prevent any CO₂ leakage risk.

The studied Alpha prospect is located in the Smeaheia area, northern North Sea, and investigated as a potential storage site by Equinor and Gassnova [2]. The main reservoir rocks comprise Upper Jurassic Sognefjord, Fensfjord, and Krossfjord formation sandstones, where the organic-rich Draupne and Heather Formation shales act as a caprock. Because of the significant amount of fine-grained sediments (i.e., clay minerals) in the caprock [3], the capillary breakthrough is very unlikely; hence, the injection-related top seal fracture is one of the main caprock failure risks in the Alpha prospect. However, estimation of caprock mechanical properties (i.e., brittleness) is very complex and uncertain. Moreover, the

stress path changes due to injection are mostly unknown in a saline aquifer. In the presence of many uncertainties, the deterministic method of caprock analysis is somewhat questionable [4]; instead, a probabilistic approach is more suitable [5], [6]. Therefore, we conducted a probabilistic analysis to evaluate the Draupne Formation reliability as a caprock using the First Order Reliability Method (FORM). Comparison analysis between deterministic value and probabilistic assessment is also carried out. Moreover, the relative importance of different uncertain parameters is also evaluated. This probabilistic analysis technique for the subsurface structure is a new approach that was recently introduced by Rahman et al. [7] for fault reliability analysis. The hypothetical failure cases are evaluated to identify the reliability failure values to compare them with the in-situ probability of failure values.

2. Geologic framework of the study area

The study area experienced two rifting events, possibly during the Permo-Triassic and the Late Jurassic to Mid-Cretaceous times [8]–[10]. A wide basin with deep-rooted faults and thick syn-depositional wedges was centered on the Horda Platform during the 1st rifting event. Several N-S trending faults were formed, which were believed to be rooted in Caledonian zones of crustal weakness [10], demarcating the area's structural elements. The Smeaheia area is bounded by two faults, where the Øygarden Fault Complex (ØFC) delineates the east, and the Vette fault outlines the western boundary shown in Figure 1a. In the Late Jurassic to Mid

Cretaceous time during the 2nd event, rifting and tilting activities shifted westward and assumed that weak stretching with the reactivation of major Permo-Triassic faults on the Horda Platform [8]–[13].

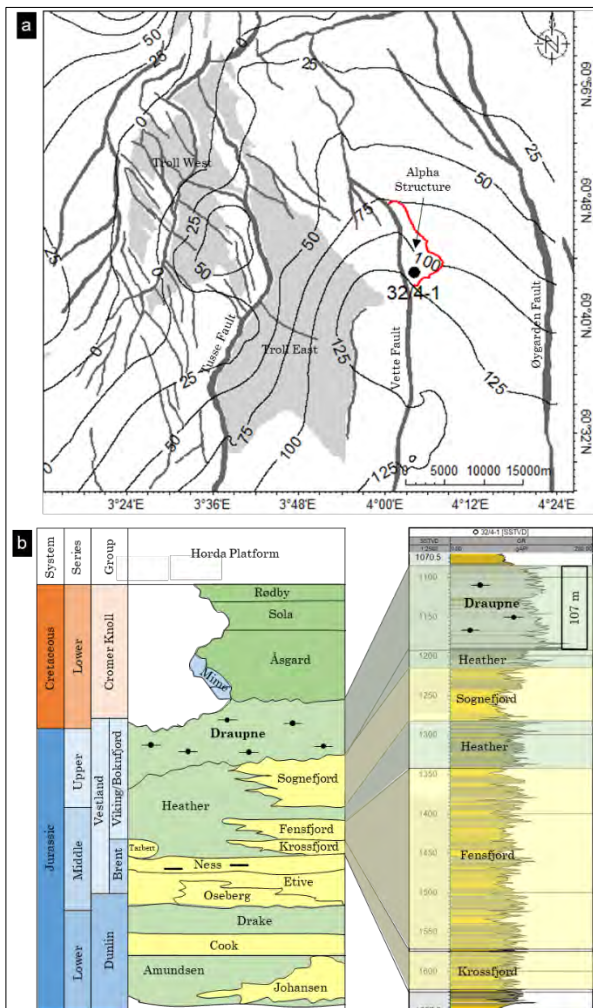


Figure 1: Location map of the Horda Platform showing the major and minor faults with Troll Fields as reference. The contour lines represent the Draupne Formation thickness adapted from [3]. The red polygon against the Vette fault is the Alpha prospect (a). A generalized stratigraphic succession of the Horda Platform showing the Jurassic and Lower Cretaceous formations and the vertical distribution of the Upper Jurassic reservoir-caprock configuration is shown in well 32/4-1 (b).

The primary caprock Draupne Formation shale is part of the Viking Group, deposited in the Late Jurassic syn-rift time within the East Shetland Basin, the Viking Graben, and over the Horda Platform area [2]. The thickness of this formation varies significantly [3], which varies between 75 to 125 m within the Alpha prospect (Fig. 1a), while the well 32/4-1 (Alpha) penetrates 107 m thick Draupne shale. The formation consists of dark grey-brown to black, non-calcareous, carbonaceous, occasionally fissile claystone deposited in an open marine environment with restricted bottom circulation and often with anaerobic conditions [14]. It is also characterized by high gamma-ray values (usually above 100 API) due to high Uranium and TOC content. Interbedded sandstone and siltstone, as well as minor limestone streaks and concretions, are also present.

Draupne Formation generally has a diachronous contact with the Heather Formation in the lower boundary. However, on the northern Horda Platform, Late Jurassic sandstones of the Sognefjord Formation mark the base of the Draupne Formation. The upper boundary of the Draupne Formation is usually characterized by Cretaceous rock (Cromer Knoll Group), which has a higher velocity and lower gamma-ray response than the over and underlying rocks [15] (Fig. 1b).

3. Material and Method

Caprock structural reliability depends on the mechanical properties of that layer and the stress state of the area. Mohr-Coulomb failure criterion approach can evaluate caprock stability. This study assesses the Draupne caprock probability of failure by an analytical model defined by the Mohr-Coulomb failure criterion. The corresponding deterministic factor of safety values is also estimated for comparison.

3.1 Model parameters

The recent study suggested that a normal faulting regime with isotropic horizontal stress conditions is a reasonable stress model for the Alpha prospect [16]. Moreover, the extended leak-off test data in the studied area reveal that the vertical stress gradient is significantly higher than the horizontal stress, reflecting a normal faulting regime (Fig. 2). Therefore, the normal faulting with isotropic horizontal stress conditions was used in this study. The hydrostatic pressure gradient shown in Figure 2 was calculated using the depth profile from well 32/4-1 drilled in the Alpha prospect. However, the vertical and horizontal stress profiles were estimated using the extended leak-off test (XLOT) data scouted from the Statoil Underground report [17].

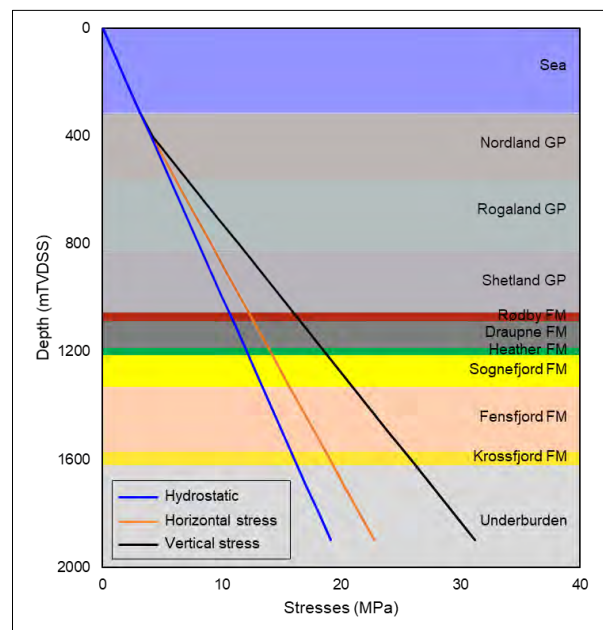


Figure 2: In-situ stress profile for the Alpha structure calculated using extended leak-off test (XLOT) data [17] indicating normal faulting regime with isotropic horizontal stress condition (adapted from [7]).

This study only focuses on the in-situ stress condition, and the dynamic CO₂ injection effect is not considered. However, the pore pressure depletion scenario due to the possible communication with the hydrocarbon production in the Troll Field was analyzed. Maximum 4 MPa depletion estimated by the Statoil studies was used as a case in this modeling work. However, we did not consider any stress path changes while running that scenario.

Moreover, the theoretical failure scenario was analyzed to get a quantitative estimation of probability failure values compared to real cases. The caprock failure scenario was estimated by decreasing horizontal stress while the other parameters (i.e., vertical stress and pore pressure) remain in the initial condition. A summary of all cases is shown in Table 1, which were evaluated to estimate the Draupne caprock probability of failure.

Table 1: Various caprock scenarios tested in this study.

	Assumptions
Case-1	Initial stress condition
Case-2	Depletion due oil/gas production from Troll
Case-3	Caprock failure due to decreasing σ_3

The Mohr-Coulomb plots of the Draupne Formation for three cases are shown in Figure 3. The initial state stress condition (case-1) represents a relatively large distance between the Mohr circle, and Coulomb failure (Fig. 3a). The pore pressure depletion scenario (case-2) further shifts the circle away from the envelope by increasing the effective stresses (Fig. 3b). Moreover, the theoretical caprock failure plots show that the case-3 shear failure occurs at 55° σ_1 plane (Fig. 3c). The theoretical caprock failure value for case-3 (σ_h^3) is estimated using the MohrPlotter software by selecting 'failure by horizontal stress' mode, and the horizontal stress value estimated was 10.57 MPa when the shear failure occurs.

The laboratory test result of rock strength parameters (i.e., cohesion and friction angle) of the Draupne Formation were scouted [16]–[20] and also estimated from the wireline log. The compressional velocity (V_p) based empirical equation proposed by Horsrud [19] was used, which stated that:

$$C_0 = 0.77V_p^{2.93} \quad (\phi = 30 - 55\%), \quad (1)$$

where C_0 is compressional strength in MPa and V_p is in km/s.

In the model, the input parameters used are shown in Table 2. It should be noted that statistical information in the table is from a limited database and should only be used to test the methodology. It may represent the field condition. Five random variables such as vertical stress (σ_v), horizontal stress (σ_h), pore pressure (P_p), cohesion (S_0), and friction angle (ϕ) are used to run the stochastic model where arithmetic average with standard deviation was used to define the ranges. However, for additional properties of case-2 and case-3 (i.e., P_p^2 & σ_h^3), the same

standard deviation (i.e., like case-1) value was used (Table 2).

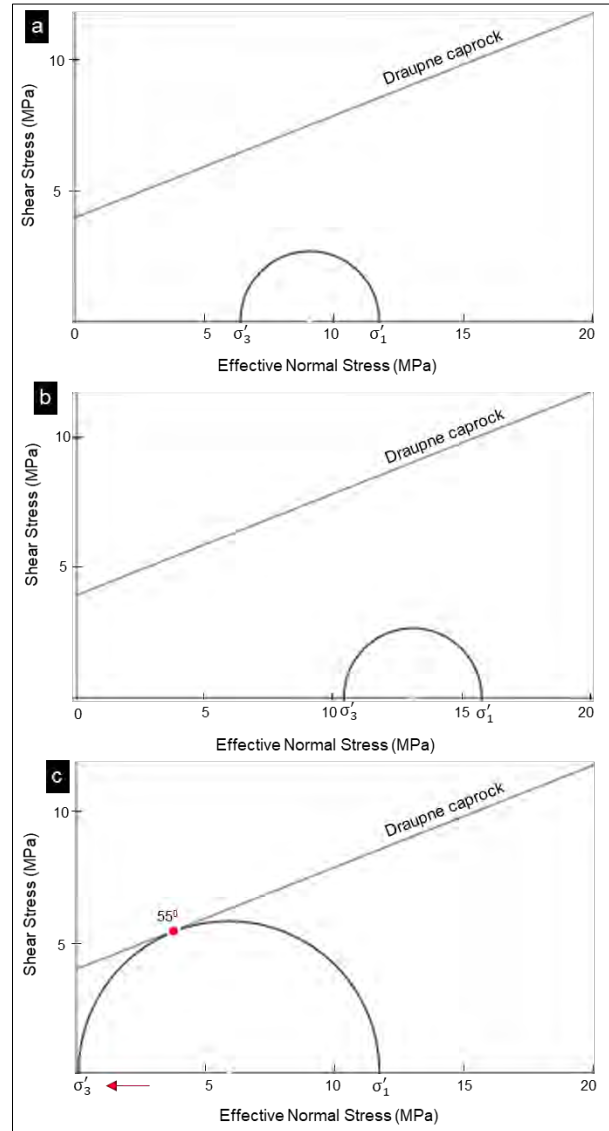


Figure 3: Mohr-Coulomb plots with Draupne Formation failure surface: (a) initial reservoir stress state condition (case-1), (b) depleted scenario due to oil/gas production from Troll (case-2), and (c) shear failure scenario due to decreasing σ_3 (case-3).

Table 2: Input parameters for the model with the type of distribution and data sources. The superscript numbers in the parameters name represent as case numbers. Note the statistical information in this table is based on a limited database and should be used only to test the methodology. It may not represent the field conditions.

Parameters	Average	Unit	Standard Deviation	Distribution
σ_v	22.25	MPa	0.65	Normal
$\sigma_h^{1,2}$	16.85	MPa	0.95	Normal
σ_h^3	10.57	MPa	0.95	Normal
$P_p^{1,3}$	10.48	MPa	1.32	Normal
P_p^2	6.48	MPa	1.32	Normal
S_0	3.93	MPa	1.05	Log-Normal
ϕ	21.63	Degree	5.14	Normal

Standard deviation can indicate the data spread and might serve as a measure of uncertainty. For example, a small standard deviation value indicates clustered closely around the mean with more precision and vice versa. Moreover, most geological processes follow a normal or log-normal law [5]; thus, we assumed normal distribution for most of the properties except caprock cohesion in this study. A log-normal distribution was used for caprock cohesion assuming the parameter cannot be physically negative within three standard deviations of average.

3.2 Model definition

The reliability of a structural component depends on the uncertainties in load (S) and resistance (R), and if both are normally distributed, the failure probability might be assessed directly by the safety margin M and denoted as:

$$M = R - S, \quad (2)$$

and the probability of failure may be assessed through:

$$P_f = P(R - S \leq 0) = P(M \leq 0), \quad (3)$$

where M is normally distributed with parameters with the mean $\mu_M = \mu_R - \mu_S$ and standard deviation $\sigma_M = \sqrt{\sigma_R^2 + \sigma_S^2}$. The failure probability may be determined by the use of the standard normal distribution function as:

$$P_f = \Phi\left(\frac{0 - \mu_M}{\sigma_M}\right) = \Phi(-\beta), \quad (4)$$

where $\mu_M/\sigma_M = \beta$ is called the safety/reliability index, which is the standard deviation by which the mean value of the safety margin M exceeds zero or most likely exceeds the failure point (Fig. 4a). However, if the resistance and the load cannot be described by only two random variables but rather by functions of the same random variables and statistically dependent, the safety margin M will be:

$$M = R - S = f_1(X) - f_2(X) = g(X), \quad (5)$$

where X is a vector with n so-called basic random variables, the function g(X) is denoted as the limit state function, which is a boundary between desired ($g(X) > 0$) and undesired ($g(X) \leq 0$) performance of any structure and defined within a mathematical model for functionality and performance [21]. In this study, the Mohr-Coulomb failure criteria-based limit state function was considered. Assuming isotropic horizontal stress condition within a normal faulting regime, the factor of safety (FoS) is defined as:

$$FoS = \frac{\left[\left(\frac{\sigma'_1 + \sigma'_3}{2}\right) + \frac{S_0}{\tan\phi}\right] \sin\phi}{\frac{\sigma'_1 - \sigma'_3}{2}}, \quad (6)$$

$$\sigma'_1 = \sigma_1 - p_p, \quad (7)$$

$$\sigma'_3 = \sigma_3 - p_p, \quad (8)$$

where, σ'_1 is effective vertical stress, σ_1 is vertical stress, σ'_3 is effective horizontal stress, σ_3 is horizontal stress, p_p is pore pressure, S_0 is cohesion, and ϕ is friction angle.

The state of the structure is safe when the factor of safety is greater than 1 and fails when it is less than 1. Therefore, the limit-state function defines as:

$$g(x) = FoS - 1, \quad (9)$$

where, g(x) is the limit-state function which is the boundary between safe ($g(x) > 0$) and failure ($g(x) \leq 0$) state.

The First Order Reliability Model (FORM) was used to estimate the failure probability of Draupne caprock. This method was proposed by Hasofer and Lind [22] and widely used in practical engineering problems [6], [23]. This method linearizes the failure surface ($g(z)$) at a design point z^* where the shortest distance is called the reliability index (β) and normal vector direction to the failure surface denoted as α (Fig. 4c). However, the inaccurate result could be estimated if the linearization design points are not correctly selected. Moreover, the reliability index value is also used as a performance indicator and directional vector to describe the random variables' relative importance. We analyzed this sensitivity factor to identify the significance of each parameter used in the model.

The Python-based open-source structural reliability analysis module PyRe [24] was used to initiate and run the FORM models. PyRe has been created using the core function of the Finite Element Reliability Using Matlab (FERUM) project, which is very flexible and extensive, making it applicable to a large number of problems. Other software such as MohrPlotter version-3 and Excel 2016 were also used for the Mohr-Coulomb plot and sensitivity plots, respectively.

The probabilistic reliability analyses deal with the structural uncertainties, provide a rational framework, and have a different approach than the deterministic estimation [6]. Although the failure probability approach is widely used for engineering purposes, it is new for caprock characterization. Therefore, a comparison between deterministic safety factors with the probability of failure was also analyzed. Such a comparison will help to understand caprock failure probability values.

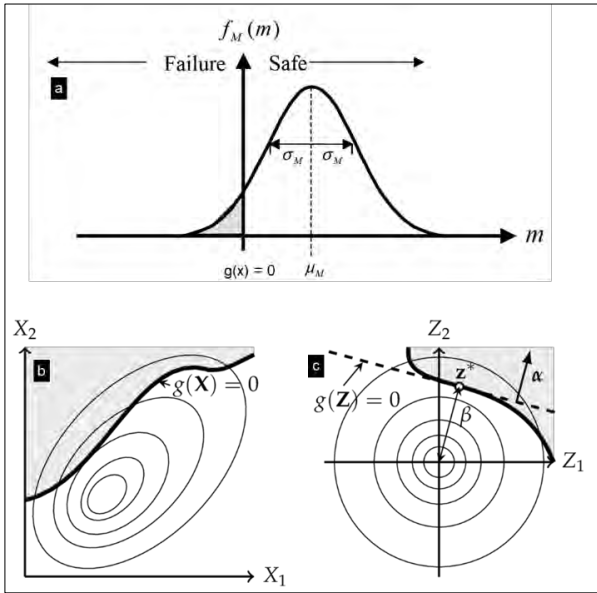


Figure 4: Structural reliability concept and model definition: (a) Gaussian distribution of the probability distribution function of safety margin M showing the failure and safe events modified after Faber [23], (b) limit state function $g(X)$ stated in the physical space using two random variables (X_1 and X_2), and (c) after normalizing the random variables into standardized normally distributed variable (Z_1 and Z_2) with the design point z^* and reliability index β . Note that the grey shaded area denoted the failure domain (modified after Madsen et al., [25]).

4. Results

The deterministic and probabilistic failure values with corresponding reliability index (β) are summarized in Table 3. In the in-situ stress condition (case-1), the Draupne Formation probability of failure (PoF) is $1.38E-08$, while the factor of safety (FoS) shows a value of 2.60. However, the depleted scenario (case-2) due to Troll Field production decreases the failure probability number ($<3.0E-08$). The safety factor also increases from 2.60 to 3.16. Although the FoS increases from case-1 to case-2, the increase is not significant compared to PoF. Moreover, the reliability index value also increases from case-1 to case-2. The FoS for theoretical shear failure scenario (case-3) shows caprock failure by representing a value=1. The corresponding PoF and β value showed $2.42E-02$ and 1.97, respectively.

Table 3: Deterministic factor of safety (FoS) and the probability of failure (PoF) of different cases. Corresponding reliability index (β) values are also shown.

	FoS	PoF	β
Case-1	2.60	$1.38E-08$	5.56
Case-2	3.16	$<3.0E-08$	<5.0
Case-3	1.00	$2.42E-02$	1.97

The comparative analysis between deterministic and probabilistic sensitivity gives a unique opportunity to explain the reliability of the proposed method (i.e., FORM). The deterministic sensitivity was estimated

using the ‘one variable at a time’ (OVAT) technique [26], [27], where each input parameter is alternatively assigned its minimum and maximum values when the other parameters are fixed to their mean values. The parameters ranges used are summarized in Table 4.

The tornado diagram of case-1 (Fig. 5) illustrated that the initial horizontal stress (σ_h^1) has the most significant impact on the factor of safety than the rest of the input parameters. Moreover, initial vertical stress (σ_v) and Cohesion (S_0) have significant influences.

Table 4: Minimum and maximum values used in the deterministic sensitivity analysis.

Parameter	Value Range
Initial vertical stress (σ_v)	21.60 - 22.90 (MPa)
Initial horizontal stress (σ_h^1)	15.90 - 17.80 (MPa)
Pore Pressure (P_p^1)	9.16 - 11.80 (MPa)
Cohesion (S_0)	2.88 - 4.98 (MPa)
Friction angle (ϕ)	$16.49 - 26.77^0$

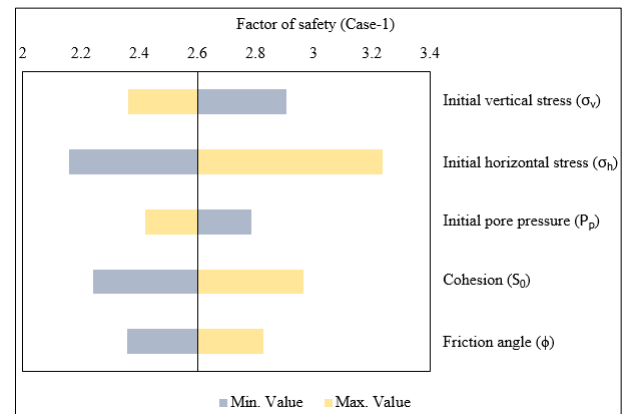


Figure 5: The tornado diagram of the case-1 scenario illustrated the relative importance of the input parameters.

The relative design sensitivity factor or the relative importance factors (α) are often referred to as probabilistic sensitivity and indicate the effect of each parameter on the reliability function [28]. This is very useful for the ranking of random variables and obtained by performing several probabilistic analyses and treating every individual parameter as a deterministic variable in each study [29], [30]. A positive value indicates a direct relationship between the variable’s value and the response, while a negative sensitivity suggests an inverse relation. However, the square of each sensitivity factor (α_i^2) is a measure of its contribution to the probability, and the sum is equal to 1. The relation between the input parameters with the probabilistic response is illustrated in Figure 6, where pore pressure and friction angle show a direct connection with the result, and horizontal stress and cohesion suggested an inverse relation. However, the vertical stress showed a significantly low positive value (approximately zero) and indicated insignificance contribution during the calculating probability of failure.

Figure 7 display the relative contribution of each input parameter within different cases. The failure probability using the FORM technique mainly depends on the horizontal stress, pore pressure, and cohesion, in which pore pressure is the most significant. A substantial pore

pressure influence was observed in case-2 (i.e., 60%), which is a depleted scenario due to Troll Field production. A gentle contribution of friction angle is illustrated in case-1; however, there is very little impact in the rest of the cases.

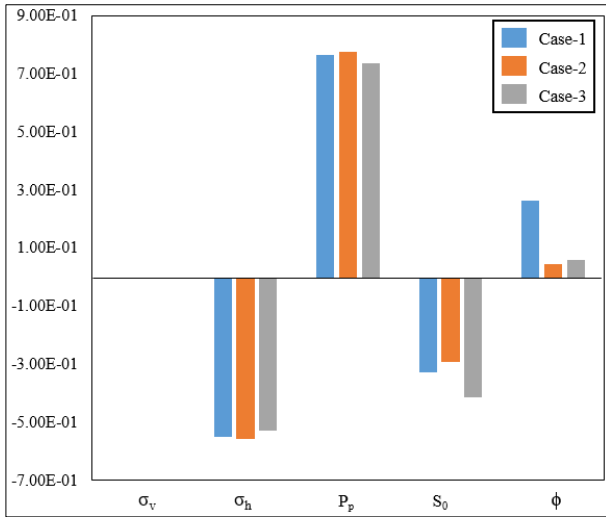


Figure 6: Sensitivity factor (α) in the probabilistic analysis of Draupne Caprock shale using FORM showing the relations between random input variables and the responses.

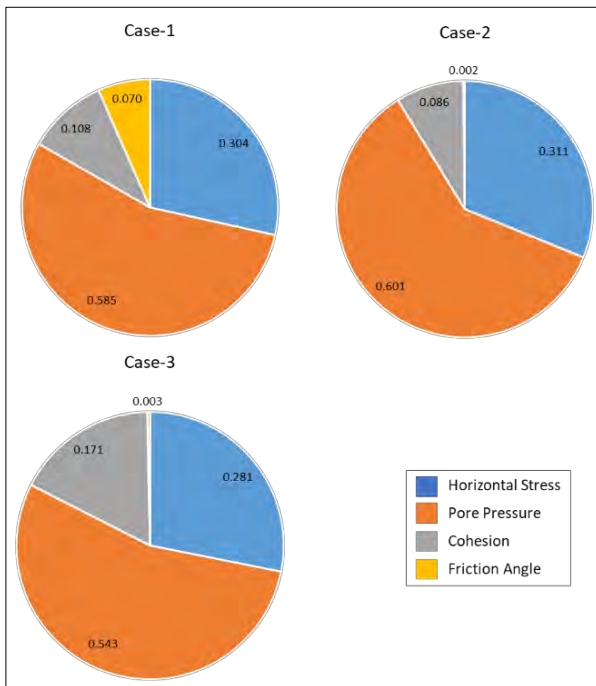


Figure 7: Square of each factor (α^2) showing the contribution variation to the probability failure analysis within different cases.

5. Discussion

The input parameters used for caprock failure analysis are often highly uncertain, and the deterministic safety factor does not reflect the corresponding failure probability [6]. The approach used in this study can

integrate all the possible uncertainties by adding the ranges and probabilistically estimating the structural reliability. For example, case-2 failure probability significantly decreases the chances of failure compared to case-1, while the increase of safety factor is insignificant (i.e., from 2.6 to 3.16). Therefore, the probabilistic reliability analysis for subsurface structures could be a useful tool to incorporate the parameter uncertainties and quantify the failure risks. However, the probabilistic method is susceptible to the input parameter ranges and should be defined very carefully. For instance, in this analysis, the standard deviation value defined for σ_v and σ_h is only 3% and 6% of the average value, indicating these properties are not very sensitive and lead to a significantly low PoF, and β value (Table 3). Moreover, the insignificance relative contribution of σ_v might be the effect of the uncertainty range. Therefore, the emphasis is needed to define the uncertain parameters range before use as an input parameter in the failure probability model.

The reliability index and probability of failure in any structure are a relative measurement of the current condition and provide a qualitative estimation of the expected performance [31]. However, integrity analysis of caprocks presents under certain pressure, and temperature conditions are very complex. Although our modeling approach considers various pressure conditions, the temperature effect on caprock mechanical behavior is beyond the scope. Moreover, the variation between the deterministic and probabilistic sensitivity indicates that further analysis is needed to examine the method's reliability. The model used in this study is a novel approach for caprock failure characterization; hence, there are no published charts for standard. However, this method is widely used in geotechnical engineering, and we compare our result with the expected performance range for embankment shown in Table 5 [31]. According to the chart, the in-situ condition (case-1) and depleted scenarios (case-2) are above the highest performance level (High). However, the theoretical failure case does not represent the same reliability index value and is classified as Poor (case-3). The probability of unsatisfactory performance illustrated that for case-3, 24 of every 1000 would result in a failure event. The failure events are significantly different from the theoretical failure due to decreased horizontal stress and pore pressure changes. However, the unsatisfactory performance number of the in-situ stress scenario (case-1) is only 13 out of 10^9 runs, making this case safer.

Table 5: The defined performance level with corresponding unsatisfactory events and reliability index values adapted from U.S. Army Corps of Engineers [31].

Expected Performance Level	Probability of Unsatisfactory Performance	Reliability Index (β)
High	0.0000003	5.0
Good	0.00003	4.0
Above average	0.001	3.0
Below average	0.006	2.5
Poor	0.023	2.0
Unsatisfactory	0.07	1.5
Hazardous	0.16	1.0

6. Conclusion

The probabilistic estimation of the Draupne Formation caprock's reliability is the critical condition for a successful Alpha prospect CO₂ injection site. This study's outcomes proved to be a valuable approach when several uncertainties are present. However, it needs a careful investigation to define the parameter ranges before using them as model input. The main observations of this study are as follows:

- In the initial condition, the reliability of Draupne caprock shales is excellent, with a very low chance of mechanical failure. Moreover, considering the Troll Field depletion scenarios, the failure probability decreases significantly.
- Pore pressure and friction angle directly relate to the probabilistic response, while horizontal stress and cohesion have an inverse relation. Overall, pore pressure and horizontal stress are the main contributors to the probability of failure value.
- Although there is a similar increasing or decreasing trend between deterministic and probabilistic values of different cases, the variations are significant in the probabilistic approach.

This study indicates that the Draupne Formation can be a safety barrier during CO₂ injection into the Alpha prospect. Nevertheless, it should be perceived that this study has focused on the feasibility of the methodology rather than the field evaluation. The injection-related potential risks can be affected by other factors (e.g., stiffness contrast between reservoir and surroundings, geometrical effects, drainage condition, stress paths, etc.) and need to be evaluated further with a better assessment of the statistical input and the numerical simulation.

Acknowledgments

We are thankful for the funding provided by the Research Council of Norway for the OASIS (Overburden Analysis and Seal Integrity Study for CO₂ Sequestration in the North Sea) project (NFR-CLIMIT project #280472) and the FME NCCS Centre (NFR project #257579/E20). We are also grateful to Schlumberger for the Petrel academic software license, Python Software Foundation for Python, and Rick Allmendinger's Stuff for MohrPlotter.

References

- [1] G. M. Ingram, J. L. Urai, and M. A. Naylor, "Sealing processes and top seal assessment," in *Norwegian Petroleum Society Special Publications*, vol. 7, Elsevier, 1997, pp. 165–174.
- [2] NPD CO₂ Atlas, "NPD CO₂ Atlas Report," 2014.
- [3] M. J. Rahman, M. Fawad, and N. H. Mondol, "Organic-rich shale caprock properties of potential CO₂ storage sites in the northern North Sea-offshore Norway," *Mar. Pet. Geol.*, vol. 122, p. 104665, 2020.
- [4] J. M. Duncan, "Factors of safety and reliability in geotechnical engineering," *J. Geotech. Geoenvironmental Eng.*, vol. 126, no. 4, pp. 307–316, 2000.
- [5] J. T. Christian, "Geotechnical engineering reliability: How well do we know what we are doing?," *J. Geotech. Geoenvironmental Eng.*, vol. 130, no. 10, pp. 985–1003, 2004.
- [6] F. Nadim, "Tools and strategies for dealing with uncertainty in geotechnics," in *Probabilistic methods in geotechnical engineering*, Springer, 2007, pp. 71–95.
- [7] M. J. Rahman, J. C. Choi, M. Fawad, and N. H. Mondol, "Probabilistic analysis of Vette fault stability in potential CO₂ storage site Smeaheia, offshore Norway" *Int. J. Greenh. Gas Control*, vol. 108, p. 103315, 2021.
- [8] R. B. Færseth, "Interaction of Permo-Triassic and Jurassic extensional fault-blocks during the development of the northern North Sea," *J. Geol. Soc. London.*, vol. 153, no. 6, pp. 931–944, 1996.
- [9] R. Steel and A. Ryseth, "The Triassic—Early Jurassic succession in the northern North Sea: megasequence stratigraphy and intra-Triassic tectonics," *Geol. Soc. London, Spec. Publ.*, vol. 55, no. 1, pp. 139–168, 1990.
- [10] P. S. Whipp, C. L. Jackson, R. L. Gawthorpe, T. Dreyer, and D. Quinn, "Normal fault array evolution above a reactivated rift fabric; a subsurface example from the northern Horda Platform, Norwegian North Sea," *Basin Res.*, vol. 26, no. 4, pp. 523–549, 2014.
- [11] A. M. Roberts, G. Yielding, N. J. Kusznir, I. Walker, and D. Dorn-Lopez, "Mesozoic extension in the North Sea: constraints from flexural backstripping, forward modelling and fault populations," in *Geological Society, London, Petroleum Geology Conference series*, 1993, vol. 4, no. 1, pp. 1123–1136.
- [12] A. M. Roberts, N. J. Kusznir, G. Yielding, and H. Beeley, "Mapping the bathymetric evolution of the Northern North Sea: from Jurassic synrift archipelago through Cretaceous–Tertiary post-rift subsidence," *Pet. Geosci.*, vol. 25, no. 3, pp. 306–321, 2019.
- [13] R. J. Steel, "Triassic–Jurassic megasequence stratigraphy in the Northern North Sea: rift to post-rift evolution," in *Geological Society, London, Petroleum Geology Conference series*, 1993, vol. 4, no. 1, pp. 299–315.
- [14] J. Vollset and A. G. Doré, *A revised Triassic and Jurassic lithostratigraphic nomenclature for the Norwegian North Sea*. Oljedirektoratet, 1984.
- [15] NPD, "NPD FactPages," 2021. <https://npdfactpages.npd.no/factpages/Default.aspx?culture=en>.
- [16] E. Skurtveit, J. C. Choi, J. Osmond, M. Mulrooney, and A. Braathen, "3D fault integrity screening for smeaheia CO₂ injection site," in *14th Greenhouse Gas Control Technologies Conference Melbourne*, 2018, pp. 21–26.
- [17] Statoil Underground report, "Feasibility study of planning and design of a CO₂ storage facility on the Norwegian Continental Shelf – Smeaheia," 2016.
- [18] M. Gutierrez, L. E. Øino, and R. Nygaard, "Stress-dependent permeability of a de-mineralised fracture in shale," *Mar. Pet. Geol.*, vol. 17, no. 8, pp. 895–907, 2000.
- [19] P. Horsrud, E. F. Sønstebo, and R. Bøe, "Mechanical and petrophysical properties of North Sea shales," *Int. J. Rock Mech. Min. Sci.*, vol. 35, no. 8, pp. 1009–1020, 1998.
- [20] E. Skurtveit *et al.*, "Mechanical testing and sealing capacity of the Upper Jurassic Draupne Formation, North Sea," *49th US Rock Mech. Symp. Am. Rock Mech. Assoc.*, 2015.

- [21] O. Ditlevsen and H. O. Madsen, *Structural Reliability Methods*, Internet e. John Wiley and Sons, 2007.
- [22] A. M. Hasofer and N. C. Lind, "Exact and invariant second-moment code format," *J. Eng. Mech. Div.*, vol. 100, no. 1, pp. 111–121, 1974.
- [23] M. H. Faber, "Basics of structural reliability," *Swiss Fed. Inst. Technol. ETH, Zürich, Switz.*, 2009.
- [24] J. Hackl, "PyRe documentation," 2018. <http://github.com/hackl/pyre>.
- [25] H. O. Madsen, S. Krenk, and N. C. Lind, *Methods of structural safety*. Courier Corporation, 2006.
- [26] Campolongo, F., Kleijnen, J.P.C., Andres, T., 2000. Screening methods. Wiley Ser. Probab. Stat.
- [27] Rohmer, J., Seyedi, D.M., 2010. Coupled large scale hydromechanical modelling for caprock failure risk assessment of CO₂ storage in deep saline aquifers. *Oil Gas Sci. Technol. l'Institut Français du Pétrole* 65, 503–517.
- [28] S. K. Easley, S. Pal, P. R. Tomaszewski, A. J. Petrella, P. J. Rullkoetter, and P. J. Laz, "Finite element-based probabilistic analysis tool for orthopaedic applications," *Comput. Methods Programs Biomed.*, vol. 85, no. 1, pp. 32–40, 2007.
- [29] NESUS Theoretical Manual, "Southwest Research Institute," San Antonio, Texas, 2011.
- [30] F. L. G. Pereira, D. Roehl, J. P. Laquini, M. F. F. Oliveira, and A. M. Costa, "Fault reactivation case study for probabilistic assessment of carbon dioxide sequestration," *Int. J. Rock Mech. Min. Sci.*, vol. 71, pp. 310–319, 2014.
- [31] USA Army Corps of Engineers, "Engineering and design introduction to probability and reliability methods for use in geotechnical engineering," Washington, D.C., 1997. [Online]. Available: www.usace.army.mil/usace-docs.

ELEGANCY – ENABLING A LOW-CARBON ECONOMY VIA HYDROGEN AND CCS

Svend T. Munkejord^{1*}, Marco Mazzotti², Mijndert van der Spek^{2,3}, Catherine Banet⁴, Nilay Shah⁵, Nixon Sunny⁵, Gunhild A. Reigstad¹, Gianfranco Guidati², Hans L. Skarsvåg¹, Roland Span⁶, Jaap Vente⁷, J.P. Martin Trusler⁵, Nils A. Røkke¹

¹ SINTEF Energy Research, Trondheim, Norway

² ETH Zurich, Zurich, Switzerland

³Current address: Heriot-Watt University, Edinburgh, UK

⁴University of Oslo, Oslo, Norway

⁵Imperial College London, London, UK

⁶Ruhr University Bochum, Bochum, Germany

⁷TNO, Petten, the Netherlands

* Corresponding author e-mail: svend.t.munkejord@sintef.no

Abstract

ELEGANCY was an ERA-Net Cofund ACT project with the aim to help fast-tracking the decarbonization of Europe's energy system via hydrogen and CCS. This has been achieved by overcoming or highlighting specific scientific, technological and economic/legal barriers and by undertaking five national case studies adapted to the conditions in the partner countries Germany, the Netherlands, Norway, Switzerland and the UK. ELEGANCY had 22 partners from industry and academia/research. This paper gives a brief overview of the project and some main results.

Keywords: CO₂ capture and storage (CCS), hydrogen, full chain

1. Introduction

The low-carbon economy needs CO₂ capture and storage (CCS), as a key technology to mitigate CO₂ emissions [21], including emissions from industrial processes that would otherwise be difficult to abate [43]. The low-carbon economy also needs hydrogen (H₂) as a low-carbon energy vector – depending on how it is produced.

The main idea behind the ELEGANCY project [4] was that combining CCS and H₂ could give a double benefit. Large amounts of clean H₂ can be produced from natural gas (NG) with CCS, thus providing the decarbonization of power, heating and transport based on an existing fuel and infrastructure. This would also provide a commercial model for industrial CCS, and it would build necessary bridges towards a system increasingly based on hydrogen produced from renewable sources.

2. Project overview

ELEGANCY R&D provides solutions to key technical challenges for H₂-CCS chains (Figure 1) – on both a systems and component level. This includes CO₂ transport, injection and storage, as well as H₂-CO₂ separation – directly increasing the TRL of selected components to 5 where large-scale demonstration is possible. The research generated and analysed new experimental data from world-class research infrastructure, such as ECCSEL and EPOS facilities. To enable application of this research, ELEGANCY developed an innovative, open-source design tool for a fully integrated H₂-CCS chain. Finally, taking a fully integrated approach, the project studied business

development opportunities, public perceptions of H₂ and CCS, and environmental aspects of H₂-CCS chains. All the research findings and tools were applied to five national case studies, each designed to account for the specific and conditions and preferences in each of the participating countries. The ELEGANCY case studies are described in more detail in Refs. [25, 26]. The work breakdown structure and technical topics included in the project are further described in Figure 2.

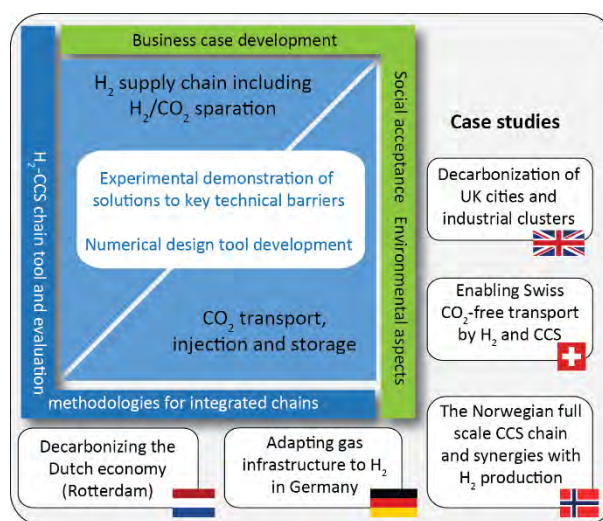


Figure 1: Overview of ELEGANCY research.

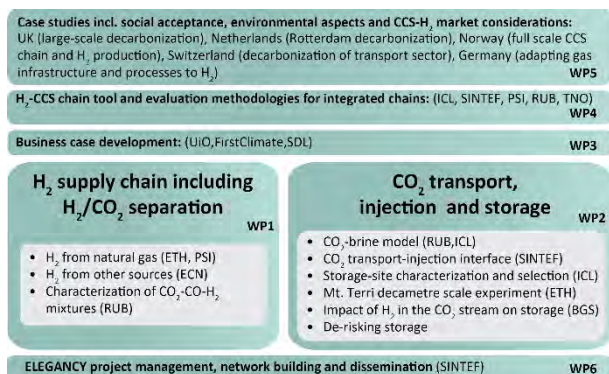


Figure 2: ELEGANCY work breakdown structure.

3. Activities and results

This section briefly summarizes the technical results achieved in the ELEGANCY work packages (Figure 2). For the cases where the results have been published at the time of writing, those publications are cited.

3.1 WP1 – H₂ supply chain and H₂-CO₂ separation

WP1 aimed to enable the production of large volumes of low-carbon H₂ at the scales of interest. To this end, WP1

- Enabled efficient H₂ production and CO₂ capture at different plant sizes.
- Found ways to increase the efficiency and productivity of natural gas/biogas reforming and CO₂/H₂ separation independently of the plant size.
- Integrated H₂ production and CO₂ capture with significant industrial processes such as steel production.
- Characterized the properties of H₂ mixed with CO₂, CO, and CH₄.

The research spanned the range from the phenomenon level (RUB) via lab-scale experiments (ETH and TNO) to the pre-pilot scale (TNO).

Task 1.1: H₂ production with ambient temperature-based technologies PSA/VPSA (ETH, UU)

The primary objective of the work was the development of vacuum pressure swing adsorption technology (VPSA) for the single cycle co-purification of H₂ and CO₂. This was first done *in silico* and for a generic gas stream [31]. The developed VPSA cycle was then applied to relevant syngases from steam reforming and autothermal reforming of natural gas [32]. The cycle was also used for the modelling and optimization of different H₂ production pathways starting from natural gas or biogas comparing the state-of-the-art technology combination for H₂ purification and CO₂ capture with VPSA [6]. In the first part of the project, we focused on VPSA cycles using existing commercial sorbents. We then evaluated novel materials for VPSA through experimental characterization [8, 33] and modelling and optimization of VPSA process performance. Finally, the new cycle was demonstrated in the ETH inhouse pilot plant: we designed, refurbished, and updated the automation of the lab-pilot and undertook breakthrough and full-cycle experiments, showcasing that the cycle works satisfactorily in practice, bringing the technology to TRL 5.

Task 1.2 H₂ production with enhanced adsorption-based technologies – SEWGS (TNO, SWERIM)

In previous projects, sorption-enhanced water-gas shift (SEWGS) has shown excellent performance under industrial gas loads such as blast furnace gas from steel mills. In ELEGANCY, SEWGS technology was prepared for demonstration as a feasible CO₂ capture technology for another high-volume steel-mill gas, namely basic oxygen furnace (BOF) gas. To produce a H₂-rich gas stream from BOF gas with SEWGS, the following was achieved:

- The catalytic testing of commercial high-temperature water-gas shift (HTWGS) catalyst with BOF gas was finalized. Results and implications have been discussed with the catalyst vendor. The versatility of the (JM) Katalco™ 71-6 WGS catalyst has been demonstrated in long-term experiments, with only 4–5% conversion loss over 1000 hours. This shows that the JM WGS catalyst can be used under the various conditions encountered with steel gases.
- Based on an extensive experimental and modelling campaign it is shown that the SEWGS process can be adapted for operation under the extreme conditions produced by the BOF gas. The experimental and modelling results conclude that large-scale operation is technically feasible with the aid of a split-flow WGS section that also helps minimize S/CO ratios. As expected, the carbon capture rate is robust to switching from blast furnace gas (BFG) to BOF.
- Cycle design and optimization for BOF gas was extensively studied. The highest productivity, at targeted carbon-capture rate (CCR) and carbon purity (CP) was achieved for SEWGS section operating at 35 bar. Obtained CCR was 96%, CP was 98%. To achieve this, two trains with 8 columns in each train is required.
- Analysis on engineering and costing of multi-column SEWGS at the SWERIM site in Luleå has been reported.
- The ELEGANCY results on SEWGS with BOF gas has resulted in the follow up INITIATE (H2020) project (November 2020 – November 2024) to further the development of SEWGS with BOF gas (for the production of Urea) in a real industrial setting at TRL7.

Task 1.3 System integration and optimization (ETH, UU)

Task 1.3 involved the integration and optimization of CO₂-capture technology into H₂-production systems (from natural gas as well as biogenic sources). First, an inventory was made of state-of-the-art H₂ production technology with CCS [7]. In addition, a techno-economic assessment framework was established and used in conjunction with the chain-tool (Sec. 3.4). Based on this work, an integrated techno-environmental assessment study of hydrogen production from natural gas and biogenic sources, combined with CCS was undertaken, identifying optimal plant-wide configurations from both technical and environmental perspective [14]. The technologies analysed are steam-methane reforming (SMR), autothermal reforming (ATR) and biomass gasification for syngas production. CO₂ capture from the

syngas was included, using the novel vacuum pressure swing adsorption (VPSA) process developed in Task 1.1, that combines hydrogen purification and CO₂ separation in one cycle. As a reference for comparison, we have included cases with conventional amine-based technology. To this end, we built a mathematical optimization routine that combines the two softwares we used, namely Matlab and Aspen Plus. With the integration of bio-sources we studied the possibility to have negative emissions while producing hydrogen with CCS.

Task 1.4 Thermodynamic property models (RUB)

Finally, at the phenomenon level, RUB managed to develop an improved thermodynamics model for prediction of vapour-liquid equilibria in mixture of H₂ with CO₂ and CH₄. To that end, data for the density of mixtures of H₂ with CO₂, carbon monoxide (CO), and methane (CH₄) were measured with the highly accurate densimeters available at RUB in a wide range of temperatures, pressures, and compositions. Also, speeds of sound were measured for mixtures of H₂ with CH₄ and CO₂. Shortcomings of the existing model were identified for the binary subsystems H₂ with CH₄, CO₂, CO and N₂. Based on this, the mixture models were improved for the systems H₂ with CH₄, CO₂, CO and N₂ impurities. In particular, this is true for the technically highly relevant phase equilibria. Finally, the improved mixture model was made available to project partners via a new version of the property software TREND (TREND 5.0).

3.2 WP2 – CO₂ transport, injection and storage

WP2 focused on CO₂ storage and on the transport-storage interface. The work utilizes a wide variety of first-class research infrastructure. The ultimate goal was to de-risk CO₂ storage. To this end, WP2

- Developed an accurate property model for CO₂-brine mixtures in the presence of impurities.
- Matured and validated tools for the safe, efficient and cost-effective design and operation of CO₂ pipelines and injection wells.
- Performed petrophysical chemical analyses for the characterization and selection of storage sites in Switzerland.
- Designed and performed decameter-scale experiments at the Mont Terri research rock laboratory to understand the role of CO₂ injection in modifying fault/fracture permeability through seismic and/or aseismic reactivation.
- Reduced uncertainties in injection, storage and monitoring of CO₂ produced by NG reforming for H₂ production.

Task 2.1 Thermodynamic property model for CO₂-brine (RUB, ICL)

The objective of this task was to develop a comprehensive model for the thermodynamic properties of reservoir brines containing dissolved gases, especially CO₂ and H₂ as an impurity. ICL performed experiments to address the lack of available data for the solubility of H₂ in brines. This necessitated the construction of new apparatus that can operate at temperatures up to 200°C

and pressures up to 700 bar [42]. The apparatus was validated by measuring the solubility of CO₂ and H₂ in pure water [41]. Measurements of H₂ solubility in a concentrated NaCl brine (2.5 mol/kg) were carried out at temperatures of 50, 100 and 150 °C with pressures up to about 400 bar. The results can be expressed in terms of a Sechenov coefficient which relates H₂ solubility in NaCl brine to that in pure water. By analysing the experimental results, together with literature data at lower temperatures, this coefficient has been determined at temperatures between 0 and 150°C [40].

The IAPWS seawater model [20] was combined with highly accurate equations of state to ensure consistent calculations of mixtures of brines with seawater-like composition and CCS-components. Therefore, a complex approach for the combination of pressure and density-explicit models was developed [29]. The model was implemented in the thermodynamic property database TREND and published to more than 150 users in academia and industry on an open-source basis. Further, a more advanced brine model based on Pitzer's equations was studied. These equations allow for flexible salt compositions and are more suitable for the description of brines at storage conditions.

Task 2.2 Well dynamics (SINTEF)

Work has been carried out to quantify thermal and flow transients in CO₂-injection wells and CO₂-transportation systems. To this end, a well-flow model accounting for multiple components and phases and employing modern numerical methods has been developed. This has been coupled to a near-well reservoir model, where the response of the reservoir model influences the well model. The results show that such a coupling is necessary to capture the correct transients in the order of hours or days, which is relevant for e.g. intermittent CO₂ injection from ships [24]. Tube-depressurization experiments have been carried out for CO₂-N₂ and CO₂-He, showing a significant influence of 2 mol-% of impurities. To our knowledge, these are the first experiments of this kind incorporating high-speed temperature measurements [23]. Finally, experimental observations of two-phase vertical flow of CO₂ have been carried out [18]. Both experimental series serve model development and validation.

Task 2.3 Petrophysics and chemistry for site characterization and selection (ICL)

The main objective for this task is to understand and characterize fluid transport in both intact (reservoir) and damaged (seal) rocks, including those from the Mont Terri field site. A major technical challenge is to quantify the impact of heterogeneities on CO₂ flow and trapping in representative rock systems, so that measurements carried out in the laboratory are useful for upscaling. Pore network model predictions of Darcy-scale multiphase flow heterogeneity were validated by two-phase flow experiments [47]. A second technical challenge is to quantify fracture properties under stress conditions and their effect on fluid transport. Understanding how caprock may fail is in fact key for the safe exploitation of

the storage complex and to design contingency measures. We successfully conducted experiments on both reference rock types [46], and on Opalinus claystone from the Mont Terri field site to investigate the interplay between mechanical deformation and flow. The experiments on Opalinus claystone are of particular note, as they reveal the self-sealing properties of the rock when exposed to brine, as a result of clay-swelling.

Task 2.4 Mont Terri experiment: Fault slip and trapping (SCCER)

The experiment (CS-D) aims at improving our understanding on the main physical and chemical mechanisms controlling the migration of CO₂ through a fault-damage zone in a caprock, and the impact of the injection on the transmissivity in the fault [48]. To this end, we performed a prolonged (12 months) injection of CO₂-saturated saline water in the damage zone of a 3 m thick fault in the Opalinus Clay, a clay formation that is a good representative of common caprocks for CO₂ storage at depth. The mobility of the CO₂ within the fault is studied at decameter scale. We collected data from different independent monitoring systems, such as a seismic network, pressure temperature and electrical conductivity sensors, fiber optics, extensometers, and in situ mass spectrometer for dissolved-gas monitoring. The observations are complemented by laboratory data on collected fluids and rock samples. While injecting at a pressure just below the limit for fault opening and reactivation, we could observe that the flow is minimal and confined in tiny fractures that cannot be detected by classical geophysical measurements. Results also indicates some potential porosity decrease in the region immediately near the injection. An exposure to relatively high pressure, prolonged for 12 months, does not further weaken the fault. No notable seismic induced event could be detected.

Task 2.5 Understanding the impact of H₂ in a CO₂-rich stream on the storage strata (BGS, SCCER)

To understand the potential for microbial activity to influence CO₂ storage in the presence of H₂ [17], a series of experiments were completed. The results indicated that the hydrogen could stimulate microbial activity leading to an increase in microbial biomass, particularly sulphate reducers which can potentially use the hydrogen as an electron donor. Sulphate reduction also occurred when hydrogen was not present but seemed to be at a much lower rate. Methanogenesis also occurred under both conditions. Evidence of sulphate reducing organisms was seen up to 15% NaCl and methanogen up to 18% NaCl. Together this new data suggests that hydrogen impurities may increase microbial activity which could have an effect on microbial gas production (particularly hydrogen sulphide) and consumption in the reservoir, and have potential impacts on mineralogy. Additional work is recommended to fully understand the potential microbial interactions that could occur in CCS connected to hydrogen production.

3.3 WP3 – Business case development for H₂-CCS integrated chains

The vision of ELEGANCY includes not only technical and scientific objectives, but also an ambition to investigate regulatory, policy, commercial and market issues around H₂-CCS chains in order to accelerate their deployment. Within this scope, WP3 was aimed at developing a publicly available business-case assessment framework and templates which included a methodology to identify and select suitable business models for H₂-CCS projects.

WP3 followed the stepwise approach for the development of the business case framework. The business case framework developed in this work package provides a standardized approach for assessing the business context of H₂-CCS opportunities, identifying and mitigating business risks and investment barriers of a project, and ultimately selecting suitable business models that can deliver the project based on appropriate public and private sector risk sharing. The framework applies to case studies within ELEGANCY as well as to CCUS infrastructure chains broadly and the relevant resources are made publicly available for external use [4] under a Creative Commons CC BY-ND license.

The business case framework comprises the following elements:

Business model development methodology: We have developed an overall methodology which may be applied to select business models for H₂-CCS and other CCUS opportunities. The process is divided into four distinct steps, from the definition of the case-study scope and assessment of the market background, to business and investment risk identification and mitigation, and ultimately business-model selection. Once a business model is selected, business cases can be defined and assessed to various levels of detail depending on the stage of the project concept. For this purpose, a supplemental methodology is available. As business model preferences can change with changing business contexts as well as with the maturity of a project, the combined selection and assessment process is iterative.

Tool-kit [4]: To accompany each step in the process, a suite of Excel-based analytical and visualization tools has been designed and produced to facilitate the identification of key issues and promote collaborations early-on in the project development process. The tools cover: (i) assessment of the macroeconomic, fiscal and policy background, (ii) analysis of market failures, (iii) identification of policy needs and financial support gaps, (iv) evaluation of business risks and investments barriers as well as available mitigation measures, (v) selection of potential business models at system and sector level, and (vi) business case definition and assessment.

Guidance materials: A full description of the concepts and approach of the framework are detailed in four public interim reports of WP3 and in available recorded webinars.

The overall results and findings, including a compilation of the Excel tools' utility and functionality, are presented in a Synthesis Report on business case development for

H₂-CCS integrated chains [28]. The Synthesis Report provides a useful catalogue and index to the detailed interim reports. In addition, the legal research has been further developed in journal publications on de-risking the hydrogen-CCS supply chain through law, and on the identification of legal principles for gas market re-design for ensuring hydrogen and CCUS compatible gas networks.

WP3 actively engaged with key stakeholders in industry, government, European institutions and NGOs throughout the course of the ELEGANCY project via a series of workshops, interviews and collaboration with the Zero Emissions Platform (a European Technology and Innovation Platform under the Commission's Strategic Energy Technologies Plan). The workshops served the dual purpose of disseminating results and obtaining feedback and input for the WP3 programme. WP3 also ensured cross-fertilization of ideas and results with the ERA-net ACT ALIGN CCUS project.

3.4 WP4 – H₂-CCS chain tool and evaluation methodologies for integrated chains

To aid the commercial implementation of a H₂-CCS network, there needs to be extensive analysis on its technical feasibility in conjunction with integrated assessment under multiple criteria. There is a need for a powerful computational tool that can analyse various potential applications for H₂-CCS chains in a robust manner. The primary focus of ELEGANCY WP4 was to address this need and provide the necessary tools and techniques for analysing large scale H₂-CCS chain networks in the form of a modelling tool-kit.

Task 4.1 Define specifications for the open-source multi-scale systems modelling framework for H₂-CCS chain tool and evaluation (ICL, SINTEF, PSI, TNO, RUB)

A consistent methodological approach was needed to ensure that all the multi-scale modelling tools formulated as part of this work package used a unified framework for analysis [34-36]. In particular, the user requirements of the various tools need a clear outline, with clear expectations of model functionalities. This task involved close interactions with anticipated users of the modelling tools to plan the integration of software modules. As an outcome, three specifications – user requirements, functional and technical requirements were developed and publicly released to provide transparency.

Task 4.2 Define performance metrics (process, economic and environmental) for integrated assessment (PSI, ICL, SINTEF, TNO, RUB)

The core utility of the chain-tool developed within this work package is its applicability to a range of design problems. To enhance the broader use of the tool, the work took input from the project consortium and potential external users, thus identifying key features of interest. These discussions have been critical in the formulation of a set of performance metrics that are relevant for decision-making in the context of H₂-CO₂ infrastructure design [9]. These performance metrics

include economic, environmental, and thermodynamic performance measures. The outcome of this task was publicly released, allowing potential users to understand the calculation methodology along with the set of working assumptions.

Task 4.3 Build detailed process and models of all components in H₂-CCS chain (ICL, SINTEF, RUB, TNO)

The model-building approach relied on multi-scale modelling, with a consistent set of working assumptions which define the characterization of an engineering process, at both a regional and network-level. This task is essential for the development of the tool as detailed component models allow users to simulate individual modules, whilst focusing on their elements of interest. The different project partners have each produced various models (e.g. hydrogen production, CO₂ separation, gas transport and compression, end-use, etc.) in a relevant simulation environment [22]. These models have all been publicly released and used for analysing regional H₂/CO₂ infrastructure design in the UK, where it has shown potential for cost-reduction through appropriate management of pipeline transmission pressures and storage infrastructure.

Task 4.4 Develop a metamodeling approach for different components of the H₂-CCS chain for use in steady state design mode and dynamic operation mode (SINTEF, ICL, PSI, TNO)

Computational complexity is a key issue that needs to be resolved when performing detailed dynamic simulations across the H₂-CCS chain. Large process systems with multiple plants, connecting infrastructure and storage often take long system times to be simulated and the computational burden may be prohibitive in certain cases. Abstractions of the more detailed process models were developed and implemented in OpenModelica. For example, a detailed thermodynamic equation of state was reduced to a simpler polynomial regression model with adapted range of validity, resulting in a significant reduction in computation time. Rather than using an ad-hoc approach to model reduction, a formal “metamodeling” tool, Consumet, was developed, enabling effective and accurate model reduction. Consumet can be used to sample a series of data points across the simulation space (using detailed models) and generate output data, which can be used for the formulation of simpler, yet accurate mathematical relations. This tool is publicly released for potential use with a range of process systems beyond H₂-CCS, allowing for greater impact [2].

In addition to the work towards the H₂-CCS chain tool, a life cycle assessment tool for passenger cars has been made openly available [1]. This was used in the Swiss case study to do economic and environmental evaluation of different types of cars under various driving and energy supply scenarios.

Task 4.5 Integrate component models into system models and deliver overall design and operational

toolkit for the H₂-CCS chain (ICL, SINTEF, RUB, PSI, TNO)

This final activity combines all the various outputs from the earlier tasks to produce an overall modelling tool that can be applied to analyse the design and operation of H₂-CO₂ networks. In particular, detailed component models are released [22], with the reduced order modelling framework from Task 4.4. Furthermore, reduced-order models are assimilated to produce an open-source and open-access operational modelling toolkit [3], which is capable of simulating over 50 individual process plants and associated infrastructure at half-hour intervals over the course of an annual time horizon, within a few minutes of CPU time on a standard laptop. Additionally, design optimization frameworks have been developed in Python and released on a software hosting platform. These tools are accompanied by life-cycle assessment datasets and appropriate documentation to enhance usability. The chain-tool can evaluate a range of regional systems and provide insights on robust deployment pathways, investment breakdowns, multi-criteria decision-making.

The chain-tool has provided insights on H₂/CO₂ infrastructure design for the decarbonization of heat and industry in the UK [37, 38], with its findings disseminated for appraisal by key national stakeholders such as the Committee on Climate Change, HMG's Department of Business, Energy & Industrial Strategy, National Grid, etc. Similarly, the Dutch case study team is in dialogue with Gasunie regarding the outputs from the case study.

3.5 WP5 – Case studies

The ELEGANCY case studies have accelerated the implementation of H₂ and CCS chains in Europe by:

- Establishing the H-vision consortium committed to decarbonizing the Rotterdam cluster industry.
- Developing a Roadmap for decarbonization of the Dutch economy.
- Quantifying the role of H₂ and CCS along with – and not in contrast to – the deployment of renewable energy and large energy-storage facilities.
- Presenting a CO₂-supply profile, validating the UK storage capacity and developing an optimal injection strategy for the most promising storage sites, sufficient for the planned decarbonization by the H21 North of England, Acorn and Cadent projects.
- Identifying the key opportunities and constraints for the design of a UK H₂ and CCS infrastructure, including significant potential H₂ storage capacity, and presenting UK business case solutions.
- Identifying the role of H₂ and CCS for reaching the Swiss climate targets. Negative emissions are required to compensate emissions from non-energy sectors, and to reach the net-zero target in 2050. These are best realized with a combination of H₂ production from biomass resources and CCS.
- Revealing the need for a two-pronged approach for CCS in Switzerland due to the characteristics of Swiss geology that are challenging for the deployment of CCS; 1) improve the understanding of

the Swiss subsurface, 2) develop alternatives, i.e. the export of CO₂ to storage sites such as planned by the Northern Lights consortium.

- Performing a multi-disciplinary evaluation of decarbonization strategies for the German gas infrastructure using public acceptance and legal insights as guidance on infrastructure concepts and macro-economic insights to understand the prerequisites for a successful transition.
- Showing that large-scale H₂ production in Norway for export and national demand can help to enable significant economies of scale in the development of a Norwegian CCS infrastructure, thus increasing the attractiveness of Norway as a large-scale storage location for European CO₂ emissions.

Further details are given in Refs. [5, 10-13, 15, 16, 19, 27, 30, 39, 44, 45].

4. Education and training

By educating and training the next-generation academics and industrials in the form of summer interns, master's students, PhD candidates and postdocs, ELEGANCY will have a lasting effect. The following number of education and training positions have been involved in ELEGANCY:

- Summer interns: 6
- Masters students: 14
- PhD candidates: 11
- Postdocs: 17

5. Dissemination

Dissemination is key to accelerating CCS deployment, not just to enhance R&D efforts, but perhaps more importantly since deployment requires industrial and political willingness as well as public acceptance. Open and engaging communication of scientific results has therefore been a core strategic activity in ELEGANCY. Major efforts have been the ELEGANCY Conference, a luncheon discussion in the European Parliament, and the ELEGANCY webinar series. Information about, and slides from these meetings can be found on the project website [4].

The website also contains a brief project description, and, importantly, an up-to-date publications page where all public deliverables can be downloaded. There is also a "news" section displaying glimpses from project work, and a newsletter that users could describe to, containing a digest of the latest news items.

In January–November 2020, there have been 8950 page views, which on average were read by the users for 1 min 50 sec. These are good numbers and indicate that the users find what they search for and read the contents of the page. The number of unique users was 1117 in 2018, increasing to 1273 in 2019 and 1587 in 2020 (until 3 December). In 2020, the users were from Norway (319), the UK (256), Germany (240), the Netherlands (151) and Switzerland (129), and also from Belgium (79), France (79), Italy (69) and the USA (69). This may be indicative of an increasing interest for CCS.

ELEGANCY has also established a Twitter account ([@ELEGANCY_ACT](https://twitter.com/ELEGANCY_ACT)) which is used to diffuse project-

related news, and videos from key events have been published on Youtube.

ELEGANCY has since its start-up year used the SINTEF Blog (a scientific blog aimed at researchers, partner organizations and other industry stakeholders) actively to communicate research results and project activities.

6. Conclusion

ELEGANCY has helped fast-tracking the decarbonization of Europe's energy system by combining CCS and H₂, by overcoming specific scientific, technological and economic/legal barriers, and by undertaking five national case studies adapted to the conditions in the partner countries.

Based on our work and the project results, we conclude as follows.

- Europe is dependent on all main available decarbonization options – including hydrogen and CCS – to address the European-parliament declared climate emergency from November 2019 and reduce CO₂ emissions by 55% by 2030 and further to net zero by 2050.
- The European parliament has also supported greater action for implementing commercial-scale CCS.
- Hydrogen can be delivered at scale – fast-tracking the 2050 net-zero emission goal.
- Fuel-switching to hydrogen will:
 - Curb emissions from distributed sources, such as transport, industrial processes, heating and cooling.
 - Quickly decarbonize heavy industry in the EU and so maintain economic activity and jobs.
- Hydrogen produced both from renewable energy sources and from natural gas with CCS will be needed.
- Climate-positive hydrogen from biomass with CCS can play an important role in compensating CO₂ emissions from hard-to-abate sectors, despite limited resources of sustainable biomass.
- CCS is an efficient and safe way to eliminate CO₂ emissions.
- The Hydrogen Pathway needs appropriate financial, regulatory and political frameworks.
- Hydrogen should become an important part of the future European energy system.
- A comprehensive hydrogen infrastructure is required, also using existing assets.
- Open-access infrastructure for CO₂ transport and storage is required – being able to permanently store CO₂ will enable new pathways to climate neutrality.
- Full-scale deployment of hydrogen with CCS should start now.
- Recommended key principles for market re-design are:
 - Integrated energy system planning and governance tools.
 - Efficient and coordinated permitting procedures.
 - Access to the grid and gas grid conversion.
 - Operation of transport networks and related infrastructures.

Acknowledgements

ACT ELEGANCY, Project No 271498, has received funding from DETEC (CH), BMWi (DE), RVO (NL), Gassnova (NO), BEIS (UK), Gassco, Equinor and Total, and is cofunded by the European Commission under the Horizon 2020 programme, ACT Grant Agreement No 691712.

References

1. Calculator web-page. <https://calculator.psi.ch/>.
2. Consumet Github. <https://github.com/act-elegancy/consumet>.
3. ELEGANCY Chain-Tool Github. https://github.com/act-elegancy/chain_tool.
4. ELEGANCY web-page. <http://www.elegancy.no>.
5. Adams B, Sutter D, Mazzotti M, Saar MO. Combining Direct Air Capture and Geothermal Heat and Electricity Generation for Net-negative Carbon Dioxide Emissions. World Geothermal Congress (WGC 2020), online, April 27, 2020. 2020. <https://doi.org/10.3929/ethz-b-000449685>.
6. Antonini C, Treyer K, Streb A, van der Spek M, Bauer C, Mazzotti M. Hydrogen production from natural gas and biomethane with carbon capture and storage – A techno-environmental analysis. *Sustainable Energy & Fuels*. 2020;4:2967-86. <https://doi.org/10.1039/D0SE00222D>.
7. Antonini C, van der Spek M, Sutter D, Streb A, Gazzani M, Mazzotti M. Report on optimal plants for production of low-carbon H₂ with state-of-the-art technologies. ELEGANCY D1.3.1 2018.
8. Asgari M, Streb A, van der Spek M, Queen W, Mazzotti M. Synergistic material and process development: application of a metal-organic framework, Cu-TDPAT, in single-cycle hydrogen purification and CO₂ capture from synthesis gas. *Chemical Engineering Journal*. 2021;128778. <https://doi.org/10.1016/j.cej.2021.128778>.
9. Bauer C, van der Spek M, Sutter D, Anantharaman R, Shah N, Iruretagoyena D, de Kler R. Definition of quantifiable environmental, economic and operability metrics for all H₂-CCS chain sections and model components - Issue 1. ELEGANCY D4.2.1 2018.
10. Benrath D, Flamme S, Glanz S, Hoffart FM. CO₂ and H₂ Infrastructure in Germany – Final Report of the German Case Study. ELEGANCY D5.5.3 2020.
11. Cox B, Bauer C, Mendoza Beltran A, van Vuuren DP, Mutel CL. Life cycle environmental and cost comparison of current and future passenger cars under different energy scenarios. *Appl Energ*. 2020;269:115021. <https://doi.org/10.1016/j.apenergy.2020.115021>.
12. de Kler R, van de Beek F, van der Veen A. ROADMAP for the introduction of a low carbon industry in the Rotterdam region. ELEGANCY D5.2.6 2020.
13. Flamme S, Benrath D, Glanz S, et al. ELEGANCY: The Interdisciplinary Approach of the German Case Study to Enable a Low Carbon Economy by Hydrogen and CCS. *Energy Proc*. 2019;158:3709-14. <https://doi.org/10.1016/j.egypro.2019.01.887>.
14. Gabrielli P, Poluzzi A, Kramer GJ, Spiers C, Mazzotti M, Gazzani M. Seasonal energy storage for zero-emissions multi-energy systems via underground hydrogen storage. *Renew Sust Energ Rev*. 2020;121:109629. <https://doi.org/10.1016/j.rser.2019.109629>.
15. Glanz S, Schönauer A-L. Towards a Low-Carbon Society via Hydrogen and Carbon Capture and Storage: Social Acceptance from a Stakeholder Perspective. *J Sust Dev Energ, Wat Env Syst*. 2021;9. <https://doi.org/10.13044/j.sdewes.d8.0322>.

16. Goldthorpe W, Avignon L. H21 Leeds and North of England risk matrix, business case template and risk reduction strategies. ELEGANCY D5.4.3 2020.
17. Gregory SP, Barnett MJ, Field LP, Milodowski AE. Subsurface Microbial Hydrogen Cycling: Natural Occurrence and Implications for Industry. *Microorganisms*. 2019;7:53.
18. Hammer M, Deng H, Liu L, Langsholt M, Munkejord ST. Upward and downward two-phase flow of CO₂ in a pipe: Comparison between experimental data and model predictions. *Int J Multiphase Flow*. 2021;138:103590. <https://doi.org/10.1016/j.ijmultiphaseflow.2021.103590>.
19. Hoffart FM, Schmitt E-J, Roos MW. Rethinking Economic Energy Policy Research—Developing Qualitative Scenarios to Identify Feasible Energy Policies. *Sustainable Development of Energy, Water and Environment Systems*. 2020. <https://doi.org/10.13044/j.sdewes.d8.0331>.
20. IAPWS. Thermodynamic properties of seawater. 2008.
21. IPCC. Climate Change 2014: Synthesis Report. Contribution of Working Groups I, II and III to the Fifth Assessment Report of the Intergovernmental Panel on Climate Change. Geneva, Switzerland: IPCC, 2014.
22. Iruretagoyena D, Sunny N, Mac Dowell N, et al. Operational component model inventory - Issue 1. ELEGANCY D4.3.1 2019.
23. Munkejord ST, Deng H, Austegard A, Hammer M, Aasen A, Skarsvåg HL. Depressurization of CO₂-N₂ and CO₂-He in a pipe: Experiments and modelling of pressure and temperature dynamics. *Int J Greenh Gas Con*. 2021;109:103361. <https://doi.org/10.1016/j.ijggc.2021.103361>.
24. Munkejord ST, Hammer M, Ervik Å, Odsæter L. Coupled CO₂-well-reservoir simulation using a partitioned approach. Effect of reservoir properties on well dynamics. *Greenh Gas Sci Technol*. 2021;11:103-27. <https://doi.org/10.1002/ghg.2035>.
25. Reigstad GA, Akhurst M, Anantharaman R, et al. Hydrogen production with CCS to accelerate the decarbonization of the European power, industrial and transport sector - Key findings from the ACT ELEGANCY project's national case studies. Accepted for GHGT-15. 2021
26. Reigstad GA, Roussanaly S, Straus J, et al. Experiences from case studies on planning hydrogen-CCS value chains and development of business case opportunities in Europe. *In preparation*. 2021.
27. Schwiieger J, Brodmann U. WP3 business case framework applied and tested on the Swiss case study. ELEGANCY M5.3.2 2019.
28. Schwiieger J, Goldthorpe W, Avignon L, Banet C. Synthesis report on business case development for H₂-CCS integrated chains. ELEGANCY D3.4.1 2020.
29. Semrau B, Span R. Report and software on a property model for CO₂-rich mixtures in contact with brines with a seawater like composition. ELEGANCY D2.1.1 2019.
30. Straus J, Roussanaly S, Anantharaman R. Norwegian H₂ value chain from a European perspective. ELEGANCY D5.6.3 2020.
31. Streb A, Hefi M, Gazzani M, Mazzotti M. Novel Adsorption Process for Co-Production of Hydrogen and CO₂ from a Multicomponent Stream. *Ind Eng Chem Res*. 2019;58:17489-506. <https://doi.org/10.1021/acs.iecr.9b02817>.
32. Streb A, Mazzotti M. Novel Adsorption Process for Co-Production of Hydrogen and CO₂ from a Multicomponent Stream—Part 2: Application to Steam Methane Reforming and Autothermal Reforming Gases. *Ind Eng Chem Res*. 2020;59:10093-109. <https://doi.org/10.1021/acs.iecr.9b06953>.
33. Streb A, van der Spek M, Jørsboe J, Asgari M, Queen W, Mazzotti M. Report on characterization of equilibria and transport phenomena in promising new adsorbents for CO₂/H₂ separation. ELEGANCY D1.1.2 2019.
34. Sunny N, Iruretagoyena D, Mac Dowell N, et al. Functional Specification - Issue 1. ELEGANCY D4.1.1b 2018.
35. Sunny N, Iruretagoyena D, Mac Dowell N, et al. Technical Specification - Issue 1. ELEGANCY D4.1.1c 2018.
36. Sunny N, Iruretagoyena D, Mac Dowell N, et al. User Requirements Specification - Issue 1. ELEGANCY D4.1.1a 2018.
37. Sunny N, Mac Dowell N, Shah N. Design of low-carbon hydrogen and CCS infrastructure for the decarbonisation of heat in the UK. H2FC Supergen Research Conference; Nottingham, UK. 2020
38. Sunny N, Mac Dowell N, Shah N. Large Scale Deployment of Low Carbon Hydrogen and CCS Value Chains for the Decarbonisation of Heat: Novel Methods and Insights. AIChE Annual Meetin; Orlando, Florida, USA. 2019
39. Sunny N, Mac Dowell N, Shah N. What is needed to deliver carbon-neutral heat using hydrogen and CCS? *Energy Environ Sci*. 2020. <https://doi.org/10.1039/D0EE02016H>.
40. Torín-Ollarves G, Trusler JPM. Solubility of H₂ in brine at reservoir conditions. ELEGANCY D2.1.6 2019.
41. Torín-Ollarves G, Trusler JPM. Solubility of H₂ in pure water at reservoir conditions. ELEGANCY D2.1.5 2019.
42. Torín-Ollarves G, Trusler JPM. Validation of experimental apparatus for measurement of H₂ solubility in water/brine. ELEGANCY D2.1.4 2018.
43. Voldsund M, Gardarsdóttir SO, De Lena E, et al. Comparison of Technologies for CO₂ Capture from Cement Production—Part 1: Technical Evaluation. *Energies*. 2019;12:559. <https://doi.org/10.3390/en12030559>.
44. Weimann L, Gabrielli P, Boldrini A, Kramer GJ, Gazzani M. On the role of H₂ storage and conversion for wind power production in the Netherlands. In: Kiss AA, Zondervan E, Lakerveld R, Özkan L, editors. *Computer Aided Chemical Engineering*; Elsevier; 2019. p. 1627-32. <https://doi.org/10.1016/B978-0-12-818634-3.50272-1>.
45. Weimann L, Gazzani M, Kramer GJ, Matser J, Boldrini A. Evaluation of the potential for hydrogen and CCS in the decarbonization of the Dutch steel industry. ELEGANCY D5.2.5 2020.
46. Wenning QC, Madonna C, Kurotori T, Pini R. Spatial Mapping of Fracture Aperture Changes With Shear Displacement Using X-ray Computerized Tomography. *Journal of Geophysical Research: Solid Earth*. 2019;124:7320-40. <https://doi.org/10.1029/2019JB017301>.
47. Zahasky C, Jackson SJ, Lin Q, Krevor S. Pore Network Model Predictions of Darcy-Scale Multiphase Flow Heterogeneity Validated by Experiments. *Water Resour Res*. 2020;56:e2019WR026708. <https://doi.org/10.1029/2019WR026708>.
48. Zappone A, Rinaldi AP, Grab M, Obermann A, Claudio M, Nussbaum C, Wiemer S. CO₂ Sequestration: Studying Caprock And Fault Sealing Integrity, The CS-D Experiment In Mont Terri. Fifth CO₂ Geological Storage Workshop. 2018. <https://doi.org/10.3997/2214-4609.201803002>.

THERMODYNAMIC PROPERTIES OF THE BINARY MIXTURE OF MONOETHANOLAMINE AND CARBON DIOXIDE

Tobias Neumann^{1,2*}, Ida M. Bernhardsen², Hanna K. Knuutila², Jana P. Jakobsen², Roland Span¹

¹ Lehrstuhl für Thermodynamik, Ruhr University Bochum, 44801 Bochum, Germany

² Department of Chemical Engineering, Norwegian University of Science and Technology, 7491 Trondheim, Norway

* Corresponding author e-mail: T.Neumann@thermo.rub.de

Abstract

Homogenous densities in the liquid phase and VLE data were measured for the monoethanolamine and carbon dioxide system. The density data were obtained on five isotherms in a temperature range between 313.15 K and 353.15 K at atmospheric pressure and for two different loadings. VLE data were acquired on the isotherms 333.15 K, 353.15 K, and 373.15 K. These new data enabled the adjustment of an e-NRTL Gibbs excess model in combination with a cubic equation of state for CO₂ to describe the gas phase. The model represents the partial pressure of CO₂ above carbon dioxide loaded pure monoethanolamine well.

Keywords: Density, phase equilibrium, measurements, monoethanolamine, carbon dioxide, e-NRTL model

1. Introduction

The global warming caused by continuously increasing concentrations of the greenhouse gas carbon dioxide in the atmosphere has to stay below a temperature increase of 1.5 °C [1] in order to prevent severe consequences of an irreversible climate change. Decreasing the CO₂ pollutions from e.g. energy or chemical industries is the main goal. Here, a key technology is carbon capture and storage (CCS). For the separation of CO₂ from for example flue gases of power plants burning fossil fuels, amine solutions are one of the most promising and mature approaches [2]. One of the most analyzed amines that is often used as a benchmark is aqueous monoethanolamine (MEA).

In most calculations and simulations, the thermodynamic properties of the multicomponent mixture MEA + CO₂ + H₂O are represented with models, which are based on combinations of binary interactions of the contained components. These models are typically adjusted to ternary data. However, it is discussed if the binary parts itself are represented properly. To our knowledge there is no data available for the non-aqueous system of only MEA + CO₂ to check this or to enhance the adjustment of the ternary model. In order to extend the possibilities of model validation, data were experimentally measured for the binary mixture of MEA + CO₂. Homogeneous density data were measured for CO₂ loadings of 0.12 mol CO₂/mol MEA and 0.22 mol CO₂/mol MEA at atmospheric pressure on the isotherms 313.15 K, 323.15 K, 333.15 K, 343.15 K, and 353.15 K. The VLE data cover the three isotherms 333.15 K, 353.15 K, and 373.15 K. The latter ones were the basis for the development of a Gibbs excess energy model in form of the e-NRTL [3]. To describe the gas phase of the phase equilibrium data, a cubic Peng-Robinson equations of state [4] for CO₂ was used.

2. Materials and Methods

Carbon dioxide (CO₂, CAS: 124-38-9), with a purity of 99.999 % was provided by AGA and monoethanolamine (MEA, CAS: 141-43-5), with a purity of ≥99.5 %, was provided by Sigma-Aldrich. MEA was used as received. The lot numbers for MEA were STBJ2248 and STBH4366.

2.1 Density Measurements

Density measurements were performed using an Anton Paar DMA 4500 M density meter (Evjen et al. [5]). The density meter is equipped with a temperature-regulated magazine which can take up to 44 samples with 10 mL solution and an Xsample 452 for automatic filling, measuring, and cleaning. The measurements were conducted in the temperature range 313 K – 353 K and for each sample two density measurements were made, with only the average value being reported. Between every sample a control sample containing Millipore water was placed. The measurements were carried out under atmospheric pressure. However, no pressure control was used. The water measurements laid the basis for estimating the uncertainty of the density measurements.

2.2 Vapor-Liquid Equilibrium (VLE) Measurements

Vapor-liquid equilibrium (VLE) measurements were carried out using the same apparatus (Figure 1) as previously used by Hartono et al. [6]. The apparatus consists of a Büchi glass reactor and a stainless-steel gas holding vessel. The pressure in the reactor and in the vessel is measured by a pressure transmitter PTX5072, with a pressure range of 0 kPa – 600 kPa (uncertainty of ±0.15 % of the full scale), and the temperature of the gas and liquid phase is measured by Pt-100 thermometers (uncertainty of ±0.1 K).

Prior to generating VLE data for the MEA + CO₂ system, the VLE apparatus was validated by measuring the solubility of CO₂ in water. Since the experimental procedure used for validating the apparatus was slightly different from the one used to generate VLE data, the procedures are described separately.

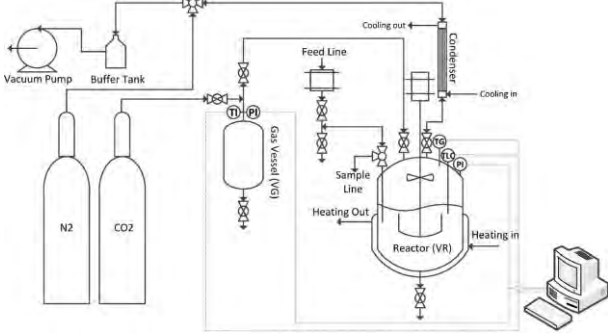


Figure 1: Illustration of the VLE apparatus. The figure is retrieved from Hartono et al. [6].

The solubility of CO₂ in water was measured in the temperature range of 313 K – 393 K and the experimental procedure was similar as described in Bernhardsen and Knuutila [7]. Briefly, the reactor was first evacuated at 293 K – 298 K, fed with a known amount of deionized water, and then evacuated again to remove potential air that entered the reactor during filling. The deionized water was then heated to desired temperatures in the range of 313 K – 393 K and, at each temperature, equilibrium was established. This resulted in a temperature-pressure profile before the addition of CO₂. At the highest experimental temperature, CO₂ was added from the gas holding vessel to the reactor. Then, the system was left to equilibrate and when equilibrium was reached, the temperature was decreased for new equilibrium points. This resulted in a temperature-pressure profile after the addition of CO₂.

At each temperature, the equilibrium partial pressure of CO₂ (p_{CO_2}) was calculated from total pressure measurements as following:

$$p_{CO_2} = p_{\text{after addition}} - p_{\text{before addition}} \quad (1)$$

This is based on the assumption that “the partial pressure of the liquid phase remains constant and is equal to the total pressure in the reactor before the first addition of CO₂” as stated in Kim et al. [8] or in Knuutila and Nannestad [9].

The concentration of CO₂ in the liquid phase, at each temperature, was calculated as given in Eq. (2) in which the amount of CO₂ added from the gas holding vessel, $n_{CO_2}^{\text{added}}$, and present in the gas phase of the reactor, $n_{CO_2}^g$, was calculated using the Helmholtz energy equation of state by Span and Wagner [10].

$$c_{CO_2} = \frac{n_{CO_2}^{\text{added}} - n_{CO_2}^g}{V_L} \quad (2)$$

The CO₂ solubility was expressed by Henry’s law constant as follows:

$$H_{CO_2} = \frac{p_{CO_2}}{c_{CO_2}} \quad (3)$$

2.2.1 VLE Measurements of the MEA + CO₂ System

VLE data for the MEA + CO₂ system were generated in the temperature range of 333 K – 373 K and the experimental procedure was the same as described in Hartono et al. [6]. Similar as above, the reactor was first evacuated, fed with a known amount of MEA, and once again evacuated. The experiments were carried out isothermally and under stirring at the experimental temperature, the system was left to equilibrate. When a stable temperature and pressure were obtained, CO₂ was added from the gas holding vessel to the reactor. The system was once again left to equilibrate before a new portion of CO₂ was added to the reactor. This procedure was repeated until the total pressure in the reactor at the experimental temperature was around 500 kPa. At the end of the experiment, a liquid sample was collected for CO₂ and amine analysis. On average, the CO₂ loading determined from the liquid analysis deviated 2 % relative to the loading from the calculated values.

The partial pressure of CO₂ was calculated from Eq. (4) by using information about the total pressure (p_{total}) and the pressure in the reactor before the addition of CO₂ (p_{initial}).

$$p_{CO_2} = p_{\text{total}} - p_{\text{initial}} \quad (4)$$

The concentration of CO₂ in the liquid phase was, as above, calculated using Eq. (2).

3. Theory and Model Description

The phase equilibrium is described in general by the equality of the chemical potential of each component i in each of the phases:

$$\mu_i^g = \mu_i^l \quad (5)$$

The gas phase can be described in the following manner:

$$\mu_i^g = RT \ln \frac{x_i^g \phi_i^g p}{p^{\text{ref}}} + \mu_i^{\text{ref}} \quad (6)$$

The gas constant $R = 8.314462618 \text{ J} \cdot \text{mol}^{-1} \cdot \text{K}^{-1}$ is defined in Newell et al. [11]. The reference pressure p^{ref} is set to 1 atm. To calculate the fugacity coefficients in the gas phase ϕ_i^g , a cubic Peng-Robinson equation of state by Peng and Robinson [4] is used. Since the models for the gas and liquid phase refer to different reference states this needs to be considered in the chemical potential with μ_i^{ref} . The description of the liquid phase is accomplished with an activity coefficient approach. It reads

$$\mu_i^l = RT \ln \frac{x_i^l \gamma_i}{\gamma_i^\infty} \quad (7)$$

The activity coefficients are derived from a Gibbs excess energy model in form of the e-NRTL according to Chen and Evans [3]. The model is based on the summation of short range interactions, which is a temperature dependent function of non-randomness and energy parameters and long range interactions describing electrostatic forces [3]. Similar to Monteiro et al. [12] and Putta et al. [13], the long range term is a Pitzer-Debye-Hückel term corrected by a Born term as published by Austgen et al. [14]. The parameters of the e-NRTL model

can be found in Table 1 and Table 2 in the appendix. Each of the components has an assigned reference state. For MEA the pure component reference state was chosen. Thus, $\gamma_{\text{MEA}}^{\infty}$ is equal to zero. CO₂ is at the reference state of a pure component in an infinite dilution of water. Because of this reference state and the general structure of the e-NRTL model, information about the contribution between water and these components are needed to calculate γ_i^{∞} . Therefore, all parameters containing water in Table 1 were adopted from a ternary e-NRTL model presented in Putta et al. [13]. It has to be noted that these parameters solely influence γ_i^{∞} because the mole fraction of water is equal to zero, which makes its influence vanish. The other parameters of the new e-NRTL model were adjusted to the VLE data reported in section 4.2 by using a particle swarm optimization algorithm from Monteiro et al. [12]. Depending on the reference state, the correction of the chemical potential in Eq. (6) for CO₂ is

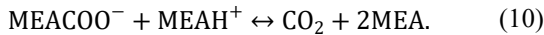
$$\mu_{\text{CO}_2}^{\text{ref}} = RT \ln \frac{p^{\text{ref}}}{H_{\text{CO}_2 \text{ in H}_2\text{O}}} \quad (8)$$

with the Henry's law constant $H_{\text{CO}_2 \text{ in H}_2\text{O}}$ taken from Carroll et al. [15] and for MEA

$$\mu_{\text{MEA}}^{\text{ref}} = RT \ln \frac{p^{\text{ref}}}{\varphi_{\text{s,MEA}} \cdot p_{\text{s,MEA}}} \quad (9)$$

with the saturation fugacity coefficient and saturation pressure of pure MEA at the specific temperature.

The mixture of MEA + CO₂ is assumed to be reactive also without the presence of water, as stated in Han et al. [16], which can be described with the following reaction equation



Hereby, MEAH⁺ and MEACOO⁻ are also at pure component reference state in an infinite dilution of water. Thus, the γ_i^{∞} used in Eq. (7) have to be calculated. The reaction is assumed to occur only in the liquid phase. Therefore, the components MEAH⁺ and MEACOO⁻ are not present in the gas phase and also do not require a correction of the chemical potential for the reference state in Eq. (6). The equilibrium constant K_{eq} was empirically determined during the adjustment of the e-NRTL parameters and reads:

$$K_{\text{eq}}(T) = \exp \left(A + \frac{B}{T} + C \cdot \ln(T/K) + D \cdot T \right) \quad (11)$$

with $A = -137.438$, $B = -6661.75 \text{ K}$,
 $C = 36.5588$, $D = -0.19082 \text{ K}^{-1}$

For the results shown in section 4.2, the chemical equilibrium was solved with an algorithm by Michelsen and Mollerup [17]. The algorithm minimizes the overall Gibbs energy of the system applying a Lagrange multiplier based approach. Further details can be found in Pinto [18].

4. Results

In the following section, the results of the density and VLE measurements are presented and discussed. The

VLE data are compared to the e-NRTL model with the newly adjusted parameters.

4.1 Density Data

The uncertainty and repeatability of the density measurements were 1 kg/m³ and 10⁻² kg/m³, respectively. The data can be found in Table 3 in the appendix and in Figure 2 with a comparison to densities of pure MEA.

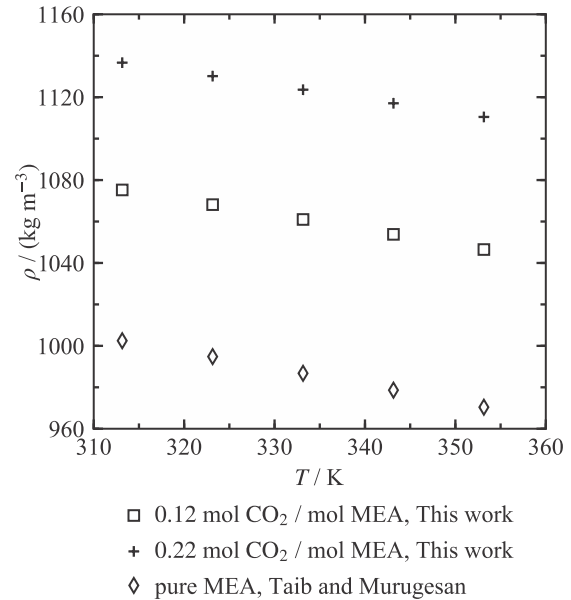


Figure 2: Homogeneous liquid densities for pure MEA [19] and CO₂ loaded 100 wt% MEA solutions at atmospheric pressure (listed in the appendix).

Similar to pure MEA, the density of the loaded solutions decreases with increasing temperature. As expected increasing the loading increases the density.

4.2 VLE Data and Model Comparison

The VLE experiments were validated by measuring the solubility of CO₂ in water in the temperature range of 40 °C – 120 °C (Figure 3, Table 4 in the appendix) and by comparing the data to the Henry's law correlation provided by Carroll et al. [15].

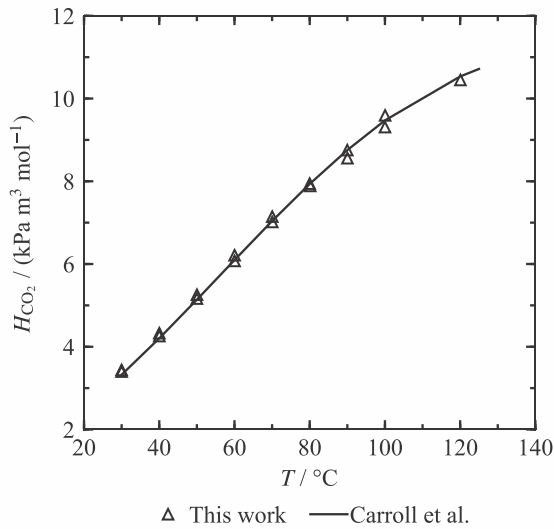


Figure 3: Experimental Henry's law constants for CO₂ in water in comparison to the correlation by Carroll et al. [15].

The average absolute relative deviation (AARD) between experimental and literature values [15] of the Henry's law constant was 1.4 % and the repeatability was on average 2 %. The VLE data are tabulated in the appendix. A comparison with the model developed in this work is shown in Figure 4.

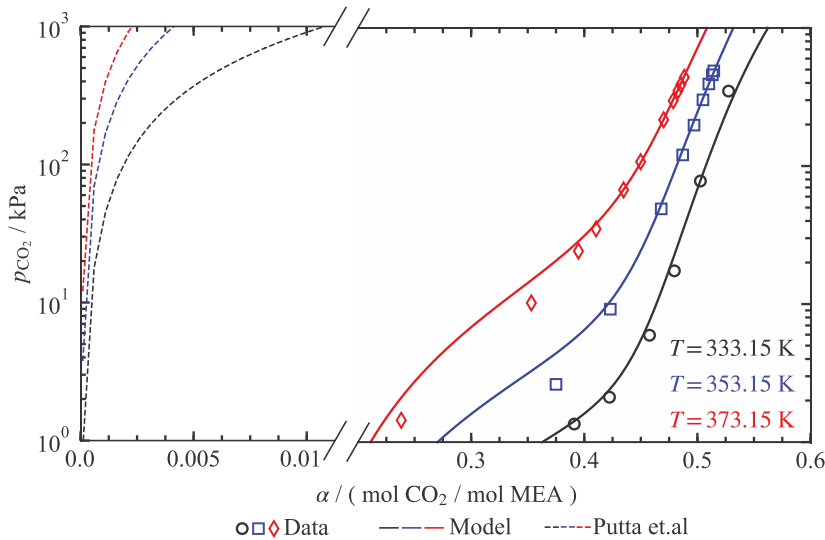


Figure 4: Experimental VLE data (listed in the appendix) in comparison to the model developed for the MEA + CO₂ system and corresponding binary parameters taken from Putta et al. [13].

The ternary model was fitted only for aqueous solutions of up to 60 wt% MEA. Since it is not possible to describe the data in Figure 4 with the corresponding binary e-NRTL parameters taken from the established e-NRTL model for the ternary system from Putta et al. [13] the adjustment of a binary model is necessary. The representation of the data with the new model is good with an AARD of 18.7 % in terms of pressure. The deviations decrease with increasing loading. Most of the data points are represented within the combined uncertainty with respect to the partial pressure of CO₂ of $u_c(p_{CO_2}) = 1.3$ kPa (cf. Table 5). Since the loading in the VLE data is greater than 0.5 mol CO₂ / mol MEA and due to the reaction equation in Eq. (10), also physical absorption has to occur. This is also captured by the new model as shown in the speciation diagram for one exemplary temperature in Figure 5.

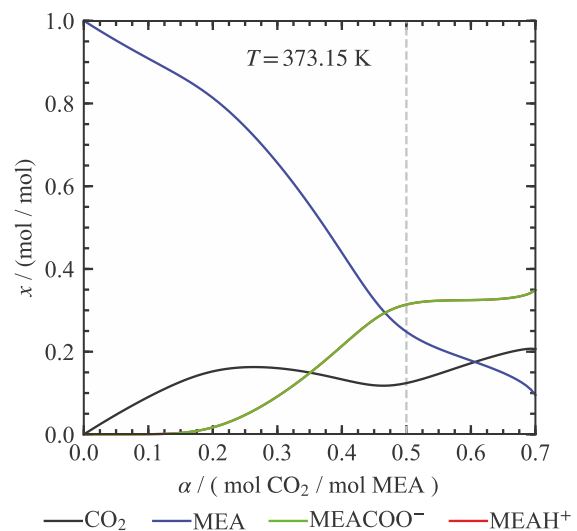


Figure 5: Speciation diagram of the developed model for the MEA + CO₂ system with respect to loading of CO₂.

The compositions of MEAH⁺ and MEACOO⁻ are the same because of the equality of charge. Therefore, the green and red line overlap exactly. The CO₂ is first physically absorbed until a loading of around 0.2 mol CO₂ / mol MEA when the reaction starts increasing the amount of MEAH⁺ and MEACOO⁻. This is also visible by the steeper decrease of MEA. At a loading of around 0.5 mol CO₂ / mol MEA, the concentrations of MEAH⁺ and MEACOO⁻ become almost constant and CO₂ starts to increase again.

5. Conclusion

The binary system of MEA + CO₂ was experimentally investigated and described in terms of a Gibbs excess model. Homogeneous density data points in the liquid phase were measured for two loadings at atmospheric pressure in a temperature range of 313.15 K – 353.15 K. The data were compared to densities of pure MEA. VLE measurements at atmospheric pressure ranges in loadings from 0.238 mol CO₂ / mol MEA to 0.528 mol CO₂ / mol MEA and the temperature from 333.15 K to 373.15 K. The combined standard uncertainty with regard to partial pressure of CO₂ is calculated to 1.3 kPa. An e-NRTL model for the liquid phase was adjusted to the VLE data considering the assumed reactive nature of the mixture forming protonated MEA and carbamate. The representation of the data with the model is qualitatively good. In most cases the experimental uncertainty could be matched. Since only the binary contributions from an established ternary model do not match the data an enhancement of the ternary models using the non-aqueous MEA + CO₂ data obtained in this work is an exciting idea for future work. The speciation shows a combination of chemically and physically absorbed CO₂ in the liquid, which is confirmed by the VLE data.

Acknowledgements

This publication has been produced with support from the NCCS Centre, performed under the Norwegian research program Centres for Environment-friendly Energy Research (FME). The authors acknowledge the following partners for their contributions: Aker Solutions, Ansaldo Energia, CoorsTek Membrane Sciences, EMGS, Equinor, Gassco, Krohne, Larvik Shipping, Lundin, Norcem, Norwegian Oil and Gas, Quad Geometrics, Total, Vår Energi, and the Research Council of Norway (257579/E20).

The authors thank Dr. D. Pinto for his support during the development of the e-NRTL model.

References

- [1] IPCC, Global warming of 1.5 °C, (2019). <https://www.ipcc.ch/sr15/>.
- [2] G.T. Rochelle, Amine Scrubbing for CO₂ Capture, *Science* (80-.). 325 (2009) 1652–1654. <https://doi.org/10.1126/science.1176731>.
- [3] C. -C Chen, L.B. Evans, A local composition model for the excess Gibbs energy of aqueous electrolyte systems, *AIChE J.* 32 (1986) 444–454. <https://doi.org/10.1002/aic.690320311>.
- [4] D.Y. Peng, D.B. Robinson, A New Two-Constant Equation of State, *Ind. Eng. Chem. Fundam.* 15 (1976) 59–64. <https://doi.org/10.1021/i160057a011>.
- [5] S. Evjen, R. Wanderley, A. Fiksdahl, H.K. Knuutila, Viscosity, Density, and Volatility of Binary Mixtures of Imidazole, 2-Methylimidazole, 2,4,5-Trimethylimidazole, and 1,2,4,5-Tetramethylimidazole with Water, *J. Chem. Eng. Data.* 64 (2019) 507–516. <https://doi.org/10.1021/acs.jced.8b00674>.
- [6] A. Hartono, R. Rennemo, M. Awais, S.J. Vevelstad, O.G. Brakstad, I. Kim, H.K. Knuutila, Characterization of 2-piperidineethanol and 1-(2-hydroxyethyl)pyrrolidine as strong bicarbonate forming solvents for CO₂ capture, *Int. J. Greenh. Gas Control.* 63 (2017) 260–271. <https://doi.org/10.1016/j.ijggc.2017.05.021>.
- [7] I.M. Bernhardsen, H.K. Knuutila, A review of potential amine solvents for CO₂ absorption process: Absorption capacity, cyclic capacity and pK_a, *Int. J. Greenh. Gas Control.* 61 (2017) 27–48. <https://doi.org/10.1016/j.ijggc.2017.03.021>.
- [8] I. Kim, K.A. Hoff, T. Mejdell, Heat of absorption of CO₂ with aqueous solutions of mea: New experimental data, *Energy Procedia.* 63 (2014) 1446–1455. <https://doi.org/10.1016/j.egypro.2014.11.154>.
- [9] H.K. Knuutila, Å. Nannestad, Effect of the concentration of MAPA on the heat of absorption of CO₂ and on the cyclic capacity in DEEA-MAPA blends, *Int. J. Greenh. Gas Control.* 61 (2017) 94–103. <https://doi.org/10.1016/j.ijggc.2017.03.026>.
- [10] R. Span, W. Wagner, A New Equation of State for Carbon Dioxide Covering the Fluid Region from the Triple-Point Temperature to 1100 K at Pressures up to 800 MPa, *J. Phys. Chem. Ref. Data.* 25 (1996) 1509–1596. <https://doi.org/10.1063/1.555991>.
- [11] D.B. Newell, F. Cabiati, J. Fischer, K. Fujii, S.G. Karshenboim, H.S. Margolis, E. de Mirandés, P.J. Mohr, F. Nez, K. Pachucki, T.J. Quinn, B.N. Taylor, M. Wang, B.M. Wood, Z. Zhang, The CODATA 2017 values of h, e, k, and N A for the revision of the SI, *Metrologia.* 55 (2018) L13–L16. <https://doi.org/10.1088/1681-7575/aa950a>.
- [12] J.G.M.-S. Monteiro, D.D.D. Pinto, S.A.H. Zaidy, A. Hartono, H.F. Svendsen, VLE data and modelling of aqueous N,N-diethylethanolamine (DEEA) solutions, *Int. J. Greenh. Gas Control.* 19 (2013) 432–440. <https://doi.org/10.1016/j.ijggc.2013.10.001>.
- [13] K.R. Putta, D.D.D. Pinto, H.F. Svendsen, H.K. Knuutila, CO₂ absorption into loaded aqueous MEA solutions: Kinetics assessment using penetration theory, *Int. J. Greenh. Gas Control.* 53 (2016) 338–353. <https://doi.org/10.1016/j.ijggc.2016.08.009>.
- [14] D.M. Austgen, G.T. Rochelle, X. Peng, C.C. Chen, Model of Vapor—Liquid Equilibria for Aqueous Acid Gas—Alkanolamine Systems Using the Electrolyte—NRTL Equation, *Ind. Eng. Chem. Res.* 28 (1989) 1060–1073. <https://doi.org/10.1021/ie00091a028>.
- [15] J.J. Carroll, J.D. Slupsky, A.E. Mather, The Solubility of Carbon Dioxide in Water at Low Pressure, *J. Phys. Chem. Ref. Data.* 20 (1991) 1201–1209. <https://doi.org/10.1063/1.555900>.
- [16] B. Han, Y. Sun, M. Fan, H. Cheng, On the CO₂ Capture in Water-Free Monoethanolamine Solution: An ab Initio Molecular Dynamics Study, *J. Phys. Chem. B.* 117 (2013) 5971–5977. <https://doi.org/10.1021/jp4022932>.
- [17] M.L. Michelsen, J. Mollerup, Thermodynamic Models: Fundamentals & Computational Aspects, Tie-

- Line Publications, 2007.
- [18] D.D.D. Pinto, CO₂ capture solvents: modeling and experimental characterization, Ph.D. Thesis, Norwegian University of Science and Technology, 2014.
- [19] M.M. Taib, T. Murugesan, Density, Refractive Index, and Excess Properties of 1-Butyl-3-methylimidazolium Tetrafluoroborate with Water and Monoethanolamine, *J. Chem. Eng. Data.* 57 (2012) 120–126. <https://doi.org/10.1021/jc2007204>.
- [20] K.S. Pitzer, Electrolytes. From dilute solutions to fused salts, *J. Am. Chem. Soc.* 102 (1980) 2902–2906. <https://doi.org/10.1021/ja00529a006>.

Appendix

Table 1: e-NRTL parameters of the short range terms for the system MEA + CO₂ with water being apparent for the reference state of infinite dilution. The non-randomness parameters were fixed to 0.2.

Molecular Parameters: $a_{m,m}$ and $b_{m,m}$			
$a_{\text{H}_2\text{O},\text{CO}_2}$	0 ^a	$b_{\text{H}_2\text{O},\text{CO}_2}$	0 ^a
$a_{\text{H}_2\text{O},\text{MEA}}$	-1.2024 ^a	$b_{\text{H}_2\text{O},\text{MEA}}$	281.3086 ^a
$a_{\text{CO}_2,\text{H}_2\text{O}}$	0 ^a	$b_{\text{CO}_2,\text{H}_2\text{O}}$	0 ^a
$a_{\text{CO}_2,\text{MEA}}$	0.86900	$b_{\text{CO}_2,\text{MEA}}$	-2997.52
$a_{\text{MEA},\text{H}_2\text{O}}$	2.7657 ^a	$b_{\text{MEA},\text{H}_2\text{O}}$	-1147.8744 ^a
$a_{\text{MEA},\text{CO}_2}$	1.62828	$b_{\text{MEA},\text{CO}_2}$	-1616.26
Molecule-Salt Parameters: $a_{m,c/a}$ and $b_{m,c/a}$			
$a_{\text{H}_2\text{O},\text{MEA}^+/\text{MEACOO}^-}$	-12.4523 ^a	$b_{\text{H}_2\text{O},\text{MEA}^+/\text{MEACOO}^-}$	1017.78 ^a
$a_{\text{CO}_2,\text{MEA}^+/\text{MEACOO}^-}$	-8.92601	$b_{\text{CO}_2,\text{MEA}^+/\text{MEACOO}^-}$	-4129.05
$a_{\text{MEA},\text{MEA}^+/\text{MEACOO}^-}$	-13.7033	$b_{\text{MEA},\text{MEA}^+/\text{MEACOO}^-}$	-2761.98
Salt-Molecule Parameters: $a_{c/a,m}$ and $b_{c/a,m}$			
$a_{\text{MEA}^+/\text{MEACOO}^-, \text{H}_2\text{O}}$	1.7486 ^a	$b_{\text{MEA}^+/\text{MEACOO}^-, \text{H}_2\text{O}}$	-496.199 ^a
$a_{\text{MEA}^+/\text{MEACOO}^-, \text{CO}_2}$	8.29695	$b_{\text{MEA}^+/\text{MEACOO}^-, \text{CO}_2}$	-3157.30
$a_{\text{MEA}^+/\text{MEACOO}^-, \text{MEA}}$	14.6325	$b_{\text{MEA}^+/\text{MEACOO}^-, \text{MEA}}$	-3310.86

^a Adopted from Putta et al. [13].

Table 2: e-NRTL parameters of the long range terms for the system MEA + CO₂ with water being apparent for the reference state of infinite dilution.

Distance of closest approach ρ_{Dist}	14.9 ^b		
Born radius r_{Born}	$3 \cdot 10^{-10}$ ^a		
Dielectric constant parameters [14]: $D_i = A_i + B_i(1/T - 1/C_i)$			
i	A_i	B_i / K	C_i / K
H ₂ O	78.54	31989.38	298.15
CO ₂	1.6	0	298.15
MEA	35.76	14836	273.15

^a Adopted from Putta et al. [13].

^b Adopted from Pitzer [20].

Table 3: Experimental density data for the MEA + CO₂ system at various temperatures.

α / (mol CO ₂ / mol MEA)	ρ / (kg/m ³)				
	313.15 K	323.15 K	333.15 K	343.15 K	353.15 K
0.12	1075	1068	1061	1054	1046
0.22	1137	1130	1124	1117	1110

Table 4: Measured Henry's constant for CO₂ in water.

T / K	H_{CO_2} / (kPa m ³ mol ⁻¹)
303.14	3.40
303.14	3.44
313.16	4.26
313.16	4.33
323.16	5.16
323.17	5.26
333.17	6.07
333.18	6.21
343.19	7.02
343.19	7.15
353.27	7.89
353.14	7.94
363.18	8.56
363.13	8.75
373.16	9.31
373.20	9.59
393.22	10.45
303.14	3.40
303.14	3.44
313.16	4.26

Table 5: Experimental vapor-liquid equilibrium data for the MEA + CO₂ system. In the table, T is temperature, p is pressure, α is the CO₂ loading with the combined standard uncertainty $u_c(\alpha)$ and w_{CO_2} is the mass fraction of CO₂ in the loaded solution with the combined standard uncertainty $u_c(w_{\text{CO}_2})$.^a

T / K	$p_{\text{tot}} / \text{kPa}$	$p_{\text{CO}_2} / \text{kPa}$	$\alpha / (\text{mol CO}_2 / \text{mol MEA})$	$u_c(\alpha) / (\text{mol CO}_2 / \text{mol MEA})$	w_{CO_2}	$u_c(w_{\text{CO}_2})$
333.15	2.5					
333.15	3.8	1.4	0.391	0.01	0.2199	0.0002
333.15	4.6	2.1	0.422	0.01	0.2333	0.0002
333.15	8.4	5.9	0.458	0.01	0.2480	0.0002
333.15	19.9	17.4	0.480	0.01	0.2568	0.0002
333.15	80.3	77.9	0.503	0.01	0.2659	0.0002
333.15	351.5	349.0	0.528	0.01	0.2754	0.0002
353.15	3.8					
353.15	6.4	2.6	0.375	0.02	0.2127	0.0003
353.15	13.0	9.2	0.423	0.02	0.2336	0.0003
353.15	52.8	49.0	0.468	0.02	0.2523	0.0003
353.15	124.2	120.4	0.487	0.02	0.2598	0.0003
353.15	201.6	197.8	0.497	0.02	0.2636	0.0003
353.15	305.5	301.6	0.505	0.02	0.2668	0.0003
353.15	397.2	393.3	0.510	0.02	0.2688	0.0003
353.15	462.1	458.2	0.513	0.02	0.2699	0.0003
353.15	492.9	489.1	0.515	0.02	0.2704	0.0003
373.15	9.3					
373.15	10.8	1.4	0.238	0.01	0.1465	0.0002
373.15	19.5	10.2	0.353	0.01	0.2029	0.0002
373.15	33.5	24.2	0.395	0.01	0.2215	0.0002
373.15	44.3	35.0	0.410	0.01	0.2282	0.0002
373.15	76.5	67.2	0.435	0.01	0.2385	0.0002
373.15	116.6	107.3	0.450	0.01	0.2448	0.0002
373.15	225.5	216.2	0.470	0.01	0.2531	0.0002
373.15	306.8	297.5	0.479	0.01	0.2564	0.0002
373.15	361.0	351.7	0.483	0.01	0.2581	0.0002
373.15	398.0	388.7	0.485	0.01	0.2591	0.0002
373.15	9.2					
373.15	17.4	8.2	0.323	0.01	0.1887	0.0002
373.15	37.5	28.3	0.398	0.01	0.2229	0.0002
373.15	81.0	71.9	0.436	0.01	0.2391	0.0002
373.15	253.8	244.6	0.474	0.01	0.2545	0.0002

^a Standard uncertainties u are $u(T) = 0.1 \text{ K}$ and $u(p_{\text{tot}}) = 0.9 \text{ kPa}$, and the combined standard uncertainties u_c is $u_c(p_{\text{CO}_2}) = 1.3 \text{ kPa}$. Due to small variations in α , three decimals are given.

ARTIFICIAL INTELLIGENCE FOR WELL INTEGRITY MONITORING BASED ON EM DATA

Seyed Ehsan Hosseini^{1*}, Simone Zonetti², Anouar Romdhane³, Bastien Dupuy³, Børge Arntsen¹

¹ NTNU, Trondheim, Norway

² SINTEF Digital, Oslo, Norway

³ SINTEF Industry, Trondheim, Norway

* Corresponding author e-mail: seyed.e.hosseini@ntnu.no

Abstract

Monitoring of integrity of plugged and abandoned (P&A'ed) wells is of interest for the oil and gas industry and for CO₂ storage. The purpose of this study is to develop artificial intelligence (AI)-based approaches to detect anomalies or defects when monitoring permanently plugged wells. The studied solution is based on the analysis of electromagnetic (EM) data. We consider an offshore setting where the EM signal is generated in presence of a P&A'ed well and the resulting electric field is recorded at the seafloor. Numerical simulations are used to train an AI algorithm to classify the modelled EM features into predefined well integrity classes. We consider four scenarios: (1) no well, (2) well with three 20 meters thick cement barriers of thickness, (3) well with three cement barriers of 60 meters thickness, and (4) well with three cement barriers of 100 meters thickness. Convolutional neural networks (CNNs) are tested as the AI algorithm in this study. After training the algorithm on 80% of the data, it shows an accuracy of 95.36% on the test data. P&A'ed well integrity monitoring currently remains limited to local observation and symptom identification, but this study shows that there is great potential for developing remote non-invasive well integrity monitoring techniques.

Keywords: *P&A'ed well integrity, non-invasive monitoring, electro-magnetic fields, Artificial intelligence, Convolutional Neural Networks (CNNs)*

1. Introduction

A well needs to be permanently plugged and abandoned (P&A'ed) when its productive life is over. Several cement plugs are installed in discrete sections of the wellbore. They seal the well structure both vertically and horizontally [1]. Moreover, the wellhead is detached, and the top portion of the well is severed several meters below the seafloor (Figure 1). Nowadays, this technique is used to prevent long-term leakage.

Heat, pressure, corrosion, seismic activity, subsidence, and formation creep exert strong mechanical loads on the wellbore construction over time [2]. It is estimated that well which reached 15 years of age might have a 50% probability of leakage [3]. It is reported that 0.9-3.7 kt yr⁻¹ of CH₄ is emitted from 1,792 wells in an area of 20,000 km² in the UK sector of the central North Sea, suggesting that the large number of wells in North Sea likely constitute a major source of methane [4]. In Pennsylvania, 6% of the methane emissions have been associated to leakage from old wells [5]. At the Groningen field in the Netherlands, 1 out of 29 wells was found to be leaking [6].

There is a need for monitoring the integrity of P&A'ed wells. As the wellhead and top pipes are removed and buried in sediments, it is difficult and expensive to use logging tools to monitor well integrity. Thus, "post-mortem" monitoring of leakage is the only possible option with observations of bubbles or growth of

bacterial mats at the seafloor in the vicinity of the well [7].

Although recent studies emphasize developing non-invasive well integrity monitoring methods [2][8], all of the current methods are variations of permanent sensing systems which monitor some parameters such as temperature, strain, pressure, chemical and acoustic sensing. They can be used both in a point sensing manner or in a distributive manner along the entire well.

There are some options for non-invasive well integrity monitoring that can be developed. One of them is acoustic systems which use guided waves for high-resolution imaging. Although these systems are already used for monitoring the pipelines in aircraft industry [9][10], they have not been customized for well integrity monitoring. They can be used at the surface of the casing or in the well's internal casing. As P&A'ed wells are cut below the seafloor, these methods are more difficult to implement because they require access to well casings.

Another option for both temporarily and permanently plugged wells is based on electric and magnetic fields. They have already seen great success in geophysical imaging of the subsurface. Magnetotellurics (MT), magnetometric resistivity (MMR), electrical resistivity tomography (ERT), and controlled-source electromagnetics (CSEM) are based on using passive or active electric-magnetic fields in different frequency bands. These systems have already some commercial applications such as hydrocarbon exploration [11], large

scale crustal imaging [12], and CO₂ storage monitoring [13][14]. Nowadays, researchers show their interest to use these systems for well integrity measurements. One example is using CSEM surveys for casing integrity measurements where steel casing is used as electrodes during CSEM surveys [15][16].

In this paper, we propose an AI algorithm which senses changes in a well structure based on seabed electric field. In the proposed method detailed in section 2, the electric field at the seabed is simulated using a finite-element simulator. We consider four scenarios, with no well in one of them, and thickness of cement plugs inside the wellbore changed for the three others. Then, a carefully designed CNN algorithm is trained to discriminate them. The methodology is described in section 2 and the results presented and discussed in section 3.

2. Method

2.1 Geometry

Here we consider a simplified well geometry consisting of a 700-meter cylinder with radius of 20 cm (Figure 2). The inner hole is filled with 9 cm brine/sea water, 1 cm metal casing, and 10 cm of cement. In addition, horizontal elements that simulate the presence of cement plugs can be introduced in the well. The well elements are placed within a large, cylindrical modelling domain with radius of several hundreds of meters. The modelling domain is layered horizontally to include a 100 m air layer at the top, a 100 m sea water layer below, and a 900 m layer of rock formation, which can fully enclose the well element. The well-head can be placed at any location at or below the sea floor. An additional geometric layer surrounds the modelling domain to apply Infinite Element Domains (absorbing boundary conditions) features in the simulation software.

2.2 Materials

In the implementation of the model, all material properties are frequency independent. This is an approximation that will be relaxed in subsequent work in order to optimize the detected signal depending on the frequency of the source. Furthermore, the materials are assumed to be perfectly homogeneous and isotropic. This can be easily relaxed by introducing both diffuse inhomogeneity and material property gradients, especially in the rock formation. Table 1 gives a summary of the EM material properties for the well elements.

2.3 Electromagnetic signals

Electromagnetic signals are excited in the model via a 1 m long perfectly conducting dipole, which can be placed anywhere in the geometry. By simulating tangential and radial polarizations for the transmitter, we can take advantage of field symmetry to reduce the modelling domain to 1/2 of the original, reducing computational requirements. The vertical position of the dipole is a free parameter, and it has been fixed to 30 m below the water surface. The position of the source and receivers can be

adapted depending on EM measurements providers. With no dependence of material properties on frequency nor field strength, the problem is linear with respect to the field amplitude, and therefore the transmitter is driven with a constant current of nominal amplitude. The operating frequency is correspond to 0.5 Hz. A schematic representation of the geometry used is provided in Figure 2. The electrical properties of the different components are also given in Table 1.

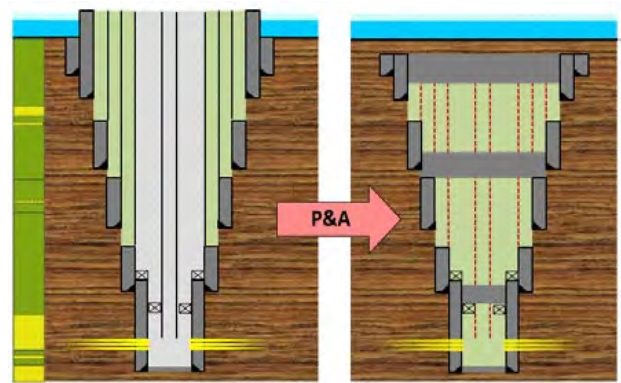


Figure 1: A typical well before (left) and after (right) permanent well plugging [2]. Cement barriers are grey in the figure.

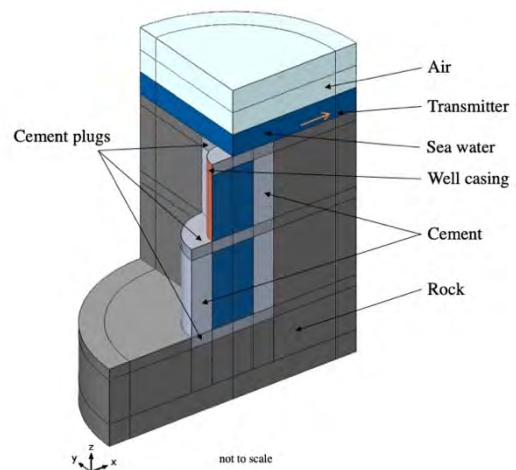


Figure 2: Schematic representation of the model's geometry, including well casing, three cement plugs and a well head at the sea floor.

Table 1: Material properties.

Material	Electrical properties	
	Conductivity [S/m]	Relative permittivity [F/m]
Rock formation	0.50	6
Cement	0.33	2.20
Steel	62500	1
Sea Water	3	78.40
Air	0	1

2.4 FEM implementation

The model is implemented using the commercial Finite Element Method (FEM) software COMSOL Multiphysics [17]. Given the operating frequency of 0.5 Hz, resulting in a local wavelength much larger than the size of the modelling domain, inductive effects can be neglected in the first approximation, and one can take advantage of the simplified formulation of Maxwell's equations implemented in the Electric Currents interface. The Infinite Element Domains feature can be the external domains of the geometry, allowing simulated fields to vanish at infinity and avoid fields reflections at the sides of the simulation model. The electrically thin steel casing at the interface between sea water (inside the well) and cement is simulated using the dedicated Distributed Impedance boundary condition, which effectively simulates the 1 cm thick material as a 2D surface, thus eliminating the need of meshing the thickness of this layer. The interior of the model is meshed using triangular elements on the sea floor surface (Figure 3), on which a tetrahedral mesh is built in the sea water domain. Mesh elements are kept small enough close to the well to ensure a sufficient discretization of the immediate vicinities of the well itself. The annulus element around the sea floor uses a mapped mesh, while the rest of the mesh is swept vertically from the top and bottom boundaries of the water layer.

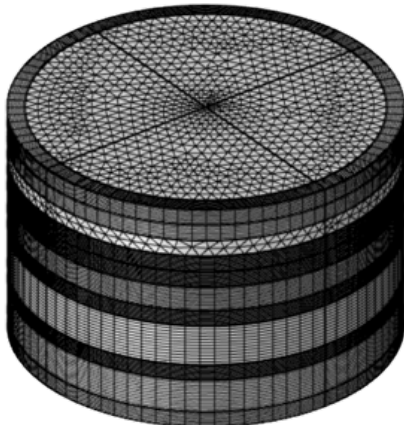


Figure 3: Example of meshed modelling domain for FEM simulations.

2.5 AI algorithm

CNN [18] is the AI algorithm which is used in this study for classification among four different scenarios including: (1) Case A: No well, (2) Case B: A well with three 20-meter cement plugs inside the wellbore, (3) Case C: a well with three 60-meter cement plugs inside the wellbore, and (4) Case D: a well with three 100-meter cement plugs inside the wellbore. The aim of the AI algorithm is to discriminate among these four scenarios using as input the electric field simulated at the seabed. The CNN structure used in this research consists of 3 blocks of convolution and 2 fully connected layers with 64 and 4 neurons respectively (Figure 4). Each of the convolutional blocks has ReLU activation function [19], and a Max-Pooling of 2 by 2 [20]. The last layer has

SoftMax activation function to report the uncertainty associated with the obtained classification. For more generalization of the network, Dropout is employed [21]. Dropout rate is 0.2 in each convolutional block (between convolution and Max-pooling layer), and it is 0.5 before the last layer.

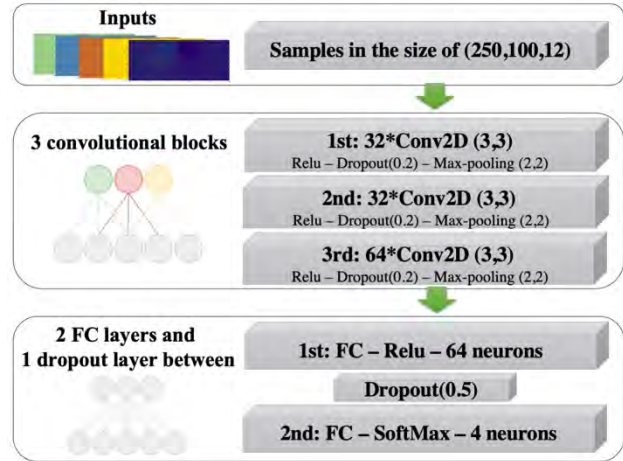


Figure 4: Proposed convolutional neural network structure.

2.6 Preprocessing and data augmentation

Since neural networks need some data to learn, different orientations of transmitter dipole antenna are used to augment the data. For each scenario, the antenna direction is changed from x-direction to y-direction with a step of one degree. Thus, there are 91 electric field data for each scenario (364 samples overall). 12 features are taken out from these electric fields including: real part, imaginary part, magnitude, and phase of electric fields in each direction. Since it would be hard to measure electric field at the seabed, we constrain the span of received electric field. We do this by cropping an area with the size of 250 by 100 meters around the well. Then, all features get sparse by setting 7/8 of values in x direction and 4/5 of values in y direction to zero (meaning no measurements at those locations). Finally, values are scaled between -1 and +1 to allow for better training in our neural network (Figure 5). These data are labeled and used to train and test our classification method. One feature map of an input sample is provided in Figure 6 for illustration.

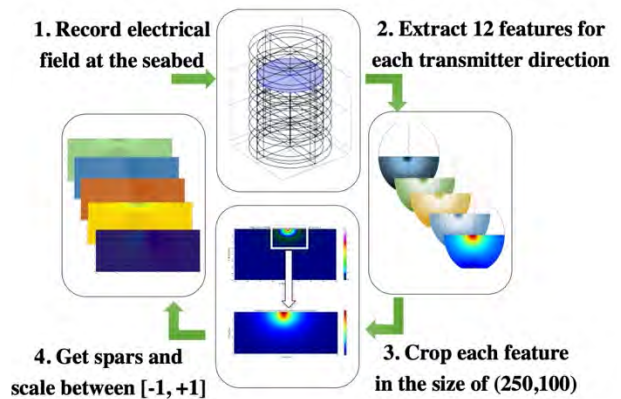


Figure 5: Preprocessing workflow.

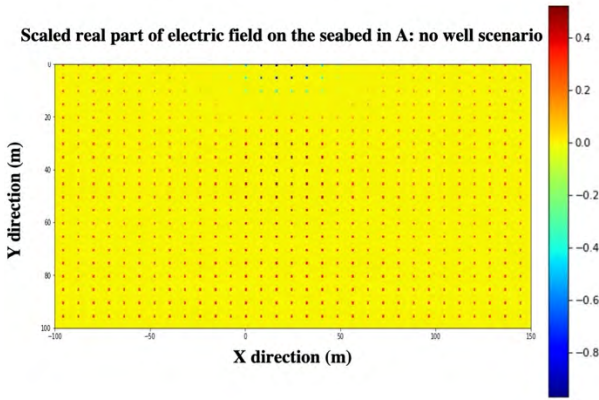


Figure 6: Example of an input feature to the CNN.

3. RESULTS

After simulating electric fields with FEM, CNN is trained in 50 epochs with batch-size of 16. To ensure that no overlap occurs between training and test content, the augmented data was divided into 80% (291 samples) for training and 20% (73 samples) for testing. Since artificial neural networks use randomness (random initial weights, shuffling, etc.) during each training epoch, a repeated stratified five-folded cross-validation is introduced to build more robust results. It means that training and testing were implemented 5 times with different test data each time. Moreover, the whole process is repeated and implemented 30 times, resulting in a more reliable evaluation of the model performance. The overall confusion matrix for all the test data after repeated stratified five-folded cross-validation is shown in Table 2. This table tells how our classification method predicts each class label after training is performed.

Table 2: Derived confusion matrix. A: no well, B: a well with three 20-meter cement plugs inside the wellbore, C: a well with three 60-meter cement plugs inside the wellbore, and D: a well with three 100-meter cement plugs inside the wellbore.

		Predicted Label			
		A	B	C	D
True Label	A	2526	71	1	132
	B	19	2685	1	25
	C	13	5	2651	61
	D	96	56	27	2551

The classifier is tested on 10920 test samples which consists of 364 unique test samples. These unique test samples are evaluated on 30 different CNNs. Table 2 shows a very low misclassification rate as most samples are classified correctly. Although the AI algorithm shows more misclassification in class (D), it shows a robust performance, and it can classify each scenario very well. In order to understand how well each scenario is classified, a normalized confusion matrix (based on each

row) is drawn in Table 3 with the corresponding percentages.

Table 3: Normalized confusion matrix. Numbers are provided in percentage in the table. A: no well, B: a well with three 20-meter cement plugs inside the wellbore, C: a well with three 60-meter cement plugs inside the wellbore, and D: a well with three 100-meter cement plugs inside the wellbore.

		Predicted Label			
		A	B	C	D
True Label	A	92.53	2.60	0.03	4.84
	B	0.70	98.35	0.03	0.92
	C	0.48	0.18	97.11	2.23
	D	3.52	2.05	0.99	93.44

Table 3 shows how well our method classifies each scenario. For instance, 92.53% of real data in scenario (A) is predicted as scenario (A). Similarly, 2.60% of real data in scenario (A) is classified as scenario (B). By looking at this table, it is obvious that scenario (A) and (D) are more prone to misclassification as the misclassification error is higher. Evaluation metrics of our classifier are provided in Table 4 (numbers in percentage). Table 4 shows classification metrics not only in each class but also in average which is based on macro- and micro-average method. Since micro-average method is more reliable than macro-average, we report our final results based on it. The overall accuracy of our classification method is 95.36% with standard deviation of 1.45% after training 30 times on different initialized models.

Table 4: Evaluation metrics of our classifier (percentages). A: no well, B: a well with three 20-meter cement plugs inside the wellbore, C: a well with three 60-meter cement plugs inside the wellbore, and D: a well with three 100-meter cement plugs inside the wellbore.

	Precision	Recall	F1-score	Accuracy
A	95.18	92.53	93.83	96.96
B	95.31	98.35	96.81	98.38
C	98.92	97.11	98.00	99.01
D	92.13	93.44	92.78	96.36
Macro-Ave	95.38	95.36	95.37	97.68
Micro-Ave	95.36	95.36	95.36	95.36

4. Conclusions

Remotely inspecting a subsea well and its structure remains limited to symptom identification around the well. By using a simple geometry and the power of deep neural networks, this study shows that it would be possible to classify plugging thickness under the seabed from recorded EM fields. The accuracy of 95.36% in our neural network-based classifier proves this claim. Our proposed method can distinguish among four different

scenarios related to changes in a wellbore by using just finite sparse electric fields at the seabed.

We aim at developing a generalized AI anomaly detection algorithm that uses different types of data (seismic, EM, etc.) recorded remotely to detect the changes in the cement plugs of a well and not just classifying some scenarios. Moreover, we will not limit the method to one specific well and we will consider more realistic models. The effects of data noise and uncertainty related to the rock formation properties will be analyzed in the future work. Evaluating other types of data, like acoustic data for well monitoring and analyzing the method in detection of some leaking scenarios will also be considered.

Although the assumptions used like considering a simple geometry or using known medium properties in this study, we believe that it will pave the way for further investigating the potential of non-invasive well integrity monitoring techniques that would be applicable also for P&A'ed wells. Accordingly, it would take the industry from a reactive state (symptom detection) to proactive state (take action before leakage occurs).

Acknowledgements

This work is performed with support from the Research Council of Norway (TOPHOLE project Petromaks2-KPN 295132) and the NCCS Centre (NFR project number 257579/E20).

References

- [1] Vrålstad, T., Saasen, A., Fjær, E., Øia, T., Ytrehus, J. D., & Khalifeh, M. (2019). Plug & abandonment of offshore wells: Ensuring long-term well integrity and cost-efficiency. *Journal of Petroleum Science and Engineering*, 173, 478-491.
- [2] A. Lavrov, M. Torsæter, *Physics and Mechanics of Primary Well Cementing*, Springer 2016.
- [3] C. Brufatto, J. Cochran Aberdeen, S. Lee Conn David Power, S. Zaki Abd Alla El-Zeghaty, B. Fraboulet, T. Griffin, S. James Trevor Munk, F. Justus Santa Cruz, B.R. Joseph Levine, C. Montgomery, D. Murphy, J. Pfeiffer Houston, T. Tiraputra Pornpoch, L. Rishmani Abu Dhabi, From Mud to Cement Building Gas Wells, *Oilf. Rev.* (2003) 62–76.
- [4] Böttner, C. et al., “Greenhouse gas emissions from marine decommissioned hydrocarbon wells: leakage detection, monitoring and mitigation strategies”, *International Journal of Greenhouse Gas Control*, 100 (September 2019), p. 103119.
- [5] T. H. Darrah, A. Vengosh, R. B. Jackson, N. R. Warner, R. J. Poreda. Noble gases identify the mechanisms of fugitive gas contamination in drinking-water wells overlying the Marcellus and Barnett Shales. *PNAS* 111,39 (2014) 14076-14081.
- [6] G. Cardon de Lichtbuer. Methane leakage from abandoned gas wells in the Netherlands, reality or fiction Master Thesis University of Utrecht, 2017-2018. Available at: <https://dspace.library.uu.nl/bitstream/handle/1874/356894/Thesis%20Guillaume.pdf?sequence=2&isAllowed=y>
- [7] L. Vielstädte, M. Haeckel, J. Karstens, P. Linke, M. Schmidt, L. Steinle and K. Wallmann. Dealing with legacy wells: Implications from subsea leakage along abandoned North Sea gas wells. Presented at 11th IEAGHG Monitoring Network Meeting, 13-15th June 2017. Available at: https://ieaghg.org/docs/11mon/Session11_Talk1_IEAGHG_lvielstaedte.pdf
- [8] Pinto, H.L. and P.M. Gouvea. Well Integrity Monitoring: Challenges and Perspectives. in *OTC Brasil. 2013: Offshore Technology Conference*.
- [9] Rose, J.L., A baseline and vision of ultrasonic guided wave inspection potential. *Journal of pressure vessel technology*, 2002. 124(3): p. 273-282.
- [10] Rocha, B., C. Silva, and A. Suleman, Structural health monitoring system using piezoelectric networks with tuned lamb waves. *Shock and Vibration*, 2010. 17(4-5): p. 677-695.
- [11] Constable, S. (2010) ‘Ten years of marine CSEM for hydrocarbon exploration’, *Geophysics*, 75(5).
- [12] Bai, D. et al. (2010) ‘Crustal deformation of the eastern Tibetan plateau revealed by magnetotelluric imaging’, *Nature Geoscience*, 3(5), pp. 358–362.
- [13] Michelle Ellis and Martin Sinha, (2010), "The potential of controlled source electromagnetic surveying in CO₂ storage monitoring," *SEG Technical Program Expanded Abstracts*: 843-847.
- [14] Kang, S. et al. (2015) ‘MCSEM inversion for CO₂ sequestration monitoring at a deep brine aquifer in a shallow sea’, *Exploration Geophysics*, 46(3), pp. 236–252.
- [15] Tietze, K., Ritter, O., Veeken, P., & Verboom, B. (2015). CSEM for monitoring reservoir oil-saturation using a borehole-to-surface set-up. In *SEG Technical Program Expanded Abstracts 2015* (pp. 937-941). Society of Exploration Geophysicists.
- [16] Daley, T. M., Marchesini, P., Wilt, M., Cook, P., Freifeld, B. M., & Lawton, D. (2017). Containment and Monitoring Institute- Baseline Geophysics for CO₂ Monitoring with Crosswell Seismic and Electromagnetics. In *EAGE/SEG Research Workshop 2017*.
- [17] COMSOL Multiphysics® v. 5.4. www.comsol.com. COMSOL AB, Stockholm, Sweden.
- [18] Yamashita, R., Nishio, M., Do, R.K.G. et al. Convolutional neural networks: an overview and application in radiology. *Insights Imaging* 9, 611–629 (2018).
- [19] G. E. Dahl, T. N. Sainath, and G. E. Hinton, “Improving deep neural networks for lvcsr using rectified linear units and dropout,” in *ICASSP*, 2013, pp. 8609–8613.
- [20] J. Nagi et al., "Max-pooling convolutional neural networks for vision-based hand gesture recognition," *2011 IEEE International Conference on Signal and Image Processing Applications (ICSIPA)*, Kuala Lumpur, 2011, pp. 342-347, doi: 10.1109/ICSIPA.2011.6144164.
- [21] Nitish Srivastava et al., “Dropout: A Simple Way to Prevent Neural Networks from Overfitting,” *Journal of Machine Learning Research* 15 (2014): 1929–1958.

A WORKFLOW FOR REGIONAL EXPLORATION OF CO₂ STORAGE SITES IN SALINE AQUIFERS

Christopher Lloyd^{1*}, Mads Huuse¹, Bonita J Barrett², Andrew M W Newton³

¹ Department of Earth and Environmental Sciences, University of Manchester, Manchester, M13 9PL, UK

² Equinor ASA, Equinor Research Centre, Arkitekt Ebbells veg 10, 7053, Ranheim, Norway

³ School of Natural and Built Environment, Queen's University Belfast, Belfast, BT7 1NN, UK

* Corresponding author e-mail: Christopher.lloyd-2@manchester.ac.uk

Abstract

Regional screening for CO₂ storage sites within saline aquifers can benefit from play-based, risk segment mapping approaches developed by the exploration industry. Here, we outline a regional workflow focusing on containment and capacity for identification of storage sites that can be applied to any aquifer. A case study is presented of the northern Utsira Fm. aquifer (northern North Sea). A large-scale exploration dataset is utilised, including regional 3D, depth-migrated broadband seismic reflection data, full waveform inverted velocity data, and 141 exploration wells. A containment confidence (CC) matrix is presented as an approach to assess the seal and overburden, whereby matrix elements are mapped to constrain the most secure areas of the aquifer. Seal internal geometry, sandstone presence and sandstone connectivity are elements assessed, but other elements (e.g. faulting) could also be incorporated, if applicable. A full characterisation of the aquifer that considers 3D variability of reservoir properties is performed to inform capacity estimations. We incorporate regional porosity, intra-reservoir barriers and baffles and fill-to-spill analysis to identify prospective storage sites. Finally, minimum depth (700 m), minimum capacity (5 Mt CO₂) and positive CC cut-offs are applied. The optimal region for storage is in the northeast, where four prospects are identified, with a combined storage capacity of 53 Mt CO₂ (using 5% storage efficiency). Additional capacity could be achieved through use of the reservoir between adjacent prospects. These prospects can be put forward for detailed appraisal. Moreover, the mapping can form the basis of static and dynamic models, well plans and mitigation options. The workflow presented provides a systematic approach for regional CO₂ storage site screening that can be readily applied by geoscientists across the industry, with typical exploration-scale datasets.

Keywords: Capacity, containment, and regional exploration

1. Introduction

Carbon Capture and Storage (CCS) is now regarded as a 'necessity, not an option' to reach global greenhouse gas emissions targets [1]. Numerous studies have evaluated the storage potential of saline aquifers across a variety of basins, showing that many have gigaton storage capacities [e.g. 2-4]. As many of these aquifers lie in prolific hydrocarbon provinces, there are abundant hydrocarbon exploration and production data that can be re-purposed for evaluation of CO₂ storage targets. With regional-scale data and exploration-style approaches, detailed and pragmatic screening can be performed upon such aquifers to highlight the most advantageous regions for storage. Prospects can be identified and storage capacity estimates refined with a rigorous assessment of an aquifer's spatial variability [5]. Moreover, 'containment confidence' (the inverse of leakage risk) can be mapped for fuller constraint on security, through regional evaluation of the seal and overburden [6]. Parallel and systematic assessments of capacity and containment are essential inputs to models, to ensure realistic and well-constrained simulations for injectivity and migration predictions.

Here, we outline a regional workflow for CO₂ storage aquifer characterisation that addresses both the seal (containment) and the reservoir (capacity). The approach could be applied and adapted to any basin, but is showcased here with the northern Utsira Formation in the northern North Sea [5-6]. A 3D broadband seismic survey and 141 exploration wells are used to deliver a series of maps and ultimately, a portfolio of prospects.

2. Requirements for CO₂ Storage

Individual CO₂ storage sites require detailed assessment across various scales before they are deemed 'injection-ready'. Each site requires analysis of: 1) *containment*, ensuring CO₂ will remain in the reservoir through a sufficient seal; 2) *capacity*, outlining the volume of CO₂ that can be stored and in which area; and 3) *injectivity*, defining the extent, timescale and impact of fluid flow through well design and development planning.

In the same way that basin-scale exploration is the typical first step to identify hydrocarbon prospects, regional screening is required to identify potential CO₂ storage sites within an aquifer. The basic principles of play analysis and mapping for hydrocarbons (source,

reservoir, seal) can be applied to CO₂ storage by adjusting the play elements (reservoir and seal equating to capacity and containment) and placing more emphasis on the overburden. Migration concepts are also transferable, as potential fluid pathways within and out of the aquifer must be constrained, including seal bypass systems, such as faults or connected sandstones. As such, the skills and risk-based approaches used in hydrocarbon exploration can be utilized for CO₂ storage site screening and form the basis of the containment and capacity workflow presented.

Injectivity is not assessed here, but upon identification of a suitable prospect, dedicated data collection for CO₂ storage from a well will provide information that includes, but is not limited to, seal integrity, sedimentology and pressure. Injectivity can then be rigorously assessed through dynamic modelling of the storage site and provide input to well planning.

2.1 Containment

The primary objective of a containment assessment is to evaluate the seal and overburden to establish whether CO₂ would remain in the reservoir. A secondary objective is to understand the potential migration route of CO₂ should it leave the reservoir. Core data are necessary to understand seal integrity, but legacy core data rarely cover seal rock intervals. As such, seal analysis in the screening phase is limited to seismic and other well data, which are suitable for assessment of: 1) seal distribution and thickness; 2) seal internal geometry; and 3) seal bypass systems. These form the basis of a regional assessment of containment confidence (CC) [6].

It is important to assess and map the presence of seal bypass systems, but also constrain their vertical connectivity through the overburden. This is achieved through subdivision of the stratigraphy above the aquifer into two units: 'Seal Interval' and 'Overburden Interval' (Fig. 1). The Seal Interval is the zone directly above the aquifer, defined as the minimum seal thickness required for CO₂ storage [6]. The absolute thickness will vary according to the aquifer. For example, the advised

minimum seal thickness in the North Sea is 50 m [2], which is used here. A lesser thickness could be sufficient for containing CO₂, but prior to detailed data collection, a pragmatic approach is to take a conservative minimum.

The Overburden Interval comprises the stratigraphy from the top of the Seal Interval to either the seabed, a shallower potential CO₂ storage reservoir, or a theoretical maximum limit of migration. Accordingly, the Overburden Interval has variable thickness, and may be absent where there is only a Seal Interval separating two potential CO₂ storage reservoirs.

A regional CC assessment allows identification of the best and worst areas in terms of storage security and so should be one of the main considerations during exploration. It should be performed on the full aquifer, and not be limited to local storage sites. This is because CO₂ could migrate contrarily to predictions/models, and potential migration routes outside of the local injection area should be pre-emptively understood.

2.2 Capacity

Capacity is the assessment of how much CO₂ could theoretically be injected and is typically calculated based on available pore volume, either for the full aquifer [e.g. 2] or for all structural traps [e.g. 8], or through simulated injection until the pressure limit is reached [e.g. 9]. Although suitable for broad estimates, these approaches do not consider 3D variability of reservoir character, hence do not differentiate between high and low quality areas of the aquifer, which is addressed in the workflow presented here.

Our capacity workflow for the aquifer considers: 1) presence and extent of intra-aquifer mudstones; 2) porosity distribution; 3) identification of structural closures; and 4) storage capacity estimations. Upon integration with the CC assessment, a portfolio of ranked prospects across the aquifer are presented. Trapping potential outside of individual prospects is not considered, but could be included when considering storage in a network of traps through a fill-to-spill process.

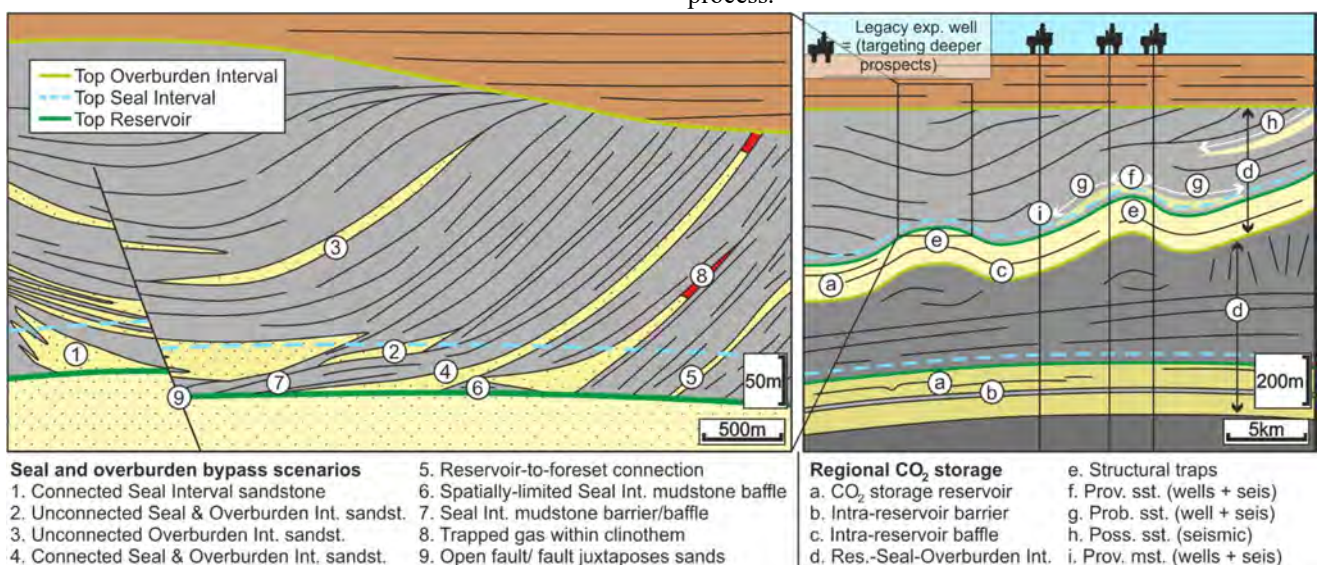


Figure 1] Schematic for regional exploration for CO₂ storage prospects - scenarios of seal bypass for the containment analysis (left) and definitions of intervals and sandstone presence (right). Prov. = proven; prob. = probable; poss. = possible; seis. = seismic.

3. Dataset and Data Preparation

The Neogene northern Utsira Formation was studied due to its large size, good reservoir properties and proximity to the current CO₂ storage license offshore Norway (Fig. 2). A 35,400 km² full 3D BroadSeis™ seismic reflection survey acquired and provided by CGG was used for the analysis (Fig. 2). The original two-way time data were converted to depth by CGG, using advanced full-waveform inversion [10]. The FWI velocity cube has been re-purposed to evaluate porosity distribution (Section 4.2.1). The seismic data were coupled with 141 exploration wells (Fig. 2). Most of the wells are clustered around hydrocarbon provinces, which combined with the shallow depth of the studied interval (<1600 m TVD) means the distribution and quality of relevant well data are highly variable. A pre-interpreted lithology column was extracted from the TGS Facies Map Browser for each well, based on petrophysical logs and completion reports (Fig. 3). The interpretations are simplified for this study into ‘sandstone’, ‘mudstone’ and ‘other’ to focus on permeable versus impermeable lithologies and to allow simpler correlation between wells [6] (Fig. 3).

Prior to data analysis, a seismic stratigraphic framework was established. The reservoir limits, and seal and overburden stratigraphy were manually mapped with the seismic data, informed by well formation tops and previously published seismic sections for the reservoir [e.g. 11] and overlying stratigraphy [e.g. 12]. Intra-unit surfaces were mapped semi-automatically with Paleoscan™ [5, 6, 13]. These were repeatedly checked for geological accuracy and were iteratively corrected. Seismic volume attributes were extracted onto mapped surfaces to assess geomorphological features.

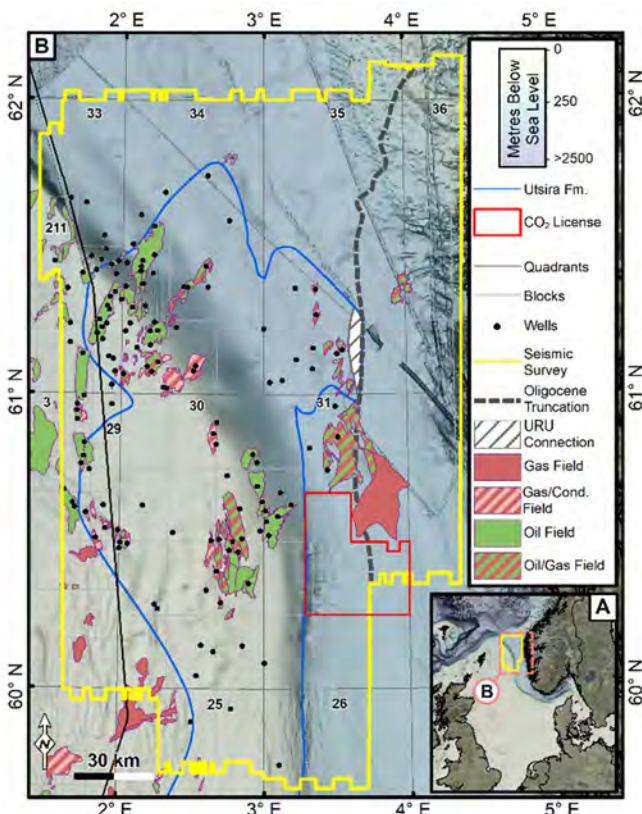


Figure 2 | Dataset for the northern Utsira Fm., northern North Sea. Only studied exploration wells (141) are shown.

4. Containment and Capacity Workflows

The parallel workflows for containment and capacity analysis are presented in Figure 3. They can be performed simultaneously, however, the resultant containment confidence map is required as an input to the prospect identification stage and should be completed before storage capacity estimations.

4.1 Containment Confidence (CC) Assessment

Here, we outline the approach for the Containment Confidence (CC) assessment, applied to the Utsira Fm. To assess containment, seal geometric properties and seal bypass systems must be considered. To do this, we assess and map: 1) seal internal geometry; 2) Seal Interval sandstone presence; 3) Overburden Interval sandstone presence; and 4) sandstone connectivity. Each are scored according to a matrix (Table 1). Additional (or fewer) elements could also require analysis depending on the geology above a given aquifer. We also perform a regional shallow gas interpretation and cross-reference it with the identified overburden migration paths.

Within the matrix, a positive CC value is assigned if the component increases our confidence in containment, e.g. a full mudstone succession in the Seal Interval. A negative CC value is assigned if the component decreases our confidence in containment, e.g. sandstones in the Seal Interval. A CC value of 0 is assigned where there are either no data, or the component does not affect CC. Each element is scored relatively to the other elements, as they present variable contributions to containment. For example, a sandstone body within the Seal Interval (CC = -7) is considered to compromise containment more than a sandstone body in the Overburden Interval (CC = -1) (Table 1). Each of the four elements are regionally mapped to show the spatial distribution of CC according to that element (Fig. 4A-4D). The final step is to overlay and sum the individual element maps to give an overall CC evaluation (Fig. 4E). The final CC scores in the matrix are arbitrary numbers and dependent on the number of elements analysed in the matrix and the perceived containment contribution by the interpreter, but represent a relative, semi-quantitative approach to distinguish areas across the aquifer according to their CC.

4.1.1 Seal Internal Geometry

An assessment of seal internal geometry is only applicable to reservoirs that are overlain by non-parallel stratigraphy, such as the Utsira Fm., which is overlain by a clinoform succession. Dipping stratigraphy (e.g. clinoform foresets) in the Seal Interval juxtapose more sub-units against the reservoir than flat-lying stratigraphy. This increases the risk of a sub-unit with a high permeability zone (e.g. a sandy channel; Fig. 1) being in contact with the reservoir and so is assigned a negative CC score (CC = -3). A low negative CC score is assigned relative to the other elements (Table 1), as seal internal geometry is a minor contributor to containment. This is because it only increases the likelihood of seal bypass, rather than presenting evidence of a permeable route. Flat-lying/parallel-to-reservoir stratigraphy is assigned a neutral CC score of 0.

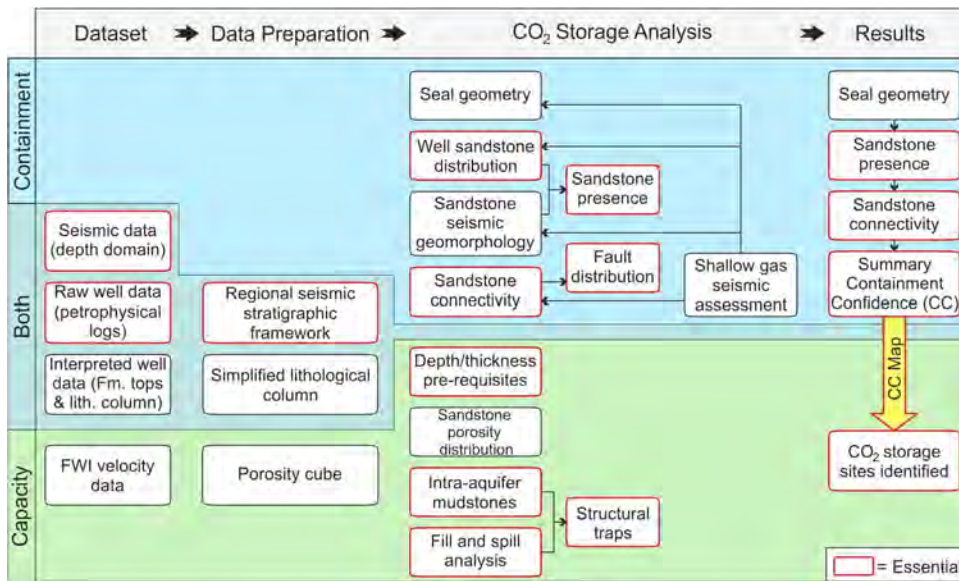


Figure 3| Workflow for containment and capacity assessment of an aquifer for CO₂ storage. The essential steps are highlighted (red perimeter). Fault presence is essential but as we encounter no major faults through the containment interval for the Utsira Fm., it is not considered here. The final output of the containment assessment (CC map) is used in the capacity assessment. The non-essential steps apply to the Utsira Fm. assessment but could also be applicable elsewhere.

The geometry of the Seal Interval is here assessed by creating a pseudo-surface at the top of the Seal Interval (50 m above the Utsira Fm. in our study). Seismic amplitudes at this surface were extracted, and in map-view, reveal the geometry of the intersection between the surface and the stratigraphy at that level. For example, alternating positive-negative amplitude bands are apparent where the surface intersects dipping stratigraphy. Broad areas of a single polarity occur where the surface intersects flat-lying or parallel-to-reservoir stratigraphy (Fig. 1 & 4A). For the Utsira Fm., dipping stratigraphy is recorded at the southeast and southwest margins. Flat-lying stratigraphy dominates in the northern and particularly north-eastern areas (Fig. 4A).

4.1.2 Sandstone Presence

Sandstone presence is essential to the CC assessment because it (and other permeable lithologies) can facilitate seal bypass. Mapping the presence of sandstone in the Seal Interval also acts to represent the absence of mudstone. Sandstones in the Overburden Interval could be migration routes if they are connected (Fig. 1). Sandstones bodies can be identified in well data and interpreted in the seismic data through correlations and identification of seismic geomorphologies that resemble sandstone features, e.g. submarine fans.

The CC score for sandstone presence depends upon two factors: 1) the stratigraphic position of the sandstones relative to the reservoir, and 2) the evidence for the sandstone. In terms of stratigraphic position, the CC assessment considers the Seal and Overburden Intervals separately, as sandstones that are proximal to the reservoir provide a greater risk to containment. For the evidence type (in the Seal Interval), the CC score is assigned according to whether the sandstones are ‘proven’, ‘probable’ or ‘possible’, based on the

informing data (Fig. 1). ‘Proven’ sandstones are those that can be correlated between wells with the seismic, and so reduce containment confidence the most (CC = -7). ‘Probable’ sandstones are an extrapolation of ‘proven’ sandstones beyond well control using seismic (CC = -5). ‘Possible’ sandstones have no well penetrations but have a seismic response or geomorphological expression indicative of a ‘proven’ or ‘probable’ sandstone (CC = -3) [6]. Positive CC scoring areas are where mudstone has either been ‘proven’ (CC = +7) or is ‘probable’ (CC = +5), based on the same classification as sandstones. There is no specific seismic evidence of a mudstone in the studied interval, and therefore there is not a ‘possible’ mudstone CC score. Where there is no lithological evidence and the lithology is unknown, the CC score is considered unchanged (CC = 0). For the Overburden Interval, presence of sandstone alone (without connectivity) is not considered to greatly compromise CC. Therefore, a CC value of -1 is assigned for evidence of sandstones, and +1 for evidence of mudstones.

Our dataset contains abundant well data, which allowed the areas of high sandstone content to be highlighted. We mapped sandstone bodies away from the wells with the seismic data, also utilising volume attributes, including sweetness, variance and spectral (frequency) decomposition [6]. Every high amplitude clinoform was mapped and assessed to identify potential sandy features. Several individual and amalgamated channels and lobes were identified on the Norwegian (east) and East Shetland Platform (ESP, west) sides of the basin, which could act as up-dip fluid migration pathways. In the Seal Interval, sandstones were primarily encountered in the west and southeast. Mudstones dominate in the northeast (Fig. 4B). In the Overburden Interval sandstones were encountered across most of the Utsira Fm. (Fig. 4C).

Element	Containment Confidence (CC) Score											
	-8	-7	-6	-5	-4	-3	-2	-1	0	+3	+5	+7
Seal Internal Geometry (SIG)						Dip			Flat			
Seal Interval Sandstones (SIS)		Prov.		Prob.		Poss.			Unknown		Mud Prob.	Mud Prov.
Overburden Interval Sandstones (OIS)								Pres.	Unknown	None		
Sandstone Connectivity (SC)	A-B-C			A-B			B-C		None			

Table 1| Containment Confidence (CC) matrix for the Utsira Formation. Prov. = proven; prob. = probable; poss. = possible.

4.1.3 Sandstone Connectivity

It is important to constrain the connectivity of the reservoir with overlying permeable routes that could allow CO₂ migration through the overburden. Connectivity is facilitated through amalgamation of sandstones or faults/fractures. Well data provide direct insight into connectivity at point locations. Away from the wells, seismic data can be used to map the thickness and amplitude of intervening mudstones; where thickness falls to zero (below seismic resolution) or amplitude response falls (reduced acoustic impedance contrast), connectivity between the sandstones is assumed.

In the CC matrix, connectivity is assessed between the reservoir (A), Seal Interval sandstones (B) and Overburden Interval sandstones (C) (Table 1). Where there is a full connection (A-B-C), CC is greatly reduced (CC = -8), as it implies a full potential migration path. Connectivity of A-B reduces CC (CC = -5), but not as substantially, because migration through the Overburden Interval is inhibited. Connectivity of B-C implies no connection to the reservoir but is still assigned a low negative CC score (CC = -3) as sandstones in the Seal Interval could be connected through sub-seismic migration routes. The CC score is only applied to the lowermost sandstone (e.g. in the Seal Interval), as this is the root of the connection. High connectivity was observed in the west around the ESP, where connected sandstones could be traced from the reservoir and up the clinoform foresets (Fig. 4D).

4.1.4 Shallow Gas Seismic Assessment

Shallow gas accumulates in sandstones and fractured mudstones, and can migrate through the stratigraphy using the same migration routes that injected CO₂ could follow, hence represent valuable observations to support the CC assessment. Strictly, shallow gas is not an element

that contributes to containment, rather it highlights other elements, and as such, is not included in the matrix.

Shallow gas can be identified in seismic data, mostly due to its effect on seismic velocity and acoustic impedance. Typical diagnostic features include anomalously high, negative (in this dataset) amplitudes, seismic attenuation, chimneys and pockmarks. However, interpretation can be cryptic due to other phenomena producing gas-like responses, such as glacial tunnel valleys causing velocity disturbances [14] or amplitude anomalies from tuning [15]. Mostly, interpreted gas pockets are not verified as wells are placed to avoid them, however, gas encounters in wells can be used to identify gas-prone layers.

Here, we take a regional approach using only the seismic data; a more forensic approach could be applied to include the wells. We undertook a broad screening using a minimum amplitude (i.e. high negative) and variance extraction of the seismic data. We mapped anomalies above an amplitude threshold taken from a known, nearby gas accumulation (Peon discovery) [6]. Individual anomalies were assessed and cross-checked with mapped sandstones from the CC assessment. Interpreted gas-sands coincided with clinoform truncations and slope channels in the southeast, and within antiforms <200 m above the Utsira Fm. in the northwest, mostly coinciding with areas of high sandstone presence (Fig. 4D) [6].

4.1.5 Summary CC Map

Summation of each individual element map produces a regional summary CC map (Fig. 4E). This shows the best and worst regions of the aquifer for containment. The areas with the highest positive CC (best areas) are in the central and northern parts of the Utsira Fm, where there are flat-lying, mudstone-dominated stratigraphy in the Seal Interval (seal internal geometry: CC = 0; Seal Interval sandstone presence: CC = +5 or +7). Sandstones

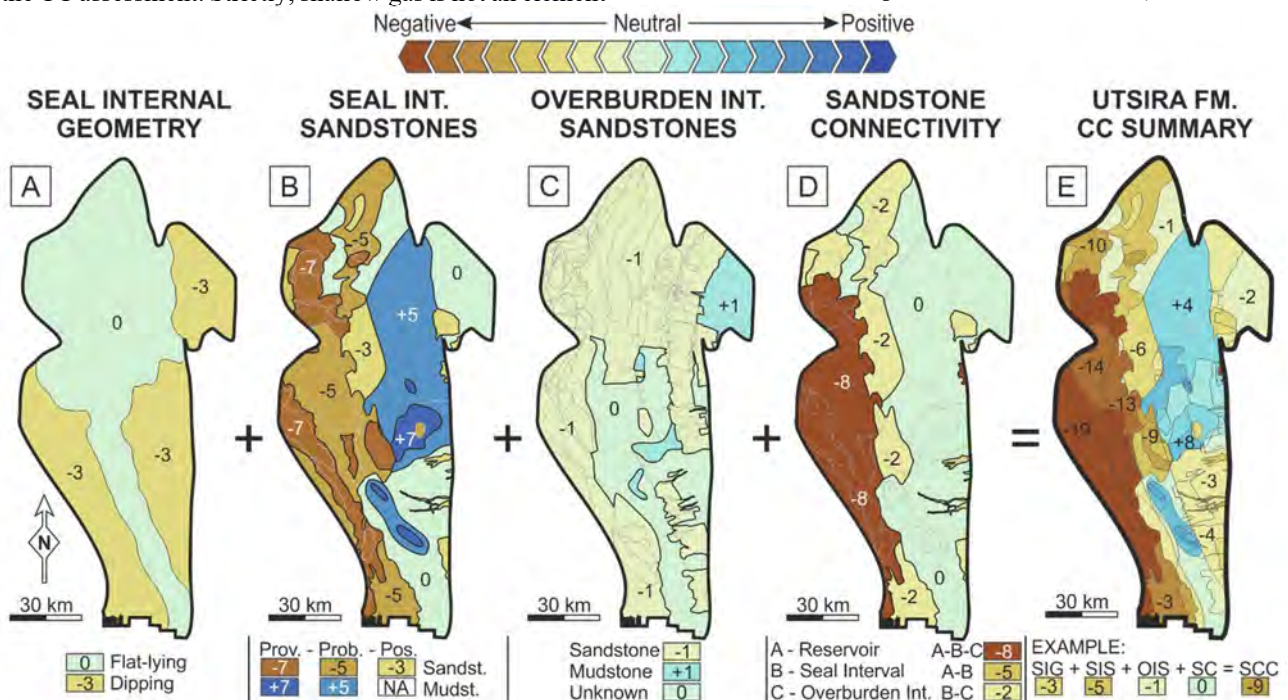


Figure 4 | Containment Confidence (CC) assessment for the Utsira Formation. A) Seal Internal Geometry (SIG), B) Seal Internal Sandstones (SIS), C) Overburden Interval Sandstones (OIS), D) Sandstone Connectivity (SC), E) Utsira Fm. CC Summary (SCC). Scoring scheme is shown in Table 1. Int. = interval; sandst. = sandstone; mudst. = mudstone.

are present in the Overburden Interval, but they are unconnected (Overburden Interval sandstone presence: CC = -1; sandstone connectivity: CC = 0) [6].

The area with the highest negative CC (worst area), is the west of the Utsira Fm. There is a difference in seal internal geometry between the southwest (dipping stratigraphy, seal internal geometry CC = -3) and northwest (flat-lying stratigraphy, seal internal geometry CC = 0). Sandstones are present in the Seal Interval that are predominantly connected between the reservoir and Overburden Interval (Seal Interval sandstone presence: CC = -7 or -5; sandstone connectivity: CC = -8). The CC summary map is used to inform the identification of suitable prospects, but it could also be used for plume migration modelling and mitigation planning.

4.2 CO₂ Capacity Assessment

For the capacity assessment, 3D variability of the aquifer is considered. Here, we assessed the porosity distribution, and the presence and extent of intra-aquifer mudstones. Structural traps were identified at the interfaces to seal rocks/barriers, apex depths were considered and storage capacity was estimated for individual prospects. The results were combined with the CC analysis to identify suitable CO₂ storage prospects, which could go forward to more detailed appraisal.

4.2.1 Porosity Distribution

Porosity is a fundamental parameter in storage capacity calculations and represents reservoir quality. Petrophysical logs were used with the FWI velocity cube to create a 3D porosity volume of the Utsira Fm. sandstones (Fig. 5A). This approach allows for porosity estimations in areas with limited well data. First, density and sonic logs were converted into porosity and velocity logs, respectively [6]. The relationship between these two properties for sandstones in the reservoir was calculated for the studied wells that contained both logs (20 wells). The resultant linear function (Equation 1; R = -0.41), was applied to the velocity cube, converting it to porosity. A separate equation relating porosity to velocity is required for deeper stratigraphy below our studied interval.

$$\text{Eq. 1: } \text{Porosity} = -0.00015251 \times \text{velocity} + 0.663317$$

An average porosity of 35% was observed across the Utsira Fm., which is consistent with the average porosity at the Sleipner injection site in the southern Utsira Fm. [7]. Porosity decreases towards the northeast as the formation becomes deeper and further from the main sediment source in the southwest (ESP). Little vertical variability in porosity was observed within the Utsira Fm., but in a broader study of the full Utsira-Skade Aquifer, the underlying Skade Fm. showed a reduced average porosity compared to the Utsira Fm. (33%) [6].

4.2.2 Intra-Aquifer Mudstone Analysis

Intra-aquifer impermeable layers can act as baffles, temporarily disrupting the CO₂ plume during injection, or barriers, inhibiting further vertical migration and trapping the CO₂. On a regional scale, it is important to constrain their thickness and extent to establish which of

the two are more likely. Regardless, mapped mudstones are also important inputs to geomodels.

Compilation of well data across the region provides a general overview of mudstone distribution. For the Utsira Fm., we measured the thickest intra-formation mudstone, along with the total net-to-gross of the interval in each well, and overlaid these onto a thickness map of the reservoir (Fig. 5B). This approach allowed quick screening to highlight mudstone-prone areas for more detailed mapping and assessment.

All the mudstones in the Utsira Fm. (in our study area) are <50 m (minimum seal thickness) and expected to only act as baffles to flow. There are few seismically-resolvable mudstones within the Utsira Fm, as most fall within a single wavelet. However, where mudstones could be mapped, channels were identified through sharp and marked reductions in amplitude. Channel erosion of the mudstone allows connection between underlying and overlying sandstones, thus resulting in a reduced acoustic impedance contrast [5]. As such, the mudstones are also not considered to be laterally-extensive. As part of a larger-scale study, considering the whole Utsira-Skade Aquifer, intra-aquifer mudstones were shown to be prevalent and in some areas, thick enough (>50 m) to contain CO₂ (top Skade Fm.) [5].

4.2.3 Fill-and-Spill Analysis

As the intra-reservoir mudstones were deemed to be baffles, only the top Utsira Fm. was considered suitable for long-term sealing of CO₂. Structural closures and potential CO₂ migration paths were mapped at this level. For this, we used a fill-and-spill simulation using Permedia™. We used 800 random source (injection) points to cover the full Utsira Fm. From each source point, fluid migrates up-dip beneath the sealing surface until it is trapped in a closure or reaches the boundary of the map (Fig. 5C). This method only considers structural gradients to determine fill-and-spill. It does not consider physical and chemical processes that act over different timescales, and their impact on fluid migration and trapping.

It is important to quality-check the simulation results, as velocity pulls-ups or onlaps onto underlying mounds (the latter of which are prevalent in our study area) can be erroneously plotted as closures. The authenticity of each individual closure was validated using seismic cross-sections.

The analysis revealed that most of the largest closures are in the centre of the Utsira Fm., and that migration paths mainly extend towards the southwest (Fig. 5C).

4.2.4 Storage Capacity Estimation

The effective storage capacity of each prospect was calculated using the following equation:

$$\text{Eq. 2: } \text{Effective storage capacity} = \text{GRV} \times \text{Porosity} \times N:G \times \text{CO}_2 \text{ density} \times SE$$

Gross Rock Volume (GRV, in MM Sm³) includes the rock within the closure (structural trap) and immediately underlying reservoir, where other trapping mechanisms could act. Porosity was taken from the closure apex,

which approximated to the average for the prospect. Sandstone net-to-gross (N:G) was taken from the closest or most appropriate well. A CO₂ density of 500 kg/Sm³ (from 800 m depth) was used [2]. Storage efficiency (SE) is the fraction of the reservoir pore space that can be filled by CO₂ [8]. Locally, this fraction depends on several factors (including reservoir character, geometry and conditions) and varies from 3-40% [16]. We used a SE of 5%, from calculated values in the same formation at Sleipner (in 2013) [17], but higher values could be used if only considering the GRV within the structural trap [5].

4.2.5 CO₂ Storage Prospect Portfolio

Not all of the identified traps are suitable for storage and so some were discarded, i.e. those with: 1) an apex depth <700 m below sea level; 2) a negative CC score; and 3) <5 Mt CO₂ storage capacity (Fig. 5E). The depth limit was applied because CO₂ would leave the supercritical phase at shallow depths. The 800 m depth contour is also plotted on Fig. 5E, which could be used as a more conservative depth limit. A 5 Mt capacity cut-off was used to focus on the largest targets for injection. However, smaller structural traps could be utilized through a fill-and-spill approach during injection.

There are four prospects in the Utsira Fm. that are deemed suitable in terms of containment and capacity (Fig. 5E). The storage capacities of these are 32, 9, 7 and 5 Mt CO₂, but could be greater using a higher storage efficiency. These should be the targets for further detailed appraisal and could be used in isolation or as a network of traps.

The results are not directly comparable to existing full aquifer studies [e.g. 2, 9 and 10], because we provide site-specific storage capacities. Moreover, we only consider traps as prospects if their capacity is >5 Mt CO₂.

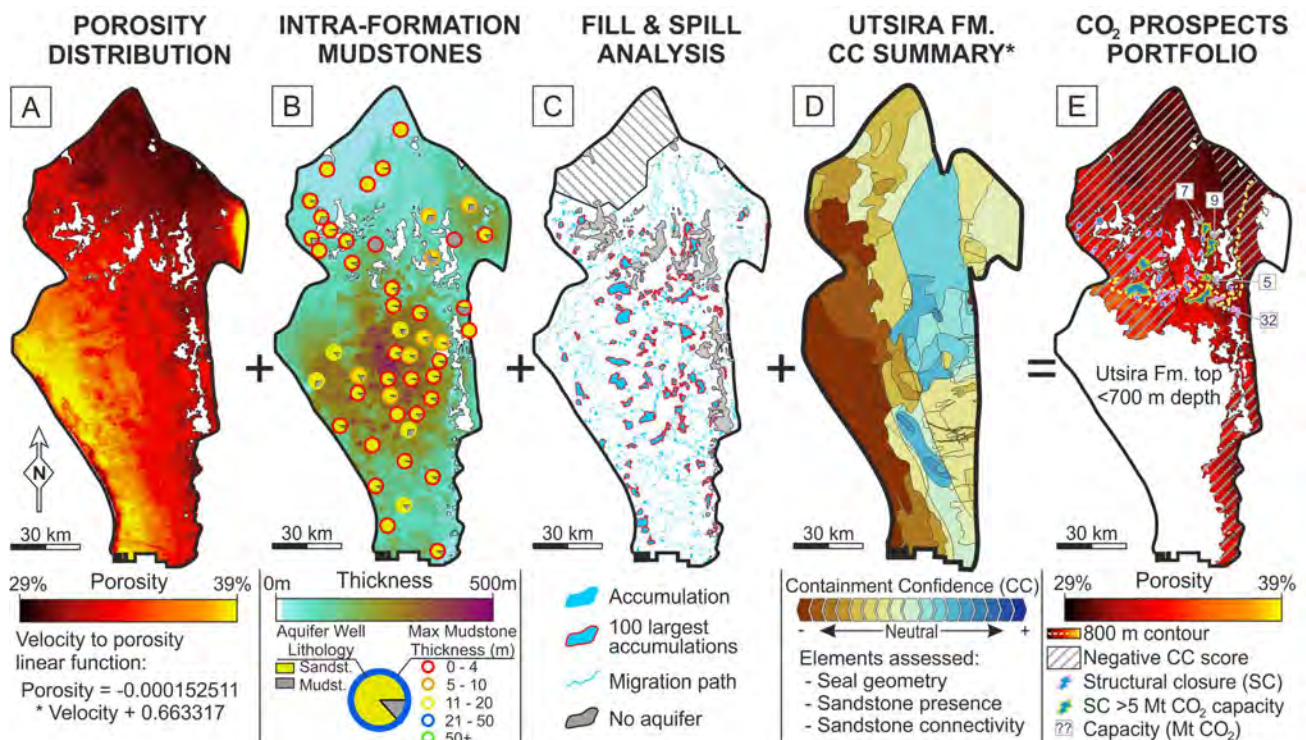
5. Discussion – Application of the Workflow

We advocate and present a play-based, risk segment mapping evaluation style for regional CO₂ storage site exploration. The objective of the workflow is to provide a screening method to identify potential storage sites in an aquifer, which would then require additional data collection and analysis for detailed appraisal.

Due to the inherent differences in geology and data availability/quality across basins worldwide, the workflows presented here are guidelines that can be tailored. For the CC assessment, through the use of a relative scoring system, elements can be added or removed and the relative scoring adjusted (although this limits comparison between aquifers). For the capacity assessment, additional elements (e.g. sedimentology, mineralogy, temperature) could be further added for aquifer delimitation and characterisation.

For the CC analysis of the Utsira Fm., we did not consider faulting or leakage from legacy wells, both of which could be important elements to include in the matrix. Faulting was not included as no large faults were observed [6]. The effect of legacy wells on leakage is debated [18] and their impact should be assessed on a local scale upon prospect identification. The number of well penetrations could be considered for comparisons and ranking of prospects [e.g. 6], however, there were no penetrations through the four identified prospects in the Utsira Fm. For the capacity analysis, alternative methods for porosity analysis could be adopted where FWI velocity data are unavailable. For example, using well logs or checkshots as point data for contouring.

Porosity (or sandstone quality) could also be considered as an element in the CC analysis, if there are sufficient data. For example, here, sandstones in the clinofolds of the seal and overburden of the Utsira Fm could be



differentiated according to their different glacial (east-derived) and non-glacial (west-derived) origins [11, 12]. However, for screening, the presence of potential seal bypass systems is of primary importance [6].

A more detailed evaluation could be performed by introducing a second order into the elements. For example, for seal internal geometry in the CC analysis, the stratigraphy could be sub-divided into flat-lying, dipping 1-2° and dipping >2°, or for the capacity analysis, the intra-formation baffles could be split according to mudstone and siltstone lithologies.

6. Conclusion

Regional screening for CO₂ storage sites can benefit from play-based, risking exploration approaches. Here, we outline a widely-applicable workflow for regional screening of a CO₂ storage aquifer, using the northern Utsira Fm. as a case study. Containment and capacity are the primary factors that are assessed to identify suitable storage prospects. A containment confidence matrix is presented as an approach for seal and overburden assessment, which allows layer-based mapping of matrix elements to spatially-constrain the aquifer to the most secure areas. Seal internal geometry, sandstone presence and sandstone connectivity are the elements assessed, but faulting and well penetrations could also be incorporated, if applicable. The capacity assessment workflow aims to capture the 3D variability of the aquifer, which is typically not considered in storage capacity estimates. We incorporate regional porosity, intra-reservoir mudstones and fill-to-spill analysis to identify prospects. Finally, minimum depth (700 m), minimum capacity (5 Mt CO₂) and positive CC cut-offs are applied. For the Utsira Fm., the optimal region is in the northeast, where there are four prospects, with a combined storage capacity of 53 Mt CO₂. This workflow is based upon classic exploration approaches and can be applied with regional-scale legacy data. A portfolio of suitable CO₂ prospects can be identified and put forward for detailed appraisal. Moreover, output maps can also form the basis of static and dynamic models, well designs, and development, mitigation and monitoring plans.

Acknowledgements

This work forms part of a PhD study funded by the NERC Centre for Doctoral Training in oil and gas (grant number: NE/R01051X/1). The authors thank CGG for the provision of 3D seismic data and TGS for their FMB lithology interpretations. Well data is publicly accessible through the NPD and OGA. AMWN was supported by NERC grant NE/R013675/1.

References

- [1] Stark, C. & Thompson, M. (2019). Net Zero - The UK's contribution to stopping global warming. Committee on Climate Change.
- [2] Halland, E., Johansen, W. & Riis, F. (2011). CO₂ Storage Atlas, Norwegian North Sea. *Publication of the Norwegian Petroleum Directorate*.
- [3] Meckel, T.A., Trevino, R. & Hovorka, S.D. (2017). Offshore CO₂ storage resource assessment of the northern Gulf of Mexico. *Energy Procedia*, 114, 4728-4734.
- [4] Sun, L., Dou, H., Li, Z., Hu, Y. & Hao, X. (2018). Assessment of CO₂ storage potential and carbon capture, utilization and storage prospect in China. *Journal of the Energy Institute*, 91, 970-977.
- [5] Lloyd, C., Huuse, M., Barrett, B.J. & Newton, A.M.W. (accepted). Regional identification of CO₂ Storage prospects in the Utsira-Skade Aquifer, North Viking Graben, North Sea. *Earth Science, Systems and Society*.
- [6] Lloyd, C., Huuse, M., Barrett, B.J., Stewart, M.A. & Newton, A.M.W. (2021). A regional CO₂ containment assessment of the northern Utsira Formation seal and overburden, northern North Sea. *Basin Research*, 33, 1985-2017.
- [7] Zweigel, P., Arts, R., Lothe, A.E. & Lindeberg, E.B. (2004). Reservoir geology of the Utsira Formation at the first industrial-scale underground CO₂ storage site (Sleipner area, North Sea). *Geological Society, London, Special Publications*, 233, 165-180.
- [8] Chadwick A., Arts R., Bernstone C., May F., Thibeau S., & Zweigel P. (eds) (2008). Best practice for the storage of CO₂ in saline aquifers. Observations and guidelines from the SACS and CO2STORE projects. BGS Occasional Publication No. 14. BGS, Keyworth, Nottingham, UK.
- [9] Gasda, S., Wangen, M., Bjørnara, T. & Elenius, M. (2017) Investigation of caprock integrity due to pressure build-up during high-volume injection into the Utsira formation. *Energy Procedia*, 114, 3157-3166.
- [10] Hayes, P., Twigger, L., Ubik, K., Latter, T., Purcell, C., Xiao, B. & Ratcliffe, A. (2018). Increasing resolution in the North Sea. *First Break*, 36, 105-111.
- [11] Eidvin, T., Riis, F., Rasmussen, E.S. & Rundberg, Y. (2013). Investigation of Oligocene to Lower Pliocene deposits in the Nordic offshore area and onshore Denmark. *NPD Bulletin*, 10, 62.
- [12] Ottesen, D., Dowdeswell, J.A. & Bugge, T., (2014). Morphology, sedimentary infill and depositional environments of the Early Quaternary North Sea Basin (56–62° N). *Marine and Petroleum Geology*, 56, 123-146.
- [13] Daynac, N., Lacaze, S. & Pauget, F. (2016). Interpretation of complex faulted deposits in the North Sea using the relative geological time model. *First Break*, 34, 55-62.
- [14] Huuse, M. & Kristensen, T.B. (2016). Pleistocene tunnel valleys in the North Sea Basin. *Geological Society, London, Memoirs*, 46, 207-208.
- [15] Barrett, B.J., Huws, D.G., Booth, A.D., Wergeland, Ø. & Green, J.M. (2017). Tuning, interference and false shallow gas signatures in geohazard interpretations: beyond the “λ/4” rule. *Near Surface Geophysics*, 15, 359-366.
- [16] Vangkilde-Pedersen, T., Anthonsen, K.L., Smith, N., Kirk, K., van der Meer, B., Le Gallo, Y., Bossie-Codreanu, D., Wojcicki, A., Le Nindre, Y.M., Hendriks, C. & Dalhoff, F. (2009). Assessing European capacity for geological storage of carbon dioxide—the EU GeoCapacity project. *Energy Procedia*, 1, 2663-2670.
- [17] Thibeau, S., Seldon, L., Masserano, F., Canal Vila, J. & Ringrose, P. (2018). Revisiting the Utsira Saline Aquifer CO₂ Storage Resources using the SRMS Classification Framework. *14th Greenhouse Gas Control Technologies Conference, Melbourne*, 21-26.
- [18] Ide, S.T., Friedmann, S.J. & Herzog, H.J. (2006). CO₂ leakage through existing wells: current technology and regulations. *8th International Conference on Greenhouse Gas Control Technologies*, 19-22.

NEGATIVE GREENHOUSE GAS EMISSIONS IN FRANCE BY 2050: TECHNO-ECONOMIC POTENTIAL ASSESSMENT

Ancuta Isbasoiu^{1*}, Paula Coussy¹

¹ IFP Energies nouvelles, 1-4 avenue de Bois-Préau, 92852 Rueil-Malmaison, France

* Corresponding author e-mail: ancuta.isbasoiu@ifpen.fr

Abstract

Climate change is one of the biggest challenges humanity faces today. The existing mitigation strategies to reduce greenhouse gas (GHG) emissions are not sufficient to deal with the major negative effects of climate change. The European Union's goal of becoming a net-zero greenhouse gas economy by 2050 represents the cornerstone of the European Green Deal, in conformity with the EU's global commitments under the Paris Agreement. To achieve climate neutrality goal by 2050, the deployment of Negative Emission Technologies (NETs) will be necessary. This paper focuses on one of these technologies, namely Bioenergy with carbon capture and storage (BECCS). In particular, it studies the French potential in terms of negative emissions and shows to what extent BECCS can represent a viable solution for achieving climate neutrality in France by 2050. We estimate the cost and potential of negative emissions for each of the nine BECCS technological options considered. Depending on the types of biomass corresponding to each technology, results show that the cost of a tonne of negative CO₂ (€/tCO₂) varies widely across the technologies: indirect gasification to Substitute Natural Gas (BioSNG) [32.7; 98.7]; gasification to liquid hydrogen [67.1; 96.2]; fast pyrolysis to liquid hydrogen [78.2; 98.5]; anaerobic digestion to biomethane [54.2; 118.9]; anaerobic digestion to electricity [73.9; 125]; gasification to liquid fuels [120.1; 163]; fast pyrolysis to electricity [150.2; 167.4]; hydrothermal liquefaction to liquid fuels [207.1; 314.4] and ethanol fermentation 53.3 €/tCO₂. Our analysis highlights that BECCS plays a key role in achieving the neutrality goal in France by 2050. For a target of 15 million tonnes negative emissions in France in 2050, if we use 50% of the available biomass distributed equally between the nine BECCS technologies studied, it will be necessary to cumulate the potentials of several BECCS technologies at a cost per tonne of CO₂ varying from 32.7 €/tCO₂ to 98.5 €/tCO₂. The marginal cost will increase with the setting of higher targets.

Keywords: *negative emissions, climate change, carbon neutrality, negative emission technologies, carbon dioxide removal.*

1. Introduction

For more than a century, human actions have influenced the Earth's climate. As a result of cumulative anthropogenic greenhouse gas (GHG) emissions and the increase of the global average temperature, following the United Nations Climate Change Conference in Paris, in 2015, no less than 196 countries have agreed on a common objective which consists in limiting global warming to "well below 2°C" and that efforts should be made to limit it below 1.5°C above pre-industrial levels [1],[2]. This ambition of the Paris Agreement on climate cannot be achieved only through a simple transition from fossil fuels to greener energy sources. According to Van Vuuren et al. [3], during the period 2000-2100, it is necessary a significant reduction of cumulative emissions and implicitly, unprecedented rates of decarbonization, both in the long and short term, in order to be able to limit¹ the climate change to 2°C. Pires [4] highlights that the reduction of GHG emissions may not be enough to mitigate climate change.

High greenhouse gas concentrations in the atmosphere can lead to dangerous levels of global warming, which is why the international scientific community puts in discussion the removal of carbon dioxide² (CO₂) from the air, through the so-called "negative emissions". The concept of negative emissions gained attention since its first inclusion in the 4th IPCC report (AR4), which included the implementation of Negative Emissions Technologies (NETs) and highlighted the essential role that negative emissions could play in the framework of climate goals. According to the IPCC AR5 report [5], most of the 2°C scenarios involve a large-scale implementation of the NETs after 2050, with the main purpose of compensating the residual CO₂ emissions from the sectors where decarbonization is difficult to achieve (for example, the aviation, agriculture, shipping, a part of car transport, cement production, etc.) [6].

NETs can play a significant role in keeping the increase of global temperature below the level of 2°C, and this with a probability higher than 66% [5],[9],[10],[11]. In this regard, Alcalde et al. [12] highlight the importance of NETs and the insufficiency of just reducing

¹ with a probability of around 66 %.

² Most research has focused on 'Carbon Dioxide Removal' (CDR), as CO₂ is the most predominant greenhouse gas [4],[7],[8].

greenhouse gas emissions from human activity. Negative Emission Technologies have the capacity to achieve long-term removal of CO₂ from the atmosphere, unlike conventional methods for reducing GHG emissions [13]. Gasser et al. [14] show that in order to reach the 2°C objective, negative emissions alone are not enough, but they are necessary even if we would dispose of very high mitigation rates. At the same time, Fuss et al. [15] point out that if there is no significant reduction of emissions in the short-term, then negative emissions will also be inefficient for achieving climate goals. To substantially remove CO₂ from the atmosphere, Integrated Assessment Models (IAMs) involve scenarios based on a large-scale implementation of NETs [5],[12],[16], the studies based on these models showing both the long-term and strategic importance of the Carbon Dioxide Removal for achieving a 2°C target [11],[17]. Fuss et al. [15] highlight that while there are some scenarios to 2°C that are not based on negative emissions, all 1.5°C scenarios are almost inconceivable without them. Mac Dowell et al. [18] also indicated that the ambitions to limit climate change to no more than 1.5°C–2°C by the end of the 21st century rely heavily on the availability of NETs.

The European Union’s goal of becoming a net-zero greenhouse gas economy by 2050 represents the cornerstone of the European Green Deal, in conformity with the EU’s global commitments under the Paris Agreement. In the 2030 climate and energy policy framework and the European Green Deal, the European Commission acknowledges that Carbon Dioxide Capture and Geological Storage (CCS) can play a key role in achieving the EU’s long-term emissions reduction goal [19],[20].

This article focuses on one of the Negative Emission Technologies (NETs), Bioenergy with carbon capture and storage (BECCS), and aims to study the French potential of negative emissions by 2050 necessary to move towards carbon neutrality. For this technology, we identify the pathways characterized by the lowest costs and the highest productivity in France.

2. France within the European climate objectives

2.1 The French National Low-Carbon Strategy

France strongly supports European objectives, and since 2015 has adopted the National Low-Carbon Strategy (SNBC), which aims to represent France’s roadmap to a transition to a low-carbon economy in all sectors of activity. With the adoption of the first National Low-Carbon Strategy in 2015, France had committed itself to reduce GHG emissions by 4 at the 2050 horizon compared to 1990 levels. With the introduction in 2017 of the Climate Plan for France by the Ministry of Ecological Transition and Solidarity, new targets have been set that replaced the initial ones (factor 4), with more ambitious ones that involve achieving carbon neutrality by 2050. This target, enrolled in law in 2019,

assumes that GHG emissions in France will have to be reduced by 6.9 compared to 1990 levels.

The latest National Low-Carbon Strategy was published in March 2020, with the main goal of achieving carbon neutrality by 2050. The objectives of reducing French greenhouse gas emissions associated with the National Low-Carbon Strategy are presented under the form of carbon budgets, expressed as an annual average per 5-year period in millions of tonnes of CO₂ equivalent (see the last three carbon budgets in Table 1) [21]. The carbon budgets initiated in 2015, in the French Energy Transition for Green Growth Act by SNBC, were also revised in 2019.

TABLE 1: Carbon budgets according to the French National Low-Carbon Strategy (SNBC). Source: IFPEN based on [21].

Period	2019-2023	2024-2028	2029-2033
Carbon budget (Emissions without LULUCF*)	422 MtCO ₂ eq/year in average	359 MtCO ₂ eq/year in average	300 MtCO ₂ eq/year in average
Carbon budget (Emissions with LULUCF*)	383 MtCO ₂ eq/year in average	320 MtCO ₂ eq/year in average	258 MtCO ₂ eq/year in average

* LULUCF – Land Use, Land-Use Change and Forestry

2.2 Negative emissions from LULUCF sector in France

In 2018, the Land Use, Land-Use Change and Forestry sector in France absorbed 17.26% more CO₂ from the atmosphere than in 1990. The negative emissions from LULUCF come from Forest Land, Grasslands and Harvested wood products. But negative emissions from the LULUCF sector will not be enough. Therefore, it is essential to study the solutions represented by artificial sinks, and implicitly Negative Emission Technologies (NETs), which, together with natural sinks, should be able to allow as much compensation as possible of emissions in the short, medium and long-term.

2.3 France’s carbon sink target for 2050

Given that neutrality must be achieved in 2050, the French National Low-Carbon Strategy assesses the residual emissions to 80 MtCO₂eq in 2050 and **-82 MtCO₂eq for sinks** (which would allow a reserve of -2 MtCO₂eq) [21],[22],[23]. CITEPA [22] suggests that of the residual³ emissions in 2050 (80 MtCO₂), 60% are assigned to agriculture and 20% to industry.

Regarding the carbon sink of France, for the year 2050, the -82 MtCO₂ are attributed:

- **to the LULUCF sector, in a percentage of 82% (soils, biomass forests, etc.)**
- **to CO₂ capture and storage (CCS) (BECCS + DACCS)⁴ in a percentage of 18%**

Based on the objectives and data from the National Low-Carbon Strategy [21] and [22], in Figure 1, we illustrate one of the scenarios that would allow obtaining carbon

³ emissions that cannot be avoided.

⁴ BECCS - Bioenergy with carbon capture and storage; DACCS - Direct Air Carbon capture and storage;

neutrality by 2050 in France. This scenario is inspired by the reference scenario of SNBC, called “With Additional Measures Scenario” (in french, scénario “Avec Mesures Supplémentaires” - AMS). Thus, according to this scenario, approximately -67 MtCO₂ would come from the LULUCF sector, and -15 MtCO₂ would have to be obtained through Negative Emission Technologies.

The interdependence between natural and artificial sinks must be taken into account (the higher the quantity of carbon absorbed by the LULUCF sector, the lower the

dependence on NETs), so that achieving the goal is done with the lowest costs, while simultaneously reducing the impact on the environment.

From the two levers that allow to obtain negative emissions, namely, LULUCF sector and CO₂ capture and storage (CCS), in this paper, we focused our analysis on the second lever that relies on Negative Emission Technologies, by studying the French potential on NETs, and implicitly the 18% (around 15 MtCO₂) necessary to obtain carbon neutrality in France by 2050.

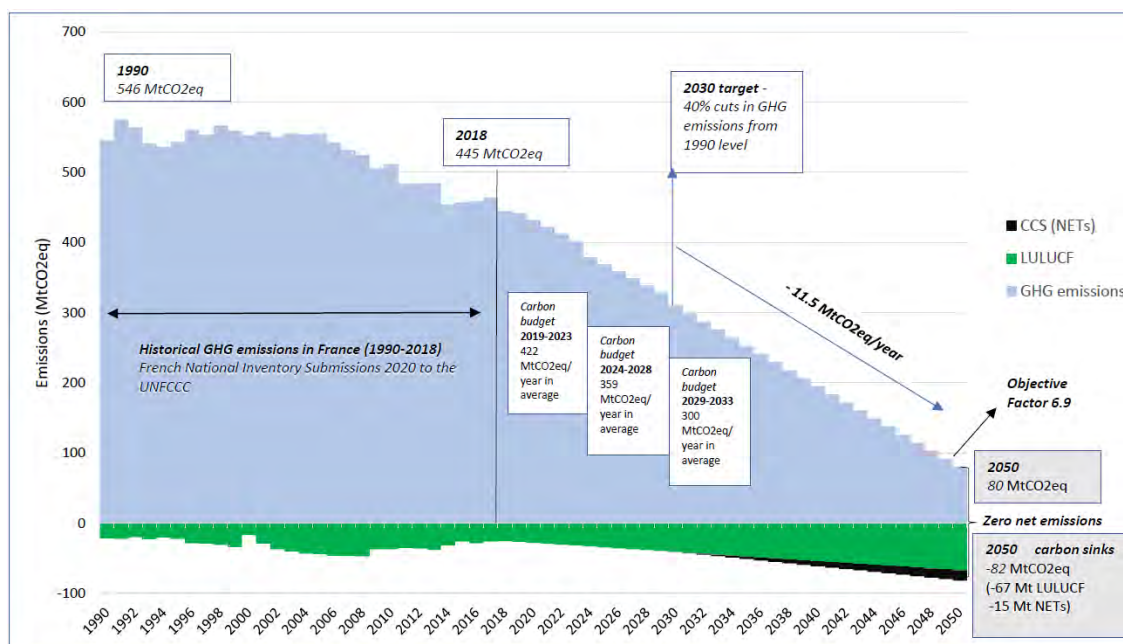


FIGURE 1: Trajectory of GHG emissions in France, in order to achieve the carbon neutrality in 2050. Source: IFPEN based on the objectives and data from the French National Low-Carbon Strategy [21],[22].

As stated by the French National Low-Carbon Strategy, the BECCS technology is seen as the starting point that would allow obtaining negative emissions in a continuous way on a very long-term, also emphasizing that at the moment, the technology is in a very early stage of development.

3. Methodology - BECCS implementation

In most climate change scenarios that use negative emission technologies, bioenergy and carbon capture and storage (BECCS) is presented as the best option and the most mature technology to decarbonize emission-intensive industries, and to allow negative emissions.

3.1 Biomass resources in France in 2050

We took into account the most important sources of biomass that are adaptable to the implementation of BECCS technologies. The main sources of biomass as raw material that we considered in this paper and that can be widely used in France are agricultural biomass, forest biomass, livestock effluents and waste.

According to the French National Biomass Mobilization Strategy [24], in France, the biomass of agricultural origin that can be used, is very diverse, France being the leading agricultural producer in the European Union. Regarding the forest biomass, it is one of the most important renewable resources in France. Livestock effluents are another important resource, with a significant use for BECCS technology. Waste can also be used for BECCS implementation.

To examine these sources of feedstock, as well as the projected availability in France, at the horizon of 2050, we used previously published studies, in particular, the French National Biomass Mobilization Strategy⁵ [24], ADEME [25], FranceAgriMer [26]. Based on the estimates⁶ from these studies, the quantity (expressed in million tonnes of dry matter) of mobilizable biomass resources in France in 2050 that we used in this paper, is summarized in Table 2.

The cost of each category of biomass considered were based on [27],[28],[29],[30]. In this paper, costs are

⁵ The French National Biomass Mobilization Strategy distinguishes two categories of biomass, without double counting: non-methanized biomass with low moisture and methanized biomass with high moisture.

⁶ The estimation of mobilizable biomass resources at the horizon of 2050, is characterized by some uncertainty, in the sense that the publications that estimate them are based on different scenarios, with a predilection for specific uses.

expressed in euro₂₀₂₀, and calculated by applying a yearly inflation rate⁷.

TABLE 2: Quantity and cost of biomass considered available in France in 2050. (Costs are expressed in €₂₀₂₀). Source: IFPEN based on data provided by [24],[25],[26],[27],[28],[29],[30].

Biomass type	Quantity (million tonnes DM/year)	Biomass cost (€ ₂₀₂₀ /tonne DM)
Forest biomass	29.23	69.43
Agricultural biomass	41.74	52.01
Livestock effluents	17.88	32.61
Waste	3.58	25.15

*DM refers to dry matter.

3.2 BECCS – portfolio of technologies

BECCS is characterized by a large portfolio of technologies at different stages of maturity. In our analysis, we consider various BECCS technologies: **Gasification**, with three different options (Gasification with Fischer-Tropsch Synthesis to Liquid Fuels; Gasification with Water-Gas Shift to Hydrogen; Indirect gasification to Substitute Natural Gas (BioSNG)), **Fast pyrolysis** with two options (Fast Pyrolysis to Hydrogen; Fast Pyrolysis to Electricity), **Anaerobic digestion** with two options (Anaerobic digestion to bio-methane; Anaerobic digestion to electricity), and **ethanol fermentation** and **hydrothermal liquefaction to liquid fuels**. In addition to the amount of CO₂ that can be captured, through the implementation of these procedures, we can obtain electricity, heat, liquid fuels, hydrogen, biomethane, synthetic natural gas, long-lived carbon products, or combinations thereof.

One of the BECCS technologies analyzed is Gasification, more precisely, Gasification with Fischer-Tropsch Synthesis to Liquid Fuels. The diagram (see Figure 2) shows an example of the circuit of carbon for this technology. To create this diagram, we used data and information from three reports [31],[32],[33]. As we can see, in a typical FT diesel plant, based on oxygen blown Circulating Fluidized Bed (CFB) gasification, 52% of the carbon in the feedstock is released as high-purity CO₂ that can be captured and stored, 37% ends up in Fischer-Tropsch diesel stream, 5% is vented as CO₂ in the flue gas of the combined heat and power unit, 6% is found in the char from the gasifier.

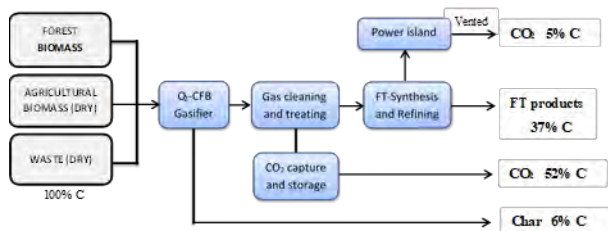


FIGURE 2: Gasification with Fischer-Tropsch Synthesis to liquid fuels. Source: IFPEN based on [31],[32],[33].

By taking into consideration the 52% of the carbon that could be captured and stored, as well as the biomass resources available in France, that are associated to this technology, namely, the forest biomass, the agricultural biomass with low moisture and the dry waste, we calculated the amount of CO₂ equivalent that can be captured and stored through this technology option.

The same principle was used for the other BECCS technologies considered (see other examples of figures in the Annexes).

3.3 BECCS - The calculation of the potential and cost of negative emissions

For each BECCS pathway that leads to negative emissions, as listed in the previous section, we have estimated both the potential and cost of negative emissions.

For the calculation of the cost of negative emissions, we used the equation (1) below, inspired by the analytical framework proposed by Baker, et al. [31]:

$$\text{Negative Emissions Cost} = \frac{TAC - PR}{NEP} \quad (1)$$

Where:

- *Negative Emissions Cost* refers to the cost of producing negative CO₂ emissions from the biomass conversion technologies studied (expressed in euro per tonne of CO₂ equivalent);
- *TAC* is the *Total Annualized Cost* (expressed in €/year), which includes the annualized capital cost (CAPEX), the fixed and variable operating cost (OPEX). The cost of biomass and the cost of capture, transport and storage are part of OPEX;
- *PR* is the *Product Revenue*, obtained from the sale of products (electricity, heat, hydrogen, liquid fuels, biomethane, BioSNG, digestate, bio-ethanol) resulting from the analyzed BECCS technologies (expressed in €/year);
- *NEP* is the *Negative Emissions Potential*, representing the annual amount of CO₂ removed due to the Negative Emissions Technology (expressed in tonnes of CO₂eq).

To calculate the potential and cost of negative emissions in France in 2050, we created an excel model, that allows us to calculate for all the BECCS technological options studied the parameters listed above.

We first calculated the annual negative CO₂ emissions quantity, for each pathway, by using the following equation:

$$NEP = \left(\sum_i Q_{Bi} \cdot CARB_i \right) \cdot C_{capt} \cdot \frac{44}{12}, \quad i=1,6 \quad (2)$$

Where:

- Q_{Bi} refers to the amount of biomass of type i in tonnes of dry matter (DM) (Forest biomass, High Moisture Agricultural Biomass, Low Moisture Agricultural Biomass, Dry Waste, Wet Waste, Livestock effluents);

⁷ <https://www.insee.fr/fr/statistiques/2122401#tableau-figure1>

- $CARB_i$ refers to the organic carbon content⁸ of biomass i (% mass);
- C_{capt} refers to the percentage of carbon that can be captured and stored in each of the analyzed BECCS technologies (%).
- $\frac{44}{12}$ refers to the conversion of one tonne of carbon equivalent into one tonne of CO₂ equivalent.

We start from the categories of biomass resources available in France in 2050, and depending on the carbon content of each category of biomass, we calculate the amount of carbon captured and stored, as well as the amount of carbon contained in the products resulting from each BECCS technology. Then, we converted the quantity of carbon captured by each process in quantity of negative bio CO₂eq.

Through the excel model created, we then determined the cost of one tonne of negative CO₂ by each BECCS technology. Thus, we considered a single facility for each of these technological paths, in which we introduced a quantity of biomass (in tonnes of dry matter) adapted to the capacity of the facility according to the data taken from various reports [34],[35],[36],[37],[38],[39]. We mention that the data taken from these differentiated plants for each technology, refer especially to CAPEX, OPEX, energy, heat and biomass consumption, which allowed us to calculate the total annualized cost, as well as the revenues obtained, according to the equation 1. The plants are assumed to be operational 8000 hours/year, with a lifetime of 15 or 20 years depending on the technology. We also mention that the role of the plants to which the reports used refer, was not to capture CO₂, but to produce various products for sale (electricity, heat, hydrogen, etc.). For the capture, transport and storage of CO₂, we considered as a hypothesis, a capture and compression cost of 40 €/tCO₂ captured, a transport cost of 20 €/tCO₂ transported and a storage cost of 30 €/tCO₂ stored. We consider the cost of transport and storage are paid as services performed by specialized companies. For technologies that allow to obtain hydrogen as a final product, we added a cost of hydrogen liquefaction of 0.5 €/kg H₂ [40].

In our analysis, we consider that in general, the CO₂ captured and stored is of high-purity. We also mention that in the case of the fast pyrolysis, the biochar obtained was not accounted in negative emissions potential calculation, although it is assumed that 80% of its carbon remains sequestered in the soil for 100 years.

For product revenues calculation, we multiplied the amount of final product that we can obtain from each BECCS technology and its wholesale price that is taken from the literature⁹ (electricity – 0.16 or 0.067 €/kWh depending on the plant size, heat – 0.054 €/kWh, digestate – 0.72 €/kg N, biomethane – 90.75 €/MWh,

hydrogen – 2.74 €/kg, BioSNG – 91.44 €/MWh, Bioethanol – 0.74 €/litre, liquid fuels – 684.75 €/t).

All costs are calculated and reported in euro₂₀₂₀, applying a yearly inflation rate.

4. Results

One of the main objectives of this model was the use of biomass resources and BECCS associated technologies in order to show to what extent BECCS can represent a viable solution for obtaining negative emissions and implicitly, for achieving climate neutrality in France by 2050.

The cost of negative CO₂ emissions is strongly influenced by various factors such as the type and cost of biomass, the electricity price, the selling price of the resulted final products, as well as the percentage of CO₂ captured corresponding to each BECCS technology analyzed. We performed an analysis of the sensitivity of the nine BECCS technologies to the cost of biomass, with the mention that each technology is characterized by certain types of biomass. For this, we varied only the cost of agricultural biomass (around the price used in the paper of 52.01 €₂₀₂₀/t dry matter), keeping constant the cost of the other parameters (see Figure 3). Results show that the cost of negative emissions through the technologies of ethanol fermentation, anaerobic digestion to biomethane and hydrothermal liquefaction to liquid fuels, is highly sensitive to the cost of biomass due to the fact that these technologies have a lower negative emissions potential per tonne of dry biomass (0.22 tCO₂/tDM, 0.30 tCO₂/tDM and respectively, 0.35 tCO₂/tDM). In contrast, gasification to liquid hydrogen and gasification to liquid fuels have the highest negative emissions potential per tonne of dry biomass (1.63 and 0.94, respectively), reason why they are less sensitive to the cost of biomass.

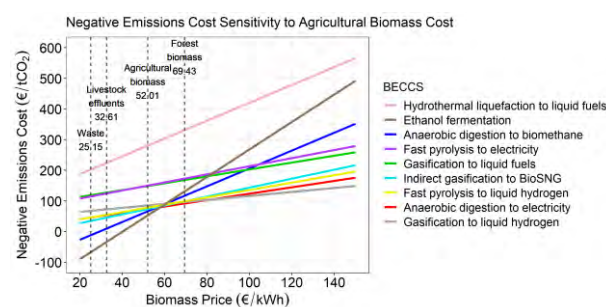


FIGURE 3: Variation of the negative emissions cost to the cost of biomass. Dashed vertical lines indicate the cost of biomass (€₂₀₂₀/tDM) used in the paper (agricultural biomass: 52.01; forest biomass: 69.43; livestock effluents: 32.61; waste: 25.15).

We also performed an analysis of the sensitivity of the BECCS technologies studied to the electricity selling price. The cost of a tonne of negative CO₂ from the

⁸ The mass organic carbon content (% mass) in biomass, considered in this paper is: 0.504 for forest biomass, 0.4688 for agricultural biomass [41]; 0.346 for livestock effluents [42] and 0.45 for waste [43].

⁹ <https://selectra.info/energie/guides/environnement/rachat-electricite-gaz-edf#biogaz>
https://eplagro55.fr/fileadmin/user_upload/pdf/Innovations/Biogaz/Rapport_gnv.pdf

https://www.ieabioenergy.com/wp-content/uploads/2019/01/Wasserstoffstudie_IEA-final.pdf
<https://atec.fr/system/files/2019-11/Position-Paper-Fili%C3%A8re-Injection-de-biom%C3%A9thane-de-synth%C3%A8se-v21-clean.pdf>
<https://www.prix-carburants.gouv.fr/>

technologies that produce and sell electricity (fast pyrolysis to electricity and anaerobic digestion to electricity) is extremely sensitive to the selling price of electricity (see Figure 4). The cost of negative emissions from the other technologies does not depend on the selling price of electricity, as they do not produce saleable electricity.

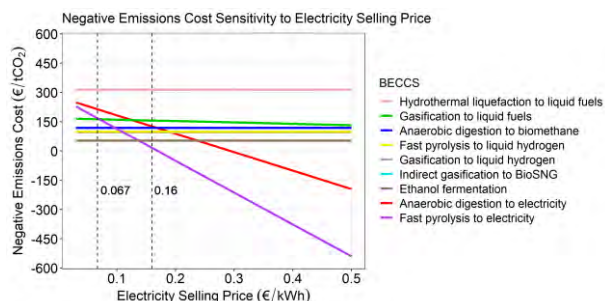


FIGURE 4: Variation of the negative emissions cost to the selling price of electricity. Dashed vertical lines indicate the electricity selling prices used in this paper: 0.067 €₂₀₂₀/kWh (installed power > 1 MW) and 0.16 €₂₀₂₀/kWh (installed power < 200 kW), depending on the power of the facility.

Among the technologies analyzed in the paper, the results show that indirect gasification to BioSNG, gasification to liquid hydrogen, fast pyrolysis to liquid hydrogen and ethanol fermentation, have the negative emissions cost below 100 €/tCO₂, regardless of the type of biomass used. In contrast, fast pyrolysis to electricity and hydrothermal liquefaction to liquid fuels, have the highest negative emissions costs, exceeding 150 €/tCO₂ (see Figure 5). An analysis of these technologies in terms of cost and potential will be presented below.

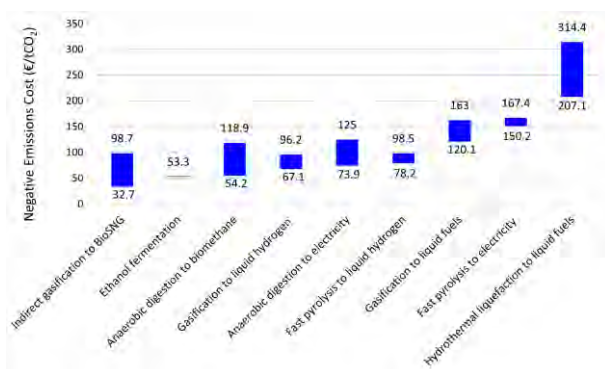


FIGURE 5: Variation of the negative emissions cost (€/tCO₂) for each BECCS technology analyzed, depending on the type of biomass used.

All these technologies require a consumption of electricity and heat that differs significantly from one technology to another. For calculating the cost and energy consumption, we used for each technology a plant of different powers, capacities, lifetime (15 or 20 years), locations¹⁰, depending on the data found in the literature, as we mentioned in the previous section. Hydrothermal

liquefaction to liquid fuels and indirect gasification to BioSNG are high consumers of electricity and heat, reported to tonnes of dry biomass, while the anaerobic digestion to electricity and biomethane are small consumers. If we refer to the tonne of negative CO₂, the technologies the most consuming of electricity and heat are gasification to liquid fuels, hydrothermal liquefaction to liquid fuels and anaerobic digestion to biomethane.

If the total available biomass in France that can be mobilized in 2050 would be distributed equally between the BECCS technologies associated to the same type of biomass¹¹, a cumulative amount of negative emissions of 62.2 MtCO₂eq would be obtained by using these nine BECCS technologies. However, this is a theoretical case, as not all the available biomass could be used for the BECCS technology in the future.

Therefore, given the fact that biomass will always be a resource for which there is competition and for a better mobilization of the types of biomass available by 2050, we decided to take in the first instance 50% of each biomass category available distributed equally between the BECCS technologies (see Figure 6 and Table 3). The results show that reaching the target of 15 Mt negative emissions in 2050, with the lowest costs, would require the implementation of all the technologies on the left of the first dashed vertical line in Figure 6 below, up to including fast pyrolysis to liquid hydrogen from forest biomass, technology with the cost of 98.5 €/tCO₂.

The estimated total electricity consumption necessary to reach this target of 15 million tonnes of negative emissions in 2050, in France, using 50% of the available biomass distributed equally, is approximately 6.08 million MWh/year (6.08 TWh/year). Compared to the electricity final consumption¹² in 2019 in France, which was 473 TWh, this estimated consumption would represent only 1.3%.

If the LULUCF sector cannot reach the target of 67 Mt negative emissions in France in 2050, then Negative Emissions Technologies will need to capture more than 15 MtCO₂. Thus, if we set a 30 Mt target for negative emissions obtained through BECCS, in 2050, it would be necessary to implement almost all BECCS options studied using all categories of biomass as input. For 30 Mt of negative emissions, using 50% of the biomass, the cost per tonne of negative CO₂ varies from 32.7 €/tCO₂ to 280.6 €/tCO₂.

If instead of using 50% of the biomass available in 2050, we only use 30% of the biomass, then reaching a target of 15 Mt negative emissions would be done at a marginal cost of 163 €/tCO₂. For a 30 Mt negative emissions target, the quantity of biomass would not be sufficient.

¹⁰ from France, United Kingdom, Switzerland, Denmark, Finland.

¹¹ BECCS technologies use different types of biomass. Biomass is distributed according to the characteristics of each technology. For example, forest biomass was divided into six parts because there are six technological options that use this type of biomass.

¹² <https://www.edf.fr/groupe-edf/espaces-dedies/l-energie-de-a-a-z/tout-sur-l-energie/le-developpement-durable/la-consommation-d-electricite-en-chiffres>
<https://www.iea.org/countries/france>

Assuming that the total amount of dry biomass in France in 2050 will be 92.4 million tonnes, then to obtain 15 Mt negative emissions it would be necessary to use 24% of the available biomass in 2050 (22.3 Mt dry matter), distributed proportionally between the BECCS technologies associated with the characteristic biomass

types: Forest biomass - 7 Mt DM; Agricultural Biomass (dry) - 1.9 Mt DM; Agricultural Biomass (wet) - 8.2 Mt DM; Livestock effluents - 4.3 Mt DM; Waste (dry) - 0.34 Mt DM; Waste (wet) - 0.53 Mt DM.

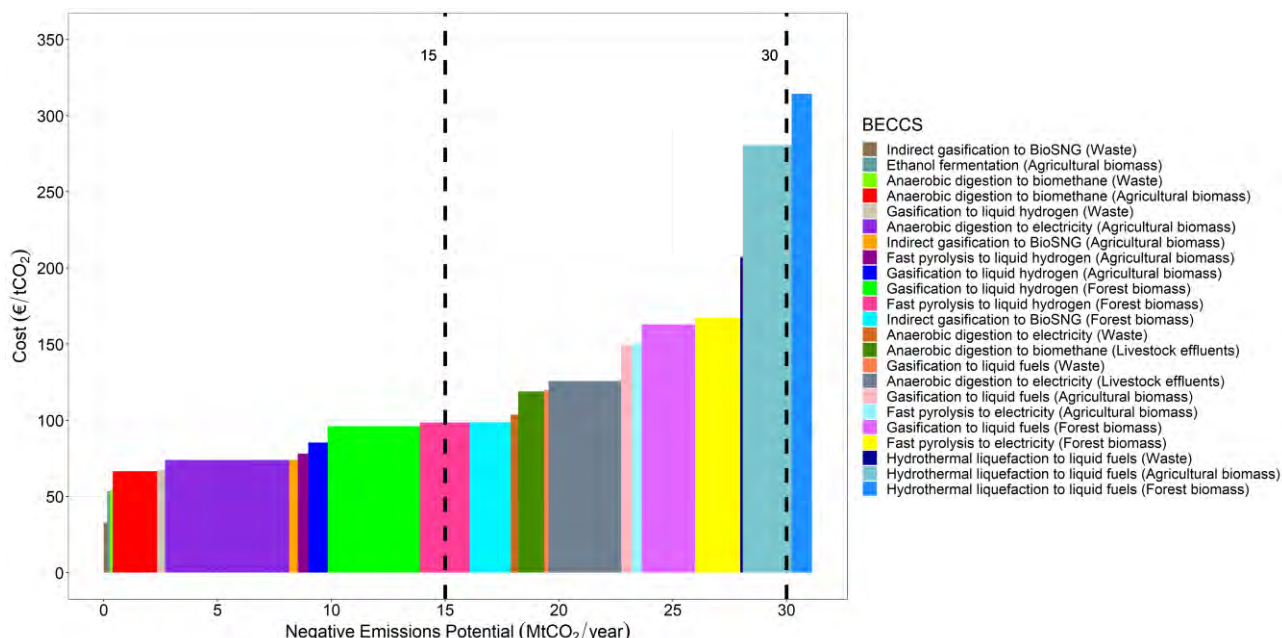


FIGURE 6: 2050 potential of negative emissions in France, when 50% of biomass is distributed equally between BECCS technologies. Biomass is distributed according to the characteristics of each technology.

TABLE 3: Negative emissions potential and cost for each BECCS technology, by using 50% of the biomass in France, in 2050. (Costs are expressed in €₂₀₂₀).

BECCS technology	Agricultural biomass		Forest biomass		Livestock effluents		Waste	
	Potential (MtCO ₂ /y)	Cost (€/tCO ₂)	Potential (MtCO ₂ /y)	Cost (€/tCO ₂)	Potential (MtCO ₂ /y)	Cost (€/tCO ₂)	Potential (MtCO ₂ /y)	Cost (€/tCO ₂)
Gasification to liquid fuels	0.49	149.0	2.34	163.0			0.20	120.1
Gasification to liquid hydrogen	0.86	85.4	4.05	96.2			0.35	67.1
Indirect gasification to BioSNG	0.38	74	1.80	98.7			0.15	32.7
Fast pyrolysis to liquid hydrogen	0.46	78.2	2.18	98.5				
Fast pyrolysis to electricity	0.42	150.2	1.99	167.4				
Hydrothermal liquefaction to liquid fuels	2.14	280.6	0.90	314.4			0.12	207.1
Ethanol fermentation	0.12	53.3						
Anaerobic digestion to electricity	5.45	73.9			3.18	125	0.34	103.7
Anaerobic digestion to biomethane	1.95	66.6			1.13	118.9	0.12	54.2
Total potential 50% biomass	31.1 MtCO₂eq							

5. Conclusions

To achieve the climate neutrality goal by 2050, the deployment of Negative Emission Technologies (NETs) will be essential. In this paper, we focused on Bioenergy with carbon capture and storage (BECCS), considered the most mature technology among NETs.

In our analysis, we studied nine BECCS technological options and identified the pathways characterized by the lowest costs and the highest productivity in France, which would allow to meet the state's goal of being carbon neutral by 2050.

The paper highlights that BECCS presents a high potential in obtaining negative emissions in France. If all the biomass estimated that can be mobilized in 2050

would be used, results showed a total potential of CO₂ negative emissions of 62.2 million tonnes of CO₂ in 2050. Given that biomass is a resource with many uses, for which there is competition, in our analysis, we focused on 50% of all biomass categories available (which would give a potential of 31.1 million tonnes negative emissions). We have estimated the cost and potential of negative emissions for each of the nine BECCS options considered. Depending on the types of biomass corresponding to each technology, results showed that the cost of a tonne of negative CO₂ (€/tCO₂) varies as follows: indirect gasification to BioSNG [32.7; 98.7]; gasification to liquid hydrogen [67.1; 96.2]; fast pyrolysis to liquid hydrogen [78.2; 98.5]; anaerobic digestion to biomethane [54.2; 118.9]; anaerobic

digestion to electricity [73.9; 125]; gasification to liquid fuels [120.1; 163]; fast pyrolysis to electricity [150.2;167.4]; hydrothermal liquefaction to liquid fuels [207.1; 314.4] and ethanol fermentation with the cost of negative emissions of 53.3 €/tCO₂. Regarding the potential of negative emissions, gasification to liquid hydrogen and anaerobic digestion to electricity are the technologies with the highest potentials.

Based on the objectives and information from the French National Low-Carbon Strategy [21] and [22], in this paper, we focused on a target of 15 Mt negative emissions by 2050, necessary to achieve the climate neutrality.

Our analysis shows that the target of 15 million tonnes negative emissions in 2050 can be obtained through BECCS implementation. If we use 50% of the biomass distributed equally between the nine BECCS technologies, it will be necessary to cumulate the potentials of certain BECCS technologies at a cost per tonne of CO₂ between 32.7 €/tCO₂ and 98.5 €/tCO₂. Results show that the quantity of 15 million tonnes of negative emissions could be obtained by using only 24% of the total available biomass in 2050.

If a higher amount of negative emissions would be needed to achieve neutrality, we also considered a target of 30 Mt. In this case, the analysis shows that it is necessary to implement all the BECCS technologies analyzed, by cumulating their CO₂ potentials using 50% of the biomass available in 2050, at a cost per tonne of negative CO₂ starting from 32.7 €/tCO₂ and reaching 280.6 €/tCO₂.

BECCS owns a portfolio of technologies with different maturity levels, which allows finding multiple ways to obtain negative emissions, playing a key role in achieving neutrality goal in France by 2050.

6. Annexes

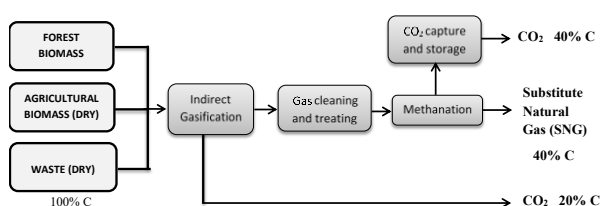


FIGURE 7: Indirect gasification to Substitute Natural Gas (BioSNG). Source: IFPEN based on [31],[32],[33].

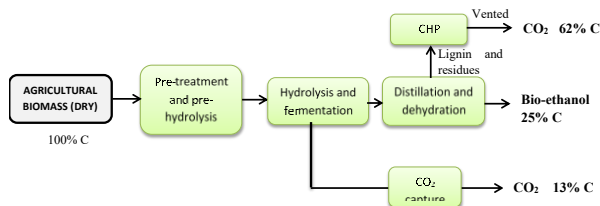


FIGURE 8: Ethanol fermentation. Source: IFPEN based on [31],[32][33]

Acknowledgements

This research is supported by the [CarMa IFP School Chair](#) entitled "Carbon Management and Negative CO₂ emissions technologies towards a low carbon future" supported by TOTAL SE in association with Fondation Tuck. The authors particularly thank the holders of the Chair and the Scientific Council for their advice throughout this research.

References

- [1] OECD (2017). *Investing in Climate, Investing in Growth*, OECD Publishing, Paris.
- [2] IPCC (2018). *Global Warming of 1.5°C. An IPCC Special Report on the impacts of global warming of 1.5°C above pre-industrial levels and related global greenhouse gas emission pathways, in the context of strengthening the global response to the threat of climate change, sustainable development, and efforts to eradicate poverty* [Masson-Delmotte, V., P. Zhai, H.-O. Pörtner, D. Roberts, J. Skea, P.R. Shukla, A. Pirani, W. Moufouma-Okia, C. Péan, R. Pidcock, S. Connors, J.B.R. Matthews, Y. Chen, X. Zhou, M.I. Gomis, E. Lonnoy, T. Maycock, M. Tignor, and T. Waterfield (eds.)]. In Press.
- [3] Van Vuuren, D. P., Deetman, S., Berg, M. v., Ruijven, B. J., & Koelbl, B. (2013). The role of negative CO₂ emissions for reaching 2 °C—insights from integrated assessment modelling. *Climatic Change*, 118, 15-27. doi:10.1007/s10584-012-0680-5
- [4] Pires, J. (2019). Negative emissions technologies: A complementary solution for climate change mitigation. *Science of the Total Environment*, 672, 502–514.
- [5] IPCC (2014). *Climate Change 2014: Mitigation of Climate Change. Contribution of Working Group III to the Fifth Assessment Report of the Intergovernmental Panel on Climate Change* [Edenhofer, O., R. Pichs-Madruga, Y. Sokona, E. Farahani, S. Kadner, K. Seyboth, A. Adler, I. Baum, S. Brunner, P. Eickemeier, B. Kriemann, J. Savolainen, S. Schlömer, C. von Stechow, T. Zwicker and J.C. Minx (eds.)]. Cambridge University Press, Cambridge, United Kingdom and New York, NY, USA.
- [6] Hilaire, J., Minx, J. C., Callaghan, M. W., Edmonds, J., Luderer, G., Nemet, G. F., Rogelj, J., Zamora, M. (2019). Negative emissions and international climate goals—learning from and about mitigation scenarios. *Climatic Change*, 157, 189–219.
- [7] Jonathan Wentworth, UK Parliamentary Office of Science and Technology. (2013). *Negative Emissions Technologies*. POST-PN-447.
- [8] McLaren, D. (2012). A comparative global assessment of potential negative emissions technologies. *Process Safety and Environmental Protection*, 90, 489–500.
- [9] IPCC (2007). *Climate Change 2007: Mitigation of Climate Change: Contribution of Working Group III to the Fourth Assessment Report of the Intergovernmental Panel on Climate Change*. ed B Metz, O R Davidson, P R Bosch, R Dave and L A Meyer (Cambridge: Cambridge University Press).
- [10] Clarke, L., Jiang, K., & Akimoto, K. (2014). *Assessing transformation pathways*. Clim. Change 2014 Mitig. Clim. Change Contrib. Work. Gr. III to Fifth Assess. Rep. Intergov. Panel Clim. Change ed O Edenhofer (Cambridge: Cambridge University Press).
- [11] Fuss, S., Lamb, W. F., & Callaghan, M. W. (2018). Negative emissions—Part 2: Costs, potentials and side effects. *Environ. Res. Lett.*, 13(063002).

- [12] Alcalde, J., Smith, P., Haszeldine, R. S., & Bond, C. E. (2018). The potential for implementation of Negative Emission Technologies in Scotland. *International Journal of Greenhouse Gas Control*(76), 85-91.
- [13] Zakkour, P., Kemper, J., & Dixon, T. (2014). Incentivising and accounting for negative emission technologies. *Energy Procedia*, 63, 6824 – 6833.
- [14] Gasser, T., Guivarch, C., Tachiiri, K., Jones, C., & Ciais, P. (2015). Negative emissions physically needed to keep global warming below 2C. *Nature communications*. doi:10.1038/ncomms8958
- [15] Fuss, S., Jones, C. D., Kraxner, F., Peters, G. P., Smith, P., Tavoni, M., Van Vuuren, D. P., Canadell, J. G., Jackson, R. B., Milne, J., Moreira, J. R., Nakicenovic, N., Sharifi, A., Yamagata, Y. (2016). Research priorities for negative emissions. *Environ. Res. Lett.*, 11(115007).
- [16] Smith, P., Davis, S., Creutzig, F., Fuss, S., Minx, J., Gabrielle, B. ...Yongsung, C. (2016). Biophysical and economic limits to negative CO₂ emissions. *Nature Climate Change*, 6, 42-50. doi:http://dx.doi.org/10.1038/nclimate2870
- [17] Kriegler, E., Weyant, J., & Blanford, G. (2014). The role of technology for achieving climate policy objectives: overview of the EMF 27 study on global technology and climate policy strategies. 123, 353–367.
- [18] Mac Dowell, N., & Fajardy, M. (2017). Inefficient power generation as an optimal route to negative emissions via BECCS? *Environmental Research Letters*, 12.
- [19] European Commission (2018). *A Clean Planet for all. A European strategic long-term vision for a prosperous, modern, competitive and climate neutral economy*. Communication from the Commission to the European Parliament, the European Council, the Council, the European Economic and Social Committee, the Committee of the Regions and the European Investment Bank. Brussels, COM(2018) 773 final.
- [20] European Commission (2019). *The European Green Deal*. Communication from the Commission to the European Parliament, the European Council, the Council, the European Economic and Social Committee and the Committee of the Regions. Brussels, 11.12.2019 COM(2019) 640 final.
- [21] Ministère de la Transition Ecologique et Solidaire (2020). *Stratégie nationale bas-carbone. La transition écologique et solidaire vers la neutralité carbone*. Ministère de la Transition Ecologique et Solidaire.
- [22] CITEPA (2019). *Inventaire des émissions de polluants atmosphériques et de gaz à effet de serre en France – Format Secten*. Citepa.
- [23] Plan national intégré énergie-climat de la France (2020). *Integrated national energy and climate plan of France*.
- [24] Stratégie Nationale de Mobilisation de la Biomasse (2018).
- [25] ADEME (2013). *Estimation des gisements potentiels de substrats utilisables en méthanisation*. Agence de la transition écologique - ADEME.
- [26] FranceAgriMer (2016). *L'Observatoire National des Ressources en Biomasse. Evaluation des ressources disponibles en France*.
- [27] Ruiz, P., Sgobbi, A., Nijs, W. N., Thiel, C., Dalla Longa, F., Kober, T., Elbersen, B., & Hengeveld, G. (2015). *The JRC-EU-TIMES model: bioenergy potentials for EU and neighbouring countries*. Luxembourg, Publications Office.
- [28] Esteban, L. & Carrasco, J., (2011). Biomass resources and costs: Assessment in different EU countries. *Biomass and bioenergy*, Volume 35, pp. 521-530.
- [29] Pekkanen, M., Bowyer, C., Forsell, N., Hünecke, K., Korosuo, A., Nanni, S., & Nuolivirta, P. (2014). *Study on impacts on resource efficiency of future EU demand for bioenergy*. Task 1 Report. Publications Office of the European Union, Luxembourg.
- [30] Piotrowski, S., Carus, M., NOVA. Deliverable D1.2: Assessment of procurement costs for the preferred feedstocks. (2012). Available online: http://www.biocore-europe.org/file/D1_2%20Assessment%20of%20procurement%20costs%20for%20the%20preferred%20feedstocks.pdf
- [31] Baker, S. E., Stolaroff, J. K., Peridas, G., Pang, S. H., Goldstein, H. M., Lucci, F. R., Li, W., Slessarev, E. W., Pett-Ridge, J., Ryerson, F. J., Wagoner, J. L., Kirkendall, W., Aines, R. D., Sanchez, D. L., Cabiyo, B., Baker, J., McCoy, S., Uden, S., Runnebaum, R., Wilcox, J., Psarras, P. C., Pilorgé, H., McQueen, N., Maynard, D., & McCormick, C. (2020). *Getting to Neutral: Options for Negative Carbon Emissions in California*. Lawrence Livermore National.
- [32] Zero Emissions Platform ZEP (2012). *Biomass with CO₂ Capture and Storage (Bio-CCS). The way forward for Europe*. European Biofuels Technology Platform.
- [33] Carbo, M. C. (2011). *Global Technology Roadmap for CCS in Industry*. ECN Energy research Centre of the Netherlands ECN-E--11-012.
- [34] agriKomp France (2017). *Etude de faisabilité pour l'implantation d'une installation de méthanisation agricole*. GAEC DE SAINT GOUDAS
- [35] Quantis (2017). *Analyse de systèmes de transformation du bois énergie*. Rapport de synthèse.
- [36] Hannula, I., & Kurkela, E., (2013). *Liquid transportation fuels via large-scale fluidised-bed gasification of lignocellulosic biomass*. VTT Technical Research Centre of Finland.
- [37] E4tech (UK) Ltd (2017). *Ramp up of lignocellulosic ethanol in Europe to 2030*. Final Report.
- [38] Pedersen, T. H., Hansen, N. H., Pérez, O. M., Cabezas, D. E. V., Rosendahl, L. A., (2018). *Renewable hydrocarbon fuels from hydrothermal liquefaction: A techno-economic analysis*. *Biofuels, Bioprod. Bioref.* 12:213–223.
- [39] Olivier Megret, Loreline Hubert, M. Calbry, Eric Trably, Hélène Carrère, et al.. (2015) *Production d'hydrogène à partir de déchets : Etat de l'art et potentiel d'émergence*. [Contrat] RECORD 13-0239/1A, Réseau Coopératif de Recherche sur les Déchets et l'Environnement, 226 p.
- [40] Académie des technologies (2020). *Rôle de l'hydrogène dans une économie décarbonée*.
- [41] Rogau, Y., (2009). La combustion du bois et de la biomasse. Pollution atmosphérique - Numéro spécial.
- [42] Kimura, S. D., Mishima, S. & Yagi, K., (2011). Carbon resources of residue and manure in Japanese farmland soils. *Nutr Cycl Agroecosyst*, Volume 89, pp. 291-302.
- [43] Yang, Y. & Heaven, S. & Venetsaneas, N. & Banks, C.J. & Bridgwater, A.V., 2018. "Slow pyrolysis of organic fraction of municipal solid waste (OFMSW): Characterisation of products and screening of the aqueous liquid product for anaerobic digestion," *Applied Energy*, Elsevier, vol. 213(C), pages 158-168.

CHALLENGES AND OPPORTUNITIES OF ACHIEVING EUROPEAN CO₂ TRANSPORTATION AND STORAGE SPECIFICATIONS FOR CARBON CAPTURE IN THE IRON AND STEEL INDUSTRY

R.T.J. Porter^{1*}, J. Barnett², P. Cobden³, E. De Coninck⁴, H. Mahgerefteh¹, G. Manzolini⁵, S. Martynov¹, F. Ruggeri⁶, V. Spallina⁷

¹ University College London, London, United Kingdom

² National Grid, Solihull, United Kingdom

³ Swerim AB, Luleå, Sweden

⁴ ArcelorMittal, Ghent, Belgium

⁵ Politecnico di Milano, Milan, Italy

⁶ Wood PLC, Corsico, Italy

⁷ University of Manchester

* Corresponding author e-mail: r.t.j.porter@ucl.ac.uk

Abstract

The application of CCS in the iron and steel industry faces particular challenges for achieving European CO₂ transportation and storage in meeting CO₂ stream impurity limit specifications due to the unique and diverse composition of the steelworks off-gases targeted for CO₂ capture and the separation efficiency of proposed CO₂ capture solutions. This paper reviews the range and levels of compounds that could form potential CO₂ impurities in steelworks off-gases and provides estimates of the quality of CO₂ products obtained in primary CO₂ capture steps from Blast Furnace Gas (BFG) using different technologies of Pressure-Swing Adsorption (PSA) and amine scrubbing. Published CO₂ specifications from European transportation and storage operators are reviewed and compared. Additional suitable purification steps that are needed in order to reduce the levels of impurities from primary CO₂ product streams in order to achieve European CO₂ impurity limit specifications are identified, characterised and the associated cost implications discussed.

Keywords: CCS, CO₂ Quality, Iron & Steel, Impurities, CO₂ Purification

1. Introduction

The iron and steel industry represents the largest energy consuming manufacturing sector in the world, with average specific emissions being around 1.83 tonnes of CO₂ per tonne of all crude steel produced and global crude steel production reaching 1.86 Gt for the year 2020 [1]. The CO₂ footprint of steel mills accounts for up to 8% [2] of anthropogenic emissions.

A unique feature of the current steel making processes is the presence of energy containing off-gases, with the three main being Coke Oven Gas (COG), Blast Furnace Gas (BFG) and Basic Oxygen Furnace Gas (BOFG). Conventionally, these off-gases are used to fuel reheating furnaces or for power generation, but are increasingly now targets for the application of Carbon Capture and Storage (CCS). CO₂ capture strategies for steelworks off-gas application aim to separate CO₂ while producing another energy containing gas stream for further use with much reduced carbon content. The general characteristics of the steelworks off-gases are shown in table 1. COG is the most energy rich of these streams containing ~65 vol% H₂ while the BOFG has significant CO content (>50 vol%). BFG represents the greatest volumetric flow, and is hence the focus of particular attention for CCS

application, but has a low energy content, consisting of ~50-60 vol% N₂ and ~20 vol% CO₂.

Table 1: Main components and characteristics of steelworks off-gases [3].

Component	COG	mol%	
		BFG	BOFG
Carbon monoxide (CO)	3.8	22.3	56.9
Carbon dioxide (CO ₂)	0.96	22.1	14.4
Hydrogen (H ₂)	59.5	3.6	2.4
Nitrogen (N ₂)	5.8	48.8	13.8
Ethane (C ₂ H ₆)	2.7	0.0	0.0
Methane (CH ₄)	23.0	0.0	0.0
Oxygen (O ₂)	0.2	0.0	0.0
Water (H ₂ O)	4.0	3.2	12.2
Lower Heating Value (LHV) (MJ/Nm ³)	17.8	3.3	8.5
Flowrate (kg/s)	0.3	158.7	14.2

The fate of the main steelworks off-gas components and a range of other contaminants when CCS systems are applied, and the degree to which these will carry over into CO₂ product streams to form impurity compounds, is an important issue for the iron and steel industry. Impurities also need to be accounted for when capturing CO₂ from many other emitting industries (e.g. cement, waste-to

energy, refineries etc.). This is because the anticipated impurities can have a range of mainly deleterious impacts on different parts of the CCS chain (i.e. on the capture process and compression/liquefaction equipment, CO₂ transportation infrastructure (pipeline and/or ship tanker), CO₂ injection well and geological storage sites). These impurity impacts include toxic effects on humans, corrosion effects on metals, metal embrittlement, along with effects on hydraulic efficiency, pipeline fracture behaviour, geological storage capacity and geochemistry (e.g. mineral dissolution and precipitation). CO₂ impurity impacts have received attention from the CCS scientific community [4][5], with some operational experience gained from CO₂ Enhanced Oil Recovery (EOR) [6]. The CO₂QUEST project [7] reviewed typical compositions of CO₂ streams from CCS and provided experimental results for the effect of impurities on pipeline rupture and CO₂ dispersion behaviour using extensively instrumented realistic-scale pipeline test facilities. Experimental and modelling results for the geological impact of impure CO₂ were also obtained while full-chain CCS techno-economic tools were developed.

In view of the impacts of CO₂ impurities, CO₂ transportation and storage providers set concentration limits for impurities, meanwhile other authors propose to determine CO₂ stream composition based on a case specific multi-criteria optimisation. Despite a significant body of knowledge acquired, the fate and impact of impurities in CCS still requires an improved understanding and characterisation in order to facilitate technology roll-out, especially in consideration of the widening scope of applications and development of future generations of CO₂ capture technologies. Research is also needed on the associated cost benefit analysis of CO₂ purification while simultaneously considering the operational and safety aspects surrounding the potential for co-transportation/-storage of CO₂ impurities.

In this paper, the range and level of impurities in steelworks off-gases are reviewed and the propensity of components to form impurities in the product streams from different primary CO₂ capture steps, including Pressure-Swing Adsorption (PSA) and amine based systems, is assessed. Following a review of current European CO₂ stream transportation and storage specifications, the requirements for the application of additional CO₂ stream clean-up technologies are identified and assessed.

2. Potential impurities in steelworks off-gases

The application of CCS to steelworks off-gases can result in new challenges due to the presence of a high number of different impurities as compared to other industrial emitters which use natural gas as a feedstock or fuel. In addition to the main components listed in table 1, other impurities may be present in low concentrations (in the parts per million (ppm) or parts per billion (ppb) region). The main compounds and their categories have been summarised by Schittkowski et al. [8] and are shown in table 2. Some of these compounds have known toxic

effects on humans (e.g. mercury (Hg)) while others pose corrosion concerns to metals, especially when present in mixtures with water (e.g. hydrogen sulfide (H₂S)), which is also poisonous and flammable, and sulfur oxides (SO_x).

Table 2: Potential impurities of exhaust gases from steel production [8].

Compound class	Compound
Hydrocarbons	CH ₄ , C ₂ H ₄ , C ₂ H ₆ , cyclopentadiene, C ₃ H ₈ , C ₃ H ₆ , C ₄ H ₁₀ , acetylene, pentene, heavy hydrocarbons
Aromatics	Phenol, benzene, toluene, xylene
PAH	Naphthalene, phenanthrene, benzopyrene,
S-compounds	SO _x (SO ₂), H ₂ S, COS, CS ₂ , thiophene, mercaptan
N-compounds	NO _x (NO ₂ , NO), NH ₃ , HCN, tar bases (C _x H _y N), pyridine, (CN) ₂
O-compounds	O ₂ , H ₂ O, tar acids (C _x H _y OH)
Heavy metal compounds	Cr, Mn, Ni, Pb, Zn, Hg, As, Cd, Cu
Halides	HCl, HF, inorganic flourides, PCDD/F, PCB
P-compounds	Trivalent phosphorus
Dust	FeO _x , alkali metals, alkali earth metals, metal oxides, CdO _x , elemental sulfur, elemental carbon, Hg

PAH: Poly aromatic hydrocarbon;

PCDD/F: Polychlorinated benzo(p)dioxin and furan.

A small number of literature resources give details of the concentration levels of impurity compounds in steelworks off-gases. The most comprehensive of these, which also includes the state-of-the art in the purification of steelworks off-gases, is the European Commission (EC) document “*Best Available Techniques (BAT) Reference Document for Iron and Steel Production*” [9]. Levels of impurity compounds in steelworks off-gases vary in different plants depending on a variety of considerations including the age of the plant and operational factors, such as the degree of pollution removal technologies employed and the type of coal selected for coke production (e.g. low or high sulfur coal). Table 3 shows the concentrations of some impurity compounds reported in [9]. BFG is known to contain different levels of H₂S; 14 mg/Nm³ given in table 3 is equivalent to 10 ppm_v which is in the lower range of other reported ranges. For example, Bender et al [10] report H₂S to be present in BFG in the range of 10–40 mg/m³. More recently, Lanzerstorfer et al. [11] measured a range of gaseous components in BFG emissions and characterised the top scrubber efficiency; they found that the clean gas emission of sulfur was dominated by carbonyl sulfide COS (at 279 mg/m³ (standard temperature and pressure - STP)) which accounted for about 85% of the total sulfur emissions, while H₂S and SO₂ accounted only for 15% and 0.6%, respectively. Although no data is available in the EC BAT document, the nitrogen containing species, HCN and NH₃ are believed to be present in BFG, but levels in the clean gas are believed to be low at 0.12 and 0.15 mg/m³ (STP), respectively, according to the recent measurements [11]. Low levels of heavy metals Mn, Pb and Zn are also

Table 3: Concentration levels of some potential steelworks off-gas impurities [9][13].

	BFG		COG (untreated)		BOFG	
	Concentration	Unit	Concentration	Unit	Concentration	Unit
Particulates	1-10	[mg/Nm ³]	-	-	15-20	g/t LS
H ₂ S	14	[mg/Nm ³]	20-700	[mg/Nm ³]	-	-
Organic sulfur	-	-	≤ 150	[mg/Nm ³]	-	-
NO _x	-	-	-	-	5-20	g/t LS
HCN	n/a	[mg/Nm ³]	0.3-1.5	[g/Nm ³]	-	-
NH ₃	n/a	[mg/Nm ³]	50-100	[mg/Nm ³]	-	-
Heavy metals:						
Mn	0.1-0.29	[mg/Nm ³]	-	-	<0.01-1.2	g/t LS
Pb	0.01-0.17	[mg/Nm ³]	-	-	0.13-0.9	g/t LS
Zn	0.03-0.17	[mg/Nm ³]	-	-	-	-
Cr	-	-	-	-	0.01-0.36	g/t LS
Cu	-	-	-	-	0.01-0.04	g/t LS
BTX	-	-	1-10	[g/Nm ³]	-	-
Naphthalene (C ₁₀ H ₈)	-	-	200-500	[mg/Nm ³]	-	-
Tar	-	-	20-31	[mg/Nm ³]	-	-
PAH	-	-	-	-	0.08-0.16	mg/t LS
PCCD/F	-	-	-	-	<0.001-0.06	µg I-TEQ/t LS

n/a: data not available; LS: (crude) Liquid Steel; BTX: Benzene, Toluene and xylene isomer;

reported for BFG in table 3. Compounds other than those reported for BFG in table 3 may be present such as O₂ and CH₄, in addition to low levels of HCl, BTX and other smaller hydrocarbons. It is also worth noting that large time-dependent fluctuations in the compound concentrations may occur during steelworks operations [12], hence the presented values may be considered as average. As also shown in table 3, COG can contain some similar inorganic compounds as BFG (i.e. sulfur compounds, NH₃, HCN), and typically contains a wide range of light and heavy hydrocarbons. COG is typically cleaned before being used as fuel in a steel plant, to remove dust, tar, naphthalene, light oil, sulfurous compounds and the cracking of ammonia to hydrogen [13]. BOFG is known to contain levels of dust and NO_x, as well as low levels heavy metals (Mn, Pb, Cr, Cu), PAH and very low amounts of PCCD/F.

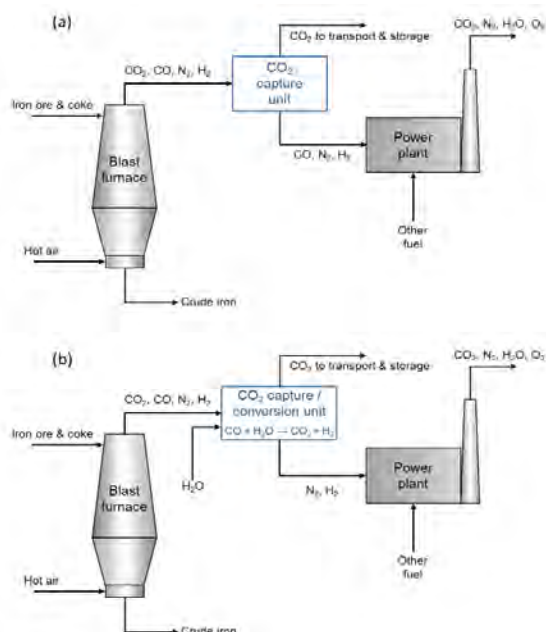


Figure 1: Simplified process schemes for (a) CO₂ capture and (b) CO₂ capture / conversion from BFG.

3. Impurities in CO₂ streams produced by capture from BFG

For a better understanding of the implications of impurities present in steelworks off-gases on CCS systems, estimates have been made of their levels in CO₂ streams captured from BFG using a mass balance technique applied to a generic CO₂ capture scheme shown in figure 1(a). Figure 1(b) also shows the case for a CO₂ capture and conversion process which can be achieved using technologies such as Sorption Enhanced Water Gas Shift (SEWGS) [3] or Calcium Assisted Steel-mill Off-gas Hydrogen (CASOH) technologies [14].

Table 4: Main impurities in CO₂ captured from BFG using PSA and amine systems estimated in this work.

	PSA low purity	PSA high purity	MEA plant
CO ₂ mol% dry	83	99.5	99.7
H ₂ O mol%	saturated	saturated	saturated
N ₂ mol% dry	10.57	0.29	0.023
CO -	5.27%	0.15%	200 ppm _v
H ₂ -	0.96%	266 ppm _v	214 ppm _v
COS ppm _v	163	214	131
H ₂ S ppm _v	50.8	66.9	41
SO ₂ ppm _v	1.1	1.4	0.9
HCN ppm _v	0.02	0.001	0.45
NH ₃ ppm _v	0.05	0.0007	0.88
HCl ppm _v	0.04	0.001	0.71
Amine ppm _v	-	-	<1

Table 4 provides the estimated concentrations of major impurities for two different CO₂ capture technologies that are considered here: PSA and amine based systems. The performance of the PSA system is based on that reported during pilot scale trials in the COURSE50 project using the Zeolum F-9H sorbent, in terms of CO₂ purity and recovery rates achieved [15]. Two PSA cases are presented comprising a low purity case, based on a CO₂ purity of 83 mol% and recovery of 67%, and a high purity case based on 99.5 mol% purity and 61% recovery.

Based on the typical behaviour of PSA systems, the sulfur species (i.e. COS, H₂S and SO₂) are assumed to enrich in the CO₂ product (adsorbate) and therefore partition completely. All other species are assumed to distribute evenly between the non-CO₂ portion of the CO₂ rich stream and the CO₂ lean streams exiting the PSA system since they have lower molecular weights. It should be noted that in the pilot-scale system testing [15], a desulfurisation unit was included prior to the PSA system, whereas this stage is neglected in the current analysis. The estimation of the CO₂ composition captured from BFG using an amine system is based on the laboratory based analysis reported by Dreillard et al [16] for monoethanolamine (MEA) and DMX solvents, which achieved CO₂ purity set at 99.7 mol% (dry basis) and a CO₂ capture rate of 90%. The concentration of CO was reported to be 375 ppm_v in the stripper top in the case of capture using MEA applied to an inlet gas representative of Top Gas Recycling (TGR) conditions with a composition of CO₂=37.04 mol%, CO=46.71 mol%, N₂=9.21 mol%, H₂=7.04 mol%, hence the value used in table 4 is proportionally scaled to account for the lower inlet concentration of CO in the typical BFG case. The concentration of amine in the CO₂ product is also based on the reported value by Dreillard et al for the TGR case. In the MEA case, sulfur containing compounds, nitrogen containing contaminants (NH₃ and HCN) and HCl are all assumed to partition completely with CO₂. HCN and SO₂ may form heat stable salts and COS may also undergo hydrolysis in amine systems [17]. The values presented here for the MEA case may therefore represent conservatively high estimates for contaminant concentration and actual values require a thorough investigation through experimental measurement.

4. European specifications for CO₂ transport and storage

Three European specifications for CO₂ transportation and storage have recently been published from the Northern Lights CCS project [18], National Grid in the UK [19] and TAQA for the PORTHOS project [20]. The Northern Lights project is part of the Norwegian full-scale CCS project, which includes the capture of CO₂ from industrial sources beginning in the Oslofjord region; the CO₂ will be liquified and shipped to a Northern Lights facility near Bergen, where it will be pumped 2,600 meters below the sea floor into a saline aquifer. The National Grid CO₂ specification has been developed since 2009 in the context of the UK Government's CCS commercialization competitions and has been based largely on the specification provided by the DYNAMIS consortium, with some adjustments for some compounds such as H₂S to ensure the pipelines do not become classed as "sour service" and the water level to prevent material degradation. The PORTHOS project associated to TAQA's CO₂ specification, will use depleted gas fields in the North Sea to store CO₂ which will be captured from industrial emitters in the Port of Rotterdam area and transported by pipelines. Table 5 shows the CO₂ specification provided in these three resources. For the

comprehensive breakdown of the rationale behind the proposed limits for each component in the three specifications, the reader is referred to the relevant reports [18][19][20].

Comparing the different specifications, it can be seen from table 5 that similarities and differences exist. TAQA's specification is the most comprehensive with precise recommendations provided for 21 components. The Northern Lights specification provides recommendation for amine and potential degradation products (NH₃, formaldehyde, acetaldehyde) and, generally sets the most stringent limits on all components barring NO_x, H₂S and HCN. The National Grid minimum concentration for CO₂ is 96% for dense phase CO₂ which is broadly in-line with the TAQA recommendation where the sum of non-condensable components must not exceed 4 vol%. No specific lower limit is set for CO₂ in the Northern Lights specification but non-condensables will be limited by their solubility in liquid CO₂ during interim storage. In all three specifications, tight limits are set for H₂O (30-50 ppm_v) and O₂ (10-40 ppm_v), while limits for NO_x range from 5 to 100 ppm_v. Some variation is observed between the three specifications in the case of sulfur species; TAQA's limit for H₂S is lowest at 5 ppm_v, followed by the 10 ppm_v limit for Northern Lights and 80 ppm_v gas and the 20 ppm_v dense phase National Grid limits. These H₂S limits are in contrast to the composition of transported CO₂ in North America for the purposes of EOR in the Weyburn Project, where around 0.9 vol% H₂S is co-injected into an oil reservoir. H₂S is known to have a beneficial effect for EOR due to the reduction of the minimum miscibility pressure for CO₂ and oil mixtures, while a range of other factors such as population density are considered to account for differences in the limits on H₂S between North American and European CO₂ transportation and storage applications. National Grid's limit on H₂S was selected to avoid selection of pipeline materials for sour service. Variation in the permitted concentrations of SO_x is also observed between specifications with Northern Lights being the lowest at 10 ppm_v and National Grid having the highest at 100 ppm_v. Only TAQA gives specific low limits for COS (at 0.1 ppm_v) and (CH₃)₂S (at 1.1 ppm_v). A large disparity on the limits for hydrogen is observed with a limit of 50 ppm_v imposed in the case of Northern Lights but much higher tolerances for National Grid at 2 vol% and TAQA at 0.75 vol%. A notable disparity also exists in the case of CO where at National Grid and TAQA allow up to 2000 and 750 ppm_v, respectively, but Northern lights has the tightest restriction at 100 ppm_v.

Given the types and levels of impurities expected in CO₂ streams captured from BFG presented in table 4 and the limits imposed for impurities in the CO₂ specifications of table 5, insights can be gleaned into which components may be problematic for the iron and steel industry in meeting the CO₂ purity requirements for the associated transportation and storage infrastructure. Notably, that in the PSA cases, CO is an issue and will need to be significantly reduced in order to meet any of the specifications. Even the CO₂ captured by the amine

Table 5: Comparison of CO₂ specifications for CO₂ transport and storage [18][19][20].

	Limiting concentration criterion		
	Northern Lights [†]	National Grid*	TAQA
CO ₂	-	≥ 91 vol% (gaseous phase) ≥ 96 vol% (dense phase)	≥ 95% ‡
H ₂ O	≤ 30 ppm _v	≤ 50 ppm _v	≤ 40 ppm _v
O ₂	≤ 10 ppm _v	≤ 10 ppm _v	≤ 40 ppm _v
NO _x (NO+NO ₂)	≤ 10 ppm _v	≤ 100 ppm _v	≤ 5 ppm _v (≤ 2.5 ppm _v + ≤ 2.5 ppm _v)
SO _x	≤ 10 ppm _v	≤ 100 ppm _v	≤ 50 ppm _v
H ₂ S	≤ 10 ppm _v	≤ 20 or 80 ppm _v §	≤ 5 ppm _v
COS	-	¶	≤ 0.1 ppm _v
(CH ₃) ₂ S	-	-	≤ 1.1 ppm _v
H ₂	≤ 50 ppm _v	≤ 2 vol%	≤ 0.75 vol%
N ₂	-	Depends on saturation P [‡]	≤ 2 mol%
Ar	-	Depends on saturation P [‡]	≤ 1 mol%
CH ₄	-	Depends on saturation P [‡]	≤ 1 mol%
CO	≤ 100 ppm _v	≤ 2000 ppm _v	≤ 750 ppm _v
Amine	≤ 100 ppm _v	¶	-
NH ₃	≤ 10 ppm _v	¶	-
HCN	-	¶	≤ 20 ppm _v
Formaldehyde	≤ 20 ppm _v	-	-
Acetaldehyde	≤ 20 ppm _v	-	-
Mercury, Hg	≤ 0.03 ppm _v	¶	-
Cadmium, Cd Thallium, Tl	≤ 0.03 ppm _v (sum)	-	-
C ₂ + (hydrocarbons)	-	-	≤ 1200 ppm _v
Aromatics (incl. BTEX)	-	-	≤ 0.1 ppm _v
C ₂ H ₄	-	-	≤ 1 ppm _v
Total VOC	-	-	≤ 750 ppm _v

* Entry may be permitted for compounds other than those listed (Hg + derived compounds, Se, MEA, Selexol, NH₃, HCl, HF, HCN, COS etc.), conditional on them not exceeding detection limits and to be determined on a case by case basis.

† Non-condensable gases are defined in the Northern Lights specification as components that, when pure, will be in gaseous form at 15 barg and -26°C, where their content will be limited by the actual solubility in liquid CO₂ in the interim storage tanks at the capture plants.

‡ The sum of non-condensable species H₂, N₂, Ar, CH₄, CO and N₂ should not exceed 4 vol%.

§ Limits of 80 and 20 ppm_v apply to gaseous (below 80 barg) and dense (below 156 barg) phases, respectively.

‡ The allowable concentration of non-condensable components is subject to confirmation that the mixture saturation pressure does not exceed 80 barg.

¶ Must not exceed levels above measurable limits and need to be discussed and agreed with National Grid.

system which has the lowest content of CO estimated at 200 ppm_v will not meet the 100 ppm_v threshold for the Northern Lights specification. Other potentially problematic impurities include reduced sulfur compounds, H₂S and COS. Reductions in the content of H₂S in CO₂ for all PSA and amine capture systems appears to be needed while a drastic reduction in COS would be required to meet the TAQA specification. Issues related to SO_x would appear to be less of a concern where all three estimated capture qualities would already meet the required threshold for all CO₂ specifications. Similarly, the nitrogen containing impurities, HCN and NH₃ appear not to need specific targeting by additional separation. To meet the strict limits on water concentration, it is clear that some form of dehydration will be needed to reduce the amounts from saturated levels from the capture systems, although this should not be of great concern due to available technologies being mature and inexpensive. Other potential impurities of concern include H₂ in the case of meeting the Northern Lights specification and O₂ where air ingress may take place in iron and steel plant or CO₂ capture systems. O₂

may also become a problematic impurity in species for other types of technologies that could be employed for CO₂ capture on iron and steel plants such as those that use oxy-combustion based approaches. In the following section, we discuss approaches that can be taken to reduce the impurities of concern in the captured CO₂ from BFG streams.

5. CO₂ purification approaches

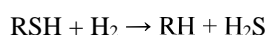
In this section, approaches to CO₂ purification suitable for CO₂ capture from BFG are discussed with emphasis on targeting the critical contaminants, reduced sulfur species and CO. Multicomponent removal solutions are also outlined.

5.1 Approaches to H₂S and COS reduction

Sulfur components can be removed either by wet scrubbing or by dry adsorption processes. In wet processes, the sulfur components can be removed by physical (e.g. Rectisol) or chemical adsorption (e.g. MEA) or by a combination of both. An example of a dry

process is the adsorption of H₂S on ZnO [21]. Technologies for sulfur reduction should be selected on the basis of inlet and target concentration, while scale is another important factor. Wet processes are characterised by high investment costs and are therefore mainly used at large scale. Dry processes are used mainly for low inlet concentrations and therefore may be suitable for targeting the levels of sulfur in BFG. The ZnO adsorbent process is widely used for H₂S removal (at levels normally <50 ppm) from natural gas or syngas at temperatures of 200–450°C. In a conventional catalytic adsorbent purification system, illustrated in Figure 2, ZnO is used in conjunction with hydrogenation catalysts based on cobalt, molybdenum and nickel. This system involves the hydrogenation of sulfur compounds such as mercaptans to H₂S, and halides such as chlorides to HCl. These compounds are then reacted with the ZnO absorbent where H₂S is converted to zinc sulfide, and HCl forms a stable chloride. Additionally, ZnO removes COS by hydrolysis to form H₂S which is then adsorbed to form zinc sulfide [22]. The general, reactions are summarised as follows:

Hydrogenation reactions:



Reactions with ZnO:

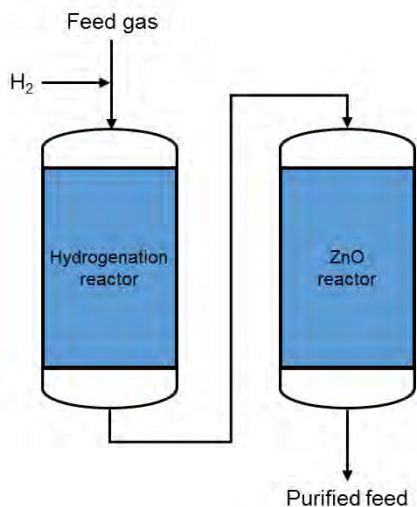
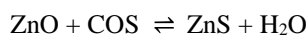
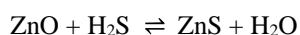


Figure 2: Conventional ZnO purification system [22].

Sulfur removal below 50 ppb_v is attainable with ZnO. However, a hydrogenation reactor may not be required in the case of processing BFG if the presence of halogens and sulfur compounds other than H₂S and COS is not a concern for the downstream impacts. A quantity of 100 kg ZnO is required to remove 39 kg S while the cost of a ZnO sorbent is ~2 \$/kg.

5.2 Approaches to CO reduction

Different approaches can be taken for reducing the CO content in captured CO₂ streams that may once again depend on the quantities involved, the inlet and target concentrations. In the case of low purity CO₂ from the

PSA based capture case with 83% purity CO₂, a cryogenic based system is an option to remove CO simultaneously with other non-condensable components. In such a system, CO₂ is liquefied to separate it from the non-condensable gases. The ULCOS program [23] explored the use of PSA and vacuum PSA (vPSA) systems with a subsequent cryogenic separation for achieving high purity CO₂. Cryogenic flash separation is commonly used to treat CO₂ streams with above 80 mol% purity. Higher grades of CO₂ can be produced using cryogenic distillation which have a history of development for oxyfuel combustion power systems, and operate at elevated pressures ~30 bar and low temperatures between -10 °C and -60 °C. The conditions in this process make it energy intensive with an energy requirements for the CO₂ Compression and Purification system (CPU) ranging from of 412 to 700 kJ/kgCO₂. Typical recovery efficiencies are in the range of 86.6 to 90.1% with CO₂ purities as high as 99.99 vol% achievable [24].

Other approaches to CO reduction can involve conversion by reaction to other compounds which are more easily separable or have higher thresholds in the CO₂ specifications. For example, the water gas shift process could be used to convert CO to CO₂ and H₂ but would necessitate both high and low temperature conversion units for deep CO reduction. Employing this process could also lead to improved overall CO₂ capture rates above 80%. Alternatively, CO could be reacted with H₂ to produce CH₄ or with O₂ to produce CO₂. Oxidation as an approach to CO reduction is covered below in the context of multi-component removal approaches.

5.3 Approaches to multicomponent reduction

Catalytic oxidation has been used as an approach to remove ppm levels of impurities from raw CO₂ streams to produce high purity CO₂ product for different applications including for the food industry. Praxair patented a technology for the removal sulfur compounds and hydrocarbons from CO₂, which is also capable of CO reduction [25]. This technology uses a sulfur tolerant catalytic oxidation system whereby contaminants are oxidised to CO₂, water and SO₂ which are then removed by adsorption and/or absorption techniques. While hydrocarbons are converted to CO₂ by the catalytic oxidation process, sulfur compounds (e.g. H₂S, CS₂, COS and mercaptans) present in the CO₂ stream react with O₂, forming their respective combustion products according to the following reactions:

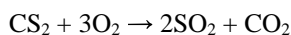
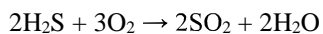


Figure 3 presents a simplified process block flow diagram for the purification system by catalytic oxidation. Crude CO₂ first passes through a compression step and liquid water is removed by a separator. In this system, O₂ is injected either as air or PSA produced O₂ to maintain an excess O₂ concentration of approximately 1000 ppm in the gas stream leaving the catalytic

oxidation reactor. The temperature of the gas entering the catalytic reactor is increased to approximately 315 to 480 °C and then passed over a sulfur tolerant metal catalyst (platinum and palladium catalysts are preferred) where the impurities react with the O₂ to form oxidised products. The temperature of the catalytic bed is typically kept below about 425 °C to minimise the oxidation of CH₄ since this contaminant can readily be removed in a subsequent CO₂ liquefaction/stripper stage. The catalytic oxidiser is operated at preferred pressure of about 17 to 22 bar. After the hydrocarbon contaminants and the sulfur compounds are converted to their respective oxides, upon exiting the catalytic oxidiser, the gas stream is cooled by means of a cooler/condenser and condensed

water is removed using a water separator. The sulfur oxides are next subsequently removed from the CO₂ stream by absorption, for high concentrations of sulfur components (e.g. ~100-5000 ppm), or by adsorption, for low concentration of sulfur components (e.g. ~1-100 ppm). The gas stream (which now is free of sulfur, hydrocarbon compounds and water) enters the CO₂ liquefier, where the non-condensables (e.g. O₂, N₂ and CH₄) are separated by distillation and vented from the liquid CO₂ stream. The process is claimed to produce CO₂ at a quality of 99.9 vol% CO₂ with N₂ < 60 ppm_v, O₂ < 30 ppm_v, sulfur species < 1 ppm_v, total hydrocarbons < 20 ppm_v and water < 20 ppm_v and at a temperature of -18 °C and pressure of 10 bar.

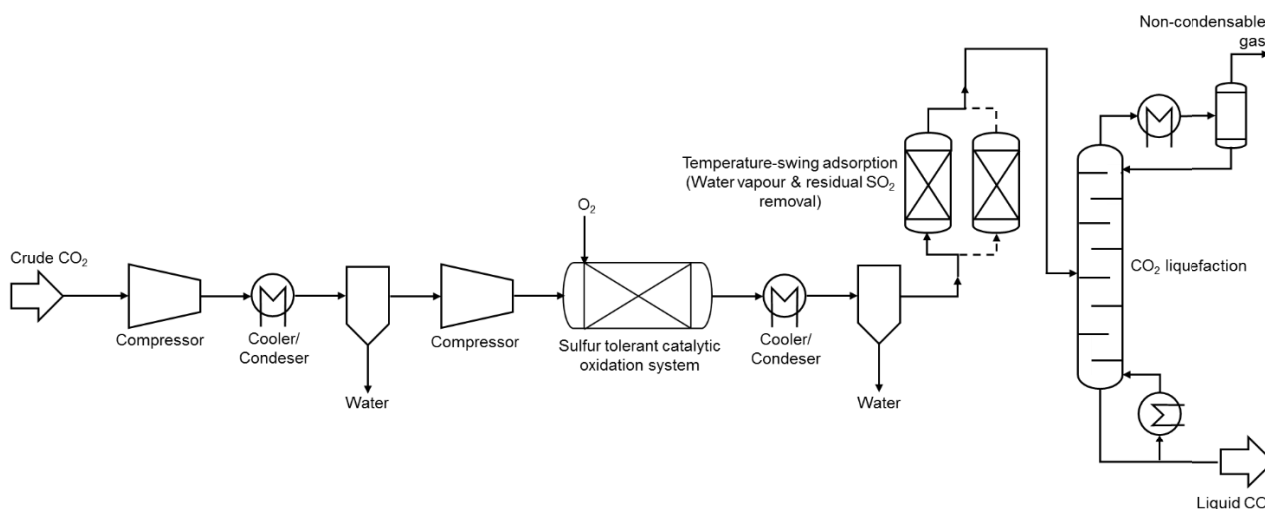


Figure 2: Block flow diagram of CO₂ purification process by catalytic oxidation (based on [25]).

Other embodiments of the above process have been proposed where the excess O₂ is chemisorbed by a bed of transition metal adsorbent (i.e., Cu or Ni) in place of a distillation system, or where the excess oxygen leaving the catalytic oxidation system is controlled to less than 30 ppm by using a “tight control” option [25].

At the time of writing, no detailed techno-economic studies of CO₂ purification by catalytic oxidation for removal of CO and sulfur components are available in the literature.

5.4 Water removal technologies

Dehydration of CO₂ streams can be carried out using several technologies, including compression and cooling, adsorption using solid desiccants, absorption using liquid desiccants, absorption with a deliquescent solid, and cooling below the initial dew point [26].

Guidelines for the selection of dehydration technology for carbon capture systems have been put forward by Kemper et al. [27] which allocates a range of technologies, such as TEG (triethylene glycol) and molecular sieve systems, applicable to certain ranges of wet gas water content and a target dry gas concentrations. These authors also noted that the presence of impurities, i.e. NO_x, SO_x and H₂S, leads to a 7% higher capital expenditure (CAPEX) but no difference in operational expenditure (OPEX) for molecular sieve systems. For the

iron and steel industry, the derived CO₂ product streams presented in table 4 and the target concentrations of European CO₂ specifications listed in table 5, molecular sieve and silica gel systems are the most likely technologies for implementation.

6. Conclusion

This paper has reviewed the range and level of impurity components in steelworks off-gases and provided estimates of their carry over into CO₂ product streams when primary capture steps of PSA (low and high purity scenarios) and amine scrubbing are applied to BFG. While useful insight can be gleaned from these estimates, they require further assessment by experimental investigation and detailed process simulation studies. European CO₂ transportation and storage specifications have been reviewed and compared, with the implications for the impurity content of CO₂ streams captured from BFG. In many cases, additional gas clean-up measures will likely be needed if the CO₂ specifications for impurity limits that are currently imposed by CO₂ transportation and storage providers are to be met. Particular CO₂ impurities of concern that require reduction for the presented applications of CCS in the iron and steel industry are CO and the reduced sulfur species H₂S and COS. Dehydration systems will also be needed for CO₂ product processing. Options for removing sulfur components suitable for the levels

present in BFG focus on adsorption based systems, while CO reduction techniques for impure CO₂ involve cryogenic separations. Multicomponent removal methods for CO and sulfur species involve catalytic oxidation followed by adsorption/absorption and cryogenic separation.

It should be noted that reasonable limits on impurities in CO₂ must be set on the basis of safety, design, operation, integrity and hydraulic efficiency of the associated transportation and storage infrastructure and these requirements have to be considered as a whole. Thresholds which are excessively stringent for impurities in CO₂ transportation and storage specifications will cause a financial burden on CO₂ emitters due to the associated costs of removal, therefore posing a potential barrier to CCS deployment. Conversely, the emission of high levels of impurities in CO₂ product streams into infrastructure could move the financial burden onto transportation and storage providers. Techno-economic analysis techniques should be employed to consider site-specific design and operation of the CCS chain during normal and abnormal operation in order to achieve an optimised balance between the cost of purification and the impacts of impurities on CO₂ transportation and storage infrastructure.

Acknowledgements

This work has received funding from the European Union's Horizon 2020 research and innovation programme under grant agreement no. 884418. The work reflects only the authors' views and the European Union is not liable for any use that may be made of the information contained therein.

References

- [1] <https://www.worldsteel.org/media-centre/press-releases/2021/Global-crude-steel-output-decreases-by-0.9--in-2020.html>
- [2] https://www.energy-transitions.org/wp-content/uploads/2020/08/ETC-sectoral-focus-Steel_final.pdf
- [3] Manzolini, G. et al. 2020. Techno-economic assessment of SEWGS technology when applied to integrated steel-plant for CO₂ emission mitigation. *Int J Greenh Gas Control*, 94, 102935.
- [4] IEAGHG, "Impact of COR2R impurity on COR2R compression, liquefaction and transportation". 2016/01, April, 2016.
- [5] Brown, A., Eickhoff, C., Reinders, J.E.A., Raben, I., Spruijt, M. and Neele, F. (2017) 'IMPACTS: framework for risk assessment of CO₂ transport and storage infrastructure', *Energy Procedia*, 114, 6501–6513.
- [6] M. Woods, M. Matuszewski. Quality Guideline for Energy System Studies: CO₂ Impurity Design Parameters NETL/DOE-341/011212 (2013).
- [7] Porter, R.T.J. et al. CO₂QUEST: An overview of aims, objectives and main findings. *Int. J. Greenh. Gas Control* 2016, 54, 662–681.
- [8] J. Schittkowski et al. Methanol Synthesis from Steel Mill Exhaust Gases: Challenges for the Industrial Cu/ZnO/Al₂O₃ Catalyst. *Chem. Ing. Tech.*, 90 (2018), pp. 1419-1429.
- [9] R. Remus, M. A. Aguado-Monsonet, S. Roudier and L. D. Sancho: Best Available Techniques (BAT) Reference Document for Iron and Steel Production, Industrial Emissions Directive 2010/75/EU, Integrated Pollution Prevention and Control, Publications Office of the European Union, Luxembourg, (2013), 1.
- [10] M. Bender, T. Roussiere, H. Schelling, S. Schuster, E. Schwab. Coupled production of steel and chemicals. *Chem Ing Tech*, 90 (2018), pp. 1782-1805.
- [11] Lanzerstorfer, C. Preitschopf, W. Neuhold, R. Feilmayr, C. Emissions and Removal of Gaseous Pollutants from the Top-gas of a Blast Furnace. *ISIJ Int.* 2019,59(3), 590–595.
- [12] Pugh, D., et al. 2013. Thermal distributive blast furnace gas characterisation, a steelworks case study. *Applied Thermal Engineering* 53 (2), pp. 358-365.
- [13] S. Caillat. Burners in the steel industry: utilization of by-product combustion gases in reheating furnaces and annealing lines. *Energy Procedia* 2017, 120, 20–27.
- [14] J.R. Fernandez, V. Spallina, J.C. Abanades Advanced packed-bed Ca-Cu looping process for the CO₂ capture from steel mill off-gases. *Front Energy Res*, 8 (2020), 146.
- [15] W.H. Saima, Y. Mogi, T. Haraoka. Development of PSA system for the recovery of carbon dioxide and carbon monoxide from blast furnace gas in steel works. *Energy Proced.* 37 (2013), pp. 7152-7159.
- [16] M. Dreillard, P. Broutin, P. Briot, T. Huard, A. Lettat. Application of the DMX™ CO₂ capture process in steel industry. *Energy Procedia*, 114 (2017), pp. 2573-2589.
- [17] Palma, V.Vaiano, V. Barba, D. Colozzi, M. Palo, E; Barbato, L. Cortese, S. Miccio, M. Study of the carbonyl sulphide hydrolysis reaction in liquid phase. *Chem. Eng. Trans.* 2019,73, 247–252.
- [18] Equinor. (2019). Northern Lights Project Concept Report.
- [19] NGC/SP/PIP/25. National Grid Carbon Specification for Carbon Dioxide Quality Requirements for Pipeline Transportation, 2019.
- [20] TAQA Energy B.V. (2019). Porthos Basis of completion design.
- [21] Hofbauer H, Rauch R, Ripfel-Nitsche K (2008) Report on gas cleaning for synthesis applications, final report, EU-ThermalNet.
- [22] Nexant Inc. Equipment Design and Cost Estimation for Small Modular Biomass Systems, Synthesis Gas Cleanup, and Oxygen Separation Equipment, Task 1: Cost Estimates of Small Modular Systems; Subcontract Report NREL/SR-510-39943; May 2006.
- [23] Keys, A, M Van Hout, and B Daniëls (2019). Decarbonisation options for the Dutch steel industry. *Tech. rep.:www.pbl.nl/en*.
- [24] Font-Palma, C. et al. Integrated oxyfuel power plant with improved CO₂ separation and compression technology for EOR application. *Process. Saf. Environ. Prot.* 2016, 103, 455–465.
- [25] EP0952111A1. CO₂ purification system, 1999.
- [26] Z. Abbas, T. Mezher, M.R.M. Abu-Zahra CO₂ purification. Part I: Purification requirement review and the selection of impurities deep removal technologies. *Int J Greenh Gas Control*, 16 (2013), pp. 324-33.
- [27] J. Kemper, L. Sutherland, J. Watt, S. Santos. Evaluation and analysis of the performance of dehydration units for CO₂ capture. *Energy Procedia*, 63 (2014), pp. 7568-7584.

ON THE DISTINCTIVENESS OF NOBLE GASES IN INJECTED CO₂ FROM BACKGROUND FLUIDS

Ulrich W. Weber^{1*}, Niko Kampman², Anja Sundal¹

¹ University of Oslo, Oslo, Norway

² Shell Global Solutions International B.V., Amsterdam, Netherlands

* Corresponding author e-mail: u.w.weber@geo.uio.no

Abstract

A comprehensive monitoring program for CO₂ storage sites is an integral part of designing CCS projects. Once a CO₂ anomaly is observed or suspected, the source of the CO₂ may be identified through evaluation of geochemical tracers. Noble gases are one of those geochemical tracers that display unique signatures for the environmental reservoirs involved in the storage site system.

The background fluids at storage prospect, such as formation water, hydrocarbons or shallow gases need to be characterized prior to injection. Typical noble gas signatures are of atmospheric, crustal/radiogenic or mantle character. Captured CO₂ can contain a large range of noble gas concentrations and ratios with typically significantly lower concentrations than the other background fluids.

Here, we collect the noble gas analysis of various environmental fluids in the storage site system relevant to the North Sea, such as hydrocarbons and shallow gases, to narrow down possible observable signatures. If samples are not available realistic values can be inferred from analogue sites/studies. Further, we show that after injection, phase partitioning, hence equilibration, of the injected CO₂ with formation water leads to adaption of a radiogenic signature from the formation water. Therefore, the initially low concentrations of the CO₂, and their associated elemental and isotopic ratios, are only preserved when remaining almost pure. These signatures can be applied to mixing calculations with the background fluids to rule out if injected CO₂ is contributing to an anomaly.

Meanwhile, noble gases are one of the environmental tracers that could be cost-effective since they are naturally inherent in the CO₂ and the storage reservoir fluids, we also model the addition of artificial noble gas tracers to increase the detectability, i.e. ability to recognize lower contributions of injected CO₂ in a background reservoir fluid. These calculations can be fed into cost calculations to estimate the economic impact of such an additional monitoring measure.

Keywords: *Monitoring and Verification, Noble gases, Tracer addition*

1. Introduction

Designing a CO₂ storage sites measurement, monitoring and verification (MMV) program is an essential part of a CCS project [1]. The Norwegian ‘Longship’ project aims to store CO₂ in the ‘Aurora’ prospect in the North Sea in the vicinity of the Troll oil and gas field. The planned, continuous MMV program does not include noble gases [2], however, with the content of ‘triggered’ environmental monitoring surveys not yet defined, this may be included there.

Noble gases are trace constituents of most environmental fluids. The concentrations of He, Ne, Ar, Kr, Xe, and their isotopic ratios constitute a signature or ‘fingerprint’ of a fluid. Due to their inertness, only physical processes influence them such that they have widespread application in deciphering physical and geochemical processes [3]. Inherent noble gas tracers were used to refute an alleged leakage from a CO₂ storage site [4].

The main groups of noble gas fingerprints are of atmospheric [5], crustal [6] and mantle character [7]. However, there are wide isotopic concentration ranges within these categories, such that characterizing the

background fluids of a storage site is key for the applicability of noble gases as tracers. Therefore, the ICO₂P project has characterized the signature of various captured CO₂ streams [8,9,10]. Noble gases showed large variation at the different sample sites and all were being depleted through the CO₂ capture process in a way that the captured CO₂ has a low noble gas content compared to other background fluids (e.g. natural gas). For background fluids at the ‘Aurora’ storage site noble gas samples have not yet been analyzed such that analogue studies e.g. describing other hydrocarbon systems in the North Sea can be used to infer the noble gas content.

One also has to consider that the CO₂ can undergo interaction with e.g. in-situ formation water or gases, subsequently altering the noble gas fingerprint. In previous work [8,9], we showed that the phase partitioning with formation water leads to the stripping of gases and inheritance of a radiogenic signature. We concluded that this provides a monitoring target in differentiating injected, “anthropogenic” CO₂ from shallow, natural CO₂ sources, e.g. biogenic or gas hydrates.

In this work, we build the foundation of noble gas signatures that may be expected for the North Sea and follow up previous calculations with mixing calculations of the injected, equilibrated CO₂ with other fluids possibly involved in anomalies.

Further, we apply the calculations to a simulated addition of noble gas tracers. This can increase the distinctiveness of the injected CO₂ relative to natural fluids. However, this comes with a cost, which can be estimated from an economic analysis including the tracer gas amounts needed and the related gas prices.

2. Baseline Concentrations

Collecting the baseline concentrations of fluids in the storage site system allows assessing differentiability of the background to injected CO₂. Tab. 1 shows a summary of the expected ranges for different environmental fluids.

Captured CO₂ has been analyzed for several capture plants in Norway [8,9,10] and other countries [11]. Noble gas concentrations are typically low and the isotopic signatures are either air-like for plants with combustion prior to capture (e.g. waste incineration) or natural gas-like (e.g. natural gas processing).

For natural gas, sample analyses for the North Sea are currently available for Sleipner Vest and the Magnus field [12,13]. The results show a typical radiogenic character, deriving from the production of ⁴He, ²¹Ne and ⁴⁰Ar through radioactive decay of the elements K, U and Th in the rocks [6]. Samples for natural, geologic CO₂ have a dominantly magmatic (mantle) signature with subsequent equilibration with radiogenic formation water. The values in Tab. 1 are from large natural CO₂ systems in the US [14,15]. Natural CO₂ in the North Sea context is typically a minor constituent of natural gas accumulations [e.g. 12] and would therefore likely have the same concentrations of associated noble gases as natural gas.

Radiogenic signatures can cover a large range since the amount of a noble gas isotope in subsurface reservoirs; natural gas, oil, natural CO₂ or in pore water, is dependent

on the exchange with other fluids from the atmosphere, crust and mantle. Further, longer time of separation from other reservoirs allows for more radiogenic accumulation. The provenance of natural gas can also have an impact i.e. stripping of noble gases during migration through formation water.

Close to the seabed gas hydrates may occur. Only elemental gas concentrations have been analyzed for gas hydrates but not the isotopic composition [16]. Those samples were collected outside the coast of Oregon, US and showed a quite specific fractionation pattern with preferential incorporation of heavier noble gases and suppression of the lighter ones (Tab. 1).

Sediment samples, i.e. the dissolved noble gases in the sediments' pore-water, are rare and for the North Sea there is no data set available. Sediment pore water concentrations are dependent on the temperature during sedimentation and if there are leakage sites, e.g. black smokers, nearby. The data from [17,18] has to be seen in the context of continental plate boundaries which may therefore not be representative for the North Sea.

Seawater, if not in the vicinity of specific fluid releases, is typically air equilibrated water at a given temperature and salinity [19]. This means atmospheric gas, including noble gases, is dissolved based on the solubility of the respective gas species at these conditions in water. In case there are seepages, ocean currents may redistribute them fast, so anomalies can be local. The atmosphere is typically well mixed and has a set noble gas signature [5].

With regards to isotopic ratios there are the three main signatures and fluids represent mixtures of these to various degrees. Typical values for the isotopes mainly affected are shown in Tab. 2.

For captured CO₂ the ratios are dependent on the source of flue gas and if combustion has taken place prior to capture, e.g. at heat and power plants. Combustion typically introduces noble gases from the air also shifting

Table 1: Observed noble gas concentrations for the different fluids in the storage site systems. Captured CO₂ from several sites [8,11]. Atmospheric values from [5]. Seawater concentrations after [19] (assuming a temperature of 7,5 °C and a salinity of 34,2 g/L). Natural gas for He, Ne and Ar compiled from the Sleipner field and Magnus oil field in the North sea from [12,13], Kr and Xe from Sleipner Field [12]. Natural CO₂ compiled from [14] and [15]. Sediment values from the South Pacific Ocean [17] and the Mediterranean ridge for helium [18]. Gas hydrates from [16].

	He	Ne	Ar	Kr	Xe
Captured CO₂	2,29E-09 – 2,9E-06	6E-11 – 4,27E-07	3,7E-10 – 1,4E-04	3,6E-12 – 6,3E-09	1,1E-13 – 1,9E-09
Natural CO₂	1E-04 – 1E-02	7,0E-08 – 1,8E-06	1,5E-05 – 2,7 E-05	1,0E-10 – 1,0E-08	5,0E-12
Natural Gas	5E-03 – 1,3E-04	0,8E-08 – 2,7E-08	1,5E-05 – 2,7E-05	9,5E-09	2,0E-09
Gas Hydrates	7,0E-10 – 9,0E-10	2,5E-09 – 6,2E-08	3,5E-05 – 5,3E-04	1,8E-08 – 3,0E-07	2,7E-09 – 9,4E-08
Sediment (cm³/g)	1,0E-04 – 1,0E-02	5,0E-09 – 5,0E-07	1,0E-05 – 1,0E-08	5,0E-08 – 1,5E-09	8,0E-09 – 1,7E-08
Seawater (cm³/g)	4,0E-08	5,7E-09	1,1E-06	8,5E-08	1,1E-08
Atmosphere	5,24E-06	1,82E-05	9,34E-03	1,13E-06	8,7E-08

	³ He/ ⁴ He (R/R _A)	²¹ Ne/ ²² Ne	⁴⁰ Ar/ ³⁶ Ar	⁸⁶ Kr/ ⁸⁴ Kr	¹³² Xe/ ¹³⁰ Xe
Atmospheric Signature	1	0,029	296	0,303	6,61
Crustal signature	~0,1	~0,033	~455	~0,303	~6,61
Mantle signature (MORB)	8	0,06	~30000	-	-

Table 2: Isotopic ratios for the main signatures: atmospheric [5], crustal [6], hence radiogenic, and mantle [7]. If “~” sign averaged from several samples.

ratios towards atmospheric values. At natural gas processing sites the radiogenic ratios are maintained [8].

Noble gas ratios associated with hydrocarbons are dependent on the geological setting of a reservoir and the provenance of the natural gas. In Tab. 2 isotopic ratios are shown for the North Sea [12]. However, especially the ³He/⁴He and ⁴⁰Ar/³⁶Ar ratio can be quite varying, e.g. natural gas from Snøhvit has an order of magnitude lower value for the He ratio [8].

3. CO₂ Signature after Injection

3.1 Phase Partitioning

We calculated phase partitioning with formation water that would occur after CO₂ injection and during migration in [8,9]. We showed that the depleted signature of the captured CO₂ is not maintained, but in contrast largely inherited from the formation water by gas stripping. Thereby, the CO₂ adopts a radiogenic signature.

In [8,9] we derived the assumed formation water concentrations based on assuming equilibrium of the water with natural gas of the Snøhvit Field. Since Snøhvit is located in a different geological setting compared to prospective sites in the North Sea, the noble gas accumulation is expectedly larger in the Snøhvit Field than in the North Sea. Therefore, in this work, we used the values from the Sleipner Field [12] to calculate the concentrations at the given gas-water ratios, V_g/V_w.

By calculating the ratio of the concentrations in the CO₂ relative to the concentrations at very low V_g/V_w, it becomes apparent that the formation water signature dominates up to high gas-water ratio (Fig. 1). The most relevant value for V_g/V_w is the maximum water saturation, S_{max} which is approximately at 1,5. Here, no more water can be replaced by CO₂. At the maximum water saturation, S_{max}, concentrations constitute 80-90% of that of the formation. The slight differences for the enrichment for the single gases derives from gas specific solubilities.

Only at very high V_g/V_w the concentrations of the injected CO₂ will be influential without tracer addition. However, this is likely not possible to be achieved considering maximum saturation. In a scenario where an area of a reservoir is repeatedly flushed by CO₂ significant parts of the original noble gas content could have been stripped, thereby making the signature of the injected CO₂ more influential or possible to be approached. This could for example be the case at CO₂-EOR (enhanced oil recovery).

3.1 Tracer Addition

The adopted signature of the formation water into injected CO₂ allows differentiation from fluids that do not have a radiogenic signature, i.e. shallower sources (see Tab. 1). The approach of modelling phase partitioning also allows to evaluate the active addition of a noble gas tracer to the injection stream with the goal to

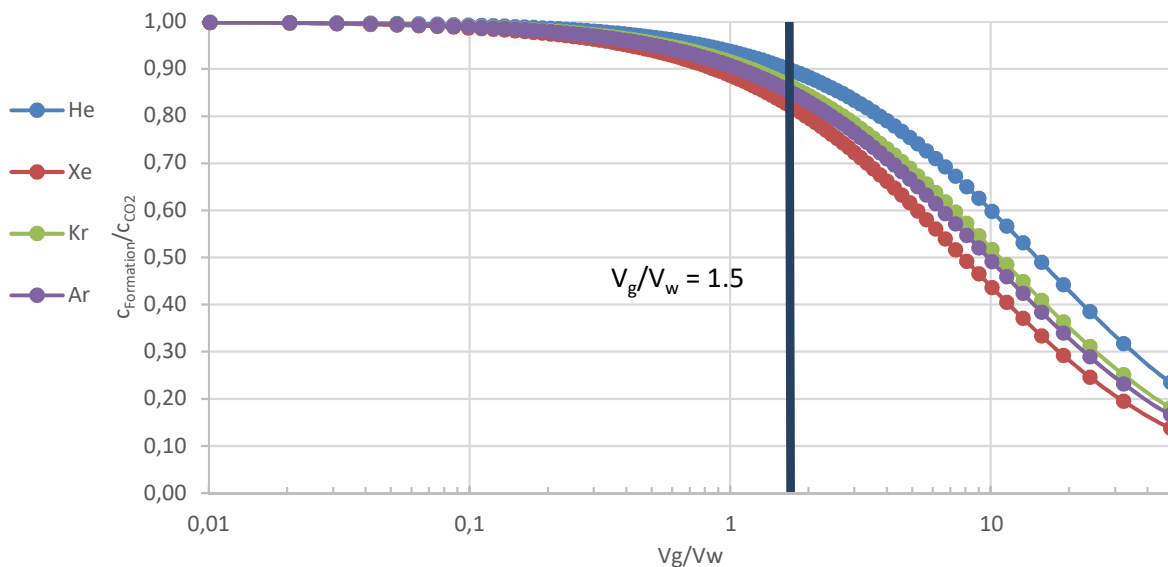
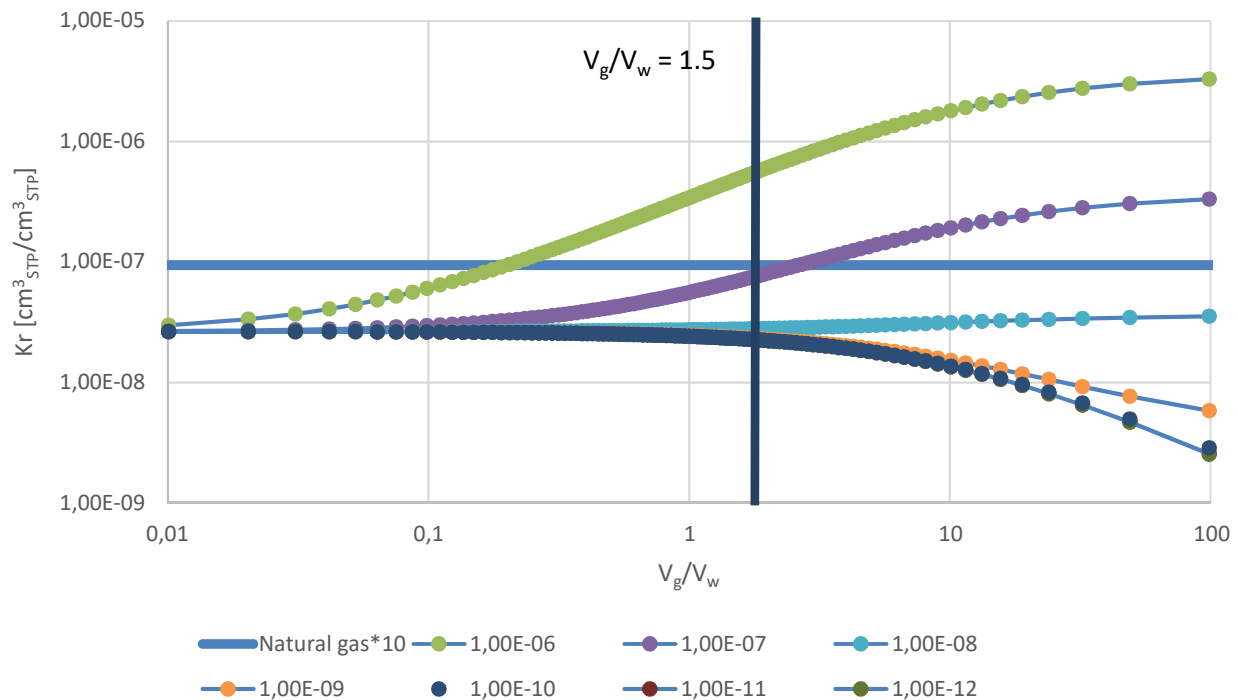


Figure 1: Phase partitioning of captured CO₂ from Klemetsrud, containing trace amounts of noble gases, with formation water with a crustal signature (equilibrated with natural gas from Sleipner. Concentration in the CO₂ relative to concentrations at a V_g/V_w of 0.0001. Modified from [9]. Up to realistic gas-water volume ratios, the formation water signature prevails.

Figure 2: Tracer concentration in injected CO₂ after equilibration for the addition of an artificial tracer; Kr in this example, in the injected CO₂ in dependence of V_g/V_{H₂O}. Lines represent values for a tracer in the given order of magnitude. Between magnitudes 5E-07 – 1E-06 cm³_{STP}/cm³_{STP} an added tracer would be one order of magnitude above natural gas concentration at S_{max} = V_g/V_w = 1.5.



maintain a significant different noble gas signature after the equilibration.

Kr and Xe are especially relevant choices for noble gas tracer addition, since they have low concentrations in background (see Tab. 1) and do not impact the main features of the radiogenic signature, in contrast e.g. to He. This could be used to differentiate the injected CO₂ from natural gas that may be in the vicinity of a storage site, as is the case at ‘Aurora’ [2].

For the addition of elemental Kr the resulting noble gas concentrations are modelled in dependence of V_g/V_w for a range of concentrations in the injected CO₂ (Fig.2). To achieve a value of one order of magnitude above the background in natural gas, to be significantly distinctive, an addition of Kr with concentrations in the injected CO₂ of 5E-07 – 1E-06 cm³_{STP}/cm³_{STP} is necessary at maximum saturation (S_{max}). At ratios lower than S_{max}, the background formation fluid signature prevails despite higher tracer concentrations. The same calculation leads to 5E-08 – 1E-07 cm³_{STP}/cm³_{STP} for Xe.

The value of one order of magnitude above a background, in this case natural gas, to reach distinctiveness is an arbitrary choice. It shall account for uncertainties in background concentrations and that a leakage may be a mixture of gases, where the CO₂ is a minor component.

The necessary amounts of a trace gas can be scaled up to a storage sites injection volume to derive the cost of such a tracer addition [20]. Including the single isotopes of the respective noble gas may reduce the amounts needed during injection. For example, ³He is significantly less abundant in the environment than ⁴He. This lower

abundance, however, typically comes with increased production cost of the respective isotope [20].

4. Mixing calculations

Having established the background concentrations (Sec. 2, Tab. 1 and 2), the concentration the captured CO₂ will likely adopt and the potential signature of a tracer addition. Mixing calculations can be performed to estimate the content of injected CO₂ in a fluid. This could for example be conducted on samples from bubbling gas on the seafloor or the production stream of a natural gas field. Once an anomaly is observed noble gas mixing calculations can be applied for leakage attribution.

The noble gas concentrations of a reservoir can vary significantly (Tab. 1). By depicting the values of some of the known signatures on a crossplot it becomes apparent that several orders of magnitude are covered (Fig. 3). Fig. 3 shows the elemental ratio of Xe/He versus Xe for the different background fluids on a double logarithmic scale. He and Xe were chosen due to the low background of Xe and the typically large difference in He between crustal and shallow signatures (Tab. 1). The addition of 1E-07 cm³_{STP}/cm³_{STP} Xe to the injected CO₂ would distinct the signature of the CO₂ after injection from the pure natural gas even further as shown in Fig. 3. Then He would still allow distinction to shallow signatures.

Three mixing calculations are performed in Fig. 3, one for mixing of injected and equilibrated CO₂ with atmosphere and mixing with gas hydrates to illustrate the content of CO₂ in a mixture being needed to change the elemental ratio. The values are derived from the binary mixture of the two end-members for a given percentage of CO₂ in the fluid mixture. Such an analysis, however,

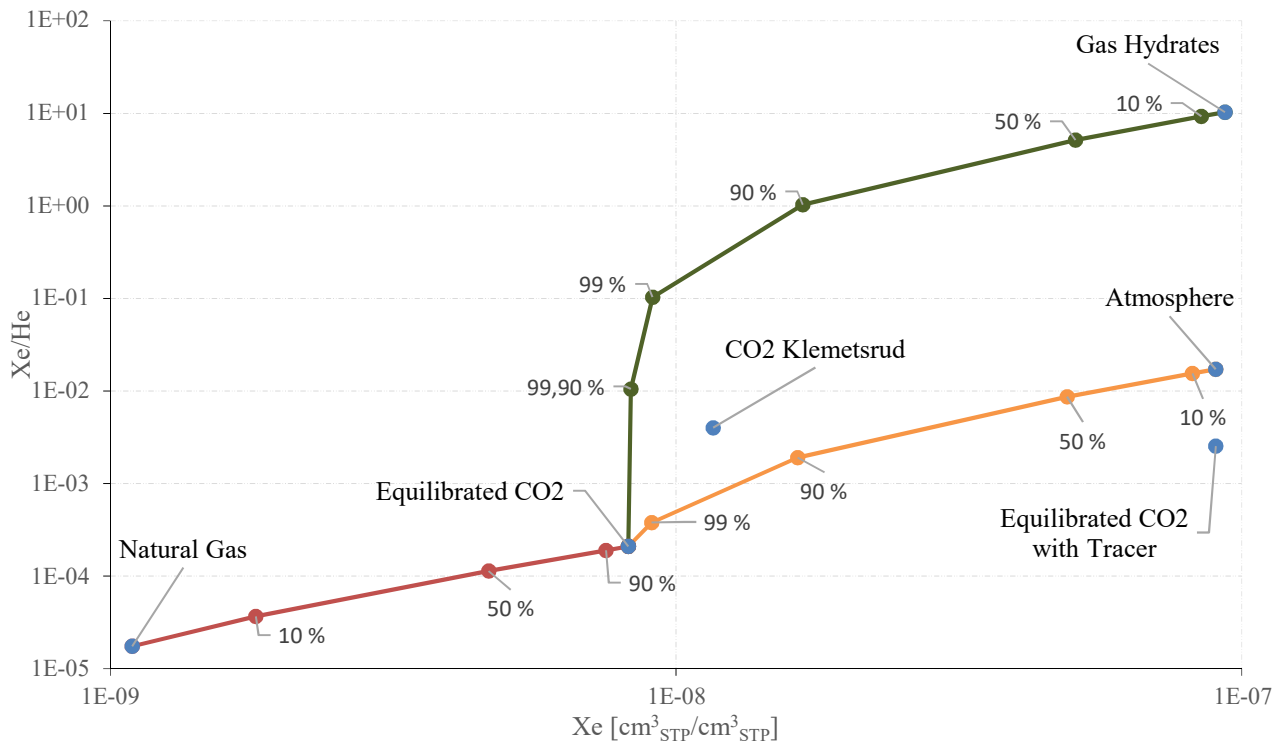


Figure 3: Xe/He vs Xe plotted with mixing lines with equilibrated CO₂ and background fluids (see Sec. 2 and Tab. 1). Mixing lines with the injected, equilibrated CO₂ and signatures of gas hydrates and the atmosphere. Also, equilibrated CO₂ with a tracer addition of 1E-07 cm³_{STP}/cm³_{STP} Xe is included. Mixing lines of injected CO₂ after equilibration with gas hydrates, atmosphere and natural gas with the content of the CO₂ in the mixture in percent.

would further have to account for analytical uncertainty and natural variation of the background fluids. At least the latter one can be addressed by performing a thorough baseline characterization of the storage site prior to injection.

5. Conclusion

The derivation of the signature of the injected CO₂ after phase partitioning with the formation water allows to evaluate differentiability of the possible signatures. Comparing the injected CO₂ to other sources depicts the identifiability and attributability of a leakage through noble gases. Here, we have shown examples how a leakage would be detectable and how the volumetric contribution of injected CO₂ can be estimated. Most notably, the difference between the adopted radiogenic signature and that of shallow fluids with atmospheric or other specific signatures, such as gas hydrates, is very pronounced. We also modelled the amounts that would be needed for tracer addition for Kr and Xe. These can be fed into cost calculations for the respective noble gases. This cost can be broken down to a price per ton and set into perspective to the cost of other monitoring measures of a storage project.

However, there are still uncertainties for some of the background fluids even though the shown inferred concentrations from analogues allow to constrain the possible observed concentrations. Thus, we aim to characterize more fluid compositions from oil and gas fields in the North Sea. Further, we aim to analyze sediment samples from the seafloor to characterize shallow signatures. The ICO₂P project will continue to focus on characterizing the area around the Aurora site,

which has been selected as the storage prospect for the ‘Longship’ project. An extended baseline database will contribute to the goal to conclude on the applicability of noble gas tracers.

Acknowledgements

The ICO₂P-project is funded by the Norwegian Research Council (project number 280551) under a CLIMIT grant (number 616220). Equinor and Shell contribute financially to the project.

References

- [1] P. Ringrose. How to Store CO₂ Underground: Insights from early-mover CCS Projects [2020], Springer, ISBN: 978-3-030-33112-2.
- [2] Furre, A.-K., Meneguolo, R., Pinturier, L., Bakke, K. [2020] Planning deep subsurface CO₂ storage monitoring for the Norwegian full-scale CCS project. First Break, Volume 38, Issue 10, Oct 2020, p. 55 – 60. doi: 10.3997/1365-2397.fb2020074.
- [3] Burnard, P. (Ed.), The Noble Gases as Geochemical Tracers, Springer Berlin Heidelberg, 2013. doi: 10.1007/978-3-642-28836-4.
- [4] Gilfillan, S.M.V., Sherk, G.W., Poreda, R.J. and Haszeldine [2017] Using noble gas fingerprints at the Kerr Farm to assess CO₂ leakage allegations linked to the Weyburn-Midale CO₂ monitoring and storage project. Int. Jour. of Greenhouse Gas Control, 63, 215-225.
- [5] Y. Sano, B. Marty, P. Burnard, Noble gases in the atmosphere, in: The Noble Gases as Geochemical Tracers, Springer Berlin Heidelberg, 2012, pp. 17-31. doi:10.1007/978-3-642-28836-4_2

- [6] Ballentine, C. J., Burnard, P., [2002] Production, Release and Transport of Noble Gases in the Continental Crust, *Reviews in Mineralogy and Geochemistry* 47 (1): 481–538. doi: 10.2138/rmg.2002.47.12.
- [7] Moreira, M.A., Kurz, M.D., Noble gases as tracers of mantle processes and magmatic degassing, in: *The Noble Gases as Geochemical Tracers*, Springer Berlin Heidelberg, 2012, pp. 371-391. doi:10.1007/978-3-642-28836-4_12.
- [8] Weber, U.W., Kipfer, R., Ringrose, P., Horstmann, E., Kampman, N., Tomonaga, Y., Brennwald, M.S., Sundal, A. [2020] Noble Gas Tracers in Gas Streams at Norwegian CO₂ Capture Plants. *Int. Jour. of Greenhouse Gas Control*, 103205, doi: 10.1016/j.ijggc.2020.103238. Noble Gases as Monitoring Tracers in CCS: A Case Study with CO₂ from the Waste-to-Energy Plant Klemetsrud, Norway
- [9] Weber, U.W. and Kampman, N., Mikoviny, T., Thomassen, J., Sundal, A. [2021] Noble Gases as Monitoring Tracers in CCS: A Case Study with CO₂ from the Waste-to-Energy Plant Klemetsrud, Norway. *Proceedings of the 15th Greenhouse Gas Control Technologies Conference* 15-18 March 2021, doi: 10.2139/ssrn.3819288
- [10] Sundal, A., Weber, U., Brennwald, M., Ringrose, P., Flø, N. and Johnsen, K., Faramarzi, L., Aagaard, P., Kipfer, R., [2018] Monitoring Real Time, In-Line Variations of Noble Gas Concentrations During CO₂ Capture Operations by Means of a Portable Mass Spectrometer. *14th Greenhouse Gas Control Technologies Conference Melbourne (GHGT-14)*, doi: 10.2139/ssrn.3366166.
- [11] Flude, S., Györe, D., Stuart, F., Zurakowska, M., Boyce, A., Haszeldine, R., Chalaturnyk, R., Gilfillan, S. [2017] The inherent tracer fingerprint of captured CO₂. *International Journal of Greenhouse Gas Control* 65, 40-54.
- [12] P.H. Barry, M. Lawson, W.P. Meurer, O. Warr, J.C. Mabry, D.J. Byrne, C.J. Ballentine, Noble gases solubility models of hydrocarbon charge mechanism in the Sleipner Vest gas field, *Geochimica et Cosmochimica Acta*, Volume 194, 2016, Pages 291-309, ISSN 0016-7037, <https://doi.org/10.1016/j.gca.2016.08.021>.
- [13] C. Ballentine, R. O'Nions, M. Coleman, A magnus opus: Helium, neon, and argon isotopes in a north sea oilfield, *Geochimica et Cosmochimica Acta* 60 (5) (1996) 831.849. doi:10.1016/0016-7037(95)00439-4.
- [14] C. J. Ballentine, M. Schoell, D. Coleman, B. A. Cain, 300-Myr-old magmatic CO₂ in natural gas reservoirs of the west Texas Permian basin, *Nature* 409 (6818) (2001) 327-331. doi:10.1038/35053046.
- [15] S. M. Gilfillan, C. J. Ballentine, G. Holland, D. Blagburn, B. S. Lollar, S. Stevens, M. Schoell, M. Cassidy, The noble gas geochemistry of natural CO₂ gas reservoirs from the colorado plateau and rocky mountain provinces, USA, *Geochimica et Cosmochimica Acta* 72 (4) (2008) 1174-1198. doi:10.1016/j.gca.2007.10.009.
- [16] Winckler, G., Aeschbach-Hertig, W., Holocher, J., Kipfer, R., Levin, I., Poss, C., Rehder, G., Schlosser, P., and Suess, E. [2002] Noble gases and radiocarbon in natural gas hydrates, *Geophys. Res. Lett.*, 29 (10), doi:10.1029/2001GL014013, 2002.
- [17] Y. Tomonaga, M. S. Brennwald, R. Kipfer [2013] Using helium and other noble gases in ocean sediments to characterize active methane seepage off the coast of New Zealand, *Marine Geology* 344 34-40. doi: 10.1016/j.margeo.2013.07.010.
- [18] M. Nuzzo, Y. Tomonaga, M. Schmidt, V. Valadares, E. Faber, E. Pinero, A. Reitz, M. Haeckel, L. Tyroller, E. Godinho, R. Kipfer, P. G. Terrinha, C. Hensen, [2019] Formation and migration of hydrocarbons in deeply buried sediments of the gulf of cadiz convergent plate boundary - insights from the hydrocarbon and helium isotope geochemistry of mud volcano fluids, *Marine Geology* 410 56-69. doi:10.1016/j.margeo.2019.01.005.
- [19] Y. Sano, N. Takahata, Measurement of noble gas solubility in seawater using a quadrupole mass spectrometer, *Journal of Oceanography* 61 (3) (2005) 465-473. doi:10.1007/s10872-005-0055-x.
- [20] J. J. Roberts, S. M.V. Gilfillan, L. Stalker, M. Naylor [2017] Geochemical tracers for monitoring offshore CO₂ stores, *International Journal of Greenhouse Gas Control* 65, 218-234, doi: 10.1016/j.ijggc.2017.07.021

IS CARBON CAPTURE A VIABLE SOLUTION TO DECARBONISE THE SHIPPING INDUSTRY?

Carolina Font-Palma*

Department of Engineering, University of Hull, HU6 7RX, Hull, UK

* Corresponding author e-mail: C.Font-Palma@hull.ac.uk

Abstract

This work presents some insights into two different options for onboard carbon capture and storage (OCCS). Previous studies have shown that solvent-based carbon capture is feasible, and that the new equipment installed for CO₂ capture would not debilitate the ship stability. This work assesses the potential for cryogenic carbon capture on LNG-fired engines due to the availability of cold conditions through a thermal analysis.

Keywords: shipping, carbon capture and storage, maritime sector, cryogenic separation

1. Introduction

The maritime sector is emitting about 2.5% of global GHG emissions. As a respond, the International Maritime Organization (IMO) has committed to a reduction of at least 40% of CO₂ emissions by 2030 from international shipping and by at least 50% by 2050 compared to 2008 emissions [1]. This need to reduce the emissions of greenhouse gases (GHG) from the shipping sector has enthused the first all-electric ferry that started operation between the island ports of Fynshav and Søby in southern Denmark to powered by a 4.3-MWh battery travels a distance of 40 km between charges [2]. Also, plans for the first liquid hydrogen fuel cell of 3.2MW with battery storage is expected by retrofitting a cruise ship by 2023 in Norway [3]. As an alternative, various options are being assessed including: fuel switching to liquified natural gas (LNG) or other fuels such as biofuels, methanol, hydrogen; electric propulsion systems, and nuclear marine propulsion; vessel improvements such as wind propulsion assistance, slow steaming, low resistance hull coatings, waste heat recovery systems; or exhaust gas treatment (e.g. carbon capture) [4]. However, some of these solutions will require adaptation of engines to new fuels and resolving sustainability challenges of those biofuels. Therefore, this work will focus on exhaust gas treatment measures.

1.1 Background on shipping decarbonisation

The CO₂ intensity of shipping is approximately 13.9gCO₂ tonne⁻¹ km⁻¹ [5]. Thus, a study has shown that the switch to LNG is not enough to achieve the target of 50% reduction of GHG emissions. The study highlights that this option will require to be combined with efficiency measures; whilst bio-based fuels that struggle to derive from sustainable sources will rely more on efficiency measures to reduce their consumption [4]. Balcombe et al. [4] and Bouman et al. [6] presented the CO₂ reduction potential from different methods to decarbonise shipping, none included carbon capture as a potential measure.

Onboard carbon capture and storage (OCCS) systems have been proposed to treat exhaust gases emitted from

the internal combustion engines on board of ships. The stored CO₂ can be unloaded at ports, and then stored underground, undergo methanation or other conversion routes for CO₂ utilisation [7]. In addition, the IMO 2020 regulation has set a cap for sulphur content on fuel from 3.5% to 0.5%, where vessels will need to either change to low sulphur fuels or be fitted with scrubbers to comply such targets [1]. Awoyowi et al. [8] proposed scrubbing using aqueous ammonia for the simultaneous removal of CO₂ and SO₂ from the flue gas from a 10,800 kW Wärtsilä 9L46F marine diesel engine and found that through waste heat recovery a 70% CO₂ capture rate at 85% load is achievable. They showed that a 75% carbon capture rate is possible to recover heat using WHRS (waste heat recovery system) for the reboiler (ammonia requires less heat for regeneration than MEA), but 12.88% more fuel was needed to deliver the same power output of 8.7 MWe at 85% load, due to power requirements for CO₂ capture and compression for storage.

In addition to ammonia, other solvents have been considered. Feenstra et al. [9] proposed carbon capture from diesel and LNG-fuelled vessels (1,280 kW dual fuel Wärtsilä 8L20DF and 3,000 kW Wärtsilä 6L34DF). They used MEA as reference case, which was evaluated against 30 wt.% aqueous piperazine (PZ). PZ showed lower costs compared to MEA cases due to the higher pressure used in the desorption process and consequently lower CO₂ compression costs. They concluded that after considering the weight of equipment and stored CO₂, equipment could be fit onboard the ship with some space reconfiguration. They compared carbon capture rates of 60 – 90%, and in most cases, it was possible to recovery heat from exhaust gases for use in the reboiler to regenerate the solvent. However, it is not clear if the compression power and NH₃ refrigeration power are provided by using more fuel or reducing the engine power output.

As a potential alternative to chemical absorption with aqueous-based solvents, cryogenic carbon capture (CCC) is emerging as a CO₂ separation technology based on phase change at very low temperatures. The CCC method

consists of the separation of CO₂ as a solid frost at conditions below its sublimation temperature (-78°C at 1 bara). The CO₂ frost is then warmed leaving a pure CO₂ stream ready for reuse or storage. One CCC approach uses packed beds to separate both water and CO₂ on the packing surface. The packed bed consists of chilled beads where water condenses, then the fuel gas is further cooled for CO₂ deposition as frost, the bed is warmed to release the CO₂, and finally the bed is cooled down ready for a new cycle. Thus, the process makes use of multiple parallel beds to allow continuous operation [10]. Another approach uses a moving bed of metallic beads, the advanced cryogenic carbon capture (A3C) process, that avoids the switching of multiple beds. This provides intensive heat transfer while avoiding the effects of heavy frost deposition, but it will need the appropriate handling of solids [11].

The A3C process has been evaluated for a shipping application. Two case studies were assessed, an LNG fuelled pure car and truck carrier (12,614 kW dual-fuel 7S60ME-C10.5-GI two stroke diesel engine), and a hybrid diesel (1,200 kW engine that burns marine gas oil, MGO) - electric/battery ferry. The study by PMW Technology found that integration of the A3C process into new built or retrofitted vessels is feasible. However, the A3C process showed that the total fuel consumption increased by 17% for LNG and 24% for MGO when capturing 90% of carbon emissions from main and auxiliary engines, and an additional load on the vessel by the liquid CO₂ storage tanks. The report concludes claiming that the cost of the A3C process for shipping could be up to 50% lower than the conversion of vessels to zero carbon fuels [12].

Carbon capture could aid decarbonise the maritime transport, whilst avoiding major design changes needed in fuel switching to ammonia or hydrogen. This sector is important worldwide. For instance, in the UK economy the maritime transport involves around 95% of imports and exports, 25% of the energy supply and 48% of food supply [13], and within the EU 40% of freight exchanges are carried out by sea.

1.1.1 Motivation and aims of this study

OCCS offers a route that avoids changes or replacement of ship engines. However, there is limited open literature on carbon capture for shipping applications.

Previous works [9], [14] have tested the use of OCCS by scrubbing using aqueous solvents, though this option will require the handling of hazardous chemicals onboard. A report [12] evaluating the cryogenic A3C process featured the potential and benefits of cryogenic separation, but the process will require refrigerants, and energy consumption for compression and liquefaction of CO₂. This works aims to compare solvent-based carbon capture against cryogenic separation. These technologies greatly depend on highly integrated configurations that intend to minimise energy consumption; therefore, identifying the benefits of hot versus cold heat integration could aid selecting the OCCS options with more potential.

2. Methodology

LNG is used as fuel, which is stored at -163°C. Table 1 shows the composition of the LNG consumed onboard. Table 2 shows the exhaust gas compositions and flow rates used in this work with and without exhaust gas recirculation (EGR). In order to reduce the energy requirements linked to the lower CO₂ content in the exhaust gases, EGR can be implemented to increase the concentration of CO₂ and thus the overall performance of the carbon capture unit, as shown in Table 2.

Table 1: Liquefied natural gas composition [14].

LNG	% wt.	% mol
Methane	91	95.41
Ethane	6.5	3.64
Propane	2.5	0.095
	100% load	85% load
Flow (kg/s)	0.55	0.45

Table 2: Data for exhaust gases of main engine Wartsila 9L46DF at 85% load and with EGR [14].

(mol %)	85% load	EGR (30%)
CO ₂	4.88	6.45
N ₂	75.24	74.04
O ₂	10.37	6.97
H ₂ O	9.50	12.54
Flow (kg/s)	16.35	12.30

2.1 Ship-based carbon capture

Figure 1 shows the proposed integrated system of cryogenic post-combustion carbon capture in an LNG fuelled engine. The system consists of an LNG storage tank, a vaporiser to regasify LNG, the ship engine, and direct contact cooler to cool down exhaust gases. Before the CCC process, the exhaust gases are further cooled and dried. The shaded area shows the CO₂ capture unit, where CO₂ is desublimed at temperatures below -100°C depending on the CO₂ content and at atmospheric pressure, and sublimed for CO₂ release using packed columns, and finally the CO₂ is compressed, liquified and stored.

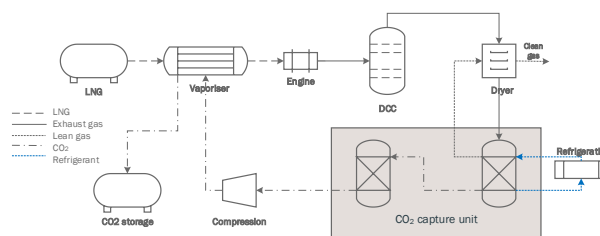


Figure 1: Schematic representation of the proposed OCCS using cryogenic packed columns

The desublimation/sublimation (CO₂ separator and CO₂ sublimator) steps could be designed to operate according to the two configurations shown in Figure 2, currently at technology readiness level (TRL) 3. One option shown in figure 2a employs alternating processes, that is whilst one precooled column is used for CO₂ removal the other columns are releasing the previously captured CO₂ and/or being cooled to the required temperatures. This

system has been previously tested at laboratory scale [10]. Another option is to make use of moving beds as proposed in the A3C process [11], where the desublimation step has been tested experimentally using precooled metallic beads as packing material [15]. This configuration would allow continuous operation, but it requires complex handling of particles, as shown in Figure 2b.

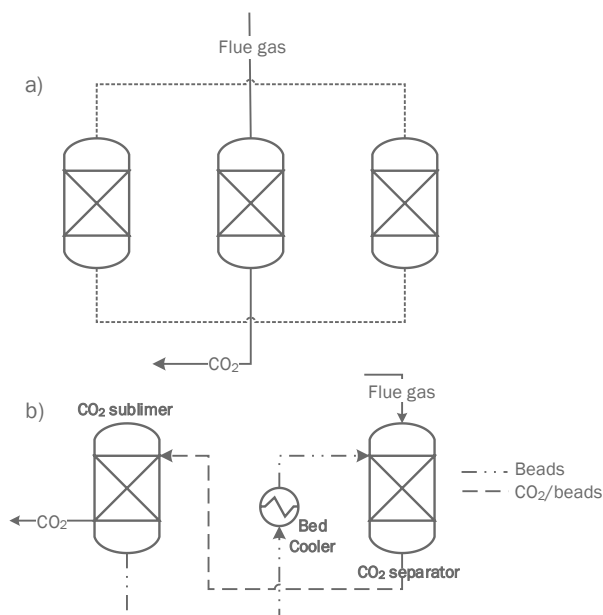


Figure 2: Schematic representation of cryogenic CO₂ capture unit: a) fixed packed columns and b) moving packed beds

In both configurations from Figure 2, prior to CO₂ desublimation, the packing material is cooled below the sublimation temperature, for an exhaust gas with 6.45% mol CO₂ content at -118°C for 95% CO₂ removal. For the fixed packed column, the packing cooling stage is switched between columns once each reach saturation. Whilst for the moving packed bed, the packing is cooled in a heat exchanger prior to entering the CO₂ separator, as shown in Figure 2b. This work aims to integrate cold sinks to minimise the need for external refrigeration. Figure 1 also shows that the evaporation of LNG could provide the cooling duty for liquifying CO₂; whilst the CCC process is integrated between the CO₂ desublimation and sublimation steps, and the cooling and drying of exhaust gases. The direct contact column (DCC) is designed so that the maximum sea water temperature rise is 5°C.

The cryogenic OCCS process was modelled using Aspen Plus® software V10. The thermodynamic method used was the Peng Robinson equation-of-state. Since only Gibbs reactors (RGibbs) can handle solids, these were used to represent the desublimation and sublimation of CO₂. The desublimation column was represented by a series of ten RGibbs blocks using phase and chemical equilibrium, allowing solids formation at each stage [16], and the standard enthalpy of formation and free energy of formation of solid CO₂ were entered to achieve more accurate energy estimations.

3. Results and Discussions

3.1 Performance of the Integrated System

3.1.1. Thermal integration of OCCS process

Feenstra et al. [9] showed that there is enough cold from the regasification of LNG to cool and liquify CO₂ at 22 bar with a storing temperature of -16°C. An analysis of heat and cold sinks made possible the integration of the cold from LNG as previously done plus other cold streams from the cryogenic process. Since the cryogenic packed column delivers a cold CO₂ at around the sublimation temperature, the cold from this stream could be recovered to cool the compressed CO₂ at a lower pressure of 11 bar to reach the temperature of -36°C needed for CO₂ liquefaction. Figure 3 shows the composite curve for hot and cold streams. Table 3 shows the duties and the streams matched.

Table 3: Heat balance analysis.

	Parameter to achieve	Duty (kW)	Supplied by
CO ₂ cooling	-36°C	80.8	Cold CO ₂
CO ₂ liquefaction	Liquid CO ₂	379.6	LNG vaporisation

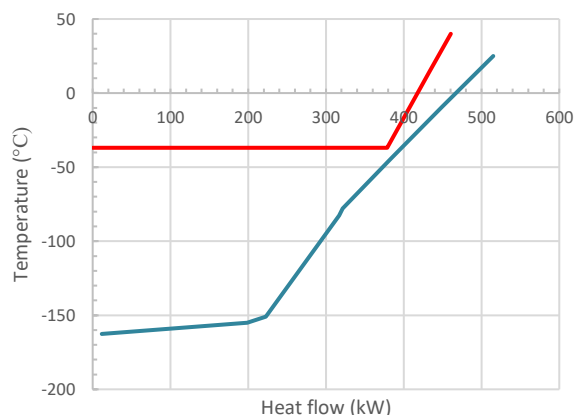


Figure 3: Composite curve for heat integration

Other alternative CCC process, developed by Sustainable Energy Solutions (SES), makes use of a cryogenic liquid to provide the cold for the desublimation of CO₂ [16]. Their Cryogenic Carbon Capture™ technology has been tested using real flue gas from power generation sources, positioning it at TRL 5. The SES CCC process has the advantage that a slurry, a mixture of the cooling liquid and solid CO₂, is produced. The slurry can then be compressed to the desired storage pressure, avoiding the need for electric power for gaseous CO₂ compression that would be further transported for permanent underground storage. However, the process requires highly integrated refrigerant loops to provide the cooling for CO₂ desublimation and for cooling the cryogenic contact liquid.

3.1.2. Performance of OCCS process

Table 2 shows the exhaust gas composition including the use of exhaust gas recirculation (EGR) that helps increasing the CO₂ content and reduces the gas flow rate. EGR was considered in this work, since Awoyowi et al. [14] reported that the engine power output was maintained similar to that without EGR.

Table 4 compares the OCCS performance with and without EGR. The results do not show a significant difference between the two cases. However, power consumption for CO₂ capture is higher for the cryogenic cases due to compression in the refrigeration unit, thus this will require higher NG consumption of around 11% to provide the same engine power output. With solvent scrubbing, the decreased gas flow rate and increased CO₂ content reduced the reboiler duty due to less solvent used, thus reducing operating costs.

This work found that the power requirements for CO₂ compression remained the same for EGR and no EGR cases. For CO₂ capture with scrubbing, the electric power consumption for CO₂ compression decreased from 0.4 MW_e with no EGR to 0.25 MW_e with EGR [14].

Table 4: Comparison of performance results.

	no EGR	with EGR	no EGR [14]	with EGR [14]
CO ₂ capture technology	cryogenic		solvent	
CO ₂ capture rate (%)	94.8	94.6	90	90
CO ₂ stored pressure (bar)	11	11	7	7
Electric power for CO ₂ compression (MW)	0.181	0.179	0.4	0.25
Specific energy consumption for CO ₂ capture (MJ/kg-CO ₂)				
electrical	0.91	0.87	0.09	0.06
thermal	-	-	3.4	2.7

Awoyowi et al. [14] also reported that less CO₂ is captured with EGR. In this work, the amount of CO₂ captured remained the same, since the increased CO₂ concentration was compensated by the reduced gas flow rate. This observation aligns with other EGR studies on gas turbines [17].

The OCCS process was also assessed through an exergy analysis. One parameter analysed was the exergy destruction, the difference between the total amount of exergy into and out of the system, which measures the unrecoverable lost capability to do work [18]. Thus, Figure 4 shows the exergy destruction contribution of different equipment in the cryogenic configuration with EGR. As can be seen, the exhaust gas cooling equipment has the most significant contribution of exergy destruction in the process (39.5%). After that, the CO₂ capture equipment has the largest impact on the exergy destruction in the system (34.7%).

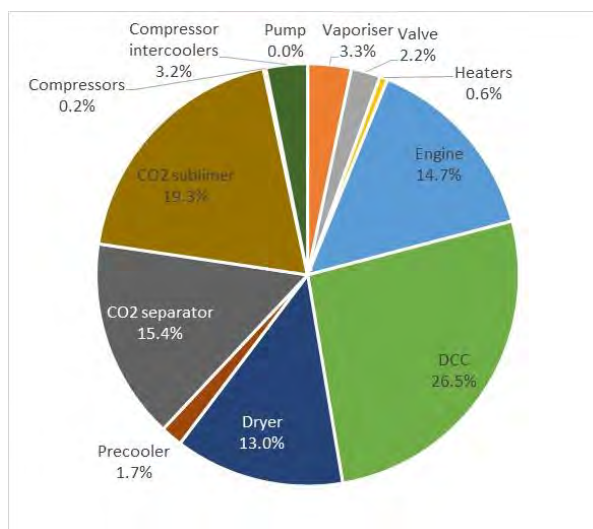


Figure 4: Percentage shares of exergy destruction based on the types of equipment in the cryogenic EGR case

4. Conclusions

This work addresses the increasing need to reduce GHG emissions from the maritime sector, this is in alignment with current targets of 50% reduction by 2050 compared to 2008 levels. Previous work evaluated the integration of solvent-based carbon capture onboard for LNG-fired ships. Thus, this work assessed the incorporation of novel cryogenic systems that complement well with the cold conditions available from LNG regasification. It was found that with a capture rate of 95%, the energy released from LNG regasification is sufficient to liquify CO₂, but the precooling needed to reach the near liquefaction temperature could be achieved from recovering cold from the cold CO₂ captured stream. Further work should look more closely into the dynamics of the integrations as well as the economic evaluation.

Acknowledgements

This Fellowship was supported by the Royal Academy of Engineering under the Leverhulme Trust Research Fellowship scheme (LTRF1920\16\18).

References

- [1] IMO, 2020. IMO Action to Reduce Greenhouse Gas Emissions from International Shipping. International Maritime Organization.
- [2] Morgan, S., 2019. World's largest electric ferry enters service in Denmark, in: Radosavljevic, Z. (Ed.). EURACTIV.
- [3] Radowitz, B., 2020. World's first liquid hydrogen fuel cell cruise ship planned for Norway's fjords. Recharge.
- [4] Balcombe, P., Brierley, J., Lewis, C., Skatvedt, L., Speirs, J., Hawkes, A., Staffell, I., 2019. How to decarbonise international shipping: Options for fuels, technologies and policies. Energy Conversion and Management 182, 72-88.
- [5] Mac Dowell N & Shah N. Shipping and CCS: A systems perspective. Sustainable Technologies, Systems and Policies, 2012 Carbon Capture and Storage Workshop:19.

- [6] Bouman, E.A., Lindstad, E., Riialand, A.I., Strømman, A.H., 2017. State-of-the-art technologies, measures, and potential for reducing GHG emissions from shipping – A review. *Transportation Research Part D: Transport and Environment* 52, 408-421.
- [7] Lee, S., Yoo, S., Park, H., Ahn, J., Chang, D., 2021. Novel methodology for EEDI calculation considering onboard carbon capture and storage system. *International Journal of Greenhouse Gas Control* 105, 103241.
- [8] Awoyomi, A., Patchigolla, K., Anthony, E.J., 2019. CO₂/SO₂ emission reduction in CO₂ shipping infrastructure. *International Journal of Greenhouse Gas Control* 88, 57-70.
- [9] Feenstra, M., Monteiro, J., van den Akker, J.T., Abu-Zahra, M.R.M., Gilling, E., Goetheer, E., 2019. Ship-based carbon capture onboard of diesel or LNG-fuelled ships. *International Journal of Greenhouse Gas Control* 85, 1-10.
- [10] Tuinier, M.J., M. van Sint Annaland, and J.A.M. Kuipers, 2011. A novel process for cryogenic CO₂ capture using dynamically operated packed beds—An experimental and numerical study. *International Journal of Greenhouse Gas Control*, 5(4): 694-701.
- [11] Willson, P., Lychnos, G., Clements, A., Michailos, S., Font-Palma, C., Diego, M.E., Pourkashanian, M., Howe, J., 2019. Evaluation of the performance and economic viability of a novel low temperature carbon capture process. *International Journal of Greenhouse Gas Control*, 86, 1-9.
- [12] Willson, P., 2020. Evaluation of the Marine Application of Advanced Carbon Capture Technology, 2019 T-TRIG Project Report. PMW Technology Limited.
- [13] DfT, 2019. Maritime 2050. Navigating the Future. Department for Transport, UK.
- [14] Awoyomi, A., Patchigolla, K., Anthony, E.J., 2020. Process and Economic Evaluation of an Onboard Capture System for LNG-Fueled CO₂ Carriers. *Industrial & Engineering Chemistry Research*. 59 (15), 6951-6960.
- [15] Cann, D., Font-Palma, C., Willson, P., 2021. Experimental analysis of CO₂ frost front behaviour in moving packed beds for cryogenic CO₂ capture. *International Journal of Greenhouse Gas Control*, 107: 103291
- [16] Jensen, M.J., Russell, C.S., Bergeson, D., Hoeger, C.D., Frankman, D.J., Bence, C.S., Baxter, L.L., 2015. Prediction and validation of external cooling loop cryogenic carbon capture (CCC-ECL) for full-scale coal-fired power plant retrofit. *International Journal of Greenhouse Gas Control* 42, 200-212.
- [17] Ali, U., Font-Palma, C., Akram, M., Agbonghae, E.O., Ingham, D.B., Pourkashanian, M., 2017. Comparative potential of natural gas, coal and biomass fired power plant with post-combustion CO₂ capture and compression, *International Journal of Greenhouse Gas Control*, 63, 184-193.
- [18] Wang, Z., Fan, W., Zhang, G., Dong, S., 2016. Exergy analysis of methane cracking thermally coupled with chemical looping combustion for hydrogen production, *Applied Energy*, 168, 1-12

MONITORING OF CO₂ WELL PLUG INTEGRITY. ELECTRICAL RESPONSE OF CEMENT/CNF SENSOR TO MECHANICAL LOAD, WATER SATURATION AND CARBONATION

Kamila Gawel^{1*}, Sigurd Wenner¹, Ali Taghipour¹, Dawid Szewczyk¹, Laura Edvardsen¹, Anette Brocks Hagen¹, Anna Stroisz¹, Bartłomiej Gawel², Ruben Bjørge¹, Amir Ghaderi¹, Pierre Cerasi¹, Malin Torsæter¹

¹ SINTEF Industry, Trondheim, Norway

² NTNU, Trondheim, Norway

* Corresponding author e-mail: kamila.gawel@sintef.no

Abstract

CO₂ storage wells will eventually need to be permanently plugged and abandoned. Subsidence, fault/fracture reactivation or chemical degradation can all adversely affect well plug integrity leading to CO₂ leakages. Thus, monitoring of well plug integrity should be of high priority for CO₂ storage.

There are materials whose properties change upon application of mechanical stress or chemical alterations that could be tested for well plug integrity sensing. One of them is cement with conductive fibres. In this paper we summarize SEP FARAWELL project results describing electrical response of conductive composites made of well cement and carbon nanofibers (CNFs) in response to load, carbonation, and water saturation changes.

The results show that bulk resistivity of well cement/CNF composites changes upon application of the three stimuli mentioned above thus the material proves promising for monitoring applications.

Keywords: well, plug, monitoring, integrity, sensor

1. Introduction

CO₂ storage wells will eventually need to be permanently plugged and abandoned. Subsidence, fault/fracture reactivation or chemical degradation can all adversely affect well plug integrity leading to CO₂ leakages. Taking responsibility for the storage projects for posterity should not only rely on better understanding of leakage mechanisms but also on taking measures to detect and prevent any future leakage events. To this end monitoring of the well plug integrity in the long perspective is needed. It is in vain to look for long-term monitoring technology in oil and gas industry. In contrast to CO₂ storage wells, the oil/gas wells are plugged when the reservoir has been depleted from gas/oil thus the system left under-pressured and not prone to further leakage. Moreover, the long-term monitoring in oil and gas industry is a controversial topic due to difficult decision making on defining responsible authorities. Defining responsibility in CO₂ storage legislation is easier.

The plugging upon abandonment aims on long term sealing of the well (preferably for infinity) in order to prevent leakage of the fluids from the reservoir to the environment [1]. This is done by setting cement plugs within the well. After the cement plug is set the plug quality is assessed by pressure testing and if no leakage at this stage is detected the well is regarded as sealed. Although the requirement for long-term (eternal) sealing seems to be very strict, there is no commercial monitoring technology for abandoned wells that could

prove that the well plug is indeed intact long after the plug was set. This implies that the responsible authorities do not know whether or not installed well plugs are fulfilling their role, or have stopped acting as barriers, as a result of chemical or mechanical degradation. The chemical degradation can be a result of interaction between the plug and reservoir fluids, while the mechanical degradation can result from e.g., subsidence or shear displacement along discontinuities (e.g., rock interfaces, fractures). Continuous in-situ monitoring of well barrier materials could allow for early stage warning of any loss of sealing capacity and intervention before any leakage occurs. Chemical or mechanical degradation processes may be detected by incorporating into the cement plug a sensor whose transducer is sensitive to both stress and changes in chemical environment. This important goal represents the main scope of the work performed within the SEP FARAWELL project at SINTEF Industry. Within this project we have proposed that electrically conductive cements with carbon nanofibers can be tested in view of plug integrity sensing.

2. Concept description

Cement materials with well-dispersed conductive fillers such as metal fibers, graphite powder, carbon nanofibers, carbon nanotubes, may show piezoresistive properties [2-9]. Piezo-resistivity is a physical property of materials defined as the change in electrical resistivity upon exposure to stress. The physical mechanism

underpinning this phenomenon is associated with the connectivity between the conductive particles. When a uniaxial compression is applied to the material with embedded electrically conductive fillers, the inter-particle distance in the filler decreases, and new conductive paths are created. The closer the conductive particles are and the more interparticle connections are created, the easier an electrical current can flow, and the resistivity of the material decreases. Provided there is no plastic deformation of the material, by unloading the composite material it returns to its primary state and the initial resistivity is recovered. The resistivity changes can also be utilized to follow irreversible changes within material occurring at higher load ranges.

The response of the material to stress takes place only above a critical concentration of conductive particles called percolation threshold. This phenomenon is well explained by the percolation theory [10, 11]. Due to their stress sensitivity, piezoelectric cement materials are considered as excellent sensors in structural health monitoring of reinforced concrete structures [3, 12] and traffic monitoring [13-15]. The SEP FARAWELL project, aimed at utilizing the stress sensitivity of cement composite materials containing carbon nanofibers in the sensing of stress changes that may occur in a permanently plugged well as a result of subsidence, fracture reactivation etc. The monitoring of a well would rely on measurements of electrical resistivity of the sensor whose transducing material is made of stress sensitive cement. It was expected that stress imparted on the cement plug with an embedded sensor would result in changes of electrical resistivity of the transducer. To prove the feasibility of the concept, the resistivity changes associated with stress changes relevant for well conditions were assessed. As the resistivity was expected to be sensitive to the water content in cement and to the temperature, the effect of the two parameters was also evaluated.

The plug being in contact with reservoir fluids may also, upon long time exposure, undergo chemical degradation. Downhole brines commonly contain carbonate and sulphate ions that tend to react with cement. The reactions are associated with density changes within the cement [16]. The density changes were expected to affect the resistivity of cement/CNF composites. This topic has not been previously researched. Therefore we also studied how the carbonation process (as an example of degradation processes) affects the signal of the potential transducer material.

Our results are also relevant for other applications where the sensing material is exposed to humidity and an environment that contains sour gases such as CO₂ and H₂S, e.g., traffic monitoring or structural health monitoring.

3. Discussion of main findings

Figure 1. shows two types of samples used to study the behavior of conductive cement composites. Cubic samples were used to study response to load while cylindrical samples were used to follow resistivity

changes upon carbonation and changes in pore saturation with water.

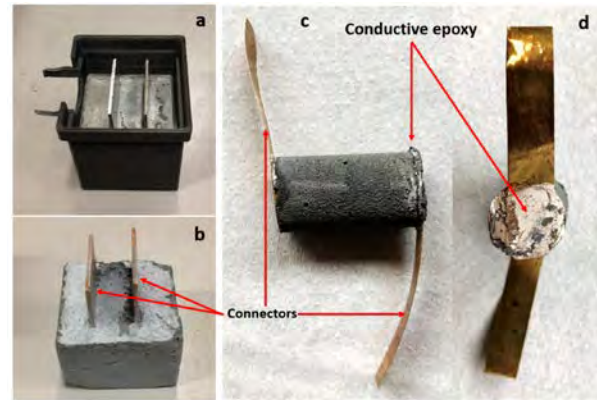


Figure 1: Photography of different samples: (1) cubic sample in a 3D printed mold before (a) and after (b) removal from the mold, and (2) cylindrical sample, side view (c) and top view (d), indicating metal connectors. (From [17])

3.1 Water saturation sensitivity

Our results (Figure 2) [17] showed that an increase in the water to cement ratio in cement slurry resulted in increased bulk resistivity.

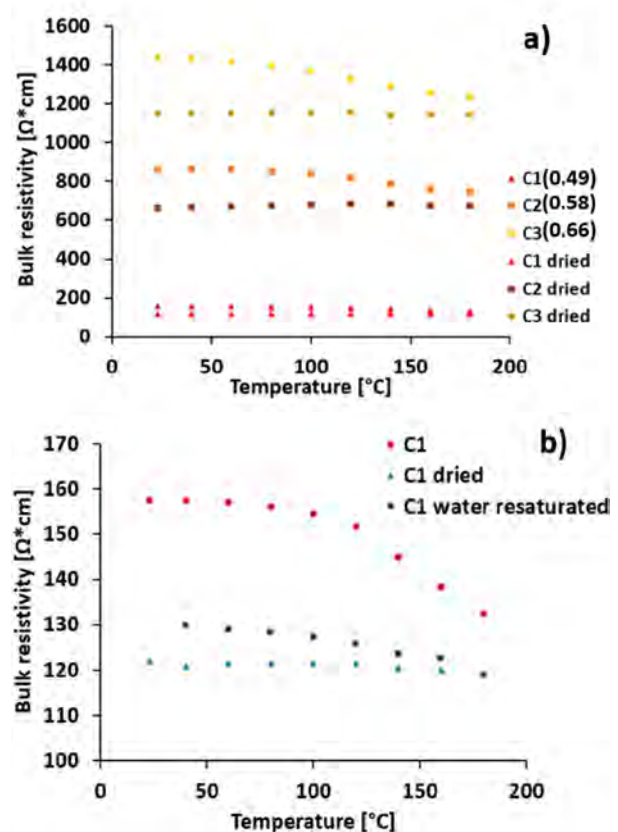


Figure 2: Resistivity changes upon temperature increase for samples with (a) different water to cement ratio: C1 (w/c: 0.49), C2 (w/c: 0.58), C3 (w/c: 0.66) and (b) different pore volume water saturation. From [17]

The decrease in nanocomposite resistivity upon a stepwise temperature increase up to 180 °C was ascribed to free water release from cement pores. The dry materials were relatively insensitive to temperature

changes and had much lower resistivity compared to wet materials. The re-saturation of pores with water did not reverse electrical resistivity. The results also highlighted the importance of the type of electrical connection. Application of electrically conductive epoxy as electrode material resulted in two orders of magnitude larger bulk resistivity compared to the same material.

3.2 Chemical changes sensitivity

We have shown that carbonation processes affect material bulk resistivity [18], thus electrical resistivity measurements may be applied to sense chemical degradation of conductive cements.

3.3 Stress sensitivity

Stress sensitivity of cement/CNF composites was studied. The samples were gradually brought to failure and resistivity changes along with acoustic emission events being followed and correlated [19]. Figure 3 presents schematically experimental setup that was used to follow changes in sample resistance and acoustic emission upon application of mechanical load.

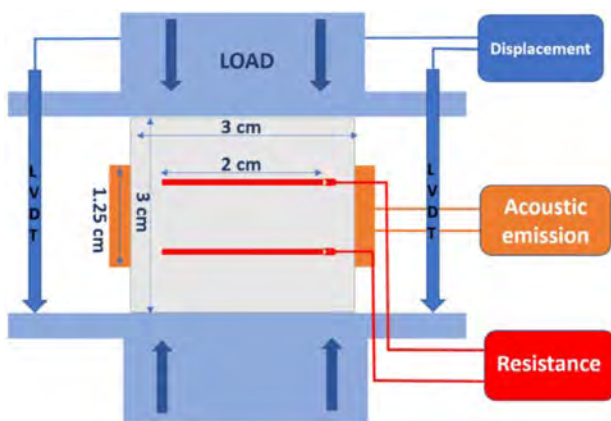


Figure 3: Schematic illustration of experimental setup (not to scale). From [19].

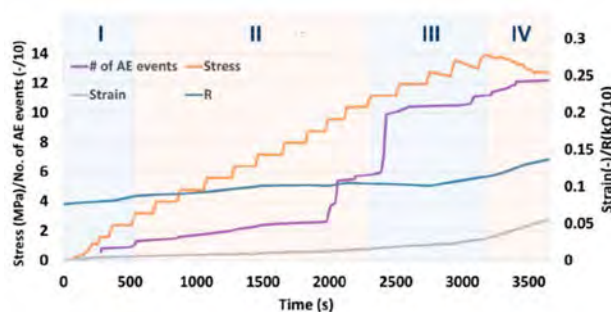


Figure 4: Resistivity changes (R) and cumulative acoustic emission events (# of AE events) upon application of mechanical load to the sample similar to that shown in Figure 1 b. The load was applied in a direction perpendicular to the surfaces of electrical connectors. Mechanical failure takes place at time of 310 seconds. From [19].

Our results (Figure 4) [19] showed that complementary acoustic emission recording and resistivity measurements can clearly indicate the onset of material mechanical failure. The increase in resistivity starts long

before failure which implies that the method can be used as indicator of increasing load.

3.4 Sensor and signal readout

In order to monitor the state of the temporary or permanent well plug, the transducer material has to be embedded within the cement plug or be used as a plug itself. There are at least two readout systems utilizing conductive cements that can be consider for sensing application: (1) direct resistivity measurements with two or four point probe methods or (2) electromagnetic EM method.

For direct resistivity method the transducer material needs to be physically connected with a power source and a signal transmitter. Signal transmission can be done in a wireless manner using e.g., radio communication. The system of many wells can likely be monitored by just one radio signal receiver. The direct measurement method can be easily used to monitor the state of the top i.e., environmental plug, however monitoring of the deeply situated plugs seems more challenging.

The electromagnetic method nowadays used as a complementary geophysical method to seismic surveys could be extended to monitor the state of permanent cement plugs containing CNF. The method requires electromagnetic transmitter and receiver that does not have to be in a direct electrical contact with the transducing material which makes the method noninvasive and thus promising.

The design of the readout system and power source was however beyond the scope of this project, and the topic requires a separate spin-off project.

3.5. Interpretation of the data

Detection of stresses that are close to the compressive strength of cement may suggest that the plug is close to failure. The increasing stress followed by sudden unloading or continued loading above the material failure threshold may suggest failure of the plug. Modelling of different mechanical failure scenarios is needed to aid in the data analysis. Both stress (close to failure) and carbonation contribute to increased resistivity of cement/CNF composites. Decoupling of the two effects as well as the effect of changing water saturation and salinity may be the biggest challenge for the field application of cement/CNF composite as selective transducers. What poses a challenge is simultaneously a benefit as the materials can sense both mechanical and chemical stimuli which makes them promising.

3. Conclusions

Project findings suggest that cements with carbon nanofibers are good candidates for transducer materials capable of transforming changes in stress as well as chemical alterations into electrical signal. The cement/CNF composites showed to be sensitive to mechanical load and chemical degradation. As the materials have been shown to be sensitive also to other factors like water saturation, the signal readout needs to be carefully designed and the interpretation of data should consider all factors.

Cement/CNF composite materials are good candidates for continuous in-situ monitoring of well barrier materials. Such monitoring could allow for early-stage warning of loss of plug integrity due to chemical or mechanical degradation. Early detection of such degradation processes could allow for leakage preventive intervention before any leakage occurs.

Acknowledgements

The authors gratefully acknowledge the financial support from SEP FARAWELL project granted within SINTEF Industry internal strategic funds as well as The Norwegian Research Council in the form of grant number 285568 "Well fossilization for P&A".

References

1. Vrålstad, T., et al., *Plug & abandonment of offshore wells: Ensuring long-term well integrity and cost-efficiency*. Journal of Petroleum Science and Engineering, 2019. **173**: p. 478-491.
2. Chung, D., *Electrically Conductive Cement-Based Materials*. Vol. 16. 2004. 167-176.
3. Meoni, A., et al., *An Experimental Study on Static and Dynamic Strain Sensitivity of Embeddable Smart Concrete Sensors Doped with Carbon Nanotubes for SHM of Large Structures*. Sensors (Basel, Switzerland), 2018. **18**(3): p. 831.
4. Carmona, F., R. Canet, and P. Delhaes, *Piezoresistivity of heterogeneous solids*. Journal of Applied Physics, 1987. **61**(7): p. 2550-2557.
5. Wang, X., X. Fu, and D.D.L. Chung, *Strain sensing using carbon fiber*. Journal of Materials Research, 1999. **14**(3): p. 790-802.
6. Sun, M., et al., *Study of piezoelectric properties of carbon fiber reinforced concrete and plain cement paste during dynamic loading*. Cement and Concrete Research, 2000. **30**(10): p. 1593-1595.
7. Newnham, R.E., et al., *Composite piezoelectric transducers*. Materials and Design, 1980. **2**(2): p. 93-106.
8. Li, Z., D. Zhang, and K. Wu, *Cement-based 0-3 piezoelectric composites*. Journal of the American Ceramic Society, 2002. **85**(2): p. 305-313.
9. Han, B. and J. Ou, *Embedded piezoresistive cement-based stress/strain sensor*. Sensors and Actuators, A: Physical, 2007. **138**(2): p. 294-298.
10. Dietrich Stauffer, A.A., *Introduction to Percolation Theory*. 1994.
11. Czyzewski, J.B., P. Gawel, K. Meisner, J., *Rapid prototyping of electrically conductive components using 3D printing technology*. Journal of Materials Processing Technology, 2009. **209**(12-13): p. 5281-5285.
12. Ramam, K. and K. Chandramouli, *Piezoelectric cement composite for structural health monitoring*. Advances in Cement Research, 2012. **24**(3): p. 165-171.
13. Monteiro, A.O., et al., *A pressure-sensitive carbon black cement composite for traffic monitoring*. Construction and Building Materials, 2017. **154**: p. 1079-1086.
14. Zhang, J., et al., *A new smart traffic monitoring method using embedded cement-based piezoelectric sensors*. Smart Materials and Structures, 2015. **24**(2).
15. Wen, S. and D.D.L. Chung, *Piezoelectric cement-based materials with large coupling and voltage coefficients*. Cement and Concrete Research, 2002. **32**(3): p. 335-339.
16. Chavez Panduro, E.A., et al., *In-Situ X-ray Tomography Study of Cement Exposed to CO₂ Saturated Brine*. Environmental Science & Technology, 2017. **51**(16): p. 9344-9351.
17. Gawel, K., et al., *Effects of water content and temperature on bulk resistivity of hybrid cement/carbon nanofiber composites*. Materials, 2020. **13**(13).
18. Kamila Gawel, S.W., Laura Edvardsen, *Effect of carbonation on bulk resistivity of cement/carbon nanofiber composites*. Under submission.
19. Kamila Gawel, D.S., Pierre Cerasi, *Self-sensing well cement. Coupling between electrical resistivity and acoustic emissions measurements in carbon nanofiber reinforced well cement composite*. Materials, 2021. **14**(5): p. 1235.

INTEGRATION OF INDUSTRIAL CO₂ CAPTURE WITH DISTRICT HEATING NETWORKS: A REFINERY CASE STUDY

Åsa Eliasson*, Elin Fahrman, Maximilian Biermann, Fredrik Normann, Simon Harvey

Division of Energy Technology, Chalmers University of Technology, 412 96 Gothenburg, Sweden

* Corresponding author e-mail: asa.eliasson@chalmers.se

Abstract

Industrial carbon capture and storage is recognized as an important technology to reach net zero emissions and mitigate global warming in accordance with the Paris agreement. Absorption-based carbon capture requires considerable amounts of low-grade heat, and a high degree of integration with the plant's energy system is thus of high importance in order to achieve low operating costs for the capture plant. In this context, it is important to redefine what is commonly referred to as process "excess heat". This work evaluates the impact of heat integration of a carbon capture plant with an existing refinery and two excess heat-powered district heating networks. The results show that a capture rate of ~60% of direct emissions at the refinery will consume all of the plant's available residual heat. However, the results also indicate that a significant amount of heat can be recovered from the capture plant and exported for district heating supply purposes. Subsequent to capture plant integration, the potential district heating supply is 87 MW, compared to 100 MW in the reference case.

Keywords: Carbon capture and storage, heat integration, district heating, excess heat, process industry, partial capture

1. Introduction

The industrial sector accounts for around 20% of global CO₂ emissions [1]. Mitigation of these emissions is therefore necessary in order to achieve current internationally agreed climate goals. Carbon capture and storage (CCS) and increased energy efficiency are viable options for reduction of direct plant emissions. Carbon capture is however an energy-intensive process, and approximately 3-4 MJ heat/kg CO₂ are required to regenerate the solvent in common absorption-based processes, which will decrease the plant's energy efficiency. The heat required is typically at a relatively low temperature (around 130°C) and residual heat (often referred to as "excess heat") at such temperature levels is often available at industrial plants. Therefore, several studies (see e.g. [2], [3]) have focused on identifying opportunities to collect and utilize excess heat to provide the heat necessary to regenerate the solvent in the capture process, with the aim of reducing both cost and emissions compared to using primary heat. However, in many cases the excess process heat may be reduced by energy efficiency measures, or is already utilized for other purposes, e.g. in steam cycles or for district heating (common in the Nordic countries). The utilization of industrial excess heat, which is usually considered as a waste stream and not burdened by emission allocations, together with the expansion of the district heating networks has provided a way to reduce direct emissions in the heating sector [4]. Furthermore, supplying heat to a district heating network provides an opportunity for industries to monetize their excess heat. CCS requires considerable amounts of heat and will have a major impact on the plant's energy system, and the relation

between heat recovery for CCS and for delivery of district heating should be investigated. A methodology for exploring the trade-offs between recovering industrial excess heat for increased use on-site or export to a regional district heating network has been developed by Eriksson et al [5]. The competition between CCS and district heating has been discussed by Bartela et al. [6] in the context of a supercritical coal-fired CHP plant. They concluded that some of the heat released by the CO₂ capture plant could be recovered and supplied to the district heating system, which reduced the economic impact of the carbon capture process on the CHP plant operation significantly.

1.1. Aim and scope

This work evaluates the theoretical potential for heat integration of absorption-based carbon capture in a refinery heat recovery system. The work quantifies the reduction of direct emissions that is achievable by utilizing available heat in the plant energy system and the impact on the existing district heating network caused by the carbon capture integration, including an estimation of the amount of heat that can be recovered from the capture plant and delivered to the district heating network. Furthermore, in relation to the heat integration between an industrial plant, the district heating network and the capture plant, a suitable definition of excess heat is proposed, including a discussion of what consequences the excess heat definition has on the district heating supply from an industrial plant subsequent to the integration of carbon capture.

2. Definition of excess heat

The definition of *excess heat* is important to process economics as it decides the allocation of emissions between energy products and is therefore discussed. It is common that industrial excess heat is simply defined as “the heat discharged from an industrial process”. Bendig et al [7] discuss the important distinction between *avoidable* and *unavoidable* excess heat. Pettersson et al. [8] propose adopting a pragmatic techno-economic perspective whereby avoidable excess heat refers to heat that could be reused internally within the process through heat recovery measures that meet the plant owner's investment performance criteria. Olsson et al. [9], on the other hand, propose a definition whereby “*excess energy [is energy] that cannot be utilized internally and where the alternative is that the heat is released into the surroundings*”, which does not consider heat (cooling) that may be avoided by internal heat integration. It is a common conclusion that utilization of excess heat (as in heat free of cost and emission allocation) may significantly reduce the specific cost of CO₂ capture. However, in accordance with the excess heat definition by [9], the claim that *excess heat* may be used for CCS implies that the capture plant is not an internal part of the industrial plant. Considering that all industrial processes must reach zero emissions to limit global warming [10], it is reasonable to consider CCS – or other CO₂ mitigation technologies - as an internal emission control technology required to meet stringent regulations, similar to e.g. desulphurization. Heat available at a temperature level suitable for recovery and use in the CO₂ capture plant should, thus, not be considered as excess heat. This work defines excess heat as: “the energy that cannot be re-used within an industrial process, including processes for emission control and zero-carbon emissions, and where the alternative is that the heat is released into the surroundings”. Instead, the heat that can be made readily available for CCS within the existing plant energy system is designated as “available heat”. “Excess heat” is heat at a quality not suitable for CCS integration.

3. Method

The studied system, illustrated in Figure 1, includes the industrial plant, the CO₂-capture plant and the district heating network. The capture plant specifications consist of both flue gas flow and composition and available heat from the industrial plant (i.e. the refinery). In the capture plant, CO₂ from the refinery flue gases is chemically absorbed into aqueous monoethanolamine (MEA), chosen for its status as benchmark solvent for CO₂ absorption. The available heat from the refinery is then utilized to regenerate the solvent and release the CO₂. Prior to capture plant integration, the input for the district heating network is available heat and excess heat from the refinery. As a result of the integration of the capture plant, potential energy flows to the district heating network consist instead of excess heat from the extended refinery heat recovery system, which includes the capture plant. Specifications regarding the refinery and the district heating network are based on previous studies ([11],[12],[13]), while the capture plant performance is based on simulations carried out in this work.

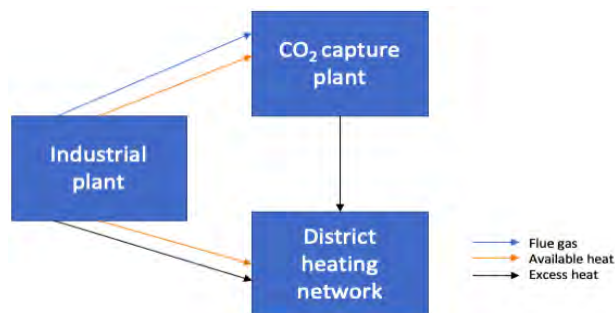


Figure 1: Overview of the studied system including the three parts and the material and energy flows between them.

3.1. Case study

The industrial plant used as a case study is a Swedish refinery with a crude oil capacity of 6 Mt/a, and direct CO₂ emissions of 0.5 Mt/a [11]. The heat needed for the internal refining processes is generated by combustion of refinery excess gas, i.e. gas that originates from the processes but cannot be utilized as a component in any of the products. CO₂ is assumed to be captured from two stacks where the flue gases from the heat generation are emitted. The CO₂ emitted from these stacks account for around 89% of direct plant CO₂ emissions [11]. It is assumed that these stacks are combined to form a single flue gas flow. The flue gas composition, presented in Table 1, was calculated assuming combustion of natural gas with 12% excess air. Furthermore, it is assumed that the refinery and the capture plant have the same operating hours, i.e. 95% availability or 8322 hr/a [12].

Table 1: Refinery flue gas characteristics.

Composition	
CO ₂ [mol%]	8.9
H ₂ O [mol%]	18.0
N ₂ [mol%]	71.1
O ₂ [mol%]	2.0
Flow [kNm ³ /h]	317
Temperature [°C]	168
Pressure [barg]	0

3.2. Heat integration

The evaluation of the theoretical potential for heat integration between the industrial plant, the CO₂ capture plant and the district heating network was carried out in two steps. A global ΔT_{\min} of 10°C between hot and cold streams was applied. The first step was an estimation of available heat based on the work by Berntsson et al. [13], who collected refinery energy system data and calculated the overall temperature profile of refinery process streams and flue gases in coolers connected to external heat sinks, which will hereinafter be referred to as “the refinery heat recovery system”. The refinery currently delivers heat to two external heating networks, i.e. the heat recovery system has to separate parts. A low-temperature network (T_{supply} 90°C; T_{return} 50°C), which supplies district heat to the local municipality. A high-temperature network (T_{supply} 140°C; T_{return} 90°C), which

supplies heat to a nearby industrial site where it is used for heating of buildings but also in the production, which is why it is delivered at higher temperatures than for ordinary district heating supply. To estimate the amount of refinery heat that could be utilized for operating the CO₂ capture plant, the reboiler temperature was assumed to be 121°C, which implies that heat at temperature levels at or above 131°C is available for CO₂ capture. The second step of the heat integration evaluation was to incorporate the heating and cooling duties of the capture plant into the existing refinery heat recovery system and thereby estimate the effect on the district heating supply. Figure 2 shows a schematic overview of the capture plant, with coolers and heaters included in the heat integration highlighted.

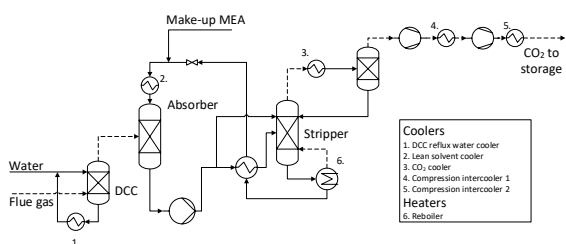


Figure 2: Process flow diagram of the capture process with rich solvent splitting. The process heaters and coolers are marked 1-6.

3.3. Capture process model

The capture process was modeled using Aspen PLUS V11 process simulation software. A standard set-up configuration with rich-solvent splitting was assumed. The set-up of the capture model was based on previous work by Garðarsdóttir et al. [14] and Biermann et al. [15]. The model was expanded to include a two-stage compression sequence with intermediate cooling. A transport pressure of 7 bar(a), suitable for ship transport, was assumed, with the CO₂ being compressed to 20 bar(a) before entering the liquefaction plant [16]. The electrolyte NRTL and RK property methods were used to estimate liquid and vapor properties, respectively, in the capture plant. In the compression sequence, the Peng-Robinson with Boston-Mathias extrapolation equation of state was used to estimate vapor properties. Table 2 lists the key specifications of the simulation set-up.

Table 2: Key specifications of the capture process simulations.

MEA concentration [wt%]	30
Lean CO ₂ loading [molCO ₂ /molMEA]	0.3
Absorber/ stripper packing height [m]	20/15
Absorber CO ₂ separation rate [%]	90
Absorber overhead pressure [bar(a)]	1.01
Lean solvent inlet temperature [°C]	40
Minimum temperature approach in cross heat exchanger [°C]	10
Stripper overhead pressure [bar(a)]	1.9
Stripper reboiler temperature [°C]	121
Discharge pressure compressor 1/2 [bar(a)]	6.3/20

4. Results and discussion

4.1. Analysis of available heat

Figure 3 and Figure 4 show the composite curves for the refinery heat recovery system connected to the low- and high-temperature networks prior to capture plant integration. There is a small process heating demand in each system (1.7 MW in the low-temperature network and 2.3 MW in the high-temperature network), however, the district heating water constitutes the main part of the cold composite curves. The curves are not balanced, indicating that trim coolers are needed to remove the remainder of the heat in both systems. The potential for district heating supply is 61 MW in the low-temperature network and 39 MW in the high temperature network. The grey dashed line in each figure represents the cold stream in the capture plant reboiler at 121°C. In the low-temperature network, 10 MW of heat currently delivered to the district heating network is available at temperatures of 131°C or higher, and can thus be supplied to the capture plant. The corresponding amount of available heat in the high-temperature network is 27 MW, thus, a total of 37 MW of heat in the current refinery heat recovery system is available for capture plant operation.

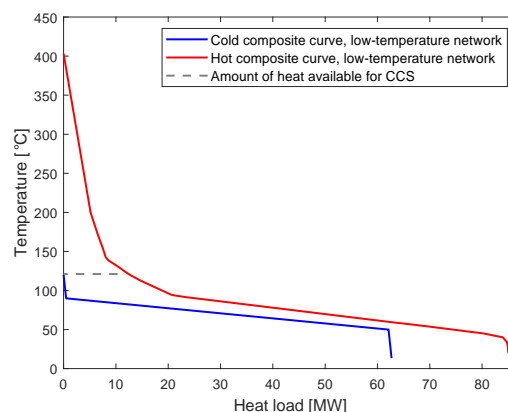


Figure 3: Low-temperature network composite curves. District heating potential (blue line between 50 and 90°C): 61 MW. The amount of heat suitable for CCS (indicated by the grey dashed line at 121°C) is about 10 MW.

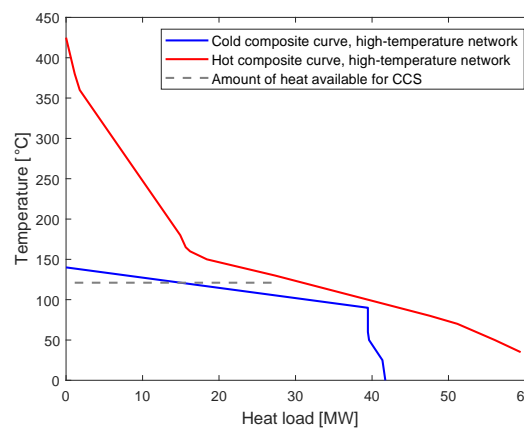


Figure 4: High-temperature network composite curves. District heating potential (blue line between 90 and 140°C): 39 MW. The amount of heat suitable for CCS (indicated by the grey dashed line at 121°C) is about 27 MW.

Table 3 presents key findings from the capture plant simulations. 37 MW of available heat is sufficient for capturing 60% of the direct plant emissions.

Table 3: Capture plant performance.

CO ₂ capture rate [kton/a]	298
Direct plant emission reduction [%]	60
Specific reboiler duty [MJ/kg CO ₂]	3.72

4.2. Evaluation of heat integration potential and effect on the district heating supply

Table 4 presents the demand for heating and cooling in the capture plant. Large amounts of heat, although at low temperatures (<56°C), are found in the DCC reflux water cooler (1) and the lean amine cooler (2). The excess heat with the highest temperature is found in the compressor intercoolers (coolers 4 and 5) as well as the stripper condenser (cooler 3). In the compressor intercoolers, the amount of heat is low, meaning that the possibility for heat recovery is limited despite relatively high temperatures. Cooler 3 has a highly curved cooling profile, due to the simultaneous water condensation and CO₂ cooling. This profile was represented by a two-segment (3a and 3b) piecewise linear approximation in the analysis. In total, 9.5 MW of excess heat may be recovered from the capture plant to supply heat to the low-temperature district heating network, which corresponds to about 26% of the amount of available heat that is supplied to the district heating networks in the reference case (i.e. prior to capture plant integration). The amount of recoverable heat from the CO₂ capture plant is however dependent on assumptions made, e.g. the chosen ΔT_{\min} . It is also dependent on technical factors regarding the capture plant itself, such as e.g. the chosen solvent and the stripper pressure level, thus, the exact amount of recoverable heat will be case specific.

Table 4: Temperature and heat duty of the heaters and coolers in the capture plant and compression sequence. See Figure 2 for numbering.

Cooler	Temperature [°C]	Heat [MW]
1.	50-20	25.6
2.	56-40	12.3
3a	99-60	8.3
3b	60-20	1.9
4	117-25	0.9
5	126-25	1.0
Heater		
6	121-121	37

Figure 5 shows the hot and cold composite curves of the new refinery heat recovery system subsequent to capture plant integration, i.e., where the heating and cooling demands of the capture plant have been included in the respective curves. Furthermore, it is assumed that the previous separate networks are combined in the new heat recovery system. The stripper reboiler duty of 37 MW corresponds to the horizontal part of the cold composite curve at 121°C, which is heated by hot streams at

temperatures of 131°C or higher. Since all available heat is used in the stripper plant, it is no longer possible to deliver heat to the high-temperature network (140°C), corresponding to a heat delivery loss of 39 MW. However, even though the supply of available heat to the low-temperature network is removed, in the new heat recovery system, the potential supply to the network can actually be extended from 61 MW to 87 MW. This is partly due to the heat recovery potential arising from the capture plant, and partly due to that even though the supply to the high-temperature network is lost because of the temperature limitations, there are considerable amounts of excess heat (i.e. heat at temperature levels less than 131°C) in the high-temperature network that can be utilized for low-temperature district heating supply in the new heat recovery system.

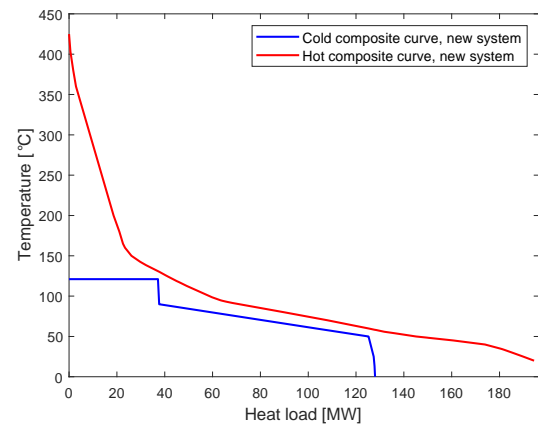


Figure 5: Composite curves of the new refinery heat recovery system, including the integrated CO₂ capture plant. The horizontal part of the cold composite curve, at 121°C, corresponds to the reboiler duty (~37 MW). The inclined part of the blue curve between 50 and 90°C indicates the potential district heating supply of 87 MW.

4.3. Excess heat: to be or not to be

The utilization of industrial excess heat for district heating has efficiently decreased the emissions from the Swedish district heating sector. Broad implementation of carbon capture for emission control will have a considerable impact on the plant energy system and thus, on the possibility to supply district heating. For example, the supply to the high-temperature network considered in this work is lost as a consequence of carbon capture plant integration. However, the heat to the high-temperature network will still have to be supplied somehow, implying that additional supply of primary energy might be needed. Thus, the implementation of CO₂ capture at the refinery might cause increased emissions elsewhere, even though the direct emissions of the industrial plant is significantly decreased. However, it is acknowledged in this work that the definition of excess heat will need to be revised in the future assuming that CO₂ capture is very likely to become a necessary feature of industrial plants, and thus is considered as an internal part of the industrial plant rather than an external application. The availability of low-cost and low-emission heat in the existing industrial energy system is important to make operation of the capture plant economically feasible. Thus, what is

often denoted industrial excess heat may rather be available heat suitable for CCS. We therefore assert that the term excess heat should only be used to refer to such heat that is at temperature levels that are too low to be utilized for CCS. Other utilization areas, such as district heating, might still be possible, and might still provide a way to valorize the excess heat, although with more stringent restrictions on the quality of the industrial heat supplied. To provide industrial heat for high-temperature district heating or process heat networks similar to the one in this work will, per definition, not be possible, since the heat provided in the reference case is at temperature levels suitable for CCS utilization. Excess heat supply for low-temperature networks, e.g. for district heating in municipalities, will however still be possible, particularly if heat pumps are used. Considering the studied system in this work, the amount of district heat delivered to the local municipality might even be increased. Furthermore, since the available heat is only sufficient for reduction of 60% of direct plant emissions, in order to reach net-zero emissions, the current refinery energy system needs to be extended, and thus, some new excess heat will most likely arise from the extension. It should however be kept in mind that the study performed in this work only considers the theoretical potential for heat integration between the refinery, the capture plant and the district heating networks. To evaluate the actual feasibility of such integration, an economic evaluation including the capture plant and the additional heat transfer equipment needed would have to be performed, as well as a study considering the practical implementation according to the refinery site conditions. Furthermore, only the current refinery heat recovery system connected to external heat sinks was investigated in this work. For a more detailed analysis, the full refinery energy system should be considered in the heat integration.

5. Conclusions

In this work, CO₂ capture powered by available industrial heat was shown to be sufficient for a reduction of around 60% of direct emissions of the studied refinery. Furthermore, by assuming a ΔT_{\min} of 10°C between the capture plant coolers and the district heating network, it can be concluded that 26% of the heat input to the capture plant can be recovered for district heating supply. In the analysis of recoverable heat, it is seen that the most important heat source in the capture plant is the stripper condenser, since it provides large amounts of heat at temperatures suitable for district heating supply. Furthermore, it can be concluded that all heat to the high-temperature network is lost as a consequence of CCS integration, since its supply temperature exceeds the temperature of the capture plant reboiler. For the low-temperature network, the potential supply can be extended by about 26 MW in the new refinery heat recovery system compared to the situation prior to capture plant integration.

Acknowledgements

The authors thank the partners of the Preem CCS project, Preem AB, SINTEF Energi AS, Aker Carbon Capture,

and Equinor, and the funding agencies: the Norwegian CLIMIT Programme and the Swedish Energy Agency.

References

- [1] Global CO₂ emissions by sector, 2018 [Internet]. IEA. 2020. Available from: <https://www.iea.org/data-and-statistics/charts/global-co2-emissions-by-sector-2018>.
- [2] Andersson V, Franck P-Å, Berntsson T. Techno-economic analysis of excess heat driven post-combustion CCS at an oil refinery. *Int. J. Greenh. Gas Control*. 2016;45:130-8.
- [3] Biermann M, Ali H, Sundqvist M, Larsson M, Normann F, Johnsson F. Excess heat-driven carbon capture at an integrated steel mill – Considerations for capture cost optimization. *Int. J. Greenh. Gas Control*. 2019;91.
- [4] Werner S. District heating and cooling in Sweden. *Energy*. 2017;126(1):419-429.
- [5] Eriksson L, Morandin M, Harvey S. (2018). A feasibility study of improved heat recovery and excess heat export at a Swedish chemical complex site. *Int J Energy Res*. 2018;42:1580–1593
- [6] Bartela Ł, Skorek-Osikowska A, Kotowicz J. Economic analysis of a supercritical coal-fired CHP plant integrated with an absorption carbon capture installation. *Energy*. 2014;64:513-23.
- [7] Bendig M, Maréchal F, Favrat D. Defining waste heat for industrial processes. *Appl. Therm. Eng.* 2013;61(1):134-142.
- [8] Pettersson K, Axelsson E, Eriksson L, Svensson E, Berntsson T, Harvey S. Holistic methodological framework for assessing the benefits of delivering industrial excess heat to a district heating network. *Int. J. Energy Res*. 2020;44(4):2634-51.
- [9] Olsson L, Wetterlund E, Söderström M. Assessing the climate impact of district heating systems with combined heat and power production and industrial excess heat. *Resources, Conservation and Recycling*. 2015;96:31-9.
- [10] Global Warming of 1.5°C [Internet]. IPCC. 2018. Available from: <https://www.ipcc.ch/sr15/>.
- [11] Johansson D, Franck P-Å, Berntsson T. CO₂ capture in oil refineries: Assessment of the capture avoidance costs associated with different heat supply options in a future energy market. *Energy Convers. Manag.* 2013;66:127-42.
- [12] Garðarsdóttir SÓ, Normann F, Skagestad R, Johnsson F. Investment costs and CO₂ reduction potential of carbon capture from industrial plants – A Swedish case study. *Int. J. Greenh. Gas Control*. 2018;76:111-24.
- [13] Berntsson T, Persson Elmeroth L, Algehed J, Hektor E, Franck P-Å, Åsblad A, et al. Towards a Sustainable Oil Refinery: Pre-study for larger co-operation projects. Chalmers University of Technology; 2008.
- [14] Garðarsdóttir SÓ, Normann F, Andersson K, Johnsson F. Postcombustion CO₂ Capture Using Monoethanolamine and Ammonia Solvents: The Influence of CO₂ Concentration on Technical Performance. *Ind. Eng. Chem. Res*. 2015;54(2):681-90.
- [15] Biermann M, Normann F, Johnsson F, Skagestad R. Partial Carbon Capture by Absorption Cycle for Reduced Specific Capture Cost. *Ind. Eng. Chem. Res*. 2018, 57, 45, 15411–15422
- [16] Deng H, Roussanaly S, Skaugen G. Techno-economic analyses of CO₂ liquefaction: Impact of product pressure and impurities. *Int J Refrig*. 2019;103:301-15.

INFLOW PERFORMANCE OF COLD CO₂ INJECTION IN DEPLETED GAS FIELDS

E. Peters^{1*}, D. Loeve¹, S. Hurter^{1,2}, F. Neele¹

¹ TNO, Utrecht, The Netherlands

² The University of Queensland, Brisbane, Australia

* Corresponding author e-mail: lies.peters@tno.nl

Abstract

Injection of CO₂ in depleted hydrocarbon fields often leads to differences in temperature between the injected CO₂ and the reservoir formation and fluids. A low pressure in the reservoir after depletion leads to decompression and cooling of the CO₂. The temperature contrast can become significant, up to tens of degrees centigrade. For safe and efficient injection and storage of cold CO₂, simulation of pressure and temperature in the pipelines, wells and reservoir is required. The reservoir is generally represented in a simplified way in pipeline and well models via multi-dimensional tables. A sensitivity analysis of CO₂ injection in a realistic reservoir model shows that for cold CO₂ injection below the critical pressure, such tables are too limited. The high variability in CO₂ properties (density and viscosity) makes the injectivity highly variable.

Keywords: CO₂ storage; Coupled models; Thermal CO₂ reservoir simulator; Well model

1. Introduction

Storage of CO₂ in the subsurface is seen as a viable option to reduce global warming, when it can be done in a safe and efficient way. A key element for the storage of carbon dioxide (CO₂) are the injection wells, which bring the CO₂ from the high-pressure surface transport pipeline to the underground storage reservoir, such as a depleted gas field or saline aquifer. Accurate prediction of the pressure and temperature in the pipelines and wells during CO₂ injection is required for both operations and conformance monitoring. Conformance monitoring entails measuring wellhead and bottom hole conditions and comparing measured values with forecasts to ascertain that the integrity and safety of the storage site is maintained [1].

The CO₂ temperature at bottom hole is likely to be significantly lower than that of the storage formation. This temperature difference is caused by the fluid (CO₂), which does not thermally equilibrate instantaneously with the geothermal gradient; especially at high flow rates a significant temperature difference is expected. The bottom hole conditions during injection depend on the conditions in the transport pipeline (pressure, temperature, CO₂ composition), the flow rate down the well, as well as on properties of the storage reservoir and the conditions in the reservoir near the well [4][9][10][11]. The latter are affected by the injection history.

The properties of the injection fluid – CO₂ fraction, density, viscosity – vary strongly over the pressure and temperature interval that is relevant for injection into depleted fields, especially when reservoir pressure and injection temperature is below the liquid-vapor phase line (lower than about 50 bar and 30 °C). Uncertainties in, for example, near-well pressure, temperature, saturation, and permeability may translate into relatively large

uncertainties in forecasts of bottom hole conditions and flow rates. The same is true for the condition at the well head. Large uncertainties in for example predicted bottom hole pressure and tubing head pressures are a problem for both operation planning and conformance monitoring.

For monitoring and risk management purposes it is important to quantify which conditions can't be explained by safe CO₂ injection, but are associated with certain risk factors (e.g. fracture propagation due to cold CO₂ around the well). A proper analysis is only possible with modelling tools that, on the one hand, take into account the direct coupling between the properties of CO₂ and the reservoir conditions and, on the other hand, the wellhead/bottom hole conditions of the CO₂ (e.g. Joule-Thomson effect in the reservoir and injection well, evaporation and dissolution) [2][4][5]. This requires the reservoir to be represented in the well and pipeline models. Mostly this is done using Inflow Performance Relationship (IPR) curves, which give inflow rate as a function of bottom hole and reservoir pressure. Because of the strong effect that temperature has, CO₂ injection simulations need to be coupled to heat transport to describe conditions at specific temperatures and pressures. Therefore, temperature is an additional parameter.

Due to the highly variable properties of the CO₂ at low pressure and low injection temperature, creating a set of IPR curves is not trivial, in particular with respect to temperature. Also these curves are limited because they do not include the effect of well interference and uncertainty.

This paper investigates the injectivity of cold CO₂ in depleted gas fields with the purpose of representing the reservoir in a well bore and network model. Sensitivity analysis is used to understand the dependence of

injectivity on injection rate and temperature and how to represent this for a well bore flow model. To ensure that the results are representative for actual depleted gas fields a realistic, multi-well reservoir model is used.

2. Approach

2.1 Model approach

To investigate the injectivity of CO₂ injection in a realistic depleted gas reservoir, a numerical modelling tool is used. The model is based on an existing gas field and has the following characteristics:

- A tilted fault block with moderately-sized aquifer
- The abandonment pressure is ~ 15 bar.
- The reservoir temperature is ~126 °C
- The field is first produced and then filled through three near-vertical wells.
- The main flow occurs in a high-permeability thin upper zone. Permeability decreases with depth.

To simulate the injection of cold CO₂, it is important to accurately account for the physical processes in the reservoir. Joule-Thomson cooling and evaporation of formation water are accurately represented. However, to keep the numerical burden manageable in a sensitivity analysis some simplifications are made:

- The initial reservoir is filled with CO₂ instead of natural gas. Although the depletion phase is simulated for natural gas, before the start of the CO₂ injection, the remaining in-situ gas is changed to CO₂. The impact of this simplification was checked and found to be negligible for the injectivity of the wells.
- To improve stability of the runs, instead of pure CO₂, some CH₄ and water (3%) were added to the injection stream. This also changed the results very little.
- CO₂ dissolution and salt precipitation and chemical reactions are not included in these simulations.
- Non-Darcy flow is not included although it is known to occur for high rate CO₂ wells [7].

The impact of mechanical effects is not included, although they could significantly affect well injectivity. In particular, the reduction in temperature can lead to thermal stress fracturing of the formation [8]. Temperatures mostly remain high enough (> 10 °C) to avoid hydrate formation [5]. Also in real applications this will normally be avoided.

An important choice for the simulation is the grid size near the well. Instead of using single-well models to represent the near-well physics in detail, a multi-well model was used. Previous models studying the behaviour of cold CO₂ injection near the critical point were mostly single well models [2][3][5]. The main reason for using a multi-well model is to incorporate interference between

wells and the influence of reservoir architecture (faults and permeability heterogeneity).

The impact of three different grid sizes was evaluated. Table 1 gives the input settings. The results make it clear that for the case of 50 x 50 m grid blocks, the behaviour was averaged to such a degree that the conditions for Joule Thomson (JT) cooling were not well met. JT cooling is strongest for low pressure and temperature (see e.g. [4]). In coarse grids, the pressure has increased substantially before the near well area is sufficiently cold to cause a strong JT effect. JT cooling and vaporization could clearly be observed in the finest grid model and the temperature in the near well bore area dropped below injection temperature. Figure 1 shows the impact on the Bottom Hole Pressure (BHP) of the three different grid sizes for the same injection rate and injection temperature. This result shows that although the detailed behaviour is less well represented using coarse grid blocks, the overall behaviour doesn't change much, except in the first moments of injection and near the phase change. For the following simulations, the model with two levels of grid refinement were used.

Table 1: Approximate sizes of grid near the well. For the thickness in the vertical (dz) the values in the main reservoir are given.

	dx = dy	dz
No refinement	40 to 50 m	in main reservoir: ~4 m
1 level	20 to 25 m	in main reservoir: ~4 m
2 levels	10 to 12.5 m	in main reservoir: ~2 m

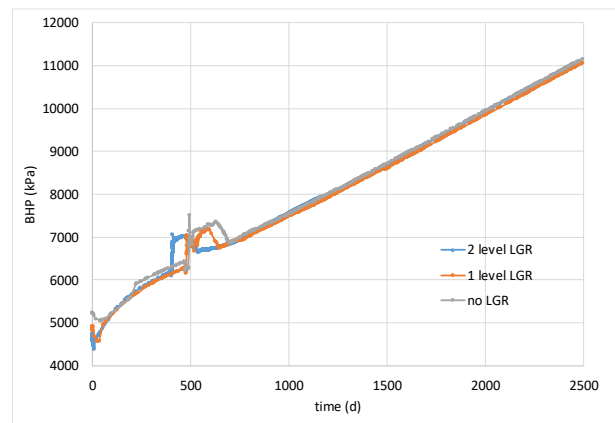


Figure 1: comparison of the impact of different near-well grid size (Table 1) on the BHP of the well for injection of 10 kg/s CO₂ at 15 °C.

2.2 Well injectivity

The Injectivity Index (II) is calculated to compare the behaviour of the well at different injection conditions. Although the definition of the injectivity index is very simple (injected mass rate divided by the pressure difference required to inject), in practice the difficulty is in defining the appropriate reservoir pressure that is used to estimate this pressure difference. In order to be appropriate for understanding the injectivity in relation to

a wellbore flow model, the reservoir pressure should represent the pressure ‘felt’ by the well. For comparison with observations, it should ideally be close to the reservoir pressure estimated from a well test.

Here, the average pressure in the area surrounding the well in the main reservoir layers is taken as the reservoir pressure for the calculation of the II. Low permeability layers beneath the main reservoir layers were not included, because the pressure in these layers lags considerably compared to the reservoir. For each well a sector surrounding each well was defined such that they do not overlap.

3. Results

3.1 Injectivity Index

As discussed, the main reason for using a multi-well reservoir model, rather than single-well models with a detailed grid, is to be able to represent the interaction between wells. As we are not interested in the very fast transients at start-up of injection, output for the first two days was omitted. In Figure 2, the difference in injectivity is plotted for injection in a single well or all three wells. It is clear that the injectivity decreases significantly due to interference with other wells. This is expected because the reservoir is well connected and the wells are not very far apart. The distance between well 1 and the nearest other well is approximately 2 km.

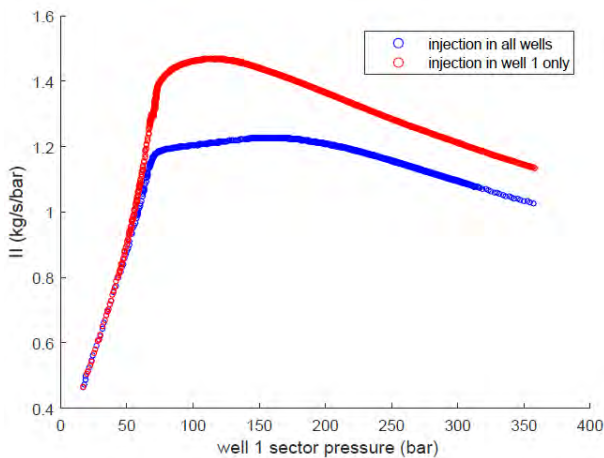


Figure 2: Difference in injectivity resulting from interference between wells (injection rate is 20 kg/s and injection temperature is 30 °C).

To investigate the impact of the injection rate and temperature a set of simulations was conducted with injection temperatures of 30, 45 and 60 °C and injection rates of 10 and 20 kg/s. The results are presented in Figure 3 and Figure 4. In Figure 3, the colour indicates the injection rate and in Figure 4 the colour indicates the injection temperature. Initially, the scenarios with the same rate have similar injectivity (Figure 3). In late time (or at higher pressure) on the other hand, the scenarios with the same injection temperature converge (Figure 4). The same behaviour was seen in the other wells (not presented here). To explain this behaviour, the properties of the CO₂ in the sector around the well are plotted in the

top figure of Figure 5 and the well bottom hole conditions in the underlying figure. Initially the density increases steeply due to the change in pressure. Since the injectivity is expressed in kg/s/bar, a higher density means a higher injectivity. In late time, the difference in viscosity due to the temperature difference dominates the difference in injectivity: the reservoir cools.

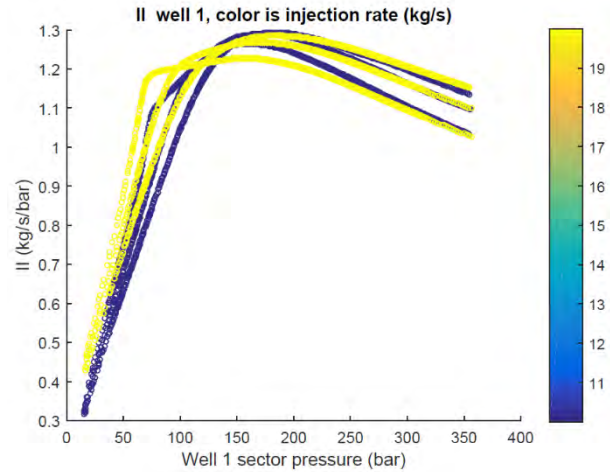


Figure 3: Injectivity index (kg/s/bar) for injection temperatures of 30, 45 and 60 °C and injection rates of 10 and 20 kg/s (indicated by colour) as a function of the well sector pressure.

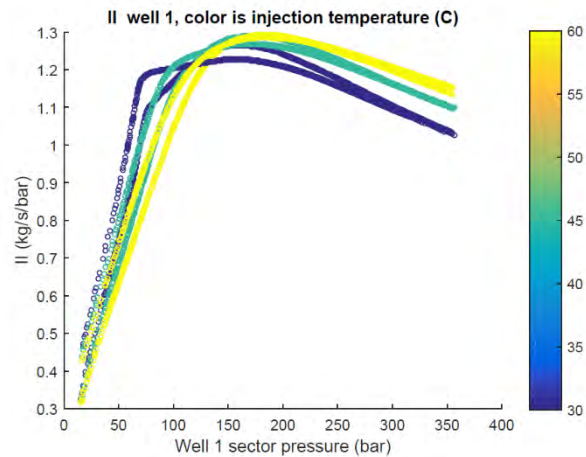


Figure 4: Injectivity index (kg/s/bar) for injection temperatures of 30, 45 and 60 °C (indicated by the colour) and injection rates of 10 and 20 kg/s as a function of the well sector pressure.

For the simulations so far, the range in injection rate and temperature was relatively small. For the initial injection period (up to a reservoir pressure of 100 bar), a more extensive range of injection rates and temperatures was simulated: 2 to 40 kg/s and 15 to 75 °C. The results are presented in Figure 6 and Figure 7. Now we can see that the range in injectivity increases considerably. The strong variations in injectivity around 40 bar are mainly caused by numerical instabilities, which can occur due to the strong changes in density and viscosity (Figure 5). Not all runs with an injection temperature of 15°C finished. For the high rate at 15°C, a more gradual ramping up of the rate would be required, but this was not conducted in this study.

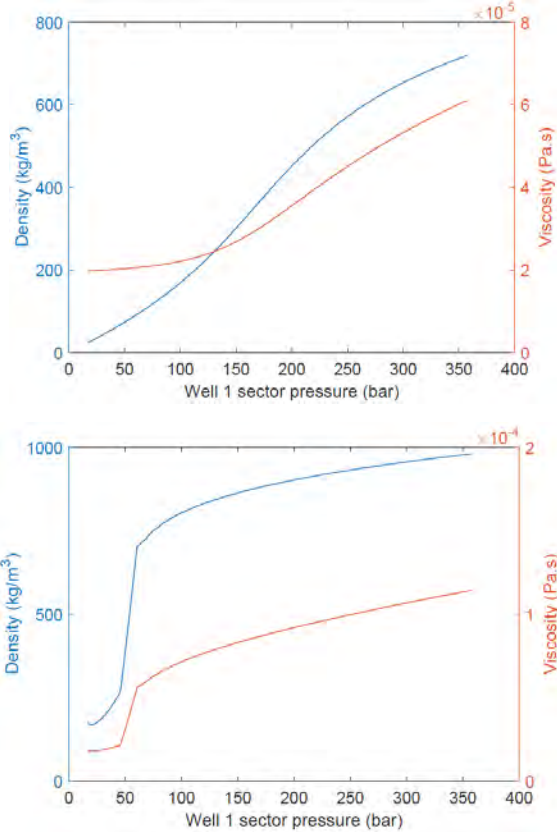


Figure 5: Properties of the CO₂ at average reservoir conditions in the sector around well 1 (top) and at well down hole conditions (bottom) for an injection rate of 20 kg/s and injection temperature of 30 °C.

From Figure 6, it is clear that initially the injection rate causes the largest span in injectivity. This can be understood from the CO₂ density and viscosity in the well which are plotted in Figure 8 and Figure 9. Injection at 15°C behaves differently than at higher temperatures because it is below the critical point. For all other injection temperatures, the impact on density and viscosity is larger for the rate than the temperature at low pressure.

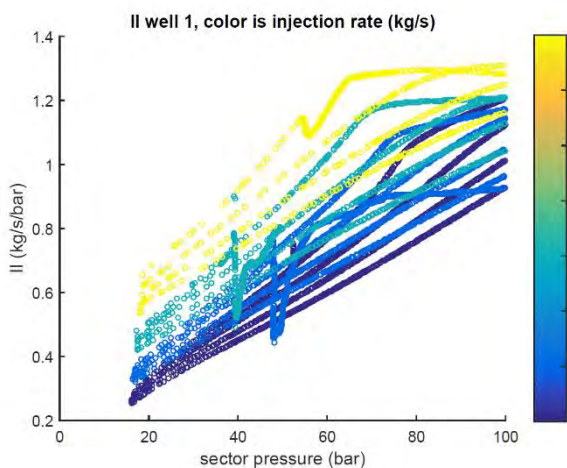


Figure 6: Injectivity Index II (kg/s/bar) for injection temperatures varying injection rate and temperature as a function of the well sector pressure (colour is injection rate).

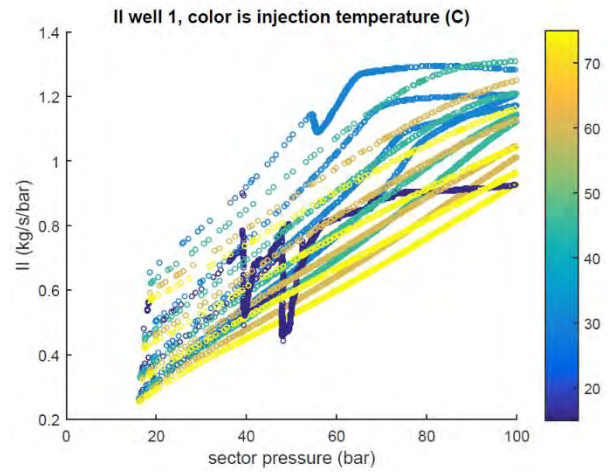


Figure 7: Injectivity Index II (kg/s/bar) for injection temperatures varying injection rate and temperature as a function of the well sector pressure (colour is injection temperature).

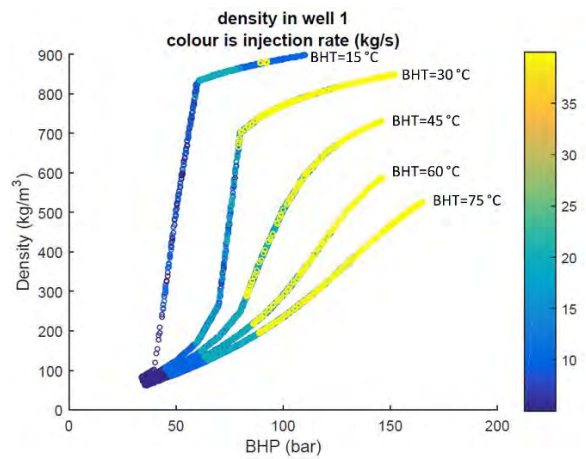


Figure 8: Density (kg/m³) in the well at down hole conditions as a function of bottom hole pressure (BHP) and bottom hole temperature (BHT).

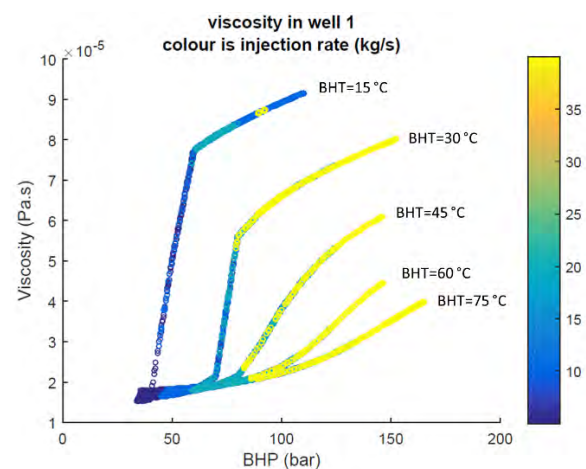


Figure 9: Viscosity (Pa.s) in the well at down hole conditions as a function of bottom hole pressure (BHP) and bottom hole temperature (BHT).

To reduce the large variability in the graphs due to the variability in density, the volumetric injectivity can be plotted instead of the mass injectivity used so far. This is similar to using a gas pseudo-pressure approach. The volumetric injectivity index is calculated by multiplying the mass rate by the CO₂ density at down hole conditions. The results in Figure 4 recalculated as volumetric injectivity index are plotted in Figure 10. Now the impact of temperature on injectivity is much more dominant, except at low pressure.

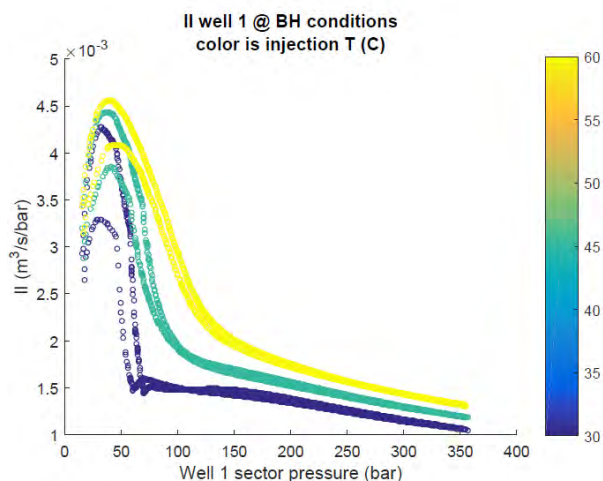


Figure 10: Volumetric Injectivity Index II (m³/s/bar) for injection temperatures of 30, 45 and 60 °C (indicated by the colour) and injection rates of 10 and 20 kg/s as a function of the well sector pressure.

These results show that if reservoir pressure and temperature are comfortably above the phase line, injection can be represented using a 4-dimensional IPR curves depending on reservoir and well pressure and temperature. However for lower temperature and pressure, such tables become unfeasible due to the high variability in the CO₂ properties. Since a full coupling of a multi-well model with well and pipeline models is currently not available and would be extremely demanding in terms of simulation effort and CPU time, a smarter solution needs to be developed. In the next step, we propose to use machine learning techniques to replace the tables for IPR curves. This will also allow to include the well interference in well-reservoir coupling.

4. Summary and conclusions

In this paper, we presented a sensitivity analysis for injection of cold CO₂ in a realistic depleted low pressure

gas reservoir tapped by three wells. The variability of the injectivity index with changes in rate and temperature below the CO₂ critical pressure is very large and would be difficult to represent in tables. We examined only a limited number of relevant processes (JT cooling and evaporation). For accurate pipeline and well modelling, the reservoir should therefore be represented in a more comprehensive way than with multi-dimensional tables.

References

- [1] Steeghs Ph., Neele F., Gittins C., Ros, M., 2014, Drafting a monitoring plan for the ROAD project under the EU CCS Directive, Energy Procedia 63 (2014) 6680 – 6687.
- [2] Oldenburg, C.M. (2007) Joule-Thomson cooling due to CO₂ injection into natural gas reservoirs. Energy Conv. Manag. 48, p 1808-1815. Doi: 10.1016/j.enconman.2007.01.010
- [3] Ziabakhsh-Ganji, Z. and H. Kooi (2014) Sensitivity of Joule-Thomson cooling to impure CO₂ injection in depleted gas reservoirs. Applied Energy 113 434-451. Doi: dx.doi.org/10.1016/j.apenergy.2013.07.059.
- [4] Carniero, J.N.E., M.A. Pasqualetto, J.F.R. Reyes, E. Krogh, S.T. Johansen; J.R.P. Ciambelli, H.T. Rodrigues, R. Fonseca Jr. (2015) Numerical Simulations of High CO₂ Content Flows in Production Wells, Flowlines and Risers. OTC-26231-MS.
- [5] Voskov, D. V., Henley, H., & Lucia, L. (2017). Fully Compositional Multi-Scale Reservoir Simulation of Various CO₂ Sequestration Mechanisms. Computers & Chemical Engineering, 96(4), 183-195. doi: 10.1016/j.compchemeng.2016.09.021
- [6] Hoteit, H., M. Fahs and M. R. Soltanian (2019) Assessment of CO₂ Injectivity During Sequestration in Depleted Gas Reservoirs. Geosciences 9. doi:10.3390/geosciences9050199.
- [7] Grigg, R.B., Z. Zeng and L.V. Bethapudi, 2004. Comparison of Non-Darcy flow of CO₂ and N₂ in a carbonate rock. SPE 89471.
- [8] Salimzadeh, S., Paluszny, A., Zimmerman, R.W. (2018) Effect of cold CO₂ injection on fracture apertures and growth, IJGGC 74, 130-141
- [9] Paterson, L., J. Ennis-King, S. Sharma (2010) Observations of Thermal and Pressure Transients in Carbon Dioxide Wells. SPE134881.
- [10] Böser, W. and S. Belfroid (2013) Flow Assurance Study. GHGT-1. Energy Procedia 37, 0.1016/j.egypro.2013.06.188.
- [11] Veltin, J. and S. Belfroid 2012. Dynamics of CO₂ Transport and Injection Strategies in a Depleted Gas Field. CMTC-151265.

EXPERIMENTAL ASSESSMENT OF THE ENVIRONMENTAL IMPACT OF ETHANOLAMINE

Vanja Buvik¹, Richard Strimbeck², Hanna K. Knuutila^{1*}

¹ Department of Chemical Engineering, NTNU, NO-7491 Trondheim, Norway

² Department of Biology, NTNU, NO-7491, Trondheim, Norway

* Corresponding author e-mail: hanna.knuutila@ntnu.no

Abstract

The environmental impact of ethanolamine, a common amine for carbon dioxide capture, was experimentally investigated in laboratory scale microcosms. By exposing the plant-soil systems to varying amounts of ethanolamine, we assessed the effects a potential leakage or spill to the surroundings of an industrial site including vegetation. The results of this study show that small amounts of ethanolamine have no significant impact of the health of the plants in the scope of three weeks after treatment. Plant health was affected negatively by larger amounts of ethanolamine, but the plants treated with larger ethanolamine concentrations also seemed to be healthier, lusher and greener after three weeks of observation. Unfortunately, this positive observation, indicating an actual fertilizing effect by ethanolamine on the plants could not be verified. In the TCCS-11 presentation we will show the results of this experimental study, their statistical interpretation, as well the implications the results have.

Keywords: biodegradation, amine stability, CO₂ capture, ecotoxicity, plant health

1 Introduction

One of the most efficient ways of performing capture of carbon dioxide (CO₂) from industrial sources is using amine solvents. This is one of the most mature technologies available for large scale CO₂ capture, as it has been developed and tested over nearly a century.¹⁻³ Amines bind chemically to the CO₂ molecules in a reaction that can be reversed upon heating up the solvent. Chemical stability of the amine is a necessity in the capture process, where it needs to withstand temperature cycling as well as oxidative conditions.⁴ If the amine reaches the environment through emissions or spills from the capture facility, however, stability may no longer be a desirable property. Anything that reaches the environment should have the ability to get incorporated into the environment as non-toxic components that can be consumed by organisms making changes to them or the environment.

Biodegradation is the process of breaking down larger into smaller molecules, performed by microorganisms. Because of the plethora of different microorganisms capable of performing biodegradation, biodegradability can follow manifold pathways. Amines used in CO₂ capture consist of hydrogen (H), carbon (C), oxygen (O) and nitrogen (N) and will ideally be broken down to CO₂, water (H₂O) and ammonia (NH₃), or other small molecules that can be available for plants to use as nutrients.

Assessment of biodegradability of chemicals which are used or considered for use in industrial applications is of immense importance, for mapping potential environmental risks of a spill or leakage of the chemical. A range of biodegradability test guidelines have been

developed by the Organisation for Economic Co-operation and Development (OECD), for testing new chemicals, and these are commonly used for assessing new chemicals for industrial use.⁵

Table 1: Summary of the results of previous biodegradation studies of MEA.

Type	Conditions	Results	Ref.
Soil	aerobic and anaerobic	MEA degraded aerobically and anaerobically	6
Soil	aerobic and anaerobic	MEA degraded aerobically and anaerobically	7
Sea water	Aerobic with varying temperatures	Overall high degradability of MEA	8
Sea water	aerobic	MEA readily biodegradable	9
Fresh water	aerobic	MEA is readily biodegradable	10
Bioreactors	aerobic	MEA successfully degraded	11
Bioreactors	aerobic and anaerobic	MEA completely degradable upon PO ₄ ³⁻ addition	12

1.1 Biodegradation of ethanolamine (MEA)

Ethanolamine is naturally occurring¹³, a feature that seems to make the amines more likely to be biodegradable than synthetic ones¹⁴. It has for decades been the benchmark solvent for CO₂ capture and many biodegradation studies have already been performed both aerobically and anaerobically in soils^{6,7}, in sea water^{8,9}, fresh water¹⁰ and in lab-scale bioreactors under aerobic

and anaerobic conditions^{11,12}. Some of these studies have also been performed according to the previously mentioned OECD guidelines. A quick summary of the findings of these studies is given in Table 1, and it can be observed that all have proven MEA to indeed be biodegradable. Additionally, Eide-Haugmo et al.⁹ found that the ecotoxicity of MEA is also acceptably low in the marine species *Skeletonema costatum*.

In this work we try to take the conclusions from all these earlier studies one step further, to assess whether there are any immediate effects of an amine leakages to surrounding plants and soils. The experimental setup is, to our knowledge, novel in the field and provides a further perspective of the biocompatibility and environmental effects of amines and specifically ethanolamine.

2 Materials and methods

2.1 Materials

Ethanolamine (CAS: 141-43-5, purity $\geq 99.0\%$) was purchased from Merck Life Science/Sigma Aldrich Norway. Flowering soil ($\frac{1}{3}$ cow manure and $\frac{2}{3}$ turf, long-term composted over three years) and a mixture of grass seeds for outdoor use, were purchased from a local garden equipment store.

2.2 Experimental design

6 sets of 6 pots of 8x8x8 cm were filled with approximately 400 mL, which was thoroughly watered before soil and grass seeds were sowed on its surface in the density recommended on the seed package. The grass was watered twice a week, from a dish under the pots for the entire duration of the experiment. After 46 days, when the grass had grown at least 5-8 cm (see Figure 1) and a root system had the time to develop in the soil, one single randomized treatment was conducted per pot.



Figure 1: Example of grass length before the single treatment with MEA was conducted.

Each set of 6 pots were given one 10 mL addition of water or MEA with Table 2. The liquid was carefully distributed over the soil surface with a disposable syringe, without applying it directly on the plants. The order of treatment was randomized within each set.

Table 2: Treatments overview. Each treatment consisted of 10 mL of the given solution.

Treatment	% MEA
T1	0 (control)
T2	1.0
T3	2.5
T4	5.0
T5	7.5
T6	10

In summary this means that for each of the 6 treatments there were 6 individual samples, randomly located in different sample sets.

2.3 Assessment of plant health

Regular visual scoring of plant health was performed according to Table 3 on day 4, 7, 11, 13, 18 and 21. Every scoring was performed by the same observer, without knowledge of which treatment each given system had been given.

Table 3: Explanation of the scoring sheet used for assessing the plant health in the experiment.

Score	Percentage of brown leaves
0	0
1	1-10
2	11-30
3	31-60
4	61-90
5	91-100



Figure 2: Browning observed in one set of 6 different, randomized plant pots 11 days after treatment with MEA.

2.4 Statistical tests

A Kruskal-Wallis test was performed to determine the statistical significance in the difference of plant health observed in these experiments. This is a non-parametric statistical test, suitable for the comparison of individual samples and it does not assume a normal distribution of residuals. Variance is quantified as adjusted p-values and an adjusted $p \leq 0.05$ represents a significant difference between two treatments at a given time. The Bonferroni method was used for p-value adjustment.

A Friedman test, which is a non-parametric test for non-replicated data with complete block design, was

performed to determine the statistical significance of the change in plant health over time. Kendall's W , as shown in Eq. 1, where X^2 is the Friedman test statistic value, N the sample size and K the number of measurements. Cohen's interpretation of effect size was used to determine the size of the effect observed within each treatment.

$$W = \frac{X^2}{N(K-1)} \quad \text{Eq. 1}$$

Bonferroni p-value adjustment was used for the identification of statistical difference between the treatments.

3 Results

3.1 Plant health

Browning was typically observed from day three to some degree, and then increasing. An example of the grass health as it was observed some days after treatment can be seen in Figure 2, The results of the plant health testing throughout three weeks after treatment with different amounts of MEA is depicted the means of each treatment in Figure 3 and medians in Figure 4. There is a clear trend seen from T4 to T6, whereas the health of the plants receiving treatments T1 (control) to T3 are more similar and no effect can be immediately distinguished. The statistical relevance of both these and the remaining results were determination by a Kruskal-Wallis test as well as a Friedman test.

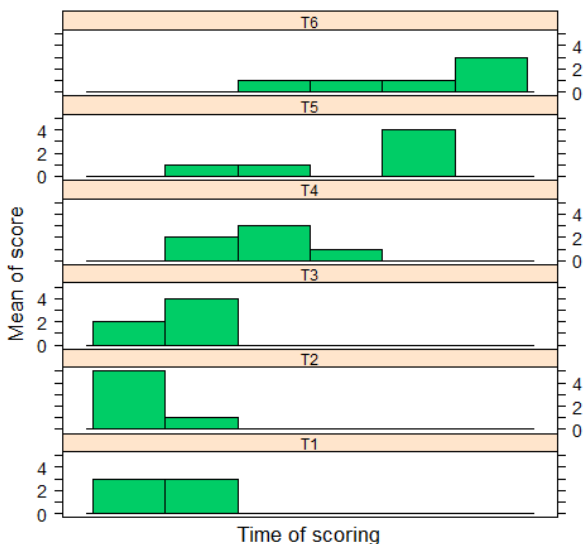


Figure 3: Means of plant health score for all treatments at different times of scoring.

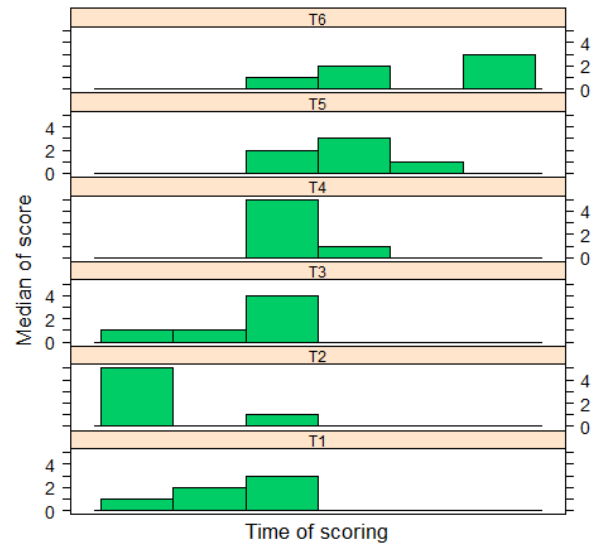


Figure 4: Medians of plant health score for all treatments at different times of scoring.

As seen in Figure 5, the Kruskal Wallis test shows that a higher degree of browning was seen on day 21 with T5 and T6 compared to T1-T3. On day 4, no significant differences were observed between any treatments, but at day 7, T6 showed more browning than T3 ($p < 0.01$). The difference between these two treatments remained significant throughout the whole experiment. After 11 days T6 had more browning than T1-T3 ($p < 0.3$ in all cases) and this is when T5 also started being browner than T2 ($p = 0.02$).

T2	1				
T3	1	1			
T4	0.9	0.4	0.9		
T5	0.03	0.01	0.03	1	
T6	0.04	0.01	0.04	1	1
	T1	T2	T3	T4	T5

Figure 5: Adjusted p-values for the average plant scores on day 21. Treatments which have $p \leq 0.05$ are statistically different from one another and can be described as giving different response in the plant health.

At no time of scoring was there a significant difference in browning between T1-T4, meaning that the addition of 1.0-5.0% MEA into the plant-soil systems makes no difference from not adding any MEA, the plant health is deemed the same.

The overall change in plant health over time was quantified by the Friedman test to be *large*. Within treatments, the effect was *small* in T1 and T2, *moderate* in T3 and T4 and *large* in T5 and T6 using Kendall's W and the Cohen interpretation of effect size. The effects of the treatments were studied using multiple pairwise comparisons and the Bonferroni adjusted p-values are given in Figure 6. According to these results treatments T3 to T6 have differences in plant health over time compared to T1 (control) to T3.

T2	0.7				
T3	1	1			
T4	$4 \cdot 10^{-3}$	$9 \cdot 10^{-6}$	$1 \cdot 10^{-4}$		
T5	$4 \cdot 10^{-6}$	$7 \cdot 10^{-8}$	$2 \cdot 10^{-7}$	0.04	
T6	$2 \cdot 10^{-8}$	$7 \cdot 10^{-10}$	$1 \cdot 10^{-9}$	$7 \cdot 10^{-5}$	1
	T1	T2	T3	T4	T5

Figure 6: Adjusted p-values for the mean of the plant scores through the entire experiment time of 21 days. Statistical significance given at $p \leq 0.05$.

Interestingly, a few weeks after the experiment was concluded, the pots containing plants treated with T5 and T6 seemed lusher and healthier than the plants where less MEA had been added. Since the observer from the duration of the experiment was not available, this data could not be logged. Attempts were made to extract remaining MEA and potential degradation compounds from the soil using a KOH extraction method followed by centrifuging and filtering. No MEA could be observed in the soil extracts in the subsequent cation IC analysis. This phenomenon could either be due to an insufficiently low detection limit, having the strong signal of K⁺ in the chromatogram, or it could be simply because the MEA was already biodegraded. Further research is needed to conclude on this matter.

4 Discussion and conclusions

Just like previous biodegradability ecotoxicity testing, these experiments show that MEA is not harmful for a plant-soil system, at least in small doses. For the three weeks after treatment with MEA there was no observable difference between plant-soil systems given up to 0.5 mL of MEA per 400 mL soil. This must mean that the buffer capacity of the soil is good enough to account for the potential pH increase when adding MEA, as well as that there's no observable toxic effect on the plants. The higher concentrations of MEA had a significant impact on the plants, making them browner in the experimental observation time of three weeks. In these cases, it can be hypothesized that the MEA has a negative impact in the soil, either by killing off some of the microbes or damaging the root systems of the plants. This is likely to be caused by the high pH of the MEA causing a chemical burn. The less likely explanation is that MEA has a toxic effect causing the plants to go brown. This is less likely because of previous testing, but also because of the subsequent healing of the plants after the end of the experiment.

The fact that the plants which had received a higher concentration of MEA actually seemed healthier after the experiment had ended, than those with less or no MEA added, indicates that the MEA that initially may have made the plants health decline, now was biodegraded into components that acted as nutrients for the plants. Nitrogen is a valuable nutrient in the plant kingdom, that the plants need to absorb from soil and water, as they are

not able to convert nitrogen from air. Hence, the addition of nitrogen in the form of MEA may initially be harmful, but then have been biologically (biodegraded) converted to bioavailable small molecules by the soil microbes. Since, unfortunately, this observation took place after the experiment was ended and could not be logged by the same observer as throughout the scorings given in this paper, this effect could not be quantified and would be interesting to study in future work. This would most definitely be an interesting starting point for any further studies of the environmental impact of amines.

Acknowledgements

This publication has been produced with support from the NCCS Centre, performed under the Norwegian research program Centres for Environment-friendly Energy Research (FME). The authors acknowledge the following partners for their contributions: Aker Solutions, Ansaldo Energia, Baker Hughes, CoorsTek Membrane Sciences, EMGS, Equinor, Gassco, Krohne, Larvik Shipping, Lundin, Norcem, Norwegian Oil and Gas, Quad Geometrics, Total, Vår Energi, and the Research Council of Norway (257579/E20).

References

- Kohl, A. L.; Nielsen, R. B., Chapter 2 - Alkanolamines for Hydrogen Sulfide and Carbon Dioxide Removal. In *Gas Purification (Fifth Edition)*, Kohl, A. L.; Nielsen, R. B., Eds. Gulf Professional Publishing: Houston, 1997; pp 40-186.
- Rochelle, G. T., Amine scrubbing for CO₂ capture. *Science* **2009**, *325* (5948), 1652-1654.
- Leung, D. Y.; Caramanna, G.; Maroto-Valer, M. M., An overview of current status of carbon dioxide capture and storage technologies. *Renewable and Sustainable Energy Reviews* **2014**, *39*, 426-443.
- Reynolds, A. J.; Verheyen, T. V.; Meuleman, E., Degradation of amine-based solvents. In *Absorption-Based Post-combustion Capture of Carbon Dioxide*, Feron, P. H. M., Ed. Woodhead Publishing: 2016; pp 399-423.
- OECD, *Detailed Review Paper on Biodegradability Testing*. 2002.
- Ndegwa, A. W.; Wong, R. C.; Chu, A.; Bentley, L. R.; Lunn, S. R., Degradation of monoethanolamine in soil. *Journal of Environmental Engineering and Science* **2004**, *3* (2), 137-145.
- Wong, R. C.; Bentley, L.; Ndegwa, A.; Chu, A.; Gharibi, M.; Lunn, S. R., Biodegradation of monoethanolamine in soil monitored by electrical conductivity measurement: an observational approach. *Canadian geotechnical journal* **2004**, *41* (6), 1026-1037.
- Brakstad, O. G.; Booth, A.; Eide-Haugmo, I.; Skjaeran, J. A.; Sorheim, K. R.; Bonaunet, K.; Vang, S. H.; da Silva, E. F., Seawater biodegradation of alkanolamines used for CO₂-capture from natural gas. *International Journal of Greenhouse Gas Control* **2012**, *10*, 271-277.
- Eide-Haugmo, I.; Brakstad, O. G.; Hoff, K. A.; da Silva, E. F.; Svendsen, H. F., Marine biodegradability and ecotoxicity of solvents for CO₂-capture of natural gas. *International Journal of Greenhouse Gas Control* **2012**, *9*, 184-192.
- Henry, I. A.; Kowarz, V.; Østgaard, K., Aerobic and anoxic biodegradability of amines applied in CO₂-capture. *International Journal of Greenhouse Gas Control* **2017**, *58*, 266-275.

11. Kim, D.-J.; Lim, Y.; Cho, D.; Rhee, I. H., Biodegradation of monoethanolamine in aerobic and anoxic conditions. *Korean Journal of Chemical Engineering* **2010**, *27* (5), 1521-1526.
12. Mrklas, O.; Chu, A.; Lunn, S.; Bentley, L. R., Biodegradation of monoethanolamine, ethylene glycol and triethylene glycol in laboratory bioreactors. *Water, air, and soil pollution* **2004**, *159* (1), 249-263.
13. DNP Dictionary of Natural Products. <http://dnp.chemnetbase.com/faces/chemical/ChemicalSearch.xhtml> (accessed 10.10.2020).
14. Eide-Haugmo, I., Environmental impacts and aspects of absorbents used for CO₂ capture. **2011**.

MODELLING AND EVALUATING CARBAMATE POLYMERIZATION OF MONOETHANOLAMINE IN POST-COMBUSTION CARBON CAPTURE

Lucas Braakhuis¹, Hanna K. Knuutila^{1*}

¹ Department of Chemical Engineering, Norwegian University of Science and Technology, 7491 Trondheim, Norway

* Corresponding author e-mail: hanna.knuutila@ntnu.no

Abstract

In this work, experimental data on carbamate polymerization of aqueous solutions of monoethanolamine (MEA) has been collected and analyzed. Three degradation models were developed describing thermal degradation of MEA in aqueous solutions to investigate the importance of taking into account MEA consumption when describing the experimental data. The models were fitted to literature data. It was found that with the same number of parameters, a better fit was obtained when considering MEA consumption. All the models showed increased deviations for longer experiments and at higher temperatures, indicating that the high concentration of degradation compounds might influence the degradation rate.

Keywords: MEA, monoethanolamine, carbamate polymerization, thermal degradation, solvent management.

1. Introduction

One of the most promising ways to reduce carbon dioxide emissions into the atmosphere is through absorption-based post-combustion carbon capture. In this process, exhaust gases from industry are treated with a water-based solvent, which selectively absorbs the CO₂ from the gas. The solvent is stripped at elevated temperatures, after which it is recycled. A fraction of the solvent is entrained in the flue gas or lost through degradation and is replaced. One of the main challenges is to reduce the loss of solvent through degradation and prevent the formation of degradation products [1].

Solvents degrade when brought into contact with oxygen in the absorber or through carbamate polymerization at increased temperatures and under the presence of CO₂. Carbamate polymerization, typically happening during solvent regeneration in the stripper, is also referred to as thermal degradation under the presence of CO₂. Aqueous 30 wt-% of monoethanolamine (MEA) solution is one of the most established solvents used for post-combustion carbon capture [2] and the solvent studied in this paper.

Figure 1 gives an overview of the predominant degradation reactions and products. The carbamate that is formed when CO₂ reacts with MEA can undergo a ring closure to form 2-oxazolidone (OZD). Concentrations of this compound are low in degraded solutions, and therefore, OZD is suspected to be an intermediate [3]. OZD can react with free MEA to form N-(2-hydroxyethyl)-ethylenediamine (HEEDA), which in turn can react with CO₂ to form 1-(2-hydroxyethyl)-2-imidazolidone (HEIA).

Léonard et al. [4] modelled the carbamate polymerization rate as the product of a temperature-dependent reaction rate coefficient and the initial concentration of CO₂. Because of the abundance of MEA, it was assumed the amine concentration did not affect the degradation rate. However, experimental data shows that the degradation rate is not constant and tends to decrease over time, especially at higher temperatures and loadings [5]. This

indicates that the consumption of MEA might play an important role when modeling laboratory-scale degradation data.

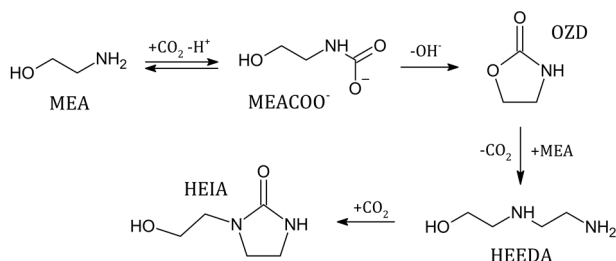


Figure 1: Overview of the most significant carbamate polymerization reactions, as proposed by [3], [5]–[7].

In this study, three different degradation models were developed, fitted, and evaluated to investigate the extent and effect of this consumption.

2. Methodology

Experimental data from carbamate polymerization studies given in Table 1 was used in this work. No additional degradation experiments were performed. The experimental methods in these studies were similar to each other. Amine solutions were prepared and loaded with CO₂ up to the specified loading. The solution was transferred into stainless steel cylinders, which were closed off. The cylinders' liquid volume and headspace varied slightly in the different experiments but were in the same order of magnitude. Next, the cylinders were placed in a heat-controlled chamber and kept at a specified temperature for a duration of time. During this time, no stirring or agitation took place. After the degradation, the cylinders were removed and cooled down. The solutions were then analyzed using different analytical methods. The MEA concentration was typically analyzed with (HP)LC-MS and/or Ion

Chromatography (IC). In some cases, analysis via GC-MS or LC-MS was used to identify and quantify degradation products. The uncertainty in these analytical methods is assumed to be the same, so each datapoint can be weighted equally.

Table 1: Overview of the experimental data on carbamate polymerization used in this study.

Datapoints	Loading, α	Temperature	Reference
30	0.2 - 0.5	100 - 150	[5]
9	0.1 - 0.4	105 - 135	[8]
25	0.1 - 0.5	135	[3]
5	0.5	135	[9]
6	0.44	120 - 140	[4]
8	0.4	135	[10]
3	0.4	125 - 145	[11]
2	0.4	135	[12]

2.1 Proposed degradation models

The model equations are given in Table 2. The first model describes linear degradation, similar to the model by Léonard et al. [4]. The initial concentration ($[MEA]_0$) has been taken into account to account for different starting concentrations of MEA. The second model takes into account the consumption of MEA, while the CO₂ concentration is kept constant at its initial concentration.

The approach behind the third model is slightly different. Considering the degradation mechanism in Figure 1, one would expect the degradation rate of MEA to be proportional to the concentration of MEA-carbamate. Therefore, this model aims to predict the carbamate concentration, which is then used to fit the reaction rate. Since no experimental data is available on the speciation at these temperatures, the carbamate concentration is modeled with an in-house vapor-liquid equilibrium model calculating activities using an eNRTL-model.

Table 2: Short description and equations of the investigated degradation models in this work.

	Description	Equations
M1	Linear degradation	$\frac{d[MEA]}{dt} = k(T) \cdot [MEA]_0 [CO_2]_0$
M2	MEA consumption	$\frac{d[MEA]}{dt} = k(T) \cdot [MEA][CO_2]_0$
M3	MEA consumption, CO ₂ SIM speciation	$\frac{d[MEA]}{dt} = k(T) \cdot [MEACOO^-]$ $[MEACOO^-] = f([MEA], [CO_2]_0)$

2.1 Adjusted form of the Arrhenius equation

For all models, the reaction rate coefficient at a specified temperature ($k(T)$) is determined using an adjusted form of the Arrhenius equation (1). Here T_r and k_r are the reference temperature and the reaction rate coefficient at reference temperature, respectively. A reference temperature of 400 K has been chosen as this is the rough average of the experiments. This adjusted form yields the same results, but provides a more meaningful expression

for the reaction rate coefficient, which allows for better model comparison and more intuitive initial estimates.

$$k(T) = k_r \cdot \exp\left(\frac{-E_A}{R} \left(\frac{1}{T} - \frac{1}{T_r}\right)\right) \quad (1)$$

2.2 Fitting the parameters

The model parameters have been fitted by minimizing the relative least square errors between the experimental data and the model results. Each experiment is treated individually and weighted equally. Optimization has been performed using the nonlinear Levenberg-Marquardt algorithm. In addition, a particle swarm optimization (PSO) algorithm was used to check if the solution was a valid global minimum. Both routines yielded the same optimized parameters for all the investigated cases.

2.3 Complete and refined dataset

There appears to be no explicit agreement between the experimental results at higher temperatures and loadings (above 145 °C or $\alpha = 0.5$). The relative deviation between the data sets is significantly larger than for experiments at more moderate temperatures and lower loadings. The reason for this difference is not known, but it may be caused by experimental challenges at high temperatures and loadings. Because only four experiments were performed at these extreme conditions, without clear agreement between them, the three models shown in Table 2 have been evaluated with both the complete dataset, taking into account all the data in Table 1 and by excluding experimental data above 145 °C or at a loading of 0.5 (refined dataset).

2.4 Pure experimental error

There were eight sets of replicate degradation experiments in the dataset (17 datapoints in total), for which the temperature, loading, initial concentration, and degradation time were the same (seven sets at 135 °C with various loadings, one at 120 °C with a loading of 0.4). These replicates were used to get an indication of the sum of pure experimental errors (SSEP). The sum of squared errors (SSE) of the model in relation to the experimental data is made up out of the SSEP and the sum of square errors caused by limitations in the model, the lack of fit (SSELOF). The part of the SSE, which the pure error cannot explain is thus caused by lack of fit.

The degree of the lack of fit of the model can be evaluated by comparing the mean error due to lack of fit (MSELOF) against the mean pure square error (MSEP). This fraction is then compared to a F-distribution at 95%-confidence, which is dependent on the total number of datapoints and the number of replicates, see equation (2). The model is considered to be inadequate if $T_{LOF} \geq 1$.

$$T_{LOF} = \frac{\frac{MSELOF}{MSEP}}{F_{0.95, v_{LOF}, v_{pure}}} \quad (2)$$

3. Results

Table 3: Fitted model parameters, confidence intervals and lack-of-fit tests for the complete dataset. Data used to fit the models covers temperature and loading range of 100 – 150 °C and α : 0.1 – 0.5.

Model	Rate parameters	Units	Confidence intervals (95%)	T_{LOF}
M1	$k_r = 6.05 \cdot 10^{-11}$ $E_A = 3.16 \cdot 10^4$	$[m^3 \cdot mol^{-1} \cdot s^{-1}]$ $[J \cdot mol^{-1}]$	$[4.97-7.12] \cdot 10^{-11}$ $[1.95-4.38] \cdot 10^4$	6.201
M2	$k_r = 7.02 \cdot 10^{-11}$ $E_A = 8.87 \cdot 10^4$	$[m^3 \cdot mol^{-1} \cdot s^{-1}]$ $[J \cdot mol^{-1}]$	$[5.68-8.36] \cdot 10^{-11}$ $[0.68-1.08] \cdot 10^5$	2.757
M3	$k_r = 3.91 \cdot 10^{-7}$ $E_A = 1.22 \cdot 10^5$	$[s^{-1}]$ $[J \cdot mol^{-1}]$	$[2.81-5.01] \cdot 10^{-7}$ $[0.90-1.54] \cdot 10^5$	3.671

Table 4: Fitted model parameters, confidence intervals and lack-of-fit tests for the refined dataset. Data used to fit the models covers temperature and loading range of 100 – 145 °C and α : 0.1 – 0.45.

Model	Rate parameters	Units	Confidence intervals (95%)	T_{LOF}
M1	$k_r = 2.71 \cdot 10^{-11}$ $E_A = 1.38 \cdot 10^5$	$[m^3 \cdot mol^{-1} \cdot s^{-1}]$ $[J \cdot mol^{-1}]$	$[2.16-3.25] \cdot 10^{-11}$ $[1.06-1.69] \cdot 10^5$	0.309
M2	$k_r = 3.34 \cdot 10^{-11}$ $E_A = 1.39 \cdot 10^5$	$[m^3 \cdot mol^{-1} \cdot s^{-1}]$ $[J \cdot mol^{-1}]$	$[2.88-4.01] \cdot 10^{-11}$ $[1.14-1.64] \cdot 10^5$	0.175
M3	$k_r = 1.76 \cdot 10^{-7}$ $E_A = 1.58 \cdot 10^5$	$[s^{-1}]$ $[J \cdot mol^{-1}]$	$[1.42-2.10] \cdot 10^{-7}$ $[1.29-1.87] \cdot 10^5$	0.187

Table 3 shows that the lack-of-fit test parameter is larger than 1 for each model. This shows that the residuals of the models are significantly larger than can be explained by the pure experimental error and thus, the full dataset cannot be fitted appropriately. The contribution of experiments at higher temperatures and loadings to the SSE was significant, however, a clear trend was not observed. There were no replicates for the experiments at higher temperatures and loadings, so the pure experimental error was the same for both datasets.

Excluding the data at high temperatures (145 °C and above) improves the models ability to represent the experimental data significantly, as seen in

Table 4. When comparing these to the results in Table 3, the fitted activation energy is higher and the reaction rates lower for the total dataset, resulting in a higher temperature dependency of the reaction rate. It would be good to investigate how reproducible the degradation experiments at temperatures above 145 °C or with a loading of 0.5 are, to evaluate their experimental error. For now, we will focus on the results from the refined dataset.

Table 4 shows also that model 2 and 3 have a much better fit than the linear model (model 1). Because model 2 considers the consumption of MEA, the reaction rate coefficient is expected to be slightly larger than for model 1, as the concentration of MEA will decrease over time. The reaction rate coefficient for model three is several orders of magnitude higher because in this model, the reaction rate coefficient is only multiplied with the concentration of MEA-carbamate, instead of both the concentration of CO₂ and MEA, which is the case for the other models. In addition, the activation energy is higher for this model. Overall, model 2 has the best fit, but there is no significant difference between model 2 and 3.

In Figure 2, several of the datapoints are compared to the fitted results of model 2. The experimental data by

Davis et al. shows less degradation in comparison to the other experiments. Overall the model fits the experimental data adequately, with a relative standard deviation of 5.02% (6.29% and 5.15% for model 1 and 3 respectively).

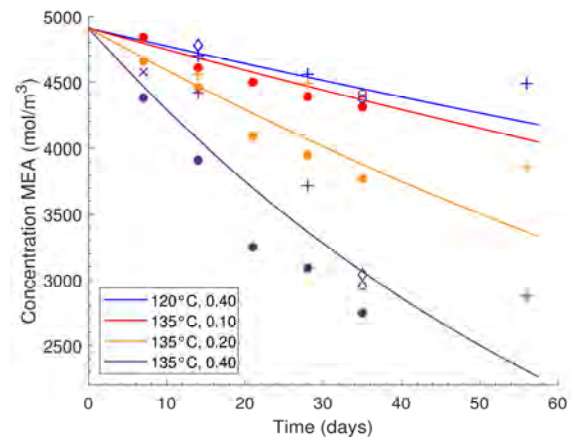


Figure 2: Model 2 results compared with experimental data. Markers indicate experiments from Grimstvedt (o), Davis (+), Fytianos (\diamond), Eide-Haugmo (\bullet), and Huang (x).

3.1 Compared model predictions

The degradation experiments can replicate operational conditions but are not necessarily comparable. The cylinders in the degradation experiments are closed off, so consumption of the solvent and CO₂ will influence concentrations and degradation rates. In a continuous capture plant there will be a constant supply of CO₂ from the flue gas and a make-up of degraded solvent, so the conditions in for example the reboiler will not change significantly.

Measurements at lower solvent concentrations are thus not representable, however, they can still be used, as they provide useful insight into the degradation mechanism. To evaluate and compare the predicted

degradation rates at continuous operation, the initial degradation rate is more interesting, because the initial conditions and concentrations of MEA and CO₂ are more representative of the actual process. The predicted degradation rates are given in Figure 3.

In comparison, the degradation models show similar trends with temperature at different loadings. Model 2, which had the best fit, predicts the most degradation. In comparison, the linear degradation model (model 1) predicts less degradation, especially at higher temperatures. This is because at higher temperatures, the concentration of MEA is reduced significantly and the degradation rate is also reduced over time.

As a result, the linear concentration slope of MEA is less steep and less degradation is predicted. The higher activation energy in model 3 also becomes apparent as the degradation rate increases more rapidly with temperature. The model by Léonard et al. ([4]) is conservative with respect to the models fitted in this study. With a loading of 0.4 and at a stripper temperature of 120 °C, the degradation rate predicted by model 2 is 47.5% higher than the degradation as predicted by the model of Léonard et al.. At the same conditions, model 2 also predicts 25.9% more degradation than model 1.

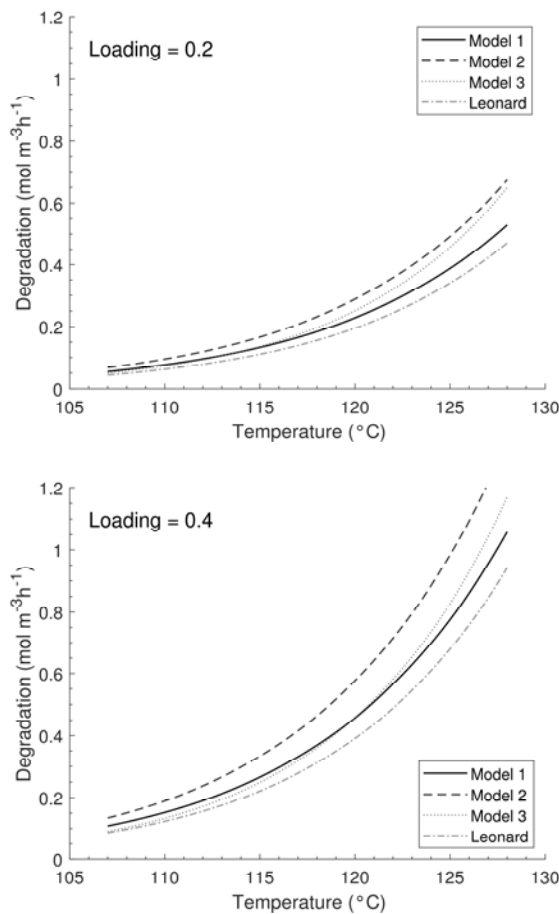


Figure 3: Predicted degradation rate due to carbamate polymerization for 30 wt-% MEA at a loading of 0.2 (above) and 0.4 (below). The kinetic model by Léonard et al. ([4]) is evaluated as a reference.

3.2 Joint confidence region

The marginal confidence intervals of the fitted parameters are relatively large. The correlation between the activation energy and the reaction rate coefficient at reference temperature was also significant for all models, but lowest for model 2 at 0.956. For this model, the approximate confidence region of 95% was determined and is given in Figure 4. From this figure, the strong correlation between the parameters is also apparent.

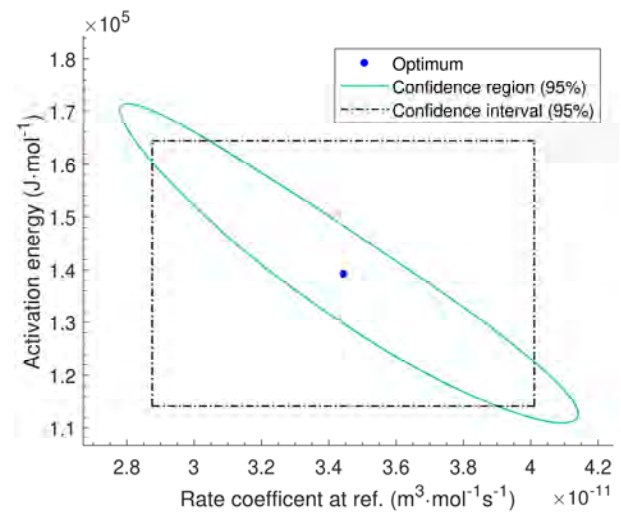


Figure 4: Marginal confidence interval and joint confidence region for the parameter estimates of model 2 on the refined dataset.

3.3 Residual plots

The residuals for model 2 are analysed in Figure 5. The errors appear to be randomly distributed as a function of the loading since no clear pattern can be observed. The temperature, on the other hand, is strongly correlated with the error. This also explains why the regression was more accurate for the refined dataset. There also appears to be a slight increase in the residuals when the experiments last longer. The effect, however, is more pronounced than in the case of temperature.

These trends indicate that the error is most likely not purely analytical and that fluctuations in experimental conditions play a role as well. These fluctuations could cause the reaction rate to deviate, resulting in larger errors in solvent concentration over time. It's thus recommended to investigate the cause and extent of these fluctuations.

Model 1 was found to underpredict the degradation at first, while overpredicting experiments with a longer duration. This shows that the model was unable to represent the non-linear degradation data, and explains the higher lack-of-fit parameter for the model.

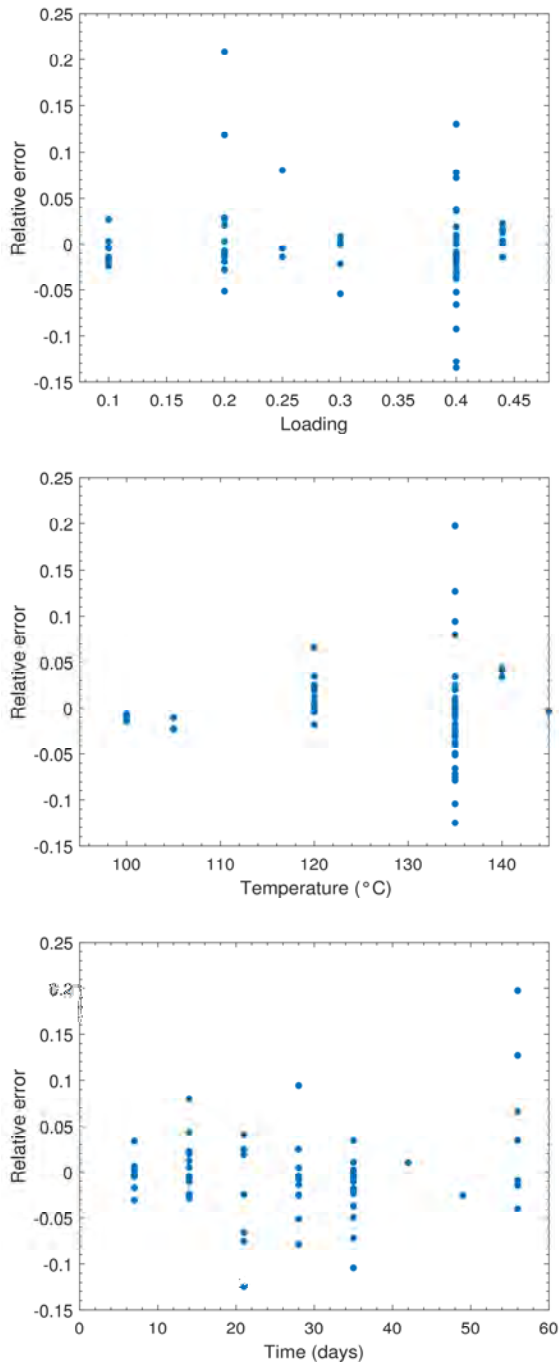


Figure 5: Relative error as a function of initial loading (top), temperature (middle), and experiment duration (bottom) for the parameter estimates of model 2 on the refined dataset.

4. Conclusion

To conclude, three models have successfully been used to evaluate and predict degradation through carbamate polymerization. Model 2, which takes into account the consumption of MEA in the rate equation, was able to explain the experimental data most accurately, with a relative standard deviation of 5.02%, compared to 6.29% and 5.15% for model 1 and 3 respectively. Model 2 predicts over 25.9% more carbamate polymerization at stripper conditions compared to model 1, the linear model, which do not take into account the concentration of MEA over time.

The use of the speciation model to determine the carbamate concentration, in Model 3, also showed promise. It would be interesting to investigate how this model behaves when the concentration of CO₂ and some of the major degradation products were also taken into account. Another recommendation is to perform more degradation experiments at increased temperatures and loadings to evaluate the experimental uncertainty.

Acknowledgements

This publication has been produced with support from the NCCS Centre, performed under the Norwegian research program Centres for Environment-friendly Energy Research (FME). The authors acknowledge the following partners for their contributions: Aker Solutions, ANSALDO Energia, CoorsTek Membrane Sciences, EMGS, Equinor, Gassco, KROHNE, Larvik Shipping, Norcem, Norwegian Oil and Gas, Quad Geometrics, Shell, TOTAL, and the Research Council of Norway (257579/E20).

References

- [1] F. Vega, A. Sanna, B. Navarrete, M. M. Maroto-Valer, and V. J. Cortés, 'Degradation of amine-based solvents in CO₂ capture process by chemical absorption', *Greenh. Gases Sci. Technol.*, vol. 4, no. 6, pp. 707–733, 2014, doi: <https://doi.org/10.1002/ghg.1446>.
- [2] C. Guedard, D. Picq, F. Launay, and P.-L. Carrette, 'Amine degradation in CO₂ capture. I. A review', *Int. J. Greenh. Gas Control*, vol. 10, pp. 244–270, Sep. 2012, doi: 10.1016/j.ijggc.2012.06.015.
- [3] I. Eide-Haugmo, 'Environmental impacts and aspects of absorbents used for CO₂ capture.', Norwegian University of Science and Technology, Trondheim, 2011.
- [4] G. Léonard, D. Toye, and G. Heyen, 'Experimental study and kinetic model of monoethanolamine oxidative and thermal degradation for post-combustion CO₂ capture', *Int. J. Greenh. Gas Control*, vol. 30, pp. 171–178, Nov. 2014, doi: 10.1016/j.ijggc.2014.09.014.
- [5] J. Davis and G. Rochelle, 'Thermal degradation of monoethanolamine at stripper conditions', *Energy Procedia*, vol. 1, no. 1, Art. no. 1, Feb. 2009, doi: 10.1016/j.egypro.2009.01.045.
- [6] H. Lepaumier, D. Picq, and P.-L. Carrette, 'New Amines for CO₂ Capture. I. Mechanisms of Amine Degradation

- in the Presence of CO₂', *Ind. Eng. Chem. Res.*, vol. 48, no. 20, Art. no. 20, Oct. 2009, doi: 10.1021/ie900472x.
- [7] E. F. da Silva *et al.*, 'Understanding 2-Ethanolamine Degradation in Postcombustion CO₂ Capture', *Ind. Eng. Chem. Res.*, vol. 51, no. 41, Art. no. 41, Oct. 2012, doi: 10.1021/ie300718a.
- [8] A. Grimstvedt, E. Falck da Silva, and K. A. Hoff, 'Thermal degradation of MEA, effect of temperature and CO₂ loading', SINTEF Materials and Chemistry, Trondheim, TCCS-7, 2013.
- [9] H. Lepaumier *et al.*, 'Comparison of MEA degradation in pilot-scale with lab-scale experiments', *Energy Procedia*, vol. 4, pp. 1652–1659, Jan. 2011, doi: 10.1016/j.egypro.2011.02.037.
- [10] S. Zhou, S. Wang, and C. Chen, 'Thermal Degradation of Monoethanolamine in CO₂ Capture with Acidic Impurities in Flue Gas', *Ind. Eng. Chem. Res.*, vol. 51, no. 6, Art. no. 6, Feb. 2012, doi: 10.1021/ie202214y.
- [11] Q. Huang *et al.*, 'Impact of Flue Gas Contaminants on Monoethanolamine Thermal Degradation', *Ind. Eng. Chem. Res.*, vol. 53, no. 2, pp. 553–563, Jan. 2014, doi: 10.1021/ie403426c.
- [12] G. Fytianos, S. Ucar, A. Grimstvedt, A. Hyldbakk, H. F. Svendsen, and H. K. Knuutila, 'Corrosion and degradation in MEA based post-combustion CO₂ capture', *Int. J. Greenh. Gas Control*, vol. 46, pp. 48–56, Mar. 2016, doi: 10.1016/j.ijggc.2015.12.028.

ELECTROCHEMICALLY ENHANCED DEPOSITION OF MINERALS FROM SYNTHETIC RESERVOIR BRINE

Laura Edvardsen*, Benjamin Udo Emmel, Mohammad Hossain Bhuiyan, Sigurd Wenner, Kamila Gawel, Malin Torsæter

SINTEF Industry, Trondheim, Norway

* Corresponding author e-mail: laura.edvardsen@sintef.no

Abstract

In this paper we ask the question whether or not electrochemically enhanced deposition of minerals can be utilized to repair leakage paths existing in cement plugs in wells. Electrical polarization of two electrodes may result in oxygen reduction and water electrolysis, where both processes change the local pH close to the two electrodes. The solution close to the anode is becoming acidic while close to the cathode it is becoming alkaline. Since solubility of many scaling minerals is pH dependent, precipitation of minerals on conductive surfaces can be induced by electrical polarization. We test whether cathodic polarization of conductive surfaces can be used to facilitate deposition of minerals from brines resembling reservoir fluids. As a model the reservoir formation water from the Gyda field was chosen. The electrochemically enhanced deposition at 23 and 120 °C from a synthetic Gyda brine was tested by polarizing at 5 V. The results show that cathodic polarization significantly enhanced precipitation of minerals from the synthetic Gyda brine.

Keywords: *electrochemical, mineralization, carbonates, well plugging*

1. Introduction

The Norwegian North Sea has an increasing amount of gas and oil fields that are depleted and shut down. These are candidates for storage of CO₂, and maybe in the future also hydrogen. The fields have a proven trapping and sealing capacity over geological timescales and might be suitable to guarantee safe storage of future renewable energy sources or CO₂. Until 2021, 24 gas and oil fields explored throughout the 1970 and 1980's have been shut down on the Norwegian continental margin [1]. Numerical studies and leakage incidents [2] indicate that wells are one of the major paths for gas (CH₄, CO₂, hydrogen) leakage [3].

At the end of the gas and oil production phase, wellbores are decommissioned *via* plugging and abandonment (P&A). To ensure that the P&A procedure seals the well and protects the surrounding (geological) environment against leakage in an eternal perspective, it is often necessary to remove long sections of steel pipes and create or repair annular barriers in the well. This is typically done by placing cement plugs inside the wells [4].

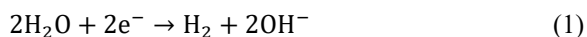
King et al. [5] compared statistics of well issues in the North Sea Norway, North Sea UK, and the Gulf of Mexico, and concluded that the major causes of well

integrity issues were leakage through tubings and cement. The most probable leakage pathways via abandoned wells have been described by Gasda et al. [6]. One of them is a damaged cement plug. The sealing ability of the plugs can be impaired by chemical or mechanical degradation processes which may lead to gas leakage.

In this paper we suggest an electrochemical method for repairing cement plug damages and eliminating leakage pathways through these plugs.

The concept relies on utilizing cathodic polarization of the casing close to the cement plug (e.g., Figure 1 b), filled with scaling fluid to induce precipitation of minerals within or above the leakage pathway in order to plug (repair) it. The concept of anodic polarization of steel pipes has already been proposed for P&A purposes and the method has been tested for facilitation of pipe removal via enhanced corrosion. In contrast to its anodic counterpart, cathodic polarization protects steel pipes from corrosion. It has been shown that cathodic polarization of conductive surfaces in contact with scaling solution can lead to enhanced precipitation of scaling minerals like e.g., calcium carbonate [7]. Precipitation of scaling minerals is enhanced at high pH condition. Such conditions are induced in the vicinity of

electrode during cathodic polarization due to production of hydroxide ions, see Eq (1) [8].



In this paper we test the concept of electrochemically enhanced deposition on a real scenario using formation water composition from the Gyda field sandstone reservoir. The electrochemically enhanced deposition at 23 and 120 °C from synthetic Gyda brine was tested. The reasons for choosing Gyda field for this case study is highlighted in Materials and Methods section.

2. Materials and method

2.1. Gyda case

The Gyda field (Figure 1.a) is in the southern part of the Norwegian North Sea, approximately 325 km southeast of Kristiansand. From 1990 to 2020 the field produced about 41 mill m³ oil from a sandstone reservoir in the Ula formation at a depth of ca. 4000 m. The field temperature is around 155 °C and a high pressure of ca. 590 bar is prevailing. The claystone's of the Mandal formation provide a ca. 30 m thick seal. Six exploration wells and 53 production wells perforate the oil field with a well density of 1.44/km². In the discovery wellbore 2/1-3, hydrocarbons occur in three different formations in a depth ranging from ca. 3000 to 4100 m: (i) in the Tor formation limestone, (ii) in the Ula formation sandstone and (iii) in the Bryne formation sandstone [1].

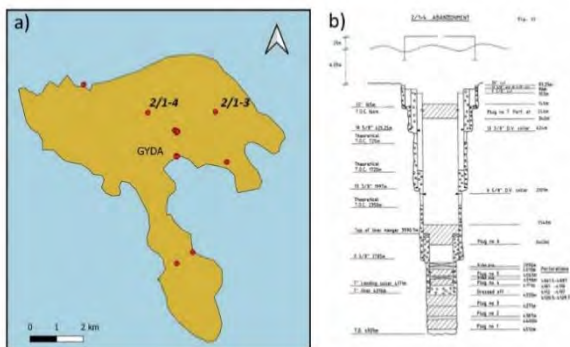


Figure 1. a) Extent of the Gyda field (brown area) with wellbore locations (red dots). b) Example of an abandonment plan for exploration well 2/1-4 [1] indicating the depth of the build plugs (grey shaded area).

Gyda formation water composition (ionic composition, pH) was calculated as an average from six formation water samples reported by Warren et al. [9].

2.2 Preparation of synthetic Gyda formation water

Synthetic Gyda formation water (brine) was made by mixing the salts listed in Table 1 with deionized water for at least 1 hour. The solution is a simplified version of

Gyda formation water reported in [9]. The initial solution is oversaturated at room temperature, thus some amount of salts remains precipitated.

Table 1. Ionic composition of synthetic and real Gyda formation water (fw) used for Phreeqc models. Salts (NaCl:130.57 g; MgCl₂·6H₂O: 17.65 g; KCl: 8.5 g CaCl₂·2H₂O: 97.42g; NaHCO₃: 0.6g; Na₂SO₄: 2.90 g and FeCl₃: 0.41 g) were mixed with deionized water to make up a total of 1 L solution.

	Synthetic Gyda fw	Real Gyda fw
Ion	Mass (g/l)	Mass (g/l)
Na ⁺	52.53	54.72
Mg ⁺	2.11	2.11
K ⁺	4.46	4.48
Ca ²⁺	26.56	26.51
Fe ³⁺	0.14	0.14
CO ₃ ²⁻	0.60	0.43
SO ₄ ²⁻	1.89	1.96
Cl ⁻	136.82	121.57
Ba ²⁺	-	0.32
Sr ²⁺	-	0.85

2.3 Geochemical modelling of pH and temperature changes

It is expected that local pH changes close to electrodes (polarized conductive surfaces) will lead to acceleration or inhibition of salt precipitation. To predict the impact of pH changes on the geochemical equilibrium between the Gyda brine and the precipitate, we modelled mineral dissolution/precipitation for different pH values and temperatures for the Gyda formation water with the composition described elsewhere [9]. The pressure, temperature and pH dependence of mineral reactions calculations have been done using the software Phreeqc with the *wateq4f.dat* data-base [10].

2.4 Electrochemical deposition

Electrochemical deposition was induced by applying a potential between two graphite electrodes immersed in an electrolyte (synthetic Gyda formation water). Graphite was chosen over metal to avoid corrosion of anode associated with the release of iron. Graphite tubes were used as cathode, anode and reference, and the potential between cathode and anode was set to 5 V. Experiments were conducted at 23 and 120 °C and the electrodes were polarized for 15 minutes. After the exposure, the electrodes were quickly flushed with deionized water to remove excess of brine and prevent excessive crystallization of the remaining salt during the drying process. Scanning electron microscopy (SEM) was used to investigate the topography of the electrode surfaces, and powder X-ray diffraction (XRD) was used to find the

mineralogical composition of the deposit. For SEM imaging of the surfaces, a Hitachi S3400 N thermal emission microscope was used with an acceleration voltage equal to 15 kV.

3. Results and discussions

3.1 Geochemical modelling

At first, we modelled the pH values that should be expected at different pressure/temperature conditions using the measured pH of the synthetic Gyda formation water (pH of 5.2 which is in line with the pH reported for Gyda brine samples [9]) as the initial value. The results in Figure 2 show the pH decrease from 5.2 to 4.7 with increasing temperature and pressure. The resulting data was further used as an input for geochemical modelling (Figure 3).

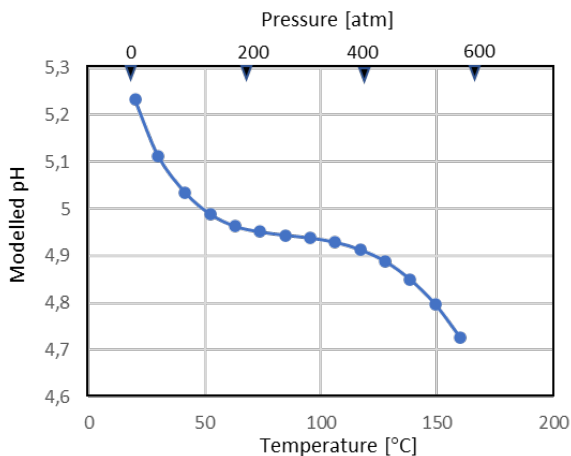


Figure 2. Modelled pH values for the Gyda formation water at different pressure/temperature conditions using Phreeqc. The initial conditions used were pH value of 5.2 at temperature of 23 °C and 1 atm pressure.

Figure 3 shows modelled saturation indices (SI) for different model assumptions:

- (i) Pressure/temperature and pH conditions at reservoir depth for the real and synthetic Gyda formation waters (T=154 °C; P=582 atm)
- (ii) Pressure/temperature and pH conditions at laboratory conditions for the real and synthetic Gyda formation water (T=23 °C; P=1 atm)

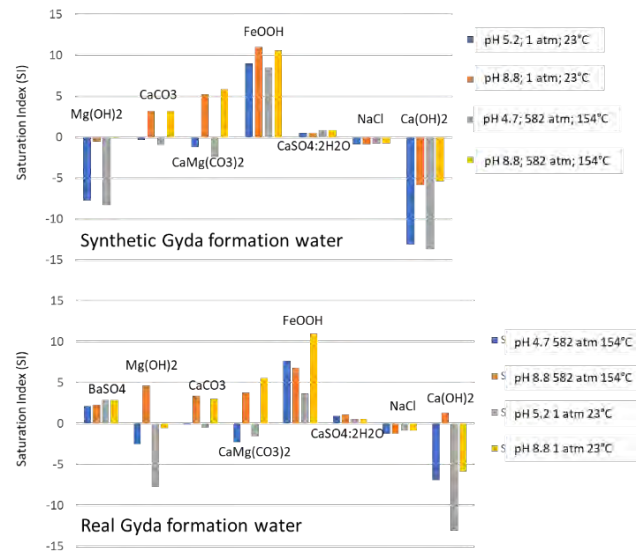


Figure 3. Saturation indices (SI) modelled for mineral phases at different pressure/temperature/pH conditions using the synthetic Gyda formation water (top) and real Gyda formation water (bottom) ionic composition.

A SI < 0 means the mineral phase is in the solution, and a SI > 0 means the solution is oversaturated and the phase will precipitate. From Figure 3 it is seen that the iron (Fe³⁺) bearing phase (goethite) reach the highest saturation for all model assumptions. The main difference between synthetic and real Gyda formation water modelling was the presence of BaSO₄ in the real composition. Also, for the real composition, Ca(OH)₂ and Mg(OH)₂ have SI > 0 at pH 8.8, 582 atm and 154 °C, which is not the case for the synthetic composition.

Figure 4 shows modelled saturation indices at different pH values under laboratory conditions (room temperature and pressure) for the synthetic and real Gyda formation water. Only the Ca-bearing mineral phases and sodium chloride (NaCl) are presented.

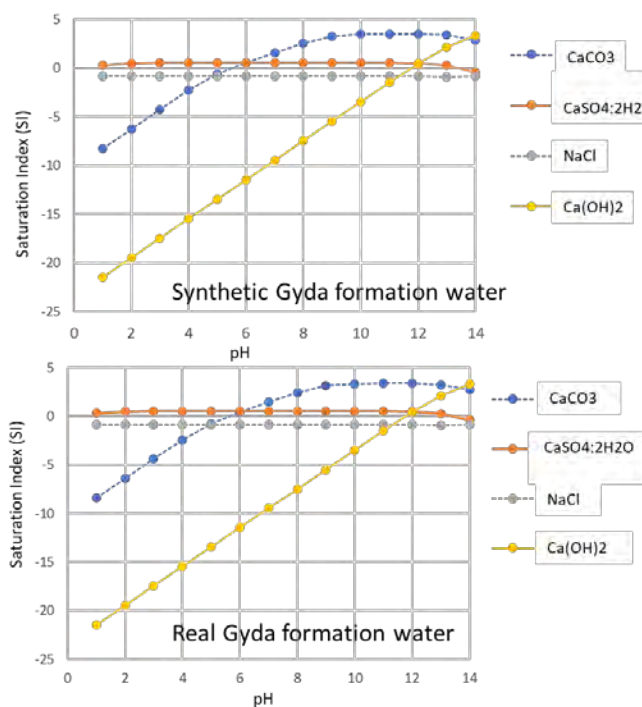


Figure 4. Modelled saturation indices (SI) for Ca-bearing mineral phases and NaCl at 23 °C, 1 atm for different pH values, using the synthetic Gyda formation water (top) and real Gyda formation water (bottom) ionic composition.

NaCl and gypsum ($\text{CaSO}_4 \cdot 4\text{H}_2\text{O}$) are relatively insensitive to pH variations. While NaCl had a SI lower than 0 for all pH values and would stay dissolved, $\text{CaSO}_4 \cdot 4\text{H}_2\text{O}$ precipitate at almost all pH values except from pH 14. At alkaline conditions ($\text{pH} > 12$) portlandite (Ca(OH)_2) and calcium carbonate (CaCO_3) were shown to precipitate. If the pH close to the electrode is less than 12 but greater than 6, only CaCO_3 has a potential to precipitate.

3.2 Electrochemical deposition on graphite tubes

Figure 5 compares the surfaces of cathode, anode, and reference sample after only 15 minutes of polarization (5 V) in synthetic Gyda brine at different temperatures. The surfaces of the two cathode tubes were covered with a thick, white layer of minerals, while on the anode only a thin layer of precipitate was present. The precipitate on the anode occurred because the electrode stayed for 2 minutes in the brine solution after the potential was switched off, before the electrode was dismantled from the experimental setup and flushed with deionized water. The reference sample had a slightly thicker layer of precipitate than the anode. The large difference in amount of precipitate between the cathode and the reference sample indicates significant impact of electrical polarization on mineral deposition. It is thus suggested that the pH close to the cathode is larger than 6 at the experimental conditions (see Figure 4) as it accelerates precipitation. The local pH close to the cathode increases

due to reduction of hydrogen and generation of hydroxide ions [11, 12]. On the contrary, the local pH close to the anode was acidic due to the production of hydrogen ions, which from Figure 4 is seen to inhibit precipitation of scaling minerals.

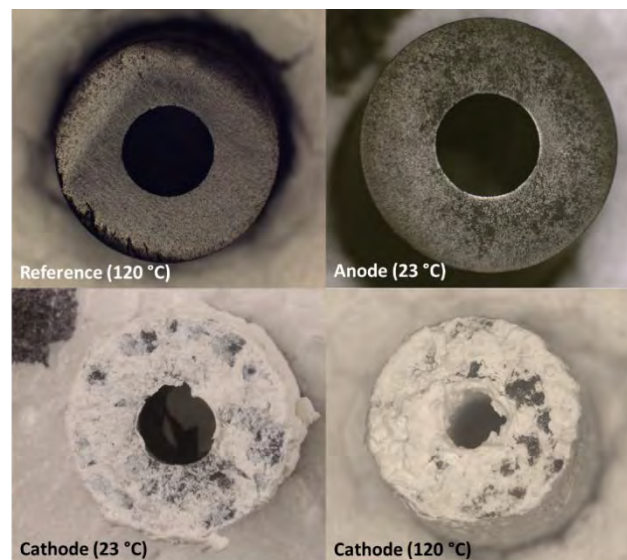


Figure 5. Photographs of graphite electrodes after 15 minutes of polarization at 5 V in synthetic Gyda formation water at 23 and 120 °C.

From Figure 5 it is also seen that an increase in temperature resulted in an increase of precipitate layer thickness on the cathode surface. This suggests that the temperature can further accelerate deposition processes.

Figure 6 presents SEM images showing the topography of precipitate deposited on the cathode surfaces after 15 minutes of polarization. Thick, partially cracked layers of precipitated material are present on both cathode surfaces.

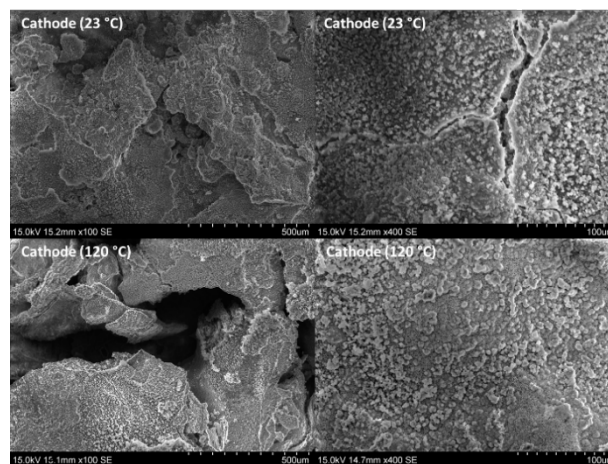


Figure 6. SEM images presenting topography of scale deposited at graphite surfaces after 15 minutes of polarization at 5 V in synthetic Gyda formation water.

X-ray powder diffraction patterns collected for the surface precipitates are presented in Figure 7. The patterns indicate the presence of peaks that are characteristic for portlandite (Ca(OH)₂), halite (NaCl) and calcite (CaCO₃). The major components found on the cathode surface were portlandite and halite, while calcite was only detected in relatively small quantities.

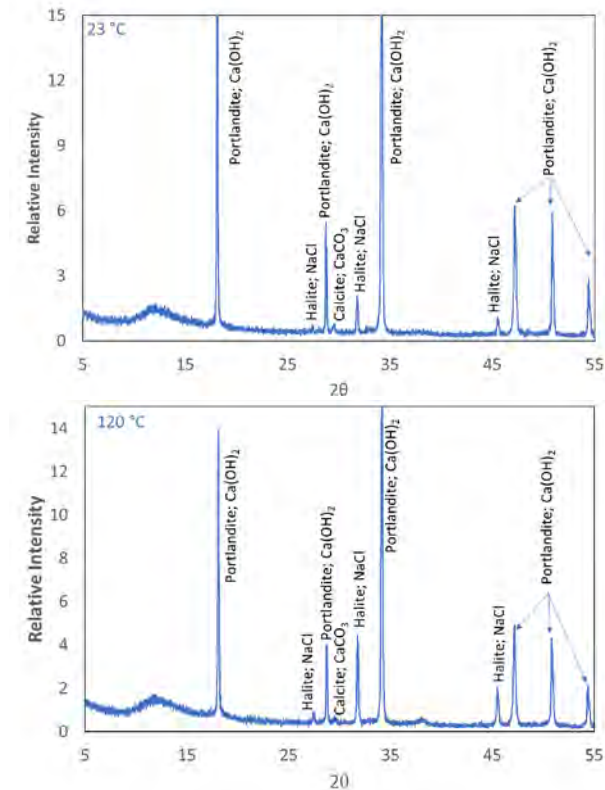
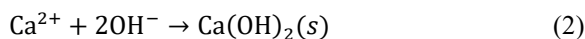
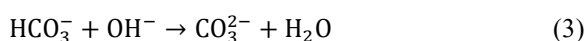


Figure 7. XRD patterns of material deposited at the surface of cathode polarized at 5 V at 23 and 120 °C. The peak characteristics for the different materials are ascribed.

Hydroxide ions are generated at the cathode, which increased the pH and promotes precipitation of portlandite through the following reaction [13]:



where the free Ca²⁺ ions come from dissolved CaCl₂ (see Table 1). The generation of hydroxide ions at the cathode also leads to an increased carbonate ion (CO₃²⁻) concentration [14]. This promotes precipitation of calcite according to Eq (3) and (4),



where the bicarbonate ions (HCO₃⁻) originates from NaHCO₃. The scaling solution is only slightly undersaturated in respect to NaCl. It is thus likely that some small amounts of NaCl will co-precipitate along with portlandite due to e.g., locally changed

concentration of sodium and chloride ions. Precipitation of calcite is known to increase with increasing temperature, but the effect of temperature is not as significant as the effect of pH [15]. The solubility of portlandite decrease with increasing temperature [16, 17] which explains the larger amount of precipitate at 120 °C compared to 23 °C. The presence of portlandite as the main mineral precipitated on the electrode surface together with the modelling results (Figure 4) suggest that the pH closest to the cathode surface was higher than 12.

3.3 Utilization of electrochemical deposition

Electrochemically enhanced mineral precipitation can be a method useful for future P&A, as well as maintenance of well integrity, to repairing plug damages and eliminate leakage pathways through cement plugs. However, utilization of electrochemical deposition in the context of CO₂ storage is highly dependent on the formation fluid. Brines needs to contain scaling ions like e.g., Ca²⁺, Mg²⁺, and carbonate and sulfate ions, which are common ions present in North Sea formation waters [9].

In this study, cathodic polarization of a graphite surface immersed in synthetic Gyda brine enhanced precipitation of portlandite. Portlandite is the main hydration product of Portland cement- a cement typically used for plugging of wells. It is expected that in contact with CO₂ brine the electrochemically precipitated portlandite could react to form calcium carbonate in a similar manner as portlandite present in cement material does [18, 19]. The reaction of portlandite with CO₂ is associated with volume increase which may additionally contribute to clogging of leakage pathways. A prerequisite to perform electrochemical clogging is good electrochemical communication between the cathode and the counter electrode. Achieving such a communication at downhole conditions may be the biggest challenge for the concept to be widely applicable.

4. Conclusions

In this paper we showed that cathodic and anodic polarization of conductive surfaces can be used to accelerate or inhibited scale deposition from reservoir brines rich in calcium like e.g., Gyda reservoir brine. Cathodic polarization at 5 V resulted in efficient precipitation of minerals from Gyda brine. The main minerals that precipitated were portlandite and smaller amounts of calcium carbonate. Increasing the temperature led to an increase in the amount of precipitate at the cathode surface. The acceleration and inhibition of scaling were driven by changes in the pH close to the electrode surfaces. Geochemical modelling

suggests that a pH value achieved at the electrode surface upon polarization at 5 V in the Gyda brine was above 12.

Acknowledgements

The authors gratefully acknowledge the financial support from The Norwegian Research Council in the form of grant number 285568 "Well fossilization for P&A" and from the strategic SINTEF Industry project number 102021203 "Electrophoretic cleaning and friction reduction for applications in drilling and well construction".

References

1. Factpages Norwegian Petroleum Directorate - Gyda. <https://factpages.npd.no/en/field/PageView/ShutDown/43492>.
2. Vielstädte, L., et al., *Quantification of methane emissions at abandoned gas wells in the Central North Sea*. Marine and Petroleum Geology, 2015. **68**: p. 848-860.
3. Alcalde, J., et al., *Estimating geological CO₂ storage security to deliver on climate mitigation*. Nature communications, 2018. **9**(1): p. 1-13.
4. Vrålstad, T., et al., *Plug & abandonment of offshore wells: Ensuring long-term well integrity and cost-efficiency*. Journal of Petroleum Science and Engineering, 2019. **173**: p. 478-491.
5. King, G.E. and D.E. King, *Environmental Risk Arising From Well-Construction Failure--Differences Between Barrier and Well Failure, and Estimates of Failure Frequency Across Common Well Types, Locations, and Well Age*. SPE Production & Operations, 2013. **28**(04): p. 323-344.
6. Gasda, S.E., S. Bachu, and M.A. Celia, *Spatial characterization of the location of potentially leaky wells penetrating a deep saline aquifer in a mature sedimentary basin*. Environmental geology, 2004. **46**(6-7): p. 707-720.
7. Edvardsen, L., et al., *Electrochemical enhancement and inhibition of calcium carbonate deposition*. Journal of Environmental Chemical Engineering, 2020. **8**(5): p. 104239.
8. Sheng, K., et al., *Formation and Inhibition of Calcium Carbonate Crystals under Cathodic Polarization Conditions*. Crystals, 2020. **10**(4): p. 275.
9. Warren, E.A., C.P. Smalley, and R. Howarth, *Part 4: compositional variations of North Sea formation waters*. Geological Society, London, Memoirs, 1994. **15**(1): p. 119-208.
10. Parkhurst, D.L. and C. Appelo, *Description of input and examples for PHREEQC version 3: a computer program for speciation, batch-reaction, one-dimensional transport, and inverse geochemical calculations*. 2013, US Geological Survey.
11. Persat, A., M.E. Suss, and J.G. Santiago, *Basic principles of electrolyte chemistry for microfluidic electrokinetics. Part II: Coupling between ion mobility, electrolysis, and acid-base equilibria*. Lab on a Chip, 2009. **9**(17): p. 2454-2469.
12. Kuhn, A. and C. Chan, *pH changes at near-electrode surfaces*. Journal of Applied Electrochemistry, 1983. **13**(2): p. 189-207.
13. Ellis, L.D., et al., *Toward electrochemical synthesis of cement—An electrolyzer-based process for decarbonating CaCO₃ while producing useful gas streams*. Proceedings of the National Academy of Sciences, 2020. **117**(23): p. 12584-12591.
14. Chavez Panduro, E.A., et al., *Real time 3D observations of Portland Cement Carbonation at CO₂ storage conditions*. Environmental science & technology, 2020. **54**(13): p. 8323-8332.
15. MacAdam, J. and S.A. Parsons, *Calcium carbonate scale formation and control*. Re/Views in Environmental Science & Bio/Technology, 2004. **3**(2): p. 159-169.
16. Justnes, H., et al., *Transformation kinetics of burnt lime in freshwater and sea water*. Materials, 2020. **13**(21): p. 4926.
17. Xinyu Zhang, F.P.G., K.L. Scrivener, *Reaction kinetics of dolomite and portlandite*. Cement and Concrete Research, 2014. **66**: p. 11-18.
18. Tiong, M., R. Gholami, and M.E. Rahman, *Cement degradation in CO₂ storage sites: a review on potential applications of nanomaterials*. Journal of Petroleum Exploration and Production Technology, 2019. **9**(1): p. 329-340.
19. Kutchko, B.G., et al., *Degradation of well cement by CO₂ under geologic sequestration conditions*. Environmental science & technology, 2007. **41**(13): p. 4787-4792.

RATE BASED MODEL AND TECHNO-ECONOMIC ASSESSMENT OF A POST-COMBUSTION CO₂ CAPTURE UNIT OPERATING WITH POTASSIUM LYSINATE FOR NGCC DECARBONISATION

Antonio Conversano^{1,2,*}, Manuele Gatti^{1,2}

¹ Dipartimento di Energia, Politecnico di Milano, via Lambruschini 4, 20156 Milano, Italia

² LEAP-Laboratorio Energia e Ambiente Piacenza, Via Nino Bixio 27/C, 29121 Piacenza (PC)

* Corresponding author e-mail: antonio.conversano@polimi.it

Abstract

The present work reports the results of process design and techno-economic assessment carried out on a CO₂ capture unit operating with an aqueous solution of potassium Lysinate (LysK) at 43.7%_{w/w}, in post-combustion arrangement for natural gas combined cycle (NGCC) decarbonisation. A dedicated rate-based model of the absorption unit has been defined and programmed in Matlab[®]. The techno-economic assessment of the reference natural gas combined cycle (frame-F gas turbine technology, 829.9 MWe without capture unit) coupled with a CO₂ capture unit with the low-maturity LysK-based solvent has been carried out in order to estimate the energy penalty due to capture, the specific primary energy consumption per unit of CO₂ avoided as well as economic indicators, such as overall capital costs, cost of electricity and the cost of CO₂ avoided. The results are compared against a case study envisaging the same reference NGCC coupled with a commercial post-combustion capture solution working with 30%_{w/w} aqueous monoethanolamine (MEA).

Keywords: amino acid salts, post-combustion capture, natural gas combined cycle (NGCC), potassium lysinate

1. Introduction

Greenhouse gas (GHG) emissions associated to human activity have reached 49 GtCO₂-eq/y in 2015[1], with 36 GtCO₂-eq/y CO₂ from fossil fuel combustion and industrial processes remaining the main responsible for global warming[1]. Within this context, a leading position is covered by the power industry, whose amount has reached 13.6 GtCO₂ in 2017[2] caused by the elevated energy demand and the still intensive use of fossil fuels in electricity and heat generation. In order to reduce the carbon emissions associated to power production from natural gas combined cycles (NGCC), solvent absorption processes in post-combustion arrangement are usually identified as the most mature and reference technology. In fact, amine-based solutions are considered effective for CCS (Carbon Capture and Storage) applications, and the specific case of aqueous MEA (monoethanolamine and its possible water-based solutions) has been taken as a benchmark in several European initiatives such as CaESAR [3] and CESAR [4] projects, while analogous amine-based solvents are applied in commercial scale CCUS facilities (e.g. Boundary Dam).

However, Monoethanolamine scrubbing shows many drawbacks that include high-energy consumption for regeneration, limited CO₂ loading capacity, equipment corrosion, generation of toxic compounds and amine volatility, hence leaving the field to a great margin of improvements. New studies on alternative solvents are, therefore, ongoing to answer the still open items on absorption technologies, moving towards the identification of more effective, energy saving and

greener solvents for a low-carbon energy production industry. Among these, recent research activities carried out from University of Texas consider piperazine (PZ) as a new potential baseline for amine-based carbon dioxide absorption, due to its higher operating temperature range and expected lower specific thermal duty [kJ/kg of CO₂ captured] for regeneration. The direct major effect of this newly identified secondary amine-based solvent is to allow stripper operations at higher pressure, with a sensitive reduction of the energy requirement for the CO₂ compression unit. In the field of amine-free solvents, amino acid salts (AAS) solutions are one of the most recent options under investigation. They are considered environmental friendly and, some of their formulations demonstrate fast reaction kinetics, lower regeneration energy and good CO₂ loading capacity; moreover, they are non-volatile and stable to oxidative degradation.

Despite their advantages, little knowledge on AAS absorption is available, as a consequence of limited experimental data (e.g.: heat capacity, vapor-liquid equilibria, heat of reaction, etc.), scarce pilot plant campaigns data and lack of comprehensive process engineering studies. With these regards, a first attempt at considering amino acids for CO₂ absorption has already been proposed in Decab, Decab Plus and Casper processes [5], however a limited range of solvents has been analyzed. Moreover, they envisage solid precipitation with a significant complication of the contacting equipment, which has discouraged technology spreading and application at industrial level.

For the above-mentioned reasons, a thorough understanding of the real potential of AAS-based non-precipitating solutions still requires further evaluations, and it has inspired the present research.

The final goal of this work is to assess the viability of non-precipitating AAS solutions applied to CO₂ absorption systems (DCC + absorber + stripper + heat exchanger network + CO₂ compression unit) treating post combustion gases from a natural gas combined cycle (NGCC, 829.9 MWe w/o capture).

Due to the high cost share of the absorber on the overall investment cost of a post-combustion unit, a proper design and sizing of this column is required ahead of costing. For this reason, the first step of this investigation consists in the definition of a rate-based absorber model developed in Matlab[®] with in-house codes. Moreover, the study is finalized by proposing a very first comprehensive techno-economic assessment on AAS based-post combustion unit coupled with NGCC, to be compared against the results of dedicated techno-economic assessments on MEA and other solvents within a consistent and comparable framework.

The target AAS molecule is potassium lysinate (LysK) at 43.7%w/w. The solution has been identified based on literature reviews and dedicated experimental tests carried out during previous works [6], [7].

The technical baseline for the study is be the European best practice guidelines for assessment of CO₂ capture technology (released by the European Benchmarking Task Force-EBTF), which makes reference to a natural gas fired power plant of 829.9 MWe_{el} without capture and outlines the performance of the same NGCC coupled with a CO₂ capture unit operating with 30%_{w/w} monoethanolamine solution.

2. Context, Approach and Methodology

In order to identify suitable alternative solvents for post combustion CO₂ capture, a bibliographic review has been run, taking into account relevant solvent properties such as operating temperatures and pressure, physical and chemical quantities (viscosity, solubility, etc.), absorption capacity and enthalpy of reaction with CO₂. The review has highlighted that amino acid salts constitute a solvent family of interest for CCS compared to traditional molecules: AAS-solutions envisage chemical reaction (chemical absorption process), they can reach high CO₂ loading capacity, fast reaction rates, and they may require less regeneration energy with reference to commercial amines. Besides, these solvents are biodegradable and environmental friendly, they present low volatility and ecotoxicity, stability against oxidation, negligible corrosion effects; hence, they look appealing in the perspective of industrial scale applications [8].

From a preliminary literature review [9]–[11], lysine-based salts (e.g.: LysK) stand out among the most noteworthy molecules for further analysis. In a recommended concentration range of 3.5-4.5 m, LysK exhibits capacities in line with a 7m MEA without

showing precipitation. Reference values are 2.66 mol_{CO₂}/kg_{LysK Solution} for a 3.5 m solution of lysinate[10] compared to 2.64 mol_{CO₂}/kg_{MEA Solution} for a 7 m solution of MEA [10] (at 297K and partial pressure of CO₂ equal to 9 kPa). Overall, the few data available from the literature on the enthalpy of absorption of aqueous LysK seems to be in line with the MEA benchmark, meanwhile higher reaction kinetics has been recorded for LyK, with consequent potential reduction of the absorber height, packing volume and costs.

In spite of their potential, no complete and comprehensive techno-economic assessment on AAS applications to post-combustion CO₂ capture analyzing both solvent effectiveness and process engineering repercussions is available. The workflow followed by the authors aims at overcoming the state-of-the-art by filling the aforementioned literature gaps:

1. Experimental tests previously run [6], [7] have been produced to assess the performance of the amino acids selected from the literature review via an initial experimental screening at Sotacarbo research campus;
2. LysK solutions have shown the highest performance. CO₂ absorption capacity data have been employed to define a target concentration of LysK aqueous solution (i.e., 43.7%_{w/w}) which guarantees the same capacity of the reference 30%_{w/w} (7m) MEA;
3. A suitable thermodynamic model based on Deshmukh and Mather approach has been reproduced for the MEA/CO₂/H₂O. The same approach has been followed in order to describe vapour-liquid equilibria and CO₂ solubility of the LysK/CO₂/H₂O system;
4. A dedicated rate-based model and preliminary design of the absorber operating with aqueous LysK has been defined via in-house coding developed in Matlab;
5. Based on the newly defined thermodynamic model, the regeneration energy for CO₂ rich LysK solutions has been estimated for the very first time, adopting a well-established literature approach [13], [14];
6. Preliminary design of the CO₂ capture unit including direct contact cooler, absorber, stripper, heat exchanger network and CO₂ capture unit has been carried out;
7. Evaluation of the solvent regeneration duty and energy penalty over the combined cycle have been necessary for a preliminary techno-economic assessment of the investigated system. Therefore, suitable energy and economic indicators such as the specific primary energy consumption per unit of CO₂ avoided (SPECCA), cost of electricity (COE) and cost of CO₂ avoided (CCA) have been calculated for LysK-based absorption and compared against the outcomes of MEA[3] scrubbing. The three techno-economic assessments provide a quantitative overview on the viability of AAS solutions for CO₂ capture from power plants.

This article presents the key outcome of steps 4 to 7.

3. Material and Methods

3.1 Thermodynamic model

During the research activities, the MEA/CO₂/H₂O system has been modelled according to Deshmukh-Mather formulation and following the framework of Weiland et al.[15]. The MEA model has set the ground for LysK analysis, it has been calibrated with MEA experimental data from Aronu et al.[16], and validated against MEA experimental results from Li and Shen[17].

The thermodynamic framework established from the MEA case has been transferred to describe the LysK system, introducing the following methodology:

- Given the scarce amount of vapor-liquid equilibrium data, the most suitable data-set (41.2%w/w LysK solution) has been selected from Shen et al.[18] to calibrate the model with experimental points from tests that are as close as possible to the identified LysK concentration (43.7w/w LysK solution);
- A Kent-Eisenberg-like approach has been used, enhancing Kent-Eisenberg model with Debye-Hückel activity coefficients in order to provide a synthetic data-set for LysK-Deshmukh-Mather model to be developed in the next step. The enhanced Kent-Eisenberg is able to mathematically fit Shen's experimental data, simultaneously estimating the coefficients of unknown equilibrium constants;
- Exploiting the estimation of the equilibrium constants and an extended pseudo data-set (i.e.: synthetic data) produced from Kent-Eisenberg after Shen's data fitting, a LysK Deshmukh-Mather model has been developed. Both Kent-Eisenberg and Deshmukh-Mather models have been extended to loading values lower than 0.8. Deshmukh-Mather can be used to evaluate vapor-liquid equilibria for the targeted 43.7%w/w LysK solution.

The Deshmukh-Mather model for LysK can be considered predictive and it can be used to evaluate the vapor-liquid equilibria for the selected aqueous solution concentration. Thus, the here mentioned thermodynamic model has been integrated in a proprietary rate-based model to design the absorber column working with 43.7%_{w/w} aqueous LysK.

Beside playing a key role in the design of absorption/stripping units, the thermodynamic model has been relevant to estimate the solvent regeneration duty required from the stripping section. In fact, the solvent regeneration duty is composed of 3 contributions: enthalpy of vaporization, sensible heat and heat of absorption; the Deshmukh-Mather and Van't Hoff equation have been adopted to investigate the contribution provided by the heat of reaction. More details on the thermodynamic model can be found in the literature produced by the authors[19].

3.2 Rate-based model

Rate-based models for MEA and LysK absorption columns have been developed in Matlab[®] and are important to draw suitable techno-economic evaluations of the capture technology. Validation of the rate-based model has been carried out applying the model to

absorption processes working with aqueous MEA at pilot scale in order to match the experimental outcomes in terms of CO₂ molar fraction in the gas phase, solvent loading as well as solvent and gas temperature profiles.

The validated absorber rate-based model evaluates mass and energy balance of the absorption unit and is inspired by the extensive literature consulted during the workflow [20]–[27]. The adopted approach follows the here-reported steps:

- A model representative of CO₂ and water mass transfer in a gas-liquid counterflow contacting reactor has been developed. The model benefits from Deshmukh-Mather thermodynamic function representative of vapour-liquid equilibria. The rate-based model runs a step-wise calculation of the heat and mass transfer envisaging chemical reaction according to the two-film theory approach;
- The model has been developed both for MEA and LysK absorption systems;
- To validate the approach, pilot plant literature data representative of a CO₂ absorption process with MEA have been reproduced in case of random and structured packing. The validation process has consisted in adapting the column's model to reproduce selected pilot set-ups; specifically, experimental data from Tontiwachwuthikul et al. [21] have been used to assess the simulation results for an absorber operating with random packing, meanwhile test results from Aroonwilas and co-workers [28] have been employed in case structured packing is required.
- A particular point of relevance is that the response of the model with MEA to replicate pilot plant data is based on purely theoretical literature mass and energy transfer correlation (Onda et al., Bravo-Rocha), hence no corrective coefficients have been used (i.e.: IAF-interfacial area factor = 1).

In the present work, a rate-based model has been developed in Matlab[®] using the two-film theory, and solving energy and mass balance drawn over the infinitesimal control volume reported in Figure 1. The system of differential equation has been solved by implementing a finite difference forward Euler approach.

Design choices and encompassed assumptions are the following:

- the chemical reaction occurs only in the liquid phase, and the bulk is at equilibrium;
- the absorption column is an adiabatic vessel;
- gas/liquid temperature at the interface is equal to the temperature in the liquid bulk;
- Axial dispersion is not accounted for;
- heat and mass transfer interfacial surface areas are equal.

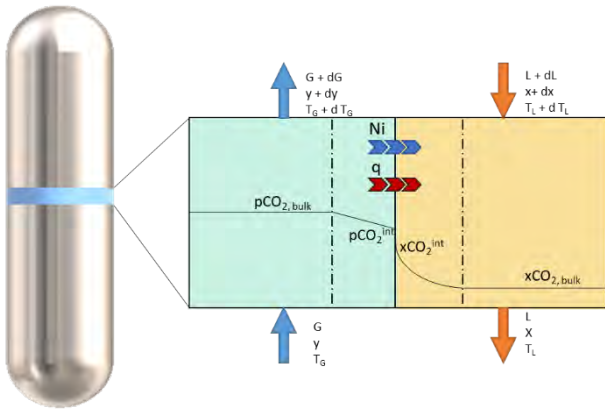


Figure 1: infinitesimal element considered to draw energy and mass balance.

3.3 Conceptual process design

The overall CO₂ conventional capture process reported in Figure 2 has been considered for a complete performance assessment: the full-scale absorption unit treating flue gas from the EBTF-NGCC combined cycle has been designed proposing two rate-based models for the aforementioned cases such as 30%w/w MEA and 43.7%w/w LysK scrubbing. The two columns have been sized and compared to evaluate eventual LysK benefits (e.g: lower required packing volume) with respect to MEA. The estimation of the absorber packing volume has to be carried out in comparative and not absolute terms as no interfacial area factors have been calibrated against pilot-plant data to support the design. In order to investigate the effect of the most relevant operating conditions, a sensitivity analysis has been run over the LysK CO₂ absorption rate-based model. More specifically, the height of the vessel has been calculated as a function of liquid-to-gas ratio (L/G) and lean loading. Reduced column heights which result into lower investment cost for the capture unit have been recorded for low values of lean loading and high L/G, which favor higher driving force. However, lower liquid-to-gas ratios imply savings in terms of circulating solvent (i.e.: lower energy penalty for pumping and regeneration). For this reason, selected L/G and loading operating window have been identified with an iterative approach, preserving an absorber packed volume equivalent to the MEA case and minimizing the reboiler duty.

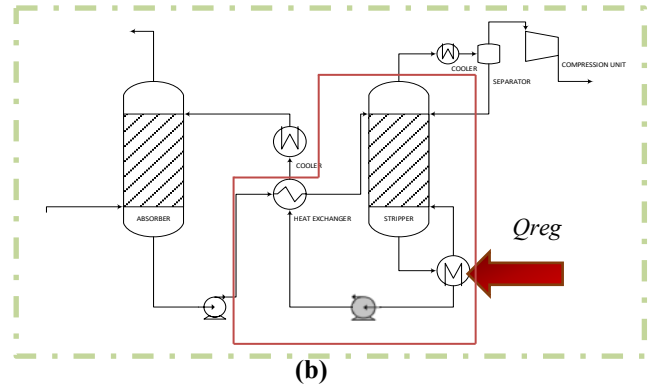
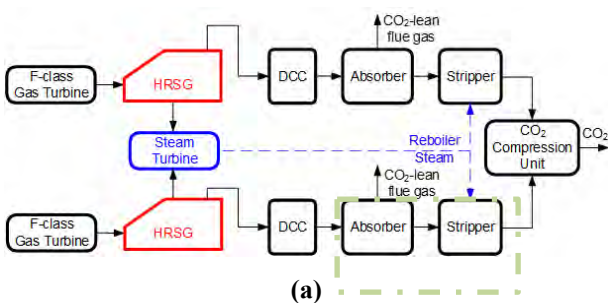


Figure 2: (a) simplified block flow diagram of the NGCC+CO₂ capture unit. The absorption and stripping units are highlighted with a dashed green square; (b) focus on the CO₂ absorption/stripping system.

4. Results and discussion

The results of the absorber unit (2 trains) design for LysK and MEA cases are reported in Table 1.

Table 1: Design of the LysK vs. MEA CO₂ capture unit.

	MEA-EBTF	LysK-Optimized	Unit
SET-UP	Power plant size (no CCS)	829.9	829.9
	Flue Gas Flowrate per train	665	665
	Flue Gas Temperature	48.7	48.7
	Flue Gas Pressure	1.06	1.06
	Absorber Packing	Mellapak 250Y	Mellapak 250Y
	Absorber Area	242.37	252.0
	CO ₂ in Flue Gas	4.02	4.02
	Solvent concentration	30	43.7
	CO ₂ capture rate	90	90
	L/G	1.5	1.4
RESULTS	Absorber Packed Height	20.4	19.5
	Packing volume	4944	4914
	Reboiler Duty	3.96	4.58

A performance analysis of the NGCC power plant coupled with the investigated capture systems working with LysK has been carried out and compared against the MEA benchmark. Results are reported in Table 2 and highlight a SPECCA value for LysK based absorption,

which is ~15% higher than the MEA reference case. This energy penalty mainly depends on the higher reboiler thermal duty for solvent regeneration, resulting in a lower net power output from the steam cycle.

Power consumption for the CCS-auxiliaries is higher than the MEA one due to the higher solvent circulating mass flow rate, higher energy penalty for heat rejection and different DCC configuration selected (upstream position of the fan in the LysK case with respect to the direct contact cooler against the configuration of the MEA EBTF benchmark where the fan follows the DCC).

Table 2: LysK vs. MEA CO₂ capture unit - performance analysis.

Process section	Quantity	N. Trains (Full Plant)	Units	LysK	MEA
				Value	Value
EBTF Combined Cycle	Fuel input	-	MWLHV	1422.6	1422.6
	Gas Turbine Power Output (2 units)	2	MWe	544.2	544.2
	Steam Cycle Net Power Output w/o CCS	1	MWe	285.7	285.7
	Net Power Output w/o CCS	-	MWe	829.9	829.9
	Steam Cycle Net Power Output with CCS	-	MWe	194.4	207.9
	Gross Power Output with CCS	-	MWe	744.8	752.1
Advanced CCS process	Total Power CO₂ Capture Auxiliaries	-	MWe	26.6	19.9
	Captured CO₂	2	kg/s	73.4	73.4
	Reboiler Thermal duty	2	MWth	336.0	290.7
	Specific thermal consumption for solvent regeneration	-	MJth/kgCO₂	4.58	3.96
	Total Power CO₂ Compression	-	MWe	22.60	22.6
Overall plant performance	Net Power Output with CCS	-	MWe	695.59	709.7
	Power Plant Net Electric Efficiency with CCS	-	%	49%	49.9%
	CO₂ emissions w/o CCS	-	kgCO₂/MWh	351.80	351.8
	CO₂ emissions with CCS	-	kgCO₂/s	8.16	7.87
	CO₂ emissions with CCS	-	kgCO₂/MWh	42.22	39.30
	EBTF Plant Net Electric Efficiency w/o CCS	-	%	58.3%	58.3%
	SPECCA	-	GJLHV/tCO₂	3.84	3.34

Process design and pricing has allowed the evaluation of relevant economic indicators such as cost of electricity (COE) and cost of CO₂ avoided (CCA), which have been calculated with a consistent approach for the MEA benchmark and LysK case. The calculation is based on a factorial costing methodology for equipment pricing as from previous literature works [29].

The economic evaluation of MEA has been carried out with reference to literature information and it has been calculated to be consistent with the LysK case. The results of the techno-economic evaluation reported in Table 3 compare the LysK case against MEA. Standing out, the slightly higher cost of CO₂ avoided of the LysK case with respect to MEA (~90 vs. 85 \$/tCO₂ respectively). This is mostly related to the higher energy penalty calculated for the amino acid salt case (SPECCA index of the LysK case is ~15% higher compared to the SPECCA index of the benchmark from Table 2).

Table 3: Economic indicators for NGCC+LysK and NGCC+MEA.

Indicator	Unit	LysK	MEA
Cost of Electricity	[\$/MWh]	72.91	71.54
Cost of CO ₂ Avoided	[\$/tCO ₂]	90.16	84.92

5. Conclusions

A new techno economic assessment of a CO₂ absorption process working with 43.7%w/w aqueous LysK solution coupled with a reference NGCC (830 MWeI without capture) has been carried out. Solvent selection is based on previous experimental campaigns and literature data, and it is justified by the higher environmental compatibility, promising capacity and fast kinetics of the chosen amino acid salt.

The present work has required the definition of a detailed thermodynamic model of the LysK/CO₂/H₂O system and the definition of a proprietary in-house rate-based model of the absorption unit. Moreover, a preliminary evaluation of the solvent regeneration duty based on Van't Hoff equation has been carried out in order to estimate the energy penalty of the capture unit over the combined cycle. Performance results and process cost have been calculated within a dedicated techno-economic assessment, which has provided suitable indicators.

Standing out, the higher cost of CO₂ avoided of the LysK case with respect to MEA, which is mostly related to the

higher energy penalty calculated for the amino acid salt case. Specifically, the SPECCA index of the LysK case is ~15% higher compared to the SPECCA index of the benchmark.

Cost of electricity (72.91 \$/MWh) and CO₂ avoided (90.16 \$/tCO₂) for the alternative case are higher with respect to the benchmark capture unit with MEA (i.e., 71.54 \$/MWh and 84.92 \$/tCO₂).

The evaluation of the energy penalty of the LysK case still requires further experimental evidences. Specifically, additional tests on vapor-liquid equilibria for the low loading region together with calorimeter analysis of the heat of reaction, as well as heat capacity and viscosity measurements of the loaded solvent are recommended.

Moreover, cyclic absorption/regeneration tests and stress testing of the solvent at different temperature and flue-gas composition would allow a better quantification of the degradation effects, consequent required solvent make-up rate and operating cost aimed at performing a more accurate techno-economic assessment of AAS-based capture technology applied to post-combustion CO₂ capture for decarbonized power production.

Acknowledgment

The results of the present research activity rely on previous experimental work focusing on an amino acid screening carried by the authors together with Sotacarbo research center.

The thermodynamic model embedded in the absorber rate-based model delivered within the present work is based on previous modelling activities carried out by the authors together with CTP group from Mines ParisTech.

The authors thank Dr. A. Porcu, Dr. M. Mureddu, Dr. A. Orsini and Dr. A. Pettinau from Sotacarbo research center for the research collaboration and the experimental analysis carried out as a baseline for this work.

The authors are also grateful to Prof. C. Coquelet, Eng. S. Delgado and the team from CTP-Mines ParisTech for the collaboration and significant contributions on the thermodynamic model that has been necessary to carry out the present study.

References

- [1] M. Crippa *et al.*, “Fossil CO₂ and GHG emissions of all world countries - 2019 Report, EUR 29849 EN, Publications Office of the European Union,” Luxembourg, 2019.
- [2] IEA, “CO₂ Emissions from Fuel Combustion,” 2019. [Online]. Available: [https://www.iea.org/data-and-statistics?country=WORLD&fuel=CO₂ emissions&indicator=CO₂ emissions by sector](https://www.iea.org/data-and-statistics?country=WORLD&fuel=CO2&emissions&indicator=CO2%20emissions%20by%20sector).
- [3] CaESAR, “European best practice guidelines for assessment of CO₂ capture technologies,” 2011.
- [4] P. van Os, “CESAR-CO₂ Enhanced Separation and Recovery,” 2006.
- [5] L. V. van der Ham, E. L. V. Goetheer, E. S. Fernandez, M. R. M. Abu-Zahra, and T. J. H. Vlucht, “5 – Precipitating amino acid solutions,” in *Absorption-Based Post-combustion Capture of Carbon Dioxide*, 2016, pp. 103–119.
- [6] A. Conversano, A. Porcu, M. Mureddu, A. Pettinau, and M. Gatti, “Bench-scale experimental tests and data analysis on CO₂ capture with potassium proline solutions for

- combined cycle decarbonization,” *Int. J. Greenh. Gas Control*, vol. 93, p. 102881, Feb. 2020.
- [7] A. Conversano, A. Porcu, M. Mureddu, A. Pettinau, and M. Gatti, “Bench-Scale Absorption Testing of Aqueous Potassium Lysinate as a New Solvent for CO₂ Capture in Natural Gas-Fired Power Plants,” *Int. J. Greenh. Gas Control*, vol. 106, p. 103268, Mar. 2021.
- [8] W. M. Budzianowski, *Energy Efficient Solvents for CO₂ Capture by Gas-Liquid Absorption*. Cham: Springer International Publishing, 2017.
- [9] Y. Zhao *et al.*, “A Comparative Study of Aqueous Potassium Lysinate and Aqueous Monoethanolamine for Postcombustion CO₂ Capture,” *Energy & Fuels*, vol. 31, no. 12, pp. 14033–14044, Dec. 2017.
- [10] B. Mai Lerche, *CO₂ Capture from Flue gas using Amino acid salt solutions*, no. August. 2012.
- [11] Y. Zhao, S. Shen, Y. Bian, Y. nan Yang, and U. Ghosh, “CO₂ Solubility in Aqueous Potassium Lysinate Solutions at Absorber Conditions,” *J. Chem. Thermodyn.*, vol. 111, pp. 100–105, 2017.
- [12] L. Li and G. Rochelle, “Amino acid solvents for CO₂ absorption,” *AIChE Annu. Meet. Conf. Proc.*, pp. 15–17, 2011.
- [13] H. Kim, S. J. Hwang, and K. S. Lee, “Novel Shortcut Estimation Method for Regeneration Energy of Amine Solvents in an Absorption-Based Carbon Capture Process,” *Environ. Sci. Technol.*, vol. 49, no. 3, pp. 1478–1485, Feb. 2015.
- [14] Y. Lin and G. T. Rochelle, “Optimum heat of absorption for CO₂ capture using the advanced flash stripper,” *Int. J. Greenh. Gas Control*, vol. 53, pp. 169–177, 2016.
- [15] R. H. Weiland, T. Chakravarty, and A. E. Mather, “Solubility of carbon dioxide and hydrogen sulfide in aqueous alkanolamines,” *Ind. Eng. Chem. Res.*, vol. 32, no. 7, pp. 1419–1430, Jul. 1993.
- [16] U. E. Aronu *et al.*, “Solubility of CO₂ in 15, 30, 45 and 60 mass % MEA from 40 to 120 °C and model representation using the extended UNIQUAC framework,” *Chem. Eng. Sci.*, vol. 66, no. 24, pp. 6393–6406, 2011.
- [17] M.-H. Li and K.-P. Shen, “Calculation of equilibrium solubility of carbon dioxide in aqueous mixtures of monoethanolamine with methyldiethanolamine,” *Fluid Phase Equilib.*, vol. 85, pp. 129–140, May 1993.
- [18] S. Shen, Y. Zhao, Y. Bian, Y. Wang, H. Guo, and H. Li, “CO₂ absorption using aqueous potassium lysinate solutions: Vapor – liquid equilibrium data and modelling,” *J. Chem. Thermodyn.*, vol. 115, pp. 209–220, Dec. 2017.
- [19] A. Conversano, *Thermodynamic Modelling and Process Design of a CO₂ Capture Unit with Amino Acid Salts Solutions for Combined Cycle Decarbonisation*. Politecnico di Milano, 2021.
- [20] M. Z. Shahid, A. S. Maulud, M. A. Bustam, H. Suleman, H. N. A. Halim, and A. M. Shariff, “Rate-Based Modeling for Packed Absorption Column of the MEA–CO₂–Water System at High-Pressure and High-CO₂ Loading Conditions,” *Ind. Eng. Chem. Res.*, vol. 58, no. 27, pp. 12235–12246, Jul. 2019.
- [21] P. Tontiwachwuthikul, A. Meisen, and C. J. Lim, “CO₂ absorption by NaOH, monoethanolamine and 2-amino-2-methyl-1-propanol solutions in a packed column,” *Chem. Eng. Sci.*, vol. 47, no. 2, pp. 381–390, Feb. 1992.
- [22] H. M. Kvamsdal, J. P. Jakobsen, and K. A. Hoff, “Dynamic modeling and simulation of a CO₂ absorber column for post-combustion CO₂ capture,” *Chem. Eng. Process. Process Intensif.*, vol. 48, no. 1, pp. 135–144, Jan. 2009.
- [23] L. L. Simon, Y. Elias, G. Puxty, Y. Artanto, and K. Hungerbuhler, “Rate based modeling and validation of a carbon-dioxide pilot plant absorption column operating on monoethanolamine,” *Chem. Eng. Res. Des.*, vol. 89, no. 9, pp. 1684–1692, Sep. 2011.
- [24] M. Afkhamipour and M. Mofarahi, “Comparison of rate-based and equilibrium-stage models of a packed column for post-combustion CO₂ capture using 2-amino-2-methyl-1-propanol (AMP) solution,” *Int. J. Greenh. Gas Control*, vol. 15, pp. 186–199, Jul. 2013.
- [25] N. A. H. Hairul, A. M. Shariff, W. H. Tay, A. M. A. v. d. Mortel, K. K. Lau, and L. S. Tan, “Modelling of high pressure CO₂ absorption using PZ+AMP blended solution in a packed absorption column,” *Sep. Purif. Technol.*, vol. 165, pp. 179–189, Jun. 2016.
- [26] J. Gabrielsen, M. L. Michelsen, E. H. Stenby, and G. M. Kontogeorgis, “Modeling of CO₂ absorber using an AMP solution,” *AIChE J.*, vol. 52, no. 10, pp. 3443–3451, Oct. 2006.
- [27] M. Saimpert, G. Puxty, S. Qureshi, L. Wardhaugh, and A. Cousins, “A new rate based absorber and desorber modelling tool,” *Chem. Eng. Sci.*, vol. 96, pp. 10–25, Jun. 2013.
- [28] A. Aroonwilas, A. Chakma, P. Tontiwachwuthikul, and A. Veawab, “Mathematical modelling of mass-transfer and hydrodynamics in CO₂ absorbers packed with structured packings,” *Chem. Eng. Sci.*, vol. 58, no. 17, pp. 4037–4053, Sep. 2003.
- [29] M. Gatti *et al.*, “Preliminary Performance and Cost Evaluation of Four Alternative Technologies for Post-Combustion CO₂ Capture in Natural Gas-Fired Power Plants,” *Energies*, vol. 13, no. 3, p. 543, Jan. 2020.

MATERIAL INTEGRITY ASPECTS OF CCS: AN OVERVIEW FOR CO₂ TRANSPORT AND STORAGE

Cécile Millet^{1,*}, Dwaipayan Mallick², Guillaume Néel¹, Leila Faramarzi³, Ali Meschi Amoli³

¹Vallourec Research Center France, 60 route de Leval, 59620 Aulnoye-Aymeries, France

²Innovateam, 114 Avenue Charles de Gaulle, 92200 Neuilly-sur-Seine

³Vallourec Head quarter, 27 avenue du General Leclerc, 92100 Boulogne Billancourt, France

* Corresponding author e-mail: cecile.millet@vallourec.com

Keywords: CO₂, Materials, CRA, CCS, corrosion, toughness

Introduction

Carbon capture and storage (CCS) are technologies aimed at capturing CO₂, followed by transportation to a storage site, injecting into one of several types of stable geological formations, trapping and preventing its subsequent emission [1]. Though CO₂ transport and injection for enhanced oil recovery (EOR) are known for over 40 years, new challenges arise when the CO₂ source is anthropogenic and not natural (as in EOR) [2]. EU Directive 2009/31/EC states that CO₂ streams from power stations or industrial plants "shall consist overwhelmingly of CO₂" but may contain associated incidental substances (e.g., SO_x, NO_x, O₂, H₂S) [3]. These anthropogenic impurities pose a bottleneck in

extending the established corrosion prediction models used in oil and gas environments to CCS [2]. They add to the system's complexity by influencing CO₂'s physical properties and the water solubility, segregating CO₂ into the aqueous phase, potentially lowering the solution pH and increasing corrosion risk [2], [4]. Figure 1 presents a schematic of the CCS process, along with the associated risks at each step.

The paper intends to briefly highlight the risks involved with the transport and storage of anthropogenic CO₂, the material selection criteria and concludes with highlighting the present challenges.

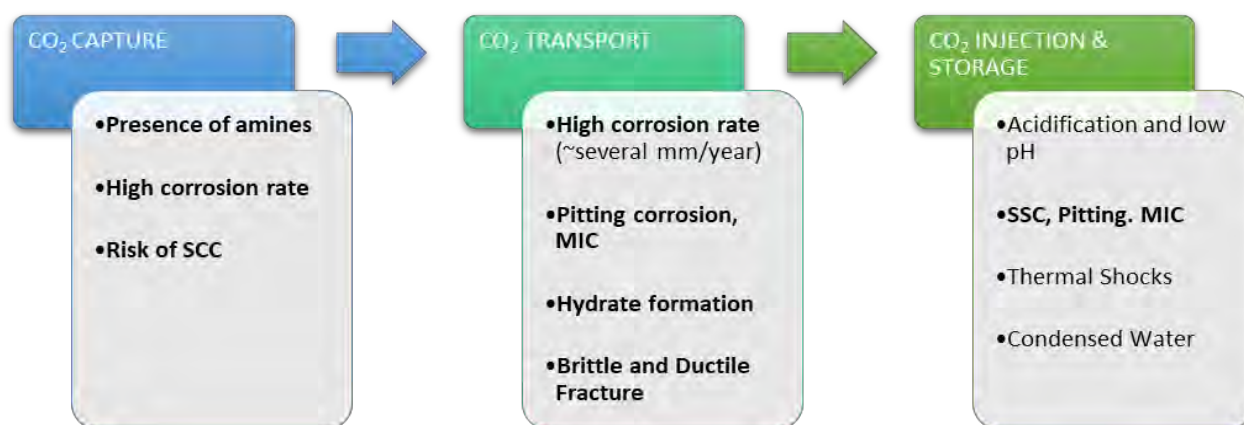


Figure 1: A schematic of the CCS process, threats and the material risks associated with each step (SSC: Sulfide Stress Cracking / MIC: microbologically induced corrosion)

Risks involved during CO₂ transport

There is currently a lack of standards for CO₂ stream quality specifications, making it difficult to accurately define the safe operating conditions for CO₂ transport and storage. There could be a distinct difference in the contaminants present in the CO₂ stream, depending on the sources [2]. The CO₂ stream will contain SO₂, NO₂, O₂ or H₂S based on the source, the capture process, and the gas treatment level.

Most CCS projects in the planning phase intend to transport and store CO₂ in a supercritical state (Figure 2). When present within the solubility limit, water content in-stream poses no significant corrosion risk; however, it will separate as an aqueous phase and wet the pipeline walls if it exceeds the saturation level. Water is a potent cause of CO₂ pipeline corrosion, mainly if the water accumulates as a liquid at low or dead points within the pipes [5]. Water and acid gas

impurities co-exist under such conditions, causing general corrosion at rates up to several mm/y, accompanied by pitting corrosion or a risk of sulphide stress cracking (SSC) in presence of H₂S. Impurities also lower the water solubility in the supercritical CO₂ stream, exacerbating the issue. A study reported among CO₂ related pipeline failures, 45% was due to corrosion, i.e. it was the single most significant cause of pipeline

failures [2]. Water may also lead to hydrates formation at low temperature in the pipeline, blocking the pipeline. Additionally, O₂ might be present in the CO₂ stream (unlike CO₂ from natural sources), increasing corrosion issues by additional cathodic reduction, inhibiting protective scale formation and possible microbiologically induced corrosion (MIC).

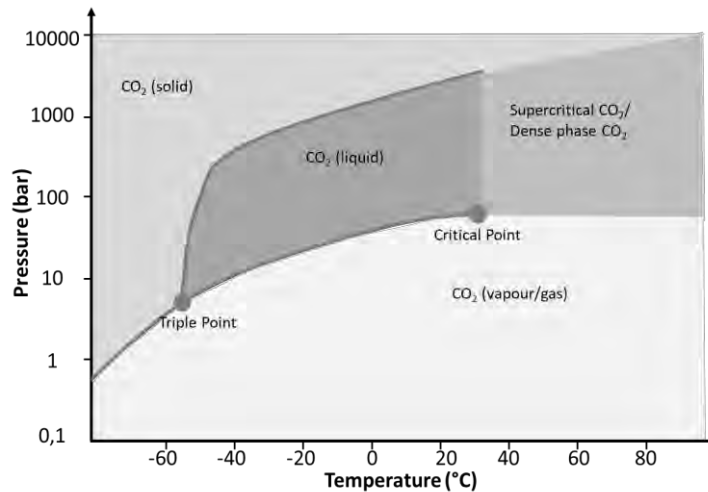


Figure 2: Pressure-temperature phase diagram for CO₂ [6]

Apart from stream composition, another difference in CCS and EOR transportation is that generally, EOR pipelines are confined to low population areas and operate well below the supercritical conditions [6]. In CCS pipelines, defects by mechanical damage, corrosion, or operational issues may result in leakage from the damaged sections, posing a threat to the population and the vicinity's local environment [7].

Risks involved during CO₂ storage

Figure 3 illustrates the process of CO₂ injection in geological reservoirs. CO₂ injection for storage requires tubing material to withstand the corrosive environment defined by the near-wellbore conditions (pressure, temperature, brine properties and injected CO₂ composition). The injection point temperature depends on the CO₂ injection rate and the reservoir conditions, ranging from 10- 120 °C. The pressure is typically 50-150 bar, for which the CO₂ will be in the liquid or supercritical state, depending on the temperature. Different brines have different salt contents, and pH is usually in the range of 3.5 – 4.5. Condensed water, which may form during shut-in, has no buffer capacity and can have pH as low as 3.0; resultantly, condensed water is much more aggressive than buffered formation water. Impurities in the CO₂ stream can reduce the pH (SO_x, NO_x and other acids) and increase corrosivity. During injection, at the bottom hole, formation water will dissolve CO₂ up to saturation. Impurities will partition to the water phase, with the acidic gases in CO₂ reacting with formation water producing strong acids. Thus, a significant corrosion risk is at the interface between formation water and CO₂. During the shut-in period, wellhead temperature decreases with CO₂ in gas

and supercritical phase co-existing at the wellhead. If residual water is present, the wellhead is exposed to corrosion issues. If H₂S gas is present in the stream, there might be a risk of SSC. Oxygen will enormously increase the localized corrosion attack and promote MIC. Finally, during prolonged storage, the tubing may be removed or stay in place, ensuring against CO₂ leakage under both conditions.

and supercritical phase co-existing at the wellhead. If residual water is present, the wellhead is exposed to corrosion issues. If H₂S gas is present in the stream, there might be a risk of SSC. Oxygen will enormously increase the localized corrosion attack and promote MIC. Finally, during prolonged storage, the tubing may be removed or stay in place, ensuring against CO₂ leakage under both conditions.

If shut-in conditions are frequent, injection well suffers from thermal shocks due to pressure changes. Therefore, an essential aspect for the material selection would be a good material impact toughness property at low temperatures. Material impact toughness is also an important consideration for material selection in case of a blow out where rapid depressurization of supercritical CO₂ will result in a huge temperature drop. Vallourec is conducting experiments to measure the impact toughness of different CRA materials in sub-zero temperatures (down to -80°C) to help with a risk-based approach for material selection for CCS applications.

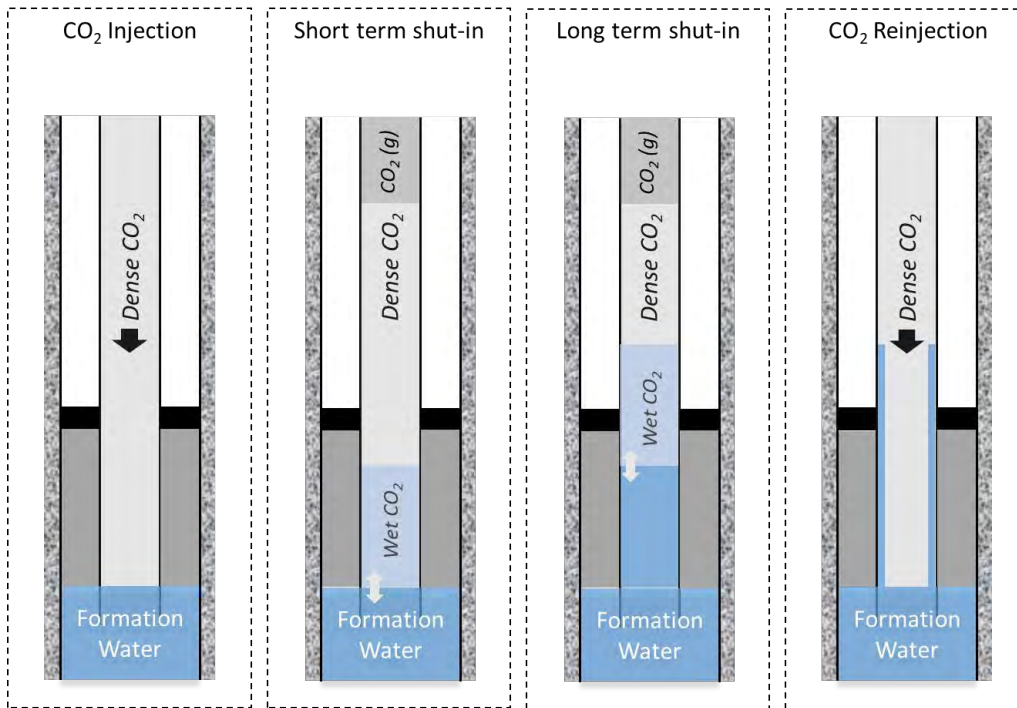


Figure 3: Sketch illustrating corrosion risks during injection and storage

Material Selection for CO₂ storage

Corrosion risks will depend on impurities

In the case of injection, recommendations and guidelines for materials selection are limited, particularly with impurities like O₂. It is common practice to assume the same material limits for CO₂ injection wells as oil and gas wells. However, the conditions can be significantly different in dense anthropogenic CO₂ depending on its composition and specific position in the well under consideration [9].

criteria based on the position within the well. Main corrosion risks to be considered for material selection occurs during shut-in and long storage.

Several corrosion resistant alloys (CRA) materials are used for well tubing in oil and gas production. 13Cr (martensitic and super martensitic) and duplex stainless steels are most common [10]. 13Cr has good resistance to CO₂ corrosion due to its high chromium content. Still, it may be susceptible to pitting and localized

corrosion, particularly at high temperatures in the presence of high chloride contents. Supermartensitic 13Cr steels are generally more resistant to pitting corrosion than conventional 13Cr [11]. Duplex stainless steels have good corrosion resistance in CO₂ environments but may be susceptible to stress corrosion cracking (SCC) under certain aggressive conditions. The SCC susceptibility depends on parameters like temperature, chloride concentration and oxygen.

The practical challenge for using duplex stainless steels is, in many cases, to decide whether the operational conditions are inside or outside the safe window. In particular, the temperature, chloride content and oxygen content are essential factors for stress corrosion cracking. In short, several materials can be used for well tubing. Still, the use can be restricted by pitting corrosion and stress corrosion cracking when oxygen and high chloride levels are present.

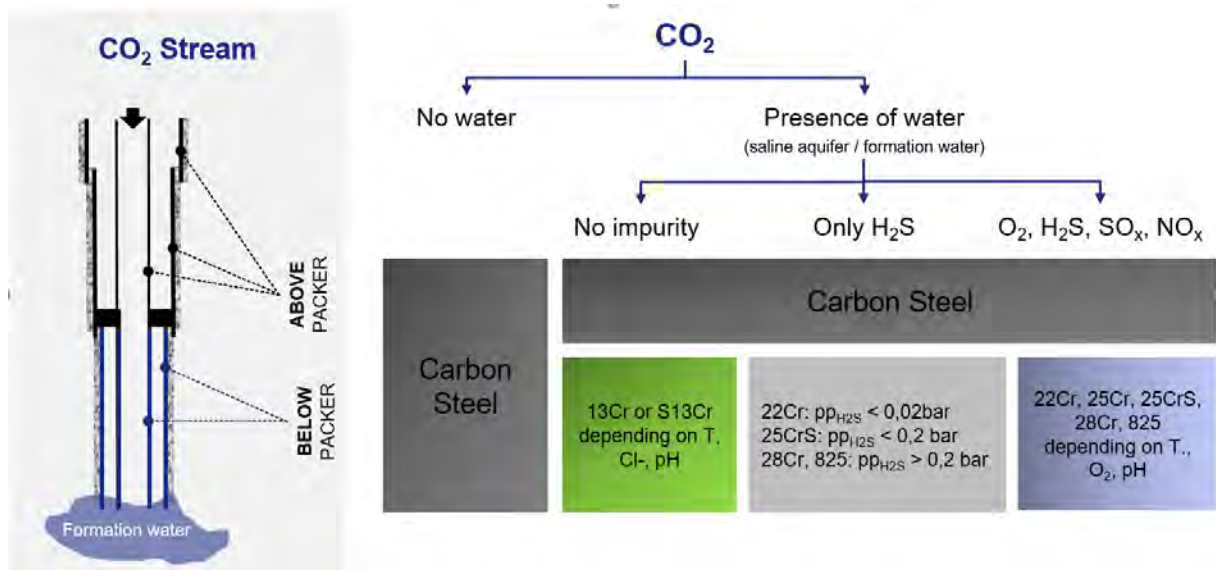


Figure 4: Material selection criteria for different sections of the CO₂ well.

Impact toughness at low temperature

The material impact toughness is the material's ability to absorb energy in the plastic region. Typically, as the temperature drops below 0°C, the hardness, yield strength, ultimate tensile strength and modulus of elasticity of a metal increase but ductility decreases.

Impact toughness is driven by alloying elements, residual elements, micro-cleanliness, microstructure, and manufacturing process. At low temperatures, in general, austenitic steels exhibit higher impact toughness than the relatively brittle martensite. Duplex stainless steels, widely used in petrochemical industries (consists of discontinuous ferrite in an austenitic matrix), exhibit impact toughness values intermediate to those of austenitic and martensitic steels.

The impact toughness value of a material is measured using the Charpy V notch method as per ASTM E23. Initially developed as a quality control test, the Charpy V notch method is currently used for materials design based on the toughness requirement. In this study, 4 different duplex stainless steels were studied for their impact toughness values. As shown in Table 1, two duplex stainless steels (22-5-3) were studied, one in cold worked (CW) condition and the other in solution annealed (SA) condition. Similarly, four super duplex stainless steels (25-7-4) were studied in solution annealed condition (SA) and cold worked condition (CW). The specimens were machined using the largest possible size of the specimen considering wall thickness of the tubes. Since the wall thickness of the tubular specimens were non identical, different size specimens were used in the study as indicated in Table 1. The impact toughness of solution annealed and cold work 25-7-4 in both transversal and longitudinal direction is plotted in Figure 5. When SA and CW materials are compared, SA materials appear to have much better impact toughness resistance than the cold worked materials.

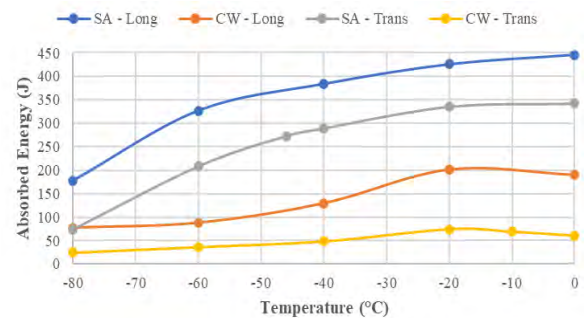


Figure 5 - Transition curves of 25-7-4 in SA and CW state with different testing orientations (converted to full size)

This is due to the highest residual stress induced by the cold hardening process which results in higher yield strength but a lower impact toughness values. Additionally, longitudinal values are always higher than transversal ones due to the grain orientation given by the extrusion process.

Table 1: Materials investigated in the study

Material	Tube OD x Wt [mm]	Specimen Size (KCV)[mm]	AYS [ksi]
22-5-3 SA	168,3 x 10	10 x 7,5	70
22-5-3 CW	114 x 10,92	10 x 5	131
25-7-4 SA	168,3 x 10,97	10 x 7,5	90
25-7-4 CW	114 x 7,05	10 x 5	142
25-7-4 SA	204 x 25,6	10 x 10	87
25-7-4 CW	179 x 10,36	10 x 7,5	137

As there is no available standards currently available for CCUS, material selection at present depends on the available standards used in oil and gas industry. According to the NORSOK M-601 specification, the minimum average impact toughness requirement for a material is 45J at -46°C. Applying the reduction factor for KCV 7.5 and KCV 5 specimens, according to

NORSOK M-601, the minimum required average impact toughness values are 37.5J and 30J respectively. On Figure 6, we compare differences between 22-5-3 Duplex and 25-7-4 Super Duplex Stainless Steel. Results show that super duplex stainless steels exhibit better impact toughness properties than the duplex stainless steel in both cold worked and solution

annealed conditions. It is evident that the investigated materials exhibit different level of toughness depending on process route. As per project requirements, product qualification would be required to confirm material suitability.

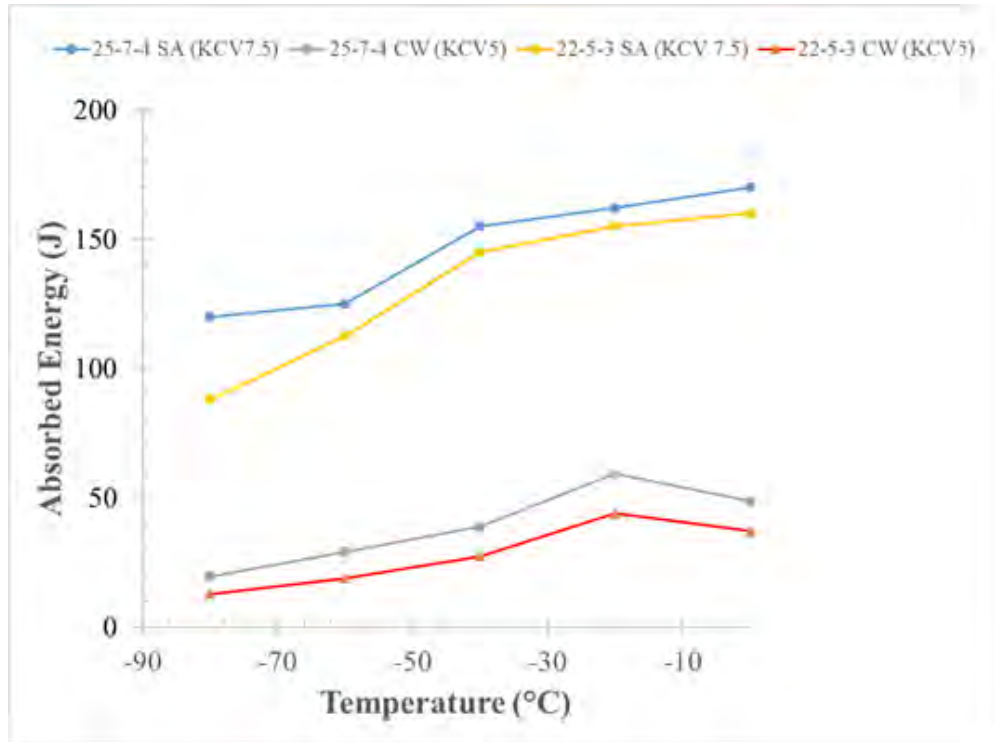


Figure 6 - Temperature dependent transversal impact toughness values of the investigated duplex and super duplex stainless steels.

Conclusion, Challenges and Research Opportunities

Conclusion

This paper aims to highlight the major challenges in the CCUS technology from a materials perspective. The key challenges identified for the material selection CO₂ storage is corrosion and material impact toughness properties. The impact toughness properties of 4 duplex and super duplex stainless steels were compared and the values were compared against the minimum requirement. It was seen that all the stainless steels show good impact toughness properties. Super duplex stainless steels show better impact toughness properties as compared to duplex stainless steels.

Challenges and Research opportunities

One of the significant experimental challenges is understanding the impurity behavior under dynamic flow conditions [12]. Another issue with non-dynamic testing is the depletion of impurity during the experiment. It could be imperative when considering tests of longer duration. In a study, IFE reported that a large part of the impurities became 'non-active' due to immobilization of the corrosive phases and reactions in the bulk phases [13].

Acknowledgment

The authors would like to express their gratitude to Mannesmann Stainless Tubes for the support and involvement in this project.

References

- [1] M. E. Boot-Handford et al., « Carbon capture and storage update », *Energy Env. Sci.*, vol. 7, no 1, p. 130-189, 2014, doi: 10.1039/C3EE42350F.
- [2] R. Barker, Y. Hua, et A. Neville, « Internal corrosion of carbon steel pipelines for dense-phase CO₂ transport in carbon capture and storage (CCS) – a review », *Int. Mater. Rev.*, vol. 62, no 1, p. 1-31, janv. 2017, doi: 10.1080/09506608.2016.1176306.
- [3] H. Rütters et al., « Towards an optimization of the CO₂ stream composition—A whole-chain approach », *Int. J. Greenh. Gas Control*, vol. 54, p. 682-701, nov. 2016, doi: 10.1016/j.ijggc.2016.08.019.
- [4] I. S. Cole, D. A. Paterson, P. Corrigan, S. Sim, et N. Birbilis, « State of the aqueous phase in liquid and supercritical CO₂ as relevant to CCS pipelines », *Int. J. Greenh. Gas Control*, vol. 7, p. 82-88, mars 2012, doi: 10.1016/j.ijggc.2011.12.008.
- [5] S. Foltran et al., « Understanding the solubility of water in carbon capture and storage mixtures: An FTIR spectroscopic study of H₂O+CO₂+N₂ ternary mixtures », *Int. J. Greenh. Gas Control*, vol. 35, p. 131-137, avr. 2015, doi: 10.1016/j.ijggc.2015.02.002.
- [6] H. Mahgerefteh, S. Brown, et G. Denton, « Modelling the impact of stream impurities on ductile fractures in CO₂ pipelines », *Chem. Eng. Sci.*, vol. 74, p. 200-210, mai 2012, doi: 10.1016/j.ces.2012.02.037.
- [7] S. Gu et al., « An experimental study on the flow characteristics during the leakage of high pressure CO₂ pipelines », *Process Saf. Environ. Prot.*, vol. 125, p. 92-101, mai 2019, doi: 10.1016/j.psep.2019.03.010.
- [8] L. Teng et al., « Experimental study of near-field structure and thermo-hydraulics of supercritical CO₂ releases », *Energy*, vol. 157, p. 806-814, aug 2018, doi: 10.1016/j.energy.2018.04.195.
- [9] L. Smith, M. A. Billingham, C.-H. Lee, et D. Milanovic, « Establishing and maintaining the integrity of wells used for sequestration of CO₂ », *Energy Procedia*, vol. 4, p. 5154-5161, 2011, doi: 10.1016/j.egypro.2011.02.492.
- [10] « Corrosion and materials selection in CCS systems », IEAGHG, p. 288, avr. 2010.
- [11] R. Moreira, C. Franco, C. J. B. M. Joia, S. Giordana, et O. R. Mattos, « The effects of temperature and hydrodynamics on the CO₂ corrosion of 13Cr and 13Cr5Ni2Mo stainless steels in the presence of free acetic acid », *Corros. Sci.*, vol. 46, p. 2987-3003, déc. 2004, doi: 10.1016/j.corsci.2004.05.020.
- [12] Y. Hua, R. Barker, et A. Neville, « Understanding the Influence of SO₂ and O₂ on the Corrosion of Carbon Steel in Water-Saturated Supercritical CO₂ », *CORROSION*, vol. 71, no 5, p. 667-683, mai 2015, doi: 10.5006/1504.
- [13] J. Brown, B. Graver, E. Gulbrandsen, A. Dugstad, et B. Morland, « Update of DNV Recommended Practice RP-J202 with Focus on CO₂ Corrosion with Impurities », *Energy Procedia*, vol. 63, p. 2432-2441, janv. 2014, doi: 10.1016/j.egypro.2014.11.265.

DESCRIPTION OF THE WORK AND PRELIMINARY RESULTS OF THE AC²OCEM PROJECT IN FACILITATING CARBON CAPTURE TECHNOLOGY IN THE CEMENT INDUSTRY USING OXYFUEL COMBUSTION

Cynthia Kroumian^{1*}, Kristina Fleiger², Ines Veckenstedt³, Mari Voldsund⁴, Otávio Cavalett⁵, Simon Roussanaly⁴, Joerg Maier¹, Volker Hoenig², Konstantina Peloriadi⁶, Günter Scheffknecht¹

¹ Institute of Combustion and Power Plant Technology, University of Stuttgart, Stuttgart, Germany

² VDZ Technology gGmbH, Düsseldorf, Germany

³ thyssenkrupp Industrial Solutions AG, Beckum, Germany

⁴ SINTEF Energy Research, Trondheim, Norway

⁵ Norwegian University of Science and Technology, Trondheim, Norway

⁶ CERTH Centre for Research and Technology Hellas, Athens, Greece

* Corresponding author e-mail: cynthia.kroumian@ifk.uni-stuttgart.de

Abstract

The Paris agreement compels CO₂ intensive industries, such as the cement industry to significantly decrease the CO₂ emissions. The source of the CO₂ emissions from the cement industry is related to the calcination and the combustion process, which is why innovative measures have to be implied to reach the CO₂ reduction goal. According to previous studies, the oxyfuel technology to facilitate the carbon capture and storage technology is the most economically feasible potential to solve the issue. In frame of the AC²OCEm project, a European consortium has come together to reduce the knowledge gap and the time to market of the oxyfuel technology in the cement industry. Experimental and analytical work on the oxyfuel technology for retrofitting existing cement plants will be focused on optimizing the calciner and the oxyfuel burner with 100 % alternative fuels. In addition to the experimental and analytical tests regarding the burner technology in pilot-scale facilities, design and optimization of retrofitting existing plants is performed, taking into consideration the boundary condition of two demonstration plants located in Slite, Sweden and Lägerdorf, Germany. For the retrofit design, the heat integration in oxyfuel condition and the effect of false air ingress for both plants is studied and it is found that a heat exchanger system would adequately supply the energy to the drying unit. A realistic value for false air has been set at 6 % as an initial design parameter of the CPU. Within the scope of the AC²OCEm project, the kiln and calciner oxyfuel burners will be promoted to higher technology readiness levels for newly-build and up-to 100 % oxygen combustion cement plants. A techno-economic analysis and life cycle assessment for retrofitted existing and new-build cement plants will also be performed.

Keywords: *Alternative fuel, CCS, Cement, Oxyfuel, SRF*

1. Introduction

The ambitious target set by the Paris agreement, 2 °C scenario by 2050, necessitates overall around 2,800 Mt CO₂ emissions reduction. The International Energy Agency (IEA) has emphasized that 40 % of the decrease in emissions must be made within the European industry, specifically those that are CO₂ intensive, such as the cement and steel industries [1]. European countries taking part in the Paris agreement have come up with several approaches to reduce the CO₂ emissions by 1,700 Mt. Further measures must be taken to account for the remaining 1,100 Mt of CO₂. For this purpose, industry and research institutions are working together to come up with technically and economically feasible methods to reduce and ultimately eliminate these emissions [2]. Both the IEA and the International Renewable Energy Agency (IRENA) have confirmed that carbon capture usage and storage (CCUS) is important to achieve the goal set by the Paris agreement [3,4].

1.1 Cement Industry

The cement industry is one of the highest energy and CO₂ intensive industries, where CO₂ is not only emitted due to the combustion process but also as the main side product of the calcination process. The process related emissions are directly proportional to the amount of clinker used, the main raw material in the cement industry. The important CO₂ reduction approaches in the cement industry include switching to low-carbon or carbon-free fuels, reducing the clinker to cement ratio and advancing the process technology [3,5,6].

The IEA has shown that these approaches can potentially achieve 44 % of the target CO₂ emission reduction [6]. In order to achieve the decarbonization of the sector and reach the 2 °C scenario goal, further measures have to be taken into account. In frame of the European Cement Research Academy (ECRA) project, the potential of carbon capture and storage (CCS) is studied and the advantages and disadvantages of the different carbon

capture methods in the cement industry, pre-combustion, post-combustion, oxyfuel technology and carbonate looping were assessed. It was concluded that the oxyfuel technology and post combustion capture showed high potential [7]. In the CEMCAP project, the oxyfuel technology, chilled ammonia-based absorption, membrane-assisted liquefaction and calcium looping were assessed and compared with MEA-based absorption. Among these technologies, the oxyfuel technology was found to have the lowest cost of CO₂ avoided, but at the same time a high risk related to the close integration with the clinker burning process was highlighted for this technology [8,9].

1.2 AC²OCem Project

Eleven partners from five European countries, Norway, Germany, Switzerland, France and Greece have formed a consortium in scope of the ACT program to evaluate the feasibility of oxyfuel combustion in the cement industry to accelerate the carbon capture and storage technology. The AC²OCem project brings together the expertise of four industrial end-users, two technology providers and five research institutions. In scope of AC²OCem, oxyfuel technology will be evaluated for retrofitting existing cement plants and for new-build plants. This paper will provide a comprehensive overview of the project goals and objectives, in addition to a brief summary of achieved results and an outlook on planned work.

The main goal of the AC²OCem project is to accelerate the deployment of CCS by closing the knowledge gaps and advancing the technology development for a successful operation of the first oxyfuel demonstration cement plants. The project will focus on reducing the CO₂ avoidance cost, and increasing the plant efficiency.

The project consists of six work packages, WP1 is for management and dissemination. Within WP2, advanced oxyfuel burners, pilot-scale experiments as well as CFD simulations will be performed to evaluate the oxyfuel kiln burner in retrofitted and new-build plants with up to 100 % alternative fuels. WP3, optimization of oxyfuel calciner, is focused on evaluating the impact of the flue gas composition on the calcination process under oxyfuel conditions, and demonstrating pilot-scale calcination tests in oxyfuel conditions using up to 100 % alternative fuels. In WP4, integration of 1st generation oxyfuel technology by retrofit to existing cement plants, Heidelberg Cement and LafargeHolcim have selected two demonstration plants in Slite, Sweden and Lägerdorf, Germany respectively to design and optimize the oxyfuel technology, transferring the technology from TRL6 to TRL8. Different flue gas recirculation ratios and raw meal qualities will be simulated to optimize the overall process and a techno-economic analysis will be performed for retrofitted cement plants (considering the two demonstration plants). In WP5, oxyfuel technology of 2nd generation for new-build cement plants, the design and optimization of the new-build oxyfuel cement plants will be evaluated, promoting the technology from TRL2 to TRL6 and a techno-economic feasibility study will be performed. In WP6, life cycle assessment, the

environmental sustainability aspects of oxyfuel technologies for retrofitted and new-build cement plants will be evaluated.

2. Oxyfuel burner technologies

The focus of this work package is on the experimental and analytical investigation of an oxyfuel burner. The first part of the work package is dedicated to the design and evaluation, experimental and analytical, of an oxyfuel burner for 100 % alternative fuel in oxyfuel atmosphere. The second part of the work package is dedicated to the design and evaluation of an advanced oxyfuel burner for the combustion of alternative fuels with up to 100 % oxygen. The experiments will take place in the 500 kW pilot-scale combustion chamber at the University of Stuttgart that has been adapted to simulate a cement kiln. The experimental data obtained will also be used to validate the CFD simulation models of the retrofitted and new-build cases performed by CERTH and SINTEF respectively.

2.1 Description of the 500 kW combustion facility at the University of Stuttgart

The 500 kW pilot-scale down-fired combustion chamber at the University of Stuttgart (Figure 1) has been optimized to simulate the atmosphere inside a cement kiln by an advantageously designed burner muffle that electrically pre-heats the secondary inlet gas up to 800 °C to account for the recirculated combustion gases from the clinker cooler [10]. The combustion chamber is 7 m in length and 0.8 m in inner diameter and measurement ports are distributed along the length of the chamber to allow axial and radial in-flame measurements.

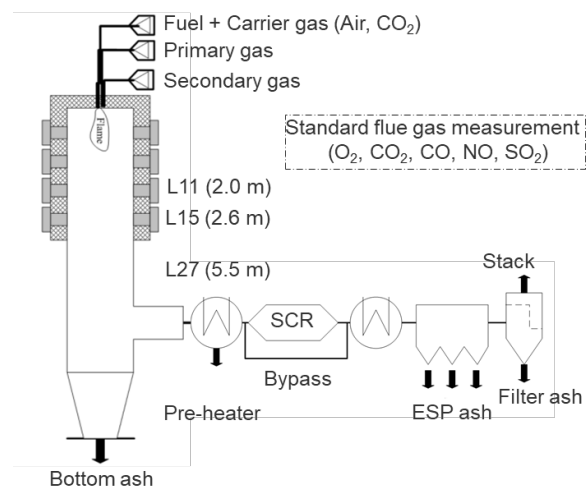


Figure 1: Sketch of 500 kW combustion chamber at IFK, University of Stuttgart

2.2 100 % SRF combustion experiments

Three different cases were performed, the first is a reference case with air and 100 % SRF (refer to Table 1 for the SRF properties, taking into account that SRF is an inhomogeneous fuel and the results are bound to have high uncertainties). In the second case, AIR28, the carrier, primary and secondary gases were air, yet an additional oxygen stream was fed into the primary gas

inlet along with air, the total oxygen concentration in the inlet gas was 28 vol. %. The third case, OXY31, is an oxyfuel case with 100 % SRF, 31 vol. % total oxygen in the inlet gases and CO₂ for the rest of the combustion gases.

Table 1: SRF properties including the proximate and ultimate raw fuel analysis

	Unit	a.r.
Moisture	wt. %	2.03
Volatile matter	wt. %	79.4
Ash	wt. %	11.0
Fixed Carbon	wt. %	7.62
Carbon (C)	wt. %	56.8
Hydrogen total (H)	wt. %	8.19
Hydrogen organic (H)	wt. %	7.96
Nitrogen (N)	wt. %	0.653
Sulfur (S)	wt. %	0.276
Net calorific value H _u	J/g	24818

The gas composition in the primary, secondary and carrier gas can be controlled independently of each other. In the AIR28 case, pure oxygen is fed directly into the primary air inlet stream at the burner resulting in 60 vol. % oxygen in the primary gas. The secondary and carrier gases are air. In the OXY31 case, the SRF carrier gas is CO₂, the primary and secondary gases contain 70 vol. % and 22 vol. % oxygen respectively. The AIR28 and OXY31 case are both evaluated based on the reference air case. In the oxyfuel case the gas radiation and heat capacity are the properties with the highest effect on the combustion process. At 1123 °C, the molar heat capacity ratio of CO₂ to N₂ is 1.7, which directly influences the flame temperature and stability [11]. Figure 2 depicts images of the SRF flame at 18, 33 and 48 cm from the burner, it is observed that at higher oxygen concentrations, in the primary gas, the flame is more compact near the burner. To achieve a stable flame and maintain the flame temperature, for coal, the total oxygen concentration must be between 25 and 42 vol. % [11]. Other researchers have shown that the type of fuel influences the total oxygen concentration necessary to maintain a similar temperature profile during oxyfuel combustion with CO₂ in comparison to the air reference case [12,13].

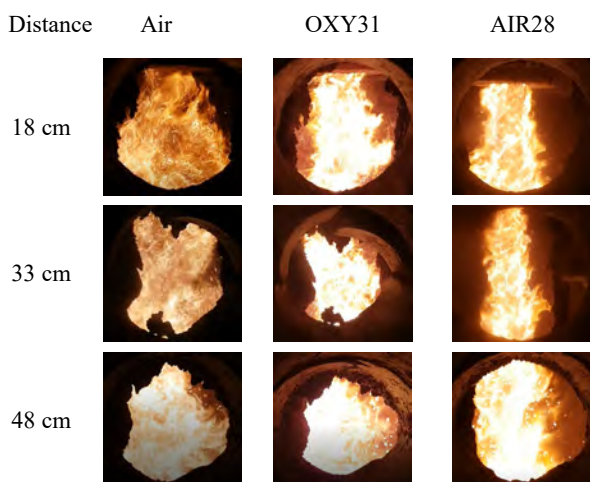


Figure 2: 100 % SRF flame captured in the Air, OXY31 and AIR28 cases at different distances from the burner

Figure 3 depicts the temperature and oxygen concentration profiles measured from the burner along the centerline of the furnace. The temperature profiles up to 48 cm are similar for the three cases despite the fluctuation of the oxygen consumption in the region. It is observed that the rate at which the temperature increases from the burner (0 cm) to the maximum measured flame temperature (measured at 116 cm from the burner for the Air and OXY31 cases and at 99 cm for the AIR28 case) is higher in the AIR28 case compared to the air and OXY31 cases. The temperature profile in the OXY31 case is on average 40 °C less than in the reference case, yet the oxygen consumption, especially in the main flame zone (between 63 and 167 cm), reacts similarly in the two cases. Higher fluctuations in the oxygen consumption is also noticed in the OXY31 case. The experiments have proven a stable SRF flame, yet one possibility to increase the flame temperature above 1200 °C would be a mixture of different alternative fuels, for example one with less volatile matter.

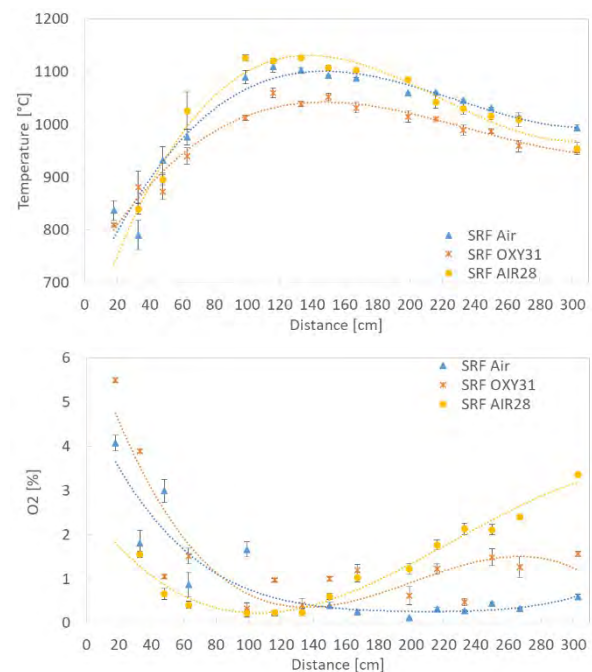


Figure 3: Oxygen concentration and temperature profiles measured from the burner along the centerline of the furnace

Figure 4 depicts the peak temperature measured in the three cases and their relative calculated adiabatic flame temperatures. Although the adiabatic temperature is over 1000 °C above the measured temperature, the trend is clear and confirms the results obtained. The adiabatic temperature and measured temperature of the OXY31 case were lower than that of the reference air case by 49 and 33 °C respectively. This result complies with the results of other researchers and suggests that the total inlet oxygen must be slightly increased to become comparable with the air reference case.

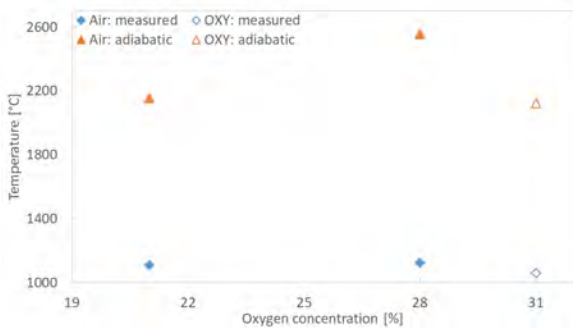


Figure 4: Adiabatic temperature calculation and maximum measured temperatures for 100 % SRF combustion with air, AIR28 and OXY31

These and future measurements will be used to verify CFD simulation performed by CERTH and SINTEF. Further measurements with higher oxygen concentration are also planned in the frame of the AC²OCem project.

3. Impact of oxyfuel technology on the calciner

The focus of work package 3 is on experimental investigations of calcination under oxyfuel conditions.

The studies will be conducted in three experimental facilities at the University of Stuttgart, thyssenkrupp Industrial Solutions AG and Air Liquide.

These experiments have been partially started and will be continued in the next months.

Several objectives are being investigated in each facility including the role of flue gas moisture level in the calciner to reduce and control the calcination temperature and minimize the risk of blockages under oxyfuel conditions as well as investigations on different oxyfuel calciner regimes. Theoretical and experimental calcination tests will be performed up to pilot-scale in a process relevant environment (TRL 6). To correlate the calcination performance in the oxyfuel environment to a reference scenario, the tests will be conducted under both air and oxyfuel conditions.

The impact of process conditions and flue gas impurities like sulfur and chlorines on calcination reaction will be evaluated at technical- and pilot-scales. Based on the results a moisture injection concept and process control strategy for retrofitted and new-build cement plants will be developed.

The experiments at the technical scale facility in the University of Stuttgart will be performed in an electrically heated entrained flow reactor (up to 50 kW), refer to Figure 5. The facility is capable of emulating co-current oxyfuel calciner conditions, which allows promising investigations under the relevant environment.

The pilot-scale facility of thyssenkrupp Industrial Solutions AG, Figure 6, consists of a calciner and a 4-stage cyclone preheater with the feed rate of around 40 kg/h. The influence of moisture content on the calcination efficiency and the calcination temperature will be fully investigated in oxyfuel environments.

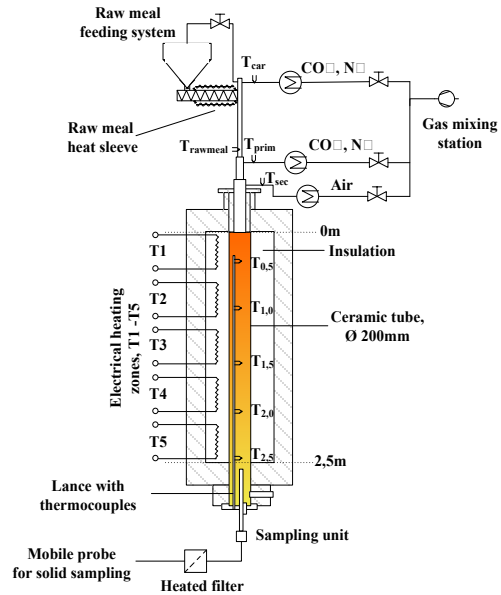


Figure 5: Sketch of the 50 kW technical-scale facility at the University of Stuttgart, Germany

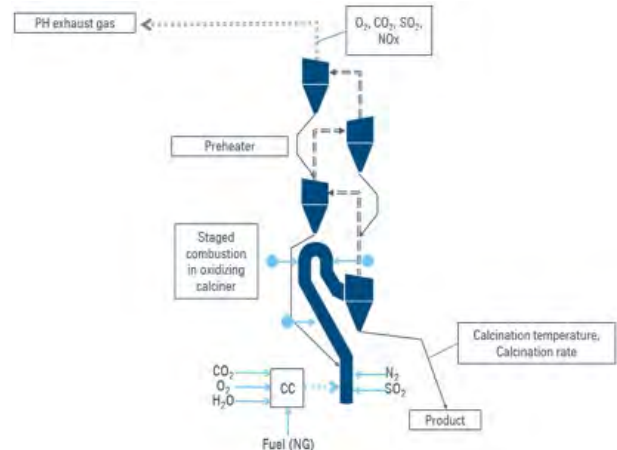


Figure 6: Sketch of the pilot-scale facility of thyssenkrupp Industrial Solutions AG, Germany

Evaluation of oxyfuel calcination process with up to 100 % alternative fuel combustion will be conducted in a 1 MW oxyfuel calciner facility of Air Liquid, Figure 7. The facility is constructed to emulate the conditions of calciners under oxyfuel conditions. The calcination of limestone is simulated thanks to the injection of cold CO₂ and fireclay in the combustion chamber.

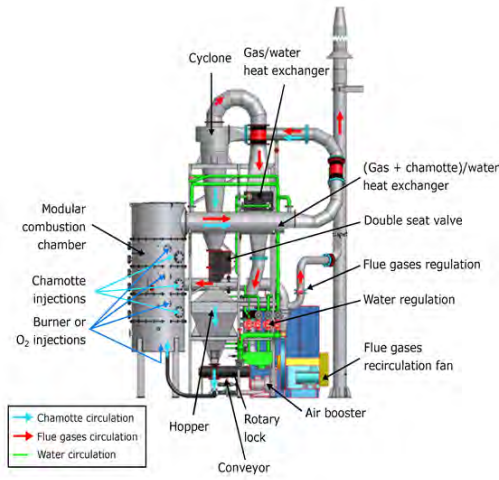


Figure 7: Sketch of the 1 MW calciner facility at Air Liquide, France

4. Integration of oxyfuel technology by retrofitting existing cement plants

4.1 Cement plants for the retrofit examples

The ability for retrofitting 1st generation oxyfuel technology to existing cement plants is evaluated within WP4 of the AC²OCem project. The project partners, HeidelbergCement and LafargeHolcim, have selected their Slite plant in Sweden and the Lägerdorf plant in Germany respectively to serve as design examples. Both plants are operated with a relatively high alternative fuel rate (70-80 %) typical for Northern Europe and therefore represent a realistic case even for the near future. The major difference of the plant is the production process influenced by the given boundary conditions of the plant location. Where the process in Slite is similar to the reference case (as described in the CEMCAP project framework), the Lägerdorf plant is operated in a so-called semi-wet process. The natural raw material from the Lägerdorf quarry shows a high moisture content of about 20 %, which influences the pre-treatment of the material prior to being fed to the burning process.

4.2 Heat integration

All available waste heat from the process has to be supplied to the drying unit (hammer mill flash-dryer), making the heat integration in oxyfuel mode a challenge. Based on the plant specific boundary conditions and taking into account the mass and energy balances performed by combined modelling approaches of SINTEF and VDZ, an optimized oxyfuel design layout has been developed for each plant with the help of the equipment supplier thyssenkrupp. In this development process, the optimal performance in terms of energy use and minimum CO₂ generation, as well as the technological risk mainly due to false air ingress, has been assessed. Usually process waste heat from the flue gas is directly used in the drying unit, which is difficult to seal especially in case of retrofit. As shown in Figure 8 the energy demand of the Lägerdorf plant for drying is significantly higher than of Slite plant (or the CEMCAP reference with 6 % raw material moisture).

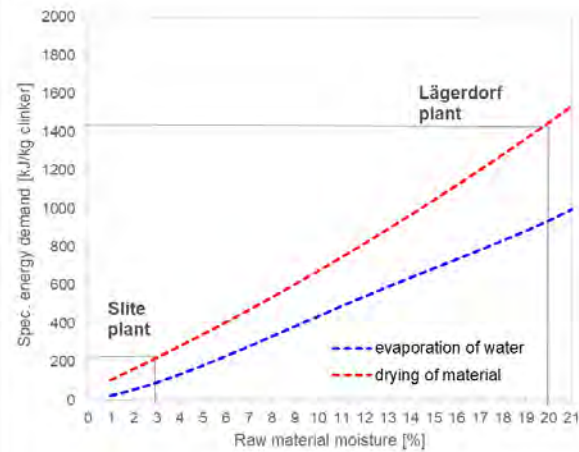


Figure 8: Energy demand for raw material drying for the Slite and Lägerdorf plants

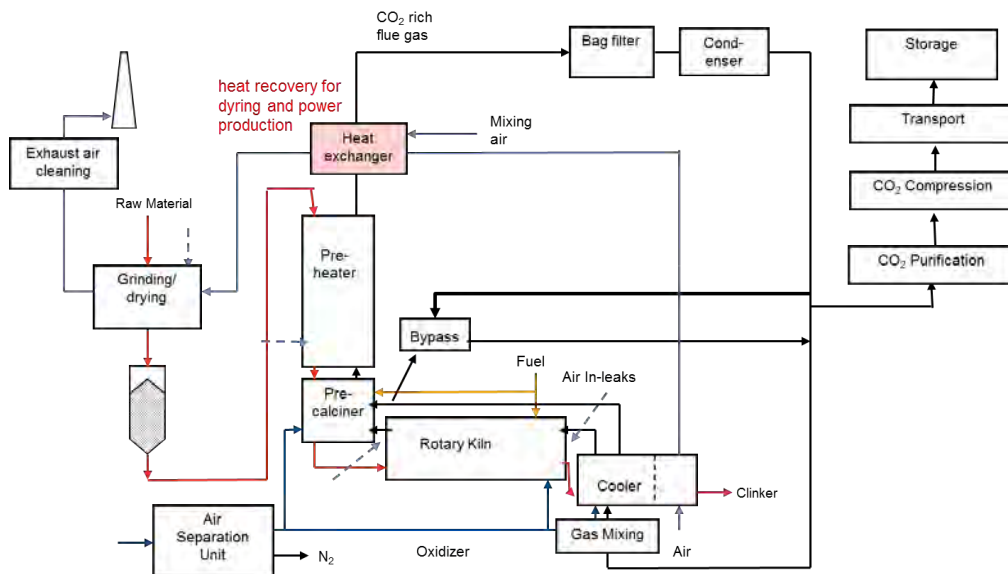


Figure 9: Oxyfuel 1st generation layout for Slite and Lägerdorf plant

The optimal location of the hammer mill dryer in the process layout played an important role. Although the direct integration is energetically reasonable, the operational risk by false air intrusion is high. In order to avoid dilution of the CO₂ and its negative impact on energy demand of the CPU, this layout has not been further developed. The overall energetic evaluation proved that a sophisticated heat exchanger system could provide enough energy (also in terms of gas volume and temperature) to the drying unit. For this reason the following layout has been chosen for both plants (Figure 9). The main technological risk for the Lägerdorf plant arises from the gas/gas heat exchanger installed in the flue gas path under hot (~500 °C) and dust loaded (~100 g/Nm³) conditions. In case of the Slite plant, the high SO_x emissions from the raw material makes an additional scrubber necessary in conventional mode. In which extend this scrubber has to be integrated into the oxyfuel layout is discussed with the supplier of CPU.

4.3 False air ingress

For each oxyfuel process false air intrusion is the major aggressor due to influence on the target of enriching CO₂ to a reasonable level for operating an energy efficient CPU. 6 % false air (related to the total flue gas volume) has been determined as an optimistic and realistic value with regard to sealing the clinker burning process. But it is likely that within the year of kiln operation false air is increased due to wear at the sealings. In case of doubling the false air ingress the CO₂ concentration is reduced from initially 81 vol. % to 71-73 vol. % on dry basis (Figure 10). As a rule of thumb, gas supplier AirLiquide named a change of +/- 2 % spec. energy demand for each +/- 1 percentage point CO₂ dry base concentration for design basis of a CPU. As a CPU is designed for a dedicated operational point (e.g. for a pessimistic CO₂ concentration), false air influences OPEX and CAPEX of the CPU.

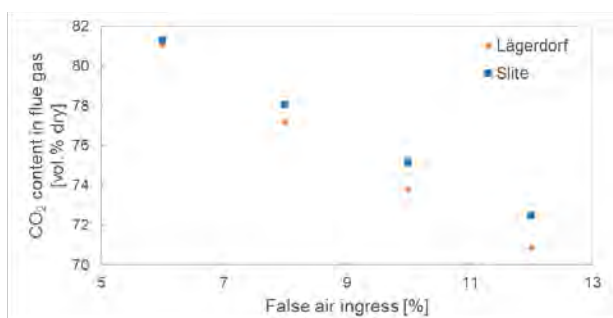


Figure 10: CO₂ concentration in flue gas depending on false air ingress

This again clearly shows the need for sophisticated long-living sealings and a good management for false air detection. Against this background the project partners have developed a guideline document for this purpose, which describes apart from the definitions, typical values, the economic effect and examples for improvement, the methods and techniques to detect false air. The resulting detection strategy (Figure 11) includes the continuous online measurement of O₂ and CO₂ (common UV, IR or paramagnetic measuring) as direct nitrogen measurement is complex and expensive. After

having traced back the intrusion to a certain unit, false air can be further localized by ultrasonic detectors, thermal cameras or absolute pressure measuring devices. After the location of the leak is identified, the maintenance department will need to decide if it can be repaired during operation or if it may require a temporary fix until a kiln stop can be scheduled.

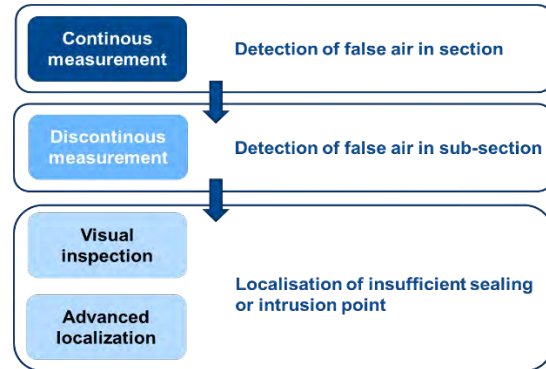


Figure 11: False air detection strategy

4.3 Techno-economic evaluation

A techno-economic evaluation will be performed for integration of oxyfuel technology in the Slite and Lägerdorf plants, where the main performance indicator will be the cost of CO₂ avoided. A bottom-up approach will be used for estimation of CAPEX related to the modifications that have to be done to the plants based on equipment cost estimated with Aspen Process Economic Analyzer® for standard process equipment and estimates from the project's industrial partners and data available in the literature for non-standard equipment. Variable operating costs, which includes fuel and raw material costs, utilities, and other consumables, will be estimated based on the process models developed in the project, while fixed operating costs will be estimated using a factor approach. Based on the analysis of the two plants and the retrofitability study performed in the CEMCAP project [9], a guideline for techno-economic decision-making will be made for retrofitting oxyfuel cement plants.

5. Oxyfuel technology for new-build cement plants

The idea of the 2nd generation oxyfuel layout developed by thyssenkrupp is to avoid the effort for flue gas recirculation with the aim to reduce CAPEX and OPEX costs. A simulation study of VDZ and SINTEF based on a reference plant (described in CEMCAP framework) will evaluate the operational performance of this layout as basis for a comparative techno-economic study to 1st generation oxyfuel. First modelling results using reference conditions showed the significant need of heat integration when using this kind of process to increase the overall use of energy. Potential to improve the SPECCA is feasible by either a change in gas ducting or the integration of a power generation unit. Further calculations will be made with regard to the use of alternative fuels (implying the integration of a bypass system) and its impact on energy efficiency.

6. Life cycle assessment

Life cycle assessment (LCA) is a widely used tool to evaluate the sustainability of a product considering all the production and use stages, e.g. from raw materials extraction to disposal. This method has been largely applied to address the carbon emissions of several cement production technologies, including pre- and post-combustion carbon capture technologies [14]. An unprecedented LCA of oxyfuel retrofitted cement plants will be provided based on realistic operational data. It will be compared with the analysis of a 2nd generation new-build cement plant, considering different production scales. The assessment will also consider the operation of oxyfuel cement plant with high shares of alternative fuels (with substantial shares of biogenic carbon), testing the possibility of reaching negative emissions in the cement production process. The LCA will include not only climate change impacts, but also other categories like non-renewable energy use, human toxicity, ecotoxicity, acidification, particulates and ozone formation. A structural path analysis will be used to identify hotspot stages with increased environmental pressure. Options to improve these pressures, including technology options and pollutants emission minimization and heat recovery measures under consideration in this project, will also be explored in scenario analyses. The quantification of net carbon benefits from decarbonization of the cement industry in Europe from a large-scale deployment of the oxyfuel technology on reducing CO₂ emissions and other environmental impacts will also be performed.

7. Conclusion

The aim of the AC²OCem project is to decarbonize the cement sector, which is a CO₂ intensive industry due to the CO₂ emissions from the calcination and the combustion process. The project focuses on designing and optimizing the oxyfuel combustion technology to promote CCS in existing and new-build plants. The boundary layer information from the Heidelberg Cement plant in Slite and the LafargeHolcim plant in Lägerdorf will allow the project partners to design and optimize layout with oxyfuel technology. The different energy demands for the raw material drying are taken into account and the effect of the false air ingress on the CPU is evaluated. Pilot-scale experiments and CFD simulations are also performed to optimize the combustion of alternative fuels under oxyfuel conditions. Additionally the effect of the oxyfuel technology on the calcination process is studied and the process is optimized. The project also focuses on new-build plants, where the burner technology will be evaluated in pilot-scale experimental set-up and evaluated analytically. An optimized process layout will be designed aiming at reducing the CAPEX and OPEX costs. A techno-economic assessment and life cycle assessment of retrofitted and new-build processes will also be evaluated. In scope of the project, the partners will publish the finding in journals and in the scope of various conferences to increase the public acceptance and knowledge regarding the oxyfuel and CCUS technology.

8. Nomenclature

Symbol	Description
AC ² OCem	Accelerating Carbon Capture using Oxyfuel technology in Cement production
ACT	Accelerating CCS Technologies
CAPEX	Capital costs
CCS	Carbon Capture and Storage
CCUS	Carbon Capture Utilization and Storage
CEMCAP	CO ₂ capture from cement production
CFD	Computational Fluid Dynamics
CPU	CO ₂ purification unit
ECRA	European Cement Research Academy
IEA	International Energy Agency
IRENA	European Cement Research Academy
LCA	Life Cycle Assessment
MEA	Monoethanolamine
OPEX	Operating costs
SRF	Solid Recovered Fuel
TRL	Technology readiness level
WP	Work package

Acknowledgements

This research is executed in scope of the AC²OCem project which is funded through the ACT program (Accelerating CCS Technologies, Horizon2020 Project No 299663).

Financial contributions are made from; The Research Council of Norway, (RCN), Norway, Federal Ministry for Economic Affairs and Energy (BMWi), Germany, Swiss Federal Office of Energy (SFOE), Switzerland, General Secretariat for Research and Development (GSRT), Greece and French Environment & Energy Management Agency (ADEME), France.



References

- [1] International Energy Agency- IEA. The Future of Hydrogen.
- [2] Frauke Schorch, Ioanna Kourti, Bianca Maria Scalet, Serge Roudier, Luis Delgado Sancho. Best Available Techniques (BAT) Reference Document for the Production of Cement, Lime and Magnesium Oxide: Industrial Emissions Directive 2010/75/EU (Integrated Pollution Prevention and Control).

- [3] © OECD/IEA and IRENA. Perspectives for the Energy Transition - Investment needs for a low-carbon energy system 2017.
- [4] IEA. Transforming Industry through CCUS. All rights reserved; 2019.
- [5] Fuel Cells and Hydrogen 2 Joint Undertaking. Hydrogen Roadmap Europe: A Sustainable Pathway for the European Energy Transition; 2019.
- [6] IEAGHG. Deployment of CCS in the Cement Industry; 2013.
- [7] ECRA. CCS Project - Report on Phase III: Technical Report; 2012.
- [8] Gardarsdottir S, Lena E de, Romano M, Roussanaly S, Voldsund M, Pérez-Calvo J-F et al. Comparison of Technologies for CO₂ Capture from Cement Production—Part 2: Cost Analysis. *Energies* 2019;12(3):542.
- [9] Voldsund M, Gardarsdottir S, Lena E de, Pérez-Calvo J-F, Jamali A, Berstad D et al. Comparison of Technologies for CO₂ Capture from Cement Production—Part 1: Technical Evaluation. *Energies* 2019;12(3):559.
- [10] Carrasco F, Grathwohl S, Maier J, Ruppert J, Scheffknecht G. Experimental investigations of oxyfuel burner for cement production application. *Fuel* 2019;236:608–14.
- [11] Toftegaard MB, Brix J, Jensen PA, Glarborg P, Jensen AD. Oxy-fuel combustion of solid fuels. *Progress in Energy and Combustion Science* 2010;36(5):581–625.
- [12] Bhupesh Dhungel. Experimental Investigations on Combustion and Emission Behaviour during Oxy-Coal Combustion. Doctorate. Germany; 2010.
- [13] Eric Croiset, Kelly Thambimuthu, Allan Palmer. Coal combustion in O₂/CO₂ mixtures compared with air. *The Canadian Journal of Chemical Engineering* 2000;78(2):402–7.
- [14] Rolfe, A., Huang, Y., Haaf, M., Pita, A., Rezvani, S., Dave, A., & Hewitt, N. J. (2018). Technical and environmental study of calcium carbonate looping versus oxy-fuel options for low CO₂ emission cement plants. *International Journal of Greenhouse Gas Control*, 75, 85-97.

DESIGN AND MULTI-OBJECTIVE OPTIMIZATION OF CO₂ VALUE CHAINS FOR A NET-NEGATIVE WASTE TO ENERGY SECTOR: A SWISS CASE STUDY

Paolo Gabrielli¹, Viola Becattini¹, Alberto Acquilino², Cristina Antonini¹, Jordi Campos Schweitzer¹, Giovanni Sansavini^{1,*}, Marco Mazzotti^{1,*}

¹Institute of Energy and Process Engineering, ETH Zurich, 8092 Zurich, Switzerland

²Music Technology, Schulich School of Music, McGill University, Montreal, Canada

* Corresponding authors e-mail: sansavig@ethz.ch, marco.mazzotti@ipe.mavt.ethz.ch

Abstract

This study investigates the optimal design of CO₂ value chains aimed at decarbonizing the waste to energy (WtE) sector on a national scale and presents the case study of Switzerland. Switzerland has 30 WtE plants that generate a total of 4.2 million tons of CO₂ emissions per year. Half of these emissions are from biogenic sources and half are fossil-based, corresponding to 4.5% of the overall Swiss emissions. On the one hand, this indicates the relevance of decarbonizing the WtE sector. On the other hand, it implies that a net-negative-emissions WtE sector can be achieved by adopting carbon capture and storage (CCS) technologies.

The CO₂ value chains considered here consist in capturing CO₂ at the WtE production sites, transporting it to the storage site, and permanently storing it underground. An optimization problem is formulated to determine the optimal design of the CO₂ value chains in terms of size and location of carbon capture technologies, and structure of the network transporting the CO₂ from the capture to the storage sites. The optimization algorithm is a mixed integer linear program that minimizes the total annual cost and CO₂ emissions of the overall system. Several transport options are assessed, namely truck, train, pipeline and ship, as well as different transport paths.

Keywords: CO₂ value chain; CO₂ network; waste-to-energy; net-negative emissions; industrial emissions; optimization.

1. Introduction

Evidences that the anthropogenic alteration of the earth carbon balance is leading to climate change clearly indicate the necessity of finding new routes for energy provision to achieve no-carbon emission by 2050 and keep global warming below 1.5 °C [1]. Within this framework, carbon capture and storage (CCS) proved to be a fundamental technology to achieve net-zero emissions in “hard-to-decarbonize” industrial sectors, such as the cement, steel and chemical industries. At the same time, CCS allows achieving net-negative emissions in sectors such as waste-to-energy (WtE), when energy is produced starting from biogenic waste.

Unlocking this CCS potential relies on the creation of a shared CO₂ infrastructure to connect the emission sources to the CO₂ permanent storage sites, thus decreasing the risk of investment and providing low-cost mitigation measures. In addition to the CO₂ emissions sources and permanent storage sites, the key component of these CO₂ ecosystems will be the CO₂ transport network. Currently, several European CCS projects are focused on building CO₂ storage hubs and clusters in various locations across Europe (e.g., in Norway, in the Netherlands, and in the UK). Among these, the Northern Lights project will most likely be the first one to enter into the operational phase, targeted for 2024-2025, and

will make CO₂ storage available to emitters from coastal and central Europe.

The CO₂ transport network may rely on different transportation modes. Nowadays, pipelines are the most common CO₂ transport mode. They are a mature technology that has been in operations since the early 1970s for enhanced oil recovery applications. In some locations, CO₂ transport by ship or barge may be an economically attractive alternative to pipelines. For example, in the perspective of a permanent storage site in the North Sea (in Norway, Netherlands or UK), water transport may be preferred, not only by coastal CO₂ emitters in Northern Europe, but also by those emitters located in the proximity of the Rhine axis that links the largest European seaports to their hinterland. For small CO₂ volumes, road and rail tankers are also viable options. In particular, in the short term and at an early stage of development of a CO₂ network, the use of insulated tankers that can be loaded onto trucks or rails seem the most feasible choice. It becomes evident that developing an optimal network design will be a key challenge to create a mature CCS industry [2].

Switzerland has 30 WtE plants that generate a total of 4.2 million tons of CO₂ emissions per year. Half of these emissions are from biogenic sources and half are fossil-based, corresponding to 4.5% of the overall Swiss

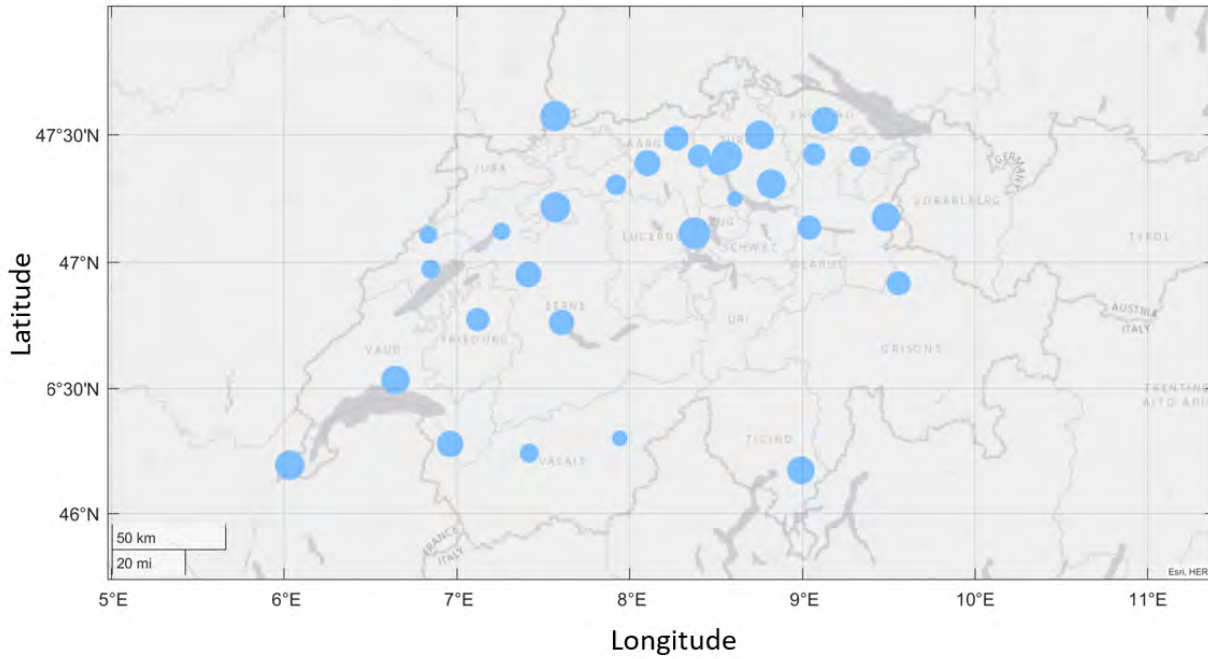


Figure 1. Schematic representation of the location of the Swiss WtE plants.

emissions. On the one hand, this indicates the relevance of decarbonizing the WtE sector. On the other hand, it implies that a net-negative-emissions WtE sector can be achieved with CCS technologies. Focusing on such a Swiss case study, this study investigates the optimal design of CO₂ value chains aimed at decarbonizing the WtE sector on a national scale.

2. System description

The CO₂ network considered here entails capturing CO₂ at the 30 Swiss WtE production sites, transporting it to the storage site, and permanently storing it underground. We evaluate the feasibility of transporting the CO₂ captured from the Swiss WtE plants to a storage site in the North Sea (i.e., the Northern Lights project off the Norwegian shore) via a continental terminal located in the port of Rotterdam, in The Netherlands.

The system components include:

- (i) The CO₂ capture sites corresponding to the WtE plants, see Figure 1. An amine-based technology with 90% capture rate and several fractions of exhaust gases treated are considered.
- (ii) The Northern Lights CO₂ storage site, where the CO₂ is permanently stored underground;
- (iii) The CO₂ transport network that consists of CO₂ paths from capture sites to the permanent storage site. The transport technologies considered in this work are truck, rail, ship, barges and pipelines. Here, we consider a brownfield design for pipelines, i.e., we force the CO₂ pipelines to follow the same route of the installed natural gas pipelines.

Our work aims at defining the *optimal* CO₂ value chain in terms of size and location of CO₂ capture technologies,

type and size of CO₂ network connections between all nodes.

3. Optimization problem

The optimal design of the CO₂ value chain is tackled by formulating and solving an optimization problem that minimizes the total annual cost and CO₂ emissions of the system by determining the optimal size and location of CO₂ capture technologies, as well as the optimal structure of the CO₂ network. Such an optimization problem is formulated as a mixed-integer linear program (MILP), which include both continuous, x , and binary variables, y , and can be written in general form as:

$$\min_{x,y} (c_1^T x + c_2^T y)$$

s.t.

$$A_1 x = b_1, \quad A_2 y = b_2$$

$$x \geq 0 \in \mathbb{R}^X, \quad y \in \{0, 1\}^Y$$

where c_1 and c_2 represent the cost vectors associated to the continuous and binary decision variables, x and y , respectively; A_1 and A_2 are the corresponding constraint matrices, and b_1 and b_2 the corresponding constraint known terms; X and Y indicate the dimensions of the vectors x and y , respectively. Here, both continuous and binary variables are optimized, with the latter being introduced to model the nonlinearities related to the presence and to the costs of network connections. The optimization problem is based on mathematical tools presented earlier [3,4,5], which are here expanded to describe all relevant features of CO₂ networks.

The input data to the optimization problem are (i) the CO₂ emissions corresponding to the WtE plants (spatially distributed), (ii) the availability of technology and

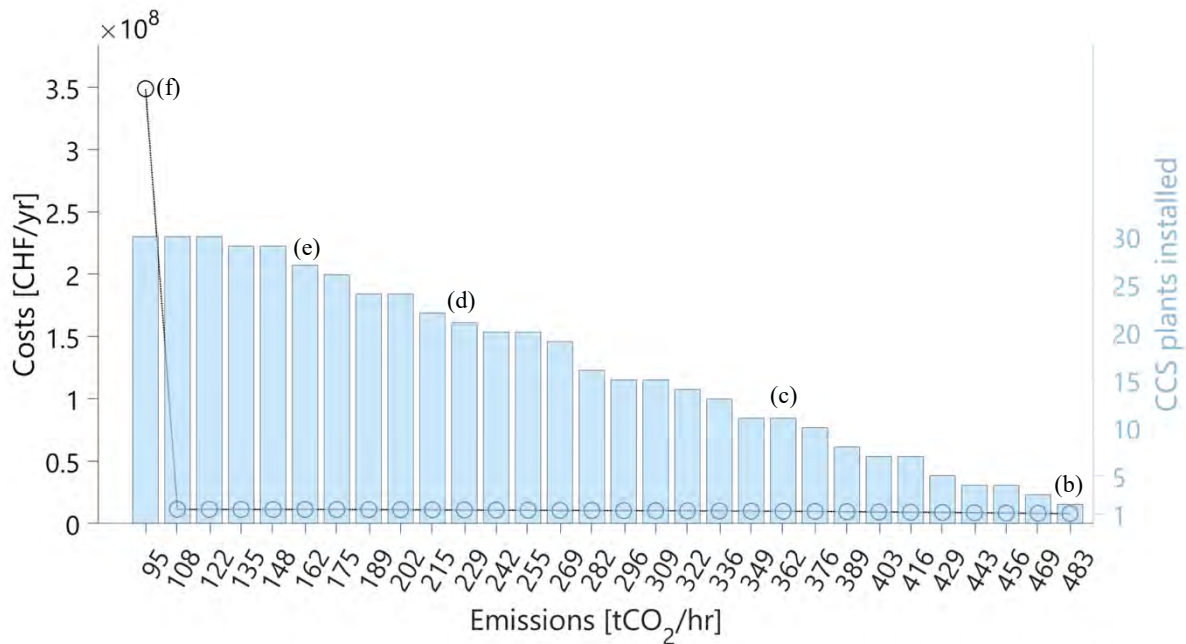


Figure 2. Cost-emissions Pareto front and number of installed capture plants as a function of total CO₂ emissions of the system.

network options (including the availability of CO₂ storage sites), (iii) the parameters defining cost and performance of the CO₂ capture and network technologies, (iv) the parameters describing the system configuration.

Based on such input data, the optimization problem determines (i) the selection and size of capture and network technologies, (ii) the CO₂ flow through network technologies, (iii) the energy required to compress and liquefy CO₂ after capture and to transport it.

The optimal solution must comply with mass and energy balances, as well as with the models of the capture and network technologies.

The optimization algorithm minimizes the total annual cost (capital, maintenance, and operational costs) and the total annual CO₂ emissions. This translates in a multi-objective optimization problem, which is solved through the ϵ -constraint method proposed by Mavrotas [8], where the cost is minimized for fixed values of CO₂ emissions.

3. Preliminary results and discussion

Figure 2 shows the cost-emissions Pareto front of the CO₂ value chains for the Swiss WtE plants, and reports the number of capture units installed (right-hand side) along the Pareto front. Two main observations can be made. First, costs and emissions cannot be minimized simultaneously, and a trade-off emerges from these two variables. As the number of capture plants installed, hence the costs, increase, the total emissions decrease. Second, the achievement of the lowest level of emissions (i.e., 95 tCO₂/h) requires a more than threefold increase in costs for only a 12% reduction in emissions. These trends can be further explored by considering the network design emerging for different points along the Pareto front.

Figures 3 and 4 show the CO₂ network design obtained for different points along the Pareto front. Moving towards lower emissions, not only the number of installed capture unit increases but the CO₂ network shifts to transport modes with lower carbon footprint. Case (a) corresponds to the maximum emissions scenario, i.e., no capture plants are installed and there are no costs associated. Designs (b), (c), and (d) mostly rely on train transport from the WtE plants to the Rotterdam terminal, from where CO₂ is transported via ship to the Northern Lights storage facilities. For those emitters without a train connection, transport of CO₂ by truck to the nearest train station is found to be the most viable solution. It can be noted how the model chooses to install first (i.e., for lower costs) capture units at plants that are geographically closer to the Northern Lights storage. In addition, capture units are preferably installed at sites with larger emissions, in order to optimize costs per amount of CO₂ transported. For a further reduction of total emissions (design (e)), the model opts for installing truck connections between the WtE plants and the Swiss terminal corresponding to Basel, from where the CO₂ is transported via barge along the Rhine until Rotterdam, and again by ship to Northern Lights. Barge-based transport, having a smaller carbon footprint than train transport, allows lowering the total emissions and, at the same time, adopting a cheaper transport solution, i.e., truck, at the national level.

Finally, the most stringent emissions reduction level (i.e., total emissions of 95 tCO₂/h) is achieved not by installing additional capture units, but by adopting pipelines as the main CO₂ transport mode, at the national and international level (design (f)). Nevertheless, even in this case few connections within Switzerland are forced to adopt truck or train transport due to the limitations on pipeline construction.

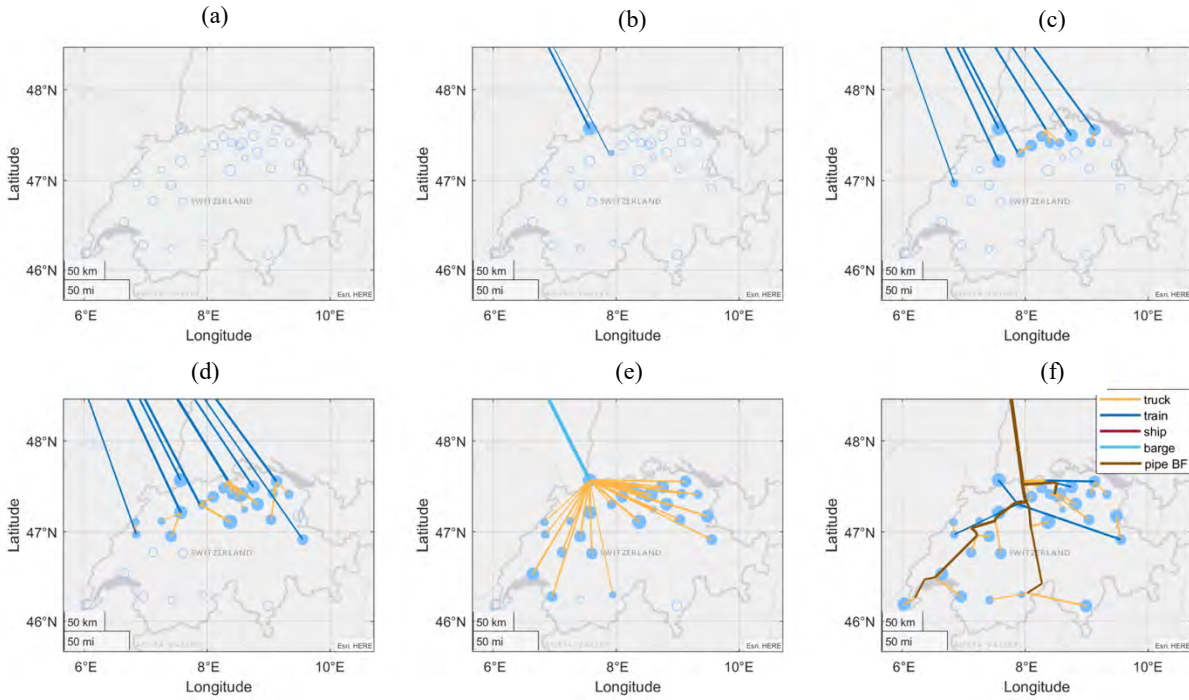


Figure 4. CO₂ network design for different points along the Pareto front (focus on Swiss national network).

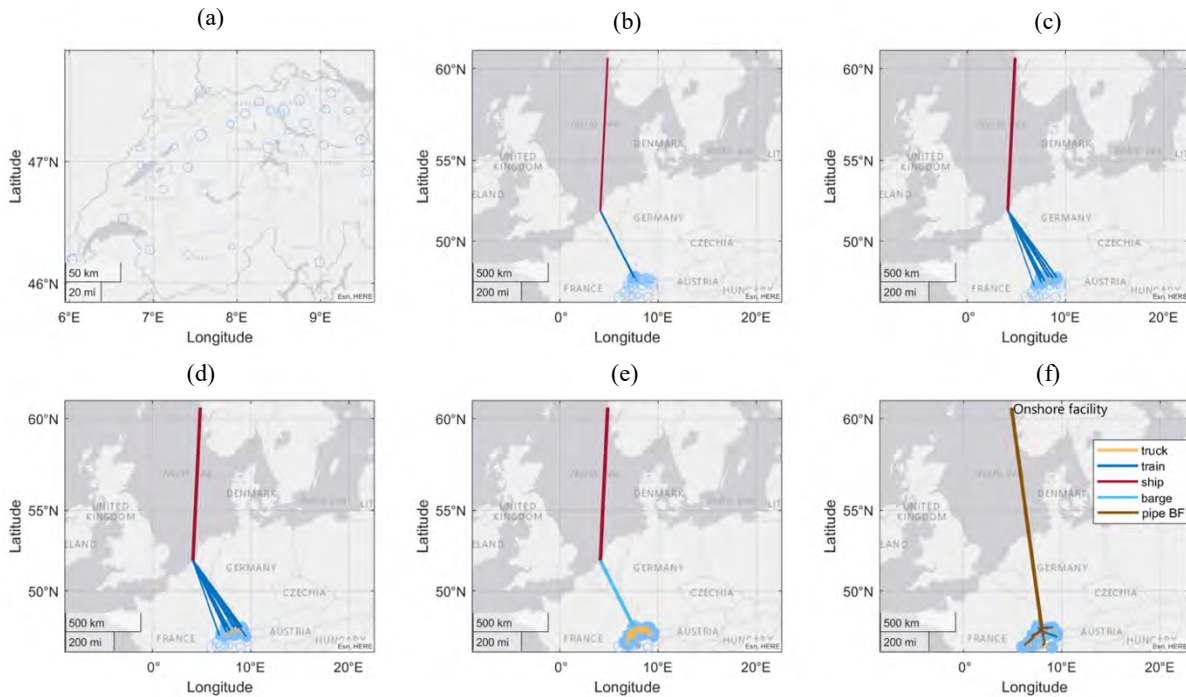


Figure 3. CO₂ network design for different points along the Pareto front (overview on international connection).

4. Conclusions

This work investigates the optimal design of CO₂ value chains aimed at decarbonizing the Swiss waste to energy sector, which comprises 30 WtE plants generating a total of 4.2 million tons of CO₂ emissions per year. The CO₂ value chains considered here consist in capturing CO₂ at the WtE production sites, transporting it to the storage site, and permanently storing it underground. An optimization problem is formulated to determine the optimal design of the CO₂ value chains in terms of size

and location of carbon capture technologies, and structure of the network transporting the CO₂ from the capture to the storage sites. Several transport options are assessed, namely truck, train, pipeline and ship, as well as different transport paths.

Acknowledgments

The authors are grateful to Marija Spokaite and Petrisa Eckle for the support and helpful discussion.

References

- [1] Masson-Delmotte V, Zhai P, Pörtner HO, Roberts D, Skea J, Shukla PR, Pirani A, Moufouma-Okia W, Péan C, Pidcock R, Connors S. Global warming of 1.5 C. An IPCC Special Report on the impacts of global warming of. 2018 Oct 8;1:1-9.
- [2] Wei YM, Kang JN, Liu LC, Li Q, Wang PT, Hou JJ, Liang QM, Liao H, Huang SF, Yu B. A proposed global layout of carbon capture and storage in line with a 2° C climate target. *Nature Climate Change*. 2021 Jan 4:1-7.
- [3] P. Gabrielli, M. Gazzani, E. Martelli, and M. Mazzotti, “Optimal design of multi-energy systems with seasonal storage,” *Appl. Energy*, vol. 219, pp. 408–424, 2018.
- [4] P. Gabrielli, F. Charbonnier, A. Guidolin, and M. Mazzotti, “Enabling low-carbon hydrogen supply chains through use of biomass and carbon capture and storage: A Swiss case study,” *Submitted*, 2019.
- [5] Gabrielli P, Poluzzi A, Kramer GJ, Spiers C, Mazzotti M, Gazzani M. Seasonal energy storage for zero-emissions multi-energy systems via underground hydrogen storage. *Renewable and Sustainable Energy Reviews*. 2020 Apr 1;121:109629.
- [6] Mavrotas G. Effective implementation of the ϵ -constraint method in multi-objective mathematical programming problems. *Applied mathematics and computation*. 2009 Jul 15;213(2):455-65.

THE ROLE OF CARBON CAPTURE, STORAGE AND UTILIZATION TO ENABLE A NET-ZERO-CO₂-EMISSIONS AVIATION SECTOR

Viola Becattini, Paolo Gabrielli, Marco Mazzotti*

Institute of Energy and Process Engineering, ETH Zurich, 8092 Zurich, Switzerland

* Corresponding author e-mail: marco.mazzotti@ipe.mavt.ethz.ch

Abstract

This contribution presents a techno-economic analysis of feasible pathways for the aviation industry to achieve net-zero CO₂ emissions. These pathways are based (i) on carbon capture and storage (CCS), where conventional fossil jet fuel is produced and the corresponding emissions are offset by capturing CO₂, either via direct air capture (DAC-CCS route) or via point-source capture (PSC-CCS route), and permanently storing it underground; and (ii) on carbon capture and utilization (CCU), where synthetic jet fuel is produced by using CO₂ as feedstock, which is either captured from air (DAC-CCU route) or from a point-source emitter (PSC-CCU route). To ensure net-zero CO₂ emissions, the feedstock of the point-source emitter, both for CCS- and CCU-based routes, must be of biogenic nature. A comparative quantitative assessment of these scenarios and of a business-as-usual (BAU) scenario, where aviation emissions are subjected to a carbon tax, is performed based on jet fuel cost and carbon price projections until 2050. Cost reductions due to economy of scale of current low-maturity technologies are accounted for. An uncertainty analysis based on Monte Carlo simulations is performed to assess the effects of the uncertainty associated with the most relevant techno-economic quantities on the observed trends. Findings show that CCS-based scenarios consistently lead to lower jet fuel costs than CCU-based scenarios across the considered time scenarios and sensitivity analyses. This is mainly due to the fact that CCU-based routes result in an energy consumption more than 20 times higher than CCS-based routes, which also implies higher CO₂ emissions when considering the carbon intensity of current electricity grids. Overall, the PSC-CCS route represents the most cost-effective solution for decarbonizing the aviation industry and it is cost-competitive with BAU already today.

Keywords: aviation; net-zero emissions; carbon capture and storage; carbon utilization; renewable fuels.

1. Introduction

According to the Intergovernmental Panel on Climate Change (IPCC) scenarios, limiting global warming to 1.5°C implies reaching net-zero CO₂ emissions globally around 2050 [1]. To achieve this target, all anthropogenic emissions should be reduced as much as possible, with the remaining unavoidable fraction being balanced by an equivalent amount of carbon removal. The mobility sector, and especially the air transport sector, will face critical decarbonization challenges due to the limited availability of mitigation strategies (e.g., low-carbon fuels, aircraft energy efficiency, operational efficiency, etc.) and to the higher demand growth with respect to other transport modes [1].

Although alternative jet fuels (JF) and direct air capture (DAC) combined with permanent CO₂ storage emerge as promising strategies to achieve carbon-neutral aviation, their high costs are hindering their commercial deployment [2, 3]. The goal of this work is to provide a quantitative assessment of the current and future projected costs of possible strategies based on carbon capture, storage and utilization to decarbonize the aviation industry, and to compare them to the business-as-usual (BAU) solution. We follow a similar approach adopted in a recent paper on the role of CCS and CCU to enable a net-zero chemical industry [4], but we expand

the focus of that work to include a full techno-economic performance analysis [5].

2. Scope of the work

Five scenarios are investigated. The BAU scenario (1) is based on the use of conventional fossil JF and relies on the extraction of crude oil. Since this results in CO₂-positive emissions, we consider these to be subjected to the payment of a carbon tax. The next four scenarios considered achieve net-zero CO₂ emissions through carbon capture and storage (CCS) or carbon capture and utilization (CCU) technologies, under the assumption that the processes are powered by carbon-free electricity, e.g., coming from carbon-free solar or wind. Scenarios (2) and (3) are based on Direct Air Capture (DAC), while scenarios (4) and (5) are based on Point-Source Capture (PSC). The DAC-CCS scenario (2) is still based on the use of fossil JF, but the corresponding CO₂ emissions are offset by CO₂ removal from the atmosphere through DAC and subsequent permanent storage. In the DAC-CCU scenario (3), carbon-neutral synthetic fuels are produced via Fischer-Tropsch reaction from CO₂ provided by DAC and H₂ supplied by water electrolysis. The PSC-CCS (4) and PSC-CCU (5) scenarios are symmetrical to scenarios (2) and (3), respectively, but they make use of biogenic CO₂ captured at a point-source emitter. Such an emitter may be a waste-to-energy (WtE) plant producing heat and electricity through the

incineration of waste, where around 60% of the carbon contained in waste is biogenic.

The five scenarios are broken down into their corresponding technology routes, for which current costs are estimated based on available data. Future costs of low-TRL (Technology Readiness Level) technologies (i.e., water electrolysis, CO₂ electrochemical reduction, DAC, and PSC) are projected using learning curves, while trends in carbon prices are taken from literature [1]. The functional unit for the comparison is the synthesis and use of one tonne or liter of jet fuel (conventional or synthetic) with costs estimated from today to 2050.

3. Comparative assessment: current costs

Estimates of the current JF cost and of the total electricity consumption for the five aforementioned scenarios are summarized in Table 1. It is worth noting that the JF cost estimated for the BAU scenario includes the payment of a carbon tax. The CCU-based scenarios result in the highest cost and electricity input as they mostly rely on low-TRL, expensive, and energy-intensive technologies, i.e., water electrolysis and electrochemical conversion of CO₂. As expected, the lower cost of PSC with respect to DAC leads to a lower jet fuel cost for the PSC-based technology routes. In particular, the PSC-CCS scenario may be already cost competitive with BAU today.

Table 1. Current jet fuel cost estimated for the five aviation scenarios and corresponding electricity input.

	JF cost		Electricity input
	[€/t]	[€/L]	[MWh _e /tJF]
BAU	670	0.53	-
DAC-CCS	2320	1.86	2
DAC-CCU	6610	4.89	50
PSC-CCS	750	0.60	-
PSC-CCU	3750	2.77	48

It should be noted that the investigated technology routes result in net-zero CO₂ emissions when considering carbon-free electricity to supply the energy required by the JF production processes and by the CO₂ capture technologies. However, operating the technology chains with currently available electricity would result in positive values of the CO₂ emissions. This is illustrated in Figure 1, which shows the amount of CO₂ emitted per unit JF as a function of the carbon intensity of the available electricity.

The BAU scenario results in about 3 tCO₂/tJF and is nearly independent of the electricity mix, since the largest share of CO₂ emissions is due to the use of fossil carbon to produce and use JF, whereas the electricity required for the production process plays a negligible role. In contrast, the CO₂ emissions of the other scenarios increase with the electricity carbon intensity, with those of CCU-based scenarios growing about 22 to 24 times faster than those of CCS-based scenarios. This is proportional to the larger electricity consumption of the CCU scenarios, which is mostly due to the electricity required to produce hydrogen and to convert CO₂ into CO.

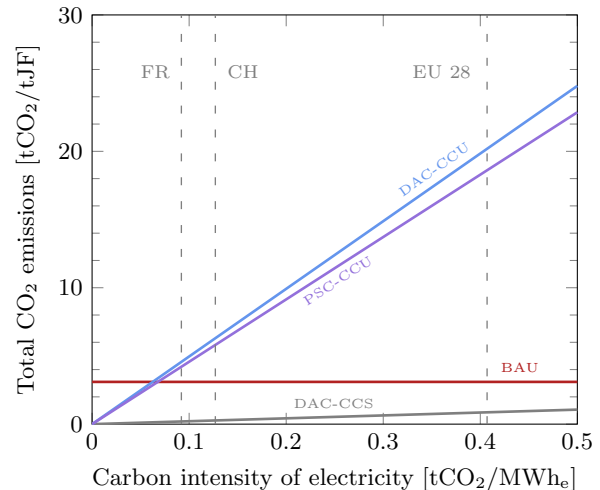


Figure 1. Total CO₂ emissions for the BAU (red), DAC-CCS (gray), DAC-CCU (blue), and PSC-CCU (purple) routes as function of the carbon intensity of electricity.

As an example, consider the electricity mixes of France (Fr, 0.09 tCO₂/MWh_e), Switzerland (CH, 0.13 tCO₂/MWh_e), and the average European Union (EU-28, 0.41 tCO₂/MWh_e). The CCU-based scenarios emit about 4, 6, and 18 t of CO₂ more than the CCS-based ones per tonne of produced JF (average of -PSC and -DAC routes), and more than the BAU case even for such low-carbon electricity grids as those of France and Switzerland.

For both CCS and CCU scenarios, the CO₂ emissions are higher when adopting DAC than PSC, due to the higher efficiency in capturing CO₂ from concentrated sources versus capturing it from air, hence to the larger electricity requirements of DAC compared to PSC.

4. Comparative assessment: future forecasts

Ranges of JF cost are estimated for several scenarios from 2020 to 2050. On the one hand, such scenarios consider the potential cost reductions for low-maturity technologies through learning-by-doing (i.e., DAC, PSC, H₂ production through water electrolysis, and CO₂ electrochemical conversion); on the other hand, possible future evolutions (increase) of the carbon price are accounted for.

Figure 2 illustrates the future projections of JF cost for the considered scenarios. The shaded areas represent computed ranges, while the solid lines represent the mid-range values of JF cost estimated for each scenario.

Different factors determine the lower and upper bounds of JF cost for the different scenarios.

- BAU. The lower and upper bounds correspond to the extreme trends assumed for the carbon tax, namely to the 1.5°C high OS and to the Below 1.5°C pathways, respectively, of the IPCC report [1].
- Net-zero scenarios. The lower and upper bounds correspond to the maximum and minimum learning rates assumed for estimating the cost reductions of low-TRL technologies.

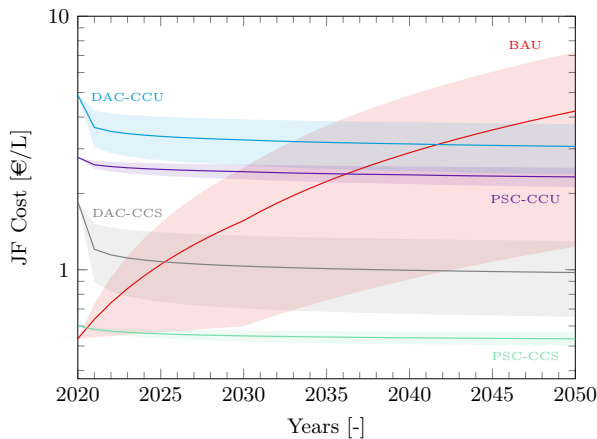


Figure 2. Cost ranges (shaded areas) and mid-range values (solid lines) of JF cost estimated for all scenarios from 2020 to 2050.

Various considerations can be made when comparing the different scenarios.

- CCS-based scenarios lead to lower JF costs than CCU-based ones across the entire time horizon, independently of the considered learning rates.
- Technology chains based on PSC result in lower JF costs and narrower cost ranges than those based on DAC. The lower JF costs are due to the lower capture cost of PSC with respect to DAC; the narrower cost ranges are because PSC is a more mature technology than DAC, hence relies less on future learning rates.
- Overall, PSC-CCS (green shaded region) represents the most cost-effective solution for a net-zero aviation going towards 2050. It is cost competitive with BAU already today, independently of the considered carbon tax evolution and learning rates.
- DAC-CCS will become cost competitive with BAU before 2035 provided that high learning rates are experienced. The higher the carbon tax, the earlier DAC-CCS becomes competitive.
- In case of high carbon taxes, CCU-based solutions become cost-competitive with BAU around 2030. The higher the carbon tax and the learning rates, the earlier CCU becomes competitive.

5. Monte Carlo analysis

Finally, we further discuss the uncertainty associated with our assumptions through a Monte Carlo analysis, which allows to determine the probability distributions associated with the JF costs of all scenarios.

The following quantities are randomly sampled between $\pm 20\%$ of their reference values: (i) the initial cost of DAC, hydrogen production, CO₂ conversion and PSC; (ii) the production cost of fossil jet fuel; (iii) the levelized cost of electricity (LCOE); (iv) the revenue resulting from the sale of diesel; and (v) the CO₂ transport and storage costs.

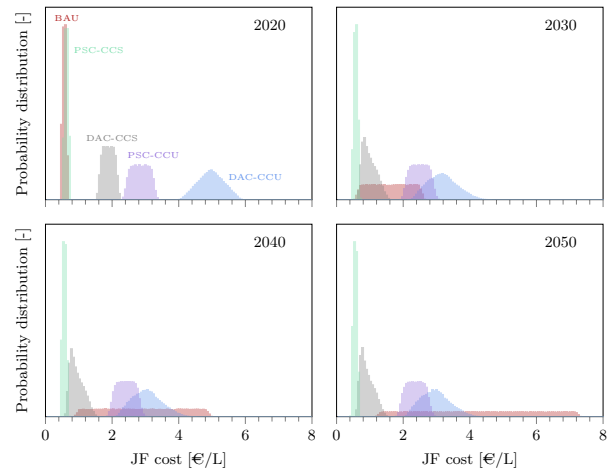


Figure 3. Probability distribution of JF cost obtained via Monte Carlo analysis for all scenarios, for years 2020, 2030, 2040 and 2050.

The carbon price during each year is randomly sampled within the range determined by the 1.5 °C high OS and the Below 1.5 °C curves [1]. The learning rate is randomly sampled between 5% and 20% and it is allowed to be different for each technology. All parameters are sampled according to a uniform distribution. Based on these, the probability distributions of JF cost for all scenarios are calculated from 2020 to 2050.

Findings are presented in Figure 3, which shows that the trends obtained for the baseline assessment, as well as considerations made in Section 4, are not significantly affected by the uncertainty and variability in the input quantities. This means that CCS-based technology routes represent the most cost-effective solutions (with PSC-CCS competing with BAU already today), and that PSC has an economic advantage over DAC.

Looking at the cost distribution, in 2020 the only scenario enabling a net-zero-CO₂-emissions aviation industry while being cost-competitive with BAU is PSC-CCS (mean JF cost of about 0.6 EUR/L).

By 2030, PSC-CCS becomes the most convenient route, DAC-CCS (mean JF cost of about 0.9 EUR/L) becomes on average more convenient than BAU, and PSC-CCU (mean JF cost of about 2.4 EUR/L) starts getting close to BAU.

From 2040 onward, all technology routes start being on average more cost-effective than BAU, whose cost increases due to the increasing carbon price.

Overall, while the cost distributions of the net-zero-CO₂-emissions scenarios maintain a similar width from 2020 to 2050 (and exhibit a slightly positive skewness), the cost distribution of BAU becomes remarkably wider because of the uncertainty associated with future values of carbon price (and it can be approximated by a uniform distribution).

6. Conclusions

This work defines, analyzes and compares possible scenarios to achieve a net-zero-CO₂-emissions aviation sector. These scenarios are based on (i) carbon capture and storage (CCS), where fossil jet fuel is produced and the corresponding emissions are offset by capturing CO₂, either from the air (DAC-CCS route) or from a point-source emitter (PSC-CCS route), and permanently storing it underground, and (ii) carbon capture and utilization (CCU), where synthetic jet fuel is produced by using CO₂ as feedstock, which is either captured from air (DAC-CCU route) or from a point-source emitter (PSC-CCU route).

A quantitative comparative assessment of these scenarios with a business-as-usual (BAU) scenario where negative externalities are subjected to an aviation carbon tax, is provided through estimates of jet fuel cost from today to 2050. The future cost of low-TRL technologies, such as DAC, hydrogen production, CO₂ conversion and PSC technologies, is estimated through learning curves. The analysis leads to the following conclusions:

1. A net-zero-CO₂-emissions aviation industry is possible, and can be accomplished by following the CCS and CCU scenarios discussed and assessed in this work. All scenarios are feasible and lead to net-zero CO₂ emissions under specific conditions, namely when considering carbon-free electricity to power the jet fuel production and the carbon capture processes.
2. A thorough assessment of the pros and cons of different technology routes requires a systemic analysis that (i) considers the key technical features of all involved technologies, (ii) covers the cost evaluation of the entire technology routes, (iii) accounts for the uncertainties associated with the quantities of interest.
3. General considerations, independent of such uncertainties, can be made concerning the techno-economic assessment of the technology routes.

Overall, CCS-based routes result in an electricity consumption (with heat requirements also met by using electricity) more than 20 times smaller than CCU-based routes. This implies that, when considering increasing levels of the carbon intensity of electricity production, the CO₂ emissions of the CCU routes grow about 20 times faster than those of the CCS routes. Besides they are above BAU emission levels for a carbon intensity of electricity above circa 0.07 tCO₂/MWh_e (for reference, France energy mix corresponds to about 0.1 tCO₂/MWh_e).

Furthermore, the smaller electricity consumption and the simpler jet fuel production processes of the CCS routes lead to lower jet fuel costs and to a smaller impact of the uncertainty associated with the future deployment of low-TRL technologies.

In fact, the CCS-PSC route is cost-competitive with BAU already today and technology-ready for wide deployment.

4. The transition to a net-zero-CO₂-emissions aviation industry based on CCS can be driven by carbon prices in the order of only 70-100 EUR/tCO₂, whereas the impact of electricity prices is limited (negligible in the case of PSC). In contrast, the transition to a CCU industry requires much higher carbon prices and/or a large increase in the availability of low cost carbon-free electricity.
5. A deep decarbonization of the aviation sector will most likely depend on a mix of different mitigation measures as there is no silver bullet for reaching this goal. In any case, it is becoming more and more evident that carbon capture, storage and utilization will be key in achieving net-zero CO₂ emissions.

References

- [1] J. Rogelj, D. Shindell, K. Jiang, S. Fifita, P. Forster, V. Ginzburg, C. Handa, H. Kheshgi, S. Kobayashi, E. Kriegler, L. Mundaca, R. Séférian and M. Vilarinho, "Mitigation Pathways Compatible with 1.5°C in the Context of Sustainable," in *Global Warming of 1.5°C. An IPCC Special Report on the impacts of global warming of 1.5°C above pre-industrial levels and related global greenhouse gas emission pathways, in the context of strengthening the global response to the threat of climate change*, V. Masson-Delmotte, P. Zhai, H. Pörtner, D. Roberts, J. Skea, P. Shukla, A. Pirani, W. Moufouma-Okia, C. Péan, R. Pidcock, S. Connors, J. Matthews, Y. Chen, X. Zhou, M. Gomis and E. Lonnoy, Eds., Geneva, IPCC, 2018, p. In press.
- [2] IEA, "Production cost and break-even crude oil price for SAFs compared with fossil jet kerosene," IEA, Paris, 2019.
- [3] G. Realmonte, L. Drouet, A. Gambhir, J. Glynn, A. Hawkes, A. C. Köberle and M. Tavoni, "An inter-model assessment of the role of direct air capture in deep mitigation pathways," *Nature Communications*, vol. 10, p. 3277, 2019.
- [4] P. Gabrielli, M. Gazzani and M. Mazzotti, "The role of carbon capture and utilization, carbon capture and storage, and biomass to enable a net-zero-CO₂ emissions chemical industry," *Industrial & Engineering Chemistry Research*, vol. 59, no. 15, pp. 7033-7045, 2020.
- [5] V. Becattini, P. Gabrielli, and M. Mazzotti. "Role of Carbon Capture, Storage, and Utilization to Enable a Net-Zero-CO₂-Emissions Aviation Sector." *Industrial & Engineering Chemistry Research*, 2021.

FROM PRE-SCREENING TO MONITORING OF PLUGGED AND ABANDONED MARINE EXPLORATION WELLS - ENABLING REUSE OF RESERVOIRS FOR CO₂ STORAGE THROUGH GEOPHYSICAL MONITORING

Benjamin Emmel^{1*}, Simone Zonetti², Anouar Romdhane¹, Bastien Dupuy¹, Malin Torsæter¹

¹ SINTEF Industry, Applied Geoscience Group, Trondheim, Norway

² SINTEF Digital, Applied Optics Group, Oslo, Norway

* Corresponding author e-mail: Benjaminudo.emmel@sintef.no

Decommissioning of platforms and permanent plugging and abandonment (P&A) of oil and gas wells is a major future financial challenge for oil producing countries. This is especially true for offshore wells in deep water, where heavy-duty drilling rigs with high day rates need to be applied for well closure. Even if well monitoring is typically not done after abandonment, this is an emerging topic – which is crucial to enable reuse of reservoirs for e.g., CO₂ or hydrogen storage. With this respect, it is important to find new cost-efficient ways of monitoring plugged offshore wells, where in-situ gas measurements, satellite- and/or air- based monitoring techniques are difficult to implement or not possible. In the present paper, we propose the first steps for a data-based, *geophysical monitoring strategy for permanently plugged wells*. The foundation is a detailed analysis of documents provided by operators towards the Norwegian authorities. Based on these open-access data, we construct numerical wells and simulate/evaluate the geophysical response of the different well barrier materials. The data can be used for future field reuse/monitoring campaigns to detect missing or damaged cement barriers in abandoned oil and gas wells. This will broaden the available sites for future large-scale CO₂ storage.

Keywords: CO₂ storage, Well integrity, Plugging and Abandonment (P&A), Numerical simulations, Geophysical monitoring, CSEM

1. Introduction

The decommissioning and permanent plugging and abandoning of wells is an *eternal* legacy of energy companies working in the North Sea. Post-abandonment monitoring is typically not performed but is an important topic if the reservoir is to be qualified for re-use as e.g., a CO₂ storage site. Since 1966, more than 750 wildcat wells have been drilled only in the Norwegian part of the North Sea. Some of these wells might pose an environmental risk by representing potential leakage paths for gases towards the seafloor, the water column, and maybe into the atmosphere [1]. Leakage along wells can occur through or along the cement plug placed within the wellbore or through/along the annular cement outside the casing pipe. Both the cement matrix and the cement-rock and cement-steel interfaces are potential leakage paths [2]. Plugging and abandonment (P&A) procedures aim at preventing such integrity failures with an *eternal* perspective by filling carefully selected discrete sections of the well with cement (cement plugging) [3]. However, as indicated by a few scientific cruises targeting decommissioned exploration wells, these locations show gas leakages from the subsurface to the seafloor [4][5][6]. As there are strict requirements for P&A on the Norwegian Continental Shelf since the start of oil and gas production, the wells are always plugged with cement – and the leak are thus most likely connected to degradation of barriers over time. Both steel and cement are materials

known to deteriorate over time in subsurface environment, as is also the bonding between them[7][8].

Current strategies for well integrity assessments are based on cased logging tools, requiring entry and access into the wellbore. This makes the monitoring of temporarily and permanently P&Aed wells costly and challenging. To our knowledge, no reliable methods for non-invasive (tophole) well integrity monitoring for plugged wells have been published in scientific literature, even though some recent studies and industry workshops have pointed out the urgent need for developing such methods – especially for reservoir re-use for CO₂ storage purposes.

Our approach is to develop such a technique through the combination of knowledge on well construction, material degradation over time and non-invasive subsurface imaging. In this context, geophysical techniques offer the potential to represent a more continuous and cost-efficient alternative to in-situ gas measurements on the seafloor, allowing early prevention and mitigation of well barrier degradation. However, before entering a geophysical monitoring stage, a good overview of the P&A status and associated well architecture, and subsurface geology is necessary. This can be achieved by evaluating old drilling operation reports and by identifying critical parameters such as parameters from drilling (e.g. drilling induced damage to the rock formation), the success of primary well cementing, any

pressure/integrity testing performed on barriers during the wells' operative lifetime, information on build-up of sustained casing pressure over time in the well, and the general subsurface conditions in the well (to estimate the degree of material degradation). All this data can be extracted from publicly available well completion reports and the webpage of the Norwegian Petroleum Directorate (NPD). After the pre-screening results are evaluated, specific wells can be selected for a detailed geophysical analysis based, in a first stage, on numerical but realistic models. Comparisons with laboratory and field experiments can be performed afterwards.

In this contribution, we report a strategy for how to proceed from pre-screening of available data reported to the NPD towards the building of numerical well models for assessing the sensitivity of selected geophysical techniques to well integrity issues.

In the future European green energy network Norway has a crucial role to store CO₂ or hydrogen in depleted gas and oil reservoirs. A monitoring strategy for abandoned wells as one of the major risks for gas leakage [9][10] will be one of the key aspects to de-risk environmental pollution and guarantee safe sub-surface future energy storage. Such a strategy will help to apply new, cost-effective P&A methods developed at SINTEF Industry, such as using shale as a natural barrier [11] or repairing damaged cement by electrochemical enhancement of mineral growth [12].

2. Methods and results

In this paper, we present two methods. We start with the pre-screening of data reported to the Norwegian authorities. Based on this public data-set we show how to build realistic numerical models and examples of geophysical numerical modelling that is part of an underway sensitivity analysis.

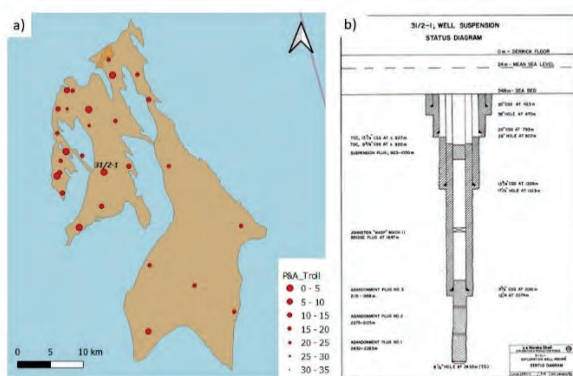


Figure 1: a) Map showing locations and P&A evaluation scores for exploration wells (red dots) from the Troll gas and oil field (brownish area). b) Decommissioning and P&A plan for well 31/2-1 showing the planned outer cement framing and the position of a "suspension" plug (923-1050 m) and three abandonment plugs between 2283 m and 1958 m. The grey shaded area should represent volume filled by cement.

2.1 Pre screening (evaluation of available data)

Well decommissioning data provided by the NPD are analysed with respect to their availability, plausibility,

and to conformance to the present P&A regulations offshore Norway [7]. Based on twelve criteria a final P&A score for 31 exploration wells in the Troll area was established (Fig. 1a) and interpreted in a Geographic Information System (GIS) environment [13]. A few of the evaluation criteria will be explained with the example of exploration well 31/2-1 (Fig 1a) which was drilled in 1979 to a total vertical depth of 2433 m and discovered oil in the sandstones of the Sognefjord Formation.

The evaluation results are given in Table 1. The first 4 criteria *sc_status* (e.g., P&A, suspended, junked etc.), *sc_entryYear* (before or after 2004), *sc_plugged_sa*, *sc_plugged_ab* relate to data given from NPD in their wellbore GIS shape-file *wlb.Point.zip* [14]. Criteria *sc_report*, *sc_cs_ver*, *sc_plug_len*, *sc_pl_ver*, *sc_mill*, *sc_ind_leak* are explained in the description of Table 1, *sc_plug_job* and *sc_cem_job* are explained more detailed in the following.

Table 1: Pre-screening evaluation results for well 31/2-1 and short description of the evaluation criteria. The pre-screening score is far below average of exploration wells from the Troll gas and oil field and thus a further investigation is necessary.

Criteria	Score	Max	Description
<i>sc_status</i>	1	3	Status descriptions for exploration wells from NPD
<i>sc_entryYear</i>	0	1	Year of drilling related to regulations
<i>sc_plugged_da</i>	0	1	Reporting of plugging operation to the authorities
<i>sc_plugged_ab</i>	0	1	Finishing date reported to the authorities
<i>sc_report</i>	2	3	Report quality
<i>sc_cem_job</i>	3,00	3	Casing cement job evaluation
<i>sc_cs_ver</i>	1	3	Casing cement job verification
<i>sc_plug_job</i>	-6	6	Abandonment, reservoir and surface plug
<i>sc_plug_len</i>	2,80	3	In the NNS the required plug length is 100 m
<i>sc_pl_ver</i>	0	3	Tagging or weight testing of plugs?
<i>sc_mill</i>	0	1	Milling of casing to improve cement integrity
<i>sc_ind_leak</i>	1	2	Leakage indicated by secondary measurements
<i>sc_total</i>	4,80	30,00	

In the casing cement job evaluation (*sc_cem_job*), we investigate the volumes of the drilled hole used cement along the full length of the wellbore (including cement used for well lead, tail and shoe, without add-ons). We assume a cylindrical shape of the borehole and the casing. The volume between the open borehole and the casing was calculated by subtracting the casing volume from the open borehole volume. The *sc_cem_job* score (between 0 and 3) is obtained by adding the individual scores for every casing interval and by normalization. For well 31/2-1, the cement job is sufficient for all four casing intervals and thus a score of 3 is given (Fig. 2a, Tab.1).

We evaluate three plug types in the *sc_plug_job* criteria. These are from the deepest to the shallowest wellbore depth: (i) Abandonment plug: this well barrier should protect against any potential source of inflow within

permeable zones. The cementing job consists in filling the deepest parts of the wellbore, including sometimes open hole sections (with no casing). (ii) Reservoir plug: added if a potential source of inflow or if the reservoir is exposed (hydrocarbons present). (iii) Environmental plug: this well barrier should isolate the surface/seabed from any potential source of inflow from the wellbore.

In the *sc_plug_job* evaluation, we mainly consider two criteria. At first, we check if all plugs are available and in the correct position, e.g., if the reservoir plug is correctly placed according to the present regulations and regional geological knowledge (e.g., top of a reservoir unit). Figure 2b shows the plug locations along the well 31/2-1. Environmental plug and reservoir plug are missing or placed incorrectly. The cement volume calculations for the abandonment plugs indicated insufficient used cement volumes for the anticipated plug lengths resulting in a *sc_plug_job* score corresponding to -6 (Tab. 1), indicating that the plugs are not placed in the right position and/or the amount of used cement was insufficient. The resulting total score of well 31/2-1 is 4.8 (Tab. 1) which is below the average score for exploration wells from the Troll gas and oil field. A further monitoring/examination of this well is therefore recommended.

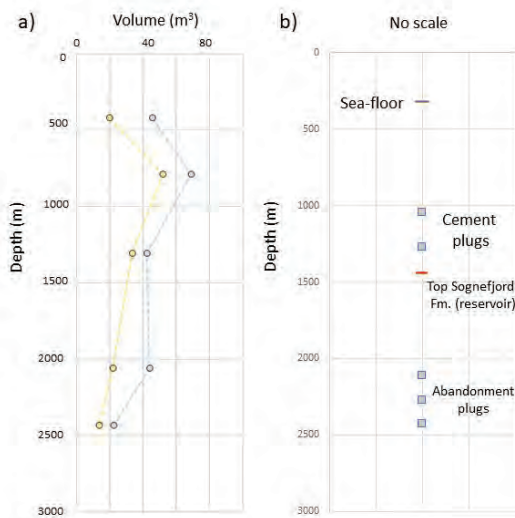


Figure 2: Graphic representation of the casing cement job and the plug position for well 31/2-1. a) The dashed yellow line indicates the volume between the open hole and the casing which should be filled by cement. The dashed blue line is the volume of cement used between every one of the 4 casing intervals. b) Schematic illustration of plug positioning in relation to the top of the reservoir and the seafloor (the plug length is not considered in the figure). In this case, the cement plugs (this work was done 1979) are not positioned according to the regulations from 2004 [7].

2.2 Numerical model set-up

The data of well 31/2-1 is used to build a numerical model to simulate electromagnetic (EM) responses using the finite element method (FEM) software COMSOL Multiphysics® v. 5.5 [15].

The cylindrical well element, radially layered to accommodate different wellbore and casing sizes, is enclosed in a large cylindrical domain with a radius larger than 500 m. The whole geometry is also layered horizontally, following the size changes in the well and the location of the plugs, with the inclusion of a water layer and an air layer at the top, and additional 400 m of rock formation below the well. Furthermore, the modelling domain is surrounded by absorbers to simulate infinitely large systems and avoid the generation of data due to the use of a limited bounded simulation domain. The geometry of the well (not to scale) is given in Figure 3.

A transmitter antenna is implemented as a perfect dipole of arbitrary length and can be placed anywhere in the simulation domain with any orientation. Taking advantage of field symmetry, simulations of radial and tangential polarisations allow to reduce computational requirements by half. Materials are characterized by their conductivity and relative permittivity and are considered, in first approximation, to be independent from the frequency of EM radiation. Formation properties are taken to be isotropic but vary with depth. The model is meshed using a triangular mesh on the seafloor surface, with element size adapted to provide sufficient local refinements in the proximity of the well, surrounded by a mapped mesh on the corresponding absorbing boundary. The resulting surface mesh is then swept along the vertical direction (Fig. 4).

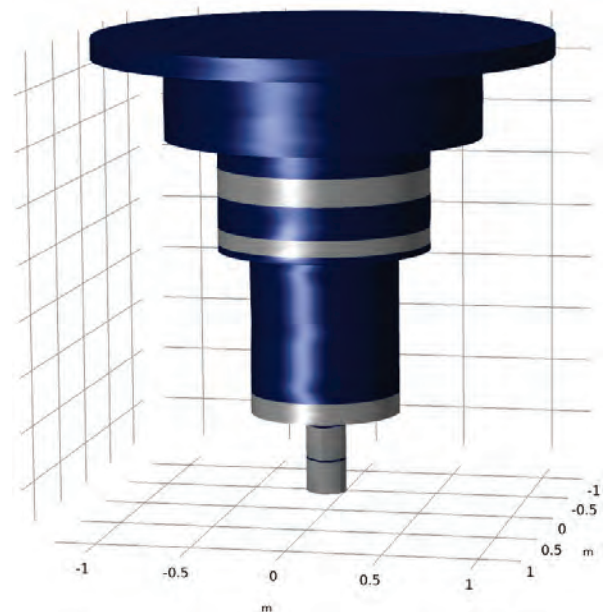


Figure 3: Visualization of the well structure implemented in COMSOL Multiphysics® [15], not to scale. Dark blue areas represent the well casing, grey areas the cement plugs.

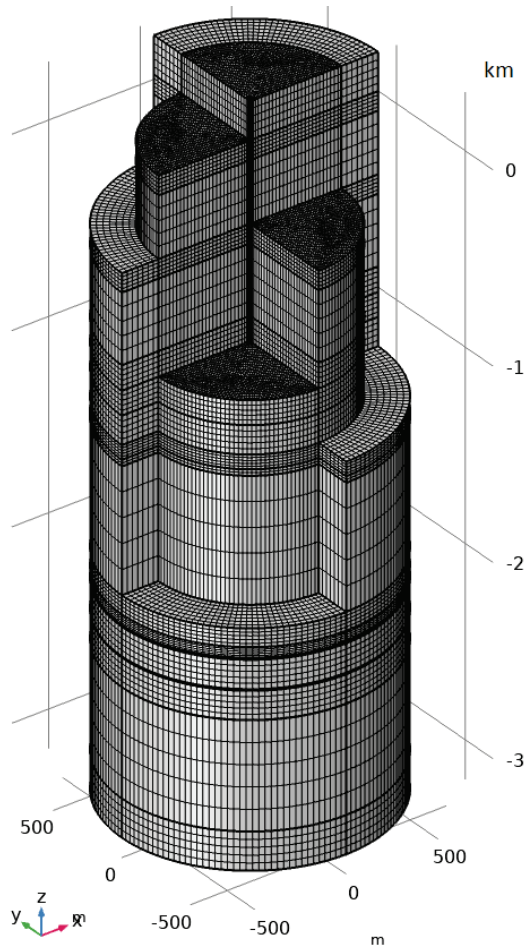


Figure 4: Example of a possible discretization of the FEM model, with a dense triangular mesh on the horizontal internal surfaces, mapped mesh on the absorbing layer, and swept mesh in the vertical direction.

2.3 Geophysical monitoring techniques

Taking advantage of a dedicated implementation of low frequency EM, including effective formulations for thin electrical layers, it was possible to study the response of well components to external EM fields, both for the purpose of well detection and well monitoring. Results from the numerical models can be used as benchmark models in a realistic field scale well integrity monitoring study.

A 40 m long horizontal dipole emitter located 30 m below the sea surface at a radial distance of 100 m from the wellbore, is considered with a frequency corresponding to 1 Hz. We derive the corresponding electric field in the simulation domain and extract the solution at the seafloor surface. Figure 5 shows an example of the resulting data where the gain in dB, calculated as $20 \cdot \log_{10}$ (scattered field / background field) for the horizontal component of the electric field, is displayed. The background and scattered fields correspond to the cases where no well is considered in the simulation domain and where a well geometry including plug is added, respectively. The result highlights the field patterns that can be observed with finite measurements of the electric field at the seafloor (CSEM receivers). It is also indicative of spatially variable sensitivity that one might expect.

Similar patterns can be derived for different orientations of the dipole emitter with respect to the wellbore location.

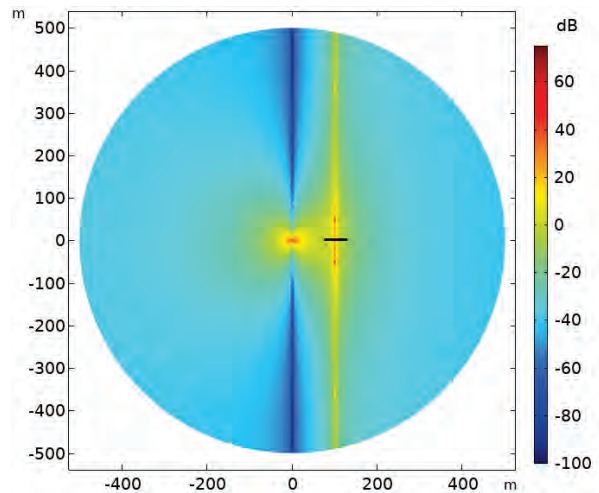


Figure 5: Example of electric field gain (x component) on the seafloor surface of the FEM model. The well is at the center of the plot. The position of the 40 m long dipole antenna relative to the sea-floor plane is pictured as a black line, 100 m away from the wellbore.

3. Discussion and conclusion

Potential leakage pathways for stored and/or natural subsurface gases can be geological (e.g., through fractures, faults, or due to caprock failure) or man-made, with the latter mainly due to leakage along deep active or abandoned wells [16]. Wells can form a direct connection between deep gas and oil reservoirs or CO₂, hydrogen storage units with the seafloor by-passing all geological sealing caprock units. The European CO₂ storage community expects a low risk due to leakage along active and onshore wells because they can be monitored very effectively through geochemical and geophysical methods [16] and observed leakage might be restricted to a few incidences [4][6]. There is, however, little information on leakage from abandoned offshore wells, which can be more severe – and uncertainty about these wells can typically jeopardize the use of a reservoir for CO₂ storage purposes. However, leakage along wells with emission of greenhouse gases must be treated as a global problem including countries with limited federal regulations [17] and cost-effective monitoring strategies are needed to be implemented as soon as possible.

Here, we propose a strategy which starts with the evaluation of documents provided by the drilling operating companies towards the Norwegian authorities. Every exploration well is unique when it comes to the design and the interaction with the surrounding geological units. The level of details in the available well documentation can vary significantly. Pre-screening criteria's are e.g.: (i) the date of drilling, P&A work, number of plugs, and quality of the cementing work are considered in our study. The obtained results suggest higher scores for the wells drilled after 2004, date of the first regulations for P&A on the Norwegian continental shelf [7], compared to the wells drilled before that date.

Here, we can assume that federal regulations have improved on average the quality of P&A work.

(ii) For the plugging, most industry standards only require isolation for zones with flow potential. This means, that for an exploration well one plug isolating a hydrocarbon reservoir might be sufficient. However, in our evaluation we include three plug types (1) abandonment, (2) reservoir and (3) surface plug considering the future usage of a depleted reservoir as a potential CO₂/hydrogen storage place. (iii) The quality of the cement work is evaluated by simplified volumetric calculations using the data given in the reports. Temperature, pressure and add-ons volumes are neglected in the volume calculations.

For the geophysical modelling, a further understanding of the sensitivity of EM measurements as function of frequency, data noise, and the orientation of the dipole emitters and receivers is required. A first practical application of such measurements consists in finding the exact location of the wells in the subsurface. If casing is still present, EM signals will be very sensitive, and should help locate accurately the wells. Another application consists in identifying and verifying the location and thickness of cement plugs. Finally, we foresee possible use of EM signals in a 4D context where the objective is to provide alerts about possible integrity issues (e.g., casing discontinuity due to corrosion). For these possible applications, EM signals must be recorded and processed to extract the relevant information (e.g., using inversion) out of the raw data. Future work will also include seismic modelling and would be the basis for the design of tailored acquisition layouts capable of detecting old P&Aed wells and in a later stage providing useful information about wellbore integrity status.

Acknowledgements

This work is performed with support from the Research Council of Norway (TOPHOLE project Petromaks2-KPN 295132) and the NCCS Centre (NFR project number 257579/E20).

References

- [1] Kang, M., Kanno, C.M., Reid, M.C., Zhang, X., Mauzerall, D.L., Celia, M.A., Chen, Y., Onstott, T.C., 2014. Direct measurements of methane emissions from abandoned oil and gas wells in Pennsylvania. *Proc. Natl. Acad. Sci. Unit. States Am.* 111, 18173–18177. <https://doi.org/10.1073/pnas.1408315111>.
- [2] Gasda, S.E., Bachu, S., Celia, M.A. (2004). Spatial characterization of the location of potentially leaky wells penetrating a deep saline aquifer in a mature sedimentary basin. *Environ. Geol.*, 46, 707-720.
- [3] Khalifeh, M., Saasen, A. (2020) Introduction to Permanent Plug and Abandonment of Wells. Springer Nature, Switzerland, <https://doi.org/10.1007/978-3-030-39970-2>.
- [4] Vielstädte, L., J. Karstens, M. Haeckel, M. Schmidt, P. Linke, S. Reimann, V. Liebetau, D. F. McGinnis, K. Wallmann, Quantification of methane emissions at abandoned gas wells in the Central North Sea, *Marine and Petroleum Geology* 68 (2015), 848-860. <https://doi.org/10.1016/j.marpetgeo.2015.07.030>.
- [5] Böttner, C., M. Haeckel, M. Schmidt, C. Berndt, L. Vielstädte, J. A. Kutsch, J. Karstens, T. Weiß, (2020). Greenhouse gas emissions from marine decommissioned hydrocarbon wells: leakage detection, monitoring and mitigation strategies, *International Journal of Greenhouse Gas Control* 100, <https://doi.org/10.1016/j.ijggc.2020.103119>.
- [6] Leifer, I, Judd, A. (2015). The UK22/4b blowout 20 years on: Investigations of continuing methane emissions from sub-seabed to the atmosphere in a North Sea context, *Marine and Petroleum Geology* 68, 706-717, <https://doi.org/10.1016/j.marpetgeo.2015.11.012>.
- [7] NORSOK D-010. Well integrity in drilling and well operations, NORSKO standard D-10 (Rev. 3), Standards Norway, Lysaker, Norway, 2004. <https://www.standard.no/pagefiles/1315/d-010r3.pdf>
- [8] Vrålstad, T., A. Saasen, E. Fjær, T. Øia, J. D. Ytrehus, M. Khalifeh (2019). Plug & abandonment of offshore wells: Ensuring long-term well integrity and cost-efficiency, *Journal of Petroleum Science and Engineering* 173, 478-491. <https://doi.org/10.1016/j.petrol.2018.10.049>.
- [9] Alcalde, J., Flude, S., Wilkinson, M. et al. (2018). Estimating geological CO₂ storage security to deliver on climate mitigation. *Nature Communications* 9, 2201. <https://doi.org/10.1038/s41467-018-04423-1>
- [10] Williams, J.P., Regehr, A., Kang, M., (2020). Methane Emissions from Abandoned Oil and Gas Wells in Canada and the United States. *Environmental Science & Technology*; 55 (1): 563 DOI: 10.1021/acs.est.0c04265
- [11] Fjær, E, Larsen, I. (2018). Shale As a Sealing Barrier Around Deep Wells. Proceedings of the ASME 2018 37th International Conference on Ocean, Offshore and Arctic Engineering. Volume 8: Polar and Arctic Sciences and Technology; *Petroleum Technology. Madrid, Spain. June 17–22*.
- [12] Edvardsen, L, Gawel, K, Wenner, S., Gawel, B., Torsæter, M. (2020). Electrochemical enhancement and inhibition of calcium carbonate deposition, *Journal of Environmental Chemical Engineering*, 8, <https://doi.org/10.1016/j.jece.2020.104239>.
- [13] QGIS.org, 2020. QGIS Geographic Information System. QGIS Association. <http://www.qgis.org>
- [14] <https://www.npd.no/en/about-us/information-services/open-data/map-services>
- [15] www.comsol.com. COMSOL AB, Stockholm, Sweden.
- [16] CO2GeoNet (2008). What does CO₂ geological storage really mean 19 pp. Available at: <http://www.co2geonet.com/resources/>
- [17] Kadafa, A. A. (2012). Environmental impacts of oil exploration and exploitation in the Niger Delta of Nigeria. *Global Journal of Science Frontier Research Environment & Earth Sciences*, 12(3).

EFFECT OF CAPROCK RELATIVE PERMEABILITY ON CO₂ FLOW THROUGH IT

Iman Rahimzadeh Kivi^{1,2*}, Victor Vilarrasa^{1,2,3}, Roman Makhnenko⁴

¹ Institute of Environmental Assessment and Water Research, Spanish National Research Council (IDAEA-CSIC), Barcelona, Spain

² Associated Unit: Hydrogeology Group (UPC-CSIC), Barcelona, Spain

³ Mediterranean Institute for Advanced Studies (IMEDEA), Spanish National Research Council (CSIC), Esporles, Spain

⁴ Department of Civil & Environmental Engineering, University of Illinois at Urbana-Champaign, Urbana, Illinois, USA.

* Corresponding author e-mail: iman.rahimzadeh@idaea.csic.es

Abstract

Geologic carbon storage is needed to meet the climate goal of limiting global warming to 1.5 °C. Injecting in deep sedimentary formations brings CO₂ to a supercritical state, yet less dense than the resident brine making it buoyant. Therefore, the assessment of the sealing capacity of the caprock lying above the storage reservoir is of paramount importance for the widespread deployment of geologic carbon storage. We perform laboratory-scale supercritical CO₂ injection into a representative caprock sample and employ numerical simulations to provide an in-depth understanding of CO₂ leakage mechanisms. We explore the effect of relative permeability curves on the potential CO₂ leakage through the caprock. We show that capillary breakthrough is unlikely to take place across a non-fractured caprock with low intrinsic permeability and high entry pressure. Rather, CO₂ leakage is dominated by the intrinsically slow molecular diffusion, favoring safe storage of CO₂ over geological time scales.

Keywords: *Geologic carbon storage, Sealing capacity, Capillary breakthrough, Molecular diffusion, Shale*

1. Introduction

The growing emissions of anthropogenic CO₂ into the atmosphere have given rise to global warming and, thus, climate change with well-known harmful environmental effects. Being aware of the urgent threat of climate change to the planet, the majority of countries worldwide adopted the Paris Agreement, which aims at limiting global warming to well below 2 °C compared to the pre-industrial level. To achieve this objective, the Intergovernmental Panel on Climate Change (IPCC) suggests different mitigation strategies [1]. All these mitigation pathways project increasing shares of renewables, energy efficiency, and Carbon Capture and Storage (CCS). By approaching the limits of efficiency and currently inevitable carbon emissions in some sectors, hundreds of gigatonnes of CO₂ should be stored over the course of the 21st century to reach zero emissions. The CCS technology is expected to be more pronounced in the second half of the century, during which huge net negative emissions have to happen.

CCS consists in capturing CO₂ from stationary sources and permanently storing it underground, mainly in deep saline aquifers. The targeted strata are preferably located deep enough (>800 m) to bring CO₂ to a supercritical state. At high temperatures (i.e., $T > 31.04$ °C) and pressures (i.e., $P > 7.38$ MPa), the supercritical CO₂ has a liquid-like density and gas-like viscosity, guaranteeing high storativity and injectivity [2][3]. However, CO₂ density never exceeds that of the resident brine at these conditions [4]. As a result, CO₂ is buoyant and floats across the injection reservoir. An appropriate injection site should include a low-permeability and high-entry

pressure caprock, lying immediately above the storage reservoir, to prevent CO₂ migration out of the storage reservoir. Otherwise, CO₂ may approach shallow aquifers, hosting potable water, or even get back to the surface, putting the primary goal of long-term CO₂ storage in danger and imposing additional negative environmental impacts [5][6]. The assessment of the caprock sealing capacity is thus of crucial significance in screening appropriate storage sites and bringing public acceptance to carbon capture and storage at large scales.

As the non-wetting fluid, CO₂ penetrates into the caprock in free phase if the differential pressure between CO₂ and brine (i.e., the capillary pressure) overcomes the capillary entry pressure P_0 of the pore network. CO₂ is expected to percolate through the caprock if another capillary threshold, called breakthrough pressure P_{brth} is exceeded [7]. Nevertheless, desaturation of the pore network establishes a two-phase flow in which the effective permeability to each phase (the intrinsic permeability multiplied by the phase relative permeability) governs the advection rate. The literature provides very limited experimental measurements of CO₂-brine relative permeability in tight clay-rich caprock representatives [8]. The lack of data on relative permeability curves imposes high uncertainties on the caprock sealing capacity assessment. Besides, CO₂ dissolves by up to 4 mol% into the resident brine under reservoir conditions, initiating diffusive transport in the aqueous phase [9]. There is a consensus that the leakage becomes advection-dominated once the breakthrough pressure is surpassed [7][10]. The reliability of this statement has yet to be investigated on the lab-scale under well-monitored

conditions. In this study, we conduct supercritical CO₂ injection experiments on a representative caprock sample, namely Opalinus Clay. We parametrize a two-phase flow model and simulate the experiment numerically to deal with the abovementioned flow complexities and the associated uncertainties. Through replicating the experimental observations, we provide an improved understanding of the flow mechanisms controlling CO₂ leakage through the caprock. We also address the sensitivity of CO₂ flow behavior to the relative permeability curve.

2. Methodology

2.1 Materials and experimental methods

We choose shaly facies of Opalinus Clay as a representative caprock for this study. Samples are retrieved from the Mont Terri underground laboratory site in Switzerland. We employ preliminary characterization techniques to measure the capillary and flow properties of the material. Mercury intrusion porosimetry provides a porosity of 12.5% and dominant pore throat diameter value of 0.015 micron. The Mercury Intrusion Capillary Pressure (MICP) curves are converted to a supercritical CO₂ intrusion into an initially brine-saturated specimen by taking a CO₂-brine interfacial tension of 30 mN/m and a shale-CO₂-brine contact angle of 40° [11]. The CO₂ saturation curve suggests a capillary entry pressure of approximately 4 MPa. The intrinsic permeability of the shale is measured in a single-phase steady-state brine flow experiment and is determined to be $3 \cdot 10^{-21}$ m² [12]. The injected brine has a chemical composition similar to the formation fluid to prevent possible chemical effects and swelling of the tested material.

After the permeability measurement, supercritical CO₂ is injected into the shale according to the procedure described in Makhnenko et al. [13]. The 10 mm thick and 35 mm in diameter specimen is tested under the oedometric conditions (Figure 1). The specimen is capped between two 6-mm thick porous stones with a porosity of 32%, an intrinsic permeability of 10^{-12} m², and low entry pressure of 0.01 MPa, which are initially saturated with brine. The upstream CO₂ controller increases the pressure to a value (~22 MPa), higher than the estimated breakthrough threshold to promote advective CO₂ flow through the specimen. The upstream valve is then closed and the upstream pressure variation resulting from CO₂ flow is continuously recorded. Meanwhile, the downstream controller keeps the downstream brine pressure constant at 8 MPa and measures the outflow volume. The temperature of all experimental equipment is also kept constant at 40 °C throughout the experiment.

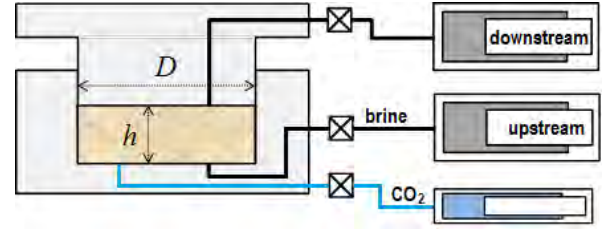


Figure 1: Schematic representation of the oedometric cell used to inject CO₂ into a cylindrical brine-saturated shale specimen of 10 mm thick and 35 mm in diameter

2.2 Numerical approach

CO₂ flow through the brine-saturated rock is a two-phase flow problem that requires solving the mass conservation for each phase (wetting and non-wetting) or each component (brine and CO₂). Adopting the latter approach, the mass balance equation writes as

$$\frac{\partial}{\partial t} (\omega_a^i \rho_a S_a \phi + \omega_c^i \rho_c S_c \phi) + \nabla \cdot (\mathbf{i}_a^i + \mathbf{i}_c^i + \omega_a^i \rho_a \mathbf{q}_a + \omega_c^i \rho_c \mathbf{q}_c) = f^i, \quad (1)$$

where ϕ is porosity and t is time, ρ_ψ and S_ψ , in which the subscript ψ stands for either aqueous ($\psi = a$) or CO₂-rich phase ($\psi = c$), denote the phase density and saturation, respectively. ω_ψ^i represents the mass concentration of component i in phase ψ . The right-hand side f^i accounts for an external mass supply of component i . Mass transport includes phase advective flux of \mathbf{q}_ψ and diffusive flux of individual components, \mathbf{i}_ψ^i .

The advective flow rate of each phase relates to pressure changes and gravity effect using Darcy's law

$$\mathbf{q}_\psi = -\frac{k k_{r\psi}}{\mu_\psi} (\nabla p_\psi + \rho_\psi g \nabla z), \quad (2)$$

where k is the intrinsic permeability, $k_{r\psi}$ is the relative permeability to the fluid phase ψ having a dynamic viscosity of μ_ψ , g is the gravity acceleration and z is the vertical position.

The molecular diffusion of components in each phase is expressed using Fick's law

$$\mathbf{i}_\psi^i = -\tau \phi \rho_\psi S_\psi D_\psi^i \nabla \omega_\psi^i, \quad (3)$$

where τ stands for the pore structure tortuosity and D_ψ^i for the diffusion coefficient of component i in phase ψ , and \mathbf{I} represents the identity tensor. The product of tortuosity and diffusion coefficient returns the effective diffusion coefficient D of each component through the rock.

It is worth mentioning that in an oedometric testing cell, the specimen is subjected to constant external stresses and hydromechanical coupling effects are minor due to relatively small pressure changes. Therefore, we here put our emphasis on the two-phase flow problem. A discussion on relevant hydromechanical coupling processes can be found in Rahimzadeh Kivi et al. [14].

Owing to the problem's symmetry, we take advantage of the low computational cost of an axisymmetric model. The model includes the shale specimen in the middle and

a set of stiff porous stone and loading platten on each upper and lower side (Figure 2). The fluid content of loading plattens reproduces the dead volumes of the testing setup.

The properties of the rock and porous stones are summarized in Table 1 and are used to calibrate a two-phase flow model. The aqueous phase saturation S_a relates to the capillary pressure p_{cap} through the Van Genuchten model [15]

$$S_{ea} = \frac{S_a - S_{ra}}{S_{max,a} - S_{ra}} = \left(1 + \left(\frac{p_{cap}}{p_0} \right)^{1/(1-m)} \right)^{-m}, \quad (4)$$

where S_{ra} and $S_{max,a}$ are residual and maximum brine saturations, respectively, S_{ea} is effective brine saturation, and m is the shape parameter of the retention curve. The parameters S_{ra} , $S_{max,a}$ and m are determined by fitting the experimentally obtained retention curves.

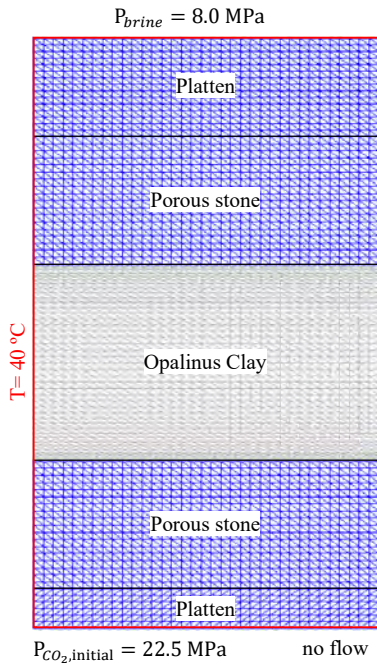


Figure 2: A sketch of the numerical model, including the mesh, for simulating the lab-scale CO₂ injection into the shale specimen

The relative permeability to each phase follows a power-law model with the corresponding effective saturation. Experimental evaluations of the relative permeability curves for clay-rich rock are rarely carried out due to their low permeability. An exponent of 6 is assumed to be appropriate for these geomaterials [8]. However, to deal with uncertainties associated with the relative permeability curves, we adapt a reference model with an exponent of 6 and perform a sensitivity analysis to this parameter. We use decreased exponent values of 5, 4 and 3. A lower one provides an increased preference for advection at a reference saturation degree (Figure 3). In this model, the relative permeability to CO₂ approaches unity at the residual brine saturation, although it can be much lower [8].

Table 1: Flow and retention properties of the Opalinus Clay and porous stones

Parameter	Opalinus Clay	Porous stones
Intrinsic permeability, k_0 (m ²)	$3 \cdot 10^{-21}$	10^{-12}
Rel. brine permeability, k_{ra}	S_{ea}^6	S_{ea}
Rel. CO ₂ permeability, k_{rc}	$(1 - S_{ea})^6$	$1 - S_{ea}$
Residual brine saturation, S_{ra}	0.13	0
Max. brine saturation, $S_{max,a}$	1	1
Residual CO ₂ saturation, S_{rc}	0	0
Gas entry pressure, P_0 (MPa)	3.83	0.01
van Genuchten constant, m	0.63	0.8
Initial porosity, ϕ_0	0.125	0.32
Diffusion coefficient, D (m ² /s)	$1.6 \cdot 10^{-9}$	$1.6 \cdot 10^{-9}$

CO₂ is injected at the bottom face and the upstream compartment is pressurized to 22.5 MPa. A no-flow boundary is then exerted and the system response to CO₂ flow is simulated. The temperature is maintained constant at 40 °C throughout the simulation. We conduct the simulation using the finite element code CODE_BRIGHT [16], extended for CO₂ injection [17].

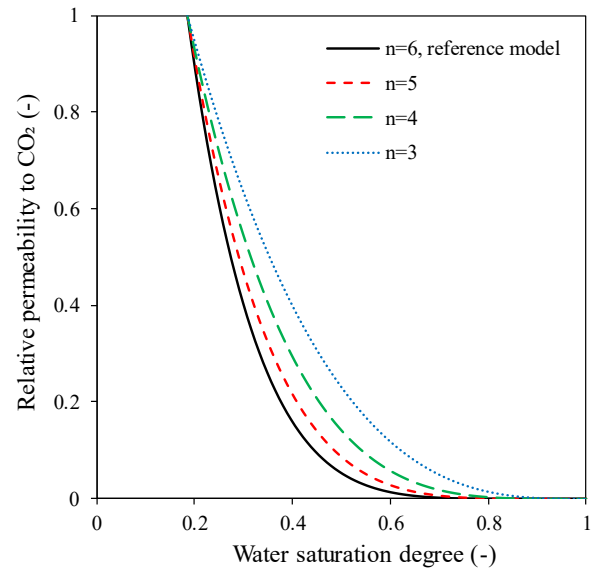


Figure 3: Relative permeability curves to CO₂ used in this study

3. Results and discussion

3.1 Reference case

Figure 4 illustrates the evolution of CO₂ pressure at the upstream side as well as the cumulative outflow volume at the downstream side. A logarithmic time scale is adopted to bring the short- and long-term responses together in one frame. The differential pressure between CO₂ and brine (~14.5 MPa) overcomes the capillary entry pressure of the specimen and CO₂ enters the pore network. Given the limited CO₂ supply at the upstream compartment, CO₂ pressure declines with time. CO₂ penetration into the specimen also gives rise to brine overpressure and an advective brine flow toward the downstream. Simulation results satisfactorily reproduce the observed pressure evolution in the short-term during

which experimental data are available. Nevertheless, simulations highly underestimate the outflow volume. This discrepancy can be attributed to the relative permeability curves we have used for the simulation and the presence of preferential flow paths through the tested shale specimen that are not considered by the model. These potential flow discontinuities may possess lower capillary entry pressure and higher permeability compared to the matrix, providing larger transported fluid volumes.

The long-term simulation results disclose a continuous CO₂ flow and pressure decrease until recovering a uniform pressure distribution throughout the specimen. To achieve a more detailed insight into the governing flow mechanisms, we draw the vertical profiles of brine saturation (Figure 5) and the individual components of CO₂ mass flux (Figure 6). CO₂ enters the pore network and commences desaturating the rock. As the CO₂ pressure propagates upward into the specimen, more interconnected pores experience drainage. However, the drainage path is not long-lasting and gives way to brine imbibition from the downstream because the upstream pressure continuously decreases. This drainage-to-imbibition transition happens after a short while (~10 hrs) at the upstream part of the specimen, while it takes more than 50 hours to occur downstream (Figure 5). From this moment on, the whole specimen imbibes brine from the downstream compartment until it becomes again fully saturated.

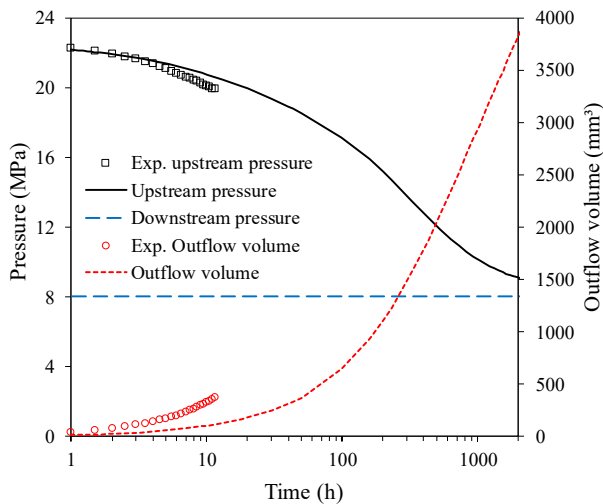


Figure 4: Results of supercritical CO₂ injection into the Opalinus Clay in terms of the upstream CO₂ pressure and downstream outflow volume. The calculated curves utilize a relative permeability model with an exponent of 6 (i.e., the reference model).

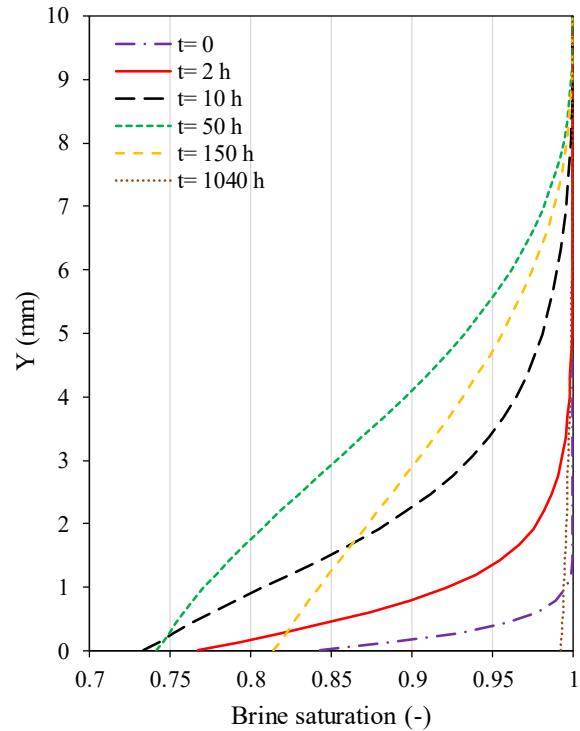


Figure 5: Distribution of brine saturation along the shale specimen and fluid compartments

Desaturation of the shale specimen promotes a two-phase flow of CO₂ and brine. According to Eq. (2), the advective CO₂ flux is directly linked to the corresponding relative permeability, which, in turn, is a function of saturation. In our reference model, an effective enhancement of the relative permeability can be expected if the brine saturation drops below 0.8 (see Figure 3). This extent of desaturation is observed only at the lowermost two millimeters of the 10-mm long specimen. For example, CO₂ saturation at a point located 2.5 mm away from the bottom face increases up to 0.17 but is insufficient to ever make CO₂ mobile. Therefore, the advective flux is quite concentrated around the bottom of the specimen and has negligible contribution to flow in the rest of the specimen (Figure 6). As a result, molecular diffusion thoroughly overwhelms the advective-driven behavior and stands merely as the dominating flow process. On the other hand, brine also advects across the specimen and conveys CO₂ in dissolution. Nevertheless, this mechanism has a negligible effect on the CO₂ mass transported and is thereby not included in Figure 6.

Interestingly, we infer from a sensitivity analysis on the specimen length (not shown here) that CO₂ injection into a longer specimen gives rise to an enhanced brine pressure buildup or equivalently decreased capillary pressure and, thus, specimen desaturation. This scale dependence can be more pronounced in the field where caprock thickness is in tens to hundreds of meters. Therefore, potential CO₂ leakage through shaly caprock favorably remains diffusion-dominated.

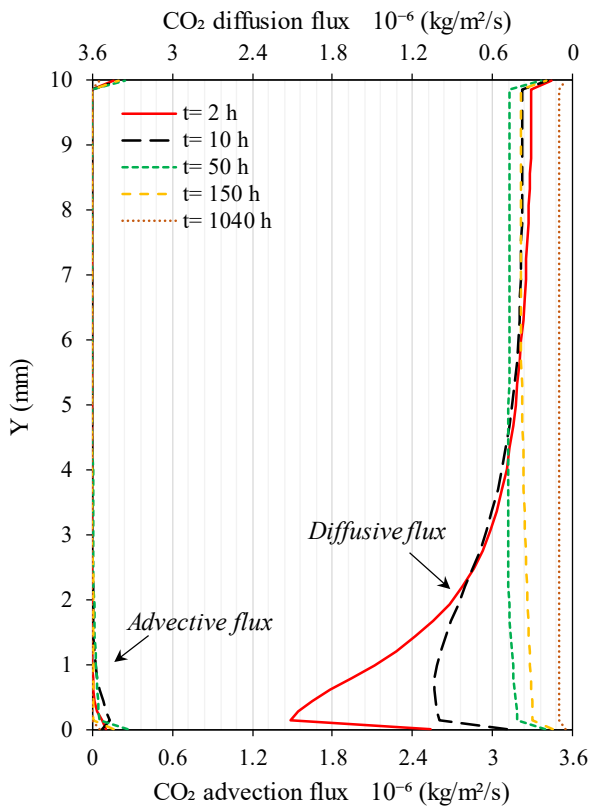


Figure 6: Vertical profiles of CO₂ flux components at several times: molecular diffusion and advection.

3.2 Sensitivity study on the relative permeability

The advancement of the advective CO₂ front depends on the relative permeability curve. The smaller the exponent n of the relative permeability model, the higher is the relative permeability and, thus, the further the advective front advances into the specimen. We here examine the sensitivity of the system behavior to relative permeabilities with lower exponents down to 3. Following our above reasoning, the worst scenario to the caprock sealing capacity is expected for the lowest exponent, i.e., $n=3$, which is presented in this study. Figure 7 displays a comparison between numerical simulations and experimental data. Provided a lower resistance to advection by the increased relative permeability, both the outflow volume and the pressure drop in the short term increase, compared to the reference case (see Figure 4). These changes provide an almost perfect fit to the recorded pressure data, though simulations are still far from a satisfactory match with the outflow volumes. However, the long-term simulation results are very similar in both cases. The upstream pressure and the outflow volume continue to evolve with time. To explore possible changes in flow mechanisms with the relative permeability curve and to reason the negligible difference between the two simulations, we plot vertical profiles of CO₂ mass flux terms in Figure 8. During early times (up to 30 hrs), the advective CO₂ flux along the specimen peaks at larger values than in the reference case. Moreover, the advective front propagates much further into the specimen (more than half of its length) compared to the reference case. CO₂ bubbles

become mobile in the middle of the specimen. The advective flux assists in CO₂ mass transport, particularly during early times, whose effects have been reflected in Figure 7 as enhanced pressure drop and fluid discharge. Nevertheless, CO₂ flow at the downstream side remains purely diffusion-dominated. Simulations with intermediate relative permeability exponents (i.e., $n=4$ and $n=5$) consistently imply that decreasing the exponent n further restricts the advective flow to the lower part of the specimen.

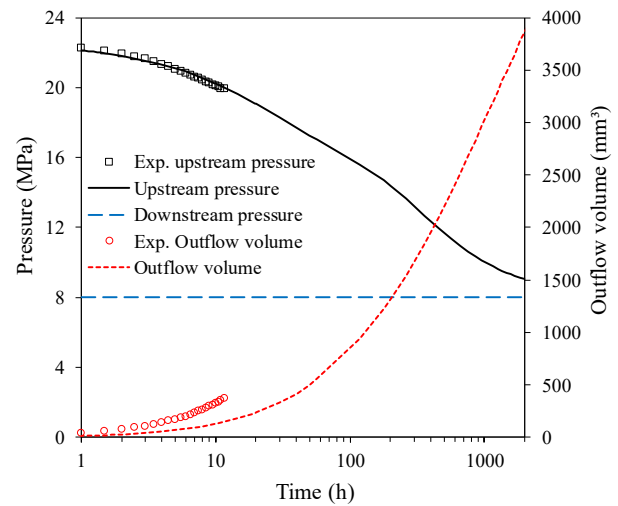


Figure 7: Results of supercritical CO₂ injection into the Opalinus Clay. The numerical simulation utilizes an enhanced relative permeability model with an exponent of 3.

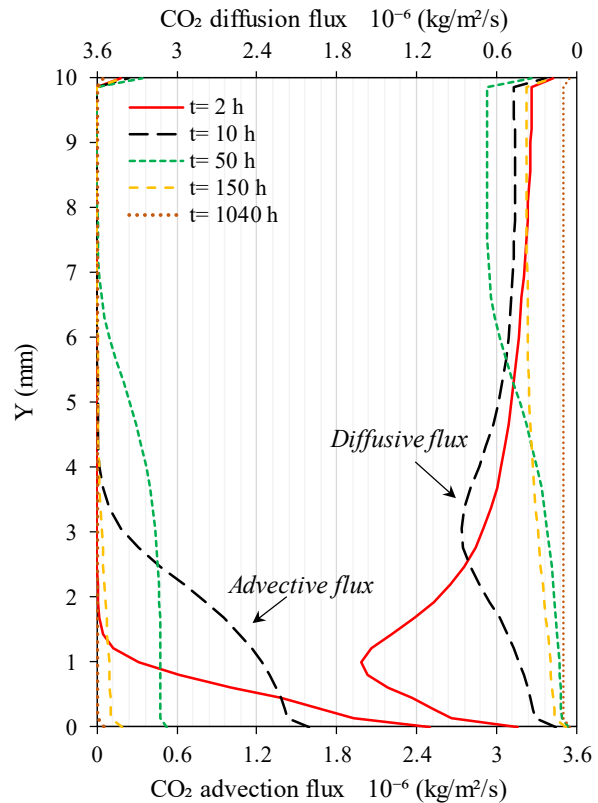


Figure 8: Vertical profiles of CO₂ flux components at several times obtained from numerical simulations with an exponent of 3 in the relative permeability model.

4. Summary and conclusions

Using numerical simulations of laboratory-scale supercritical CO₂ injection into a low-permeability Opalinus Clay (shale) we assess flow mechanisms governing potential CO₂ leakage through a non-fractured caprock. By overcoming the capillary entry pressure, CO₂ enters the rock and develops a two-phase flow. The advective CO₂ flow peaks at early times and the bottom face of the specimen experiences imbibition. The relative permeability to CO₂ locally increases and CO₂ advection remains confined to the lowermost portion of the rock with negligible contribution to flow. Even by changing the relative permeability curve, which leads to enhanced effective permeability to CO₂, the advective front does not bridge the specimen. Our analyses show that CO₂ transport through the representative caprock is dominated by molecular diffusion. Over the length and time span of interest in the field-scale CO₂ injection, it is unlikely that capillary breakthrough takes place and compromises the caprock sealing capacity. Yet, small fractions of CO₂ may diffuse across the caprock over geological time scales.

Acknowledgements

I.R.K. and V.V. acknowledge funding from the European Research Council (ERC) under the European Union's Horizon 2020 Research and Innovation Program through the Starting Grant GGeoREST (www.georest.eu) (Grant agreement No. 801809). IDAEA-CSIC is a Centre of Excellence Severo Ochoa (Spanish Ministry of Science and Innovation, Project CEX2018-000794-S). R.M. is thankful for the support from US DOE through CarbonSAFE Macon County Project DE-FE0029381.

References

- [1] IPCC, 2018: "Global Warming of 1.5°C. An IPCC Special Report on the impacts of global warming of 1.5°C above pre-industrial levels and related global greenhouse gas emission pathways, in the context of strengthening the global response to the threat of climate change, sustainable development, and efforts to eradicate poverty" [Masson-Delmotte, V., P. Zhai, H.-O. Pörtner, D. Roberts, J. Skea, P.R. Shukla, A. Pirani, W. Moufouma-Okia, C. Péan, R. Pidcock, S. Connors, J.B.R. Matthews, Y. Chen, X. Zhou, M.I. Gomis, E. Lonnoy, T. Maycock, M. Tignor, and T. Waterfield (eds.)].
- [2] Bachu, S. (2003). Screening and ranking of sedimentary basins for sequestration of CO₂ in geological media in response to climate change. *Environmental Geology*, 44(3), 277-289.
- [3] Celia, M. A. (2017). Geological storage of captured carbon dioxide as a large-scale carbon mitigation option. *Water Resources Research*, 53(5), 3527–3533.
- [4] Vilarrasa, V., Bolster, D., Dentz, M., Olivella, S., Carrera, J., 2010. Effects of CO₂ compressibility on CO₂ storage in deep saline aquifers. *Transp. Porous Media*, 85, 619-639.
- [5] Birkholzer, J. T., Zhou, Q., Tsang, C.-F. (2009). Large-scale impact of CO₂ storage in deep saline aquifers: a sensitivity study on pressure response in stratified systems. *International Journal of Greenhouse Gas Control*, 3, 181–194.
- [6] Vilarrasa, V., Rutqvist, J., & Rinaldi, A. P. (2015). Thermal and capillary effects on the caprock mechanical stability at In Salah, Algeria. *Greenhouse Gases: Science and Technology*, 5(4), 449–461
- [7] Hildenbrand, A., Schlomer, S., & Krooss, B. M. (2002). Gas breakthrough experiments on fine-grained sedimentary rocks. *Geofluids* 2(1), 3–23.
- [8] Bennion, B., & Bachu, S. (2008). Drainage and imbibition relative permeability relationships for supercritical CO₂/brine and H₂S/brine systems in intergranular sandstone, carbonate, shale, and anhydrite rocks. *SPE Reservoir Evaluation & Engineering*, 11(3), 487-496.
- [9] Gherardi, F., Xu, T., & Pruess, K. (2007). Numerical modeling of self-limiting and self-enhancing caprock alteration induced by CO₂ storage in a depleted gas reservoir. *Chemical Geology*, 244, 103–129.
- [10] Espinoza, D. N., & Santamarina, J. C. (2017). CO₂ breakthrough-caprock sealing efficiency and integrity for carbon geological storage. *International Journal of Greenhouse Gas Control*, 66, 218–229.
- [11] Espinoza, D. N., & Santamarina, J. C. (2010). Water-C-mineral systems: interfacial tension, contact angle and diffusion—Implications to CO₂ geological storage. *Water Resources Research*, 46, (W07537)
- [12] Kim, K., & Makhnenko, R. (2020). Coupling between poromechanical behavior and fluid flow in tight rock. *Transport in Porous Media*, 135, 487-512.
- [13] Makhnenko, R. Y., Vilarrasa, V., Mylnikov, D., & Laloui, L. (2017). Hydromechanical aspects of CO₂ breakthrough into Clay-rich caprock. *Energy Procedia*, 114, 3219–3228.
- [14] Kivi, I. R., Vilarrasa, V., & Makhnenko, R. Y. (2020). Laboratory and numerical assessment of potential CO₂ leakage through the caprock. *CouFrac2020*, November 11–13, 2020, Seoul, Korea, in press.
- [15] Van Genuchten, M. T. (1980). A closed-form equation for predicting the hydraulic conductivity of unsaturated soils. *Soil Science Society of America Journal*, 44(5), 892.
- [16] Olivella, S., Carrera, J., Gens, A., & Alonso, E. E. (1994). Nonisothermal multiphase flow of brine and gas through saline media. *Transport in Porous Media*, 15(3), 271–293.
- [17] Vilarrasa, V., Bolster, D., Olivella, S., & Carrera, J. (2010). Coupled hydromechanical modeling of CO₂ sequestration in deep saline aquifers. *International Journal of Greenhouse Gas Control*, 4(6), 910–919.

EXPERIMENTAL INVESTIGATION OF THE INFLUENCE OF INJECTION PRESSURE AND CLAY SMEAR ON FAULT REACTIVATION FOR CO₂ STORAGE

Luke Griffiths¹, Joonsang Park¹, Pierre Cerasi², Laura Edvardsen², Andreas Wüstefeld³

¹ NGI - Norwegian Geotechnical Institute, Oslo, Norway

² SINTEF Industry, Trondheim, Norway

³ NORSAR, Kjeller, Norway

* Corresponding author e-mail: luke.griffiths@ngi.no

Abstract

Abstract

Induced microseismicity from subsurface engineering projects such as geothermal heat exploitation and CO₂ storage can be a show-stopper and halt the development of a site. While microseismicity correlates with fluid injection in the ground, the magnitudes of events are difficult to predict and some faults in the underground release significant energy, while others do not. Here, we test in the laboratory the hypothesis that clay content in the fault gouge may dampen asperity breakage upon shear slip and explain why certain faults release less elastic energy. We performed two triaxial tests on a sample of Castlegate sandstone to simulate fault reactivation as a result of pore pressure increase due to CO₂ (or water) injection, whilst measuring axial and radial P-wave velocities and monitoring acoustic emissions (AE; laboratory scale microseismicity). A through-going fracture was created by axial loading of the sample to failure. The axial stress was then reduced to 80% of the residual strength of the sample, and the fracture was reactivated by pore pressure pulses at rates of 3, 6, 12 and 24 MPa/hr. Although no CO₂ or second phase fluid was injected, the pressure pulse simulates the pressure propagation ahead of the injected fluid. Following the test, the sample was separated along the fracture plane, and the fracture was filled with a clay (kaolinite) gouge, reassembled, and the test procedure was repeated. For both tests we analysed AE locations, rate, and magnitude distribution, and determined source mechanisms. AE during the first test on the intact sample occurred throughout the sample during axial loading until coalescing along the macroscopic fault plane observed using 3D CT imaging. AE during the reactivation stages were located predominantly along the fracture. For the clean fracture, the pore pressure increase rate had no clear effect on the pressure for reactivation, i.e., no weakening at higher injection rates. For the sample containing a clay-filled fracture, we observed very little AE activity during all test stages and we were unable to reach stable sliding of the in-filled fracture during axial loading as for the clean fracture. We observed a slight increase in the pore pressure reactivation pressure at higher pressurisation rates which we attribute to plastic deformation of the fault gouge. These results suggest that, for the pressurisation rates observed, CO₂ injection rates may only have a negligible effect on fault stability, which is controlled rather by the absolute pressure changes.

Keywords: CO₂ reservoir, sandstone, fault, clay smear, microseismicity

1. Introduction

Carbon capture and storage (CCS) could play an essential role in meeting net-zero global CO₂ emission [1]. Currently, North Sea saline aquifers are targets for large-scale geological storage of CO₂. At such storage sites, pressure changes due to CO₂ injection may cause undesired deformation, and even slip on faults within and around the reservoir [2]. This could produce permeable pathways for fluid migration towards the surface, as well as microseismic activity. An assessment of the risk of leakage of CO₂ to the seabed requires a deep understanding of the mechanical properties of the reservoir and the potential for fracturing or reactivation of existing fractures and faults [3]. Specifically, it is important to know the influence of CO₂ injection rate translated into pore pressure increase on fault instability to develop an injection strategy to prevent, and limit, microseismicity and potential for leakage. If better

understood, microseismicity could be employed as a monitoring tool; this presupposes that one has the means to keep magnitudes below levels felt by humans on the ground (and obviously below levels capable of causing structural damage in built-up areas). The assumption is that microseismicity could monitor the pressure plume preceding the injected CO₂ fluid plume, and thus give an early warning on lack of conformance with predictions.

To better understand the influence of pressurisation rate on fault reactivation within reservoir sandstone, mechanical testing may be performed under controlled fluid saturation and stress conditions in the laboratory. When deforming rock samples in the laboratory, the macroscopic stress state is known and, through monitoring the laboratory-scale microseismic events (or Acoustic Emissions: AE), the initiation and location of any failure plane can be monitored as it develops. AE monitoring is a well-established technique to study failure processes in rocks [4]–[9].

In this study, we performed two triaxial tests on a sandstone sample relevant to North Sea CCS. First, we created a through-going fracture within the sample by axial loading at a constant axial deformation rate, which was then reactivated by pore pressure pulses at different rates. The sample was separated along the fracture and the fracture was filled with a clay gouge. The sample was then reassembled, and the test was repeated. We compare the mechanical and microseismic response of the samples to reactivation of the fracture through axial deformation, and then by pore pressure increase at different rates.

2. Materials and methods

2.1 Materials

Castlegate sandstone was selected for this study as it is a relatively homogeneous, clay-free rock, and has previously been used as part of a study on fracture reactivation by pore pressure increase [10]. The sandstone sample was a cylinder of 119.85 mm in length and 49.815 mm in diameter. Two tests were performed on the same sample. Test 1 was performed on the initially intact sample (Figure 1a), where a through-going fracture was created by axial loading, and the fracture was reactivated by pore pressure increase at different rates. In Test 2 the same sample was used, but with kaolin spread along the fracture (Figure 1b) as an analogue to clay-smear along a fault.

2.2 Testing equipment

Tests were performed within a triaxial apparatus at NGI (schematic shown in Figure 1c; [4], [11]) which can independently control the axial (vertical) and radial (horizontal or confining) stresses and the pressure of the pore fluid within the rock. The sample is held between two platens through which pore fluid may be injected. Steel filters between each end of the sample and the pistons prevent particles from entering the pore line tubing and ensure pressure is evenly distributed across the sample faces. The sample is contained within a nitrile sleeve to isolate it from the confining oil. Axial deformation is measured using two LVDTs mounted to the top and bottom platens (Figure 1c). The radial deformation is measured using strain gauges attached to a cantilever, fixed directly to the sample mid-height via 4 pins. The axial load (via a pressure chamber above the upper piston), confining pressure, and pore pressure are controlled by GDS pumps. The initial consolidation stresses were chosen to be the same as used by Cerasi et al. (2018) on samples of the same material: 5 MPa total isotropic stress and 2 MPa pore pressure.

Ultrasonic P-wave velocities in the axial and radial directions were measured during the tests at regular intervals through pairs of piezo transducers embedded within the platens and at the sample mid-height (Figure 2). AE monitoring was performed using 12 piezoelectric transducers (pinducers from Ergotech Ltd, UK), sensitive to displacement, and attached through the jacket to the lateral surface of the sample (Figure 1c). The transducers have a resonant frequency of around 1MHz, with most energy centered on 0.5 MHz [4]. The Milne acquisition system (Itasca Consulting, UK) is used to record

waveforms during velocity measurements and detect and record AE events. An event is recorded when the trigger voltage is surpassed at more than 4 of the 16 sensors (12 pinducers and 4 piezo-transducers). We recorded waveforms at 10 MHz sampling rate and 12-bit amplitude resolution, over durations of 409.5 μ s. Waveforms recorded through AE monitoring and active surveys were filtered using a band-pass filter with 10 kHz low-cut and 1 MHz high-cut frequencies.

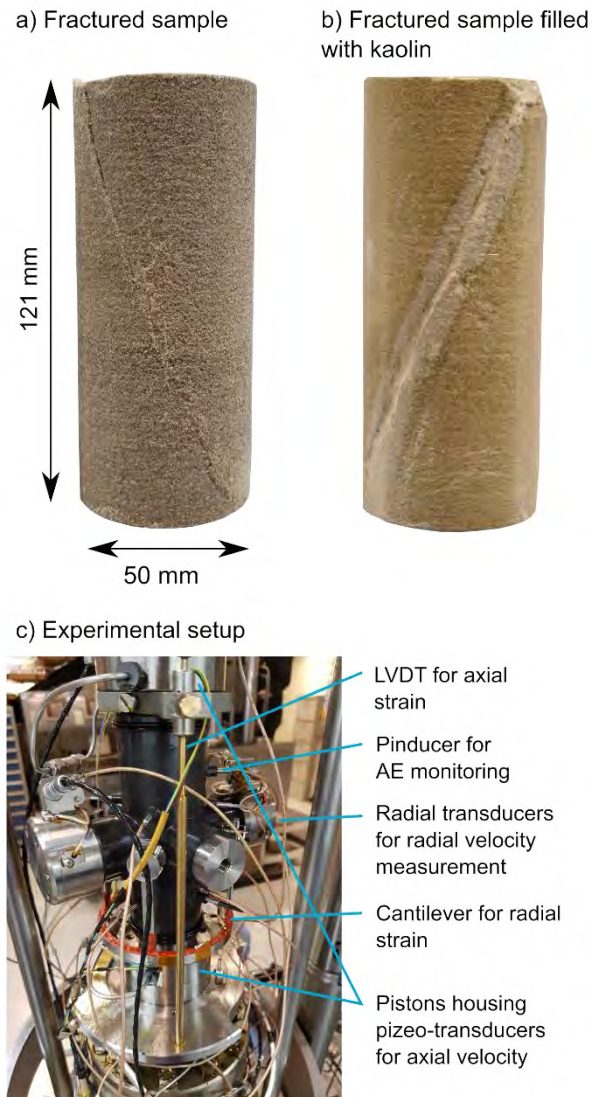


Figure 1: (a) The fractured sample following Test 1. (b) The same sample is used for Test 2 but with kaolin filling the through-going fracture. (c) The jacketed sample and instrumented sample within the triaxial apparatus.

To calibrate the voltage amplitudes at each sensor, we recorded across all 16 channels several pulses emitted from the larger axial and radial sensor pairs used for the velocity surveys (Figure 1c). The voltages at each of the 16 sensors were then scaled by a multiplicative factor so that each sensor gave the same relative "location magnitude" for the pulses, relative to a reference sensor. The relative magnitude (m) is given by equation (1), in the case where voltages at multiple (N) sensors are considered, V_{RMS} is the RMS voltage, and d_m is the distance between the event and the receiver (from Pettitt

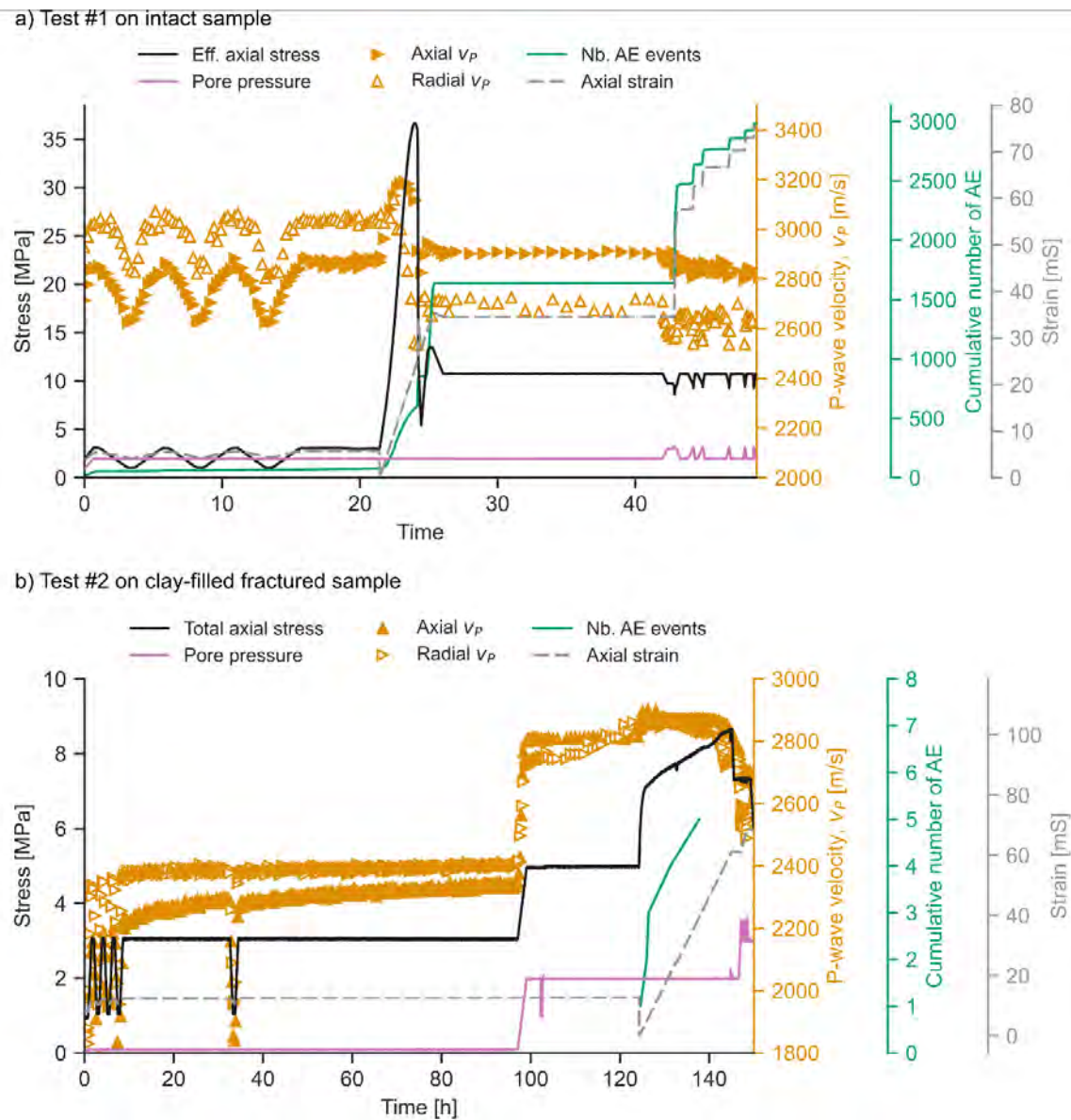


Figure 2: Timelines for triaxial tests on Castlegate sandstone: (a) Test on an initially intact sample; (b) test on the same sample, with kaolinite along the fracture.

and Young (2007)). The calibration waveforms were acquired at the consolidation stresses prior to shearing. Measurements were made for multiple pulses from each sensor to verify the consistency of the voltage signals. The calibration highlighted a greater sensitivity of the sensors located within the platen compared to the smaller radial sensors. We therefore excluded the sensors within the platens from the location and source mechanism calculation to avoid any bias.

$$m = \log_{10} \left(\frac{\sum_{m=1}^N V_{RMS} \cdot d_m}{N} \right) \quad (1)$$

2.3 Stress paths

2.3.1. Sandstone containing clean fracture

Figure 2a depicts a timeline of Test 1 on the initially intact Castlegate sandstone sample. The sample was first held under vacuum and pressurized to 1 MPa confining

pressure. Brine (35g/L NaCl) was then allowed to enter the sample, and the pore pressure was increased to 0.1 MPa. AE trigger thresholds were adjusted for each sensor to be just above the noise level of the equipment and velocity surveys were scheduled every 15 minutes. The cell pressure was increased to 5 MPa and the pore pressure to 2 MPa over 70 minutes. Cell pressure was cycled from 5 to 3 MPa at 1 MPa/hr (three cycles), with 30 min between ramps to allow for stabilization of strain due to any adjustment of the sample and the loading frame.

To create a through-going fracture, the sample was axially deformed at a constant strain rate of 3 mS/hr to beyond the peak stress (26.6 MPa effective axial stress), until the axial stress had stabilized at the residual strength of the fractured sample (13.5 MPa effective axial stress; Figure 2a). The axial stress was then decreased to 80 % of the of residual stress (10.8 MPa) at a rate of 3.75 MPa/hr.

The fracture was then reactivated multiple times by increasing pore pressure from 2 MPa at 3 MPa/hr. The pore pressure was increased until we observed an acceleration of the axial strain as the fracture began to slip (giving the pore pressure reactivation pressure), at which point we then decreased the pore pressure to 2 MPa at the same rate. Reactivation at 2 MPa/hr was repeated three times at rates of 6, 12 and 24 MPa/hr, unloading at reactivation to 2 MPa in 7 minutes (~10 MPa/hr). Finally, the axial stress was unloaded at 3.75 MPa/hr to isotropic conditions and the sample was removed from the cell.

2.3.2. Sandstone containing clean fracture

Test 2 was performed on the same sample as used in Test 1. Prior to testing, the sample was separated into two pieces when wet, and dried in an oven for 48 hr (mass change between 24 and 48 hours was 0.02-0.04 g). Kaolin (Speswhite™) mixed with distilled water was applied to each side of the fracture, resulting in a coating with 1-2 mm thickness (Figure 1c). X-ray micro-computed tomography (μ -CT) was used to assess the coverage of the clay within the fracture, which was found to be continuous across the fracture surface, and completely filling the fracture aperture.

The sample was then placed within the nitrile jacket with the same orientation as during Test 1. As for Test 1, the sample was pressurised to 1 MPa confining pressure and saturated with 35 g/L NaCl brine. The AE trigger thresholds were individually adjusted to just above the noise level. Cell pressure was increased to 5 MPa and pore pressure to 2 MPa. The cell pressure was decreased from 5 to 3 MPa and back, at a rate of 1 MPa/hr (three times), with 30 min between ramps. Following a period of 24 hours at the consolidation stresses, the cell pressure was cycled again at the same rate, to see whether there were any long-term changes in the mechanical properties of the sample in presence of clay (which there were not).

Axial stress was increased to deform the sample at a constant strain rate of 3 mS/hr. We expected the stress to reach a peak value and stabilize at the residual strength of the fracture, as for Test 1. Instead, the axial stress continued to increase within the deformation range of the test, and the axial loading was stopped at an arbitrary value of 7.3 MPa effective axial stress. The effective axial stress was then decreased to 80 % of this value: 5.3 MPa, at which stress the axial and radial strain remained stable.

The clay-filled fracture was reactivated multiple times by increasing the pore pressure at rates of 3 MPa/h (three times), and 6, 12, and 24 MPa/hr (one time) until an acceleration of the axial strain was observed (at the pore pressure reactivation pressure). Finally, the axial stress was unloaded at 3.75 MPa/hr to isotropic conditions and the sample was removed from the cell.

3. Results

3.1 Fracture reactivation

Table 1 gives the fracture reactivation pore pressure for the different rates of pore pressure increase used in Tests

1 and 2. The fracture reactivation pressures were determined at the onset of slip by an increase in axial deformation and drop in axial stress. For Test 1 the initial fracture reactivation had the highest reactivation pressure at 3.27 MPa, compared to around 3.1 MPa for all subsequent reactivations, regardless of the rate of increasing pore pressure. For Test 2 a slight increase in reactivation pressure with pore pressure increase rate was observed: from 3.21 MPa for the first reactivation at 3 MPa/hr, to 3.39 MPa for the final reactivation at 24 MPa/hr (Table 1). We note, however, that the overall influence of pore pressure increase rate on the absolute reactivation pressure was low.

Table 1: Pore pressures for fracture reactivation for different pore pressure increase rates for Test 1 on a "clean" fractured sandstone, and Test 2 on fractured sandstone with clay fault.

Test	Cell pressure [MPa]	Axial stress [MPa]	Initial pore pressure [MPa]	Pore pressure increase rate [MPa/hour]	Pore pressure reactivation pressure [MPa]
1	5	10.8	3	3	3.27
			2	2	3.07
				3	3.08
				6	3.12
				12	3.14
24	3.1				
2	5	7.3	2	3	3.21
			3	3	3.3
				3	3.28
				6	3.31
				12	3.35
24	3.39				

3.2 Passive and active acoustic monitoring

3.2.1 P-wave velocities and AE locations

Figure 2a shows the P-wave velocities in the radial (at the sample mid-height) and axial directions, calculated from the P-wave travel times between opposing source-receiver pairs and the sample dimensions (accounting for sample deformation).

Also shown in Figure 2 are the number of located AE during each test. For Test 1 (Figure 2a), across all test phases, a total of 2904 AE events were detected, with arrival times picked on at least five sensors and located within the cylinder as defined by the piezo-transducers. A grid search algorithm within the InSite software (Itasca; Pettitt and Young, 2007), was used to locate the events, considering a time-dependent transverse isotropic velocity model constrained by the measured axial and radial velocities (Figure 2a). The locations of the detected events are illustrated using 3D visualization of the μ -CT data of the sample post-testing and coloured by test phase (Figure 3). During the consolidation phase, 68 events were detected as the effective isotropic stresses reached 3 MPa. Only a few events were detected during the isotropic cycling stage, located predominantly in proximity to the radial sensors. This was likely due to rearrangement and friction between the large radial transducers and the sample.

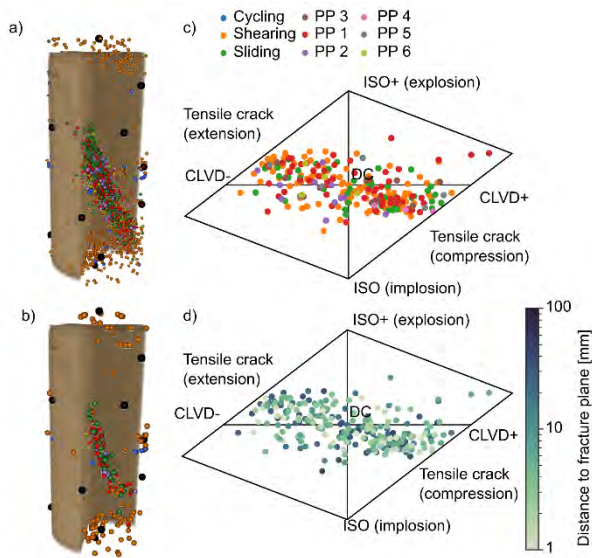


Figure 3. Acoustic emission locations and source mechanisms for Test 1 on the initially intact Castlegate sandstone: a) all AE event locations coloured by test phase (PP: pore pressure reactivation) within a 3D visualization of μ -CT data of the sample post testing. Black spheres give the location of the piezo-transducers for velocity surveys and AE monitoring. b) AE event locations of high SNR events used for moment tensor inversion. (c) and (d) Hudson plots [13] of the decomposition of moment tensors of events in (b) into their isotropic (ISO), double-couple (DC), compensated linear vector dipole (CLVD) by (c) test phase, and (d) by distance to the macroscopic fracture plane.

During the shearing stage, 781 events were detected and located. Events during shearing are initially located near the sample's end surfaces, close to the rock-platens interface. Similar observations were made in [14], and are expected to result from localised frictional slip due to strain incompatibility at the interface between the steel platens and the rock sample ends. In the later stages of shearing, AE events were located towards the centre of the sample, before forming a fracture plane (Figure 3).

For Test 1, the fracture plane formed by the AE events matches the location of the fracture as observed within the μ -CT scan of the sample following the test (Figure 3a; plane with azimuth 286.8° and dip 11.14°). During the stable sliding stage—between the stress drop and unloading to 80 % of the residual strength of the fracture—732 AE events were located. During the six pore pressure pulses, 833, 161, 120, 85, 67 and 57 were located (Figure 3a). Following the formation of the through-going fracture, almost all events were located in close proximity to the fracture.

During Test 2 on the sample containing a clay-filled fracture, only 5 AE events were located within the sample, all occurring during the axial loading phase (Figure 3b). No events were detected during pulse pressure reactivation, and therefore further study of the AE will focus on the results of Test 1.

3.2.1 AE characteristics

Figure 4 shows histograms of the relative magnitudes of AE events during each phase of Test 1 on the clean

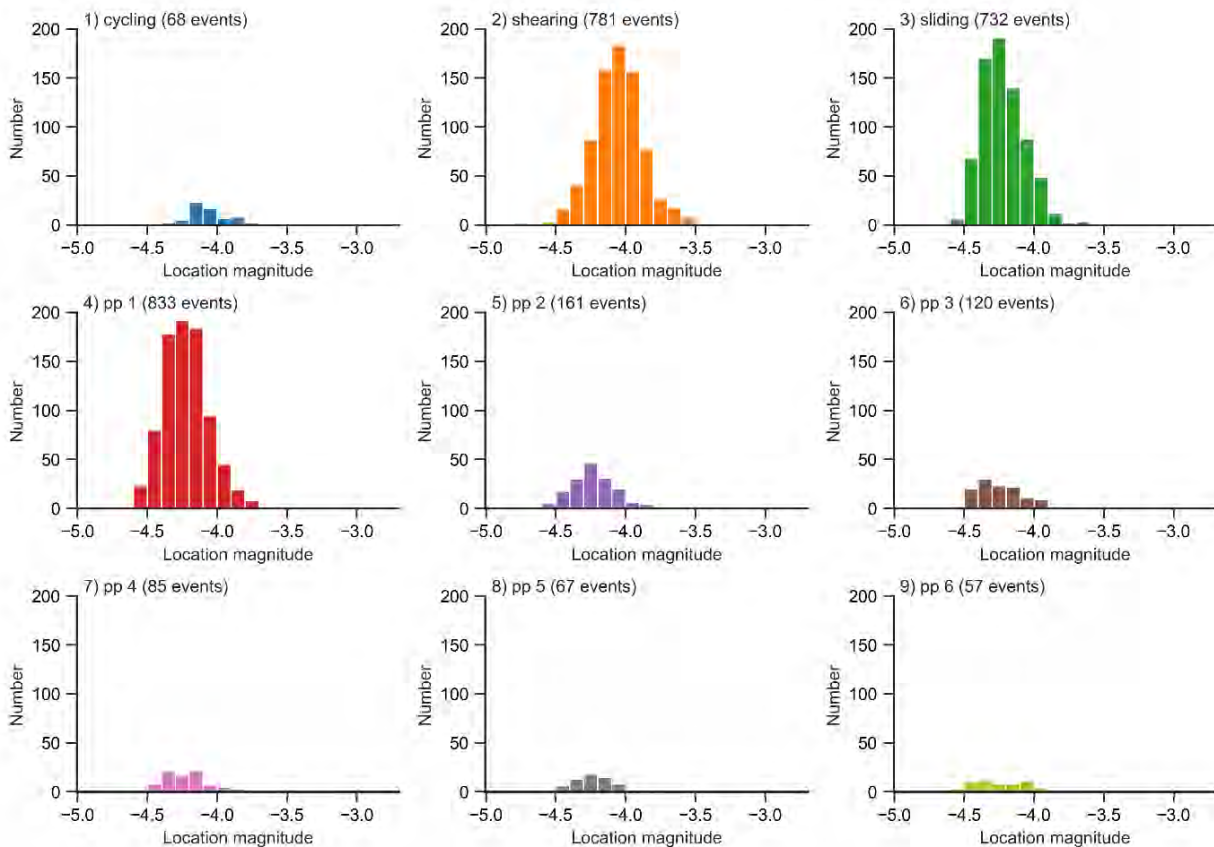


Figure 4. Histograms of the relative magnitudes of AE events during each phase of Test 1 on the clean sandstone (PP: pore pressure reactivation), calculated using Eq. (1).

sandstone, calculated using Eq. (1). The relative magnitudes of events during shearing were overall higher (relative magnitudes centered around -4.0) than during other test phases (relative centered around \sim -4.25).

AE can provide insights into fracture source mechanisms by statistical evaluation of P-wave first motion polarities ([15], [16]), or by seismic moment tensor inversion. Moment tensors – a description of the equivalent forces acting at a seismic point source – are commonly inferred from microseismic data and may be decomposed into isotropic, double-couple, and compensated linear vector dipole parts ([17]) and their relative contributions may be analysed ([4], [18]).

Here we selected AE events during Test 1 with P-wave arrival times and amplitudes picked on a minimum of 10 sensors, and with a signal-noise-ratio of the P-wave arrivals of more than 20 for moment tensor inversion. We calculated the moment tensors using a linear inversion of the P-wave amplitudes in the time domain ([12], [19]) considering a homogeneous, time-dependent velocity model updated throughout the experiment from the velocity surveys (Figure 2a). We see that events close to the fracture plane had generally a lower isotropic component than events occurring away from the macroscopic fracture (Figure 3d).

4. Discussion

4.1 Influence of fault gouge on fault stability

During the post peak deformation of Test 1, the sample with a clean fracture reached a residual "strength" for stable sliding of the fracture. The sample containing a clay-filled fault, however, became stronger during the axial shearing phase, with no stabilization stress (Figure 2b).

For the clean fracture, we observed a slightly higher pore pressure at reactivation during the very first reactivation phase (3.3 MPa pore pressure; Table 1). For each of the subsequent reactivations of the fracture, including at different rates of pore pressure increase, the reactivation pressure was lower and similar for all (at \sim 3.1 MPa).

For the sample containing a clay-filled fracture, higher pore pressure increase rates lead to slightly higher reactivation pressures (3.28 MPa at 3 MPa/hr to 3.39 MPa at 24 MPa/hr; Table 1). The pore pressure rate may influence the pore pressure reactivation pressure in presence of the fault gouge, which we attribute to time-dependent, plastic deformation of the clay.

4.1 AE response with and without fault gouge

During Test 1, on the initially intact sample, AE detected during shearing and creation of a through-going fracture were more energetic than during the subsequent fracture reactivation phases (Figure 3). We attribute the higher energy AE to the breaking of cement and grains during the fracturing of the intact sample, releasing more energy than AE resulting from sliding, rolling and fracturing of grains on an already fractured surface.

During each pore pressure reactivation phase of Test 1, the AE events had a similar relative magnitude (Figure

3), and the number of events increased quasi-linearly with strain (Figure 2a), regardless of the pore pressure increase rate.

For the sample containing a clay-filled fracture, we detected very few AE events in comparison, and only during the shearing phase (Figure 2b). The difference in AE response suggests that within the observable frequency range (50 kHz – 1MHz), slip along the clay-filled fracture is aseismic.

4.3 Implications for CCS

These experiments were performed to assess the response of faults to different rates of pore pressure change which may be associated with CCS. While brine was used as the saturating pore fluid, we do not expect our results to strongly differ in presence of CO₂ –the presence of CO₂ in clay-filled fractures have been shown in the lab to not affect fault stability (e.g. [20]).

Here we see that the laboratory faults are not strongly affected by pore pressurisation rate effects, and it rather is the absolute pressure which governs whether the fault may reactivate. For CCS, CO₂ injection rates could potentially be adjusted to avoid unwanted fault reactivation and microseismicity. Our results suggest, however, that the rate of pore pressure change is not expected to induce any change in fault properties – with or without fault gouge. This means that injecting at lower rates may only limit fracture reactivation if it results in lower absolute pore pressures.

We expect rather that fluid mobility and the progression of the pressure front governs where faults and fractures may reactivate. For example, microseismic monitoring at the Decatur CO₂ sequestration site has highlighted the significance of hydraulic heterogeneity on CO₂ migration, including a hydraulic connection between the reservoir and the basement [21]. Field-scale studies have shown microseismic characteristics—including event magnitude and the size and shape of the microseismic cloud [22], [23]—to be related to the type of fluid injected and its mobility, with fluid viscosity thought to be a key influencing parameter.

5 Conclusion

We performed two triaxial tests on a sample of Castlegate sandstone to simulate fault reactivation, whilst measuring axial and radial P-wave velocities and monitoring acoustic emissions. A through-going fracture was created by axial loading, which was then reactivated by pore pressure pulses at rates of 3, 6, 12 and 24 MPa/hr. Following the test, the sample was separated along the fracture plane, and the fracture was filled with a clay (kaolinite) gouge, before being subject to the same test procedure.

For the test on the initially intact rock, AE characteristics (relative magnitudes, locations, source mechanisms) differed between AE events resulting from fracturing and from reactivation of the fracture. AE had similar characteristics for each of the reactivation phases, regardless of pore pressure increase rate. However, for the sample containing a clay-filled fracture, we observed very little AE activity during all test stages.

The pore pressure increase rate had no clear effect on the pressure for reactivation of the clean fracture, i.e. no weakening at higher injection rates. For the sample containing a clay-filled fracture, higher pore pressure increase rates lead to only slightly higher reactivation pressures. These results suggest for the pressurisation rates observed, injection rates may only have a negligible effect on fault stability, which is controlled by the absolute pressure changes.

Acknowledgements

This work has been produced with support from the SINTEF-coordinated Pre-ACT project (Project No. 271497) funded by the Research Council of Norway RCN, Gassnova (Norway), BEIS (UK), RVO (Netherlands), and BMWi (Germany) and co-funded by the European Commission under the Horizon 2020 program, ACT Grant Agreement No 691712. We also acknowledge the industry partners for their contributions: Total, Equinor, Shell, TAQA. This research was also supported by RCN via CLIMIT grant no. 268520/E20, IGCCS: Induced-seismicity geomechanics for controlled CO₂ storage in the North Sea. Additional funding was also given by the European Union's Horizon 2020 research and innovation program under grant agreement number 764531, "SECURE—Subsurface Evaluation of Carbon capture and storage and Unconventional risks".

References

- [1] V. Masson-Delmotte et al., "IPCC, 2018: Summary for Policymakers," 2018.
- [2] V. Vilarrasa and J. Rutqvist, "Thermal effects on geologic carbon storage," *Earth-science reviews*, vol. 165, pp. 245–256, 2017.
- [3] M. Rongved and P. Cerasi, "Simulation of stress hysteresis effect on permeability increase risk along a fault," *Energies*, vol. 12, no. 18, p. 3458, 2019.
- [4] E. Aker, D. Kühn, V. Vavryčuk, M. Soldal, and V. Oye, "Experimental investigation of acoustic emissions and their moment tensors in rock during failure," *International Journal of Rock Mechanics and Mining Sciences*, vol. 70, pp. 286–295, Sep. 2014, doi: 10.1016/j.ijrmms.2014.05.003.
- [5] L. Griffiths, O. Lengliné, M. J. Heap, P. Baud, and J. Schmittbuhl, "Thermal Cracking in Westerly Granite Monitored Using Direct Wave Velocity, Coda Wave Interferometry, and Acoustic Emissions," *Journal of Geophysical Research: Solid Earth*, Mar. 2018, doi: 10.1002/2017JB015191.
- [6] P. Baud, E. Klein, and T. Wong, "Compaction localization in porous sandstones: spatial evolution of damage and acoustic emission activity," *Journal of Structural Geology*, vol. 26, no. 4, pp. 603–624, Apr. 2004, doi: 10.1016/j.jsg.2003.09.002.
- [7] M. C. Eppes et al., "Deciphering the role of solar-induced thermal stresses in rock weathering," *Geological Society of America Bulletin*, vol. 128, no. 9–10, pp. 1315–1338, May 2016, doi: 10.1130/B31422.1.
- [8] D. Lockner, "The role of acoustic emission in the study of rock fracture," *International Journal of Rock Mechanics and Mining Sciences & Geomechanics Abstracts*, vol. 30, no. 7, pp. 883–899, décembre 1993.
- [9] D. A. Lockner, J. D. Byerlee, V. Kuksenko, A. Ponomarev, and A. Sidorin, "Quasi-static fault growth and shear fracture energy in granite," *Nature*, vol. 350, no. 6313, pp. 39–42, Mar. 1991, doi: 10.1038/350039a0.
- [10] P. Cerasi, A. Stroisz, E. Sønseth, S. Stanchits, V. Oye, and R. Bauer, "Experimental investigation of injection pressure effects on fault reactivation for CO₂ storage," *International Journal of Greenhouse Gas Control*, vol. 78, pp. 218–227, Nov. 2018, doi: 10.1016/j.ijggc.2018.08.011.
- [11] T. Berre, "Triaxial testing of soft rocks," *Geotechnical Testing Journal*, vol. 34, no. 1, pp. 61–75, 2010.
- [12] W. S. Pettitt and R. P. Young, "InSite seismic processor—user operations manual version 2.14," *Applied Seismology Consultants*, Shrewsbury, UK, 2007.
- [13] J. A. Hudson, R. G. Pearce, and R. M. Rogers, "Source type plot for inversion of the moment tensor," *Journal of Geophysical Research*, vol. 94, no. B1, p. 765, 1989.
- [14] L. Griffiths et al., "Inferring microseismic source mechanisms and in situ stresses during triaxial deformation of a North-Sea-analogue sandstone," *Advances in Geosciences*, vol. 49, pp. 85–93, Sep. 2019, doi: 10.5194/adgeo-49-85-2019.
- [15] S. Stanchits, S. Vinciguerra, and G. Dresen, "Ultrasonic velocities, acoustic emission characteristics and crack damage of basalt and granite," *Pure and Applied Geophysics*, vol. 163, pp. 974–993, 2006.
- [16] A. Zang, F. Christian Wagner, S. Stanchits, G. Dresen, R. Andresen, and M. A. Haidekker, "Source analysis of acoustic emissions in Aue granite cores under symmetric and asymmetric compressive loads," *Geophys J Int*, vol. 135, no. 3, pp. 1113–1130, Dec. 1998.
- [17] L. Knopoff and M. J. Randall, "The compensated linear-vector dipole: A possible mechanism for deep earthquakes," *Journal of Geophysical Research* (1896-1977), vol. 75, no. 26, pp. 4957–4963, 1970.
- [18] G. Kwiatek, T. H. W. Goebel, and G. Dresen, "Seismic moment tensor and b value variations over successive seismic cycles in laboratory stick-slip experiments," *Geophys. Res. Lett.*, vol. 41, no. 16, p. 2014GL060159, Aug. 2014, doi: 10.1002/2014GL060159.
- [19] G. De Natale and A. Zollo, "Earthquake focal mechanisms from inversion of first P and S wave motions," in *Digital seismology and fine modeling of the lithosphere*, Springer, 1989, pp. 399–419.
- [20] J. Samuelson and C. J. Spiers, "Fault friction and slip stability not affected by CO₂ storage: Evidence from short-term laboratory experiments on North Sea reservoir sandstones and caprocks," *International Journal of Greenhouse Gas Control*, vol. 11, pp. S78–S90, Nov. 2012, doi: 10.1016/j.ijggc.2012.09.018.
- [21] B. P. Goertz-Allmann, S. J. Gibbons, V. Oye, R. Bauer, and R. Will, "Characterization of induced seismicity patterns derived from internal structure in event clusters," *Journal of Geophysical Research: Solid Earth*, vol. 122, no. 5, pp. 3875–3894, 2017, doi: 10.1002/2016JB013731.
- [22] S. J. Ha, J. Choo, and T. S. Yun, "Liquid CO₂ Fracturing: Effect of Fluid Permeation on the Breakdown Pressure and Cracking Behavior," *Rock Mechanics and Rock Engineering*, vol. 51, no. 11, pp. 3407–3420, Nov. 2018, doi: 10.1007/s00603-018-1542-x.
- [23] J. P. Verdon, J.-M. Kendall, and S. C. Maxwell, "A comparison of passive seismic monitoring of fracture stimulation from water and CO₂ injection," *GEOPHYSICS*, vol. 75, no. 3, pp. MA1–MA7, May 2010.

FROM NATIONAL TO INTERNATIONAL FOCUS – RESULTS AND IMPACTS FROM THE NORWEGIAN NATIONAL RD&D PROGRAMME FOR CCS (CLIMIT)

Aage Stangeland^{1*}, Åse Slagtern¹, Ragnhild Rønneberg¹, Lars Ingolf Eide¹, Ingrid Sørum Melaaen²

¹ The Research Council of Norway, Oslo, Norway

² Gassnova SF, Porsgrunn, Norway

* Corresponding author e-mail: ast@rcn.no

Abstract

The Norwegian national program for RD&D within CCS (CLIMIT) changed focus towards more international collaboration in 2017. The program has since then allocated approximately 20 percent of the available budget for international joint calls, primarily through the calls set up by the ACT transnational partnership. ACT is the abbreviation for *Accelerating CCS technologies*, and funding agencies from 16 countries, provinces and regions are collaborating on joint calls and knowledge sharing within this partnership. The effect of allocating a fifth of the available CLIMIT funds to international calls, has led to a shift from basic to applied research and consequently to larger projects of higher industrial interest. The international projects have managed to raise awareness of CCUS as a tool to combat global warming in a much more pronounced way than is normally seen in national RD&D projects.

Keywords: CCS, international project, RD&D funding

1. Introduction

CO₂ Capture and Storage (CCS) is a key technology to combat global warming, as highlighted by the International Energy Agency [1]. CCS has a large potential for global CO₂ emission reductions and if combined with other technologies, like biomass, it can lead to CO₂ removal from the atmosphere. Realizing the potential for CCS requires large scale demonstration of the CCS technology in parallel with ambitious research and development and demonstration.

The Norwegian government launched the Longship project in the autumn 2020 [1] which is scheduled to be in operation by 2024 to demonstrate a full scale CCS chain. The project includes CO₂ capture from a cement plant, CO₂ transport by ship, and permanent storage in an underground aquifer in the North Sea. Several other large-scale projects are also being planned in other countries [3].

The Norwegian national program for research, development and demonstration (RD&D) within CCS, the CLIMIT program [4] has since it was launched in 2005 supported national RD&D projects within capture, transport and storage of CO₂. Until 2015 most of the annual budget for the CLIMIT program was allocated to national calls for RD&D applications. Since 2016 and onwards a significant share of the budget for the CLIMIT program has been allocated to international calls.

The aim of this paper is to analyze the effects and impacts of allocating national Norwegian RD&D budget to international joint calls.

Section 2 analyzes how the new international focus has changed the project portfolio of the CLIMIT program. Effects and impacts when international calls are prioritized are highlighted in Section 3 followed by a

discussion on the way forward for Norwegian RD&D within CCS in Section 4. Conclusions are given in Section 5.

2. Analysis of project portfolio

The CLIMIT program is administrated in cooperation between the Gassnova State Enterprise and the Research Council of Norway (RCN). RCN supports research and innovation at lower Technology Readiness Level (TRL), whereas Gassnova supports demonstration and development at higher TRL. The CLIMIT program supported 142 projects in 2020 with a total of NOK 218 M. The projects typically run for three to four years.

The program has a joint secretariat with representatives from Gassnova and RCN and a board that takes decisions on strategic priorities, investment plans and project funding. The annual budget for the program is allocated by the Norwegian Ministry for Petroleum and Energy (MPE) over the National Budget.

The following project types can be supported:

- Basic research with up to 100 percent funding rate from CLIMIT.
- Competence building project led by research organization with support from industrial partners. Typical funding rate from CLIMIT is 80 %.
- Innovations projects led by industry. Support from CLIMIT is regulated by state aid guidelines.
- Demonstration and development projects where industrial partners have key roles in projects addressing development, piloting or demonstration at smaller scale. Support from CLIMIT is regulated by state aid guidelines.

- International RD&D projects where CLIMIT fund the Norwegian part of the projects. Funding rate regulated by state aid guidelines.
- Coordination activities.

CLIMIT has since 2016 allocated funding to international calls and bilateral projects. RCN is coordinating the international RD&D initiative called *Accelerating CCS Technologies* (ACT) where 16 countries and regions are collaborating on joint calls [5]. CLIMIT has made significant contribution to the three ACT calls launched in 2016, 2018, and 2020, respectively - with allocations from 60 to 70 million Norwegian kroner (NOK) to each call.

In addition, CLIMIT is open for and welcomes bilateral projects. This has led to the Preem CCS project [6], receiving funding from CLIMIT and the Swedish Energy Agency (Energimyndigheten) The project aims at CO₂ capture at the Preem refinery in Lysekil, Sweden.

Figure 1 shows the annual support from CLIMIT distributed on the different project types.

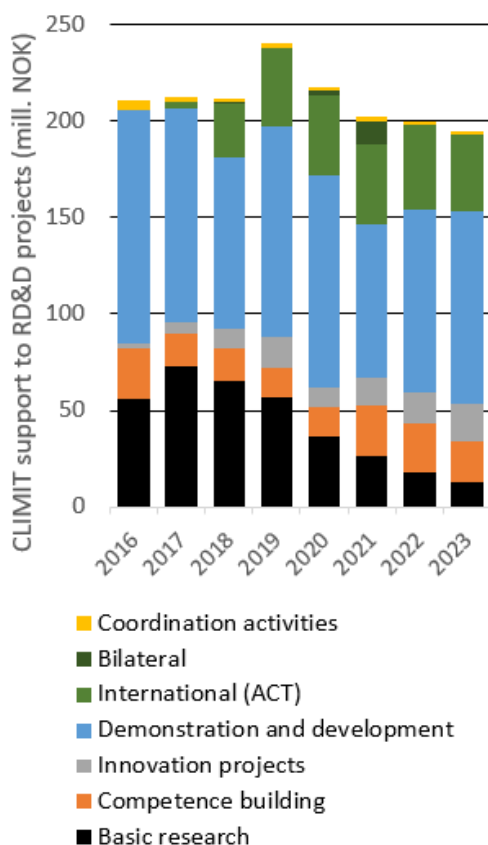


Figure 1: Annual support from the CLIMIT program to RD&D projects split on different project types.

The data in Figure 1 is based on historical support to projects and stipulated spending for the coming years. The figure shows a spending of approximately NOK 200 M annually until 2018, then an increase in 2019, partly due to allocation of significant funds to projects funded through the ACT calls. The decline after 2019 is a result of a 14 percent reduction in the National Budget for the CLIMIT program in 2020.

Figure 2 shows the shares of the total annual CLIMIT spending in 2016 and predicted spending in 2021. The figure shows that while there were no international projects in the portfolio in 2016, the share of international ACT projects has increased to 20 percent in 2021. In addition, there is also a 6 percent share for bilateral projects in 2021. The share of international ACT projects has stayed at the level of approximately 20 percent since 2019 and is stipulated to be stabilized at level for the coming years.

Please note that there is some international collaboration in many of the projects not classified as bilateral or international ACT projects in Figure 1 and Figure 2. The budget for such international collaboration is, however, limited. The projects highlighted as international projects in Figure 1 and 2 are projects funded by several funding agencies from several countries, but only the national Norwegian funding is shown in the figures.

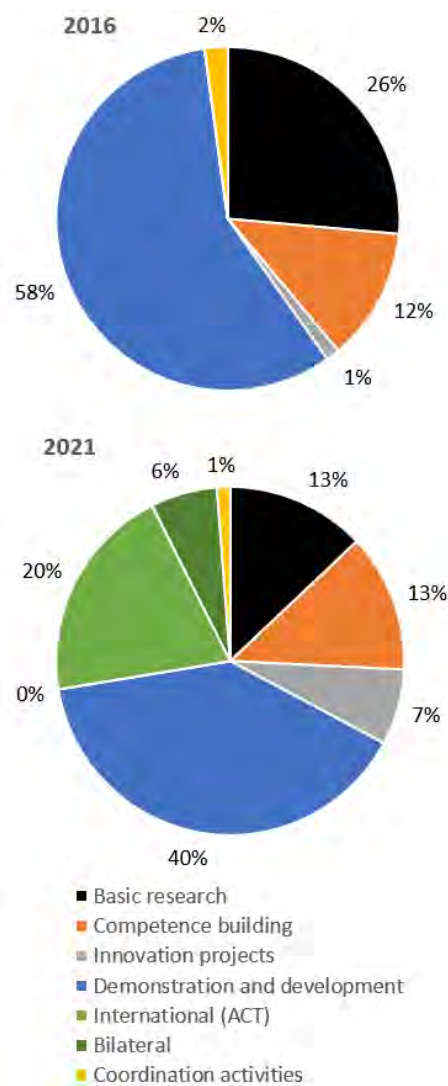


Figure 2: The share of different project types in the CLIMIT portfolio.

One consequence of increasing the share of the international projects is a decreasing share of national basic research projects. This has been a strategic planned change because the CLIMIT board wants to prioritize

international projects and projects with industrial involvement. Currently, as Norway is investing in the Longship project, it will be important to support projects on higher TRL which can build on the Longship project and close gaps that may appear during the construction and commissioning of the Longship. Moreover, it is expected that new large-scale projects will arise, and that they will have the potential to connect to the large-scale Norwegian infrastructure for CO₂ transport and storage that will be built as a part of the Longship project.

2.1 The ERA NET Cofund ACT initiative

ACT is the main international activity supported by CLIMIT. ACT started as an ERA NET cofund in 2016 with eight European countries participating in the first call. ACT has since then expanded beyond the European borders and there are now funding agencies from 16 countries, provinces and regions participating. Figure 3 shows the contributions from each ACT partner to the three ACT calls that have been set up until now.

Norway is the largest contributor to the ACT calls, closely followed by UK, Germany, the Netherlands, and the European Commission (EC). The first ACT call was cofounded by EC and their contribution was distributed among all countries participating in the first ACT call.

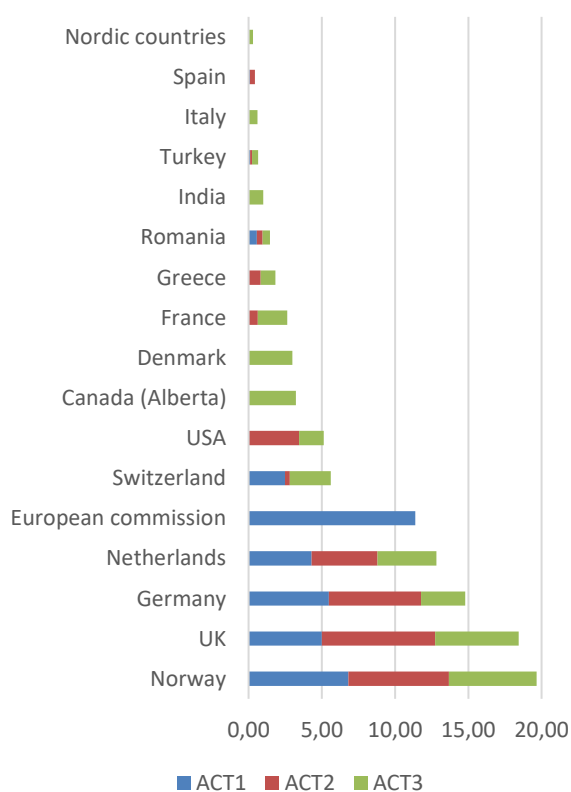


Figure 3: Countries, provinces and regions participating with funding for the three ACT calls.

The available funding for the three ACT calls have been in the range from € 31 to 36 M and the total budget for the three calls summarize to € 103 M. The first two ACT calls resulted in 20 projects granted € 67 M in support from ACT. The total budget for the 20 projects is € 94 M, including financial support from ACT, own financing, and contributions from industry.

3. Effects and impacts

3.1 Effects of increased international cooperation

The main effect after CLIMIT allocated more funding to international calls is that there are more projects in the CLIMIT portfolio where Norwegian researchers work closely together with researchers from other countries.

A consequence of prioritizing international collaboration is that other areas get less financing. In this case for the CLIMIT program, the funding for basic research has gone considerably down, from NOK 56 M in 2016 to expected spending of NOK 26 M in 2021.

ACT has a positive effect due to the cost sharing. ACT projects receives funding from several countries and the financial burden is distributed on several funding agencies. Furthermore, ACT has a positive structural effect on international RD&D because it contributes to aligning research objectives and activities across national borders. It is also believed that some countries have more comprehensive RD&D activities within CCS because of ACT than they would have had without ACT. However, this is difficult to quantify.

RCN is the coordinator of the ACT initiative. This is a resource demanding task, and RCN has therefore allocated an additional employee for coordination and management of ACT.

While most ACT projects perform applied research, there are also ACT projects with work packages addressing basic research. ACT projects addressing applied research have more industrial oriented approaches and deliverables are often designed to meet industrial needs. Consequently, there are often less peer-reviewed scientific paper publications in the ACT projects focusing on applied research compared to national basic research projects. This has only a minor effect on the total publication rate in the CLIMIT portfolio. The total number of peer-review publications from CLIMIT and ACT projects funded by RCN has been quite stable the last five years as shown in Figure 4.

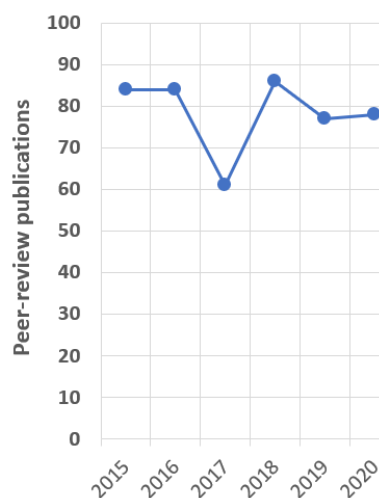


Figure 4: Number of peer-reviewed publications from CLIMIT and ACT projects funded by RCN.

Knowledge sharing is high on the agenda within the ACT consortium and within the projects funded by ACT. The projects are requested to emphasize on dissemination, and results created by ACT funded projects are therefore to a large extent available for the international environment of researchers, industrial stakeholders, and decision makers interested in CCS.

3.2 Impacts of increased international cooperation

There has been a strong industrial interest for the ACT projects. The industrial interest is higher for ACT projects compared to an average national CLIMIT project at similar Technology Readiness Level. With international collaboration on joint calls it has been possible to establish large projects that have better abilities to address industrial needs.

ACT projects have undoubtedly played a crucial and important role for the Norwegian CCS community. Representatives from industrial partners in the Longship project have stated that ACT projects are delivering results and competence needed for the Longship project. One example is the ACT funded project Pre-ACT [7] that has delivered new knowledge on how to handle pressure build-up during CO₂ injection. Industrial stakeholders have said that this knowledge is of high value for the Northern Light [8] project where the CO₂ storage solution for Longship is designed and constructed.

The ACT calls have addressed strategic priorities from the EU SET-plan [9] and the Mission Innovation (MI) [10] in the call texts. Projects funded by ACT are therefore important tools for generating results that are needed to achieve the ambitions of the EU SET-plan and Mission Innovation.

There are several important fora for international cooperation within CCS at a strategic level. Representatives from Norwegian authorities participate in several of them. The most important, in addition to two already mentioned (SET-Plan and MI) are the Carbon Sequestration Leadership Forum (CSLF), the Clean Energy Ministerial (CEM) CCUS Initiative, the IEA GHG, the Zero Emission Platform (ZEP), the bilateral Memorandum of Understanding (MoU) between Norway and USA, and the MoU between Norway and UK. When significant resources are spent at the strategic level it is important to make sure that there are activities that can lead to achievement of strategical ambitions. ACT has turned out to be an important tool to meet the strategic ambitions of the mentioned strategic fora.

Several ACT projects have joined forces to set up seminars in Brussels where key results are communicated to stakeholders and decision makers. There have been several CCUS seminars in the period from 2017 and the start of the corona lockdown spring 2020. One example is the ELEGANCY Conference 2018, set up in Brussels 8 November 2018 to address how hydrogen can contribute to decarbonization of the European energy system [11]. This conference, together with results from the ELEGANCY project, has contributed significantly to ensure that Hydrogen production combined with CCS is on the radar at political and industrial level in Europe.

Several ACT projects, together with other European CCS projects, set up at conference in Brussels 10 September 2019 to showcase the research results within CO₂ storage with special relevance for energy, environment and climate policy [12]. Events like this are very important for raising awareness of CCS as an important and necessary tool to combat global warming. National CLIMIT projects have not been able to address awareness in a similar way.

The shift in Norwegian RD&D within CCS from national to international projects also has some weaknesses. The share of basic research in the CLIMIT portfolio is decreasing. A consequence is limited funds available for studying new concepts that potentially could evolve to the highly needed next generation CCS technologies. Furthermore, the number of PhD candidates and Postdoctoral researchers in the CLIMIT portfolio is decreasing as shown in Figure 5. Educating the future CCS experts is important and CLIMIT is contributing less than the program did some years ago. Please note that Figure 5 only includes PhDs and Postdoctoral researchers financed by RCN. There are in addition some PhD candidates and Postdoctoral researchers in the CLIMIT projects financed by Gassnova. The figure focus on RCN only because educating future experts is an important key performance indicator (KPI) for RCN.

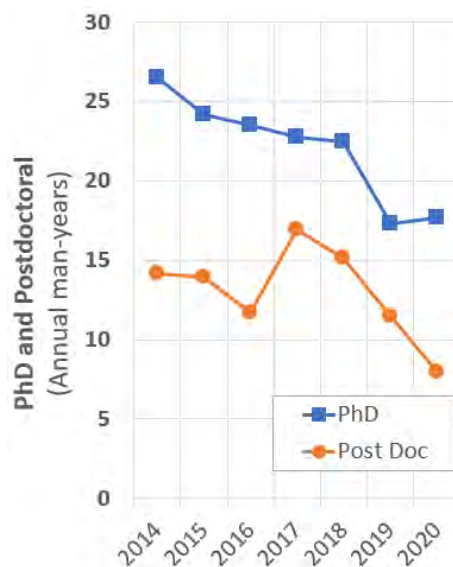


Figure 5: Annual man-years for PhD candidates and Postdoctoral researchers financed by the Research Council of Norway through the CLIMIT program.

4. The way forward for international cooperation on RD&D

When ACT started in 2016 a five-year grant agreement was signed with the EC. Now that this contract is coming to an end, there is ambitions among the ACT partners to continue the collaboration. The Clean Energy Transition Partnership (CETP) which is planned under Horizon Europe is seen as a good basis for continuing the collaboration. However, this depends on an effective governance structure being established that fits with the ACT governance model. ACT will continue the

collaboration with partners outside Europe and CETP will only be an alternative for ACT if it opens for effective collaboration beyond the European borders. ACT aim at continuing with USA, Canada and India as partners and also opens up for other countries to join ACT.

5. Conclusions

The Norwegian national program for RD&D within CCS, CLIMIT, changed focus towards more international collaboration in 2016. Since then about 20 % of the annual budget has been allocated to international calls.

Most of the CLIMIT budget allocated to international calls have been directed to the joint calls set up by the ACT partnership. In ACT, a total of 16 countries, provinces and regions are collaborating on bi-annual transnational joint calls and multinational knowledge sharing.

The shift from national to international joint calls have given the following positive impacts for CLIMIT:

- With international collaboration on joint calls it has been possible to establish larger projects that are able to efficiently address industrial needs.
- ACT projects have delivered results and competence needed and taken up in the large-scale Longship project.
- The ACT calls have addressed strategic priorities from the EU SET-plan [9] and Mission Innovation [10].
- Several ACT projects have joined forces to set up international seminars where key results have been communicated to stakeholders and decision makers. These events have been very important for raising awareness of CCS as an important and necessary tool to combat global warming. National CLIMIT projects have not been able to address awareness in a similar way.

There are also some disadvantages when international calls are prioritized instead of national calls:

- More funding allocated to international calls means less funding to national calls. Funding for basic research has decreased in the CLIMIT portfolio after international collaboration became more prioritized. Consequently, there are limited funding available for studying new concepts that potentially could evolve into next generation CCS technology.
- The number of PhD candidates in the portfolio has decreased. Educating the future CCS experts has become less pronounced in the CLIMIT portfolio when the focus has shifted from national to international collaboration.

Acknowledgements

The EC is acknowledged for funding ACT through the grant 691712. All funding agencies taking part in ACT are acknowledged for fruitful and effective collaboration and for taking part in the three joint international ACT calls and for actively contributing to substantial knowledge sharing.

References

- [1] Energy Technology Perspectives 2020, Special Report on Carbon Capture, Utilisation and Storage, The International Energy Agency (IEA), 2020. <https://webstore.iea.org/ccus-in-clean-energy-transitions>
- [2] Longship – Carbon capture and storage, Meld. St. 33 (2019–2020) Report to the Storting (white paper) <https://www.regjeringen.no/contentassets/943cb244091d4b2fb3782f395d69b05b/en-gb/pdfs/stm201920200033000engpdfs.pdf>
- [3] Carbon Sequestration Leadership Forum (CSLF), Task Force on Clusters, Hubs, and infrastructure for CCS, September 2020, [Microsoft Word - Clusters report 2020 September update.docx](https://www.cslforum.org/Clusters_report_2020_September_update.docx) ([cslforum.org](http://www.cslforum.org))
- [4] The CLIMIT program, www.climit.no/en
- [5] Accelerating CCS Technologies (ACT), <http://www.act-ccs.eu/>
- [6] The Preem CCS project, <https://climit.no/project/techno-economic-feasibility-study-of-the-implementation-of-carbon-capture-from-major-emission-sources-at-preemraff-lysekil-preem-ccs/>
- [7] The Pre-ACT project, <https://www.sintef.no/pre-act/>
- [8] Northern Light [Northern Lights – A European CO₂ transport and storage network \(northernlightsccs.com\)](http://www.northernlightsccs.com)
- [9] SET-PLAN TWG9 CCS and CCU Implementation Plan, Report from the SET-Plan ACTION no. 9, September 2017. https://setis.ec.europa.eu/system/files/set_plan_ccus_implementation_plan.pdf
- [10] Accelerating Breakthrough Innovation in Carbon Capture, Utilization, and Storage, Report of the Mission Innovation Carbon Capture, Utilization, and Storage Experts' Workshop, Mission Innovation, September 2017. <https://www.energy.gov/sites/prod/files/2018/05/f51/Accelerating%20Breakthrough%20Innovation%20in%20Carbon%20Capture%2C%20Utilization%2C%20and%20Storage%200.pdf>
- [11] The ELEGANCY Conference 2018, Brussels 8 November 2018, <https://blog.sintef.com/sintefenergy/elegancy-conference-2018/>
- [12] EU CCS Storage Research Projects Science-Policy Showcase, Brussels 10 September 2019, <https://webgate.ec.europa.eu/maritimeforum/en/node/4417>

CO₂-ENHANCED GEOTHERMAL SYSTEMS FOR CLIMATE NEUTRAL ENERGY SUPPLY

Anna Sowizdzal^{1*}, Paweł Gładysz¹, Trond Andresen², Maciej Miecznik³, Bjørn S. Frengstad⁴, Marcin Liszka⁵, Anna Chmielowska¹, Marcel Gawron⁵, Sigurd W. Løvseth², Leszek Pająk¹, Lars A. Stenvik⁴, Barbara Tomaszewska¹

¹ AGH University of Science and Technology, Kraków, Poland

² SINTEF Energy Research, Trondheim, Norway

³ Mineral and Energy Economy Research Institute, Polish Academy of Sciences, Kraków, Poland

⁴ Norwegian University of Science and Technology, Trondheim, Norway

⁵ EXERGON Sp. z o.o, Gliwice, Poland

* Corresponding author e-mail: anna.sowizdzal@agh.edu.pl

Abstract

The main objective of the research carried out by the Polish-Norwegian scientific team is to analyze the potential for implementation and efficiency of enhanced geothermal systems (EGS) using CO₂ as a working fluid (CO₂-EGS). This technology has attracted much interest of the scientific community in the last two decades due to the additional benefit of CO₂ geological storage that is occurring during the power generation process. The purpose of this technology is to mitigate climate change by producing clean geothermal energy and simultaneously reduce carbon dioxide emissions to the atmosphere coming from the combustion of fossil fuels. Within the paper, the scope of the EnerGizerS project is indicated. Moreover, the preliminary results of case study locations for the CO₂-EGS in both Poland and Norway are presented.

Keywords: *enhanced geothermal system, CO₂ utilization, CO₂ storage, techno-economic assessment, environmental assessment*

1. Introduction

Geothermal energy is a renewable source of heat and power, which unlike some other renewable sources can be used for baseload supply without additional energy storage. Although conventional (hydrothermal) geothermal resources have been used for over 100 years, and energy systems based on them are considered as mature, they do not develop at a rate that would significantly reduce greenhouse gases emissions globally due to the limited access to favorable geological conditions worldwide. Compared to conventional hydrothermal resources, enhanced geothermal systems (EGS) have the advantage of accessing much more abundant heat that is available in most parts of the world. As the heat content in the upper crust is several orders of magnitude higher than annual global energy consumption [1-3], the use of these energy reserves is gaining the growing attention of scientists in many parts of the world. Since the 1970s, over a dozen EGS reservoirs have been created by artificial stimulation of naturally impermeable rocks at depths exceeding 5 km. Numerous reports and publications of leading research centers [3] predict that the use of enhanced geothermal systems will develop at a much faster rate than geothermal energy based on hydrothermal reservoirs. Current EGS reservoirs use injected water as a heat carrier. However, due to the

beneficial properties of carbon dioxide as a working fluid, research on the use of this greenhouse gas has been ongoing for nearly two decades [4-6].

The first EGS project was developed in Los Alamos National Laboratory, USA, utilizing the Earth's heat at Fenton Hill in closed geothermal systems by an artificial increase of the hydraulic flow rate of a geothermal reservoir. The Fenton Hill is an installation that uses water as a working fluid, like all EGS installations currently operating around the globe.

The utilization of CO₂ as a working fluid in geothermal systems has not been implemented commercially so far but is under research due to potential benefits compared with water. For instance, an EGS experiment and CO₂ sequestration test were carried out at the Ogachi EGS site (Japan) [1]. A considerable number of issues regarding the functioning of CO₂-EGS still remain unresolved. One important aspect is to understand the behavior of CO₂, both regarding its interaction with the reservoir rocks and in the operation of the subsurface installation.

Another important issue is to render the reservoir available, which is done by fracturing. Hydraulic fracturing technology has been known since the 1920s, and its first successful commercial application took place in 1949. The technology has developed rapidly since then due to the increasing scope of its application

[7]. Initially, it was used in conventional oil wells, now it is used on unconventional reservoirs and enhanced geothermal systems.

It is also very important to consider the effect of impurities in CO₂ working fluids, where the inclusion of components other than CO₂ will influence thermodynamic fluid properties such as phase transition curves, density, and viscosity. Zhang et al. [8] investigated thermodynamic impacts of using impure CO₂ as a working fluid in CO₂-EGS, and a slightly altered behavior and lower efficiency with increased impurity content were reported. Further, in order to correctly model the CO₂-EGS working fluids, access to experimental data of thermodynamic properties of the specific fluid mixture at system-relevant conditions is important to ensure model accuracy and reliability. Relevant impurity components would greatly depend on the composition of the CO₂ injected into the reservoir to be used as a working fluid, but also on the native chemistry of the geological reservoir, which is determined by location and well depth. One important impurity is naturally H₂O, where a survey performed by NTNU and SINTEF [9] showed a significant lack of data in the CO₂-rich liquid and supercritical phase. There is even less data if salts are present. Furthermore, although the ratio of density to viscosity is proportional to the mass flow through the geothermal reservoir, there are large gaps in experimental data on viscosity and density of CO₂ and CO₂-rich mixtures at relevant processing temperatures and pressures [10-11]. SINTEF has an extended track-record in measuring phase equilibrium of CO₂-rich fluids, where accurate measurements of binary and ternary systems of CO₂ with impurities such as CO, N₂, O₂, CH₄ and Ar have been performed using a custom-made phase equilibrium cell [12-17].

Norwegian leading research organizations spearheaded the resurgence of CO₂ as a working fluid in the early 1990s, and they have since had research and technology development on aspects related to CO₂ heat pumping and power cycles as the main focus area. Rankine cycles with CO₂ are actively investigated on a global scale. In addition to concentrated solar and nuclear power, the technology is still highly relevant in specific waste heat applications, for example, offshore gas turbine exhaust. There have been considerable research activities on CO₂ transcritical power cycles, including constructing and operating a laboratory-scale CO₂ Rankine cycle, through projects such as ROMA (2007-2013) and CREATIV (2009-2013), funded by the Research Council of Norway. Later projects continued technology development towards specific applications such as offshore gas turbine bottoming cycles (EFFORT 2010-2014) and industrial waste heat (COPRO 2016-2019), in addition to confidential demonstration projects with the industry. Internationally, a few companies have developed such technology into larger prototypes and arguably even to commercial maturity.

The idea of merging CO₂-EGS systems with other energy systems has also been investigated in the literature. As an example for Polish conditions, results

of an investigation of a biomass-fired combined heat and power plant with CO₂ capture integrated with a CO₂ enhanced geothermal system [18-20] indicated the need to study the behavior of CO₂ as a working fluid. Further, it was concluded that the real possibilities of implementing such a solution in other countries should be assessed. From an economic point of view, only CO₂-EGS systems were proven competitive to conventional storage of captured CO₂ [19].

Geothermal conditions in Poland are relatively well recognized and have been studied since the 1980s [21]. Comprehensive information about Poland's geothermal resources is provided by a series of Geothermal Atlases, covering the areas of the Polish Lowland, Carpathians, and the Carpathian Foredeep. These works indicate the possibilities of using hydrogeothermal resources gathered in groundwater for various purposes, mainly heating, but also balneotherapy, recreation and the like. In recent years, research was conducted also to evaluate the energy potential of using petrogeothermal reservoir potential EGS systems [22-24].

Mainland Norway consists with few exceptions of Precambrian and Paleozoic crystalline rocks with low porosity and permeability. Temperature logging of boreholes down to 500-1600 m has revealed moderate geothermal gradients between 13.0 and 21.7 K/km [25-28]. Offshore Norway in the North Sea and the Norwegian Sea, there are many deep boreholes for oil exploration and extraction. Baird [29] describes thermal gradients between 33.0 and 42.2 K/km for Norwegian North Sea reservoirs, which might make them interesting for extraction of geothermal heat. The Arctic archipelago of Svalbard might be another candidate for geothermal heat with general gradients of 30 K/km and some measurements in the range of 40-50 K/km [30].

2. Planned research with EnerGizerS project

On October 1st, 2020, a joint Polish-Norwegian research and development project was launched. The main objective of this project, entitled "CO₂-Enhanced Geothermal Systems for Climate Neutral Energy Supply" (EnerGizerS), is to progress the technology of enhanced geothermal systems (EGS) using CO₂ as a working fluid closer to industrial deployment. The project consortium, constituted of AGH University of Science and Technology (Poland), SINTEF Energy Research (Norway), Mineral and Energy Economy Research Institute of the Polish Academy of Sciences (Poland), Norwegian University of Science and Technology (Norway) and EXERGON (Poland), will pursue the goals of the project through 36 months of extensive theoretical and experimental research activities.

To achieve the project objectives, the consortium partners will conduct research aimed at detailed identification of potential geological structures for the location of CO₂-EGS systems, combining the requirements for both EGS and carbon capture and storage (CCS) systems both in Poland and Norway. Moreover, novel laboratory research on CO₂ mixtures

with reservoir fluids will be performed to enhance the 3D geothermal simulations. The pinnacle of the EnerGizerS project will be a high-performance system concept for heat and/or electricity production along with professional techno-economic analysis.

2.1. Work Package 1

Work Package 1 consists of analytical tasks, where the Cross Impact method will be used to select a list of factors that are key for the indication of optimal locations suitable for CO₂-EGS systems. The results, in combination with CO₂ sources and other energy systems assessments, will be used to select locations and technologies related to CO₂-EGS installation, thus defining the case studies to be investigated in detail both in Norway and Poland. For the selected geological structures, core samples will be gathered for further research activities.

2.2. Work Package 2

In Work Package 2, core samples gathered in Work Package 1 will be subjected to laboratory tests. Petrophysical, thermal and mechanical tests will be performed on drill-core samples taken from appropriate geological structures. Based on the results, the database containing archival petrophysical and mechanical data as well as new laboratory measurements of rocks will be developed.

2.3. Work Package 3

The goal of Work Package 3 is to provide high quality experimental data on phase behavior and viscosity and density properties of CO₂-EGS to cover the most critical knowledge gaps identified so far, thus allowing to improve existing fluid models of CO₂-EGS relevant working fluids based on generated fluid property data. New data will be produced using state-of-the-art ECCEL ERIC infrastructure [12-17,31-33]. The fluid systems, properties, and conditions of the experimental investigations will be selected based on the knowledge of reservoir fluids and available CO₂ of the EGS locations selected in WP1, combined with a survey of existing data on relevant systems.

2.4. Work Package 4

Work Package 4 will be dedicated to the assessment of possible scenarios of the fracturing process for geological structures specified in WP1, the nature of possible fractures, their orientation and the resulting increase in permeability. Further on, the injection pressure required to circulate the CO₂ in the reservoir while maintaining the thermosiphon effect will be assessed. The optimum well separation distance in order to minimize pressure drop in the reservoir, while avoiding thermal drawdown at the production well, will be estimated. Assessment of possible CO₂ reaction with rock-forming minerals and reservoir brine and consequences on EGS behavior over time (i.e. CO₂ amount permanently stored, increase or decrease in permeability through dissolution or precipitation of minerals) will be carried out. Finally, the heat quantity and quality (temperature, enthalpy) produced from the

EGS reservoir under various scenarios will be estimated.

2.5. Work Package 5

Within Work Package 5, the high-performance topside system concepts for producing heat and/or electric power from geothermal energy, using CO₂ circulating in the EGS reservoir as the direct working fluid, will be developed. Mathematical modeling will be carried out using existing and demonstrated frameworks [34]. The heat exchanger models [35-36] use geometry data as input to calculate parameters such as hydraulic diameters, perimeters and cross-sectional areas for each fluid stream and pass. Based on the geometry specification and the fluid inlet conditions, the outlet conditions are found through the integration of the fluid passes (with a 4th order Runge Kutta routine) and iteration on the wall temperature profile (with DNSQE from SLATEC). Geometry-specific, state-of-the-art models for heat transfer and pressure drop will be applied. For a set of operating conditions, these models will be used to optimize the geometry within given operational and physical constraints. A similar framework will be developed for system-level analyses, which will enable connecting heat exchangers and other component models such as pumps, turbines, valves, and reactors in any type of arrangement to evaluate and optimize complex processes and systems.

2.6. Work Package 6

In Work Package 6, the techno-economic framework and guidelines will be developed, following some of the best practices used in research and industry. Most of the technical-oriented costs will be gathered based on extended literature review, and the experience of the project partners, and will be expressed as “power functions”, “unit costs” or “cost functions”. For the geographical-oriented costs and prices, a literature review will be performed, including governmental reference documents. Similarly, an environmental assessment framework will be developed, which in general will follow the ISO standards (ISO 14040:2006 and ISO 14044:2006) for the environmental management - Life Cycle Assessment (LCA). Due to the early stage of research, the comprehensive LCA analysis will not be performed. Best practices from LCA studies, together with the environmental assessment methods based on saved production of electricity and heat (and associated environmental effect) will be combined to formulate an adequate framework.

3. CO₂-EGS system case study definition

3.1. Cross Impact method results

Structural analysis is, first of all, a tool for structuring ideas. It gives the possibility to describe a system with the help of a matrix connecting all its components. By studying these relations, this method provides an opportunity to reveal variables essential to the system's evolution. It is possible to use it alone (as a support for reflection and/or decision making), or as part of a more complex forecasting activity (scenarios).

Within the analysis, the Micmac Forecasting method was used [37]. During the study, a group of 20 experts pointed out 193 variables important for the CO₂-EGS system and its location. As a result of variables' aggregation, their number was reduced to 49 and assumed as important for the CO₂-EGS systems development and exploitation. The experts were asked to assess the strength of interconnections among all variables. Results of the analysis indicated groups of factors, that are: key factors, targets, results, auxiliary factors, determinants, motors and breakers, regulating factors and autonomous. For an onshore system location as the most important variables were identified, viz.

- existing wells and other infrastructure;
- geological recognition level;
- reservoir temperature;
- depth of the EGS system;
- physical and petrogeothermal parameters of reservoir rocks;
- availability of the CO₂ sources;
- formal constraints related to local nature protected area;
- distance of CO₂-EGS site to thermal energy users and electricity grid.

3.2. Case study definition

For both Norway and Poland, all relevant CO₂ sources were identified, assessed and categorized in terms of potential CO₂ capacity from the capture process, as well as other relevant factors like CO₂ purity, time perspective of availability (especially important for Poland due to the forthcoming decarbonization of the energy system) and type of CO₂ source (power generation, industry). In addition, all existing wells in Norway and Poland suitable for the EGS system development were identified and assessed, taking into account, for example, the depth of the reservoir, expected temperatures, and permeability. Moreover, the local heat demand in selected areas was also identified, as the CO₂-EGS system's operation could potentially be a source of decarbonized heat supply for district heating systems. All these data were put on an interactive map, as an aid in the selection procedure (ranking) of potential CO₂-EGS locations in both Poland and Norway.

3.3. Selection procedure

Taking into account the identified key factors related to location, identified by means of the Cross Impact method, as well as the gathered data on the CO₂ sources and promising geological structures, the appropriate procedure was defined to allow selection of the most suitable locations for the CO₂-EGS system and definition of the case study, which include for example the subsurface installation design.

3.4. Preliminary results

3.4.1. Poland

Taking into account geological criteria, including first of all thermal and petrophysical parameters of rocks, 5 potential regions for CO₂-EGS were indicated. Preliminary analyzes were conducted of the various types of rocks: crystalline, volcanic and sedimentary. The results of the analyzes indicate the following areas as those in which further works aimed at selecting this prospective location should be concentrated: Karkonosze area, Gorzów Block, Szczecin Trough, Mogilno-Łódź Trough, Upper Silesian. These are areas with a varied geological structure, but also with a different degree of geological recognition

An assessment of environmental issues that may limit the implementation of proposed solutions was also carried out for these zones. Following key factors were used for the environmental assessment:

- existence of mining areas - licensed/concession areas designated for the exploitation of minerals;
- existence of licensed/concession areas related to the exploration and recognition of mineral resources (in particular for crude oil, natural gas, healing and geothermal waters, etc.);
- existence of Natura 2000 protected areas;
- the presence of other forms of nature protection - National Parks, National Park buffer zones;
- limitations in accordance to hydrogeological condition - groundwater protection zones, main groundwater reservoirs, groundwater bodies;
- limitation in accordance to hydrological condition - especially as flood hazard zones.

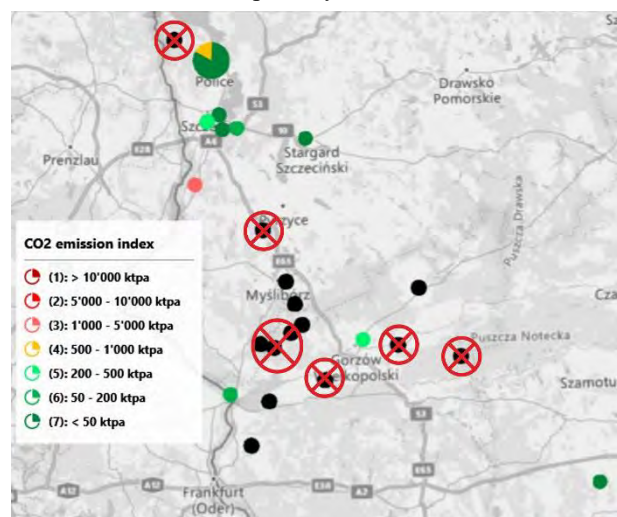


Figure 1: Map showing existing deep wells in the Gorzów Block. Wells not suitable for the CO₂-EGS system due to formal and environmental restrictions were crossed in red.

Although the granite massifs of the Karkonosze Mountains (SW Poland) were also interesting due to potentially high temperatures and presumably homogenous lithology of reservoir rocks, the complete lack of drilling data for depths exceeding 2 km and

numerous environmental limitations resulted in the rejection of this region for further analyzes. In the case of Gorzów Block, it should be mentioned that not all of the existing wells are suitable for the development of the CO₂-EGS system due to the aforementioned environmental constraints (marked red in Figure 1).

For Mogilno-Łódź Trough (Kutno area), a detailed analysis regarding the potential CO₂ sources, as well as nearby (from 2 to 15 km) heat demand in district heating systems, was done. As presented in Figure 2, the area has potentially favorable temperatures between 160 and 190 °C at depths of 5000 to 6000 meters below sea level. In the near vicinity, significant perspective industrial CO₂ sources were identified, associated with the refineries and their power generation plants. Other nearby CO₂ sources, mainly the lignite-fired power plant in Pałnów, are rather not suitable long-term sources of carbon dioxide, due to the planned decommissioning in the coming years.



Figure 2: Map showing the Kutno area, three district heating systems in nearby municipalities and potential (perspective and not perspective) CO₂ sources.

Further on, more detailed studies are planned to investigate options for long-term CO₂ supply and heat demand in regions considered as possible for the CO₂-EGS systems development as the feasibility of such systems must be determined.

4.3.2. Norway

Wellbore logs accessed from the Norwegian Petroleum Directorate [38] have revealed six favorable formations (fm) offshore Norway, see Figure 3. These are the Are fm in the Norwegian Sea, and Devonian rocks (no formation defined), Lunde fm, Skagerrak fm, Tor fm and Ula fm in the North Sea.

The formations display temperatures between 100 and 170 °C, depths between 2400-4700 meters below seafloor, and seawater depths ranging from 60 to 380 meters. The most realistic CO₂ source and energy user would be offshore oil and gas installations, since all formations locate far from the coastline. However, all formations are located within 15 km from oil and gas platforms already in place. Still, further analysis must be conducted to assess the feasibility of such a fully offshore CO₂-EGS system.

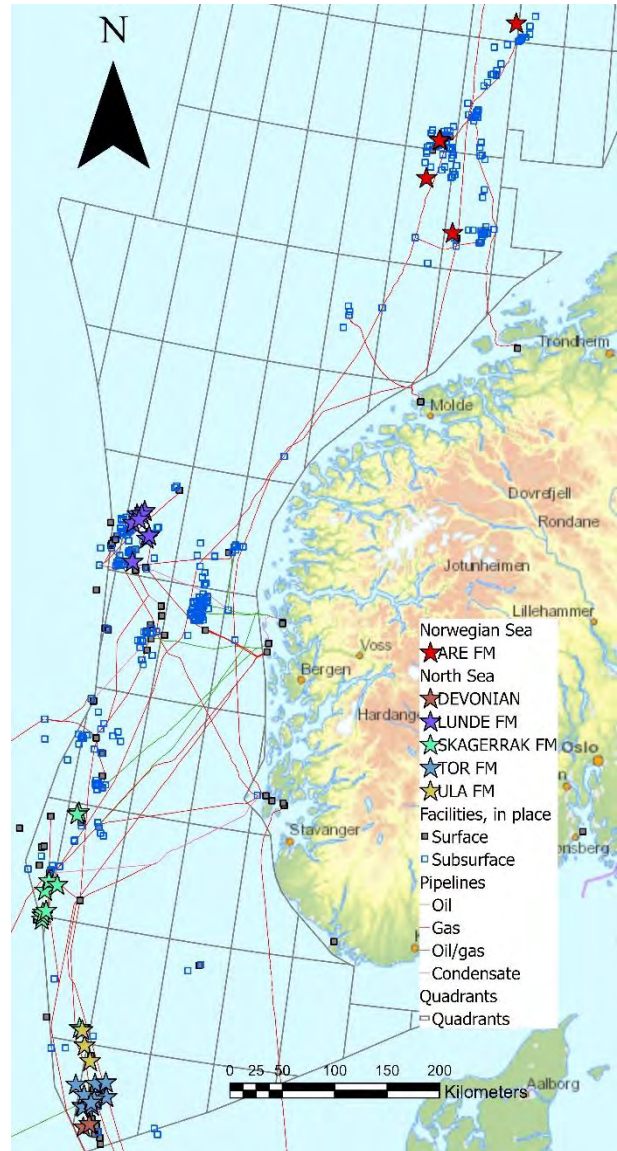


Figure 3: Map showing the location of six promising formations for CO₂-EGS utilization offshore Norway. In place, infrastructure is also indicated.

4. Conclusions and further studies

Hot dry rocks characterized by high temperatures are reservoirs of geothermal energy with great potential for application in many regions of the world. This potential can be exploited with enhanced geothermal systems, which is a forward-looking, yet immature technology. Therefore, numerous research is underway to develop this technology. One of them is the EnerGizerS project, carried out by a Polish-Norwegian consortium. The main purpose of the project is to analyze the effectiveness of the operation of unconventional geothermal systems using CO₂ as a working fluid. Due to the excellent thermodynamic properties of CO₂ and the need to reduce its emissions to the atmosphere, the EGS system, which uses CO₂ instead of water as a working fluid, is of great interest. An important aspect of the system is an additional environmental benefit resulting from the geological storage of a fraction of CO₂ used during the power generation process.

Researchers from Poland and Norway will cooperate to analyze the effectiveness of CO₂-EGS systems in their

respective countries. Six work packages will be completed during the project, under which a number of analytical and laboratory research will be performed, including laboratory tests on drill-core samples taken from appropriate geological structures, mathematical modeling, including structural modeling of the geological reservoir, modeling of the fracturing process of solid rocks and 3D modeling for multi-variant simulations of CO₂ injection and exploitation with forecasts of reservoir behavior over time, experimental determination of properties and behavior of CO₂-EGS working fluids as well as mathematical modeling of CO₂-based topside systems for heat and power production. All performed tests and analyzes will form the basis for conducting techno-economic and environmental assessments of the proposed technology. The current progress in the implementation of the EnerGizerS project allows us to initially indicate the most convenient locations for the first CO₂-EGS installations in both Poland and Norway.

Acknowledgements

The research leading to these results has received funding from the Norway Grants 2014-2021 via the National Centre for Research and Development. The results are part of the Polish-Norwegian project: CO₂-Enhanced Geothermal Systems for Climate Neutral Energy Supply, acronym EnerGizerS, registration number NOR/POLNOR/EnerGizerS/0036/2019.

References

- [1] Shyi-Min, L. A global review of enhanced geothermal system (EGS). *Renewable and Sustainable Energy Reviews* 2018; 81:2902-2921.
- [2] Dickson, M. H., & Fanelli, M. (2004). What is geothermal energy? International Geothermal Association, Bochum.
- [3] Tester, J., et al. (2006). The Future of Geothermal Energy. Impact of Enhanced Geothermal Systems (EGS) on the United States in the 21st Century. Massachusetts Institute of Technology. Report no. INL/EXT-06-11746. MIT. Cambridge, MA, USA.
- [4] Brown, D. W. (2000). A Hot Dry Rock Geothermal Energy Concept Utilizing Supercritical CO₂ Instead of Water. Proceedings, Twenty-Fifth Workshop on Geothermal Reservoir Engineering, Stanford University, January 2000.
- [5] Pruess, K. Enhanced geothermal systems (EGS) using CO₂ as working fluid — A novel approach for generating renewable energy with simultaneous sequestration of carbon. *Geothermics* 2006; 25:351-367.
- [6] Olasolo, P., Juárez, M. C., Morales, M. P., D'Amico, S., & Liarte, I. A. Enhanced geothermal systems (EGS): A review. *Renewable and Sustainable Energy Reviews* 2016; 56:133-144.
- [7] Biagi, J., Agarwal, R., & Zhang, Z.. Simulation and optimization of enhanced geothermal systems using CO₂ as a working fluid. *Energy* 2015; 86(6):627-637.
- [8] Zhang, F., et al. Thermodynamic analysis of enhanced geothermal systems using impure CO₂ as the geofluid. *Applied Thermal Engineering* 2016; 99:1277-1285.
- [9] Aasen, A., et al. Thermodynamic models to accurately describe the PVTxy-behavior of water /carbon dioxide mixtures. *Fluid Phase Equilibria* 2017; 442:125-139.
- [10] Li, H., et al. PVTxy properties of CO₂ mixtures relevant for CO₂ capture, transport and storage: Review of available experimental data and theoretical models. *Applied Energy* 2011; 88(11): 3567-3579.
- [11] Munkejord, S. T., et al. CO₂ transport: Data and models – A review. *Applied Energy* 2016; 169:499-523.
- [12] Westman, S. F., Stang, H. G. J., Løvseth, S. W., Austegard A., & Størset, S. Ø. Vapor-liquid equilibrium data for the carbon dioxide and nitrogen (CO₂ + N₂) system at the temperatures 223, 270, 298 and 303 K and pressures up to 18 Mpa. *Fluid Phase Equilibria* 2016; 409:207-241.
- [13] Westman, S. F., Stang, H. G. J., Løvseth, S. W., Austegard, A., Snustad, I., & Ertesvåg I. S. Vapor-liquid equilibrium data for the carbon dioxide and oxygen (CO₂ + O₂) system at the temperatures 218, 233, 253, 273, 288 and 298 K and pressures up to 14 Mpa. *Fluid Phase Equilibria* 2016; 421:67-87.
- [14] Løvseth, S. W., Austegard, A., Westman, S. F., Stang, H. G. J., Herrig, S., Neumann, T., & Span R. Thermodynamics of the carbon dioxide plus argon (CO₂ + Ar) system: An improved reference mixture model and measurements of vapor-liquid, vapor-solid, liquid-solid and vapor-liquid-solid phase equilibrium data at the temperatures 213–299 K and pressures up to 16 Mpa. *Fluid Phase Equilibria* 2018; 466:48-78.
- [15] Petropoulou, E., Voutsas, E., Westman, S. F., Austegard, A., Stang, H. G. J., & Løvseth, S. W. Vapor - liquid equilibrium of the carbon dioxide/methane mixture at three isotherms. *Fluid Phase Equilibria* 2018; 462:44-58.
- [16] Westman, S. F., Austegard, A., Stang, H. G. J., & Løvseth, S. W. Vapor-liquid equilibrium data for the carbon dioxide and carbon monoxide (CO₂ + CO) system at the temperatures 253, 273, 283 and 298 K and pressures up to 13 Mpa. *Fluid Phase Equilibria* 2018; 473:37-49.
- [17] Ottøy, S., Neumann, T., Stang, H. G. J., Jakobsen, J. P., Austegard, A., & Løvseth, S. W. Thermodynamics of the carbon dioxide plus nitrogen plus methane (CO₂ + N₂ + CH₄) system: Measurements of vapor-liquid equilibrium data at temperatures from 223 to 298 K and verification of EOS-CG-2019 equation of state. *Fluid Phase Equilibria* 2020; 509:112444.
- [18] Gładysz, P., Sowiżdżał, A., Miecznik, M., & Pająk, L. Carbon dioxide-enhanced geothermal systems for heat and electricity production: Energy and economic analyses for central Poland. *Energy Conversion and Management* 2020; 220: 113142. <https://doi.org/10.1016/j.enconman.2020.113142>.
- [19] Gładysz, P., Sowiżdżał, A., Miecznik, M., Hacaga, M., & Pająk, L. Techno-Economic Assessment of a Combined Heat and Power Plant Integrated with Carbon Dioxide Removal Technology: A Case Study for Central Poland. *Energies* 2020; 13: 2841. <https://doi.org/10.3390/en13112841>.
- [20] Sowiżdżał, A., Gładysz, P., & Pająk, L. Sustainable Use of Petrothermal Resources—A Review of the Geological Conditions in Poland. *Resources* 2021; 10(1):8. <https://doi.org/10.3390/resources10010008>.
- [21] Sowiżdżał, A. Geothermal energy resources in Poland – Overview of the current state of knowledge, *Renewable and Sustainable Energy Reviews* 2018; 82(part 3):4020-4027.
- [22] Sowiżdżał, A., Papiernik, B., Machowski, G., & Hajto, M. Characterization of petrophysical parameters of the Lower Triassic deposits in prospective location for

- Enhanced Geothermal System (central Poland). *Geological Quarterly* 2013; 57(4):729–743.
- [23] Sowizdżał, A., & Kaczmarczyk, M. Analysis of thermal parameters of Triassic, Permian and Carboniferous sedimentary rocks in central Poland, *Geological Journal* 2016; 51(1):65-76.
- [24] Sowizdżał, A.. Possibilities of petrogeothermal energy resources utilization in central part of Poland, *Applied Ecology and Environmental Research* 2016; 14(2):555–574.
- [25] Elvebakk, H. 2012a. Geofysisk logging av borehull ved Arnestad skole, Asker [In Norwegian]. NGU-report 2011.016. Trondheim: NGU.
- [26] Elvebakk, H. 2012b. Geofysisk logging av tre borehull i Hurdal [In Norwegian]. NGU-report 2011.011. Trondheim: NGU.
- [27] Elvebakk, H. 2018. Logging av dype energibrønner på Oslo Lufthavn, Gardermoen. [In Norwegian]. NGU-report 2018.020. Trondheim: NGU.
- [28] Maystrenko, Y. P., Slagstad, T., Olesen, O., Elvebakk, H. K., Venvik, G., & Rønning, J. S. New heat flow data from three boreholes near Bergen, Stavanger and Moss, southern Norway. *Geothermics* 2015; 56:79-92.
- [29] Baird, R. A. V. W. C. (1991). Relation between Liquid Hydrocarbon Reserves and Geothermal Gradients--Norwegian North Sea. Virginia Water Co. USA.
- [30] Betlem, P., Midttømme, K., Jochmann, M., Senger, K., & Olaussen, S. (2018). Geothermal Gradients on Svalbard, Arctic Norway. Conference Proceedings, First EAGE/IGA/DGMK Joint Workshop on Deep Geothermal Energy, November 2018. <https://doi.org/10.3997/2214-4609.201802945>
- [31] ECCSEL ERIC. 2021. Available at: <http://www.eccsel.org/> (Accessed 20 January 2021).
- [32] Stang, H. G. J., Løvseth, S. W., Størset, S. Ø., Malvik, B., & Rekestad, H. Accurate Measurements of CO₂ Rich Mixture Phase Equilibria Relevant for CCS Transport and Conditioning. *Energy Procedia* 2013; 37:2897-2903.
- [33] Løvseth, S. W. Impact of impurities in the CO₂ on fluid density, viscosity and thermal conductivity, and CCS processes. Conference Proceedings. CLIMIT Digit, Round 1 - Transport & CO₂-EOR.. <https://gyroconference.no/climit/#1-1>, February 2021.
- [34] Nikolaisen, M., & Andresen, T. System impact of heat exchanger pressure loss in ORCs for smelter off-gas waste heat recovery. *Energy* 2021; 215(part B):118956. <https://doi.org/10.1016/j.energy.2020.118956>.
- [35] Skaugen, G., Kolsaker, K., Walnum, H. T., & Wilhelmsen, Ø. A flexible and robust modelling framework for multi-stream heat exchangers. *Computers & Chemical Engineering* 2013; 49:95-104. <https://doi.org/10.1016/j.compchemeng.2012.10.006>.
- [36] Hagen, B. A. L., Nikolaisen, M., & Andresen, T. A novel methodology for Rankine cycle analysis with generic heat exchanger models. *Applied Thermal Engineering* 2020; 165:114566. <https://doi.org/10.1016/j.applthermaleng.2019.114566>.
- [37] La prospective. 2021. MicMac Structural Analysis. Available at: <http://en.lapropective.fr/methods-of-prospective/softwares/59-micmac.html> (Accessed 21 January 2021).
- [38] Norwegian Petroleum Directorate. 2020. Factpages. Available at: <https://factpages.npd.no/nb-no> (Accessed 14 December 2020).

NUMERICAL STUDIES OF CO₂ LEAKAGE REMEDIATION BY MICP-BASED PLUGGING TECHNOLOGY

D. Landa-Marbán^{1*}, K. Kumar², S. Tveit¹, S.E. Gasda¹

¹ NORCE Norwegian Research Centre AS, Bergen, Norway

² University of Bergen, Bergen, Norway

* Corresponding author e-mail: dmar@norce-research.no

Abstract

Microbially induced calcite precipitation (MICP) is a technology for sealing leakage paths to ensure the safe storage of CO₂ in geological formations. In this work we introduce a numerical simulator of MICP for field-scale studies. This simulator is implemented in the open porous media (OPM) framework. We compare the numerical results to simulations using an upgraded implementation of the mathematical model in the MATLAB® reservoir simulation toolbox (MRST). Finally, we consider a 3D system consisting of two aquifers separated by caprock with a leakage path across the width of the reservoir. We study a strategy where microbial solution is injected only at the beginning of the treatment and subsequently either growth solution or cementation solution is injected for biofilm development or calcite precipitation. By applying this strategy, the numerical results show that the MICP technology could be used to seal these leakage paths.

Keywords: leakage remediation and mitigation, mathematical modeling, microbially induced calcite precipitation

1. Introduction

Carbon capture and storage (CCS) in the subsurface is one of the most promising scalable technologies for reduction of greenhouse gases through large scale carbon sequestration. For the successful implementation of this technology, the captured carbon must remain stored and any possibility of its migration back to the surface through the complex subsurface geometric structures such as faults, fractures, and abandoned wells must be reduced. Geological sequestration of CO₂ involves the injection of CO₂ into underground formations such as oil-bearing formations and saline aquifers allowing it to be trapped by the caprocks as has been practically achieved in the Norwegian continental shelf, e.g., in the Sleipner field. Many investigations have been conducted on assessment of CO₂ leakage (see e.g., [1-4]). The migration of CO₂ either to the freshwater aquifer or to the surface threatens not just the viability of the technology but also poses a risk to the precious ground water resource. This underlines the need for developing technologies that ensure closure of any potential leakage pathway for the trapped CO₂. Fig. 1 shows a schematic representation of injection of CO₂ for storage in deep subsurface, where leakage paths in caprocks lead to contamination of fresh water.

Microbial induced calcite precipitation (MICP) is an in-situ sealing technology that utilizes the biochemical processes to create barriers by calcium carbonate cementation. It involves injection of a mix of components including microbes, growth medium, and other chemical substances into a reservoir where the microbes produce calcite that reduces the in-situ permeability reducing the chances of CO₂ leakage. The field studies indicate that this strategy works in practice; [5] showed that MICP under field conditions improved the strengthening of the

soil and concluded that MICP can be used for large-scale applications. One of the potential MICP applications is on reservoirs where leakage mitigation is relevant before CO₂ is injected. If the location of these leakage paths is known, then an injection strategy could be applied to create barriers by calcium carbonate precipitation in the leakage paths. Besides the sealing technology for prevention of CO₂ leakage, the MICP also has potential applications in biomineralized concrete [6], wastewater treatment, and erosion control.

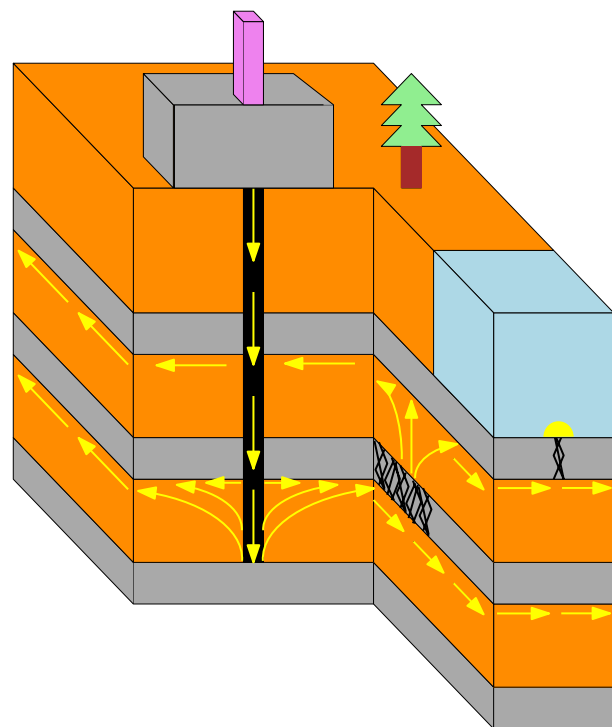


Figure 1: Contamination of water by CO₂ leakage.

The complexity and economics of the laboratory experiments at field scale necessitate the development of mathematical models that can enable simulation of the process. This development is built on the laboratory experiments conducted at the pore and core scales. Bai et al. [7] performed MICP experiments in microfluidic cells to study the calcite precipitation at the pore scale enabling the determination of certain coefficients in the mathematical model. The core-scale experiments by [8-10] help us identify the key processes involved. Based on these, detailed mathematical models have been proposed in literature. We refer to the model of [11] for a comprehensive pore-scale model for MICP and [12] for a comprehensive core-scale model. Based on the pore- and core-scale models, [13-14] developed simplified mathematical models for MICP at the field scale. An optimization study under parameter uncertainty using a simplified MICP model is presented in [15]. In this work, we will be relying on the model developed in [14].

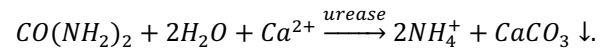
Our motivation is to develop mathematical models and numerical tools that simulates the MICP at the field scale. The process is quite complex taking place at several scales, with the flow and transport in complex geometry, and involving a set of reactions at multiple temporal and spatial scales. This yields a system of coupled partial differential equations and a set of ordinary differential equations with heterogeneous coefficients, nonlinearities, and degeneracies, e.g., multiphase flows coupled to reactive transport. Performing numerical simulations of such a complex set of mathematical equations is quite difficult and often intractable even with the usual techniques of local grid refinement, multiscale approaches, or improving the time stepping. Another challenge in considering highly detailed models is the unavailability of the laboratory data at field scale to estimate the increasing number of parameters involved as the complexity of models is increased. We are thus motivated by the following consideration: we would like to consider models that are simple enough to let us perform simulations at the field scale, yet capture the essence of the physical and chemical processes keeping the number of parameters as small as we can. The simplicity of the model considered here will also allow us to perform optimization of the injection strategy.

In this proceeding, we consider a field-scale model for MICP and use this to study the remediation of a fractured zone in a caprock to prevent the potential leakage of CO₂. More specifically, we consider both 2D and 3D geometries with potential leakage pathways and inject microbes mixed in water, a growth medium, and cementation solution to allow the calcite precipitation. We then study the evolution of the in-situ porosity and the flux of the CO₂. This allows us to simulate the process and study its effectiveness as a sealing technology. In this work, we implement the mathematical model in the open porous media (OPM) framework which is an open-source tool for simulating multiphase flow and transport in subsurface porous media [16]. We compare the results with those from the proto-type model developed in MRST, a MATLAB® based reservoir simulation toolbox [17]. The use of open-source toolbox allows us also to benefit from the existing implementation of other

modules of a reservoir simulator such as multiphase modules, and handling of complex geometry. Finally, we study a 3D system consisting of two aquifers separated by caprock with a leakage path across the width of the reservoir. We conclude with the discussions on the numerical findings and the further work that we plan to undertake.

2. Methodology

MICP is a complex bio-geochemical process resulting in mineralization of CO₂ in the form of calcite as a result of microbial metabolic activities. A rough description of the process consists of an impermeable biofilm formation where microorganisms produce an adhesive matrix of extracellular polymeric substance (EPS), microbes catalyze urea to produce ammonium ions and carbonate, the calcium-rich environment then reacts with the carbonate ions to produce calcite. We consider accordingly a set of unknown variables consisting of biofilm, water, calcite, microbes suspended in water, oxygen (acting as the electron acceptor), and urea. A simplified representation of the MICP reactions is given by



We consider the rate-limiting components in the injected solutions to be suspended microbes, oxygen, and urea respectively. We assume that the MICP treatment is applied before CO₂ injection. Thus, only water is presented in the aquifer. After MICP treatment, CO₂ is injected to the reservoir. Given these assumptions, we describe simplified models for MICP and CO₂ sequestration in the following subsections.

2.1 Mathematical model of MICP technology

A comprehensive presentation of the MICP model can be found in [14]. Here we shortly describe this mathematical model.

We consider a reservoir characterized by its initial porosity ϕ_0 and permeability \mathbb{K}_0 . We denote ϕ_b and ϕ_c as the volume fractions of biofilm and calcite respectively. Then the rock porosity reduction is

$$\phi = \phi_0 - \phi_b - \phi_c.$$

Since the biofilm and calcite are assumed immobile, the mass balance equations only involve the storage term,

$$\frac{\partial(\rho_\chi \phi_\chi)}{\partial t} = R_\chi, \quad \chi \in \{b, c\},$$

where ρ_χ are densities and R_χ reaction terms described later in this section.

We denote ϕ_{crit} as the value of porosity when the permeability reaches a minimum value K_{min} ($\phi \leq \phi_{crit}$). The following relationship is used to model the permeability reduction as a consequence of the porosity reduction ($\phi_{crit} < \phi$)

$$\mathbb{K} = \left[\mathbb{K}_0 \left(\frac{\phi - \phi_{crit}}{\phi_0 - \phi_{crit}} \right)^\eta + K_{min} \right] \frac{\mathbb{K}_0}{\mathbb{K}_0 + K_{min}},$$

where η is a fitting factor.

The mass conservation equation and Darcy's law for the water are

$$\frac{\partial \phi}{\partial t} + \nabla \cdot \mathbf{v}_w = q_w, \quad \mathbf{v}_w = -\frac{\mathbb{K}}{\mu_w} (\nabla p_w - \rho_w \mathbf{g}),$$

where \mathbf{v}_w is the discharge per unit area, ρ_w the fluid density, p_w the reservoir pressure, \mathbf{g} the gravity, μ_w the water viscosity, and q_w the source/sink term.

The mass balances for the suspended microbes (m), oxygen (o), and urea (u) are

$$\frac{\partial (c_\xi \phi)}{\partial t} + \nabla \cdot (c_\xi \mathbf{v}_w) = c_\xi q_w + R_\xi, \quad \xi \in \{m, o, u\},$$

where c_ξ are mass concentrations and R_ξ reaction terms described next.

The reaction term for the suspended microbes is

$$R_m = c_m \phi \left(Y \mu \frac{c_o}{k_o + c_o} - k_d - k_a \right) + \phi_b \rho_b k_{str} \phi \|\nabla p_w - \rho_w \mathbf{g}\|^{0.58},$$

where Y is the growth yield coefficient, μ is the maximum specific growth rate, k_o is the half-velocity coefficient of oxygen, k_d is the microbial death coefficient, k_a is the microbial attachment coefficient, and k_{str} is the detachment rate.

The reaction term for the oxygen is

$$R_o = -(c_m \phi + \rho_b \phi_b) F \mu \frac{c_o}{k_o + c_o},$$

where F is the mass ratio of oxygen consumed to substrate used for growth.

The reaction term for the urea is

$$R_u = -\rho_b \phi_b \mu_u \frac{c_u}{k_u + c_u},$$

where μ_u is the maximum rate of urea utilization and k_u is the half-velocity coefficient for urea.

The reaction term for the biofilm is

$$R_b = \rho_b \phi_b \left[Y \mu \frac{c_o}{k_o + c_o} - k_d - \frac{R_c}{\rho_c (\phi_0 - \phi_c)} - k_{str} \phi \|\nabla p_w - \rho_w \mathbf{g}\|^{0.58} \right] + c_m \phi k_a.$$

The reaction term for the calcite is

$$R_c = -\rho_b \phi_b Y_{uc} \mu_u \frac{c_u}{k_u + c_u},$$

where Y_{uc} is a yield coefficient (units of produced calcite over units of urea utilization).

2.2 Mathematical model of CO₂ storage

For simulation of CO₂ sequestration, we consider a simple immiscible two-phase flow model. We denote water saturation as s_w and CO₂ saturation as s_{CO_2} , where $s_w + s_{CO_2} = 1$. The mass conservation and extended Darcy's law for each α phase ($\alpha = w, CO_2$) are

$$\phi \frac{\partial s_\alpha}{\partial t} + \nabla \cdot \mathbf{v}_\alpha = q_\alpha, \quad \mathbf{v}_\alpha = -\frac{k_{r,\alpha}}{\mu_\alpha} \mathbb{K} (\nabla p_\alpha - \rho_\alpha \mathbf{g}),$$

where $k_{r,\alpha}$ are relative permeabilities. The relative permeabilities are set as a linear function of the

saturation ($k_{r,\alpha} = s_\alpha$) and the capillary pressure is neglected ($p_{CO_2} = p_w$).

2.3 Implementation

The open porous media (OPM) initiative, a free open-source software for reservoir modeling and simulation, is used to implement the MICP mathematical model [16]. The source code for OPM and its related modules can be obtained at <http://github.com/OPM> and a description of the simulator can be found in the OPM Flow manual [18]. The implementation of this MICP model is made in the 2020.10 release of OPM. The source code for the implementation of this MICP model in MRST can be obtained at <https://www.sintef.no/projectweb/mrst/> and <https://github.com/daavid00/ad-micp.git>. We have upgraded the first version of the ad-micp module to make it compatible with GNU Octave.

The MICP model is solved on domains with vertex-centered grids. The leakage paths are discretized with three-dimensional elements. This approach has shown to be in good agreement with comparable simulations using different approaches such as discrete fracture networks (see e.g., [19]). Two-point flux approximation (TPFA) and backward Euler (BE) are used for the space and time discretization respectively. The resulting system of equations is linearized using the Newton-Raphson method. We consider constant-pressure production wells on the domain boundaries to model an infinite acting aquifer. We use the MRST functionalities to produce the grids and write the corresponding grid file in GRDECL format which is read by the OPM simulator. We use OPM Flow to assess the CO₂ leakage.

2.4 Model parameters and reservoir properties

Here we have separated model inputs in two parts. Table 1 shows the model parameters regarding the fluid properties and MICP processes. These values are selected from previous studies and full references to the sources can be found in [14].

Table 1: Table of model parameters for the numerical studies.

Parameter	Sym	Value	Unit
Density (biofilm)	ρ_b	35	kg/m ³
Density (calcite)	ρ_c	2710	kg/m ³
Density (CO ₂)	ρ_{CO_2}	479	kg/m ³
Density (water)	ρ_w	1045	kg/m ³
Detachment rate	k_{str}	2.6×10^{-10}	m/(Pa s)
Half-velocity coefficient (oxygen)	k_o	2×10^{-5}	kg/m ³
Half-velocity coefficient (urea)	k_u	21.3	kg/m ³
Maximum specific growth rate	μ	4.17×10^{-5}	1/s
Maximum rate of urea utilization	μ_u	1.61×10^{-2}	1/s
Microbial attachment rate	k_a	8.51×10^{-7}	1/s
Microbial death rate	k_d	3.18×10^{-7}	1/s
Oxygen consumption factor	F	0.5	[-]
Viscosity (CO ₂)	μ_{CO_2}	3.95×10^{-5}	Pa s
Viscosity (water)	μ_w	2.54×10^{-4}	Pa s

Yield coefficient (growth)	Y	0.5	[-]
Yield coefficient (calcite/urea)	Y_{uc}	1.67	[-]

Table 2 shows the reservoir properties we consider for the simulations. These properties are set to common values for numerical studies.

Table 2: Table of reservoir properties for the simulations.

Parameter	Sym	Value	Unit
Aperture (leak)	a	1	m
Fitting factor	η	3	[-]
Gap (lower aquifer)	g_l	15	m
Gap (upper aquifer)	g_u	5	m
Height (aquifer)	H	5	m
Height (caprock)	h	20	m
Length (aquifer)	L	100	m
Gap (potential leakage)	l	15	m
Permeability (aquifer)	K_A	10^{-14}	m^2
Permeability (leakage)	K_L	$2K_A$	m^2
Permeability (minimum)	K_{min}	10^{-20}	m^2
Porosity (aquifer/leakage)	ϕ_0	0.15	[-]
Porosity (critical)	ϕ_{crit}	0.1	[-]
Tilt angle (leak)	θ	135	$^\circ$
Width (aquifer)	W	20	m
Width (leak)	w	6	m

2.5 Injection strategy

Both laboratory experiments and numerical studies have shown that by separating the injection of solutions (microbial, growing, and cementation solutions) with no-flow periods then limited clogging is expected to occur near the injection site (see e.g., [8,12]). We adopt this strategy, where first the microbial solution is injected (t_1^I) and after only water is injected to displace the microbes deeper in the aquifer (t_2^I). After closing the system to allow the suspended microbes to attach themselves to the rock (t_3^I), growth solution is injected (t_4^I) to stimulate the biofilm formation, followed by only water injection (t_5^I) and a non-flow period (t_6^I). Next, the cementation solution is injected (t_7^I) followed by only water (t_8^I) and a non-flow period (t_9^I) to allow the calcite precipitation to occur. All these nine injection times are denoted as phase I. Several phases can be applied to seal the leak.

For the numerical studies we fix the injected concentrations, and we keep the injection rate constant in each of the phases. The injected concentrations are set to $c_m = 0.01 \text{ kg/m}^3$, $c_o = 0.04 \text{ kg/m}^3$, and $c_u = 300 \text{ kg/m}^3$. The value of injection rate Q_w is different for the different flow systems and its value is given in each example.

3. Results and Discussion

In this section, three examples are presented to demonstrate the validity and application of the implementation in OPM. The first example verifies the simulator against a previous implementation in MRST. In the second example, we show the evolution of the MICP processes during injection of one MICP treatment

on a 2D flow domain with a diagonal leakage path. In the last example, we describe a successful injection strategy to mitigate CO₂ leakage on a reservoir with a leakage path along the width of the caprock.

3.1 Example 1: comparison of the model implementation in OPM to the one in MRST

The comparison between implementations is performed on a 1D flow horizontal system as shown in Fig. 2.

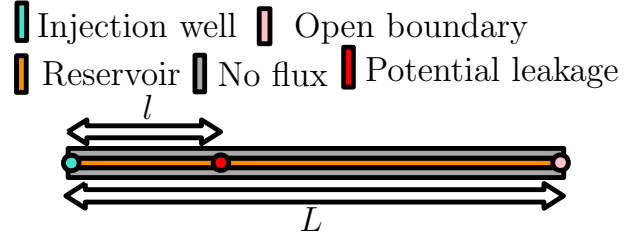


Figure 2: 1D domain with a potential leakage zone.

The injection well is located on the left and the production well on the right side. The potential leakage zone is located at [12.5 m, 17.5 m] from the injection well. The size of the domain is $100 \times 1 \times 1 \text{ m}$ and the dimension of the grid is $100 \times 1 \times 1$. The injection rate is set to $2.31 \times 10^{-5} \text{ m}^3/\text{s}$. Fig. 3 shows the simulation results obtained from both implementations.

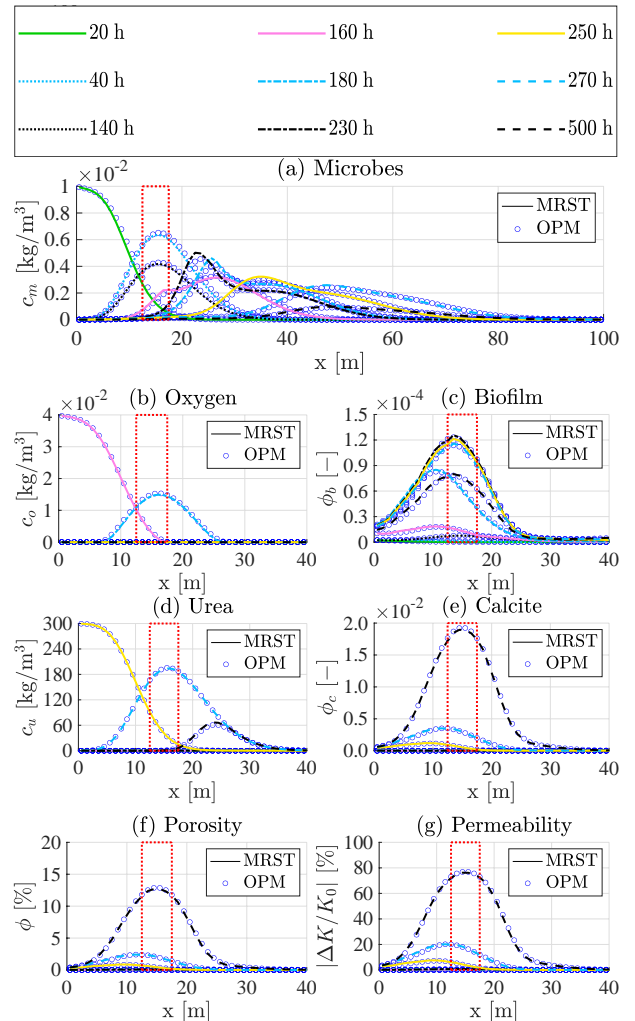


Figure 3: Comparison between implementations in OPM and MRST.

As shown in Fig. 3, the results verify that there is a good agreement in the spatial distribution of the model variables over time computed by OPM and MRST. For this example, the simulation time using OPM (2.82 s) is ca. 20 times faster than using MRST (55.81 s).

3.2 Example 2: MICP on a 2D flow domain with a diagonal leak

To demonstrate the use of the MICP simulator in the presence of a leakage path, we consider the 2D flow system shown in Fig. 4.

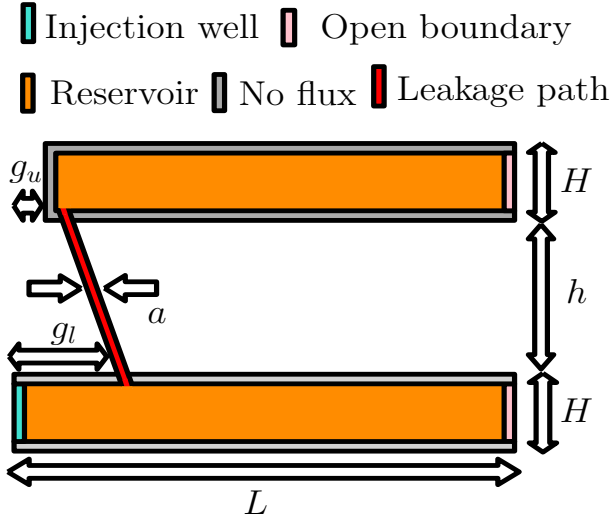


Figure 4: 2D domain with a leakage path.

The times for the injection strategy are $t_1^I = 15$ h, $t_2^I = 22$ h, $t_3^I = 100$ h, $t_4^I = 130$ h, $t_5^I = 135$ h, $t_6^I = 160$ h, $t_7^I = 200$ h, $t_8^I = 210$ h, and $t_9^I = 300$ h and the injection rate is set to 2.31×10^{-4} m³/s. Fig. 5 shows the spatial discretization and simulation results after application of one phase of MICP treatment.

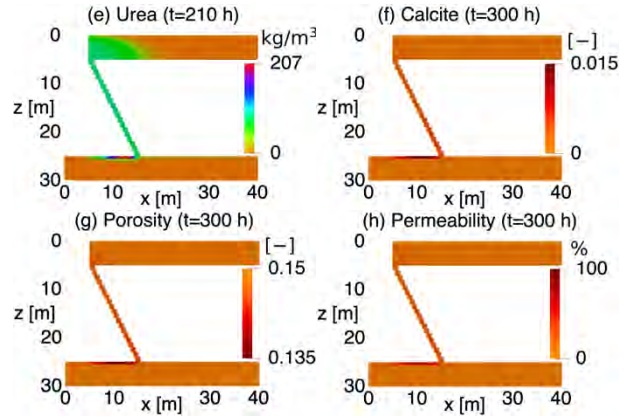
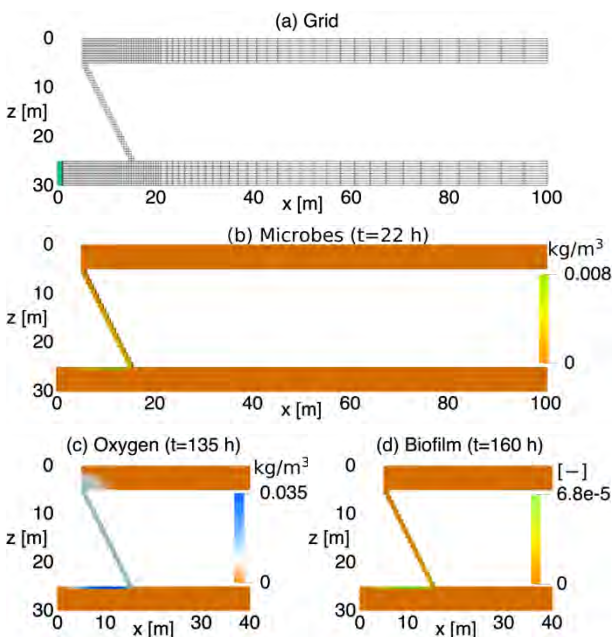


Figure 5: (a) Grid with well and spatial distribution of (b) suspended microbes, (c) oxygen, (d) biofilm, (e) urea, (f) calcite, (g) porosity, and (h) permeability reduction at different times of the MICP treatment.

In Fig. 5h we observe a significant permeability reduction on the leakage path (max ca. 30%) after only one phase of MICP treatment.

3.3 Example 3: leakage mitigation on a 3D flow domain with a diagonal leak

The implementation of the MICP mathematical in OPM allows for computationally challenging simulations. We consider the 3D system shown in Fig. 6.

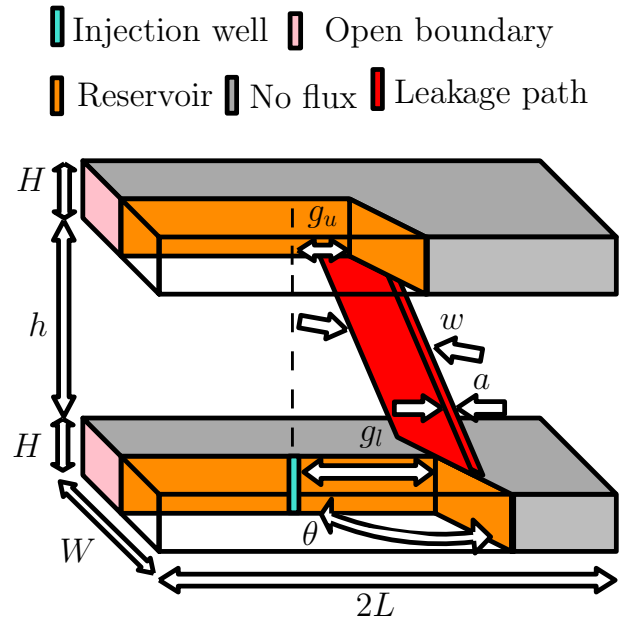


Figure 6: 3D domain with a leakage path.

We proceed to design an injection strategy for the sealing of the leakage path. Here we use an ad-hoc approach where we run simulations and change manually the injection times and rates. The following times and rates result in the successful sealing of the leakage path after five phases of MICP treatment: $Q_w^I = Q_w^{II} = Q_w^{III} = 8.70 \times 10^{-3}$ m³/s, $t_1^I = 15$ h, $t_2^I = 22$ h, $t_3^I = 100$ h, $t_4^I = 130$ h, $t_5^I = 135$ h, $t_6^I = 160$ h, $t_7^I = 200$ h, $t_8^I = 210$ h, $t_9^I = 300$ h, $t_4^{II} = 330$ h, $t_5^{II} = 340$ h, $t_6^{II} = 341$ h, $t_7^{II} = 371$ h, $t_8^{II} = 381$ h, $t_9^{II} = 431$ h, $t_7^{III} = 461$ h, $t_8^{III} = 471$ h, $t_9^{III} = 571$ h, $t_4^{IV} = 601$ h, $t_5^{IV} =$

611 h, $t_6^{IV} = 612$ h, $t_7^{IV} = 642$ h, $t_8^{IV} = 652$ h, $t_9^{IV} = 702$ h, $t_7^V = 732$ h, $t_8^V = 742$ h, and $t_9^V = 800$ h. In this injection strategy microbial solution is injected only at the beginning of the treatment and subsequently either growth solution or cementation solution is injected for biofilm development or calcite precipitation. The grid and simulation results are shown in Fig. 7.

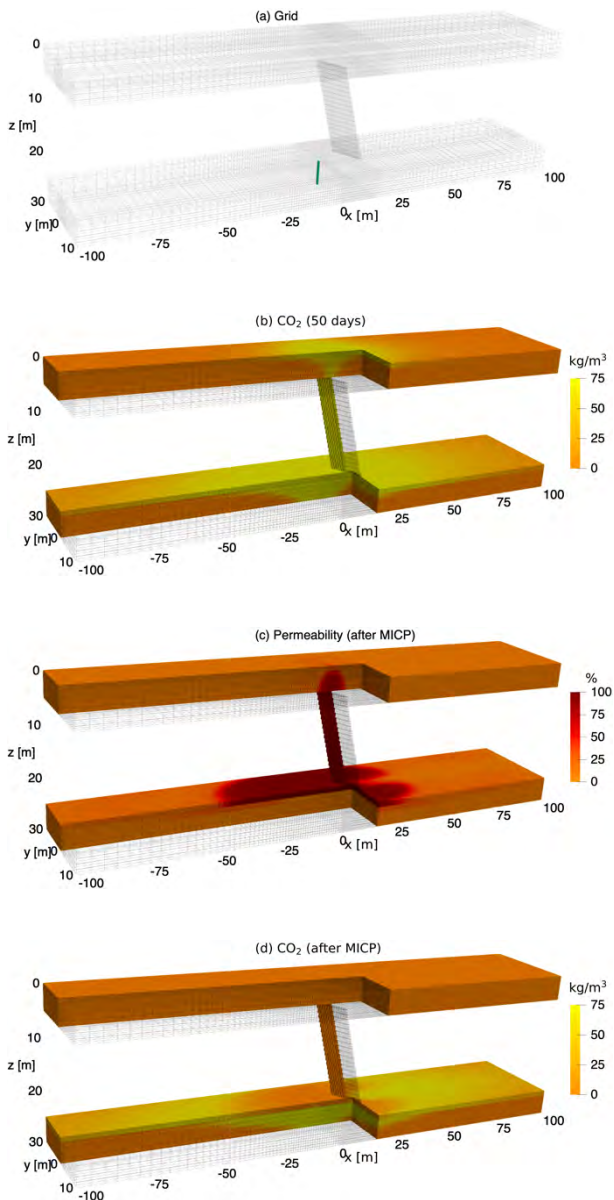


Figure 7: (a) Grid with well and spatial distribution of (b) CO₂ without MICP treatment, (c) permeability reduction, and (d) CO₂ after MICP treatment.

For a better visualization of the CO₂ rate through the leakage path, we plot the average normalized value of CO₂ flux along the width of the leakage path over time with and without MICP treatment in Fig. 8. The CO₂ was injected at a rate of $2.31 \times 10^{-4} \text{ m}^3/\text{s}$.

We observe from the plot without MICP treatment that after few days of injection the CO₂ reaches the leakage path, and a significant amount of CO₂ leak to the upper aquifer. This leak is mitigated after application of the MICP technology.

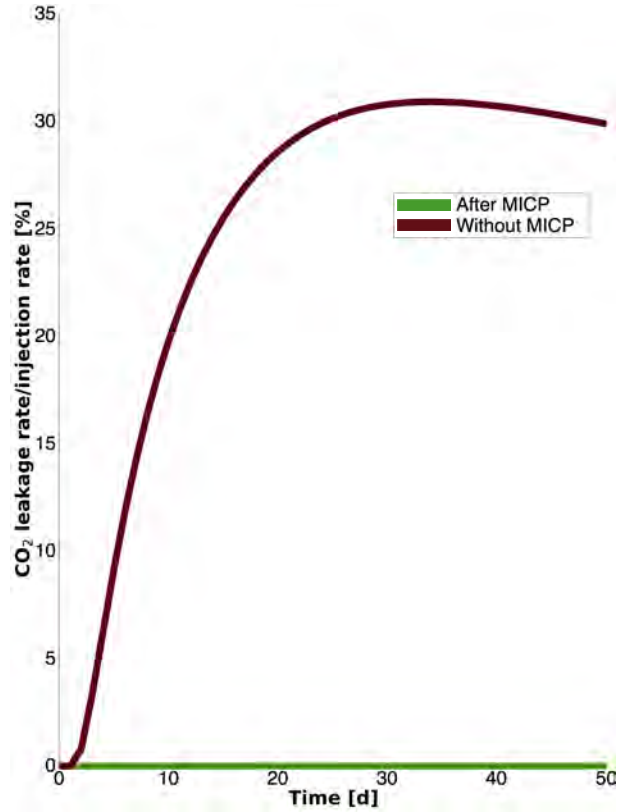


Figure 8: Leakage rate of CO₂ through the leakage path (at z=5 m) in the caprock.

4. Conclusions

This paper presents the application of the MICP technology for CO₂ leakage remediation using the OPM simulator. The implementation of the MICP mathematical model in OPM is compared against an implementation in MRST resulting in a good agreement between numerical results. Subsequently the application of the MICP simulator in OPM is demonstrated in a 2D flow domain with a leakage path. Finally, we design an injection strategy to seal a leakage path in a complex 3D system with a diagonal leakage path along the width of the caprock. This study demonstrates that it is possible to use MICP technology to plug a leakage pathway across the width of the reservoir.

Currently we are focusing on adding dispersion effects and making the implementation of the MICP model a part of OPM Flow, which in turn will make the model available as open-source code. Further work is to use this implementation to perform optimization and sensitivity analysis studies.

Acknowledgements

The authors are grateful for the financial support from Research Council of Norway through the project “Efficient models for microbially induced calcite precipitation as a seal for CO₂ storage (MICAP)” (grant 268390).

References

- [1] Ebigbo, A., Class, H., Helmig, R., 2007. CO₂ leakage through an abandoned well: problem-oriented benchmarks. *Comput. Geosci.* 11, 103–115.
- [2] Nakajima, T. et al., 2014. Numerical simulation of CO₂ leakage along fault system for the assessment of environmental impact at CCS site. *Energy Procedia* 63, 3234-3241.
- [3] Newell P. and Martinez, M.J., 2020. Numerical assessment of fault impact on caprock seals during CO₂ sequestration. *Int. J. Greenh. Gas Control* 94, 102890.
- [4] Wu, R. et al., 2019. Significance of fault seal in assessing CO₂ storage capacity and leakage risks – An example from offshore Norway. *Eur. Assoc. Geosci. Eng.* 2019.
- [5] Whiffin, V.S., van Paassen, L.A. and Harkes, M.P., 2007. Microbial carbonate precipitation as a soil improvement technique. *Geomicrobiol. J.* 24(5), 417-423.
- [6] Lee, C., Lee, H. and Kim, O.B., 2018. Biocement fabrication and design application for a sustainable urban area. *Sustainability* 10(11), 4079.
- [7] Bai, Y et al., 2017. Experimental and visual research on the microbial induced carbonate precipitation by *Pseudomonas aeruginosa*. *AMB Express* 7, 57.
- [8] Ebigbo, A. et al., 2012. Darcy-scale modeling of microbially induced carbonate mineral precipitation in sand columns. *Water Resour. Res.* 48(7), W07519.
- [9] Gomez, M.G. et al., 2017. Large-scale comparison of bioaugmentation and biostimulation approaches for biocementation of sands. *J. Geotech. Geoenviron. Eng.* 143(5), 04016124.
- [10] Xiao, Y. et al., 2021. Homogeneity and mechanical behaviors of sands improved by a temperature-controlled one-phase MICP method. *Acta Geotech.*
- [11] Zhang, T. and Klapper, I., 2010. Mathematical model of biofilm induced calcite precipitation. *Water Sci. Technol.* 61(11), 2957–2964.
- [12] Hommel, J. et al., 2015. A revised model for microbially induced calcite precipitation: improvements and new insights based on recent experiments. *Water Resour. Res.* 51, 3695–3715.
- [13] Tveit, S. et al., 2018. Numerical study of microbially induced calcite precipitation as a leakage mitigation solution for CO₂ storage. *Eur. Assoc. Geosci. Eng.* 2018.
- [14] Landa-Marbán, D. et al., 2021. Practical approaches to study microbially induced calcite precipitation at the field scale. *Int. J. Greenh. Gas Control* 106, 103256.
- [15] Tveit, S., Pettersson, P., and Landa-Marbán, D., 2020. Optimizing sealing of CO₂ leakage paths with microbially induced calcite precipitation under uncertainty. *Eur. Assoc. Geosci. Eng.* 2020.
- [16] Rasmussen, A.F. et al., 2021. The open porous media flow reservoir simulator. *Comput. Math. Appl.* 81, 159-185.
- [17] Lie, K.-A., 2019. An introduction to reservoir simulation using MATLAB/GNU Octave: user guide to the MATLAB reservoir simulation toolbox (MRST). Cambridge University Press.
- [18] Baxendale, D. et al. 2020, OPM Flow Documentation Manual, Open Porous Media Initiative. https://opm-project.org/?page_id=955.
- [19] Berre, I. et al., 2021. Verification benchmarks for single-phase flow in three-dimensional fractured porous media. *Adv. Water Resour.* 147, 103759.

RAPID OPTIMISATION OF THE NEW SLEIPNER BENCHMARK MODEL

Francesca Watson^{1*}, Odd Andersen¹, Halvor Møll Nilsen¹

¹ SINTEF Digital, Oslo, Norway

* Corresponding author e-mail: francesca.watson@sintef.no

Abstract

A new Sleipner benchmark model has recently been released. Basic petrophysical parameters are included in the dataset but it is intended that further modelling work should be carried out in order to refine parameter estimates. In this study we have developed a rapid calibration workflow, in the open source Matlab Reservoir Simulation Toolbox (MRST). We use this workflow to calibrate model parameters such that results match plume outlines interpreted from seismic data, also provided in the benchmark dataset. This is made feasible by the use of hybrid vertical equilibrium (VE) modelling and adjoint-based, continuous optimisation, using automatic differentiation. Parameters have been found which lead to simulation results that provide a reasonable match to the plume outline in the top layer, when using a slightly modified model top surface. This workflow provides a useful tool which allows us to use monitoring data to improve simulation models during and after CO₂ injection.

Keywords: *Sleipner, Vertical Equilibrium, Optimisation, MRST, Reservoir simulation*

1. Introduction

Underground CO₂ storage has been undertaken at the Sleipner site since 1996. During this time a whole host of geophysical monitoring data, in particular seismic data, has been collected from the site, allowing us to infer information about the temporal evolution of the CO₂ plume as well as information about the internal structure of the reservoir. Importantly, seismic observations of the CO₂ plume reveal a more detailed picture of the layered internal structure of the reservoir [1].

In conjunction with geophysical monitoring data we can use simulations to better understand the dynamic processes occurring in the subsurface and reduce uncertainties in simulation parameters (e.g. model geometry, petrophysical parameters). Initial simulation work at Sleipner involved simplified models with basic geometry to investigate the layered structure and CO₂ plume migration [2].

In 2011 a Sleipner benchmark model was released, with realistic geometry inferred from seismic data [3]. This model covered the uppermost layer of the reservoir, layer 9, where we have the most accurate seismic coverage.

Several studies used this model as a starting point to identify parameters which give simulation results that best match the CO₂ spread at the top of the reservoir, identified in the seismic data [3] [4] [5] [6]. As this benchmark only comprises the top layer of the reservoir, assumptions have to be made regarding the amount of CO₂ in the layer and the location it is first introduced into the model.

These studies generally showed the strong influence of the permeability heterogeneity and the topography of the top surface on the resulting plume shape but several things are still debated. For example the mass distribution within the layers, the density of the plume and the vertical migration mechanism through the shale layers, capillary flow vs higher permeability pathways.

A new Sleipner benchmark model was released by Equinor in 2019 [7]. It includes an updated reservoir model which covers the whole depth of the reservoir including the injection well. It also contains supplementary information such as injection rates, the suspected location of possible feeder chimneys through the shale, based on the changes in the nature of the seismic signal, and the extent of the plume at the top of each layer after 15 years injection, also based on the seismic data.

The base model has been populated with a basic set of parameters (uniform permeability and porosity for the sand, uniform permeability and porosity for the shale) which can be used as a starting point to determine a more realistic parameter set.

In this study we have developed a rapid optimisation workflow which uses hybrid vertical equilibrium modelling [8] and adjoint-based continuous optimisation to run simulations on the new benchmark model and find more realistic parameters, constrained by the observed data. Here we have used the plume outlines given in the dataset as the data we would like to match our simulations to. Further work has been undertaken in [9] where multiple types of monitoring data have been used in combination to further constrain the reservoir parameters. Simulations have been carried out using the Matlab Reservoir Simulation Toolbox (MRST) [10]. MRST is open source and highly flexible allowing for rapid prototyping and easy modification of model equations. It also contains functionality for vertical equilibrium modelling and gradient-based optimisation using adjoints.

The combination of the hybrid VE framework with adjoint based optimisation and automatic differentiation is key to allowing us to run automatic optimisation, with a flexible objective function, on a model as large as the

Sleipner benchmark (~1.9 million cells in the original benchmark simulation grid).

2. Methodology

2.1 Governing equations

We use the equations for multiphase flow in porous media and a finite-volume discretisation. The mass conservation of phase α is given by:

$$\frac{\partial(\phi\rho_{\alpha}s_{\alpha})}{\partial t} = -\nabla \cdot (\rho_{\alpha}\mathbf{u}_{\alpha}) + \rho_{\alpha}f_{\alpha} \quad (1)$$

where ϕ is porosity, ρ_{α} is phase density, s_{α} is phase saturation (volume fraction), f_{α} is the sum of any sinks / sources and \mathbf{u}_{α} is the Darcy flux of phase α . The multiphase equation for the Darcy flux is:

$$\mathbf{u}_{\alpha} = -\frac{\mathbf{k}k_{r\alpha}}{\mu_{\alpha}}(\nabla P_{\alpha} + \rho_{\alpha}\mathbf{g}) \quad (2)$$

with permeability \mathbf{k} , relative permeability, which is a function of the wetting phase saturation $k_{r\alpha} = k_{r\alpha}(s_{\alpha})$, phase viscosity μ_{α} , phase pressure P_{α} and gravity vector \mathbf{g} . All phase saturations sum up to unity.

2.2 The hybrid vertical equilibrium model

The hybrid VE model is a modification of the standard VE model and is described in detail by [8].

In the standard VE model we solve a form of the governing equations which have been integrated vertically such that we are solving for the vertically integrated horizontal fluxes in the model. The vertical configuration of fluids can then be calculated from the results based on the assumption that fluids in a grid cell have reached vertical equilibrium. Thus we do not need to discretise the model in the vertical direction, leading to a large reduction in the number of grid cells required. This method has been shown to work well for systems with large buoyancy contrasts such as brine-CO₂ systems [11] [12].

The internal layering of the new benchmark model requires a modification to this method. Here, the layers are in vertical equilibrium internally but there is still flux between layers and up through the reservoir. As a whole, the reservoir is not vertically equilibrated due to the low permeability shale layers, as indicated by the layered structure of the CO₂ plume seen in the seismic data.

The hybrid VE framework we have used allows us to have a hybrid grid, with volumes being modelled as VE cells connected to volumes modelled as fully resolved cells (normal 3D simulation). This means we can setup a simulation grid which uses VE simulation internal to each layer but which has fully resolved cells that represent the possible feeder chimneys and allow us to model vertical flow at these locations.

2.3 Model setup

The benchmark simulation grid contains approximately 1.9 million cells. We convert the 9 sandstone layers in the grid into a series of stacked VE layers with impermeable boundaries between the layers to represent the low permeability shales. There are fully resolved cells in the locations of the suspected feeder chimneys (Fig. 1). In total the hybrid VE grid contains 76527 cells, which is about 4 percent of the original cell count.

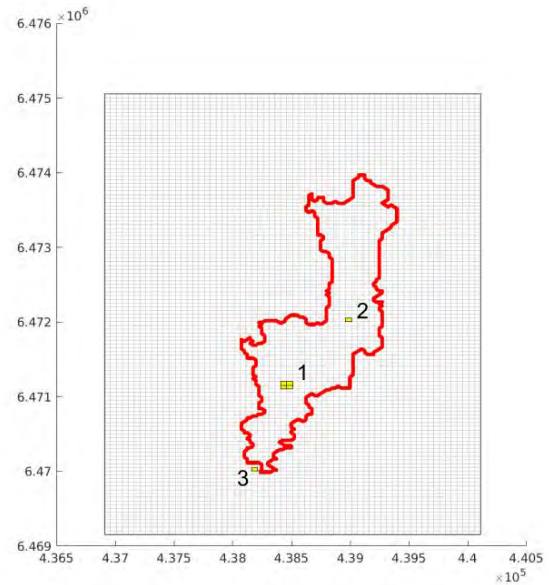


Figure 1: The three possible feeder locations included in the dataset. Red line is the plume outline at the top of layer 9. Numbers 1, 2 and 3 correspond to the permeability factors shown in Fig. 6. The main feeder chimney can be identified on the seismic data and intersects the whole of the reservoir up to layer 9. The other two chimneys are less clear in the seismic data and intersect only layer 5 and layer 7 respectively.

The location of the injection well is taken from the benchmark dataset. Injection rates are given in [13].

Petrophysical properties for the model are given in the benchmark dataset. Fluid properties for CO₂ are calculated based on temperature and pressure using the CoolProp library [14] [15]. Although temperature is not modelled in the simulation we impose a background temperature gradient with an injection temperature of 41 °C and a temperature at the top of the reservoir of 37 °C. Fluid properties are shown in Table 1.

Table 1. Simulation fluid properties.

Brine density [kg m ⁻³]	1020
CO ₂ density [kg m ⁻³]	318 - 497
Brine viscosity [Pa s]	8.00×10 ⁻⁴
CO ₂ viscosity [Pa s]	6.00×10 ⁻⁵
Brine compressibility [bar ⁻¹]	4.37×10 ⁻⁵
CO ₂ compressibility [bar ⁻¹]	4.37×10 ⁻⁴

2.4 Adjoint based optimisation

Adjoint based optimisation is implemented in MRST as described in [5] [16].

The aim of the optimisation is to update model parameters so that simulated plume outlines match the plume outlines given in the benchmark dataset. Plume outlines, provided as polygons, show the extent of the CO₂ plume at the top of each layer in the 2010 seismic survey. The objective function, J_{plume} , is given by:

$$\begin{aligned}
 J_{inside,i} &= \left(\frac{h_i - h_{min}}{H_i - h_{min}} \right)^2, & h_i < h_{min} \\
 J_{inside,i} &= 0, & h_i > h_{min} \\
 J_{outside,i} &= \left(\frac{h_i - h_{min}}{-h_{min}} \right)^2, & h_i > h_{min} \\
 J_{outside,i} &= 0, & h_i < h_{min} \\
 J_{plume} &= \sum_i J_{inside,i} + \sum_i J_{outside,i} \quad (3)
 \end{aligned}$$

where h_i is the height of CO₂ in cell i , h_{min} is the assumed minimum CO₂ column height required for the plume in that cell to be visible in the seismic data and H_i is the total height of cell i .

We have chosen individual layer and chimney permeabilities, porosity and CO₂ density as the parameters to be optimised. Varying the parameters is carried out by multiplying them by a scalar value which is allowed to vary within a certain range. The ranges for porosity and permeability are chosen based on the range of values given in the dataset.

We have chosen to vary the CO₂ density as there is some uncertainty in the temperature distribution in the reservoir which may have a large impact on the density distribution in the plume.

3. Results

3.1 Matching the benchmark model

Fig. 2 shows the simulated CO₂ saturation after 15 years injection for the unoptimised benchmark model. Plume outlines from the benchmark data are shown in red. Using the base case model does not give a good match between the observed and simulated plume outlines.

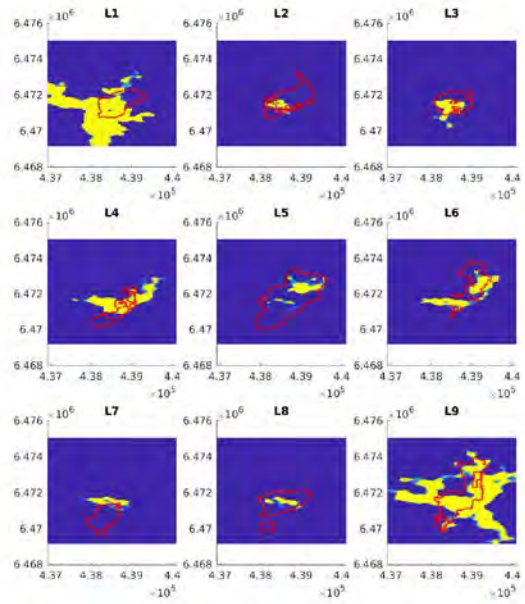


Figure 2: CO₂ saturation at the top of all layers. Unoptimised benchmark model. Plume outlines from the benchmark are shown in red.

After running the optimisation, where we are only concerned with matching the outline in layer 9, we find that we are still unable to get a good match between the simulated plume in layer 9 and the plume outline (Fig. 3).

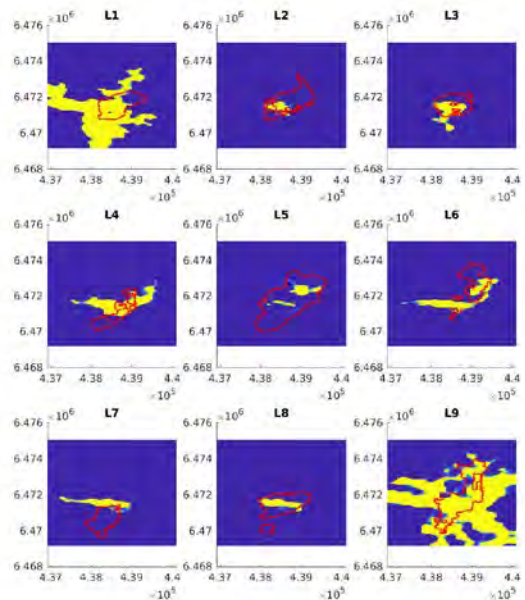


Figure 3: CO₂ saturation at the top of all layers. Optimised model matched to plume outlines in layer 9. Plume outlines from the benchmark are shown in red.

Consistent with previous studies, all our simulations lead to outcomes where CO₂ collects locally as a plume beneath each vertical flow barrier, with a shape that closely reflects the shape of the overlying confining layer. Closer inspection of the topography of the top layer

of the model (Fig. 4) shows that it is incompatible with the plume shape and therefore it is impossible for us to match the plume shapes with the topography that we have.

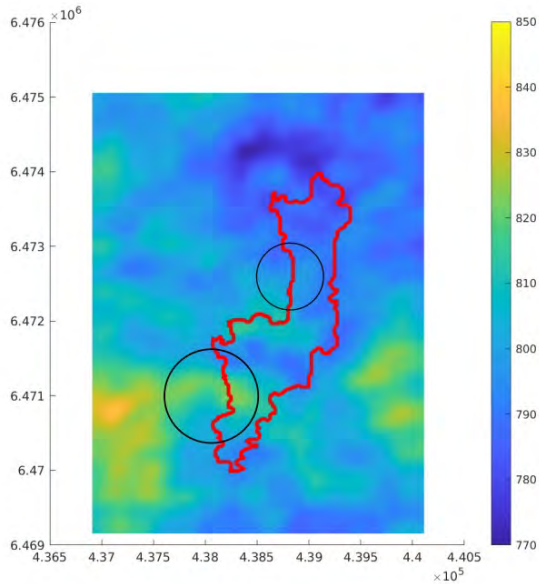


Figure 4: Depth of top surface of the benchmark model with plume outline for layer 9 on top. Notice the bottom circle shows a dip in the surface which cuts across the plume edge. A similar feature can be seen in the top circle. If these areas are to be covered by the plume then CO₂ will also be able to migrate outside of the plume outline, as happens in Fig. 3.

3.2 Modified top surface

Based on past studies which have had some success matching the plume outlines in the older benchmark model [5], we have adjusted the top surface of the new benchmark model such that it has the same topography as the older model given in [3]. Each column of grid cells has been shifted by a certain amount, this means all layers are affected by the shift in the vertical direction.

Results from matching to the layer 9 plume with the modified top surface are greatly improved although there is still some CO₂ outside of the plume outline (Fig. 5). We also see much better results for plume shapes in the underlying, internal layers even though matching plume outlines lower down the reservoir was not included in the objective function of this particular optimisation.

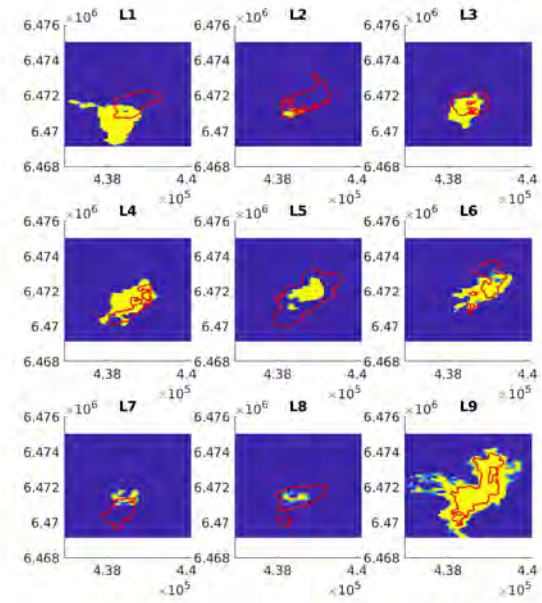


Figure 5: CO₂ saturation at the top of all layers after 15 years injection with the modified top surface. Optimised model matched to plume outlines in layer 9. Plume outlines from the benchmark are shown in red.

Looking at the resulting optimisation factors (Fig. 6, row 2) shows an increase in CO₂ density and a reduction in permeability for the main feeder chimney, this reduces the amount of CO₂ reaching the top of the model and makes it spread out less. However, this is also in conjunction with an increase in permeability in layer 9 which will conversely make the CO₂ spread out more. It is the interplay between all these factors, as well as the topography of the layer, which controls the geometry of the plume. In this way, it is possible that the result, in terms of optimisation factors, could be ambiguous. We could reduce the uncertainty by constraining with other data such as gravity measurements or specified mass in each layer [15].

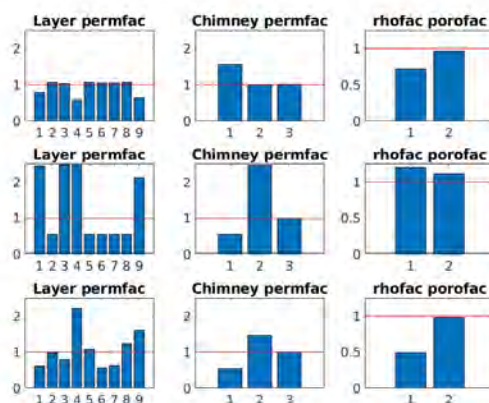


Figure 6: Optimised parameter factors. From top to bottom the rows pertain to: Matching layer 9 with the benchmark top surface, Matching L9 with the modified top surface, Matching all layers with the modified top surface.

We also observe an increase in permeability for chimney 2 which is in the north-eastern part of the reservoir between layers 5 and 6. This suggests that more CO₂ is required in the in the north-east part of the plume in layer 6 to fit the plume outline better.

Our modelling framework allows us to specify which individual outlines we would like to include in the optimisation. Fig. 7 shows the results when we optimise to fit plume outlines in all layers. Here the match in lower layers is improved compared to Fig. 5 at the expense of the match in the top layer. As there is much greater uncertainty in the outlines in lower layers, being able to get a good match to outlines in all layers is relatively unrealistic.

Matching to plume outlines is only possible if the topography of the model is compatible with their shapes. This means that we cannot hope to obtain a close match without being able to modify the actual model geometry. Arguably the plume outlines only provide limited information on the CO₂ spatial distribution. Although corresponding z coordinates are given, these are not of much use as they do not generally correspond to the topography of the surface. For more detailed information about CO₂ migration we require a better measure of how the mass of CO₂ is distributed in the plume.

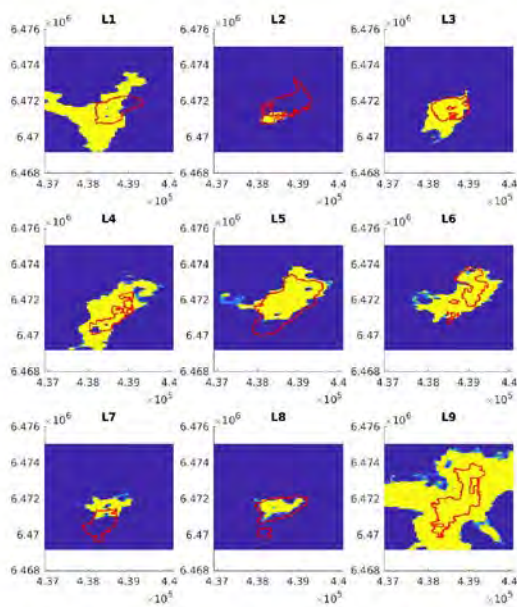


Figure 7: CO₂ saturation at the top of all layers after 15 years injection with the modified top surface. Optimised model matched to plume outlines in all layers. Plume outlines from the benchmark are shown in red.

3.2 CO₂ mass distribution

Fig. 8 shows that for both optimisations we reduce the CO₂ mass in the top layer from the unoptimised case. There is some redistribution of CO₂ in the layers in the middle of the reservoir (layers 3, 4, 5, 6). For fitting all

plumes we see increased CO₂ mass in layer 5 compared to fitting only the layer 9 plume, this is where the optimisation algorithm tried to fit the larger plume outline of layer 5.

In [17], the authors tried to estimate CO₂ mass in each layer. In the future it would be interesting to use our model and attempt to match a certain CO₂ mass in each layer as well as the plume outlines. This would be relatively easy to implement in our framework due to the rapid prototyping capabilities of MRST.

It should be noted that CO₂ mass is also closely connected to the density profile in the model. Here we have used an initial vertical density profile computed from local pressure and temperature using an equation of state, and then modified the density of CO₂ in the whole model using a single scalar multiplier. This will lead to slightly unrealistic estimates of plume density as CO₂ is highly non-linear in the region close to the conditions in the reservoir, i.e. a slight change in pressure and temperature can lead to a large change in CO₂ density. Also, the temperature at the injection well is fairly well constrained but there are large uncertainties in the temperature at the top of the reservoir and therefore in the temperature gradient. To investigate the density profile of CO₂ at Sleipner we should extend our model so that we can use the temperature gradient as an optimisation parameter instead of density.

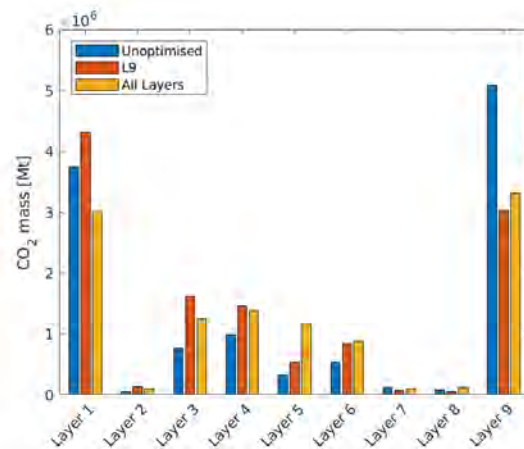


Figure 8: CO₂ mass in each layer when matching to different plume outlines.

4. Conclusions

We have used a hybrid VE model, implemented in the open-source code, MRST, to efficiently simulate the new Sleipner, multi-layered, benchmark model. A framework for rapid optimisation has been developed and we have optimised selected properties of the simulation model to match plume outlines given in the benchmark dataset. Closer inspection of the benchmark model shows that the topography of the surfaces is not compatible with the observed plume outlines, at least without significantly departing from the generally agreed assumptions of rapid gravity segregation and local CO₂ pooling. Results from modifying the geometry so that the top surface resembles the 2011 benchmark model show a closer match to the

plume although an exact match cannot be found without being able to modify the top surface automatically.

Being able to use more geophysical data in a combined fashion will allow us to better constrain the parameters we have and reduce the ambiguity in optimisation results.

Future work should also focus on investigating the temperature and therefore density profile of the plume which may help our understanding of vertical migration within the reservoir.

In general, this workflow can provide a valuable tool to integrate monitoring data acquired during and after CO₂ injection into dynamic simulation models. Thereby improving the accuracy of the simulation models and helping to elucidate processes occurring in the subsurface.

Acknowledgements

This publication has been produced with support from the NCCS Research Centre, performed under the Norwegian research program Centres for Environment-friendly Energy Research (FME). The authors acknowledge the following partners for their contributions: Aker Solutions, Ansaldo Energia, Baker Hughes, CoorsTek Membrane Sciences, EMGS, Equinor, Gassco, Krohne, Larvik Shipping, Lundin, Norcem, Norwegian Oil and Gas, Quad Geometrics, Total, Var Energi, and the Research Council of Norway (257579/E20). This work has also been funded by Gassnova under the CLIMIT-demo project 619210.

References

- [1] R. Chadwick, R. Arts, O. Eiken, G. Kirby, E. Lindeberg and P. Zweigel, *4D seismic imaging of an injected CO₂ plume at the Sleipner field, central North Sea: Geological Society, London, Memoirs, 29, 311–320, doi: 10.1144/GSL.MEM.2004.*
- [2] R. A. Chadwick and D. J. Noy, "History-matching flow simulations and time-lapse seismic data from the Sleipner CO₂ plume," in *Geological Society, London, Petroleum Geology Conference series*, 2010.
- [3] V. P. Singh, A. Cavanagh, H. Hansen, B. Nazarian, M. Iding, P. S. Ringrose and others, "Reservoir modeling of CO₂ plume behavior calibrated against monitoring data from Sleipner, Norway," in *SPE annual technical conference and exhibition*, 2010.
- [4] C. Zhu, G. Zhang, P. Lu, L. Meng and X. Ji, "Benchmark modeling of the Sleipner CO₂ plume: Calibration to seismic data for the uppermost layer and model sensitivity analysis," *International Journal of Greenhouse Gas Control*, vol. 43, p. 233–246, 2015.
- [5] H. M. Nilsen, S. Krogstad, O. Andersen, R. Allen and K.-A. Lie, "Using sensitivities and vertical-equilibrium models for parameter estimation of CO₂ injection models with application to Sleipner data," *Energy Procedia*, vol. 114, p. 3476–3495, 2017.
- [6] L. R. Cowton, J. A. Neufeld, N. J. White, M. J. Bickle, G. A. Williams, J. C. White and R. A. Chadwick, "Benchmarking of vertically-integrated CO₂ flow simulations at the Sleipner Field, North Sea," *Earth and Planetary Science Letters*, vol. 491, p. 121–133, 2018.
- [7] CO2DataShare, "Sleipner Benchmark Dataset 2019," 2019.
- [8] O. Møyner and H. M. Nilsen, "Multiresolution coupled vertical equilibrium model for fast flexible simulation of CO₂ storage," *Computational Geosciences*, vol. 23, p. 1–20, 2019.
- [9] F. Watson, H. Møll Nilsen, O. Andersen, P. Eliasson and A. Romdhane, "Improved technology for the integration of simulation and monitoring data for CO₂ storage.," *International Energy Agency Greenhouse Gas R&D Programme (IEAGHG), 15th Greenhouse Gas Control Technologies Conference 2020 (GHGT-15)*, 2021.
- [10] K.-A. Lie, *An introduction to reservoir simulation using MATLAB/GNU Octave*, Cambridge University Press, 2019.
- [11] H. M. Nilsen, P. A. Herrera, M. Ashraf, I. Ligaarden, M. Iding, C. Hermanrud, K.-A. Lie, J. M. Nordbotten, H. K. Dahle and E. Keilegavlen, "Field-case simulation of CO₂-plume migration using vertical-equilibrium models," *Energy Procedia*, vol. 4, p. 3801–3808, 2011.
- [12] K. W. Bandilla, M. A. Celia and E. Leister, "Impact of model complexity on CO₂ plume modeling at Sleipner," *Energy Procedia*, vol. 63, p. 3405–3415, 2014.
- [13] A. Callioli Santi, "Factors impacting multi-layer plume distribution in CO₂ storage reservoirs," 2018.
- [14] CoolProp, "www.coolprop.org".
- [15] I. H. Bell, J. Wronski, S. Quoilin and V. Lemort, "Pure and Pseudo-pure Fluid Thermophysical Property Evaluation and the Open-Source Thermophysical Property Library CoolProp," *Industrial & Engineering Chemistry Research*, vol. 53, p. 2498–2508, 2014.
- [16] O. Møyner, S. Krogstad, K.-A. Lie and others, "The application of flow diagnostics for reservoir management," *SPE Journal*, vol. 20, p. 306–323, 2015.
- [17] A. J. Cavanagh and R. S. Haszeldine, "The Sleipner storage site: Capillary flow modeling of a layered CO₂ plume requires fractured shale barriers within the Utsira Formation," *International Journal of Greenhouse Gas Control*, vol. 21, p. 101–112, 2014.

HOW FAULT INTERPRETATION METHOD MAY INFLUENCE THE ASSESSMENT OF A FAULT-BOUND CO₂ STORAGE SITE

E.A.H.Michie¹, A. Braathen¹, B. Alaei²

¹ University of Oslo, Oslo, Norway

² Earth Science Analytics, Oslo, Norway

* Corresponding author e-mail: e.m.haines@geo.uio.no

Abstract

Interpretation of faults in the subsurface hinges on utilizing an optimum picking strategy, i.e. the seismic line spacing. Differences in line spacing lead to significant changes in subsequent fault analyses such as fault growth, fault seal and fault stability, all of which are crucial when analyzing a fault-bound CO₂ storage site. With the ever-advancing technologies, machine learning techniques, such as Deep Neural Networks (DNN), used for fault extraction are becoming increasingly common, however their limitations and corresponding uncertainty is still largely unknown. Here, we show how fault extraction using DNN compares with faults that have been picked manually, and with using different line spacing. Uncertainty related to both manual and automated fault extraction methods are heavily reliant on seismic quality. As such, faults that are well-imaged show a closer similarity between those that have been manually picked and automatically extracted. In cases of poorly imaged faults, DNN picking on narrower line spacing creates a fault that is more irregular and with a lower predicted stability than the smoother and simpler fault model created by manual picking. Thereby, DNN creates fault surfaces that are less stable than those that have been picked manually, which is assumed to be associated with the increased irregularity of the fault segments. We conclude that fault picking by DNN without in-depth expertise works for well-imaged faults; poorly imaged faults require additional considerations and quality control for both manually and DNN picked faults.

Keywords: Fault interpretation, fault stability, machine learning, uncertainty, CO₂ storage

1. Introduction

In order to achieve targets to reduce emissions of greenhouse gases as outlined by the European Commission [1], methods of carbon capture and storage can be utilized to reach the 2°C goal of the Paris Agreement [2]. One candidate for a CO₂ storage site has been identified in the Norwegian North Sea, which is the focus of this study: the saline aquifer in the Sognefjord Formation at the Smeaheia site [3] (Figure 1). The Alpha prospect identified for this site is located within a tilted fault block bound by a deep-seated basement fault: the Vette Fault Zone (VFZ) [3], and hence a high fault sealing capacity is required to retain the injected CO₂. Further, it is necessary for the fault to have no reactivation potential. Both of these parameters hinge on generating an accurate geological model, performed using suitable picking strategies.

The process by which seismic is interpreted has developed significantly over the years. Initially, seismic interpretation involved the manual picking using printed seismic sections [4], which has since developed to provide users with the ability to interpret using a suite of digital environments [5]. The ease and accuracy of seismic interpretation is continually increasing, associated with advanced geophysical and rock physics tools, as well as the increased use of automated technologies. While technology has progressed to allow user to quickly interpret horizons using facilities such as auto-tracking, the ability for machine learned algorithms

for automated fault extraction has, until recently, been lacking. New technology has emerged that uses Deep Learning (i.e. Deep Neural Networks inspired machine learning) to automatically extract faults from seismic, with minimal manual seismic fault interpretation [6]. However, it is crucial to understand any uncertainties when using these automated methods, and how they may impact any further fault analyses.

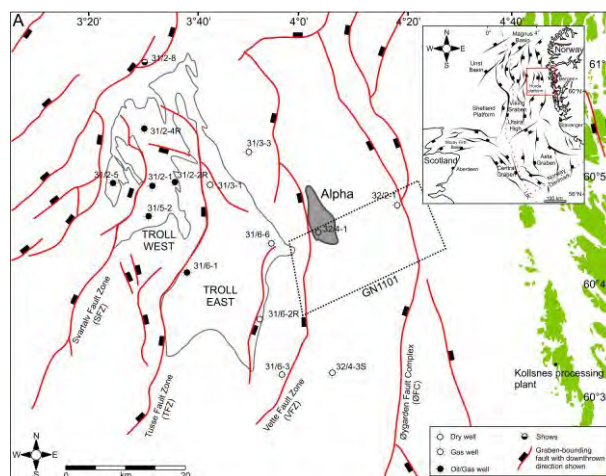


Figure 1. Location of the potential CO₂ storage site, known as Smeaheia.

2. Methodology

In this contribution, we compare manual fault interpretation with that from supervised DNN fault extraction for the prospect-bounding Vette Fault within the Smeaheia potential CO₂ storage site. Further, we also compare differences between interpretation using different line spacing, as this has proven to be crucial for in-depth fault analyses such as fault stability analysis. Specifically, we have examined how the predicted dilation tendency varies when faults are picked on every line (25 m), 2nd line (50 m), 4th line (100 m), 8th line (200 m), 16th line (400 m) and 32nd line (800 m). Dilation tendency is the relative probability of a plane to dilate within the current stress field (Table 1), taking into consideration the cohesion and frictional coefficient of the fault rock, which are set as 0.5 MPa and 0.45, respectively. Dilation tendency is a ratio between 0 and 1, where the higher the value, the more likely a fault will go into tensile failure.

	Gradient (MPa/m)	Stress (MPa)	Depth (m)	Direction (degrees)
SHmin	0.0146	23.07	1699.5	090
SHmax	0.0146	23.07	1699.5	180
Sv	0.0215	32.37	1699.5	
PP	0.01	16.94	1699.5	

Table 1: *In situ* stress data used for geomechanical analysis, from [6].

GN1101 3D seismic survey was used in this study. The survey has a 25x12.5 m inline and cross line spacing and 4 ms vertical sampling interval. Data is prestack time migrated. Data quality is overall good. Seismic imaging challenges caused by large faults (i.e. the Vette Fault Zone) caused some poor imaging around fault zones. Wells around the survey were used to build a simple velocity model for depth conversion purposes.

3. Results

3.1 Manual Fault Interpretation

Although fault stability is influenced by external factors, specifically the *in situ* stress conditions, it is also heavily influenced by intrinsic fault attributes, namely strike and dip. Since the stress conditions used in this study are isotropic, fault dip has a primary control on fault stability over fault strike. Here, we show how fault dip, and hence geomechanical analysis, varies with picking strategy.

3.1.1. Dip

Fault dip varies down the VFZ. There is low fault dip within the top 1000 m, particularly in the Northern section, where the fault penetrates younger stratigraphy, specifically the Cromer Knoll and the Shetland Groups. Here, the dip decreases to approximately 35 degrees, but can be as low as 15 degrees at the very top of the fault (Figure 2). The fault then steepens in dip to approximately 70 degrees at 1500 – 4000 m depth,

beyond which the dip decreases again to approximately 40 degrees at the base of the fault.

Fault dip is also shown to vary according to picking strategy. The shallowly dipping portion at the top of the fault is smoothed with increasing picking distance, such that the lowest dip for faults picked on every 400 m and 800 m line spacing is 35 degrees. However, the shallowest dip for faults picked on every 25 m and 50 m line spacing is 15 degrees. Further, small, bulls-eye areas of steeper dip are also removed and smoothed when line spacing is increased (Figure 2, red circles). Similarly, the steeper portion of the fault is smoothed as the line spacing used for picking is increased. This decreases the range of dips, and smooths any bulls-eye patches of steeper or shallower dip (Figure 2, black circles).

Although rigorous quality control has been performed to improve continuity between each inline, there remains several places where slight differences in picking has occurred between lines. This human error leads to an increased irregularity of the fault surface, often creating these bulls-eye areas of inconsistent dip, associated with the triangulation algorithm trying to honour each point along the fault segments. Since fault stability is influenced by fault dip, these areas will be brought through to geomechanical modelling. The uneven nature of the fault surface is most severe when every inline line has been picked on. The irregularity decreases with increased picking spacing.

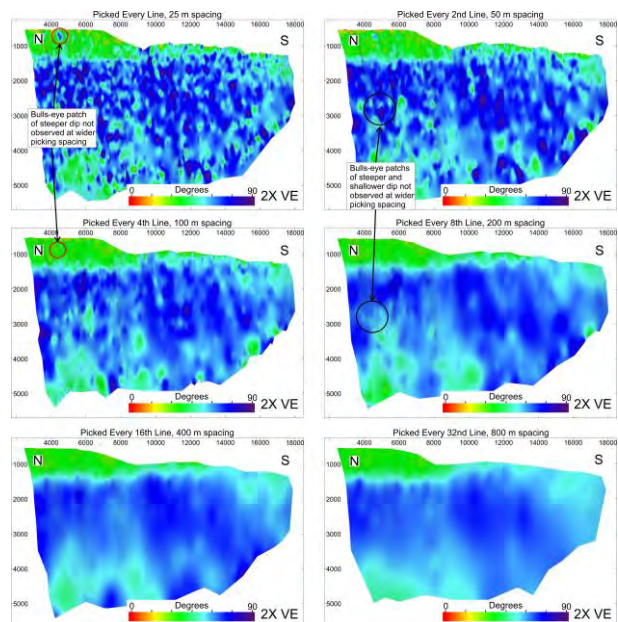


Figure 2. Fault plane diagrams showing fault dip attribute displayed on the fault surfaces for each manual picking strategy: 1, 2, 4, 8, 16 and 32 lines. Fault dip is observed to vary with line spacing used for fault picking. A highly irregular fault surface is observed when every line is used for picking, when compared to the overly smooth surface when every 32nd line is used for picking. X- and y-axes represent the lateral and vertical scales in metres, respectively. Note that unconstrained triangulation is used for fault surface generation.

3.1.2. Dilation Tendency

Since dip varies with picking strategy, as does the predicted fault stability. Along fault-strike there are minor patches where the fault is more stable than the surrounding values and patches where the fault is less stable. These patches are most apparent when every line is picked on, with irregularity decreasing in severity until every 100 m to 200 m line spacing is used for picking, where the frequency of these irregular patches is reduced. Since the fault surface is smoothed with greater picking spacing (i.e. >200 m line spacing), the results for fault stability are also smoothed, reducing the range of values of the predicted dilation tendency (Figure 3). Hence, interpretation of fault stability will vary with picking strategy, and may in fact lead to incorrect fault stability assumptions. For example, areas where the fault is close to failure are only observed when a narrower line spacing picking strategy is used (Figure 3). These areas are smoothed out and not visible when a coarser line spacing picking strategy is used. However, if these irregular areas are not a product of human error or triangulation method, the overall stability would be overestimated within this location if a coarser line spacing was used. Patches where the fault is more or less stable than the average surrounding values that occur when a narrower line spacing picking strategy is used, could be a product of human error and/or triangulation method, but may also in fact be geologically plausible due to the inherent irregularity of faults in nature. Therefore, a question is presented regarding optimum picking strategy that retains sufficient detail but remove any data that is caused by human error and/or triangulation method. Human error combined with triangulation method complications are most apparent at narrower line spacing. Conversely, over-smoothing occurs at coarser line spacing. For the studied fault system, we propose an optimum picking strategy of every 100 m line spacing. Best-practice is however likely to be case-dependent.

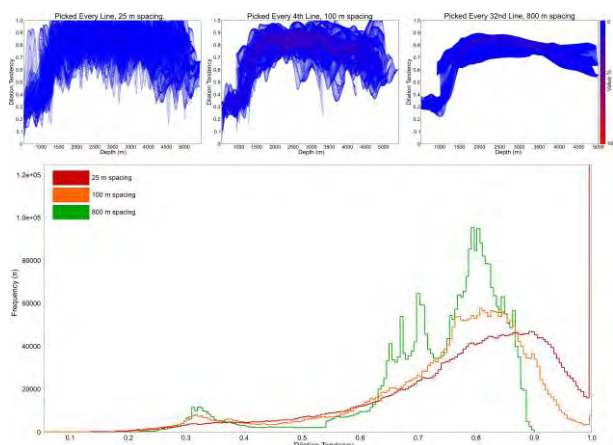


Figure 3. Top: plots showing dilation tendency with depth, for scenarios manually picked on every line (left), every 4th line (middle) and every 32nd line (right). Colour intensity reflects the frequency of those values, where blue is 1% and red is 100% frequency. Bottom: Histogram showing frequency of dilation tendency for scenarios picked on every line (red), every 4th lines (orange) and every 32nd line (green). Note that when every line is picked, a large portion of the values are above 1 (i.e. in failure). This decreases as the spacing decreases.

3.2. Deep Learning Fault Interpretation

For the DNN approach, we used supervised learning which means providing some fault picks to be used for training with seismic full stack data. The trained DNN models are checked against input picked faults through confusion matrix and visual review. We have also predicted faults using a pretrained fault model which trained on 20 surveys (excluding the GN1101 survey). We have then generated ensemble fault results of four DNN models. This enables us to see the confidence of predicted faults. Such information is useful when used to verify fault geometric attributes such as dip in this study. Comparisons have been made between fault surfaces that have been picked using traditional manual picking methods and machine learning techniques, at different picking intervals. Here we show how fault surfaces and the subsequent attributes and fault analyses vary when picked on every line, every 4th line and every 32nd line. We then describe how faults identified by different seismic quality influence the results from machine learned automated fault extraction. The Vette Fault Zone has relatively poor seismic resolution, with a wide fault zone shown by decreased seismic quality. Conversely, minor faults surrounding the Vette Fault Zone show significantly improved seismic resolution. Differences in seismic quality show variations in the results of DNN models.

3.2.1. Vette Fault Zone: Poorly imaged fault

Starting with the coarse picking strategy of every 32nd line, we can see significant disparities in the modelled fault surfaces between manual verses machine learned fault picking (Figure 4). Despite the overall smoothing that tends to exist when a coarse line spacing is chosen as the picking strategy, there remains a high propensity of the fault to appear highly irregular when machine learning techniques are used, compared to manual picking. The irregularity of the fault surface increases when the spacing for the picking strategy is decreased, as seen when examining the results for picking on every 4th line and on every line. As shown previously, when fault segments are manually picked using every crossing line, this can lead to a rugose fault surface, despite rigorous fault QC'ing. However, a fault surface with increased irregularity is formed when machine learned techniques are used. This is observed by the increased triangles, wider spread in triangle size as well as clustering of different sized triangles that is formed through machine learned techniques, related to irregular fault segments. The increased irregularity formed from both used machine learned techniques and also a narrower line spacing may lead to potential inaccuracies during any further fault analyses performed if not real.

Not only does the irregularity of the fault surface vary with picking strategy and between machine learning and manual methods, the extents of the fault surface produced is also observed to differ. Specifically, there are places where the height of the fault surface is observed to be

increased or decreased when machine learning methods are used. For example, the top of the fault is observed to extend to shallower levels in only a portion of the Southern section of the fault when machine learning methods are used, which is not observed through manual interpretation. Since identifying the location of the base of the fault is highly ambiguous due to poor seismic resolution, machine learned techniques creates a fault surface with an increased irregular fault base, where the depth of the fault base varies more across the entire fault (as seen in figures 4 and 5).

3.2.1. Dip

Fault surface irregularity is significantly higher when machine learning techniques are employed over manual interpretation, as described above. This is reflected in the increased number of irregular ‘bulls-eye’ patches of varying dip values displayed on the fault, observed on all three line spacing scenarios: every line, every 4th line and every 32nd line (Figure 4). Moreover, these patches of irregular dips tend to be steeper than the surrounding. Conversely, the patches of irregular dip when manual interpretation is performed is a combination of both steeper and shallower dips than the surrounding. The fault is smoothed such that no patches of irregular dip is observed when the fault is picked manually using a picking strategy of 32nd line spacing. The irregularities remain at the 32nd line spacing when machine learned techniques are used. However, they show both lower and higher dip compared to the background and are larger in size compared to irregularities observed in dip images of every 4 lines (Figure 4).

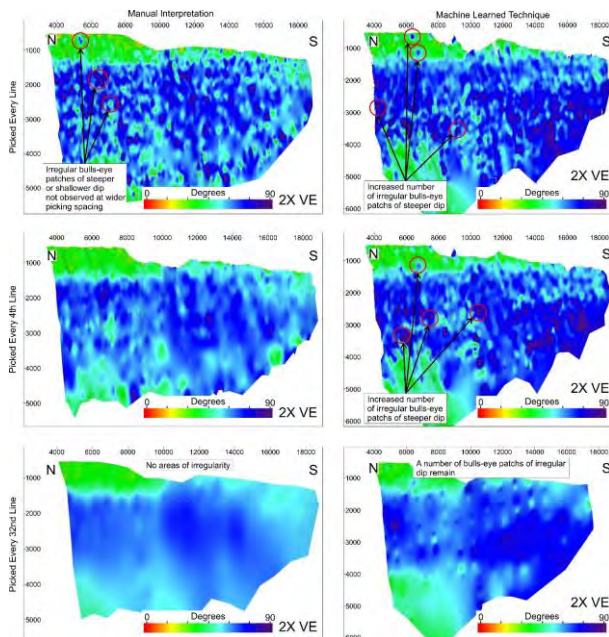


Figure 4. Fault dip attribute displayed on the fault surfaces for manual interpretation versus machine learned techniques picking on every line, every 4th line and every 32nd line. Fault dip is observed to vary with line spacing used for fault picking. A highly irregular fault surface is observed when every line is used for picking, when compared to the overly smooth surface

when every 32nd line is used for picking. Moreover, fault extraction using DNN creates an increased irregularity to the fault surface when compared to manual interpretation. X- and y-axes represent the lateral and vertical scales in metres, respectively. Note that unconstrained triangulation is used for fault surface generation.

3.2.2. Dilation Tendency

Upon examining how the predicted dilation tendency of the Vette Fault Zone changes with manual versus machine learned picking techniques, we can see distinct differences. Regardless of picking strategy spacing, we can observe an increased predicted dilation tendency when machine learned techniques are employed over manual interpretation (Figure 5). Manual interpretation using different line spacing shows a gradual increase in predicted dilation tendency with a decrease in line spacing, where a fault is predicted to be at the failure envelope at 25 m line spacing, and further away from the failure envelope at 800 m line spacing. This trend of a decrease in fault stability with a decrease in line spacing is also observed when machine learned techniques are used. However, in all scenarios the fault is predicted to be at the failure envelope, regardless of line spacing used for fault surface generation. Specifically, all three scenarios (25 m, 100 m and 800 m line spacing) show areas on the fault where the dilation tendency is 1 or over. This means that any increase in pore fluid pressure, e.g. through CO₂ injection, is likely to cause the fault to fail (under these specific input parameters).

We can observe that the bulls-eye patches of higher dips correspond to those areas of high dilation tendency (Figure 4 versus Figure 5), and hence it is these areas that have an increased likelihood of failure upon injection of CO₂. Since these irregular high dip patches occur to a lesser degree when manual interpretation occurs, the likelihood of the fault to fail is interpreted to be lower through manual interpretation, particularly for those scenarios where the fault has been picked using a coarser line spacing.

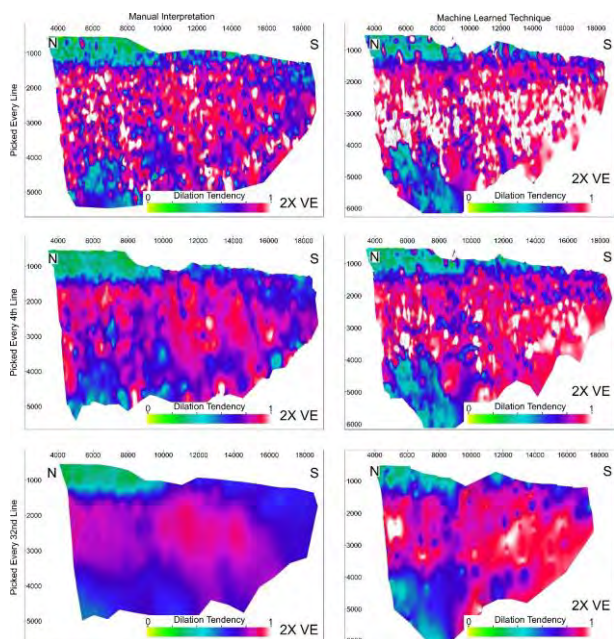


Figure 5. Dilation tendency attribute displayed on the fault surfaces for manual interpretation versus machine learned techniques picking on every line, every 4th line and every 32nd line. Since fault dip varies with line spacing and with picking technique (manual versus machine learned), as does dilation tendency. The increased irregularity to the fault surface when DNN methods are used leads to a fault that would be interpreted to be more unstable in all cases. X- and y-axes represent the lateral and vertical scales in metres, respectively. Note that unconstrained triangulation is used for fault surface generation.

3.2.2. Well imaged minor faulting

While machine learning techniques have shown to be challenging for areas of poor seismic quality, other smaller faults that are better imaged show improved identification. Specifically, minor faults (up to 100 m displacement) within the footwall of the Vette Fault Zone show accurate identification and have a significantly reduced segmentation (Figure 6), despite in several places not showing any sharp cutoffs, but rather identified by subtle folding. To qualitatively and quantitatively assess this improved fault extraction of the minor faults, we compare calculated dilation tendency using machine learning techniques with manual interpretation for one fault within the footwall of the Vette Fault Zone: fault ‘FW 01’ (see [3] for location details of this fault). We can observe that FW 01 has significantly less segmentation than those picked for the Vette Fault Zone, and in fact, the majority of lines pick only one segment for this fault. Moreover, the predicted dilation tendency is very similar between the machine learned and manually interpreted faults, which would lead to the same overall interpretation of fault stability (Figure 6). The only slight difference between machine learned and manual interpretation is the size of the fault: machine learned techniques do not extrapolate deeper than manual interpretation, which is simply a product of the poor seismic resolution at greater depths.

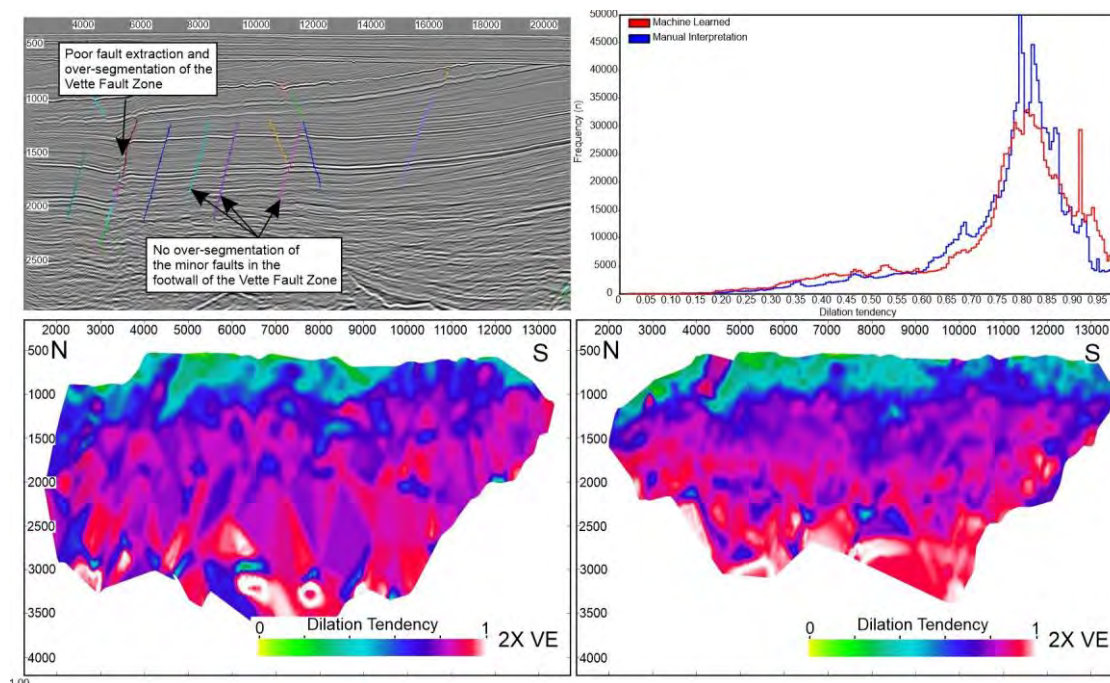


Figure 6. Comparison of manual interpretation versus machine learned interpretation of a fault in the footwall of the Vette Fault Zone. Bottom left: Fault surface produced through manual interpretation. Bottom right: Fault surface produced through machine learning. Highly similar surfaces are produced from both techniques, with the interpretation of the fault stability being almost identical.

4. Discussion

Ensuring the correct picking strategy has been chosen when manually interpreting faults, and understanding the

uncertainties involved in both manual and automated fault extraction methods, is crucial to provide the most likely estimate of any subsequent fault stability analysis. Manual picking on every line creates significant

irregularities to the fault surface, which is brought through to such analysis. Choosing this method will lead to the assumption that the fault is at/near failure, which may be inaccurate, despite any assumptions that picking using every available data may provide the best-case example. Conversely, picking using a wide line spacing, such as every 32nd line, creates an overly smoothed fault, which is interpreted to be more stable, which is likely to be incorrect. Since differences in picking strategies can over- or underestimate the fault stability, it is crucial to get the picking strategy correct for accurate predictions of fault stability analysis when assessing a storage site for CO₂ storage. We have shown that picking using every 4th line spacing is likely to create the most geologically accurate representation of the faults in the subsurface; incorporating inherent irregularities of the fault surface, while adding some smoothing to reduce the impact of human error (Figure 7). Further, an important factor to be considered is the line spacing of surveys that are used for interpretation. In our case with 4 line spacing, we are ignoring any irregularity less than 75 m in inline direction.

It is important to note that although injecting CO₂ into the Sognefjord Formation will increase the pore pressure, which in turn increases the likelihood of the fault to fail; such analysis will not have the ability to indicate precisely where on the fault failure may occur. This analysis simply provides an indication of the likelihood of failure.

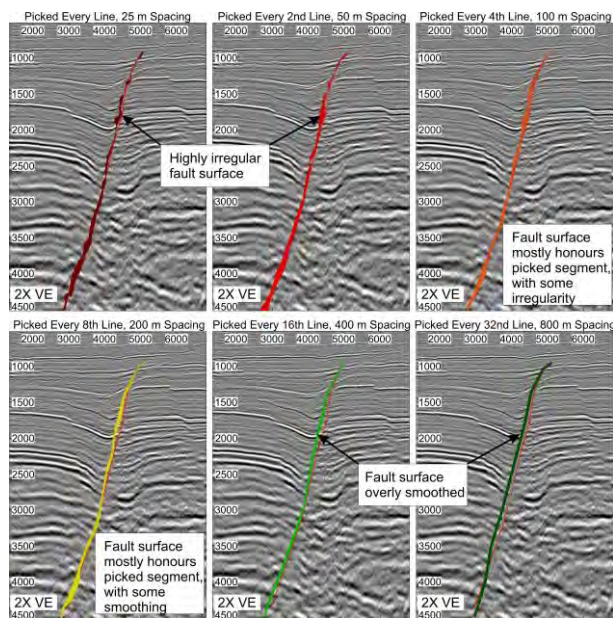


Figure 7. Differences in fault surface generation depending on picking strategy: 25 m, 50 m, 100 m, 200 m, 400 m or 800 m line spacing. Picked fault segment shown as red line. Note the smoothing that occurs at greater line spacing, and the irregularity at narrower line spacing.

Seismic data quality is an issue, which influences both manual and DNN results. The survey used in this study is prestack time migrated which is not the best imaging approach in cases with structural complexity as well as large lateral variations in velocity. Fault shadow effect is

observed in the data which deteriorate the quality of seismic data underneath fault planes and causes challenges for both manual and DNN based fault picking.

Utilising modern advances in fault picking, i.e. automated fault extraction using supervised DNN, is a fast approach to the normally time-consuming manually interpretation strategy. However, as with any new technology, it is crucial to understand the influence of how, and to what extent, machine learning may influence subsequent fault analyses such as fault stability. In our case study, DNN based results showed more irregularity for the fault surfaces, especially for the poorly imaged Vette Fault. It could be argued that fault surfaces are highly irregular in nature and hence the overly irregular faults produced could be due to automated extraction picking every kink or bend in a fault, that may be missed by manual interpretation. Large amounts of data exist in geophysical studies, hence a neural network might find hidden irregularities in the data that manual interpreters may have overlooked [8]. However, it may also be due to areas of false positive interpretation by the DNN models that we applied, particularly in areas of poor seismic resolution. As with manual fault picks, errors associated with machine learning techniques will be integrated in the fault model. Identifying short-comings through quality control may indicate the need for continued machine learning retraining to improve the model, by either further hyperparameters tuning and/or improving the input labels.

Our applied DNN models provided vertically segmented images for the Vette Fault. The networks use features on seismic data that can represent discontinuity. This segmentation can happen, for example, in areas with weak discontinuities on seismic data (e.g. packages with very low reflectivity). Hence, this could be an explanation for the increased irregularity. In manual interpretation, we usually ignore such weak reflectivity areas and extend picks over them. One approach to overcome this issue was to take ensemble of multiple DNN results. Figure 8B and D show the improvement of vertical and lateral continuity by using ensemble results.

Areas with a severe decrease in seismic quality, creating a high degree of ambiguity often lead to poor picking through machine learned techniques. For example, areas surrounding the relay zone to the Southern end of the Vette Fault (known as Vette_2, see [3]) have been poorly identified (Figure 8B). The high complexity assumed for the basin-scale Vette Fault results in a poorer seismic resolution at the fault. This leads to poor predictions of the location of the fault, and some areas of the fault being missed. In areas of poor quality seismic, manual interpretation is also model-based and can be non-unique. On the contrary, well-imaged minor faulting show excellent correlation between manual and machine learned fault picking, with the resulting predicted dilation tendency being very similar between these two methods. Hence, improved seismic quality will reduce the uncertainty of DNN based fault picking.

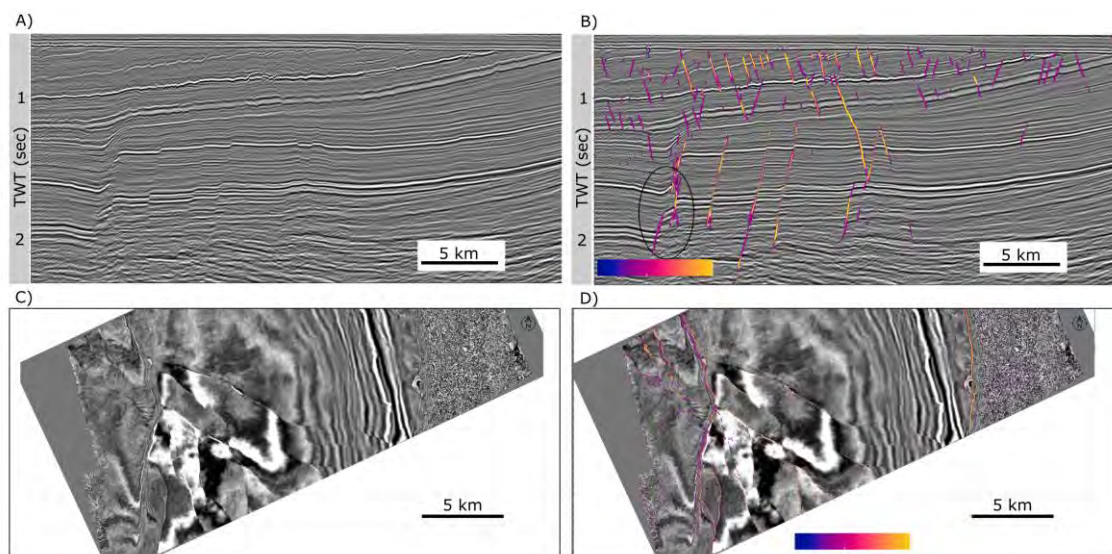


Figure 8. Examples of fault predictions using the supervised DNN models. The predicted faults are ensemble of four different models and the colour represents the confidence of predicted faults. The yellow colour means that all four models predicted faults. A) Inline without predicted results B) Inline with predicted faults. The area inside the ellipse shows poor quality seismic zone. C) Time slice without predicted faults D) Time slice with predicted faults. Note the segments of the Vette fault with less confidence in the prediction.

5. Summary

Line spacing chosen to pick fault segments will influence any subsequent analysis, e.g. fault stability, with the results varying with picking strategy. Manually interpreting using a wider line spacing creates a fault that is predicted to have an increased stability. Conversely, picking using every line spacing creates a highly irregular fault, such that the stability is predicted to be significantly reduced, and in fact will lead to the prediction of an unstable fault.

Automated methods of fault extraction is sensitive to the quality of seismic data. Poorer imaging of faults creates fault surfaces with increased irregularity when compared to manual interpretation, leading to higher predicted dilation tendency values in all line spacing scenarios. Using ensemble models, a larger coverage of faults was imaged using DNN with additional information of the confidence of predicted fault. Further fine-tuning of hyperparameters and fault label picks can potentially improve the results. On the contrary, picking of well-imaged, smaller faults show noticeable similarity in results between manual and automated methods.

Acknowledgements

This is a contribution of the FRISK project, supported by the Research Council of Norway (RCN# 295061). Support from the NCCS Centre is acknowledged, performed under the Norwegian research program Centres for Environment-friendly Energy Research (FME). The authors acknowledge the following partners for their contributions: Aker Solutions, Ansaldo Energia, CoorsTek Membrane Sciences, EMGS, Equinor, Gassco, Krohne, Larvik Shipping, Lundin, Norcem, Norwegian Oil and Gas, Quad Geometrics, Total, Vår Energi, and the Research Council of Norway (RCN# 257579/E20). Badley Geoscience Ltd. and Earth Science Analytics are

thanked for their academic licenses of T7 and EarthNet, respectively.

References

- [1] EU Commission, 2018. Communication from the commission to the European parliament, the European Council, the Council, the European economic and social committee, the committee of the regions and the European investment bank, in: A Clean Planet for All. A European Strategic Long-Term Vision for a Prosperous, Modern, Competitive and Climate Neutral Economy. Brussels.
- [2] Rogelj, J., Den Elzen, M., Höhne, N., Fransen, T., Fekete, H., Winkler, H., Schaeffer, R., Sha, F., Riahi, K. and Meinshausen, M., 2016. Paris Agreement climate proposals need a boost to keep warming well below 2 C. *Nature*, 534(7609), pp.631-639.
- [3] Mulrooney, M.J., Osmond, J.L., Skurtveit, E., Faleide, J.I. and Braathen, A., 2020. Structural analysis of the Smeaheia fault block, a potential CO₂ storage site, northern Horda Platform, North Sea. *Marine and Petroleum Geology*, p.104598.
- [4] Sheriff, R.E., 1982. *Structural interpretation of seismic data* (No. 23). American Association of Petroleum Geologists.
- [5] Al-Shuhail, A.A., Al-Dossary, S.A. and Mousa, W.A., 2017. *Seismic Data Interpretation Using Digital Image Processing*. John Wiley & Sons.
- [6] Zhao, T. and Mukhopadhyay, P., 2018. A fault detection workflow using deep learning and image processing. In *SEG Technical Program Expanded Abstracts 2018* (pp. 1966-1970). Society of Exploration Geophysicists.
- [7] Statoil, 2016. Subsurface Evaluation of Smeaheia as part of 2016 Feasibility study on CO₂ storage in the Norwegian Continental Shelf. OED 15/1785. Document A – Underground report Smeaheia (Internal Report – Available on Request Only).
- [8] Russell, B., 2019. Machine learning and geophysical inversion—A numerical study. *The Leading Edge*, 38(7), pp.512-519.

A PRELIMINARY ASSESSMENT OF RIO BONITO FORMATION (PARANÁ BASIN, BRAZIL) SUITABILITY FOR CO₂ STORAGE

Nathália Weber^{1,2*}, Saulo B. de Oliveira^{1,3}, Julio Romano Meneghini^{1,2}, Colombo Celso Gaeta Tassinari^{1,3}

¹ Research Centre for Gas Innovation (RCGI), University of São Paulo, São Paulo, Brazil

² Polytechnic School of University of São Paulo, São Paulo, Brazil

³ Institute of Energy and Environment of University of São Paulo, São Paulo, Brazil

* Corresponding author e-mail: webermasulino@usp.br

Abstract

Brazil presents a great potential for Carbon Capture and Storage (CCS) projects due to the various exploited oil and gas reservoirs on its coast, with many possibilities to replicate the results of the ongoing commercial project of carbon dioxide (CO₂) injection in the Lula oilfield. However, the distances from main sources of CO₂ emissions and the lack of sufficient transport infrastructure impose significant barriers for CCS deployment related to power plants and industrial activities. The Paraná Basin has a strategic location for onshore geological carbon storage in Brazil due to the proximity to a large concentration of CO₂ stationary sources. This work presents an initial assessment of Rio Bonito Formation sandstones suitability for CO₂ storage. Main parameters and properties related to reservoir quality, sealing quality and other leak risks, data coverage, regional proximity analysis, and social context analysis were compared to desirable characteristics for site selection. The analysis suggests a good potential of petrophysical available data for storage capacity and indications of effective containment of the injected CO₂ due to the presence of mudstone layers. However, it is required further characterization of the geological system and trapping mechanisms and assessments of public perception on CCS in the region.

Keywords: *Geological carbon storage, CO₂ storage site characterization, Rio Bonito Formation, Parana Basin*

1. Introduction

Brazil has several sedimentary basins with promising potential for CO₂ storage [1] [2] [3]. Offshore basins such as Campos and Santos Basins are vastly explored due to the intense upstream activity of petroleum industry. Its oil and gas depleted reservoirs are relevant candidates for CO₂ injection – whether for Enhanced Oil Recovery (EOR) or exclusively for carbon sequestration [4]. However, the distance from these sites to the Brazilian coast and especially to areas with large concentrations of stationary carbon sources imposes big logistical challenges to transport the large quantities of CO₂ to be captured. Considering Brazil's dimensions, these long distances impose greater risks to the viability of CO₂ pipelines, with higher costs for implementation and operations, in addition to higher regulatory risks. Previous studies revealed that CO₂ transportation infrastructure to oilfields constitutes a relevant constraint for economic feasibility to the deployment of CCS projects [5] [6].

In this sense, onshore sedimentary basins offer great opportunities to reduce these risks, favouring the viability of CO₂ transport by shorter routes, close to the stationary sources. Currently, one technical challenge to the development of CCS with onshore geological carbon storage in Brazil is the low level of knowledge regarding CO₂ injection capacity potential and related safety aspects. One of the most promising onshore sedimentary basins for CO₂ storage in the country is the Paraná Basin. It comprises an area that can be considered strategic for

the implementation of CCS due to the presence of large concentrations of CO₂ emissions stationary sources and deep sandstone layers in the Rio Bonito Formation. In addition to industries with intensive use of fossil fuels, the regions comprised by the Paraná Basin also have a great activity of bioenergy production, which provides opportunities for the development of BECCS, with potential for negative emissions.

The present work proposes an assessment of the suitability for CO₂ storage in Rio Bonito Formation and its geological context in the Paraná Basin (Fig. 1), in order to strengthen the comprehension of critical aspects that may favour or impose challenges to CCS deployment. In addition, it is aimed to identify the main lacks in critical data and information and prior research needs to a further characterization of Rio Bonito Formation as a potential geological CO₂ storage site.

The assessment was based on literature reviews regarding: (i) main parameters related to site screening and reservoir characterization for CO₂ storage; (ii) other relevant non-geological parameters involving CCS activities; and (iii) Rio Bonito Formation and Paraná Basin available data and previous studies published.

2. Basic geological criteria for CO₂ storage suitability

Reservoir properties criteria for CO₂ storage comprises [7]:

- Sufficient depth to ensure the CO₂ supercritical phase.
- Sealing integrity to contain the CO₂ in the designated reservoir, avoiding undesirable migrations.
- Sufficient storage capacity to receive CO₂ from its stationary sources.
- Effective petrophysical reservoir properties (porosity and permeability) to ensure that CO₂ injection can be economically viable and that sufficient CO₂ can be retained.

Several previous works that include the pre-feasibility stage of geological characterization for CO₂ storage propose new workflows and methodology [8] [9] [10] and present studies focused on regional or field scale site assessment [11] [12] [13] [14] [1] [16] [17]. Most of these works show similar macro arrangements, comprehending the evaluation of geological features that indicate the reservoir potential quality of storage capacity, injectivity and containment of the injected fluid. Some publications add non-geological aspects to the evaluation requirement, mentioning logistics of the whole CCS chain and regional proximity information, and social context.

To this present proposal of a primary assessment of Rio Bonito Formation suitability to CO₂ storage, the selected site screening criteria considered the limitations of geological data availability. The analysis was focused on an initial regional site assessment in a pre-feasibility stage, aiming at finding the suitability of the geological formation for CO₂ sequestration as well as the main required data and research needs for further evaluations.

Halland et al. presented a methodology for characterization of aquifers and structures with a classification of main properties as follows [18]:

- Reservoir properties: aquifer structuring, traps, pore pressure, depth, reservoir homogeneity, net thickness, average porosity, and permeability.
- Sealing properties: sealing layer, seal thickness, seal composition, faults, and other breaks.
- Other leak risks: the presence of exploration or production wells drilled through the seal.
- Data coverage: seismic and wells.

In this context, specific reservoir properties of interest and their typical high scores parameters [18] were listed as the basis for comparison with Rio Bonito Formation data. In addition, it was included a tectonic activity in the “other leak risk” category.

Other non-geological parameters and criteria for assessing sedimentary basins for CO₂ geological sequestration presented in Bachu [8] were also considered in the present work. These additional topics for comparison include logistics issues related to accessibility to the injection site, infrastructure availability and concentration of CO₂ sources.

3. Evaluation of Rio Bonito Formation suitability to CO₂ storage

The assessment of Rio Bonito Formation characteristics for each site screening criteria formerly presented is described in the following subsections. Table 1 summarises the results compared to the desirable characteristics for geological CO₂ long-term storage.

3.1 Reservoir quality

The Rio Bonito Formation consists of interbedded orthoconglomerates, sandstones, mudstones, and coals, deposited in fluvial, deltaic, estuarine, and shallow marine environments during the early Permian [19] [20] [21]. The stratigraphic succession is subdivided into three major members, labelled from base to top: Triunfo (coastal and fluvial sandstones), Paraguaçu (marine mudstones and fine-grained sandstones) and Siderópolis (coastal and fluvial sandstones) [21]. The Rio Bonito sandstones present promising permoporous properties, with peaks of 20% of porosity in some portions [22], favouring Rio Bonito as a CO₂ sink candidate. The total thickness varies from 60 to 135 m [20], which agrees with the 20 m minimum recommended by international guides [23] [24].

However, the Rio Bonito sandstones are quite heterogeneous, and when considering a mineral trapping for CO₂ storage, we must analyse in detail the mineralogical cementation composition of these sandstones, which can vary from calcitic, dolomitic, sideritic, kaolinitic, and pyritic, as described by Ketzer et al. [20] [25].

Aquifers in the Rio Bonito Formation with a level of total dissolved solids (TDS) in the water greater than 10,000 ppm are reported in the Rio Grande do Sul State, in the southern portion of Paraná Basin [26]. However, more data and studies are still needed to delimit the spatial continuity and extension of these saline aquifers.

Geological environments considered for CO₂ storage were categorized into five major systems: oil and gas reservoirs, saline formations, unmineable coal areas, shale, and basalt formations. In these systems, four trapping mechanisms are considered [27]: structural and stratigraphic trapping (physical), residual CO₂ trapping (physical), solubility trapping (geochemical), and mineral trapping (geochemical). The Rio Bonito Formation presents most of these geological systems with a high potential for CO₂ geological storage. The sandstones of the Triunfo and Siderópolis members could be considered in possible structural and stratigraphic traps where the mudstones of Paraguaçu member and Palermo Formation would act as sealing rocks. The cement with carbonatic composition in some sandstones of the Rio Bonito Formation could present an interesting potential for mineral trapping. The occurrence of saline aquifers in the Rio Bonito Formation could be better studied considering solubility trapping. Coal deposits of the Rio Bonito Formation in the southern Paraná Basin area comprise Brazil’s largest coal reserve [18].

Unmineable coal areas in this region could be focused on site locations that meet the specifications for CO₂ storage.

3.2 Sealing quality

The Rio Bonito Formation has its upper contact with mudstones of Palermo Formation or Tatuí Formation, both of which are stratigraphically equivalent, having an average thickness of 100 m [21]. The base of the Rio Bonito Formation overlies the sequence of Itararé Group, commonly with sandstones superimposed over the Taciba Formation shales. Thus, the Rio Bonito sandstones are in contact with sealing rocks both at the top and at the base. Mudstones from Paraguaçu Formation can also act as local sealants depending on their occurrence, which is erratic along the basin, and may sometimes be absent [21].

A comprehensive characterization of the sealing quality requires studies relative to the reactivity of the mineral content reactions of each of these sealing candidates, considering that some preliminary sample tests have indicated the creation of preferential pathways due to dissolution process [28].

3.3 Other leak risks

The Paraná Basin is tectonically related to a divergent margin with no relation with fold belts [29], thus being in a tectonically favourable location for CO₂ reservoir and is subject to the low level of seismic activity typical of intra-plate regions [30], as recommended by IEA-GHG [24].

Although the Paraná Basin has a high potential for hydrocarbons, there are currently no active oil or gas production fields.

3.4 Data coverage

The Paraná Basin presents an extensive data set with 123 hydrocarbon exploration well data, carried out by Petrobras Company during the 1950s until the 2000s, and 2D seismic surveys covering most of its extension, as well as some local electromagnetic, magnetic and gamma surveys (<http://geo.anp.gov.br/mapview>). The database has already been provided by the Brazilian National Petroleum Agency (ANP) including petrophysical data of all wells and will be analysed together with seismic surveys in the next steps of this research to generate an integrated 3D geological model to better characterize specific locations with potential for CO₂ storage, mainly in the region of the state of São Paulo.

3.5 Regional proximity analysis

An initial regional approach of the Rio Bonito Formation as source-sink was conducted by Rocket et al. [33] considering only the optimal depths for CO₂ storage (800 – 2,000m) and CO₂ stationary sources location in the entire Paraná Basin (Fig. 2). The map highlights the central-northern portion of the state of São Paulo as the most favourable region for selecting CO₂ storage sites.

This region accounts for one the highest concentration of stationary CO₂ emitting sources in Brazil, which could reduce risks and costs for CO₂ transportation. In addition, the presence of bioenergy production in São Paulo can lead to opportunities to implement chains for negative emissions with BECCS. In 2020, 149 production installations in the state generated around 52 thousand cubic meters of ethanol, which represented 8% of national production [31] [32].

On the other hand, existing infrastructure in the region does not present a dense pipeline network that could be considered to find synergies for CO₂ transportation.

3.6 Social context analysis

Public perception studies regarding CCS in Brazil are still at an initial stage and none is focused specifically on the region that concerns Rio Bonito Formation potential sites for CO₂ injection. Commercial CCS activities in Brazil are conducted in oil and gas reservoirs in the Lula field [34], aiming to improve petroleum production with Enhanced Oil Recovery (EOR) technique, and present no significant impacts on public perception since it is an offshore project.

A primary approach to social factors with potential influence on public acceptance of CCS with onshore CO₂ storage was conducted by Netto et al. [35]. The study was applied to Recôncavo Basin, a sedimentary basin with intensive oil production in Brazil's Northeast region. Although this studied basin is far from Rio Bonito Formation, Netto et al. [35] indicate relevant points that could be applied to other onshore potential CO₂ injection sites. The outcomes of the research conducted with communities located in the prospective areas for CCS in Recôncavo Basin point to: (i) the lack of knowledge regarding the concept of CCS; (ii) the relevance of the previous relationship with oil and gas companies to the comprehension of benefits and advantages of CCS activities; and (iii) the trust in government and private companies can improve the community's support for CCS projects [35].

Table 1: Rio Bonito Fm. available data compared to desired reservoir properties for CO₂ storage (after Bachu [8], Halland et al. [18] and Rodosta et al. [10]).

Criteria	Properties of interest	Desirable characteristics	Rio Bonito Fm.
Reservoir quality	Aquifer structuring	Possible closures	n/a
	Traps	Defined sealed structures	Mapped layers of mudstones
	Pore pressure	Hydrostatic or lower	n/a
	Depth	800- 2500 m	800 - 4000 m
	Reservoir homogeneity	Homogeneous	High heterogeneity
	Net thickness	> 50 m	100 m (formation average)
	Average porosity	> 25 %	20%
Sealing quality	Permeability	> 500 mD	n/a
	Sealing layer	More than one seal	Some portions with more than one seal
	Seal thickness	> 100 m	100 m
	Seal composition	High clay content, homogeneous	High clay content, homogeneous
	Faults	No faulting of the seal	n/a
Other leak risks	Other breaks	No fracture	n/a
	Wells (exploration/production)	No drilling through seal	Few drillings through seal
Data coverage	Tectonic activity	Low level of seismicity	Low level of seismicity
	Availability of data from seismic and wells	3D seismic, wells through the actual aquifer/structure	2D seismic, 123 hydrocarbon exploration well data
Regional proximity analysis	Accessibility to injection site	Easy	Easy / onshore reservoir
	Infrastructure availability	Extensive	Minor
	CO ₂ sources concentration	Major	Major
Social context analysis	Assessments of public perceptions on CCS	Regional assessments with indications of public support	No regional or national level assessment

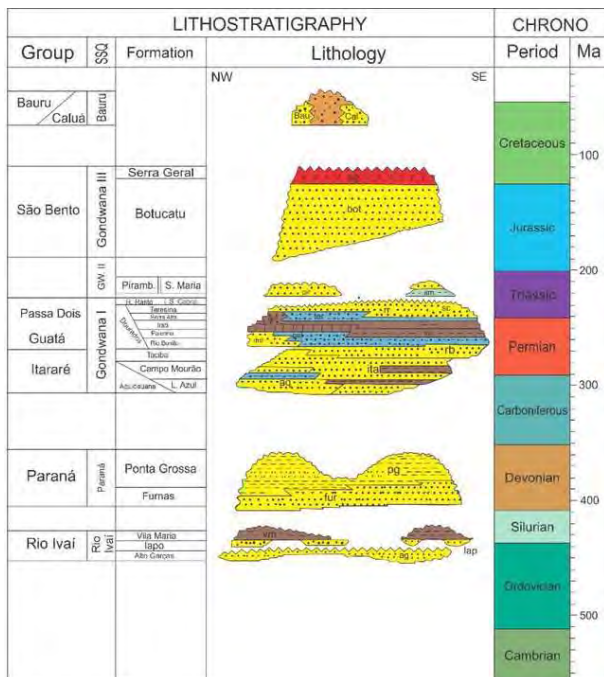


Fig. 1: Stratigraphic chart of Paraná Basin (simplified from Milani et al. [36] and Teramoto et al. [36])

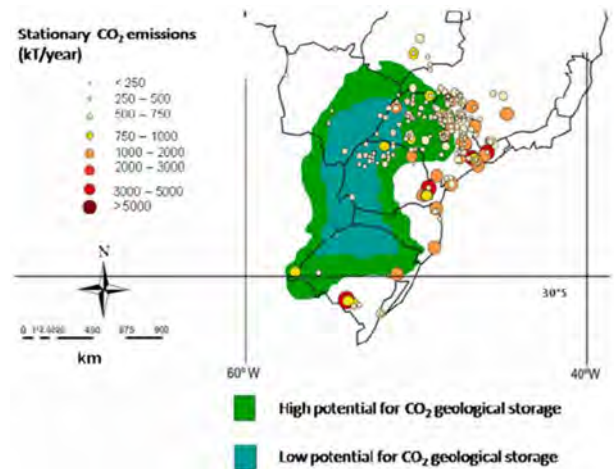


Fig. 2: CO₂ geological storage potential in Rio Bonito Fm., Paraná Basin, considering a minimum of 800 m and maximum of 2,000 m depth and CO₂ stationary sources (after Rockett et al. [33]).

Conclusions

The proposed initial assessment of the Rio Bonito Formation suitability for long-term carbon storage has indicated some relevant positive geological characteristics and qualitative analysis regarding the potential region for CO₂ injection. Four geological environments favourable to CO₂ storage should be further assessed in detailed studies considering: (i) structural and stratigraphic trapping in the sandstones of the Triunfo and Siderópolis members, considering the mudstones of Paraguaçu member and of Palermo Formation as sealing rocks; (ii) potential for mineral

trapping with the carbonate cement of some sandstones. (iii) saline aquifers; and (iv) unmineable coal areas.

The reservoir quality of the Rio Bonito sandstones presents good potential for sufficient storage capacity and petrophysical reservoir properties, especially due to average depth and thickness. Also, the presence of mudstone layers above the Rio Bonito Formation suggests a promising sealing quality, with low seismicity activity. Regional proximity analysis showed good accessibility to potential sites for CO₂ injection, considering its onshore location and the great concentration of stationary CO₂ emitting sources.

Despite the considerable availability of data from seismic and exploration wells in the Paraná Basin, the site selection for long-term CO₂ injection must consider local geological structures and properties that require further studies and analysis, e.g. permoporosity conditions, pore pressure, and the presence of faults and natural fractures. The evaluation of the sealing effectiveness is also critical to determine the best portions of the formation to assure the containment of the injected CO₂. In addition, public perception of CCS assessments also play a relevant role in the identification of regions with higher risks of strong opposition to CO₂ injection activity deployment. So far, there is no related assessment focused on the region nor at the national level.

Finally, for initial evaluations and analysis of Rio Bonito Formation potential for CO₂ storage capacity, injectivity and containment, we suggest that priority research efforts should be addressed to:

- Further characterization of the geological system – reservoir and sealing layers – through the refinement of geological properties and identification of faults and fractures.
- Site selection of best portions of Rio Bonito Formation for CO₂ injection.
- Analysis of reservoir simulations for potential plume migration and evolution of trapping mechanisms.
- Public perception on CCS assessment focused on targeted regions.

Acknowledgments

We are grateful for the support of FAPESP and Shell through the "Research Centre for Gas Innovation - RCGI" (Fapesp Proc. 2014 / 50279-4), organized by the University of São Paulo, and the strategic importance of the support granted by the ANP (National Agency of Petroleum, Natural Gas and Biofuels of Brazil) through the R&D clause.

References

- [1] Machado, C. X., Rockett, G. C., Ketzner, J. M. M. (2013) Brazilian renewable carbon capture and geological storage map: Possibilities for the Paraná Basin. *Energy Procedia* 37:6105-6111. doi: <https://doi.org/10.1016/j.egypro.2013.06.539>
- [2] Iglesias, R. S., Ketzner, J. M., Melo, C. L., Heemann, R., Machado, C. X. (2015). Carbon capture and geological storage in Brazil: an overview. *Greenhouse Gases: Science and Technology* 5:119-130. doi: <https://doi.org/10.1002/ggh.1476>
- [3] Ketzner, J. M. M., Machado, C.X., Rockett, G. C., Iglesias, R. S. (2016). Atlas brasileiro de captura e armazenamento geológico de CO₂. EDIPUCRS, Porto Alegre.
- [4] Rockett, G. C., Ketzner, J. M. M., Ramírez, A., van den Broek, M. (2013). CO₂ Storage Capacity of Campos Basin's Oil Fields, Brazil. *Energy Procedia* 37:5124-5133. doi: <https://doi.org/10.1016/j.egypro.2013.06.427>
- [5] Merschmann, P. R. C., Szklo, A. S., Schaeffer, R. (2016). Technical potential and abatement costs associated with the use of process emissions from sugarcane ethanol distilleries for EOR in offshore fields in Brazil, *International Journal of Greenhouse Gas Control*, Volume 52, 2016, Pages 270-292, ISSN 1750-5836, <https://doi.org/10.1016/j.ijggc.2016.07.007>.
- [6] da Silva, F.T.F., Carvalho, F. M., Corrêa, J.L.G., Merschmann, P.R.C., Tagomori, I. S., Szklo, A., Schaeffer, R. (2018). CO₂ capture in ethanol distilleries in Brazil: Designing the optimum carbon transportation network by integrating hubs, pipelines and trucks, *International Journal of Greenhouse Gas Control*, Volume 71, 2018, Pages 168-183, ISSN 1750-5836, <https://doi.org/10.1016/j.ijggc.2018.02.018>.
- [7] Vosgerau, H., Kirk, K. L., von Dalwigk, I., and Vangkilde-Pedersen, T. (2008). Site Selection Criteria. EU GeoCapacity deliverable D23 (2008) 13.
- [8] Bachu, S., (2003). Screening and ranking of sedimentary basins for sequestration of CO₂ in geological media in response to climate change. *Environ. Geol.* 44, 277–289. <https://doi.org/10.1007/s00254-003-0762-9>.
- [9] Raza, A., Rezaee, R., Gholami, R., Bing, C. H., Nagarajan, R., Hamid, M. A. (2016). A screening criterion for selection of suitable CO₂ storage sites. *Journal of Natural Gas Science and Engineering*, Volume 28, 2016, Pages 317-327, ISSN 1875-5100. <https://doi.org/10.1016/j.jngse.2015.11.053>.
- [10] Rodosta, T. D., Litynski, J. T., Plasynski, S. I., Hickman, S., Frailey, S., Myer, L. (2011). U.S. Department of Energy's site screening, site selection, and initial characterization for storage of CO₂ in deep geological formations. *Energy Procedia* 4:4664-4671. doi: <https://doi.org/10.1016/j.egypro.2011.02.427>
- [11] Bachu, S., (2000). Sequestration of CO₂ in geological media: criteria and approach for site selection in response to climate change. *Energy Conversion Management* 41, 953-970.
- [12] Bradshaw, J., Bradshaw, B.E., Allison, G., Rigg, A., Nguyen, V., Spencer, L., (2002). The potential for geological sequestration of CO₂ in Australia: preliminary findings and implications for new gas field development. *Australian Petroleum Production and Exploration Association Journal* 42, 25e46. part 1.
- [13] Gibson-Poole, C.M., Root, R.S., Lang, S.C., Streit, J.E., Hennig, A.L., Otto, C.J., Unterschultz, J.R., (2005). Conducting comprehensive analyses of potential sites for geological CO₂ storage. In: Rubin, E.S., Keith, D.W., Gilboy, C.F. (Eds.), *Proceedings of the 7th International Conference on Greenhouse Gas Control Technologies*, 5e9 September, Vancouver, Canada. Elsevier, Oxford, pp. 673-681.
- [14] Varma, S., Unterschultz, J., Dance, T., Langford, R., Esterle, J., Dodds, K., van Gent, D., (2009). Regional study on potential CO₂ geosequestration in the Collie

- Basin and the southern Perth Basin of Western Australia. *Marine and Petroleum Geology* 26, 1255e1273.
- [15] Dance, T. (2013). Assessment and geological characterisation of the CO₂CRC Otway Project CO₂ storage demonstration site: From prefeasibility to injection. *Marine and Petroleum Geology*, Volume 46, 2013, Pages 251-269, ISSN 0264-8172, <https://doi.org/10.1016/j.marpetgeo.2013.06.008>.
- [16] Anthonsen, K. L., Aagaard, P., Bergmo, P. E. S., Gislason, S. R., Lothe, A. E., Mortensen, G. M., Snæbjörnsdóttir, S. O. (2014). Characterisation and Selection of the Most Prospective CO₂ Storage Sites in the Nordic Region. *Energy Procedia*, Volume 63, 2014, Pages 4884-4896, ISSN 1876-6102, <https://doi.org/10.1016/j.egypro.2014.11.519>.
- [17] Sun, L., Dou, H., Li, Z., Hu, Y., Hao, X. (2018). Assessment of CO₂ storage potential and carbon capture, utilization and storage prospect in China, *Journal of the Energy Institute*, Volume 91, Issue 6, 2018, Pages 970-977, ISSN 1743-9671, <https://doi.org/10.1016/j.joei.2017.08.002>.
- [18] Halland EK, Gjeldvik IT, Johansen WT, Magnus C, Meling IM, Pedersen S, Riis F, Solbakk T, Tappel I.(2011). CO₂ Storage Atlas Norwegian North Sea. Norwegian Petroleum directorate; 2011.
- [19] Holz, M. (2003). Sequence stratigraphy of a lagoonal estuarine system—an example from the lower Permian Rio Bonito Formation, Paraná Basin, Brazil. *Sedimentary Geology* 162:305-331. doi: [https://doi.org/10.1016/S0037-0738\(03\)00156-8](https://doi.org/10.1016/S0037-0738(03)00156-8)
- [20] Ketzer, J. M., Holz, M., Morad, S., Al-Aasm, I. S. (2003). Sequence stratigraphic distribution of diagenetic alterations in coal-bearing, paralic sandstones: evidence from the Rio Bonito Formation (early Permian), southern Brazil. *Sedimentology* 50:855-877. doi: 10.1046/j.1365-3091.2003.00586.x
- [21] Holz, M., França, A. B., Souza, P. A., Iannuzzi, R., Rohn, R. (2010). A stratigraphic chart of the Late Carboniferous/Permian succession of the eastern border of the Paraná Basin, Brazil, South America. *Journal of South American Earth Sciences* 29:381-399. doi: <https://doi.org/10.1016/j.jsames.2009.04.004>
- [22] ANP - Agência Nacional do Petróleo, Gás Natural e Biocombustíveis (2017). Bacia do Paraná: sumário geológico e setores em oferta. Superintendência de Definição de Blocos. Available at: <<http://rodadas.anp.gov.br/pt/>>.
- [23] Chadwick, R. A., Arts, R., Bernstone, C., May, F., Thibeau, S., Zweigel, P. (2008). Best practice for the storage of CO₂ in saline aquifers. *British Geological Survey Occasional Publication*, 14. Keyworth, Nottingham
- [24] IEA-GHG – International Energy Agency Greenhouse Gas R&D programme (2009). CCS Site characterisation criteria In: Bachu S, Hawkes C, Lawton D, Pooladi-Darvish M, Perkins E (eds). Cheltenham, United Kingdom, pp 112.
- [25] Ketzer, J. M., Iglesias, R., Einloft, S., Dullius, J., Ligabue, R., de Lima, V. (2009). Water–rock–CO₂ interactions in saline aquifers aimed for carbon dioxide storage: Experimental and numerical modeling studies of the Rio Bonito Formation (Permian), southern Brazil. *Applied Geochemistry* 24:760-767. doi: <https://doi.org/10.1016/j.apgeochem.2009.01.001>
- [26] Machado, J. L. F., Freitas, M. (2005). Projeto mapa hidrogeológico do Estado do Rio Grande do Sul – Relatório final. CPRM, Porto Alegre, Brasil, pp 65.
- [27] Metz, B., Davidson, O., De Coninck, K., Loos, M., Meyer, L., eds. (2005), IPCC special report on carbon dioxide capture and storage, p. 431.
- [28] de Lima, V., Einloft, S., Ketzer, J.M., Jullien, M., Bildstein, O., Petronin, J-C. (2011). CO₂ Geological storage in saline aquifers: Paraná Basin caprock and reservoir chemical reactivity. *Energy Procedia* 4:5377-5384. doi: <https://doi.org/10.1016/j.egypro.2011.02.521>
- [29] Milani, E. J., Thomaz Filho, A. (2000). Sedimentary basins of South America In: Cordani UG, Milani EJ, Thomaz Filho A, Campos DA (eds) Tectonic Evolution of South America. In-Fólio Produção Editorial, Rio de Janeiro, Brazil, pp 389-449.
- [30] Berrocal, J., Fernandes, C., Bassini, A., Barbosa, J. R. (1996). Earthquake hazard assessment in southeastern Brazil. *Geofísica Internacional* 35:257-272.
- [31] ANP – Agência Nacional do Petróleo, Gás Natural e Biocombustíveis. Mapa Dinâmico: Produtores de Etanol. Available at: <https://app.powerbi.com/view?r=eyJrIjoizWU1MTc0ZjYtMjVhYi00YTEwLWJhODMtODQ0MDdhNmJiMwYwliwidCI6IjQ0OTlmNGZmLTI0YTUyYtNGI0Mi1iN2VmlTEyNGFmY2FkYzcxMyJ9&pageName=ReportSecti on8aa0cee5b2b8a941e5e0%22>.
- [32] ANP – Agência Nacional do Petróleo, Gás Natural e Biocombustíveis. Painel Dinâmico: Produção de Etanol. Available at: <https://app.powerbi.com/view?r=eyJrIjoizWU1MTc0ZjYtMjVhYi00YTEwLWJhODMtODQ0MDdhNmJiMwYwliwidCI6IjQ0OTlmNGZmLTI0YTUyYtNGI0Mi1iN2VmlTEyNGFmY2FkYzcxMyJ9&pageName=ReportSecti on8aa0cee5b2b8a941e5e0%22>.
- [33] Rockett, G. C., Machado, C. X., Ketzer, J. M. M., Centeno, C. I. (2011). The CARBMAP project: Matching CO₂ sources and geological sinks in Brazil using geographic information system. *Energy Procedia* 4:2764-2771. doi: <https://doi.org/10.1016/j.egypro.2011.02.179>
- [34] Iglesias, R. S., Ketzer, J. M., Melo, C. L., Heemann, R., Machado, C. X. (2015). Carbon capture and geological storage in Brazil: an overview. *Greenhouse Gases Science and Technology*, 5 (2) (2015), pp. 119-130, <https://doi.org/10.1002/ghg.1476>.
- [35] Netto, A. N. A., Câmara, G., Rocha, E., Silva, A. L., Andrade, J. C. S., Peyerl, D., Rocha, P. (2020). A first look at social factors driving CCS perception in Brazil: A case study in the Recôncavo Basin, *International Journal of Greenhouse Gas Control*, Volume 98, 2020, 103053, ISSN 1750-5836, <https://doi.org/10.1016/j.ijggc.2020.103053>.
- [36] Teramoto, E. H., Gonçalves, R. D., Chang, H. K. (2020) Hydrochemistry of the Guarani Aquifer System modulated by mixing with underlying and overlying hydrostratigraphic units. *Journal of Hydrology: Regional Studies* 30:100713. doi: <https://doi.org/10.1016/j.ejrh.2020.100713>
- [37] Milani, E. J., França, A.B., Medeiros, R.A. (2007) Roteiros Geológicos Boletim de Geociências da Petrobras, 15 (1), pp. 135-162

USING THE URBAN STOCK AS A CARBON SINK: A CASE STUDY FROM THE GERMAN FEDERAL STATE OF NORTH RHINE – WESTPHALIA

Ali Abdelshafy^{1*}, Grit Walther¹

¹ Chair of Operations Management – RWTH Aachen, Aachen, Germany

* Corresponding author e-mail: ali.abdelshafy@om.rwth-aachen.de

Abstract

The decarbonization of the industrial sector will not be feasible without carbon capture and utilization (CCU) or storage (CCS) due to unavoidable process emissions. Due to the lack of geological storage in Germany, the low social acceptance and the legal challenges, CO₂ utilization has become a favorable route to sequester the process emissions.

This paper presents a case study from North Rhine – Westphalia (NRW) in order to highlight the importance of using the urban stock (e.g. construction and demolition waste & concrete products) as a carbon sink for process emissions by means of carbonation, quantify the amounts of emissions that can be permanently stored, and illustrate the significance of the locational aspects that will affect the prospective supply chain. The analyses show that the average distance between the selected carbon sources and sinks is 55.6 Km, nevertheless, some plants have a comparative advantage in terms of the average transportation costs, which range between 2 and 31.6 EUR/ton for the shortest and longest distance respectively (8.8 Km and 142.3 Km).

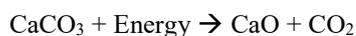
Keywords: Carbon Capture and Utilization (CCU), Urban stock, Process emissions, Carbon sink

1. Introduction

1.1 Industrial process emissions

The German national strategy of energy transition (Energiewende) aims at achieving carbon neutrality by 2050 [1, 2, 3]. There are various roadmaps aiming at investigating the potentials of using decarbonization enablers (e.g. electrification and hydrogen) in the industrial sector. Nevertheless, decarbonizing the industrial sector still represents a major challenge, not only due to the heterogeneity of the industrial processes and the risk of carbon leakage, but also due to the significant amounts of process emissions that cannot be avoided even if the fuel and energy emissions are decarbonized. In 2018, the process emissions represented 8% of the total German GHG-emissions (65 Mt CO₂ eq.) [4].

Four major industries are responsible for more than 70% of the process emissions in Germany; namely steel, cement, lime and basic chemicals [4]. The introduction of hydrogen and electrification technologies will play a vital role in decreasing the gross and process emissions of steel and chemicals. However, the specific process emissions per ton of clinker and lime (clinker = 60% & lime = 69% of the total emissions [5]) cannot be reduced by such technologies [5] as they are chemically associated with the production process (calcination) (i.e. the chemical reaction of transforming calcium carbonates into calcium oxides as shown in the following equation).



The case study discussed in this paper focuses on NRW as an important industrial hub in Germany with unique locational characteristics that qualify it as an appropriate region to be investigated.

Currently, CO₂ pipelines that would allow to transport CO₂ emissions to ports from where they could be shipped to be stored (Carbon Capture and Storage – CCS) are controversially discussed. Even if a pipeline network exists, it wouldn't be able to cover all locations in NRW. Many plants of the iron and steel industry are located close to waterways and thus would be able to ship their emissions easily. In contrast, cement and lime plants are located near the raw materials (limestone), which is far away from the industrial clusters in the Ruhrgebiet as shown in Figure 1. Against this background, this paper focuses on options for cement and lime plants to utilize their process emissions (Carbon Capture and Utilization – CCU).

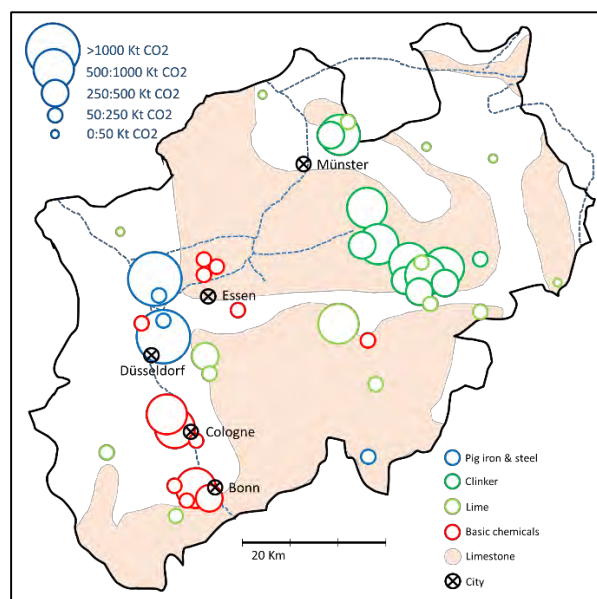
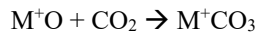


Figure 1: GHG emissions per annum of some industrial sectors in NRW, visualized based on [6, 7, 8]

1.2 Carbonation

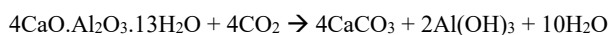
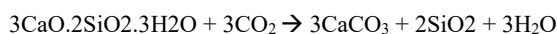
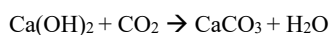
Carbonation refers to the CO₂ reaction with oxides that results in forming stable and insoluble compounds (carbonates) as the reverse reaction of calcination. The reaction is exothermic and occurs naturally which is known as “silicate weathering” phenomena. However, the natural reaction rate is very slow as it depends on the silicate dissolution [9, 10].



Stimulated by the endeavors to find suitable routes to reduce the GHGs, various studies have been implemented in the recent years in order to utilize the primary and secondary raw materials as a carbon sink. Some natural minerals can be used for carbonation such as Olivine, Serpentine and Wollastonite as shown in the following reactions [11]. Despite the proven technical feasibility, the amounts needed, geographical availability and logistical complexities associated make it unsecured supply chains [12].



Cement hydration results in a set of compounds such as portlandite, CSH, CAH and other compounds. The reaction of these compounds with CO₂ dissolved in water results in stable compounds (calcium carbonate/ CaCO₃) as shown in the following equations [13, 14]. The carbonation of cementitious materials happens naturally during the lifetime of the construction object as an ageing effect, but it is also too slow and has a limited capacity which is known as “**passive carbonation**”.



“**Active carbonation**” of cementitious materials utilize these reactions for specific technical, economic and ecological purposes (i.e. carbon sequestration) [15]. Hence, construction and demolition waste (CDW) and concrete products are promising carbon sinks and have various advantages in comparison to natural minerals such as avoided mining, continuous supply and domestic availability. Moreover, compared to other CCU pathways, concrete carbonation is characterized by low energy input and sometimes, even savings in energy and CO₂ emissions result as the conventional precast curing processes is avoided [16]. Also, in contrast to geological storage, carbonation does not require high CO₂ specifications. Geological storage normally requires very low amounts of impurities due to the associated risks such as leaks, rock erosion, mineral dissolution in saline aquifers and pipeline corrosion. Strict requirements imply higher costs due to additional purification and analysis operations [17, 18]. Hence, avoiding these phases in the carbonation process would make the technology more cost-efficient.

When designing a prospective carbonation supply chain, the quantities and locations of CDW and of concrete & precast products as well as the amount of CO₂ emissions will be the most important factors. Low transportation costs and sustainable supply will provide a comparative advantage to compensate for the investments needed to retrofit the plants and to install carbonation chambers.

Due to the novelty of the technology, the majority of investigations focus on the technical feasibility and are mostly applied on a lab scale as could be seen in different research projects such as [19, 20, 21]. According to our best knowledge, no systematic analyses have been implemented to analyze the regional resources and potentials as presented in this paper.

The specific sequestration capacity is a controversial point as each study has different curing conditions (e.g. curing duration, CO₂ pressure, temperature, etc.). As a result, the amount of CO₂ that can be stored per kilogram of cement ranges between 63 and 350 gram [22, 14, 19, 23, 24]. Similarly, there is no consensus on the technology readiness level (TRL). While some studies classify the maturity of the technology as moderate such as [25], others grade it as high [21]. Nonetheless, there is consensus on the large future potential. Some optimistic views project that between 16.3% to 41.3% of the global concrete production can be used for carbonation by 2030 [26]. Some companies have already existing products and carbonation technologies such as Solidia and CarbonCure [27, 28, 29].

A clear distinction is to be made between different types of concrete products as this has various implications in terms of TRL and hence the expected market penetration rate. First, products can be classified into reinforced and non-reinforced products as the carbonation process results in a low pH that can lead to steel corrosion and hence affect the durability. Nonetheless, some experts expect that this hurdle can be overcome in the coming years [25]. Secondly, products can be classified into ready-mix concrete (RMC) and precast products due to the different manufacturing operations and product features that will affect the carbonation process, technical limits and economies.

In contrast to the concrete and precast products, CDW carbonation does not face technical restrictions like the risk of durability and steel corrosion. Moreover, it does not need high CO₂ purity, some technical reports even emphasize that the carbonation process can take place by directly using cement flue gas with a high CO₂ concentration (>20%) [21]. This can actually be a game changer as it will significantly reduce the carbon sequestration costs. Considering that the capturing process contributes significantly to the total sequestration cost [30, 31], saving these costs will help in boosting the carbonation technology. Similar to concrete carbonation, some major companies already started to invest in CDW carbonation technology such as [32, 33, 34, 35].

Nevertheless, a robust CDW recycling system and enhancing policies are a precondition for establishing a

carbonation supply chain. Within an established and efficient CDW recycling system, carbonation could even be a valorization. If these prerequisites are missing, the costs of using the secondary materials as carbon sink, i.e., the sum of collection, transportation and processing costs, would be much higher. In the following, we will analyze the conditions in terms of spatial characteristics and resources for NRW. Table 1 summarizes the key carbonation performance data used in the following sections.

Performance	Value	Reference
Cement content in concrete (concrete, precast and recycled aggregates)	11% ¹	[36, 37]
Carbonation (ton CO ₂ /ton cement) (concrete, precast and recycled aggregates)	0.35	[23, 24]
Waste cement/waste concrete (ton/ton)	0.17	[14, 38]
Concrete content in recycled rubble (ton/ton)	0.51	[39, 40]
Bricks content in recycled rubble (ton/ton)	0.1	[39, 40]
Mixed waste content in recycled rubble (ton/ton)	0.39	[39, 40]
Carbonation (ton CO ₂ /ton waste cement)	0.27	[41, 14]
Carbonation product 1 (ton limestone/ton waste cement)	0.61	[42, 41, 23]
Carbonation product 2 (ton residue/ton waste cement)	0.66	[42, 41, 23]
No. of cement plants	12	[6]
No. of lime plants	14	[6]
No. of carbon sinks (districts)	53	[43]
Transportation cost (Long Heavier Vehicles LHV) (EUR/ton.Km)	0.095	[44]
Transportation cost (Tractor + trailers) (EUR/ton.Km)	0.127	[44]
Average transportation cost (EUR/ton.Km)	0.111	[44]

Table1: Key carbonation performance data

1.3 Construction activities & demolition waste in NRW

NRW is the most populous and densely populated state in Germany. Hence it has a strong and dynamic construction sector especially close to the industrial cities and urban centers adjacent to the Rheine river such as Cologne, Bonn, and Düsseldorf, Duisburg and Essen (Figure 2 and 3). The non-residential sector has been stable since the eighties with an average of 4.7 million m² constructed per year. On the other hand, the residential sector has witnessed a boom in the nineties but stabilized afterwards with an average of 42 thousand apartments constructed per year in the last decade (Figure 4).

In terms of the raw materials and intermediate products, the state produces 9.7 Mt of cement, of which 6.3 Mt are consumed domestically to produce 8.8 million cubic

meters or 21.1 Mt of RMC, 8.6 Mt of precast concrete and 1.5 Mt of other products in dry format (e.g. mortar) [45, 39]. The total cement consumption is split almost equally to three main sectors; non-residential construction = 34%, residential construction = 33% and infrastructure = 33% [46].

In terms of the demolition activities, every year, around 4,000 houses are demolished in NRW. Together with the demolition activities in the infrastructure sector demolished quantities result in 10 Mt of rubble (plus other waste streams). Eighty percent of the resulted rubble is recycled into “secondary aggregates”, which is close to the average rate in Germany (78%) [47]. These recycling rates are higher than in many EU countries [48], and are in accordance with the European goal of reaching a 70% recycling rate [49].

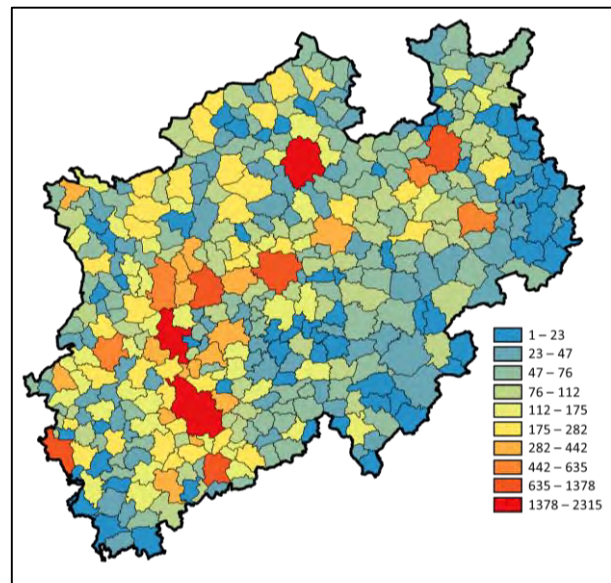


Figure 2: Residential construction (apartments) in NRW in 2019, visualized based on [39]

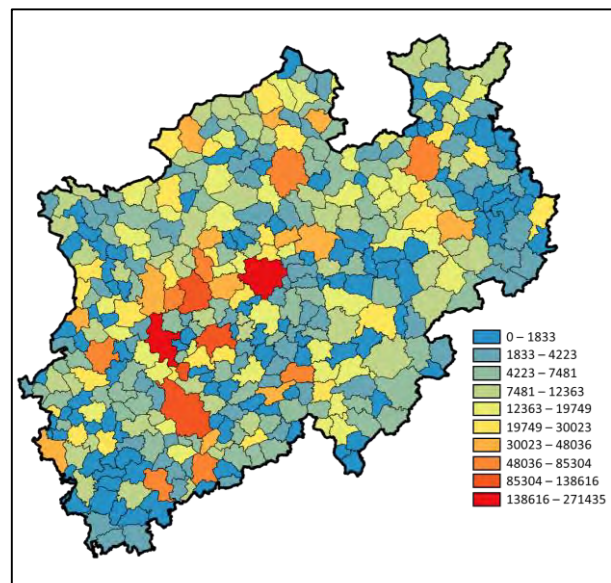


Figure 3: Non-residential construction (usable area in m²) in NRW in 2019, visualized based on [39]

¹ Average cement content ($\frac{7\%+15\%}{2}$)

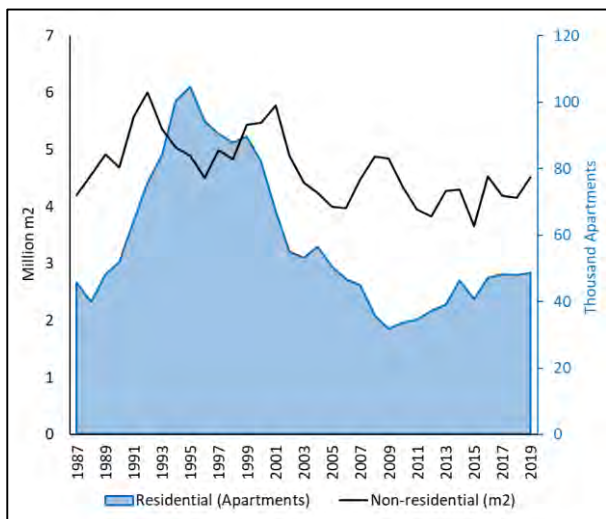


Figure 4: Construction activities in NRW, based on [39]

As Figure 5 shows, the total amounts of recycled rubble (recycled aggregates) per year has been stable during the last 15 years (Min 6.1 Mt in 2006 and max 8.5 Mt in 2018), which implies that the supply of these materials is evidently secured. Geographically, the pattern of current demolition activities match with the pattern of construction areas as shown in Figure 6.

It should be noted that 79% of the apartments in NRW were constructed after the second world war WWII [50, 39], and survival analyses show that some age classes of the apartments built after WWII have already reached or will soon enter the demolition phase (Figure 7). Therefore, CDW amounts are expected to increase in the coming decades.

In terms of composition, the rubble waste stream in Germany is composed of 51% concrete, 10% bricks and tiles while the rest is a mixture of all. Assuming an average cement content of 11% would result in a total sequestration capacity of 167 kt CO₂ in NRW. This is a quite conservative estimation as it considers only the separated concrete waste stream. Taking into account the stream mixed with bricks and tiles would result in higher capacities, but it should be preceded by a techno-economic evaluation.

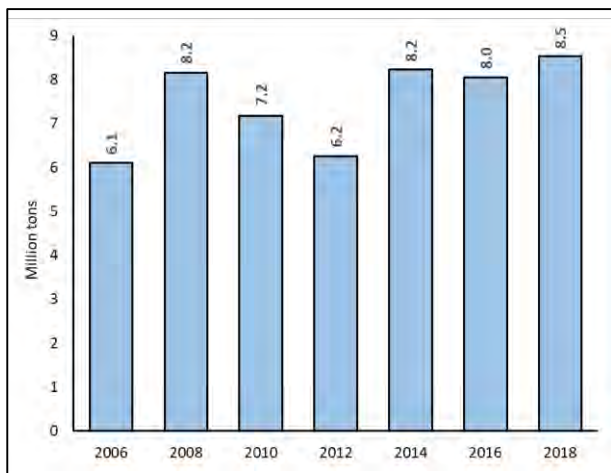


Figure 5: Amounts of rubble generated in NRW in 2019, based on [39]

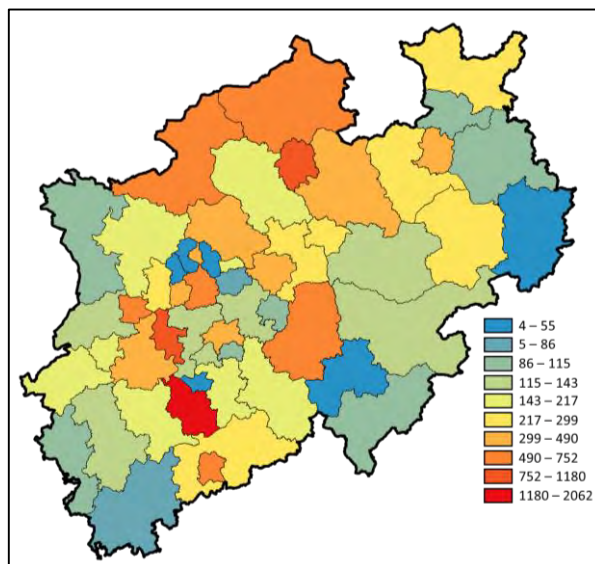


Figure 6: Locations of demolition activities (demolished rooms) in NRW in 2019, visualized based on [39]

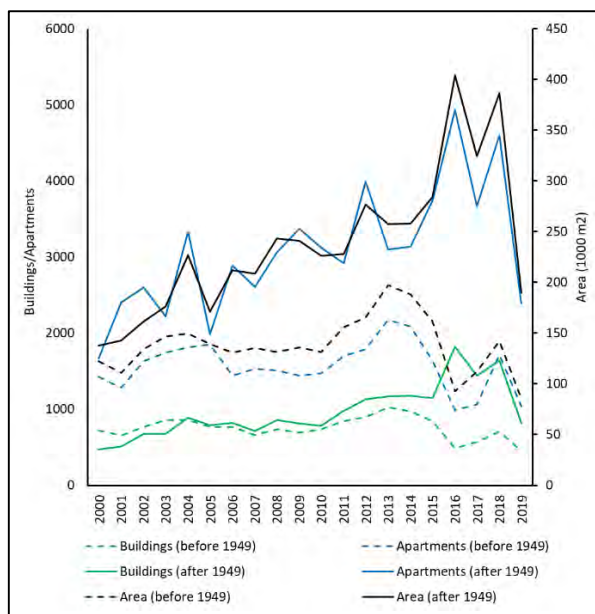


Figure 7: Demolition activities in NRW in 2019 based on [39]

Business Opportunities
In terms of the business opportunities, as mentioned, precast carbonation offers cost deductions resulting from energy savings. On the other hand, the outputs of CDW carbonation depend on the process adopted. CDW carbonation can be classified into recycled concrete aggregates (RCA) and cement waste (CW) [14].

Carbonating RCA would result in better mechanical properties than conventional recycled aggregates [51, 14] which are normally used to substitute natural aggregates. On the other hand, CW carbonation yields new physical products rather than cost savings or enhanced properties. CW can be generated during the recycling process, after pulverizing the CDW and classifying it into aggregates and WC (diameter $\leq 10 \mu\text{m}$) [14, 41].

The main products of CW carbonation are limestone flour and residue which is composed mainly of silica dioxide. Additionally, there are CO₂ residues coming out

of the carbonation chamber which can be compressed and recycled again [42, 41]. Similar to the specific carbonation capacity (ton CO₂/ton substance), the ratio of each output depends on the various factors (e.g. composition, curing process, duration, conditions, etc.).

According to [14, 23, 41, 42], each ton of concrete waste contains 0.17 ton WC and after carbonation each ton of waste cement can sequester 0.27 ton CO₂ and produce 0.61 ton limestone flour and 0.66 residue (silica dioxide). Considering that 740 kt WC can be yielded annually in NRW, 199.8 kt CO₂ can be sequestered via carbonation in addition to 451.4 kt limestone flour and 488.4 kt residue.

Several industries consume significant amounts of limestone flour such as power, paper, glass, etc. for various purposes [52]. Figure 8 shows the limestone flour production in NRW, the yield and production value have been stable in the last ten years (average = 2.1 Mt & 28.9 EUR/ton). In addition, 16 Mt of low-value limestone are mined and consumed by cement and lime industries. Comparing the current domestic yield with the expected one from CW carbonation, it is clear that the additional amounts from carbonation will not have a negative impact on the market.

It should be noted that this figure shows only the average product value (i.e. the price at the factory gate) which does not include the value-added tax and additional profits gained by traders. The figure also represents the average value of all limestone qualities. The limestone flour produced via CW carbonation is a very high-purity limestone (> 98%) qualified to be sold at the highest price [53].

The second by-product (silica dioxide) can be used as recycled sand [42]. Figure 9 shows the annual yield and production value of construction sand in NRW, which also have been stable during the last decade (average = 17.3 Mt & 5.4 EUR/ton). Due to the low ratio between both values (488.4 kt : 17.3 Mt), the recycled sand (silica dioxide) produced via carbonation cannot cause an oversupply and thus will not have a noticeable impact on the market.

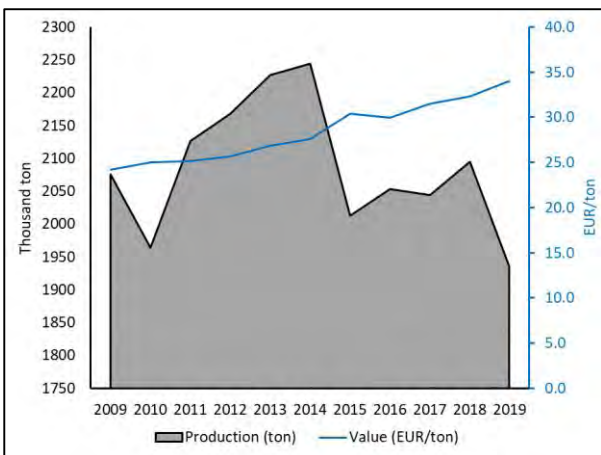


Figure 8: Limestone flour in NRW (production & value), based on [39]

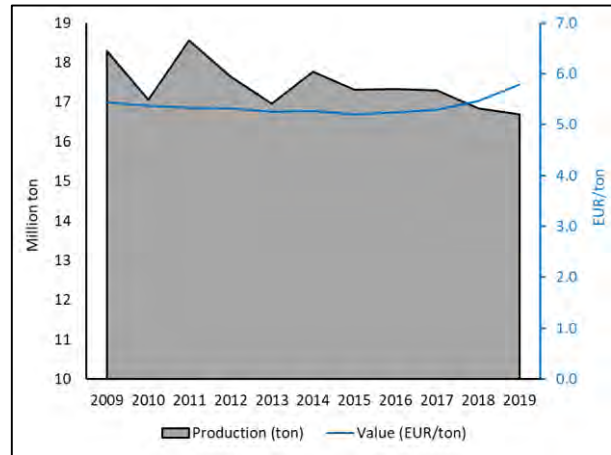


Figure 9: Construction sand in NRW (production & value), based on [39]

Nevertheless, revenues of selling these secondary products should not be considered as the sole profits resulting from carbonation. Being initially an alternative to CCS, emitters are also expected to pay a fee on each ton of carbon sequestered.

2. Case study: Using the residential and non-residential sectors as a carbon sink

A location-allocation model has been designed in order to minimize the transportation costs by means of allocating the CO₂ supply (from cement and lime plants) to the demand (carbon sinks) while considering the capacity of each sink (demand point). The model considers the concrete and precast products consumed by the residential and non-residential sectors. Due to the lack of precise data on the locations of the infrastructure activities, this sector has been omitted from the model.

To simplify the model, the cement consumed by each municipality (396 municipalities) has been aggregated on the district level (53 districts). Centers of the districts have been used to represent the locations of the carbon sinks. The supply is represented by 12 cement plants and 14 lime plants (with total process emissions of 3.2 and 2.7 Mt CO₂ respectively) as shown in Figure 8.

The residential and non-residential construction activities (Figure 2 and 3) have been used as an indicator to cement consumption in each sector. In order to illustrate the full potential, the model assumes that all concrete products are suitable for carbonation and that the maximum carbonation capacity is valid (0.35 t CO₂ per ton of cement consumed). This will result in a total sequestration capacity of 1.4 Mt CO₂. Nevertheless, it should be noted that this is an assumption regarding positive future developments and that these parameters are not yet achieved considering the state-of-the-art technology.

2.1 Methodology

As each carbon sink has a limited capacity, Capacitated P-Median problem (CPMP) has been used to allocate the lime and cement plants to the carbon sinks as

algorithmically described in Equations 1 – 6 [54, 55, 56]. ArcMap 10.7.1 has been used to solve and visualize the model as shown in Figure 10.

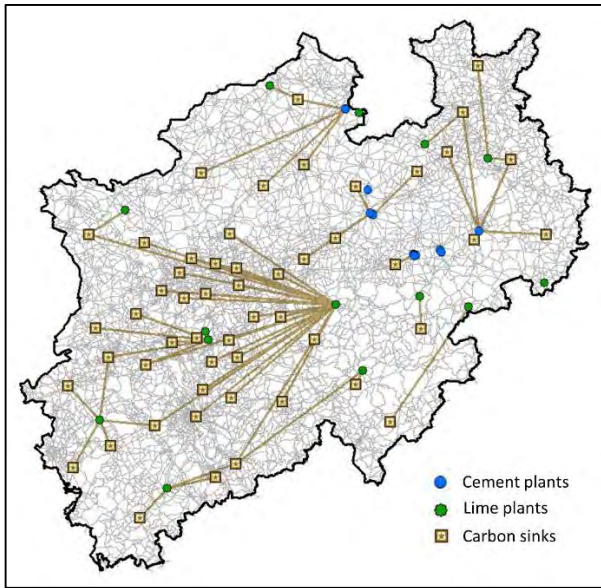


Figure 10: Location-allocation model

$$\text{MIN } f(x) = \sum_{i \in I} \sum_{j \in J} w_i \cdot d_{ij} \cdot X_{ij} \quad (1)$$

Subject to:

$$\sum_{j \in J} X_{ij} = 1 \quad \forall i \in I \quad (2)$$

$$\sum_{j \in J} Y_j = P \quad (3)$$

$$\sum_{i \in I} w_i \cdot X_{ij} \leq b_j \cdot Y_j \quad \forall j \in J \quad (4)$$

$$Y_j \in \{0,1\} \quad \forall j \in J \quad (5)$$

$$X_{ij} \in \{0,1\} \quad \forall i \in I, j \in J \quad (6)$$

I set of lime and cement plants ($i \in I = \{1, \dots, n\}$)

J set of potential carbon sinks ($j \in J = \{1, \dots, m\}$)

d_{ij} the distance between plant $i \in I$ and sink $j \in J$

w_i the amount of process emissions at $i \in I$

P the number of carbon sinks

b_j the capacity of a carbon sink located at $j \in J$

$$Y_j = \begin{cases} 1, & \text{if a carbon sink is located at site } j \in J \\ 0, & \text{otherwise} \end{cases}$$

$$X_{ij} = \begin{cases} 1, & \text{if a plant } i \in I \text{ is assigned to a sink } j \in J \\ 0, & \text{otherwise} \end{cases}$$

2.2 Results & discussion

The model shows that the average transportation distance from the emission sources to the carbon sinks is 55.6 km. Although road transportation has the highest costs in comparison to rail and water, it is still the best transportation mode due to the low quantities of CO₂ transported and the distribution of carbon sources and sinks all over NRW. Nevertheless, the transportation costs still represent a big ratio of the carbonation costs.

In order to analyse the impact of transportation costs, a cost parameter of 0.111 EUR/ton.Km is considered representing the average of two common road transportation modes (Long Heavier Vehicles LHV) and (Tractor + trailers) with average transportation costs of 0.095 EUR/ton.Km and 0.127 EUR/ton.Km respectively [44]. Applying those figures on the average transportation distance (55.6 Km) will result in average transportation costs of 12.3 EUR/ton (round trip).

Nonetheless, the transportation costs vary significantly between the plants. Figure 11 shows the cumulative capacity utilization of carbon sinks as a function of the distance between the source and the closest available sink (presented model). Utilizing all the sequestration capacity available in the state implies that some CO₂ quantities will need to be transported 142.3 km resulting in average transportation costs of 31.6 EUR/ton, while transportation over shortest distance (8.8 Km) would cost the operators only 2 EUR/ton.

Due to the high transportation costs, the carbon price and the availability of other CO₂ sequestration options will play a major role in determining the maximum distance to be travelled between the plant and the carbon sink. This will consequently have an impact on the deployment of this technology and on the amount of CDW and concrete products that can be carbonated in the future.

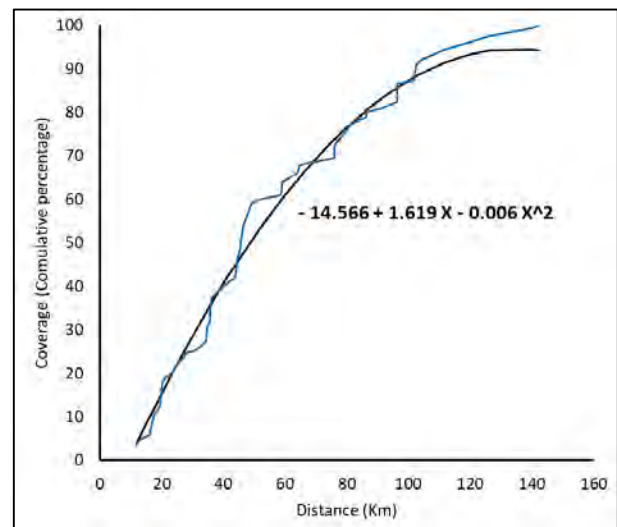


Figure 11: Distance vs. coverage of carbon sinks

In terms of the CO₂ source, the results show that more than 70% of the carbon sink capacities have been allocated to the lime plants based on the distance (transportation costs). This can be explained due to the

existence of the lime plants in the western part of the state, where a lot of construction activities take place in the urban centres along the Rhine river. Thus, the lime plants have a comparative advantage in terms of the accessibility.

3. Conclusions & Outlook

Carbonation as CCU technology has potentials to be an effective substitute to CCS within certain regions, especially if there are logistics and acceptance challenges for CCS. Nevertheless, due to the limited sequestration capacity of the urban stock in NRW, carbonation will not be able to satisfy the demand solely and a combination between CCU and CCS will be needed.

Investigating the development of the construction sector, the CDW recycling system and the demolition behavior in the coming decades is essential in order to quantify the capacities and reduce the investment risks associated with such novel value chains.

The locational aspects have a vital influence on the future business models of carbonation. Due to the relative small capacity of the urban carbon sinks and its distribution over the whole state (in contrast to geological storage), trucks would be the optimum transportation mode. Nonetheless, truck transportation still has the highest cost per ton and needs to be optimized.

In order to confirm the advantages of carbonation as CCU technology, RMC and recycling plants need to be investigated further from a techno-economic perspective in order to estimate the retrofitting investments. Also, it must be analyzed how the carbonation cycle and curing chamber can be integrated within the production and recycling processes.

A full life cycle assessment LCA is required to prove the environmental benefits of the technology. Moreover, pilot projects are needed to validate the technical feasibility. Cities with high cement consumption and CWD quantities such as the urban centers (e.g. Cologne and Düsseldorf in NRW) are very suitable candidates.

Acknowledgements

This research has been financed by SCI4climate.NRW project (funded by Ministry of Economic Affairs, Innovation, Digitalization and Energy of the State of North Rhine-Westphalia) [57].

References

- [1] H. Kuittinen and D. Velte, "Case Study Report - Energiewende," 2018.
- [2] BMWi, "Ein gutes Stück Arbeit - Die Energie der Zukunft - Vierter Monitoring-Bericht zur Energiewende," 2015.
- [3] D. Pescia and P. Graichen, "Understanding the Energiewende - FAQ on the ongoing transition of the German power system - Background," 2015.
- [4] O. Lösch, F. Toro, N. Ashley-Belbin, F. Reitze and M. Schön, "Prozessemissionen in der deutschen Industrie und ihre Bedeutung für die nationalen Klimaschutzziele – Problemdarstellung und erste Lösungsansätze. Institut für Ressourceneffizienz und Energiestrategien GmbH (IREES)," 2018.
- [5] M. Stork, W. Meindersma, M. Overgaag and M. Neelis, "Technical Report - A competitive and efficient lime industry - Cornerstone for a sustainable Europe. The European Lime Association (EuLA)," 2014.
- [6] EC, "European Union Transaction Log. The European Commission," 2020.
- [7] VDZ, "Zementindustrie im Überblick 2019/2020. Verein Deutscher Zementwerke e.V.," 2019.
- [8] WV Stahl, "Fakten zur Stahlindustrie in Deutschland. Wirtschaftsvereinigung Stahl," 2019.
- [9] V. Prigiobbe, M. Hänchen, M. Werner, R. Baciocchi and M. Mazzotti, "Mineral carbonation process for CO₂ sequestration," *Energy Procedia*, 2009.
- [10] C. D. Hills, N. Tripathi and P. J. Carey, "Mineralization Technology for Carbon Capture, Utilization, and Storage," *Front. Energy Res. (Frontiers in Energy Research)*, 2020.
- [11] M. Mazzotti, J. C. Abanades, R. Allam, K. S. Lackner, F. Meunier, E. Rubin, J. C. Sanchez, K. Yogo, R. Zevenhoven, B. Eliasson and R. T. M. Sutarnegara, "Carbon dioxide capture and utilization: Chapter 7 - Mineral carbonation and industrial uses of carbon dioxide. Intergovernmental Panel on Climate Change (IPCC)," 2005.
- [12] J. C. Picot, D. Cassard, F. Maldan, D. Greffié and F. Bodéan, "Worldwide potential for ex-situ mineral carbonation," 2011.
- [13] Y. Shao, "Beneficial Use of Carbon Dioxide in Precast Concrete Production," p. 2014.
- [14] S. K. Kaliyavaradhan and T. C. Ling, "Potential of CO₂ sequestration through construction and demolition (C&D) waste—An overview," *Journal of CO₂ Utilization*, 2017.
- [15] B. Šavija and M. Luković, "Carbonation of cement paste: Understanding, challenges, and opportunities," 2016.
- [16] V. Rostami, Y. Shao and A. J. Boyd, "Carbonation curing versus steam curing for precast concrete production," 2012.
- [17] A. Murugan, R. J. Brown, R. Wilmot, D. Hussain, S. Bartlett, P. J. Brewer, D. R. Worton, T. Bacquart, T. Gardiner, R. A. Robinson and A. J. Finlayson, "Performing quality assurance of carbon dioxide for carbon capture and storage," 2020.
- [18] IEAGHG, "Effects of impurities on geological storage of CO₂. IEA Greenhouse Gas R&D Programme," 2011.
- [19] J. Skocek, M. Zajac and M. Ben Haha, "Carbon Capture and Utilization by mineralization of cement pastes derived from recycled concrete," 2020.
- [20] B. R. Ellis, V. C. Li and S. J. Skerlos, "Storing CO₂ in built infrastructure: CO₂ carbonation of precast concrete products," 2019.
- [21] J. G. M. Monteiro, E. Goetheer, E. Schols, P. Van OS, J. F. Pérez Calvo, H. Hoppe, H. S. Bharadwaj, S. Roussanal, P. Khakharia, M. Feenstra and A. De Jong, "CEMCAP - D5.1 revision 1 Post-capture CO₂ management: options for the cement industry," 2018.

- [22] Y. Shao, S. Monkman and A. J. Boyd, "Recycling carbon dioxide into concrete: a feasibility study," 2010.
- [23] H. El-Hassan and Y. Shao, "Carbon Storage through Concrete Block Carbonation Curing," *JO CET (Journal of Clean Energy Technologies)*, 2014.
- [24] Y. Shao and H. El Hassan, "CO₂ utilization in concrete," *3rd International Conference on Sustainable Construction Materials and Technologies*, 2013.
- [25] S. Alberici, P. Noothout, G. U. Rehman Mir, M. Stork, F. Wiersma, N. Mac Dowell, N. Shah and P. Fennell, "Assessing the potential of CO₂ utilisation in the UK," 2017.
- [26] GCI and ICEF, "Global Roadmap for Implementing CO₂ Utilization. The Global CO₂ Initiative & The Innovation for Cool Earth Forum," 2016.
- [27] J. Rissman, "Cement's role in a carbon-neutral future," p. 2018.
- [28] V. Meyer, S. Sahu and A. Dunster, "Properties of Solidia Cement and Concrete," 2019.
- [29] CarbonCure, "Who knew greener could mean stronger? CarbonCure Concrete Technology - Recycling CO₂ to make simply better concrete," 2018.
- [30] P. Markewitz, L. Zhao, M. Ryssel, G. Moumin, Y. Wang, C. Sattler, M. Robinius and D. Stolten, "Carbon capture for CO₂ emissions reduction in the cement industry in Germany," 2019.
- [31] R. Anantharaman, C. Fu, S. Roussanaly and M. Voldsund, "Design and performance of CEMCAP cement plant with MEA post combustion capture," 2016.
- [32] LH, "LafargeHolcim inaugure son démonstrateur FastCarb pour accélérer la carbonatation des granulats de béton recyclé et réduire l'empreinte carbone de la construction. LafargeHolcim," 2020.
- [33] HC, "Sustainability Report 2019. HeidelbergCement," 2020.
- [34] BMBF, "CO₂Min - CO₂ - Capturing durch mineralische Rohstoffe zur Erzeugung marktfähiger Produkte. Bundesministerium für Bildung und Forschung (BMBF)," 2017.
- [35] L. Schmitt and J. M. Torrenti, "The FastCarb National Project. Concrete Technology," 2020.
- [36] PCA, "How concrete is made. Portland Cement Association," 2021. [Online]. Available: <https://www.cement.org/cement-concrete/how-concrete-is-made>. [Accessed 03 May 2021].
- [37] M. W. Tait and W. M. Cheung, "A comparative cradle-to-gate life cycle assessment of three concrete mix designs," 2016.
- [38] K. S. You, S. H. Lee, S. H. Hwang and J. W. Ahn, "Effects of CO₂ carbonation on the chemical properties of waste cement: CEC and the heavy metal adsorption ability," 2011.
- [39] IT NRW, "Landesdatenbank NRW. Information und Technik Nordrhein-Westfalen-Statistisches Landesamt," 2020.
- [40] GENESIS, "GENESIS-Online. Statistisches Bundesamt," 2021.
- [41] A. Iizuka, M. Fujii, A. Yamasaki and Y. Yanagisawa, "Development of a new CO₂ sequestration process utilizing the carbonation of waste cement," 2004.
- [42] A. Iizuka, A. Yamasaki and Y. Yanagisawa, "Cost evaluation for a carbon dioxide sequestration process by aqueous mineral carbonation of waste concrete," 2013.
- [43] IT NRW, "Information und Technik - Nordrhein-Westfalen. OpenGeodata.NRW," 2021.
- [44] S. Van der Meulen, T. Grijspaardt, W. Mars, W. Van der Geest, A. Roest-Crollius and J. Kiel, "Cost figures for freight transport - final report," 2020.
- [45] BTB, "Jahresbericht 2020 – Gutes Klima. Bundesverband der Deutschen Transportbetonindustrie e.V.," 2020.
- [46] VDZ, "Zementindustrie im Überblick 2020/2021. Verein Deutscher Zementwerke e.V.," 2020.
- [47] KB, "Mineralische Bauabfälle Monitoring 2016. Bericht zum Aufkommen und zum Verlieb mineralischer Bauabfälle im Jahr 2016. Kreislaufwirtschaft Bau," 2019.
- [48] EC, "Directive contract on management of construction and demolition waste - SR1 - Final report task 2. The European Commission," 2011.
- [49] EC, "Directive 2008/98/EC of the European Parliament and of the council of 19 November 2008 on waste and repealing certain directives. The European Commission," 2008.
- [50] DESTATIS, "Wohnungen nach Baujahr und Bundesländern 2018," 2020.
- [51] B. Zhan, C. S. Poon, Q. Liu, S. Kou and C. Shi, "Experimental study on CO₂ curing for enhancement of recycled aggregate properties," 2014.
- [52] E. Lewicka, J. Szlugaj, A. Burkowiec and K. Galos, "Sources and markets of limestone flour in Poland," 2020.
- [53] Y. Katsuyama and A. Yamasaki, "Development of a process for producing high-purity calcium carbonate (CaCO₃) from waste cement using pressurized CO₂," 2005.
- [54] C. A. Irawan, A. Imran and M. Luis, "Solving the bi-objective capacitated p -median problem with multilevel capacities using compromise programming and VNS," *Intl. Trans. in Op. Res. (International Transactions in Operational Research)*, 2020.
- [55] M. El Amrani and Y. Benadada, "Multi-Stage algorithms for solving a generalized capacitated p-median location problem," (*IJACSA*) *International Journal of Advanced Computer Science and Applications*, 2018.
- [56] S. S. R. Shariff, N. H. Moin and M. Omar, "An alternative heuristic for capacitated p-median problem (CPMP)," *IEEE Business Engineering and Industrial Applications Colloquium (BEIAC)*, 2013.
- [57] "SCI4climate.NRW," 2021. [Online]. Available: <https://www.in4climate.nrw/en/stakeholders/scientific-community/>. [Accessed 2021].

CO₂-SPICER – CZECH-NORWEGIAN PROJECT TO PREPARE A CO₂ STORAGE PILOT IN A CARBONATE RESERVOIR

Vit Hladik^{1*}, Robert Prochac¹, Vladimir Opletal², Milan Pagac², Petr Jirman¹, Roman Berenblyum³, Anton Shchipanov³, Eric Ford³, Anders Nerموen³

¹ Czech Geological Survey (CGS), Brno, Czech Republic

² MND a.s., Hodonin, Czech Republic

³ NORCE, Bergen, Norway

* Corresponding author e-mail: vit.hladik@geology.cz

Abstract

Carbon capture and storage (CCS) is one of key technologies to decarbonise the emission-intensive industries in the Czech Republic and reach the 2050 carbon-neutral economy target. An important step on the road to the deployment of the technology is to prepare and realise a CO₂ storage pilot project in the country. The newly launched CO₂-SPICER project has been designed to make significant progress in this direction. It is the first project in Europe, targeting an onshore hydrocarbon field situated in carbonates as a pilot CO₂ storage site. Achieving the main project objective - to reach the implementation-ready stage of site development - would allow direct follow-up to project activities, using main project results as ready-made input. The target Zar-3 site is a hydrocarbon field located in the SE part of the Czech Republic. It is situated in an erosional relict of fractured carbonates of Jurassic age on the SE slopes of the Bohemian Massif, covered by Paleogene deposits and Carpathian flysch nappes. The field was discovered in 2001 and is now nearly depleted. This relatively “young age” of the field, together with active participation of field operator in the consortium and ongoing hydrocarbon production provide many advantages, such as direct access of the reservoir, availability of field monitoring data, generally good condition of wells, well-preserved core material and detailed reservoir description. However, the geology of naturally fractured carbonates brings specific research challenges. This paper provides a brief overview of the storage site and the project, its objectives, planned activities and expected outcomes.

Keywords: CO₂ geological storage, pilot project, Czech Republic, hydrocarbon field, fractured carbonates

1. Introduction

Up to now, storage of captured CO₂ in geological formations in the Czech Republic has only been developed on research level. The Technology Readiness Level for CO₂ geological storage in Czechia is between 4 (technology validated in lab) and 5 (technology validated in relevant environment).

In the case of underground CO₂ storage, TRL5 means its validation by realisation of a pilot project in geological conditions similar to future industrial-scale projects. The first steps for rising CO₂ geological storage in the Czech Republic towards TRL5 were made in the REPP-CO2 project [1] led by CGS, supported by IRIS (now NORCE), VSB - Technical University of Ostrava and a few other Czech entities, and focused on the depleted LBr-1 hydrocarbon field in SE Moravia as a possible pilot CO₂ storage site.

During discussions on possible further steps in the effort to prepare a CO₂ storage pilot in the Czech Republic, a dialogue was established with MND, the leading Czech oil and gas E&P company. This opened up the opportunity to consider active hydrocarbon fields as storage candidates. Among them, the Zar-3 field, a depleting oil and gas field in SE Czech Republic (Fig. 1) was identified as the most promising candidate for a CO₂ storage pilot.

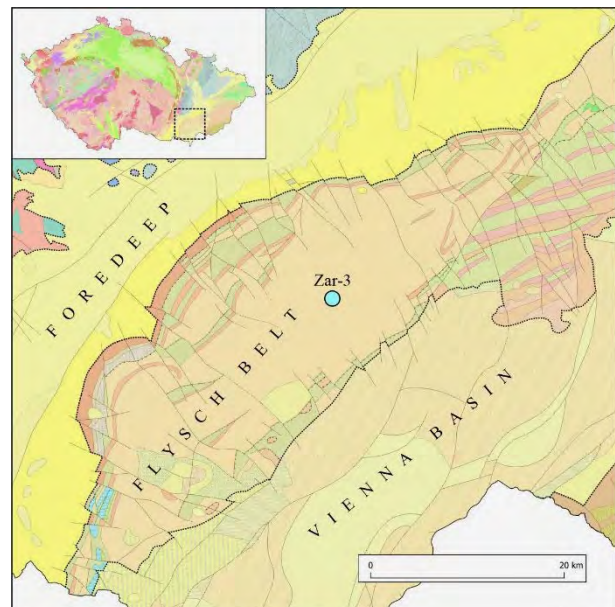


Figure 1: Position of Zar-3 site displayed on geological map of the Czech Republic [2]

CO₂-SPICER (CO₂ Storage Pilot In a CarbonatE Reservoir) is the next logical step in a series of projects and activities performed by CGS and its project partners on the road to realise a CO₂ storage pilot project in the

country. The project is the first of its kind in Europe targeting an onshore hydrocarbon field situated in fractured carbonates.

2. Overview of geology and the site

2.1 Brief overview of regional geology

The Zar-3 structure is located at the contact zone between the European foreland plate, represented by the Bohemian Massif and the Western Carpathian thrust belt (Fig. 1). Rock complexes in this region belong to three main structural levels, the Cadomian, Variscan and Mesozoic. All are buried below the overthrust flysch complexes of the Western Carpathians [3][4].

The Cadomian level is represented by the Brunovistulian unit, composed of Precambrian metamorphic rocks, granitoids to quartz diorites and rare ultrabasic rocks.

The lower part of the Variscan rock complex is composed of prevalingly red-coloured, coarse-grained Cambrian to Middle Devonian lithofacies. Overlying Upper Devonian to Lower Carboniferous rocks are represented mainly by facies of carbonate platforms and basins. The carbonate deposition was replaced in the Early Carboniferous by flysch (Culm) facies, followed in the Late Carboniferous by the molasse deposition of mostly sandstones containing coal seams (Namurian-A).

After a Permian hiatus, the Mesozoic sequence began in the area by deposition of the Middle Jurassic mostly terrigenous and shallow marine clastic deposits. They are followed by the Upper Jurassic facies, characterised by deposition of platform carbonates in the shallow marginal and uplifted zones and by sedimentation of marine marly shales in deeper basinal environment.

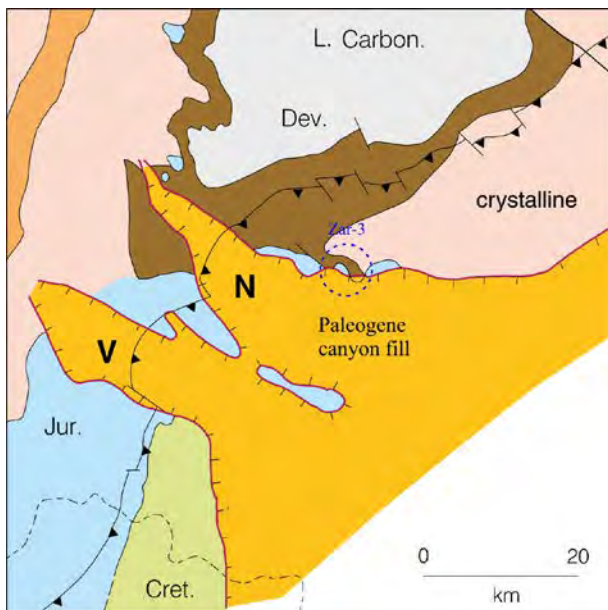


Figure 2: Pre-Neogene subcrop map showing the Nesvacilka (N) and Vranovice (V) paleovalleys [5]

During the Late Cretaceous to Early Paleogene the terrain was deeply eroded by rivers in the tectonically predisposed Nesvacilka and Vranovice depressions (Fig. 2) that turned into more than 1500 m deep submarine canyons. In both depressions most of the

Mesozoic sediments were removed. The heavily eroded pre-Tertiary basement in both depressions was gradually filled by the Upper Cretaceous to Paleogene detrital deposits, mainly by flysch sediments of deep-water gravity flows.

During the Late Paleogene and Early Miocene, the flysch sequences were deformed and thrust over the European foreland due to the late phases of the Alpine orogeny. The Carpathian thrust belt in Moravia is composed of Upper Jurassic to Lower Miocene sequences of the flysch belt, with several rootless tectonostratigraphical units, including the marginal Pouzdrany, the Zdanice-Subsilesian, the Silesian, and the Magura units [3][4][6].

2.2 Zar-3 structure

The Zar-3 structure (Fig. 3) comprising an oil field with a gas cap and an active aquifer is located in an erosional relict of Jurassic rocks on the north-eastern slope of the Nesvacilka depression (Fig. 2). The field was discovered in 2001 by the ZA3 well in the depth interval of 1565 – 1872 m (Fig. 3). The reservoir is represented by the Jurassic Vranovice carbonates, formed mostly by dolomites with some limestones and sandstones. Sealing of the reservoir is provided by a combination of the Paleogene side valley fill, the Jurassic Mikulov marls and, due to its complex tectonic settings, partially also by the Lower Carboniferous deposits.

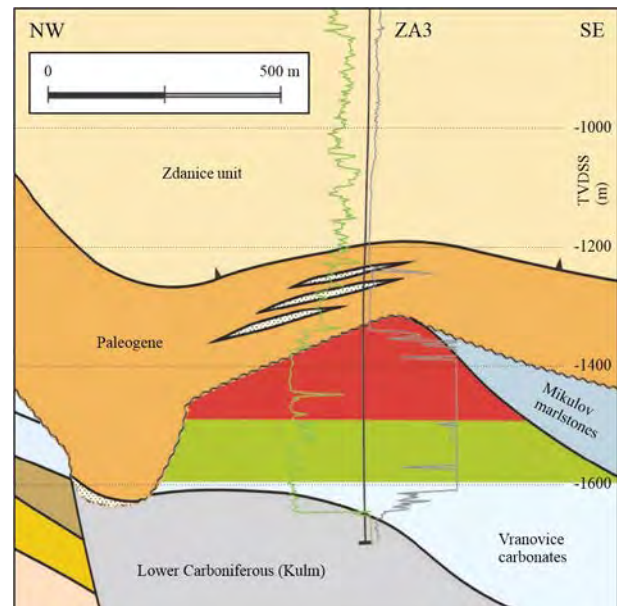


Figure 3: Schematic geological cross-section of NW – SE direction through the Zar-3 structure [6]

The porosity of the reservoir varies significantly, depending on the position within the structure and the resulting lithology (dolomitization degree, clastic and carbonate components content) and the distribution of fracture network (secondary porosity). This results in a considerable range of reservoir porosities from 2 to 20 %, based on well-log data [7]. The porosity determined from the cores shows an approximate average value of 12 %. Based on hydrodynamic tests [7], the reservoir permeability was estimated to 190 – 630 mD.

The gas cap reaches thickness up to 150 m, the original oil zone was ca. 105 m thick. Hydrocarbon reserves were estimated to 1.2 million cubic meters of original oil in place, 77 million cubic meters of solution gas and 100 million cubic meters of original gas in place in the gas cap.

The geological settings of the Zar-3 structure are relatively well known on the basis of deep drilling results and 3D seismic data covering the whole structure. The area of Zar-3 reservoir (and surrounding) comprises a total of 26 deep wells (14 in the reservoir itself) with well logging data available for about 20 wells. Check-shot surveys have been registered in 3 wells.

Even though a significant level of knowledge has been developed during the exploration and production phases of the Zar-3 field, a certain extent of geological uncertainty still exists. The main uncertainty is related to heterogeneity of the storage reservoir, in particular, the spatial distribution of rock properties and complexity of the geological settings.

3. CO₂-SPICER project

The CO₂-SPICER project is part of a broader long-term concept to realise a pilot project on geological storage of CO₂ in the Czech Republic. The project benefits from knowledge and experience gathered during previous pilot project preparation activities at the LBr-1 site [2][8] in previous REPP-CO₂ and ENOS projects, even though the geology differs and some special investigation approaches are required to qualify the Zar-3 field for injection. The Zar-3 site has many advantages compared to LBr-1:

- ongoing oil and gas production and existence of operating injection and observation wells, enabling access to the reservoir and wells for logging, testing and sampling;
- better condition of the wells penetrating the reservoir due to later discovery of the field;
- availability of well-preserved archive cores;
- significantly more information on the reservoir, including advanced well monitoring during production history;
- reduced probability of conflicts of interest, in particular no trans-boundary issues;
- active participation of the field operator (MND) in the consortium, enabling significant speed-up of developing the project towards CO₂ injection.

The geology of carbonates brings, however, specific research challenges to the project in comparison with the clastic sediments that were investigated in previous projects. These include, in particular, fluid flow in naturally fractured rocks and chemical reactivity of carbonates with CO₂, which may cause changes in mineral composition and reservoir (porosity, permeability) and geomechanical properties. These challenges must be identified and evaluated, and possible

mitigation actions must be taken in the specific site design and monitoring system.

3.1 Project objectives and approach

The main objective of CO₂-SPICER is to prepare implementation of a CO₂ geological storage pilot project at the mature Zar-3 oil and gas field in the SE part of the Czech Republic. To achieve this, the following set of sub-objectives has been set:

- build a 3D geological model of the storage complex;
- evaluate geomechanical and geochemical properties of the storage complex and identify if the injected CO₂ could affect reservoir integrity;
- simulate various CO₂ injection scenarios;
- assess risks related to CO₂ storage on the pilot site;
- prepare a site monitoring plan;
- evaluate scenarios for future site development, including design of CO₂ injection facilities.

Research methods will include collection and quality control of data from archives, core sampling, collection of fluid samples from the reservoir, laboratory experiments, field data acquisition both on the surface and in wells, data processing and interpretation, geological modelling, reservoir simulations and synthesis of results. The work will be carried out in close cooperation of all project partners - CGS, MND, NORCE, VSB - Technical University of Ostrava and Institute of Geophysics of the Czech Academy of Sciences.

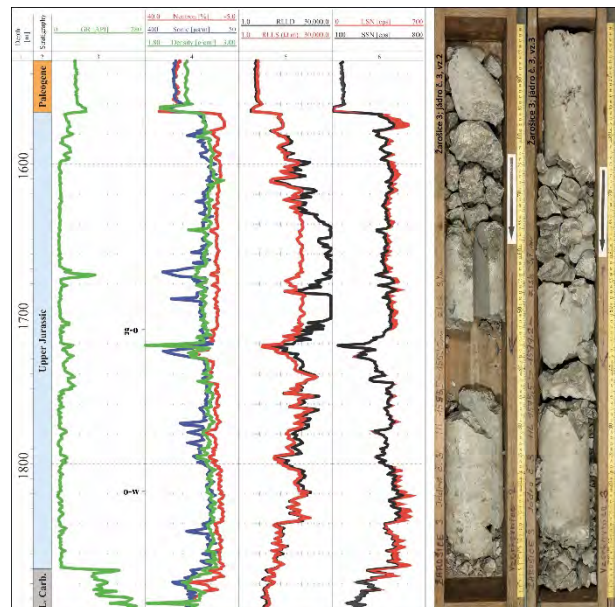


Figure 4: Well-logs of the reservoir (on the left, [6]) and core samples from the upper part of the reservoir (on the right, photos from MND core repository)

The field operator and project partner MND will provide 3D seismic data for the site (Fig. 5). The data cube will cover the whole site area, allowing the project team to prepare a detailed fault and structural plan of the net storage and the whole storage complex. The data and its

interpretation will be prepared for input to the 3D geological model.

The 3D geological model of the storage complex is one of the most important outcomes of the project. Individual steps of 3D model construction will include definition of covered spatial area, import of data, spatial well-log correlation and seismic interpretation, construction of layer boundaries (bases and surfaces), interpretation of tectonics, modelling of distribution of petrophysical parameters and distribution of fluids. The model will serve as an input into other parts of the project, especially the reservoir simulations of CO₂ injection, assessment of risks and possible CO₂ leakage pathways and setting up the site monitoring plan.

Another important outcome of the project will be the results of reservoir simulations of CO₂ injection focusing on various injection scenarios. These will serve as an input into risk assessment and preparation of a monitoring plan. Moreover, they will be directly used in all future stages of site development: applying for storage permit, carrying out the storage pilot and subsequent full-field CO₂ injection and storage.

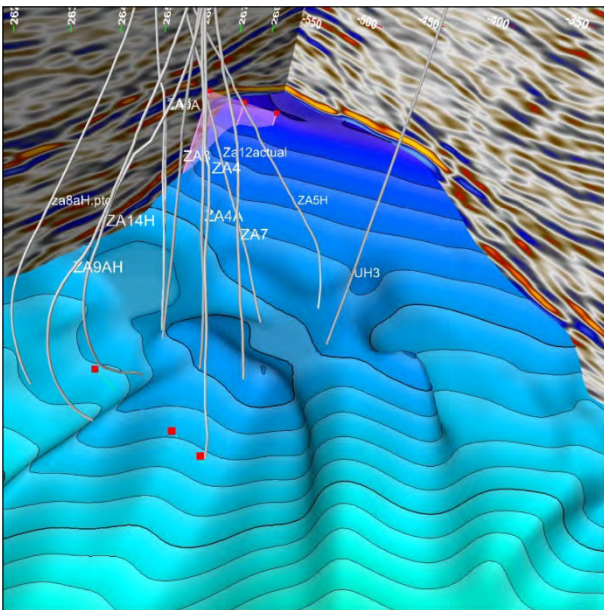


Figure 5: 3D view of the Zar-3 structure on 3D seismic data with interpreted reservoir top (MND data and interpretation)

Many novel approaches and methods will be used in the project, including handling of geological uncertainty through multiple geological realisations, evaluation and modelling of dynamic fracture behaviour, assessment of modern monitoring techniques such as time-lapse pressure transient analysis and seismic monitoring, as well as evaluation of the possibility to combine CO₂ storage with in-situ bacterial methanogenesis.

A comprehensive work programme consisting of ten work packages, spreading over 3.5 years (11/2020 – 04/2024), has been prepared to achieve the project objectives.

3.2 Expected outcomes

CO₂-SPICER project results will include a 3D geological model of the whole storage complex, containing the reservoir itself as well as its over- and under-burden. The model will comprise a set of derived structural geological maps and cross-sections illustrating distribution of reservoir parameters at defined stages of future reservoir development, using various CO₂ injection scenarios. The studied parameters will include CO₂ and other reservoir fluid saturations, pressure distribution, all in dynamics according to simulated scenarios, which will range from a basic CO₂ storage pilot up to full field-scale storage.

Project results will be prepared to enable their immediate application in practice by the industry partner MND for future development and implementation of the CO₂ storage pilot at the Zar-3 field. Many outcomes, e.g. the CO₂ injection scenarios, may be implemented very soon after the project completion, provided that parallel efforts to prepare a full-chain CCS pilot project involving a suitable industrial source of captured CO₂ in combination with the Zar-3 field as the storage site are successful.

The main precondition for the implementation of the pilot project is the availability of a suitable source of captured CO₂. This will require liaison with a company interested in reducing CO₂ emissions by means of CCS technology. Relatively large amounts of emissions are produced by industrial facilities in the Czech Republic, amounting to about 16.4 mil. tonnes annually (Tab. 1). Opportunities of cooperation have been investigated during the project preparation and some of the potential partners have expressed their intent to join the project End-User Club.

Table 1: Overview of CO₂ emissions in industrial sectors in the Czech Republic (data from the year 2018). Source: <https://portal.cenia.cz/irz/unikyPrenosy.jsp>

Industrial sector	CO ₂ emission (t / year)
Iron and steel	5 564 686
Refinery	4 089 807
Cement plants	2 997 169
Pulp and paper mill, millwork	1 116 245
Chemical plants	1 109 317
Lime works	1 071 379
Glass factory	285 022
Cooking plant	119 847
Total all sectors	16 353 472

4. Summary

The CO₂-SPICER project aims for preparation of a CO₂ storage pilot in the Czech Republic to the implementation-ready stage, where project results would feed in directly as a design concept. By this, CO₂-SPICER will significantly increase the Technology Readiness Level of CO₂ geological storage in the Czech Republic and make an important step towards practical deployment of the CCS technology in the country, as well as in Central & Eastern Europe.

Addressing an operational hydrocarbon field located in naturally fractured carbonates as potential storage site makes this project a unique showcase for CCS deployment in onshore Europe, having large application potential for brown and abandoned carbonate fields. The close collaboration with the field operator is crucial for achieving the project objectives.

Acknowledgements

The CO₂-SPICER project benefits from a € 2.32 mil. grant from Norway and Technology Agency of the Czech Republic.

References

- [1] Hladik, V., Berenblyum, R., Pereszlenyi, M., Krejci, O., Francu, J., Riis, F., Ford, E. P., Kollbotn, L., & Khrulenko, A. (2017). LBr-1 – Research CO₂ Storage Pilot in the Czech Republic. *Energy Procedia*, 114, p. 5742 – 5747.
- [2] Czech Geological Survey ArcGIS server map services <http://www.geology.cz/extranet/mapy/mapy-online/esri>.
- [3] Adamek, J. (1990). New findings on the deep structure of the southeastern slopes of the Bohemian Massif (“southern section” – Nemečický block). In Minarikova, D. & Lobitzer, H., eds., *Thirty years of geological cooperation between Austria and Czechoslovakia*. Fed. Geol. Survey Vienna, Geol. Survey Prague, p. 10 – 16.
- [4] Adamek, J. (2005). The Jurassic floor of the Bohemian Massif in Moravia – geology and paleogeography. *Bulletin of Geosciences*, 80, 4, p. 291 – 305.
- [5] Picha, F. J., Stranik, Z., & Krejci, O. (2006). Geology and Hydrocarbon Resources of the Outer Western Carpathians and Their Foreland, Czech Republic. In Golonka, J., & Picha, F. J., eds., *The Carpathians and their foreland: Geology and hydrocarbon resources*. AAPG Memoir 84, p. 49 – 175.
- [6] Kostelnicek, P., Ciprys, V., & Berka, J. (2006). Examples of recently discovered oil and gas fields in the Carpathian foredeep and in the European foreland plate underneath the Carpathian thrust belt, Czech Republic. In Golonka, J., & Picha, F. J., eds., *The Carpathians and their foreland: Geology and hydrocarbon resources*. AAPG Memoir 84, p. 177 – 189.
- [7] Durica, D., Suk, M., & Ciprys, V. (2010). Energetické zdroje – včera, dnes a zítra (Energy resources – yesterday, today and tomorrow). *Moravské zemské muzeum, Brno*, 165 p.
- [8] Berenblyum, R., Khrulenko, A., Kollbotn, L., Nermoen, A., Shchipanov, A., Skadsem, H., Zuta, J., Hladik, V. (2017). Integrated Approach to CO₂ EOR and Storage Potential Evaluation in an Abandoned Oil Field in Czech Republic. *19th European Symposium on Improved Oil Recovery, 24-27 April*. Stavanger, Norway: EAGE. doi:10.3997/2214-4609.201800046

ESTIMATION OF MUTUAL SOLUBILITY OF CO₂-H₂O IN SALINE AQUIFER SYSTEMS USING EPC-SAFT EQUATION OF STATE

Mohammad Masoudi^{1*}, Anja Sundal¹, Helge Hellevang¹

¹ Department of Geosciences, University of Oslo, Oslo, Norway

* Corresponding author e-mail: mohammad.masoudi@geo.uio.no

Abstract

A primary assessment of mutual solubility of CO₂ and water for estimated max and min temperatures and pressures of the prospective reservoir formations of Aurora; Cook (at >2650 m depth) and Johansen (at >2700 m depth) have been done using ePC-SAFT equation of state. Mole fraction of CO₂ in H₂O ranges from 0.025 to 0.027, and H₂O in CO₂ from 0.016 to 0.023 over pressure-temperature ranges of 265 – 283 bar and 95 – 110 °C. The potential for drying out effects (H₂O to CO₂) is significant, and there would be risk of salt precipitation in the near well area.

Keywords: Carbon Storage; mutual solubility; ePC-SAFT; Thermodynamics; Aurora

1. Introduction

An accurate determination of the distribution of components among different fluid and solid phases is crucial for efficiency and risk assessment in Carbon Capture and Storage (CCS) projects. An important step in quantification is modelling of different physical phenomena specific to a given reservoir/site. Among these, CO₂ concentration in water and water content of CO₂ have a superior priority, as saline aquifers are by far the most common type of repository, and evaporation of water into CO₂ stream causes salt precipitation and permeability impairment. However, a system such as H₂O-CO₂-Salt represents a complex fluid type due to highly non-ideal intermolecular interactions, such as association (hydrogen bonding), polarity, ionic bonds, and chain forming reactions. From a thermodynamic modelling perspective, it is not trivial to estimate the exact location of the phase boundaries and components distribution of such a complex system, by using standard engineering equations-of-state of the Van der Waals type (Peng-Robinson, Soave-Redlich-Kwong). Densities of the dense phase is especially challenging. To account for the non-ideal interactions, a good alternative is incorporating a predictive thermodynamic model that considers additional interactions (forces) between molecules: The Statistical Association Fluid Theory (SAFT). [1,2]

SAFT is a promising framework built on a reference term, which – unlike Van der Waals equations – can capture chain length (molecular shape) and molecular association [3]. Because of its accuracy and predictive capabilities, we used the ePC-SAFT [4–6] version to predict phase behaviour of H₂O-CO₂-Salt. This is at present the most advanced and accurate predictive tool for quantification of salt precipitation, and thus essential input to risk evaluations related to clogging.

2. Reservoir setting and data

The Norwegian Longship full value-chain CCS project [7] has selected deeply buried saline aquifers just offshore West Norway as suitable storage reservoirs for CO₂. The Johansen and Cook storage formations are siliciclastic, highly porous (20–30 %) Jurassic sandstones at burial depths in the order of 2.6-2.7 km below the sea floor [8]. The site has been studied extensively in the last decade [8–12]; however, there were no well data (P, T, porosity, permeability, mineralogy, fluid chemistry etc.) available from the storage license until 2020, when a CO₂ storage exploration well was drilled: 31/5-7 EOS [13]. Equinor and their Northern Lights Team, has made a data repository available [14].

Estimates of pressure (P), temperature (T) and salinity vary in previous studies and according to parameters for projections from analogue data (e.g. from Warren & Smalley, 1995[15]), and different studied locations. In [8,10,11,15] ranges are: P: 200-350 bar, T: 70-120 C and salinity 20 000 – 100 000 ppm. With new data, we now have proper input values for both the upper (Cook) and the lower (Johansen) reservoirs, and we applied formation water with TDS of 73000 - 73500 ppm, and P, T max/min scenarios of 95/110 °C, 265-283 bar [14].

2. Theory and model

The Perturbed Chain Statistical Association Fluid Theory (PC-SAFT) treats molecules as a chain composed of (m) spherical segments of equal sizes, bonded tangentially together and interacting via an intermolecular potential, *i.e.* Lennard-Jones (LJ), square-well (SW) etc. SAFT-type equations-of-states are usually formulated in terms of the residual Helmholtz energy. Considering the various types of molecular interactions we have taken into account in this work, the residual Helmholtz energy is defined as:

$$a^{res} = a^{hc} + a^{disp} + a^{assoc} + a^{ionic} \quad (1)$$

Where \tilde{a}^{res} is the difference between the total Helmholtz energy per mole for the real gas or liquid and the ideal gas Helmholtz energy per mole at the same temperature and density. The superscripts refer to terms accounting for the hard-chain, dispersion, association, and ionic interactions, respectively. All other thermodynamic properties can be estimated through derivatives of the residual Helmholtz free energy. The fugacity coefficient, ϕ , of the components can be calculated with:

$$\ln \phi_i = \tilde{a}^{res} + \left(\frac{\partial \tilde{a}^{res}}{\partial x_i} \right)_{T, \rho, x_{j \neq i}} - \sum_{j=1} x_j \left(\frac{\partial \tilde{a}^{res}}{\partial x_j} \right)_{T, \rho, x_{k \neq j}} + Z - 1 - \ln Z \quad (2)$$

where x_i is the mole fraction of component i , T is temperature, ρ is density, and Z is the compressibility factor and calculated with

$$Z = 1 + \rho \left(\frac{\partial \tilde{a}^{res}}{\partial \rho} \right)_{T, x} \quad (3)$$

The derivatives of the residual Helmholtz energy with respect to density can be calculated both numerically and analytically (here we used analytical derivatives). However, we generally recommend analytical derivation for the residual Helmholtz energy with respect to compositions, as we noticed that derivatives with respect to compositions are highly sensitive. The analytical derivation for hard chain and dispersion contribution of the free Helmholtz energy can be found in [16–18], for association contribution in [19], and for ionic contribution in [20].

The model requires three parameters for each compound, namely: m , the number of segments, σ , the segment diameter, and ε , the segment energy. For associative molecules, two additional parameters are needed, the association volume, κ^{AB} , and the well depth of the association energy, ε^{AB} .

We developed the model based on the following considerations:

- It is assumed that the association term can capture the polarity contribution of the molecules.
- The ePC-SAFT considers the hydrogen bonding through cross-association between unlike sites (i.e., O–H).
- The model for water molecules is based on the two-site single segment model proposed by [6], in which two associating sites of type (H) and type (O) represent the proton-donor sites and electron lone pairs, respectively. Two sites of the same type (i.e., O–O or H–H) do not associate.
- CO₂ is not considered as an associative molecule.
- Dispersion interaction is not considered between ions [6].
- Since the model is initially benchmarked for the CO₂-H₂O-NaCl system, we assumed total salinity as NaCl (i.e. TDS in formation water samples).

PC-SAFT parameters for water, Na⁺, and Cl⁻ are taken from [6]. PC-SAFT parameters for CO₂ are taken from

[17]. PC-SAFT parameters for all the components are reported in Table 1. Binary interaction parameters reported in [20] for the H₂O-CO₂-NaCl system is used.

Table 1. ePC-SAFT parameters for H₂O, CO₂, and ions

	m	σ (Å)	ε/k (K)	κ_{AB}	$\varepsilon_{AB}/k(K)$
H ₂ O	1.0953	2.8898	365.956	0.034868	2515.671
CO ₂	2.0729	2.7852	169.21	0	0
Na ⁺	1	1.6262	119.806	0	0
Cl ⁻	1	3.5991	359.660	0	0

Given a pressure P , a temperature T , and a mixture with global composition z , multi-phase flash calculations (vapour-liquid (V-L)) were performed to compute the phase fraction and the distribution of the components.

To perform multiphase flash calculations, the Rachford-Rice equation [21] is modified to account for the solid phase as follows:

$$\sum_{i=1}^{N_c} \frac{(K_i - 1)z_i}{1 + F_G(K_i - 1)} = 0 \quad (4)$$

Where N_c is the number of components, F_G is gas phase molar fraction and K_i is the equilibrium constant of component i . K_i is defined as:

$$K_i = \frac{y_i}{x_i} \quad (5)$$

$$x_i = \frac{z_i}{1 + F_G(K_i - 1)} \quad (6)$$

$$y_i = \frac{z_i K_i}{1 + F_G(K_i - 1)} \quad (7)$$

x_i is composition of component i in aqueous phase and y_i is composition of component i in gas phase.

More details of phase equilibria calculations can be found in our previous works [20,22].

3. Results and discussions

3.1 Model verification

The electrolyte and association contribution of the developed model are benchmarked for associative binary systems reported in [1] and water-salt systems reported in [6].

3.1.1 Association term

To validate the association contribution, we considered two systems. The first one is a Benzene-1-Propanol system. Benzene is a non-associating molecules and 1-propanol is an associating molecule. Figure 1.A shows isothermal vapor-liquid equilibria of this binary, self-associating mixture in which both compounds are below their critical point.

The second system is a mixture with two associating substances, Methanol and 1-Octanol. The results of isobaric vapor-liquid equilibria of this system is shown in Figure 1B.

The results confirm the ability of the model to simulate the phase behavior of systems containing associating molecules. We got the same results as [23] and matched the experimental data from [24,25].

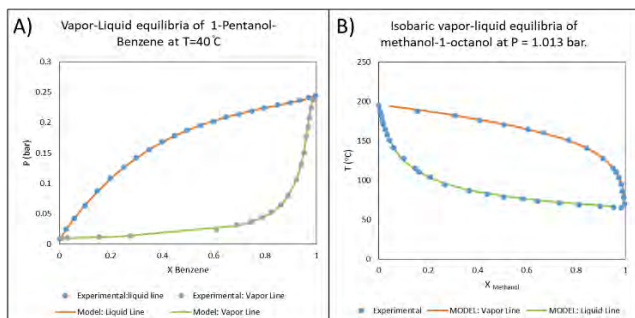


Figure 1: Vapor-liquid equilibria of: A) a system which contains one associating substance[24], and B) a system with two associating substances[24].

3.1.2 Ionic term

To validate the ionic contribution to Helmholtz energy, we considered two aqueous solutions containing monovalent ions (NaCl) and the bivalent ion (Na₂SO₄). The vapor pressure of aqueous solutions are calculated at different temperatures. The results show the ability of the model to cover the phase behavior of electrolyte solutions (Figure 2). We got the same results as [6] and matched the experimental data from [26,27].

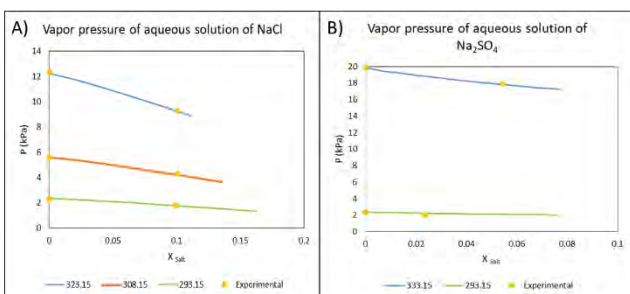


Figure 2: Vapor pressures of aqueous solutions of NaCl [26] and Na₂SO₄ [27] at different temperatures.

3.2 Mutual solubility

Figure 3 shows the mutual solubility of CO₂ and water in the CO₂-H₂O-NaCl system for 73,000 ppm salinity and CO₂ to brine ratio of 1:10 over a wide range of pressure

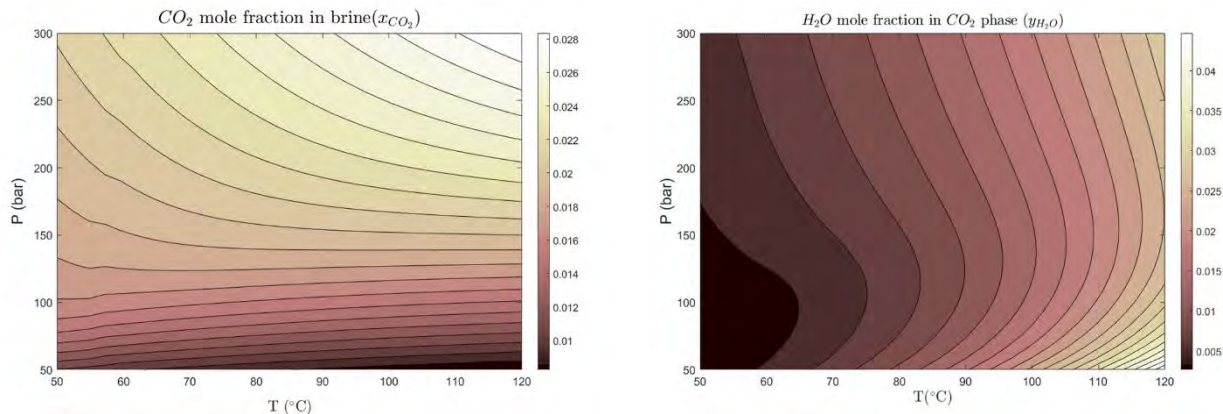


Figure 3: Mutual solubility of CO₂ in brine with 73,000 ppm NaCl and H₂O in CO₂ at varying reservoir conditions.

and temperature. The details of the mutual solubility for a combination of the expected max and min temperatures and pressures reported for the prospective reservoir formations of Aurora; Cook and Johansen, are reported in Table 2. Mole fraction of CO₂ in H₂O ranges from 0.025 to 0.027, and H₂O in CO₂ form 0.016 to 0.023 over pressure-temperature ranges of 265 – 283 bar and 95 – 110 °C.

Table 2: Mutual solubility of CO₂ and water for estimated max and min temperatures and pressures of the Johansen Fm. at >2700 m depth, and the Cook Fm. at >2650 m depth.

	T(°C)	P(bar)	x_{CO_2}	y_{H_2O}
Fluid 1	95	272	0.0258	0.0166
	110	272	0.0272	0.0231
	95	283	0.0261	0.0169
	110	283	0.0276	0.0234
Fluid 2	95	265	0.0255	0.0164
	110	265	0.0269	0.0229
	95	270	0.0257	0.0166
	110	270	0.0271	0.0230

4. Conclusion and recommendation

The PC-SAFT model set up presented here proves valid for estimating mutual solubility for CO₂-NaCl-H₂O systems, analogous to storage reservoir conditions. The estimated solubility for CO₂ in water (0.0255 – 0.0276 mol CO₂/H₂O) are in the same order of magnitude as in previous studies of the Aurora reservoirs. However, the potential for drying out effects (H₂O to CO₂) is significant, and there would be risk of salt precipitation in the near well area.

To have a better risk assessment a thorough simulation including sensitivity analysis on different salts and ions would have to be applied.

Acknowledgements

This publication has been produced with support from the project "Preventing loss of near-well permeability in CO₂ injection wells (POREPAC), funded by the Research Council of Norway through the CLIMIT program (280651/E20), and from the NCCS Centre (257579/E20), performed under the Norwegian research program Centres for Environment-friendly Energy Research

(FME). The authors acknowledge the following partners for their contributions: Aker Solutions, Ansaldo Energia, Baker Hughes, CoorsTek Membrane Sciences, EMGS, Equinor, Gassco, Krohne, Larvik Shipping, Lundin, Norcem, Norwegian Oil and Gas, Quad Geometrics, Total, and Vår Energi. Finally, the authors acknowledge Equinor and Northern Lights for making available the well data repository from EOS.

References

- [1] J. Gross, G. Sadowski, Application of the perturbed-chain SAFT equation of state to associating systems, *Ind. Eng. Chem. Res.* 41 (2002) 5510–5515.
- [2] R. Miri, P. Aagaard, H. Hellevang, Examination of CO₂–SO₂ Solubility in Water by SAFT1. Implications for CO₂ Transport and Storage, *J. Phys. Chem. B.* 118 (2014) 10214–10223. <https://doi.org/10.1021/jp505562j>.
- [3] W.G. Chapman, K.E. Gubbins, G. Jackson, M. Radosz, SAFT: Equation-of-state solution model for associating fluids, *Fluid Phase Equilib.* 52 (1989) 31–38.
- [4] X. Ji, C. Held, G. Sadowski, Modeling imidazolium-based ionic liquids with ePC-SAFT, *Fluid Phase Equilib.* 335 (2012) 64–73. <https://doi.org/10.1016/J.FLUID.2012.05.029>.
- [5] C. Held, T. Reschke, S. Mohammad, A. Luza, G. Sadowski, ePC-SAFT revised, *Chem. Eng. Res. Des.* 92 (2014) 2884–2897. <https://doi.org/10.1016/J.CHERD.2014.05.017>.
- [6] L.F. Cameretti, G. Sadowski, J.M. Mollerup, Modeling of Aqueous Electrolyte Solutions with Perturbed-Chain Statistical Associated Fluid Theory, *Ind. Eng. Chem. Res.* 44 (2005) 3355–3362. <https://doi.org/10.1021/ie0488142>.
- [7] Norwegian Government, The Government launches ‘Longship’ for carbon capture and storage in Norway, (2020). <https://www.regjeringen.no/no/aktuelt/regjeringa-lanserer-langskip-for-fangst-og-lagring-av-co2-i-noreg/id2765288/>.
- [8] E.K. Halland, J. Mujezinovic, F. Riis, CO₂ Storage Atlas: Norwegian Continental Shelf, Norwegian Petroleum Directorate, PO Box 600, NO-4003 Stavanger, Norway, 2014, URL [http://Www.Npd.No/En/Publications/Reports/Compiled-CO₂-Atlas](http://Www.Npd.No/En/Publications/Reports/Compiled-CO2-Atlas). (2014).
- [9] A. Sundal, H. Hellevang, Using Reservoir Geology and Petrographic Observations to Improve CO₂ Mineralization Estimates: Examples from the Johansen Formation, North Sea, Norway, *Miner.* 9 (2019). <https://doi.org/10.3390/min9110671>.
- [10] A. Sundal, R. Miri, T. Ravn, P. Aagaard, Modelling CO₂ migration in aquifers; considering 3D seismic property data and the effect of site-typical depositional heterogeneities, *Int. J. Greenh. Gas Control.* 39 (2015) 349–365. <https://doi.org/https://doi.org/10.1016/j.ijggc.2015.05.021>.
- [11] L. Wei, F. Saaf, Estimate CO₂ storage capacity of the Johansen formation: numerical investigations beyond the benchmarking exercise, *Comput. Geosci.* 13 (2009) 451. <https://doi.org/10.1007/s10596-008-9122-x>.
- [12] G.T. Eigestad, H.K. Dahle, B. Hellevang, F. Riis, W.T. Johansen, E. Øian, Geological modeling and simulation of CO₂ injection in the Johansen formation, *Comput. Geosci.* 13 (2009) 435.
- [13] NPD factpages, n.d. <https://factpages.npd.no/nb-no/facility/pageview/fixed/all/723056>.
- [14] Equinor Open Data, Northern Lights Repository, n.d. <https://data.equinor.com/dataset/NorthernLights>.
- [15] E.A. Warren, P.C. Smalley, North Sea formation waters atlas, *Oceanogr. Lit. Rev.* 6 (1995) 471.
- [16] R. Privat, R. Gani, J.-N. Jaubert, Are safe results obtained when the PC-SAFT equation of state is applied to ordinary pure chemicals?, *Fluid Phase Equilib.* 295 (2010) 76–92. <https://doi.org/https://doi.org/10.1016/j.fluid.2010.03.041>.
- [17] J. Gross, G. Sadowski, Perturbed-Chain SAFT: An Equation of State Based on a Perturbation Theory for Chain Molecules, *Ind. Eng. Chem. Res.* 40 (2001) 1244–1260. <https://doi.org/10.1021/ie0003887>.
- [18] S. Mohebbinia, Advanced equation of state modeling for compositional simulation of gas floods, The University of Texas at Austin, 2013. <http://hdl.handle.net/2152/23098>.
- [19] W.G. Chapman, K.E. Gubbins, G. Jackson, M. Radosz, New reference equation of state for associating liquids, *Ind. Eng. Chem. Res.* 29 (1990) 1709–1721.
- [20] S. Parvin, M. Masoudi, A. Sundal, R. Miri, Continuum scale modelling of salt precipitation in the context of CO₂ storage in saline aquifers with MRST compositional, *Int. J. Greenh. Gas Control.* 99 (2020) 103075. <https://doi.org/https://doi.org/10.1016/j.ijggc.2020.10.3075>.
- [21] H.H. Rachford Jr, J.D. Rice, Procedure for use of electronic digital computers in calculating flash vaporization hydrocarbon equilibrium, *J. Pet. Technol.* 4 (1952) 13–19.
- [22] M. Masoudi, R. Miri, H. Hellevang, S. Kord, Modified PC-SAFT characterization technique for modeling asphaltenic crude oil phase behavior, *Fluid Phase Equilib.* 513 (2020) 112545. <https://doi.org/https://doi.org/10.1016/j.fluid.2020.11.2545>.
- [23] J. Gross, G. Sadowski, Application of the perturbed-chain SAFT equation of state to associating systems, *Ind. Eng. Chem. Res.* 41 (2002) 5510–5515. <https://doi.org/10.1021/ie010954d>.
- [24] J.M. Rhodes, T.A. Griffin, M.J. Lazzaroni, V.R. Bhethanabotla, S.W. Campbell, Total pressure measurements for benzene with 1-propanol, 2-propanol, 1-pentanol, 3-pentanol, and 2-methyl-2-butanol at 313.15 K, *Fluid Phase Equilib.* 179 (2001) 217–229. [https://doi.org/https://doi.org/10.1016/S0378-3812\(00\)00502-1](https://doi.org/https://doi.org/10.1016/S0378-3812(00)00502-1).
- [25] A. Arce, A. Blanco, A. Soto, J. Tojo, Isobaric vapor-liquid equilibria of methanol+ 1-octanol and ethanol+ 1-octanol mixtures, *J. Chem. Eng. Data.* 40 (1995) 1011–1014.
- [26] A. Apelblat, E. Korin, The vapour pressures of saturated aqueous solutions of sodium chloride, sodium bromide, sodium nitrate, sodium nitrite,

potassium iodate, and rubidium chloride at temperatures from 227 K to 323 K, *J. Chem. Thermodyn.* 30 (1998) 59–71. <https://doi.org/https://doi.org/10.1006/jcht.1997.0275>.

[27] A. Apelblat, E. Korin, The vapour pressure of water

over saturated solutions of sodium sulfate, calcium bromide, ferric chloride, zinc nitrate, calcium nitrate, and lithium nitrate at temperatures from 278.15K to 323.15K, *J. Chem. Thermodyn.* 34 (2002) 1621–1637. [https://doi.org/https://doi.org/10.1016/S0021-9614\(02\)00201-X](https://doi.org/https://doi.org/10.1016/S0021-9614(02)00201-X).

A MODEL TO ESTIMATE CO₂ LEAKAGE AND IDENTIFY CO₂ HYDRATE STABLE CONDITIONS FOR OFFSHORE CCS

Hariharan Ramachandran^{1*}

¹ CAGE - Centre for Arctic Gas Hydrate, Environment and Climate, Department of Geosciences, UiT-The Arctic University of Norway, Tromsø, Norway

* Corresponding author e-mail: hariharan.r@uit.no

Abstract

Offshore CCS (Carbon Capture and Storage) is an attractive option to clamp down on carbon emissions. Two major advantages are 1) existing infrastructure for injection and 2) well characterized reservoirs due to previous oil and gas operations. One of the biggest concerns is the possibility of leakage. Leakage is likely when CO₂ plume encounters improperly abandoned wellbores, pre-existing conductive faults, or reactivated faults amongst others. The hazard of leakage strongly depends on the leakage fluxes and rates. Hydrates may form and throttle leakage if the pressure-temperature conditions within the pathway reach hydrate stable conditions. Thus, a useful component of risk assessment is to model CO₂ leakage and assess potential for hydrate formation conditions. In this short paper, we describe a model for flow of CO₂ along a leakage pathway. We assume single phase flow of CO₂ with variable fluid properties and a continuous leakage pathway with constant thickness. These assumptions help obtain worst-case estimates of leakage fluxes and rates. Expected leakage fluxes and rates are estimated along with the effect of pathway permeability and reservoir overpressure on it. Pressure-temperature conditions are checked if they fall within the CO₂ hydrate stable conditions for typical Norwegian Continental Shelf (NCS) Storage projects (Sleipner, Snøhvit and Aurora projects). Formed hydrates reduce the permeability of the pathway and has the potential to temporarily block leakage or redirect leakage in different directions. The aim of this study is to understand the relationship between pathway properties, regional conditions, leakage pressure profile and hydrate formation on leakage fluxes and rates.

Keywords: CO₂ leakage; Hydrates; Offshore CCS; Modeling; Leakage risk; Leakage flux

1. Introduction

Global effort has been undertaken with the announcement of Paris agreement to limit the average temperature rise to 2 °C and CO₂ concentration to 450 ppm by the end of the 21st century [1][2]. One key suggestion to clamp down on carbon emissions is to add the Carbon Capture and Storage (CCS) for existing and new fossil-fuel based power sources and other energy intensive industries [3]. Captured CO₂ is transported and injected in deep geological formations. In some sense, CCS is the process of returning carbon to where it was produced from, albeit in an altered form [4]. Previous studies [5] have shown that large volumes of CO₂ can be stored in aquifers by dissolution, trapping and mineralization. The most considered storage formations [6] are depleted oil and gas fields [7], deep saline aquifers [8] and unminable coal seams [8][9]. Depleted oil and gas reservoirs are especially an attractive option because of existing infrastructure and well characterized storage formation.

One of the biggest risks associated with storage is the possibility of leakage [6][10]. CO₂ may escape (Refer Figure 1) through man-made pathways, such as poorly completed and/or abandoned wells pre-dating storage operations [11][12], or through pre-existing or reactivated faults/fractures [13]. Besides providing a direct release of leaking CO₂ at seafloor/surface, they also spread them at shallower depths with a possibility to contaminate [6][10][14]. This provides a motivation to analyze the leakage along such pathways. A good physics-based model to predict leakage characteristics

will be helpful during the site selection phase from risk assessment perspective [15].

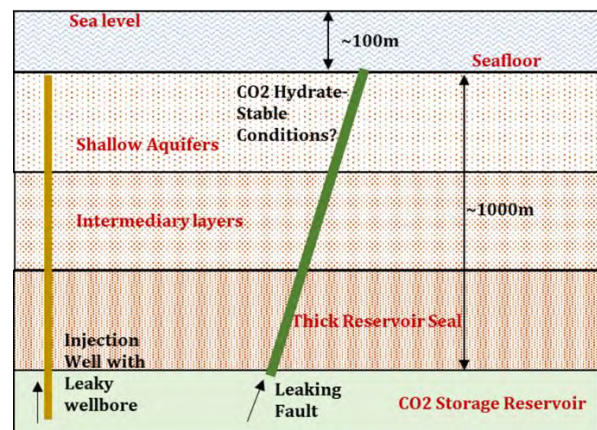


Figure 1: Schematic representation of offshore leakage scenario. CO₂ leaks through a fault or wells with leaky wellbore. The leakage pathway terminates at the seafloor. Does CO₂ encounter hydrate-stable conditions as it reaches the seafloor?

Understanding the pressure and temperature conditions occurring during leakage and its implications on CO₂ properties is critical for modeling leakage [20][21][22]. CO₂ is in supercritical state at typical storage conditions. The temperature and pressure profile of a vertical fault at hydrostatic and geothermal equilibrium is shown on a CO₂ phase diagram in Figure 2. The seafloor depth and reservoir depth are taken from Figure 1. Pressure and temperature decrease from the leakage source to the

seafloor. The key observation from Figure 2 is that CO₂ can exist in different phases during leakage. Since the pressure and temperature decrease continuously, there will be a substantial variation in CO₂ properties such as density, viscosity etc. This decompressive nature will also affect the pressure profile within the fault [20][21][22]. It's instructive to check if the new pressures reach hydrate stable conditions. Accounting for above factors is critical in getting a good leakage estimate.

Several studies have developed analytical and semi-analytical models to estimate leakage fluxes [16][17][18][19] through faults and wellbores. The fluxes were estimated with an isothermal assumption mostly (non-isothermal assumption was used in certain section of the pathway [19]) and issues related to the permeability of the pathways and the pressure at the leakage source were well addressed. The non-isothermal nature of leakage throughout the pathway and multiphase coexistence considerations (condensation, evaporation, and hydrate formation) were studied extensively too [20][21][22][23].

In this study, we present a simplified steady state model to predict leakage fluxes and rates in non-isothermal and hydrate stable conditions. The simplified approach help predict the worst-case fluxes when leakage occurs. This model is used to predict leakage for wide variety of pathway geological properties and regional constraints such as geothermal gradients. This model can also assess if hydrate stable conditions exist during leakage.

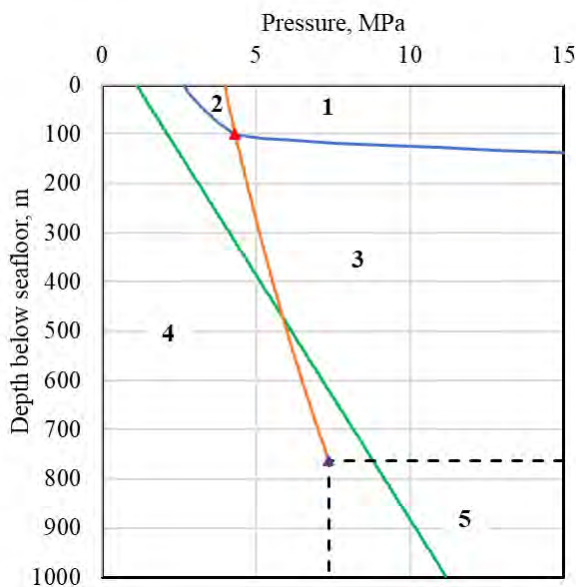


Figure 2: Typical pressure-temperature profile for a slow leaking fault (green line) shown in Figure 1. This profile is superimposed on the phase diagram of CO₂. Orange line is the Saturation line for CO₂ and purple triangle is the critical point. Gas and liquid phase coexist in this pressure-temperature condition. Region 3 has liquid phase and region 4 has gas phase. CO₂ exists in supercritical conditions in region 5. The hydrate forming conditions for CO₂-H₂O mixtures is shown by the blue curve and the red triangle is the quadruple point. CO₂ hydrate exists in region 1 and 2.

2. Methods

The simplified steady-state flow model is presented in this section. A leakage pathway is assumed to intersect the storage reservoir. The injected CO₂ is assumed to have reached the base of the leakage pathway and 100% CO₂ is assumed to leak. The leakage pathway is a generic term. It refers to faults under high permeability and leaky wellbore under low permeability [19]. Analysis for other types of leakage pathways can be performed by altering the pathway properties in this model [21][23]. The pathway is assumed to be a 1-D vertical porous medium with specific geometry (effective width, breadth), rock properties (porosity, permeability) and rock-fluid properties (relative permeability, initial saturations). The complexities related to the geology of fault core / leaky wellbore and the damaged zone surrounding it is simplified. Averaged values were used along the horizontal directions, but they can vary with depth. Complex pathway characteristics related to in-situ stress, stress-dependent properties, fracture branching amongst other geomechanical factors are not included in this model. The aqueous phase is assumed to be at residual saturation. This assumption is intended to calculate the worst-case fluxes when leakages occur.

Summary of the assumptions used to derive the mass balance are:

- 1) Steady state 1-D flow of CO₂ in the vertical pathway.
- 2) Constant pressure and temperature at the bottom and top of the pathway.
- 3) Multiphase Darcy's law is applied to flow in pathway.
- 4) Capillary pressure is neglected.
- 5) Residual water saturation in pathway after steady state flow of CO₂ reached.
- 6) Hydrates will only affect the permeability in the formed region.
- 7) The temperature in the pathway is assumed to have equilibrated with the geothermal temperature

The overall mass balance constraint equation is given as,

$$\frac{dm}{dz} = 0 \quad 2-1$$

The multiphase flowing effects are ignored and only CO₂ (in gas, liquid, or supercritical conditions) can flow and assumed to establish steady saturation. The flow rate is,

$$\dot{m} = -\frac{\rho_j k k_{rj} A}{\mu_j} \left(\frac{dP}{dz} - \rho_j g \right) \quad 2-2$$

Where m is the total mass rate, A is the area perpendicular to flow, k is the absolute permeability of the pathway, k_{rj} is the relative permeability of phase j , μ_j is the viscosity of phase j and ρ_j is the mass density of phase j . Hydrate formation is assumed to affect the permeability alone. Several experiments [24][25] have been reported showing the effect of CO₂-hydrates on rock permeability and calibrated the correlation between the permeability and hydrate saturation as,

$$k_{new} = (1 - S_h)^{n_h} k \quad 2-3$$

The new permeability, k_{new} in the hydrate region is only a function of the hydrate saturation, S_h , and a hydrate exponent, n_h . An exponent of 3 was used for this study based on the experimental results [24][25]. The CO₂ hydrate stable pressures for a given temperatures and seawater salinity conditions were published [26] and a correlation was developed using this data,

$$P_{hyd} = \sum_{i=0}^7 A_i T^i \quad 2-4$$

Table 1: Constant Values for Equation 2-4

Constant	If T ≤ 281.58K	If T > 281.58K
A ₀	-1.4022673445909542 * 10 ¹⁰	+2.252510579962195 * 10 ¹²
A ₁	+3.5856298042175686 * 10 ⁸	-4.738766839485371 * 10 ¹⁰
A ₂	-3.9292771701155193 * 10 ⁶	+4.1538268190587914 * 10 ⁸
A ₃	+2.392087196483884 * 10 ⁴	-1.9418959119972903 * 10 ⁶
A ₄	-87.37405622572473	+5106.4822557848065
A ₅	+0.1914826448303001	-7.16163577830236
A ₆	-2.331279266183065 * 10 ⁻⁴	+4.184920304845536 * 10 ⁻³
A ₇	+1.2163909288497183 * 10 ⁻⁷	0.0

P_{hyd} is the hydrate stable pressure in MPa for the given temperature, T in K and A_i is equation constants given in Table 1. It is assumed that all the water (with seawater salinity) available is converted to hydrates when the pressure-temperature condition is hydrate stable. This is a reasonable assumption for low water saturations. CO₂ properties vary along the pathway as both temperature and pressure vary with depth. Span-Wagner multi-parameter Equation Of State for CO₂ [27] is employed for phase behavior and fluid properties estimation and a corresponding state model for viscosity [38][39]. The pressure at the seafloor is given as,

$$P_{sf} = P_{atm} + D_{sf} * HG \quad 2-5$$

P_{sf} is the pressure at the seafloor in MPa, D_{sf} is the seafloor depth, P_{atm} is the atmospheric pressure taken as 0.101325 MPa and HG is the hydrostatic gradient in MPa/m. The temperature and pressure below the seafloor are given as,

$$T = T_{sf} + D * GG \quad 2-6$$

$$P = P_{sf} + D * HG \quad 2-7$$

T_{sf} is the seafloor temperature in K, D is the sediment depth below seafloor in m and GG is the geothermal gradient in K/m. The mass flux and pressures are the unknowns that are solved for using the model. The mass balance equation (2-1) together with mass flux equation (2-2 and 2-3) is solved to obtain the leakage flux. The pathway is discretized into blocks and the equations are solved iteratively until the mass balance constraint is

honored. The temperature within the blocks is determined using equation (2-6) and the pressure boundary conditions are determined using equation (2-5 and 2-7) This model is coded in Julia [33].

3. Results

3.1 Base Case

This section discusses a synthetic base case for the model. A homogenous vertical pathway from the seafloor to a depth of 1000 mbsf (meters below seafloor) with a permeability of 1 Darcy is considered. The cross-sectional area allowable for flow is kept constant. The seafloor depth, seafloor temperature and geothermal gradient typical for Norwegian Continental Shelf (NCS) were obtained from previous studies [28]. The initial pathway pressure is described by the hydrostatic gradient. The bottom of the pathway is assumed to be connected to a continuous source of CO₂ at constant pressure and temperature. The storage reservoir is overpressurized due to the injection and storage (Overpressure, $\Delta P_s = P_{reservoir} - P_{hydrostatic}$). An overpressure of 2 MPa is assumed. The pathway is assumed to be at residual water saturation of 0.2 and constant gas relative permeability of 0.8. The geological description is shown in Table 2 and schematic representation is shown in Figure 3.

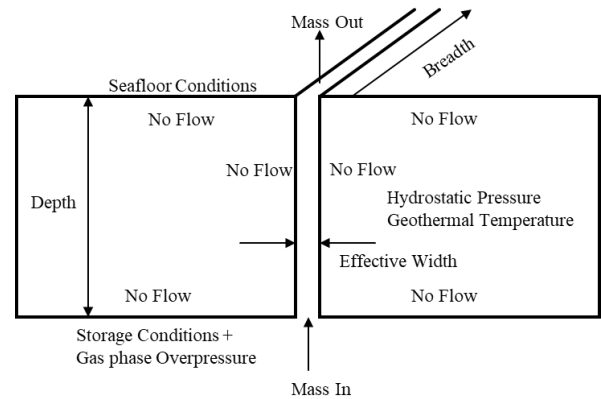


Figure 3: Schematic representation of leakage pathway system used for synthetic base case to represent NCS.

Table 2: Input parameters for synthetic base case

Geological Description	Values
Pathway porosity, ϕ	0.3
Pathway effective width (m), w	0.1
Pathway permeability (D), k	1.0
Pathway breadth (m), b	10.0
Pathway depth (mbsf), D	1000.0
Initial Conditions	
Seafloor depth (m), D_{sf}	100.0
Seafloor temperature (K), T_{sf}	278.15
Geothermal gradient (K/m), GG	0.034
Hydrostatic gradient (MPa/m), HG	0.01
Overpressure at leakage source (MPa), ΔP_s	2.0
Pressure at seafloor (MPa), P_{sf}	1.008
Pressure at leakage source (MPa), P	13.16
Temperature at leakage source (K), T	312.065

The resulting pressure-temperature profiles within the pathway at the onset of leakage is shown in Figure 4. The pressure in the pathway is higher than the corresponding hydrostatic pressure at every depth but lower than the hydrate-stable pressure for the given temperature conditions. Although this might provide a driving force for CO₂ to leak-off from the pathway into intersecting permeable layers if any, higher pressures will provide a signal to nearby observation wells during monitoring phase which may lead to quicker remediation.

The leakage flux is calculated to be 0.044 kg/s/m² or 1399.2 ton/year/m². For the sake of comparison, leakage flux from an isothermal model is calculated to be 0.066 kg/s/m² or 2100.9 ton/year/m². Calculations for the isothermal model are performed with density and viscosity of CO₂ averaged between leakage source conditions and seafloor conditions. The results indicated that the isothermal model overestimated leakage flux by 50% compared with current model. Direct consequences of such overestimation are 1) the risk associated with leakage is overestimated affecting the site selection process and 2) the leakage pathway properties such as permeability is underestimated from the obtained monitoring data [23].

The leakage flux is expressed independent of the area. Assuming 1 m² of leakage area, the leakage rate is approximately 1,399.2 ton/year. This result is sensitive to the area of the pathway and to attenuation to intersecting permeable layers among other factors. Both these factors affect the final leakage rate. In the context of long-term risk assessment, this leakage rate for 100 years would yield 0.14 million tons of escaped CO₂, approximated to 0.7% for a 20 million tons storage project, well below the 1% target [6]. The fluxes estimated by the model report the worst-case fluxes and not necessarily the real-world scenario.

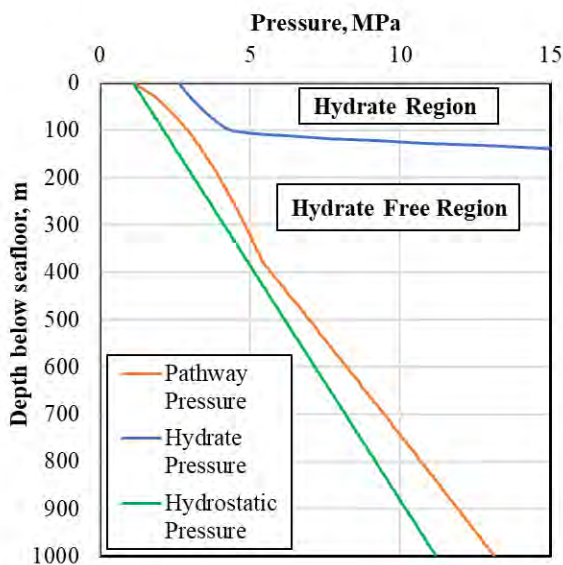


Figure 4: Pressure profile with depth for synthetic base case. The pathway pressure is in the single-phase regions and don't reach hydrate formation conditions.

3.2 Effect of Permeability

Leakage flux increased in a log-linear fashion with the increase in permeability as shown in Figure 5. A sensitivity study was performed on permeability to estimate its effect on leakage flux keeping all other parameters same as the base case. The variation in permeability does not affect the fluid properties. For an order of magnitude permeability increase, the leakage flux increased by a factor of 10. For comparison, the CO₂ background flux at earth's surface is 0.2 mg/s/m² [29]. The intention here is to set the calculated fluxes in context with background fluxes and not to comment on whether the values are large or small enough to neglect when compared. This provides confidence that the leaks can be easily identified during monitoring for permeability greater than 10 μD.

Flux through leaky faults are quite high with a possibility for runaway discharge and compromise the storage operation. Leakage fluxes are around 0.1 ton/year/m² for 0.0001 Darcy pathway signifying typical leaky wellbore [12][19]. Assuming 1 m² of leakage area, 15,000 leaky wellbores need to be encountered to reach 1% leakage over 100 years for a 20 million tons storage project and the above leakage flux. From overall leakage perspective, leaky wellbores provide less of risk than leaky faults. In the context of long-term risk assessment, all the wellbores/faults and other pathways in contact with the reservoir needs to be accounted for. Specifically, whether they are leaky or not and their permeability distribution.

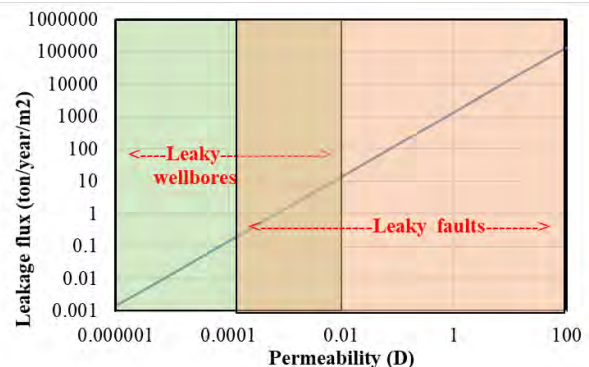


Figure 5: Leakage rate as function of permeability. Green region is typical permeability reported [12][19] for leaky wellbores and red region reported [21] for leaky faults.

3.3 Effect of Overpressure

The CO₂ storage reservoir is typically at hydrostatic pressure. The pressure in the reservoir increases during injection assuming no production or leakage. The increase in pressure above hydrostatic is referred to as overpressure. CO₂ typically occupies the top of the reservoir, and the length of this connected CO₂ phase is attributed to an increase in pressure. Typical pressure profiles within a reservoir are discussed in previous studies [19][20][23]. A simplified version of this effect is used here as constant overpressure in all our simulations. A sensitivity study was performed on overpressure to estimate its effect on leakage flux keeping all other parameters same as the base case. Leakage flux increases

with increase in overpressure as shown in Figure 6. Besides the concerns with respect to the unintended fracturing, higher rate of injection will increase the overpressure and the leakage flux. It is preferable to inject slower and longer than faster and shorter when concerned about minimizing the leakage flux. Thus, reservoir pressure management plays an active role in minimizing leakage.

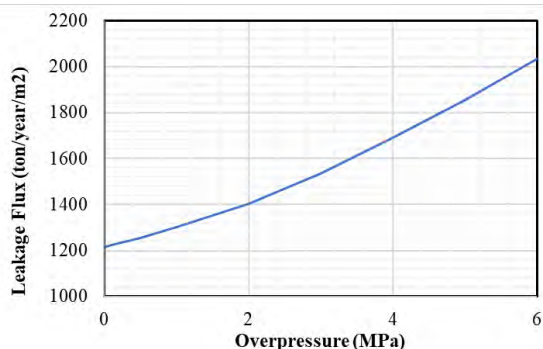


Figure 6: Leakage flux as function of constant reservoir overpressure.

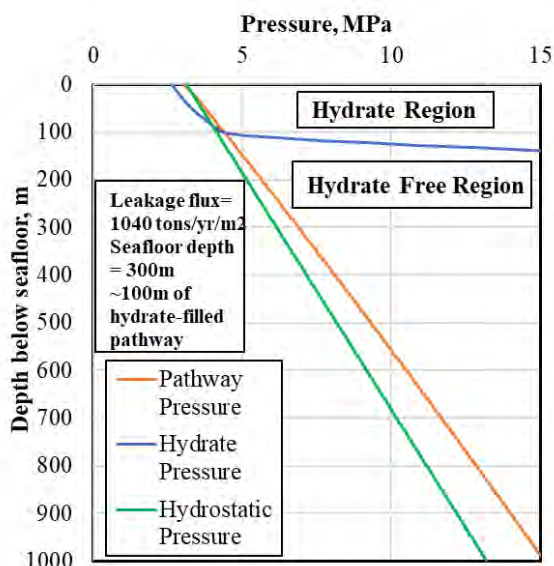


Figure 7: Pressure profile with depth for base case with a different seafloor depth of 300m. Close to 100m of CO₂-hydrate filled zone is present in the pathway

3.4 CO₂- Hydrate Stable Conditions

Pressures within the pathway for base case conditions (Figure 3) was far away from hydrate stable conditions. But it is instructive to find out what conditions facilitate hydrate formation within the pathways. Increase in reservoir depth, colder conditions (low geothermal gradient) and larger overpressure conditions were not found to assist hydrate formation. On analysis, two factors strongly assisted hydrate formation. They were colder seafloor temperatures and greater seafloor depths as shown in Figure 7 and Figure 8. Amount of aqueous phase present will determine the hydrate saturation within this region. Over time, there is potential for formed hydrates to accumulate enough to block pathways

as observed in marine methane seeps, gas chimneys and active pockmarks [30] [31][32]. Formed hydrates act as a signal during the shallow subsurface monitoring phase. Recent studies show even a minor change in gas or hydrate saturation could be detected using the time-lapse seismic approach [37].

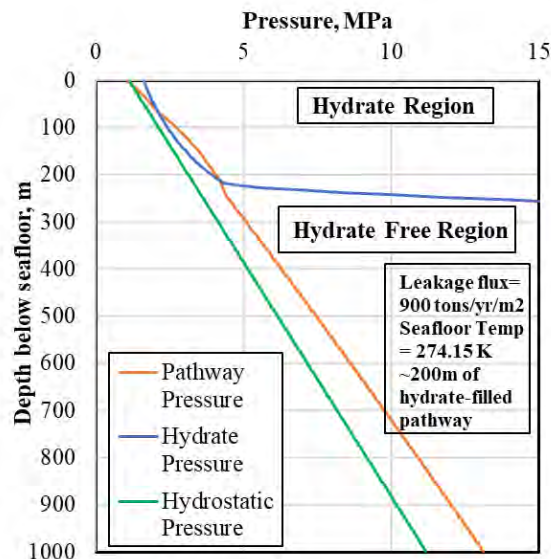


Figure 8: Pressure profile with depth for base case with different seafloor temperature of 274.15K. Close to 200m of CO₂-hydrate filled zone is present in the pathway.

3.5 Leakage Analysis for Storage Sites in NCS

Hypothetical leakage scenario from CCS projects (Sleipner project, Snøhvit project and Aurora/ Northern Lights project) in Norwegian Continental Shelf (NCS) is analyzed in this section and the corresponding data is shown in Table 3 [28][34][35][36]. The maximum uncertainty is on the seafloor temperature and geothermal gradient. From previous section, geothermal gradient was found to have minimal impact when compared with seafloor temperature on leakage pathway reaching CO₂ hydrate stable conditions.

Table 3: Input parameters for hypothetical leakage analysis on real field information [28][34][35][36].

Geological Description	Sleipner	Snøhvit	Aurora
Pathway porosity, ϕ		0.3	
Pathway effective width (m)		0.1	
Pathway permeability (D)		1	
Pathway breadth (m)		10	
Initial Conditions	Sleipner	Snøhvit	Aurora
Seafloor depth (m)	80	330	300
Seafloor temperature (K)	278.15	277.15	276.15
Geothermal gradient (K/m)	0.034	0.035	0.036
Overpressure at leak source (MPa)	2		
Pathway depth (m)	700	2600	2700

The pressure conditions in the pathway along with CO₂ hydrate stable pressure and hydrostatic pressure is shown in Figure 9 (for Sleipner project), Figure 10 (for Snøhvit

project) and Figure 11 (for Aurora project). The pathway pressure is far away from hydrate stable conditions for the Sleipner project, but they reach CO₂ hydrate stable conditions in the upper 150m for the Snøhvit and Aurora project. Although there are considerable uncertainties here, the results indicate that in the event of leakage, it is very likely for hydrates to form at the Snøhvit and Aurora projects they might temporarily block the pathways [30][31][32]. The leakage fluxes were considerably lower for Snøhvit and Aurora project (~900 ton/year/m²) when compared with Sleipner project (~1500 ton/year/m²). Larger seafloor depth (> 300 m) coupled with colder seafloor temperatures (< 277 K) were found to be amenable for CO₂ hydrate formation along the pathway during leakage.

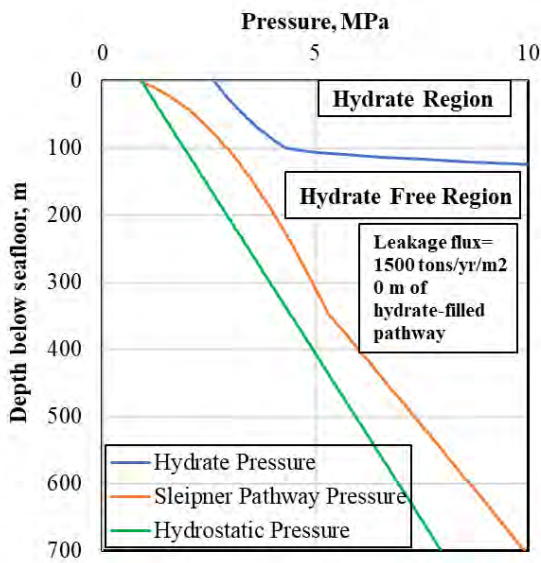


Figure 9: Pressure profile with depth for Sleipner project. No CO₂-hydrates are present in the pathway.

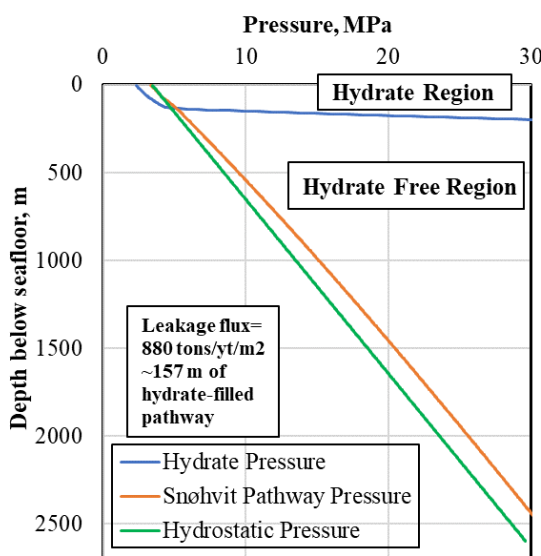


Figure 10: Pressure profile with depth for Snøhvit project. Close to 157m of CO₂-hydrate filled zone is present in the pathway.

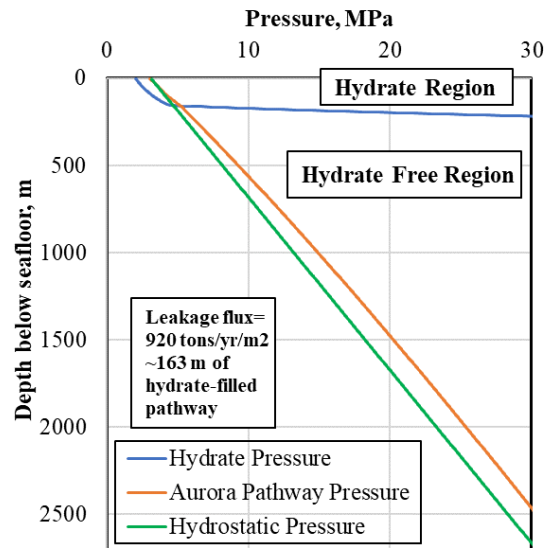


Figure 11: Pressure profile with depth for Aurora project. Close to 163m of CO₂-hydrate filled zone is present in the pathway.

4. Conclusion

The steady-state leakage model estimates leakage fluxes along all types of leakage pathway. Additionally, it has the capability to assess for hydrate stable conditions and estimate the impact of formed hydrates on permeability and leakage fluxes. This model allows quick estimation of fluxes, follows physics-based approach, and fits well into the risk assessment framework. Example calculations were shown for highly idealized representation of leakage pathway and regional conditions commonly observed in Norwegian continental shelf (to mimic offshore CCS operation).

Results indicate permeability has a first-order effect on leakage fluxes. Other factors such as overpressure affect the fluxes, but not as much as the factor of permeability. Open faults leak more than leaky wellbores. Larger seafloor depth (> 300 m) and colder seafloor temperatures (< 277 K) were found to be amenable for CO₂ hydrate formation along the pathway during leakage. Hypothetical leakage at Snøhvit and Aurora project were found to reach CO₂ hydrate stable conditions along the pathway and no hydrates at Sleipner project. Further analysis is needed to check if this may lead to potential blockages and gas chimney formation.

The leakage fluxes estimates shown here should be considered as relative values based on the idealized assumptions rather than predictions of actual values. The geometry and properties of an actual fault will be much more complex than assumed in these simple models. However, the leakage fluxes calculated using a numerical reservoir simulator with a more realistic description of a fault is a challenging task and is also subject to many uncertainties. The results in this paper indicate the importance of taking the multiphase and non-isothermal nature of leakage in such simulations.

Acknowledgements

This work was supported by the SEAMSTRESS project. SEAMSTRESS project is supported by starting grants from the Tromsø Research Foundation and the Research Council of Norway (grant nr. 2878659) awarded to Andrea Plaza-Faverola.

References

- [1] UNFCCC. (2015a). Decision 1/CP.21, in report of the conference of the parties on its twenty-first session, held in Paris from 30 November to 13 December 2015. Addendum Part two: Action taken by the Conference of the Parties at its twenty-first session (FCCC/CP/2015/10/Add.1).
- [2] UNFCCC. (2015b). Synthesis report on the aggregate effect of the intended nationally determined contributions (FCCC/CP/2015/7).
- [3] Leung, D. Y., Caramanna, G., & Maroto-Valer, M. M. (2014). An overview of current status of carbon dioxide capture and storage technologies. *Renewable and Sustainable Energy Reviews*, 39, 426-443.
- [4] RISCs, (2014). A Guide to Potential Impacts of Leakage from CO₂ Storage. *British Geological Survey*, 70.
- [5] Kumar, A., Noh, M. H., Ozah, R. C., Pope, G. A., Bryant, S. L., Sepehrmoori, K., & Lake, L. W. (2005). Reservoir Simulation of CO₂ Storage in Aquifers. *SPE Journal*, 10(03), 336-348.
- [6] IPCC (Intergovernmental Panel on Climate Change), (2005). Special Report on Carbon Dioxide Capture and Storage. Cambridge University Press, Cambridge, UK, New York, NY, USA.
- [7] Stevens, S. H., Kuuskraa, V. A., Gale, J. and Beecy, D. (2001), CO₂ Injection and Sequestration in Depleted Oil and Gas Fields and Deep Coal Seams: Worldwide Potential and Costs. *Environmental Geosciences*, 8: 200–209.
- [8] White, C.M., Strazisar, B.R., Granite, E.J., Hoffman, J.S. and Pennline, H.W., 2003. Separation and capture of CO₂ from large stationary sources and sequestration in geological formations—coalbeds and deep saline aquifers. *Journal of the Air & Waste Management Association*, 53(6), pp.645-715.
- [9] Reeves, S.R. and Schoeling, L., 2001. Geological sequestration of CO₂ in coal seams: reservoir mechanisms field performance, and economics.
- [10] Jimenez, J.A. and Chalaturnyk, R.J., 2003, January. Are Disused Hydrocarbon Reservoirs Safe for Geological Storage of CO₂? In *Greenhouse Gas Control Technologies-6th International Conference* (pp. 471-476). Pergamon.
- [11] Gasda, S.E., Bachu, S. and Celia, M.A., 2004. Spatial characterization of the location of potentially leaky wells penetrating a deep saline aquifer in a mature sedimentary basin. *Environmental geology*, 46(6-7), pp.707-720.
- [12] Tao, Q. and Bryant, S.L., 2014. Well permeability estimation and CO₂ leakage rates. *International Journal of Greenhouse Gas Control*, 22, pp.77-87.
- [13] Rutqvist, J., Birkholzer, J., Cappa, F. and Tsang, C.F., 2007. Estimating maximum sustainable injection pressure during geological sequestration of CO₂ using coupled fluid flow and geomechanical fault-slip analysis. *Energy Conversion and Management*, 48(6), pp.1798-1807.
- [14] Jones, D.G., Beaubien, S.E., Blackford, J.C., Foekema, E.M., Lions, J., De Vittor, C., West, J.M., Widdicombe, S., Hauton, C. and Queirós, A.M., 2015. Developments since 2005 in understanding potential environmental impacts of CO₂ leakage from geological storage. *International Journal of Greenhouse Gas Control*, 40, pp.350-377.
- [15] Pawar, R.J., Bromhal, G.S., Carey, J.W., Foxall, W., Korre, A., Ringrose, P.S., Tucker, O., Watson, M.N. and White, J.A., 2015. Recent advances in risk assessment and risk management of geologic CO₂ storage. *International Journal of Greenhouse Gas Control*, 40, pp.292-311.
- [16] Celia, M.A., Bachu, S., Nordbotten, J.M., Gasda, S.E. and Dahle, H.K., 2005. Quantitative estimation of CO₂ leakage from geological storage: Analytical models, numerical models, and data needs. In *Greenhouse Gas Control Technologies 7* (pp. 663-671). Elsevier Science Ltd.
- [17] Nordbotten, J.M., Celia, M.A. and Bachu, S., 2005. Injection and storage of CO₂ in deep saline aquifers: analytical solution for CO₂ plume evolution during injection. *Transport in Porous media*, 58(3), pp.339-360.
- [18] Chang, K.W., Minkoff, S.E. and Bryant, S.L., 2009. Simplified model for CO₂ leakage and its attenuation due to geological structures. *Energy Procedia*, 1(1), pp.3453-3460.
- [19] Tao, Q., Checkai, D., Huerta, N. and Bryant, S.L., 2011. An improved model to forecast CO₂ leakage rates along a wellbore. *Energy Procedia*, 4, pp.5385-5391.
- [20] Pruess, K., 2004. Numerical simulation of CO₂ leakage from a geologic disposal reservoir, including transitions from super- to subcritical conditions, and boiling of liquid CO₂. *Spe Journal*, 9(02), pp.237-248.
- [21] Ramachandran, H., Pope, G.A. and Srinivasan, S., 2014. Effect of thermodynamic phase changes on CO₂ leakage. *Energy Procedia*, 63, pp.3735-3745.
- [22] Ramachandran, H., Pope, G.A. and Srinivasan, S., 2017. Numerical Study on the Effect of Thermodynamic Phase Changes on CO₂ Leakage. *Energy Procedia*, 114, pp.3528-3536.
- [23] Ramachandran, H., 2017. Modeling CO₂ leakage through faults and fractures from subsurface storage sites (Doctoral dissertation).
- [24] Kumar, A., Maini, B., Bishnoi, P.R., Clarke, M., Zatepina, O. and Srinivasan, S., 2010. Experimental determination of permeability in the presence of hydrates and its effect on the dissociation characteristics of gas hydrates in porous media. *Journal of petroleum science and engineering*, 70(1-2), pp.114-122.
- [25] Masuda, Y., 1997. Numerical calculation of gas production performance from reservoirs containing natural gas hydrates. In *Annual Technical Conference, Soc. of Petrol. Eng., San Antonio, Tex., Oct. 1997*.
- [26] Duan, Z. and Sun, R., 2006. A model to predict phase equilibrium of CH₄ and CO₂ clathrate hydrate in aqueous electrolyte solutions. *American Mineralogist*, 91(8-9), pp.1346-1354.
- [27] Span, R. and Wagner, W., 2003. Equations of state for technical applications. III. Results for polar fluids. *International Journal of Thermophysics*, 24(1), pp.111-162.
- [28] Allen, R., Nilsen, H.M., Lie, K.A., Møyner, O. and Andersen, O., 2018. Using simplified methods to explore the impact of parameter uncertainty on CO₂ storage estimates with application to the Norwegian Continental

- Shelf. *International Journal of Greenhouse Gas Control*, 75, pp.198-213.
- [29] Allis, R., Bergfeld, D., Moore, J., McClure, K., Morgan, C., Chidsey, T., Heath, J. and McPherson, B., 2005, May. Implications of results from CO₂ flux surveys over known CO₂ systems for long-term monitoring. In Fourth annual conference on carbon capture and sequestration, DOE/NETL.
- [30] Plaza-Faverola, A., Bünz, S., Johnson, J.E., Chand, S., Knies, J., Mienert, J. and Franek, P., 2015. Role of tectonic stress in seepage evolution along the gas hydrate charged Vestnesa Ridge, Fram Strait. *Geophysical Research Letters*, 42(3), pp.733-742.
- [31] Bünz, S., Polyakov, S., Vadakkepuliambatta, S., Consolaro, C. and Mienert, J., 2012. Active gas venting through hydrate-bearing sediments on the Vestnesa Ridge, offshore W-Svalbard. *Marine Geology*, 332, pp.189-197.
- [32] Daigle, H. and Dugan, B., 2010. Origin and evolution of fracture-hosted methane hydrate deposits. *Journal of Geophysical Research: Solid Earth*, 115(B11).
- [33] Bezanon, J., Edelman, A., Karpinski, S. and Shah, V.B., 2017. Julia: A fresh approach to numerical computing. *SIAM review*, 59(1), pp.65-98.
- [34] Eiken, O., Ringrose, P., Hermanrud, C., Nazarian, B., Torp, T.A. and Høier, L., 2011. Lessons learned from 14 years of CCS operations: Sleipner. In Salah and Snøhvit. *Energy Procedia*, 4, pp.5541-5548.
- [35] Tasianias, A., Mahl, L., Darcis, M., Buenz, S. and Class, H., 2016. Simulating seismic chimney structures as potential vertical migration pathways for CO₂ in the Snøhvit area, SW Barents Sea: model challenges and outcomes. *Environmental Earth Sciences*, 75(6), p.504.
- [36] Wu, L., Thorsen, R., Ottesen, S., Meneguolo, R., Hartvedt, K., Ringrose, P. and Nazarian, B., 2021. Significance of fault seal in assessing CO₂ storage capacity and containment risks—an example from the Horda Platform, northern North Sea. *Petroleum Geoscience*.
- [37] Waage, M., Singhroha, S., Bünz, S., Planke, S., Waghorn, K.A. and Bellwald, B., 2021. Feasibility of using the P-Cable high-resolution 3D seismic system in detecting and monitoring CO₂ leakage. *International Journal of Greenhouse Gas Control*, 106, p.103240.
- [38] Vesovic, V., Wakeham, W.A., Olchowy, G.A., Sengers, J.V., Watson, J.T.R. and Millat, J., 1990. The transport properties of carbon dioxide. *Journal of physical and chemical reference data*, 19(3), pp.763-808.
- [39] Fenghour, A., Wakeham, W.A. and Vesovic, V., 1998. The viscosity of carbon dioxide. *Journal of physical and chemical reference data*, 27(1), pp.31-44.

SYNTHESIS PROPERTIES OF FeCO₃: UNDERSTANDING THE UNDERGROUND REACTIVE ROCK

*Randi Neerup, Isaac A. Løge, Philip L. Fosbøl**

Center for Energy Resources Engineering (CERE), Department of Chemical and Biochemical Engineering, Technical University of Denmark (DTU), Søtofts Plads 229, 2800, Kgs. Lyngby, Denmark

* Corresponding author e-mail: plf@kt.dtu.dk

Abstract

Combatting anthropogenic CO₂ emissions is one of the humanities considerable challenges, and carbon capture and storage (CCS) technologies are one of the tools that has been proposed for this. FeCO₃ is attracting attention as it has been proposed to be a potential storage unit for CO₂ injection in underground basaltic rock. Through mineral carbonation, dissolved CO₂ reacts with underground reactive divalent metal-containing rock. However, the properties of FeCO₃ is not well understood, and optimal permanent storage hinges on knowledge of the properties of the reactive species. We investigate the influence of synthesis parameters through a variation study, such as temperature, synthesis duration, and pressure. We then investigate the material properties, where the crystal structure and crystalline domains size is examined through XRD, thermal degradation stability with TGA and particle size with SEM. Through this investigation, a fundamental understanding of FeCO₃ was gained, which will enhance the understanding of underground storage in reactive basaltic rock.

Keywords: CCS, Divalent metal carbonates, physiochemical investigation

1. Introduction

Man-made climate change is currently the most significant challenge we face as humanity. A possible mitigation strategy gaining popularity is capturing CO₂ through direct air capture and storing it for future use. Recently, a large-scale pilot experiment on Iceland performed a successful project, where CO₂ was captured and injected into reactive basaltic rock [1]. These rocks consist of Mg, Ca, and Fe. It is essential to understand the different processes occurring to optimize the efficiency of the storage procedure. Calcium carbonation is a well-investigated system. However, to optimize efficiency, it is essential to create knowledge on the carbonation of Fe and Mg. Currently, there exists conflicting evidence on the properties of FeCO₃ [2]. No joint agreement on the colour of the synthesis product can be reached, and the solubility limit is also a debated topic [2]. FeCO₃ can either be used synthetically or as extracted from underground, in the form of siderite. Other species (Mg, Ca) can be incorporated into the crystal lattice as an extracted material, affecting its properties. To investigate

synthetic FeCO₃, it must be consistently the same synthesis product with identical properties when synthesized across the globe. As FeCO₃ reacts readily with the oxygen in the atmosphere, it is not commercially available. Therefore, to ensure that researchers investigate the same product, knowledge must exist of the influence of various synthesis variables.

This study uses a patented synthesis method, utilizing an anoxic environment provided by a glovebox. We explore the synthesis parameter-space to investigate the influence of temperature, synthesis duration, and temperature on FeCO₃ physiochemical properties. By probing the microscopic properties through XRD, macro properties through SEM, and couple these with the thermal stability through TGA, we create a correlation between synthesis parameters and what happens in the nm, μm, and mm scale.

2. Methods

2.1 Materials

FeCl₂·4H₂O, NaHCO₃, and Na₂HCO₃ were obtained from Sigma-Aldrich without purification. Stock solutions of FeCl₂·4H₂O, NaHCO₃, and Na₂HCO₃ were prepared with degassed with N₂ ultra-pure Milli-Q water. The oxygen concentration was acquired with a multimeter (Hach Lange, HQ40D) connected to dissolved oxygen (DO) sensor (Hach Lange, LDO101).

2.2 FeCO₃ synthesis

The FeCO₃ synthesis was prepared in a glovebox (MBRaun) with an anoxic environment. The atmosphere inside the glovebox was via catalyst to trap oxygen species and water.

FeCl₂·4H₂O and NaHCO₃/Na₂CO₃ were mixed in a Fe/CO₂ ratio of 1:4 in a titanium piston cylinder. The piston-cylinder was taken out of the glovebox, pressurized and placed in an oven at a constant temperature. The reaction was terminated by extracting the cylinder. After transferring the cool piston to the glovebox, the supernatant was decanted. FeCO₃ was washed. FeCO₃ was let to dry in the glovebox for two to three days. The adjustable synthesis variables are summarized in Table 1.

Table 1. Parameters for the FeCO₃ synthesis. T=Temperature, P=pressure, R=reaction time

Fe/CO ₂	T (°C)	P (Bar)	R (h)
1:4	130	10	24
1:4	80	10	24
1:4	25	10	24
1:4	130	1	24
1:4	130	5	24
1:4	130	15	24
1:4	130	10	4
1:4	130	10	6
1:4	130	10	12
1:4	130	10	24
1:4	130	10	72
1:4	130	10	96

2.3 Sample characterization

2.3.1 X-ray powder diffraction

The crystal structure of FeCO₃ was determined by x-ray powder diffraction (XRPD) at room temperature. The powder diffraction patterns were collected with a Huber G670 powder diffractometer in the 2θ range 3 to 100° in steps of 0.005° using CuKα₁ radiation (λ = 1.54056 Å) for 10 min. The data were collected in transmission mode from a rotating flat plate sample inclined 45° relative to the primary beam.

Crystalline sizes were determined from the diffractograms via the Scherrer equation. To obtain the sizes through the Scherrer equation, the diffractograms

were fitted to Gaussian first order models from which the FWHM was determined.

2.3.2 Scanning electron microscopy

Scanning electron microscopy (SEM) images have been acquired in a FEI QEISCAN with an acceleration voltage of 20 kV under a high vacuum. Samples were transported in an airtight environment from the glovebox to the SEM. During transfer to the SEM environment, the samples were exposed to less than 1 minute atmospheric conditions. The images were analysed in ImageJ and Gwyddion to obtain the particle sizes. Size distributions were obtained by measuring the diameter of more than 400 particles on each set of data.

2.3.3 Thermogravimetric analysis

Decomposition of FeCO₃ was performed using thermogravimetric analysis (TGA) (TA Instruments, Discovery TGA). The measurements were conducted in a nitrogen atmosphere and in the temperature range 27 to 900 °C with a temperature rate of 10 °C/min.

3. Results and Discussion

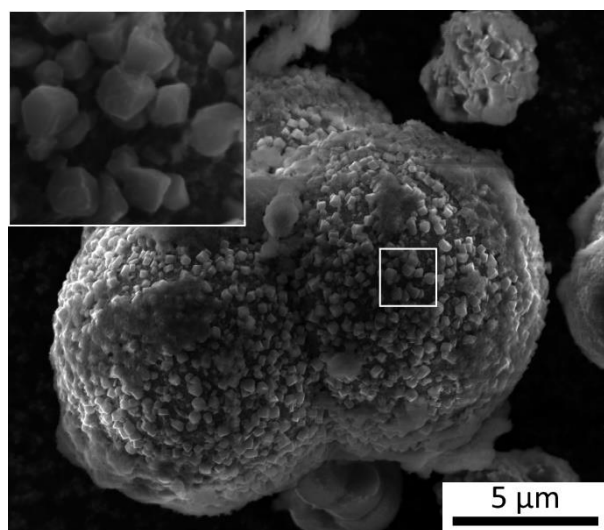


Figure 1. SEM image of FeCO₃

FeCO₃ is known to have a rhombohedral crystal shape associated with that of carbonate crystals. In this work, we observed a hierarchical growth where rhombohedral crystals grow on larger aggregates. The larger particles act as a nucleation centre for the rhombohedral FeCO₃ crystals, see Figure 1. These spherical particles were previously reported as amorphous FeCO₃ (AFC). In our study, the particles were analysed utilizing TEM. It was shown that these particles exhibit crystallinity and can therefore not be AFC. In the following, this terminology will be used throughout. From Figure 2-2, the diameter of the large particle has been referred to as the particle size. At the same time, the individual crystallites are called either by crystallite size or by scattering coherence length. The crystallite sizes and particles sizes are

measured as a function of synthesis parameters, as presented in the following sections.

3.1 Microstructure

The size of the crystalline domains was estimated based on the Scherrer equation. The result can be seen in Figure 2-1. From these sizes, it can readily be concluded that the synthesis temperature and duration affect the resulting crystallite domain size. It should be noted that the synthesis performed for shorter than 24 h and below a temperature of 130 °C all have a crystalline domain size smaller than 3.5 Å. The pressure does not influence the crystallite size, and all synthesis resulted in crystallite size larger than 3.5 Å.

3.2 Macrostructure

The particle size was measured through a statistical analysis of SEM images. From this investigation, it was shown how there was a correlation between the macro properties of the particles and the synthesis parameters.

Particle sizes increased as both temperature, duration and pressure were increased. The most significant increase between process parameters is the pressure. Here the particle diameter is shown to increase from 3 μm to 7.5 μm from 1 bar to 15 bar respectively.

3.3 Influence of micro and macro on the thermal stability

Through TGA, the thermal properties of each product from the different synthesis was determined, see Figure 2-3. From the TGA results, two characteristic degradation paths could be estimated. One with only one steep slope, with a total mass loss of 36 % occurring at 350 °C. This was in agreement with previous observations on FeCO₃. This behaviour was shared for the particles with a crystalline size large than 3.3 Å. This included the ones synthesized for longer than 24 h, at 130 °C and was observed for all pressure. The weight loss of ~36 % would agree with a decarbonisation through the following reaction:

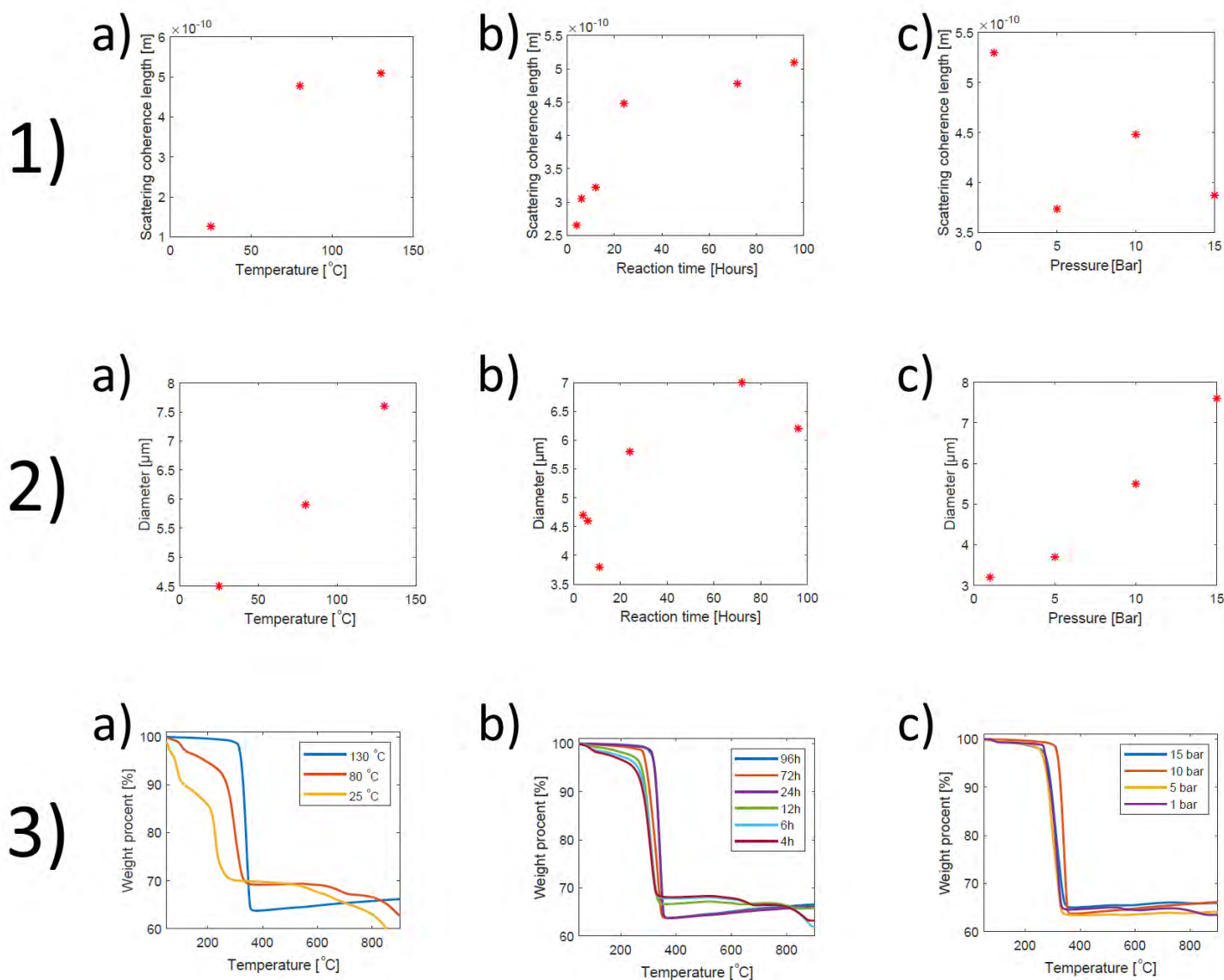
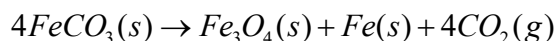
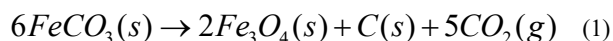


Figure 2. Physicochemical properties of FeCO₃. a), b) and c) denotes a change in synthesis temperature, reaction duration or pressure. 1) The Scattering coherence length. 2) The particle diameter. 3) Thermogravimetric analysis



The second degradation path had a gradual mass loss observed from 100 °C to 350 °C, and above 350 °C, there was a total mass loss of 32%. After 350 °C several weight losses are observed at 340, 600, and 800 °C. This was seen for particles with a crystallite size smaller than 3.3 Å. This indicates a critical crystalline size, under which there is a change of degradation path. The weight loss of 32 % can be explained by the reaction presented below



3. Conclusion and future implications

The main findings of this work can be summarized as follows:

- There exists a correlation between synthesis duration and temperature with the micro properties of FeCO₃. Longer synthesis and higher temperatures lead to large crystallite domains. However, the crystallite domain size is invariant with synthesis pressure.
- Macrosized (the particle diameter), increase with an increase in all synthesis variables
- The thermal degradation of FeCO₃ is not dependent on macro size, while it is heavily

affected by the micro properties. Crystalline domains larger than 3.3 Å all exhibit a sharp weight loss at 350 °C, while smaller domains show a gradual weight loss.

These findings show the importance of accurately knowing the variables under which the synthesis was performed. All products would be characterized as FeCO₃ through XRD. However, by a closer analysis, it became evident that the physicochemical properties were greatly dependent on the synthesis. As Fe constitutes a significant part of basaltic rock, and FeCO₃ is one of the products formed upon CO₂ injection it becomes apparent that mapping the parameter space of the synthesis is of utmost importance.

Acknowledgements

This work received funding from the Danish Hydrocarbon Research and Technology Centre (DHRTC) through the on-going project "CO₂ impact on corrosion product (FeCO₃) solubility"

References

- [1] J. M. Matter et al., "The CarbFix Pilot Project - Storing carbon dioxide in basalt," *Energy Procedia*, vol. 4, pp. 5579–5585, 2011.
- [2] P. L. Fosbøl, K. Thomsen, and E. H. Stenby, "Review and recommended thermodynamic properties of FeCO₃," *Corrosion Engineering Science and Technology*, vol. 45, no. 2, pp. 115–135, Apr-2010.

POST-COMBUSTION CO₂ CAPTURE: A COMPARISON BETWEEN COMMERCIALLY READY TECHNOLOGIES

Stefano E. Zanco, Jose-Francisco Pérez-Calvo, Viola Becattini and Marco Mazzotti*

Institute of Process Engineering, ETH Zurich, Sonneggstrasse 3, Zurich, 8092, Switzerland

* Corresponding author e-mail: marco.mazzotti@ipe.mavt.ethz.ch

Abstract

Retro-fitting of post-combustion CO₂ capture units to coal fired power plants is key to the transition to a net-zero CO₂ emission reality. Different separation technologies have been found suitable for CO₂ capture, but a more comprehensive approach is required to identify the most viable option among those commercially available. In this study we analyze the three most established technologies, namely absorption, adsorption and membrane separation, comparing both their exergetic efficiency and their total cost. This assessment provides an overview of the technical differences among the three capture routes and a realistic estimate of the expenditures associated with post-combustion CO₂ capture, as of today.

Keywords: Post-combustion CO₂ capture; techno-economic analysis; piperazine; TSA; membranes

1. Introduction

Pursuing the global goal of zero carbon-emissions by 2050 and keeping global warming below 1.5°C, carbon capture technologies offer a way to decarbonize a range of sectors, including the energy and the heavy industry sectors, where it is proving difficult to meaningfully reduce emissions in a near future[1,2,3].

More specifically, CO₂ capture via a post-combustion capture system represents the most immediate and viable option to retrofit existing plants, as it represents the only possibility to reduce the emissions at the stack without affecting the manufacturing process[3,4]. As regards post-combustion systems, the availability of a range of commercial-ready technologies suitable for point sources of different size and typology is crucial to reduce the price of the emission reduction, thus speeding up the

transition toward a net-zero-emission reality, before the complete decommission of fossil fuel combustors.

Amine wash is acknowledged as the least energy intensive among post-combustion technologies[3], and it is the only one whose operability has been already proven through pilot testing on a variety of scales[5,6]. Adsorption-based and membrane-based processes have been instead broadly studied and tested at lab or pilot scale. They benefit from a more basic process structure, where fewer sub-processes and devices are involved[7]. Although each one of these components is in general expensive (both in terms of capital and operational costs) and their cost tends to scale up linearly with the plant size, the price of the avoided CO₂ can be positively affected by the overall process simplicity. However, both technologies suffer from a strong limitation: Both commercial sorbents and commercial membranes for CO₂ separation cannot cope with the moisture of the flue gas, thus requiring a pretreatment unit for dehydration (Figure 1).

With this contribution, we aim at ranking the performance, in terms of both efficiency and capture costs, of adsorption and membranes in comparison to the most established absorption technology. The twofold nature of the detailed techno-economic analysis we have performed allows us both to highlight the differences in the final results, and to justify them consistently with the intrinsic features of the chemical separation processes involved.

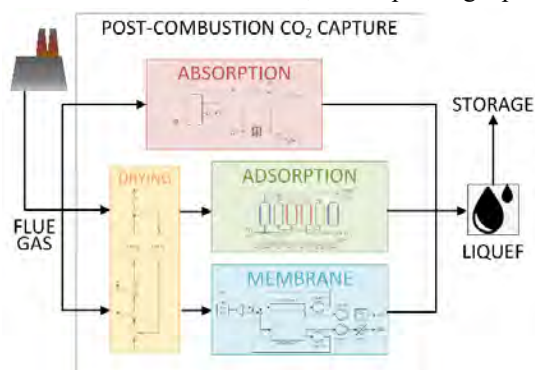


Figure 1. Schematic representation of the three post-combustion capture alternatives investigated within a general CCS system. The coal combustion flue gas is conveyed to the carbon capture plant, after a dehydration treatment in the case of adsorption or membrane. After the separation, CO₂ is ready to be liquefied and then transported to storage.

2. Methods

To compare the three technologies, an example case of post-combustion application has been chosen. Our reference emitter consists in a large point source, which

releases a flow rate of 10'000 tons per day of flue gas with a concentration of 12% vol. CO₂ (dry based), typical of a coal fired combustion. The capture units considered are required to meet those separation performance that are commonly assumed for Carbon Capture and Storage (CCS) applications, i.e. a rate of CO₂ recovery of 90% and a final CO₂-product purity of at least 96%.

A very straightforward path to the identification of the most suitable process design for each technology would be that of optimizing the process design subject to the minimization of the total plant cost. This approach has though a major drawback. In fact, the universality of the assumptions required to perform a cost analysis is rather limited, and the uncertainties deriving from the specificity of each assumption might impact the definition of an optimal design that could be considered as such from a more general prospective.

For this reason, in this study a two-step approach is preferred:

- First of all, each separation process is optimized from a merely technical point of view, aiming at maximum plant productivity and minimum exergy consumption, which can be reasonably considered technical proxies of the Capital Expenditures (CapEx) and Operational Expenditures (OpEx), respectively, associated with the realization and operation of a capture plant. This two-objective optimization yields a set of equivalent optima (a Pareto set).

- In a second step, the process designs forming the Pareto set are screened by means of a detailed cost analysis, assessing the CapEx and OpEx involved, estimating the total cost of capture, in terms of monetary annualized cost per ton of avoided CO₂ emission, and thus identifying the single economic optimum among the Pareto set.

Detailed rate-based models have been deployed for the simulation of the core process of each technology (i.e. the absorption columns, the adsorption column and the fibers of the membrane modules), and the cost estimations have been extended to include all the equipment involved in the CO₂ capture process[8,9,10,11].

Table 1. Boundary conditions for the operation of the CO₂ capture unit.

Parameter	Unit	Value
Flue gas composition	%	12/88 CO ₂ /N ₂
Flue gas relative humidity	%	95 @ 30°C
Flue gas temperature	°C	30
Flue gas pressure	bar(a)	1.3
CO ₂ recovery rate	%	90
CO ₂ purity	%	≥ 96

3. Technologies

The real potential of each separation technology for post-combustion CO₂ capture must be evaluated consistently with its state of technical development as of today, consistently with the fact that the retro-fitting of an emitting plant is a fast implementable solution, which can compensate on the short run for the unavailability of stable, economically viable and reliable carbon free

energy sources. Keeping in mind this concept, in this study we have sensibly decided to opt for ready-to-build process designs, which resort to commercially available materials and equipment.

3.1 Absorption

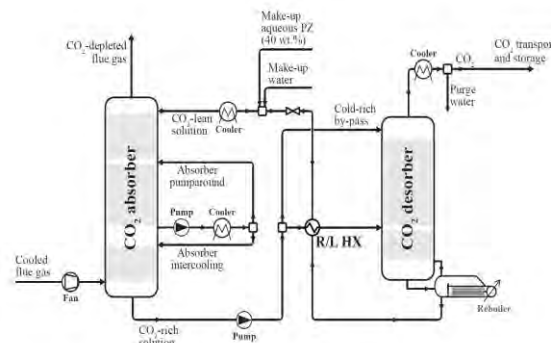


Figure 2. Process scheme of absorption capture unit.

The core of the process consists of two absorption columns, an absorber and a desorber. In the former CO₂ is removed from the flue gas by means of an aqueous solution of piperazine, a broadly studied solvent capable of fast absorption kinetics, high resistance to chemical and thermal degradation, low energy requirements for regeneration and few volatility and corrosion issues[3,12,13,14,15].

In the desorber this solvent is regenerated by providing thermal power, thus releasing a CO₂-rich gaseous product stream, which leaves the capture plant with a high water vapor content. In order to minimize the energy required for solvent regeneration, a significant share of the heat transferred to the cold loaded solvent is recovered by heat exchange with the hot lean solvent stream that exits the reboiler of the desorber, in the so-called Rich/Lean Heat Exchanger.

The most simple absorber-desorber process scheme has been also complemented with two process modifications that have been proven to improve significantly performance of the amine-based capture processes, without being capital-intensive[16]. These are: On the one hand, the intercooling of the liquid stream and the partial pump-around recycle at the absorber; on the other hand, the cold-rich bypass at the desorber. The process plant scheme is shown in Figure 2.

3.2 Adsorption

Temperature Swing Adsorption (TSA) processes use high temperatures to regenerate the sorbent after it has been saturated by the CO₂ withdrawn from the flue gas. The virtue of this solution resides in two key advantages over pressure dependent regeneration routes: 1) the possibility of using thermal energy at relatively low temperature[17,18], which is exergetically less valuable than mechanical energy and opens the way to the exploitation of recovered waste heat fluxes, and 2) the avoidance of any pre-compression of the large flue gas flow rate.

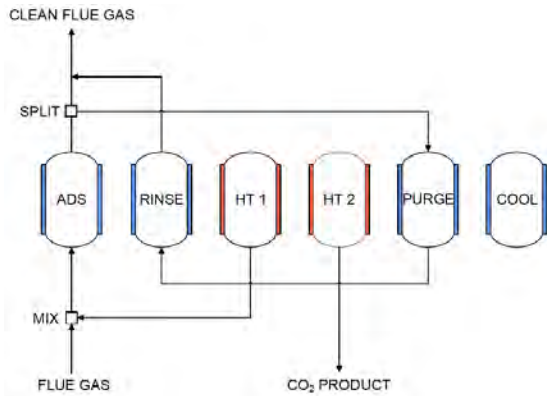


Figure 3. Process scheme of TSA cycle configuration.

The adsorption cycle configuration adopted in this study is the cycle D configuration proposed by Joss et al.[19], which improves the performance of the most standard TSA cycle by means of the introduction of a purge-rinse open loop, which recycles any CO₂ left at the end of the regeneration into the adsorption phase[20], and of a heating step split, a solution finalized at an increase in purity of the CO₂-rich product. The conceptual scheme of the adsorption cycle is displayed in Figure 3.

As regards the adsorbent, a conservative choice has been made in considering zeolite 13X, a very well known CO₂ sorbent, suitable for this type of separations and still believed to be a competitive alternative to more expensive, tailor-made materials[21,22,23]. Due to the high selectivity of zeolites towards water[24], a relevant implication of the use of this sorbent is the need for the pre-dehydration of the flue gas ahead of the separation, as previously mentioned. In this study, the flue gas is dried down to a water content of 100 ppm by means of a simple two-step TSA process, where water is adsorbed on silica gel.

3.3 Membranes

The high modularity offered by the membrane based separation systems, together with the relatively low cost of the membrane materials and the easy operation of the modules, advocate membrane separation as an interesting alternative to absorption and adsorption technologies[10,25,26,27].

In the recent years, some commercial applications specifically aimed at post-combustion CO₂ capture have

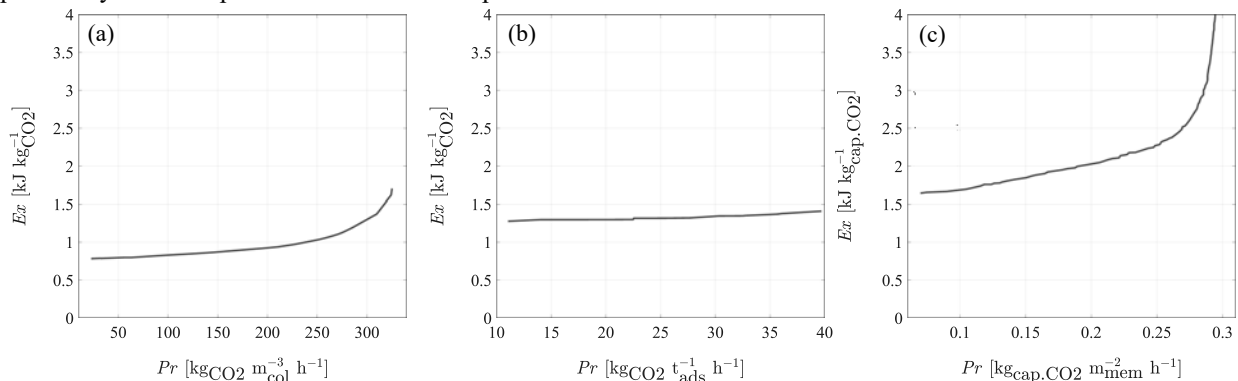


Figure 5. Comparison of the Productivity-Exergy Pareto fronts for the three post-combustion separation technologies (a) absorption, (b) adsorption, and (c) membranes.

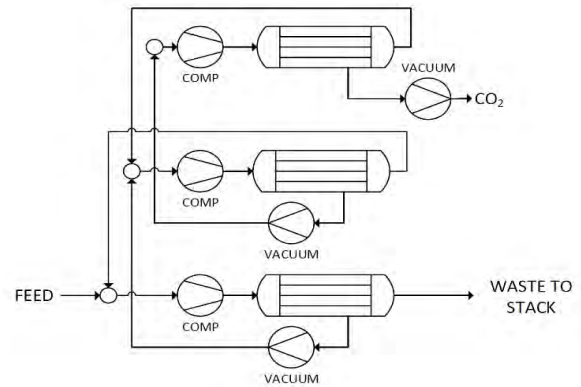


Figure 4. Process scheme of membrane capture unit.

appeared on the market. An example of this is Polaris, a polymeric membrane developed, produced and commercialized by MTR[28,29], whose favorable features place its performance close to Robenson's Upper Bound[30]. The suitability of this membrane for CO₂ capture from a binary CO₂/N₂ mixture has been also proven by several studies[29,31,32].

The capture unit analyzed in this study adopts the Polaris membrane in a series of three different separation stages, all interconnected. At each stage the retentate is recirculated back to the previous stage, while the permeate is processed further in the following one, as shown in Figure 4. At each stage, the pressure ratio required for permeation is guaranteed by the combined contribution of vacuum pumps at the permeate side and compressors at the retentate side.

As in the case of adsorption, due to the loss in performance associated with the presence of moisture, the flue gas is dehydrated ahead of the separation in a dedicated TSA unit.

4. Technical analysis

The process design of the three technologies have been optimized subject to the maximization of the unit productivity and the minimization of the exergy requirements for separation. In order to evaluate this performances, the two indicators Pr and Ex are here adopted to show the comparative results.

The definition of the exergy consumption, Ex, is common to the three technologies. Within this index

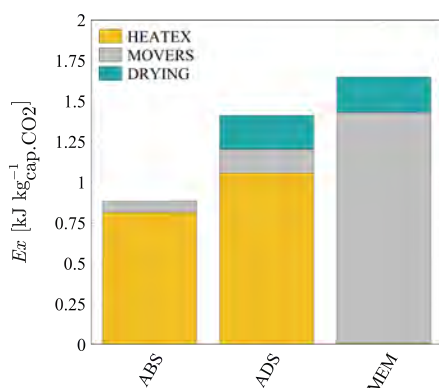


Figure 6. Breakdown of the exergy contributions of each separation technology.

different energetic contributions are considered, each of them weighted according to its exergetic content, in order to make them comparable, consistently with the concept of second principle efficiency. The total consumption is expressed in specific terms of exergy per unit CO₂ captured.

The definition of the productivity, Pr , is instead technology dependent, as it would be impossible to identify a single unit of measurement that could represent the specificity of each separation mean. In order to identify the optimum design, it is preferable to resort to an indicator which directly relates to the deployed separation material. For this reason, for each technology, the flow rate of captured CO₂ is divided here by a different denominator, that is:

- for absorption, the unit volume of vessel (including adsorber, desorber and rich/lean heat exchanger), which is also representative of the amount of piperazine solution required for the separation;
- for adsorption, the unit mass of sorbent;
- for membranes, the surface of the membrane.

The results obtained for the three technologies are displayed in figure 5. A few observations can be drawn at a first glance:

- The technologies can be ranked rather univocally in terms of exergy demand, with absorption once again proving to be the least energy intensive among the three (with a minimum at 0.8 MJ per ton of CO₂ captured), followed by adsorption, and eventually membranes.
- For all of three, the tradeoff between a lower exergy consumption and a higher plant productivity is evident, although for adsorption the curve is significantly more flat than in the other two cases, this identifying that for a TSA cycle optimizing the process configuration has a higher impact on the sizing of the plant than on the actual energy demand.

As previously mentioned, the analysis of the exergy consumption allows for the comparison of different energy sources. In fact, three technologies rely differently on heat sources and mechanical power for both regeneration and pretreatment of the flue gas (the pre-drying unit of adsorption and membranes), and clearly illustrated in Figure 6. Here the different terms forming the total exergy consumptions have been categorized according to the piece of equipment they are associated with, as follows:

- **MOVERS**, including fans, compressors and vacuum pumps for gas streams, as well as pumps for liquid streams, and thus related to the consumption of mechanical power, which in this study is assumed to be available in the form of electricity;
- **HEATEX**, including all heat exchangers, either internal or related to the provision of heat from a hot source, which in this study is identified as stream of condensing steam at the temperature required by the process;
- **DRYING**, including all pieces of equipment constituting the pre-dehydration TSA unit (only present in the case of adsorption and membrane technologies).

From a quick observation of the diagram, it is possible to infer how absorption and adsorption strictly depend on the provision of a thermal power made available by a hot source, which is the main contributor to the energy required for the regeneration of both the solvent (for the piperazine) or the sorbent (for zeolite 13X). The membrane process, instead, resorts almost completely to the mechanical power required for to move vacuum pumps and compressors.

Moreover, both adsorption and membranes pay an additional consumption fee because of the impossibility of processing a moist flue gas, which accounts for a considerable share of the total energy requirement.

5. Cost analysis

Following the same approach adopted by Hasan et al.[33,34], the cost analysis of this study is finalized to the identification of a single economic index, the Total Annualized Cost (TAC) of the capture plant, specific for unit mass of CO₂ avoided. Considering the amount of CO₂ avoided instead of the amount of CO₂ captured allows taking into account also the impact of the energy sources on the final cost of capture, consistently with the fact that the deployment of post-combustion capture units like these is realistic within a scenario where fossil fuels still play a major role in the panorama of power production.

The total annualized cost is the sum of two main contributions, i.e. the Capital Expenditures (CapEx) and Operational Expenditures (OpEx):

$$TAC = CapEx + OpEx$$

The latter includes all costs related to the utilities required for process operation (mainly the energy supplies), whereas the former is computed as the sum of the initial purchase costs of all the installed pieces of equipment. This capital investment is subject to annualization, and must be added to a further maintenance cost

$$CapEx = \phi TPC + AMC$$

with TPC being the total plant cost, AMC the annual maintenance cost, and ϕ the capital recovery factor, which relates the discount rate i and the number of annuities n (equal to the plant lifetime) and is commonly defined as

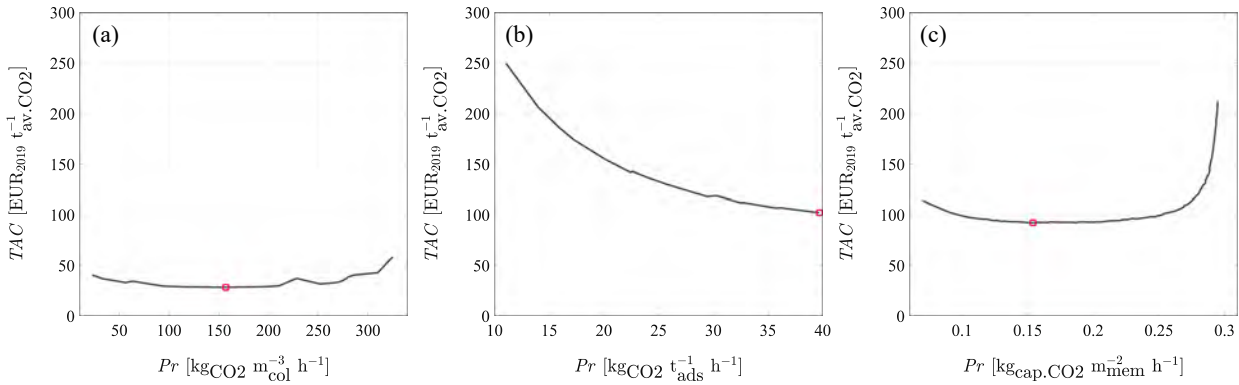


Figure 7. Comparison of Productivity-TAC curves for the three post-combustion separation technologies (a) absorption, (b) adsorption and (c) membranes. For each technology, the point corresponding to the process design associated with the minimum cost is indicated by a red square.

$$\phi = \frac{i(i+1)^n}{(i+1)^n - 1}$$

All costs are calculated according to Hasan et al. and reported in EUR referred to the year 2019. A list of assumptions made for the cost analysis is available in Table 2.

Table 2. Main parameters for the cost analysis and the calculation of the CO₂ avoided emissions.

Parameter	Unit	Value
capital recovery factor, ϕ		0.154
annual operation time	h	8000
CO ₂ footprint of steam [35]	tCO ₂ /TJ	62.3
CO ₂ footprint of electricity [36]	tCO ₂ /MWh	0.41
cost of steam	\$ ₂₀₁₉ /ton	6
cost of electricity	\$ ₂₀₁₉ /kWh	0.07
cost of piperazine solution	\$ ₂₀₁₉ /ton	6000
cost of zeolite 13X	\$ ₂₀₁₉ /ton	1300
Cost of MTR Polaris membrane	\$ ₂₀₁₉ /m ²	50

The costs have been analyzed for each technology for the chosen example case, corresponding to a daily flow rate of 10'000 tons of flue gas. The allocation of the costs is reported dividing them into a few main categories, which correspond to those already used for the analysis of the exergy consumption, apart from the additional TECH, which considers all technology specific pieces of equipment and flows.

In Figure 7 the curves of the costs corresponding to the Pareto sets of Figure 5 are displayed.

The tradeoff between CapEx and OpEx, as foreseen by the two performance indicators Ex and Pr, is evident both for the absorption and for the membrane case, where at low productivity the impact of a bigger plant size negatively affects the overall capture cost, while at high exergy consumption the cost related with the provision of mechanical and thermal power compromises the advantages offered by a more intensive exploitation of the separation mean.

The case of adsorption is, instead, different. The flat trend of the Pareto front in the productivity-exergy domain causes the cost curve to be strictly decreasing with the plant size, given that the cost related to the energy supply is rather constant along the Pareto set.

To better understand this trends, it is helpful to analyze the different shares of CapEx and OpEx for the optimum design identified along the cost curves, i.e. the process design associated with the minimum total cost. The shares for the three technologies are reported in Figure 8. The relevant role played by the cost of the equipment in the case of the TSA process is reflected in the high share of CapEx on the total cost for adsorption. The purchase cost of the adsorption columns is so high that it overcompensates the lower exergy consumption of the TSA cycle compared to the membrane process, which, in the end, is less efficient in thermodynamic terms, but nevertheless less expensive.

The advantage of the piperazine wash is, in terms of total cost, twofold. On the one hand, the low energy intensity of this capture process allows for the containment of the OpEx; on the other hand, the scalability of the absorption vessels eases the exploitation of the economies of scale that are involved in the costing of the purchased equipment, making it particularly convenient at large scale. It is to consider that in the case of both adsorption and membranes, the core separation unit (adsorption column and membrane module, respectively) cannot offer the same flexibility in terms of unit sizing. Therefore, for these two technologies a scale-out approach, rather than a scale-up one, is necessarily implemented when shifting towards larger plant sizes, resorting to large numbers of adsorption columns or membrane modules that operate in parallel. This reduces sensibly the benefit deriving from the economies of scale.

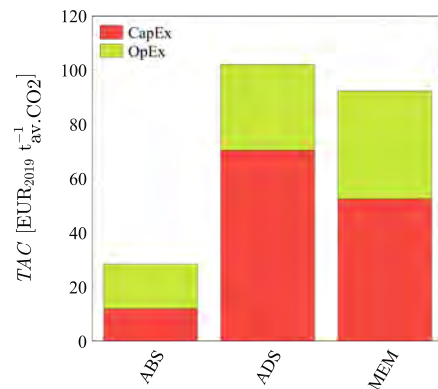


Figure 8. TAC cost for the optimum process design of each technology, highlighting the contribution of CapEx and OpEx.

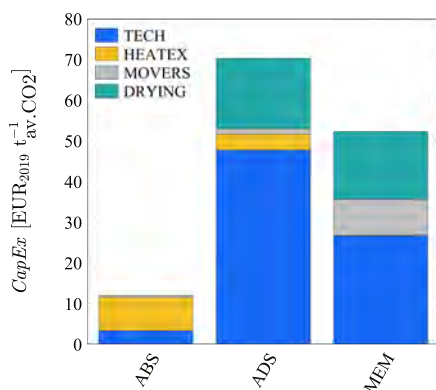


Figure 9. Cost breakdown of the CapEx associated with the optimum process design of each technology.

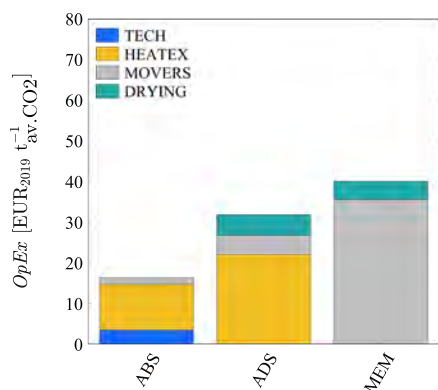


Figure 10. Cost breakdown of the OpEx associated with the optimum process design of each technology.

This effect is clearly identifiable when looking at the allocation of the cost terms for both CapEx and OpEx, as shown in Figure 9. For both adsorption and membranes, the TECH share of the cost. This includes the adsorption columns (together with their internal heat exchanging system, while HEATEX accounts for additional heat exchangers required for the conditioning of the gas streams along the recycles) and the membrane modules, for TSA and membranes respectively, and covers the largest share of the capital expenditures. Notably, the second largest share is that associated with the pre-drying unit.

As regards the operational costs, it is worth noticing that the absorption process is the only one featuring a technology related term of OpEx. It consists in the cost of the make-up flowrate of piperazine solution, made necessary by the partial volatilization and degradation of the solvent. Differently from the zeolite beads and the polymeric membrane, which require to be replaced only few times during the plant lifetime, a flowrate of solvent must be continuously fed to the amine wash plant, and is therefore accounted for as an operational cost. It accounts for about 15% of the total OpEx for absorption.

The rest of the operational cost is strictly related to the energy inputs of the systems, and thus represented by the cost of electricity for the membrane case, and of the hot steam for the other technologies.

6. Conclusions

With the present work, we have presented a comparison between three commercially ready technologies for post-combustion CO₂ capture, namely absorption, adsorption, and membranes. The process design of each of them has been firstly optimized for the capture of CO₂ out of a coal combustion flue gas, aiming at identifying a set of optimal operation designs that could express the tradeoff between low energy intensity and high plant productivity. Among this set of optima, the final process design has been elected based on total cost minimization, taking into consideration both the capital and the operational expenditures deriving from the capture process.

In conclusion, absorption has been confirmed as the least energy intensive, as well as the least expensive among the three technologies. However, the comparison has identified the rationale behind these results, highlighting how the differences in cost reflect intrinsic features of the three separation routes, in particular:

- the use of different energy sources, mainly hot utilities or mechanical power, and the consequence of their impact in terms of further CO₂ emissions, which should be accounted for by looking at the specific costs per unit CO₂ avoided;
- the technical limitations of the separation mean (solid sorbents and polymeric membranes) to perform CO₂ capture in presence of moisture;
- the technical limitations in the sizing of the pieces of equipment, which commits to the choice of a scale-out approach rather than a full scale-up when moving towards larger plant sizes, thus preventing any profit from the economies of scale.

References

- [1] Masson-Delmotte V, Zhai P, Pörtner HO, Roberts D, Skea J, Shukla P, Pirani A, Moufouma-Okia W, Péan C, Pidcock R, et al., Global warming of 1.5°C: An IPCC special report on the impacts of global warming of 1.5°C above pre-industrial levels and related global greenhouse gas emission pathways, in the context of strengthening the global response to the threat of climate change, sustainable development, and efforts to eradicate poverty, <https://www.ipcc.ch/sr15/>, 2018, accessed on: 27-10-2020
- [2] Gabrielli P, Gazzani M, Mazzotti M, The role of carbon capture and utilization, carbon capture and storage, and biomass to enable a net-zero-CO₂ emission chemical industry, *Ind. Eng. Chem. Res.* 59, 2020, pp. 7033-7045
- [3] Bui M, Adjiman CS, Bardow A, Anthony EJ, Boston A, Brown S, Fennell PS, Fuss S, Galindo A, Hackett LA, Hallett JP, Herzog HJ, Jackson G, Kemper J, Krevor S, Maitland GC, Matuszewski M, Metcalfe IS, Petit C, Puxty G, Reimer J, Reiner DM, Rubin ES, Scott SA, Shah N, Smit B, Trusler JPM, Webley P, Wilcox J, Mac Dowell N, Carbon capture and storage (CCS): the way forward, *Energy Environ. Sci.* 11 (5), 2018, pp.1062-1176
- [4] Hills T, Leeson D, Florin N, Fennell P, Carbon capture in the cement industry: technologies, progress, and retrofitting, *Environ. Sci. Technol.* 50 (1), 2016, pp 368-377
- [5] Boot-Handford ME, Abanades JC, Anthony EJ, Blunt MJ, Brandani S, Mac Dowell N, Fernandez JR, Ferrari MC, Gross R, Hallett JP, Haszeldine RS, Heptonstall P, Lyngfelt A, Makuch Z, Mangano E, Porter RTJ, Pourkashanian M,

- Rochelle GT, Shah N, Yao JG, Fennell PS, Carbon capture and storage update, *Energy Environ. Sci.* 7 (1), 2014, pp. 130–189
- [6] MacDowell N, Florin N, Buchard A, Hallett J Galind A, Jackson G, Adjiman CS, Williams CK, Shah N, Fennell P, An overview of CO₂ capture technologies, *Energy Environ. Sci.* 3 (11), 2010, pp. 1645-1669
- [7] Ebner AD, Ritter J, State-of-the-art adsorption and membrane separation processes for carbon dioxide production from carbon dioxide emitting industries, *Sep. Sci. Tech.* 44 (6), 2009, pp. 1273-1421
- [8] Pérez-Calvo JF, Müller C, Cordiano B, Mazzotti M, Rigorous technical optimization and cost analysis of solvent-based CO₂ capture processes applied to different flue gas compositions: A case study using aqueous piperazine solutions as absorbent, 2021, in preparation
- [9] Casas N, Schell J, Pini R, Mazzotti M, Fixed bed adsorption of CO₂/H₂ mixtures on activated carbon: experiments and modeling, *Adsorption* 18, 2012, pp 143-161
- [10] Gabrielli P, Gazzani M, Mazzotti M, On the optimal design of membrane-based gas separation processes, *J. Memb. Sci.* 526, 2017, pp. 118-130
- [11] Zanco SE, Pérez-Calvo JF, Gasós A, Cordiano B, Becattini V, Mazzotti M, Post-combustion CO₂ capture by solvents, sorbents and membranes: a tech-economic comparative assessment, 2021, in preparation
- [12] Rochelle GT, Wu Y, Chen E, Akinpelumi K, Fischer KB, Gao T, Liu CT, Selinger JL, Pilot plant demonstration of piperazine with the advanced flash stripper, *Int. J. Greenh. Gas Control* 84, 2019, pp. 72-81
- [13] Lin YJ, Chen E, Rochelle GT, Pilot plant test of the advanced flash stripper for CO₂ capture, *Faraday Discuss.* 192, 2016, pp. 37-58
- [14] Zhang Y, Sachde D, Chen E, Rochelle G, Modeling of absorber pilot plant performance for CO₂ capture with aqueous piperazine, *Int. J. Greenh. Gas Control* 61, 2017, pp. 300-313
- [15] Tsay C, Pattinson RC, Zhang Y, Rochelle GT, Baldea M, Rate-based modeling and economic optimization of next-generation amine-based carbon capture plants, *Appl. Energy* 252, 2019, n. 113379
- [16] Le Moulec Y, Neveux T, Al Azki A, Chikukwa A, Hoff KA, Process modifications for solvent-based post-combustion CO₂ capture, *Int. J. Greenh. Gas Control* 31, 2014, pp. 96-112
- [17] Harlick PJ, Tezel FH, An experimental adsorbent screening study for CO₂ removal from N₂, *Microp. Mesop. Mater.* 76 (1-3), 2004, pp 71-79
- [18] Samantha A, Zhao A, Shimizu GK, Sarkar P, Gupta R, Post-combustion CO₂ capture using solid sorbents: a review, *Ind. Eng. Chem. Res.* 51 (4), 2012, pp. 1438-1463
- [19] Joss L, Gazzani M, Mazzotti M, Rational design of temperature swing adsorption cycles for post-combustion CO₂ capture, *Chem. Eng. Sci.* 158, 2017, pp 381-394
- [20] Reynolds SP, Mehrotra A, Ebner AD, Ritter JA, Heavy reflux PSA cycles for CO₂ recovery from flue gas: Part I, performance evaluation, *Adsorption* 14 (2-3), 2008, pp. 399-413
- [21] Merel J, Clause M, Meunier F, Experimental investigation of CO₂ post-combustion capture by indirect thermal swing adsorption using 13X and 5A zeolites, *Ind. Eng. Chem. Res.* 47 (1), 2008, pp. 209-215
- [22] Subramanina Balashankar V, Rajendran A, Process optimization-based screening of zeolites for post-combustion CO₂ capture by vacuum swing adsorption, *Sustain. Chem. Eng.* 7 (21), 2019, pp. 17747-17755
- [23] Hefti M, Marx D, Joss L, Mazzotti M, Adsorption equilibrium of binary mixtures of carbon dioxide and nitrogen on zeolite ZSM-5 and 13X, *Microp. Mesop. Mater.* 215, 2015, pp. 215-226
- [24] Hefti M, Mazzotti M, Postcombustion CO₂ capture from wet flue gas by temperature swing adsorption, *Ind. Eng. Chem. Res.* 57, 2018, pp. 15542-15555
- [25] Brunetti A, Scura G, Barbieri G, Drioli E, Membrane technologies for CO₂ separation, *J. Memb. Sci.* 359 (1-2), 2010, pp. 115-125
- [26] Luis P, Van Gerven T, Van der Bruggen B, Recent developments in membrane-based technologies for CO₂ capture, *Progress in En. Comb. Sci.* 38 (3), 2012, pp 419-448
- [27] Xu J, Wu H, Wang Z, Qiao Z, Zhao S, Wang J, Recent advances on the membrane processes for CO₂ separation, *Chinese J. Chem. Eng.* 26 (11), 2018, pp. 2280-2291
- [28] Robeson LM, The upper bound revisited, *J. Memb. Sci.* 320 (1-2), 2008, pp. 390-400
- [29] Lin H, He Z, Sun Z, Vu J, Ng A, Mohammed M, Knip J, Merkel TC, Wu T, Lambrecht RC, CO₂-selective membranes for hydrogen production and CO₂ capture – Part I: membrane development, *J. Memb. Sci.* 457, 2014, pp. 149-161
- [30] White LS, Wei X, Pande S, Wu T, Merkel TC, Extended flue gas trials with a membrane-based pilot plant at a one-ton-per-day carbon capture rate, *J. Memb. Sci.* 496, 2015, pp. 48-57
- [31] Merkel Tc, Lin H, Wei X, Baker R, Power plant post-combustion carbon dioxide capture: an opportunity for membranes, *J. Memb. Sci.* 359 (1-2), 2010, pp. 126-139
- [32] Turi DM, Ho M, Ferrari MC, Chiesa P, Wiley DE, Romano MC, CO₂ capture from natural gas combined cycles by CO₂ selective membranes, *Int. J. Greenh. Gas Control* 61, 2017, pp. 168-183
- [33] Hasan MM, Baliban RC, Elia JA, Floudas CA, Modeling, simulation and optimization of postcombustion CO₂ capture for variable feed concentration and flow rate. 1. Chemical absorption and membrane processes, *Inf. Eng. Chem. Res.* 51 (48), 2012, pp. 15642-15664
- [34] Hasan MM, Baliban RC, Elia JA, Floudas CA, Modeling, simulation and optimization of postcombustion CO₂ capture for variable feed concentration and flow rate. 2. Pressure swing adsorption and vacuum swing adsorption processes, *Inf. Eng. Chem. Res.* 51 (48), 2012, pp. 15665-15682
- [35] Voldsund M, Gardarsdottir MO, De Lena E, Pérez-Calvo JF, Jamali A, Berstad D, Fu C, Romano MC, Roussanaly S, Anantharaman R, Hoppe H, Sutter D, Mazzotti M, Gazzani M, Cinti G, Jordal K, Comparison of technologies for CO₂ capture from cement production—Part 1: technical evaluation, *Energies* 12 (3), 2019, n. 559
- [36] Moro A, Lonza L, Electricity carbon intensity in European member states: impacts on GHG emission of electric vehicles, *Transp. Res. Part D: Transp. Environ.*, 64, 2018, pp. 5-14

EFFECTIVE PERMEABILITY OF DEFORMATION BANDS IN FAULT DAMAGE ZONES – CAN DEFORMATION BANDS REDUCE THE RISK OF FAULT LEAKAGE?

Runar L. Berge^{1*}, Sarah E. Gasda¹, Eirik Keilegaveln², Tor H. Sandve¹

¹ NORCE, Bergen, Norway

² Department of Mathematics, University of Bergen, Bergen, Norway

* Corresponding author e-mail: rube@norce-research.no

Abstract

Faults are major geological structures that can dominate the flow paths in subsurface reservoirs by, e.g., connecting otherwise unconnected layers. In CO₂ storage sites where the faults act as the main structural trap, the sealing properties of the faults must be fully understood, thus, requiring an accurate representation of the fluid flow close to the faults on all scales. This paper study the effects low permeable deformation bands have on the fluid flow in the near fault region. Deformation bands are generated stochastically, and numerical simulations that include the deformation bands explicitly in the simulation domain are performed to obtain an upscaled effective permeability. The numerical examples show that using a simple harmonic average to calculate the effective permeability may overestimate the effective permeability by up to an order of magnitude. A new analytical approximation of the effective permeability based on the deformation band length, density, and rotation is given, and this approximation fits the numerical simulations better than the harmonic average. The results confirm that deformation bands significantly alter the fluid flow close to faults and may decrease the potential leakage of CO₂ through faults.

Keywords: *Deformation bands – Effective permeability – CO₂ storage integrity – Fault zones – Leakage Risk*

1. Introduction

Fluid flow and migration in sedimentary basins have for centuries been a challenge to modelling in a variety of applications, such as groundwater management, hydrocarbon production [1], and recently CO₂ storage [2]. To implement large-scale CO₂ storage, a wide range of reservoir types must be exploited, including reservoirs where faults form the main structural trapping mechanism. A challenge with faults as structural traps is to validate their sealing potential due to the difficulty to predict the properties of the faults. For hydrocarbon reservoirs the fault sealing can be validated by drilling exploratory wells to confirm the existence of hydrocarbons, whereas this is not applicable to aquifers. Mitigating risks related to fault sealing by improving our understanding of the broad range of fluid flow dynamics around faults is therefore needed to unlock storage reservoirs where faults form the main structural trapping mechanism for CO₂.

Fluid flow around faults is governed by geometrically complex structures at a range of scales. There are two different fluid paths that are important to characterize with respect to fault leakage and loss of containment of CO₂. We divide these two paths into the vertical fluid flow along the slip surface in the fault core, and horizontal fluid flow across the fault, see Figure 1 for a conceptual model. The Shale Gouge Ratio of a fault has been identified as a controlling parameter for the sealing

properties of faults [3], and the current state-of-the art fault-seal analysis [4] are developed around the shale content as a controlling parameter. However, these methods only capture across-fault flow [5, 6] and not the complexity of the damage zone or fluid flow vertically along faults.

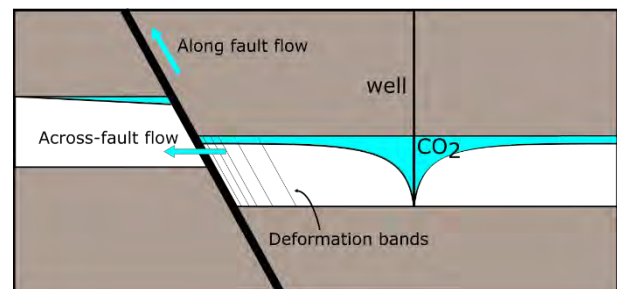


Figure 1: Conceptual model of two possible leakage paths of CO₂ when faults form the main structural trapping mechanism; across-fault flow and along fault flow. Deformation bands that form parallel to the fault may reduce both across-fault flow and along-fault flow by reducing the effective permeability.

One of the structures that is found in the damage zone is deformation bands, which are millimeter-thick low-displacement deformation zones [7]. Deformation bands can have a one to six orders of magnitude lower permeability than the host rock [8, 7, 9], which has led to investigations regarding the impact of deformation bands on fluid flow [10, 11, 12]. These studies have shown that deformation bands can alter the fluid flow paths in a

reservoir, especially if the permeability contrast is lower than four orders of magnitude, but also if the permeability contrast is as low as one order of magnitude [13]. The number of deformation bands around a fault can be related to fault throw [14] and can reach tens of bands per meter close to the fault core. In a potential storage site for CO₂ the individual deformation bands will be unknown and their distribution must be derived from analogue outcrops and models. A quantity that is possible to measure on seismic imaging is the throw of a fault. This triggers the question if it is possible to quantify the effects of deformation bands based on the fault throw. In this paper we give insight into how geometric parameters of the deformation bands impact fluid flow within the damage zone around faults and relate these to fault throw. We do this by generating deformation bands stochastically using recent quantifications of deformation bands in the damage zone [14], and upscale the effective permeability of the generated networks by numerical simulations and analytical approximations.

The Smeaheia storage prospect in the North Sea is considered as a possible storage site for CO₂ [15]. The site is confined by the Vette fault which is predicted to be a structural trap. Including deformation bands in a reservoir scale model will improve our understanding of the fluid flow around the Vette fault and help mitigate the leakage risks of the Smeaheia storage site. In reservoir scale simulations, the size of grid cells is typically on the order of 10 m to 100 m, while the length of the deformation bands is on the order of 10 cm to 100 m. Further, the aperture of the deformation bands is on the millimeter scale. This makes it clear that it is impossible to include deformation bands explicitly in a reservoir scale simulation. Instead, the deformation bands are typically included by considering an effective permeability that represents the combined permeability of the deformation bands and the host rock. This will in general lead to an anisotropic permeability tensor because of the geometric structure of the deformation bands [16]. The effectiveness of this approach is dependent on how well the effective permeability is estimated. An approach that has been used to calculate the effective permeability of the combined porous media of deformation bands and host rock is by a harmonic averaging procedure [12]. While this gives a lower bound on the effective permeability, it will miss the contribution of the geometry of the deformation bands, which has the potential to affect the fluid flow in complicated manners.

The main contributions of this work are twofold. First, we propose a new analytical model for the effective permeability that includes geometry effects of the deformation bands. The derived expression can be used to calculate the effective permeability in other geological settings than around faults, however, this paper only validates the model with data generated from fault zones. Secondly, we perform fine-scale numerical simulations of fluid flow that resolve individual deformation bands explicitly in the simulation domain. In this study we vary the band permeability, band geometry, and band density

to investigate how the different parameters affect the effective permeability in the damage zone around faults.

The remainder of the paper is outlined as follows. The next section discusses the geometric setup and how this relates to faults. Section 3 defines the governing equations for single-phase flow, and Section 4 presents the numerical method used to solve the governing equations with explicitly represented deformation bands in the domain. Section 5 presents our new approximation of the effective permeability and validates it against cases where the band density is constant in the domain. Section 6 contains the main results of this paper, a parameter study of the effective permeability in the damage zone of faults. Here we compare both the numerical simulations and the proposed analytical approximation from Section 5. The final section contains discussion and conclusions.

2. Geometric setup

Deformation bands are thin surfaces that close to a fault tend to form parallel to the fault. While the horizontal extent of the deformation bands can vary from centimeters to hundreds of meters, the deformation bands are often bedding constrained in vertical direction [17, 18]. To reduce the computational cost, we therefore collapse the vertical dimension of the permeable layer and run simulations on two-dimensional domains.

In this work, the deformation bands are generated stochastically by a similar procedure as described in [19]. Deformation bands are represented by straight-line segments, and the line segments can be described by the band centers and the rotations from the y -axis, θ , both stochastic variables. The distributions will be specified in each section. The length of the bands is denoted by l , and the band density, ρ , is defined as the expected number of band centers per unit area. Similarly, the directional density, ρ_α , is defined as the expected number of bands intersecting a scan-line per unit length in the direction α .

3. Governing equations

We consider an incompressible single-phase fluid in a porous media. The porous media consists of two materials, the host rock and the deformation bands. Quantities related to the host rock are denoted by a subscript m and quantities related to the deformation bands are denoted by a subscript b . The permeability within the host rock and deformation bands are assumed to be each homogenous and isotropic and defined by the scalars, k_m and k_b , respectively. The fluid flux, \mathbf{q} , is related to the pressure, p , through Darcy's law. Together with conservation of mass this defines our governing equations:

$$\mathbf{q} = -k\nabla p, \quad \nabla \cdot \mathbf{q} = 0,$$

where $k = k_m$ in the host rock and $k = k_b$ in the deformation bands. In addition, we assume appropriate boundary conditions to be defined.

Lower-bound on effective permeability

A lower-bound of the effective permeability, $K_{\alpha,e}$, can be obtained by taking the harmonic average of the deformation band permeability and the host rock permeability along the scanline α :

$$\frac{K_{\alpha,e}}{K_m} \geq \frac{1}{(1 - \rho_\alpha a) + \frac{\rho_\alpha a K_m}{K_b}} \approx \frac{1}{1 + \frac{\rho_\alpha a K_m}{K_b}}. \quad (1)$$

Here, a , is the aperture of the deformation bands. This lower-bound is obtained if the fluid is not able to flow around the deformation bands but must cross all bands that intersect the scanline in the direction α . In the numerical results we observe that the lower bound is approached as the band length and/or band density increases.

The error of the approximation in Equation (1) is small if $\rho_\alpha a \ll 1$. Out of the 106 outcrop scanlines studied in [14] none of the scanlines had a maximum band density of more than 110 bands per meter, with the mean being 34 bands per meter. If the deformation bands have an aperture $a \approx 1$ mm, the error of the approximation is small. When $\rho_\alpha a \ll 1$, we observe that the reduction in permeability given by the harmonic average in Equation (1) is only dependent on the dimensionless quantity $\rho_\alpha a K_m / K_b$. Thus, a single dimensionless quantity may describe the effect of the deformation bands! Finally, when the density is varying in the domain the averaged value should be used. Specifically, for the logarithmic density in Section 6 (Equation (4)), the density in Equation (1) can be replaced by $-B$.

4. Numerical method

Before we describe the numerical method, we would like to make two comments. The aperture of the deformation bands, a , is typically on the order of magnitude of milli meters, while their lengths can span up to several hundred meters [7]. In addition, the permeability in the deformation bands, k_b , is lower than the permeability in the host rock. We will therefore disregard the fluid flux in the tangential direction of the deformation bands. To represent the permeability reduction caused by the deformation bands, the computational grids are constructed to conform to the bands. That is, the deformation bands will be discretized by the faces in the computational grid. To discretize the governing equations, we use the two-point flux approximation. The two-point flux approximation is sufficient for our purposes because we are only interested in the reduction in effective permeability relative to the homogeneous case. In addition, we are using a completely unstructured grid that reduces the consistency error. By neglecting the tangential flow, assuming small apertures, and using a conforming grid, the deformation bands can be included in the discretization as a face transmissibility multiplier, as described in the following paragraphs.

Let σ be a face between cell L and cell R . The fluid flux from cell L to cell R is approximated by

$$F_\sigma = -T_\sigma (p_R - p_L),$$

where T_σ is the transmissibility and p_R and p_L are the cell center pressure. If the face between the cells do not lie on a deformation band the transmissibility is calculated by the harmonic average of the two half transmissibilities:

$$T_\sigma = \frac{T_{\sigma L} T_{\sigma R}}{T_{\sigma L} + T_{\sigma R}}, \quad T_{\sigma k} = \frac{k_m A_\sigma \mathbf{n}_{\sigma k} \cdot \mathbf{d}_{\sigma k}}{\mathbf{d}_{\sigma k} \cdot \mathbf{d}_{\sigma k}}, \quad k \in \{L, R\}.$$

Here, A_σ is the area of the face, $\mathbf{n}_{\sigma k}$ is the unit normal vector of σ that points out of cell k , and $\mathbf{d}_{\sigma k}$ is the distance vector from the cell center to the face center. If the face is on a deformation band, the transmissibility is modified to include the effect of the bands by taking the harmonic average of the band transmissibility and the half transmissibility of each cell:

$$T_\sigma = \frac{T_{b\sigma L} T_{b\sigma R}}{T_{b\sigma L} + T_{b\sigma R}}, \quad T_{b\sigma k} = \frac{k_b T_{\sigma k}}{k_b + \frac{T_{\sigma k} a}{2A_\sigma}}, \quad k \in \{L, R\}.$$

5. Layered approximation of the effective permeability

In this section we propose a new approach to estimate the effective permeability. This approach approximates the effective permeability in the domain by using some well-educated simplifications. In this section we assume that the band density, ρ , is constant in the domain.

When the fluid approaches a deformation band, parts of the fluid will cross the band and parts of the fluid will flow around the band. The effective permeability is approximated by considering the path across the band and the path around the band as a layered porous media with two layers. This conceptual model is depicted in Figure 2 for fluid flow in the x -direction.

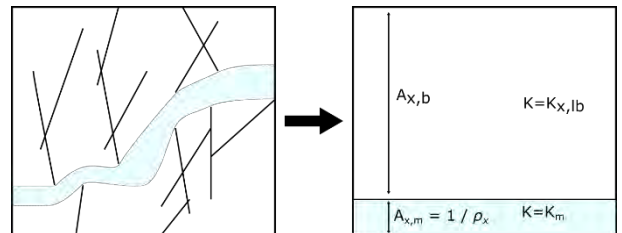


Figure 2: Conceptual model of fluid flow in the x -direction. The complex geometry of the deformation bands is simplified to an area where the fluid only flow through the rock matrix (blue), and an area where the fluid crosses the deformation bands (white).

Given the conceptual model of the porous media consisting of two layers, the effective permeability in the direction α can be calculated as

$$K_{\alpha,e} = \frac{K_{\alpha,lb} A_{\alpha,b} + K_m A_{\alpha,m}}{A_{\alpha,b} + A_{\alpha,m}}, \quad (2)$$

where $A_{\alpha,b}$ and $A_{\alpha,m}$ are the areas available for flow in the band layer and host rock layer, respectively (see Figure 2). The permeability in the band layer, $K_{\alpha,lb}$, is obtained by calculating the harmonic mean of the band

permeability and rock matrix permeability, using the approximation of small band aperture:

$$\frac{K_{\alpha,lb}}{K_m} = \frac{1}{1 + \frac{K_m a \rho_\alpha}{K_b} c_\alpha}$$

Here, the constant c_α defines the fraction of the number of bands within the band layer the fluid must cross. When the rotation of the bands is normally distributed, $\theta = \mathcal{N}(0, \sigma)$, we use

$$c_x = 1, \quad c_y = \sin(E(|\theta|)),$$

where $E(|\theta|)$ is the expected value of the absolute value of the rotation. The challenging part of this approach is to obtain good estimates on the area available for flow around, $A_{\alpha,m}$, and across, $A_{\alpha,b}$, the deformation bands, and the remaining of this section will focus on this.

Let us consider an arbitrary deformation band, called r . Each other deformation band in the domain has a certain fixed probability of crossing this band. When ρ is independent of position and the bands are independently distributed, the number of intersections, N , band r has with other bands is Poisson distributed. The probability of the band having zero intersections can be calculated as

$$P(N = 0) = \exp\left(-l^2 \rho \int_{-\infty}^{\infty} \int_{-\infty}^{\infty} |\sin(\theta)| f(\theta + \eta) f(\eta) d\theta d\eta\right),$$

where $f(\theta)$ is the probability density function of the rotation of the bands. If the rotation of the bands is uniform, the integral simplifies to $2/\pi$. If the rotation of bands is normally distributed the integral can be calculated numerically. Since N is Poisson distributed, the expected value can be calculated as

$$E(N) = -\log(P(N = 0)). \quad (3)$$

Figure 3 shows a comparison of the Poisson distribution with expectation $E(N)$ and the probability density function calculated numerically by populating a domain with 10 000 deformation bands stochastically. The fit is good and gives no reasons to doubt that the number of intersections is Poisson distributed with expected value given by Equation (3).

Let M denote the number of bands you must pick at random before picking a band with 0 intersections. The expected value of M can be calculated as:

$$E(M) = \frac{1 - P(N = 0)}{P(N = 0)^2}.$$

When the deformation bands intersect, they may form long chains of bands. When a band is added to the chain the chain grows in a random direction, and we postulate that the growth of the chain follows the same scaling as Brownian motion, that is, the length grows with the square root of the number of bands. We have confirmed this scaling numerically. We therefore suggest that the area available for flow across deformation bands is

$$A_{\alpha,b} = l_\alpha^T + \sqrt{0.5 l_\alpha^T E(M)}.$$

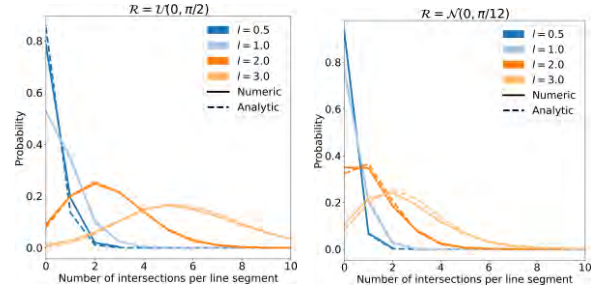


Figure 3: The probability of a band having N intersections. The solid lines show the probability calculated numerically by distributing 10 000 bands randomly in a domain, while the dashed lines show the Poisson distribution. In the left figure the band rotation is uniformly distributed, while in the right figure the band rotation is normally distributed.

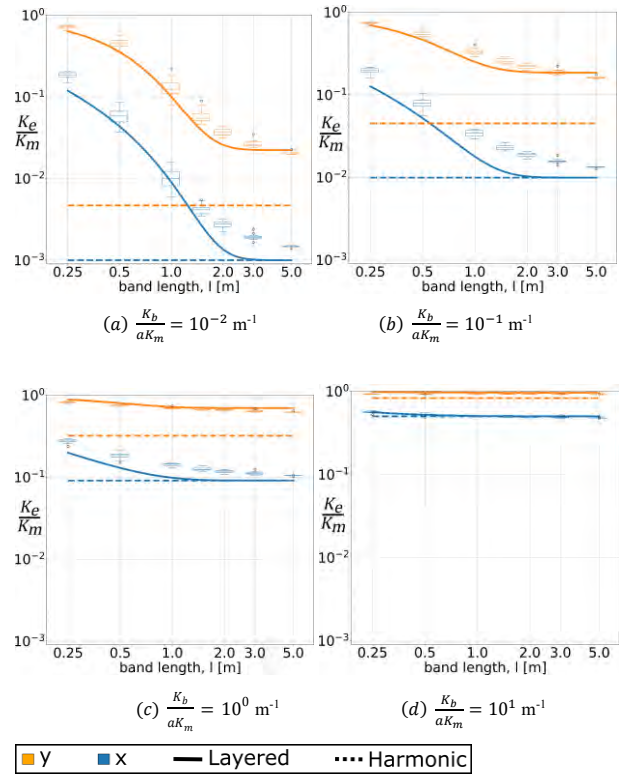


Figure 4: The effective permeability (y -axis) as a function of the band length (x -axis) for a band density independent of position in the domain. The box plots show the effective permeability obtained from numerical simulations, the solid lines correspond to the effective permeability obtained by the layered analytical approximation, and the dashed lines to the harmonic average. The orange color corresponds to the effective permeability in y -direction, while the blue color corresponds to the effective permeability in x -direction. Each figure shows the result of a different permeability ratio of the rock and the deformation bands.

Here, l_α^T is the expected band length in the direction perpendicular to α . If the rotation is normally distributed with standard deviation σ , $\mathcal{R} = \mathcal{N}(0, \sigma^2)$, and $\sigma \ll 1$, we obtain

$$l_x^T = l \cos\left(\frac{\sigma\sqrt{2}}{\pi}\right), \quad l_y^T = l \sin\left(\frac{\sigma\sqrt{2}}{\pi}\right), \quad \rho_\alpha = \rho l_\alpha^T.$$

For the conceptual layer of the host rock, the area available for flow is the area between bands. We

therefore suggest that the area for the host rock in our conceptual model scales as

$$A_{\alpha,m} = 1/\rho_{\alpha}.$$

Comparison to numerical simulations

To test the suggested analytical solution for the effective permeability as a layered porous media we compare the analytical approximation given by Equation (2) to the effective permeability calculated from the numerical simulations. We let $\mathcal{R} = \mathcal{N}(0, (\pi/12)^2)$ and fix the density to $\rho = 1 \text{ m}^{-2}$. The band length, l , is varied between 0.25 m and 5 m. The comparisons between the analytical approximations and numerical solutions are shown in Figure 4. Using the harmonic average approximation given by Equation (1) consistently underestimates the permeability; up to two orders of magnitude in the worst case. The analytical approximation given by Equation (2) gives a much better approximation and is able to capture the increase in effective permeability as the deformation band network becomes disconnected. Finally, we note that as the deformation band length increases or the permeability ratio decreases, the error of the harmonic average becomes smaller.

Figure 5 shows the comparison of the numerical simulations and the analytical approximation as a function of band density, ρ . The band length is fixed to $l = 1 \text{ m}$. The analytical approximation of the effective permeability given by Equation (2), is able to capture the effective permeability both when the band network is disconnected (the band density is small), and when it is highly connected (band density is large), while the harmonic average given by Equation (1) is only applicable when the band density or the band transmissibility, $\frac{K_f}{aK_m}$, is large. This is the same qualitative behavior as observed in Figure 4.

6. Application to fault damage zones

Around faults the number of deformation bands is not constant but varies as a function of the distance from the fault. In this section we assume the density function along a scanline normal to the fault (x -direction) follows the logarithmic law given in [14]:

$$\rho_x(x) = A + B \ln\left(\frac{x}{1\text{m}}\right), \quad (4)$$

where A and B are two constants that can be used to fit the density function to a specific fault. We will use the average values from the data given in [14]:

$$B = -8.33 \text{ m}^{-1},$$

$$A = 13.33 \ln\left(\frac{W_5}{1 \text{ m}}\right) \text{ m}^{-1} - 5 \left(\ln\left(\frac{W_5}{1 \text{ m}}\right) - 1\right) \text{ m}^{-1},$$

where W_5 is the distance from the fault to where the band frequency is 5 m^{-1} , that is $\rho(W_5) = 5 \text{ m}^{-1}$. We refer to this value as the damage zone width. The damage zone width can be related to fault throw, T , as (see [14])

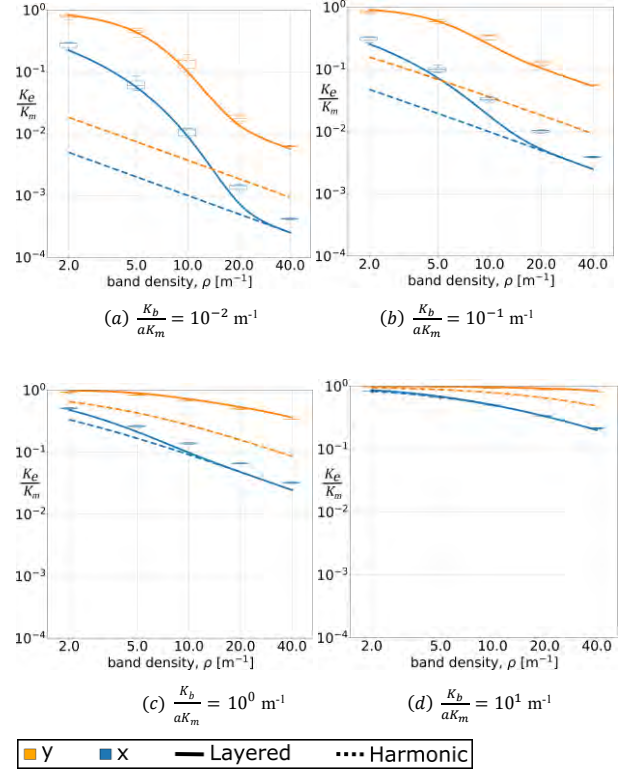


Figure 5: The effective permeability (y-axis) as a function of the band density (x-axis) for a density that is independent of position in the domain. The box plots show the effective permeability obtained from numerical simulations, the solid lines correspond to the effective permeability obtained by the layered analytical approximation, and the dashed lines to the harmonic average. The orange color corresponds to the effective permeability in y -direction, while the blue color corresponds to the effective permeability in x -direction. Each figure shows the result of a different permeability ratio of the rock matrix and the deformation bands.

$$W_5 = 1.74 \left(\frac{T}{1 \text{ m}}\right)^{0.43} \text{ m},$$

which allows us to generate deformation band networks based on only the fault throw.

Figure 6 shows three examples of generated deformation band networks using the logarithmic density function. The figure illustrates that increasing values of W_5 both widens the damage zone and increases the frequency of the bands within the zone. The deformation zone widths are 1 m, 5 m, and 10 m, which correspond to fault throws of 0.28 m, 12 m, and 58 m, respectively.

The analytical expression using the approximation of the effective permeability given in Equation (2) was derived for domains where the density was constant, however, if the density is varying slowly enough, we expect that Equation (2) gives a good point estimate of the effective permeability. By integrating the point estimate of the effective permeability, the effective permeability of the whole domain can be obtained.

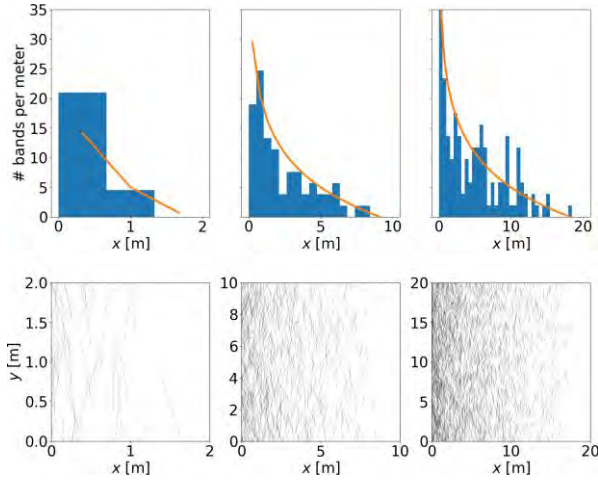


Figure 6: Example of three generated deformation bands networks that follow the logarithmic density function (bottom row). The damage zone width is $W_5 = 1, 5,$ and 10 meters from the left figure to the right figure. The top row shows the histograms of the deformation bands crossing the horizontal scan line through the center of the domain, while the orange line shows the density function given by Equation (4). The fault is parallel to the y -axis and located at $x = 0$. Note the different axis is each plot.

We will test the analytical approximation by comparing it to numerical simulations. Three tests are performed, varying the parameters going into the model independently.

Common setup

The following parameters are used in all the following examples. The coordinate system is chosen such that the fault is parallel to the y -axis, and the x -axis defines the distance from the fault. In the numerical simulations the effective permeability in x - (resp. y -) direction is calculated by imposing a unit drop in pressure in x - (resp. y -) direction and imposing a no-flow condition on the top and bottom (resp. left and right) boundaries.

The computational domain is a square, $[X, Y]$. The height, Y , is set to be 8 times the band length. This domain height has been found to be sufficiently large so that a doubling of the domain height does not alter the results. The domain width, X , is set equal the width at which no deformation appears, that is, $\rho_x(X) = 0$.

In all test cases the band transmissibility is defined as the permeability ratio divided by the aperture. In each test case the band transmissibility is varied four orders of magnitudes, $\frac{K_b}{aK_m} = \{10^{-2}, 10^{-1}, 10^0, 10^1\} \text{ m}^{-1}$. The lowest band transmissibility corresponds to, e.g., an aperture of 1 mm and permeability ratio of 5 orders of magnitude.

In all test cases the rotation of the bands, θ , is assumed normally distributed with standard deviation σ , $\mathcal{R} = \mathcal{N}(0, \sigma^2)$.

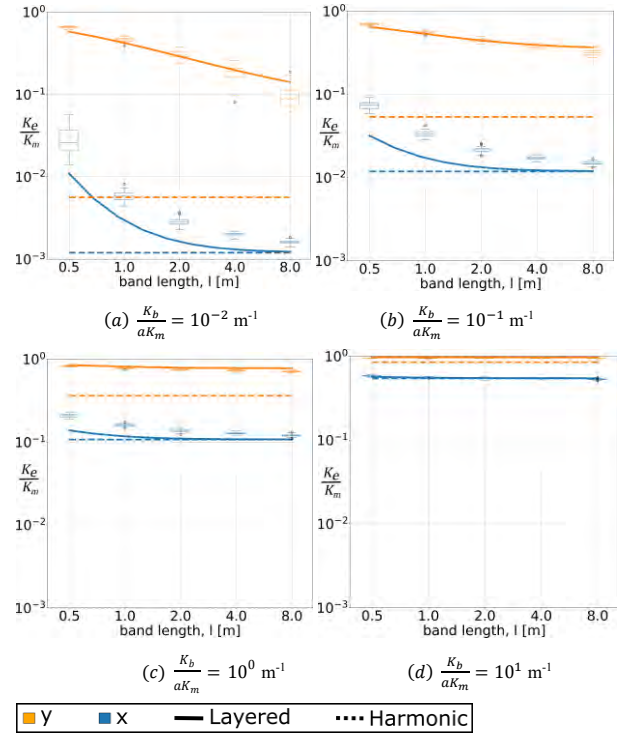


Figure 7: The effective permeability of the fault damage zone as a function of the band length. The box plots show the effective permeability obtained from numerical simulations, the solid lines correspond to the effective permeability obtained by the layered analytical approximation, and the dashed lines to the harmonic average. Blue color is the permeability normal to the fault, while the orange color is the permeability parallel to the fault.

6.1 Effective permeability vs. band length

In this test, the damage zone width is fixed to $W_5 = 5$ m, which corresponds to a throw of 12 m. The standard deviation of the rotation is set to $\sigma = \pi/12$. The band length is varied between simulations and takes values 0.5, 1, 2, 4, and 8 meters. For each band length a total of 48 simulations were run.

Figure 7 shows the effective permeability in x - and y -direction as a function of band length. As the length of the bands increase, the effective permeability approaches the lower-bound given by the harmonic average in Equation (1). The layered approximation in Equation (2) gives quite good match with the numerical results. We observe that the effective permeability varies an order of magnitude between band lengths of 0.5 m and band lengths of 4.0 m and has an anisotropy up to two orders of magnitude in the normal and parallel directions.

6.2 Effective permeability vs rotation

In this test case the expected band length is fixed to $l = 1$ m, and the damage zone width to $W_5 = 5$ m. Varying the standard deviation in the normal distribution, σ , changes how much the deformation bands intersect. When the standard deviation is 0 all bands are parallel, and no bands intersect. When the standard deviation is more than $\pi/5$ there is not much structure in the deformation bands and the generated network resembles that of a uniform distribution. In the numerical tests, we consider this full range of rotations. For each value of σ

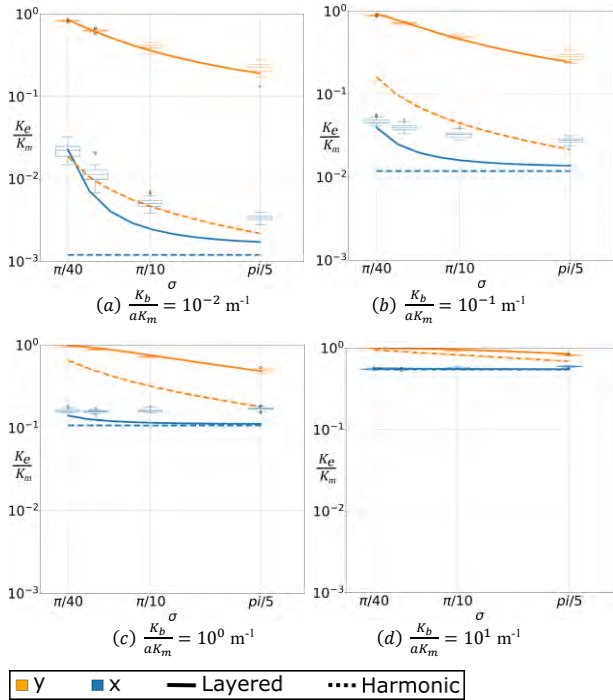


Figure 8: The effective permeability of the fault damage zone as a function of the band rotation. Each subplot shows the result for a different permeability ratio. The box plots show the effective permeability obtained from numerical simulations, the solid lines correspond to the effective permeability obtained by the layered analytical approximation, and the dashed lines to the harmonic average. Blue color is the permeability normal to the fault, while the orange color is the permeability parallel to the fault.

a total of 48 realizations of the deformation band network was created.

Figure 8 shows the effective permeability for each case. The effective permeability decreases as the rotation increases because the bands tend to intersect each other more which creates long connected chains of deformation bands that the fluid must cross. The permeability parallel to the fault is approximately 2 orders of magnitude larger than the permeability normal to the fault for the fault transmissibility 10^{-2} m^{-1} , but decreases as the fault transmissibility increases.

6.3 Effective permeability vs damage zone width, W_5

We upscale the effective permeability for the damage zone widths $W_5 = 1, 2, 3, 5, 7, 10, 20$ meters numerically by generating 48 realizations of the deformation bands for each length. These damage zone widths correspond to a throw of 0.28, 1.4, 3.5, 12, 25, 58 and 293 meters, respectively.

The effective permeability is plotted in Figure 9. The variance of the effective permeability decreases with increasing damage zone width, however, the value of the effective permeability appears to be constant. That the effective permeability is independent of fault throw is also predicted by both the harmonic average approximation in Equation (1), and the layered

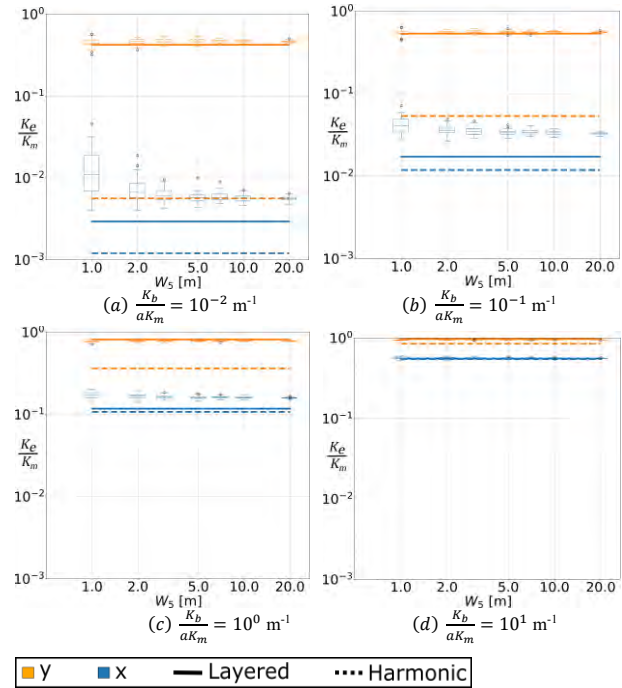


Figure 9: The effective permeability in the damage zone as a function of damage zone width. Each subplot shows the result for a different permeability ratio. The box plots show the effective permeability obtained from numerical simulations, the solid lines correspond to the effective permeability obtained by the analytical approximation, and the dashed lines to the harmonic average. Blue color is the permeability normal to the fault, while the orange color is the permeability parallel to the fault.

approximation in Equation (2). The reason for this is that the choice of A and B causes the total number of deformation bands in the domain divided by the damage zone width to be constant. That band density averaged over the damage zone is independent of damage zone width is consistent with field observations [14]. This causes the width of the damage zone to increase at the same rate as the number of bands in the damage zone. Thus, the changes in these two parameters cancel each other in the calculation of the effective permeability. Note that this is only true for the effective permeability averaged over the whole damage zone; the point value of the effective permeability, e.g., 1 m from the fault is much lower for a fault throw of 300 m than a fault throw of 2 m.

8. Discussion and conclusion

In this paper a novel analytical expression for the effective permeability of a porous media with deformation bands is presented. The analytical expression assumes the porous media can be represented as two layers, one with deformation bands and one without. The analytical solution is validated by numerical simulations over a wide range of parameters.

The results from the numerical simulations show that deformation bands can significantly alter the effective permeability in the damage zone of faults. It is also

shown that the geometry of the deformation bands is important when estimating the effective permeability. Counting the number of deformation bands along a scan line from a fault and taking the harmonic average between the deformation bands and host matrix can overestimate the reduction in permeability by an order of magnitude. The main mechanism that increases the effective permeability is that the geometry allows the fluid to bypass bands without crossing them. This effect is especially important when the permeability ratio of the deformation bands and the rock matrix is smaller than three orders of magnitude.

In the results presented in this paper it is assumed that deformation bands are placed randomly in the domain by a stochastic process and that each deformation band is independent of all others. This is an assumption that not necessary holds true for a field case, and an important part of further work will be to quantify the difference between the proposed method and field observations. In this work it will be necessary to explore appropriate methods for including the suggested model in a reservoir simulation. The discrepancy in scales between the damage zone and grid cell size may cause a straightforward upscaling of the grid cell permeability to underestimate the effects of the bands. Special care should then be taken close to faults where, due to the logarithmic density function of deformation bands, the deformation band density varies significantly, and a representative elementary volume of the combined deformation bands and host rock may not exist.

Acknowledgements

This work has been founded in part by the Norwegian Research Council grant 294719.

References

- [1] D. Faulkner, C. Jackson, R. Lunn, R. Schlische, Z. Shipton, C. Wibberley and M.O. Withjack, "A review of recent developments concerning the structure, mechanics and fluid flow properties of fault zones," *Journal of Structural Geology*, vol. 32, no. 11, pp. 1557-1575, 2010.
- [2] F. Cappa and J. Rutqvist, "Modeling of coupled deformation and permeability evolution during fault reactivation induced by deep underground injection of CO₂," *International Journal of Greenhouse Gas Control*, vol. 5, no. 2, pp. 336-346, 2011.
- [3] Y. Pei, D. A. Paton, R. J. Knipe and K. Wu, "A review of fault sealing behaviour and its evaluation in siliciclastic rocks," *Earth-Science Reviews*, vol. 150, pp. 121-138, November 2015.
- [4] R. J. Knipe, "Juxtaposition and Seal Diagrams to Help Analyze Fault Seals in Hydrocarbon Reservoirs," *AAPG Bulletin*, vol. 81, no. 2, pp. 187-195, 1997.
- [5] A. Braathen, J. Tveranger, H. Fossen, T. Skar, N. Cardozo, S. E. Semshaug, E. Bastesen and E. Sverdrup, "Fault facies and its application to sandstone reservoirs," *AAPG Bulletin*, vol. 93, no. 7, pp. 891-917, 2009.
- [6] M. Fachri, J. Tveranger, A. Braathen and P. Røe, "Volumetric faults in field-sized reservoir simulation models: A first case study," *AAPG Bulletin*, vol. 100, no. 5, pp. 795-817, 2016.
- [7] H. Fossen, R. Schultz, Z. Shipton and K. Mair, "Deformation bands insandstone - a review," *Journal of the Geological Society*, vol. 164, no. 4, pp. 755-769, 2007.
- [8] M. Antonellini and A. Aydin, "Effect of faulting on fluid flow in poroussandstones: petrophysical properties," *AAPG Bulletin*, vol. 78, no. 3, pp. 355-377, 1994.
- [9] G. Ballas, R. Soliva, J.-P. Sizun, A. Benedicto, T. Cavailles and S. Raynaud, "The importance of the degree of cataclasis in shear bands for fluid flow in porous sandstone, Provence, France," *AAPG Bulletin*, vol. 96, no. 11, pp. 2167-2186, 2012.
- [10] S. Matthäi, A. Aydin, D. Pollard and S. Roberts, "Numerical simulation of departures from radial drawdown in a faulted sandstone reservoir with joints and deformation bands," in *Faulting, fault sealing and fluid flow in hydrocarbon reservoirs*, G. Jones, Q. Fisher and R. Knipe, Eds., London, Geological Society, Special Publications, 1998, pp. 157-191.
- [11] K. Sternlof, J. Chapin, D. Pollard and L. Durlofsky, "Permeability effects of deformation band arrays in sandstone," *AAPG Bulletin*, vol. 88, no. 9, pp. 1315-1329, 2004.
- [12] H. Fossen and A. Bale, "Deformation bands and their influence on fluid flow," *AAPG Bulletin*, vol. 91, no. 12, pp. 1685-1700, 2007.
- [13] A. Rotevatn, H. S. Fossmark, E. Bastesen, E. Thorsheim and A. Torabi, "Do deformation bands matter for flow? Insights from permeability measurements and flow simulations in porous carbonate rocks," *Petroleum Geoscience*, vol. 23, no. 1, p. 104-119, 2017.
- [14] S. Schueller, A. Braathen, H. Fossen and J. Tveranger, "Spatial distribution of deformation bands in damage zones of extensional faults in porous sandstones: Statistical analysis of field data," *Journal of Structural Geology*, vol. 52, pp. 148-162, 2013.
- [15] OED, "Feasibility study for full-scale CCS in Norway," 09 2019. [Online]. [Accessed 19 02 2021].
- [16] K. R. Sternlof, M. Karimi-Fard, P. D. D. and L. J. Durlofsky, "Flow and transport effects of compaction bands in sandstone at scales relevant to aquifer and reservoir management," *Water Resources Research*, vol. 42, no. 7, p. W07425, 2006.
- [17] R. A. Schultz and H. Fossen, "Displacement-length scaling in three dimensions: the importance of aspect ratio and application to deformation bands," *Journal of Structural Geology*, vol. 24, no. 9, pp. 1389-1411, 2002.
- [18] M. L. Cooke and C. A. Underwood, "Fracture termination and step-over at bedding interfaces due to frictional slip and interface opening," *Journal of Structural Geology*, vol. 23, no. 2-3, pp. 223-238, 2001.
- [19] C. Xu and P. Dowd, "A new computer code for discrete fracture network modelling," *Computers & Geosciences*, vol. 36, no. 3, pp. 292-301, 2010.
- [20] A. Aydin, R. Borja and P. Eichhubl, "Geological and mathematical framework for failure modes in granular rock," *Journal of Structural Geology*, vol. 28, no. 1, pp. 83-98, 2006.

RESULTS FROM CESAR-1 TESTING WITH COMBINED HEAT AND POWER (CHP) FLUE GAS AT THE CO₂ TECHNOLOGY CENTRE MONGSTAD

Scott A. Hume,² Muhammad I. Shah,¹ Gerard Lombardo,¹ and Eirik Romslo Kleppe¹

¹ CO₂ Technology Centre Mongstad (TCM), 5954 Mongstad, Norway

² Electric Power Research Institute, Inc., 3420 Hillview Avenue, Palo Alto, CA 94394, USA

* Corresponding author e-mail: shume@epri.com

Abstract

CO₂ Technology Centre Mongstad (TCM) houses a demonstration-scale test facility for CO₂ capture solvents termed the “amine plant,” where multiple test campaigns have been performed on numerous solvents that the owners of TCM, TCM DA, have conducted since its inauguration in 2012. The large number of public, industrial, research, and academic participants involved in these campaigns have enriched the projects and ensured that the significant results serve a broad audience. The main objective of these campaigns was to produce knowledge that can be used to reduce the cost as well as the technical, environmental, and financial risks for the commercial-scale deployment of post-combustion CO₂ capture (PCC). This includes demonstration of a model-based control system, dynamic operation of the amine plant, investigation of amine aerosol emissions, and establishment of the baseline performance with monoethanolamine for residual fluid catalytic cracker (RFCC) and combined-cycle gas turbine (CCGT)-based combined-heat-and-power plant (CHP) flue gases. The RFCC flue gas is sourced from a nearby Equinor refinery that emulates coal flue gas in composition with 13%–14% vol CO₂ content and the CHP flue gas represents flue gas from CCGT power plants with a 3.5% vol CO₂ content. In addition to baseline testing, specific tests targeted at reducing CO₂ avoided cost have also been conducted utilizing both flue gas sources. This paper focuses on the testing of the CESAR-1 solvent, a blend of 2-amino-2-methyl-1-propanol and piperazine.

The Electric Power Research Institute, Inc. (EPRI) assessed the performance of the process using an independent verification protocol (IVP) developed previously. The IVP provides a structured testing procedure for assessing the thermal and environmental performance of PCC processes under normal operating conditions. Throughout the CESAR-1 testing, TCM manually collected extractive samples from the depleted flue gas and product CO₂ outlets sequentially. As part of the IVP, EPRI also assessed critical plant instrumentation at TCM for accuracy and precision error based on a comparative analysis done during testing operations and against calibration checks.

The CESAR-1 process was evaluated during 16 individual test periods over four days in June 2020. During the tests, extractive samples were taken to measure process contaminants such as aldehydes, ketones, amines, and ammonia. Sulfur oxides and nitrogen oxides were continuously monitored using Fourier-transform infrared (FTIR) analysers on the depleted flue gas and product CO₂ streams. TCM has installed multiple measurements (FTIR, non-dispersive infrared sensor, and gas chromatography) of the CO₂ concentration allowing comparative confirmation during the test periods. The capture rate was calculated via four methods along with evaluation of the CO₂ recovery, which is indicative of the overall mass balance. The overall thermal performance (energy consumption) was assessed based on measured data taken during each of the sampling periods. The CO₂ capture rate achieved during the CESAR-1 testing was 97–99%, with steam reboiler duties of 3.41–3.54 GJ/tonne-CO₂, and the CO₂ gas mass balance closures were close to 100%. These data and the associated assessments, along with the results of TCM sampling during these tests, are presented in this paper.

Keywords: CO₂ capture; EPRI; Post-combustion capture; CO₂ Technology Centre Mongstad; TCM; CESAR-1

1. Introduction

The CO₂ Technology Centre Mongstad (TCM) is located next to the Equinor refinery in Mongstad, Norway. TCM DA is a joint venture owned by Gassnova representing the Norwegian state, Equinor, Shell, and Total. TCM is home to one of the largest post-combustion CO₂ capture (PCC) test centers in the world. This facility entered the operational phase in August 2012 and is dubbed the “amine plant.”

A unique aspect of the facility is that either a flue gas slipstream from a natural gas-fired combined-heat-and-

power (CHP) plant or an equivalent volumetric flow from a residual fluid catalytic cracker (RFCC) unit can be used for CO₂ capture. The CHP flue gas contains about 3.5 vol% CO₂ and the RFCC flue gas contains about 13–14 vol% CO₂, the latter of which is comparable to CO₂ levels seen in a coal-fired flue gas. The amine plant, designed and constructed by Aker Solutions and Kværner, is a highly flexible and well-instrumented facility that can accommodate a variety of technologies with capabilities of treating flue gas streams of up to 60,000 Sm³/hr.

The plant is offered to developers of solvent-based CO₂ capture technologies to test the performance of their

solvent technology and to verify systems aimed to reduce the atmospheric emissions and environmental impact of solvent emissions and degradation products from these processes.

The objective of TCM DA is to test, verify, and demonstrate CO₂ capture technologies suitable for deployment at full scale. A significant number of vendors, including Aker Solutions, Alstom (now GE Power), Cansolv Technologies Inc., and Carbon Clean Solutions Ltd., have already successfully tested using the TCM DA facilities to assess their CO₂ capture technologies.

Multiple tests using the CESAR-1 solvent have been carried out at TCM to define the baseline performance of the solvent for defined operating conditions using CHP flue gas boosted to 5 vol% CO₂ content using recycle in accordance with an independent verification protocol (IVP), which provides a structured testing procedure, developed by the Electric Power Research Institute, Inc. (EPRI) [1]. These tests are compared with prior MEA testing at TCM using the CHP flue gas without recycle at 3.5 vol%.

2. Amine Plant

The TCM 234 tonnes-CO₂/day amine plant was designed to be flexible to allow testing of different configurations. The amine plant is configured to remove CO₂ from a natural gas-fired combustion turbine-based CHP plant flue gas or a RFCC off-gas. The typical characteristics of these two flue gas streams are shown in Table 1.

Table 1: Nominal characteristics of flue gas supplied to TCM

Parameter	Units	CHP Flue Gas	RFCC Flue Gas
Temperature	°C	185	27
N ₂ +Ar	% vol, dry	81.5	82.5
O ₂	% vol, dry	14.8	4.3
CO ₂	% vol, dry	3.7	13.2
SO ₂	ppmv, dry	very small	20 to 60
NO	ppmv, dry	<5	50 to 115
NO ₂	ppmv, dry	<0.5	3
SO ₃	ppmv, dry	very small	7 to 10*
CO	ppmv, dry	-	0 to 3
NH ₃	ppmv, dry	<5	1
Particulates	mg/Nm ³	very small	14 to 41*
Chloride	mg/Nm ³	-	< 0.1

* controlled via candle filter

For these tests, a portion of the product CO₂ was recycled to the CHP flue gas inlet stream in a controlled way to maintain the incoming CO₂ concentration at 5% vol, dry. A process flow diagram showing high-level equipment contained within the amine plant along with key existing instrumentation is shown in Figure 1.

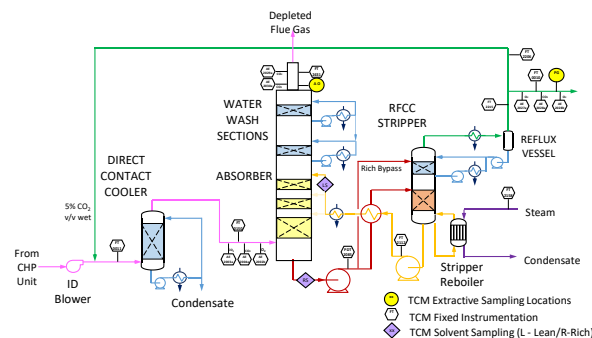


Figure 1: Process flow diagram for the TCM amine plant with CO₂ recycle

Major systems include:

- An induced draft (ID) blower to overcome pressure drops and blow the flue gas through the plant with an output capacity of up to 270 mbar and 70,000 Sm³/hr.
- A direct-contact cooler (DCC) system to initially lower the temperature of and saturate the incoming flue gas by a counter-current water flow to improve the efficiency of the absorption process and provide pre-scrubbing of the flue gas. The DCC system has two individually operated packed columns for operations with the CHP flue gas and the RFCC flue gas, respectively. The DCC column designed for CHP gas operations is 3-m diameter and a total 16 m height. The section where water counter currently contacts the flue gas is 3.1 m high with Flexipac 3X structured stainless-steel packing of Koch Glitsch.
- An absorber to remove CO₂ from the flue gas. The absorber has a rectangular, polypropylene-lined concrete column with a 3.55 x 2 m cross-section and a total height of 62 m. The lower regions of the tower, where the amine solution contacts the flue gas, consist of three sections of Koch-Glitsch Flexipac 2X structured stainless-steel packing of 12 m, 6 m, and 6 m of height, respectively. Water-wash systems are located in the upper region of the tower to scrub and clean the flue gas, particularly of any solvent carry over, and consist of two sections of Koch-Glitsch Flexipac 2Y HC structured stainless-steel packing, each 3 m in height. The lower water-wash section is used to cool the depleted flue gas for overall plant water balance by adjusting the temperature of the circulating water. The uppermost water-wash section was operated as an adiabatic acid-wash stage for further emission mitigation. Liquid distributors, liquid collector trays, and mesh mist eliminators (Koch-Glitsch) are located at various locations in the tower, and the final mesh mist eliminator at the top of the tower is by Sulzer. The CO₂ depleted flue gas exits the absorber column to the atmosphere through a stack located at the top of the column.
- Stripper columns to recover the captured CO₂ and return CO₂-lean solvent to the absorber. The amine plant consists of two independent stripper columns with a common overhead condenser system. The two stripper columns are operated independently considering the CO₂ content in the flue gas due to column design, hydraulics, and gas velocity effects. The smaller diameter stripper column is used when treating CHP flue gas or RFCC gas

diluted with air, whereas the larger diameter column is used when treating flue gases of undiluted (i.e., higher CO₂ content) RFCC gas or when operating with CHP using CO₂ recycle, as is the case with these tests. The CHP stripper is 1.25 m in diameter and 28 m in height tangent-to-tangent. The RFCC stripper is 2.2 m in diameter and is also 28 m tangent-to-tangent. The lower regions of both stripper columns, where the amine solution is stripped, consist of Koch-Glitsch Flexipac 2X structured stainless-steel packing 8 m high. The upper regions of the strippers consist of a rectifying water-wash section of Koch-Glitsch Flexipac 2Y HC structured stainless-steel packing 1.6 m high. Liquid distributors, liquid collector trays, and mesh mist eliminators (all by Koch-Glitsch) are located at various locations in the strippers. Each stripper column is connected to its respective steam-heated reboiler, providing the necessary heat required for the stripping process. Both strippers circulate solvent to the reboilers by thermosiphon. The RFCC stripper also has a circulating pump to assist at low-load operation and during startup. The RFCC reboiler is a shell-and-tube arrangement and the CHP reboiler is a plate-in shell heat exchanger.

- A lean-solvent trim cooler that uses seawater to cool the lean solvent leaving the cross heat exchanger to a desired temperature before admission to the absorber column.
- A set of pumps used to move the CO₂-lean and CO₂-rich solvent streams between the absorber and stripper and through a cross heat exchanger to recover heat from the lean stream.
- A reflux drum, condenser, and pumps to dry the product CO₂ that exits the stripper. A portion of the product CO₂ can also be recycled back to the inlet of the CHP DCC to increase the concentration of the CO₂ in the inlet flue gas stream when using CHP flue gas.

The TCM facility can test virtually any PCC solvent-based process as the amine plant has been designed to accommodate a variety of technologies. The facility also has excellent instrumentation and an on-site lab for detailed analysis.

An IVP was developed to be used as part of the overall performance assessment of amine-based processes and has been updated over time to apply to either CHP or RFCC operation on the TCM amine facility. The IVP is designed to provide a structured testing procedure for assessing thermal and environmental performance of PCC processes under normal operating conditions. Uncertainty for key flow measurements was carried out as part of the IVP previously [2].

3. CESAR-1 CHP Campaign Overview

The CESAR-1 solvent is a blend of 2-amino-2-methyl-1-propanol (AMP) and piperazine (PZ). CHP flue gas capture performance assessment periods were conducted in June 2020. During the testing, personnel from TCM manually collected extractive samples from the depleted gas outlet and the product CO₂ line downstream of the RFCC stripper. In previous tests, this was sometimes performed by an independent testing contractor.

However, TCM’s competency related to performing this testing was deemed adequate by EPRI during prior monoethanolamine (MEA) baseline campaigns, especially since TCM is not commercially involved in the outcome and hence can be considered to be unbiased.

Data logs for all sampling periods containing pertinent flows, temperatures, pressures, and concentrations measured by permanent plant instruments were supplied by TCM for the entire test period. The sampling time periods, and sampling period designators are shown in Table 2 along with additional sampling undertaken on each day.

Table 2: CESAR-1 CHP sampling periods

Date	#	Time	Stream	Samples
June 24, 2020	1	9:26–11:39	CO ₂	AMP, PZ, NH ₃
	2	11:45–12:27	CO ₂	Aldehyde/Ketones
	3	12:15–12:25	ABS	Aldehyde/Ketones
	4	12:48–13:48	ABS	AMP, PZ, NH ₃
June 25, 2020	5	10:16–12:16	ABS	AMP, PZ, NH ₃
	6	10:32–12:37	CO ₂	AMP, PZ, NH ₃
	7	12:28–12:58	ABS	Aldehyde/Ketones
	8	12:43–13:20	CO ₂	Aldehyde/Ketones
June 26, 2020	9	9:33–11:33	ABS	AMP, PZ, NH ₃
	10	9:43–11:50	CO ₂	AMP, PZ, NH ₃
	11	11:42–12:12	ABS	Aldehyde/Ketones
	12	11:54–12:30	CO ₂	Aldehyde/Ketones
June 30, 2020	13	10:17–12:17	ABS	AMP, PZ, NH ₃
	14	10:27–12:33	CO ₂	AMP, PZ, NH ₃
	15	12:24–12:54	ABS	Aldehyde/Ketones
	16	12:38–13:13	CO ₂	Aldehyde/Ketones

The plant operated in a stable condition through the entire test period, as shown in Figures 2 and 3 with controlled flue gas flow at 59,000 Sm³/h and CO₂ controlled at 5 vol%, dry using recycled product gas.

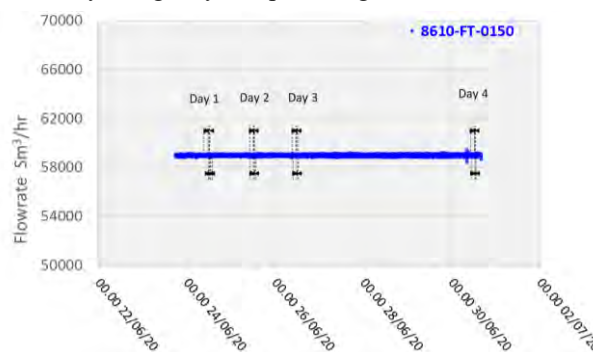


Figure 2: Flue gas flowrate through testing period

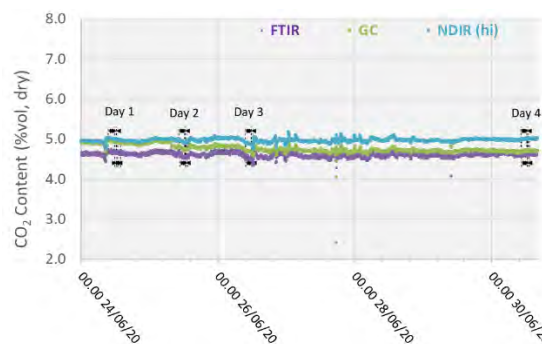


Figure 3: Inlet CO₂ concentration through testing period

3.1 CO₂ Capture Efficiency and Recovery

CO₂ capture efficiency can be quantified in several ways depending on how measurements have been taken and the expected accuracy of each individual measurement. Using different combinations of the measured parameters at the boundary of the process, four individual methods can be applied as detailed in Table 3.

These methods can rely on combinations of the available information to determine a capture efficiency, using the measured gas flowrates in combination with the CO₂ analyzer measurements.

Method 4 simplifies the measurement uncertainty by utilizing only CO₂ concentration data and making the well-founded assumption that all incoming inert gases (such as nitrogen and oxygen) will be unchanged through the absorption process. Hence, Method 4 can be used to compare against the other methods that utilize the flow measurements.

Table 3: CO₂ capture efficiency calculation methods

Method	Formula
1	$Efficiency = \frac{CO_2(\text{product})}{CO_2(\text{supply})}$
2	$Efficiency = \frac{CO_2(\text{product})}{CO_2(\text{product}) + CO_2(\text{depleted})}$
3	$Efficiency = \frac{CO_2(\text{supply}) - CO_2(\text{depleted})}{CO_2(\text{supply})}$
4	$Efficiency = 1 - \frac{O_{CO_2} (1 - I_{CO_2})}{(1 - O_{CO_2}) I_{CO_2}}$

The “CO₂ recovery” calculation is defined as the ratio of the sum of the CO₂ flow in depleted flue gas and the product CO₂ flow divided by the CO₂ flow in the flue gas supply.

$$Recovery = \frac{CO_2(\text{depleted}) + CO_2(\text{product})}{CO_2(\text{supply})}$$

The CO₂ recovery is a measure of the closure of the CO₂ mass balance, being the fraction of CO₂ mass flow in the flue gas supply that is accounted for by measured CO₂ mass flows in the depleted flue gas and product CO₂.

Table 4 shows the four calculation methods of CO₂ capture and recovery for the test periods. Note that CO₂ product flow can be based on either the measured CO₂ product flow or by using the difference between the non-dispersive infrared-measured CO₂ supply and depleted flows. CO₂ capture rates calculated by all methods were in good agreement within each test period. It should be noted that Methods 3 and 4 are equivalent due to using the conserved oxygen and nitrogen method for outlet gas flow determination.

Table 4: CESAR-1 CHP sampling periods

#	Method 1, %	Method 2, %	Method 3, %	Method 4, %	Recovery %
1	96.70	97.85	97.88	97.88	98.80
2	97.77	97.85	97.86	97.86	99.92
3	97.43	97.91	97.92	97.92	99.50
4	97.35	98.03	98.05	98.05	99.29
5	97.28	97.95	97.96	97.96	99.30
6	97.23	97.95	97.97	97.97	99.24
7	96.99	97.90	97.91	97.91	99.05
8	97.28	97.87	97.89	97.89	99.38
9	97.57	98.23	98.25	98.25	99.31
10	97.61	98.25	98.26	98.26	99.34
11	98.94	98.37	98.36	98.36	100.6
12	98.31	98.47	98.47	98.47	99.84
13	97.06	98.84	98.87	98.87	98.17
14	96.80	98.81	98.84	98.84	97.94
15	96.77	98.72	98.75	98.75	98.00
16	96.84	98.73	98.76	98.76	98.05

Regardless of the method used, the CO₂ capture rate was consistently >96% as measured during all test periods. As the recovery rate was close to 100%, this implies consistency between the flue gas measurements and CO₂ concentration determination at all 3 locations.

3.2 Thermal Use

The reboiler heat duty or the heat released in the reboiler is calculated as the difference between steam enthalpy at reboiler inlet and the saturated water enthalpy at the reboiler condensate temperature. The specific thermal use (STU) is then calculated by dividing the reboiler heat duty by the product CO₂ flow.

$$STU_{\text{product}} = \frac{\dot{m}_{\text{steam}}(H_{\text{steam}} - H_{\text{condensate}})}{CO_2(\text{product})}$$

$$STU_{\text{captured}} = \frac{\dot{m}_{\text{steam}}(H_{\text{steam}} - H_{\text{condensate}})}{CO_2(\text{supply}) - CO_2(\text{depleted})}$$

The two corresponding values for specific thermal energy consumption are shown in Table 5 and were consistent during all test periods.

Table 5: Stripper reboiler specific thermal use

#	Heat Duty, MJ/hr	Product CO ₂ Flow, kg/hr	Specific Thermal Use, GJ/t-CO ₂	Captured CO ₂ , kg/hr	Specific Thermal Use, GJ/t-CO ₂
1	17,329	5014	3.46	5075	3.41
2	17,403	5045	3.45	5049	3.45
3	17,434	5023	3.47	5049	3.45
4	17,562	5009	3.51	5045	3.48
5	18,097	4969	3.64	5003	3.62
6	18,103	4952	3.65	4990	3.63
7	18,046	4928	3.66	4975	3.63
8	18,081	4941	3.66	4971	3.64
9	18,839	4928	3.82	4963	3.80
10	18,863	4927	3.83	4960	3.80
11	19,148	4948	3.87	4919	3.89
12	18,872	4883	3.86	4891	3.86
13	17,692	5005	3.53	5098	3.47
14	17,683	4994	3.54	5099	3.47
15	17,730	5008	3.54	5110	3.47
16	17,751	5017	3.54	5117	3.47

Prior testing at TCM using conventional 5M MEA solvent with CHP flue gas (3.5 vol% CO₂) at approximately an 80 tonnes-CO₂/day load yielded a regeneration energy range of 3.61–3.66 GJ/t-CO₂ using the product CO₂ flow and 3.58–3.60 GJ/t-CO₂ using the capture method, all carried out at 85% capture rate [3]. The CESAR-1 CHP tests (5 vol% CO₂) achieved circa 119 tonnes-CO₂/day load and achieved a regeneration energy range of 3.45–3.87 GJ/t-CO₂ using product flow and 3.41–3.89 GJ/t-CO₂ using the gas-side difference method.

It can be seen that the regeneration energy initially was near the bottom of the range for Tests 1 to 4 on June 24, and steadily increased in subsequent Tests 5 to 12. It was identified by TCM that excess foam formation in the stripper caused additional water condensation in the overhead stripper and an associated steam consumption increase. An antifoam agent was injected in the morning of June 30 by TCM operators with a subsequent rapid reduction in the regeneration energy measured in Tests 13 to 16, implying that the baseline CHP CESAR-1 regeneration energy is more in the range of 3.45–3.54 GJ/t-CO₂ using product flow and 3.41–3.48 GJ/t-CO₂ using the gas-side difference method when foaming is absent.

Importantly, the capture rate is 98% for these tests, far higher than the 85% capture rate for the MEA baseline tests, showing CESAR-1 solvent performs well at high capture rates as the regeneration energy is lower than MEA (when foaming was controlled) despite a capture rate of nearly 100%.

Recent testing at the Niederaussem pilot plant showed CESAR-1 solvent at 98% capture rate required only 3.22 GJ/tonne regeneration energy, however the inlet CO₂ concentration was 15.2% vol, dry as the flue gas source is from coal combustion [4]. Although the lower CO₂ concentration during these tests resulted in higher regeneration energy than observed at Niederaussem, some of the difference can also be attributed to the use of the RFCC stripper for these tests that is oversized for this regeneration load, operating at only 50% capacity. The CHP stripper was not used for these tests due to a combination of the 5% vol, dry inlet CO₂ concentration and the targeted 98% capture rate.

3.3 Process Contaminants

3.3.1 Aldehydes and Ketones

Formaldehyde, acetaldehyde, and acetone concentrations were determined by extractive sampling during the CESAR-1 CHP test periods. The data are shown in Table 6 for the depleted flue gas and in Table 7 for the CO₂ product.

Table 6: Depleted flue gas aldehyde/ketone concentrations

#	Formaldehyde, mg/Sm ³	Acetaldehyde, mg/Sm ³	Acetone, mg/Sm ³
3	0.0635	0.0931	1.14
7	0.0406	0.0596	1.42
11	0.0546	0.0801	2.85
15	0.0190	0.0279	1.13

The formaldehyde levels are lower than the previous MEA CHP baseline testing, which measured concentrations of 0.72 mg/Sm³ by an external contractor. The acetaldehyde levels are also considerably lower with CESAR-1 than the MEA CHP test samples of 16 mg/Sm³.

Acetone levels measured during the MEA tests were sufficiently low at or below the detection limit of 1 mg/Sm³, while with CESAR-1 they were measurable at between 1–3 mg/Sm³ even though the upper water wash was configured as an acid wash for these tests and not in the MEA campaign. These species were also measured continuously with the Proton-Transfer-Reaction mass spectrometer (PTR-MS) that exhibits a very low detection limit capability (measuring in the ppb range). A sample of the data collected is shown in Figure 4, with higher formaldehyde levels (700–800 ppb) than measured by extractive samples (20–50 ppb), and comparable acetaldehyde and acetone measurements.

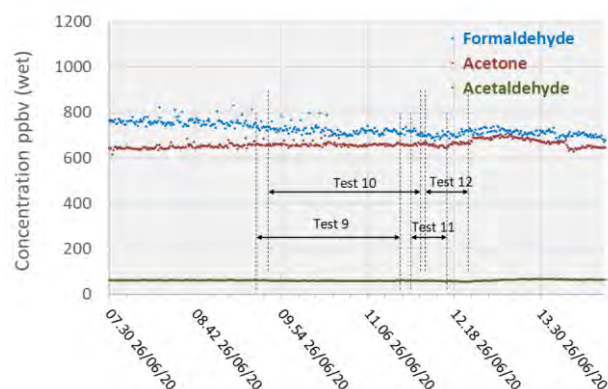


Figure 4: Depleted flue gas PTR-MS aldehyde and ketone measurements

For the CO₂ product, the formaldehyde levels detected were 2–4x higher than the manual-sampled measurements during the MEA CHP baseline campaign (0.14 mg/Sm³) and the acetaldehyde levels were considerably lower than the previous level of 150 mg/Sm³ measured for MEA.

Unlike the MEA tests, acetone was easily detected in the CO₂ product for CESAR-1, whereas in the previous MEA baseline all measurements taken were below the detection limit of 0.9 mg/Sm³.

Table 7: Product CO₂ aldehyde/ketone concentrations

#	Formaldehyde, mg/Sm ³	Acetaldehyde, mg/Sm ³	Acetone, mg/Sm ³
2	0.63	0.93	21.7
8	0.42	0.61	23.1
10	0.39	0.57	28.5
16	0.18	0.27	16.7

The concentration of the depleted flue gas will be impacted by the CO₂ recycle stream, passing a portion of the contaminants shown back to the absorber inlet. With the exception of acetone, these components in the flue

gas for the CESAR-1 testing were significantly lower than previous MEA measurements. This in turn suggests that these components are not significant degradation compounds from AMP and PZ, or that these solvents were not degraded to the same condition as for MEA.

3.3.2 Ammonia and Solvent Components

TCM measured concentrations of solvent components (AMP and PZ) along with ammonia during the CESAR-1 testing. Results of these manually extracted samples are shown in Table 8.

Table 8: Depleted flue gas stream ammonia and solvent component concentrations

#	AMP, mg/Sm ³	PZ, mg/Sm ³	Ammonia, mg/Sm ³
4	0.06	0.01	0.04
5	0.04	<0.007	0.03
9	0.03	<0.007	0.02
13	0.03	<0.007	0.03

'<' denotes the limit of detection

The solvent components of CESAR-1 appear to show higher vapor pressure than is associated with MEA solvent, which was previously measured by an external contractor at 0.006 mg/Sm³ during testing on CHP flue gas. PZ was barely detected, only showing up in Test 4, which shows that perhaps a longer extraction sample period would help to improve determination of this species at the ppb level. Ammonia levels are far lower than the previous MEA CHP tests results, measured at 13 mg/Sm³, suggesting that ammonia does not represent a significant degradation product of CESAR-1.

With the exception of the first test, the AMP measurements were lower than the extractive samples. However, both strategies were likely near their method detection limits as levels were measured below 20 ppb in all cases. PZ was not detected by the PTR-MS instrument and hence was not included in Figure 5, however Acetonitrile was detected at 0.1 ppmv.

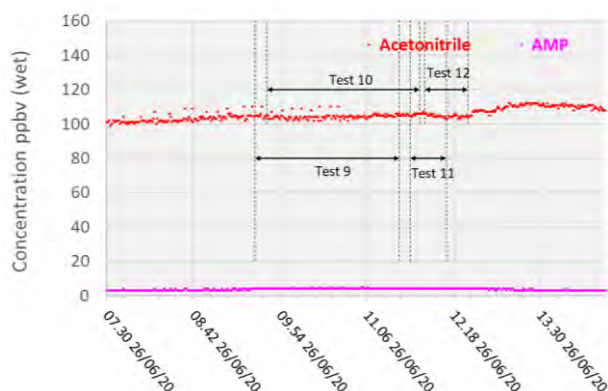


Figure 5: Depleted flue gas PTR-MS solvent measurements

Extractive solvent and ammonia samples were taken from the CO₂ product, and the results are shown in Table 9.

Table 9: Product CO₂ ammonia and solvent component concentrations

#	AMP, ppmvd	PZ, ppmvd	Ammonia, ppmvd
1	7.73	0.07	2.89
6	9.07	0.12	3.20
10	7.49	0.09	4.60
14	0.29	<0.007	3.59

'<' denotes the limit of detection

Similar to the depleted flue gas measurements, the AMP measurements were higher than the equivalent MEA samples, at 0.076 mg/Sm³, and up to 2 orders of magnitude higher for AMP. PZ was detected in 3 of the 4 samples, but was present at very low concentrations.

Although ammonia desorption into the product gas is 2 orders of magnitude higher than the depleted flue gas levels, this is 4 times lower than the ammonia detected from the MEA CHP tests at 16 mg/Sm³.

3.3.3 SO₂ and NO_x

The TCM Fourier-transform infrared units installed for the flue gas supply and the depleted flue gas were configured to measure SO₂, NO, and NO₂ concentrations. The reported data are shown in Figures 6 and 7.

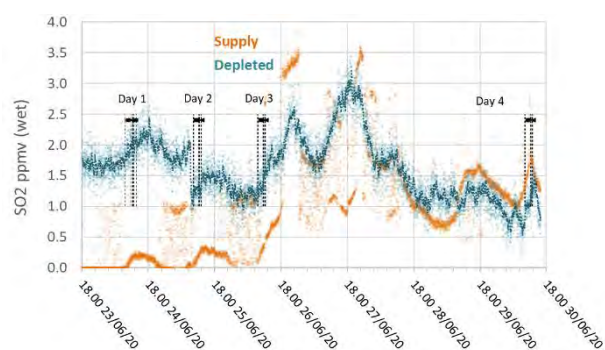


Figure 6: Supply and depleted flue gas SO₂ measurements throughout the test period

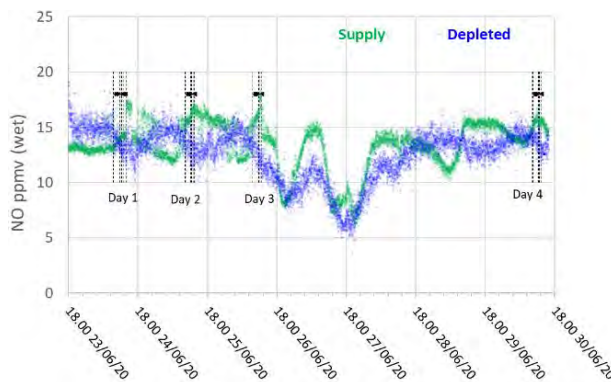


Figure 7: Supply and depleted flue gas NO measurements throughout the test period

During previous MEA testing, SO₂ levels leaving the absorber were consistently lower than the inlet measurement, likely due to absorption. This doesn't appear to be the case for CESAR-1 solvent, though the inconsistency in the incoming flue gas data doesn't allow a strong relationship to be established. Therefore, there

was no way to determine SO₂ absorption rates for this solvent from the tests.

The NO data shows similar levels at the inlet and outlet, indicating minimal absorption into the CESAR-1 solvent. While absorbed NO₂ is known to contribute to the formation of nitrosamines in some solvents, the NO₂ data for the depleted gas were not recorded for these test periods. The average measured values in the flue gas for both NO and SO₂ leaving the absorber are shown in Table 10.

Table 10: Depleted flue gas SO₂ and NO concentrations

#	SO ₂ , ppmvd	NO, ppmvd
1	2.02	14.9
2	2.20	14.2
3	2.28	13.6
4	2.19	14.0
5	1.38	14.5
6	1.40	14.3
7	1.36	13.9
8	1.43	14.2
9	1.39	14.0
10	1.41	13.9
11	1.64	13.1
12	1.68	12.8
13	1.10	15.0
14	1.11	14.9
15	1.34	15.2
16	1.38	14.4

4. Conclusions

CESAR-1 solvent was tested at the TCM amine plant over 16 individual tests, during which extractive samples were taken, an overall summary of the tests is given in Table 11.

Table 11: Summary of CESAR-1 testing

Baseline Year	2020
Packing Height (m)	18
Flue Gas Flow (Sm ³ /h)	59,000
Flue Gas Supply Temperature (°C)	38
Flue Gas Supply Pressure (bar)	0.02
Lean Amine Flow (kg/h)	58,000
Lean Loading	0.10
Rich Loading	0.52
Stripper Bottom Temperature (°C)	121
CO ₂ Capture (%)	98
SRD (GJ/t-CO ₂)	3.61

The plant was operated at 119 tonnes/day of CO₂ production with capture rates of 96–99%, exhibiting a near 100% mass balance.

Foaming was identified as causing stripper performance issues; however, when foaming was controlled, the regeneration energy for CESAR-1 solvent was 3.41–3.54 GJ/t-CO₂, lower than prior baseline testing of MEA at a lower capture rate of 85% at 3.58–3.66 GJ/t-CO₂.

Degradation products including formaldehyde, acetaldehyde and ammonia, were measured at lower levels for CESAR-1 solvent with acid water wash compared to results from MEA testing. As the solvent is a blend of AMP and PZ, both species were sampled showing higher levels of AMP than was measured for MEA and PZ being barely detectable due to the low vapor pressure of PZ.

5. Acknowledgements

The authors gratefully acknowledge the staff of TCM DA, Gassnova, Equinor, Shell, and Total for their contribution and work at the TCM DA facility.

The authors also gratefully acknowledge Gassnova, Equinor, Shell, and Total as the owners of TCM DA for their financial support and contributions.

6. References

- [1] Thimsen et al., Energy Procedia 63, 5938–5958; 2014.
- [2] Flue Gas Composition and Energy & Mass Balance Accuracy Studies at CO₂ Technology Centre Mongstad (TCM DA): Results Related to the Amine Capture Unit.” K-E Frøysa and R. Sakariassen. CRM-12-F14016-RA-2: 7 June 2012
- [3] Faramarzi et al., Energy Procedia 114, 1128–1145; 2017.
- [4] Moser et al., ALIGN-CCUS: Results of the 18-Month Test with Aqueous AMP/PZ Solvent at the Pilot Plant at Niederaussem – Solvent Management, Emissions and Dynamic Behavior. Proceedings of the 15th Greenhouse Gas Control Technologies Conference 15-18 March 2021, <http://dx.doi.org/10.2139/ssrn.3812132>

SCREENING MICROORGANISMS FOR REMEDIATION OF WELLS VIA CARBONATE PRECIPITATION

Megan J. Barnett¹, Simon P. Gregory¹, Audrey Ougier-Simonin¹

¹British Geological Survey, Keyworth, UK

* Corresponding author e-mail: megan@bgs.ac.uk

Abstract

Borehole infrastructure in near end-of-life oil and gas reservoirs can potentially be reused for CCS operations when repurposing fields for use as CO₂ storage reservoirs. The integrity of such wells may not be sufficient for immediate applications; however remediation could make them suitable for reuse. Microbial induced carbonate precipitation (MICP) is ubiquitous in nature and had been proposed as a suitable technological solution for reducing permeability in several geotechnical scenarios. However, the relatively high temperatures, and high pH of down well environments provide challenges to microorganisms. We present a suite of screening techniques and simplified flow apparatus to enable screening of MICP microorganisms and optimization of parameters to better understand the application of novel microorganisms for remediation in deep subsurface conditions.

Keywords: MICP, bioprecipitation, borehole remediation, CCS, microbiology

1. Introduction

A large number of oil and gas reservoirs are coming to end-of-life and are of interest as potential sites for large scale CCS. REX-CO₂ is a multidisciplinary project addressing the potential for reuse of existing oil and gas wells for CCS. Assessing well integrity and exploring potential remediation techniques form part of this work.

Microbial induced carbonate precipitation (MICP) is a biochemical process that is widespread in nature, both in terms of environments and organisms involved [1]. Several different biochemical pathways can result in carbonate precipitation; primarily from the carbon, nitrogen and sulfur cycles. These all differ in the details of the pathway. However, MICP generally relies on the microbial production of carbonate or bicarbonate compounds and microbial induction of local increases in pH. Then, if there are suitable cations in the environment, precipitation occurs chemically.

MICP is utilised in biotechnology applications e.g. Biocalcis® for soil stabilization (Soletanche Bachy, France) and is a rapid area of development for subsurface geotechnical applications such as borehole sealing [2], and self-healing cement [3]. Field scale borehole sealing at 340m depth was demonstrated using a wireline dump bailer, delivering fluids at depth. It was achieved by introducing alternating solutions of microbial growth media containing either *Sporosarcina pasteurii* or Ca ions and achieved flow rate decrease from 1.9L min⁻¹ to 0.47L min⁻¹ after 4 days treatment [2].

The bacterium *S. pasteurii* induces MICP via urea hydrolysis, and is commonly used as a focus of biotechnology development as precipitation proceeds by a well-defined pathway, and can lead to high carbonate yields [1]. Modifying factors such as microbiological media composition or flow rate can affect precipitation and therefore permeability [2]. However, MICP via the ureolytic pathway is not suitable in all applications due to environmental and other constraints [4].

We explored non-ureolytic nitrogen microbial metabolic pathways for down well remediation, it was essential that microbial isolates were capable of carbonate precipitation in fluids at the moderate temperatures (due to depth) and higher pH (due to cement) that may be encountered when remediating oil and gas wells. Several suitable environments were targeted for bacterial isolation and simple screening techniques were applied to identify essential and desirable properties of the microorganisms. Additional simple flow experiments were developed to enable the optimization of parameters, such as media concentration, prior to application in a laboratory scale remediation test with aged cement and suitable reservoir or caprock.

2. Materials and Methods

2.1 Field sites and isolation of novel bacteria

MICP microorganisms are commonly found in carbonaceous soils, so a lime-rich field site was selected as source of microorganisms. As growth at elevated temperatures was also of interest two thermal springs were sampled, both of which passed through carbonate rocks. Lime-rich soil samples were taken from a stream draining a lime waste site near Buxton, Derbyshire, UK (soil identification from landis.org). Initially two samples were selected to test a range of precipitation media, and modified B4 microbiological growth agar was selected for further isolations. Modified B4 agar (per L): yeast extract (4g), glucose (1g), calcium acetate (2.5g), Tris HCl (4.42g), Tris base (7.72g), phenol red (12mg) and agar (15g). Final pH 8.5. Glucose and calcium acetate were added as 0.2 µm filter-sterile fluids after autoclave sterilization of the remaining media components. An additional ten samples were collected along a transect of the stream. Spring water was collected from Buxton St Anne's Well (~27°C) and Thermae Bath Spa (~40°C), 500mL to 4 L was filtered onto sterile 0.22 µm membranes, split in half then pressed onto modified B4 agar. Plates from all sites were incubated at 30 and 50°C.

Table 1: Selected screening results from unique isolates

Isolate	Provisional identification	Metabolic pathways		Carbon source						pH		Anaerobic	Liquid	50 °C
		Urease	Am.	G+ Ac	YE+ G	YE+ Ac	G	YE	Ac	9.5	10.0			
BH01	<i>Bacillus flexus</i>	Y	Y	W	Y	Y	W	Y	W	W	W	N	Y*	N
BH03	<i>B. paralicheniformis</i>	N	Y	Y	Y	Y	Y	Y	W	Y	Y	Y	Y*	Y
HH11	<i>Microbacterium maritopicum</i>	Y	Y	W	W	W	N	W	W	W	W	Y	xls	W
HH18	<i>Arthrobacter gandavensis</i>	N	Y	Y	Y	xls	xls	Y	xls	Xls	xls	N	xls	Y
HH19	<i>Brevibacterium frigoritolerans</i>	Y	Y	Y	Y	xls	Y	Y	xls	Xls	W	Y	xls	W
HH21	<i>M. oxydans</i>	Y	N	xls	Y	xls	xls	W	W	W	W	W	xls	N
HH26	<i>B. licheniformis</i>	N	Y	Y	Y	xls	W	Y	xls	Y	Y	Y	xls	W

Am. Ammonification, YE yeast extract, G – glucose, Ac – Ca acetate. Y – growth, N – no growth, W - weak growth, xls - growth with visible crystals observed.

* no crystal could be seen but thick biofilms formed, potentially containing crystals

2.2 Screening techniques

Visually unique isolates with evident crystal growth were selected and re-streaked on modified B4 agar. Bacterial isolates were identified by partial DNA sequencing of the 16s rRNA gene, and potential pathogens discarded. Further adjustments were made to modified B4 agar to test for the following properties of each of the bacterial isolates:

- Growth with Na acetate replacing Ca acetate
- Growth with single or dual carbon sources (yeast extract, glucose and Ca acetate)
- Crystal formation in liquid media (these were static to preserve local pH changes around cells)
- Growth at different temperatures: 25, 35 and 50°C
- High pH tolerance: 9.0, 9.5 and 10.0

Isolates were tested by resuspending a single colony in sterile saline and spotting three volumes of 10µL onto appropriate agar or 10µL into 20mL fluid.

Selective media for urease production and ammonification were also used to test the bacterial isolates. Urease agar (per L): peptone (1g), NaCl (5g), glucose (1g), urea (20g), phenol red (12mg), agar (15g). Final pH 6.5. Urea and glucose were added as filter sterile solutions. Ammonification agar (per L): peptone (5g), yeast extract (3g), NaCl (5g), phenol red (12mg), agar (15g). Final pH 7.0. For both tests, positive identification is associated with a colour change in agar surrounding the isolate. A pink colour is seen as the pH increases.

2.3 Development of low-cost flow experiments

Simple flow experiments were developed to enable test for MICP of bacterial isolates in the presence of unconsolidated materials. *S. pasteurii* (DSMZ33, purchased from DSMZ, Germany) was tested alongside the seven isolates identified from the initial screening stage of this study. Figure 1 shows an example set-up. All isolates and were grown in liquid broth for three days at 35°C. Suspension was then centrifuged at 4000 x g to

concentrate microbial cells and 0.5 mL of concentrated isolate was added to top of syringe barrel, and topped up with 2.5mL unbuffered liquid media (i.e. modified B4 without Tris buffer components or agar). Experiments were left for 4 hours to allow for attachment of cells (three-way valve closed). Then, unbuffered B4 media was supplied to the top of the syringes at nominal flow rate of 0.5 mL h⁻¹. The three-way valve was opened, allowing for excess fluid to flow out via tubing under gravity.

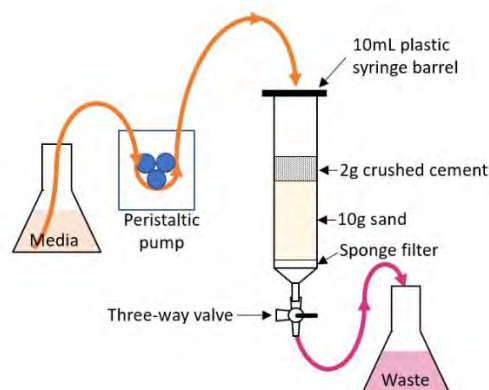


Figure 1: Example set up of low-cost flow apparatus. The syringe barrels are housed in incubator.

At the end of experiment DI water was flowed through system for 24 hours, at 0.5 mL h⁻¹. If out flow under gravity was not possible, excess fluid was removed using syringe at time intervals between 4 to 8 hours. Syringes barrels and contents were then dried at 35°C. The end of the syringe barrels were cut off with craft knife and contents ejected using syringe plunger. The samples were imaged using Olympus TG-6 in macro mode.

3. Results

3.1 Colony Screening

Thirty-one isolates (showing crystal growth) were picked for further screening (Figure 2), of which seven unique

isolates were identified by colony morphology and subsequent DNA sequencing (Table 1). Five were isolated from sediments (HH), and the remaining two from Thermae Bath Spa water (BH). All isolates were capable of growth with Na acetate replacing Ca acetate and at 35°C (data not shown), with five capable of growth at 50°C. All isolates were capable of growth at all pHs tested, and could grow with just yeast extract, however it was observed that spots were generally slightly larger with the addition of glucose.

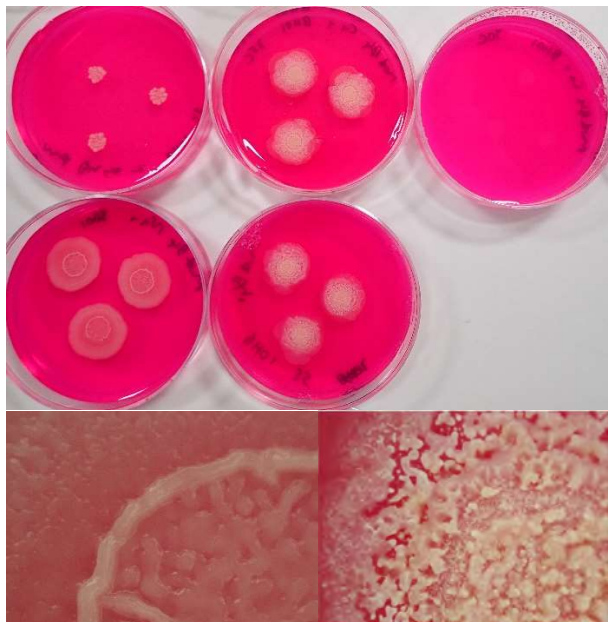


Figure 2: example of isolate screening with isolate BH01. Petri dishes are 55 mm diameter. Top row left to right, growth at 25°C, 35°C and 50°C. Middle row, growth at 35°C left with Na acetate, and centre 50% Ca acetate. Bottom row, close up images showing differences between growth in the absence (left) and presence (right) of Ca ions. Image width ~3 mm.

All seven isolates, along with *S. pasteurii*, were tested in the first round of flow experiments as all were capable of growth at 35°C, pH 10.0 and likely to produce crystals in liquid media.

3.2 Flow experiments

Phenol red is a pH sensitive dye and was added to the microbiological media as carbonate precipitation is pH dependent and is favoured at higher pH. The unbuffered B4 media starts orange (~7.0), and will turn yellow at pH < 6.2 and pink at pH > 8.0. During microbial growth in unbuffered B4 the growth media initially turns yellow, likely through organic acid production during glucose consumption. After this the solution turns pink e.g. through ammonification. In the flow experiments the media turns pink once added to the crushed cement. After 24 hours of flow through the cements and sand the colour, hence pH, varied among the isolates from orange to pink (lowest to highest) in the following order: HH26, HH10, HH19, *S. pasteurii*, BH03, BH01, HH18 and HH21. The higher pH indicates a more favourable environment for carbonate precipitation.

Waste flow under gravity was no longer possible in BH01 and BH03 after 7 days, and all flow experiments were stopped after 8 days. Blockages were likely to be a

combination of crystal and biomass growth. After drying, crystals and finer powdered material were seen on the surfaces of the crushed cement. Some consolidation of the crushed cement was observed with all isolates, this was not quantified however was noticeably weaker with HH26 (Figure 3).

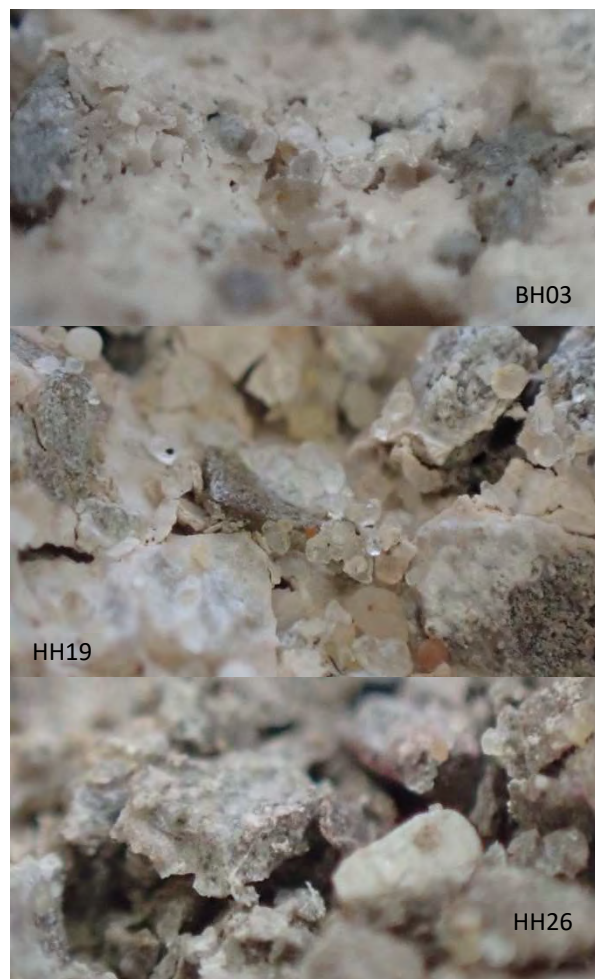


Figure 3: Crystal growth on upper surface of crushed cement. Image width ~2.5 mm.

Given that all isolates met the essential characteristics and were capable of growth with just yeast extract, the desirable characteristics and performance in flow tests were used for further screening. Only BH03 has strong growth in the remaining two desirable characteristics (50°C and anaerobic growth). HH11, HH18 and HH19 are also of interest as they show strong growth in one of the desirable characteristics and either weak growth in the other, or promise in flow experiments.

4. Discussion and Conclusion

Screening was divided into two different categories, those that are essential for bioremediation at depth and those which are desirable as they support practicalities and reduce cost implications of bioremediation. Due to selection of appropriate field samples and initial isolation criteria (modified B4 agar and minimum 30°C growth) it is not unsurprising that all seven isolates satisfied the essential characteristics (growth at moderate temperature, 35°C, and precipitation of minerals at moderate temperatures at high pH and in liquid media). The desirable characteristics were higher growth

temperature (50°C), reduced nutrient requirements and anaerobic growth. For biotechnology applications fast growth would also be desirable, and could be estimated by recording size of spot after a given time, this was not recorded systematically during screening, but could be estimated from images. The provisional identifications of the good (*B. paralicheniformis*), and potential (*M. maritypicum*, *A. gandavensis* and *Br. Frigoritolerans*) candidates come from a range of genera but limited to two classes of soil associated bacteria.

Due to the high cost of Tris buffer this was excluded for the flow experiments, as would drastically increase the cost of industrial applications. Phenol red, a pH sensitive dye, was included during these experiments as it allows for easy trouble shooting, but would be unnecessary during upscaling. Screening has demonstrated that only yeast extract was required for growth, and the low-cost flow experiments developed here are perfectly suited to test effect of media composition on carbonate precipitation, leading to increased efficiency and cost reduction.

Successful consolidation of the crushed cement by six of the seven isolates (and *S. pasteurii*) demonstrates that simple flow experiments can be used as a basis for microbial screening and testing precipitation parameters. The flexibility of this system can be easily adapted to different flow regimes, *i.e.* bottom fed, and along with precise measurements of mass change can be used to quantify the effect of these changes on precipitation. This system will also be used to refine parameters such as media composition, starting cell density or pulsed flow, before being used in more complex laboratory test systems [5,6].

Laboratory test systems for bioprecipitation, including those planned as part of REX-CO₂ project, generally involve complex, or large-scale systems and can include high pressure pumps, pressure vessels, cored material, or sand tanks along with instrumentation to monitor changes in pressure and flow. Although these systems provide essential insight into how these systems behaving in near real-world scenarios [5, 6], their nature means that only a limited number of parameters can be measured.

Down hole MICP technologies have a huge potential in geotechnical engineering including the remediation of oil and gas wells for CCS. Similar technologies have already been demonstrated to promote borehole sealing at 340 m depth in oils and gas wells through urea hydrolysis by *S. pasteurii* [2]. This presented here has identified one good (provisional identification *B. paralicheniformis*), and three potential candidates (provisional identifications *M. maritypicum*, *A. gandavensis* and *Br. Frigoritolerans*) for

bioremediation of oil and gas wells. As urea was not used in these experiments an additional pathway for MICP must be involved, potentially via the ammonification of the nitrogen sources in the yeast extract. As urease hydrolysis is not appropriate in all environments, microorganisms capable of MICP via alternative metabolic pathways are required to fulfil the full potential of MICP as a geotechnical tool.

Acknowledgements

The project REX-CO₂ is funded through the ACT programme (Accelerating CCS Technologies, Horizon2020 Project No. 294766). Financial contributions made from ADEME (FR); RVO (NL); Gassnova and RCN (NO); UEFISCDI (RO); BEIS, NERC, and EPSRC (UK); and US-DOE (USA) are gratefully acknowledged. Also thanks to Leigh Sanderson from Bath and North East Somerset Council for access to Bath Spring Water.

References

- [1] Zhu, T and Dittrich, M (2016). Carbonate Precipitation through Microbial Activities in Natural Environment, and Their Potential in Biotechnology: A Review. *Front. Bioeng. Biotechnol.* 4:4. doi: 10.3389/fbioe.2016.00004
- [2] Phillips, AJ, Cunningham, AB, Gerlach, R, Hiebert, R, Hwang, C, Lomans BP, Westrich J, Mantilla C, Kirksey J, Esposito R and Spangler L (2016). Fracture Sealing with Microbially-Induced Calcium Carbonate Precipitation: A Field Study. *Environmental Science & Technology* 50 (7), 4111-4117 DOI: 10.1021/acs.est.5b05559
- [3] Jonkers, HM, Thijssen, A, Muyzer, G, Copuroglu, O and Schlangen, E. (2010). Application of bacteria as self-healing agent for the development of sustainable concrete *Ecological Engineering* 36 (2) p97-246 <https://doi.org/10.1016/j.ecoleng.2008.12.036>
- [4] Reeksting BJ, Hoffmann TD, Tan L, Paine K and Gebhard S. (2020). In-Depth Profiling of Calcite Precipitation by Environmental Bacteria Reveals Fundamental Mechanistic Differences with Relevance to Application. *Appl Environ Microbiol.* 86(7):e02739-19. Published 2020 Mar 18. doi:10.1128/AEM.02739-19
- [5] Mitchell, AC, Phillips, AJ, Schultz, LN, Parks, SL, Spangler, H, Cunningham, AB and Gerlach, R (2013). Microbial CaCO₃ mineral formation and stability in an experimentally simulated high pressure saline aquifer with supercritical CO₂ " *International Journal of Greenhouse Gas Control*, July 2013 15: 86–96 <https://doi.org/10.1016/j.ijggc.2013.02.001>
- [6] Nassar, MK, Gurung, D, Bastani, M, Ginn, TR, Shafei, B, Gomez, MG, Graddy, CMR, Nelson, DC and DeJong, JT (2018). Large-scale experiments in microbially induced calcite precipitation (MICP): Reactive transport model development and prediction. *Water Resources Research*, 54, 480– 500. <https://doi.org/10.1002/2017WR021488>

UPSCALED GEOCELLULAR FLOW MODEL OF POTENTIAL ACROSS- AND ALONG-FAULT LEAKAGE USING SHALE GOUGE RATIO.

T.I. Bjørnarå^{1*}, E.M. Haines², E. Skurtveit^{1,2}

¹ NGI, Oslo, Norway, ² University of Oslo, Norway

* Corresponding author e-mail: tore.ingvald.bjornara@ngi.no

Abstract

Every CCS project has an inherent risk of leakage. Faults are difficult to characterize because they are structurally complex and limited subsurface field-data is typically available; hence the properties need to be inferred elsewhere, e.g. well-logs and seismic. For example, the shale gouge ratio (SGR) is typically used today in the oil and gas exploration to estimate sealing properties of faults, by utilizing VShale well logs.

Here we extend the methodology to account for along-fault flow where the complex structural composition of a fault is conceptually described by a geocellular model that is stochastically constructed using modelled SGR from a real fault (Vette Fault) in the Horda platform, North Sea, offshore Norway. A detailed geocellular fault model can be extremely computationally expensive, therefore an upscaled formulation is defined and validated. This formulation also extends the applicability of a multi-layered geocellular model by allowing slip-surface(s) to be a natural component of the fault core. The validation model is applied to a single-phase fluid flow problem, simulating fluid migration from a pressurized reservoir and across and up along a fault that intersects the reservoir; a scenario directly relevant to CO₂ storage where the fault is (temporary) outside the reach of the injected CO₂ plume.

The presented upscaled formulation of a multi-layered geocellular model was found to have a high and consistent accuracy, relative to a full-dimensional reference model, with generally less than 4 % error (or less than 8 % within 95 % confidence interval) in calculated along- and across-fault flow. The focus here is on proof of concept and validation of a generic upscaled multi-layered geocellular model, but some general observations can be made. For across-fault flow, an increase in variability in fault composition resulted in a reduced flow-rate and less spread in flow-rate. For along-fault flow, increasing variability in fault composition had little effect on mean flow-rate, but resulted in smaller spread.

Keywords: CO₂ storage, across- and along-fault flow, Shale Gouge Ratio (SGR), fault leakage

1. Introduction

Recently, the Norwegian government launched Longship, a first project for full-scale Carbon Capture and Storage (CCS) in Norway. The Aurora storage site in the Norwegian Horda Platform area is currently under development of CO₂ injection, but the area also has large potential for upscaling the storage volumes. The Smeaheia fault block, located between the Troll gas field and the Norway west coast has shown promising storage potential within the Sognefjord Formation, bounded by two regional fault systems, the Vette Fault Zone (VFZ) and the Øygarden fault complex (ØFC), in the west and east, respectively, see Figure 1. The future success of this faulted block as offshore CO₂ storage is highly dependent on maturing the geological understanding and fault seal potential of the area (Mulrooney et al., 2020, Wu et al., 2021).

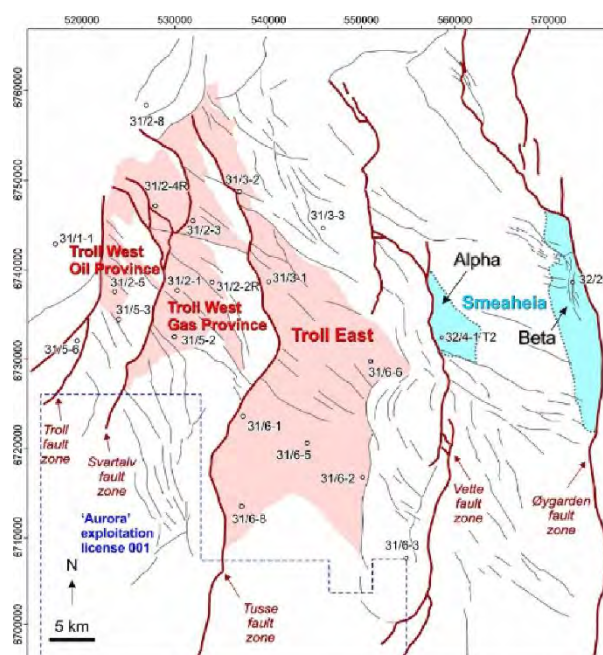


Figure 1: Structural map of the Troll field area (Wu et al., 2019). The Smeaheia-site is shown with two storage prospects (Alpha and Beta) bounded laterally to the west and east by the Vette Fault (VF) and Øygarden Fault (ØGF), respectively.

The challenge with CO₂ storage is to ensure its integrity against leakage of injected CO₂. Three potential leakage pathways for CO₂ are: (i) migration and diffusions through intact caprock, (ii) migration by fracturing of the caprock and (iii) migration along pre-existing fractures and faults (Niemi et al., 2017). Besides (iv) leakage up wellbores, (iii) is potentially the most critical mechanism and most difficult to characterize in terms of leakage risk. Faults can have both sealing or conductive properties, making them complex geological structures that can both limit the storage capacity and be detrimental to the storage integrity.

There is a general need for improved understanding of fluid flow in faults, particularly for large regional-scale faults. The geometry may be constrained by seismic and missing fault attributes can be approximated using correlations, e.g. Torabi & Berg (2011). However, the main challenge is to characterize hydraulic properties of faults from available data. One of the aspects that makes large faults complex is the unknown variability and distribution of associated fault rocks (gouge, breccia, cataclasite, mylonite, etc.) within the fault core (Grant, 2020), and the resulting hydraulic properties.

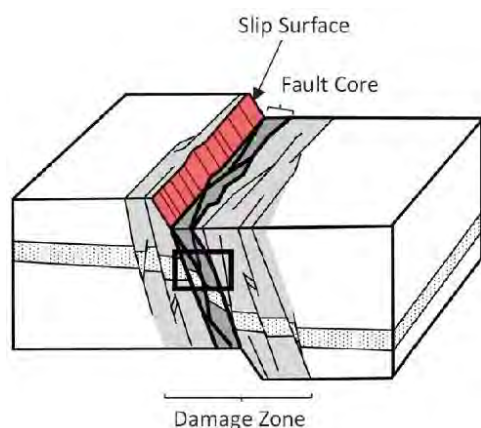


Figure 2: Illustration of a typical fault architecture, as originally defined by Caine et al. (1996) (figure from Grant 2020, originally modified from Torabi & Berg, 2011).

The two most common representations and/or conceptualizations of faults and its hydraulic structure are the single- and two-component description of a fault, see Figure 2 and Figure 3. In the single-component model, the fault zone (FZ) is homogenized to an isotropic or anisotropic permeability structure with principal permeabilities in the across- and along-fault directions. In the two-component fault model, the fault zone is divided into a fault core (FC) surrounded by a damage zone (DZ). This latter model was further characterized by Caine et al. (1996) by distinguishing the fraction of FC width and DZ width relative to the total FZ width and recognizing that, in general, the FC promotes sealing (barrier) properties while the DZ promotes conductive (conduit) properties. Fault classification by Caine et al. (1996) is based on geometric properties of FC and DZ, but other modified two-component fault classifications have been proposed, e.g. by Matonti et al. (2012) which is based on fracturation, p -wave velocity and porosity.

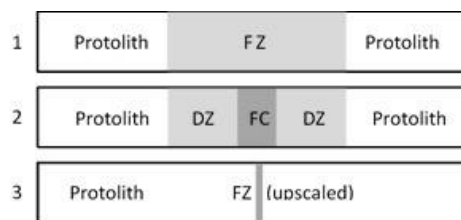


Figure 3: Typical conceptualizations of faults found in the literature. (1) Single-component model of a fault zone (FZ). (2) Two-component model where the fault zone is divided into a fault core (FC) surrounded by a damage zone (DZ). (3) Upscaled/dimensionally reduced version of single- and/or two-component fault model where the FZ, or FC and DZ, is mathematically described as a surface in 3D, or a line in 2D, with virtual thicknesses.

Another way to distinguish the fault properties is to divide the FZ into a zone of low- and high-strain, or displacement. The high-strain zone corresponds to the fault core with the largest deformations and where the fault rock is developed. The low-strain zone corresponds to the damage zone. The host rock material, before faulting, decides what properties the strain-zones will have after faulting. This conceptualization has resulted in several mixing models, or clay smear models, where sequences of alternating sandstone and shales are displaced by faults: shale smear factor model (SSF, Lindsay et al., 1993), clay smear potential model (CSP, Lehner and Pilaar, 1997), shale gouge ratio model (SGR, Yielding et al., 1997) and extensions of these.

SGR is a measure of the net shale/clay content at a location along the slip direction of a fault. It has been shown that the clay-content typically has an exponential influence on the fault core permeability, and there are several correlations between fault core permeability and SGR, e.g. Sperrevik et al. (2012), and Childs et al. (2007). Further, a relationship has been defined between the predicted SGR and measured column heights (Yielding et al., 2010). Hence, SGR is commonly used to predict the sealing potential of a fault and its ability to contain a maximum hydrocarbon column.

There have been several attempts in advancing the characterization of hydraulic properties of faults. The single- and two-component models illustrated in Figure 3 are not adequate because an average model cannot capture the variability, across and along the fault, and therefore may not capture potential spill-points along a seemingly sufficiently tight caprock. This has led to the development of geocellular fault models, where the fault core is approximated by geocells and the geocell properties are populated stochastically, e.g. fault rock facies (Fault Facies Project at the University of Bergen, e.g. Fredman et al., 2007, Kolyukhin & Tveranger, 2015, and references therein) or upscaled SGR from seismic and well-logs (Manzocchi et al., 1999). This is done by converting the locally upscaled SGR-value to a permeability, which is then used to calculate a transmissibility multiplier for across-fault flow characterization that can be used in reservoir-scale models (Manzocchi et al., 1999).

An important component of a fault is the slip-surface(s) in the high-strain FC. The slip-surface(s) of a fault can be straight or undulating (anastomosing), they can occur

single or in an arrangement, e.g. en echelon. A distinct feature of a slip-surface is that it has an extremely large aspect ratio and is therefore missing in geocellular models. However, slip-surface(s) can be an important factor when considering activation of a fault and the dynamic changes in its sealing properties. Slip-surfaces, like discrete fractures, are almost always defined as a dimensional reduced object with a virtual thickness.

Here we present a model that combines the fault variability of the geocellular model with the inclusion of slip-surface(s) in the fault. We use the geocellular approach to characterize fluid flow both across and along a regional-scale fault. Then we formulate the geocellular fault using upscaled equations for single-phase fluid flow. The upscaled multi-layer geocellular model is validated by solution-comparison with a model using the full-dimensional formulation. The strength of the upscaled formulation of a geocellular fault is that it uses an already applied methodology based on SGR (hence, also transmissibility multiplier), and the upscaled formulation is identical to a dimensionally reduced slip-surface and can therefore easily be added as an integral part of the fault description. Also, the less complex and numerically efficient upscaled formulation opens the possibility to do a wide range of investigations and what-if analyses related to faults, both in 2D and 3D, and some preliminary analysis are also presented.

2. Model and method

The focus in this manuscript is on the validation of an upscaled geocellular model, and in particular the across- and along-fault fluid flow and flow rates out of storage reservoir. Hence, the material properties of surrounding formations, including the reservoir, are generic and therefore not discussed in detail. This simplification also applies to the geometry, e.g. we do not consider the displacement (throw) of the fault and therefore the host rocks on opposite sides of the fault are not shifted relative to each other.

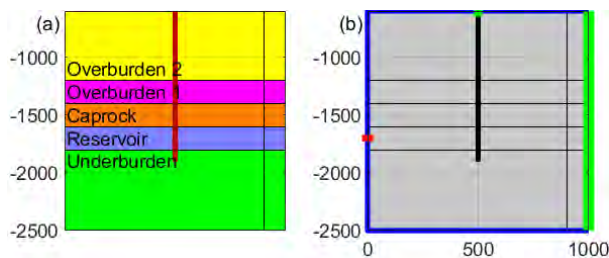


Figure 4: Geometry of validation model with the various lithologies indicated. The total height of the model is 1900 m (from -2500 m to -600 m). The total width of the model is 10 km. (a) The various formations in the model. The fault core (FC), indicated by the red vertical line, is 15 m thick and located app. 500 m from the left boundary. In the full-dimensional model the fault is defined by a domain, and in the upscaled model the fault is defined by a zero-thickness line (internal boundary in the model). (b) Boundary conditions: Inlet (pressure, red), no-flow (blue) and outlet (reference pressure, green).

The scenario that is treated here is a pressurized reservoir, e.g. due to injection of CO₂. The reservoir is intersected

by, and hydraulically connected to, a vertical fault that extends up to the top of the overburden, at -600 m bmsl, see geometry in Figure 4. Although the scenario presented here is related to CO₂ storage, the fault is assumed, for simplicity, to be outside the reach of the CO₂ plume and is therefore a single-phase fluid flow problem.

The complex structural composition of the FC is conceptually described by a geocellular model. The cells, stochastically constructed, have a randomly generated height between 10-100 m. The geocells allow for variability in the permeability structure, which can be populated stochastically from either fault facies (e.g. Wilson et al., 2020, Grant, 2020) or SGR (Yielding et al., 1997). Here we use a vertical cross-section (red line in Figure 5, center) of a 3D model of the SGR for a real fault on the Horda platform in the North Sea (Vette Fault, see Figure 1, a 2 km wide section is shown in Figure 5, left) as basis for the considered scenario. The vertical cross-section is the mean SGR-profile and using a normal probability distribution function with a standard deviation of 14 % (derived from Foxford et al., 1998; Freeman et al., 2008), the geocellular fault is populated. In Figure 5 (right) a geocellular fault (core) with 8 parallel layers is shown, the grey dots indicate the corresponding statistical spread in SGR-values along the vertical profile (each grey dot represents a geocell).

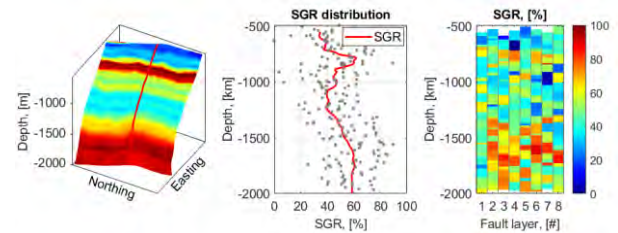


Figure 5: Left: A 2 km wide section of SGR (%) along the Vette fault (cold blue to hot red represents SGR-values of 28-62 %, respectively). Center: Red line is the average SGR-profile shown in left panel. Right: Example of a geocellular model of SGR. The SGR-values in the geocells are shown by the grey dots in the center figure.

2.1 Numerical model

The numerical model is a reservoir-scale model with a geometry as schematically shown in Figure 4. The fluid flow is described by the mass conservation equation for the fluid combined with Darcy's law for the volumetric flux rate \mathbf{q} [m/s]:

$$S\rho\frac{\partial p}{\partial t} + \nabla \cdot (\rho\mathbf{q}) = 0, \mathbf{q} = -\frac{k}{\mu}(\nabla p - \rho\mathbf{g}) \quad \text{Eq. 1}$$

where ρ [kg/m³] is the fluid density, k [m²] is the permeability, μ [Pa·s] is the fluid viscosity, \mathbf{g} [m/s²] is the gravity vector and where the storage coefficient S [1/Pa] is defined by:

$$S = \frac{b - \phi}{K_s} + \frac{\phi}{K_f} + \frac{b^2}{\lambda + 2G} \quad \text{Eq. 2}$$

where b [-] is the Biot's coefficient, ϕ [-] is the porosity, K_s [Pa] is the bulk modulus of the solid grains, K_f [Pa] is the inverse of the fluid compressibility and λ [Pa] and

G [Pa] Lamé coefficients that are the bulk elastic moduli for the formations. Note that the permeability is isotropic but heterogeneous inside the fault (core), $k = k(x, y)$, and homogeneous in the surrounding formations.

The boundary conditions are illustrated with the geometry in Figure 4 (right). The inlet is a pressure condition: $p_{in} = p_0 + \Delta p$, where p_0 [Pa] is the initial pore pressure and Δp is the pressure increase (due to CO₂ injection in the scenario defined here). The blue boundaries have no-flow condition and the green boundaries are open boundaries with a fixed pressure: $p = p_0$. Note that the boundary conditions here are constructed so that flow can only exit the model either through the top boundary of the fault or on the opposite side of the inlet to better compare the along- and across-fault flow behavior in the upscaled model with the full-dimensional model.

2.2 Upscaled fault flow

The upscaled formulations for fluid flow are particularly useful when modelling structures with high aspect ratio, e.g. slip-surfaces and layers of geocells (as shown in Figure 5, right). The fluid flow in a fault can be composed of two main flow contributions; along-fault flow and across-fault flow. The along-fault flow can be described as tangential flow along the upscaled fault while the across-fault flow can be described as a balance of the fluid flux normal to the upscaled fault that corresponds to the fluid exchange to the surrounding protolith and/or neighboring fault component(s), see illustration in Figure 6.

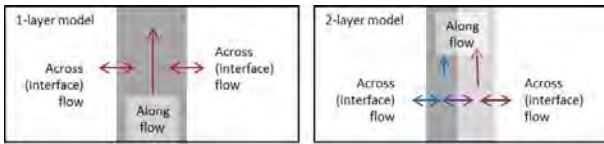


Figure 6: Flow characteristics used in an upscaled model. Left: Single-layer fault model of a fault zone (FZ). Right: Two-layer model of a fault. In a multi-layered (≥ 2 layers) FZ can be further discretized into fault core FC and damage zone(s) DZ.

The tangential fluid flow formulation can be found by integrating the mass conservation equations for the fluid phase across the thickness w_n [m] of a fault layer or component. When assuming that the properties in the fault layer/component are constant, as well as the Darcy-flux, the upscaled (tangential) form of the fluid-flow equations can be expressed as:

$$w_n \left[S_n \rho \frac{\partial p}{\partial t} \nabla_t \cdot (\rho \mathbf{q}_t) \right] = \mathbf{q}_{\Delta, n} \quad \text{Eq. 3}$$

where we have included the fault layer index n and the subscript t indicates tangential component. The Darcy-flux in Eq. 3 is now expressed as:

$$\mathbf{q}_t = -\frac{k_n}{\mu} (\nabla_t p - \rho \mathbf{g}) \quad \text{Eq. 4}$$

The source-term on the right side, $\mathbf{q}_{\Delta, n}$ [kg/m²/s], comes directly from the integration procedure and describes the fluid exchange with the surrounding protolith and/or neighboring fault component(s): across-fault flow.

In the case of no fluid exchange, e.g. if the surrounding protolith and/or neighboring fault component(s) are impermeable, or in the case of continuity in pore pressure, we have that $\mathbf{q}_{\Delta, n} = 0$. However, here we are describing a pore pressure discontinuity and therefore need to describe the fluid exchange. The across-fault flow can be described using a thin-layer approximation of the fluid flux (conceptually similar to Nernst diffusion layer approximation). Flux across an interface, over a distance δ [m] can be expressed as:

$$q = -\rho \frac{\bar{k} \Delta p + \rho g n_z}{\mu \delta} \quad \text{Eq. 5}$$

Here n_z [-] is the vertical component of the normal vector, \bar{k} is the average (harmonic mean) permeability of the domains on both sides of the interface:

$$\bar{k} = \frac{\sum(w_i)}{\sum(w_i/k_i)} \quad \text{Eq. 6}$$

The interface thickness is approximated as:

$$\delta = \sum(w_i) \quad \text{Eq. 7}$$

As mentioned, an advantage with the upscaled formulation is that it is easily extendable (into n -layers) and a layer can, by using the same mathematical formulation, describe flow in a fracture/slip-surface. Eq. 3 and Eq. 4 are the same equations used when modelling fluid flow in a fracture by redefining the porous media permeability k_n to the fracture flow permeability k_f [m²]:

$$k_f = \frac{w_i^2}{12f} \quad \text{Eq. 8}$$

where w_n is now equivalent to the fracture aperture and f [-] is the roughness/friction coefficient. The fracture transmissivity becomes $T_i = w_i^3/(12f)$.

2.3 Model validation

To validate the upscaled formulation of the geocellular fault, a model with a full-dimensional geocellular fault is compared to a model with an upscaled geocellular fault description. The geocells are populated based on SGR, but for simplicity, here only for the permeability. The other material properties vary between the layers according to Table 1.

There are many correlations in the literature that relates SGR and fault permeability (typically the core; FC) and they should be considered site-specific. These correlations are typically exponentially decaying with shale/clay content (e.g. Childs et al., 2002). Here we define such a correlation (for FC) that is linear in SGR and with two end-member permeabilities representing the pure components:

$$\log(k_n) = \text{SGR}_n \cdot \log\left(\frac{k_c}{k_s}\right) + \log(k_s) \quad \text{Eq. 9}$$

where k_c [m²] and k_s [m²] are the permeability of the shale (clay-rich component) and the sandstone, respectively. Here we use that $k_c = 1 \mu\text{D}$ and $k_s = 1 \text{D}$. An alternative correlation for FC is given by Manzocchi et al. (1999):

$$\log(k_n) = 0.4 - 4\text{SGR} - \frac{1}{4}\log(D) (1 - \text{SGR})^5 \quad \text{Eq. 10}$$

where D [m] is the fault throw (here we use that $D = 10$ m). These correlations are compared in Figure 7.

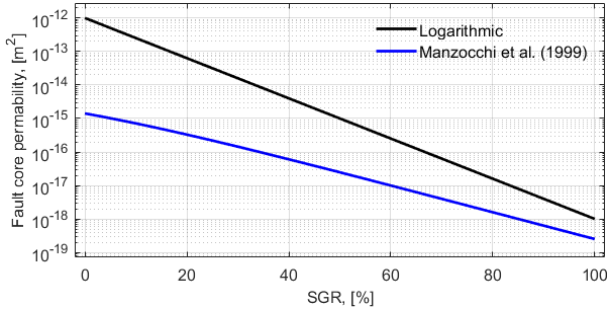


Figure 7: Correlation between SGR and permeability of the fault core from Eq. 9 and Eq. 10.

In this validation we use the correlation in Eq. 9 and it was chosen, over the correlation by Manzocchi et al., (1999), for the purpose of validation of a mathematical model because it gives more (measurable) flow up along and across the fault (has a higher permeability).

The hydro-mechanical properties of the various formations are given in Table 2. Again, note that the values are generic.

Table 1: Hydro-mechanical properties of the fault layers.

Fault layer, [#]	1	2	3	4	5	6	7	8
Perm. k , [m ²]	Varying, based on SGR (Eq. 9)							
Porosity, ϕ , [-]	0.1	0.2	0.3	0.1	0.1	0.2	0.3	0.1
Young's modulus, E , [GPa]	1	2	3	1	2	1	2	3
Poisson's ratio, ν , [-]	0.2	0.3	0.4	0.3	0.2	0.3	0.4	0.3
Biot's coeff. b , [-]	0.9							

Table 2: Hydro-mechanical properties of the formations.

Formation	Underburden	Reservoir	Caprock	Overburden 1	Overburden 2
Permeability, k , [mD]	0.1	1000	0.1	10	1
Porosity, ϕ , [-]	0.1	0.2	0.3	0.1	0.1
Young's mod., E , [GPa]	1	2	3	1	2
Poisson's ratio, ν , [-]	0.2	0.3	0.4	0.3	0.2
Biot's coeff., b [-]	0.9				

3. Results and discussion

In this section we present and discuss the results of the validation model and make some preliminary observations on fluid flow across and along a fault given a specific average SGR profile.

3.1 Validation model

To compare a model with a full-dimensional geocellular fault (full-dimensional model, FM) to a model with an upscaled geocellular fault description (upscaled model, UM), four cases are defined. In all cases, the fault is 15 m thick, but the number of layers in the geocellular description varies: 1, 2, 4, and 8 layers, respectively. Note that in a multi-layered model (2 layers or more), the geocellular layers can describe DZ and FC. However, in this study we do not make that distinction. The fault width is one of the fault attributes that are correlated to other attributes such as length, throw, etc. The value used here is in the higher range of such correlations, see e.g. Torabi & Berg (2011). Considering Figure 5 (right), in case A the vertical profile of the fault is defined using the profile in fault layer 1. For case B, the fault is split into a 2-layered fault where each layer is 7.5 m thick and the vertical profile of the fault layers are defined by fault layer 1 and 2. The same concept is used on case C and case D (4- and 8-layered model, respectively) such that the geocellular SGR-profile for various cases look like Figure 8.

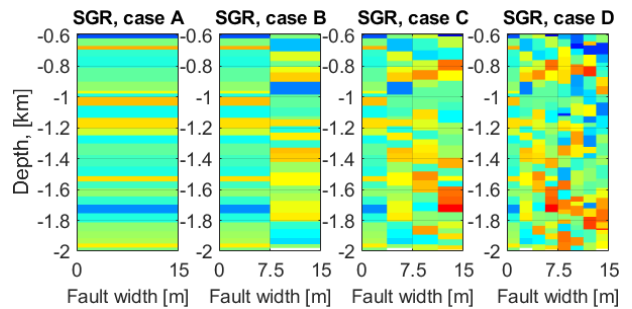


Figure 8: Example of SGR distribution in the fault for the various validation cases. Color-scale is from cold blue to hot red, 0-100 %, respectively.

For every simulation a new randomly generated SGR-"palette" is generated. To validate the UM, a total of 5327 simulations is performed. The mass flow-rate into the reservoir (Q_{in} [kg/s], red boundary in Figure 4) and out of the fault at the top boundary, (Q_{out} [kg/s], green top boundary in Figure 4), were calculated and compared. Note that in the UM the fault at the top boundary is represented by a point. The ratio of the calculated Q_{in} and Q_{out} of the UM versus the FM is shown in Figure 9: $Q_{out,UM}/Q_{out,FM}$ (blue histogram) and $Q_{in,UM}/Q_{in,FM}$ (red histogram). The mode/mean and standard deviation (calculated using Weibull, Wb, and log-logistics, LL, probability distribution functions) are shown in the legends.

The results in Figure 9 shows that the UM (model with upscaled fault) has a tendency of underestimating the flow-rate as the mean values for the ratio between UM and FM are below 1. The more layers in the geocellular

description, the more similar the two models perform, as the mean ratios approach 1.

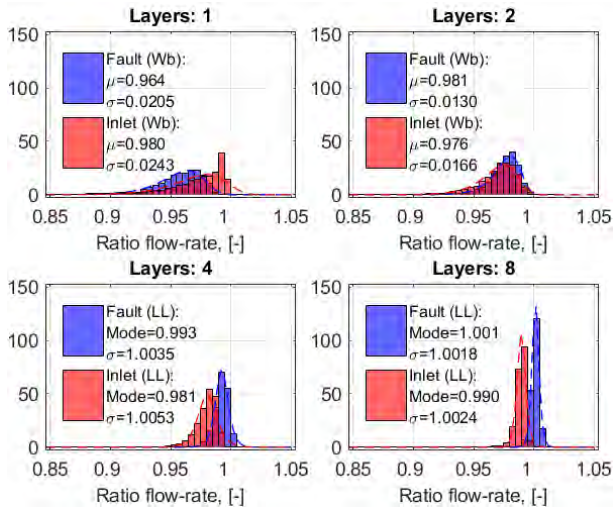


Figure 9: Validation results. Histograms show the ratio of the flow-rate along the fault (blue) and at the inlet (red) between FM and UM for the four cases. Y-axes is probability density estimate (mode/mean and standard deviation: Weibull (Wb) and Log-logistics (LL) probability distribution functions).

The discrepancy between the two models is mainly attributed to the geometrical differences between the models: in the FM the fault has a physical width while in the UM the fault has a virtual thickness, and this impacts the fluid flow tortuosity around the fault. For instance, if the location (boundary) of an SGR-geocell is very close to a formation boundary, there might be situations when it is favorable to by-pass a low-permeable geocell by flowing around it because the flow-path (due to tortuosity) has a lower total resistance to flow. But in general, the UM captures the physical processes related to the upscaled fault with a high accuracy.

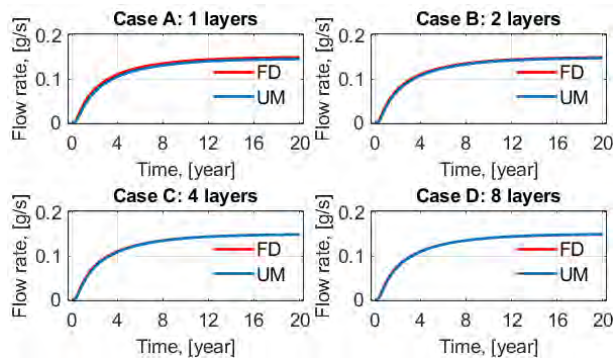


Figure 10: Transient along-fault flow-rate [g/s].

So far, only the steady-state (static) results for the validation model has been shown. To validate the transient solution, we show the comparison for the default average SGR-profile (red curve in Figure 5). The simulation is run for 20 years and the flow rate out of the fault at the top boundary for the two models are compared and shown in Figure 10. The comparison of transient solution is consistent with the comparison of the static solution in Figure 9.

3.2 Preliminary results from a geocellular model

Validation of the UM (upscaled fault model) opens the possibility to many case-studies, including a more thorough analysis of the storage units along the Vette Fault. The model defined so far is generic, with the exception of the chosen SGR-profile, but including the correlation between SGR and the fault permeability. Therefore, here we only include some preliminary results from the validation model.

Note that in the following results we use the inlet flow-rate as a proxy for the across-fault flow-rate. This can be done since the fluid entering the inlet will either exit at the top boundary, by flowing up along the fault, or out the lateral (right) boundary. Some of the fluid may by-pass the fault, by flowing underneath it. However, the permeability in the underburden is low, and combined with a relatively low flow-rate up along the fault, it can be approximated that the flow-rate at the inlet has similar magnitude as the across-fault flow.

The flow-rate at the inlet and up along the fault for the four cases are shown in Figure 11. The flow-rates from the average SGR-profile (not stochastically generated geocells) are shown by the red and blue vertical lines.

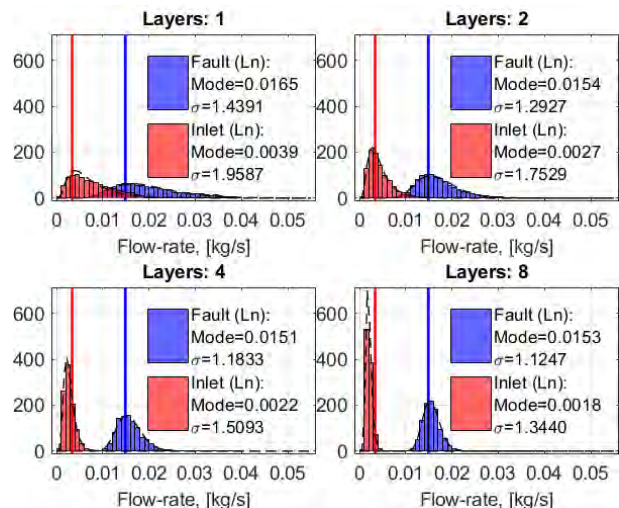


Figure 11: Flow-rate from 1, 2, 4 and 8 layered geocellular models. Note that the along-fault flow-rate is multiplied with a factor 100. The thick vertical lines are the flow-rates calculated using the average SGR-profile across the whole thickness of the fault (fault, blue: 0.0149 kg/s; inlet, red: 0.0034 kg/s). Y-axes is the probability density estimate (mode and standard deviation: Log-normal probability distribution function).

The distribution around the mean value becomes increasingly narrow with increasing number of geocellular layers. This indicates that with increased variability in the composition of the fault the average profile becomes more appropriate to use, particularly for the along-fault flow where the average SGR-profiles match with the mean flow-rates (blue histogram, Figure 11), for all cases considered, see also Figure 12 (left). However, for the across-fault flow (using inlet flow-rate as proxy), using the average SGR-profile seems to overestimate the flow-rate with increasing variability in the fault (increasing number of layers). This is better illustrated in Figure 12: blue and green histogram means

are consistent, while the red and magenta histogram means show a shift towards lower flow-rate with increasing number of geocellular layers.

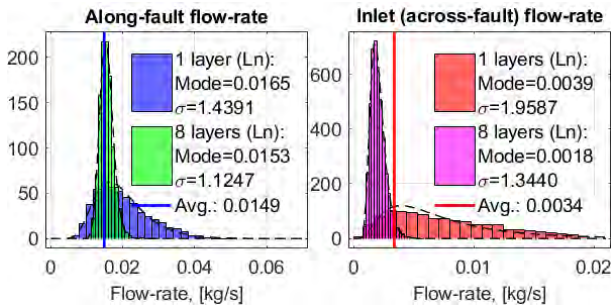


Figure 12: Flow-rate from 1 and 8 layered geocellular models. Note that the along-fault flow-rate (left figure) is multiplied with a factor 100 (for visualization purposes). The thick vertical lines are the flow-rates calculated using the average SGR-profile across the whole thickness of the fault. Y-axes is the probability density estimate (mode and standard deviation: Log-normal probability distribution function).

The flow-rates for a 1-layered geocellular model is compared to flow rates for 2-, 4- and 8-layered models in Figure 13.

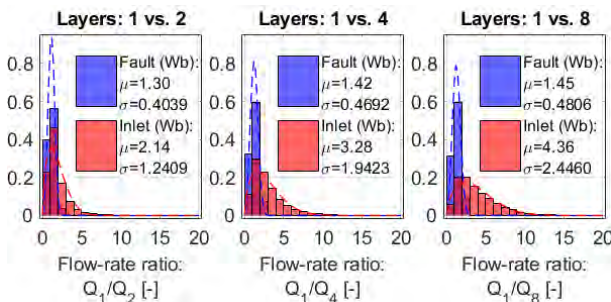


Figure 13: Ratio of flow-rate along-fault (blue) and across-fault (red) for a single layered geocellular model (Q_1) versus 2-, 4- and 8-layered geocellular model; Q_2 , Q_4 and Q_8 . Y-axes is the probability density estimate (mean and standard deviation: Weibull probability distribution function).

In Figure 14 we show the ratio of the along-fault to the across-fault flow-rate.

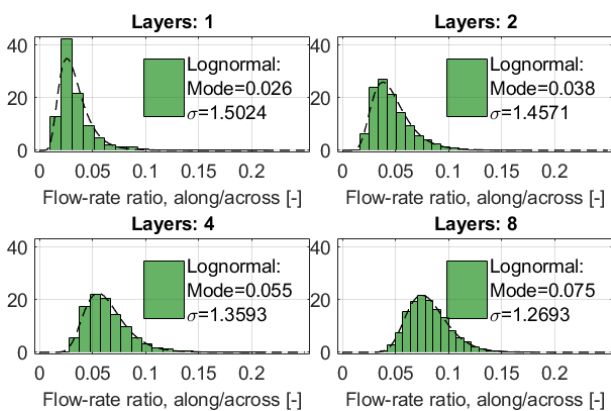


Figure 14: Ratio of flow-rate for along-fault vs. across-fault, y-axes is the probability density estimate (mode and standard deviation: Log-normal probability distribution function).

The comparison in Figure 13 shows that the ratio of the along-fault flow-rate is almost constant and independent of number of layers (ratio around 1.3-1.45, blue histograms). However, the spread in the ratio for across-

fault flow-rate is increasing with increasing number of layers (red histograms). The increasing spread is because the increasing number of layers makes the possibility of across-fault connectivity more homogeneous. Figure 14 shows the ratio of the along-fault to the across-fault flow-rate. The ratio is increasing by a factor three when going from 1 to 8 layers, indicating that increasing fault variability stimulates less fluid to migrate across-fault (since along-fault flow rate is almost constant, e.g. see Figure 10).

3.3 Implications for CO₂ storage

Since fluid migration along pre-existing fractures and faults is the most likely leakage mechanism for CO₂ storage projects, the methodology shown here can be used in a fault derisking workflow. Also, in the case of a sealing FC, but a conductive DZ (implying that across-fault flow is negligible while along-fault flow can be significant), a multi-layered approach is necessary.

Here the fault can be characterized as an assemblage of components with various permeability. However, capillary threshold pressure can also be estimated from clay content, hence leakage of CO₂ is not only relying on favorable permeability along the migration path of the fault, but also on how the driving pressure compares to the capillary pressure threshold.

The geomodel defined in this study, has a static permeability structure. An additional challenge related to faults, is to include stress-dependency into the properties. Pressure increase due to injection is the main driving force for fluid flow across/along a fault, but it also has the potential to reactivate a fault and further stimulate fluid migration. Permeability changes in the fault are related to failure and slip mechanisms, but less dramatic are the non-linearities in hydro-mechanical properties, due to changes in effective stress, e.g. pore-pressure change. It has been shown that stress-strain behavior in rocks is dominated by the softer parts (Liu, 2017) at low effective stress. What constitutes as low effective stress is relative and material dependent. This soft behavior is manifested in large strain of relatively small features, such as (micro-) fractures and/or other soft components and show an exponential correlation between effective stress and hydraulic properties, such as permeability, porosity and fracture aperture, as well as mechanical properties such as stiffness. Note that a fault zone is usually weaker than the original host rock and has lower failure attributes, such as friction coefficient and cohesion, hence pressure dependency on material properties may be more significant in fault rocks compared to host rocks.

4. Conclusion

Here we address the short-comings of standard geocellular fault models by defining and validating an upscaled multi-layered geocellular description of a fault. The upscaled formulations greatly reduce both the geometrical complexity and computational demand, by collapsing the spatial extent of the fault to a face or a line

with a virtual thickness and, importantly, add the advantage of including slip-surface(s) to the fault.

The upscaled multi-layered geocellular model was validated by comparing the results with a model where the fault was fully-resolved. Cases of 1, 2, 4 and 8 geocellular layers were solved and it was found that, although the upscaled formulation slightly underestimated the flow-rates, the accuracy was found to be high and consistent with generally less than 4 % error (or less than 8 % with 95 % confidence interval). The more layers the more accurate the upscaled model compared to the full-dimensional model. The validation was demonstrated on a 2D model, however, the concept, formulations and methodology are extendable to 3D.

The focus in this work was on validating the model concept and an updated formulation for a multi-layered geocellular fault, but some observations from the validation model were made. Increasing variability in fault composition results in more consistent hydraulic properties, or less spread in results. At the same time, the along-fault flow is relatively stable for various number of geocellular layers (fault variability), while across-fault flow was decreasing with more layers.

Acknowledgements

The work has been performed with support from the project FRISK - Quantification of fault-related leakage risk, under grant number 294719 and the Norwegian CCS Centre, grant number (257579/E20). Many thanks to research partners at NGI, NORCE, UiO and UiB.

References

- [1] Caine, J. S., Evans, J. P., and Forster, C. B. (1996). Fault zone architecture and permeability structure. *Geology*, 24(11):1025-1028.
- [2] Childs, C., Manzocchi, T., Nell, P., Walsh, J., Strand, J., Heath, A., and Lygren, T. (2002). Geological implications of a large pressure difference across a small fault in the Viking Graben. In *Norwegian Petroleum Society Special Publications*, volume 11, pages 187–201. Elsevier.
- [3] Childs, C., Walsh, J. J., Manzocchi, T., Strand, J., Nicol, A., Tomasso, M., Schöpfer, M. P., and Aplin, A. C. (2007). Definition of a fault permeability predictor from outcrop studies of a faulted turbidite sequence, Taranaki, New Zealand. *Geological Society, London, Special Publications*, 292(1):235-258.
- [4] Foxford, K.A., Walsh, J.J., Watterson, J., Garden, I.R., Guscott, S.C. and Burley, S.D., (1998). Structure and content of the Moab Fault Zone, Utah, USA, and its implications for fault seal prediction. *Geological Society, London, Special Publications*, 147(1), pp.87-103.
- [5] Fredman, N., Tveranger, J., Semshaug, S., Braathen, A., and Sverdrup, E. (2007). Sensitivity of fluid flow to fault core architecture and petrophysical properties of fault rocks in siliciclastic reservoirs: a synthetic fault model study. *Petroleum Geoscience*, 13(4):305–320.
- [6] Freeman, S., Harris, S., and Knipe, R. (2008). Fault seal mapping-incorporating geometric and property uncertainty. *Geological Society, London, Special Publications*, 309(1):5-38.
- [7] Grant, N. T. (2020). Stochastic modelling of fault gouge zones: implications for fault seal analysis. *Geological Society, London, Special Publications*, 496(1):163-197.
- [8] Lehner, F. and Pilaar, W. (1997). The emplacement of clay smears in synsedimentary normal faults: inferences from field observations near Frechen, Germany. In Møller-Pedersen, P. and Koestler, A., editors, *Hydrocarbon Seals*, volume 7 of *Norwegian Petroleum Society Special Publications*, pages 39-50. Elsevier.
- [9] Lindsay, N., Murphy, F., Walsh, J., Watterson, J., Flint, S., and Bryant, I. (1993). Outcrop studies of shale smears on fault surfaces. The geological modelling of hydrocarbon reservoirs and outcrop analogues, 15:113-123.
- [10] Liu, H.-H. (2017). Fluid Flow in the Subsurface -History, Generalization and Applications of Physical Laws, volume 28 of *Theory and Applications of Transport in Porous Media*. Springer International Publishing, 1 edition. DOI: 10.1007/978-3-319-43449-0.
- [11] Manzocchi, T., Walsh, J. J., Nell, P., and Yielding, G. (1999). Fault transmissibility multipliers for flow simulation models. *Petroleum Geoscience*, 5(1):53-63.
- [12] Matonti, C., Lamarche, J., Guglielmi, Y., and Mari e, L. (2012). Structural and petrophysical characterization of mixed conduit/seal fault zones in carbonates: Example from the Castellans fault (SE France). *Journal of Structural Geology*, 39:103-121.
- [13] Niemi, A., Bear, J., and Bensabat, J., editors (2017). *Geological Storage of CO₂ in Deep Saline Formations*, volume 29 of *Theory and Applications of Transport in Porous Media*. Springer Netherlands.
- [14] Sperrevik, S., Gillespie, P. A., Fisher, Q. J., Halvorsen, T., and Knipe, R. J. (2002). Empirical estimation of fault rock properties. In Koestler, A. G. and Hunsdale, R., editors, *Hydrocarbon Seal Quantification*, volume 11 of *Norwegian Petroleum Society Special Publications*, pages 109 -125. Elsevier.
- [15] Torabi, A. and Berg, S. S. (2011). Scaling of fault attributes: A review. *Marine and Petroleum Geology*, 28(8):1444-1460.
- [16] Wilson, P., Smith, S., Povey, D., and Harris, S. (2020). Ranking and selecting fault models using flow-indicator fault properties and simple streamline simulations. *Petroleum Geoscience*.
- [17] Wu, L., Thorsen, R., Ottesen, S., Meneguolo, R., Hartvedt, K., Ringrose, P., and Nazarian, B. (2021). Significance of fault seal in assessing CO₂ storage capacity and containment risks - an example from the Horda Platform, northern North Sea. *Petroleum Geoscience*.
- [18] Wu, L., Thorsen, R., Ringrose, P., Ottesen, S., and Hartvedt, K. (2019). Significance of fault seal in assessing CO₂ storage capacity and leakage risks - An example from offshore Norway. In *Fifth International Conference on Fault and Top Seals*, volume 2019, pages 1-5. European Association of Geoscientists & Engineers.
- [19] Yielding, G., Freeman, B., and Needham, D. T. (1997). Quantitative fault seal prediction. *AAPG bulletin*, 81(6):897-917.
- [20] Yielding, G.P.B.S., Bretan, P. and Freeman, B., (2010). Fault seal calibration: a brief review. *Geological Society, London, Special Publications*, 347(1), pp.243-255.

TECHNO-ECONOMIC PERFORMANCE OF DORA WITH MEA AND CESAR1

**Tanya Srivastava^{1*}, Roberta V. Figueiredo¹, Tarjei Skaar¹, Niels Warning¹, Paul Gravesteijn¹,
Juliana Monteiro¹, Peter van Os¹, Earl Goetheer¹**

¹ TNO, Leeghwaterstraat 46, 2628CA, Delft, Netherlands

* Corresponding author e-mail: tanya.srivastava@tno.nl

Abstract

Solvent degradation is one of the major challenges to widespread implementation of post combustion CO₂ capture (PCCC) using amine based capture solvents. The presence of oxygen in the flue gas leads to degradation and formation of heat stable salts (HSS). Oxidative degradation can be limited by removal of dissolved oxygen from the capture solvent. TNO has developed DORA (**D**issolved **O**xygen **R**emoval **A**pparatus) as a counter measure for oxidative degradation using membranes. DORA was tested in an industrial environment at PlantOne in Rotterdam with TNO's mobile CO₂ capture plant using 30 wt% MEA. The experimental campaign showed that DORA was effective in oxygen removal and stabilizing the amount of degradation products in the solvent. However, during this campaign it was also observed that porous hollow fiber membranes are not suitable for long-term use. The membrane was damaged due to pore wetting and amine leakages towards the end of the campaign. A more advanced membrane developed by NTNU was tested at TNO laboratories and it was observed that this membrane has a dissolved oxygen removal efficiency greater than 90% for 30wt% MEA. Similar tests were also performed with CESAR1 to demonstrate the solvent independent nature of the technology. To quantify the impact of DORA a techno economic assessment was carried out for 30 wt% MEA and CESAR1. The amount of heat stable salts formed when operating a PCCC plant with DORA was calculated using a degradation network model. It was estimated that the amount of heat stable salts formed would be reduced by 86%. This decrease also leads to a reduction in the number of thermal reclaiming cycles needed to maintain solvent quality. The costs of thermal reclaiming with and without DORA have been estimated in this work.

Keywords: Oxygen removal, oxidative degradation, CO₂ capture, solvent management

1. Introduction

The acceleration of CO₂ capture process implementation is critical to achieving climate goals. Post combustion CO₂ capture using absorption technology has been widely investigated. Absorption technology using aqueous amines, has been demonstrated at industrial scale and has shown promising results [1],[2].

However, solvent degradation in absorption based capture plants poses a challenge to widespread implementation. Some of these challenges include corrosivity, waste management and emissions. Amine degradation by thermal and oxidative mechanisms leads to increased operational costs.

Oxygen present in the flue gas dissolves when in contact with the solvent and leads to several irreversible reactions. Therefore, removal of dissolved oxygen from the solvent is a possible strategy to overcome oxidative degradation. This can be done by several approaches such as use of inhibitors (oxygen scavengers), or by promoting the oxygen separation (by nitrogen sparging, or using membranes) [3].

1.1 DORA as a tool for solvent management

DORA (**D**issolved **O**xygen **R**emoval **A**pparatus) is a membrane based technology developed by TNO as a mitigation strategy for oxidative degradation. The solvent passes through the DORA (an online tool) and the oxygen is removed by means of a sweeping gas (such as

nitrogen or CO₂). This prevents direct contact of the solvent with other chemicals or gases avoiding undesirable effects such as side reactions and foaming [4], [5]. A commercially available porous membrane and a dense layer membrane fabricated by NTNU [6] were previously tested for dissolved oxygen removal from MEA.

Demonstrating the solvent independent nature of DORA was achieved with experiments using CESAR1. These experiments were used to perform a techno-economic evaluation to determine impact and relevance of DORA for CO₂ capture plants at different scales.

2. Experimental work

2.1 Tests with porous membrane

As part of ERA-ACT ALIGN and NCCS projects, previous tests were done at TNO using the DORA in combination with TNO's capture plant (Miniplant). The membrane used was a commercially available porous membrane from Liqui-Cel® which was connected in a bypass configuration after the sump of the absorber allowing the flexibility to operate inline or in the bypass mode.

The campaigns consisted of operation with and without the DORA illustrating its impact on solvent degradation. During two months, the Miniplant was operational and the gas outlet of the absorber was monitored. Ammonia emissions were used as an indication of degradation since

it is one of the major degradation compounds that is formed in the process. Figure 1 shows that during the operation with the DORA the ammonia levels were constant and controlled. In contrast, when the membrane was not in operation, the ammonia levels increased and showed significant variations. The same behavior was observed during the second operation of the DORA. The gas outlet of the DORA was also monitored to ensure that the decrease in ammonia levels was not due to ammonia escaping through the membrane.

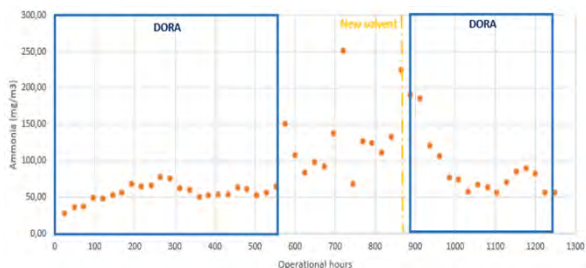


Figure 1 - Miniplant operation with and without the DORA

The previous experiments were carried out with artificial flue gas at TNO, however, a follow-up campaign was performed with the Miniplant at PlantOne (facility in Rotterdam that provided real flue gas) to characterize the DORA operation in relevant conditions.

The Miniplant was operated for 9 months and the DORA was once more coupled to the system after the absorber sump and was online at different times. In these experiments, it was decided to monitor the accumulation of oxidative degradation products in the liquid phase. The concentration of acetate, formate and oxalate in the liquid were analyzed by an external lab.

Figure 2 shows the results of the formic acid analysis and the periods in which the DORA was operated. The same is shown in Figure 3 for acetic acid and oxalate. Although the operation of DORA was not continuous, a clear correlation was observed between the operation and the stabilization degradation products and the control of degradation of MEA.

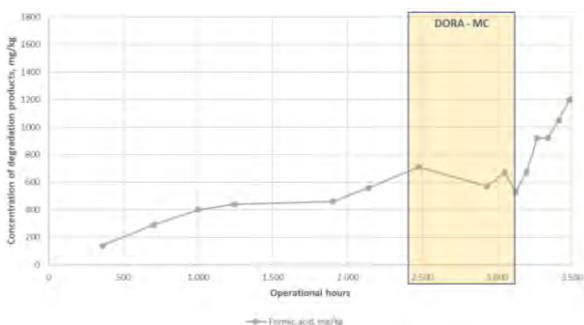


Figure 2 - DORA operation integrated in the Miniplant, formate content (expressed as formic acid). The yellow rectangle indicates the period in which DORA was operational.

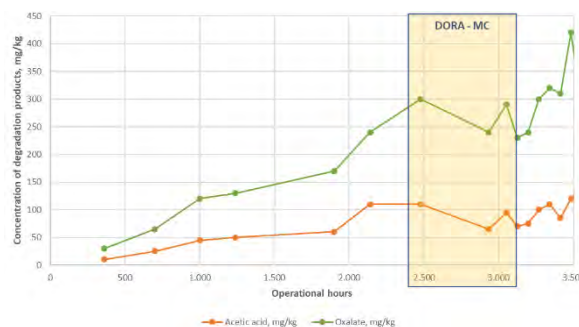


Figure 3 - DORA operation integrated in the Miniplant, acetate (expressed as acetic acid) and oxalate contents

The operation of DORA at PlantOne showed promising results for the DORA technology, however, it gave insights on the sensitivity of the porous membrane. Leakages and wetting of the pores were observed which lead to a decay in the oxygen removal efficiency towards the end of the campaign.

To overcome these issues an advanced membrane developed by NTNU was tested at TNO and compared with the damaged porous membrane Figure 4.

The tests show that oxygen removal rate with the NTNU membrane was acceptable, whereas the damaged porous membrane was completely inefficient. For this reason, further tests were done with the NTNU membrane at TNO setup ODIN (Oxygen Depletion Installation) which are shown in Section 2.2

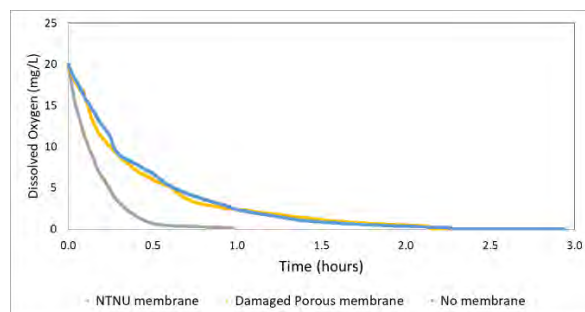


Figure 4 - Oxygen removal/degradation rates of the NTNU membrane, damaged Liqui-Cel® membrane and the set-up with no membrane

2.2 Tests with the dense layer membrane

Oxygen depletion tests without a membrane were done at TNO to characterize the behavior and performance of the NTNU membrane for the removal of oxygen. These tests were done in the ODIN setup of TNO (Figure 5), using MEA and an oxygen sensor from Endress+Hauser model COS81D-11L5/0 to measure the dissolved oxygen activity during the tests. The sensor used is an optical sensor with a membrane on the top, that when in contact with the liquid, allows the oxygen to permeate through and the activity to be measured [5].

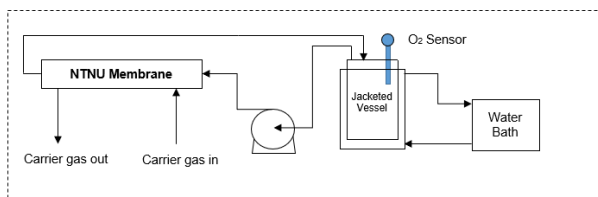


Figure 5 - Schematic of laboratorial setup for dense membrane tests (ODIN)

A set of tests was performed to check the influence of liquid and gas flow rates, temperature and CO₂ loading. Relative to the liquid flow, the liquid mass transfer resistance was observed to be the dominant factor meaning that, although the oxygen removal increases with higher flows, the increase is not proportional to the increase in the liquid flow rate. The trend for the gas flow experiments was similar, in addition to the fact that the flow rate increase is only significant until a “critical flow rate value” after which the removal rate is quite stable.

Varying the temperature of the liquid showed that higher temperatures lead to a faster depletion of oxygen, partly due to the lower solubility of gases at higher temperatures and also due to increased consumption of oxygen through oxidative degradation mechanisms, Figure 6.

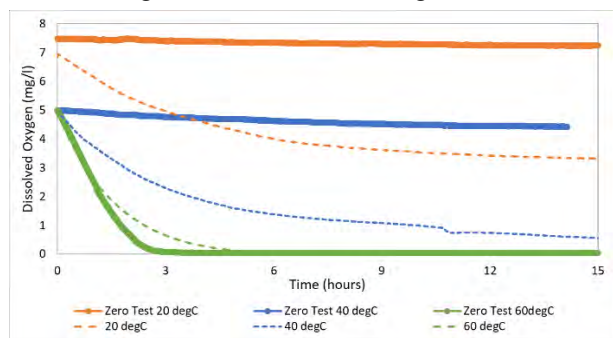


Figure 6 - The effect of temperature on oxygen removal rate. In these tests, a liquid circulation rate of 4.5 l/h is used, and the nitrogen flow is 100 l/h.

Investigating the effect of CO₂ loading on oxygen removal and consumption rate was also crucial as it was expected that the correlation between the two could be quite strong. The oxygen decay was much faster for higher loadings and pure oxygen was used instead of air to make sure the values would not get under the lower detection limit of the oxygen sensor. It was observed that, at 0.2 mol CO₂/mol MEA, the complete consumption of oxygen took place in about 25 minutes. At rich conditions, and at typical flue gas oxygen content (therefore lower initial dissolved oxygen concentration), it is likely that the oxygen is totally consumed within the absorber sump (typical residence time 10-15 minutes), Figure 7.

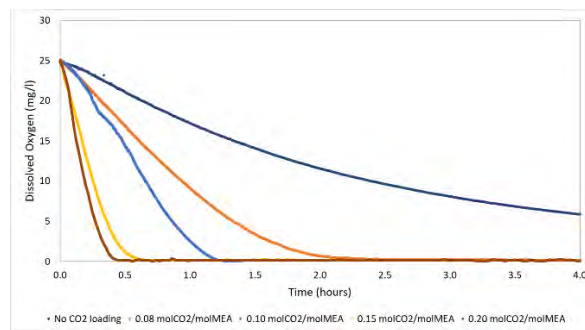


Figure 7 - The effect of CO₂ loading (in molCO₂/molMEA) on oxygen removal rates

The tests were key for the development of a model for the DORA to characterize the mass transfer of oxygen through the membrane.

2.3 Solvent Independent Nature of DORA

DORA has been developed as a solvent independent tool to reduce oxidative degradation of amines. To demonstrate this independence, DORA was tested with CESAR1, a second generation solvent blend of 2-Amino-2-methyl-1-propanol (AMP) and Piperazine (PZ).

First, tests without a membrane were carried out in the Oxygen Depletion Installation, ODIN (Figure 5). The purpose of these tests was to estimate the extent of oxygen consumption in CESAR1 over time. These tests were followed by experiments with NTNU’s dense layer membrane described in the previous section. For both tests – without and with membrane, the solvent was loaded with air at 40°C. A liquid circulation rate of 3 l/h and carrier gas (N₂) flow rate of 75 l/h was used for these tests. As shown in Figure 8, it was observed that DORA is capable of removing more than 70% of dissolved oxygen from CESAR1.

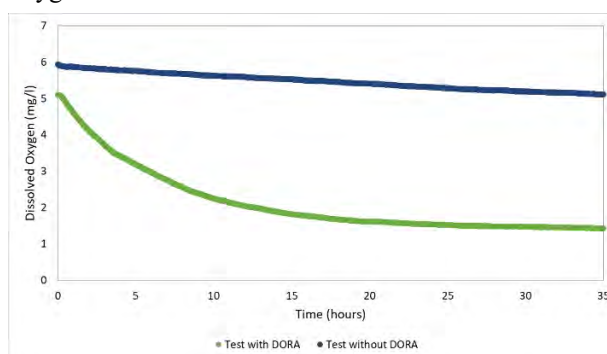


Figure 8 - Oxygen removal from CESAR1: tests with and without DORA

3. Techno-economic evaluation of DORA

A techno-economic evaluation of DORA was carried out to evaluate the impact of DORA for large scale CO₂ capture plants. Thermal reclaiming is one of the most advanced solvent management techniques. However, the process is energy intensive. The cost associated with thermal reclaiming can be reduced by means of heat integration [7]. This cost can also be reduced significantly by overall reduction of oxidative degradation using DORA.

3.1 Impact of DORA on oxidative degradation

In order to estimate the impact of DORA, the extent of oxygen consumption due to oxidative degradation was estimated with a degradation network model (DNM). This model was developed to quantify the consumption of oxygen under different operation conditions and was developed by TNO during ALIGN CCUS [8].

The oxidative degradation of capture solvents is dependent on various plant specific factors like residence times and temperatures in various units (absorber, absorber sump, piping, cross heat exchanger), quality of the flue gas and plant operation.

In order to develop an effective solvent management strategy, it is essential to understand where the most amount of solvent is degraded. From the DNM it was concluded that majority of the oxygen consumption occurs in the absorber sump. Thus, removing dissolved oxygen from the solvent before it enters the sump will be an effective strategy to reduce the extent of oxidative degradation. Integration of DORA in the capture plant before the sump will remove the oxygen and prevent the formation of degradation products.

The DNM was validated using data from the 18-month campaign with MEA conducted at the CO₂ capture pilot at Niederaussem in Germany [9]. The DNM was used to calculate the amount of formate, acetate and oxalate formed and was compared with results from sample analysis. From Figure 9, it is clear that the DNM can predict the formation of degradation products well up to 200 days. After 200 days, degradation of MEA enters and exponential regime and is not predicted well by the model.

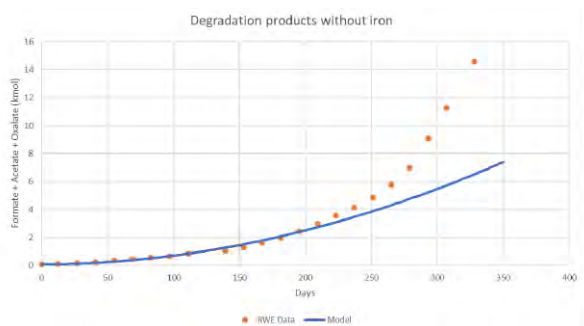


Figure 9 - Validation of DNM with campaign data from RWE

The DNM was used to calculate the amount of formate, acetate and oxalate formed in the presence of DORA. A sensitivity analysis was carried out to determine the impact of DORA with different oxygen removal efficiencies in the linear regime of MEA degradation. It was found that with 50% oxygen removal the amount of formate, acetate and oxalate formed will reduce by 47%, followed by 75% for 80% oxygen removal and 86% in the case that 90% oxygen is removed. This analysis can be seen in Figure 10.

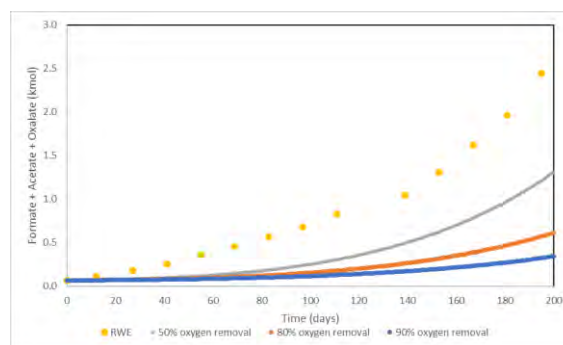


Figure 10 - Impact of DORA on formation of heat stable salts

3.2 Economic impact of DORA with 30wt% MEA

For stable operation of CO₂ capture plants, the total heat stable salt content of the solvent should be controlled. For MEA, the maximum solvent content as heat stable salt is normally controlled between 1% and 5%. Thermal reclaiming can be used to maintain heat stable salts within this range. An economic evaluation of the cost of thermal reclaiming was performed for the situation with and without DORA (base case), using the dense layer membrane. The analysis was carried out for a hypothetical CO₂ capture plant in The Netherlands with 90% capture, flue gas flowrate of 100 kt/h at 40°C and CO₂ concentration 8 vol%.

3.2.1 Base case with thermal reclaiming

Assuming thermal reclaiming can recover 90% of the degraded solvent, the costs associated with solvent replacement, reclaimer operation and waste handling for reclaimer sludge was calculated. The assumptions are listed in Table 1.

Table 1 - Assumptions for calculation of reclaiming costs for 30wt% MEA

Solvent cost (per kg)	€ 2,1 [10]
Reclaimer energy consumption (per kg HSS)	10 kWh [11]
Reclaimer waste disposal (per ton)	€ 375 [10]

The number of reclaiming cycles needed per year for maintaining a certain level of heat stable salts (formate, acetate, oxalate) in the plant was estimated from RWE campaign data (Table 2).

Table 2 - Number of reclaiming cycles required

HSS content	1%	2%	3%	4%	5%
No. of cycles	6.6	3.5	2.5	2.2	2.1

To determine the cost of thermal reclaiming a range of electricity prices were assumed (Case1: 3 €cents/kWh; Case2 : 5 €cents/kWh; Case3: 7 €cents/kWh and Case4: 10 €cents/kWh). The normalized cost for thermal reclaiming for 30wt% MEA against overall cost per ton of CO₂ captured are shown in Figure 11.

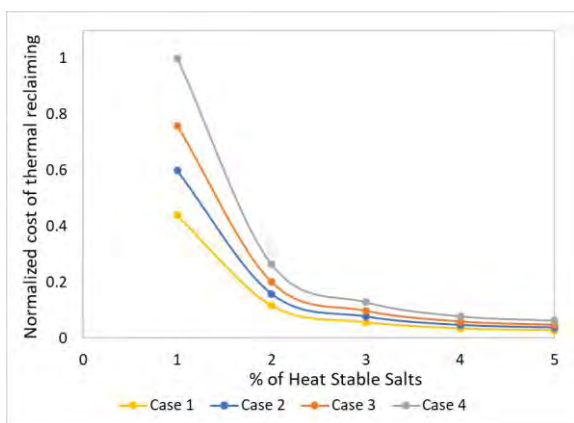


Figure 11 - Normalized cost of thermal reclaiming for 30wt% MEA

3.2.2 Thermal reclaiming with DORA

Integration of DORA in the CO₂ capture plant will lead to reduction of oxidative degradation. As a result, the amount of heat stable salts formed also reduces. In turn, the number of thermal reclaiming cycles needed to maintain a solvent quality with a pre-determined level of heat stable salts also decreases. The number of cycles necessary for maintaining these levels was determined using the DNM as described in the previous section (Table 3). It was assumed that DORA is integrated in the capture plant before the absorber sump can remove 90% of dissolved oxygen from the solvent.

Table 3 - Number of reclaiming cycles needed with DORA

HSS content	1%	2%	3%	4%	5%
No. of cycles	2.1	1.3	1.0	0.8	0.7

Figure 12 shows the impact of DORA on cost of thermal reclaiming for 30wt% MEA. The costs are reduced by 60% to 70% for the different cases.

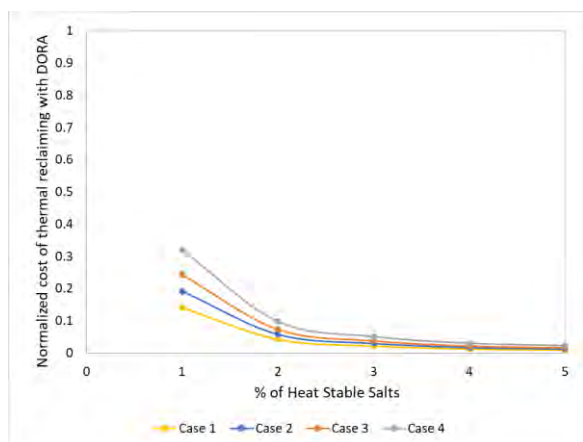


Figure 12 – Normalized cost of thermal reclaiming for 30wt% MEA with DORA

3.3 Economic impact of DORA with CESAR1

An analysis similar to the one described in section 3.2 was carried out for CESAR1. For this case, the following assumptions were taken into account (Table 4).

Table 4 - Assumptions for calculation of reclaiming costs for CESAR1

Solvent cost (per kg)	€ 8,1 [10]
Reclaimer energy consumption (per kg HSS)	8 kWh [11]
Reclaimer waste disposal (per ton)	€ 375 [10]

Figure 13 and Figure 14 show the normalized cost of thermal reclaiming for CESAR1 compared to 30wt% MEA. For this calculation it was assumed that the number of reclaiming cycles required per year is the same as 30 wt% MEA. Updated estimates of the reclaiming cycles will be made by development of the DNM for CESAR1. The estimated reduction of annual reclaiming costs with DORA is between 60% and 70% for the different cases.

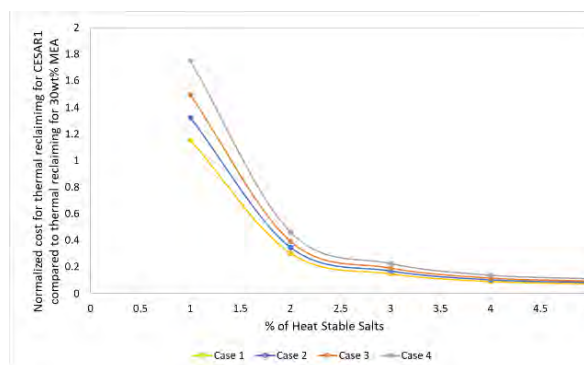


Figure 13 - Normalized costs for thermal reclaiming for CESAR1 compared with thermal reclaiming for 30wt% MEA

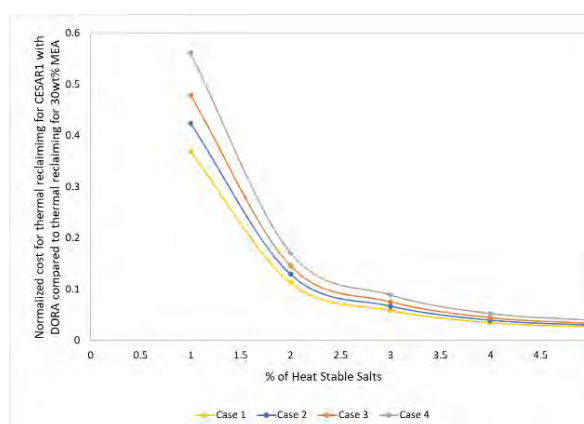


Figure 14 - Normalized costs for thermal reclaiming for CESAR1 with DORA compared to thermal reclaiming for 30wt% MEA

4. Conclusions and recommendations

Demonstration of DORA at PlantOne showed that it is capable of removing up to 90% dissolved oxygen from the solvent. This was achieved with a porous membrane that got damaged during operation due to pore wetting

and leakages. Therefore, a better membrane is needed for this application. A more advanced membrane developed at NTNU was tested at laboratory scale with 30wt% MEA and CESAR1. Oxygen removal efficiencies of greater than 90% and 70% were observed for 30wt%MEA and CESAR1 respectively. For applications that require low oxygen in the CO₂ product, such as enhanced oil recovery and storage, DORA can be an effective tool to remove oxygen concentration from the captured CO₂.

A techno-economic evaluation of DORA with the advanced dense layer membrane was carried out to estimate its impact on solvent handling costs. DORA is capable of removing 86% of heat stable salts from 30wt% MEA. This reduction allows for a decrease of 60% to 70% in costs associated with thermal reclaiming. This reduction follows from the fact that fewer thermal reclaiming cycles are required to maintain solvent quality.

The economic analysis for CESAR1 indicated that the annual cost of reclaiming is expected to be higher due to increased solvent costs. However, this analysis was carried out assuming that the number of reclaiming cycles remains the same as 30wt% MEA. This estimate will be improved in future work by extending the degradation network model for CESAR1.

From the laboratory experiments it is evident that DORA is an effective solvent management tool. It assists in reduction of oxidative degradation and has the potential to reduce overall cost of CO₂ capture.

Acknowledgements

This publication has been produced with support from the NCCS Research Centre, performed under the Norwegian research program Centres for Environment-friendly Energy Research (FME). The authors acknowledge the following partners for their contributions: Aker Solutions, Ansaldo Energia, Baker Hughes, CoorsTek Membrane Sciences, EMGS, Equinor, Gassco, Krohne, Larvik Shipping, Lundin, Norcem, Norwegian Oil and Gas, Quad Geometrics, Total, Vår Energi, and the Research Council of Norway (257579/E20).

ACT ALIGN CCUS Project No 271501. This project has received funding from RVO (NL), FZJ/PtJ(DE), Gassnova(NO), UEFISCDI (RO), BEIS (UK) and is cofunded by the European Commission under the Horizon 2020 programme ACT, Grant Agreement No. 691712. www.alignccus.eu.

The LAUNCH project is funded through the ACT programme (Accelerating CCS Technologies, Horizon2020 Project No 294766). Financial contributions are made from: Netherlands Enterprise Agency (RVO), Netherlands; Bundesministerium für Wirtschaft und Energie (BMWi), Germany; Gassnova SF (GN), Norway; Department for Business, Energy & Industrial Strategy (BEIS) together with extra funding from NERC and EPSRC research councils, United Kingdom; US-Department of Energy (US-DOE), USA.

All funders are gratefully acknowledged.

References

- [1] K. Stéphenne, "Start-up of world's first commercial post-combustion coal fired ccs project: Contribution of shell cansolv to saskpower boundary dam iccs project," Elsevier B.V., 2014.
- [2] J. Jenkins, "Financing Mega-Scale Energy Projects: A Case Study of the Petra Nova Carbon Capture Project," 2015.
- [3] P. T. Nielsen and G. T. Rochelle, "Effects of Catalysts, Inhibitors, and Contaminants on Piperazine Oxidation," *Energy Procedia*, vol. 114, pp. 1919–1929, 2017, doi: <https://doi.org/10.1016/j.egypro.2017.03.1323>.
- [4] A. J. Sexton and G. T. Rochelle, "Catalysts and inhibitors for oxidative degradation of monoethanolamine," *Int. J. Greenh. Gas Control*, vol. 3, no. 6, pp. 704–711, 2009, doi: [10.1016/j.ijggc.2009.08.007](https://doi.org/10.1016/j.ijggc.2009.08.007).
- [5] V. Buvik *et al.*, "Measurement and prediction of oxygen solubility in post-combustion CO₂ capture solvents," *Int. J. Greenh. Gas Control*, no. March, p. 103205, 2020, doi: [10.1016/j.ijggc.2020.103205](https://doi.org/10.1016/j.ijggc.2020.103205).
- [6] L. Ansaloni, R. Rennemo, H. K. Knuutila, and L. Deng, "Development of membrane contactors using volatile amine-based absorbents for CO₂ capture: Amine permeation through the membrane," *J. Memb. Sci.*, vol. 537, no. February, pp. 272–282, 2017, doi: [10.1016/j.memsci.2017.05.016](https://doi.org/10.1016/j.memsci.2017.05.016).
- [7] CO2CRC Limted, "Retrofitting an Australian brown coal power station with post-combustion capture," 2018.
- [8] G. Wiechers *et al.*, "ALIGN-CCUS D1.2.6 Guidelines for effective solvent management," 2020.
- [9] P. Moser *et al.*, "Results of the 18-month test with MEA at the post-combustion capture pilot plant at Niederaussem – new impetus to solvent management, emissions and dynamic behaviour," *Int. J. Greenh. Gas Control*, vol. 95, no. September 2019, p. 102945, 2020, doi: [10.1016/j.ijggc.2019.102945](https://doi.org/10.1016/j.ijggc.2019.102945).
- [10] S. Garcia *et al.*, "ALIGN-CCUS D1.4.3 Guidelines and Cost-drivers of capture plants operating with advanced solvents," 2020.
- [11] A. J. Sexton, K. Fisher, C. Beitler, and G. T. Rochelle, "Evaluation of amine reclaimer operation and waste disposal from post-combustion CO₂ capture," in *Laurance Reid Gas Conditioning Conference*, 2016.

SOLVENT RECLAIMING AT A POST COMBUSTION CO₂ CAPTURE PLANT AT TWENCE (WTE FACILITY)

**Tanya Srivastava^{1*}, Juliana Monteiro¹, Arjen Huizinga¹, Jill Jansen¹, Paul Gravesteijn¹,
 Ronald de Vries², Mathijs Vos², Kirsten Telgenkamp², Peter van Os¹**

¹ TNO, Leeghwaterstraat 46, 2628CA, Delft, The Netherlands

² Twence B.V., PO Box 870, Hengelo, 7550 AW, The Netherlands

* Corresponding author e-mail: tanya.srivastava@tno.nl

Abstract

Solvent degradation in post combustion CO₂ capture (PCCC) impacts process economics and the environment. The degradation of solvents and the accumulation of degradation products leads to reduced cyclic capacity, change of solvent characteristics like viscosity and density, increased fouling and increased corrosivity [1]. This accumulation can be mitigated by solvent replacement, which is simple and effective, but affects process economics adversely, and leads to losses of non-degraded solvent. Thus, techniques like thermal reclaiming, which allow for recovering most of the non-degraded solvent while removing degradation products and impurities to a large extent, are seen as a preferred solvent management strategy.

Solvent thermal reclaiming was implemented at the PCCC pilot at Twence, a Waste-To-Energy plant in the east of The Netherlands. A standalone batch reclaiming unit was designed based on laboratory experiments and a ProTreat® model. From the laboratory experiments it was found that dilution of degraded MEA solvent (DMS) enhances MEA recovery, as expected and in line with previous literature [2]. This dilution, however, increases the energy demand of the reclaiming unit. Heat integration was carried out in ProTreat® to preheat the dilution water with the recovered MEA stream. The reclaiming commissioning campaign was carried out at Twence and it was found that the reclaiming unit was effective in removing impurities such as formate, acetate, oxalate, metals (Fe, Cr, Ni) and impurities (chloride, nitrate and nitrite) to below detection limit. The reclaiming unit was operated with different operating conditions: without dilution, with dilution and with neutralization with sodium hydroxide. As expected, addition of sodium hydroxide at the start of the reclaiming campaign led to enhanced MEA recovery (~20 wt% MEA in the distillate).

Keywords: CO₂ capture, aerosol-based emissions, solvent management, thermal reclaiming

1. Introduction

Post combustion CO₂ capture (PCCC) is critical for reduction of greenhouse gas emissions. Amine-based CO₂ capture has been implemented for capture of CO₂ from several types of flue gas sources. This method of CO₂ capture, using 30wt% monoethanolamine (MEA) is also being used at Twence, a Waste-To-Energy plant located in the east of The Netherlands. The PCCC pilot at Twence was commissioned in 2014. This pilot reduces the CO₂ footprint of the CHP (combined heat and power generation from waste incineration), thereby enabling renewable energy generation, circularity and production of biobased and CO₂ based products (Figure 1) [3].

The current CO₂ pilot installation at Twence captures up to 500 kg/h of CO₂ by treating 1.5 vol% of flue gas from a waste incinerator line. It is a multi-component hybrid system, which can produce liquid CO₂ and/or sodium bicarbonate. The liquefied CO₂ can be sold as a product to greenhouses and the sodium bicarbonate is used to remove acidic contaminants from the flue gas. The PCC pilot installation at Twence is shown in Figure 2.

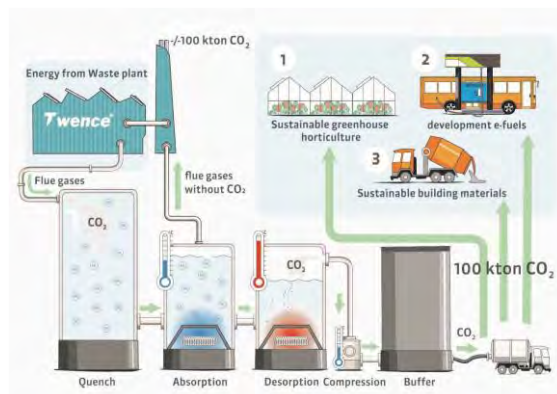


Figure 1 - CO₂ Utilization at Twence [4]

Solvent degradation affects the overall economic and environmental impact of PCCC. Amine based solvents degrade through three main mechanisms – thermal, oxidative and thermal degradation with CO₂ [5]. These mechanisms lead to the formation of degradation products that accumulate in the solvent over time, causing reduced solvent capacity [6], change of solvent properties like viscosity and density, increased fouling and corrosivity etc. The accumulation of the degradation products can also accelerate degradation due to increase

in corrosion [1]. This leads to additional costs due to solvent replacement and increased maintenance.

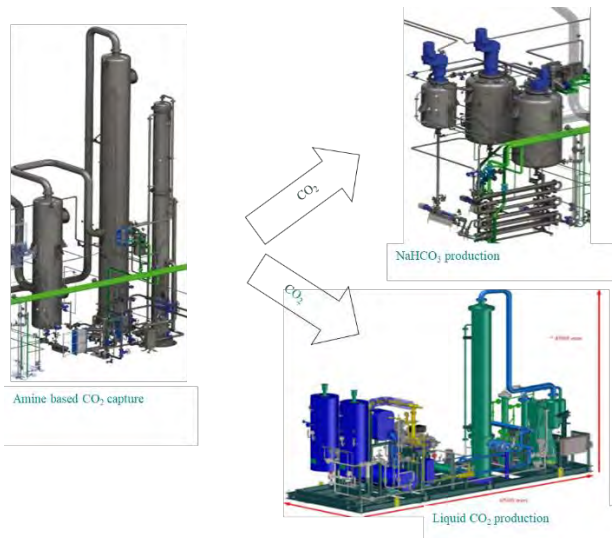


Figure 2 - PCCC pilot installation at Twence

Additionally, the solvent replacement leads to large volumes of waste that adversely impacts overall process economics. Thermal reclaiming of amine based solvents is an effective counter measure that can recover up to 90% of amines from the degraded solvent [1], [7], [8]. Thermal reclaiming has been demonstrated for different solvents, and is considered a mature and effective method for reclaiming MEA [2]. This reduces the costs associated with solvent replacement and also the environmental impact due to reduction of waste streams. A stand-alone batch thermal reclaiming unit was designed to reclaim degraded solvent from the Twence PCCC pilot installation. This unit was commissioned at Twence in April 2021 and results of the experimental campaign are discussed in this work.

2. Solvent Management

2.1 Laboratory experiments

Laboratory experiments were carried out at TNO to determine the optimum operating conditions to reclaim degraded solvent, obtained from the Twence pilot PCCC plant. Experiments were carried in a batch wise evaporator operated at atmospheric pressure. The operating temperature was maintained at 130°C. This was done to limit the thermal degradation which occurs at higher temperatures [9]. The aim of the experiments was to recover at least 90% MEA. Initial experiments indicated that dilution of degraded MEA with water assists the thermal reclaiming process. Thus, a series of experiments with different dilution factors were carried out for a fixed batch time. As shown in Figure 3, dilution factors above 5 lead to MEA recovery greater than 90%.

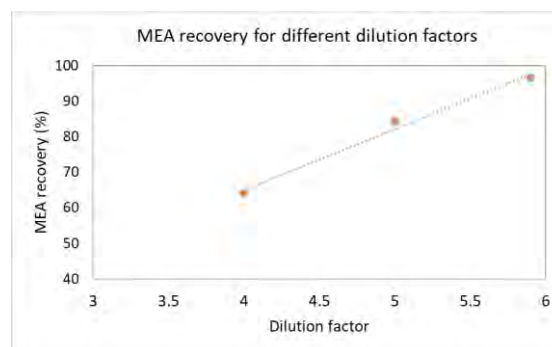


Figure 3 - MEA recovery for different dilution factors

However, this dilution greatly increases the energy consumption and, thus, a standalone thermal reclaiming system is expected to have a high energy demand and associated operational costs. To minimize these costs heat integration with the stripper of the capture plant is recommended [10]. It should be noticed, however, that for the current work heat integration with the PCCC plant was not performed.

3.2 Reclaimer Modelling

In order to reduce the cost of thermal reclaiming, it was decided to pre-heat the dilution water with the hot reclaimer MEA stream. A model was created in ProTreat® to determine the size of the equipment (heat exchanger, reclaimer vessel) required for this integration and achieving 90% MEA recovery. Figure 4 shows this model where a stream of lean degraded MEA is mixed with preheated dilution water is sent to a reclaiming vessel.

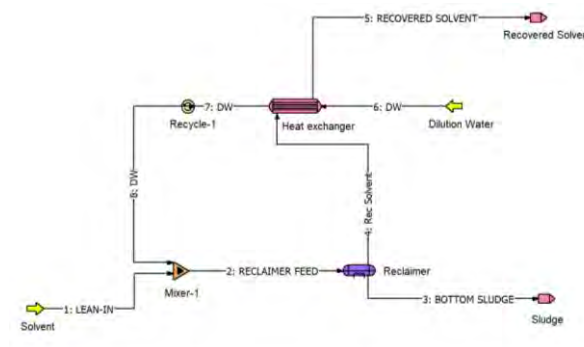


Figure 4 - ProTreat® model for MEA recovery

The dilution water is preheated to 110°C with the top stream of the reclaimer.

A sensitivity analysis was also carried out to determine the optimum operating pressure of the reclaiming vessel. According to Figure 5, it was observed that reclaiming efficiency increases at lower pressures. However, in the interest of costs, it was decided to operate the reclaimer at atmospheric conditions.

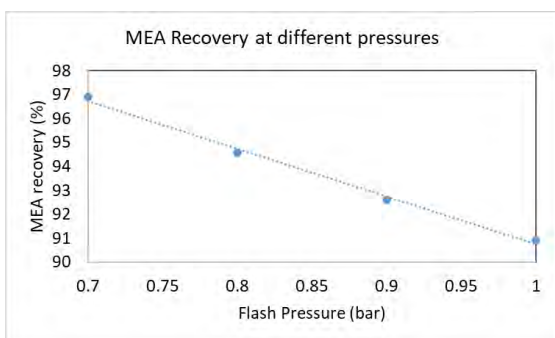


Figure 5 - MEA recovery at different reclaimer pressures

The model was also used to carry out a sensitivity study for dilution factor and was compared to the experimental results. Figure 6 illustrates that the model prediction follows the same trend as the experiments with better recoveries in the experiments. This may be attributed to the model not having an accurate representation of the degraded solvent (ProTreat® allows for including some heat stable salts to the simulations, but thermal degradation products are not present).

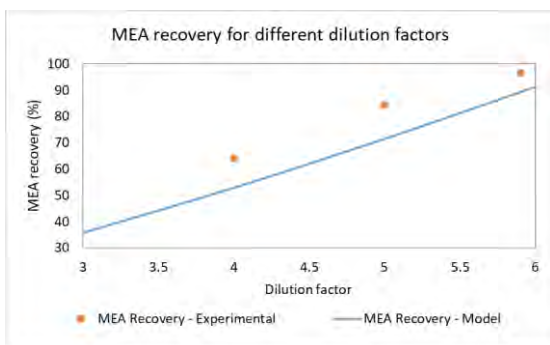


Figure 6 - Effect of dilution factor on reclaiming efficiency

3.3 Reclaiming campaign at Twence

A standalone batch reclaimer was designed and constructed based on prior laboratory experiments and the ProTreat® model results (Figure 7). The reclaimer has the capacity to process 0.5 m³ of degraded solvent per batch. Degraded MEA solvent from the Twence plant was treated in the batch reclaimer and the distillate was collected and analyzed. The reclaimer was heated using three electrical heating elements installed in the reclaimer sump. Different operational settings were investigated during the commissioning tests held over three days in March and April 2021.



Figure 7 - Batch reclaiming unit

At the start of the tests, degraded MEA was added to the reclaimer. The degraded MEA solvent was heated and it was observed that the reclaimer distillate comprised mostly of water and the amount of reclaimed MEA in the distillate marginally increased at higher temperatures.

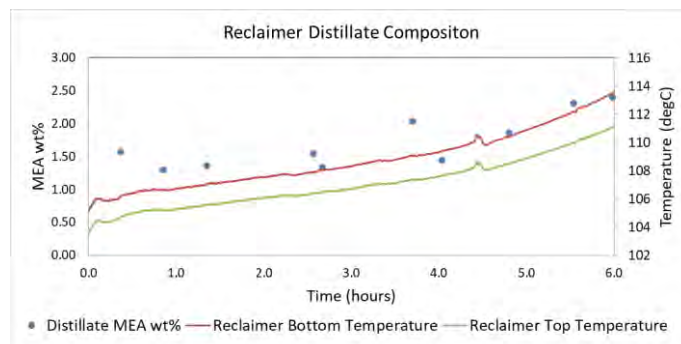


Figure 8- Reclaimer distillate composition with degraded MEA

Then, sodium hydroxide was added to the degraded MEA solvent to neutralize the solvent. Upon neutralization, the MEA recovery in the distillate increased considerably and the composition reached between 10wt% and 29wt% MEA. During this campaign the operating temperature of the reclaimer also increased. To maintain the temperature below 130°C, demi water was added to the reclaimer twice. The MEA recovery decreased immediately after the addition of water and then increased as shown in Figure 9.

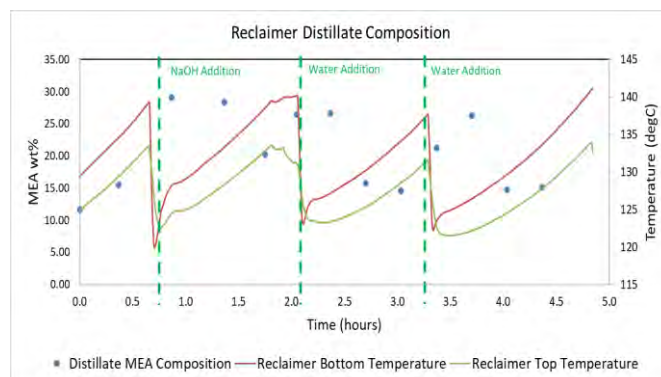


Figure 9 - Reclaimer distillate composition with neutralized MEA

Several samples were taken during the commissioning campaign and were analyzed for some degradation products, impurities and metals. The sludge at the bottom of the reclaimer was also analyzed. These results have been summarized in Table 1.

Table 1 - Laboratory analysis for degraded MEA, distillate sample and sludge sample

Component (mg/kg)	Start sample	Distillate sample	Bottom Sludge Sample
Acetic Acid	641.5	< 10	1826.1
Formic acid	1454.4	< 10	5028.0
Oxalic acid	627.2	< 10	10436.8

Chloride	103.0	< 10	587.7
Nitrate	1116.9	< 10	5252.5
Nitrite	29.4	< 10	26.5
Chromium	0.78	< 0.02	27.70
Iron	3.67	< 0.09	140.68
Nickel	0.43	< 0.02	15.38

From the laboratory analysis it can be clearly seen that the reclaiming operation was successful in removal of degradation products and impurities listed above. The bottom sludge was observed to be more viscous than the start sample and as the analysis shows contains the degradation products and impurities accumulated in the bottom sludge (Table 1).

4. Conclusions

Amine loss due to solvent degradation has significant economic and environmental impacts. For large scale implementation of PCCC, it is important to reduce the impact of these issues.

Laboratory experiments were carried out to determine the optimum operating conditions. It was found that a dilution factor of 6 and operating temperature of 130°C at atmospheric pressure lead to MEA recovery greater than 90%. A model was developed in ProTreat® to optimize the design of the thermal reclaimer, including a heat integration strategy. This reduces the energy demand of the reclaiming unit. Based on the experiments and model results, a standalone thermal reclaimer was designed and operated at Twence. The overall energy demand can be further reduced by integrating the reclaimer with the stripper of the capture plant in industrial scale installations.

The reclaimer was successfully commissioned and the MEA recovery was enhanced after neutralization with sodium hydroxide. The amount of sodium hydroxide to be added for neutralization needs to be better estimated to improve the overall solvent recovery and enhance the reclaiming efficiency. The use of reclaiming allows for reduction of waste volumes thereby reducing the overall waste handling costs. Additionally, the reuse of reclaimed MEA also improves process economics.

The commissioning campaign at Twence provided a first insight into the operation of thermal reclaimers. The operational parameters for maximal solvent recovery, and the design of a process control philosophy will be investigated next. The possibility of using the reclaimer for continuous operation and for blends will be investigated in the future. This mobile batch reclaimer unit can be a valid instrument in evaluating reclaimability of different solvents, and TNO is evaluating the use of it in different research projects. The results of the commissioning campaign of the reclaimer at Twence contributes to the understanding of use of thermal reclaiming as a solvent management strategy for amine based post combustion CO₂ capture in the Waste-to-Energy sector.

Acknowledgements

The authors acknowledge the project “Pilot CAMAK”, that has received funding of the “Topsector Energiesubsidie” of the Ministry of Economic affairs in the Netherlands

References

- [1] O. Gorset and V. Andersson, “Amine thermal reclamation; Technology development from lab to large-scale pilot testing,” *Energy Procedia*, vol. 37, pp. 6357–6364, 2013, doi: 10.1016/j.egypro.2013.06.565.
- [2] N. E. Flø *et al.*, “Results from MEA Degradation and Reclaiming Processes at the CO₂ Technology Centre Mongstad,” *Energy Procedia*, vol. 114, no. November 2016, pp. 1307–1324, 2017, doi: 10.1016/j.egypro.2017.03.1899.
- [3] R. de Vries, A. Roeloffzen, and C. Offereins, “Carbon Capture and Usage (CCU) at Twence,” in *ISWA World Congress Bilbao*, 2019.
- [4] R. de Vries and W. de Jong, “CCU at Twence Status from Pilot to Demonstration,” in *Workshop on EU funding opportunities for CCU projects*, 2019.
- [5] S. A. Bedell, “Amine autoxidation in flue gas CO₂ capture-Mechanistic lessons learned from other gas treating processes,” *Int. J. Greenh. Gas Control*, vol. 5, no. 1, pp. 1–6, 2011, doi: 10.1016/j.ijggc.2010.01.007.
- [6] A. L. Cummings and S. M. Mecum, “Increasing Profitability and Improving Environmental Performance by Maintaining Amine Solvent Purity,” in *Proceedings of the Laurance Reid Gas Conditioning Conference*, 2000, pp. 9–20.
- [7] T. Wang, J. Hovland, and K. J. Jens, “Amine reclaiming technologies in post-combustion carbon dioxide capture,” *J. Environ. Sci.*, vol. 27, pp. 276–289, 2015, doi: https://doi.org/10.1016/j.jes.2014.06.037.
- [8] N. E. Flø *et al.*, “Results from MEA Degradation and Reclaiming Processes at the CO₂Technology Centre Mongstad,” *Energy Procedia*, vol. 114, no. November 2016, pp. 1307–1324, 2017, doi: 10.1016/j.egypro.2017.03.1899.
- [9] G. Léonard, D. Toye, and G. Heyen, “Experimental study and kinetic model of monoethanolamine oxidative and thermal degradation for post-combustion CO₂ capture,” *Int. J. Greenh. Gas Control*, vol. 30, pp. 171–178, 2014, doi: 10.1016/j.ijggc.2014.09.014.
- [10] CO₂CRC Limted, “Retrofitting an Australian brown coal power station with post-combustion capture,” 2018.

SIMULATIONS OF SUBSEA CO₂ LEAKAGE SCENARIOS

Anusha L. Dissanayake^{1*}, Tor Nordam^{1,2}, Jonas Gros³

¹ SINTEF Ocean, Trondheim, Norway

² Department of Physics, NTNU, Trondheim, Norway

³GEOMAR Helmholtz center for ocean research Kiel, Kiel, Germany

* Corresponding author e-mail: Anusha.Dissanayake@sintef.no

Abstract

Subsea carbon dioxide leakages from geological storage complexes and transmission lines may pose a threat to the marine ecosystem in their vicinity. For high leakage flow rates (100 kg/s), buoyant dynamic plumes will form and, in shallow water depths (100-300 m) such as in continental shelves, they may reach the water surface thereby releasing gases to the atmosphere. Here, we present simulations of subsea releases of CO₂ at varying scales, such as seeps, point source plumes and line source plumes, and we discuss their behaviors. The simulated release conditions and water depths are representative of potential storage area on the Norwegian Continental Shelf. Simulations are performed with the TAMOC model, a multiphase-integral plume modeling suite developed and validated for subsea gas and oil releases.

Keywords: *subsea CO₂ leakages, integral plume model, multi-phase plumes, pipeline fracture*

1. Introduction

Potential leakages of carbon dioxide (CO₂) [1] from subsea geological storage (such as decommissioned oil and gas wells) and transmission facilities have a potential to impact marine ecosystems negatively. When CO₂ gets dissolved in water, the acidity increases depending on the amount dissolved and on the total alkalinity. Potential leakages of CO₂ cover a range of scales from seeps [2] to large-scale blowout scenarios [3][4], which create dynamic momentum and buoyancy-dominated plumes. The two release types will behave differently. Modeling tools are useful in predicting the behaviors of the different types of leakage scenarios and provide guidance in planning and enable assessment of the impact on ecosystems.

In this short paper, we present simulations of several subsea CO₂ leakage scenarios that are possible on the Norwegian Continental Shelf. The models used are described briefly, and results are presented to show varying capabilities of modeling tools and their applications.

2. Numerical Methods and Simulations

2.1 Models used for the simulations

We use modules from the Texas A&M Oilspill Calculator (TAMOC) [5][6][7] to simulate three different potential release scenarios as described in subsection 2.3. This modeling suite has been developed to simulate subsea releases of gas and oil mixtures and is extensively validated with both laboratory and field data [2][8][9][10]. The multi-phase plume models in TAMOC are integral models that consider the conservation of

mass, momentum, and buoyancy, and provide estimates of cross-sectional averages of these parameters along the plume trajectory. The models track the mass transfer of gas from bubbles to the ambient, and expansion as the pressure drops when the plume rises in the water column. The temperature and pressure dependent properties of gas mixtures are estimated based on the Peng-Robinson equation of state. The Single Bubble Model [8][6][10] is used to simulate the behaviors of seeping CO₂ bubbles in three-dimensional space in the water column. The Bent Plume Model (BPM, Figure 1b) [11] uses a Lagrangian based approach and it can simulate point source releases in stratified and cross-flow dominated ambient conditions. The Stratified Plume Model (SPM, Figure 1a) [12][13] is based on the Eulerian double-plume model theory and simulates point source plumes in the absence or near-still cross flow conditions in the stratification-dominated regime. To simulate a release from a pipeline fracture with linear geometry in the absence of cross-flow, a Stratified Plume Model extension for line source diffusers (where the width of the release opening is small when compared to its length) [11] can be utilized. The ambient water entrainment into plumes is driven by both the cross flow for BPM and shear between the ambient and rising plume in both BPM and SPM. The shear entrainment coefficient considers the stratification in the ambient in terms of the local densimetric Froude number [14]. These models predict the distribution of gas and dissolved gas in the water column, along with the approximate surfacing volume, time, and location with respect to the plume release point.

To account for the enhanced density of seawater containing dissolved CO₂, we have used the following formulation [15],

$$\rho_c = \rho + (M - \rho\nu)C$$

where ρ_c is the density of seawater containing CO₂ (kg m⁻³), ρ is the seawater density based on the standard equation of state (kg m⁻³), ν is the molar volume of CO₂ (m³ mol⁻¹), C is the total dissolved inorganic carbon (mol m⁻³), and M is the molar mass of CO₂ (kg mol⁻¹).

pH variation in the water column can easily be estimated, based on the dissolved concentrations predicted from the different plume models described earlier in the section and assuming equilibrium within the carbonate system [2] [16] [17]. The advection of the dissolved gas in the water column can be simulated following [18], but is not presented here.

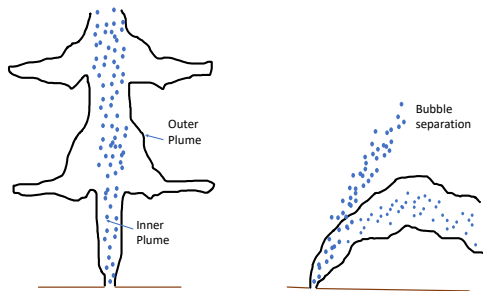


Figure 1: Schematic diagram of (a) Stratified Plume Model and (b) Bent Plume Model [5]

2.2 Validation with experimental data

We compared the model predictions for the behavior of CO₂ bubbles with recent experimental data from [19] (Figure 2). Similar validations of the dissolution of CO₂ bubbles were published in [2] and [16]. The experiments were carried out in a laboratory setup using seawater from Trondheimsfjord in Norway. Because the natural seawater contained dissolved atmospheric gases, we simulated the mass transfer of CO₂, nitrogen, and oxygen between the seawater and the bubble [2][7][9][20]. We used an initial bubble size of 2.55 mm in the simulation fitted to the data. Further model validations for subsea releases of bubbles and plumes at 1–1,500 m water depth are presented in references given in section 2.1. However, experimental data for subsea CO₂ blowout plumes that can be used for model validations are not widely available in the literature.

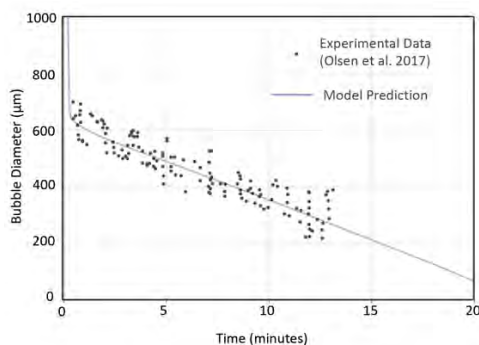


Figure 2: Bubble size variation with time according to model prediction and experimental laboratory data, for an initially pure CO₂ bubble

2.3 Simulated scenarios

We present simulations of seeps, point source releases in stratification and a line source release which is a possible scenario from a geological faultline [20] or from a pipeline fracture [22]. Water depths of the simulated releases are representative of potential CO₂ storage sites in Norway. The Norwegian Petroleum Directorate (NPD) reported that the area in the northern part of the North Sea, about 100 km west of Bergen is a good candidate for CO₂ storage. We selected a location in the area as shown in Figure 3 based on approximate drilling location tested by NPD [23]. The reported typical water depth at this location is about 307 m. Typical salinity, temperature, and dissolved oxygen profiles at the location were extracted from NOAA's World Ocean Atlas [24]. Dissolved nitrogen and CO₂ profiles in the water column that are not available in the World Ocean Atlas, were estimated by considering the equilibrium of atmospheric gases with the water column. Release water depths and flowrates used in the simulations are listed in Table 1. The diameter of the point source plume and the width of the line source plume are both 0.15 m.

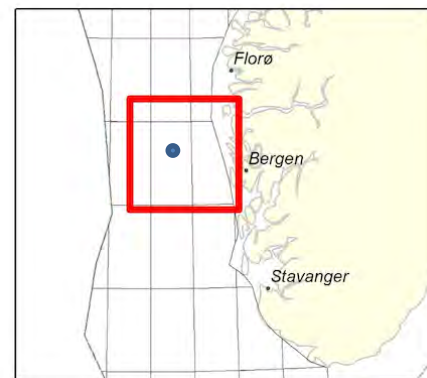


Figure 3: Location of the simulated release shown as a blue dot (map:www.npd.no)

Table 1: Simulated release conditions

Model	Release Water Depth (m)	Released amount
Seep	300	10 mm bubble
	100	10 mm bubble
Point source with ambient stratification	300	100 (kg/s)
	150	100 (kg/s)
Line source with ambient stratification	300	100 (kg/s/m)
	150	100 (kg/s/m)

3. Results and Discussion

The evolution of bubble rise depth, velocity, diameter and remaining mass fraction of CO₂ in the bubble are shown in Figure 4 and Figure 5 for the bubbles released at 100 m and 300 m depth respectively. The bubble

released at 100 m depth rises about 30 m through the water column within five minutes before getting completely dissolved, while the bubble released at 300 m depth only rises to about 20 m within a similar time span. The bubble released at the deeper depth carries more mass in its volume due to higher compression than the bubble at 100 m depth with same volume. However, bubbles released at both depths experienced dissolution of 99.9 % of their CO₂ within 7- 8 m rising distance from seafloor. The simulated remaining fraction of the initial CO₂ mass in bubbles as they rise in the water column is depicted on Figs.4d and 5d. Thus, the seep at the deeper release concentrates more dissolved mass in a similar water column height compared to the shallower release, for a given leakage volume flow rate. The reason being the CO₂ in the gas mixture in the bubbles released at higher pressure at 300 m is more soluble in seawater when compared to 100 m depth release.

Figure 6 shows the plume entrained upwelling and detraining flowrates within the inner and outer plumes for a 300 m depth release simulated with the stratified plume model. The inner plume is the core of rising bubbles and upwelling entrained water that gets arrested and form intrusions when it reaches a neutral buoyancy level. The detraining water from the plume makes an intrusion and creates an outer plume shrouding the inner plume [13][25]. If the bubbles in the inner plume do not get completely dissolved by the time that the first intrusion is formed, they can escape the plume and rise further in the water column with possible subsequent intrusion formation. The release shown in Figure 6 shows a single intrusion formed between depth levels 50 – 170 m. All the CO₂ released gets dissolved in the water column, thus the plume is not reaching the sea surface. The inner plume contains a higher concentration of dissolved CO₂ than the outer plume (Figure 7).

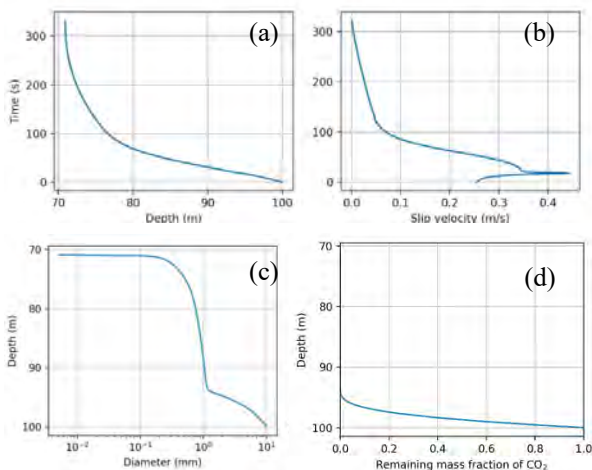


Figure 4: Evolution of bubble (a) rise depth (b) terminal slip velocity (c) size and (d) remaining CO₂ mass fraction with depth for the seep bubble release at 100 m depth.

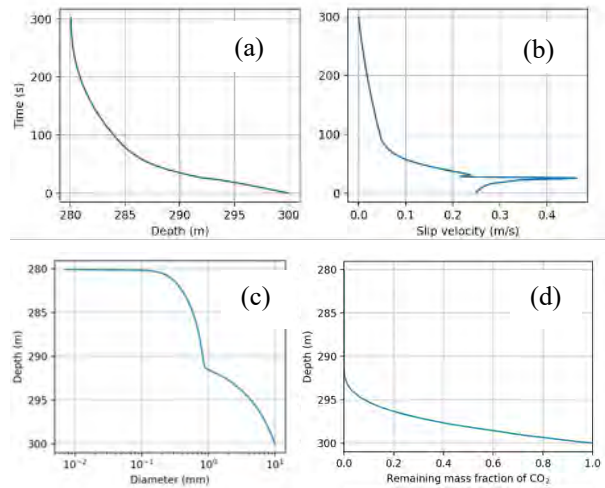


Figure 5: Evolution of bubble (a) rise depth (b) terminal slip velocity (c) size and (d) remaining CO₂ mass fraction with depth for the seep bubble release at 300 m depth.

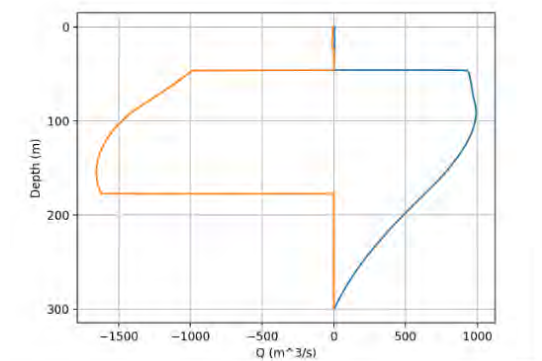


Figure 6: Entrained water flowrate (Q) in the inner plume (right) and outer plume (left) of subsea CO₂ release of 100 kg/s from a point source at 300 m depth.

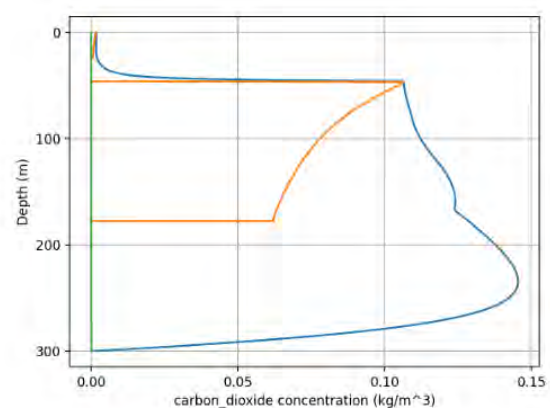


Figure 7: Concentration of dissolved CO₂ (total inorganic carbon) in the inner plume (inner) and outer plume (orange) of subsea CO₂ release of 100 kg/s from a point source at 300 m depth.

For a point-source leakage having the same 100 kg/s flowrate released at 150 m water depth, the plume reaches the water surface (Figure 8). The highest concentration of dissolved CO₂ in both the inner and outer plumes are seen in the surface water (Figure 9). This

in contrast with the deeper release of the same scale (Figure 7).

A linear geometry source plume released at 300 m depth with a rate of 100 kg/s/m shows that the plume reaches the water surface, unlike the release rate from a point source release of 100 kg/s as shown in Figure 6. The main reason is that the point source has a release velocity close to 95 m/s and more water gets entrained into the plume at release, in comparison to line geometry source plume, which only has about 20 m/s release velocity at the source. When more water gets entrained, the plume slows down and tends to make intrusions within a shorter rise distance than the plume with lower ambient water entrainment. Figure 11 and Figure 12 respectively show the predicted concentration of dissolved CO₂ in the inner and outer plumes considering 7.5 mm and 10 mm bubbles, for the same linear geometry source release from 300 m depth with 100 kg/s/m release flowrate. The inner plume with 10 mm bubbles has only about 0.15 kg/m³ concentrations below 200 m depth, while the inner plume with 7.5 mm bubbles has a higher concentration of 0.25 kg/m³ below 200 m depth. This illustrates the importance of using the correct bubble sizes at the plume source when simulations are performed, due to the high sensitivity of the results to the initial conditions. However, to date a well validated bubble size prediction model for subsea gas blowout plumes is only available in the literature for idealized scenarios (circular orifice) [26]. Especially for a gas like CO₂ which is rapidly dissolved in the water, changing the initial bubble size may lead to significant difference in the plume behavior, and the local environmental impact.

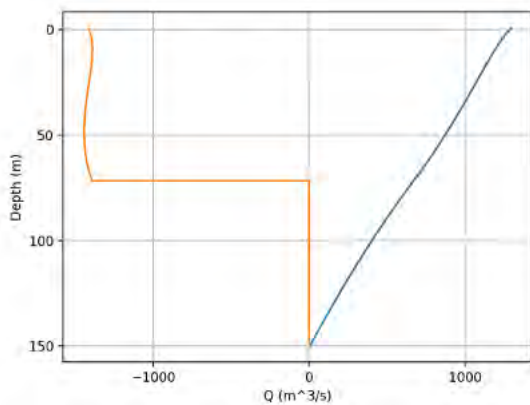


Figure 8: Entrained water flowrate (Q) in the inner plume (right) and outer plume (left) of subsea CO₂ release of 100 kg/s from a point source at 150 m depth.

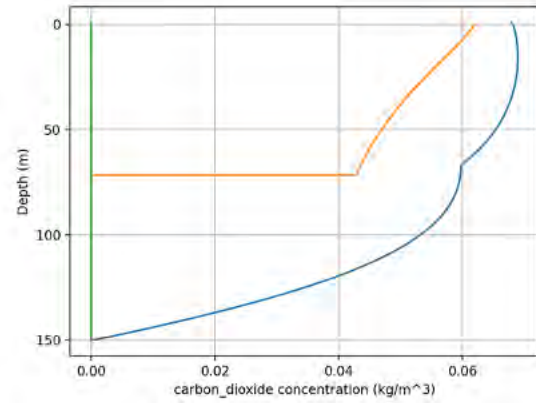


Figure 9: Concentration of dissolved CO₂ in the inner plume (blue) and outer plume (orange) of subsea CO₂ release of 100 kg/s from a point source at 150 m depth.

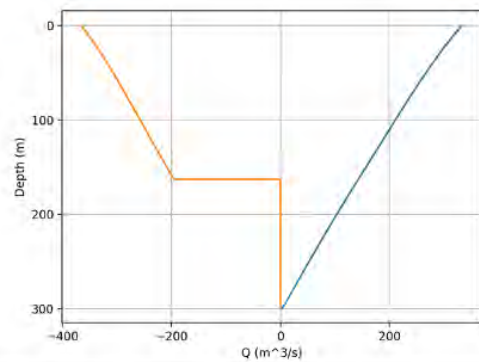


Figure 10: Entrained water flowrate (Q) in the inner plume (right) and outer plume (left) of subsea CO₂ release of 100 kg/s/m from a line source at 300 m depth.

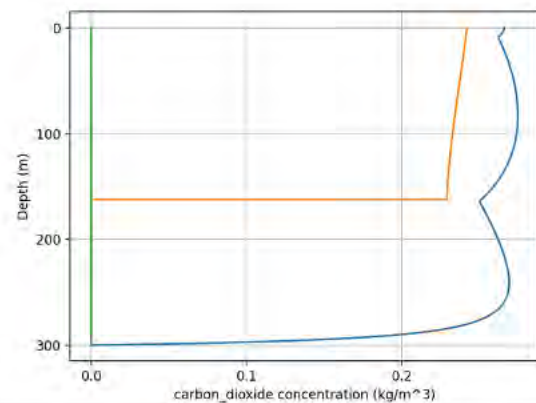


Figure 11: Concentration of dissolved CO₂ in the inner plume (blue) and outer plume (orange) of subsea CO₂ release of 100 kg/s/m from a line source at 300 m depth. The bubble size used in the simulation is 7.5 mm.

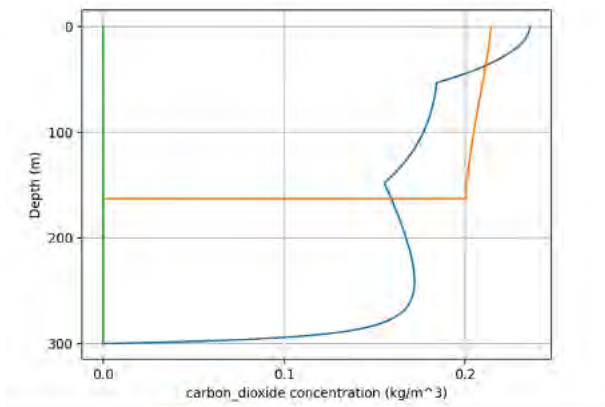


Figure 12: Concentration of dissolved CO₂ in the inner plume (inner) and outer plume (orange) of subsea CO₂ release of 100 kg/s from a line source at 300 m depth. The bubble size used in the simulation is 10 mm.

4. Summary and Conclusions

We have presented details of a modeling suite that can be used to simulate subsea releases of CO₂ at varying scales. The size distribution of the formed bubbles, the release depth, the release flowrate, and the release geometry are shown to have significant effect on the distribution of dissolved CO₂ in the water column. Dissolved CO₂ that reduces the pH in water leading to higher acidity may pose a potential threat to marine ecosystems in the vicinity of subsea CO₂ releases. Hence understanding the controlling parameters that determine the behavior of dissolved CO₂ from plumes and improving these in modeling tools will be useful for purposes of planning and risk assessment. Furthermore, integral plume models are very efficient in calculations compared to CFD models that are solving for three-dimensional detailed behavior of the plumes, as CFD models generally require far more computational time and resources. Hence, integral models are a very useful tool in predicting the behaviors of subsea CO₂ releases. Improving the capability of predicting the bubble size distributions from blowouts and seeps as well as the interaction of the plumes with the water surface are important areas for future studies of subsea bubble plume releases.

Acknowledgements

The authors acknowledge Jørgen Skancke at SINTEF Ocean for his valuable input and discussions for the model validation.

References

[1] Bellwald, Benjamin, Malin Waage, S. Planke, Nina Lebedeva-Ivanova, S. Polteau, Alexandros Tasianas, Stefan Bünz et al. "Monitoring of CO₂ Leakage Using High-Resolution 3D Seismic Data—Examples from Snøhvit, Vestnesa Ridge and The Western Barents Sea." In Fifth CO₂ Geological Storage Workshop, vol. 2018, no. 1, pp. 1-5. European Association of Geoscientists & Engineers, 2018.

[2] Gros, J., Schmidt, M., Dale, A. W., Linke, P., Vielstädte, L., Bigalke, N., & Sommer, S. (2019).

Simulating and quantifying multiple natural subsea CO₂ seeps at Panarea Island (Aeolian Islands, Italy) as a proxy for potential leakage from seabed carbon storage sites. *Environmental science & technology*, 53(17), 10258-10268.

[3] Oldenburg, C. M., & Pan, L. (2020). Major CO₂ blowouts from offshore wells are strongly attenuated in water deeper than 50 m. *Greenhouse Gases: Science and Technology*, 10(1), 15-31.

[4] Olsen, J. E., & Skjetne, P. (2020). Summarizing an Eulerian–Lagrangian model for subsea gas release and comparing release of CO₂ with CH₄. *Applied Mathematical Modelling*, 79, 672-684.

[5] Socolofsky, S. A., Dissanayake, A. L., Jun, I., Gros, J., Arey, J. S., & Reddy, C. M. (2015, June). Texas A&M Oilspill Calculator (TAMOC): Modeling suite for subsea spills. In *Proceedings of the Thirty-Eighth AMOP Technical Seminar* (pp. 153-168). Environment Canada Ottawa.

[6] Gros, J., Socolofsky, S. A., Dissanayake, A. L., Jun, I., Zhao, L., Boufadel, M. C., & Arey, J. S. (2017). Petroleum dynamics in the sea and influence of subsea dispersant injection during Deepwater Horizon. *Proceedings of the National Academy of Sciences*, 114(38), 10065-10070.

[7] Dissanayake, A. L., Gros, J., & Socolofsky, S. A. (2018). Integral models for bubble, droplet, and multiphase plume dynamics in stratification and crossflow. *Environmental Fluid Mechanics*, 18(5), 1167-1202.

[8] Gros, J., Reddy, C. M., Nelson, R. K., Socolofsky, S. A., & Arey, J. S. (2016). Simulating gas–liquid–water partitioning and fluid properties of petroleum under pressure: implications for deep-sea blowouts. *Environmental science & technology*, 50(14), 7397-7408.

[9] Gros, J., Arey, J. S., Socolofsky, S. A., & Dissanayake, A. L. (2020). Dynamics of live oil droplets and natural gas bubbles in deep water. *Environmental Science & Technology*, 54(19), 11865-11875.

[10] Jun, I. (2018). A numerical model for hydrocarbon bubbles from natural seeps within hydrate stability zone (Doctoral dissertation, Texas A&M University).

[11] Dissanayake, A. L., Rezvani, M., Socolofsky, S. A., Bierlein, K. A., and Little, J. C., (2021). Bubble plume integral model for line-source diffusers in ambient stratification, *Journal of Hydraulic Engineering*, 147, no. 5 (2021): 04021015.

[12] Socolofsky, S. A., & Bhaumik, T. (2008a). Dissolution of direct ocean carbon sequestration plumes using an integral model approach. *Journal of Hydraulic Engineering*, 134(11), 1570-1578.

[13] Socolofsky, S. A., Bhaumik, T., & Seol, D. G. (2008b). Double-plume integral models for near-field mixing in multiphase plumes. *Journal of Hydraulic Engineering*, 134(6), 772-783.

- [14] Jirka, G. (2004). Integral model for turbulent buoyant jets in unbounded stratified flows. Part I: Single round jet. *Environmental Fluid Mechanics*, 4(1), 1-56.
- [15] Alendal, G., & Drange, H. (2001). Two-phase, near-field modeling of purposefully released CO₂ in the ocean. *Journal of Geophysical Research: Oceans*, 106(C1), 1085-1096.
- [16] Dissanayake, A. L., DeGraff, J. A., Yapa, P. D., Nakata, K., Ishihara, Y., & Yabe, I. (2012). Modeling the impact of CO₂ releases in Kagoshima Bay, Japan. *Journal of Hydro-environment Research*, 6(3), 195-208.
- [17] Zeebe, R. E., & Wolf-Gladrow, D. (2001). *CO₂ in seawater: equilibrium, kinetics, isotopes* (No. 65). Gulf Professional Publishing.
- [18] Nordam, T., Dissanayake, A.L. Brakstad, O. G, (2021) Methane seeps, A desktop study, SINTEF Ocean, Trondheim, Norway. Report Number OC2021 A-006, ISBN, 978-82-7174-408-3, <https://hdl.handle.net/11250/2730544>
- [19] Olsen, J. E., Dunneber, D., Davies, E., Skjetne, P., & Morud, J. (2017). Mass transfer between bubbles and seawater. *Chemical Engineering Science*, 161, 308-315.
- [20] McGinnis, D. F., Greinert, J., Artemov, Y., Beaubien, S. E., & Wüest, A. N. D. A. (2006). Fate of rising methane bubbles in stratified waters: How much methane reaches the atmosphere?. *Journal of Geophysical Research: Oceans*, 111(C9).
- [21] Kano, Y., Sato, T., Kita, J., Hirabayashi, S., & Tabeta, S. (2009). Model prediction on the rise of pCO₂ in uniform flows by leakage of CO₂ purposefully stored under the seabed. *International Journal of Greenhouse Gas Control*, 3(5), 617-625.
- [22] Guo, X., Xu, S., Chen, G., Yan, X., & Cao, Q. (2021). Fracture criterion and control plan on CO₂ pipelines: Theory analysis and full-bore rupture (FBR) experimental study. *Journal of Loss Prevention in the Process Industries*, 104394.
- [23] <https://www.npd.no/en/facts/news/>
- [24] Levitus, Sydney; US DOC/NOAA/NESDIS, National Oceanographic Data Center (2013). NODC Standard Product: World Ocean Atlas 2009 (NCEI Accession 0094866).
- [25] Yang, D., Chen, B., Socolofsky, S. A., Chamecki, M., & Meneveau, C. (2016). Large-eddy simulation and parameterization of buoyant plume dynamics in stratified flow. *Journal of Fluid Mechanics*, 794, 798.
- [26] Wang, B., Socolofsky, S. A., Lai, C. C., Adams, E. E., & Boufadel, M. C. (2018). Behavior and dynamics of bubble breakup in gas pipeline leaks and accidental subsea oil well blowouts. *Marine pollution bulletin*, 131, 72-86.

TECHNO-ECONOMIC ASSESSMENT OF FLUIDIZED BED CALCIUM LOOPING FOR THERMOCHEMICAL ENERGY STORAGE WITH CO₂ CAPTURE

Guillermo Martinez Castilla*, Diana Carolina Guío-Pérez, Stavros Papadokonstantakis, David Pallarès, Filip Johnsson

Chalmers University of Technology, Gothenburg, Sweden

* Corresponding author e-mail: castilla@chalmers.se

Abstract

The multicyclic carbonation-calcination of CaCO₃ in fluidized bed reactors is a promising process for both thermochemical energy storage (TCES) and CO₂ capture. In this paper, a techno-economic assessment of the calcium loop (CaL) process with simultaneous TCES and CO₂ capture from an existing CO₂-emitting facility is carried out. Inputs to the process are non-dispatchable high temperature heat and a stream of flue gas, while the process outputs are electricity (both dispatchable and non-dispatchable) and CO₂ for compression and storage. The process is sized so the charging section can run steadily during 12h per day and the discharging section to operate steadily 24h per day. The study assesses the economic performance of the process through the breakeven electricity price (BESP) and cost per CO₂ captured. The study excludes the costs of the renewable energy plant and the CO₂ transport and storage. The sensitivity of the results to the main process and economic parameters is also assessed. Results show that the BESP of the case with the most realistic set of economic predictions ranges between 141 and -20 \$/MWh for varying plant size. When assessed as a carbon capture facility with a revenue made from both the electricity sale and the carbon capture services, the cost ranges between 178 and 4 \$/tCO₂-captured. The investment cost of the reactors is found to be the largest fraction of the computed costs, while the sensitivity analysis points at the degree of conversion in the carbonator as the most crucial parameter, with large cost reductions for increased conversion.

Keywords: solid cycles, heat to power, dispatchability, storage cost

1. Introduction

Anthropogenic carbon dioxide (CO₂) emissions represent the main cause of climate change [1]. Despite the continuous efforts in the deployment of renewable energy generation technologies to replace fossil fuels [2], the increasing energy demand has made the share of fossil fuel in the primary energy demand to remain constant at 80% [3] and thereby the global CO₂ emissions have kept growing [4] (yet with a reduction during 2020 due to the reduced economic activity resulting from the Covid pandemic). A large share of the renewable expansion during the last decades have been in the form of wind and solar power, driven by large reductions in costs for these technologies. Due to the variability of wind and solar power generation, their value to the electricity system is reduced as their share in the system increases [5] as well as they may cause instabilities in the grid [6]. Thus, to maintain the value of wind and solar, different forms of energy storage and flexibility measures need to be implemented. There are different forms of storage such as batteries, pumped hydro and thermal energy storage can all have their role in the energy system. Of particular importance is storage which is able to handle variations of several days or weeks corresponding to the time characteristics of wind power. Thermochemical energy storage (TCES) is gaining special attention since, compared to thermal energy storage (TES), TCES displays larger energy density [7] as well as the possibility for long term storage and shipping [8]. Among other alternatives, gas-solid cycles are the most promising TCES systems due to their high reversibility, stability, and enthalpy of reaction. Although packed beds (moving or stationary) have been typically used for investigations of TCES through solids cycling at bench-, lab- and pilot-scale [9], fluidized beds should be an efficient reactor

technology for commercial-scale due to the significantly higher mixing required in larger units.

In addition, to increased share of renewable energy most future scenarios which comply with the Paris Agreement includes substantial amounts of carbon capture and storage (CCS) [10]. Several CCS technologies have been investigated and tested, with a special focus on post-combustion systems. The energy penalty associated to the operation of these processes remains however the major drawback in the commercial deployment of CCS [11].

The calcium looping (CaL) process has been investigated both as a CCS and a TCES technology, indicating that it can potentially be of double use in the energy transition [2]. The CaL process is based on the multicyclic calcination-carbonation of CaCO₃, which can be obtained from limestone, a cheap and abundant material. Thus, it is based on the following reactions:



When applied for CO₂ capture, the CaL process represents a promising capture technology with respect to efficiency and costs [12]. If implemented as TCES, it increases the dispatchability of renewable energy facilities able to provide high-temperature streams such as concentrated solar power (CSP) plants [13], [14]. In addition, if the TCES facility is installed close to a CO₂ emitting source, the CaL process could simultaneously produce dispatchable electricity while mitigating atmospheric CO₂ emissions from the nearby source. A review of the implications of the CaL process scale-up for both CO₂ capture and TCES applications has recently been

published by Ortiz et al. [15], including an analysis of different gas-solid reactor systems. When it comes to the TCES-CSP application, Ortiz et al. [13] published an in-depth review of different process schemes, conditions and materials advantageous for the operation. Bayon et al. [16] provide a techno-economic comparison of 17 gas-solid TCES systems (excluding the reactors), computing a CaL-TCES cost of 54 \$/kWh, (note that this cost is expressed per storage capacity) as compared to the cost estimated by Muto et al. [17] for a CaL-TCES process using a synthetic sorbent; 56-59 €/MWh. Nevertheless, studies on the costs associated to the CaL-TCES process are scarce due to the early stage of development [18], [19] and, thus, they are often based on the more abundant cost studies of the more mature CaL process as CO₂ capture technology (see [20] for an overview). Among these, it is worth mentioning the work by Michalski et al. [21], where a method for assessing the economic feasibility of CaL-CCS processes was suggested based on commercial technology appraisal tools. According to another study by Mantripragada et al. [22] the reactors represent the largest cost of the CaL plant together with the solids handling.

In summary, although the economic feasibility of the CaL process has been widely studied for CO₂ capture, there is little work when it comes to assess the economics of applying it as a

2. Process description

The present section describes the CaL process scheme used for the current investigation. The work by Chacartegui et al. [23] has been used as the basis for the study, i.e. adapting the process layout, although some process conditions have been modified and additional assumptions have been made according to the nature of the present work (i.e. combined TCES and CO₂ capture). Furthermore, the process scheme considers fluidized beds for both the carbonator and calciner reactors, which adds some requirements related to the presence of fluidization agents. The energy input to the process is assumed to come from a renewable energy source capable to provide high temperature heat intermittently, e.g. a concentrated solar power collector. Figure 1 shows a schematic representation of the process studied in this work. The charging and discharging sections can be operated independently. Correspondingly, solids storage at ambient conditions is considered for both charged and discharged particles, which, although decreasing the process efficiency, allows the potential introduction of shipping and make-up streams to the process without altering the thermodynamic performance. Yet, although shipping of the solids would allow the more efficient use of non-dispatchable sources, it is left outside the scope of the present work.

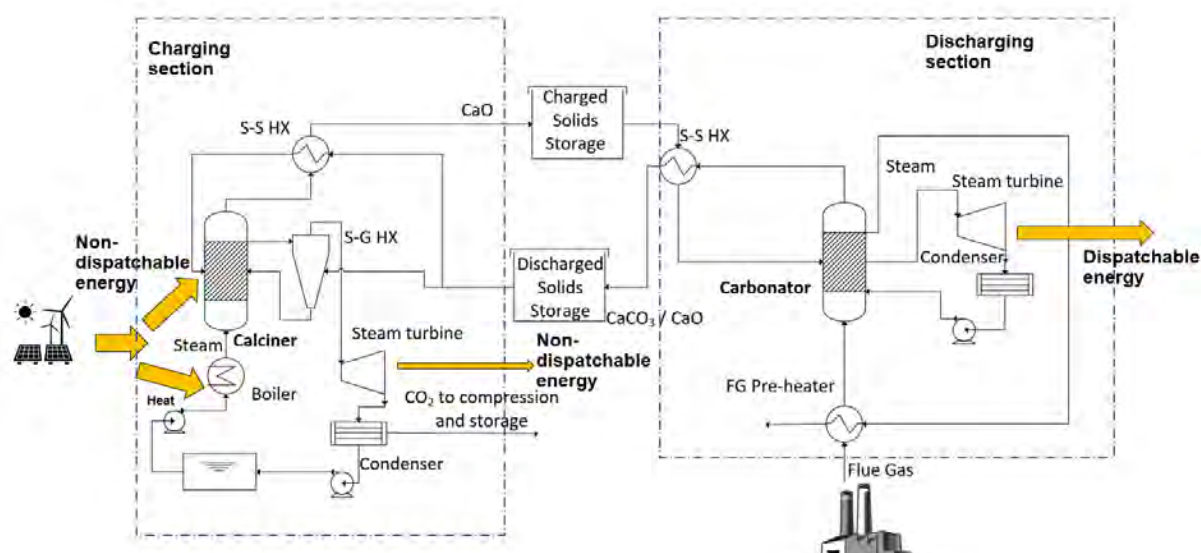


Figure 1. Schematic diagram of the investigated process. Note that the non-dispatchable energy input is in the form of high-temperature heat and the produced energy is in the form of electricity.

TCES scheme, especially when combined with CO₂ capture. Thus, the aim of this work is to estimate the cost of the CaL process when deployed for TCES in a renewable energy generation facility and combined with the capture of the CO₂ emitted by an existing facility located nearby (i.e. not accounting for transportation and storage of CO₂). Such scenario is motivated by the need of combustion facilities to operate until the initial investment is paid-off, which under an increasing cost for CO₂ emissions, will require the capture of the emitted CO₂. The process scheme here presented is developed taking a previous thermodynamic study on CaL for TCES [23] as starting point, and adapting the process for the integration of carbon capture. The cost of the process is calculated through a bottom-up approach and presented in the form of breakeven electricity selling price (BESP) and per CO₂ captured. The sensitivity of the computed cost to process size, material degree of conversion and income associated to the CO₂ captured and electricity sales is also investigated.

Energy in the form of heat at high temperature (850 °C, see below) is used to run the charging section, comprised by the calcination reactor and a steam generator that evaporates and superheats steam for fluidizing the reactor. As reported in [24], calcination under superheated steam decreases the temperature required for calcination and increases the conversion of the solids in the carbonation side. Lower calcination temperatures are desired since simpler and cheaper energy collectors can be utilized [13]. In this work the calciner conditions have been fixed to 850 °C and 1 bar, following the conclusions from [13]. The gas stream exiting the calcination reactor (consisting mainly of H₂O and CO₂) is used to preheat part of the total the inflow of discharged solids (with the split fraction taken from [23]) and is subsequently expanded in a turbine down to the condensing pressure (set by the cooling water temperature), enabling also the separation of steam and leaving the carbon dioxide ready for compression. A water tank allows the feedwater to be stored when the calciner is not in operation. The process incorporates two solid-solid heat exchangers to preheat the feeding solids with the hot streams leaving the reactors.

The energy discharging is achieved with the use of a Rankine cycle that runs the dispatchable steam turbine using the heat released in the carbonator reactor, which is fluidized with the flue gas from a nearby facility. This condition sets the carbonation conditions of the investigated process to 650 °C and 1 bar. Since the optimization of the process performance falls outside the scope of this work, a simplistic approach has been followed for the power cycle conditions. Steam at 550 °C and 120 bar is generated and expanded in one step to condensing pressure. Note that pre-heating of the feedwater line has been left out of the study.

3. Methodology

3.1 Mass and energy balances

In order to carry out the economic assessment of the process defined in Section 2 including both the capital and operational costs of the plant, a thermodynamic analysis is performed, followed by the computation of mass and energy balances and the corresponding equipment sizing. Table 1 presents the values of process parameters assumed in this study and referred in the following sections as the base case. A charging time t_{charge} is defined as the hours per day that the charging side is assumed to be running, i.e. when the intermittent renewable energy source can be harnessed and has been fixed to 12h. Thus, the storage is sized to provide the amount of charged solids (CaO) required to run the discharging side during 24- t_{charge} hours per day. The calciner is sized so it can convert the available heat input Q_{calc} into stored chemical energy while the carbonator is sized to operate continuously.

Both reactors are computed as stirred tank reactors, with all output streams leaving at the reactor temperature. The flue gas entering the process is assumed to contain 15% of CO₂ and the capture rate in the carbonator has been fixed to 90% according to [25]. All gas flows are assumed ideal and no pressure drop calculations are included in the study. Each solid-solid heat exchanger (SS-HX) is computed as a series of two bubbling fluidized bed solid-gas heat exchangers, whose volumes are estimated based on the heat-transfer coefficient reported in [26]. The solid-gas heat exchangers (SG-GX) are in turn sized as cyclones [27] according to the method available at [28], while solid storage tanks are sized using the method suggested by Bayon et al. [16]. No solid losses in cyclones and fluidized beds have been accounted. The rest of conventional fluid-fluid heat exchangers have been sized using heat transfer coefficients from [29].

Table 1. Main process assumptions and parameters of the base case. Values with (*) are modified in the sensitivity analysis (Section 4).

Parameter	Value	Unit
Plant size as net heat input into the process, Q_m	100 (*)	MW
Percentage of steam in the calciner	50	%
Charging time, t_{charge}	12	h
Storage temperature	20	°C
Cooling water temperature	20	°C
Minimum temperature difference SS-HX	20	°C
Minimum temperature difference SG-HX	15	°C
Minimum temperature difference condensers	15	°C
S-G heat transfer coefficient	480	W/m ² K
Fluid-fluid heat transfer coefficients	1500	W/m ² K
Flue gas CO ₂ content	15	%v
Capture rate	90	%
Available cooling water discharge temperature	70	°C
Cooling water pumping distance (m)	1000	m
Solids porosity, Φ	0.5	-
Turbomachinery isentropic efficiency, η_{is}	0.89	-
Fraction of discharged solids preheated in the SS-HX	0.85	-
Conversion in the calciner, x_{calc}	1	-
Conversion in the carbonator, x_{carb}	0.25 (*)	-
Solids conveying energy requirement	10	MJ/t/100m
Equivalent solids conveying length	100	m

3.2 Economic assessment

The assessment of the economic performance of the plant is done using as indicator the break-even electricity selling price (BESP). This is computed by setting the calculated net present value (NPV) of the plant to zero, i.e. calculating an electricity selling price such that the revenues balance the cost over the lifetime of the plant. Thus, the NPV is computed in this work as the sum of the discounted annual cash flows during the lifetime of the project, see Equation 3.

$$NPV = \sum_{i=1}^n \frac{CF_i}{(1+r)^i} \quad (3)$$

A bottom-up approach is used to compute the annual cash flows, i.e. breaking down the plant costs into basic components and subsequently adding installation and indirect costs. The total plant cost methodology followed in this work is based on [30]. Table 2 shows the cost functions used to estimate the erected cost of each process component, which are based on the cost of a reference component of size S_0 and scaled through the scaling parameter f (Equation 4):

$$C = C_0 \left(\frac{S}{S_0} \right)^f \quad (4)$$

Although several works [31],[32] have focused on the calciner reactor design that would allow the heat transfer from the CSP plant, this is assumed to be outside of the scope of this work and instead the calciner cost is estimated based on an oxy-circulating fluidized bed (CFB) furnace reference cost [33], assuming the heat transfer surfaces are used to add heat into the reactor. Similarly, the carbonator is assumed to be similar to a conventional CFB-boiler [33]. Due to lack of available data, the cost of solid-solid heat exchangers is estimated as two times the cost of a bubbling fluidized bed dryer. The only liquid vessel

present in the process (to store the feedwater in the charging side) is assumed cylindrical and similar to standard water vessels [34], with a total specific cost of 83 \$/m³ [16].

Table 2. Capital cost functions (in M\$) used in the study

Equipment	Cost function	Reference
Calciner	$C = 5.87 \cdot 10^2 \cdot \left(\frac{Q_{in}}{2514}\right)^{0.67}$	[33]
Carbonator	$C = 5.60 \cdot 10^2 \cdot \left(\frac{Q_{out}}{1521}\right)^{0.67}$	[33]
Solid-gas heat exchanger	$C = 3.98 \cdot 10^{-9} \cdot D_{cyc}^2 + 2.73 \cdot 10^{-6} \cdot D_{cyc} + 0.016$	[27]
Solid-solid heat exchanger	$C = 2 \cdot 3.5 \cdot 10^{-1} \cdot \left(\frac{D_b \cdot u_g}{2}\right)^{0.73}$	[29]
Gas-gas heat exchanger	$C = (2546.9 \cdot A_{HX}^{0.67} \cdot P_{gas}^{0.28}) \cdot 10^{-6}$	[21]
Cooler	$C = (2546.9 \cdot A_{HX}^{0.67} \cdot P_{fluid}^{0.28}) \cdot 10^{-6}$	[21]
Solids Storage	$C = V_{steel} \cdot C_{steel}$	[16]
Steam turbine	$C = 473 \cdot 10^{-6} \cdot \left(\frac{W_{turb}}{25}\right)^{0.67}$	[35]
Electric generator	$C = 84.5 \cdot 10^{-6} \cdot (P_{el} \cdot 10^3)^{0.95}$	[21]
Steam generator	$C = 2.85 \cdot \left(\frac{\dot{m}_{steam}}{14}\right)^{0.35}$	[29]
Pump	$C = \left(\frac{P_{el}}{197}\right)^{0.60}$	[21]

The values selected for the key economic parameters assumed in this work are listed in Table 3. The income received for capturing the CO₂ of a nearby facility (*IncomeCC*) has been taken as 50 \$/ton, which is the estimated cost for capturing CO₂ from a flue gas stream as the one included here [36]. The CO₂ compression and storage are not included in the study since their cost would be transferred to the emitting industry and are therefore not considered to play a role in the process feasibility. Moreover, the cost of the renewable energy input has also been left out since it is assumed not to be part of the cost of the storage technology here investigated. Lastly, the make-up and purge/loss of solid material has been neglected.

Table 3. Main assumptions and input data for the economic analysis. Values with (*) are modified in the sensitivity analysis (Section 4).

Parameter, Unit	Value
Plant lifetime (years)	20
Capacity factor (%)	100
Discount rate (%)	4.75
Limestone cost (\$/ton)	10
Carbon capture-derived income, <i>IncomeCC</i> (\$/ton)	50 (*)
Electricity selling price, <i>ESP</i> (\$/MWh)	40 (*)

In order to compare the process cost with other CO₂ capture technologies the total cost of the plant is also expressed in the typical capture cost metric, \$/tCO₂-captured (note that this is done only to allow the comparison, since the CO₂ capture is treated in this study as an income cashflow and therefore it is not an actual cost). To do so, the NPV includes the selling of the generated electricity and the revenue obtained for the CO₂ capture as positive cashflows. For this, the electricity is assumed to be sold at a price of 40 \$/MWh in the base case [37].

To scrutinize the economic assessment of the process, a sensitivity analysis has been carried out. Firstly, the impact of size has been evaluated, varying the instantaneous net energy input from 50 to 1000 MW. Secondly, since often reported as a crucial limiting performance parameter [38], [15], the effect of the degree of conversion of the solids in the carbonator has been investigated. Lastly, the value for the income stream associated to carbon capture has been varied from 10 to 100 \$/tCO₂ captured, which is directly related to the forecasted cost of emitting CO₂, whereas the assumed electricity selling price (*ESP*) has been varied from 20 to 80 \$/MWh.

4. Results and discussion

Figure 2 presents the simplified energy flow calculated for the base case process (see Table 1). The top scheme illustrates the energy distribution when the charging side is operating (renewable energy source is available), while the bottom diagram shows the energy flows when only the discharging side operates. It can be noted that the efficiency of the base process on a heat-to-dispatchable power is rather low (28%) mostly due to the heat lost in the condensers, in the solids storage and the heat exchanger losses connected to the high amount of inactive solids due to the low conversion efficiency in the carbonator ($x_{carb}=0.25$ for the base case). This is partially due to that the process is far from being optimized, with the two power blocks defined as basic Rankine cycles. Literature studies have shown that the efficiency of the optimized process (for the TCES scheme) can reach up to 45% [39], [23]. Also, the vast majority of the losses are in the form of heat, and this work does not assess the possibility to include heat streams in the product portfolio of the plant (in the form of district or industrial heating), in which case some part of this loss would turn into a revenue stream. It is worth pointing out that the use of superheated steam to fluidize the calciner implies an added energy loss in the steam generator that is partly recovered in the non-dispatchable turbine, which produces most of the energy when the charging side is in operation. Varying the percentage of steam in the calciner (0.5 has been used in the base case) has an impact on the total energy output shares, with lower steam contents increasing the dispatchability of the process, i.e. the weight of the dispatchable turbine on the total energy output increases.

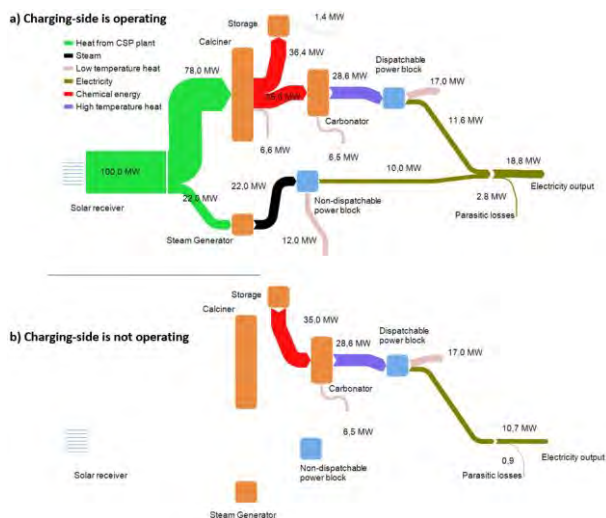


Figure 2. Simplified energy flow of the process for the base case when (a) both charging and discharging side are operating and (b) when the calciner is not operating. Note that the scheme has been simplified and recycle streams are not presented here, as well as some of the losses have been merged.

Figure 3 maps the total plant cost disclosure for different net energy inputs. It is seen that the reactors represent the main fraction of the total cost, especially at larger sizes (i.e. over 80% of the total cost for the 1000-MW case against 75% for the 50-MW case), which is in line with the study in [22]. Note that in the present work the reactor costs also include heat transfer surfaces, both for transferring heat into the calciner and for steam generation and superheating in the carbonator. These results highlight the importance of reactor costing when assessing TCES processes, which should be borne in mind when choosing a specific reactor type and design [13]. The heat exchangers and fixed operational and maintenance (O&M) costs are the second and third largest expenses, respectively, with the latest gaining weight at larger plant sizes since they scale-up linearly while the heat exchangers capital cost is favored by the economy of scale.

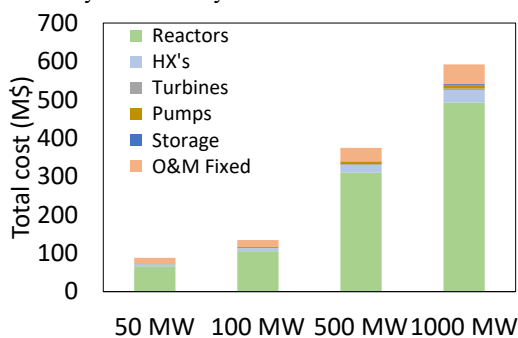
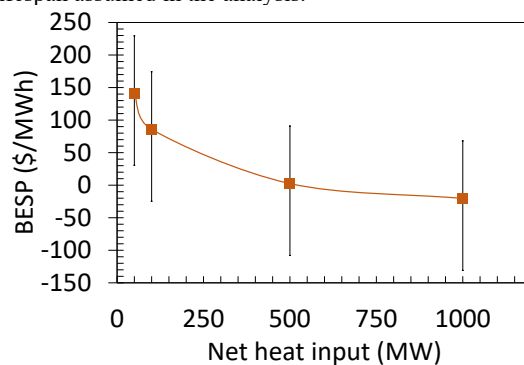


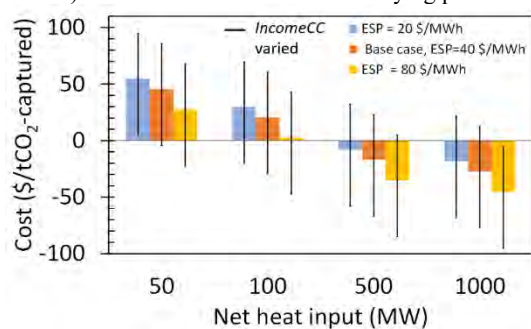
Figure 3. Disclosure of the total costs (in M\$) of the base case process for different net heat input

As expected, the BESP decreases with process size, as seen in Figure 4a, ranging from 141 \$/MWh for the smaller size to -20 \$/MWh for the 1 GW case (all other process parameters were fixed to the base case values). Note that a negative BESP indicates that the process would be profitable with only the income connected to the carbon capture services. A similar trend is observed when the cost is expressed as \$/tCO₂-captured, ranging between 45 and -27 \$/tCO₂-captured. The figure shows that the cost variation is steeper in the range 0-500 MW, becoming less sensitive in the 500-1000 MW range. In order to quantify the impact of the revenue stream related to

CO₂ capture, the base case assumption of *IncomeCC* (50 \$/tCO₂-captured) has been changed and the variation has been plotted as vertical error bars (10 to 100 \$/tCO₂) in Figure 4. It can be seen that the net impact on the cost is constant with size, which is caused by the fact that the amount of CO₂ captured scales linearly with the net heat input. Consequently, the income associated to the CO₂ capture has a stronger influence on the total plant economics at larger sizes. When the assumed electricity selling price (ESP) used for the computation of the capture cost is varied, it is observed in Figure 4b that for most of the cases the plant would breakeven before the 20 years lifespan assumed in the analysis.



a) BESP of the base case for varying process size



b) \$/tCO₂-capture for varying process size and electricity selling price (ESP)

Figure 4. Computed plant cost of the base case process for different sizes when a) expressed as BESP (\$/MWh) and b) expressed as capture cost (\$/tCO₂ captured) for different electricity selling prices (ESP). The vertical error bars represent the sensitivity of the cost to the assumption of income related to CO₂ capture *IncomeCC* (considered to range from 10 to 100\$/tCO₂)

The main results from varying the material degree of conversion in the carbonator to evaluate the impact on the plant costs are presented in Figure 5, both in terms of BESP (Figure 5a) and \$/tCO₂-captured (Figure 5b). Note that the size of the process, the CO₂ capture income and electricity price assumptions have been fixed to their base case values (100 MW, 50 \$/tCO₂ and 40 \$/MWh respectively). The relatively strong impact of x_{carb} on the plant cost can be confirmed with reductions on the BESP of 24 \$/MWh when x_{carb} is increased from 0.15 to 0.25, although it becomes less prominent for $x_{carb} > 0.5$. This impact is also noticeable when the cost is expressed in terms of captured CO₂, where low carbonation degrees yield higher capture costs.

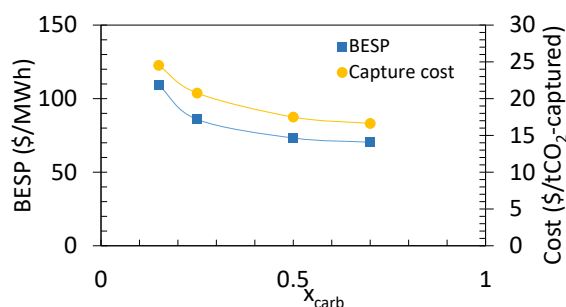


Figure 5. Sensitivity of the plant cost for different material reactivities in the carbonator when expressed as BESP (\$/MWh) and as \$/tCO₂ captured. All other process parameters are set according to the base case

It is important to mention that the critical importance of the material conversion on the process performance and had previously been identified by several authors [15], although not for a system like the one presented here and not in terms of economic performance. Though important for most of the TCES solid-gas systems [9], this parameter gains special relevance in the CaL process since its value can change by a factor of 2.5 depending on the reactor conditions [13] and whether the process is designed for TCES-only or for TCES-CCS like the one here presented. These findings highlight the need for material developments for successful deployment of the CaL process.

If the energy source is a solar receiver characteristic of CSP plants, its cost and design are other aspects that need to be addressed in more detailed economic assessments of the process here presented. The calciner conditions chosen in this work (850 °C) allow the use of cheaper equipment but the impact of such cost on the overall techno-economic performance is still unknown.

The results of the current work can be compared to other energy storage processes through the BESP as well as to other CO₂ capture systems through the cost expressed in \$/tCO₂-captured. As examples of the former, Ganwal et al. [17] reported a cost of 56-59 \$/MWh for a CaL storage process with a synthetic material of $x_{carb} = 0.4$, which would be comparable to the cost obtained in this work (see Figure 5a). Michalski et al. [21] reported a levelized cost of electricity (LCOE) of 80-95 \$/MWh, although their result is for retrofitting a coal power plant. Cormos [40] also carried out a retrofitting study concluding that the LCOE of a retrofitted CaL-power plant would range from 68-74 \$/MWh. Some of the main publications addressing the cost of CaL-CCS [20] report a cost range of 20-40 \$/tCO₂-captured, which is comparable to the computed costs in this work for carbonation reactivities higher than 0.5. Furthermore, the work published by MacKenzie et al. [41] state that the cost was mostly sensitive to the material deactivation and limestone cost. Although neglected in the present work, these factors could play important roles in the long-term, given the low degree of solids conversion in CCS applications [15].

5. Conclusions

A techno-economic investigation of a fluidized-bed calcium looping process for both thermochemical energy storage and CO₂ capture is presented. The process layout used for the current study is based on state-of-the-art literature works on the CaL process and is applied under the assumption that high temperature heat provided by renewables such as from a concentrated solar power plant is available intermittently. Such heat is used to feed the charging section (calcination) and dispatchable electricity is produced in the discharge section while capturing CO₂ from an existing emitting facility nearby.

A bottom-up approach is used to compute the electricity price that would make the process viable as well as the cost expressed by means of captured CO₂.

The analysis points at the investment costs of the reactors as the major costs of the process, which indicates that the overall cost of the process would not vary much when handling storage times larger than the ones considered here. For the conditions investigated, the calculated BESP ranges from 141 to -20 \$/MWh for the 50-1000 MW size span, which corresponds to 45 and -27 \$/tCO₂-captured. A sensitivity analysis shows that these numbers are lowered with increasing future carbon prices and with an increased degree of conversion in the carbonator. The latest is found to play a large role on the techno-economic performance, since it affects both the process energy flow and the amount of CO₂ captured and consequently the side-revenue of the process. The study also shows the importance of further analysis and optimization when it comes to choosing optimal conditions in the reactors and concentration of fluidization gas. Note that for the sake of simplicity, the results shown here do not include the cost of the renewable energy input nor the revenues associated to the heat streams.

Future work includes the optimization of the current setup and the subsequent evaluation of parameters such as reactors conditions and mechanical properties of the solids, which requires more advanced process and reactor models. Especially when it comes to evaluate the flexible operation of the charging process in the presence of various intermittent sources, dynamic models capable to describe the transient operation are required, allowing the computation of start-up and shut off times as well as investigation of different control strategies.

References

- [1] T.F. Stocker, D. Quin, IPCC 2013: CLIMATE CHANGE 2013 - The Physical Science Basis, Contribution of Working Group I to the Fifth Assessment Report of the Intergovernmental Panel on Climate Change, Cambridge University Press, 2013. <https://doi.org/10.1017/CBO9781107415324.Summary>.
- [2] International Renewable Energy Agency, IRENA (2019), Global Energy Transformation: A Roadmap to 2050, 2019. <https://www.irena.org/publications/2019/Apr/Global-energy-transformation-A-roadmap-to-2050-2019Edition>.
- [3] F. Johnsson, J. Kjærstad, J. Rootzén, The threat to climate change mitigation posed by the abundance of fossil fuels, *Clim. Policy*. 19 (2019) 258–274. <https://doi.org/10.1080/14693062.2018.1483885>.
- [4] IEA, World Energy Outlook (2020), Paris, 2020. <https://www.iea.org/reports/world-energy-outlook-2020>.
- [5] L. Hirth, The market value of variable renewables. The effect of solar wind power variability on their relative price, *Energy Econ.* 38 (2013) 218–236. <https://doi.org/10.1016/j.eneco.2013.02.004>.
- [6] J.G.L.G.S.N.M.B. David Steen, Challenges of integrating solar and wind into the electricity grid, (2014) 94. <http://publications.lib.chalmers.se/publication/210515-challenges-of-integrating-solar-and-wind-into-the-electricity-grid>.
- [7] P. Pardo, A. Deydier, Z. Anxionnaz-Minvielle, S. Rougé, M. Cabassud, P. Cognet, A review on high temperature thermochemical heat energy storage, *Renew. Sustain. Energy Rev.* 32 (2014) 591–610. <https://doi.org/10.1016/j.rser.2013.12.014>.
- [8] J. Sunku Prasad, P. Muthukumar, F. Desai, D.N. Basu, M.M. Rahman, A critical review of high-temperature reversible thermochemical energy storage systems, *Appl.*

- Energy. 254 (2019) 113733.
<https://doi.org/10.1016/j.apenergy.2019.113733>.
- [9] A.J. Carrillo, J. González-Aguilar, M. Romero, J.M. Coronado, Solar Energy on Demand: A Review on High Temperature Thermochemical Heat Storage Systems and Materials, *Chem. Rev.* 119 (2019) 4777–4816.
<https://doi.org/10.1021/acs.chemrev.8b00315>.
- [10] IEA, CCUS in Clean Energy Transitions, Paris, 2020.
<https://www.iea.org/reports/ccus-in-clean-energy-transitions>.
- [11] M.E. Boot-Handford, J.C. Abanades, E.J. Anthony, M.J. Blunt, S. Brandani, N. Mac Dowell, J.R. Fernández, M.C. Ferrari, R. Gross, J.P. Hallett, R.S. Haszeldine, P. Heptonstall, A. Lyngfelt, Z. Makuch, E. Mangano, R.T.J. Porter, M. Pourkashanian, G.T. Rochelle, N. Shah, J.G. Yao, P.S. Fennell, Carbon capture and storage update, *Energy Environ. Sci.* 7 (2014) 130–189.
<https://doi.org/10.1039/c3ee42350f>.
- [12] M. Zhao, A.I. Minett, A.T. Harris, A review of techno-economic models for the retrofitting of conventional pulverised-coal power plants for post-combustion capture (PCC) of CO₂, *Energy Environ. Sci.* 6 (2013) 25–40.
<https://doi.org/10.1039/c2ee22890d>.
- [13] C. Ortiz, J.M. Valverde, R. Chacartegui, L.A. Pérez-Maqueda, P. Giménez, The Calcium-Looping (CaCO₃/CaO) process for thermochemical energy storage in Concentrating Solar Power plants, *Renew. Sustain. Energy Rev.* 113 (2019) 109252.
<https://doi.org/10.1016/j.rser.2019.109252>.
- [14] A.A. Khosa, T. Xu, B.Q. Xia, J. Yan, C.Y. Zhao, Technological challenges and industrial applications of CaCO₃/CaO based thermal energy storage system – A review, *Sol. Energy.* 193 (2019) 618–636.
<https://doi.org/10.1016/j.solener.2019.10.003>.
- [15] C. Ortiz, J. Manuel Valverde, R. Chacartegui, L.A. Pérez-Maqueda, P. Gimenez-Gavarrell, Scaling-up the Calcium-Looping Process for CO₂ Capture and Energy Storage, *KONA Powder Part. J.* (2021) 1–20.
<https://doi.org/10.14356/kona.2021005>.
- [16] A. Bayon, R. Bader, M. Jafarian, L. Fedunik-Hofman, Y. Sun, J. Hinkley, S. Miller, W. Lipiński, Techno-economic assessment of solid–gas thermochemical energy storage systems for solar thermal power applications, *Energy.* 149 (2018) 473–484.
<https://doi.org/10.1016/j.energy.2017.11.084>.
- [17] A. Muto, T. Hansen, Demonstration of high-temperature calcium-based thermochemical energy storage system for use with concentrating solar power facilities, 2018.
<https://www.osti.gov/servlets/purl/1523643>.
- [18] Socrates Project, (2021). <https://socrates.eu/>.
- [19] G. Flamant, H. Benoit, M. Jenke, A.F. Santos, S. Tescari, G. Moumin, A. Rodriguez, A. Azapagic, L. Stamford, J. Baeyens, Y. Boes, F. Pron, M. Prouteau, P. Dumont, N. Abdenouri, H. Mazouz, Solar processing of reactive particles up to 900°C, the SOLPART project, *AIP Conf. Proc.* 2033 (2018). <https://doi.org/10.1063/1.5067013>.
- [20] P. Fenell, B. Anthony, Calcium and Chemical Looping Technology for Power Generation and Carbon Dioxide (CO₂) Capture, Woodhead Publishing Series, Cambridge, 2015.
- [21] S. Michalski, D.P. Hanak, V. Manovic, Techno-economic feasibility assessment of calcium looping combustion using commercial technology appraisal tools, *J. Clean. Prod.* 219 (2019) 540–551.
<https://doi.org/10.1016/j.jclepro.2019.02.049>.
- [22] H.C. Mantripragada, E.S. Rubin, Calcium looping cycle for CO₂ capture: Performance, cost and feasibility analysis, *Energy Procedia.* 63 (2014) 2199–2206.
<https://doi.org/10.1016/j.egypro.2014.11.239>.
- [23] R. Chacartegui, A. Alovísio, C. Ortiz, J.M. Valverde, V. Verda, J.A. Becerra, Thermochemical energy storage of concentrated solar power by integration of the calcium looping process and a CO₂ power cycle, *Appl. Energy.* 173 (2016) 589–605.
<https://doi.org/10.1016/j.apenergy.2016.04.053>.
- [24] S. Champagne, D.Y. Lu, A. MacChi, R.T. Symonds, E.J. Anthony, Influence of steam injection during calcination on the reactivity of CaO-based sorbent for carbon capture, *Ind. Eng. Chem. Res.* 52 (2013) 2241–2246.
<https://doi.org/10.1021/ie3012787>.
- [25] Y.A. Criado, B. Arias, J.C. Abanades, Calcium looping CO₂ capture system for back-up power plants, *Energy Environ. Sci.* 10 (2017) 1994–2004.
<https://doi.org/10.1039/c7ee01505d>.
- [26] F. Scala, Fluidized bed technologies for near-zero emission combustion and gasification, Woodhead Publishing Series, Cambridge, 2013.
- [27] E. De Lena, M. Spinelli, M. Gatti, R. Scaccabarozzi, S. Campanari, S. Consonni, G. Cinti, M.C. Romano, Techno-economic analysis of calcium looping processes for low CO₂ emission cement plants, *Int. J. Greenh. Gas Control.* 82 (2019) 244–260.
<https://doi.org/10.1016/j.ijggc.2019.01.005>.
- [28] U. MUSCHELKNAUTZ, E. MUSCHELKNAUTZ, Abscheideleistung von Rückführzyklonen in Wirbelschichtfeuerungen, *VGB Kraftwerkstechnik.* 79 (1999) 58–63.
- [29] R.D. Woods, Rules of Thumb in Engineering Practice, Wiley-VCH, Weinheim, 2007.
- [30] G. Manzolini, E. MacChi, M. Gazzani, CO₂ capture in Integrated Gasification Combined Cycle with SEWGS - Part B: Economic assessment, *Fuel.* 105 (2013) 220–227.
<https://doi.org/10.1016/j.fuel.2012.07.043>.
- [31] DOE/NETL, Cost and Performance for Low-Rank Pulverized Coal Oxycombustion Energy Plants, *Tech. Rep.* (2010) 442.
<https://www.globalccsinstitute.com/archive/hub/publications/119786/cost-performance-low-rank-pulverized-coal-oxycombustion-energy-plants.pdf>.
- [32] S. Walas, *Chemical Process Equipment*, Elsevier, 1988.
<https://doi.org/https://doi.org/10.1016/C2009-0-25916-2>.
- [33] A. Pizzolato, F. Donato, V. Verda, M. Santarelli, A. Sciacovelli, CSP plants with thermochemical energy storage and integrated steam generator – Techno-economic modeling and design optimization, *Energy.* 139 (2017) 231–246.
<https://doi.org/10.1016/j.energy.2017.07.160>.
- [34] P. Psarras, S. Comello, P. Bains, P. Charoensawadpong, S. Reichelsten, J. Wilcox, Carbon Capture and Utilization in the Industrial Sector, *Environ. Sci. Technol.* 51 (2017) 11440–11449.
- [35] Y. Yan, K. Wang, P.T. Clough, E.J. Anthony, Developments in calcium/chemical looping and metal oxide redox cycles for high-temperature thermochemical energy storage: A review, *Fuel Process. Technol.* 199 (2020) 106280.
<https://doi.org/10.1016/j.fuproc.2019.106280>.
- [36] C. Ortiz, M.C. Romano, J.M. Valverde, M. Binotti, R. Chacartegui, Process integration of Calcium-Looping thermochemical energy storage system in concentrating solar power plants, *Energy.* 155 (2018) 535–551.
<https://doi.org/10.1016/j.energy.2018.04.180>.
- [37] C.C. Cormos, Techno-economic implications of flexible operation for super-critical power plants equipped with

calcium looping cycle as a thermo-chemical energy storage system, *Fuel*. 280 (2020) 118293. <https://doi.org/10.1016/j.fuel.2020.118293>.

- [38] A. MacKenzie, D.L. Granatstein, E.J. Anthony, J.C. Abanades, Economics of CO₂ capture using the calcium cycle with a pressurized fluidized bed combustor, *Energy and Fuels*. 21 (2007) 920–926. <https://doi.org/10.1021/ef0603378>.

EFFICIENCY OF CO₂ FOAM MOBILITY CONTROL WITH HETEROGENEOUS RESERVOIR PROPERTIES

Alv-Arne Grimstad^{1*}, Øystein Strengehagen Klemetsdal²

¹ SINTEF Industry, Postboks 4763 Torgarden, NO-7465 Trondheim, Norway

² SINTEF Digital, Postboks 124 Blindern, 0341 Oslo, Norway

* Corresponding author e-mail: alv-arne.grimstad@sintef.no

Abstract

We investigate how reservoir heterogeneity affects the efficiency of CO₂ mobility control in saline aquifer storage. An ensemble of reservoir models is set up for simulation of CO₂ injection with a quarter-five-spot well pattern where CO₂ is injected, and brine is produced for pressure control at opposite corners. Results with and without mobility control are compared. Additionally, results are generated for a modified foam model where the mobility reduction factor scales with reservoir permeability. An empirical foam model with partitioning of surfactant between the CO₂ and brine phases is used.

Keywords: CO₂ storage, CO₂ mobility control, CO₂-brine foam.

1. Introduction

Previous work has demonstrated that mobility control in saline aquifer storage of CO₂ can significantly increase storage efficiency [1]. The reservoir model in [1] had homogeneous permeability and porosity and was used to investigate the efficiency of mobility control for various combinations of mobility reduction factor, surfactant concentration and size of surfactant solution slug. Both CO₂-soluble and water-soluble surfactant was considered. The results showed that injection of a foam-stabilising surfactant solution in the first years of a CO₂ storage operation can significantly improve the storage efficiency, predominantly close to the injection well, and thereby delay the break-through time of CO₂ at wells used for pressure control by formation brine production.

In the present work the reservoir properties are not homogeneous, but randomly generated using a gaussian variogram. An ensemble with different realizations of the permeability and porosity is used to obtain statistics on the difference between foam effect in homogeneous and heterogeneous formations. Foam properties such as mobility reduction factor and partition coefficient are kept fixed in all simulations. This enables an investigation of the effect of reservoir heterogeneities on the efficiency of mobility control for CO₂ storage. Reservoirs with heterogeneous permeability and porosity may contain high-permeability streaks between injection and production wells, leading to significantly reduced storage capacity, since breakthrough of injected CO₂ at a pressure control well would necessitate shutting this well down. Pressure management in the storage reservoir would then be much reduced and rising pressure in the reservoir would rapidly diminish attainable injection rates.

Experiments with foam in porous media have indicated that contrasts in the mobility of injected gas can be smoothed out with use of foam [2][3]. The experiments

also indicate that the mobility reduction factor for foam increase with increasing permeability. This smoothing effect would give an additional improvement to storage efficiency in heterogeneous reservoirs.

2. Method

We consider a geological model spanning a volume of 1400×1400×100 m, discretized by a 30×30×20 Cartesian grid. The top of the model is set to 800 m depth, with zero dip. To capture the propagating CO₂ front more accurately, the top six grid cell layers have a vertical thickness of 1.67 m. Vertical cell thickness increases linearly from layer six to the bottom, and the bottom six layers have a thickness of 8.33 m. CO₂ is injected through an injection well that perforates the bottom four layers in one corner of the model, at a constant injection rate of 366 000 m³/day at surface conditions (equivalent to 250 kt/year), constrained at a maximum bottom-hole pressure of 150 bar. A brine production well perforates the bottom four layers in the opposite corner and is set to operate at a constant bottom-hole pressure of 90 bar.

Both brine and CO₂ relative permeabilities are represented by Corey-type curves with exponent 2. Residual saturations are set to 0.3 for CO₂ and 0.2 for brine. Capillary entry pressure for CO₂ in the storage formation is set to 0.15 bar. All boundary conditions for the model (except for the wells) are set to no-flow.

We simulate injection of CO₂ first for four years with timesteps starting at 0.35 days, and gradually increasing to 90 days. During this period, we also inject surfactant dissolved in the CO₂ stream at 1% wt. The surfactant is assumed to have a partition coefficient of 1.0, meaning that at equilibrium where both brine, CO₂ and surfactant are present in the reservoir the mass concentration of surfactant in brine and CO₂ will be equal. We assume that the surfactant works to stabilise CO₂-brine foam wherever the surfactant concentration is large enough. The empirical foam model of Vassenden and Holt [5] is

indicated by the black vertical dashed line in the figure. Results from the simulation on a homogeneous model, an increase of 70 % is indicated by the red vertical dashed line. Figure 3 shows a correlation plot of the storage efficiency for each ensemble realization with and without foam. The storage efficiency without foam ranges mainly from 12 to 22 %, with an outlier at 24 %. With foam the storage efficiency ranges from 21 to 39 %, with an outlier at 42 %.

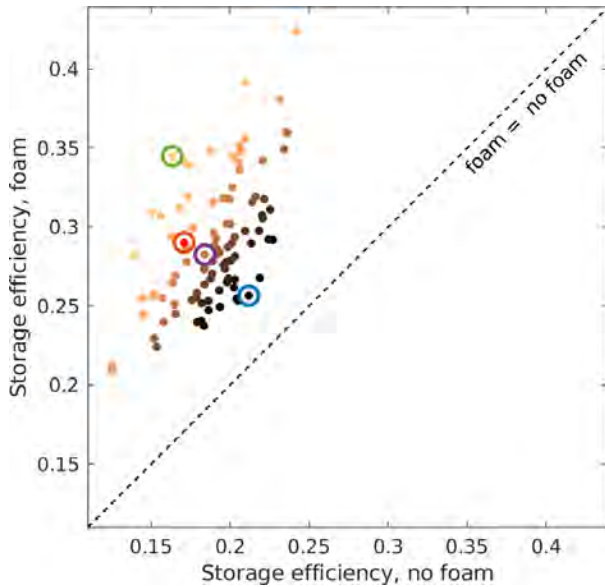


Figure 3. Correlation plot reporting storage efficiency (in pore volume fraction) using foam vs. no foam. The dashed line corresponds to zero gain, and the red dot represents the simulation with homogeneous rock properties.

In the correlation plot the three ensemble realizations with smallest, largest and an intermediate increase in storage efficiency are marked with blue, green and purple circles. These same ensemble realizations are marked similarly in the other correlation plots later. In addition, the result for the model with homogeneous porosity and permeability is marked with a red circle.

3.2. P-foam vs no foam

Figure 4 and Figure 5 show the results from the simulations with p-foam, compared to simulations without foam. The relative increase in storage efficiency (Figure 4) is now larger and range from 50 to 335 %, with an average value of 138 %. For the homogeneous model, the relative increase in storage efficiency is 70 %, the same as for normal foam vs no foam. This is as expected, since the foam strength in the homogeneous case will be the same for both normal foam and p-foam with the scaling given in Eq. (2). For the heterogeneous models, the foam strength scaling will cause reduced flow in the high-permeable regions compared to normal foam, and an increased sweep of low-permeable areas close to the injection well, thereby increasing the amount of stored CO₂.

The correlation plot (Figure 5) shows that the range of storage efficiency is shifted to 29 to 57 % for the p-foam cases. It also shows that other realizations than for

ordinary foam score highest and lowest in storage efficiency increase.

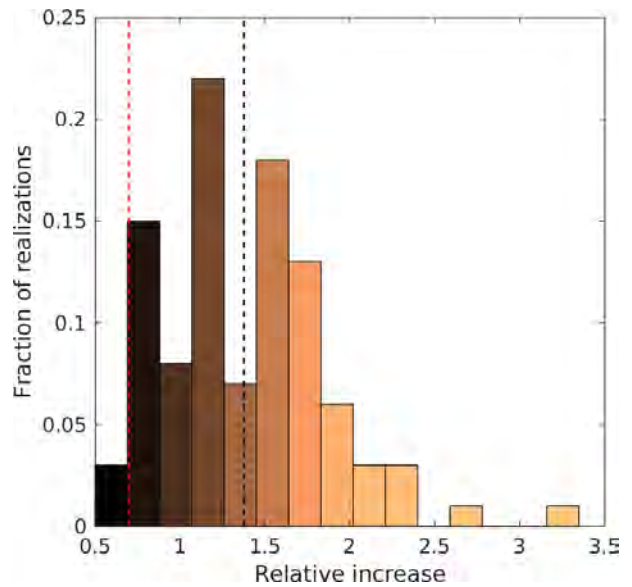


Figure 4. Histogram of relative increase in stored CO₂ mass by using p-foam compared to no foam. The mean is indicated by a black, dashed line, and the red, dashed line shows the relative increase for the same simulations using homogeneous permeability/porosity.

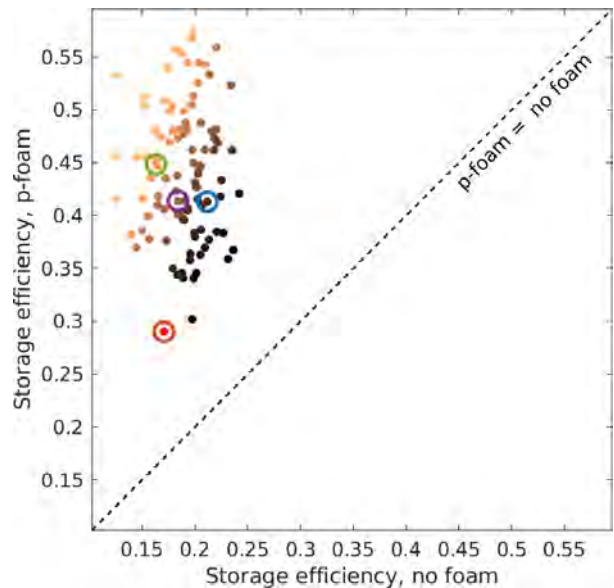


Figure 5. Correlation plot reporting storage efficiency (in pore volume fraction) using p-foam vs. no foam. The dashed line corresponds to zero gain, and the red dot the simulation with homogeneous rock properties.

3.3. Foam vs p-foam

Finally, Figure 6 and Figure 7 show a comparison of the results from p-foam simulations with the simulations using normal foam. We see that most realizations see an increase in the amount of stored CO₂, some as high as 150 %. However, for a few realizations the increase is only minor, and two realizations even see a small reduction in the amount of stored CO₂ for p-foam simulations (Figure 7). The mean increase is 56 %.

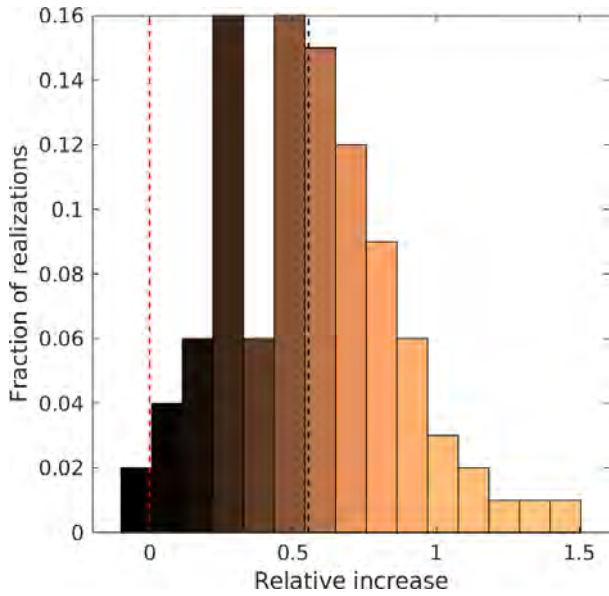


Figure 6. Histogram of relative increase in stored CO₂ mass by using p-foam, compared to normal foam. The mean is indicated by a black, dashed line, and the red, dashed line shows the relative increase for the same simulations using homogeneous permeability/porosity.

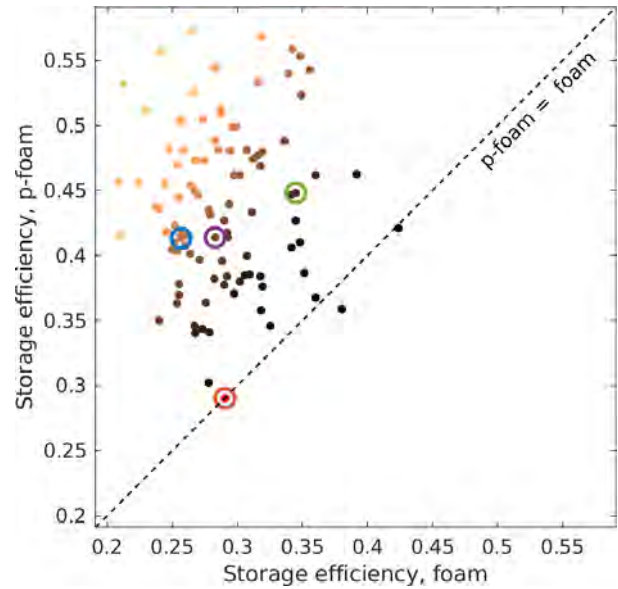


Figure 7. Correlation plot reporting storage efficiency (in pore volume fraction) using p-foam vs. normal foam. The dashed line corresponds to zero gain, and the red dot the simulation with homogeneous rock properties.

3.4. Distribution of injected CO₂

The distribution of injected CO₂ at breakthrough is illustrated in Figure 8 for a selection of realisations and foam properties. For this figure the CO₂ saturation at the end of the simulations (at break-through) is pore-volume

averaged in the vertical direction and the resulting values plotted with the position of the injection well in the lower left corner and the pressure control well in the upper right corner in each subplot (shown only in the upper left subplot). Simulations without foam are shown in the top row; simulations with normal foam in the middle row and

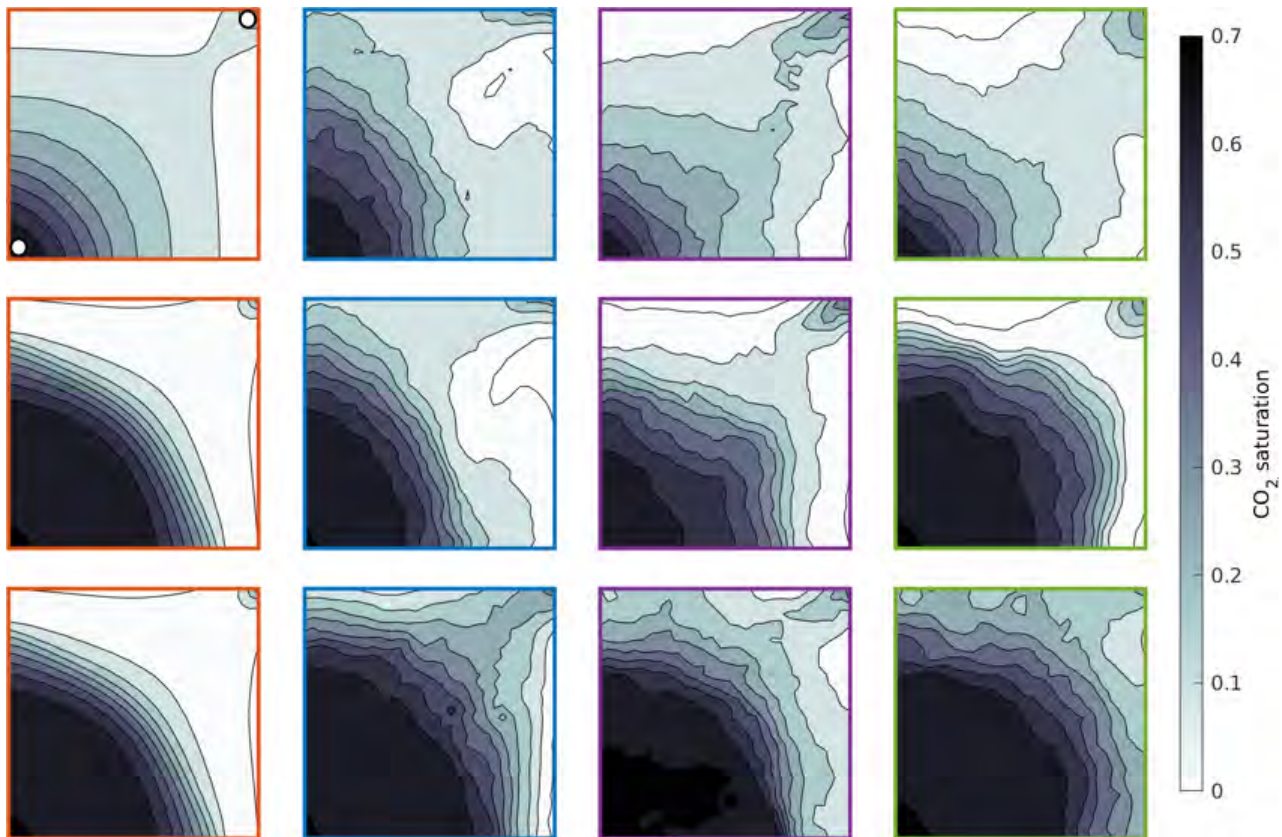


Figure 8. CO₂ plume for four selected cases. From top to bottom: no foam, foam, p-foam. From left to right: Homogeneous rock followed by the realizations with lowest gain, mean gain and largest gain from the ensemble simulation with foam vs no foam (Figure 3). The border colour of each subplot corresponds to the colour of the circles in the correlation plots in Figure 3, 5 and 7.

with p-foam in the bottom row. The columns, with different-coloured borders show results with the homogeneous model, and results from the realizations with lowest, mean and maximum storage efficiency increase in the foam vs no foam comparison (Figure 3). The colour of the border for each subplot corresponds to the models with similarly coloured markers in Figure 3, 5 and 7.

It is seen that, as expected, simulations with high storage efficiency have high average CO₂ saturations in a large region out from the injection well. We note that the transition from high to low saturation is sharper in the foam cases than in the no-foam case, indicating a more piston-like displacement of brine by the injected CO₂ even for the relatively high density difference between CO₂ and brine. We also note a tendency for more circular shape of the high-saturation CO₂ plume in the p-foam cases than for the normal foam and no-foam cases, indicating that the effect of heterogeneities on the shape of the CO₂ plume is diminished for the p-foam simulations. Figure 9 shows CO₂ saturation pore-volume averaged along the x axis for the same realizations as in Figure 8 at the time of CO₂ breakthrough in the pressure control well. The perforations in the injection and pressure control wells are indicated in the upper left subplot. We observe that the CO₂-plume is thicker for the foam cases (second and third row) and thickest for the p-foam case (third row), although the effect is only minor for the ordinary foam case with the least increase in storage efficiency (second subplot on the second row).

4. Discussion and conclusions

The BHP constraint imposed in the injection well cause throttling of the injection rate in most of the cases with foam and for all cases with p-foam, for part of the injection period. This can be expected, due to the larger pressure gradients in the near-well region when mobility control is used. Shear-thinning of foam, which is not included in the present simulations, would give weaker

mobility reduction close to the injection well and thereby reduce the impact on injection rates. A reduced injection rate due to too high BHP would not be desirable in a storage project where a constant injection rate has been agreed upon in a contract with the owner of the CO₂ source. New simulations with shear-thinning included should be run to examine more closely the impact that can be expected on injection rates.

Simulation results presented here demonstrate that the storage efficiency can be significantly increased with mobility control both for homogeneous and heterogeneous reservoir properties. The relative increase in the amount of CO₂ injected at the time of break-through in the pressure control well range from 20 to 110 % simulations with permeability-independent foam strength (normal foam) and from 50 to 335 % for the simulations where the foam strength scales with the permeability (p-foam). The average relative increase in amount of stored CO₂ is 54 % for normal foam and 138 % for p-foam.

The results show, however, that the relative increase in stored amount from normal foam to p-foam for some members of the ensemble is quite small. In the limiting case of homogeneous permeability this is easily explained, since the foam strength for normal foam and p-foam in that case is by definition equal. For the heterogeneous cases the difference would depend on the shape of permeability/porosity patterns in the reservoir.

In our results, introducing permeability-dependent foam strength significantly increases storage efficiency compared to using normal foam. However, we emphasize that we have only considered a single type of permeability dependence in this work, and further investigations of different models are needed to draw firm conclusions. We also mention that introducing permeability dependence in the mobility reduction factor makes the setup significantly more challenging to simulate. For some of the ensemble members, this

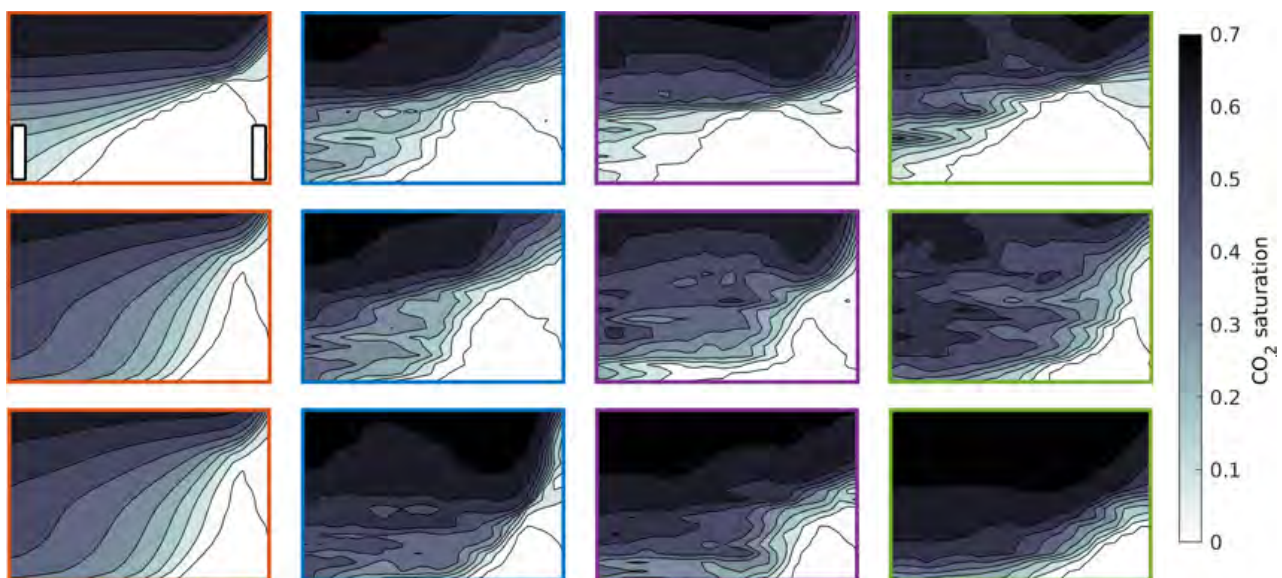


Figure 9. Vertical plot of the CO₂ saturation along the diagonal between injection and pressure control wells for selected cases. From top to bottom: no foam, foam, p-foam. From left to right: Homogeneous rock followed by the realizations with lowest gain, mean gain and largest gain from the ensemble simulations with foam vs no foam (Figure 3). The border colour of each subplot corresponds to the colour of the circles in the correlation plots in Figure 3, 5 and 7.

resulted in shorter timesteps and effectively less numerical diffusion for the p-foam ensemble. This may lead to an additional bias towards later breakthrough times compared to the no-foam and foam ensembles.

Acknowledgements

This publication has been produced with support from the NCCS Research Centre, performed under the Norwegian research program Centres for Environment-friendly Energy Research (FME). The authors acknowledge the following partners for their contributions: Aker Solutions, Ansaldo Energia, Baker Hughes, CoorsTek Membrane Sciences, EMGS, Equinor, Gassco, Krohne, Larvik Shipping, Lundin, Norcem, Norwegian Oil and Gas, Quad Geometrics, Total, Vår Energi, and the Research Council of Norway (257579/E20).

References

- [1] Grimstad, A.-A., Bergmo, P., Nilsen, H.M., Klemetsdal, Ø. 2018. CO₂ storage with mobility control. GHGT-14, Melbourne, Australia.
- [2] Chowdiah, P., Misra, B.R., Kilbane, J.J., Srivastava, V.J., Hayes, T.D. 1998. Foam propagation through soils for enhanced in-situ remediation. *Journal of Hazardous Materials*, 62 (3).
- [3] Farajzadeh, R., Lotfollahi, M., Eftekhari, A.A., Rossen, W.R., Hirasaki, G.J.H. 2015. Effect of permeability on implicit-texture foam model parameters and the limiting capillary pressure. *Energy & Fuels*, 29 (5).
- [4] Lie, K.-A. 2019. An introduction to reservoir simulation using MATLAB/GNU Octave: User guide for the MATLAB Reservoir Simulation Toolbox (MRST). Cambridge: Cambridge University Press. Doi:10.1017/9781108591416.
- [5] Vassenden, F., Holt, T. 2000. Experimental foundation for relative permeability modelling of foam. *SPE Reservoir Evaluation and Engineering*, 3 (2).
- [6] Wood, A., Chan, G. 1994. Simulation of Stationary Gaussian Processes in $[0, 1]^d$. *Journal of Computational and Graphical Statistics*, 3 (4).

AEROSOL EMISSION AT A POST COMBUSTION CO₂ CAPTURE PLANT AT TWENCE (WTE FACILITY)

Juliana Monteiro^{1*}, Tanya Srivastava¹, Jasper Ros¹, Arjen Huizinga¹, Paul Gravesteijn¹, Peter van Os¹, Ronald de Vries², Mathijs Vos², Kirsten Telgenkamp², Susanna Sprauten Uhre³, Hallvard Fjøsne Svendsen³, Hanna K Knuutila³

¹ TNO, Leeghwaterstraat 46, 2628CA, Delft, The Netherlands

² Twence B.V., PO Box 870, Hengelo, 7550 AW, The Netherlands

³ Department of Chemical Engineering, Norwegian University of Science and Technology (NTNU), NO-7491 Trondheim, Norway

* Corresponding author e-mail: juliana.monteiro@tno.nl

Abstract

Amine emissions in post combustion CO₂ capture (PCC) have a significant impact on process economics and the environment. The volatile nature of amine-based solvents in combination with aerosol formation can lead to amine emissions much higher than the design limit of PCCC plants. Aerosol management methods were implemented at the PCC pilot at Twence, a Waste-to-Energy plant in the east of The Netherlands. TNO carried out measurement campaigns at Twence with the aim to quantify amine emissions (both volatile and aerosol-based). The measurements indicated the necessity of implementing an aerosol mitigation technology, and a Brownian Demister Unit (BDU) was installed at the plant. The BDU removed more than 99% of the small particles (diameter below 5µm) from the flue gas, effectively controlling the MEA emissions at an average of 2.7 mg/Nm³ at the pilot installation outlet.

Keywords: CO₂ capture, aerosol-based emissions, solvent management, Brownian Demister Unit

1. Introduction

Post-combustion CO₂ capture (PCC) is critical for reduction of greenhouse gas emissions, particularly in hard-to-decarbonize industrial sectors, such as Waste-to-Energy (WtE). Amine-based technology has been implemented for capturing CO₂ from several types of flue gas sources. CO₂ capture, using aqueous 30wt% monoethanolamine (MEA) is considered as the benchmark technology [1], and is also being used at pilot scale at Twence, a WtE plant located in the east of The Netherlands. Twence has formulated a multi year development roadmap based on three pillars: (1) Renewable energy generation, (2) Circular economy by closing energy and material loops and (3) Biobased economy by production of materials from biogenic waste streams. PCC can act as a bridging technology since it improves CO₂ footprint of CHP and can act as a building block molecule for production cycles. This is represented in . Thus, Twence has been a first mover in accelerating WtE PCC.

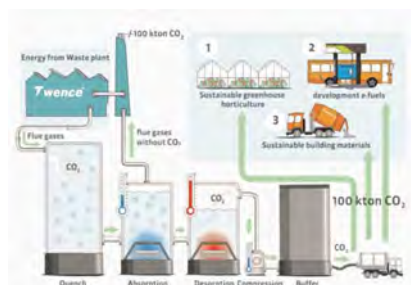


Figure 1. Twence's CO₂ capture and utilization roadmap [2]

The CO₂ capture pilot used in this study was commissioned in 2014 [3], and has been operational since then. The pilot treats ca. 1.5 vol% of the flue gas from Twence's waste incinerator line (ca. 3300 Nm³/h), and produces up to 500 kg/h of CO₂. Part of the CO₂ is used to produce sodium bicarbonate, which is in turn used in the flue gas de-sulfurization process. The remainder of the CO₂ is purified, liquified, and sold for external use (e.g., as food-grade CO₂ in the horticulture sector), see Figure 2.



Figure 2. Schematics of Twence's CO₂ capture pilot plant

There are economic and environmental challenges associated with the wide spread implementation of PCC. Emission of aqueous amine solvents, not only increases

the environmental impact of PCC, but also leads to higher operating costs. The volatile nature of amines contributes to emissions and observed MEA emissions in the treated flue gas at pilot plant operations are typically either below 10 mg/Nm³ or in the range of 100–1500 mg/Nm³ [4]. The high emission range is caused by aerosol-based emissions, and is significantly higher than the emission limit of 15 mg/Nm³ proposed at the TCM plant [5]. Traditionally, water wash and demisters are used as emission management techniques. But these counter measures are not sufficient for mitigating aerosol-based amine emissions, which are caused by the presence of aerosol particles in the gas, with diameter below 5 μm [4]. The most mature technology (TRL7) for controlling aerosol-based amine emissions is the Brownian Demister Unit (BDU), a filter capable of removing small particles from the flue gas [4]. While the BDU was used at different campaigns at the TCM pilot plant, the publications on those campaign focus on reporting the efficiency in particle removal, but fail to report on the impact on amine emissions reduction [5], [6].

This work presents the use of an BDU at Twence to reduce aerosol emissions. It reports data measured by TNO during the CAMAK project in 2020 and 2021 (funded under the Dutch Topsector Energy program, project number DEI219004).

2. Aerosol Management

2.1 Measurement of aerosol-based emissions

In order to better understand and quantify amine emissions at the Twence pilot, measurement campaigns were carried out by TNO in April 2020. The emissions were measured using an Electrical Low Pressure Impactor (ELPI) for determination of particle size distributions and concentrations. Additionally, amine emissions were monitored using a Fourier Transform Infrared Spectrometer (FTIR). The ELPI was used for measurements at three different points in the plant, namely upstream the quench column, in between the quench and absorber columns, and downstream the water wash section of the absorber, as illustrated in Figure 3. This was done to understand the extent of formation of aerosols in the quench, and to correlate the observed emissions (FTIR data) with the particle number concentration (PNC, ELPI data).

ELPI emissions

In the measurements performed upstream the quench, the flue gas temperature was ca. 160°C. The three measurements performed at this location are given in Figure 4, and are in relative good agreement. The average total PNC measured was $6.4 \cdot 10^5 \text{ cm}^{-3}$. Approximately 90% of the particles were registered in the last impactor (D50% 6nm). Given the temperature at the sampling point, these particles are expected to be solid. While the three measurements can be interpreted as repetitions, variations in the sampling procedure were performed. In the first experiment (“normal”), the ELPI line was connected at the gas sampling port. In the second experiment, a probe was used. In the third experiment, a filter was placed in the ELPI line. While the differences

registered are not significant, it is interesting to notice that the experiment with the filter allowed for registering particles throughout the measurement range (from 6nm to 5.44 μm), whereas for the other experiments, zero readings were recorded for some of the intermediate diameters. This measurement procedure is adopted in all measurements reported in this work from this point onwards. All measurements reported in Figure 4 were carried out on the 15th of April 2020.

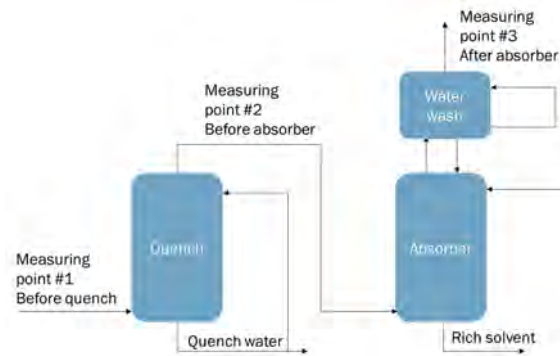


Figure 3 - Measurement points for the ELPI at Twence's capture pilot

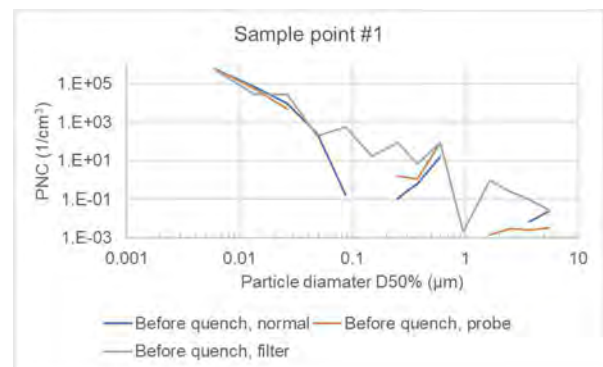


Figure 4 - Particle measurements in hot flue gas before quench, data from April 15th 2020

Measurements carried out downstream the quench (and upstream the absorber) were performed on the 7th and 15th of April 2020, and the observed PNC is given in Figure 5. The average total number of particles measured on the 7th was $3.4 \cdot 10^7 \text{ cm}^{-3}$, while on the 15th it was significantly higher: $1.2 \cdot 10^8 \text{ cm}^{-3}$. The reason for this variation is not known, and one hypothesis is that it is caused by variations in the WtE flue gas composition.

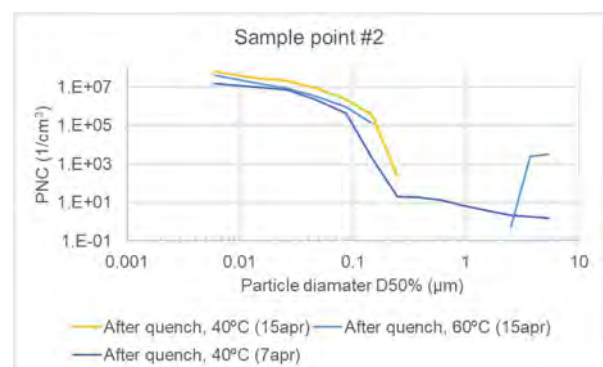


Figure 5 - Particle measurements before the absorber

The quench column is designed and operated to bring the temperature of the flue gas down from ca. 160°C to ca. 40°C. This is done by directly contacting cooling the gas with water. This leads to supersaturation of the gas phase, which contains acidic components such as HCl and SO₃. Nucleation in such environments is a well-known phenomenon in industrial wet scrubbing [7]. Both homogeneous and heterogeneous nucleation are possible in the Twence system, as foreign particles are present.

The total PNC measured at Twence after the quench is 2 orders of magnitude higher than before the quench. While the particles measured downstream the quench mostly have diameter below 0.1 μm (see in Figure 5), the typical particle sizes of HCl aerosols is 1-3 μm, whereas H₂SO₄ leads to smaller particles, from 0.3-1.5 μm [7].

Measurements were also carried out after the absorber. An 80% decrease was observed in the total number of particles. The measured particles were approximately $7 \cdot 10^6 \text{ cm}^{-3}$, while the PNC distribution shifted, as observed in Figure 6. This shift in the particle size distribution has an important effect: before the absorber, the total volume of the measured aerosols (considering perfect spheres) was $5.6 \cdot 10^{-10} \text{ cm}^3/\text{cm}^3$, whereas after the absorber this increased to $1.4 \cdot 10^{-9} \text{ cm}^3/\text{cm}^3$.

The measured concentration of aerosol particles require that dedicated mitigation technologies are employed. A review of available technologies is given in [4]. For the Twence pilot plant case, it was decided to install a Brownian Demister Unit (BDU) downstream the quench column.

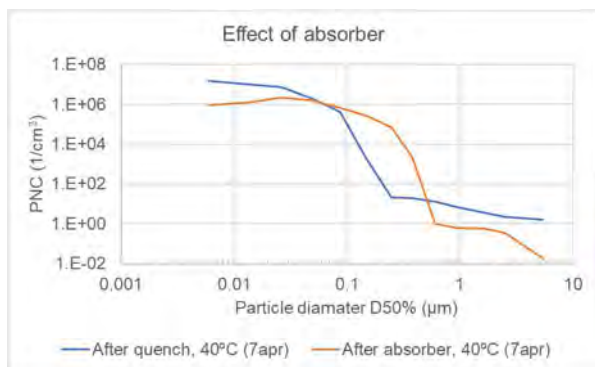


Figure 6 - Particle measurements after the absorber

FTIR measurements

The FTIR was used to measure MEA emissions at the absorber outlet (sample point #3). Emissions between 150 and 400 mg/Nm³ were observed, as illustrated in Figure 7 (showing data for the 6th and 7th of april 2020). It should be noticed that the gas from the absorber outlet is mixed into the flue gas in the stack, and therefore the MEA concentration is diluted by ca. 70 times before it is emitted to the atmosphere. Therefore, the MEA emissions to the atmosphere, when the emissions at the pilot plant was at a peak value of 400 mg/Nm³, was ca. 6 mg/Nm³, which is in-line with emissions from other pilots and below the emission limit of 15 mg/Nm³ proposed at the TCM plant [5]. As Twence doesn't have a specific emission limit for MEA this value is adopted in this study as a reference limit. Therefore, the emissions from the Twence pilot did not pose a risk to the

environment or the plant operation. On the other hand, identifying the aerosol-based emissions at pilot scale allows for evaluating alternative mitigation solutions which can be implanted also at full scale (at Twence, but for amine-based PCC in general). These evaluations are described next.

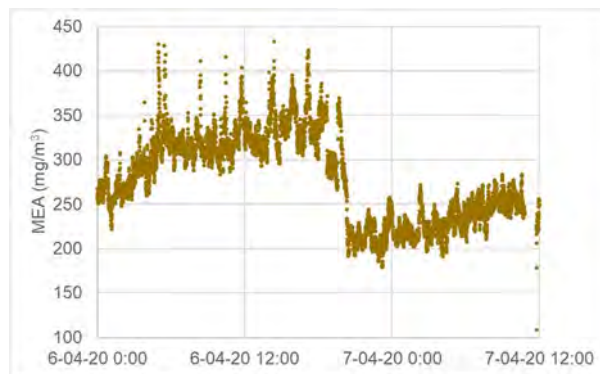


Figure 7 - MEA emissions at the absorber outlet, April 2020

2.2 Aerosol mitigation through plant operation

During the measurement campaign at the Twence pilot, operational parameters such as cooling in the quench and temperature of the lean solvent were varied. ELPI measurements were carried out at different operational settings to measure the impact of these strategies.

One mitigation strategy considered was to reduce the cooling in the quench to limit the degree of supersaturation, thereby limiting the increase in number of particles measured before the quench. During this test, the flue gas was cooled to 60°C, instead of 40°C, which lead to a decrease in the PNC (see Figure 5), from $1.2 \cdot 10^8 \text{ cm}^{-3}$ to $7 \cdot 10^7 \text{ cm}^{-3}$. While this is a relevant decrease, it is not enough to reduce the PNC to the point of mitigating aerosol-based emissions, so this would not be an effective counter measure.

Another mitigation strategy explored was increasing the temperature of the lean solvent to accelerate the particle growth within the absorber. Measurements were carried out for lean solvent at 40°C and 50°C. However, the number of particles measured was similar for both cases ($9.9 \cdot 10^6$ and $1.2 \cdot 10^7$ respectively). Thus, this strategy also was deemed ineffective.

2.3 Use of Brownian Demister Unit (BDU)

Following the measurement campaign, it was concluded that additional mitigation strategies were required to enable further emissions management. A Brownian Demister Unit (BDU) was installed at the Twence pilot in March 2021 and TNO conducted a measurement to evaluate the efficiency of this emission mitigation technology.

The BDU is installed between the quench and the absorber columns. Therefore, the gas entering the BDU is saturated at 40°C. The system is designed so that the BDU can easily be by-passed, to allow for tests with and without the BDU system inline ("BDU on/off").

A new series of ELPI measurements was performed on the 29th and 30th of March, 2021. The PNC was measured at the BDU inlet and outlet, as shown in Figure 8. The particle removal efficiency was above 99% throughout the measured particle diameter range. Two measurements were taken at the BDU inlet (1 and 2), one at the BDU outlet, and two at the water wash outlet (1 and 2), within an interval of 25 hours. During this interval, variations in the PNC were observed.

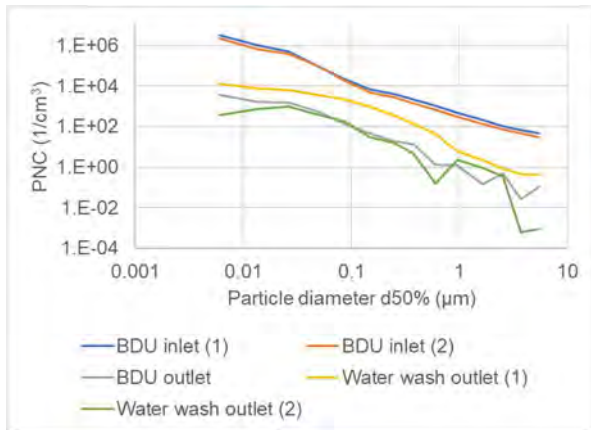


Figure 8 – Particle measurements around the BDU

The highest observed variation was in the water wash outlet (measuring point #3, see Figure 3). A long-term campaign is advised, to establish a correlation between the waste incinerator feeding process and the PNC.

The FTIR, connected downstream the absorber water wash, shows the effect on the MEA emissions. As made clear by Figure 9, the BDU has a clear effect of controlling the emissions. At stable operation with the BDU inline (BDU on), the MEA measurements averaged 2.7 mg/Nm³, which is a low value and inline with measurements from other pilots [8], [9]. When the BDU was by-passed (BDU off), the emissions immediately increased, and averaged 750 mg/Nm³ when stable. The dynamic response of switching the BDU “on” again is different than that of by-passing it, as can be observed in Figure 9. The measurements did not last long enough to determine how long it would take for the emissions would go back to the previous level.

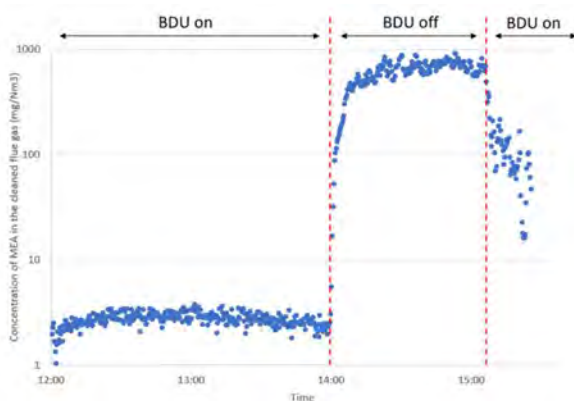


Figure 9 – MEA emissions at the pilot with and without the BDU

Again, it should be emphasized that the flue gas from the pilot is mixed with the stack flue gas before being emitted. The MEA emissions to the atmosphere, when the emissions at the pilot plant was at a peak value of 750 mg/Nm³, are estimated at ca. 11.3 mg/Nm³, below the reference limit of 15 mg/Nm³.

2.4 Aerosol modelling

An aerosol model was used to simulate selected experimental cases to predict the chemical composition of the aerosol droplets and gain insight into the experimental results. Details of the model can be found elsewhere [10]–[12]. Based on an inlet droplet size distribution, the model predicts droplet growth and how the composition change throughout the absorber and water wash sections. A demister model was included showing the effect of a demister.

The model inputs are the flow rate, composition and temperature of the gas phase, the inlet droplet composition, number concentration and size distribution, and finally, a simulation showing the bulk liquid phase compositions and temperatures as a function of position in the absorber and water washes. These simulations were run using the simulation tool CO2SIM. A selected experimental run at the Twence capture plant was simulated. Both the absorber (height of 6 meters with the packing type Flexipac 250X), and water wash section of 1 meter were simulated. In the simulations, a demister is placed after the water wash. The agreement between the experimental rich loading, gas outlet temperature, and temperature profile in the absorber and simulation results was good, the main difference being the temperature profile in the absorber. The simulated temperatures in the absorber were compared to the experimental values.

Three aerosol cases were simulated. The number concentration of droplets entering the absorber was increased to see the effect on the emissions. As the presence of sulfuric acid can have a large impact on the emissions as it can act as nuclei in the aerosol formation and as the concentration of H₂SO₄ in nuclei entering the absorber was unknown, the effect of H₂SO₄ was studied by changing the concentration of sulfuric acid in the absorber inlet. An overview of the results is shown in Table 1.

Figure 10 shows the outlet droplet diameters in the absorber and water wash. The droplets grow heavily in the water wash at the same time as the MEA concentration in the droplets drops sharply. As the demister removes the largest droplets with the biggest impact on emissions, the emissions after the demister are significantly lower for all three cases (see Table 1). Table 1 also shows that increasing the number concentration will result in a higher MEA emissions due to larger interfacial area and droplet volume. Higher inlet H₂SO₄ concentration gives higher emissions of MEA. The baseline MEA emissions predicted by the model are in acceptable agreement with the measurements performed at the Twence pilot plant. Figure 11 shows a comparison

of outlet droplet size distribution compared with experimental data for Cases 1 and 2.

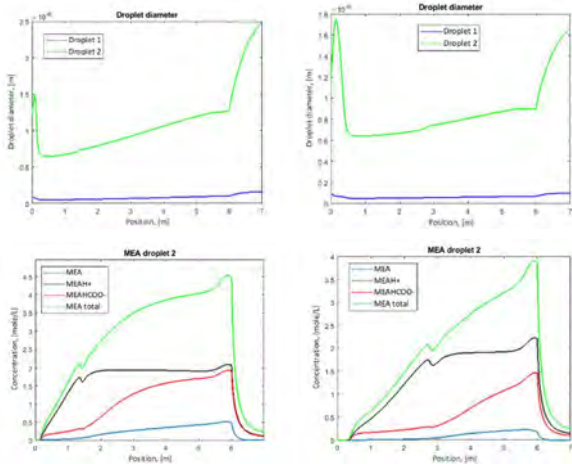


Figure 10 – Diameter of the droplets and MEA concentration as a function of position in the absorber (0-6 meters) and water wash (6-7 meters). On the left-hand side Case 1 and on the right-hand side Case 2.

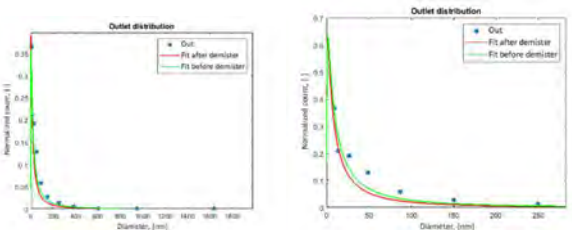


Figure 11 – Outlet distribution of droplets compared to experimental data. On the left-hand side Case 1 and on the right-hand side Case 2.

Table 1 – Summary of the modelling results

	Case 1	Case 2	Case 3
Droplets at the absorber inlet (droplets/cm ³)	11.7 · 10 ⁶	50 · 10 ⁶	50 · 10 ⁶
P _{H2O} at absorber inlet (kPa)	5.7	5.7	5.0
Inlet H ₂ SO ₄ concentration (mol/L)	0.1	0.1	0.02
MEA after absorber (ppmv)	371	482	410
MEA before demister after water wash (ppmv)	135	189	142

MEA after demister (ppmv)	57	104	80
Droplets after demister (droplets/cm ³)	11.6 · 10 ⁶	49.83 · 10 ⁶	49.86 · 10 ⁶

4. Conclusions

Amine emission due to aerosol formation pose a risk to PCC plants right to operate. For large scale implementation of PCC, it is important to both understand and know how to control these emissions.

The measurement campaign at the Twence pilot illustrated the need for an additional mitigation strategy to counter aerosol-based amine emissions, thereby improving economic and environmental performance. A BDU was installed and an experimental campaign was carried out to measure its impact. The measurements show that the BDU was able to remove more than 99% of the particles in the ELPI detection range. As a result, the MEA emissions are controlled at around 2.7 mg/Nm³.

A model was used to predict aerosol-based emissions, with acceptable agreement with the measurements performed on-site. The results of the performed research are appropriate within the multi year development roadmap of Twence and add to PCC for WtE knowledge development.

Acknowledgements

Acknowledgements goes to the project “Pilot CAMAK”, that has received funding of the “Topsector Energiesubsidie” of the Ministry of Economic affairs in the Netherlands.

References

- [1] E. Sanchez Fernandez, E. L. V Goetheer, G. Manzolini, E. Macchi, S. Rezvani, and T. J. H. Vlugt, “Thermodynamic assessment of amine based CO₂ capture technologies in power plants based on European Benchmarking Task Force methodology,” *Fuel*, vol. 129, pp. 318–329, 2014, doi: <https://doi.org/10.1016/j.fuel.2014.03.042>.
- [2] R. de Vries, A. Roeloffzen, and C. Offerreins, “Carbon Capture and Usage (CCU) at Twence,” 2019.
- [3] P. Huttenhuis, A. Roeloffzen, and G. Versteeg, “CO₂ Capture and Re-use at a Waste Incinerator,” *Energy Procedia*, vol. 86, pp. 47–55, 2016, doi: <https://doi.org/10.1016/j.egypro.2016.01.006>.

- [4] J. Monteiro, J. Ros, H. Svendsen, H. Knuutila, and N. P. Moser, “Guidelines for Emissions Control,” 2020. [Online]. Available: [https://www.alignccus.eu/sites/default/files/\[WEBSITE\] ALIGN-CCUS D1.1.7 Guidelines for emission control_0.pdf](https://www.alignccus.eu/sites/default/files/[WEBSITE] ALIGN-CCUS D1.1.7 Guidelines for emission control_0.pdf).
- [5] G. Lombardo *et al.*, “Results from Aerosol Measurement in Amine Plant Treating Gas Turbine and Residue Fluidized Catalytic Cracker Flue Gases at the CO₂ Technology Centre Mongstad,” *Energy Procedia*, vol. 114, pp. 1210–1230, 2017, doi: <https://doi.org/10.1016/j.egypro.2017.03.1377>.
- [6] M. Bade, Otto, O. Gorset, F. Graff, Oscar, and S. Woodhouse, “Method and plant for amine emission control,” WO 2010/102877 A1, 2010.
- [7] H. Gretscher and K. Schaber, “Aerosol formation by heterogeneous nucleation in wet scrubbing processes,” *Chem. Eng. Process. Process Intensif.*, vol. 38, no. 4, pp. 541–548, 1999, doi: [https://doi.org/10.1016/S0255-2701\(99\)00051-3](https://doi.org/10.1016/S0255-2701(99)00051-3).
- [8] P. Moser *et al.*, “Results of the 18-month test with MEA at the post-combustion capture pilot plant at Nederaussem – new impetus to solvent management, emissions and dynamic behaviour,” *Int. J. Greenh. Gas Control*, vol. 95, 2020, doi: [10.1016/j.ijggc.2019.102945](https://doi.org/10.1016/j.ijggc.2019.102945).
- [9] A. K. Morken *et al.*, “Emission Results of Amine Plant Operations from MEA Testing at the CO₂ Technology Centre Mongstad,” *Energy Procedia*, vol. 63, pp. 6023–6038, 2014, doi: <https://doi.org/10.1016/j.egypro.2014.11.636>.
- [10] H. Majeed, H. K. Knuutila, M. Hillestad, and H. F. Svendsen, “Characterization and modelling of aerosol droplet in absorption columns,” *Int. J. Greenh. Gas Control*, vol. 58, pp. 114–126, 2017, doi: <https://doi.org/10.1016/j.ijggc.2017.01.006>.
- [11] H. Majeed, H. Knuutila, M. Hillestad, and H. F. Svendsen, “Gas phase amine depletion created by aerosol formation and growth,” *Int. J. Greenh. Gas Control*, vol. 64, pp. 212–222, 2017, doi: <https://doi.org/10.1016/j.ijggc.2017.07.001>.
- [12] H. Majeed and H. F. Svendsen, “Effect of water wash on mist and aerosol formation in absorption column,” *Chem. Eng. J.*, vol. 333, pp. 636–648, 2018, doi: <https://doi.org/10.1016/j.cej.2017.09.124>.

THE COSTS OF CO₂ CARBONATION IN THE CEMENT INDUSTRY

Till Strunge^{1,2*}

¹ Institute for Advanced Sustainability Studies e.V., Potsdam, Germany

² Research Centre for Carbon Solutions, School of Engineering and Physical Sciences, Heriot-Watt University, Edinburgh, UK

* Corresponding author e-mail: till.strunge@iass-potsdam.de

Abstract

Rising climate change requires rapid changes in high emitting industries such as the cement industry. A concept developed in recent years which attracts researchers, entrepreneurs and policy makers alike is the so-called Carbon Capture and Utilisation (CCU). A major hurdle for implementing CCU technologies is often their economic viability. A process of particular interest for cement producers in the field of CCU are the so-called CO₂ carbonation processes, where CO₂ reacts with minerals to form stable carbonates. We assessed the main direct carbonation routes showing that Supplementary Cementitious Materials produced via CO₂ carbonation (SCM_{CCU}) could be produced at scale with Levelised Cost of Product of 120€/t_{SCM} which lies in the range of current selling prices of cement. Hence, using SCM_{CCU} could potentially become an economically viable way of reducing emission in this sector.

Keywords: *Techno-economic assessment, CO₂ carbonation, cement*

1. Introduction

Climate change poses a threat to life on earth as humans know it, and possibly even humanity itself. Anthropogenic emissions of greenhouse gases have been identified as a major cause for this effect. Among these is the molecule CO₂, which is commonly emitted through combustion of fossil fuels such as oil.¹ In order to tackle climate change, a majority of the countries in the world decided to reduce their CO₂ emissions in the upcoming years and decades with the Paris agreement in 2015.² Because approximately 30% of the anthropogenic CO₂ emissions are bound to industrial processes, with the largest emitting sectors being the steel and cement industry, a rapid change is needed to fulfil the emission reduction goals in this division.¹

A concept developed in recent years, which could possibly procure CO₂ emission reductions for many sectors is the so-called “Carbon Capture and Utilisation” (CCU). It has become a model which attracts researchers, policy makers and entrepreneurs in search of climate change mitigation solutions. The general idea is not to emit CO₂ directly, but to use the produced CO₂ to create products from it. Usually this concept is demarcated from the concept “Carbon Capture and Sequestration” (CCS), where CO₂ is (geologically) stored and no product is formed. At the end of their lifetime, many CCU products can be incinerated and the resulting CO₂ can be circled back again³. The concept is depicted in Figure 1. CCU can possibly play a large role in the de-fossilization of certain industry sectors and foster the development towards circularity in industrial processes.

It has been argued that a main advantage of the CCU concept is that industry does not need to completely change all existing processes, but it can rather be a supplement to current production routes, which makes

the transition to an environmentally sustainable society faster and more likely. Additionally, in particular instances, it might be possible to gain economic profit from it.³

A major hurdle for implementing CCU technologies is often their economic viability. Therefore, economic assessments of these technologies are of major importance for decision-makers in industry and politics, but also for upcoming entrepreneurs.⁴

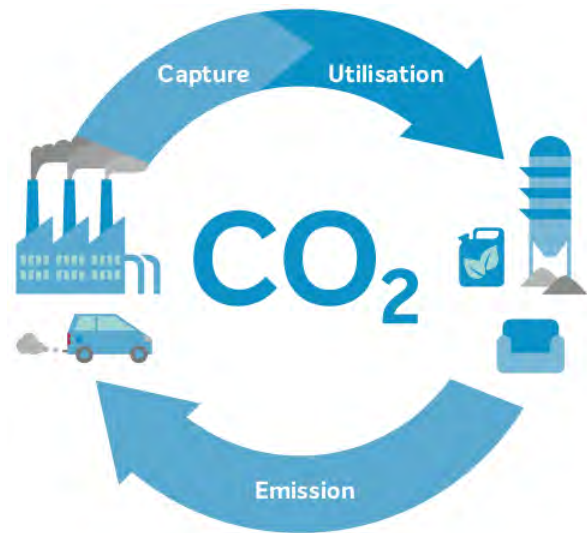


Figure 1: The economic carbon cycle taken from Zimmermann et al.³

Being among the biggest emitters of anthropogenic CO₂, the cement industry in particular requires rapid solutions in order to foster a development towards a sustainable future.⁵ A closer look at the processes reveals that roughly 60% of the cement industries emissions are process-inherent emissions and are emitted via the calcination of limestone and therefore they are not energy

related and need a distinctive mitigation approach.^{6,20} As long as the same reactions and feedstocks are used process-inherent emissions will still occur. Hence, solutions such as electrification of the process which only tackle energy related emissions and do not alter process-inherent emissions, will not be sufficient to reach net zero emissions in the cement industry. Hereby, CCU technologies could potentially be a part of the solution.⁵ A technological concept developed in this field is CO₂ carbonation often also referred to as CO₂ mineralisation. CO₂ is reacted with activated minerals to form stable carbonates.^{7,8} While many CCU products offer limited CO₂ storage potential since stored CO₂ might be released at the end of their life cycle, carbonates are a mean to store CO₂ permanently. The global storage potential of CO₂ carbonation has been estimated to be at least 10 000Gt carbon due to an abundance of mineral feedstock.^{8,9} Carbonation products could potentially be used for multiple purposes, such as fillers, Supplementary Cementitious Materials (SCM) or for land reclamation projects.^{9,10,11,12}

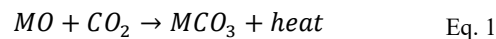
The concept of CO₂ carbonation is not new to the sustainability community. It has been researched as a storage solution for CO₂ (CCS) in recent years without focusing on the formation of a product, which can possibly create additional revenue for the emitter of CO₂ and potentially substitute carbon intensive products such as cement.⁸

Some policy advise reports¹³ use CO₂ carbonation process as a positive example for using CO₂ as a feedstock, because unlike most other CO₂ utilisation concepts, the mineralisation reaction is energetically favored.¹⁴ Controversially, a literature review revealed the lack of detailed economic assessments for these processes as a CCU technology. Additionally, it was found that when economic assessments are performed in this field they are habitually not comparable, due to the use of different assumptions and often an economic evaluation is solely done on the basis of energy consumption.^{8,9,15} Energy consumption itself might be a major driver for the operational costs using a CCU technology, but research has shown that investment decisions are not always bound to this criteria.¹⁶ Therefore, a systematic comparison of multiple mineralisation pathways is needed to provide decision-makers with the information necessary to verify the feasibility of successfully implementing such technologies. Moreover, a detailed assessment can also be used for additional purposes, such as evaluating under which circumstances a novel technology becomes economically feasible and to detect key factors which can be influenced in order to reach economic feasibility. It is also crucial to investigate additional factors that can influence whether a technology will be deployed.

This contribution aims to uncover the costs of different proposed CO₂ carbonation routes as well as their scaling effects through a rigorous techno-economic assessment (TEA).

2. Carbonation processes

In literature direct aqueous carbonation reactions have been extensively studied.^{8,15,17,18,19} Magnesium or calcium-rich rocks such as olivine or serpentine have been proposed as feedstocks for the carbonation reaction.^{15,19} The general reaction can be described as follows in which M represents MgO and CaO:



In proposed direct aqueous carbonation routes captured CO₂ is reacted in an autoclave using increased pressure and temperature in an aqueous slurry reaction. To counteract slow reaction kinetics rocks a mechanically or thermally activated (grinding and calcination) and additives such as NaCl, or NaHCO₃ are added.^{15,19}

When silicate rich feedstocks such as olivine or serpentine are used for the carbonation the by-product silica (SiO₂) is obtained, which is often a part of many Supplementary Cementitious Materials such as steel slag used in cement blends today. Hence, it is foreseen that carbonation products can be used as SCMs in the cement industry.^{11,12,20}

3. Methods

Unlike life cycle assessment (LCA), techno-economic assessments do not follow an ISO standard resulting in less homogeneous results among published studies. For this study recently published guidelines⁴ as well as the proposed methodology by Rubin et al.^{21,22} were followed. This process begins with the scope definition.

2.1 Scope of the assessment

The process can be distinguished by multiple process units, which have to be included into the scope of the assessment (see Figure 2). We choose ton of cement replacement produced (hereafter referred to as Supplementary Cementitious Material from CCU, short SCM_{CCU}) as the functional unit. We define the SCM as 40% SiO₂ and 60% MgCO₃. Gravity separation in the post-treatment is used to obtain this composition.²³

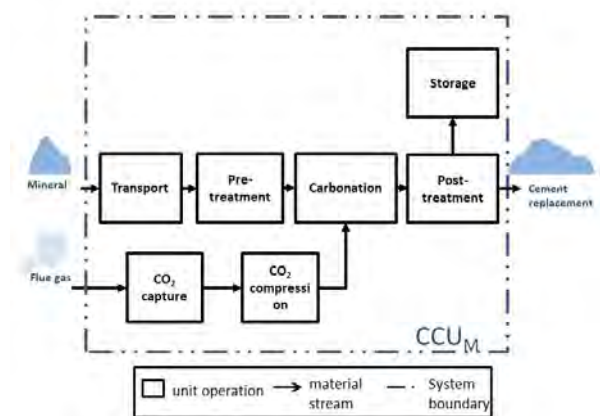


Figure 2: System boundaries for the assessment of carbon capture and utilisation through the means of mineralisation (CCU_M). Adapted from Ostovari et al.²⁰

2.1 Calculating the costs of CO₂ carbonation

The indicator chosen for this assessment is Levelised Cost of Product (LCOP) per ton of SCM_{CCU} produced. This incorporates both capital (CapEx) and operational (OpEx) expenditures needed to produce the carbonated product. The capital costs are discounted using the interest rate and the lifetime of the plant to evaluate the true cost of capital for the proposed plants (see Eq. 2 and Eq. 3).

$$LCOP = \alpha \cdot CapEx + OpEx \quad \text{Eq. 2}$$

$$\alpha = \left(\frac{i}{1 - (1 + i)^{-L}} \right) \quad \text{Eq. 3}$$

We calculate the CapEx using the Total Plan Cost (TPC) and Total Direct Costs (TDC) (see Eq. 4).

$$TPC = \sum TDC \cdot (1 + f_{indirect}) \cdot (1 + f_{process}) \cdot (1 + f_{project}) \cdot (1 + f_{owner}) \quad \text{Eq. 4}$$

Here, $f_{indirect}$, $f_{process}$, $f_{project}$, f_{owner} represent indirect costs, process contingencies, project contingences and owners costs.

To derive the TDC for each process unit we use both a bottom-up approach for all process units of which costs have not been widely studied (i.e. carbonation reactor) as well as a top down approach for units that have been studied thoroughly in literature. The top down approach is used for the CO₂ capture (monoethanolamine (MEA) post combustion capture) as well as the CO₂ compression. Here, published estimations by Voldsund et al.²⁴ (CO₂ capture) and Van der Spek et al.²⁵ (CO₂ compression) are used. The top down approach is shown in Eq. 5.

$$TDC_{top\ down} = TDC_{old} \cdot \left(\frac{\dot{m}_{new}}{\dot{m}_{old}} \right)^n \cdot \left(\frac{I_{new}}{I_{old}} \right) \quad \text{Eq. 5}$$

The plant capacity is used by \dot{m}_i in [t/a]. n represents the scaling factor and I capital cost index for a certain year to account for inflation. Here, the chemical Engineering Plant Cost Index (CEPCI)²⁶ is used. For all other process units, a bottom up approach is used to derive TDC. In the bottom up approach Aspen Capital Cost estimator is used to derive estimations of the TDC of each unit directly.

The overall CapEx are derived incorporating learning effects following Rubin et al.^{21,22} (see Eq. 6 and Eq. 7).

$$CapEx = \left(\frac{TPC}{\dot{m}_{SCM}} \right) \cdot N^{-E} \cdot \dot{m}_{SCM} \cdot (1 + i)^{t_{construction}} \quad \text{Eq. 6}$$

$$E = \frac{\ln(1 - LR)}{\ln(2)} \quad \text{Eq. 7}$$

N characterizes the number of plants necessary, LR the learning rate, E the experience factor, i the interest during construction and $t_{construction}$ the estimated time for construction.

The operational expenditures are derived using mass and energy balances for the costs of utilities and feedstocks, the costs of material transport and the costs of labour (see Eq. 8).

$$OpEx = \sum w_i \cdot \pi_i + \dot{m}_{mineral,in} \cdot \sum \pi_j \cdot d_j + OpEx_{fixed} \quad \text{Eq. 8}$$

The amount of feedstock or utility needed is represented by w_i , π_i is the price for feedstock or utility π_j is the price of transportation mean (i.e. truck, train or ship) and d_j the distance for material transported. The fixed operational expenditures $OpEx_{fixed}$ consist of cost for labor, insurance and local tax, maintenance and administration and support. The following assumptions are used for the calculations (see Table 1 to Table 4):

Table 1: Process assumptions

Descript ion	Serpe ntine 37µm (X=0.6) ¹⁵	Olivin e 37µm (X=0.3) ¹⁵	Olivin e 37µm (X=0.5) ¹⁵	Olivin e 10µm (X=0.6) ¹⁹	Olivin e 10µm (X=0.8) ¹⁹
Yield	0.6	0.3	0.5	0.6	0.8
particle size [µm]	37	37	37	10	10
P [bar]	115	150	150	100	100
T [°C]	155	185	185	190	190
c _{NaHCO₃} [mol/l]	0.64	0.64	0.64	0.5	0.5
c _{NaCl} [mol/l]	1	1	1	0.75	0.75

Table 2: Economic Assumptions: * median of multiple values used.

Variable	Value	Reference
Working hours	8000h/year	Deolalkar ²⁷
Lifetime	30 years	Own estimation
Overall interest* (including interest on equity and dept)	7.69%	European Central Bank ²⁸ , Gurufocus ²⁹ , Macrotrends ^{30,31}
Extraction Costs Mineral*	12€/t	Brown, et al. ³²
Transport distance (1000km)	60km truck 200km train 740km ship	Ostovari, et al. ²⁰ , own estimation
Transport costs	0.04€/tkm truck 0.032€/tkm train 0.0032€/tkm ship	Brown, et al. ³²
Electricity price*	62€/MWh	European Commission ³³
Natural gas price*	32€/MWh	Duić, et al. ³⁴
Price NaHCO ₃ *	209€/t	Comparison of vendor prices ³⁵
Price NaCl*	61.6€/t	Comparison of vendor prices ³⁵
Price MEA*	1320€/t	Comparison of vendor prices ³⁵

Table 3: Factors used for CapEx calculation.

Description	Value	Reference
Indirect costs	14%	Anantharaman et al. ³⁶
Process contingencies	40%	EPRI ³⁷ , AACE ³⁸
Project contingencies	30%	EPRI ³⁷
Owner's costs	7%	Grande et al. ³⁹
Learning rate	10.5%	Rubin et al. ⁴⁰
Number of plants	20	Greig et al. ⁴¹

Table 4: Factors used for OpEx calculation

Description	Value	Reference
Insurance and local tax	2% of TPC	Anantharaman et al. ³⁶
Maintenance	2.5% of TPC	Anantharaman et al. ³⁶
Administration and support	30% of operating and maintenance	Anantharaman et al. ³⁶

3. Results

The results are shown in Figure 3. Overall, the results indicate that cost reductions due to size (economies of scale) are most significant for plant sizes up to roughly 15-20kt/a. Surpassing this size building a bigger plant will only lead to minor production cost reductions. Additionally, the suggested process routes show a difference in calculated production costs of roughly 50€/t of SCM_{CCU}, which translates to a 40% increase from lowest costs to highest costs.

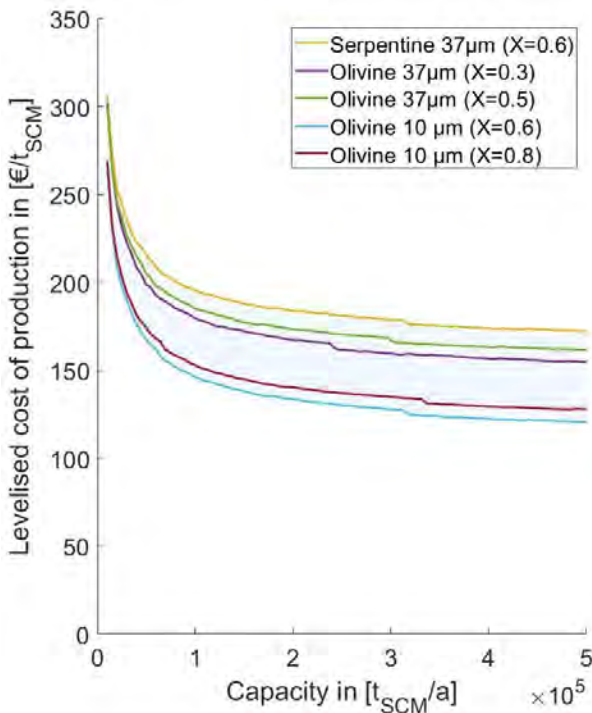


Figure 3: Levelised Cost of Product for SCM_{CCU}

The process proposed by Eikeland et al.¹⁹ shows the lowest costs with a LCOP of 120€/t_{SCM} at a capacity of

500kt_{SCM}/a. Here, olivine is used as a feedstock which is grinded to 10µm. Hence, higher operational costs due to higher energy demand for grinding as well as increased CapEx for grinding mills are off-setted by the lowered cost due to higher reaction extends compared to processes where 37µm grinding is proposed. Additionally it is shown that overall a yield of 0.6 appears to be lower in costs for producing a SCM with the same properties, compared to a yield of 0.8 for the same reaction conditions (see Figure 3, Olivine 10µm (0.6) and Olivine 10µm (0.8)).

4. Conclusion

Emission reduction in high emission sectors often comes with additional costs. The results show that large CO₂ carbonation plants might be economically feasible. With cement prices in Europe ranging from 70 to 150€/t_{cement}⁴², the calculated prices appear to be in a competitive price range, suggesting that emission reductions could become economically feasible through the means of CO₂ carbonation. Although, studies showed that using direct carbonation can reduce the emission of cement production significantly when applied in the large scale²⁰ further assessments should be performed analysing differences in costs and emissions for selected SCM product specifications (i.e. SiO₂ contents). The final costs of the system can be determined, when product specifications are set for SCM via CCU.

Acknowledgements

Parts of this work have been carried out within the project "CO2MIN" (033RC014). The project was funded by the German Federal Ministry of Education and Research (BMBF). I would like to deeply thank Dr. Mijndert Van der Spek and Dr. Phil Renforth for detailed guidance and support of this work as well as Mr. Hesam Ostovari and Mr. Dario Kremer for detailed feedback.

References

- [1] Pachauri, R. K. et al. Climate change 2014: synthesis report. Contribution of Working Groups I, II and III to the fifth assessment report of the Intergovernmental Panel on Climate Change. (Geneva, 2014).
- [2] Rogelj, J. et al. Paris Agreement climate proposals need a boost to keep warming well below 2 C. Nature 534, 631 (2016).
- [3] Zimmermann, A. et al. CO₂ utilisation today: report 2017. (2017).
- [4] Zimmermann, A. et al. Techno-Economic Assessment & Life Cycle Assessment Guidelines for CO₂ Utilization (Version 1.1). (2020).
- [5] Favier, A., De Wolf, C., Scrivener, K. & Habert, G. A sustainable future for the European Cement and Concrete Industry: Technology assessment for full decarbonisation of the industry by 2050. (ETH Zurich, 2018).
- [6] Andrew, R. M. Global CO₂ emissions from cement production. Earth System Science Data 10, 195 (2018).
- [7] Pan, S.-Y., Shah, K. J., Chen, Y.-H., Wang, M.-H. & Chiang, P.-C. Deployment of accelerated carbonation using alkaline solid wastes for carbon mineralization and

- utilization toward a circular economy. *ACS Sustainable Chemistry & Engineering* 5, 6429-6437 (2017).
- [8] Sanna, A., Uibu, M., Caramanna, G., Kuusik, R. & Maroto-Valer, M. M. A review of mineral carbonation technologies to sequester CO₂. *Chem Soc Rev* 43, 8049-8080, doi:10.1039/c4cs00035h (2014).
- [9] Sanna, A., Hall, M. R. & Maroto-Valer, M. Post-processing pathways in carbon capture and storage by mineral carbonation (CCSM) towards the introduction of carbon neutral materials. *Energy & Environmental Science* 5, 7781, doi:10.1039/c2ee03455g (2012).
- [10] Kremer, D. et al. Geological Mapping and Characterization of Possible Primary Input Materials for the Mineral Sequestration of Carbon Dioxide in Europe. *Minerals* 9, doi:10.3390/min9080485 (2019).
- [11] Benhelal, E. et al. The utilisation of feed and byproducts of mineral carbonation processes as pozzolanic cement replacements. *Journal of Cleaner Production* 186, 499-513 (2018).
- [12] Woodall, C. M., McQueen, N., Pilorgé, H. & Wilcox, J. Utilization of mineral carbonation products: current state and potential. *Greenhouse Gases: Science and Technology* 9, 1096-1113 (2019).
- [13] WWF Deutschland. Wie klimaneutral ist CO₂ als Rohstoff Wirklich? - WWF Position zu Carbon Capture and Utilization (CCU). (2018).
- [14] Rackley, S. A. in *Carbon Capture and Storage (Second Edition)* (ed Stephen A. Rackley) 253-282 (Butterworth-Heinemann, 2017).
- [15] Gerdemann, S. J., O'Connor, W. K., Dahlin, D. C., Penner, L. R. & Rush, H. Ex situ aqueous mineral carbonation. *Environmental science & technology* 41, 2587-2593 (2007).
- [16] Buchner, G. A., Zimmermann, A. W., Hohgräve, A. E. & Schomaecker, R. A techno-economic assessment framework for the chemical industry-based on technology readiness levels. *Industrial & Engineering Chemistry Research* (2018).
- [17] Stopic, S. et al. Synthesis of Nanosilica via Olivine Mineral Carbonation under High Pressure in an Autoclave. *Metals* 9, 708 (2019).
- [18] Stopic, S. et al. Synthesis of magnesium carbonate via carbonation under high pressure in an autoclave. *Metals* 8, 993 (2018).
- [19] Eikeland, E., Blichfeld, A. B., Tyrsted, C., Jensen, A. & Iversen, B. B. Optimized carbonation of magnesium silicate mineral for CO₂ storage. *ACS applied materials & interfaces* 7, 5258-5264 (2015).
- [20] Ostovari, H., Sternberg, A. & Bardow, A. Rock 'n' use of CO₂: carbon footprint of carbon capture and utilization by mineralization. *Sustainable Energy & Fuels*, doi:10.1039/D0SE00190B (2020).
- [21] Rubin, E. S. et al. A proposed methodology for CO₂ capture and storage cost estimates. *International Journal of Greenhouse Gas Control* 17, 488-503 (2013).
- [22] Rubin, E. S. et al. in *Towards improved guidelines for cost evaluation of carbon capture and storage* (eds Simon Roussanaly, Edward S. Rubin, & Mijndert Van der Spek) (2021).
- [23] Kremer, D. & Wotruba, H. Separation of Products from Mineral Sequestration of CO₂ with Primary and Secondary Raw Materials. *Minerals* 10, 1098 (2020).
- [24] Voldsund, M. et al. D4. 6: CEMCAP Comparative Techno-Economic Analysis of CO₂ Capture in Cement Plants. H2020 Project: CO₂ Capture from Cement Production (2018).
- [25] van der Spek, M., Ramirez, A. & Faaij, A. Challenges and uncertainties of ex ante techno-economic analysis of low TRL CO₂ capture technology: Lessons from a case study of an NGCC with exhaust gas recycle and electric swing adsorption. *Applied Energy* 208, 920-934 (2017).
- [26] The Chemical Engineering Plant Cost Index. Chemical Engineering. <https://www.chemengonline.com/pci-home>. (2021).
- [27] Deolalkar, S. P. in *Designing Green Cement Plants* (ed S. P. Deolalkar) 83-86 (Butterworth-Heinemann, 2016).
- [28] European Central Bank. Cost of borrowing for corporations - Euro area, <<https://sdw.ecb.europa.eu/browseSelection.do?type=series&q=MIR.M.U2.B.L22.A.R.A.2240.EUR.N+MIR.M.U2.B.A2I.AM.R.A.2240.EUR.N&node=SEARCHRESU LTS>> (2021).
- [29] Gurufocus. ROE % Sector Distribution, <<https://www.gurufocus.com/term/ROE/OTCPK:HDEL Y/ROE-Percentage/HeidelbergCement%20AG>> (2020).
- [30] Macrotrends. Holcim Debt to Equity Ratio 2010-2020, <<https://www.macrotrends.net/stocks/charts/HCLMY/holcim/debt-equity-ratio>> (2020).
- [31] Macrotrends. HeidelbergCement AG Debt to Equity Ratio 2008-2020, <<https://www.macrotrends.net/stocks/charts/HDELY/heidelbergcement-ag/debt-equity-ratio>> (2020).
- [32] Brown, T. J. et al. Underground mining of aggregates. Main report. (2010).
- [33] European Commission. Communication from the commission to the European Parliament, the Council, the European Economic and Social Committee and the Committee of the regions - Energy prices and costs in Europe (COM (2019) 1 final). (Brussels, 2019).
- [34] Duić, N. et al. Heat Roadmap Europe: EU28 fuel prices for 2015, 2030 and 2050 - Deliverable 6.1: Future fuel price review. (University of Zagreb, Zagreb, 2017).
- [35] Alibaba. Product search at Alibaba.com, <<https://www.alibaba.com/>> (2020).
- [36] Anantharaman, R., Berstad, D., Cinti, G., De Lena, E., Gatti, M., Hoppe, H., . . . Voldsund, M.. CEMCAP Framework for Comparative Techno-economic Analysis of CO₂ Capture From Cement Plants-D3., doi: 10.5281/zenodo.1257112 (2018).
- [37] EPRI. TAGTM Technical Assessment Guide Volume 1: Electricity Supply—1993, TR-102276-V1R1. Electric Power Research Institute (Palo Alto, 1993).
- [38] AACE. Cost estimate classification system – as applied in engineering, procurement, and construction for the process industries, AACE International Recommended Practice No. 18R-97 (Rev. November 29, 2011). AACE International. (Morgantown, 2011).
- [39] Grande, C., Roussanaly, S., Anantharaman, R. & Lindqvist, K. CO₂ Capture in Natural Gas Production by Adsorption Processes for CO₂ Storage, EOR and EGR. IEAGHG. (2016).
- [40] Rubin, E.S., Azevedo, I.M.L., Jaramillo, P., Yeh, S.. A review of learning rates for electricity supply technologies. *Energy Policy* 86, 198–218. (2015).
- [41] Greig, C., Garnett, A., Oesch, J. & Smart, S. Guidelines for scoping and estimating early mover ccs projects. Univ. Queensland. (Brisbane, 2014).
- [42] de Vet, J.-M., Pauer, A., Merkus, E., Baker, P., Gonzalez-Martinez, A. R., Kiss-Galfalvi, T., . . . Rincon-Aznar, A. Competitiveness of the European Cement and Lime Sectors. WIFO Studies. (2018)

PVT AND FLOW BEHAVIOR OF IMPURE CO₂ IN AQUIFERS

O. Sævareid^{1*}, S.E. Gasda¹, T.S. Mykkeltvedt¹

¹ NORCE, Bergen, Norway

* Corresponding author e-mail: ovsa@norce-research.no

Abstract

We combine compositional modelling of a Brine-CO₂ system with detailed resolution of the well interface and the near-well reservoir region. Via a small selection of case studies, we explore how impurities added to a CO₂ injection stream impacts reservoir flow and well response.

Keywords: CO₂ injection, Impurities, Density, Viscosity, Well-Reservoir

1. Introduction

The planning and control of CO₂ injection operations depends crucially on accurate and efficient simulation tools. Uncertainty regarding reservoir description, temperature conditions and the amount and type of impurities inherent in the CO₂ stream, are some of the aspects that must be explored.

This paper considers the near-well reservoir under injection, and address sensitivity of mixture properties in interaction with some simple reservoir structures. Towards this end, first we apply an in-house PVT tool [1] to explore some basic properties of impure CO₂ mixtures. For reservoir flow we have used a model available via the OPM framework [13]. This is a compositional model for a CO₂-Brine system based on a nonlinear complementary formulation [4][9]. The model relies on [5][15][16] for mutual dissolution between CO₂ and brine. Density and viscosity for the liquid (H₂O-rich) phase are based on [2][3][8], while the properties for the “gas” (CO₂-rich) phase are modelled according to [6][14][17].

2. Sensitivity of mixture PVT properties

Our focus here will be sensitivity of density and viscosity of the CO₂-rich phase with respect to impurities.

We consider a mixture of about 50% mole fraction water, while the remaining fraction consists of CO₂ where “impurities” are added by replacing 5-10% of the CO₂ by combinations of N₂ and CH₄.

We base our study on an in-house PVT tool using the Peng-Robinson equation of state and use the group contribution method, see [12] and references therein, to compute binary interaction parameters (BIP).

Table 1: Temperature dependent binary interaction coefficients computed by group contribution method for two different temperatures. Below diagonal coefficients for T=293K and above diagonal coefficients for T=353K.

	H ₂ O	N ₂	CO ₂	CH ₄
H ₂ O		0.5453	-0.0735	0.4485

N ₂	0.7826		-0.0811	0.0456
CO ₂	-0.1039	-0.0554		0.1230
CH ₄	0.5873	0.0424	0.1098	

For a set of alternative interaction parameters, we have also collected coefficients from the online calculator at https://checcalc.com/solved/multi_flash.html. These are partially based on correlations given by Gao et.al [7], and coefficients obtained for our fluid system are shown in Table 2 below.

Table 2: Alternative binary interaction coefficients.

	H ₂ O	N ₂	CO ₂	CH ₄
H ₂ O				
N ₂	0.0753			
CO ₂	0.1200	-0.0170		
CH ₄	0.0444	0.0311	0.0919	

Variability across choices of interaction parameters, is clearly significant, but the sensitivities regarding impurities are of similar magnitude.

2.1 Density

Densities for the CO₂-rich phase obtained from various mixtures and based on the parameters from Table 2, are depicted in Figure 1 and Figure 2 for temperatures of 293K and 353K, respectively.

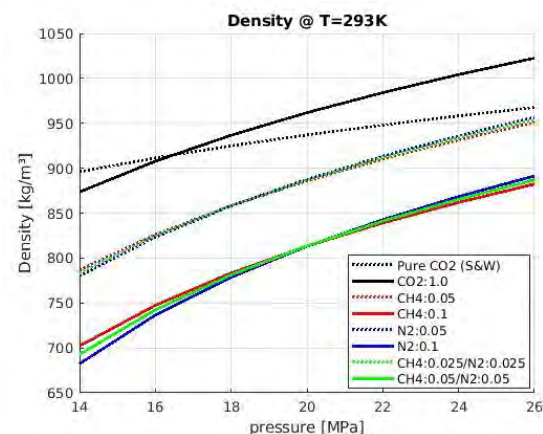


Figure 1: Density for CO₂-rich phase at “low” temperature.

The mole fractions shown in the curve legends refer to the feeding gas mixture, i.e., before brought into equilibrium with an abundant water-rich phase. Thus, the solid black line refers to the CO₂-rich phase of CO₂-H₂O system. For comparison, the density of pure CO₂ is shown as dotted black lines, based on Span& Wagner [14]. The colored lines represent various impure feeding gas mixtures, while solid and dotted indicates 90% respectively 95% mole fraction of CO₂. Red lines represent impurities in terms of methane, blue is nitrogen, and green is an equal weight (mole fraction) combination of the two.

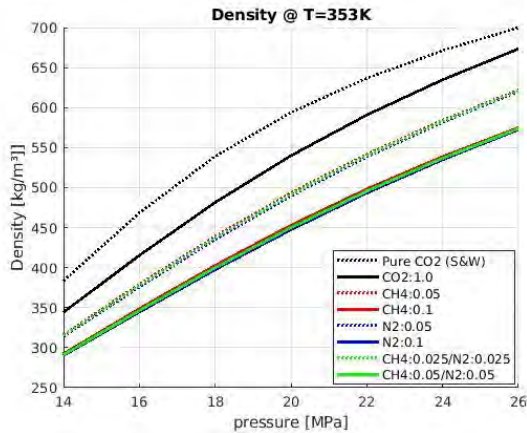


Figure 2: Density for CO₂-rich phase at “high” temperature.

The model shows clear sensitivity for the magnitude of impurity, while the quality appears to be much less important for the substances and compositions considered here. For pressure 22MPa and temperature 353K we observe densities for impure mixtures at approximately 80% and 90% of that of the pure CO₂-water system. For temperature 293K, the relative impact is slightly less.

2.2 Viscosity

Viscosities are calculated using both the original and improved LBC models, refer [10][11]. The two models give essentially identical output for the CO₂-rich phase, and results for temperatures 293K and 353K are shown in Figure 3 and Figure 4 below. The organization of line types and legends correspond to the above density plots.

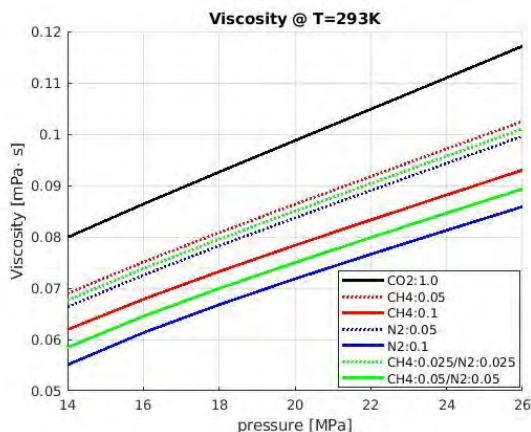


Figure 3: Viscosity for “cold” CO₂ mixtures.

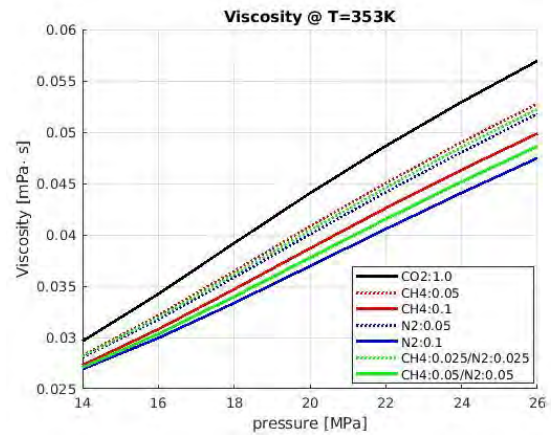


Figure 4: Viscosity for “hot” CO₂ mixtures.

Compared to the density results where the magnitude of the impurities was the dominating factor, we note that the viscosities display a clear sensitivity also regarding the quality of the impurities. For pressure 22MPa and temperature 293K we observe viscosities for the equal weighted impurities (green lines) approximately 75% and 85% of that of the pure CO₂-water system. For temperature 353K, the relative impact is less.

A more complete view of the viscosities is shown in Figure 5 and Figure 6 below, corresponding to mixtures of 90% and 95% mole fraction CO₂, respectively.

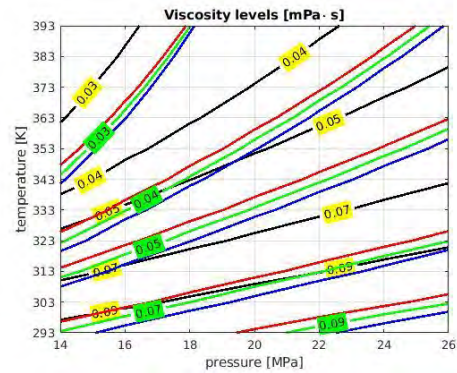


Figure 5: Viscosity contours for 90% CO₂ mole fraction.

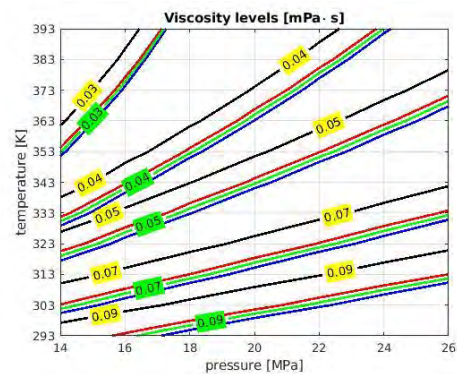


Figure 6: Viscosity contours for 95% CO₂ mole fraction.

The above computations verify the common knowledge that adding relevant impurities to a CO₂ stream, typically decrease both density and viscosity. From an injection perspective, these changes will partly cancel each other. Lower densities require more volume injected to deposit the same mass, while smaller viscosity will promote flow. Added chemical complexity increases risk for permeability altering precipitation. From a storage perspective, the plume will be larger, more buoyant, and presumably less leakage resistant.

3. Impact on reservoir flow

Here, we will first establish a simple reservoir model and then apply it to investigate how basic properties of the injected CO₂ stream influence the flow behavior in the reservoir. Model geometry is outlined in Figure 7 below, and some basic quantities are listed in Table 3.

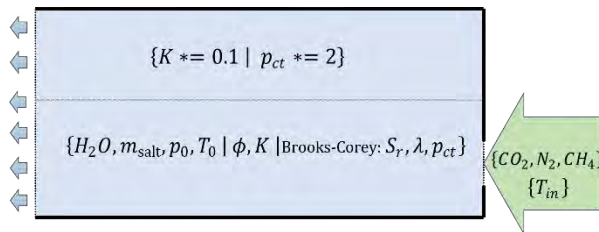


Figure 7: Computational domain for flow sensitivity study.

We consider an annular sector extending from an inner radius of 0.1m, aiming for a direct representation of the well-reservoir interface. The reservoir has a height of 40m, and the well is completed for inflow between 5m and 15m from the bottom as indicated along the right edge in Figure 7. Flow is specified in terms of uniformly distributed mass rates. The radial extent used for the computations shown here is 90m. Top and bottom boundaries are closed, while the outer radius is open for flow. Initially the reservoir is filled with water where small amounts of salt and CO₂ are dissolved. The fluid is in hydrostatic equilibrium (datum 250MPa at reservoir bottom) and at uniform temperature T₀=353K. The reservoir is partitioned into two layers, confer the horizontal dotted line in Figure 7, where the upper region (18m) is assumed to have a more fine-grained structure, more adverse to CO₂ intrusion.

Table 3 Reservoir and flow characteristics for the lower, coarse grained part of the reservoir. The upper, fine grained material has one-tenth the K and twice the p_{ct} .

Property	Value
Permeability (K)	1 Darcy
Porosity (Φ)	0.3
Brooks-Corey parameter (λ)	2.0
Capillary threshold pressure (p_{ct})	5000 Pa
Residual brine saturation	0.2
Residual CO ₂ saturation	0.0

3.1 Base case

Our baseline injection stream corresponds to pure CO₂, and the temperature T_{in}=353K equals the initial reservoir temperature T₀. The injection rate is set to approximately 170000 Sm³/day. Selected snapshots of the developing flow are depicted in Figure 8.

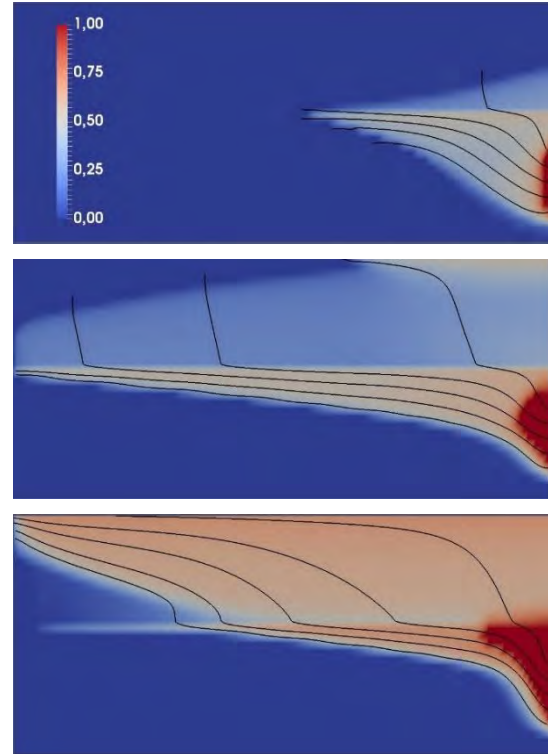


Figure 8 Saturation and streamlines for the CO₂-rich phase. Base case behavior at day 10, 100 and 1000, respectively.

Initially the bulk of the injection stream is confined below the material interface, fingering through the brine, and establishing a channel connecting to the outflow boundary. Gradually the buoyancy overcomes the vertical obstacle, and a continuous phase is formed also in the upper, fine-grained material, allowing the CO₂-rich phase an alternative escape route. This self-reinforcing process eventually erodes the original channel through the coarse-grained sand, and in the end, the whole injection stream is directed upwards. From Figure 9 we conclude that in terms of CO₂ retained, a steady state is reached after slightly more than one year of injection for our baseline scenario.

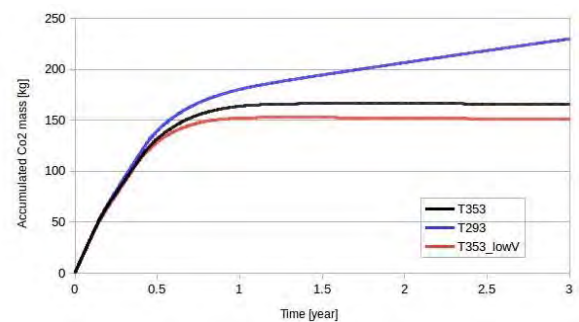


Figure 9 CO₂ mass retained in the reservoir. Base case (black), low viscosity (red), and cold (blue).

The scenario outlined in Figure 8 is observed for all parameter combinations considered in this study. However, we have essentially confined ourselves to explore the impact of varying viscosity and temperature for the injection mixture. Extending the scope to also include e.g., the parameters of Table 3, might reveal different behavior.

From Figure 8, we observe that the brine phase disappears in the vicinity of the well. With a residual saturation of 0.2, this indicates that the brine originally present has evaporated into the CO₂-rich phase. The associated salt precipitation causing permeability alterations is a well-known reason for injectivity problems. We will not pursue this aspect further here but note that our simulations easily can be adapted to include this effect.

3.2 Low viscosity injection mixture

We mimic an impure CO₂ injection stream by reducing the viscosity to 80% compared to base case, confer the discussion in section 2.2 above. Injection rate and temperature are kept as for the base case.

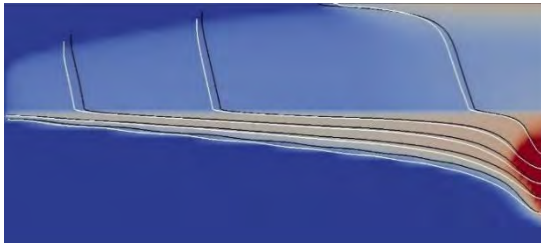


Figure 10 Saturation and streamlines for CO₂-phase. Low viscosity injection mixture at 100 days. White streamlines show base case behavior.

Compared to the base case, Figure 10 indicates a slightly leaner channel that penetrates at a higher speed through the brine to reach the outflow boundary. Also, the migration of the CO₂-rich phase into the upper, fine-grained region, as well as the erosion of the primary channel, are faster. That the less viscous mixture also displaces less brine and thus leads to less CO₂ retained, confer Figure 9, is also to be expected.

3.3 Cold injection mixture

We here lower the injection temperature. Setting $T_{in}=293K$ yields a contrast of 60K compared to the initial reservoir temperature T_0 . Our calculations from section 2 indicates typically 50% increased density and viscosity for the CO₂-rich phase.

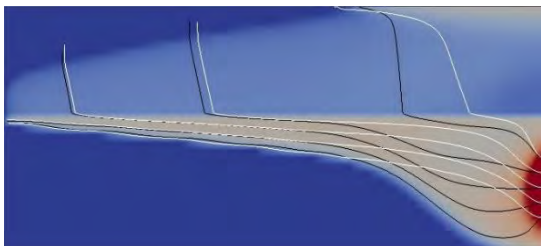


Figure 11 Saturation and streamlines for CO₂-phase. Cold injection mixture at 100 days. White streamlines are corresponding base case behavior.

We see from Figure 11 that after 100 days of injection the difference versus the base case is most pronounced in the vicinity of the well. Here the effect of the cold injection stream is more immediate, and the reservoir volume to be influenced is relatively small.

From Figure 9, we also note that for the cold injection stream, the amount of CO₂ retained increases steadily for the hole injection period. This effect must be attributed to a continuous cooling of the reservoir, leading to a gradually denser and more viscous CO₂-rich phase providing more efficient displacement and storage capabilities.

3.4 Injection well

The pressures (CO₂-rich phase) depicted in Figure 12, are the difference between the flowing pressure at the well-reservoir interface and the initial hydrostatic pressure. They are all sampled at the midpoint of the open well segment, located 10m from the reservoir bottom, corresponding to the origin of the central streamline. The absolute size of the pressure buildup obviously depends on the injection rate and for low to moderate rates it can be supposed to scale linearly with the rate. Thus, the sensitivities indicated by Figure 12 and Figure 13 can be extrapolated with some degree of confidence.

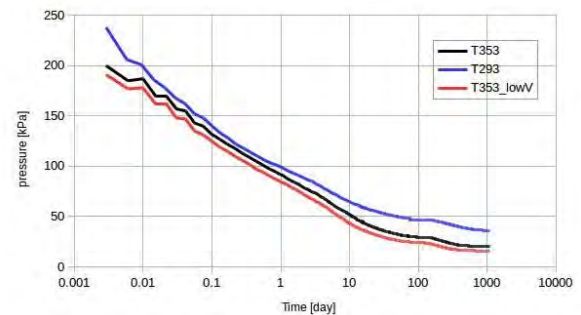


Figure 12 Well pressure buildup. Logarithmic time axis to show the early transient period. Base case (black), low viscosity (red), and cold (blue).

Figure 13 depicts the pressure along the radial (horizontal) direction extending from the well interface into the reservoir (time=100 in Figure 12 corresponds to radius=0.1 in Figure 13). The locations of transition to single phase brine regions are evident.

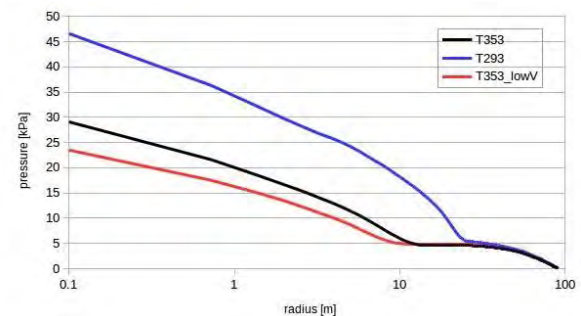


Figure 13 Radial pressure along well centerline at 100 days. Logarithmic radial axis to detail the near well behavior. Base case (black), low viscosity (red), and cold (blue).

Our approach aims at a direct resolution of the well reservoir interface. Depending on the application, various measures can be applied to improve the computational accuracy. The wiggles observed in Figure 12 for the first hours indicates a potential for more careful control of the time stepping. The discrete spatial resolution, currently ~0.5m in the well vicinity, can likewise be modified. If the early transients are important, gradually ramping up the injection rate is operationally realistic and promotes numerical stability.

4. Conclusion

Focusing on the well-reservoir interface and the near-well region, we have performed sensitivity studies on the effects of impurities and temperature variations in CO₂ injection streams.

A more systematic exploration of the parameter space remains, regarding both PVT behavior and rock properties. However, we believe that our preliminary results shed some light on the variability of accumulation and well response due to changing properties of the injection stream.

Combining geometrical resolution and detailed compositional fluid modelling has potential use as a detailed planning or control tool for well operations. Another application will be calibration and verification of simplified pseudo models for integration in large scale field simulations.

Depending on application and required level of completeness, our approach might benefit from the inclusion of a detailed wellbore model that can interact directly with the reservoir model via mutual boundary conditions at the well interface.

The current reservoir model is originally a Brine-CO₂ compositional model where we have manipulated high level properties (density/viscosity) to mimic impact of impurities. For exploration of more subtle effects like mutual dissolution or precipitation, more fine-grained control can be added.

Acknowledgements

This publication has been produced with support from research program CLIMIT and the NCCS Research Centre, performed under the Norwegian research program Centres for Environment-friendly Energy Research (FME) and the Research Council of Norway (257579/E20 and 280394).

References

- [1] Aavatsmark, I., Kometa, B.K., Gasda, S.E., Sandve, T.H. & Nilsen, H.M. (2016). A generalized cubic equation of state with application to pure CO₂ injection in aquifers. *Comput Geosci* 20, 623–635
- [2] Adams, J. and Bachu, S., 2002, Eq. of state for basin geofluids: algorithm review and intercomparison for brines, Alberta Geological Survey, Edmonton, Canada.
- [3] Batzle, M. and Wang, Z., 1992, Seismic properties of pore fluids, *Geophysics*, Vol. 57, No. 11, 1396 – 1408.
- [4] Bui, Q.M. & Elman, H.C. (2020). “Semi-smooth Newton methods for nonlinear complementarity formulation of compositional two-phase flow in porous media.” *Journal of Comp. Physics*, 407, 109163
- [5] Duan, Z., Sun, R., 2003. An improved model calculating CO₂ solubility in pure water and aqueous NaCl solutions from 257 to 533 K and from 0 to 2000 bar. *Chemical Geology* 193, 257–271.
- [6] Fenghour, A., Wakeham, W., and Vesovic, V.. (1998). The Viscosity of Carbon Dioxide. *Journal of Physical and Chemical Reference*. 27:31-44
- [7] Gao, G., Daridon, J.-L., Saint-Guirons, H. Xans, P. & Montel, F. (1992). “A simple correlation to evaluate binary interaction parameters of the Peng-Robinson equation of state: binary light hydrocarbon systems.” *Fluid Phase Equilibria* Volume 74, 85-93.
- [8] Garcia, J. (2001) “Density of Aqueous Solutions of CO₂”. Tech Report, LBNL Report 49023; Lawrence Berkeley National Laboratory: Berkeley, CA, USA.
- [9] Lauser, A., Hager, C., Helmig, R. & Wohlmuth B. (2011) “A new approach for phase transitions in miscible multi-phase flow in porous media” *Adv. Water Resour.*, 38, 957-966
- [10] Lansangan, R.M., Taylor, M., Smith, J.L. and Kovarik, F.S. (1993). “An improved viscosity correlation for CO₂ / reservoir oil systems.” *SPE Advanced Technology Series*, 1(2), 134–141.
- [11] Lohrenz, J., Bray, B.G. and Clark, C.R. (1964) “Calculating viscosities of reservoir fluids from their composition.” *Journal of Petroleum Technology*, 16(10), 1171–1176.
- [12] Qian, J.W., Privat, R. & Jaubert, J.N. (2013). Predicting the Phase Equilibria, Critical Phenomena, and Mixing Enthalpies of Binary Aqueous Systems Containing Alkanes, Cycloalkanes, Aromatics, Alkenes, and Gases (N₂, CO₂, H₂S, H₂) with the PPR78 Equation of State. *Industrial & Engineering Chemistry Research* 52 (46), 16457-16490
- [13] Rasmussen, A.F., Sandve, T.H, Bao, K., Lauser, A., Hove, J., Skaflestad, B., Klöfkorn, R., Blatt, M., Rustad, A.B., Sævareid, O., Lie, K.-A. & Thune, A. (2021). “The Open Porous Media Flow Reservoir Simulator.” *Computers & Mathematics with Applications*, 81, 159-185 - See also: <https://opm-project.org> and <https://github.com/OPM>.
- [14] Span, R., and Wagner, W. (1996). A New Equation of State for Carbon Dioxide Covering the Fluid Region from the Triple-Point Temperature to 1100 K at Pressures up to 800 MPa. *Journal of Physical and Chemical Reference Data*. 25:1509-1596.
- [15] Spycher, N., Pruess, K. 2005. CO₂-H₂O mixtures in the geological sequestration of CO₂. II. Partitioning in chloride brines at 12-100 °C and up to 600 bar. *Geochimica Cosmochimica Acta*, 69 (13), 3309-3320.
- [16] Spycher, N., Pruess, K., and Ennis-King, J., 2003. CO₂-H₂O mixtures in the geological sequestration of CO₂. I. Assessment and calculation of mutual solubilities from 12 to 100°C and up to 600 bar. *Geochimica Cosmochimica Acta*, 67, 3015–3031.
- [17] Vesovic, V., Wakeham, W.A., Olchowky, G.A., Sengers, J.V., Watson, J.T.R., and Millat, J. (1990). The Transport Properties of Carbon Dioxide. *Journal of Physical and Chemical Reference Data*. 19:763-80

ENERGY-INTENSIVE INDUSTRY AS A PRACTICAL AND COST-EFFECTIVE VECTOR FOR BLUE HYDROGEN EXPORTS – A NORWEGIAN CASE STUDY

Schalk Cloete*, Jan Hendrik Cloete

SINTEF Industry, Trondheim, Norway

* Corresponding author e-mail: schalk.cloete@sintef.no

Abstract

As political will gathers behind the ideal of rapid decarbonization, the future looks increasingly dim for oil & gas exporters. CCS offers a pathway for continued operation in the longer-term as the world decarbonizes, but this is not a straightforward solution. Many oil & gas importers are opposed to CCS and are instead looking to replace oil & gas imports with greener alternatives. The alternative solution of converting cheap locally produced hydrocarbons to hydrogen and electricity with CCS substantially increases the cost and complexity of energy exports. This study explores an alternative solution: local utilization of clean hydrogen from natural gas to produce energy intensive industrial products like steel. Such products are much easier to export than hydrogen or electricity. The system-scale modelling assessment presented in this study shows that the energy costs of clean steel using blue hydrogen in Norway is 174 €/ton cheaper than when it is produced using green hydrogen in Germany. This difference amounts to about a third of total steel production costs, giving oil & gas exporters like Norway a large competitive advantage.

Keywords: CO₂ capture and storage, Hydrogen, Energy system modeling, Oil & gas, Energy-intensive industry

1. Introduction

The future of oil and gas exporting regions appears highly uncertain. Momentum is building behind the vision of carbon neutrality by mid-century, with Europe leading the way in terms of ambition. The ongoing COVID-19 pandemic appears only to have strengthened this resolve, despite the economic impact.

As a result, the International Energy Agency's World Energy Outlook report [1] paints a bleak future for oil & gas producers. Relative to pre-pandemic estimates, the net-present value of all oil and gas production up to 2040 is cut in half in the Sustainable Development Scenario, which still falls well short of carbon-neutrality by 2050.

Clearly, the oil & gas industry requires a fundamental re-evaluation of its longer-term role in a decarbonizing world. CO₂ capture and storage (CCS) must play a central role in any such strategy (and in the broader global decarbonization effort [2]). There is a great deal of technology transfer possibilities between oil & gas extraction and distribution and CO₂ transport and storage. In addition, CO₂ enhanced oil (or gas) recovery can increase the profitability of such synergies. In a European context, these issues are of high relevance to Norway, which possesses much of the continent's oil & gas reserves and CO₂ storage potential.

However, a key challenge with such a strategy is that the clean energy products resulting from local CCS, mainly hydrogen and electricity, are much harder to export to the international market than oil & gas [3]. Hydrogen has a volumetric energy density less than a third that of natural gas and liquifies at considerably lower temperatures, making it inconvenient for exports. Electricity exports are even more costly and, given the challenge of longer-

term electricity storage, no country will be willing to build up a large electricity import dependence.

A much more practically and economically attractive alternative is to convert locally produced clean hydrogen and electricity into energy-intensive industrial products (e.g., metals, cement, chemicals), which are much simpler to export. In addition, it can be argued that such a value-added approach to using local energy resources will produce more local value in terms of jobs, skills, and local technology development. However, despite the apparent benefits of such an approach, prominent Norwegian roadmaps, such as the Norwegian Hydrogen Strategy [4] and the Energy Transition Norway 2020 forecast from DNV GL [5], place a much larger emphasis on blue hydrogen and electricity (from hydro- and wind power) exports to Europe, than on local usage to produce energy-intensive industrial products for export.

This study therefore presents a system-level assessment of the economic benefits of using energy-intensive industrial products as a Norwegian energy export vector. Specifically, clean steel production is considered as an example and the energy costs for production in Norway and Germany are compared.

2. Methodology

The study is conducted based on a previously published model of an integrated electricity and hydrogen system in Germany [6]. The model optimizes investment and hourly dispatch of a range of electricity and hydrogen generation, transmission, and storage infrastructure to minimize total system costs (including a price on CO₂). The model is solved using the General Algebraic Modelling System (GAMS) software.

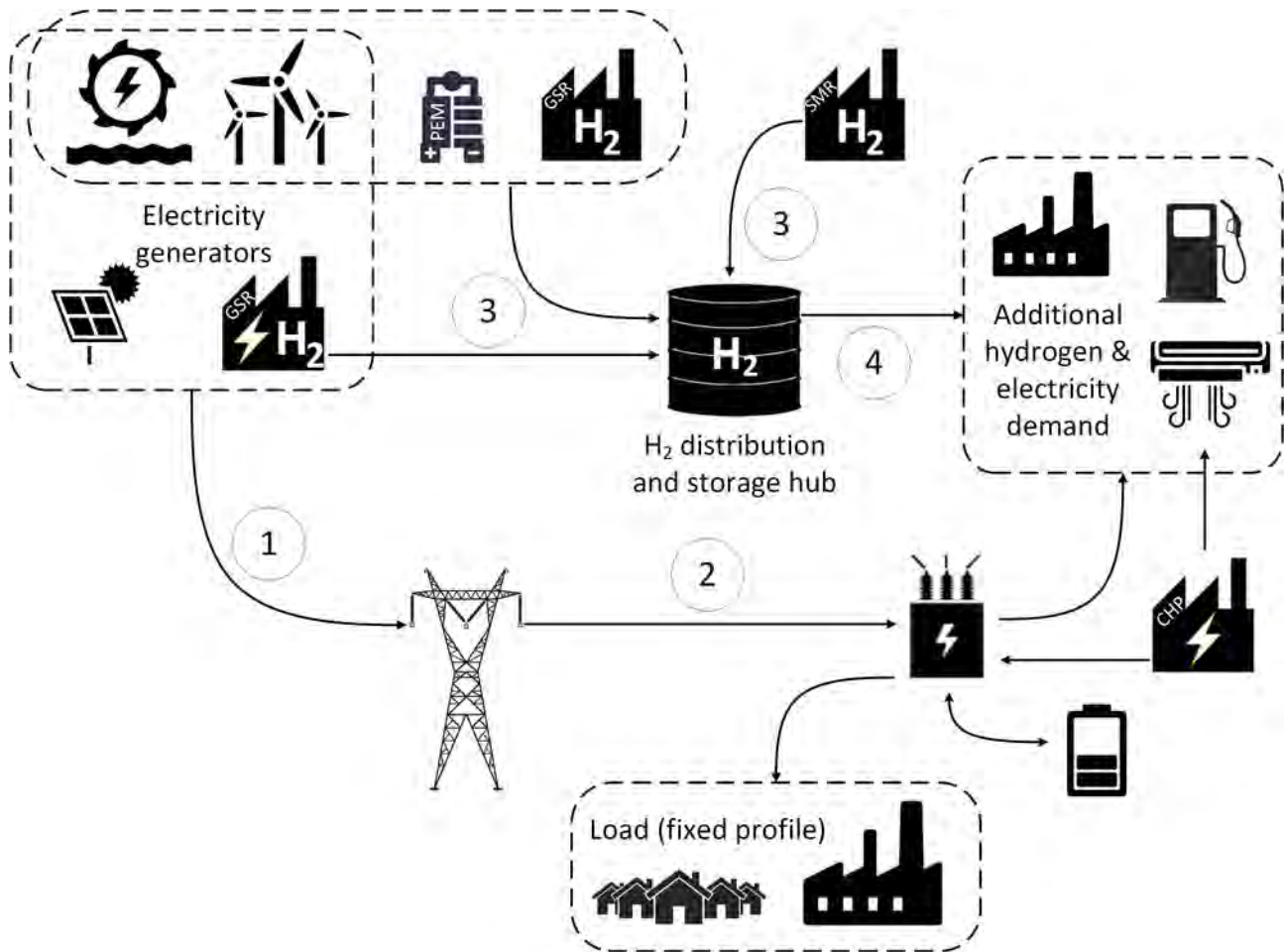


Figure 1: A schematic of the modelled energy system for Norway. The different types of transmission are indicated by numbers: 1) added transmission for wind, solar, and hydro due to their spatial mismatch with demand centers, 2) conventional transmission proportional to peak system electricity demand, 3) hydrogen transmission pipelines from various producers to central storage and distribution hubs, and 4) hydrogen distribution to serve a flat hydrogen demand profile.

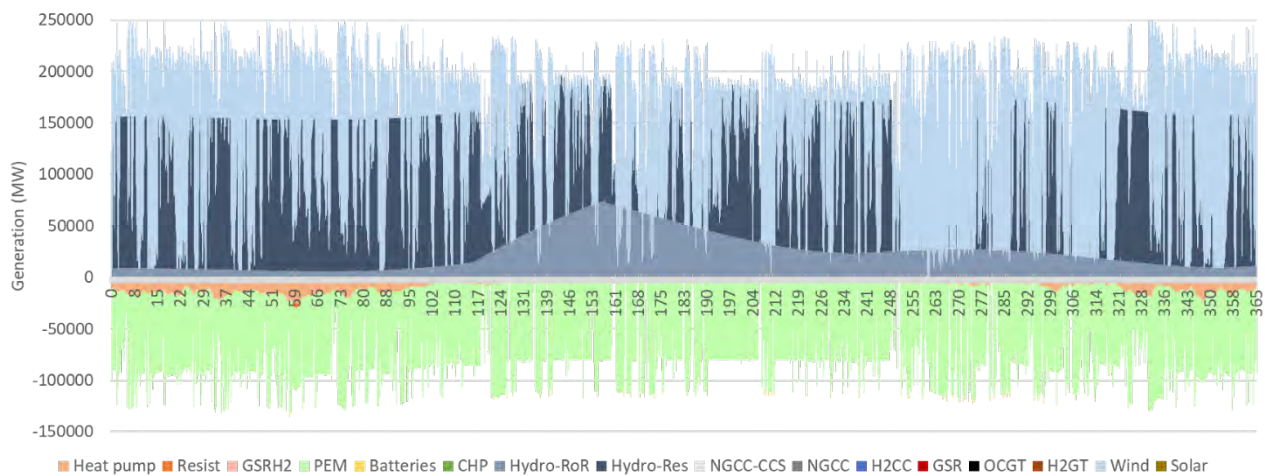


Figure 2: An example of the hourly electricity generation profile in Norway for a green hydrogen scenario (CCS technologies not allowed). Consumption from electrolysis and heat pumps is also shown. The x-axis indicates the days in the year.

2.1 System description

In the present work, this model was extended for optimizing the long-term (2040) Norwegian energy system. Aside from adopting appropriate hourly load and renewable energy availability profiles for Norway from the Open Power System Database [7] and the Renewables Ninja database [8], the following important modifications were made relative to the aforementioned study [6] based on Germany:

1. Hydropower was included, accounting both for run-of-the-river and reservoir hydro.
2. Offshore wind was preferred due to the large public resistance to onshore wind in Norway.
3. A heat balance was incorporated to separate energy demands for heating applications from electricity demand.

The simulated Norwegian energy system is summarized in Figure 1. A constraint was imposed that all electricity must be generated via renewable sources while natural gas can be used for generating hydrogen with CCS (blue hydrogen). An additional transmission cost of 200-300 €/kW was imposed for hydro, wind, and solar power due to their location dependence that does not align perfectly with demand. To minimize this cost, it was assumed that electrolyzers (green hydrogen) and gas switching reforming (GSR) [9, 10] technology (blue hydrogen) that also consumes some electricity are co-located with the location specific renewable electricity generators. Thus, the large electricity demand from these consumers does not need to be transmitted over long distances, instead requiring cheaper hydrogen transmission to demand centers, saving significant system costs.

The electricity not consumed for hydrogen production on site is transmitted to two different demand centers: a load profile that varies by hour (representing existing residential, commercial, and industrial demand) and an additional constant load profile representing future additional demand for clean energy to decarbonize areas that are currently not electrified (like transportation and additional energy-intensive industry for exports). This second demand center is subject to large uncertainty, both in its overall magnitude and in the split between electricity and hydrogen. It will therefore be subject to a sensitivity analysis in this study. Battery storage can also be deployed to help balance supply and demand.

In addition, the model optimizes a separate energy balance for heating. Currently, most of Norway's heating is done using simple resistance heating, which is a very inefficient use of its valuable clean hydropower resource. It also creates large seasonal variations with much more electricity demand in winter, leading to an oversized electricity transmission and distribution network that is poorly utilized in summer months. Hence, the model also includes the possibility of heat pumps and biomass combined heat and power (CHP) plants with CCS as options for satisfying the heating demand during winter months. The coefficient of performance of the heat pumps are adjusted according to the population-weighted ambient temperature profiles of Norway's three largest

cities to reflect the decline in heat pump performance on colder days. The CHP plant is equipped with a variant of the swing adsorption reactor cluster (SARC) CO₂ capture technology [11, 12] that is capable of running on electricity in winter months and heat in summer months to ensure that these plants can supply maximal heat output when it is most needed.

Figure 2 shows a typical output from the model for a scenario where no CCS technologies are allowed. The seasonal availability of run-of-the-river hydropower (Hydro-RoR) is clearly visible in the electricity supply profiles. During spring when the snow melts, a large amount of electricity is generated, peaking in early summer before settling at a lower constant generation until freezing takes place at the start of winter. During winter months, run-of-the-river generation is minimal. Of much greater value to the energy system is reservoir hydropower (Hydro-Res) that can be ramped up and down depending on system needs due to the large reservoirs that store potential energy for on-demand deployment. In this example, it can clearly be seen how reservoir hydro is used to balance the fluctuating output of wind power.

Table 1: Selected technology cost and performance assumptions. The type of energy by which the capital costs are scaled is given in brackets.

Technology	Capital cost (€/kW)	Lifetime (years) Fixed O&M (%/year)	Performance
Run-of-the-river hydro	1370 (electric)	40 2%	Capacity factor: 33% Maximum generation: 55 TWh/year
Reservoir hydro	1560 (electric)	40 2%	Maximum reservoir storage level: 50 TWh Annual inflow: 108 TWh/year
Offshore wind	1655 (electric)	25 2.8%	Capacity factor: 55%
Dedicated GSR H ₂ plant	862 (H ₂)	40 3%	Efficiency: 86.8% H ₂ (LHV), -5.4% electric
CHP CCS	1500 (winter heat)	40 3%	Efficiency winter/summer: 75%/30% heat and 13%/18% electric
Heat pump	411 (electric)	20 2%	Coefficient of performance: ~3 during winter

The large electricity consumption of electrolyzers (PEM) is also clearly visible in Figure 2. Electrolyzers also

contribute to balancing fluctuating wind power, although to a lower extent than reservoir hydro. The model prefers to run electrolyzers at a higher capacity factor to reduce their levelized capital costs and to reduce the costs related to transmitting and storing large fluxes of intermittently produced hydrogen. Finally, significant electricity consumption from heat pumps can also be identified during winter months. This consumption fluctuates significantly depending on the ambient temperature.

Cost and performance assumptions are based on the year 2040 and the technologies not included in the previous study on the German system [6] are detailed in Table 1. It should also be mentioned that natural gas prices of 4 and 6 €/GJ are assumed for Norway and Germany, respectively, to reflect the added costs involved in transporting natural gas to Germany. A CO₂ price of 100 €/ton is used in this study.

2.2 Scenario and case definitions

Two scenarios are investigated:

1. Green H₂: In this scenario no CCS is allowed and all hydrogen must be produced via electrolysis.
2. Blue H₂: In this case, CCS is allowed to compete with electrolysis.

Both scenarios are completed for Norway, using the setup described in section 2.1, and for Germany, using a similar setup as in our previous study [6]. Additional constraints are imposed to maximize renewable electricity generation, enforcing Norwegian and German power production to be at least 100% and 70% renewable, respectively.

It is assumed that in a future energy system, both countries will experience a substantial increase in clean energy demand (in the form of renewable electricity and hydrogen) to power the transport and industrial sectors. Therefore, in each scenario, eight different cases are simulated to investigate uncertainties associated with this additional demand:

- 4 different levels of increased total demand with a 50/50 split between electricity and hydrogen: 100, 200, 300, and 400 TWh/year.
- 4 different H₂/electricity splits at 300 TWh/year of additional demand with 20%, 40%, 60%, and 80% H₂ share.

3. Results and discussion

Results will be presented and discussed in three sections: Norway, Germany, and the implications for steelmaking using the HYBRIT process.

3.1 Norway

The cost-optimal generation mixes for the 8 different cases in the two different scenarios are illustrated in Figure 3. For the Green H₂ scenario, an increase in clean energy demand strongly increases the demand for electricity, both due to direct demand for clean electricity and due to electricity demand from electrolyzers. As more electricity is demanded, the share of wind power

strongly increases, while hydropower is constrained to a maximum according to Table 1. In the case with the lowest additional energy demand, the model chooses to deploy offshore wind instead of run-of-the-river hydro, which only runs in the summer when demand is lowest.

The increase in clean energy demand in the Blue H₂ scenario is much milder because all hydrogen demand is met through natural gas reforming using the GSR technology. A small amount of additional generation from biomass CHP plants is also visible. These plants are the reasons for the negative CO₂ emissions intensity in these cases.

When considering the cases with different shares of hydrogen in the clean energy mix, total electricity demand increases with hydrogen share in the Green scenario (due to greater electrolyzer losses) and decreases in the Blue scenario (due to more clean energy being supplied by blue hydrogen instead of electricity).

Figure 4 shows the minimum system costs achievable in each case. Increases in clean energy demand naturally increase the total system cost, but also the levelized energy cost. This increase is mainly due to the limitation on reservoir hydro, which is highly economical but limited in available capacity. As offshore wind must produce an ever-increasing share of electricity, the average energy cost goes up. This trend is less severe in the Blue H₂ scenario because of the smaller reliance on offshore wind.

When increasing the share of hydrogen, the Green scenario becomes gradually more expensive, whereas the Blue scenario becomes cheaper. This is because green hydrogen must be more expensive than the electricity used to produce it, whereas blue hydrogen from natural gas costing 4 €/GJ is attractively cheap. Overall, the Blue H₂ scenario is considerably cheaper than the Green H₂ scenario, especially when greater shares of hydrogen are required.

Finally, Figure 5 breaks down the cost components not shown in Figure 4. In the Green scenario, greater electricity demand increases the added VRE (variable renewable energy) transmission and regular transmission costs. More hydrogen demand naturally increases electrolyzer costs, while hydrogen storage costs also increase substantially as electrolyzers need to play an increasingly important balancing role, producing more intermittent hydrogen outputs.

Hydrogen storage costs are absent in the Blue scenario because hydrogen is produced at steady state. Grid related costs are also lower due to the smaller deployment of offshore wind power.

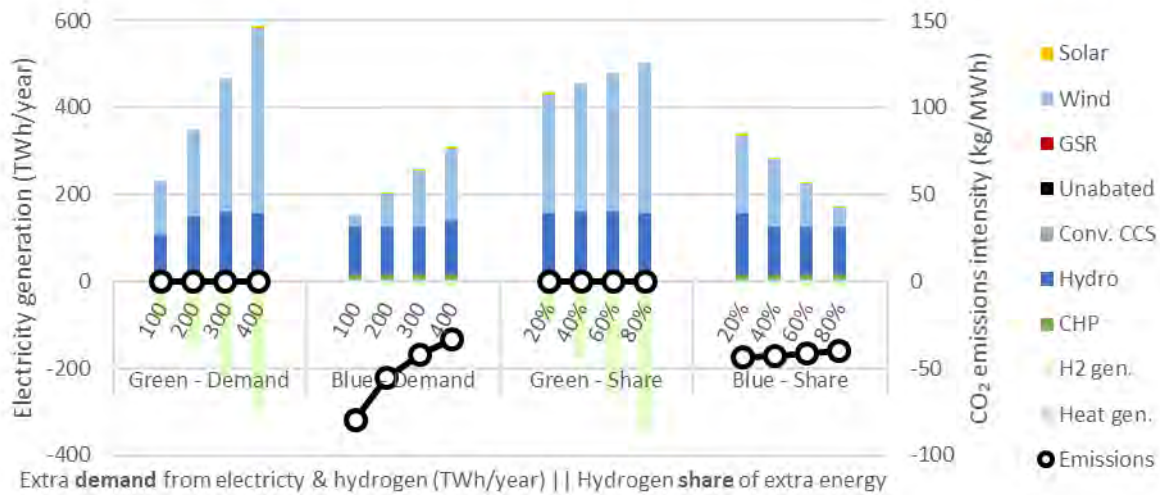


Figure 3: Breakdown of electricity generation and emissions intensity for all cases in Norway.

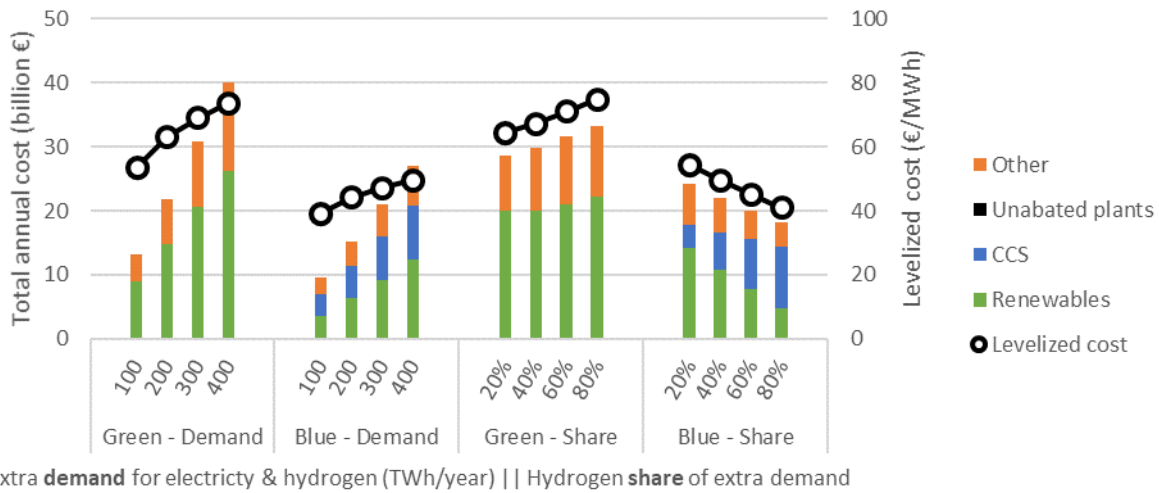


Figure 4: Breakdown of costs for all cases in Norway. Levelized costs lump together electricity, hydrogen, and heat.

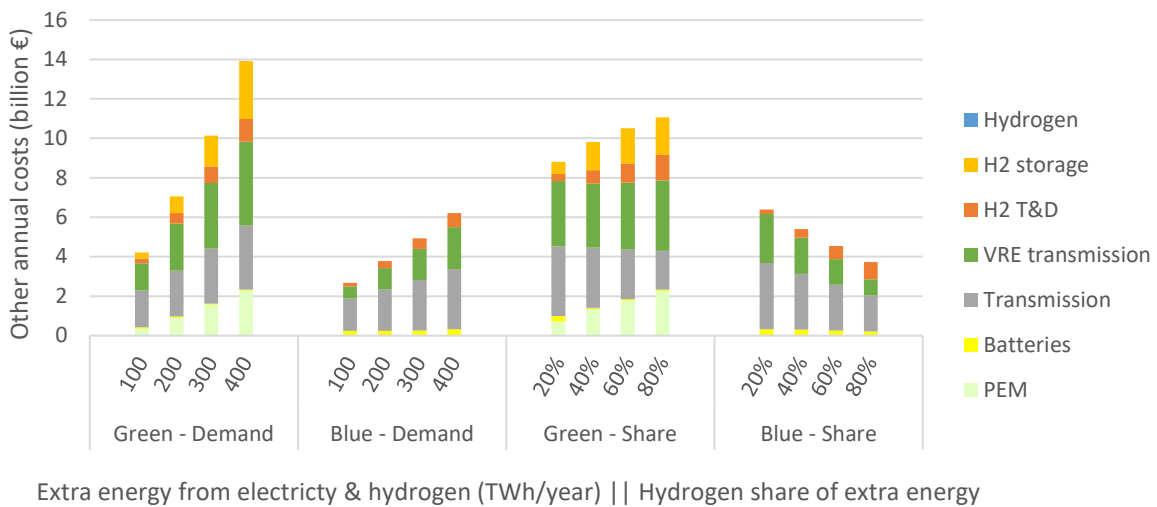


Figure 5: Breakdown of the "Other" costs in Figure 4.

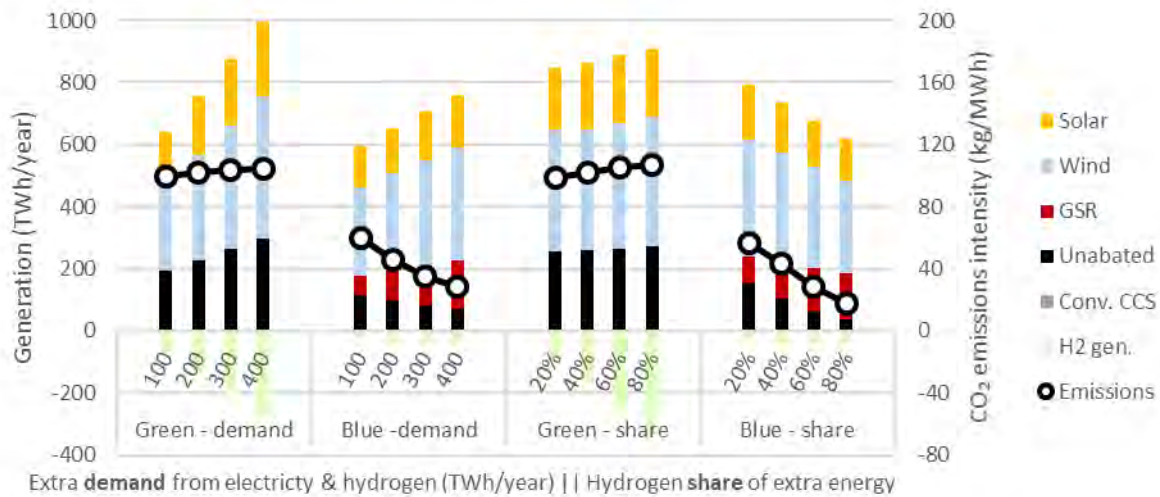


Figure 6: Breakdown of electricity generation and emissions intensity for all cases in Germany.

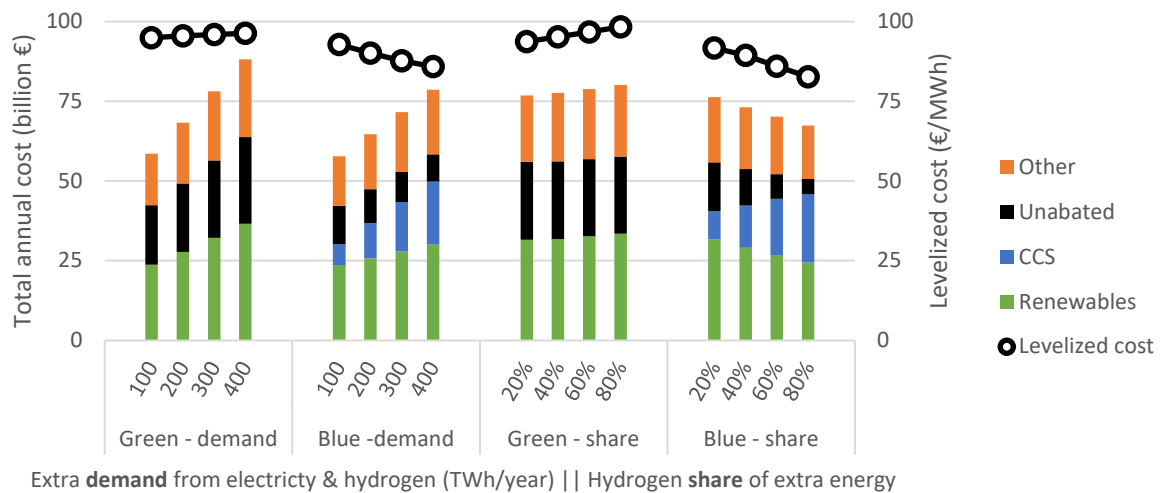


Figure 7: Breakdown of costs for all cases in Germany. Levelized costs lump together electricity, hydrogen, and heat.

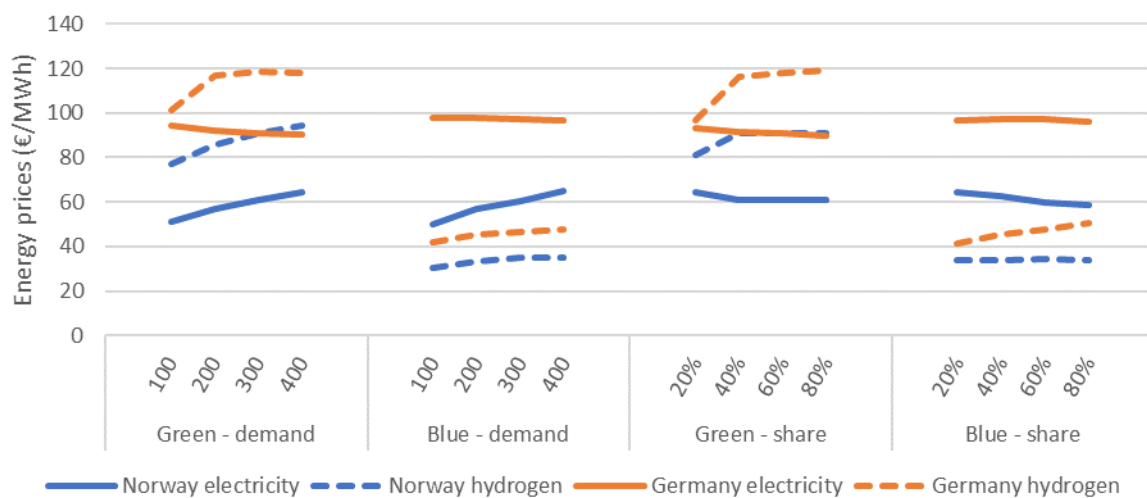


Figure 8: Volume-weighted electricity and hydrogen prices in Norway and Germany for all cases.

3.2 Germany

The electricity generation trends in Figure 6 are broadly similar to Figure 3, although the relative changes are smaller because of the much larger size of the German energy system. In addition, Germany lacks Norway's hydropower reserves and relies much more on solar power than Norway. In the Green H₂ scenario, the model relies on the maximum allowable share of unabated natural gas power generation (despite the 100 €/ton CO₂ price) to meet demand during extended periods of limited wind and sun. In the Blue H₂ scenario, the flexible power and hydrogen production from GSR [13] can increasingly be used to balance wind and solar more cost effectively as hydrogen demand increases. In general, the Green H₂ scenarios show substantially greater emissions due to the relatively high share of unabated power production required to balance variable renewables.

Cost trends in Figure 7 are also similar to Figure 4, only less pronounced because of the smaller relative changes in the overall energy system. However, levelized costs are considerably higher than in Figure 4 due to Norway's superior energy resources (hydropower, better wind resources, and cheaper natural gas). Trends in "Other" costs are also similar to that shown in Figure 5 and will therefore not be repeated here. A more detailed analysis of the German system can be found in our previous study [6].

3.3 Industrial implications (steelmaking example)

In this section, the implications for energy-intensive industry will be analyzed, using the HYBRIT steelmaking process as an example. This process uses direct-reduced iron and electric arc furnaces to produce steel, requiring 1.84 MWh of hydrogen and 0.86 MWh of electricity per ton of steel [14]. A smaller quantity of biomass is also required as a carbon source.

Using this information, the energy costs of clean steelmaking can be estimated with the modelled energy prices displayed in Figure 8. When considering electricity prices, Norway holds a large advantage over Germany due to its hydropower resources and better quality wind (which is well balanced by reservoir hydro). In the Green H₂ scenario, hydrogen prices reflect the electricity prices used to produce green hydrogen.

In the Blue H₂ scenario, electricity prices are similar to the Green scenario, but hydrogen prices are much lower. Also, the gap between Norwegian and German blue hydrogen prices is relatively small, influenced mainly by the higher natural gas cost in Germany. The large cost advantage of blue hydrogen over green hydrogen results mainly from the low natural gas price relative to the wind and solar power that must be used to produce green hydrogen. Furthermore, green hydrogen production is more intermittent, creating additional costs related to transmitting and storing large hydrogen fluxes.

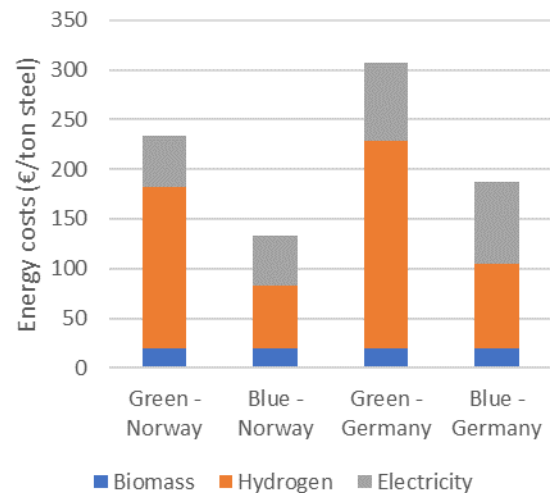


Figure 9: Energy costs for producing a ton of steel in the two different scenarios and countries.

Using the prices in Figure 8, the energy costs per ton of steel can be calculated as shown in Figure 9. Clearly, the Blue H₂ scenario produces substantially lower costs in both countries. Norway also has a sizable cost advantage over Germany in both scenarios.

Given that CCS enjoys much greater policy support in Norway than in Germany, a likely future scenario is that Blue Norway will compete with Green Germany. In this case, the energy cost difference between the two countries is 174 €/ton steel – about a third of total steel production costs.

4. Conclusions

This system-scale modelling study has illustrated the potential for oil & gas producers like Norway to export clean energy in the form of energy-intensive industrial products like steel. If CCS fails to gain political backing in energy importing regions like mainland Europe, blue hydrogen production for local consumption in heavy industry appears to be a viable way forward. If Europe does embrace CCS, the industrial cost advantage is considerably smaller, but in that case, conventional natural gas exports can continue, potentially with CO₂ being piped back for permanent storage, creating an additional revenue stream.

The robustness of these conclusions was checked by looking at a pessimistic and optimistic Blue H₂ scenario in Norway. In the pessimistic scenario, the novel and efficient GSR and biomass CHP technologies are not available, relying on conventional steam methane reforming with CCS and heat pumps for hydrogen and heat, respectively. In the optimistic scenario, half of hydrogen production is handled by membrane-assisted autothermal reforming [15], a novel technology which becomes highly attractive when hydrogen can be produced at the low pressures used for the HYBRIT process. In addition, a 20 €/ton enhanced oil recovery credit is assumed in the optimistic case.

Relative to the baseline scenario, the pessimistic case increased steel energy costs by 7.8% and the optimistic case decreased costs by 11.3%. These relatively small

changes do not impact the main conclusion that energy-intensive industry fueled by local blue hydrogen appears to be a promising path forward for oil & gas producers in an uncertain decarbonizing world.

Acknowledgements

This study was funded internally by SINTEF Industry.

References

1. IEA, *World Energy Outlook*. 2020, International Energy Agency.
2. IEA, *CCUS in Clean Energy Transitions*, in *Energy Technology Perspectives*. 2020.
3. Saadi, F.H., N.S. Lewis, and E.W. McFarland, *Relative costs of transporting electrical and chemical energy*. *Energy & Environmental Science*, 2018. **11**(3): p. 469-475.
4. Olje- og energidepartementet and Klima- og miljødepartementet, *Regjeringens hydrogenstrategi på vei mot lavutslippssamfunnet*. 2020.
5. DNV GL, *Energy Transition Norway 2020*. 2020.
6. Cloete, S., O. Ruhnau, and L. Hirth, *On capital utilization in the hydrogen economy: The quest to minimize idle capacity in renewables-rich energy systems*. *International Journal of Hydrogen Energy*, 2020.
7. Neon. *Open Power System Database*. 2020; Available from: <https://open-power-system-data.org/>.
8. Pfenninger, S. and I. Staffell, *Long-term patterns of European PV output using 30 years of validated hourly reanalysis and satellite data*. *Energy*, 2016. **114**: p. 1251-1265.
9. Wassie, S.A., et al., *Hydrogen production with integrated CO₂ capture in a novel gas switching reforming reactor: Proof-of-concept*. *International Journal of Hydrogen Energy*, 2017. **42**(21): p. 14367-14379.
10. Nazir, S.M., et al., *Pathways to low-cost clean hydrogen production with gas switching reforming*. *International Journal of Hydrogen Energy*, 2020.
11. Dhoke, C., et al., *Demonstration of the Novel Swing Adsorption Reactor Cluster Concept in a Multistage Fluidized Bed with Heat-Transfer Surfaces for Postcombustion CO₂ Capture*. *Industrial & Engineering Chemistry Research*, 2020. **59**(51): p. 22281-22291.
12. Cloete, S., et al., *Economic assessment of the swing adsorption reactor cluster for CO₂ capture from cement production*. *Journal of Cleaner Production*, 2020. **275**: p. 123024.
13. Szima, S., et al., *Gas switching reforming for flexible power and hydrogen production to balance variable renewables*. *Renewable and Sustainable Energy Reviews*, 2019. **110**: p. 207-219.
14. SSAB, LKAB, and Vattenfall, *Summary of findings from HYBRIT Pre-Feasibility Study 2016–2017*. 2018.
15. Cloete, S., M.N. Khan, and S. Amini, *Economic assessment of membrane-assisted autothermal reforming for cost effective hydrogen production with CO₂ capture*. *International Journal of Hydrogen Energy*, 2019. **44**(7): p. 3492-3510.

ROUTING DEPLOYMENT OF CC(U)S IN THE BALTIC SEA REGION

Monika Ivandic^{1*}, Alla Shogenova², Farid Karimi³, Adam Wójcicki⁴, Kazbulat Shogenov²

¹Uppsala University, Uppsala, Sweden

²Tallinn University of Technology, Tallinn, Estonia

³Novia University of Applied Sciences, Finland

⁴Polish Geological Institute – National Research Institute

* Corresponding author e-mail: monika.ivandic@geo.uu.se

Abstract

Much potential exists in the Baltic Sea region (BSR) regarding CC(U)S and at least on the research side, there has been a steady stream of activities over the years. Potential storage sites are localized in the Baltic Basin within several countries such as Sweden, Latvia, Lithuania, Poland and Russia. However, the BSR is still lagging behind in deploying a large-scale CC(U)S due to the national policy and regulatory frameworks which create unfavorable conditions for the technology, as well as the low public awareness and acceptability in most of the countries in the region. Consequently, CO₂ injection is forbidden in Lithuania, CO₂ storage on an industrial scale is banned in Estonia, Latvia and Finland and some federal states of Germany, while in Denmark, Poland and Sweden is permitted with limitations. However, it should also be noted that some positive developments and attitudes towards CC(U)S have also taken place recently in some of the BSR countries. This paper provides an overview of the current CC(U)S status and development in the BSR.

Keywords: CCUS, Baltic Sea Region, CO₂ storage, CCS regulations, Social acceptance, CCS

1. CC(U)S in the Baltic Sea Region

Deployment of full-scale CC(U)S on a global scale is key to meet the objectives of the Paris Agreement and mitigate climate change [1]. In the power sector, CCS is considered to be a key technology for fossil fuel-based generation, critical for delivering the deep emission reductions needed across fossil fuel-based power and many industrial applications while providing the opportunity for “negative emissions” [2]. It could also help the security of supply in a clean electricity system with increasing shares of variable renewable energy (VRE).

In the Baltic Sea Region (BSR), deployment of full-scale CC(U)S requires regional cooperation with equal conditions, standards, information, framework and understanding. Implementation of the technology on a regional scale for clusters of CO₂ emitters using common transboundary transport and storage infrastructure can significantly decrease the overall costs and affect public attitude. Moreover, an establishment of storage hubs to sequester CO₂ from several emission sources might be necessary to achieve large-scale deployment. A good example is the Northern Lights project in Norway, which offers an infrastructure for transport and storage of CO₂ across Europe, and the pilot capture plants planned by Fortum in the BSR: Fortum Oslo (Norway), Stockholm Exergi (Sweden), Klaipeda (Lithuania) and Zabrze CHP (combined heat and power; Poland) [3]. Northern Lights is the transport and storage component of the Longship project, promoted and supported by Norwegian State.

Although the project has been developed under circumstances that are unique to Norway, the experience is relevant for the setup and development of other CC(U)S projects. It demonstrates that, with long-term cooperation between state agencies, research institutions, academia and industrial partners, it is possible to develop CCS technology further and deploy a full-scale project.

The knowledge gained in the Northern Lights may be especially relevant for the BSR, which forms not only a political but a natural geographical area for collaboration needed for such a large-scale infrastructure development. Issues such as economic and environmental concerns, and safe transport and storage solutions are key areas of common regional interest. There will be a clear need for the use of joint and transboundary solutions for transportation and storage of CO₂ between the BSR countries. For example, since Russia and Germany are two of the largest CO₂ emitters on aggregate-level in the world, with 1792 Mt and 703 Mt of CO₂ emitted in 2020, respectively, and Poland is one of the largest CO₂ emitters in Europe (318 Mt/year) [4], the BSR needs to scale up development and deployment of CCUS as a climate change mitigation measure to meet the Paris Agreement and the EU climate goals. Regarding the geological storage possibilities, potential storage sites are localized in the Baltic Basin within the borders of several countries such as Sweden, Latvia, Lithuania, Poland and Russia. A study conducted by Anthonsen et al. [5] shows that Denmark, Norway and Sweden alone have the theoretical capacity to store the total CO₂ emission from

all European stationary point sources as mapped by the EU GeoCapacity project [6], though mostly under the North Sea. However, in the BSR CO₂ storage on an industrial scale (>100 Kt per year) is currently either permitted with different limitations (Denmark, Germany, Poland, Sweden) or prohibited for various reasons (Finland, Estonia, Latvia and Lithuania), or CC(U)S laws are not yet introduced (Russia and Belorussia). Thus, enabling policy and regulatory changes for industrial-scale projects are required in the entire region.

This paper gives an overview of the current situation in the BSR regarding both the possibilities and obstacles for implementation of the CC(U)S technology in the region.

2. The need for the CC(U)S technology in the BSR

The EU's CCS strategy presented in the Commission's proposal for 2030 climate and energy policy framework acknowledges the role of CCS in reaching the EU's long-term emissions reduction goal. As process-related emissions are unavoidable in some sectors, CCS may be the only option available to reduce direct emissions from industrial processes on the scale needed in the longer term. Moreover, as the key technology in the clean energy transition, during which fossil fuels still have the major share in the global primary energy consumption, the CC(U)S can help countries to ensure their energy security and security of supply. For instance, in the example of Estonia, an increase of CO₂ emission allowance price up to 25-30 Euro per ton in EU ETS in 2019 has led to an increase in the oil-shale based energy price, making it not competitive to the cheaper Russian energy. As a result, the largest Estonian national energy company Eesti Energia was forced to decrease energy production to reduce the high CO₂ emissions by five million tons in 2019 [7].

CC(U)S projects could also cooperate with renewable energies and produce revenues through CO₂ use options. For instance, considering that Finland is a large consumer of power and heat (per capita), the country has a unique opportunity to integrate CCS with combined heat and power (CHP) plants. Also, as Finland is a large consumer of biomass, adding CCS to bioenergy solutions, i.e., bioenergy carbon capture and storage, (BECCS), would enable removal of (biomass originated) CO₂ from the atmosphere. Furthermore, Finland's electricity supply depends on import of electricity from Russia which imposes security risk to the country whereas a clean energy system utilising CC(U)S could decrease this dependency on the non-EU energy supply. When it comes to the Finnish technology developers and providers, CCS could provide a significant market share in the future, such as in the area of oxyfuel combustion and chemical looping combustion. However, as the Finnish bedrock does not have any formations suitable for underground storage of CO₂, other alternatives need to be considered. Several options for using CO₂ as a raw

material for production of inorganic carbonates, chemicals and fuel components also seems promising [8].

Bioenergy is far more widespread in Sweden than in any other country in the region. By introducing various incentives like a CO₂ tax, green electricity certificates, tax exemption of biofuels for transport and direct investment support, there has been a major increase in the use of biofuels. In fact, in 2019, Swedish energy utility Stockholm Exergi AB has inaugurated the country's first BECCS pilot plant at its Värtan biomass-fired CHP plant in Stockholm partnering the Northern Lights project.

CC(U)S could also help to fully decarbonise heavy industry like cement and steel, where CO₂ is produced by industrial processes in addition to using energy from fossil fuels. In Sweden, for example, the cement industry produces 5% of the country's total CO₂ emissions [9]. Therefore, decarbonization of the cement industry will play a vital role in achieving Sweden's climate goals. One of the main ways in which production of cement can be made more sustainable and emissions deeply cut is through the application of CC(U)S. This has been already recognized by HeidelbergCement in Norway. Their plan to realise the first industrial-scale CCS project at a cement production facility in the world at Brevik involves capturing 400,000 tons of CO₂ annually and transporting it for permanent storage¹.

Currently, the largest industrial use of CO₂ is in enhanced oil recovery (EOR), whereby pressurized CO₂ is injected into existing oil and gas reservoirs to extract more hydrocarbons. Today, EOR is the only industrial use of CO₂ that has reached an appreciable scale. Evaluation of CO₂ injection for EOR has already been performed by oil companies in Lithuania and Russia. In Lithuania, pilot injections have been made in three oil exploitation wells to investigate the potential of CO₂ for EOR. The results showed high oil recovery percentage and about 100-200 Mt CO₂ storage capacity in the Gargzdai oil zone [14, 16]. A comprehensive study on the potential of Russia to implement CO₂-EOR showed that the geological, mining, geographical, and economic conditions of some regions in Russia have a very good potential for the technologically feasible and economically efficient implementation of CO₂-EOR technologies in depleted oil fields [10]. The most promising of the estimated regions are located in the North-Western, Volga, and Ural Federal districts.

In Poland, there are currently two candidate fields for enhanced oil recovery (EOR): the B3 oil field in the north-east part of the Polish sector [13] and Kamień Pomorski in the northwestern coastal region [14]. Another nearby hydrocarbon field, B8, with a good theoretical storage potential and with commercial production running since 2016, could be another potential site in the country for enhanced hydrocarbon recovery (EHR).

¹ www.heidelbergcement.com

Captured CO₂ can be also used in processes where underground minerals are utilised to mineralise CO₂, or in enhanced geothermal systems (EGS) where CO₂ would be used, instead of water, as heat transmission fluid, and would achieve geologic storage of CO₂ as an ancillary benefit. Research on CCUS started in many countries, including geothermal-CCS projects in France [11], Germany [12], Poland and Norway².

3. The geological storage potential in the BSR

A modelling study conducted in 2014 on the potential CO₂ storage sites in the southern Baltic Sea and surrounding onshore areas has identified a relatively large theoretical CO₂ storage capacity in the subsurface: about 16 Gt in the Middle Cambrian sandstone beneath 900 m of caprock and 1.9 Gt in the Dalders Monocline [13]. It has been also concluded that areas to the northeast of the Dalders Monocline, such as the eastern Swedish sector of the Baltic Sea and offshore part of Latvia where limited data is available, may have better reservoir qualities which would allow a higher injection rate, and thus would be more suitable for regional industrial CO₂ storage.

In addition to that, there is a possibility to use hydrocarbon and saline structures located both onshore and offshore Latvia. The estimated storage capacity of these structures is more than 880 Mt CO₂ [15, 16]. The reservoir rock properties in five onshore and offshore structures were experimentally analyzed and estimated from good to high quality, or from appropriate to very appropriate for CO₂ storage [17].

A number of studies have identified and assessed the storage capacity of reservoirs within the Baltic Basin, which is potentially suitable for CO₂ storage [18, 19, 20, 21, 22, 23]. Four potential test sites located in the BSR have been then identified and described: Southern Gotland (Sweden), South Kandava (Latvia), Vaškai structure (Lithuania) and Kamień Pomorski (Poland) (Figure 1).

There are also many places in Danish subsoil with suitable reservoirs. Anthonsen et al. [5] estimate that the subsoil can probably contain up to 22 GT of CO₂ (both onshore and offshore). This corresponds to between 500 and 1000 years of total Danish emissions at the current level. Furthermore, CO₂ storage could be established both on land and at sea, as the underground reservoirs are the same³. A few decades of research on CCS in Denmark have gathered good knowledge about the CCS potential.

In Poland, the latest national studies estimated the country's underground CO₂ storage capacity to be 10-15 Gt (predominantly onshore) [24]. The storage capacity

corresponds to 50-75 years of Polish ETS industrial installations emissions at the current level.

A fairly different situation exists in Russia where, based on the data from the former Soviet Union, estimated geological storage capacity is about 560 Gt [10], however, with most of the reservoirs being located far distant from large fossil-based power plants. CO₂ injection would therefore require construction of a gigantic pipeline system.

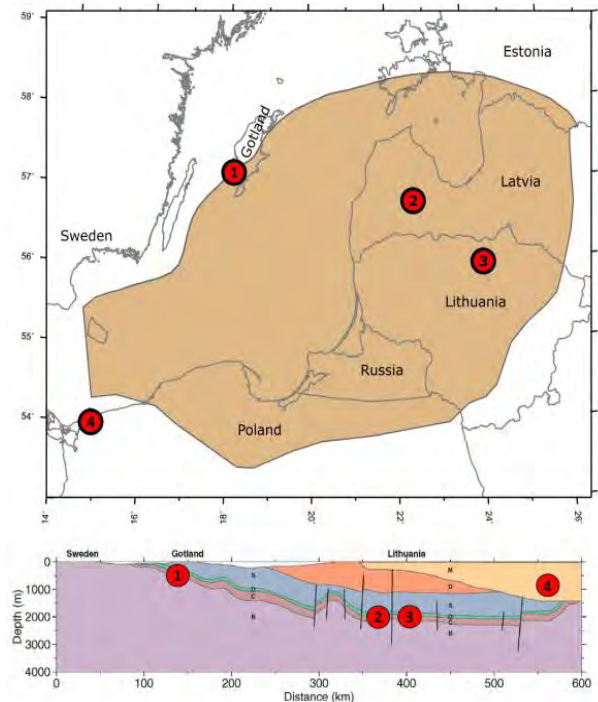


Figure 1: The area marked in brown shows the approximate area where Cambrian sandstones are present below 500 m depth where potential CO₂ storage reservoirs can exist. The locations of the four potential storage sites identified in the study are shown on the map (upper figure). Schematic cross section shows the general stratigraphic placement of the four pilot sites. B, C, O, S, D denote Basement, Cambrian, Ordovician, Silurian and Devonian, respectively. M denotes Strata which is younger than Devonian (lower figure) (Source: Nordbäck, N. et al. [14]).

On the other hand, in countries that lack potential for geological CO₂ storage, such as Finland and Estonia, captured CO₂ would need to be transported to other countries with suitable geology and storage infrastructure options. A study performed by Lauri et al. [25] has shown that the cost for transporting CO₂ from Finland to final geological CO₂ storage sites abroad is higher compared to that from the coastal regions in countries around the North Sea. However, significant cost reductions for CO₂ transport can be reached by joint transport infrastructure projects. For instance, transportation of CO₂ from the Gulf of Finland by ships could be carried out more

²www.sintef.no/en/projects/2020/energizers-co2-enhanced-geothermal-systems-for-climate-neutral-energy-supply

³ www.geus.dk/

economically by employing an infrastructure of ship terminals where CO₂ is collected into intermediate storage facilities from several capture units.

4. National CCS regulations

Article 6 of the London Protocol prohibits “export of wastes or other matter to other countries for dumping or incineration at sea” [26]. The article has been interpreted by contracting parties as prohibiting the export of CO₂ from a contracting party for injection into sub-seabed geological formations [27]. In 2009, the article was amended by contracting parties to allow cross-border transportation of CO₂ for sub-seabed storage [28], but the amendment must be ratified by two-thirds of contracting parties to enter into force.

In October 2019, the London Protocol Parties adopted a resolution to allow provisional application of an amendment to article 6 of the Protocol to allow sub-seabed geological formations for sequestration projects to be shared across national boundaries. This provisional application allows countries to agree to export and receive CO₂ for offshore geological storage. It removes the last significant international legal barrier to CCS and means that CO₂ can be transported across international borders to offshore storage.

This may enable CCS deployment in the BSR countries, as it permits countries to transport their captured CO₂ to offshore storage sites in Norway. Poland, Finland, and Germany could see this as an opportunity to decrease their CO₂ emission significantly.

The current situation in the BSR regarding the implementation of the CCS technology varies significantly from country to country. CO₂ storage is currently either permitted with different limitations or prohibited for various reasons, or CCS/CCUS laws are not yet introduced, such as in the case of Russia and Belarus (Table 1).

In Poland, CO₂ storage is prohibited until 2024 except for offshore demonstration projects in the Cambrian reservoir. CO₂ use for Enhanced Oil and Gas Recovery (EOR/EGR) is not restricted, but the status of the associated CO₂ storage possibilities both onshore and offshore is unclear.

In Germany, according to the Carbon Capture and Storage Act (KSpG), the total admissible annual storage volume is limited to four million tons of CO₂ in total, with a maximum annual storage volume of 1.3 million tons of CO₂ per storage site. Applications for storage site authorisations had to be made by the 31st of December 2016, so new storage sites can no longer be permitted as the legislation stands at present. In the evaluation report,

which was presented and discussed in the parliament in December 2018, the German federal government stated that there was no need to modify these regulations. As a result, CO₂ storage is still not permitted in Germany on an industrial scale [29, 30]. The federal government is however looking into tapping the sizable carbon storage potential under the North Sea⁴.

Table 1: National CCS regulations in the BSR countries.

Country	CO ₂ permitted for industrial scale	
	Onshore	Offshore
Denmark	No	Yes - for EOR
Estonia	No	No
Finland	No	No
Germany	No	No
Latvia	No	No
Lithuania	No	No
Poland	Not permitted, except for demo-projects	
Sweden	No	Yes
Norway	No	Yes
Russia	NE	NE
Belarus	NE	NE

In Estonia, Finland and Latvia, CO₂ storage is prohibited except for research and development, although underground CO₂ storage potential in Finland and Estonia is almost non-existent.

In Sweden and Norway, industrial-scale CO₂ storage is permitted only offshore. Sweden has also recently accepted the Amendment to article 6 of the London Protocol⁵. Previously, only Estonia, Finland, Norway, The Netherlands, UK and Iran have done that. A number of capture pilot projects have started or are in preparation to start in several places in the country with the aim to transport CO₂ to Norway from Swedish power plants,

⁴ www.cleanenergywire.org

⁵ shippingregs.org/Reference/IMO-Regulations/IMO-Circulars/2020

since an offshore CO₂ storage site in Sweden has not yet been established.

Significant changes have happened in Lithuania recently, where CO₂ geological storage was allowed both onshore and offshore until October 2019, when the new government of Lithuania adopted the new Subsurface Law. Since then, injection and storage of CO₂ in natural or artificial underground cavities or aquifers have been prohibited. This ban came into force in July 2020 [31].

In contrast, positive changes have been observed in Denmark. In the Danish Council on Climate Change report on Denmark's climate action towards 2030, CCS is presented as one of the main tools in order to reach CO₂ neutrality⁶. Although it is not possible at present to obtain permits for CO₂ storage in the Danish subsoil, the Danish Government works towards uncovering the regulatory obstacles to CC(U)S within the sectors in which the technology may be of relevance [32]. Also, based on the assessments of the Global CCS Institute undertaken in 2015⁷, Denmark has the most developed framework for CCS among the BSR countries, while the rest of the region demonstrates limited or very few CCS-specific existing laws applicable to all aspects of the CCS project lifecycle.

The enabling legislation for CCS in the BSR is regulated by national laws and international conventions. Since several BSR countries are not yet parties of the London Protocol (Finland, Poland, Latvia, Lithuania and Russia), bilateral and international agreements and local permits will be needed for transboundary offshore CO₂ storage.

Furthermore, several challenges still remain for the large-scale implementation of CCS projects in Europe. These include high investment costs and lack of public and consequently political support for onshore storage.

As concluded in the study by Shogenova et al. [30], the implementation of the CCUS technology requires regional and national incentives to be further developed in the BSR. For the realization of transboundary CCUS scenarios and construction of regional networks, both international and national legislation should be updated and implemented in a way that enables CCUS projects on an industrial scale. Furthermore, cooperation through clustering of CO₂ emitters and CO₂ storage sites and using common infrastructure could decrease costs, improve the communication with governments and local residents and create new opportunities in the BSR.

5. Politics and social aspects of CCS in the region

Advancing CC(U)S deployment is a multi-dimensional question including technological, socio-political, legal, economic and environmental dimensions. Although the

⁶www.klimaraadet.dk/da/nyheder/klimaraadet-ny-rapport-om-vejen-til-70-procentsmaalet-i-2030

⁷www.globalccsinstitute.com/resources/publications-reports-research/global-ccs-institute-ccs-legal-and-regulatory-indicator/

BSR has a unique potential for joint efforts on climate change mitigation, the level of CCS knowledge and understanding varies significantly between the countries. Various perceptions, concerns and values among stakeholders hamper the process of development and deployment of CC(U)S in the region. Furthermore, these diverse perceptions have led to fragmented governance, not least on the regional level. Strong sentiment against CCS exists among various stakeholders such as NGOs and the public in Germany [33], and to some extent, in Poland [34]. However, an exception is Norway's case where NGOs support CCS as a measure for combating climate change. This highlights different CCS perceptions in various countries attributable to various values, economic and political settings of the countries (for instance, see [33] and [34]).

In stark contrast to the development of CCS in Finland, there is fairly positive to neutral perceptions of and opinions about the technology among the public and industrial stakeholders, not least about BECCS [35], [36], [37].

In sum, the current state of stakeholders' acceptance in the BSR countries is the following: significant lack of acceptance in Germany; neutral to moderate lack of acceptance in the Baltic States and Poland; neutral to moderate acceptance in Finland, Sweden and Denmark; and acceptance and support in Norway.

Perceptions, reactions, and acceptance significantly affect the development of sustainable energy technology and the energy transition at local [37], regional, and global levels [38], [39]. Sovacool and Ratan [40] argue that social acceptance will emerge among stakeholders in the presence of the following: robust institutions, political commitment, supportive laws and regulations, competitive costs, a sophisticated communication system, and comprehensive financing.

Finally, we recommend that a comprehensive BSR campaign for social outreach would be worthwhile, including effective and transparent communication with the public concerning the cost, economic benefit and (dis-) advantages of CC(U)S. To pursue this successfully, consideration of the differences in cross-cultural and social settings between the countries is important.

6. Conclusion

International cooperation both within a region, such as the BSR, and outside the region borders is crucial to expedite CCUS development given the costly infrastructure and limited geologically suitable storage sites. Issues such as environmental concerns, safe transport and storage, public perceptions, and acceptability are of common regional interest. Therefore, it is vital to start processes which would enable such

cooperation, such as creating an EU Project of Common Interest (PCI) where all interested parties and countries could be involved, signing the London Protocol and ratifying the 2009 amendment by those countries that have not done yet, and reconsidering the current ban for CO₂ storage in Latvia and Lithuania.

The CC(U)S challenges in the various BSR countries are different. CO₂ storage capacity, for instance, is abundant in Norway but not available in Finland. This means that combining challenges, competence and possibilities in the different countries would lead towards creating more possibilities for establishing complete and optimal CC(U)S value chains in the region. Therefore, addressing the issues related to the current unfavorable national regulations that prevent full deployment of CC(U)S at an industrial scale in most of the countries in the BSR is urgently needed.

In sum, despite having relatively a shared vision in the BSR countries for expediting tackling climate change based on the EU goals and the Paris Agreement, this region is not homogenous, particularly when it comes to challenges of deployment of technologies such as CC(U)S. Also, various risk and benefit perceptions exist among the stakeholders. When it comes to the policy and politics of CC(U)S, one notable challenge is the need to deal with the existing fragmented governance concerning the deployment of the CC(U)S in the region.

Acknowledgements

This work was supported by the RouteCCS project funded by the Swedish Institute (01199/2020).

References

- [1] IEA (2016). 20 Years of Carbon Capture and Storage. Paris: International Energy Agency.
- [2] IEA report, 'Five Keys to Unlock CCS Investment, 2018, www.iea.org.
- [3] Thomassen, J., 2019. Fortum's CCUS initiatives in the Baltic Sea Region. Baltic Carbon Forum – BASRECCS Conference 22-23.10.2019, Tallinn, Estonia, <https://bcforum.net/presentations2019/02-05-Fortums-Initiatives-in-the-Baltic-Sea-Region.pdf>
- [4] Crippa, M., Guizzardi, D., Muntean, M., Schaaf, E., Solazzo, E., Monforti-Ferrario, F., Olivier, J.G.J., Vignati, E., Fossil CO₂ emissions of all world countries - 2020 Report, EUR 30358 EN, Publications Office of the European Union, Luxembourg, 2020, ISBN 978-92-76-21515-8, doi:10.2760/143674, JRC121460.
- [5] Anthonsen KL, Frykman P., Nielsen CM, 2016. Mapping of the CO₂ storage potential in the Nordic region. Geological Survey of Denmark and Greenland 35:87-90, doi: 10.34194/geusb.v35.4946
- [6] Vangkilde-Pedersen, T. et al. 2009. Assessing European capacity for geological storage of carbon dioxide – the EU GeoCapacity project. Energy Procedia 1, 2663–2670.
- [7] Shogenova, A., 2020. Carbon Neutral Baltic States: Do We Have CCUS Among Accepted Options? Baltic Carbon Forum 2020.
- [8] Teir S. et al., 2013. CCSP Carbon Capture and Storage Program, Mid-term report 2011–2013, (Eds.). Espoo 2013. VTT Technology 125. 76 p.
- [9] Tillväxtanalys. (2016). Klimatneutral cementindustri – Koldioxidavskiljning och lagring i Sverige? Retrieved from: <https://www.tillvaxtanalys.se/english/publications/direct-response/direct-response/2016-11-10-a-climateneutral-cement-industry---carbon-capture-and-storage-in-sweden.html>
- [10] Cherepovitsyn, A. Fedoseev, S., Tcvetkov, P., Sidorova, K., Kraslawski A. (2018). Potential of Russian Regions to Implement CO₂-Enhanced Oil Recovery. Energies 2018, 11, 1528; doi:10.3390/en11061528.
- [11] Galièguea, X., Laudeb, A. (2017). Combining Geothermal Energy and CCS: From the Transformation to the Reconfiguration of a Socio-Technical Regime? Energy Procedia 114 (2017), 7528 – 7539.
- [12] McDonnell, K., Molnár, L., Harty, M., Murphy, F. (2020) Feasibility Study of Carbon Dioxide Plume Geothermal Systems in Germany - Utilising Carbon Dioxide for Energy. Energies 2020, 13, 2416; doi:10.3390/en13102416
- [13] Final report on prospective sites for the geological storage of CO₂ in the southern Baltic Sea, 2014, www.globalccsinstitute.com
- [14] Nordbäck, N., Sopher, D., Niemi, A., Juhlin, C., et al. (2017). CGS Baltic seed project (S81). Project substance report. 1–84., <https://bcforum.net/storage.php>.
- [15] Šliaupa S, Lojka R, Tasáryová Z, Kolejka V, Hladík V, Kotulová J, Shogenov K, et al. 2013. CO₂ storage potential of sedimentary basins of Slovakia, the Czech Republic, Poland and the Baltic States. Geological Quarterly; 219 - 232.
- [16] Shogenov K, Shogenova A, Forlin E, Gei D., 2017. Synergy of CO₂ storage and oil recovery in different geological formations: case study in the Baltic Sea. Energy Procedia, 114: GHGT-13, Lausanne, Switzerland, 14-18 November 2016. The Netherlands: Elsevier: 7047–7054. [/doi.org/10.1016/j.egypro.2017.03.1846](https://doi.org/10.1016/j.egypro.2017.03.1846).
- [17] Shogenov, K., Shogenova, A., Vizika-Kavvadias, O., Nauroy, J. F. 2015. Reservoir quality and petrophysical properties of Cambrian sandstones and their changes during the experimental modelling of CO₂ storage in the Baltic Basin. Journal of Earth Sciences, 64 (3), 199–217.
- [18] Shogenova, A., Šliaupa, S., Vaher, R., Shogenov, K., Pomeranceva, R., 2009. The Baltic Basin: structure, properties of reservoir rocks and capacity for geological storage of CO₂. Estonian Journal of Earth Sciences, 58(4), 259 - 267.
- [19] Erlström, M., Fredriksson, D., Juhojuntti, N., Sivhed, U., Wickström, L., 2011. Lagring av koldioxid i berggrunden - krav, förutsättningar och möjligheter. Sveriges Geologiska Undersökning Rapporten och meddelanden 131, 7–94.
- [20] Vernon R., O'Neil N., Pasquali R. Nieminen M., 2013. Screening of prospective sites for geological storage of CO₂ in the Southern Baltic Sea. Espoo 2013. VTT Technology 101, 58 p. + app. 1 p. (final report of the BASTOR project).

- [21] Sopher, D., Juhlin, C., Erlstrom, M., 2014. A probabilistic assessment of the effective CO₂ storage capacity within the Swedish sector of the Baltic Basin. *International Journal of Greenhouse Gas Control*, 30, 148-170.
- [22] Lothe, A., Emmel, B., Bergmo, P., Mortensen, G. M., Frykman, P., 2015. Updated estimate of storage capacity and evaluation of Seal for selected Aquifers (D26). NORDICCS Technical Report D 6.3.1401 (D26). 80 pp.
- [23] Yang Z, Tian L., Jung B, Joodaki S, Fagerlund F, Pasquali R., 2015. Assessing CO₂ storage capacity in the Dalders Monocline of the Baltic Sea Basin using dynamic models of varying complexity. *International Journal of Greenhouse Gas Control*. 2015; 43:149-60.
- [24] Wójcicki A., Nagy S., Lubaś J., Chečko J., Tarkowski R., 2014. Assessment of formations and structures suitable for safe CO₂ storage (in Poland) including the monitoring plans (summary). PGI-NRI, Warsaw (report available at PGI website; skladowanie.pgi.gov.pl).
- [25] Lauri, K., Jouko, R., Nicklas, N. and Sebastian, T., 2014. Scenarios and new technologies for a North-European CO₂ transport infrastructure in 2050. *Energy Procedia* 3 (2014) 2738 – 2756.
- [26] Convention on the Prevention of Marine Pollution by Dumping of Wastes and other Matter (London Convention 1972). London Protocol (1996) – protocol thereto. www.imo.org
- [27] IMO. Report of the Thirtieth Consultative Meeting and the Third Meeting of Contracting Parties, LC 30/16. London: IMO; 2008.
- [28] IMO. Report of the Thirty-First Consultative Meeting and the Fourth Meeting of Contracting Parties, LC 31/15. London: IMO; 2009.
- [29] Bals, C., Bellmann, E., Bode, A., Edenhofer, O., et al. (2019). CCU and CCS – Building Blocks for Climate Protection in Industry. Analysis, Options and Recommendations (acatech – Deutsche Akademie der Technikwissenschaften e.V., Ed.). München: utzverlag GmbH.
- [30] Shogenova, A., Nordback, N., Sopher, D., Shogenov, K. et al. (2021). Carbon Neutral Baltic Sea Region by 2050: Myth or Reality? 15th International Conference on Greenhouse Gas Control Technologies, GHGT-15, 15-18 March 2021, Abu Dhabi, UAE. Elsevier, SSRN, 1–12. DOI: 10.2139/ssrn.3817722.
- [31] Pakeisti Lietuvos Respublikos žemės gelmių įstatymą Nr. I-1034 ir jį išdėstyti taip, www.infolex.lt/ta/556859:str1
- [32] Danish Ministry of Climate, Energy and Utilities. The ugly duckling – CCS and CCU in Denmark. Baltic Carbon Forum 2020. 14. October.
- [33] Karimi, F., Komendantova, N., 2017. Understanding experts' views and risk perceptions on carbon capture and storage in three European countries, *Geojournal* 82 (1), 185–200.
- [34] Karimi, F., and Toikka A., 2018. 'General Public Reactions to Carbon Capture and Storage: Does Culture Matter?' *International Journal of Greenhouse Gas Control* 70 : 193–201. <https://doi.org/10.1016/j.ijggc.2018.01.012>.
- [35] Rodriguez, Emily, Adrian Lefvert, Mathias Fridahl, Stefan Grönkvist, Simon Haikola, and Anders Hansson. 2021. 'Tensions in the Energy Transition: Swedish and Finnish Company Perspectives on Bioenergy with Carbon Capture and Storage'. *Journal of Cleaner Production* 280 (January): 124527. <https://doi.org/10.1016/j.jclepro.2020.124527>.
- [36] Kojo, Matti, and Eeva Innola. 2017. 'Carbon Capture and Storage in the Finnish Print Media'. *Risk, Hazards & Crisis in Public Policy* 8 (2): 113–46. <https://doi.org/10.1002/rhc3.12111>.
- [37] Karimi, F. and Rodi, M., 2021. Energy-Transition Challenges in the Baltic Sea Region: An Overview of Socio-Political and Legal Gaps. From Economic to Energy Transition, pp.457-487.
- [38] Wolsink, M. 2018. Social Acceptance Revisited: Gaps, Questionable Trends, and an Auspicious Perspective. *Energy Research & Social Science*, 46, 287– 295.
- [39] Sütterlin, B., & Siegrist, M. 2017. Public Acceptance of Renewable Energy Technologies from an Abstract Versus Concrete Perspective and the Positive Imagery of Solar Power. *Energy Policy*, 106, 356–366.
- [40] Sovacool, B. K., & Lakshmi Ratan, P. 2012. Conceptualizing the Acceptance of Wind and Solar Electricity. *Renewable and Sustainable Energy Reviews*, 16 (7), 5268–5279.

REGULATION OF CCS STORAGE SITES IN NORWAY AND COMPLIANCE WITH EEA LAW

Viktor Weber^{1*}

¹ Scandinavian Institute of Maritime Law, University of Oslo, Norway

Corresponding author e-mail: viktor.weber@jus.uio.no

Abstract

Carbon capture and storage (CCS) has been deployed in Norway since 1996. Originally, this activity came under the country's mineral legislation. In the late 2000s, the European Union established a detailed legal framework for the safe deployment of CCS, which was often considered by the industry to be burdensome. Being applicable in Norway as well, this article examines how the Norwegian legal system has adopted the European CCS legislation and how it addressed the challenges posed by it.

Keywords: CCS Directive, implementation, liability, flexibility, Norway, EEA

1. Introduction

Carbon (dioxide) capture and storage (CCS) is a technology whereby carbon dioxide (CO₂) is separated from flue gases at large emission sources like power stations and factories, compressed, and injected into geological formations like depleted oil and gas fields, saline aquifers, and basalt formations. CCS is supported both at the international¹ and the European level,² and it is understood to be part of the portfolio of measures that have to be deployed to reach the Paris goal of 1.5°C.³

Carbon capture and storage exists in Norway since 1996. The Sleipner T platform in the North Sea injects CO₂ into the Utsira formation beneath it. The CO₂ originates from the production of natural gas from the Sleipner West reservoirs. Since 2014 the Sleipner T platform also injects CO₂ from the Gudrun field. Since 2008 the Snøhvit site also stores produced CO₂ in the Barents Sea. CCS has been deployed on these platforms in response to the carbon tax that the Norwegian government introduced for petroleum activities in 1991.⁴

¹ UNFCCC 'Decision 7/CMP.6, Carbon Dioxide Capture and Storage in Geological Formations as Clean Development Mechanism Project Activities' UN Doc FCCC/KP/CMP/2010/12/Add.2 (15 March 2011); and UNFCCC 'Decision 10/CMP.7, Modalities and Procedures for Carbon Dioxide Capture and Storage in Geological Formations as Clean Development Mechanism Project Activities' UN Doc FCCC/KP/CMP/2011/10/Add.2 (15 March 2012).

² CCS has been the fourth part of the EU's 20-20-20 climate and energy package.

³ See in particular V Masson-Delmotte et al (eds), *Global Warming of 1.5°C* (Intergovernmental Panel on Climate Change 2018) 14. This source shows four model pathways to reach the 1.5°C goal with no or limited overshoot. Only one of these models does not include CCS technology.

⁴ CO₂ Tax Act on Petroleum Activities (LOV-1990-12-21-72). In 2021, this tax is NOK 543 (about EUR 55) / ton of CO₂. This tax is independent from and additional to the allowances that have to be purchased in the European Emission Trading Scheme (ETS). See: <https://www.norskpetroleum.no/en/environment-and-technology/emissions-to-air/>.

Today, Norway is ready for its first full-scale, full-chain CCS project, called Longship. At the moment, the project is planned to store the CO₂ captured at Norcem's cement plant in Brevik. In time, the Longship project is hoped to expand into a North-West European CCS network and that other states in Europe embark on their own CCS projects. However, CCS technology requires substantial investment, and the related legal framework is considered to be burdensome.

The legal challenges associated with this framework have been widely discussed before.⁵ Earlier experience indicates that the general answer to these challenges is a close cooperation between the industry and the authorities and the commercially reasonable interpretation of the legal terms in question and the making of commercially reasonable estimates.⁶ The present article aims at examining the Norwegian experience against this background.

2. The relevance of European legislation

At the European level, the legal framework for CCS comprises of three instruments: the CCS Directive,⁷ the Environmental Liability Directive,⁸ and the Emission Trading Scheme Directive.⁹ Each of these instruments are so-called 'instruments with EEA relevance'. This means that they are made part of the European Economic Area Agreement. Norway being a member of the EEA, the provisions of these directives are applicable to it. Thus, the Norwegian experience is highly relevant to other EEA and EU states. Initially, Norway was averse to the European efforts to introduce CCS legislation. However, over time it became supportive.¹⁰ In fact, Norway took an active role in the shaping of the international and European legal framework for CCS.¹¹ Despite Norway's involvement, the national implementation of the CCS Directive was a long and contentious process both at the level of stakeholder interests and at

⁵ The following concerns have been raised in the past: How to show 'complete and permanent' containment? Is it possible? What is 'leakage'? How will the competent authority evaluate that the hand-over criteria are met? The default 20-year post-closure period is too long. What should the financial security cover? How to estimate the future price of emission allowances? The liability is not limited. Guidance Document 4 on the Financial Security can be read as too rigid and demanding.; For discussion, see for example: A Pop, 'The EU Legal Liability Framework for Carbon Capture and Storage: Managing the Risk of Leakage while Encouraging Investment' 6 *Aberdeen Student Law Review* 2015, 32-56; V Weber, 'Uncertain liability and stagnating CCS deployment in the European Union: Is it the Member States' turn?' 27 *Review of European, Comparative and International Environmental Law* 2018, 153-161.

⁶ See for example: Carbon Sequestration Leadership Forum, 'Practical Regulations and Permitting Process for Geological CO₂ Storage' November 2017, available at <https://www.cslforum.org/cslf/sites/default/files/documents/7thMinUAE2017/7thMinAbuDhabi17-PG-RegulationTaskForceReport.pdf>; ROAD CCS, 'Case Study of the ROAD Storage Permit, A Report by the ROAD Project' (ROAD CCS 2013), available at <https://www.globalccsinstitute.com/resources/publications-reports-research/case-study-of-the-road-storage-permit/>; V Weber (fn.5).

⁷ Directive 2009/31/EC of 23 April 2009 on the geological storage of carbon dioxide [2009] OJ L140/114 (CCS Directive).

⁸ Directive 2004/35/EC of 21 April 2004 on environmental liability with regard to the prevention and remedying of environmental damage [2004] OJ L143/56 (ELD).

⁹ Directive 2003/87/EC of 13 October 2003 on establishing a scheme for greenhouse gas emission allowance trading within the Community [2003] OJ L275/32, as amended by Directive 2009/29/EC [2009] OJ L140/63.

¹⁰ T Jevnaker, 'Norway's implementation of the EU climate and energy package - Europeanization or cherry-picking?' FNI Report 7/2014 (Fridtjof Nansen Institute, 2014), p.32; See also: T Jevnaker, 'Implementation in Norway' ch.9 in J B Skjærseth et al., 'Linking EU Climate and Energy Policies' (Edward Elgar, 2017) pp.184-186.

¹¹ *Ibid.*

the level of EU-Norway relations.¹² The main concerns on the substance related to the liability that may arise for the operator, with particular regard to ETS liability, and the terms of transferring responsibility for the storage site to the State.¹³ The implementation was further complicated, by geo-political arguments (the application of the EEA Agreement on the continental shelf), by the loss of political momentum between 2013 and 2015, and by the fact that two ministries rivalled for the responsibility of implementation.¹⁴

3. Implementation and authorization requirements

In the event, the CCS Directive has been implemented through the new Storage Regulations¹⁵ and amendments to the Petroleum Regulations¹⁶ (especially new chapter 4a) and Pollution Regulations¹⁷ (new chapter 35).¹⁸

The Pollution Regulations apply to all forms of CCS and fall under the competence of the Ministry of Climate and Environment. The other two regulations are applicable depending on the type of CCS conducted. Where CCS is linked to a petroleum activity, the Petroleum Regulations apply. When CCS is conducted in itself, the Storage Regulations apply. These regulations come under the competence of the Ministry of Petroleum and Energy. After public consultation,¹⁹ the Ministry noted that difficult questions of financial and legal nature would arise if the earlier, petroleum production-related CCS operations came under the new Regulations. Consequently, the Ministry deemed that it would be the most appropriate to regulate CCS linked to petroleum activities under the petroleum legislation as earlier (with some modifications) and to apply the new Storage Regulations to CCS where the source of the CO₂ is not from the petroleum industry.

It has been raised during the public consultation that there is an overlap between new chapter 35 of the Pollution Regulations and the other two regulations. The Ministry of Petroleum and Energy justified the inclusion of the parallel provisions into the Storage Regulations and the Petroleum Regulations by stating that the provisions in these regulations concern resource management considerations while the provisions in the Pollution Regulations concern environmental considerations. These considerations are different, and practice has shown (at the Sleipner and Snøhvit storage sites) that the resource authorities also need such rules.

¹² Jevnaker (fn.10), pp.32-37.

¹³ Ibid.

¹⁴ Ibid.

¹⁵ FOR-2014-12-05-1517.

¹⁶ FOR-1997-06-27-653.

¹⁷ FOR-2004-06-01-931.

¹⁸ For general discussions on the Norwegian implementation regime see S F Vold, 'CCS Legislation in Norway - The EU CCS Directive and its Implementation into Norwegian Law' ch. 18 in M M Roggenkamp and C Banet (eds.), 'European Energy Law Report XIII' Cambridge University Press, 2020; C Banet, 'Regulering av karbonfangst, transport og lagring i norsk rett' in H C Bugge (ed.), 'Klimarett' (Universitetsforlaget, 2021).

¹⁹ See: Cabinet Papers, PRE-2014-12-05-1517, PRE-2014-12-05-1518 Gjennomføring av EUs lagringsdirektiv: Forskrift om utnyttelse av undersjøiske reservoarer på kontinentalsokkelen til lagring av CO₂ og om transport av CO₂ 2 på kontinentalsokkelen, og Forskrift om endring av forskrift 27. juni 1997 nr 653 om petroleumsvirksomhet.

This is a surprising justification. The Pollution Regulations are authorized under section 9 of the Pollution Control Act (PCA).²⁰ While the PCA applies to offshore operations, it does so in a partial manner. Section 4 provides:

“The provisions of this Act also apply, subject to any restrictions deriving from international law and from the Act itself (cf. Chapter 8 [Compensation for pollution damage]), to exploration for and production and utilization of natural subsea resources on the Norwegian part of the continental shelf, including decommissioning of facilities. The provisions of section 7 [Duty to avoid pollution], first paragraph, cf. Chapter 3, *on the duty to obtain a permit* [see s.11] and of section 9 on regulations nevertheless *apply only to those aspects of such activity that regularly result in pollution*. Nor do the provisions of section 7, second paragraph, cf. fourth paragraph, apply to measures to prevent or stop acute pollution.”²¹

Thus, it appears that in principle the PCA and thus the Pollution Regulations apply to offshore activities with respect to ‘operational pollution’ (pollution associated with boring, waste water etc.).²² Meanwhile, the petroleum framework concerns the specific provisions on accidental pollution by oil or gas.²³

The focus of the CCS Directive is the specific act of storing CO₂ with its potential consequences²⁴ and not offshore operations in general. Consequently, the most logical place for implementation is the petroleum law framework, i.e. the Storage Regulations and the Petroleum Regulations. By virtue of section 4 of the PCA, the general offshore aspects of CCS come under the pollution framework automatically, just like the general aspects of petroleum operations do. In this light, the separate implementation into the Pollution Regulations appears to be a legally questionable result of the above-mentioned rivalry between the two Ministries.

A consequence of the double regulation is that the environmental permitting regime is a hybrid system. All CCS operations must obtain a permit from the Ministry of Climate and Environment under section 11 of the PCA with respect to the boring activity and under section 35(4) of the Pollution Regulations for the actual injection and storage. In practice, these two permits are in one document (the ‘environmental permit’).

As regards the resource authorities, operators of CCS connected to a petroleum activity must obtain from the Ministry of Petroleum and Energy an exploitation permit under section 30(e) of the Petroleum Regulations; operators of standalone CCS must obtain the corresponding permit under section 4(1) of the Storage Regulations.

In 2015, Statoil (today Equinor) had to reapply for permits under the new legislation. While the permits under the Pollution Regulations are publicly available, the permits under the Petroleum Regulations have not been made available to the author. In the case of the storage site used by the Longship project, the author has received a copy of the permit under the Storage Regulations. This permit sets out the coordinates of the area in which the CO₂ operation can take place and restates various statutory obligations for the operator with particular attention to

²⁰ LOV-1981-03-13-6.

²¹ Ibid., s.4, emphasis added.

²² See also: NUT 1977:1 Utkast til lov om vern mot forurensing og forsøpling med motiver, pp. 114-115; NOU 1982:19 Generelle lovregler om erstatning for forurensningsskade, p. 261.

²³ See: Petroleum Act (LOV-1996-11-29-72) ss. 1(6)(a) and 7(1).

²⁴ See CCS Directive (fn. 7), art. 1.

environmental obligations. By contrast, the environmental permit under the Pollution Regulations has not been issued yet. The application for this permit is expected to be submitted in 2022.²⁵ It is assumed here that the available permits under the Pollution Regulations of the running projects are indicative of what should be expected in the corresponding permit of the Longship project. Thus, the discussion below will rely on the Sleipner field's environmental permit, which provides illustration of the flexible approach that authorities need to take in order to allow CCS.

4. Compliance

4.1 Risk assessment

The European framework prescribes a risk assessment as part of the permit application procedure. For the purposes of the risk assessment, an injection phase and a post-injection phase of 50 years have been defined for the Sleipner project.²⁶ The various risks taken into account have been: migration of CO₂ outside the storage formation, migration of CO₂ to production wells, leakage to the seafloor or the air through the cap rock or faults, damage to the reservoir due pressure increase, leakage through closed exploration wells, leakage to the air from the capture process, and erroneous measurement of the stored CO₂, and erroneous composition analysis of the CO₂ stream.²⁷ Two risks were noted in particular: the risk of leakage to the seafloor and a change in water acidity (pH) as a result of the leakage. The former risk was found to have a low probability of 0,0001 during injection and 0,001 in the post-injection period.²⁸ Likewise, no significant effect on sealife is predicted even in a worst-case leakage scenario. Thus, the two risks combined mean that the environmental risk was deemed low.²⁹

4.2 Financial security and financial mechanism

In its Article 19, the CCS Directive prescribes that the operator of the storage site must furnish proof that the obligations in the storage permit can be financially met. This is known as the financial security. Further to this, under Article 20 the operator must provide a lump sum payment to the competent authority before the latter takes over responsibility for the storage site in order to cover at least 30 years of monitoring costs and other costs that may arise. This is known as the financial mechanism. The European Commission elaborated further on these two provisions in a guidance document³⁰ and the Norwegian Environment Agency published further guidelines.³¹ In the Norwegian implementation the terms of the financial security are established jointly by the Ministry of Climate and Environment and the Ministry of Petroleum

²⁵ Personal correspondence with the Norwegian Environment Agency, dated 19 April 2021.

²⁶ Miljødirektoratet, 'Tillatelse til lagring av CO₂ ved Sleipner-feltet' ('Sleipner environmental permit'), Ref: 2013/4083, 16. juni 2016, s.4.1.2.

²⁷ Ibid.

²⁸ Ibid.

²⁹ Ibid.

³⁰ Commission (EU), 'Implementation of Directive 2009/31/EC on the Geological Storage of Carbon Dioxide – Guidance Document 4 – Article 19 Financial Security and Article 20 Financial Mechanism' (European Commission 2011) (Guidance Document 4).

³¹ Miljødirektoratet, 'Nærmere bestemmelser om finansiell sikkerhet for CO₂ lagring - Forurensningsforskriften § 35-15' Veileder M-521, 2016.

and Energy; meanwhile, the administration of the financial mechanism falls under the competence of the Ministry of Petroleum and Energy.³²

The financial security must be able to cover monitoring obligations, corrective measures, site closure, post-closure obligations, potential emission allowance obligations.³³

While Statoil noted that it is difficult to predict future prices on a 20 to 25-year time horizon, in 2015 it estimated the related monitoring costs of the Sleipner site to be between 87 and 104 million NOK. Crucially, the environmental permit of the Sleipner field states:

“The cost of emissions allowance obligations were not estimated, but Statoil points to the risk assessment where it concludes that the most likely leakage scenario is in the range of 0,1-100 tons/year. With such leakage rate, the emission allowance obligations will probably not constitute a significant cost even with a high allowance price in the future.”³⁴

As for the form of the security, Statoil provided a parent company guarantee. This is a less preferred form of security, but for the encouragement of the industry and the importance of reducing GHG emissions, it was accepted by the Ministry.

The exact modalities of the financial security are decided on a case-by-case basis.³⁵ Indeed, some of the costs can be estimated or partly confirmed once the storage operation is in place.³⁶

Apart from the financial security requirement, the operator must show that it is financially solid and reliable and has professional and technical competence.³⁷ According to the permit these criteria have been met by Statoil through its earlier experience in the petroleum industry.³⁸

4.3 Certain technical points

At the Sleipner field, the so-called Utsira formation is used for the storage of CO₂. This formation has been studied in great detail in the past 30 years. Statoil argued that it would be inappropriate to update the models in line with Annex I of the Pollution Regulations due to size of the Utsira formation and because the existing 4D data is better suited to describe the CO₂ plume.³⁹ This deviation was allowed.

For the monitoring plan, 4D seismic surveys have been chosen as primary method.⁴⁰ This can be complemented with gravimetry, and well pressure and temperature during the injection phase.⁴¹

³² Cabinet Papers (fn. 19), s.8.

³³ Miljødirektoratet (fn. 26), s.4.2.5.

³⁴ Ibid., author's translation.

³⁵ Miljødirektoratet (fn. 31), p.2.

³⁶ Ibid.

³⁷ Pollution Regulations (fn. 17), s. 35(4)(d).

³⁸ Miljødirektoratet (fn. 26), s. 4.1.3.

³⁹ Ibid., s. 4.1.1.

⁴⁰ Ibid., s. 4.2.3.

⁴¹ Ibid.

In the meaning of section 35(8) the CO₂ received for storage must consist *overwhelmingly* of CO₂. In the case of the Sleipner field this criterion was defined at 96-99 mol% CO₂, which corresponds to the characteristics of the amine process used for the separation of CO₂.⁴²

The Sleipner operation being part of a petroleum activity, it is subject to a decommissioning plan under ss.43-45 of the Petroleum Act. It has been agreed that the operator would furnish the post-closure plan required by section 30(n) of the Petroleum Regulations at a later stage as part of the decommissioning plan. Since the Longship project is a stand-alone CCS operation, this option will not be available, and a defined post-closure plan should be expected in its environmental permit once issued.

5. Compensation in case of pollution damage

In this last section, it is necessary to include a brief a discussion on the environmental liability that may arise from CO₂ storage. In the case of standalone CCS operations, the specific provisions are set out in chapter 8 of the Storage Regulations. The liable person is the permit holder, and the liability attaches regardless of fault. However, the liability provisions are equally applicable to a non-permit holding operator when the Ministry decides so by the authorization of the operator. In such case, claims should be directed against the operator first. If the operator cannot cover the whole claim, the permitholders must cover the outstanding amount in proportion to their share in the permit. In case of *force majeure*, the liability can be reduced as appropriate. The liability is channelled to the permit holder (or operator) who can have a recourse claim against the tortfeasor in case the tort was committed with intention or gross negligence. Chapter 9 of the Storage Regulations contain specific rules on compensation to Norwegian fishermen.

Regarding CCS linked to a petroleum activity, the Petroleum Regulations (including chapter 4a) do not contain provisions on compensation. This is because the related provisions on compensation are in chapters 7 and 8 of the Petroleum Act, the authorizing act of the Regulations. Interestingly, the definition of pollution damage has not been amended in the Petroleum Act.⁴³ Thus, formally, the relevant provisions would not cover damage caused by CO₂. It is assumed here that the relevant provisions are intended to cover damage caused by CO₂ as much as by petroleum and an amendment to this effect is recommended.

The Pollution Regulations (including chapter 35) do not contain provisions on compensation either. The corresponding provisions are in chapter 8 of the authorizing legislation, the PCA. In line with the argument made above in section 3, in principle, these compensation provisions should apply to environmental damage arising from offshore operations in general (boring etc.) and not to specific environmental damage caused by leaking CO₂.⁴⁴

⁴² Ibid., s.4.2.2.

⁴³ Section 7(1) defines pollution damage as "... damage or loss caused by pollution as a consequence of *effluence or discharge of petroleum* from a facility, including a well, and costs of reasonable measures to avert or limit such damage or such loss, as well as damage or loss as a consequence of such measures ..." (emphasis added). Cf. Storage Regulations, s8(1).

⁴⁴ See fn. (22).

6. Conclusion

This short paper has described how the European CCS legal framework has been implemented into Norwegian law and the specificities of the related permitting system; it provided some examples of how the framework can be applied to an operation storage site in anticipation of the environmental permit of the Longship project. Finally, a note was made on the related liability provisions.

It follows from the discussion above that the provisions of the CCS Directive could have been implemented in a more logical and efficient way. If revising the whole implementation is not feasible in the current administrative arrangement, at least the minor amendment to the Petroleum Act suggested above should be put in place to achieve a more coherent system.

Regarding the terms of CCS operations, the Norwegian experience coincides with the experience of earlier projects: close cooperation is necessary between the industry and the authorities, and the various legal concepts have to be given a practical interpretation with reasonable and justified estimates. The potential liability for future emissions trading quotas stands out in particular when this approach is taken; it becomes an insurable risk.

A NEW FACILITY ON ACCURATE VISCOSITY AND DENSITY MEASUREMENTS

Bahareh Khosravi¹, Sigurd W. Løvseth^{2*}, Anders Austegard², Caroline Einen², H. G. Jacob Stang², Ingrid Snustad², Jana P. Jakobsen¹, Håvard Rekstad¹

¹ Norwegian University of Science and Technology, Trondheim, Norway

² SINTEF Energy Research, Trondheim, Norway

* Corresponding author e-mail: Sigurd.W.Lovseth@sintef.no

Abstract

A new facility for accurate measurement of viscosity and density of CO₂-rich mixtures relevant for CO₂ Capture and Storage (CCS) has been constructed. The facility includes a two-capillary viscometer with several novel solutions to enable high performance over a range between 213.15 K and 473.15 K (-60 and 200 °C) in temperature and up to 100 MPa (1000 bar) in pressure. There are currently very little data available on viscosity of liquid CO₂-rich mixtures relevant for CCS, needed for instance in simulations of injection processes and reservoirs. Integrated in the setup is also a densimeter which is controlled to the same temperatures and pressures. Apart from providing density data, this enables accurate conversion between kinematic and dynamic viscosity. The total uncertainty target of the facility is 0.1 % (95% confidence level), except close to the critical point.

Keywords: *Thermophysical properties, viscosity, density, impure CO₂, CO₂ transport and storage.*

1. Introduction

In CO₂ capture, transportation, and storage (CCS), accurate predictions of thermophysical properties are required to optimize design and operations with respect to safety and costs. Thermophysical properties such as viscosity and density are crucial factors to determine the key design and operational characteristics of CO₂ transportation, storage, and injection infrastructure such as pipeline diameter, the pump/compressor power consumption and performance of heat exchangers, [1-3].

Viscosity is a necessary parameter for simulating laminar reservoir flow, where the resistance or pressure drop is proportional to the viscosity. Reservoir injectivity index is inversely proportional to viscosity, and viscosity also strongly affects plume evolution and storage efficiency. Viscosity is necessary to predict convection and diffusion processes, and the sweep efficiency of CO₂ EOR depends strongly on the CO₂/reservoir fluid viscosity contrast. Viscosity also has impact on history-matching and seismic interpretation, long-term CO₂ migration, and potential for leakage[4-6].

Since CCS processes cover a large range of fluid conditions and involve multi-component mixtures, there is a cost trade-off between purification of the captured CO₂ streams and designing and operating a transport and storage systems to handle larger quantities of the involved impurities [7]. Impurities have significant impact on thermophysical properties, particularly close to the critical point [8, 9]. However, as of today, there are still large gaps in the published viscosity and density data for CO₂ with impurities at conditions relevant for CCS, which are crucial for building good reservoir models and simulation tools. In particular, CO₂ is typically compressed to a liquid or dense phase for efficient transportation [1]. This requires accurate measurement

data for viscosity of CO₂ mixtures at these conditions, which are currently missing to a large extent, and more experiments are needed to fill these gaps and develop more accurate reservoir models and simulation tools in vicinity of the critical point [3, 8] For liquid phase viscosity and relevant compositions, only two rather limited data sets from a single lab have been identified [10]. Little data are also available for the gas phase [8, 11]. The situation for density is better, but most binary systems still have important knowledge gaps or limited data. Lack of experimental data typically leads large uncertainties in model predictions. Uncertainties in these properties can lead to costly overdesign and/or risks of inefficient or unsafe transport, injection and storage [12]. Therefore, it is important to focus on gathering reliable data with well-defined uncertainty levels that cover the phase space of interest.

The aim of the ImpreCCS project is to reduce CCS cost and risk through improving thermo-physical knowledge of pure CO₂ and CO₂-rich mixtures with impurities and at conditions characteristic for CO₂ transport and storage by acquiring high quality data. ImpreCCS is coordinated by SINTEF Energy Research within the framework of Norwegian CCS Research Centre (NCCS), and Norwegian University of Science Technology (NTNU), NORCE, University of Western Australia are important research partners, and NIST is an associated partner.

In order to address the lack of experimental viscosity data, a new novel two-capillary viscometer has been designed and constructed to cover the temperature range between 213.15 K and 473.15 K and pressures up to 100 MPa. This facility, which is part of ECCSEL ERIC [13] is designed for pure and mixed liquid, supercritical or gaseous states at high accuracy. Density is measured at the same conditions as viscosity, using a commercial

vibrating tube densimeter, enabling both closures of data gaps in density and direct conversion between kinematic and dynamic viscosity. The total uncertainty target of the facility is generally 0.1 % (95% confidence level), but this is not feasible in close vicinity to the critical point.

In this work, a description of the new facility and its measurement principle is presented.

2. Experimental Methodology

Quantifying the resistance to flow through a capillary is one of the most common and oldest principles for viscosity measurements [14, 15]. In 2004 [16], Berg described a Quartz Capillary Flow Meter (QCFM) for the measurements of gas flow rates with an uncertainty of less than 0.03 % at the National Institute of Standards and Technology (NIST). Berg also introduced a hydrodynamic model based on the Hagen–Poiseuille equation with relevant correction factors. The idea, after several modifications [17-21], was extended from using the flow meter as a single viscometer for absolute measurements to introduction of a two-capillary viscometer based on ratio measurements at low densities in the temperature range from 200 to 400 K with uncertainty ranging between 0.024% and 0.077 %. However, measurement of flow rate is required independently. Using the viscosity of helium calculated *ab initio* [22] as reference viscosity is recommended for the ratio measurements due to the high accuracy of current molecular dynamics methods. Applying the underlying principles introduced by Berg [16] and May [20] to build a modified two capillary system to measure viscosity of pure and mixed gases at high accuracy and high density is the main objective of this research work.

2.1 Fluid Dynamic Model

The principle of the capillary viscometers is based on Hagen–Poiseuille equation. The volumetric flow rate Q for an incompressible and Newtonian fluid in laminar flow through a capillary tube with internal radius r and length L is determined from [23]:

$$Q = \frac{\pi r^4 \Delta P}{8\eta L} = \frac{\pi r^4 (P_1 - P_2)}{8\eta L}, \quad \text{Eq. 1}$$

$$Q = \frac{\dot{n}}{\rho_m}. \quad \text{Eq. 2}$$

Here ΔP is the pressure drop, P_1 and P_2 are pressures at inlet and outlet of the capillary, respectively, η is the dynamic viscosity of the fluid, r is the inner diameter of the capillary, L is the capillary length, \dot{n} is molar flow rate, and ρ_m is the molar density. However, for a compressible fluid at temperature T and pressure P at locations z along the tube, the relation between pressure drop and viscosity can be found using the following relation:

$$\int_{P_1,T}^{P_2,T} \frac{\rho_m(T,P)}{\eta(T,P)} dP = \int_0^L -\frac{8\dot{n}}{\pi r^4} dz \quad \text{Eq. 3}$$

As discussed above, ratio viscosity measurements are employed in this work, where the known viscosity of helium at low pressure and 25 °C is used as a reference

[18]. Helium should be measured just after or before the test gas, such that capillary geometry effects are canceled out. However, for liquids and fluids in dense phase the ideal gas law is no longer applicable. As will be further discussed below, we will in our case use two-capillary viscometers, where the upstream capillary is at test pressure and temperature, and the downstream reference capillary operates at a constant low pressure (around 0.1 MPa) and reference temperature 298.15 K. The following working equation can be defined to estimate the viscosity of the test fluid, $\eta_{P,T}^{fld}$:

$$\eta_{P,T}^{fld} = \eta_{0,298}^{He} \left(\frac{\eta_{0,T}^{He}}{\eta_{0,298}^{He}} \right)_{ab\ initio} \left(\frac{\eta_{P,T}^{He}}{\eta_{0,T}^{He}} \right) \times \left(\frac{\eta_{0,298}^{fld}}{\eta_{0,298}^{He}} \right) (R_{T,298}^{fld,He})_{P,0} \quad \text{Eq. 4}$$

This equation includes five factors:

- 1) $\eta_{0,298}^{He}$: viscosity of helium at zero density and 298.15 K which is calculated with an *ab initio* method from quantum mechanics and statistical mechanics, with uncertainty less than 0.01 %.
- 2) $\left(\frac{\eta_{0,T}^{He}}{\eta_{0,298}^{He}} \right)_{ab\ initio}$: is the temperature-dependent ratio for the viscosity of He at 298.15 K and desired temperature T which is calculated *ab initio* with uncertainty less than 0.01 % in the range 200 K < T < 400 K.
- 3) $\left(\frac{\eta_{P,T}^{He}}{\eta_{0,T}^{He}} \right)$: the temperature-dependent ratio for He viscosity at desired pressure P and the zero density. This could be obtained with the two-capillary viscometer by setting both baths at temperature T and operating the upstream capillary first at low pressure and then at high pressure P .
- 4) $\left(\frac{\eta_{0,298}^{fld}}{\eta_{0,298}^{He}} \right)$: a reference value for the viscosity ratio, measured at 298.15 K for both He and test fluid.
- 5) $R_{T,298}^{fld,He}$: measurement of the temperature-dependent ratio of viscosity ratios which is determined from:

$$(R_{T,298}^{fld,He})_{P,0} = \frac{\left(\frac{\eta_{P,T}^{fld}}{\eta_{0,T}^{fld}} \right)}{\left(\frac{\eta_{P,T}^{He}}{\eta_{0,T}^{He}} \right)} \quad \text{Eq. 5}$$

3. Experimental Infrastructure- Apparatus description

A simplified schematic of the viscometer is shown in Figure 1. Two-capillary viscometer principle is based on measuring the flow rate of the fluid flowing through the capillary tube and the pressure differential between capillary's ends. The new design is employing a new configuration, with a total of 2×2 coiled capillaries with different inner diameters to cover variation of fluid properties corresponding to the wide range of

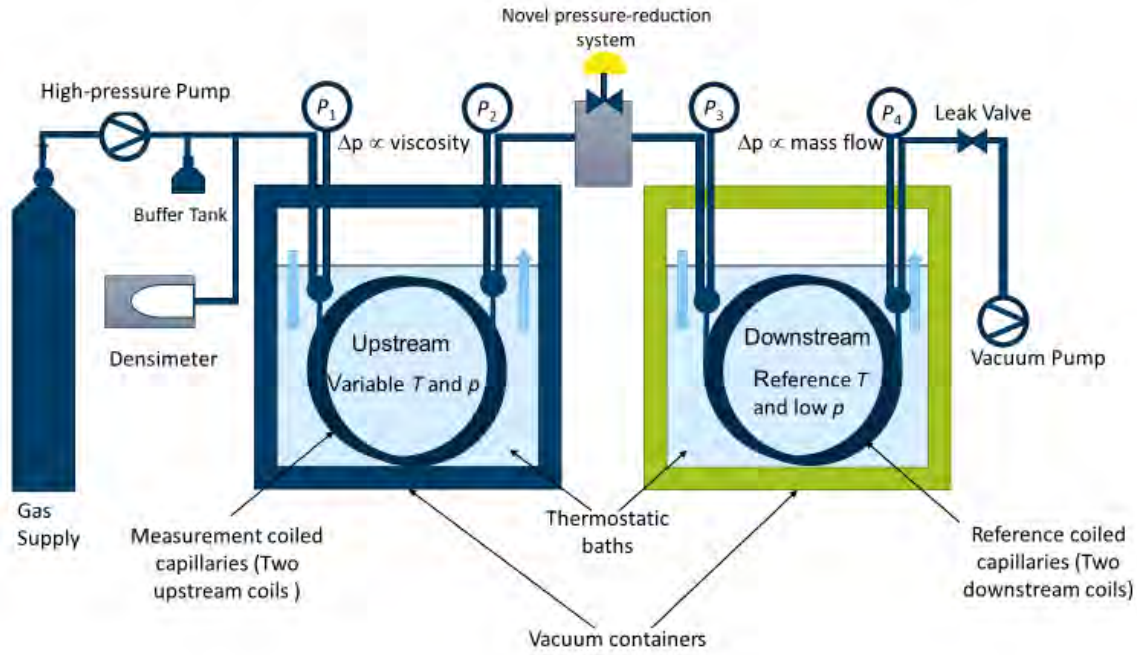


Figure 1: A simplified schematic of two- capillary viscometer.

temperatures and pressure for which it is specified. The pressure and temperature of the capillaries are precisely controlled. Their temperatures are controlled using thermostatic baths. Further, the containers with the capillaries are vacuum insulated to decrease heat loss to the surroundings and provide high temperature uniformity. Precise temperature control is important because the viscosity variations with temperature are significant. Since, the apparatus is comprised of different parts and complex processes, as illustrated in the 3-D sketch of Figure 2, the following section will discuss the main functions of the setup in more detail: 1) capillaries design and configuration, 2) high pressure gas source, 3) pressure and flow control, 4) Pressure measurements, 5) temperature measurements and control, 5) mass flow calibration, 6) density measurements.

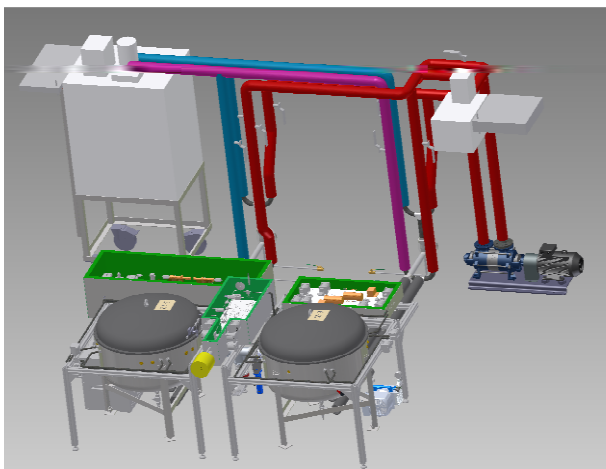


Figure 2: 3-D sketch of the facility

3.1 Capillaries Design and Configuration

The capillary tubes are the core components of the viscometer as measurements of the pressure drop across

the capillaries are used to calculate the viscosity. For this purpose, capillaries made of fused silica are used. The capillary tubes have an outer diameter of 1/32" and are coated with polyimide for mechanical protection. One difference compared with previous two-capillary setups is the possibility to use in total 4 (2×2) different capillary configurations. There are two coiled capillaries at measurement conditions (upstream) and two coiled capillaries at reference condition (downstream), but only a single measurement capillary and a single reference capillary are used simultaneously. The two measurement capillaries, with an inner diameter of 75 and 200 μm, are at the measurement temperature and with the test fluid at the measurement pressure. The other two capillaries have an inner diameter of 250 and 500 μm and are used for measurements at reference temperature (298.15 K) and at low pressure, normally around atmospheric. By using different combinations of these four capillaries, viscosity can be measured for a wide range of temperatures, pressures and different fluids at flow rates and pressure drops that minimize the impact of the various uncertainty terms.

Table 1: Geometric parameters for capillary coils.

Capillary No.	Cap. 1	Cap. 2	Cap. 3	Cap. 4
Inner diameter (μm)	75	200	250	500
Outer diameter (μm)	794	794	794	794
No. of coils around stainless-steel grid	8.5	7.5	4.5	5.5
Capillary length (m):	13.225	11.671	7.009	8.563
Coil curvature radius (m), R_{curve} :	0.25	0.25	0.25	0.25

The capillary coil specifications are based on analysis of mass and volume flow, pressure drop, capillary diameter, temperature change, Dean number $De = Re \times \sqrt{r/R_{curve}}$ and Reynolds number $Re = 2M\dot{n}/$

$\pi r \eta(T, p)$), (where M is the molar mass) with respect to feasibility and uncertainty terms.

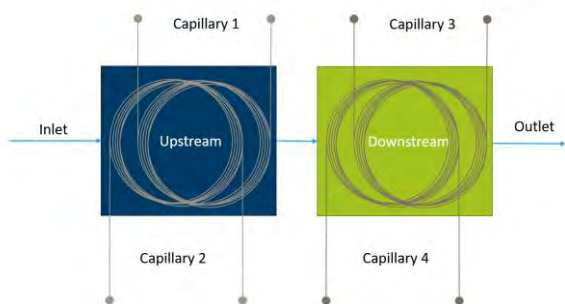


Figure 3: A Simplified schematic of 2x2 coiled capillaries with the two upstream coils and two reference coils.

In order to fit the capillaries to the other tubing of the viscometer, a metal sleeve was glued around each end of the capillaries using a special epoxy specified for the wide temperature range. The capillary mounts were tested with He and water at a wide range of pressures and temperatures before assembly. Each of these sleeves is fitted to a T-union, with the fluid inlet/outlet and pressure measurement system fitted to the other arms. The two capillaries of each container are mounted around a stainless-steel grid. Each grid with coiled capillaries in a horizontal orientation is immersed in a vacuum insulated thermostatic container in order to control their temperature. There are multiple high precision platinum resistance thermometers (PRTs) in the bath to allow temperature measurement and control and verify uniformity.

3.2 High pressure gas supply and upstream pressure control

The system is supplied with pure or mixed gas from gas cylinders. For investigation of mixtures, the composition must be known to high precision. Therefore, gravimetrically prepared mixed gases are provided from the CO₂Mix facility of SINTEF [24, 25]. The CO₂, CO₂ mixture, or He cylinder is connected to a high-pressure syringe pump (TOP-industry, PMHP model: 50-1000). The syringe pump pressurizes the system and keeps the upstream pressure P_1 constant during the measurements. The pump is connected to a buffer volume to stabilize the upstream pressure. After the target upstream pressure has been reached, the fluid flows through measurement capillary. The pump is linked to the densimeter and thereby measurement of density at the same pressure as viscosity is enabled.

3.3 Pressure and flow control

Since the pressure drop is proportional to the viscosity for laminar flow, a sophisticated pressure control system is employed, which can control the pressure at the desired values with high accuracy and stability. Four different critical pressure measurement systems are required. As discussed above, the pressure P_1 before the first two coils is controlled by the high-pressure syringe pump. The second critical pressure measurement is of P_2 at the outlet

of the measurement capillary, which together with P_1 provides the pressure drop through the measurement capillary and hence the viscosity of the fluid under test. The pressures before the reference capillary, P_3 , is controlled by a novel pressure-reduction system. The pressure of the measurement capillary can be from close to ambient to 100 MPa and the pressure for the reference capillary should normally be below 0.2 MPa and must be stabilized to high relative precision. No control valve was identified that could operate to the precision required for this large span of temperature differences and flow rates. Hence, controlling the pressure drop between the upstream and reference capillaries has been a challenge requiring innovation. The chosen solution includes a cascade system of six shut-off valves, five capillary coils with high flow resistance, and a control valve as illustrated in Figure 4. The general idea behind the design is that depending on the upstream pressure, which is controlled by the pump, and the flow, the shut-off valves will be closed or opened, directing the flow through a selection of capillary coils providing a high scalability in flow resistance. These five capillaries are similar to the capillaries used for the main viscosity measurements, but with smaller outer diameter (363 μm) and lengths (up to 5 m). The inner diameters vary between 25 and 75 μm . Hence, the pressure is reduced to an acceptable value for the control valve to reduce the pressure further down to the specified value. The fourth pressure system is the pressure drops across the reference capillary, the difference between P_3 and P_4 in Figure 2, is regulated by a variable leak valve (VAT Series 590) at the outlet, connected to a vacuum pump downstream. The pressure drop through the reference coils is a function of the flow and should be maximum 0.2 MPa. This pressure drop corresponds to a mass flow which can be calculated through a fluid specific calibration, which will be further explained in mass flow calibration section.

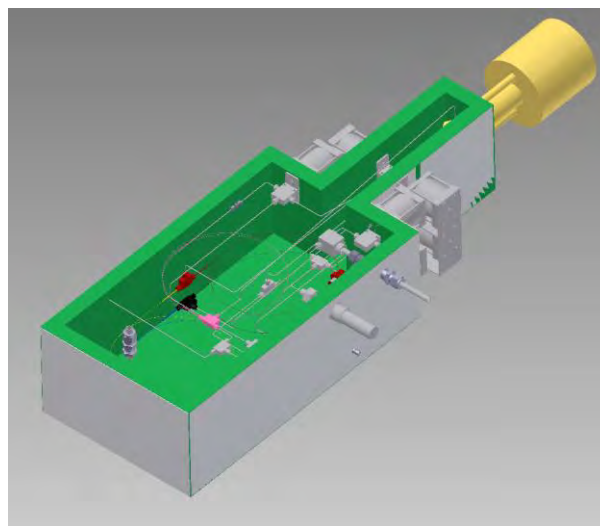


Figure 4: A 3-D sketch of the pressure control system between high- and low-pressure coils to reduce pressure to 0.2 MPa

3.4 Pressure measurements

A 3-D sketch of the pressure measurement system for P_1 and P_2 is shown in Figure 5. The pressure measurements

of P_1 and P_2 are performed using arrays of custom-made precision pressure transmitters with different full-scale pressures of 2.1, 6.9 and 13.8 MPa (Paroscientific) and 100 MPa (Keller) are used. This assortment in full-scale pressures allow for more precise low-pressure measurements, but also corrosion resistance must be taken into account, which is why arrays of two pressure transmitters with full-scale pressures of 6.9 MPa and 0.21 MPa (Paroscientific) are used for the pressure measurements of P_3 and P_4 . In addition, there are two auxiliary pressure transmitters, one for measuring the pressure of high-pressure syringe pump and one transmitter to assess the pressure before the control valve used in the customized pressure-reduction system.

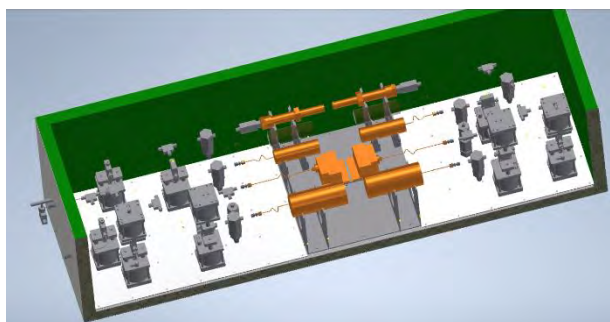


Figure 5: A 3-D sketch of the pressure measurement system-arrangement for P_1 and P_2

3.4 Temperature measurement and control

As mentioned, the experimental setup is designed for a process temperature range between 213.15 K and 473.15 K. The measurement capillaries are operating at a variable temperature and the temperature of the reference capillaries should normally be kept at reference temperature (298.15 K). However, as mentioned in Section 2.1, there is a need to keep both reference and measurement capillaries at the measurement temperature for full calibration with helium. The temperature of the measurement and reference capillaries are controlled by immersing them in circulating and thermo-stated liquids inside vacuum-insulated containers. Two Julabo thermostatic circulators with different temperature ranges are the main temperature providers to these two thermostated containers, The low-temperature circulator (FP89-HL) is employed between 213.15 K to 373K, using ethanol below its flash point temperature and water or silicon oil at the highest temperature. The high-temperature circulator (MA-12 w/ cooling water option) is used between 293.15 K to 423.15 K with water or silicon oil as working fluids.

The flow from the circulators are further temperature stabilized by using a small heater right before the inlet to the containers with the capillaries. The vacuum insulation, combined with careful design of the flow path in the setup, ensures high degree of thermal uniformity inside the tank.

The temperature is measured by several platinum resistance thermometers (PRTs). Two 25 Ω Standard

PRTs (SPRTs), calibrated with fixed point cells, are used for very high absolute accuracy. In addition, several PT100s are used to investigate uniformity and stability and enable control. In total, and based on experience from previous work [25], a thermal uniformity and accuracy of the order of 10 mK is expected.

3.5 Mass flow calibration

In order to calculate the viscosity, the mass flow of fluid must be known. In the two-capillary viscometer, reference capillary acts as a mass flow meter, if calibrated against the reference and test gas. For this purpose, a custom-made gravimetric setup is used. Mass flow is calibrated gravimetrically, by running a constant mass flow from a sphere into the reference capillary and measuring the flow duration and pressure before and after the reference coil during the flow period. In order to determine the mass of the gas that has flowed through the reference coil, the mass of the cylinder with content is carefully and very accurately determined before and after the flow experiment. The impact of various error sources, in particular varying buoyancy and nonideal repeatability /linearity of the scale, is reduced by applying the so-called ABBA scheme using a comparator [25-27]. The principle depends on comparing the object to be weighed (A) with a calibrated reference mass (B) by alternately placing the two objects on the comparator. In order to reduce impact of varying buoyancy, the objects should have similar shape and volume. In our case, object A is the sphere containing the test gas. B is a similarly the reference sphere which is empty. The mass of the two objects is made as equal as possible using calibrated weights, such that any impact of nonlinearity from the comparator is minimized. The weight of the gas that has left the sphere is hence found from the difference in mass of the calibrated weights used as well as the difference in comparator reading before and after the flow period.



Figure 6: Mass flow calibration measurements.

3.6 Density Measurement

The density measuring cell DMA HPM (oscillating tube) manufactured by Anton Paar can be used within a temperature range of 263.15 K (223.15 K with lower

accuracy) to 473.15 K and a pressure up to 100 MPa. During a density measurement, the sample is introduced into the tube, which is excited to vibrate at its characteristic frequency. This frequency changes depending on the test fluid's density. By a precise determination of the frequency and a mathematical conversion, the density of the sample can be derived. The density meter will be calibrated as a function of pressure and temperature using fluids with density known to high accuracy.

4. Experimental procedures

During ordinary viscosity measurements both the upstream and reference capillary are precisely controlled. The upstream capillary's set-point temperature is the measurement temperature T and the downstream capillary's set-point is the reference temperature 298.15 K. As mentioned above, helium should be measured just after or before the test gas and such that capillary geometry effects are canceled out. Then, either helium or test gas is flowed through the two capillaries while the pressure drops across them are measured. During a measurement, the pressures P_1 , P_3 , and P_4 are controlled to reach the desired measurement pressure (P_1) and flow and output pressure (P_3 and P_4), while the measurement of P_2 is used to estimate the viscosity. This is to a large degree automated using a LabVIEW control and data acquisition program. However, some manual operations are necessary.

Also, it is required that the measurement plan should be prepared in advance by modeling of the system using e.g. REFPROP, EOS-CG, in-house models or measurement data. This is required in order to estimate density, viscosity, and phase behavior. Measurement in the two-phase regions is meaningless, and solid-state regions must be avoided. In the pump and buffer tank, fluids of more than one component must be always kept in a single fluid phase during measurements in order to avoid changes in the composition of the fluid injected into the viscometer.

Further, an optimum flow must be determined to minimize uncertainty. The maximum flow rate is limited due to the need to be well within the laminar regime and to avoid a too large variation of fluid properties along the capillary. The minimum flow rate is limited by the accuracy of the pressure measurements.

In order to prepare for the measurements, the vacuum containers should be evacuated using vacuum pump (including a pre-vacuum pump and a turbo molecular pump for high vacuum pressure). The thermostatic systems are filled with the correct fluids and properly configured which are part of manual operations. Due to the long time required to heat and cool the containers, viscosity is measured isotherm per isotherm, from low temperatures to high temperatures. Then, after making sure the temperature of both containers are stable, automated measurements can be started. Desired pressures P_1 , P_3 , P_4 are regulated using the high pressure syringe pump, pressure reduction system, and leak valve. In order to improve measurement precision, the bias between inlet and outlet pressure transmitters is

measured before and after each measurement point. For these complex purposes, different valve configurations are involved. Finally, for each fluid to be investigated, the mass flow is calibrated.

5. Estimation of uncertainty

The overall combined standard uncertainties for the viscosity measurements $u_c(\eta(T, p, x))$ is determined from:

$$U_c(\eta(T, p, x)) = \sqrt{u(\eta)^2 + \left[\left(\frac{\partial \eta}{\partial T} \right)_{p,x} u(T) \right]^2 + \left[\left(\frac{\partial \eta}{\partial p} \right)_{T,x} u(p) \right]^2 + \left[\left(\frac{\partial \eta}{\partial x} \right)_{T,p} u(x) \right]^2} \quad \text{Eq. 6}$$

Here, $u(\eta)$, $u(T)$, $u(p)$ and $u(x)$ are the standard uncertainties in viscosity, temperature, pressure, and composition. One important contribution to the combined uncertainty is the viscosity measurements (first term of Eq. 6 $u(\eta)$), mainly related to the pressure drop along the capillaries. The facility has been designed for an overall combined expanded uncertainty ($k = 2$, with ~98% confidence) for the viscosity measurements, $U_c(\eta)$ is 0.1%, except close to the critical point. Complete uncertainty analysis will be provided with the experimental data in reference journal publications.

5. Conclusion

Acquiring high-quality data requires a well characterized experimental apparatus with a well-defined uncertainty level. A new ECCSEL ERIC facility is designed specifically for CCS to accurately measure viscosity and density of CO₂ and CO₂-rich mixtures. The apparatus includes a modified two-capillary viscometer with several novel solutions to enable high performance over a wide range in pressure and temperature. The experimental procedure relies on measuring the pressure drop through capillaries which is proportional to both the flow and the viscosity for laminar flow. Currently, the various systems of the facility have been assembled and are under final testing and calibration, and we hope to set up and run the measurements on the first fluids within 2021. For validation of the facility, the plan is to have pure CO₂ and N₂ among the first investigated fluids.

Acknowledgements

This publication has been produced with support from the research program CLIMIT and NCCS Centre, performed under the Norwegian research program Centres for Environment-friendly Energy Research (FME). The design and construction of the facility has been supported by ECCSEL Norway CCS RI Phase 1 under the INFRASTRUKTUR programme. The authors acknowledge the following partners for their contributions: Aker Carbon Capture, Allton, Ansaldo Energia, Baker Hughes, CoorsTek Membrane Sciences, Equinor, Fortum Oslo Varme, Gassco, KROHNE, Larvik

Shipping, Lundin Norway, Norcem, Norwegian Oil and Gas, Quad Geometrics, Stratum Reservoir, Total, Vår Energi, Wintershall DEA, and the Research Council of Norway (225868, 257579/E20 and 280394). Markus Hunka is acknowledged for his effort on the control system.

References

- [1] S. Peletiri, N. Rahmanian, and I. Mujtaba, "CO₂ pipeline design: a review," *Energies*, vol. 11, no. 9, p. 2184, 2018.
- [2] Y. Tan, W. Nookuea, H. Li, E. Thorin, and J. Yan, "Property impacts on Carbon Capture and Storage (CCS) processes: A review," *Energy Conversion and Management*, vol. 118, pp. 204-222, 2016.
- [3] S. T. Munkejord, M. Hammer, and S. W. Løvseth, "CO₂ transport: Data and models—A review," *Applied Energy*, vol. 169, pp. 499-523, 2016.
- [4] J. M. Nordbotten, M. A. Celia, and S. Bachu, "Injection and storage of CO₂ in deep saline aquifers: analytical solution for CO₂ plume evolution during injection," *Transport in Porous Media*, vol. 58, no. 3, pp. 339-360, 2005.
- [5] M. J. Patel, E. F. May, and M. L. Johns, "High-fidelity reservoir simulations of enhanced gas recovery with supercritical CO₂," *Energy*, vol. 111, pp. 548-559, 2016.
- [6] J. R. Wilkinson, A. Leahy-Dios, G. F. Teletzke, and J. L. Dickson, "Use of CO₂ containing impurities for miscible enhanced oil recovery," in *International Oil and Gas Conference and Exhibition in China*, 2010: Society of Petroleum Engineers.
- [7] B. Wetenhall *et al.*, "Impact of CO₂ impurity on CO₂ compression, liquefaction and transportation," *Energy Procedia*, vol. 63, pp. 2764-2778, 2014.
- [8] H. Li, Ø. Wilhelmsen, Y. Lv, W. Wang, and J. Yan, "Viscosities, thermal conductivities and diffusion coefficients of CO₂ mixtures: Review of experimental data and theoretical models," *International Journal of Greenhouse Gas Control*, vol. 5, no. 5, pp. 1119-1139, 2011, doi: 10.1016/j.ijggc.2011.07.009.
- [9] S. W. Løvseth, "ImpreCCS: Lower CCS cost and risk through better CO₂ viscosity and thermal conductivity knowledge." [Online]. Available: <https://blog.sintef.com/sintefenergy/impreccs-lower-ccs-cost-risk-co2-viscosity-thermal-conductivity/>
- [10] I. Al-Siyabi, "Effect of impurities on CO₂ stream properties," Heriot-Watt University, 2013.
- [11] M. Nazeri, A. Chapoy, R. Burgass, and B. Tohidi, "Viscosity of CO₂-rich mixtures from 243 K to 423 K at pressures up to 155 MPa: New experimental viscosity data and modelling," *The Journal of Chemical Thermodynamics*, vol. 118, pp. 100-114, 2018.
- [12] H. Li, Ø. Wilhelmsen, and J. Yan, "Properties of CO₂ Mixtures and Impacts on Carbon Capture and Storage," *Handbook of Clean Energy Systems*, pp. 1-17, 2015.
- [13] "ECCSEL ERIC." <http://www.eccsel.org/> (accessed).
- [14] J. L. M. Poiseuille, "Recherches expérimentales sur le mouvement des liquides dans les tubes de très petits diamètres; I. Influence de la pression sur la quantité de liquide qui traverse les tubes de très petits diamètres," *C. R. Acad. Sci.*, vol. 11, pp. 961-67, 1840.
- [15] J. L. M. Poiseuille, "Recherches expérimentales sur le mouvement des liquides dans les tubes de très petits diamètres; IV. Influence de la température sur la quantité de liquide qui traverse les tubes de très petits diamètres.," *C. R. Acad. Sci.*, vol. 12, pp. 112-15, 1841.
- [16] R. F. Berg, "Quartz capillary flow meter for gases," *Review of scientific instruments*, vol. 75, no. 3, pp. 772-779, 2004.
- [17] R. F. Berg, "Simple flow meter and viscometer of high accuracy for gases," *Metrologia*, vol. 42, no. 1, p. 11, 2005.
- [18] R. F. Berg, E. F. May, and M. R. Moldover, "Viscosity ratio measurements with capillary viscometers," *Journal of Chemical & Engineering Data*, vol. 59, no. 1, pp. 116-124, 2013.
- [19] R. F. Berg and M. R. Moldover, "Recommended viscosities of 11 dilute gases at 25 °C," *Journal of Physical and Chemical Reference Data*, vol. 41, no. 4, p. 043104, 2012.
- [20] E. F. May, M. R. Moldover, R. F. Berg, and J. J. Hurly, "Transport properties of argon at zero density from viscosity-ratio measurements," *Metrologia*, vol. 43, no. 3, p. 247, 2006.
- [21] E. F. May, R. F. Berg, and M. R. Moldover, "Reference viscosities of H₂, CH₄, Ar, and Xe at low densities," *International Journal of Thermophysics*, vol. 28, no. 4, pp. 1085-1110, 2007.
- [22] J. J. Hurly and M. R. Moldover, "Ab initio values of the thermophysical properties of helium as standards," *Journal of research of the National Institute of Standards and Technology*, vol. 105, no. 5, p. 667, 2000.
- [23] W. A. Wakeham, "Measurement of the transport properties of fluids," *Experimental thermodynamics*, 1991.
- [24] H. Jacob Stang, S. W. Løvseth, S. Ø. Størset, B. Malvik, and H. Rekstad, "Accurate Measurements of CO₂ Rich Mixture Phase Equilibria Relevant for CCS Transport and Conditioning," *Energy Procedia*, vol. 37, pp. 2897-2903, 2013.
- [25] S. F. Westman, H. G. J. Stang, S. W. Løvseth, A. Austegard, and S. Ø. Størset, "Vapor-liquid equilibrium data for the carbon dioxide and nitrogen (CO₂ + N₂) system at the temperatures 223, 270, 298 and 303 K and pressures up to 18 MPa," *Fluid Phase Equilibria*, vol. 409, pp. 207-241, 2016, doi: <http://dx.doi.org/10.1016/j.fluid.2015.09.034>.
- [26] C. M. Sutton and M. T. Clarkson, "A General Approach to Comparisons in the Presence of Drift," *Metrologia*, vol. 30, no. 5, p. 487, 1994. [Online]. Available: <http://stacks.iop.org/0026-1394/30/i=5/a=004>.
- [27] "Weights of classes E₁, E₂, F₁, F₂, M₁, M₁₋₂, M₂, M₂₋₃ and M₃. Part 1: Metrological and technical requirements," Organisation Internationale de Métrologie Légale (OIML), 2004.

MOLECULAR TO PROCESS SCALE: A REVIEW OF HOLISTIC DIRECT AIR CAPTURE CONTACTOR DESIGN

Quirin Grossmann¹, Valentina Stampi-Bombelli¹, Marco Mazzotti^{1*}

¹ETH Zurich, Institute of Energy and Process Engineering, Zurich, Switzerland

* Corresponding author e-mail: marco.mazzotti@ipe.mavt.ethz.ch

Abstract

Air-sorbent contactors are an essential part of direct air capture processes. Their design can have a great influence on the process energy demand and efficiency. Three aspects of this design have been identified and differentiated by length scale. On a molecular scale, the adsorption sites are defined by the chemisorbent-containing molecules, generally amines. The support of these amines defines the second length scale and plays an important role in mass and heat transfer. These two length scales have been studied in detail in academic literature and a short overview is given. The third length scale is the process scale, or contactor module scale. Together with the first two length scales, it is necessary to characterize the third to perform adequate process optimization. Research on this third length scale is scarce in academic literature, though it has been researched in industry. The direction of research tends towards structured sorbents due to their ability to process large volumes of air and academic research in this area should be expanded.

Keywords: Direct Air Capture, Amines, CO₂ Capture, Contactor Design

1. Introduction

Anthropogenic carbon dioxide CO₂ and other greenhouse gases (GHGs) have to date caused a temperature increase of approximately 1°C [1]. Following the current path of emissions, humankind is likely to increase this above the 2°C target set by the Paris Agreement in 2015 [2]. Consequently, an increasing number of countries have pledged to meet net-zero CO₂ emissions targets within the next 40 years. This will entail the deployment of negative emission technologies (NETs) in addition to conventional mitigation options such as reduction of emissions of GHGs [3]. A key component of these NETs is the direct capture of CO₂ from ambient air (*Direct Air Capture*, DAC) combined with the permanent storage of the collected CO₂ [4]. This offers the ability to offset the emissions from hard-to-decarbonize sectors such as agriculture, aviation, and the chemical industry, as well as offsetting emissions from the past.

DAC is currently achieved through absorption in aqueous basic solutions or through adsorption on solid sorbents [5]. The absorption of CO₂ in aqueous basic solutions is followed by a regeneration step at around 900°C to retrieve the bound CO₂ [6], [7]. In contrast, the regeneration of solid sorbents generally requires lower temperatures between 80 and 120°C [8], [9], [10]. Processes using solid sorbents therefore enable the use of lower quality heat, while additionally completely removing the need for the corrosive and volatile solvents used in absorption processes [11], [12].

Both processes face challenges to become economical. This is due to their current energy inefficiency and the low value of the product [13]. Aside from the unavoidable thermodynamic inefficiencies, which stem

from the low concentration of CO₂ in air, the air-sorbent contactor is the main source of inefficiencies in the DAC process. The energy required for the process is dominated by parasitic heat losses caused by the heating of the support material and sorbent during regeneration [14]. The large amount of air required for the process and the corresponding pressure drop also contributes a sizeable amount to the energy requirements [15], [16], [17]. On a smaller level, mass and heat transfer can affect cycle times and therefore influence the productivity of the process. It follows that there is a need to design and optimize the contactor with respect to the aforementioned aspects.

2. Contactor Design from Molecular to Module Scale

2.1 Molecular Scale

Much research has focused on developing materials for carbon capture applications. Commercial zeolites, such as 13X, are a material of choice for post-combustion capture from flue gases of between 4-15% CO₂ concentration due to their high selectivity towards CO₂ and process robustness [18]. Adsorption occurs on these materials through physisorption within the pores. However, the same adsorption sites have a higher selectivity towards H₂O. Pre-drying the gas therefore offers more efficient processing [19].

In this respect, materials for post-combustion differ significantly from materials capture for DAC applications. In comparison to industrial flue gas, ambient air contains much higher H₂O to CO₂ ratios, making pre-drying highly uneconomical. Materials for DAC processes must therefore be unaffected by the

presence of H₂O, while maintaining a high selectivity towards CO₂.

Research has focused on amine functionalized materials due to their favorable CO₂ uptake in the presence of H₂O. In contrast to zeolites and physisorbents, the adsorption mechanism on these materials is through chemisorption, the formation of a chemical bond with the primary and secondary amine groups. Different reaction pathways have been suggested in hydrous and anhydrous conditions, as depicted in figure 1 [5]. Adsorption via this mechanism is not only highly selective towards CO₂, but also enhanced in the presence of H₂O. In the absence of H₂O, two adjacent amine sites are required to bind a CO₂ molecule, whereas the presence of H₂O enables each amine site to bind a CO₂ molecule.

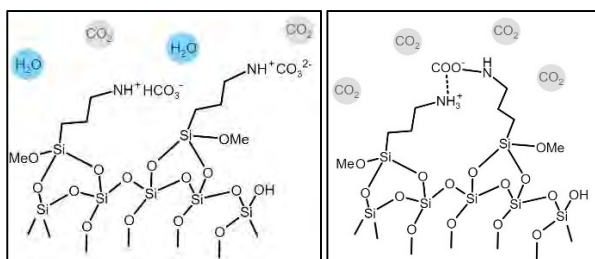


Figure 1: CO₂ capture mechanisms on silica supported amine sorbents with H₂O (left) and without H₂O (right)

As amine molecules are generally in liquid form under ambient conditions, they are tethered to solid supports to give the advantages of adsorption processes. Tethering can occur through physical impregnation via hydrogen bridges or covalent bonding, also known as grafting. Grafted amine-containing molecules are generally smaller than impregnated molecules, therefore the CO₂ adsorption capacity is generally lower [20]. However, due to the covalent bond, grafted molecules are less prone to leaching during the adsorption and desorption processes [24]. Typical materials often used for impregnation are poly(ethylenimine) (PEI) and tetraethylpentamine (TEPA), whereas silane containing molecules, such as aminopropyltrimethoxysilane (APTMS), are used for grafting. Both procedures can be accomplished in one step, though physical impregnation is generally considered the easier process [20].

2.2 Support Scale

The amine-containing molecules mentioned above must be supported on a solid material to remain in the solid phase at ambient and process conditions. The support characteristics can profoundly affect process performance. These characteristics include material, surface area, and pore structure.

The supports currently proposed in research can be divided to a large extent into oxide materials and metal-organic frameworks (MOFs). MOFs can offer extremely high adsorption capacities and are, therefore, promising candidates for DAC processes. However, their relative novelty means that more research is needed to make them industrially viable for DAC [21]. Oxide materials have been comparatively well studied and offer tunable high surface areas, pore sizes, and pore volumes [22].

Heat capacity and conductivity of the support directly influence the heat needed for regeneration. During the regeneration step, the support material is unavoidably heated together with the adsorbing molecules. This parasitic heat loss can make up almost 40% of the total energy requirement of the process [14]. A low heat capacity of the sorbent is, therefore, desirable in terms of process energy efficiency. High conductivity enables fast heating of the sorbent and, therefore, a shorter regeneration time, increasing productivity.

$$Productivity = \frac{CO_2 \text{ captured}}{\text{adsorbent volume} \times \text{process time}}$$

Isotherms define the thermodynamic equilibrium adsorption capacity at a certain temperature as a function of the partial pressure [23]. They are critical in calculating the equilibrium working capacity of a sorbent for a specific process. They correlate directly with the amount of accessible adsorption sites of a sorbent and are generally presented per mass of sorbent. For the design of process equipment, however, the per volume of sorbent values can be of more interest. In the case of amine-functionalized sorbents, the accessible adsorption sites are the accessible amine groups on the surface.

Generally, the surface area of the support directly affects the adsorption capacity per unit volume of sorbent (volumetric capacity). Intuitively, a high specific surface area is preferable to enhance the volumetric loading of the adsorbing molecules. However, it has been found that that for amine-functionalized oxides, pore size, and volume play a more important role in the number of amines present on the surface [27].

Pore size plays an important role in mass transfer. In the case of DAC processes, mass transfer is a measure of how fast CO₂ is transported to the adsorbing molecules. Faster mass transfer is desirable as shorter residence times are possible, thereby decreasing process time and increasing productivity [25]. Mass transfer can be tuned by adjusting the amount of amine molecules on the support [26]. In general, an optimum must be found between fast mass transfer and high volumetric loading, as higher loadings tend to lead to clogged pores and slow mass transfer [27]. Large pores are preferable from a mass transfer perspective and larger surface amine densities have been observed for such materials even with lower surface areas [24].

2.3 Contactor Module Scale

The above-mentioned support materials can come in various geometric configurations. The most common are honeycomb monoliths, pellets, and foams. The geometries can be either made of the support material or a different material which is then coated with the support material. Each configuration has its advantages and disadvantages, which make them more or less suited for individual applications.

Honeycomb monoliths have been used in catalysis for applications that require low pressure drops and high throughputs [28]. They have suffered from high mass transfer resistance, but recently thinner walls have

overcome this setback [29]. Compared to pellets, they have a low volumetric capacity [17].

Pellets generally offer high mass transfer rates and high volumetric capacities but suffer from higher pressure drops especially at high flow rates [17]. They are generally cheaper to produce, easier to handle, and offer a high flexibility in further geometric configurations (packed column, radial flow reactors, thin manifold beds etc.). Some examples are given in the next section.

Foams are characterized by high mass transfer due to the turbulence produced by the tortuous channels [29]. The pressure drop is, therefore, increased compared to honeycomb monoliths but decreased compared to pellets due to higher porosity. In terms of mass transfer and pressure drop, they have been found to be inferior to honeycomb monoliths [30].

3. Contemporary Contactor Design

There are many contactor configurations used or proposed for adsorption and filtration process conditions similar to those experienced in DAC. Some of these have been adapted to be used in DAC processes, whereas some may still be evaluated. This section gives an overview of some contactor designs that are already used for or could possibly fulfill the specifications of a DAC process. In all the figures, the blue arrows show the direction of the gas flow.

3.1 Diesel Particle Filters

Diesel particle filters are used to remove the soot particles from the exhaust gas of internal combustion engines. They must deal with high throughputs and offer low back pressures.

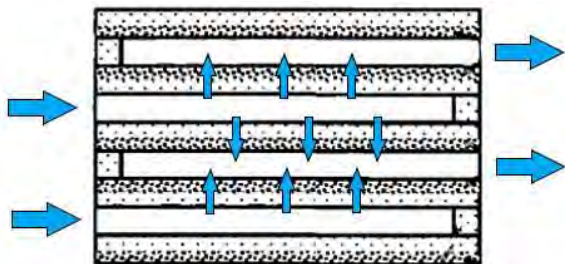


Figure 2: Diesel particle filter as suggested by Beall et al. [31].

3.2 Hollow Polymeric Fibres

Hollow fibres made of a porous polymer matrix with embedded sorbent particles offer a low pressure drop contactor for post combustion CO₂ capture. The inner duct can be used as a novel heat integration strategy for rapid temperature swing regeneration [32].

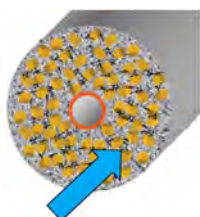


Figure 3: Porous polymer fibres as suggested by Lively et al. [32].

3.3 Radial flow adsorbers

Radial flow adsorbers have been used for a wide variety of applications and offer lower pressure drops than conventional packed beds, while still using conventional pellet sorbents. Yu and Brillman [13] suggested its use for DAC capture purposes due to high mass transfer and low pressure drop.

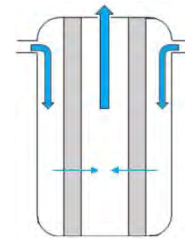


Figure 4: Radial flow adsorber suggested by Yu and Brillman [13].

3.4 Functionalized Honeycomb Monoliths

Honeycomb monoliths have been extensively used as catalyst supports in high throughput, low back pressure applications. These qualities also make them interesting for DAC applications, with MOF functionalized monoliths [34] and amine-functionalized monoliths [28] proposed in literature and in industry [35].

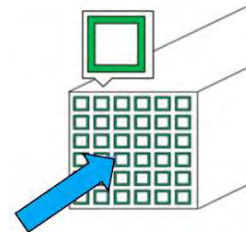


Figure 5: MOF functionalized (green) honeycomb monolith as proposed by Darunte et al. [34].

3.5 Thin manifold pellet bed

A thin bed configuration with the goal of reducing pressure drop of a pellet bed and optimizing volumetric loading within a contactor module has been patented by Climeworks [36].

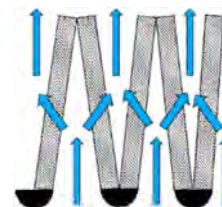


Figure 5: Manifold configuration of a pellet bed as proposed by Climeworks [36].

4. Outlook

Research in direct air capture has been mainly driven by start-ups, such as Climeworks, Global Thermostat, and Carbon Engineering. Open academic research has focused on creating novel materials, but there is a significant lack of research into optimal contactor configurations for typical DAC processes. Additionally, materials and process research has to date been conducted mostly independently, even though these are

inherently coupled. Filling the gap in academic research and combining the two main areas of DAC research is essential to further its standpoint in a net-zero future.

Acknowledgements

This work was supported by the Swiss National Science Foundation grant number 197221.

References

- [1] Masson-Delmotte, V.; Zhai, P.; Pörtner, H.-O.; Roberts, D.; Skea, J.; Shukla, P. R.; Pirani, A.; Moufouma-Okia, W.; Péan, C.; Pidcock, R., et al. Summary for policymakers. *Global Warming of 1.5°C. An IPCC Special Report on the impacts of global warming of 1.5°C above pre-industrial levels and related global greenhouse gas emission pathways, in the context of strengthening the global response to the threat of climate change, sustainable development, and efforts to eradicate poverty*, 2018, 1, 1–32.
- [2] United Nations Framework Convention on Climate Change (UNFCCC), Adoption of the Paris Agreement. 2015.
- [3] Kriegler, E.; Bauer, N.; Popp, A.; Humpenöder, F.; Leimbach, M.; Strefler, J.; Baumstark, L.; Bodirsky, B. L.; Hilaire, J.; Klein, D., et al. Fossil-fueled development (SSP5): an energy and resource intensive scenario for the 21st century. *Global Environmental Change*, 2017, 42, 297–315.
- [4] Negative emission technologies: what role in meeting Paris agreement targets?, *EASAC policy report 35*, 2018.
- [5] Sanz-Pérez, E. S.; Murdock, C. R.; Didas, S. A.; Jones, C. W. Direct Capture of CO₂ from Ambient Air. *Chem. Rev.*, 2016, 116, 11840–11876.
- [6] Baciocchi, R.; Storti, G.; Mazzotti, M. Process design and energy requirements for the capture of carbon dioxide from air. *Chem. Eng. Process. Process Intensif.* 2006, 45, 1047–1058.
- [7] Keith, D.W.; Holmes, G.; St. Angelo, D.; Heidel, K. A Process for Capturing CO₂ from the Atmosphere. *Joule*, 2018, 2, 1573–1594.
- [8] Serna-Guerrero, R.; Belmabkhout, Y.; Sayari, A. Further investigations of CO₂ capture using triamine-grafted pore-expanded mesoporous silica. *Chem. Eng. J.* 2010, 158, 513–519.
- [9] Gebald, C.; Wurzbacher, J. A.; Tingaut, P.; Zimmermann, T.; Steinfeld, A. Amine-Based Nanofibrillated Cellulose as Adsorbent for CO₂ Capture from Air. *Environ. Sci. Technol.* 2011, 45, 9101–9108.
- [10] Lee, J. J.; Yoo, C.-J.; Chen, C.-H.; Hayes, S. E.; Sievers, C.; Jones, C. W. Silica-Supported Sterically Hindered Amines for CO₂ Capture. *Langmuir* 2018, 34, 12279–12292.
- [11] Rochelle, G. T. Thermal degradation of amines for CO₂ capture. *Curr. Opin. Chem. Eng.* 2012, 1, 183–190.
- [12] Fredriksen, S.; Jens, K.-J. Oxidative Degradation of Aqueous Amine Solutions of MEA, AMP, MDEA, Pz: A Review. *Energy Procedia* 2013, 37, 1770–1777.
- [13] Yu, Q.; Brilman, D. Design strategy for CO₂ adsorption from ambient air using a supported amine-based sorbent in a fixed bed reactor. *Energy Procedia* 2017, 114, 6102–6114.
- [14] Kulkarni, A. R.; Sholl, D. S. Analysis of Equilibrium-Based TSA Processes for Direct Capture of CO₂ from Air. *Ind. Eng. Chem. Res.* 2012, 51, 8631–8645.
- [15] Zhang, W.; Liu, H.; Sun, C.; Drage, T. C.; Snape, C. E. Capturing CO₂ from ambient air using a polyethyleneimine-silica adsorbent in fluidized beds. *Chem. Eng. Sci.* 2014, 116, 306–316.
- [16] Brilman, D.; Veneman, R. Capturing Atmospheric CO₂ Using Supported Amine Sorbents. *Energy Procedia* 2013, 37, 6070–6078.
- [17] Rezaei, F.; Webley, P. Structured Adsorbents in Gas Separation Processes. *Sep. Purif. Technol.* 2010, 70, 243–256.
- [18] Chue, K. T.; Kim, J. N.; Yoo, Y. J.; Cho, S. H.; Yang, R. T. Comparison of Activated Carbon and Zeolite 13X for CO₂ Recovery from Flue Gas by Pressure Swing Adsorption. *Ind. Eng. Chem. Res.* 1995, 34, 591–598.
- [19] Hefti, M.; Mazzotti, M. Postcombustion CO₂ Capture from Wet Flue Gas by Temperature Swing Adsorption. *Ind. Eng. Chem. Res.* 2018, 57, 15542–15555.
- [20] Didas, S.A.; Choi, S.; Chaikittisilp, W.; Jones, C.W. Amine-oxide hybrid materials for CO₂ capture from ambient air. *Acc. Chem. Res.* 2015, 48, 2680–2687.
- [21] Piscopo, C.G.; Loebbecke, S. Strategies to Enhance Carbon Dioxide Capture in Metal-Organic Frameworks. *ChemPlusChem*, 2020, 85(3), pp.538-547.
- [22] Harlick, P.J.; Sayari, A. Applications of pore-expanded mesoporous silica. 5. Triamine grafted material with exceptional CO₂ dynamic and equilibrium adsorption performance. *Industrial & Engineering Chemistry Research*, 2007, 46(2), pp.446-458.
- [23] Ruthven, D.M. Principles of adsorption and adsorption processes. John Wiley & Sons, 1984.
- [24] Lashaki, M.J.; Sayari, A. CO₂ capture using triamine-grafted SBA-15: The impact of the support pore structure. *Chem. Eng. J.*, 2018, 334, 1260-1269.
- [25] Bos, M. J.; Kroeze, V.; Sutanto, S.; Brilman, D. W. Evaluating regeneration options of solid amine sorbent for CO₂ removal. *Ind. Eng. Chem. Res.* 2018, 57(32), 11141-11153.
- [26] Gelles, T.; Rezaei F. Diffusion kinetics of CO₂ in amine-impregnated MIL-101, alumina, and silica adsorbents. *AIChE J.*, 2020, 66(1), e16785.
- [27] Zhang, H.; Goeppert, A.; Kar, S.; Prakash, G.S. Structural parameters to consider in selecting silica supports for polyethyleneimine based CO₂ solid adsorbents. Importance of pore size. *J. CO₂ Util.*, 2018, 26, pp.246-253.
- [28] Sakwa-Novak, M.A.; Yoo, C.J.; Tan, S.; Rashidi, F.; Jones, C.W. Poly(ethyleneimine)-Functionalized Monolithic Alumina Honeycomb Adsorbents for CO₂ Capture from Air. *ChemSusChem*, 2016, 9(14), pp.1859-1868.
- [29] Rezaei, F.; Webley, P. Optimum structured adsorbents for gas separation processes. *Chem. Eng. Sci.*, 2009, 64(24), pp.5182-5191.
- [30] Patcas, F.C.; Garrido, G.I.; Kraushaar-Czarnetzki, B. CO oxidation over structured carriers: A comparison of ceramic foams, honeycombs and beads. *Chem. Eng. Sci.*, 2007, 62(15), pp.3984-3990.
- [31] Beall, D. M.; Heibel, A. K.-E.; Tinghon, T. Low Pressure Drop Coated Diesel Exhaust Filter. US Patent Application 2007/0140928 A1, June 21, 2007.
- [32] Lively, R. P.; Chance, R. R.; Kelley, B. T.; Deckman, H. W.; Drese, J. H.; Jones, C. W.; Koros, W. J. Hollow Fiber Adsorbents for CO₂ removal from flue gas. *Ind. Eng. Chem. Res.* 2009, 48, 7314–7324.
- [33] Tian, Q.; He, G.; Wang, Z.; Cai, D.; Chen, L. A Novel Radial Adsorber with Parallel Layered Beds for Prepurification of Large-Scale Air Separation Units. *Ind. Eng. Chem. Res.* 2015, 54, 7502–7515.

- [34] Darunte, L. A.; Terada, Y.; Murdock, C. R.; Walton, K. S.; Sholl, D. S.; Jones, C. W. Monolith-Supported Amine-Functionalized Mg₂(dobpdc) Adsorbents for CO₂ Capture. *ACS Appl. Mater. Interfaces* 2017, 9, 17042–17050.
- [35] Eisenberger, P. Carbon Dioxide Capture/Regeneration Method Using Monolith. US Patent 9,227,153 B2, January 5, 2016.
- [36] Wurzbacher, J. A.; Repond, N.; Ruesch, T.; Sauerbeck, S.; Gebald, C. Low-Pressure Drop Structure of Particle Adsorbent Bed for Improved Adsorption Gas Separation Process. US Patent Application 2020/0001224 A9, January 2, 2020.

CSEM FOR CO₂ STORAGE – FEASIBILITY STUDY AT SMEAHEIA TO OPTIMISE ACQUISITION

Romina Gehrman¹, Anouar Romdhane², Joonsang Park³, Peder Eliasson²

¹ University of Southampton, Southampton, UK

² SINTEF, Trondheim, Norway

³ NGI, Oslo, Norway

* Corresponding author e-mail: r.a.gehrmann@soton.ac.uk

Abstract

In this work, we evaluate the use of controlled-source electromagnetics (CSEM) for CO₂ monitoring at Smeaheia, a possible candidate for future phases of the Norwegian full-scale CCS project. CSEM is sensitive to electrically resistive material replacing conductive pore water in the pore space, which enables to infer volumetric estimates of the injected CO₂ in the formation. CSEM is often used in combination with high-resolution seismic reflection data due to the sensitivity of the two methods to complementary physical properties. Here, we present a technique to optimise the CSEM survey parameters for efficient 4D surveying. Realistic synthetic models prior to and after injection are derived from reservoir modelling and converted to electrical resistivities. Inversion tests are carried out in 2D for the baseline and monitor cases considering realistic data errors. We show that the resistivity changes due to CO₂ injection can be monitored using CSEM. We discuss the optimal orientation of the receivers, frequency range and transmitter-receiver offset. We finally discuss a strategy for optimal survey design based on the sensitivity to the CO₂ plume.

Keywords: CO₂ storage, Smeaheia, CSEM, acquisition design

1. Introduction

An accurate and efficient monitoring strategy is essential for safe CO₂ storage in compliance with laws and regulations. The reliability of monitoring technology is also crucial for the public acceptance of CCS, especially in case of large-scale storage and import of CO₂ from other countries. The cost of a comprehensive monitoring program, covering the different phases of a storage project, however, could quickly become prohibitively high, if not carefully optimised. In this context, geophysical monitoring methods play a key role in any proposed measurement, monitoring, and verification (MMV) plan aiming to derive, from measured data, estimates of the spatial distribution of selected physical properties of the subsurface.

While seismic surveys will most likely be the backbone of any CO₂ storage geophysical monitoring program, controlled-source electromagnetics (CSEM) can be a valuable complement. By providing an additional, yet essential, earth parameter (electrical resistivity), CSEM contributes to significantly better-constrained estimates of the pressure and saturation changes caused by CO₂ injection, and mitigates uncertainties in seismic data interpretation. The improved capability of quantitative characterisation by combining seismic and CSEM will therefore reduce risks and support the development of better tailored, sparser (in time and space) geophysical surveys and will consequently help to reduce costs.

The resolution of CSEM is inherently lower than that of seismic and therefore resolution capabilities, time-lapse approaches, and optimum ways of combining seismic

and CSEM data should be carefully investigated. Time-lapse CSEM has not been used frequently in the past for CO₂ storage or hydrocarbon monitoring. While several synthetic studies have concluded that time-lapse changes are detectable and resolvable (e.g., Colombo and McNeice, 2013), acquisition must be done very carefully to achieve sufficient repeatability (Tietze et al., 2018). Several publications have investigated the sensitivity to production-induced reservoir changes, e.g., movement of the injected waterfront (e.g., Lien and Mannseth, 2008; Orange et al., 2009; Zach et al., 2009). They have shown that CSEM monitoring is feasible, i.e., the responses from production-induced changes in hydrocarbon saturation exceed the measurement uncertainty, at least for simple models of the evolving fluid distribution. However, the feasibility of time-lapse CSEM in realistic 3D reservoir geometry (e.g., based on seismic interpreted structure) has not been fully considered. Also, realistic, highly spatially variable small-scale changes of subsurface resistivity due to CO₂ injection have not been studied (Streich, 2016).

The use of CSEM imaging for onshore CO₂ sequestration sites has been evaluated in some studies (Grayver et al., 2014). Experience with marine CSEM for CO₂ sequestration monitoring, however, is very limited, and restricted to simple feasibility studies (Park et al., 2019; Shantsev et al., 2020, Morten and Bjørke, 2020) and a case study at Sleipner (e.g., Bøe et al., 2017) using real data monitor vintage.

Large research efforts have been made during the last decades to improve solving large-scale non-linear

problems. This has resulted in CSEM inversion becoming tractable in 3D (e.g., Amaya et al., 2016; Patzer et al., 2017). Much less attention is, however, given to survey design strategies which conceptually aims at selecting the data acquisition that optimally resolve the subsurface model parameters (accuracy/resolution) of interest. Standard procedures are often suggested, and data redundancy considered to mitigate issues related to data inadequacy, but may result in unnecessary additional costs. In this context, experimental design can be used to find the best trade-off between data value and data collection cost. An overview of the techniques that can be used is provided in Maurer et al., 2010. Examples of applications to electromagnetics surveying are given in Maurer et al., 2000, Roux and Garcia, 2014, and Romdhane and Eliasson, 2018.

In this work, we evaluate the use of CSEM for CO₂ monitoring at Smeaheia, a possible candidate for future phases of the Norwegian full-scale CCS project and analyse ways to optimise the survey design. In a first stage, the paper introduces the techniques used for CSEM inversion and for the acquisition design optimisation. The results from the synthetic study at Smeaheia are then described for the baseline and monitoring case (25 years after injection). Finally, the results from the optimal survey design analysis are presented and discussed in regard to electric field components, spatial distribution of instrumentation and signal frequency content.

2. Methodology

This section briefly describes the algorithm used for CSEM inversion and for the acquisition design analysis.

2.1 CSEM inversion

The code used to invert the synthetic data for this study is the freely available modelling and inversion MARE2DEM software that can model magnetotelluric and CSEM data in frequency domain and incorporate anisotropic resistivity models (Key, 2016). The forward modelling is performed in 2.5-D (Key and Oval, 2011) and adaptively refines the forward modelling grid for an optimum accuracy. The inversion is based on the Occam minimisation algorithm (Constable et al., 1987) with possibilities for incorporating available prior information and regularisation. The misfit function being minimised can be written as:

$$U = \|\mathbf{R}\mathbf{m}\|^2 + \|\mathbf{P}(\mathbf{m}-\mathbf{m}^*)\|^2 + \mu^{-1}\|\mathbf{W}(\mathbf{d}_{\text{obs}} - \mathbf{d}_{\text{cal}})\|^2$$

where \mathbf{m} is the model parameter vector for \log_{10} (resistivity) values, \mathbf{m}^* is the prior model vector describing available prior information which can be weighted with the non-zero diagonal values in \mathbf{P} . The diagonal matrix \mathbf{W} contains the inverse standard errors for the observed data \mathbf{d}_{obs} . The data fit (last term) is the difference of the observed to the calculated data \mathbf{d}_{cal} divided by their respective errors squared. \mathbf{R} denotes the model roughness regularisation. The Lagrange multiplier μ is used to trade-off the data fit against the other two

terms and is optimised automatically during the inversion.

2.2 Acquisition design

We quantify the quality of a given acquisition layout through the computation of the eigenvalue spectrum of the approximate Hessian on a defined target region.

The approximate Hessian can be defined as:

$$\mathbf{H}_a = \Re \{ \mathbf{J}^T \mathbf{C}_d \mathbf{J}^* \}$$

Where \Re denotes the real part of a complex number. The superscripts T and $*$ correspond to the ordinary matrix transpose and complex conjugate, respectively. \mathbf{C}_d is the data covariance matrix describing data uncertainties. \mathbf{J} is the Jacobian or sensitivity matrix including spatial derivatives which can be defined as:

$$\mathbf{J} = \frac{\partial \mathbf{d}_{\text{cal}}}{\partial \mathbf{m}}$$

To efficiently compute the eigenvalue spectrum of the approximate Hessian, randomised SVD can be used following the approach described in Halko et al., 2011 and Eliasson and Romdhane, 2017. General sensitivity in the dipole transmitter/receiver domain to changes in the model space can be performed in a selected target (Romdhane and Eliasson, 2018) which can be derived from reservoir modelling. In a CO₂ storage context, the target would correspond to the spatial evolution of the plume within the storage reservoir. The spectra corresponding to a selected data trace can then be analysed and compared to the reference spectrum (Maurer et al., 2010).

3. Smeaheia case study

3.1 Geology and injection scenario

A feasibility report on a full-scale CCS project in Norway (Gassnova, 2016) suggests the Smeaheia site, which is a fault block located east of the Troll gas field, north-west of Bergen, as one of the most viable storages in the Horda platform (Figure 1).

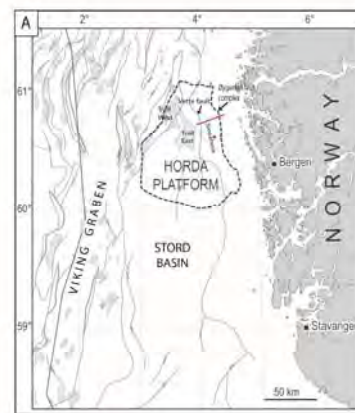


Figure 1: Location of the Smeaheia site. The red line depicts the location of the CSEM profile used in this study (modified from Dupuy et al., 2018).

Significant efforts in research and development targeting a better characterisation and monitoring concepts for

Smeaheia are conducted, since the site is considered a good candidate for future phases of the full-scale CCS.

The reservoir in Smeaheia consists of the Sognefjord, Krossfjord, and Fensfjord formations, which are well known in relation to the neighbouring Troll gas-producing field. The CO₂ injection is recommended to be done at 1200 to 1500 m depth in the Alpha structure located East of the Vette fault complex (Figure 1). More geological description of the reservoir is available in Dupuy et al., 2018.

3.2 Resistivity models

A reservoir modelling study carried out by the Northern Lights consortium considered the injection scenario in the Alpha structure with a CO₂ injection rate of 1.3 Mt/year for 25 years. In this injection scenario, both Vette and Øygarden faults are assumed to be sealing (no fault transmissibility), although this has been identified as a source of uncertainties at Smeaheia (Lothe et al. 2018; Mulrooney et al., 2020). The derived pressure and saturation maps can be used to build synthetic dynamic geophysical models describing key properties like elastic properties or resistivities. In our study, the saturation changes (see example in Figure 2) are converted to resistivity changes using Archie's relationship (Archie, 1942) with a saturation exponent equal to 2 and available information from CSEM survey data in the same area (Park et al., 2019).

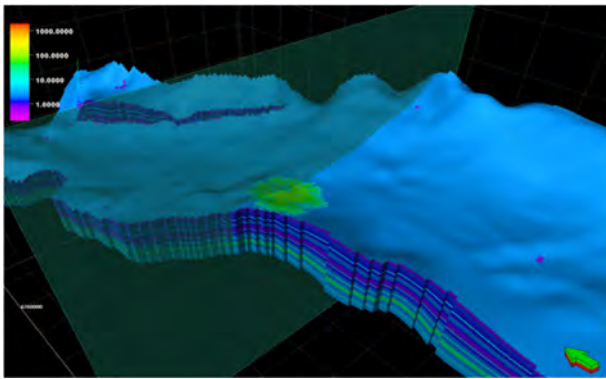


Figure 2: Reservoir saturation model after 25 years of injection (Park et al., 2019).

The resulting 2D resistivity models for the baseline (i.e., before any injection) and after 25 years of injection are displayed in Figure 3, with the effect of the CO₂ plume being observed as an increase of resistivity. The plume has a varying thickness between 10 and 50 m and a lateral extent of about 3000 m. These models are used to generate the reference data for the synthetic study.

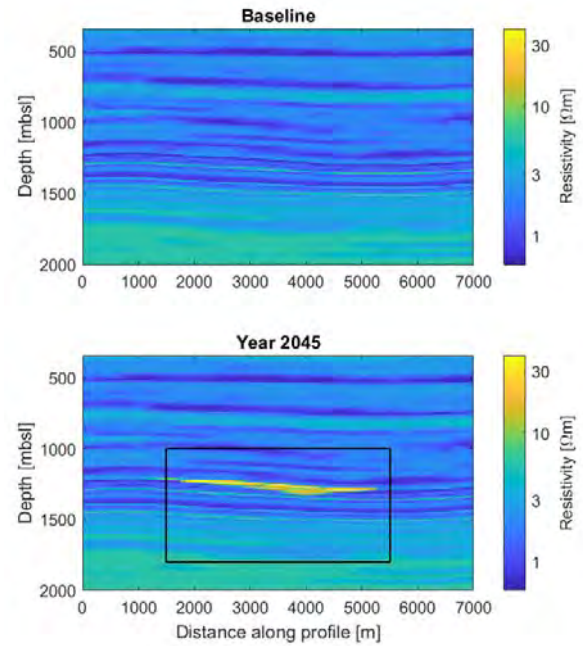


Figure 3: (Top): Baseline resistivity model. (Bottom): Resistivity model after 25 years of injection. Rectangle outlines the targeted area for the acquisition optimisation (section 3.4).

3.3 CSEM synthetic study

3.3.1. Forward modelling and data errors estimate

To generate the reference data for the baseline and monitor cases, we consider a similar acquisition layout to the one used in Park et al., 2019. A horizontal electric dipole transmitter is towed at 30 m above the seabed with a regular spacing of 300 m, resulting in 41 transmitter positions. The signal is measured using 17 dipole receivers recording the horizontal (in line with the transmitter) and vertical electric fields. The receivers are positioned at the seabed with a spacing of 500 m. The modelled frequencies correspond to 0.1, 0.25, 0.5, 0.75, 1, 2, 3, 4, and 5 Hz. An example of the modelled data is shown in Figure 4.

At a first glance, the amplitude and phase data show sensitivity to the increased resistivity in the reservoir layer. The phase data are relatively more sensitive with several degrees difference between the observed and modelled data. The amplitude data show differences up to two magnitudes smaller than the actual data. The detectability will depend on the size of the data error as well. We therefore perform a data error analysis by perturbing navigational parameters (e.g., Gehrman et al. 2019) including:

- transmitter and receiver azimuth errors with an error value corresponding to 3°,
- errors (3 m) due to the transmitter depth and transmitter dip (3°), and
- errors for dipole receiver positions along the x and y directions (3 m).

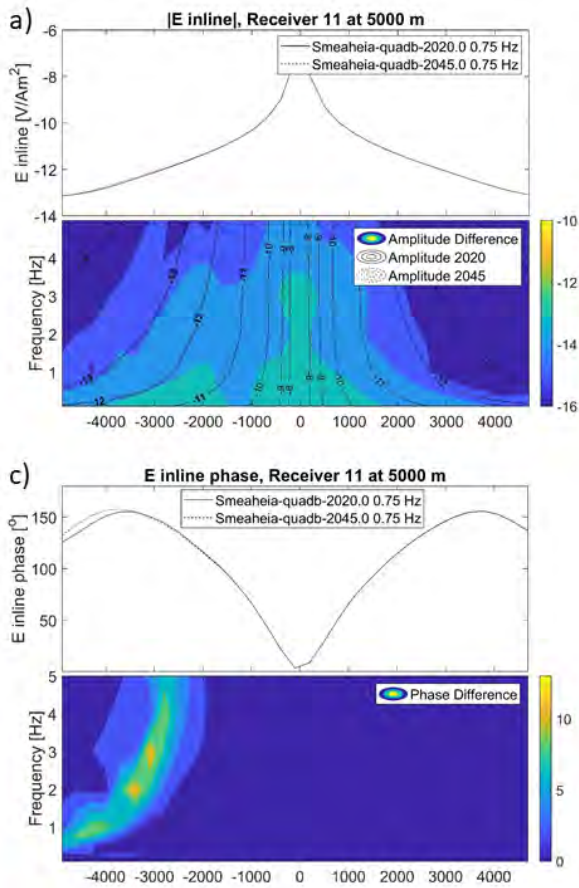


Figure 4: Synthetic data for inline electric field amplitude (a) and phase (c) for 0.75 Hz for baseline model (solid line) and model after 25 years of injection (dotted line). Data difference over frequency and transmitter-receiver offset with contours for amplitude data. Amplitude is on a logarithmic scale.

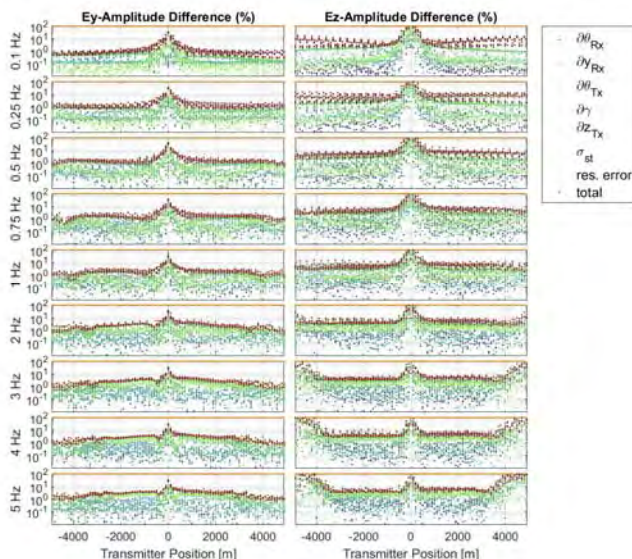


Figure 5: Data error analysis for transmitter position relative to all receivers at position 0. The total error (red) is the result of the summation of all individual data differences for each perturbation in quadrature. Perturbations are done for azimuth Θ and dip γ and variation in x , y and z for the transmitter (T_x) or receiver (R_x).

Forward modelling is performed for each perturbation and the total error is derived by adding data difference in

quadrature. Figure 5 shows the individual data anomaly resulting from the difference between the cases without and with navigation perturbations. Differences for the inline (E_y) and for the vertical component (E_z) are considered. The differences are displayed in percentage (%) for the amplitude and show that the fields are most sensitive to the lateral position of the receivers and vertical position of the transmitter.

3.2.2. Inversion results

In a first stage, we run the inversion with the baseline data. We add noise based on the navigation error estimates from the previous section assuming a Gaussian distribution. The starting model for the inversion contains a water layer with fixed resistivity of 0.3 Ωm and a homogeneous half space with a resistivity of 1 Ωm . Individual inversions for the inline (E_y) and vertical (E_z) components (Figure 6) converge to root mean squared (rms) misfit values of 1.1 and 1.3 respectively, possibly not reaching the target misfit of 1 due to the data errors being too small when compared to the numerical noise. Both data sets are sensitive to the vertical structure.

The inversion for both components using 14 iterations results in rms misfit of 1.2. The recovered resistivity model (Figure 7a) revealed sensitivity to the alternating conductive and resistive layers but with less vertical resolution than the true model. The first resistive layer is resolved, while the two thin conductive layers in ~ 500 and ~ 700 m depth are resolved as one layer in the inversion. Especially with greater depth the inversion tends to resolve one thick layer instead of several thin ones, which is due to the roughness regularisation preventing large resistivity contrasts when the data loses resolution with depth. Data residuals are random and Gaussian distributed (Figure 8).

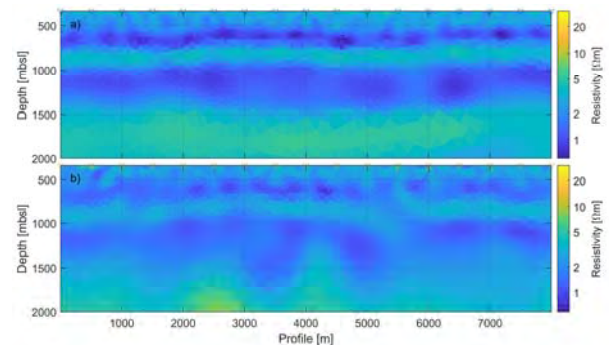


Figure 6: Baseline model inferred from CSEM inversion using (a) inline (E_y) and (b) vertical (E_z) components of the electric field.

In a second stage, we run the inversion with monitor data. We adopted a sequential time-lapse strategy where the resistivity model from the inversion of the baseline data is used as starting model for the inversion of the monitor data. The inversion parameters are the same as for the baseline case. The recovered resistivity model is displayed together with the reference model for comparison in Figure 7b. Updates compared to the result from the baseline inversion can be observed, especially

an increase of resistivity at depth between 1300 and 1600 m (Figure 7c). The observed resistivity increase is located slightly below the true target location. Such deviation can be attributed to the smoothing regularisation.

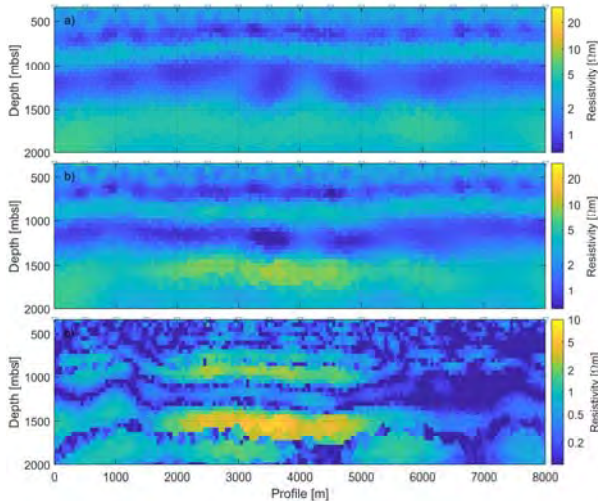


Figure 7: (a) Resistivity model inferred from CSEM inversion using inline and vertical components of the electric field for the baseline case; (b) for the monitor case, 25 years later; (c) Difference between the resistivity model in a and b.

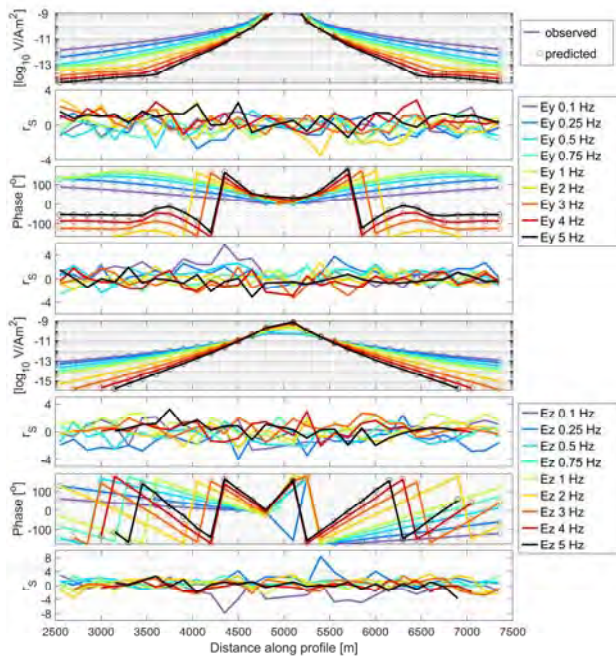


Figure 8: Amplitude and phase data for the inline (top four panels) and vertical (bottom four panels) component as well as standardised residuals (r_s) for final resistivity model shown in Figure 7a

3.3 Acquisition design

After showing that the CSEM inversion can detect a resistivity change in the expected area, using all available transmitters, receivers, data components, and

frequencies, we turn to the investigation of acquisition design. Data components here refer to inline or vertical components and amplitudes or phases. Following the eigenvalue spectrum approach described in Section 2.2, we identify the parts of the CSEM data containing most information for inversion of model parameters in a target region with lateral extension from 1500-5500 m and a depth range from 1000-1800 m, cf. Figure 3. The first selected data trace (transmitter-receiver pair for a specific frequency and data component) is the one that is most sensitive to resistivity changes in the target area, consequently offering the best possibilities to constrain/determine the target area properties during inversion. New traces are then selected iteratively based on how much additional information they bring to the previous traces. For the preliminary Smeaheia study described here, only 50 measurements are selected. This is a tiny fraction of more than 17000 used for the inversion described in Section 3.2. Visual inspection of the eigenvalue spectrum showed that the information content in this small subset of traces is, not surprisingly, smaller than in the full data set. However, an impressive amount of information is captured using those few traces, and they are, for example, shown to provide more information than 500 randomly picked traces (an otherwise often efficient way of decimating data with relatively little loss).

While future work will study in detail how the inversion result itself is affected by using smaller, but optimised, surveys, we present here instead a few examples of what is considered optimal using the described strategy. Figure 9 illustrates how the selected transmitter-receiver pairs always have a certain minimum offset (no markers along the diagonal). The traces are predominantly based on the phase of the electric field (more circles than squares). Lower frequencies are preferred, especially 0.1 Hz.

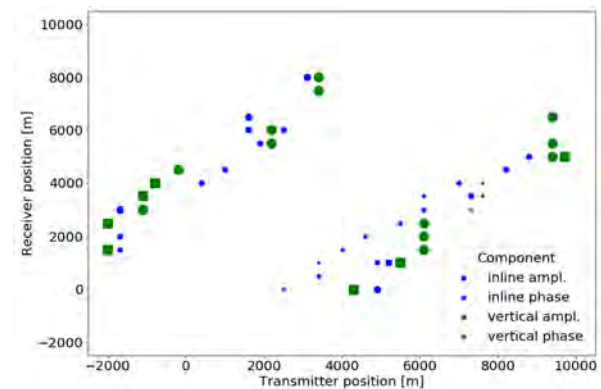


Figure 9: Illustration of 50 selected optimal data traces using a survey design strategy based on eigenvalue spectrum analysis. The axes of the plot refer to the inline positions of transmitter-receiver pairs. The color indicates whether the inline (blue) or vertical (green) electric field has been chosen, and the shape whether the amplitude (square) or phase (circle) is used. In addition, the size of the markers represents different transmitter frequencies (from 0.1-5 Hz). Larger markers denote lower frequencies.

The preference of lower frequencies becomes even clearer when plotting offset vs frequency, see Figure 10. This figure also shows an interesting trend in that the

lower frequencies in general are associated with longer offsets, while the selected higher frequencies are associated to pairs with small offsets. This is intuitively a good choice, since the lower frequencies have larger penetration depths. This figure also shows that in general favoured offsets range from 2.5-5 km, which is about twice the depth of the target.

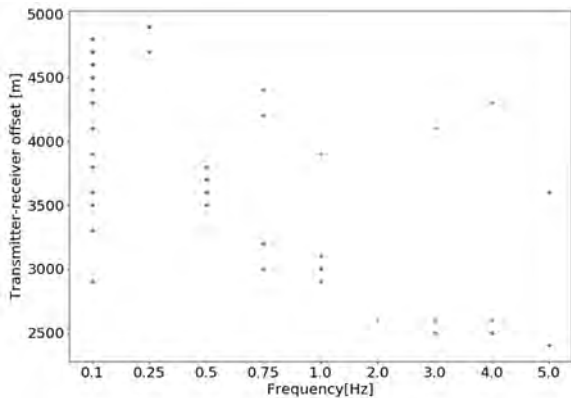


Figure 10: Transmitter-receiver offset vs frequency for 50 data traces identified using survey optimisation based on eigenvalue spectrum analysis.

Conclusions

In this work, we evaluate the use of CSEM for CO₂ monitoring at Smeaheia, a possible candidate for future phases of the Norwegian full-scale CCS project. Realistic synthetic models prior to and after 25 years of injection are derived from reservoir modelling and converted to resistivities. A CSEM time-lapse feasibility study is carried out showing the sensitivity of both vertical and horizontal electric field dipoles to resistivity changes due to CO₂ injection. The optimal acquisition analysis reveals the highest sensitivity to the storage region at 1200 m depth for transmitter-receiver offsets between 2500 and 5000 m. When considering electric field components, phase data contain more information than amplitude, which emphasises the requirement for accurate time logging during surveying. The chosen frequency range between 0.1 to 5 Hz is sensitive to the target area, but lower frequencies are preferred, especially for long offsets. Our work illustrates the benefit of an optimal survey design study using realistic subsurface models as

Eliasson, P., & Romdhane, A. (2017, June). Uncertainty Evaluation in Waveform-based Imaging Methods-A Case Study at Sleipner. In 79th EAGE Conference and Exhibition.

Gassnova (2016). Feasibility study for full-scale CCS in Norway. Technical report, Gassnova.

Gehrmann, R. A., Haroon, A., Morton, M., Djanni, A. T., & Minshull, T. A. (2020): Seafloor massive sulphide exploration using deep-towed controlled source electromagnetics: Navigational uncertainties. *Geophys. J. Int.*, 220(2), 1215-1227.

Grayver, A. V., Streich R. and Ritter O. (2014): 3D inversion and resolution analysis of land-based CSEM data from the Ketzin CO₂ storage formation, *Geophysics*, 79:2, E101-E114

a prerequisite for efficient time-lapse CSEM surveying. The CSEM method is sensitive to the presence of fluids in the pore space, including resistive CO₂, offering the possibility to complement industry 4D-seismic surveying and quantify the volume of the CO₂ in the reservoir.

Acknowledgements

The study is performed with support from the Research Council of Norway (CLIMIT-KPN 295212) and the NCCS Centre (NFR project number 257579/E20), performed under the Norwegian research program Centres for Environment-friendly Energy Research (FME).

References

Amaya, M., Morten, J. P., & Boman, L. (2016): A low-rank approximation for large-scale 3D controlled-source electromagnetic Gauss-Newton inversion. *Geophysics*, 81(3), E211-E225.

Archie, G.E. (1942): The electrical resistivity log as an aid in determining some reservoir characteristics. *Petroleum Transactions of AIME*. 146: 54-62.

Bøe, L. Z., Park, J., Vøge, M., & Sauvin, G. (2017). Filtering out seabed pipeline influence to improve the resistivity image of an offshore CO₂ storage site. In EAGE/SEG Research Workshop.

Colombo, D. and McNeice, G. W. (2013): Quantifying surface-to-reservoir electromagnetics for waterflood monitoring in a Saudi Arabian carbonate reservoir, *GEOPHYSICS*, 78:6, E281-E297

Constable, S. C., Parker, R. L., Constable C. G. (1987): Occam's inversion: a practical algorithm for generating smooth models from electromagnetic sounding data. *Geophysics*, 52(3): 289-300.

Dupuy, B., Torres, V., Romdhane, A., & Ghaderi, A. (2018, October). Norwegian large-scale CO₂ storage project (Smeaheia): baseline geophysical models. In 14th Greenhouse Gas Control Technologies Conference Melbourne (pp. 21-26).

Halko, N., Martinsson, P. G., & Tropp, J. A. (2011): Finding structure with randomness: Probabilistic algorithms for constructing approximate matrix decompositions. *SIAM review*, 53(2), 217-288.

Key, K. and Owall, J. (2011): A parallel goal-oriented adaptive finite element method for 2.5-D electromagnetic modelling. *Geophys. J. Int.*, 186, 137-154.

Key, K. (2016): MARE2DEM: a 2-D inversion code for controlled-source electromagnetic and magnetotelluric data. *Geophys. J. Int.*, 207(1), 571-588.

Lien, M., & Mannseth, T. (2008): Sensitivity study of marine CSEM data for reservoir production monitoring. *Geophysics*, 73(4), F151-F163.

Lothe, A. E., Bergmo, P. E. S., Emmel, B., & Eliasson, P. (2018, October): Effects of uncertainties in fault interpretations on pressure depletion and CO₂ storage injection at Horda Platform, offshore Norway. In 14th Greenhouse Gas Control Technologies Conference Melbourne (pp. 21-26).

Maurer, H. R., D. E. Boerner, and A. Curtis, 2000, Design strategies for electromagnetic geophysical surveys: Inverse Problems, 16(5), 1097–1118.

Maurer, H., Curtis, A., & Boerner, D. E. (2010): Recent advances in optimized geophysical survey design. *Geophysics*, 75(5), 75A177-75A194.

Morten, J. P., & Bjørke, A. (2020): Imaging and Quantifying CO₂ Containment Storage Loss Using 3D CSEM. In 82nd EAGE Annual Conference & Exhibition, 2020(1), 1-5. European Association of Geoscientists & Engineers.

Mulrooney, M. J., Osmond, J. L., Skurtveit, E., Faleide, J. I., & Braathen, A. (2020): Structural analysis of the Smeaheia fault block, a potential CO₂ storage site, northern Horda Platform, North Sea. *Marine and Petroleum Geology*, 121, 104598.

Orange, A., Key, K., & Constable, S. (2009). The feasibility of reservoir monitoring using time-lapse marine CSEM. *Geophysics*, 74(2), F21-F29.

Park, J., Bjørke, A. K., Sauvin, G., Morten, J. P., & Nazarian, B. (2019): Marine CSEM for CO₂ Storage Monitoring-North Sea Sensitivity Study. In 81st EAGE Conference and Exhibition 2019(1), 1-5. European Association of Geoscientists & Engineers.

Patzer, C., Ritter, O., & Tietze, K. (2017). Time-lapse CSEM inversion using focusing regularization techniques for reservoir monitoring. In SEG Technical Program Expanded Abstracts (pp. 5870-5874). Society of Exploration Geophysicists.

Romdhane A, Eliasson P. Optimized Geophysical Survey Design for CO₂ Monitoring—A Synthetic Study. In 14th Greenhouse Gas Control Technologies Conference Melbourne 2018 Oct (pp. 21-26).

Roux, E., & García, X. (2014): Optimizing an experimental design for a CSEM experiment: methodology and synthetic tests. *Geophys. J. Int.*, 197(1), 135-148.

Shantsev, D. V, Nerland, E. A. and Gelius, L.-J., (2020): Time-lapse CSEM: how important is survey repeatability?, *Geophys. J. Int.*, 223(3), 2133–2147.

Streich, R. (2016). Controlled-source electromagnetic approaches for hydrocarbon exploration and monitoring on land. *Surveys in geophysics*, 37(1), 47-80.

Tietze, K., Ritter, O., Patzer, C., Vesken, P., Dillen, M. (2019): Repeatability of land-based controlled-source electromagnetic measurements in industrialized areas and including vertical electric fields. – *Geophys. J. Int.*, 218(3), pp. 1552—1571

Zach, J. J., Frenkel, M. A., Ostvedt-Ghazi, A. M., De Lugao, P., & Ridyand, D. (2009, August). Marine CSEM methods for 3D hydrocarbon field mapping and monitoring. In 11th

International Congress of the Brazilian Geophysical Society & EXPOGEF 2009, Salvador, Bahia, Brazil, 24-28 August 2009 (pp. 480-485). Society of Exploration Geophysicists and Brazilian Geophysical Society.

THE EFFECT OF NEW USER SECTORS ON THE CCS INNOVATION SYSTEM

Jørgen Finstad^{1*}, Allan Dahl Andersen¹, Jakoba Sraml Gonzalez¹

¹ TIK Centre for Innovation, Technology and Culture, University of Oslo, Oslo, Norway

* Corresponding author e-mail: jorgen.finstad@tik.uio.no

Abstract

In most mitigation scenarios compatible with achieving the goals of the Paris Agreement, carbon capture and storage (CCS) develops and diffuses at a very rapid pace over the coming decades. The technology is frequently discussed as a mitigation option in a variety of industries and sectors, including the power sector, the cement industry, and as a tool for negative emissions through direct air capture and/or bioenergy with CCS. Different sectors and industries have distinct requirements, characteristics, and institutional needs which may require significant adaptations to a technology and its innovation system as it is adopted and used in new sectors. In this short paper, we propose using the technological innovation system perspective (TIS) to explore potential innovation challenges and opportunities CCS faces as the technology is adapted to new and different sectors. We argue that developing a socio-technical understanding of CCS innovation will be important, and present preliminary insights from our ongoing case-study on the effect of new user sectors on the Norwegian CCS innovation system. Preliminary findings include that sector changes may have affected the actor composition of the Norwegian CCS TIS, as well as the legitimacy of CCS in Europe. Our research also indicates that being aware of institutional and physical differences between industries – including differences in innovation modes – may be important for the diffusion of CCS going forward.

Keywords: *Technological innovation systems, multi-sector innovation, carbon capture and storage*

1 Introduction

In most mitigation scenarios compatible with achieving the goals of the Paris Agreement, carbon capture and storage (CCS) plays an important role in the global mitigation efforts. In many of these modelled pathways, the global CCS capacity expands from today's capacity of roughly 40 million tons of CO₂ captured per year to an industry capturing several billion tons of CO₂ per year in a matter of a few decades [1-3]. While possible in modelled pathways and in theory, there are questions about the feasibility of various modelled developments and how these developments can be best achieved [4-6]. It is important to be aware that the models behind most mitigation scenarios include “oversimplification of social realities, a limited attention for actors and behaviours (struggles, beliefs, strategies), (...) while portraying transitions as emerging smoothly over time” [7]. Because of this, scholars have called for a better link between the insights from transition and innovation studies and the output of models [7-9], and highlighted a need for “real-time assessments of the state of a system in transition, including the interactions between the technical, institutional, social, political and normative dimensions of a transition” [7].

For CCS, the potential discrepancy between current developments and modelled pathways can be implied by looking at the coming decade. Of the over 200 scenarios assessed in the IPCC's Special Report on the 1.5 °C-target (SR1.5), only one avoids CCS this century, and the scale of CCS in the median scenario is 914 million tons of CO₂ captured per year (MtCO₂/yr) already in 2030 [1]. To put these numbers in perspective, the total

capacity of all *planned* and *operating* CCS facilities in 2020 was a bit above 100 MtCO₂/yr [3, 10]. Traditionally, CCS facilities have been large-scale projects with long lead times – often around 10 years [11]. If this trend continues, the CCS capacity in 2030 will, to a large extent, be decided over the next few years.

Such rapid growth from early stages of innovation to global industry may present a series of innovation-based challenges. We propose that a *socio-technical* view of innovation can be an important contribution to exploring these challenges. The basis for this short paper is a notion that utilizing insights from innovation and transition studies to explore ongoing CCS developments can help identify potential opportunities, blockages, and barriers which may help or hinder the development and diffusion of CCS. We argue the *technological innovation system perspective* (TIS) is especially fruitful here, since it “contributes with an analytical framework for understanding the complex nature of the emergence and growth of new industries and a focus on analysing obstacles to this process” [12]. In this short paper, we focus on how adaptation to new and different user sectors may influence CCS technology and its broader innovation system. As discussed in the theory section of this short paper, adapting to new user sectors can provide a series of challenges (and opportunities) for the development of a technology. Since CCS is frequently discussed in relation to a wide variety of sectors, industries, and use-cases – understanding how interactions with different use sectors may influence the technology and its innovation system could prove crucial at this stage of CCS' innovation journey.

The paper is structured as follows, first we present some theoretical insights into how innovation and transitions studies understand change and technological development. Here we also introduce concepts from the technological innovation systems (TIS) perspective, and how these concepts relate to the introduction of new user sectors into an (existing) innovation system. Finally, we present some preliminary findings from our ongoing longitudinal case study of how new user sectors have influenced the Norwegian CCS innovation system.

2 Theoretical background

2.1 Innovation and transitions as socio-technical processes

Both transition and innovation studies understand change and the development of new technologies as *socio-technical processes* which require and lead to changes in the *socio-technical systems* of society. *Socio-technical systems* can be defined as the networks of actors, institutions, and norms, as well as the infrastructure, knowledge, and material artifacts which compose various societal subsystems [13]. Examples of such systems include the electricity sector and the agro-food sector [14].

Both innovation processes and sustainability transitions can be highly complex and contested and are difficult to steer and control. They are understood as multi-dimensional process, involving a multitude of actors, technologies, considerations, opinions, and include power struggles and discursive struggles between various actors and views [15, 16]. Both the development and diffusion of new (and sustainable) technologies, and the destabilization and change of existing systems are complex long-term process which often take decades to unfold, and which evolve in a non-linear fashion [14, 17]. This puts the insights from these fields in contrast with some of the assumptions of many of the models behind mitigation scenarios, which tend to be characterized by more linear innovation dynamics based on neo-classical economic principles [7, 9, 18, 19].

The technological innovation systems (TIS) perspective, in particular, is argued to be a good framework for identifying the challenges and barriers a technology (and its related innovation system) is facing [13]. While CCS has been analyzed through the lens of TIS before (e.g. [20] and [21]), an updated TIS analysis of CCS may provide several valuable insights and a better ‘real-time assessment’ of the CCS innovation journey. This is especially true when looking at CCS diffusion in sectors other than the power sector, since, as highlighted by Bui et al, “*relative to the power sector, there is a paucity of academic studies of industrial carbon capture*” [22]. The TIS framework is briefly outlined below.

2.2 Technological innovation system

A *technological innovation system* is frequently defined as “*network(s) of agents interacting in a specific technology area under a particular institutional infrastructure to generate, diffuse, and utilize*

technology” [23]. A core idea in the innovation systems approach is that the innovation and diffusion of technology stems from both individual actors and firms, but also from the broader context – including specific technological characteristics, institutional and economic structures, and various adoption mechanisms [24]. The formative phase of a new technological innovation system involves the entry of firms and organizations, the forming of networks between these actors, and (re-)aligning institutional configurations in line with the new TIS.

If we want to understand how to speed-up the development and diffusion of a technology we must understand what is blocking the current of rate development from going faster [25]. As such, weaknesses in the TIS must be identified. To do this, scholars have developed a “*functions of innovation systems*” approach. This approach introduces a layer of key system functions which are important for a TIS to grow and develop [25, 26]. The functions describe the ongoing developments within a TIS and are considered good indicators of the overall performance of the innovation system [25]. The seven functions are: 1) *knowledge development and diffusion*, 2) *entrepreneurial experimentation*, 3) *influence on the direction of search*, 4) *market formation*, 5) *legitimation*, 6) *resource mobilization* and 7) *development of positive externalities* [27].

Simply put, in the TIS framework, the successful diffusion and development of a technology is understood to result from successfully fulfilling all or most of these seven functions. Over the past twenty years the functions approach to analyzing TIS developments has been prominent and fruitful – especially when analyzing the development of sustainable technologies [14, 26, 28]. A benefit to the functions approach is that it allows the analyst to identify ““*system failures*” or *weaknesses, expressed in functional terms*” [27]. The approach can be used to identify the main challenges a TIS is facing, which again may help identify where actors and policymakers should focus their attention, and which policies may prove most suitable [24, 27]. Another benefit to the functions approach is that it allows the study of the dynamics of a TIS and what is driving (and hindering) innovation within the TIS both at a given moment and over time [24, 29]. Taken together, these aspects make the TIS perspective an excellent framework for taking stock of the status of CCS and the potential innovation opportunities and challenges the technology may be facing.

2.3 On innovation as a multi-sectoral process

In later elaborations of the TIS framework, scholars have conceptualized a sectoral configuration of TIS to capture sectoral interdependencies and dynamics related to a focal technology’s evolution [30-32]. In this approach, technology is seen as a system consisting of components and sub-components [33, 34] that are applied in and produced by different sectors—upstream, technology-producing and downstream, technology-using sectors

[30, 35].¹ Each sector is inhabited by a population of firms with similar capabilities, and has a particular underlying ‘knowledge base’ and mode of innovation [36, 37]. Each technology value chain thus involves several heterogeneous sectors whose alignment and complementarities influence the performance of the focal technology [38-40]. A technology value chain approach emphasizes important inter-sectoral dynamics. That each sector differs explains why adaptation is needed [32]. As a technology evolves, its sectoral configuration changes too. Change can happen via changes to subsystems and/or changes in the design hierarchy that coordinates the division of labour between them [41]. This can involve changes to raw materials, knowledge bases, and changes in user sectors [42, 43].

When a technology is introduced into a new user sector it typically requires a good deal of adaptation and innovation and it may lead to “speciation” events, i.e. the creation of a new version or design of the technology which may even entail new technology suppliers and new functionalities [44]. Such changes in the user-sectoral configuration of a technology have historically been important for further deployment and growth in areas such as steam engines and solar PV (ibid). Engagement with new (user) sectors can also influence a technology’s innovation system in various ways. Different sectors may have differing institutional needs, pulling a TIS in new and different directions [12]. Incorporation of new user sectors can also open opportunities for market formation, knowledge development, and resource mobilization, as well as changes to the legitimacy of a technology.

These dynamics can be important when analyzing CCS – as the technology has the potential of being utilized in a wide range of sectors and has moved from being primarily discussed in a few sectors (e.g. gas processing, fossil power production) to being discussed as a tool for dealing with residual emission in several sectors (e.g. cement production, steel production, bioenergy, etc.) and for providing options for carbon dioxide removal from the atmosphere (through CCS on bioenergy and/or direct air capture technologies). Some preliminary thoughts on how these changes in user sectors may affect the development of CCS is discussed in coming section(s) of this short paper, but first we will briefly introduce our methods.

3 Methods

To study the effects and dynamics of new user sectors entering the CCS TIS, we perform a longitudinal case study on the Norwegian CCS TIS.

We have analyzed close to 600 newspaper articles from three different Norwegian newspapers/magazines (Aftenposten, Dagens Næringsliv, Teknisk Ukeblad) over the period 2005-2020. This media analysis can be used to inform whether there have been changes to which sectors CCS is discussed in relation to over time. It can

also inform changes in some of the seven TIS functions – this includes changes to *legitimacy* over time, tracking number of new (actor) entrants into the TIS (which can inform the *entrepreneurial experimentation* function), as well as developments which may influence the *market formation* and *resource mobilization* functions.

We plan to supplement this analysis with interviews with key actors in the Norwegian CCS TIS, as well as document analysis of various databases and document sources (such as the CLIMIT database of past CLIMIT funded R&D projects). These data sources will be used to inform further changes to the TIS functions, as well as changes to actors and networks included in the Norwegian CCS TIS. Interviews with industry actors is particularly important for informing if/how/why user sector changes have influenced the Norwegian CCS TIS.

4 Preliminary findings

4.1 CCS innovation challenges from a multi-sector TIS perspective

Our preliminary findings show a series of ways user sector changes may influence the development of CCS. These questions and challenges will be elaborated on in coming months, but here we present some preliminary thoughts. We also present some insights from the cement industry as an example of the institutional needs of a sector/industry. In a future (longer) paper, the industrial requirements of the cement industry will be compared with the requirements of other industries.

4.1.1 Adapting to physical and institutional differences

Different sectors and industries may have very different physical characteristics relevant for CCS. Difference in the composition of the flue-gas require adaptation of the various capturing technologies and may influence which capturing technology/solution is best suited for different industries. Similarly, the availability of physical space at facilities will vary across industries. Both of these physical differences can have important implications for the potential of a dominant capturing technology design to emerge. If different technologies/designs end up dominating different industries, this may also affect the potential for cost reduction and learning-by-doing effects across industries and the different capturing technologies. A common assumption is that CCS costs will rapidly decline as the technology diffuses, but if standardization and modularization across industries proves difficult, there is no guarantee that this will be the case for the capture part of CCS – not all technologies decline in cost over time (e.g., nuclear energy), and standardization is an important contributor to rapid cost reductions.

¹ Upstream and downstream sectors are delineated in relation to a particular technology value chain. The focal sector is where the technology is applied, while upstream sectors are those that produce important components and subcomponents of the technology. Note that the focal, downstream sector (in a

transition) is viewed as broader than upstream sectors. The main difference is that the former includes users of sector output (e.g. electricity or mobility services) while for the latter, users are based in other sectors. The purpose of this differentiation is to explicate inter-sectoral relationships.

Different sectors and industries may also have very different institutional requirements and traditions. For instance, the cement industry – an industry often seen as a high potential industry for mitigation through CCS – has several characteristics which *could* provide obstacles for CCS diffusion in the sector. Some examples of this are outlined below.

4.1.2 *An example of institutional characteristics – the cement industry*

The cement industry, generally, has low profit margins and operates in competitive markets. Globally, cement production and cement demand are evenly matched, leaving little space for new entrants. This also means many firms cannot raise the cost of their product without losing market share [45, 46]. The cement industry is capital intensive, and much of the cost is CAPEX. New plants can cost hundreds of millions of dollars, and generally take years to plan and build. However, once a cement plant is built, they can last for several decades, with lifetimes up to 50 years. [45]. These characteristics make it difficult for new entrants to compete with large established firms, and the advantages of scale (supply chain efficiencies etc.) have contributed to high concentration of the industry between a few large actors. [46]. The latter implies fewer opportunities for innovative niche producers, production methods, and products [45]. Long asset lifetimes also mean that radical innovation can lead to major sunk cost. Because of this, the cement industry has historically been rather conservative with regards to innovation, and resource mobilization for innovation has been a challenge for the industry [47]. In addition, current cement supply is sufficient enough to meet cement demand, and with the long lifetime of existing and newly built plants, this leaves little room for new and innovative production facilities.

A further characteristic of the cement industry is the generally short distance between producer and consumer. High transportation costs means producers tend to serve local markets, often limited to a radius of a few hundred kilometers from the production plant [47]. As noted in Victor, Geels [46], “only 3% of global production trades across borders, and that mostly occurs among geographically close neighbours” Victor, Geels [46]. Because of this, the industry is geographically spread out over large areas rather than clustered in regions or specific locals [47].

Taken together, these aspects of the cement industry *could* influence the diffusion of CCS in the industry. For an industry with low-profit margins, including the cost of carbon capture could prove challenging. Due to the long lifetime of facilities, retrofitting of carbon capture may be the only way to introduce CCS to the cement industry in many regions. This could, for instance, limit the available capturing technology options in these regions, since cement producer may focus on technologies which can be easily/quickly retrofit. At the same time, actors in

the cement industry are already used to high upfront cost for new facilities, and, as such, might be less daunted by the upfront costs of installing carbon capture.

Many argue a key for further CCS diffusion is the clustering of industrial CO₂-sources, since this can reduce cost, and simplify transportation and storage. With a dispersed industry like the cement industry, this could prove a challenge – as it may be difficult connecting the dispersed production sites of the cement industry to the carbon transportation and storage infrastructure required for CCS. However, the dispersed nature (and low trade across borders) could also be a benefit for the diffusion of CCS in the cement industry. Given the high transportation cost, it may prove harder for cement producers to relocate to new regions if stringent emission taxes/regulations are introduced, potentially lowering the risk of ‘carbon leakage’² in the cement industry.

Taken together, the industrial requirements and characteristics of the cement industry highlights why understanding how the CCS TIS can adapt to various industries with completely different institutional characteristics could prove very important if CCS is to diffuse at the rate and scale seen in mitigation scenarios. As CCS enters a variety of new sectors, being aware of how these different industrial requirements and characteristics may affect the CCS innovation system, and how the innovation system should adapt to the different sectors, could prove crucial for the successful diffusion of the technology. Exploring these questions is the aim of our current study.

4.2 *Effect of sector changes on the Norwegian CCS TIS*

In our current work, we are focusing on understanding how adaptation to new user sectors has influenced the Norwegian CCS TIS over the last fifteen years. To do this we are performing a longitudinal case study on the Norwegian CCS TIS – tracking how the entry of new user sectors has influenced the TIS over time. While our work is still in an early phase and needs to be supplemented with further document analysis and interviews, we present some preliminary results from our media analysis below.

² Carbon leakage refers to when an industry or business relocates to a new region or country to avoid stringent emission taxes/regulations in the original region/country.

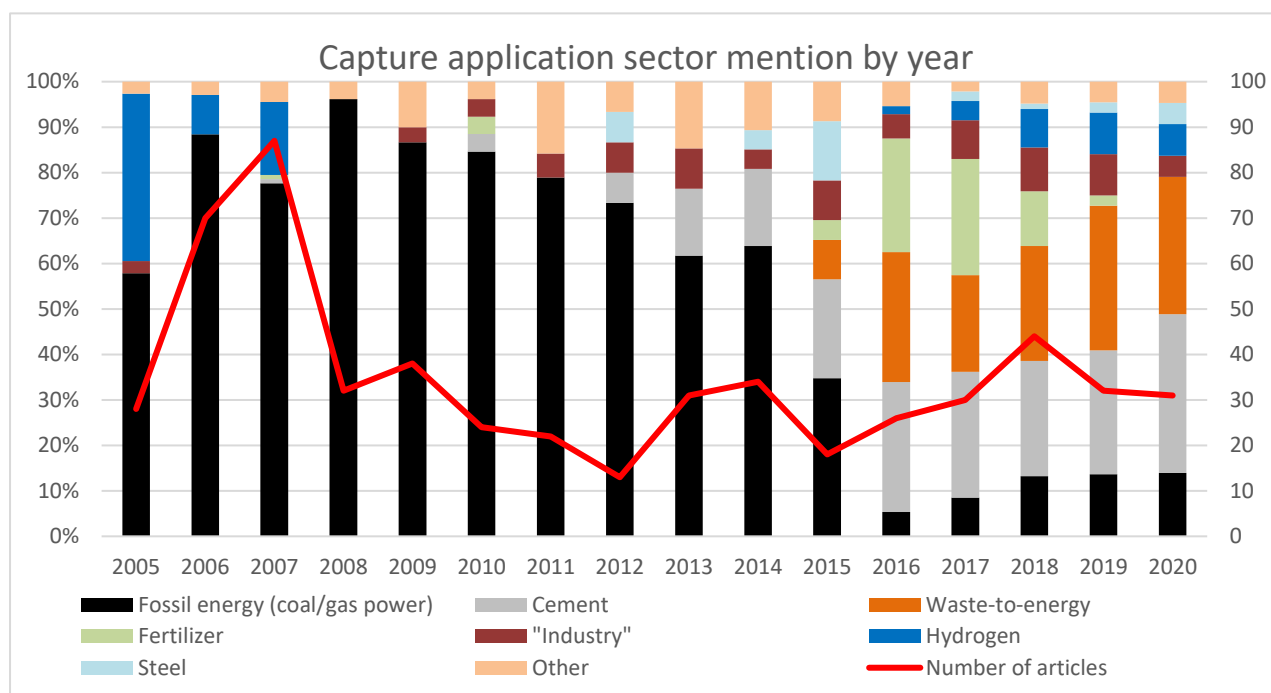


Figure 1: The figure shows which sectors CO₂-capture was discussed in relation to in the newspaper articles by year. The columns show capture application sector mentions as a percentage of all capture application sector mentions that year. The red line shows the total number of articles per year.

4.2.1 Sector changes

Unsurprisingly, our media analysis shows a significant change in which sectors and industries CO₂-capture technologies are discussed in relation to in the Norwegian newspapers over the period 2005-2020. In the period 2005-2012 capture on fossil energy was mentioned in 61-84% of the analyzed articles, while in the period 2015-2020 this number drops to 12-39%.

The move from discussing CO₂-capture on fossil energy (primarily gas power) to various other industries is, of course, heavily influenced by the change in focus in the big government funded Norwegian CCS projects. The government focus in the early period of the study (2005-2013/14) was on full-scale CCS in gas power (for instance at Mongstad and Kårstø), while the later period has focused on CO₂-capture on cement and waste-to-energy.

While unsurprising, these developments highlight how the Norwegian CCS TIS has moved into new user sectors over the past fifteen years, and, as such, form a good case for studying *how* user sector changes may influence the CCS TIS.

4.2.2 Legitimacy

As an example of how TIS functions may be affected by user sector changes we assessed how the legitimacy of CCS changed over time in the analyzed newspaper articles. While this is only a preliminary analysis of one of the TIS functions, our full analysis will include all TIS functions and include more data sources.

In our analysis of Norwegian newspapers, we find that the legitimacy of CCS in Norwegian news has generally been quite high in the period. The main exception to this is the period between 2010-2013. The flagship

government projects on CCS on gas power suffered a series of setbacks, delays, and cancellations in this period, and as such the finding is not surprising. The quick recovery of CCS legitimacy post-2013 is very interesting – and as our analysis moves forward it will be interesting to see if the change in user sectors may have had an effect in *restoring* legitimacy, or if the reduction in legitimacy was primarily a blip linked to the delays/cancellations of flagship projects.

The media analysis in Norway cannot alone support the hypothesis that sector change has influenced the legitimacy of CCS, since CCS has maintained high legitimacy for most of the period. Hints that the hypothesis may still apply to other countries does show up in our media analysis (and in preliminary interviews). An example of this appears in an article, where a representative from WWF in Germany explains how CCS lost legitimacy in Germany because it was linked to coal power, but that WWF Germany now supports CCS on hard-to-abate industrial emissions.

4.2.3 Actor changes

4.3.1 Capture technology developers

Our preliminary analysis shows that a change in user sectors, may have had an effect on the CO₂-capture technology developers involved in the Norwegian CCS TIS. Some actors show up as part of the media analysis

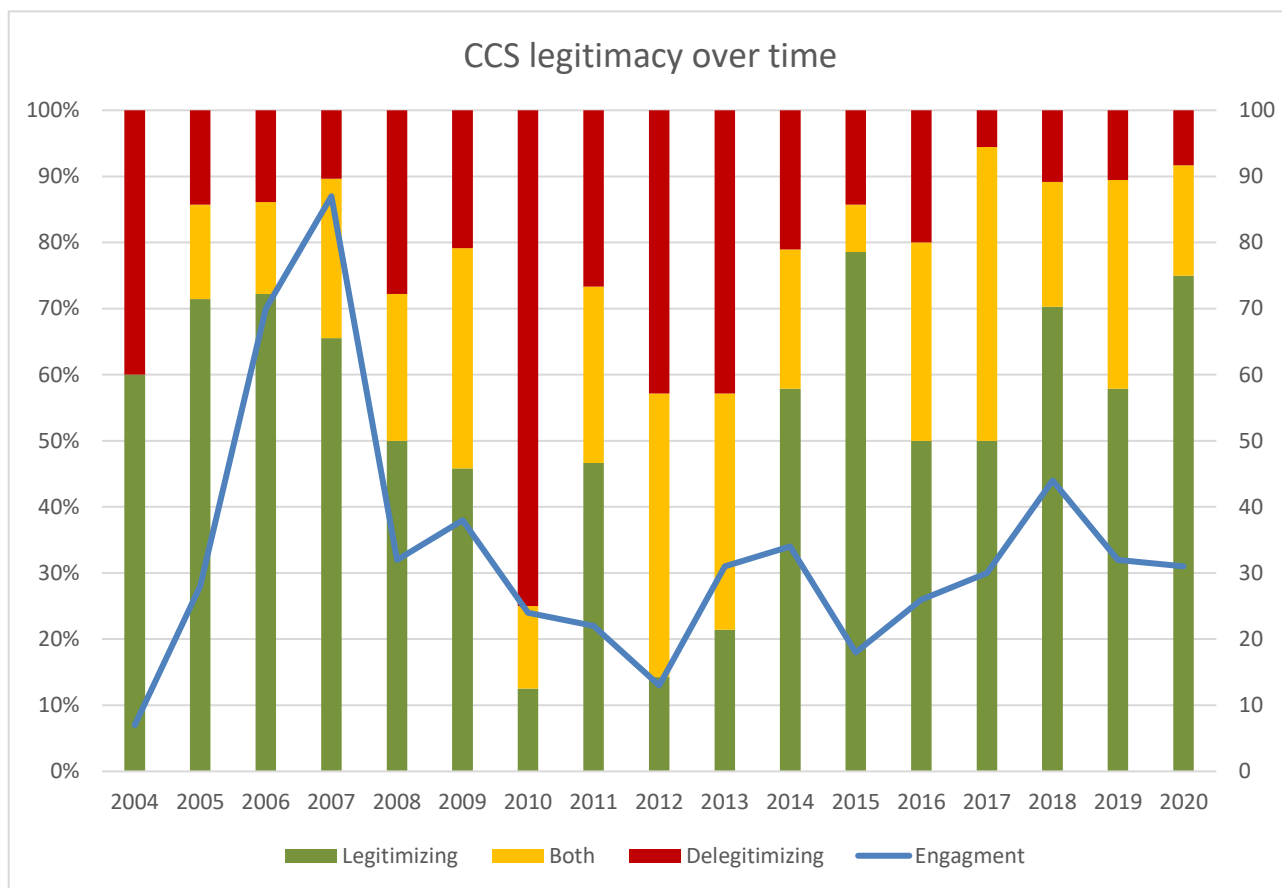


Figure 2: The columns show the number of articles with legitimizing, delegitimizing, and both legitimizing and delegitimizing storylines per year as a total of all articles with legitimizing or delegitimizing storylines. The blue line shows the total number of articles per year.

when the focus was on capturing CO₂ from fossil power (2005-2014) but disappear as the focus shifts to new sectors. This includes big international actors like Siemens, Alstom, and Mitsubishi Heavy Industries, and the Norwegian company Sargas³. In later years, new companies show up in the media analysis – these capture technology companies appear to focus more on applications for CO₂-capture other than capture to reduce emissions on fossil power directly. Examples include focus on direct air capture and technologies that combine CO₂-capture and hydrogen production. Companies like Shell and Aker have been involved in the Norwegian CCS TIS over the entire period of our analysis and have been involved in capture on both gas power and on the new industries like cement and waste-to-energy. Understanding how these actors (Shell, Aker, Sargas/Capsol) have adapted their technologies and approaches to fit new and different sectors is something we aim to explore further in interviews going forward.

5.0 Final comments

Our preliminary work indicates that new user sectors can have an impact on many parts of the innovation system. These in turn pose new challenges and opportunities for firms and policymakers that we will explore in more depth. As an example, changes in user sectors lead to new opportunities for market formation, resource

mobilization, and changes to the legitimacy of the TIS, but may also lead to new challenges when it comes to standardization and adapting to the institutional requirements of new sectors. While the analysis presented here only hints at these effects, we aim to elaborate on the broader effects of user sector changes on the Norwegian CCS TIS going forward.

Acknowledgements

Add acknowledgements here, if needed.

References

1. Huppmann, D., et al., *IAMC 1.5 C Scenario Explorer and Data hosted by IIASA*. Integrated Assessment Modeling Consortium & International Institute for Applied Systems Analysis. <https://data.ene.iiasa.ac.at/iamc-1.5c-explorer>, release, 2018. 1.
2. IEA, *World Energy Outlook 2019*. 2019.
3. GCCSI, *Global Status of CCS 2020*. 2020, Global CCS Institute.
4. Jewell, J. and A. Cherp, *On the political feasibility of climate change mitigation pathways: Is it too late to keep warming below 1.5°C?* Wiley Interdisciplinary Reviews: Climate Change, 2019.
5. Riahi, K., et al., *Locked into Copenhagen pledges – Implications of short-term emission targets for the cost and feasibility of long-term climate goals*.

³ The company Sargas went defunct in 2014, but the patents live on through the company Capsol AS.

6. van Sluisveld, M.A.E., et al., *Comparing future patterns of energy system change in 2 °C scenarios with historically observed rates of change*. Global Environmental Change, 2015. **35**: p. 436-449.
7. Hof, A.F., et al., *Understanding transition pathways by bridging modelling, transition and practice-based studies: Editorial introduction to the special issue*. Technological Forecasting and Social Change, 2019.
8. Geels, F.W., F. Berkhout, and D.P. van Vuuren, *Bridging analytical approaches for low-carbon transitions*. Nature Climate Change, 2016. **6**(6): p. 576-583.
9. van Sluisveld, M.A.E., et al., *Aligning integrated assessment modelling with socio-technical transition insights: An application to low-carbon energy scenario analysis in Europe*. Technological Forecasting and Social Change, 2018.
10. GCCSI, *Global Status of CCS 2019*. 2019.
11. Lipponen, J., et al., *The Politics of Large-scale CCS Deployment*. Energy Procedia, 2017. **114**: p. 7581-7595.
12. Bergek, A., et al., *Technological innovation systems in contexts: Conceptualizing contextual structures and interaction dynamics*. Environmental Innovation and Societal Transitions, 2015. **16**: p. 51-64.
13. Markard, J., R. Raven, and B. Truffer, *Sustainability transitions: An emerging field of research and its prospects*. Research Policy, 2012. **41**(6): p. 955-967.
14. Köhler, J., et al., *An agenda for sustainability transitions research: State of the art and future directions*. Environmental Innovation and Societal Transitions, 2019. **31**: p. 1-32.
15. Meadowcroft, J., *Engaging with the politics of sustainability transitions*. Environmental Innovation and Societal Transitions, 2011. **1**(1): p. 70-75.
16. Geels, F.W., D. Tyfield, and J. Urry, *Regime Resistance against Low-Carbon Transitions: Introducing Politics and Power into the Multi-Level Perspective*. Theory, Culture & Society, 2014. **31**(5): p. 21-40.
17. Grubler, A., *Energy transitions research: Insights and cautionary tales*. Energy Policy, 2012. **50**: p. 8-16.
18. Turnheim, B. and B. Nykvist, *Opening up the feasibility of sustainability transitions pathways (STPs): Representations, potentials, and conditions*. Research Policy, 2019. **48**(3): p. 775-788.
19. van Vuuren, D.P., et al., *Alternative pathways to the 1.5 °C target reduce the need for negative emission technologies*. Nature Climate Change, 2018. **8**(5): p. 391-397.
20. van Alphen, K., M.P. Hekkert, and W.C. Turkenburg, *Accelerating the deployment of carbon capture and storage technologies by strengthening the innovation system*. International Journal of Greenhouse Gas Control, 2010. **4**(2): p. 396-409.
21. Lai, X., et al., *Carbon capture and sequestration (CCS) technological innovation system in China: Structure, function evaluation and policy implication*. Energy Policy, 2012. **50**: p. 635-646.
22. Bui, M., et al., *Carbon capture and storage (CCS): the way forward*. Energy & Environmental Science, 2018. **11**(5): p. 1062-1176.
23. Carlsson, B. and R. Stankiewicz, *On the nature, function and composition of technological systems*. Journal of Evolutionary Economics, 1991. **1**(2): p. 93-118.
24. Hekkert, M.P., et al., *Functions of innovation systems: A new approach for analysing technological change*. Technological Forecasting and Social Change, 2007. **74**(4): p. 413-432.
25. Bergek, A., M.P. Hekkert, and S. Jacobsson, *Functions in Innovation Systems: a framework for analysing energy system dynamics and identifying goals for system building activities by entrepreneurs and policy makers*, in *Innovation For A Low Carbon Economy: Economic, Institutional and Management Approaches*, T.J. Foxon, J. Köhler, and C. Oughton, Editors. 2008, Edward Elgar Pub.
26. Hekkert, M.P. and S.O. Negro, *Functions of innovation systems as a framework to understand sustainable technological change: Empirical evidence for earlier claims*. Technological Forecasting and Social Change, 2009. **76**(4): p. 584-594.
27. Bergek, A., et al., *Analyzing the functional dynamics of technological innovation systems: A scheme of analysis*. Research Policy, 2008. **37**(3): p. 407-429.
28. Bergek, A., *Technological innovation systems: a review of recent findings and suggestions for future research*, in *Handbook of Sustainable Innovation*. 2019. p. 200-218.
29. Bergek, A., *Shaping and exploiting technological opportunities: the case of renewable energy technology in Sweden*. 2002: Chalmers University of Technology Goteborg.
30. Stephan, A., et al., *The sectoral configuration of technological innovation systems: Patterns of knowledge development and diffusion in the lithium-ion battery technology in Japan*. Research Policy, 2017. **46**(4): p. 709-723.
31. Malhotra, A., T.S. Schmidt, and J. Huenteler, *The role of inter-sectoral learning in knowledge development and diffusion: Case studies on three clean energy technologies*. Technological Forecasting and Social Change, 2019. **146**: p. 464-487.
32. Andersen, A.D. and J. Markard, *Multi-technology interaction in socio-technical transitions: How recent dynamics in HVDC technology can inform transition theories*. Technological Forecasting & Social Change, 2020. **151**.
33. Arthur, W.B., *The Nature of Technology: What It Is and How It Evolves*. 2009: Free Press. 256.
34. Murmann, J.P. and K. Frenken, *Toward a systematic framework for research on dominant designs, technological innovations, and industrial change*. Research Policy, 2006. **35**(7): p. 925-952.
35. Sandén, B.A. and K.M. Hillman, *A framework for analysis of multi-mode interaction among technologies with examples from the history of alternative transport fuels in Sweden*. Research Policy, 2011. **40**(3): p. 403-414.
36. Malerba, F., *Sectoral systems: how and why innovation differs across sectors*, in *The Oxford handbook of innovation*, J. Fagerberg, D. Mowery, and R. Nelson, Editors. 2005, Oxford University Press, USA.
37. Smith, K., *What is the "Knowledge Economy"? Knowledge Intensity and Distributed Knowledge Bases*, in *Discussion Paper Series*. 2002, United Nations University, INTECH: Maastricht.
38. Pasinetti, L., *Structural economic dynamics: a theory of the economic consequences of human learning*. 1993: Cambridge University Press.

39. Lundvall, B.-Å., *Product Innovation and User-Producer Interaction*. Industrial Development Research Series, Aalborg University Press, 1985.
40. Robertson, P.L., E. Pol, and P. Carroll, *A new typology for economic sectors with a view to policy implications*. *Economics of Innovation and New Technology*, 2002. **11**(1).
41. Henderson, R.M. and K.B. Clark, *Architectural Innovation: The Reconfiguration of Existing Product Technologies and the Failure of Established Firms*. *Administrative Science Quarterly*, 1990. **35**(1): p. 9-30.
42. Clark, K.B., *The interaction of design hierarchies and market concepts in technological evolution*. *Research Policy*, 1985. **14**(5): p. 235-251.
43. Tushman, M.L. and L. Rosenkopf, *Organizational determinants of technological-change-toward a sociology of technological evolution*. *Research in organizational behavior*, 1992. **14**: p. 311-347.
44. Frenken, K., *The early development of the steam engine: an evolutionary interpretation using complexity theory*. *Industrial and Corporate Change*, 2004. **13**(2): p. 419-450.
45. Bataille, C.G.F., *Low and zero emissions in the steel and cement industries Barriers, technologies and policies*. 2019.
46. Victor, D.G., F.W. Geels, and S. Sharpe, *Accelerating the low carbon transition*. 2019.
47. Dewald, U. and M. Achternbosch, *Why more sustainable cements failed so far? Disruptive innovations and their barriers in a basic industry*. *Environmental Innovation and Societal Transitions*, 2016. **19**: p. 15-30.
- [1]

HEAT OF ABSORPTION OF CO₂ IN NOVEL ENERGY REDUCING SOLVENTS FOR BIOGAS UPGRADING

Sai Hema Bhavya Vinjarapu^{1*}, Teresa Regueira Muniz¹, Philip Loldrup Fosbøl¹

¹ Technical University of Denmark, Lyngby, Denmark

* Corresponding author e-mail: shbvin@kt.dtu.dk

Abstract

Biogas upgrading is done for the removal of CO₂ to produce clean bio-methane. CO₂ capture is a method that can accomplish this task. This project focuses on the chemical absorption process using amine as a baseline. The energy required for CO₂ capture can be optimized by the use of new additives termed vapour reduction additives (VRAs). The heat of absorption of CO₂ in aqueous solutions of (30wt%) monoethanolamine (MEA) and (7.5wt% and 30wt%) VRAs have been measured at two temperatures (313K and 393K) at a pressure of 250 psi. The measurements were conducted by a SETARAM C80 calorimeter consisting of a flow-mixing cell. The enthalpies of mixing of CO₂ in the solvents have been obtained as a function of loading α (mol CO₂/mol MEA).

Keywords: Biogas upgrading; Carbon Capture; Heat of absorption; Vapor reduction additives

1. Introduction

The increasing levels of CO₂ in the atmosphere have proven to be a cause for serious concern. Energy productions of all forms contribute to 72% of greenhouse gas emissions [1]. Demand for energy across the globe is on the rise due to the rapid growth of economies. A majority of the world's energy needs are still met by fossil fuels. Renewable energy sources are expected to account for 34% of all energy sources by 2050. Even in this scenario, the CO₂ emissions are projected to be 22% higher than required, to limit the global temperature rise to 2°C [1]. Therefore, there is an increasing urgency in switching to CO₂-neutral sources while ensuring their cost-efficiency and economic viability.

One such potential alternative is Biogas. Biogas is produced by anaerobic digestion of organic waste from wastewater sludge, industrial wastes, and agricultural wastes. The composition of biogas depends on the raw organic material used. However, it generally comprises 60-70% Methane, 30-40% CO₂, and minor impurities of water vapour and H₂S [1]. Owing to the high CO₂ concentration, biogas has a low calorific value, making it a less appealing replacement to energy-dense fossil fuels. To increase its energy density, this CO₂ is removed. This process of biogas purification is called biogas upgrading and the technology used for achieving this goal is carb

on capture. Of the numerous CO₂ capture technologies available, chemical absorption by primary amines is state-of-the-art. Amines like Monoethanolamine (MEA), which are basic, react reversibly with acidic CO₂ gas. The process involves an absorber where CO₂ from the biogas dissolves in MEA, releasing pure bio-methane. The CO₂-rich solvent then enters a desorber where it is heated to regenerate MEA and a pure CO₂ stream. The regenerated MEA is recycled to the absorber and the pure CO₂ obtained is either sequestered or utilized as a raw

material. MEA has a high absorption capacity of CO₂ and a high reaction rate, which make it a suitable solvent.

Conventionally, the CO₂-rich solvent is heated to 105°C by lean-amine before being pumped to the top of the desorber, which is at 110°C. The reboiler at the bottom of the column is at 120°C. A high-energy requirement is the main limitation of this technology. The heat required for the solvent's regeneration is given as the sum of three terms [3]:

$$Q_{reb} = Q_{sens} + Q_{vap,H_2O} + Q_{abs,CO_2} \quad (1)$$

where, Q_{sens} is the sensible heat required to raise the temperature of the solvent to that of the reboiler's, Q_{vap,H_2O} is the heat of evaporation required to produce the stripping steam in the reboiler, and Q_{abs,CO_2} is the heat of absorption of CO₂ into the solvent. The equivalent amount of heat released by the exothermic absorption of CO₂ should be supplied to desorb it. The energy required for regeneration accounts for 70-80% of the whole process. Additionally, the high-temperature conditions result in degradation of the solvent leading to corrosion of the equipment. All of these result in significant operating costs. These disadvantages inhibit the wide-scale implementation of the process.

To optimize the regeneration of the solvent, new additives, known as vapour reduction additives are being investigated. Typically, a 30 wt% aqueous MEA solvent is used for the capture process. The high water content implies a high heat of vaporization, increasing the heat of regeneration and solvent losses. The vapour reduction additives (VRAs) are designed to replace water, thereby reducing the solvent's vapour pressure. This abates the amount of water evaporated along the column, thereby decreasing the energy requirements at the condenser situated at the top of the desorber. Further, the size requirements of the desorber are expected to decrease resulting in a decline in both capital and operating costs.

The heat required for regeneration of the solvent, as mention in equation (1), is dependent on the heat of absorption of CO₂ in the solvent. It is, therefore, important to determine the heat of absorption of CO₂ in the presence of the new additives and establish that they do not significantly increase the $Q_{\text{abs, CO}_2}$. Experimentally determining the heat of absorption for these solvents is also expected to aid in the development of accurate thermodynamic models like the Extended UNIQUAC model for representing the new solvent systems.

2. Experimental Setup

The heat of absorption of CO₂ in aqueous solutions of MEA and VRAs was measured using a flow mixing-cell adapted to a Setaram C-80 Calorimeter.

A schematic of the experimental setup is presented in Figure 1.

The system consists of three sub-units: the pre-heater, the mixing cell, and the calorimetric block. The pre-heater heats the fluids to the measurement temperature before they enter the mixing cell. The mixing cell consists of two parallel tubes for the flow of the solvent and CO₂. The tubes are coiled together at the lower end, where the mixing of the two fluids takes place. The outlet tube leaves the calorimeter and the pre-heater parallel to the inlet tubes. There are two mixing cells, one used for the mixing of the fluids, and the other as a reference cell.

The mixing cells are situated in a calorimetric block. The heat emitted by the absorption of CO₂ in the MEA solvent is transmitted to the calorimetric block through the wall of the vessel in an isothermal mode and is detected by thermopiles.

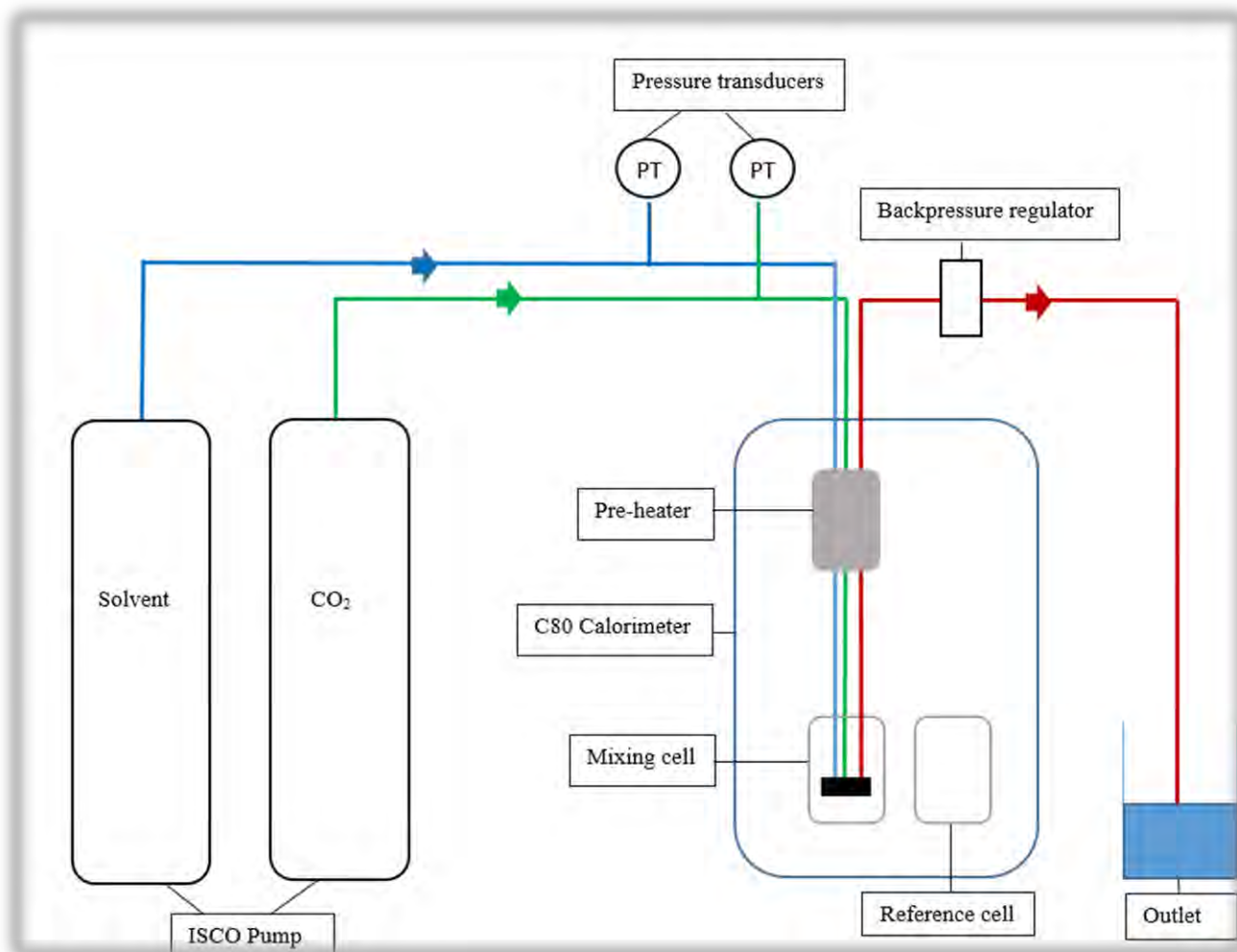


Figure 1: Schematic of the experimental setup

2.1 Operating conditions

The experiments were conducted at 40°C and 120°C, which is the temperature range of the CO₂ capture process. The pressure in the system was maintained at 250 psi by means of a backpressure regulator. The flow rate of the solvent was varied in the range of 0.02-0.3 ml/min while the flow of CO₂ was maintained constantly,

either at 0.4 or 0.6 g/h. The inlet pressure of CO₂ was maintained in the range of 32-35 bar. However, the inlet pressure of CO₂ does not have any impact on the measurements. Experiments were done for loadings in the range of 0.1-0.5 mol CO₂/mol MEA. The loading of the solvent was determined by the ratio of the molar flow rates of CO₂ and MEA, given as:

$$\alpha = \frac{n_{\text{CO}_2}}{n_{\text{MEA}}} \quad (2)$$

Both the fluids were pumped into the system by use of ISCO pumps. The molar flow rate of the solvent was determined from the volumetric flow rate, density, and concentration of the solvent. The density of the solvent was measured at 298K and atmospheric pressure. The flow of CO₂ was controlled by the use of a Coriolis mass flow controller. The molar flow rate of CO₂ was determined directly from this mass flow rate, eliminating the need for density estimation. Experiments were conducted for 30wt% MEA with and without the VRAs. The experiments are summarized as follows:

- Solvent: 30 wt% MEA
- Additives: 7.5 wt% and 30 wt% of VRA1 and VRA2
- CO₂ loading: 0.1-0.5 mol CO₂/mol MEA
- Temperature: 313 and 393K
- Pressure: 250 psi

2.2 Experimental Procedure

The solvent was first pumped through the system. A small baseline heat signal was observed. This was due to the difference in the temperature of the solvent and the temperature of the calorimetric block. The baseline signal could be reduced by adjusting the temperature of the pre-heater, but could not be eliminated. The solvent was allowed to flow through the system until a steady baseline signal was achieved. CO₂ was then pumped through the system at a pressure higher than the system pressure. This was done to ensure that the solvent does not enter the gas line. The solvent and the gas were allowed to flow through the calorimeter for an hour until a steady heat signal was observed. The loadings of CO₂ were changed in steps of 0.1. This was achieved by maintaining a constant flow rate of CO₂ and adjusting the solvent's flow rate.

The enthalpy of mixing is defined as the heat released per mole of fluid A or B. This enthalpy is obtained from the calorimetric signal S (μV). However, due to the temperature difference between the fluid entering from the pre-heater and the calorimetric block, a baseline signal occurs for the solvent. This signal is to be deducted from the heat signal resulting due to mixing and absorption. Therefore, the enthalpy of absorption is calculated as the ratio of the difference in calorimetric signal and the molar flow rate of CO₂.

$$\Delta H_{abs} = \frac{S_{abs} - S_{BL}}{Kn} \quad (3)$$

Where S_{abs} is the heat of absorption signal, S_{BL} is the baseline signal, K is the sensitivity ($\mu\text{V}/\text{Mw}$) which converts the calorimetric signal to heat power, and n is the molar flow rate of the fluid. In the current work, the standard sensitivity coefficient as a function of temperature, which was delivered with the C80 calorimeter was used.

3. Results and Discussion

3.1 Validation of the results

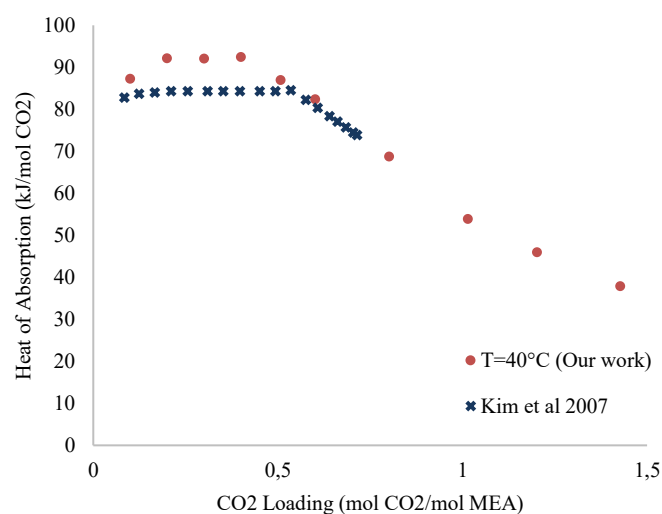


Figure 1: ΔH_{abs} of CO₂ in 30 wt% MEA at 40°C

The experimental results were validated by determining the heat of absorption of CO₂ in 30 wt% MEA at 40 and 120°C and comparing them to data found in the literature. The results for 40°C are presented in Figure 1. From Figure 1, it can be observed that the experimental data are fairly close to the data found in Kim et al [4]. However, a maximum in the heat of absorption is observed in our work. Theoretically, the heat of absorption is expected to be a constant value until saturation. This increasing trend can be considered as an experimental error as it lies within the uncertainty range of $\pm 3\%$. The difference between the experimental values and the data from literature was also observed to lie with a range of $\pm 5\%$. The validation of the method was also carried out for 30 wt% MEA at 120°C.

3.2 Results for 30 wt% MEA and VRA1

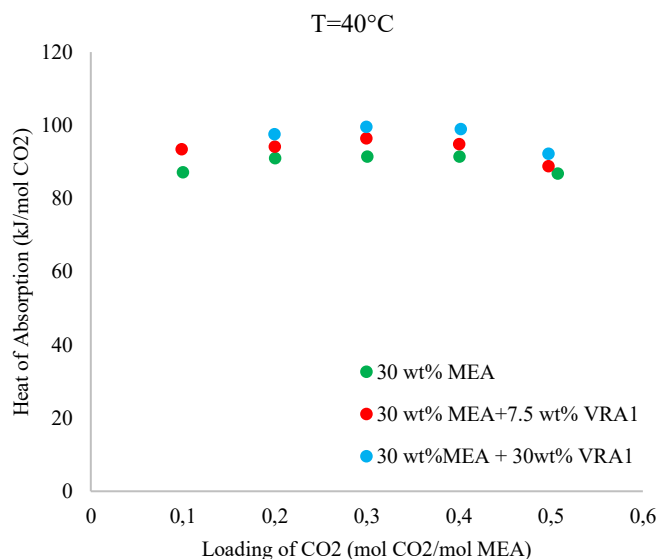


Figure 3: ΔH_{abs} of CO₂ in 30 wt% MEA + VRA1 at 40°C

Figure 3 represents the heat of absorption of CO₂ in 30wt% MEA and 7.5, 30 wt% VRA1 at 40°C. It can be observed that the heat of absorption in the presence of VRA1 is slightly higher than the base case scenario. The heat of absorption in the presence of 7.5 wt% VRA1 is higher by 4.4% than 30 wt% MEA and 30 wt% VRA1 is higher by 8.3%. Owing to the presence of uncertainty, these values are not significantly higher than 30 wt% to impact the $Q_{\text{abs,CO}_2}$ for the regeneration of the solvent. Experiments were also carried out for the remaining operating conditions.

4. Conclusion

Energy reduction of the solvent regeneration process plays a crucial role in the extensive establishment of biogas upgrading plants. The new solvent technology has the potential to meet these requirements. The vapour reduction additives are capable of reducing the energy requirements. Through this work, it has been established that the heat of absorption of CO₂ in MEA based solvents is not significantly higher in the presence of these additives. As a result, these additives can aid in reducing the energy consumed for solvent regeneration. Future work aims at estimating the heat of absorption of these solvents by use of thermodynamic models such as the Extended UNIQUAC model.

Acknowledgements

This project is co-funded by the Danish Government through the EUDP (Energy Technology Development Program) Agency.

References

- [1] Global Energy Perspective 2019. (n.d.). Retrieved July 23, 2019, from <https://www.mckinsey.com/industries/oil-and-gas/our-insights/global-energy-perspective-2019>
- [2] Arcis, H., Ballerat-Busserolles, K., Rodier, L., & Coxam, J. Y. (2011). Enthalpy of solution of carbon dioxide in aqueous solutions of monoethanolamine at temperatures of 322.5 K and 372.9 K and pressures up to 5 MPa. *Journal of Chemical & Engineering Data*, 56(8), 3351-3362.
- [3] Oexmann, J., & Kather, A. (2010). Minimising the regeneration heat duty of post-combustion CO₂ capture by wet chemical absorption: The misguided focus on low heat of absorption solvents. *International Journal of Greenhouse Gas Control*, 4 (1), 36-43.
- [4] Kim, I., & Svendsen, H. F. (2007). Heat of absorption of carbon dioxide (CO₂) in monoethanolamine (MEA) and 2-(aminoethyl) ethanolamine (AEEA) solutions. *Industrial & engineering chemistry research*, 46(17), 5803-5809

ENABLING CCS VIA FISCAL METERING

Sigurd W. Løvseth^{1*}, Yessica Arellano¹, Han Deng¹, Francesco Finotti¹, Edward Jukes², Gérard Bottino³

¹ SINTEF Energy Research, Trondheim, Norway

² KROHNE Ltd, Wellingborough, United Kingdom

³ Baker Hughes, Billerica, Massachusetts, USA

* Corresponding author e-mail: Sigurd.W.Loevseth@sintef.no

Abstract

Carbon Capture and Storage (CCS) will have to turn into a massive industry in order to play a significant role in the mitigation of anthropogenic climate change. The EU Emissions Trading Scheme (ETS) directive establishes that emissions captured, transported, and stored are considered as ‘not emitted.’ Accurate measurements will enable businesses who have implemented CO₂ capture to omit buying or selling their CO₂ Emission Unit Allowances (EUAs) under the ETS, when transferring the CO₂ to geological storages. In this context, fiscal metering technologies, calibrated and verified for CCS relevant streams, would allow rightful checks and balances in CO₂ trade. The present work provides a benchmarking study, looking into the applicability of various metering technologies for CO₂ flow measurements. The requirements to further verify the potential of such technologies in the context of industrial needs are also examined. These requirements are then incorporated into the basic design of an experimental facility with focus on operational flexibility, accurate and traceable composition and flow rate, and controlled operating conditions. The study encompasses a thorough evaluation of the metering market, including first-hand proprietary information, detailed engineering considerations for all subsystems of the experimental facility, and considerations for industrial needs based on undergoing CCS projects and plans. The study results show that although Coriolis and Ultrasonic meters seem like promising technologies for CCS, further verification at relevant conditions is required. This verification entitles a high level of innovation, particularly for accurate reference measurements for CO₂ mass and volume flow meter calibration to comply with the current regulatory framework. The results presented constitute the first step towards the construction of the world’s first large-scale test facility for CCS fiscal metering technologies. The implications of such a facility are enabling fair business throughout the CCS value chain, hence leveraging CCS towards widespread deployment.

Keywords: *CCS, Fiscal Metering, Benchmark, Measurement*

1. Introduction

Carbon capture and storage (CCS) will be a vital industrial process to avoid the catastrophic consequences of global climate change caused by continued largely unchecked emissions of CO₂ and other greenhouse gases (GHG) to the atmosphere. This view is strongly supported by recent international studies [1, 2].

According to the IEA's sustainable development scenario [1][3], the estimated annual needs for CO₂ capture, transport, and storage will be at least 5 gigatonne/year by 2050. This is approximately twice the mass of natural gas transported today. With the Emissions Trading Scheme (ETS) prices above 30 € per tonne, as of January 2021, the total value of the CO₂ to be transported and stored annually according to this scenario will be more than 150 billion €. There are currently natural gas pipelines with a capacity higher than 70 MSm³/d [3], or 20 megatonne/year on the Norwegian continental shelf. Pipelines of similar capacity can be expected for CO₂, transporting the equivalent of 600 M€ annually under the current ETS price. This scenario implies a high relevance of fiscal metering also for individual operators.

Within EU / EEA, the measurement instruments directive [4] establishes an accuracy for liquid CO₂ of 1.5% for the

measurement systems and 1% for the flow meter itself. Flow metering technology complying with the EU regulation on the monitoring and reporting on greenhouse gas emissions (ETS M&R Regulation) [5] is needed to avoid purchasing Emission Unit Allowances (EUAs), which is vital for a viable business model for commercial CCS. Thus, finding solutions for fiscal metering is central for future industrial-scale CCS.

This framework yields the necessity for accurate metering along the CCS value chain, especially every time the ownership of CO₂ changes hands, although not limited only to custody transfer operations. In addition to being required for trading, operators will also need metering to keep track of their inventories, and governments will need accurate and certified metering to regulate the industry. Hence, accurate fiscal metering is an enabling technology for a CCS marketplace and, consequently, large-scale CCS deployment.

CCS can leverage measurement experiences fostered in the oil and gas industry, where numerous metering techniques coexist. These comprise volumetric methods such as pressure drop (e.g., orifice or Venturi), turbine, optical, ultrasonic metering, and mass flow meters such as Coriolis. However, given the notable difference in the behavior and properties of CO₂ under varying CCS

conditions, against those of natural gas, the applicability of such techniques to CCS systems needs to be evaluated.

CO₂ poses specific challenges for flow measurement. It will be transported as pressurized liquid or dense phase, a state quite different from, e.g., pipeline conditions of water or natural gas. Further, bulk shipping is expected to take place at low temperatures, down to -50 °C, to reduce pressure. With the whole vapor-liquid equilibrium curve of CO₂ being close to relevant transport states, from the triple point to the critical point, properties could change rapidly with temperature and pressure.

Currently, it is not clear how traceable fiscal metering will be achieved at a relevant scale for CCS. The only technology with published studies claiming accuracies below the EU requirements is Coriolis [6], but only for pure CO₂ and at flow rates (3600 kg/h) far below what will be required ahead. For CO₂ with impurities, there are no verified results at even this scale with sufficient accuracy. Further, CO₂ sound attenuation is higher than for many other fluids, and the performance of ultrasonic time-of-flight (TOF) meters is yet to be independently confirmed for pure CO₂.

At a system level, procedures and infrastructure for traceability must be developed, taking into account relevant industrial conditions.

Against this backdrop, NCCS [7] is addressing the challenges described above through continuous dialogue with industrial stakeholders and systematic benchmarking of technologies to close knowledge gaps. The present work looks into measurement technologies with opportunities to fast-track fiscal metering for CCS deployment.

The benchmarking of the measurement principles presented in this study aims to better understand the potential of the existing commercial metering technology for CCS. The combination of proprietary know-how and research method is exploited for a thorough characterization of the most promising sensing principles and infrastructure needs for further development and verification. A discussion of the design of a test facility is presented here as a first step towards fiscal metering calibration and verification at an industrial scale.

The remainder of this paper is organized into five sections as follows. Section 2 provides an overview of the relevant regulatory framework for fiscal metering within CCS. Section 3 benchmarks promising metering technologies and discusses the planned actions to answer some of the pending questions for ultrasonic metering applicability. Section 4 establishes the need for a fiscal metering test facility and discusses the specifications and basic design for pertinent industrial utilization. The main conclusions of this study are summarized in Section 5.

2. Regulatory framework

2.1 EU regulations and directives

2.1.1 EU Emission Trading System (ETS) regulations

The current basis for fiscal metering regarding the European ETS is provided by the ETS M&R Regulation

2018/2066 [5]. From the text in Article 49, regulations for the transfer of CO₂, and Annex VIII, Section 1, Tier 4, it can be deduced that the required accuracy for measuring the net captured CO₂ mass is 2.5 % on an annual basis. This is a relaxation from the previous and often quoted limit of 1.5 % specified by the now superseded Commission Decision 2010/345.

Article 42 of the M&R Regulation specifies the legal requirements to establish these estimates, which is to follow standards where available. Where no applicable published standards exist, suitable draft standards, industry best practice guidelines, or other scientifically proven methodologies shall be used. Hence, developing such best practice/scientifically proven methodologies is a significant motivation for the fiscal metering activity of NCCS.

2.1.2 EU measurement instrument directive (MID)

The EU MID (Directive 2014/32) [4] was written to harmonize the laws of the EU and EEA member countries on measurement devices. It has been in force since 2016. Of particular relevance for CCS, Annex VII provides regulations for continuous measurements of liquids other than water. Different accuracy classes are defined, and for liquid CO₂, the accuracy class 1.5 is specified. This means that the whole measurement system should have an accuracy of 1.5 %, but the meter must have an accuracy of 1.0 %. Further, a minimum 4:1 turndown ratio is specified. It also sets specific accuracy limits for associated measurements needed to convert the measurements into a mass flow. The accuracy limits are 0.5 °C in temperature and 2 kg/m³ in density. For pressure, the limits are 50 kPa below 10 bar, 5 % between 10 and 40 bar, and 200 kPa above 40 bar.

2.2 Other standards and recommendations relevant for CO₂ fiscal metering

2.2.1 OIML R 117

OIML is the international organization for legal metrology. The principal recommendation of interest to CCS is OIML R 117 ‘Dynamic measuring systems for liquids other than water.’

The metrological and technical requirements applicable to dynamic measuring systems for liquids other than water are specified in the OIML R 117-1 [8]. Based on the field of application, the measuring systems are classified into four accuracy classes. The measuring systems for liquefied CO₂ belong to Accuracy Class 1.5, which requires an overall accuracy of the complete measuring systems of 1.5 %. This is in agreement with EU MID. Also, R117-1 specifies that the maximum permissible errors for a meter under rated operating conditions is 1 % for the measuring system of Accuracy Class 1.5.

2.2.2 NIST Handbook 44 – 2017

NIST is the US National Institute for Standards and Technology. NIST Handbook 44 – 2017 [9]. Section 3.38 covers the code requirements applicable to liquid-measuring devices used to measure liquid CO₂, though

not all of it applies to large-scale flow. The measurement of liquid CO₂ is classified as Accuracy Class 2.5 with an acceptable tolerance for the measuring devices of 1.5 %, and the test liquid shall be CO₂ in a compressed liquid state.

2.2.3 ISO standards

There are several ISO standards relating directly to different metering technologies. Some of these standards only cover high-level guidance, e.g., ISO 10790:2015 [10] for Coriolis meters. Others, such as ISO 5167-2:2003 [11] for orifice plates, are very detailed. There are also standards ISO 12242:2012 [12] and ISO 17089-2:2012 [13] for ultrasonic meters for liquids and gas, respectively. ISO/IEC 17025:2017 [14] establishes the general requirements for the competence of testing and calibration laboratories.

2.3 Comparison between NCCS specifications on accuracy and existing regulations, standards, and recommendations

As seen above, the M&R regulation, which specifies a mass accuracy of 2.5 %, appears not to be entirely in agreement with the MID and OIML R 117, which defines a measurement system mass flow accuracy of 1.5 %. One interpretation could be that the MID regulates the accuracy needed for a measurement system at a given point, and the additional 1 % allowed under the M&R Regulation accounts for other uncertainties in the CCS chain regarding the stored CO₂ mass. It should also be noted that the ETS regulations are still under regular review. In either case, 1.5 % mass flow accuracy seems like a sensible criterion when evaluating mass flow metering systems after considering the available regulations and recommendations. Note that both MID and OIML R 117 establish a 1.0 % accuracy for the flow meter itself.

Verification of a fiscal meter requires a reference flow with accuracy much higher than the meters' specification.

3. Benchmarking of flow metering methods for CCS

3.1 Flow metering technologies with potential for CCS

There exists a great variety of flow metering technologies, including Coriolis flowmeters, orifice plates, ultrasonic meters, turbine meters, venturi meters, vortex meters, tomography, radiation attenuation densitometry, SONAR-based meters, and nucleonic-based meter. Three technologies that have been identified as particularly relevant for CCS applications will be discussed in the following.

3.1.1 Coriolis flowmeters

Coriolis flowmeters use the Coriolis effect to directly measure the amount of mass moving through the meter. Thus, it has the advantage over volumetric flowmeters that pressure and temperature measurements by separate

equipment are not required to convert volumetric flow rate into mass flow rate. Coriolis flowmeters have been tested for pure CO₂ in gas, liquid, two-phase, and supercritical phases covering a limited condition, such as a temperature range of 17 – 30 °C and pressure range of 54 – 85 bar [6, 15, 16]. The uncertainty is higher with impurities [17-19] but probably still acceptable for ETS. However, no verification has so far been performed at flow rates relevant for full-scale CCS, lower temperatures, or other normal operational conditions. The influence of temperature variations of fluid or the ambient environment has not been systematically studied yet.

3.1.2 Ultrasonic flowmeters

The ultrasonic flowmeters (USMs) measure the velocity of a fluid with ultrasound to calculate volume flow, using time of flight or frequency. Over recent years, ultrasonic technologies have been developed to overcome the measurement challenges of CO₂, which includes the use of more sophisticated and powerful signal processing features and diagnostics. USMs have been evaluated in the application of CO₂-rich natural gas [20, 21], and flow meter suppliers have expressed that the issue of acoustic attenuation can be handled. Nevertheless, this remains a main uncertainty regarding the applicability of USMs for CCS in different relevant functions. Apart from signal attenuation, the measurement uncertainty of USMs is dependent on the accuracy of density measurement, flow conditions, temperature and pressure process conditions, etc. The ultrasonic flowmeters have the potential to provide high accuracy, non-invasive CCS measurement system, and zero to no pressure drop, provided their performance is fully characterized for the given high sound attenuation of CO₂.

3.1.3 Orifice plates

The orifice metering technology measures the pressure drop before and after an orifice plate, and the flow rate can be obtained from Bernoulli's equation using coefficients established from extensive research. The orifice plates have been used in the facility in the In Salah CCS demonstration project and a pilot capture plant operated by Vattenfall AB. There are, however, no demands on accuracy since no regulatory reporting requirements were involved in these schemes. Orifice plates are attractive due to their inherent simplicity. In addition to an unavoidable pressure drop, the main weakness of orifice plate meters is probably their inflexibility regarding the fluid flow rate and properties. Compared with many other fluids, CO₂ properties have a rather high sensitivity to temperature, pressure, and small amounts of impurities at relevant conditions.

3.2 Benchmarking

Table 1 summarizes the potential of the metering technologies assessed for CO₂ transport.

Table 1: Summary of benchmarking study for the potential metering technologies

	Coriolis	Ultrasonic	Orifice plate
Fiscal accuracy class (OIML R117)	0.3	0.3	-
Measurement range (10")	~1,000 tonnes/hr (nominal)	1824 m ³ /hr	Similar to Coriolis, but small turndown permissible without affecting accuracy
Process pressure limit	SS316, 100 barg, SS318 / Hastelloy C22 200 barg	No fundamental limit for clamp-on for liquids or inline (>176 bar installed).	Not a limitation in practice
Process Temperature range	Sufficient (e.g., KROHNE commercial models can be specified from -200 to +400 °C)	Sufficient (-190 to +500 °C depending on options and models)	Pressure transducer dependent, but little flexibility once calibrated for a fluid
Ambient temperature (°C)	-40 to +65 °C	-40 to +65 °C	Pressure transducer dependent
Composition ranges	In principle, unlimited and flexible as long as single-phase is ensured, but must be verified	Higher impurity level can give higher signal strength, but more uncertain density (if based on EOS)	In principle, unlimited and flexible as long as single-phase is ensured, but more uncertain density (if based on EOS)
Pressure drop	Yes	Can be negligible	Yes, and it could be strongly tied to accuracy
Multi-phase	To a limited degree and with lower accuracy	Normally not	No
Density relation	The meter can inherently also be used as a densimeter, but density does not have a first-order effect on the mass flow measurement	First-order impact, external measurement, or model estimate required	First-order impact, external measurement, or model estimate required
Weight and footprint (10")	~900 kg, 0.85 m ²	0.09 m ² / 4 beams ~530 kg	Relatively small
Recalibration interval /method	Interval not specified. Method depends on required uncertainty	Interval not specified. Method depends on required uncertainty	Interval not specified. Method depends on required uncertainty
Long-term measurement stability	Not defined	Not defined	Not defined
Installed costs	High	High	Low
Flange dimension	10" may be a practical limit for the purpose	TBC, most likely no limitations	Any
TRL (Scale of EC and for CO ₂ transport)	4	4	9
Knowledge gaps	Verification at varying conditions	Properties, especially attenuation, transients	Properties
Zero stability (10" pipe)	< 50.0 kg/hr	< 0.18 m ³ /h	High uncertainty with high turndown
Flow conditioning	Not required	For a 4 path meter, either: <ul style="list-style-type: none"> • 20D upstream - flow meter - 5D downstream, or • 5D upstream - flow conditioner - 10D upstream - flow meter - 5D downstream D is the nominal diameter	Flow conditioner required

3.3 Further evaluation

In NCCS, actions are being undertaken to perform static tests of an ultrasonic flow meter as a first step to evaluate the use of such technology for fiscal metering of large-scale CCS systems and partially close pending knowledge gaps identified above. The planned tests will monitor signal strength, speed of sound, and receiver diagnostics at relevant temperature and pressure ranges for CO₂ transport. The tests will also verify zero flow measurement when using the flow meters for liquid CO₂.

An ultrasonic multipath, transit-time-based meter will be tested at SINTEF Energy Research laboratories in

Trondheim. The experiments consist of filling the meter's body with liquid CO₂ and measuring the signal output at various conditions relevant for CO₂ transport, as illustrated in Figure 1. The response of the sensors will be characterized as a function of fluid temperature and pressure. The temperature will be controlled within ±1 °C by enclosing the vessel in a temperature-controlled chamber.

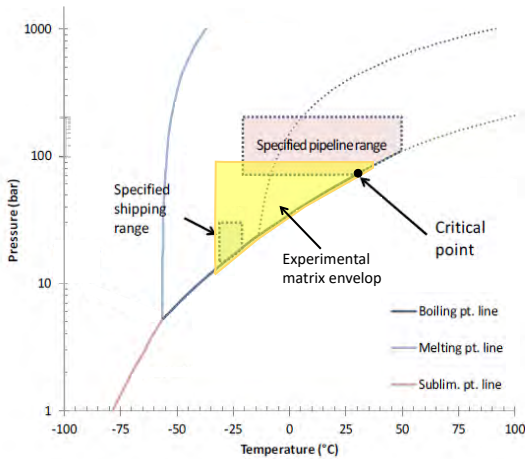


Figure 1: Experimental envelop for ultrasonic CO₂ static tests

4. Flow loop for fiscal metering testing

The benchmarking above discussed the potential of orifice plates, Coriolis, and ultrasonic meters for CCS. Each technology has an operational envelope that makes them suitable for particular applications. The complexity of the CCS process, as different industrial CO₂-rich sources are incorporated into the value chain, precludes the development of a generic fiscal metering solution enveloping all possible conditions. This, however, creates a potential for distinct application niches for the various metering solutions, hence providing opportunities for utilization for a variety of technologies.

A recent ZEP report [22], targeting opportunities and challenges of Trans-European CO₂ transportation infrastructure for CCUS, highlights that testing different measurement technologies, under representative conditions and compositions, is a necessary step towards determining suitable metering solutions. To do so, a large-scale test facility for CCUS pipeline and metering technologies needs to be constructed, as no full-scale test facilities for calibration of flow meters under real liquid or two-phase CO₂ process conditions exist today [23].

Within NCCS and a national project for CCS research infrastructure for ECCSEL ERIC [24] (ECCSEL NFS), the design of such a facility has been thoroughly addressed. The following subsections provides the specifications defined for the planned experimental facility. The design aims to be industry-relevant and target high TRLs in measurement technologies. A high-level description of the basic design is also provided.

4.1 Facility specifications

The design parameters for the research facility and subsystems were defined following two workshops and several discussions with NCCS industrial partners, including end-users and operators. The premises for the facility's specification on capacity and accuracy comprise:

- The accuracy in mass and volumetric flow measurement should be significantly higher than the ETS requirements [5], the EU MID [4], and the NIST [9] recommendations.
- Fluid under tests must be in single (liquid) phase.

- The flow rate should be in the range of 200-600 tonnes per hour to make the facility relevant for flow metering in full-scale projects.

- The facility's pressure range should be as close to real transport conditions as possible to mimic real transport scenarios.

- The facility should be able to satisfy stability and accuracy requirements in line with the General requirements for the competence of testing and calibration laboratories standard ISO/IEC 17025.

-The facility's loop size should be as close as possible to the actual measuring instrument sizes (8-12" range).

The specifications provided in Table 2 encompass capacity, temperature, pressure and composition ranges, and accuracy of the measuring variables, i.e., mass flow, volume flow, and density.

Table 2: Specifications for CO₂ fiscal meter test facility

Parameter	Specification
Mass flow accuracy	0.25 %
Volumetric flow accuracy	0.25 %
Accuracy in density	1.2 kg/m ³
Max flow rate (t/h)	600
Min flow rate (t/h)	50
Max flow (m ³ /h)	800
Phase state	Liquid / dense phase
Pressure (bara) ^a	Up to 120
Process temperature (°C)	4 to 40
Ambient temperature (°C)	-20 to 25
Composition range (mole fractions)	
CO ₂	≥75 mol%
N ₂	≤ 25 mol%
Ar	≤ 25 mol%
H ₂ (TBC)	≤ 10 mol%
CH ₄ (TBC)	≤ 23 mol%
H ₂ O	≤ 350 ppm
O ₂	≤ 10 ppm
H ₂ S	0
CO ^b	-
SO _x ^b	-
NO _x ^b	-
Amines	0
Reference fluids	Pure water
Meter pressure drop (bar)	< 2
Test section length	20 m
Development length (upstream / downstream meter)	15 m / 4 m
Pipe dimension (inches)	10
Reference normative	ISO 17025, OIML R 117

^a Minimum pressure is the evaporating pressure at a given temperature plus a safety margin to avoid vapor phase formation.

^b May occur as impurity in other source gases.

4.2 Basic operation and design

The facility has been designed to enable testing and calibration of sensing technologies and flow meters for CO₂-relevant mixtures; the focus is on traceability, flexibility, and accuracy.

An overview of the facility is sketched in the diagram shown in Figure 2. The system encompasses a highly instrumented recirculating loop filled and pressurized from an external source into a buffer tank. The circulation of the CO₂ mixture is provided by a liquid pump. A

cooling unit downstream the pumping system ensures thermal control of the process.

A flow straightener upstream of the metering technologies under test (MUT) ensures a fully developed flow profile without distortions at the inlet of the flow meters. Flexibility in the design allows for the testing section to be easily substituted with one of different dimensions to accommodate various flow meter sizes.

Accurate densimeters are placed upstream and downstream of the MUT. These measurements will be compared with integrated density measurements which some flow meter types and models have.

Mixture composition is measured using a gas chromatograph (GC). The fluid must be in single-phase, i.e., liquid or dense phase, throughout the circuit during the test runs; otherwise, the composition of the mixture will vary, and GC sampling would yield unrepresentative results.

Accurate measurement of volume or mass flow is ensured through a two-step process. A primary reference is used to calibrate an array of flow meters. These calibrated meters will henceforth be applied as secondary references for tests/calibration of the MUT. The array of meters is designed to be chain calibrated against the primary reference unit. The capacity of the primary reference must match that of the second reference flow meters. The number of flow meters in the array is determined by the capacity of these meters, and hence of the primary reference, and the targeted maximum flow (600 t/h). The aim is to have a reconfigurable system to accommodate for a primary-secondary reference calibration of all the meters. The strategy of using multiple parallel secondary references is employed by other labs, e.g., for LNG [25, 26] or natural gas [27]. These must, however, be calibrated against a traceable reference at steady state under the temperature and pressure conditions specified in the test matrix.

Depending on the type of MUT, it could be of interest to reference both for volume and mass flow rate. Reference measurements of liquid mass flow are usually based on gravimetry and timing, while a reference for volume flow rate could be based on volume and time measurements. For mass, volume, and time, there are measurement practices resulting in accepted estimates of uncertainty [8, 28-30].

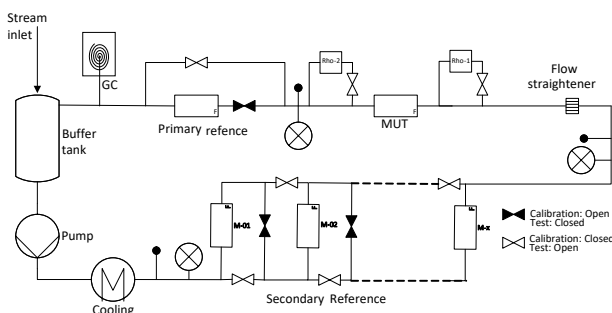


Figure 2: Schematic of an experimental facility for CO₂ metering

4.2.1 Primary reference technologies

The primary reference is the single most crucial system in the loop for accuracy and traceability. Following, two possible solutions for primary references of CO₂ streams are discussed.

One possible method consists of diverting the flow to a closed container. This, however, involves accurate back pressure control at the tank inlet to maintain the pressure. Such a valve and control system, suitable for the high flow rates and pressure drops that will occur, requires advanced custom-made components. The possibility of dry ice formation must also be taken into consideration. During the rig operation, close control of the pressure, above boiling point, must be ensured in the buffer tank. Avoiding fast boil-off and subsequent temperature drop, in hand with control of the fast dynamics of the system's temperature, guarantees uniform composition of the circulated stream.

Another solution is that of readily available direct volumetric primary reference combined with derived mass calculation. Volumetric meter proving is a method that has been long implemented in the industry, ever since advancement in the pulse interpolation techniques allowed for the development of provers of smaller scale, i.e., small volume provers (SVP)[31]. Volume proving consists of a traveling piston, which is used to measure volume flow. The position of the piston within the proving cylinder, which corresponds to a calibrated volume, is detected by optical switches located at different positions along the piston trip. The addition of a densitometer and accurate pressure and temperature measurement would allow direct and indirect, respectively, estimates of mass flow from the measured volume flow. API standard section 4 [32] establishes that Provers must have an uncertainty of less than $\pm 0,01\%$ for all measurements relating to meter proving, including uncertainties in temperature, flow, and pressure. SVPs are made for applicable flow rates and pressures, and both Emerson and Honeywell claim repeatability of the order of 0,02% [33, 34] for water flow. However, no accuracy numbers are provided, and it is an open question how accurate and repeatable the provers are with more compressible liquids like CO₂.

4.2.2 Secondary reference: preliminary uncertainty assessment

A preliminary uncertainty analysis was performed for the secondary reference array proposed in the facility schematic. Assuming the meters of each reference stage i has a relative repeatability of $u(i)$, the uncertainty contribution for each meter is $\sqrt{2}u(i)$. The total relative uncertainty contribution of the calibration stage is then in the interval $\sqrt{2}u(i) \left[\frac{1}{\sqrt{N_{p,i}}} \quad 1 \right]$, where $N_{p,i}$ is the number of parallel arms of stage i . The maximum is reached if the fluctuations of the meters in the arms of the stage have a correlation of 1. The minimum value is assumed if the fluctuations of the stage meters are independent of each other. The real case is probably somewhere in between. Assuming that the relative repeatability of the meters of each stage is the same $u = u(1) = u(2) \dots$, and the

number of parallel meters in each stage is the same $N_p = N_{p,1} = N_{p,2} = \dots$ we get the limiting cases provided in Table 3, where N_s is the number of stages. Hence, $N_s = 1$ in the base case scenario of Figure 2.

Table 3: Preliminary uncertainties of secondary reference

	Independent arms & stages	Independent arms, correlated stages	Correlated arms, independent stages	Correlated arms & stages
	$\sqrt{\frac{2N_s}{N_p}}u$	$N_s \sqrt{\frac{2}{N_p}}u$	$\sqrt{2N_s}u$	$N_s \sqrt{2}u$
$N_s = 1$ $N_p = 9$	$\sqrt{\frac{2}{9}}u = 0,47u$	$\sqrt{\frac{2}{9}}u = 0,47u$	$\sqrt{2}u = 1,41u$	$\sqrt{2}u = 1,41u$

5. Conclusions and further work

There are several potential issues associated with the accurate measurements of CO₂ mass flow in CCS systems due to the behaviour and properties of CO₂ and the expected CCS conditions. Three flow metering technologies were found most promising; after being reviewed, their benefits and limitations with respect to the measurement of CO₂ in CCS schemes were addressed. Coriolis seems like a promising technology for CCS due to its high accuracy and no apparent showstoppers for CCS except perhaps scalability and pressure drop, but this remains to be verified. Similarly, for ultrasonic meters, which have become popular for natural gas, the impact of the high acoustic absorption of CO₂ flow requires dedicated assessment. In this sense, in NCCS, efforts are being undertaken to evaluate the attenuation of sound at relevant pressure and temperature conditions of liquid CO₂ transport.

The benchmarking study also showed that there is no current single metering system that can fulfil all of the requirements for the various CO₂ metering needs, in particular when impurities are present, or the physical conditions are varying. Further, at present, no technology has been verified at the accuracy required by ETS at industrially relevant flow rates for pure CO₂. Existing measurement technologies should hence be further developed and validated for different CCS applications and be experimentally evaluated and verified to the accuracy required by ETS.

There are no test facilities or established methodology for testing CO₂ flow meters at an industrial scale under transport conditions. Methodologies and procedures used for gases or incompressible liquids must be modified for accurate verification of CO₂ flow metering technology. The specifications of an industrial-sized facility for verification of CO₂ fiscal metering were provided, along with a high-level discussion on the basic design of such facility and subsystems. Primary reference measurements of CO₂ mass and volume flow will require innovative solutions and specialized components (pumps, valves, temperature control, etc.).

Acknowledgments

This publication has been produced with support from the NCCS Centre, performed under the Norwegian research

program Centres for Environment-friendly Energy Research (FME) and the ECCSEL NFS project, performed under the INFRASTRUKTUR program.

The authors acknowledge the following partners for their contributions: Aker Carbon Capture, Allton, Ansaldo Energia, Baker Hughes, CoorsTek Membrane Sciences, Equinor, Fortum Oslo Varme, Gassco, KROHNE, Larvik Shipping, Lundin Norway, Norcem, Norwegian Oil and Gas, Quad Geometrics, Stratum Reservoir, Total, Vår Energi, Wintershall DEA, and the Research Council of Norway (257579/E20 and 296486).

References

- [1] "Energy Technology Perspectives 2017," International Energy Agency, Paris, France, <http://www.iea.org/etp/>, 2017.
- [2] V. Masson-Delmotte *et al.*, Eds. *Global Warming of 1.5°C*. <https://www.ipcc.ch/sr15/>: IPCC 2018.
- [3] "World Energy Outlook 2020," International Energy Agency, Paris, France, 2020. [Online]. Available: <https://www.iea.org/weo>
- [4] *Directive (EU) 2014/32 Measuring instruments directive (MID)*, 2014.
- [5] *Regulation (EU) No 2018/2066 on the monitoring and reporting of greenhouse gas emissions*, E. Commission, 2018.
- [6] L. Sun, Y. Yan, T. Wang, X. Feng, and P. Li, "Development of a CO₂ two-phase flow rig for flowmeters calibration under CCS conditions," presented at the FLOMEKO 2016, Sydney, Australia, 2016.
- [7] "NCCS: Norwegian CCS Research Centre – Industry driven innovation for fast track CCS deployment." <http://www.sintef.no/nccs> (accessed).
- [8] "Measuring systems for liquids other than water. Part 1: Metrological and technical requirements," in "International Recommendation," Organisation Internationale de Métrologie Légale, 2007.
- [9] *Handbook 44*, NIST, 2017. [Online]. Available: https://www.nist.gov/system/files/documents/2016/11/10/hb44-2017-web_final.pdf
- [10] *ISO 10790:2015 Measurement of fluid flow in closed conduits — Guidance to the selection, installation and use of Coriolis flowmeters (mass flow, density and volume flow measurements)*, ISO, 2015.
- [11] *ISO 5167-2:2003 Measurement of fluid flow by means of pressure differential devices inserted in circular cross-section conduits running full*, ISO, 2003.
- [12] ISO, "ISO 12242:2012 Measurement of fluid flow in closed conduits — Ultrasonic transit-time meters for liquid," 2012.
- [13] ISO, "ISO 17089-2:2012 Measurement of fluid flow in closed conduits - Ultrasonic meters for gas " Part 2: Meters for industrial applications., 2012.
- [14] *ISO/IEC 17025:2017 General requirements for the competence of testing and calibration laboratories*, ISO, 2017.
- [15] C.-W. Lin, M. Nazeri, A. Bhattacharji, G. Spicer, and M. M. Maroto-Valer, "Apparatus and method for calibrating a Coriolis mass flow meter for carbon dioxide at pressure and temperature conditions represented to CCS pipeline operations," *Applied Energy*, vol. 165, pp. 759-764, 2016.
- [16] L. Wang, J. Liu, Y. Yan, X. Wang, and T. Wang, "Mass flow measurement of two-phase carbon dioxide using Coriolis flowmeters," in *2017 IEEE International Instrumentation and Measurement*

- Technology Conference (I2MTC), 2017: IEEE, pp. 1-5.
- [17] M. Nazeri, M. M. Maroto-Valer, and E. Jukes, "Performance of Coriolis flowmeters in CO₂ pipelines with pre-combustion, post-combustion and oxyfuel gas mixtures in carbon capture and storage," *International Journal of Greenhouse Gas Control*, vol. 54, pp. 297-308, 2016.
- [18] K. Adefila, Y. Yan, L. Sun, and T. Wang, "Flow measurement of CO₂ in a binary gaseous mixture using an averaging Pitot Tube and Coriolis mass flowmeters," *Flow Measurement and Instrumentation*, vol. 54, pp. 265-272, 2017.
- [19] K. Adefila, "Flow measurement and leakage detection of gaseous CO₂," University of Kent, 2015.
- [20] J. L. Keith Harper, Toralf Dietz, "Field Experience of Ultrasonic Flow Meter Use in CO₂-Rich Applications," in *North Sea Flow Measurement Workshop*, 2009: NFOGM.
- [21] J. Wenzel, "Evaluations on CO₂ Risch Natural Gas," presented at the Flow Measurement Workshop 2015, Noordwijk, 2015. [Online]. Available: https://sportdocbox.com/Scuba_Diving/100525697-Evaluations-on-co2-rich-natural-gas-jorg-wenzel-sick.html.
- [22] A. M. Moe *et al.*, "A Trans-European CO₂ Transportation Infrastructure for CCUS: Opportunities & Challenges," Advisory Council of the European ZeroEmission Technology and Innovation Platform (ETIP ZEP), <https://zeroemissionsplatform.eu/a-trans-european-co2-transportation-infrastructure-for-ccus-opportunities-challenges/>, 2020.
- [23] J. M. Kocbach, et al, "Where do we stand on flow metering for CO₂ handling and storage?," presented at the 38th International North Sea Flow Measurement Workshop, 2020.
- [24] "ECCSEL ERIC." <http://www.eccsel.org/> (accessed.
- [25] P. Lucas *et al.*, "World's first LNG research and calibration facility," presented at the FLOMEKO 2016, Sydney, 2016.
- [26] M. v. d. Beek, P. Lucas, O. Kerkhof, M. Mirzaei, and G. Blom, "Results of the evaluation and preliminary validation of a primary LNG mass flow standard," *Metrologia*, vol. 51, pp. 539-551, 2014.
- [27] A. Johnson and T. Kegel, "Uncertainty and Traceability for the CEESI Iowa Natural Gas Facility," *Journal of Research of the National Institute of Standards and Technology*, vol. 109, no. 3, pp. 345-369, 2004.
- [28] "Weights of classes E₁, E₂, F₁, F₂, M₁, M₁₋₂, M₂, M₂₋₃ and M₃. Part 1: Metrological and technical requirements," Organisation Internationale de Métrologie Légale (OIML), 2004.
- [29] "Evaluation of measurement data — Guide to the expression of uncertainty in measurement (GUM)," JCGM, 2008.
- [30] *Measurement of liquid flow in closed conduits -- Weighing method*, 1980.
- [31] G. Williams, "Fundamentals of meter provers and proving methods," *American School of Gas Measurement Technology*, 2016.
- [32] *Manual of Petroleum Measurement Standards* A. P. Institute, 1998.
- [33] *Daniel™ Compact Prover*. (2011). Emerson Process Management. [Online]. Available: <http://www.emerson.com/documents/automation/daniel-provers-compact-prover-data-sheet-en-43910.pdf>
- [34] *Enraf® Small Volume Prover*. (2011). Honeywell. [Online]. Available: <https://www.honeywellprocess.com/library/marketing/brochures/Smallvolumeprover-Brochure.pdf>

CCS PUBLIC PERCEPTION LEARNINGS APPLIED TO BRAZIL

Karen Louise Mascarenhas^{1,3*}, Julio Romano Meneghini^{2,3}

¹ Institute of Psychology, University of São Paulo, São Paulo, Brazil

² Polytechnical School, University of São Paulo, São Paulo, Brazil

³ Research Centre for Gas Innovation, University of São Paulo, São Paulo,

* Corresponding author e-mail: karenmascarenhas@usp.br

Abstract

Carbon Capture and Storage (CCS) is considered a relevant technology to deal with climate change mitigation. However, the technology is not yet known to the various audiences, be it by the government and legislators, by industry, by academia, by media, or by society, which are far from being aware of such technologies and their impacts. This paper aims to discuss the Brazilian citizens' public perception of onshore and offshore CCS projects. Based on the international literature on CCS public perception and a few studies conducted in the Brazilian context, some highlights and recommendations are drawn. The results show Brazil as a vast country of significant diversity and inequality that requires research approaches covering local, regional and national dimensions. A substantial part of the Brazilian population believes that global warming is happening and demands immediate mitigation actions. Such a mindset could be favourable to accept CCS projects as one of the possible solutions.

Keywords: 3 - 5 keywords (Keywords) *Public Perception, acceptance, resistance, risk perception, knowledge*

1. Introduction

Carbon Capture and Storage (CCS) and Carbon Capture, Usage and Storage (CCUS) are considered relevant technologies to deal with climate change mitigation. These technologies consist in capturing carbon dioxide (CO₂) and other greenhouse gases resulting from industrial processes such as steel and cement production, combustion of fossil fuels in energy production and transportation to store these gases in onshore or offshore facilities. The storage could be made in geological reservoirs in depleted oil and gas fields, saline formations, coal beds [1], rock salt caverns [2] and absorption by plants through photosynthesis. The latter is a form of natural storage, although CO₂ will be released further in the process, requiring it to be cyclical to mitigate emissions. Mitigating or reducing the level of CO₂ in the atmosphere is critical to avoid dreadful climate impacts such as droughts, wildfires, intense heatwaves, ice melting in the pole areas, sea-level rises, floods and destruction due to severe storms, among many other possibilities [3]. Keep the rise of the average temperature of the planet limited to 2°C, preferably 1.5°C, is seen by scientists as the most recommended scenario [4], in which it is expected that human life may adapt. Through the Paris Agreement, launched in 2015 and signed by 193 countries, these have committed to take actions to limit the emissions with targets for 2030 and 2050 aiming for zero emissions and, in some cases, negative emissions.

Although CCS is a potential tool to achieve such targets, it does not come without controversy. Some argue that CCS has a local impact on the community or ecosystems close to the site where it is implemented. Impacts could

be environmental landscape or land use resulting from the transport, drilling and storage on onshore locations. Other risks are related to CO₂ concentrated leakages driving water and atmosphere contamination, affecting human health, or possible seismic activity, even worse in denser populated areas [5]. However, there is also a positive aspect of economic growth, providing employment and commercial development, apart from the "clean" use of fossil fuel and decarbonising the economy [6].

However, the technology is still evolving and is not yet known to the various audiences, be it by the government and legislators, responsible for establishing laws and deciding on regional projects; by the industry, which still has no clear understanding of all the technical, economic and social aspects involved; by academia, that keeps furthering the analysis of the issues; by the media, which requires a better preparation to convey correct information; or by society, which is far from being aware of such technologies and their impacts. Understanding how people perceive and relate to energy technologies has been an essential aspect of the CCS process [7].

The objective of this paper is to discuss citizen CCS public perception within the Brazilian context. The following section details Brazil's scenario and opportunities to develop CCS projects. Section 3 presents the main aspects of public perception in the international literature, and section 4 aggregates the Brazilian studies. Section 5 discusses Brazilian CCS public perception, and section 6 concludes with the final remarks.

2. CCS opportunities in the Brazilian landscape

The increase in energy consumption in developing countries with the consequent escalation in greenhouse gas emissions has been highlighted [8]. To deal with such challenges, Román [8] points out that some of these countries could reduce the adverse effects by implementing large-scale CCS projects. However, CCS technology is relatively expensive and competes with resources for local priority economic development.

Among other developing countries, such as India and South Africa that have significant coal participation in their energy mix, Brazil has a comparable cleaner and renewable matrix, through hydropower, responsible for 73 per cent of its energy production. The high level of 83 per cent CO₂ eq emissions results from agriculture, land-use change and forest management [8].

Even though CCS is not a strong strategy for Brazil in emissions reduction planning, it has received government approval. Petrobras, the Brazilian oil and gas company, has developed two CCS projects, one in a saline aquifer and the other on enhanced coal bed methane (CBM).

Favourable conditions, such as the estimated capacity of 2000 Gt of CO₂ storage in onshore and offshore petroleum fields, saline aquifers, and deep coal, which corresponds to close to 20 per cent of the world's storage capacity, contrast with potential environmental impacts and development concerns [8]. One of the leading ecological limitations to the onshore storage of CO₂ in Brazil, despite the sizeable underground reservoir capability, is the Guarani aquifer that runs from the Paraná region in Brazil through Argentina, Paraguay and Uruguay. The risk of any CO₂ leakage can threaten the quality of drinking water, demanding the settlement of monitoring systems and ruling of long-term responsibilities [8, 9].

Conversely, the offshore pre-salt oil and gas fields discovered in 2006 on the coast of five states in Brazil represent another attractive alternative for CCS. The high content of CO₂, which represents between 10 to 40 per cent of the associated gas, could be stored, preventing it from being ventilated to the atmosphere [10, 11]. Technologies to separate these gases in salt caverns in the pre-salt layer before extraction are being developed by a group of researchers in the Research Centre for Gas Innovation at the University of São Paulo [10–13]. That would represent a great innovation that could boost CCS efforts in the pre-salt layer offshore, preventing the release of CO₂ into the atmosphere.

Brazil, contrary to many developing countries, has a particular situation with a cleaner energy matrix. In that sense, economic development that leads to raising the demand for energy production is seen as decoupled from high greenhouse gas emissions, which impacts climate change [8]. However, the growing needs for energy alongside the pre-salt production availability may provide more fossil fuel in the Brazilian energy mix, scenario, in which CCS could be a possible solution, as it could enable the sustainable use of fossil fuel.

In favour of CCS development in Brazil, the source and sink match proximity is analysed by [8] as an advantage. In this sense, oil and gas are extracted in the pre-salt field, which may also store CO₂ in the same area, reducing the burden of transportation. Although offshore opportunities in Brazil are located very far from the coast, about 200 to 300 km away and in ultra-deep waters, meaning 2,000 to 5,000 meters below the ocean level. Technology to deal with such challenges is still under development, and the construction of salt caverns offshore is costly. If the CO₂ could be separated in the process of oil and gas exploitation, it could be kept under the ocean in salt caverns with minimal impact on people and ecosystems [11]. The challenge currently lies in the possible use of the gas commercially. This would require, for example, the construction of extensive pipelines or arrangements for long journeys of maritime transportation to the consumer centres.

For example, pipelines significantly increase the cost in offshore facilities, although, compared to onshore pipelines in densely populated areas, the latter can be even more costly [8]. We argue that onshore and offshore alternatives in Brazil require further studies.

Onshore options include the Recôncavo Basin in the State of Bahia, which presents potential characteristics for CO₂ storage [14]. Another promising onshore technology is bioenergy with CCS, named biomass carbon capture and storage (BECCS). The carbon-neutral bioenergy, combined with CCS adoption, is potentially an enabler to net-zero or even below zero emissions [15].

Noticeable for Brazil, the opportunities for developing CCS projects are an alternative to avoid the release of CO₂ from the offshore extraction of oil and gas by storing it in caverns in the pre-salt formation. How would Brazilian citizens perceive such offshore endeavours? Would this public react differently towards onshore projects?

To further discuss the perception of the Brazilian population, the next section will present a brief international literature summary of the main aspects related to the theme.

3. CCS public perception

3.1 Main features of CCS public perception in the literature

Public perception has become a relevant factor in implementing CCS and other large projects, as public opposition can lead to project cancellation. An iconic example is the Barendrecht project in the Netherlands [16, 17] that is often discussed in the literature. In that case, the project, which had neutral or positive support from the politicians, ended up cancelled, in part due to the strong public opposition that emerged and influenced the decision-makers to vote against its implementation [16]. That situation points to the need to understand the public views, opinions and attitudes towards CCS to develop adequate and timely communications.

From the start, relationships should be developed based on trust, which is also valid when planning and implementing CCS projects. The most successful ones created a dialogue space with society, articulating stakeholders divergencies and interacting with the local community through an open debate [18, 19].

Therefore, building awareness, meaning that people understand the technology, considering its benefits and risks, is crucial, as it seems to be low in general. The technology involves three stages: capture, transport, and storage, each comprising various possible technological applications. Such processes are complex and somewhat technical for the understanding of the lay public. Hence, it is essential to develop reliable communication enhancing public knowledge of CCS and its role in climate change mitigation. This effort can be challenging, as the level of non-believers on climate change has increased in the United States, according to [20], despite scientific advice that argues based on the anthropogenic effect over the planet. In this narrative, humankind intervention in nature is leading to global warming [21, 22].

Beyond awareness and knowledge, benefit and risk perception influence the public acceptance of a CCS project. Possible risks are described in the literature as CO₂ leakages and water contamination that may affect human and animal health [23]. Seismic activity is another risk that might impact property value in the vicinity [24].

Another well-known reaction to new technologies is NIMBY, "Not In My Back Yard" syndrome, in which people disapprove of the project implementation in their area. This kind of opposition is described in many large-scale projects, such as CCS, nuclear power plants, and renewables, when people oppose wind turbines in their land or neighbourhood [25].

Socio-demographics, culture, specific circumstances, previous experience with the technology, or the stakeholders responsible for the project also play a part in how the public perceives new technologies, including CCS. However, there is no 'one fits all' formula to deal with the diversity of reactions resulting from these factors.

In some locations, a part of CCS financing is expected to be coming from the energy consumer's bill to provide cleaner and greener energy [26]. Research demonstrates that people's willingness to pay for new technologies, including CCS, may be affected by the acceptance and preferences between technologies, as people have different perspectives about the energy transition they would support [26]. The discussion is mostly on whether CCS is a technology that would bridge the path out of fossil fuels towards renewables or would be a solution to maintain 'business as usual' [27].

Governmental policies often result from the interactions among stakeholders sharing their interests, which are not always aligned to the society's views. However, policies in similar areas may support new ones to approach emerging technologies such as CCS.

3.2 Cross-country studies in CCS public perception

Many studies about CCS public perception were developed in the United States, United Kingdom, Australia, Norway, China, Canada and Europe [17, 28, 29]. As a top common finding, they identify low public awareness and a tendency of unstable public opinions, as people oscillate depending on several circumstances [30].

In research that investigated the perception of CCS in six European countries [30], the level of awareness among male respondents was higher than among females. Group ages and level of education also varied. Older people (65-75 years old) were less aware of the technology than the middle age group (50-64 years old), and those with higher education responded as being more informed about it. Another factor the research pointed out is that in Norway and in the Netherlands, the general level of knowledge of CCS is 62.6% and just over 50%, respectively. In Norway, Romania and Greece, about 75% of the respondents never heard about such technology. The authors argue that "information and education strategies regarding CCS technologies must be tailored to the specific context of each country and group being targeted" [30].

When considering the best way to contain global warming [30], a study comparing CCS with other energy technologies such as nuclear power, wind, and solar, CCS is one of the least favourably evaluated, excepting nuclear. Nevertheless, the overall reactions to CCS are neutral or slightly positive [30]. However, CCS projects have still been very recently implemented, demanding more time to better verify people's thoughts and feelings in the long term within the region the technology is in operation.

Changing perceptions was also evaluated in the six European countries [30], denoting that for some of them, when the population was offered negative information, the tendency was driven to negative perception, and the opposite, when exposed to positive information, the results tended to move towards a slightly more positive perception. Curiously, Romania respondents with relatively little knowledge moved to a somewhat more positive response even though exposed to negative information. In turn, Germany moved to a slightly more negative position when exposed to positive data.

These results are an invitation for researchers to look into their assumptions and search for more in-depth aspects of human behaviour, understanding the irrational decision making and attitudes that people often assume. The outbreak of the global coronavirus pandemic in 2020 evidenced the diversity of people's reactions when exposed to uncertain and controversial subjects such as climate change and mitigation actions. Denial of the situation, and the severity of the consequences, discredit of scientific evidence, the growth of misinformation and social media fake news, conspiracy theories and many other interpretations of reality.

Therefore, the need to discuss and further investigate public perception is stressed. This summary of features affecting the public perception and acceptance will

support the discussion of these aspects in the specific Brazilian case, the aim of this paper, and presented in the next section.

4. CCS public perception in Brazil

4.1 Brazil and global warming perception

Considering the aspects pointed out in the international literature when analysing CCS projects implementation in Brazil, it is essential to comprehend the country's specificities. Brazil is a vast country with continental territorial dimensions, occupying 8.516 million km². It is the fifth-largest country on the planet, after Russia, Canada, the United States and China, and the largest in Latin America. Currently, Brazil has over 210 million inhabitants unequally distributed within five regions and 5,568 municipalities [31]. Brazil is also well known for its diversity of regional landscapes, rich in coast and inland cities, that vary in size, with large and cosmopolitan busy towns, such as São Paulo, beautiful coastal cities, such as Rio de Janeiro, the natural ecosystems of the Amazon forest, and many diverse human settlements.

Nevertheless, a new survey conducted in October 2020 [32] with 2600 participants from the five regions of Brazil showed that 92 per cent of Brazilians believe that global warming is happening and it is urgent to protect the planet. Seventy-seven per cent believe it is caused by human activity and that government (35 per cent), industry (32 per cent), citizens (24 per cent) and NGO (4 per cent) can best contribute to the solution. Seventy-four per cent of the respondents adopted waste separation practices for disposal and recycling. For 72 per cent of the participants, global warming can severely damage the current generation, and for 88 per cent, it will significantly harm future generations.

The survey also pointed out that 77 per cent of Brazilians consider it more important to protect the environment, even though such a position could reduce economic growth and employment. However, the federal government currently in charge has been adopting opposed actions, drastically reducing environmental defence policies and minimising the control of areas of environmental protection in the country.

4.2 Research in CCS public perception in Brazil

One of the very few studies related to CCS public perception in Brazil was published in 2020 [14]. The authors analyse 57 interviews with local citizens in the Recôncavo Basin region in the State of Bahia, an area of ten potential CCS onshore injection fields, primarily aiming at enhanced oil recovery (EOR). The results point out the familiarity of the local population with the oil business as the members live close to or within areas of previous oil exploration. This proximity is perceived on the one hand as positive, as the industry enables the creation of jobs, takes care of the road maintenance, and qualifies the payment of royalties. On the other hand, during the previous exploration phase, no money from

royalties was paid to those who leased the land for oil prospectation because the regulation was not in place. The traffic of heavy trucks has damaged the roads and cracked the walls of houses by the roadway. Part of the group has complaints about the lack of information about risks and guidance about dealing with possible water contamination or other accidents. Even though it is not conclusive or subject to generalisation, the data from this limited sample offers some insights into the local population's troubles and expectations. The interviewees mentioned their interest in sharing their opinions and being heard by the stakeholders in charge, providing them with a sense of empowerment. The majority of the interviewees was optimistic about the possibility of influencing decisions, especially in locations with higher density.

As in other countries, the level of awareness about the technology is low, and in this research [14], no one was knowledgeable about CCS application. Consequently, reactions of opposition were not manifested at that time, probably because the situation was new. The majority had a reasonable level of trust in the oil and gas company, despite some mistrust related to the company not presenting the complete picture of pros and cons when communicating the impacts of applied technologies.

Noticeably, the planning and implementation of CCS projects in Brazil are incipient. However, it is imperative to consider the social aspects and establish communication channels with the local community of prospect areas for CCS implementation.

5. Discussion

The [32] survey results indicate that the Brazilian population is sensitive to global warming and is concerned with the environment. Therefore, this evidence suggests possible support for technologies such as CCS to prevent global warming. When communicating the benefits of CCS projects, this feature should be stressed. However, job creation and economic growth require to be balanced with environmental preservation to meet the local community's expectations and the broader Brazilian population.

The Brazilian population demonstrates a willingness to change behaviours if they understand their contribution to shaping a low carbon society. The substantial number (74 per cent) of adopters of separating waste for disposal and recycling suggest so [32].

Brazil is a country of great inequality, with a significant part of the population with a low level of education. In this scenario, implementing CCS projects in impoverished locations can be well received as the opportunity for job creation, and economic growth would be attractive. Social justice elements become relevant, balancing the needs of progress and preserving the local environment and the community's culture.

As noticed by [14], familiarity with oil and gas companies may be favourable to reduce opposition if the relationship is positive. In this situation, community members of denser settlements might feel optimistic and

empowered to make themselves heard and take actions otherwise.

As trust in stakeholders has a positive influence on acceptance [33], open and frequent public conversations are highly recommended to keep the community informed of the activities and their consequent impacts. However, the lack of efficient communication channels between the stakeholders and the community can lead to mistrust, NIMBY reactions, and rejection, threatening project continuity.

More research is required to assess the local population's risk and benefit perception in sites where CCS project are intended to be settled. Nevertheless, some of the risk issues are related to the safety of the technology, water and air contamination, damage and dust caused by heavy trucks in the area. The perceived benefits are job creation and economic growth, and with the current regulation of royalties, financial reward from the land leasing.

Brazil has a good set of environmental protection laws that the federal government is currently amending to benefit economic development. However, there is not a specific regulation about CCS technologies. The previous government approval [8] should be further discussed to produce appropriate standards for CCS projects.

As there are very few CCS projects in operation in Brazil, many aspects should be further investigated, such as the financing modelling, building different scenarios that support decision making. If one of the options considers the contribution from energy consumers, the willingness to pay for the technology and the preferences among low carbon technologies should be further investigated.

CCS public perception seems to be critical in onshore projects, as described previously. Although the public might not be very interested in technologies being developed and implemented offshore, there are few studies, for example, Tomakomai offshore storage [34], that prove otherwise, in which fishermen and the fishing industry were concerned about the effect of CO₂ leakages in the maritime ecosystems and ocean acidification. Offshore CCS public perception studies in Brazil would be highly recommended.

6. Final remarks

The literature on CCS public perception has highlighted the main features that are attributed to diverse populations. Namely, awareness, knowledge, NIMBY, benefits and risk perception, socio-demographic factors, willingness to pay for CCS, trust, acceptance and preferences between technologies, governmental policy and interaction between stakeholders [1] should be further investigated in Brazil.

As Brazil is a vast country with significant inequality, it would be recommended to pursue research at many levels, approaching local, regional, and national dimensions to understand the 'publics perceptions'. Onshore and offshore CCS public perception must be investigated to comprehend the nuances in each situation

and contribute to the bulk of knowledge to support CCS projects.

Considering such diversity within the country, lessons learned indicate communication will be more effective if direct and straightforward, supported with visual aids that facilitate apprehension by everyone, regardless of age or educational level. Democratic, open and frequent communication with the community is highly recommended to build and to maintain trust between the public and stakeholders.

This study is limited by the insufficient literature on CCS public perception in Brazil and the lack of field studies that could expand the analysis. Therefore, carrying out research to fill this gap is crucial.

Acknowledgements

The authors gratefully acknowledge support from Shell Brasil together with FAPESP through the 'Research Centre for Gas Innovation – RCGI' (Fapesp Proc. 2014/50279-4), hosted by the University of São Paulo, and the strategic importance of the support given by ANP (Brazil's National Oil, Natural Gas and Biofuels Agency) through the R&D levy regulation. Mascarenhas also thanks CNPq (Brazilian National Council for Scientific and Technological Development) for its partial financial support for this study.

References

1. Tevetkov, P., Cherepovitsyn, A., & Fedoseev, S. (2019). Public perception of carbon capture and storage: A state-of-the-art overview. *Heliyon*, 5(12), e02845. <https://doi.org/10.1016/j.heliyon.2019.e02845>
2. Jiang, K., & Ashworth, P. (2021). The development of Carbon Capture Utilization and Storage (CCUS) research in China: A bibliometric perspective. *Renewable and Sustainable Energy Reviews*, 138(November), 110521. <https://doi.org/10.1016/j.rser.2020.110521>
3. Global CCS Institute (2019). *Global Status of CCS 2019: Targeting Climate Change*. Global CCS Institute. https://doi.org/10.1007/springerreference_15392
4. Leemans, R., & Vellinga, P. (2017). The scientific motivation of the internationally agreed 'well below 2 °C' climate protection target: a historical perspective. *Current Opinion in Environmental Sustainability*, 26–27, 134–142. <https://doi.org/10.1016/j.cosust.2017.07.010>
5. Wallquist, L., Visschers, V. H. M., & Siegrist, M. (2010). Impact of knowledge and misconceptions on benefit and risk perception of CCS. *Environmental Science and Technology*, 44(17), 6557–6562. <https://doi.org/10.1021/es1005412>
6. Anderson, K., Bows, A., Mander, S., Shackley, S., Agnolucci, P., & Ekins, P. (2006). Decarbonising Modern Societies: Integrated Scenarios Process and Workshops. *Policy Studies*, (March).
7. Chrysostomidis, I., Perumalpillai, S., Bohm, M., Crombie, M., Beynon, E., & Lee, A. (2013). CO₂ capture project's CCS stakeholder issues review and

- analysis. *Energy Procedia*, 37, 7832–7839. <https://doi.org/10.1016/j.egypro.2013.06.676>
8. Román, M. (2011). Carbon capture and storage in developing countries: A comparison of Brazil, South Africa and India. *Global Environmental Change*. <https://doi.org/10.1016/j.gloenvcha.2011.01.018>
 9. KETZER, J. M. M., MACHADO, C. X., ROCKETT, G. C., & IGLESIAS, R. S. (2016). *Atlas brasileiro de captura e armazenamento geológico de CO₂*.
 10. Maia da Costa, A., V. M da Costa, P., D. Udebhulu, O., Cabral Azevedo, R., F. F. Ebecken, N., C. O. Miranda, A., ... Breda, A. (2019). Potential of storing gas with high CO₂ content in salt caverns built in ultra-deep water in Brazil. *Greenhouse Gases: Science and Technology*, 9(1), 79–94. <https://doi.org/10.1002/ghg.1834>
 11. Mascarenhas, K. L., Peyerl, D., Moretto, E. M., & Meneghini, J. R. (2019). Challenges for the Implementation of Carbon Capture and Storage (CCs) in Brazil: a Socio-Technical Approach. *Polytechnica*, 2(1–2), 1–8. <https://doi.org/10.1007/s41050-019-00016-z>
 12. Mascarenhas, K. L., Peyerl, D., Weber, N., Mouette, D., Cuellar, W. O. S., Meneghini, J. R., & Moretto, E. M. (2020). Sustainable Development Goals as a Tool to Evaluate Multidimensional Clean Energy Initiatives. In W. Leal Filho, P. Borges de Brito, & F. Frankenberger (Eds.), *International Business, Trade and Institutional Sustainability* (World Sust., pp. 645–657). Springer, Cham. https://doi.org/10.1007/978-3-030-26759-9_37
 13. Román, M. (2011). Carbon capture and storage in developing countries: A comparison of Brazil, South Africa and India. *Global Environmental Change*, 21(2), 391–401. <https://doi.org/10.1016/j.gloenvcha.2011.01.018>
 14. Netto, A. L. A., Câmara, G., Rocha, E., Silva, A. L., Andrade, J. C. S., Peyerl, D., & Rocha, P. (2020). A first look at social factors driving CCS perception in Brazil: A case study in the Recôncavo Basin. *International Journal of Greenhouse Gas Control*, 98(April), 103053. <https://doi.org/10.1016/j.ijggc.2020.103053>
 15. Moreira, J. R., Romeiro, V., Fuss, S., Kraxner, F., & Pacca, S. A. (2016). BECCS potential in Brazil: Achieving negative emissions in ethanol and electricity production based on sugar cane bagasse and other residues. *Applied Energy*, 179, 55–63. <https://doi.org/10.1016/j.apenergy.2016.06.044>
 16. Feenstra, C. F. J., Mikunda, T., & Brunsting, S. (2011). What happened in Barendrecht? Case study on the planned onshore carbon dioxide storage in Barendrecht, the Netherlands. *Policy Studies*, 44. Retrieved from <http://www.csiro.au/files/files/pybx.pdf>
 17. Ashworth, P., Bradbury, J., Wade, S., Ynke Feenstra, C. F. J., Greenberg, S., Hund, G., & Mikunda, T. (2012). What's in store: Lessons from implementing CCS. *International Journal of Greenhouse Gas Control*, 9, 402–409. <https://doi.org/10.1016/j.ijggc.2012.04.012>
 18. Reiner, D. (2011). Evaluating global Carbon Capture and Storage (CCS) communication materials: A survey of global CCS communications. *Work*, (June), 1–46.
 19. Dowd, A. M., Itaoka, K., Ashworth, P., Saito, A., & de Best-Waldhober, M. (2014). Investigating the link between knowledge and perception of CO₂ and CCS: An international study. *International Journal of Greenhouse Gas Control*, 28, 79–87. <https://doi.org/10.1016/j.ijggc.2014.06.009>
 20. Xifra, J. (2016). Climate Change Deniers and Advocacy: A Situational Theory of Publics Approach. *American Behavioral Scientist*. <https://doi.org/10.1177/0002764215613403>
 21. Scott, V., Gilfillan, S., Markusson, N., Chalmers, H., & Haszeldine, R. S. (2013). Last chance for carbon capture and storage. *Nature Climate Change*, 3(2), 105–111. <https://doi.org/10.1038/nclimate1695>
 22. Poortinga, W., Spence, A., Whitmarsh, L., Capstick, S., & Pidgeon, N. F. (2011). Uncertain climate: An investigation into public scepticism about anthropogenic climate change. *Global Environmental Change*, 21(3), 1015–1024. <https://doi.org/10.1016/j.gloenvcha.2011.03.001>
 23. Fogarty, J., & McCally, M. (2010). Health and safety risks of carbon capture and storage. *JAMA - Journal of the American Medical Association*, 303(1), 67–68. <https://doi.org/10.1001/jama.2009.1951>
 24. Benson, S. M., Bennaceur, K., Cook, P., Davison, J., Coninck, H. de, Farhat, K., ... Global Energy Assessment Writing Team. (2012). Carbon Capture and Storage. In J. Ahearne (Ed.), *Global Energy Assessment: Toward a Sustainable Future* (pp. 993–1068). Cambridge University Press. <https://doi.org/10.1017/CBO9780511793677.019>
 25. Braun, C. (2017). Not in My Backyard: CCS Sites and Public Perception of CCS. *Risk Analysis*, 37(12), 2264–2275. <https://doi.org/10.1111/risa.12793>
 26. Kraeusel, J., & Möst, D. (2012). Carbon Capture and Storage on its way to large-scale deployment: Social acceptance and willingness to pay in Germany. *Energy Policy*, 49, 642–651. <https://doi.org/10.1016/j.enpol.2012.07.006>
 27. Jiang, J., Ye, B., & Liu, J. (2019). Research on the peak of CO₂ emissions in the developing world: Current progress and future prospect. *Applied Energy*, 235(October 2018), 186–203. <https://doi.org/10.1016/j.apenergy.2018.10.089>
 28. Watson, J., Kern, F., & Markusson, N. (2014). Resolving or managing uncertainties for carbon capture and storage: Lessons from historical analogues. *Technological Forecasting and Social Change*, 81(1), 192–204. <https://doi.org/10.1016/j.techfore.2013.04.016>
 29. Guo, Y., Ashworth, P., Sun, Y., Yang, B., Yang, J., & Chen, J. (2019). The influence of narrative versus statistical evidence on public perception towards CCS in China: Survey results from local residents in Shandong and Henan provinces. *International Journal of Greenhouse Gas Control*, 54–61. <https://doi.org/10.1016/j.ijggc.2019.02.021>
 30. Pietzner, K., Schumann, D., Tvedt, S. D., Torvatn, H. Y., Næss, R., Reiner, D. M., ... Ziogou, F. (2011). Public awareness and perceptions of carbon dioxide capture and storage (CCS): Insights from surveys administered to representative samples in six European countries. *Energy Procedia*, 4, 6300–6306. <https://doi.org/10.1016/j.egypro.2011.02.645>
 31. IBGE. (2013). *Censo 2010. Atlas censo demográfico*.

32. IBOPE Inteligência. (2020). *Mudanças climáticas: a percepção dos brasileiros*.
33. Yang, L., Zhang, X., & McAlinden, K. J. (2016). The effect of trust on people's acceptance of CCS (carbon capture and storage) technologies: Evidence from a survey in the People's Republic of China. *Energy*, 96, 69–79. <https://doi.org/10.1016/j.energy.2015.12.044>
34. Mabon, L., Kita, J., & Xue, Z. (2017). Challenges for social impact assessment in coastal regions: A case study of the Tomakomai CCS Demonstration Project. *Marine Policy*, 83, 243–251. <https://doi.org/10.1016/j.marpol.2017.06.015>

IMPACT OF UNCERTAINTY OF PHYSICAL PROPERTIES ON CO₂ ABSORPTION DESIGN

Lars Erik Øi^{1*}, Sumudu Karunarathne¹

¹ Faculty of Technology, Natural Sciences and Maritime Studies, University of South-Eastern Norway, Porsgrunn, Norway

* Corresponding author e-mail: lars.oi@usn.no

Abstract

The mass transfer coefficients, interfacial area and pressure drop of a packed bed are essential properties that need to be evaluated prior to the design of a CO₂ absorption column. Various mathematical models have been proposed to predict these properties under different process conditions. This work has compared several mathematical models for pressure drop, mass transfer coefficients and interfacial area and discussed how the uncertainty of physical properties and process conditions affect the evaluation of packed bed height in a CO₂ absorption column. A case study has been performed to study the propagation of uncertainty in input variables through the packed bed height design equations. Here, it was found as 12% from uncertainty in physical properties and 60% from uncertainty in choice of mathematical model of the calculated packed bed height. A recommended safety factor for the absorption packing height is 60 % for a generic packing, but this safety factor can be reduced considerably if experimental data for pressure drop and mass transfer coefficients are available for the specific packing.

Keywords: CO₂ capture, mass transfer coefficients, pressure drop, column design, uncertainty

1. Introduction

Physicochemical properties like density, viscosity and surface tension are vital in the design of process equipment such as absorption and desorption columns, heat exchangers, reboilers, condensers and pumps in post combustion amine-based CO₂ capture. In the design of a CO₂ absorption column, the gas side and liquid side mass transfer coefficients and interfacial area can be calculated by proposed mathematical models under different liquid and gas flow rates. The proposed models for mass transfer coefficients are based on physical theories of wetted wall theory and penetration theory [1]. In addition to the traditional methods, the applicability of ANN (artificial neural networks) correlations for mass transfer coefficients and interfacial area have been discussed by Piche and co-workers [2].

In our previous work, the propagation of uncertainty of physical properties through mass transfer models was discussed [3]. It was observed that the uncertainty of viscosity has a high influence on mass transfer coefficients. These uncertainties further propagate through design equations for sizing of the packed bed in absorber columns. Therefore, it is important to decide a safety factor for packing height to acquire the desired CO₂ removal efficiencies. This study discusses the mass transfer coefficients, interfacial area and pressure drop calculations from available mathematical models in the literature. Further, the study discusses the effect of uncertainty of physical properties and other process parameters on the evaluation of packed bed height. The work performed by Nookuea *et al.* [4] discussed the impact of physical properties of gas and liquid on design of an absorption column. Kvamsdal and Hillestad [5],

and Razi and Svendsen [6] investigated mass transfer and physical property models considering CO₂ absorption into aqueous MEA. Mathias *et al.* [7] performed a quantitative analysis of the effects of uncertainty in property models on the simulation of CO₂ capture. And Nookuea *et al.* [8] indicates that the density and diffusivity show opposite effect to viscosity in the estimation of packing height. A review of property impact on carbon capture and storage processes has been performed by Tan *et al.* [9].

2. Mass transfer coefficients, interfacial area and pressure drop calculations

Liquid hold-up and pressure drops have been calculated using Excel spreadsheets, by the methods in Rocha *et al.* [10], Billet and Schultes [11] and Stichlmair *et al.* [12]. All these correlations are based on the dimensionless numbers defined below (2 to 5):

$$d_E = 4 \cdot \frac{\varepsilon}{a_N} \quad (1)$$

$$Re_L = \frac{v_L \cdot d_E \cdot \rho_L}{\mu_L} \quad (2)$$

$$We = \frac{v_L^2 \cdot d_E \cdot \rho_L}{\sigma} \quad (3)$$

$$Fr = \frac{v_L^2}{g \cdot d_E} \quad (4)$$

$$Sc_G = \frac{\mu_G}{\rho_G \cdot D_G} \quad (5)$$

$$v_{REL} = \frac{v_G}{(1 - h_L) \cdot \varepsilon \cdot 0.7071} \quad (6)$$

The h_L was calculated using a correlation from Billet and Schultes [11] which is valid up to the loading point:

$$h_L = \left[\frac{12 \cdot \mu_L \cdot v_L \cdot a_N^2}{g \cdot \rho_L} \right]^{0.333} \quad (7)$$

The liquid hold-up was calculated to 0.087 and 0.089 at the specified top and bottom conditions. A constant value of 0.09 was then used in later calculations of the other parameters in all the correlations.

Dry packing pressure drop and total pressure drop have been calculated by the correlations for pressure drop from Stichlmair *et al.* [12], from Billet and Schultes [11] and from Rocha *et al.* [10]. The equations used may differ slightly from the original correlations and are given in earlier work [13].

Pressure drops in dry packing (with only gas) and total pressure drop (with gas and liquid) for the conditions in Table 1 are calculated in Excel and the results for total drop are shown in Figure 1:

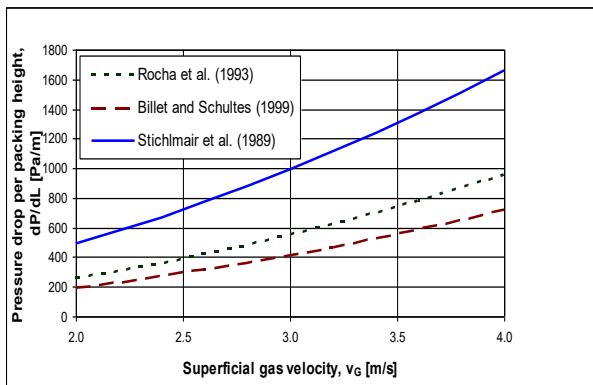


Figure 1: Calculated pressure drop from correlations using packing type Mellapak 250Y at typical CO₂ absorption column top conditions as a function of gas velocity. From [13].

As shown in Figure 1, the pressure drop increases with the increase of superficial gas velocities. The pressure drop from the correlation given by Stichlmair *et al.* [12] shows relatively large deviations from Billet and Schultes [11] and Rocha *et al.* [10] especially at high superficial gas velocities.

The effective relative interfacial areas for the conditions in Table 1 were determined based on estimation methods

proposed in Rocha *et al.* [10], Billet and Schultes [11] and deBrito *et al.* [14]. The equations used are (8-10).

$$a_{EFF} = 0.465 \cdot \left(\frac{v_L \cdot \rho_L}{\mu_L \cdot a_N} \right)^{0.3} \quad (8)$$

$$a_{EFF} = 1.5 \cdot (a_N \cdot d_E)^{-0.5} \cdot Re_L^{-0.2} \cdot We^{0.75} \cdot Fr^{-0.45} \quad (9)$$

$$a_{EFF} = \frac{0.35 \cdot 29.12 \cdot (We \cdot Fr)^{0.15}}{Re_L^{0.2} \cdot \varepsilon^{0.6} \cdot (1 - 0.93 \cdot 0.9) \cdot 0.7071^{0.3}} \quad (10)$$

The calculated a_{EFF} from Rocha *et al.* [15], Billet and Schultes [11] and deBrito *et al.* [14] are presented in Figure 2.

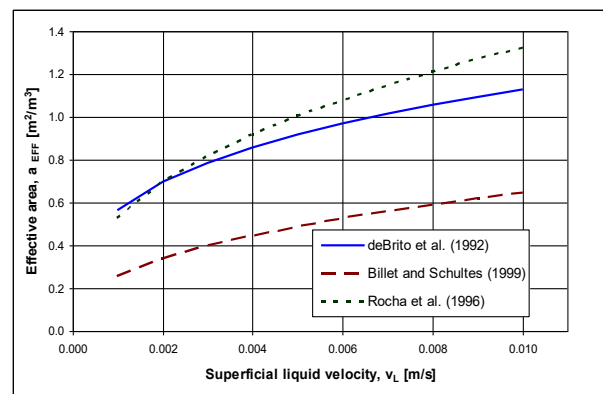


Figure 2: Calculated effective relative interfacial area from correlations at typical CO₂ absorption column top conditions as a function of superficial liquid velocity. From [13].

The interfacial area increases with superficial liquid velocity as shown in Figure 2 for all correlations. The model proposed by Billet and Schultes [11] underestimates the property compared to the other two models.

Gas side mass transfer coefficients have been calculated in a spreadsheet using the estimation methods from Rocha *et al.* [15], Billet and Schultes [11] and deBrito *et al.* [14]. The equation forms are the versions in Brunazzi *et al.* [16]. The equations used are defined in [13].

The packing type assumed in the calculations are Mellapak 250Y from Sulzer. The packing specific parameter (0.41) is specified to the average of the values from Billet and Schultes [11] for the Montz packings B1-200 and B1-300 which are similar packings with nominal specific areas of 200 and 300 m²/m³.

The physical properties liquid viscosity, gas viscosity and diffusion coefficients are calculated from the equations described in [13]. The calculated k_G from Rocha *et al.* [15], Billet and Schultes [11] and deBrito *et al.* [14] are presented in Figure 3.

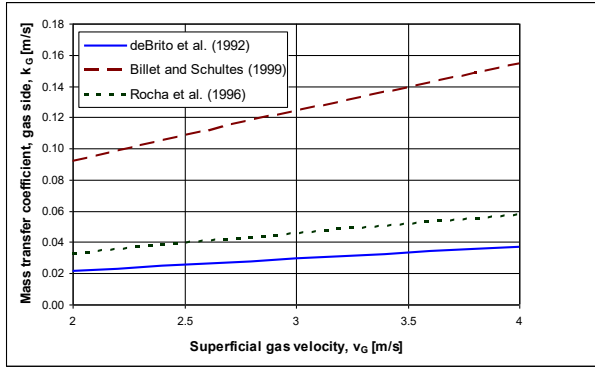


Figure 3: Calculated gas side mass transfer coefficients at typical CO₂ absorption column top conditions as a function of gas velocity. From [13].

The gas side mass transfer coefficient increases with the increase of superficial gas velocity. The considered models behave similarly with the variation of superficial gas velocity. A relatively high deviation is reported by Billet and Schultes [11] at both lower and higher superficial gas velocities compared to Rocha *et al.* [10] and deBrito *et al.* [14] as illustrated in Figure 3.

The liquid side mass transfer coefficients have been calculated in an Excel spreadsheet using the estimation methods from Rocha *et al.* [15], Billet and Schultes [11] and deBrito *et al.* [14]. The equation forms are the versions in Brunazzi *et al.* [16] and the equations are defined in [13]. The calculated k_L from Rocha *et al.* [15], Billet and Schultes [11] and deBrito *et al.* [14] are presented in Figure 4.

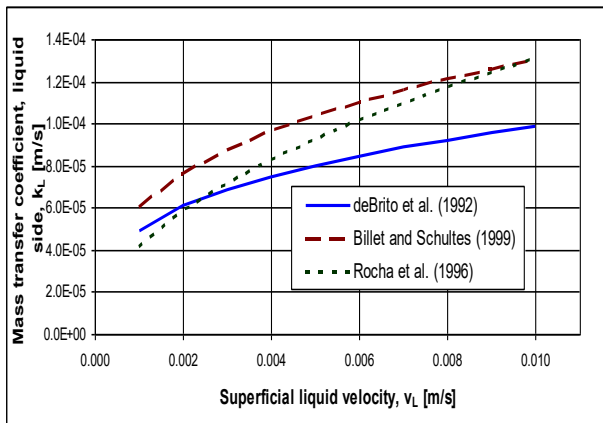


Figure 4: Calculated liquid side mass transfer coefficients as a function of liquid velocity. From [13].

The predicted liquid side mass transfer coefficient increases with the increase of liquid superficial velocity as shown in Figure 4. The deviations between the predictions from different models are less compared to the predictions for the gas side mass transfer coefficient. The model from deBrito *et al.* [14] underpredicts the liquid side mass transfer coefficient compared to models Billet and Schultes [11] and Rocha *et al.* [10] at higher superficial liquid velocity.

Table 1: Specifications for estimation of pressure drop, effective interfacial area and mass transfer coefficients at top condition in the absorber column.

Parameter	Top
Temperature, T [°C]	49
Pressure, P [bar(a)]	1.01
Gas superficial velocity, v_G [m/s]	3.5
Liquid superficial velocity, v_L [m/s]	0.0041
Liquid density, ρ_L [kg/m ³]	1050
Gas density, ρ_G [kg/m ³]	1.02
Liquid viscosity, μ_L [kg/(m·s)]	0.0023
Gas viscosity, μ_G [kg/(m·s)]	0.000019
Surface tension, σ , [N/m]	0.055
Liquid CO ₂ diffusivity, D_{CO_2} [m ² /s]	$1.2 \cdot 10^{-9}$
Void fraction, ϵ [m ³ /m ³]	0.97
Nominal surface area, a_N [m ² /m ³]	250
Side of corrugation, S [m]	0.017
Liquid hold-up, h_L [m ³ /m ³]	0.09

3. Uncertainty in height calculation in absorption column

The height of the absorber packing is a function of several parameters like molar gas flow rate per unit cross sectional area G [mol/(m²·s)], overall gas phase mass transfer coefficient K_G [mol/(m²·Pa·s)], total pressure P [Pa], interfacial surface area a [m²/m³] and mole fractions y [-] of the gas inlet and outlet of the absorber. Typical design equations found in chemical engineering textbooks are (11 to 13).

$$Z = f(G, P, K_G, a, y_{CO_2}) \quad (11)$$

$$Z = \frac{G}{K_G \cdot a \cdot P} \int_{y_{CO_2 \text{ out}}}^{y_{CO_2 \text{ in}}} \frac{dy_{CO_2}}{(y_{CO_2} - y_{CO_2}^*)} \quad (12)$$

$$Z = \frac{G}{K_G \cdot a \cdot P} \ln \left[\frac{y_{CO_2 \text{ in}}}{y_{CO_2 \text{ out}}} \right] \quad (13)$$

Figure 5 shows the cause-and-effect diagram to illustrate the uncertainty sources and their effect on absorber packing height calculation. The input variables in Equation 11 are identified as the main uncertainty sources and drawn as main branches. For the mass transfer coefficient and interfacial area, the physical properties of density, viscosity and surface tension were identified as uncertainty sources as they appear in most of the correlations. There can be other uncertainty sources in addition to the sources shown in Figure 5 and those are not discussed in here.

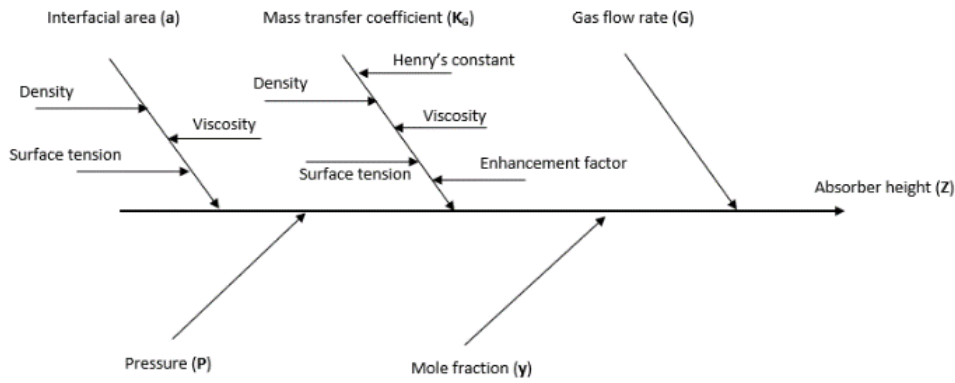


Figure 5: Cause and effect diagram

The uncertainties of the variables involved in Equation 13 are combined taking Root Sum Square (RSS). There the height of the packing is partially differentiated with respect to all the variables involved and combined as given in Equation 14.

$$\delta Z = \sqrt{\sum_{i=1,n} C_i^2 \cdot u(x_i)^2} \quad (14)$$

The individual contribution to the overall uncertainty was found from the term $|C_i \cdot u(x_i)|$. There, x_i and $u(x_i)$ are independent variables and associated uncertainties shown in Equation 14. The C_i are sensitivity coefficients evaluated as $C_i = \partial Z / \partial x_i$.

The following scenario with assumptions is considered in the evaluation of packed bed height. A column with a 2 m diameter was considered to calculate the gas flow rate into the column. Superficial gas and liquid flow rates were considered as given in Table 1. The expected CO₂ removal efficiency was 90%. Finally, the packed bed height was determined as 14.2 m according to the specification given in Table 1 for the absorption conditions at the column top.

Table 2: Uncertainties of the input variables.

Parameter	Uncertainty	
	Scenario 1 Karunaratne et al., 2017	Scenario 2 Øi, 2012
Gas flowrate (G)	1%	1%
Mass transfer coefficient (K _g)	5%	50%
Interfacial area (a)	4%	20%
Pressure drop (dP)	10%	30%
Mole fractions (y)	1%	1%

The considered uncertainties for this work are listed in Table 2. In scenario 2 the uncertainties for the mass transfer coefficient, interfacial area and pressure drop were decided from the experience from previous studies based on uncertainty evaluations of mass transfer

coefficient and interfacial area of proposed mathematical models in literature for random packings [13]. In scenario 1 the uncertainties raised due to the propagation of uncertainties in physical properties of density, viscosity and surface tension through mass transfer and interfacial area models were considered in Karunaratne *et al.* [3]. The uncertainty in pressure drop was considered due to the pressure drop of the column and other uncertainties were due to the possible variations in the feed conditions.

The calculated error from Equation 14 is the standard uncertainty for the absorber packing height. In this case, it is ±1.7 m and it is 12% of the calculated packing height for the uncertainties based on Karunaratne *et al.* [3]. The uncertainty in packing height is ±9 m and it is 60% of the calculated packing height for the uncertainties Øi [13]. The increased uncertainties in mass transfer coefficient, interfacial area and column pressure caused to increase the uncertainty in packed bed height. The uncertainty in absorber packing height from uncertainty in physical properties was calculated to 12%. The uncertainty in absorber packing height from uncertainty due to different correlations was calculated to 60%.

The calculated individual contributions to the overall uncertainty are shown in Figure 6 and 7 for the two scenarios given in Table 2.

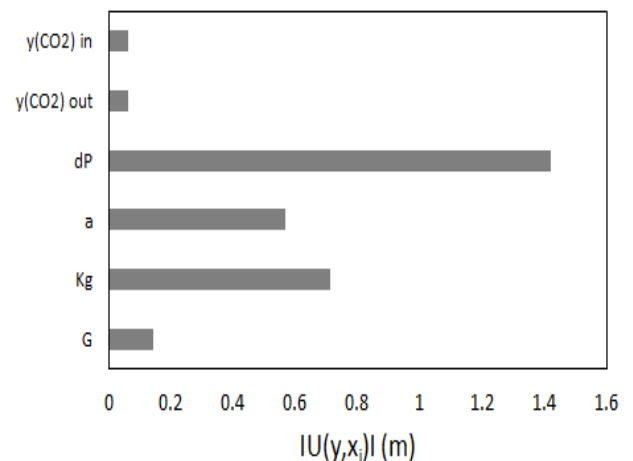


Figure 6: Uncertainty contributions from different uncertainty sources for scenario 1.

For the uncertainties considered in scenario 1, the highest individual contribution for the uncertainty of packing height was the pressure drop. For the scenario 2, the uncertainty of mass transfer coefficient has the highest uncertainty among the other uncertainty sources and it gives the highest individual contribution for the uncertainty of packing height.

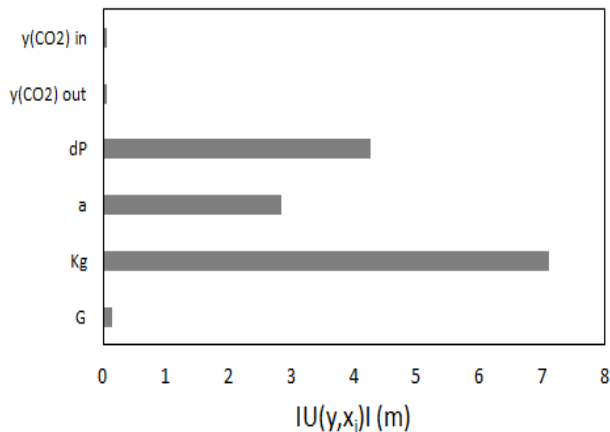


Figure 7: Uncertainty contributions from different uncertainty sources for scenario 2.

To keep a design within the uncertainty, a safety factor of 60 % in absorber packing height is calculated in this work. To reduce this large safety factor, especially the uncertainty in the correlations for the gas side mass transfer coefficient and for the pressure drop should be reduced.

For a generic packing, an uncertainty in pressure drop of 30 % as in this work is regarded as reasonable. However, for a specific packing with experimental pressure drop data, this uncertainty can be reduced.

For a generic packing, an uncertainty in gas side mass transfer coefficient of 50 % is regarded as reasonable. For specific conditions with a specified packing, a much lower uncertainty can be expected.

As a result a recommended safety factor for the absorption packing height is 60 % for a generic packing, but this safety factor can be reduced considerably with available experimental data for pressure drop and gas side mass transfer coefficients at actual conditions.

4. Conclusion

This study discusses the calculation of pressure drop, mass transfer coefficient and interfacial area of packing in an absorption column using mathematical models available in the literature. All the models show similar behaviours under the variation of gas and liquid superficial velocity.

The uncertainties in process conditions and physical properties affect the height of a packed bed in an absorber column. An uncertainty analysis as discussed leads to an evaluation of the safety margins that need to be considered in absorber design. Two scenarios were discussed considering different values for the uncertainty sources and observed how it affects the height calculation

of the packed bed in an absorption column. In the first scenario, the uncertainty in pressure drop gave the largest impact and in the second scenario the uncertainty in mass transfer coefficient gave the largest impact.

A recommended safety factor for the absorption packing height is 60 % for a generic packing, but this safety factor can be reduced considerably if experimental data for pressure drop and mass transfer coefficients are available for the specific packing.

Nomenclature

Latin symbols

a	Specific area (m ² /m ³)
D	Diffusivity coefficient (m ² /s)
d	Diameter (m)
Fr	Froude's number
G	Molar gas flow rate per unit cross sectional area (mol/(m ² ·s))
g	Acceleration of gravity (m/s ²)
h_L	Liquid hold-up
K_G	Overall mass transfer coefficient (kmol/(m ² ·Pa·s))
P	Pressure (Pa), (bar)
Re	Reynold's number
Sc	Schmidt's number
v	Velocity (m/s)
We	Weber's number
y	Mole fraction

Greek symbols

ε	Void fraction
ρ	Density (kg/m ³)
μ	Viscosity (kg/(m·s))
σ	Surface tension (N/m)

Subscripts

EFF	Effective
G	Gas
L	Liquid
N	Nominal
REL	Relative

References

- [1] Wang, G. Q., Yuan, X. G., & Yu, K. T. Review of mass-transfer correlations for packed columns. *Ind. Eng. Chem. Res.*, 2005. 44(23): p. 8715-8729.
- [2] Piché, S., Grandjean, B. P. A., & Larachi, F. Reconciliation procedure for gas-liquid interfacial area and mass-transfer coefficient in randomly packed towers. *Ind. Eng. Chem. Res.*, 2002. 41(19): p. 4911-4920.
- [3] Karunarathne, S. S., Eimer, D. A., & Øi, L. E. Model uncertainty of interfacial area and mass transfer coefficients in absorption column packings. Paper presented at the proceedings of the 58th SIMS, 2017. Reykjavik, Iceland.
- [4] Nookuea, W., Tan, Y., Li, H., Thorin, E., & Yan, J. Impacts of thermo-physical properties of gas and liquid phases on design of absorber for CO₂ capture using monoethanolamine. *Int. J. Greenhouse Gas Control*, 2016. 52: p. 190-200.

- [5] Kvamsdal, H. M., & Hillestad, M. Selection of model parameter correlations in a rate-based CO₂ absorber model aimed for process simulation. *Int. J. Greenhouse Gas Control*, 2012. 11: p. 11-20.
- [6] Razi, N., Svendsen, H. F., & Bolland, O. Validation of mass transfer correlations for CO₂ absorption with MEA using pilot data. *Int. J. Greenhouse Gas Control*, 2013. 19: p. 478-491.
- [7] Mathias, P. M., & Gilmartin, J. P. Quantitative evaluation of the effect of uncertainty in property models on the simulated performance of solvent-based CO₂-capture. *Energy Procedia*, 2014. 63: p. 1171-1185.
- [8] Nookuea, W. Tan, Y. Li, H. Thorin, E., & Yan, J. Sensitivity study of thermo-physical properties of gas phase on absorber design for CO₂ capture using monoethanolamine. *Energy Procedia*, 2015. 75: p. 2305-2310.
- [9] Tan, Y., Nookuea, W., Li, H., Thorin, E., & Yan, J. Property impacts on carbon capture and storage (CCS) processes: A review. *Energy Convers. Manage.*, 2016. 118: p. 204-222.
- [10] Rocha, J. A., Bravo, J. L., & Fair, J. R. Distillation columns containing structured packings: a comprehensive model for their performance. 1. Hydraulic models. *Ind. Eng. Chem. Res.*, 1993. 32(4): p. 641-651.
- [11] Billet, R., & Schultes, M. Prediction of mass transfer columns with dumped and arranged packings: Updated summary of the calculation method of Billet and Schultes. *Chem. Eng. Res. Des.*, 1999. 77(6): p. 498-504.
- [12] Stichlmair, J., Bravo, J. L., & Fair, J. R. General model for prediction of pressure drop and capacity of countercurrent gas/liquid packed columns. *Gas Sep. Purif.*, 1989. 3(1): p. 19-28.
- [13] Øi, L. E. (2012). Removal of CO₂ from exhaust gas. (PhD). Telemark University College, Porsgrunn, Norway.
- [14] De Brito, M. H., von Stockar, U., & Bomio, P. Predicting the liquid phase mass transfer coefficient k_L for the Sulzer structured packing Mellapak. Paper presented at the institution of chemical engineers symposium series, 1992.
- [15] Rocha, J. A., Bravo, J. L., & Fair, J. R. Distillation columns containing structured packings: A comprehensive model for their performance. 2. Mass-transfer model. *Ind. Eng. Chem. Res.*, 1996. 35(5): p. 1660-1667.
- [16] Brunazzi, E., Paglianti, A., & Petarca, L. Design of absorption columns with equipped with structured packing. *La Chimica e l'Industria*, 1996. 78: p.459-467.

CO₂ IMPACT ON FeCO₃ CORROSION PRODUCT

Randi Neerup, Isaac A. Løge, Caroline G. Rudbeck, Philip L. Fosbøl*

Center for Energy Resources Engineering (CERE), Department of Chemical and Biochemical Engineering, Technical University of Denmark (DTU), Søtofts Plads 229, 2800, Kgs. Lyngby, Denmark

* Corresponding author e-mail: plf@kt.dtu.dk

Abstract

Reduction of the emissions of CO₂ and other greenhouse gases is a global challenge. Carbon capture and storage (CCS) is one of the most ready to use technologies applicable for industries such as biogas upgrading, cement, and in general, gas cleaning. Even though the technology is mature, optimization is still needed to reduce costly production losses and shutdowns. CO₂ corrosion is a significant problem in the industry, and therefore, fundamental information regarding the corrosion product, FeCO₃, is needed. FeCO₃ creates a protective barrier on the steel surface under the right conditions, and therefore information on the solubility is important. In this study, the solubility of FeCO₃ in water and under the influence of CO₂ is investigated. Results revealed that the FeCO₃ solubility in water (with and without the presence of CO₂) is constant with temperature. A global maximum in the FeCO₃ solubility was seen when increasing CO₂ pressure. This phenomenon is not seen in the typical carbonate systems.

Keywords: CO₂, FeCO₃, Corrosion, Solubility

1. Introduction

To combat greenhouse gas emissions and significantly reduce the CO₂ content in the atmosphere, carbon capture and storage (CCS) technology is one of the most viable options.

The CCS technology is easily retrofitted to existing plants, however, optimization is still important to minimize costs and shutdowns.

CO₂ corrosion is a huge problem as it can lead to expensive production losses and shutdowns due to maintenance. In the process of capturing CO₂ from a process stream, the CO₂ is absorbed using a chemical solvent at approximately 40 °C. The CO₂ rich solvent can be regenerated heating the solvent to 120 °C and to a pressure of approximately 1.8 bar. Corrosion in the CCS technology would be seen when the solvent is loaded with CO₂ and also near the reboiler due to the heating. Transporting CO₂ after the capture process would also lead to the risk of corrosion if water is not removed from the gas stream.

As gaseous CO₂ dissolves in aqueous solutions, carbonic acid is formed. As it diffuses to the steel surface, it reacts electrochemically, and Fe²⁺ is released [1], [2]. Released

Fe²⁺ reacts with carbonates in the aqueous solutions and leads to the formation of a solid corrosion product, FeCO₃. Under the right conditions (pH, temperature, particle size), precipitation of FeCO₃ creates a protective layer on the steel surface, which will create a barrier for further corrosion [3]–[10].

Detailed knowledge about the solubility of FeCO₃ is needed to understand and predict CO₂ corrosion. The literature is sparse about experimental FeCO₃ solubility data. In the review by Fosbøl et al. [11], he summarizes available literature data on solubility. A conclusion is that the lack of anoxic conditions biases the experimental data. Another conclusion was that the purity of the synthesized FeCO₃ was questionable.

In this study, the solubility of FeCO₃ in water is measured experimentally as a function of:

- Temperature
- CO₂ pressure
- Equilibrium time

The aim is to understand the impact of CO₂ on the FeCO₃ solubility to predict when the protective layer is formed. The data would help further optimization processes related to preventing CO₂ corrosion in pipelines.

2. Methods

2.1 Materials

For the synthesis of FeCO₃, the chemicals: FeCl₂·4H₂O, NaHCO₃, and Na₂HCO₃ were purchased from Sigma-Aldrich. All chemicals had a purity of ≥99.0 %.

Solutions of FeCl₂·4H₂O, and NaHCO₃/Na₂HCO₃ were prepared with degassed with N₂ ultra-pure Milli-Q water.

2.2 FeCO₃ synthesis

The synthesis of FeCO₃ was prepared in a glovebox (MBRaun) with an anoxic environment of less than 0.1 ppm.

Solutions of FeCl₂·4H₂O and NaHCO₃/Na₂CO₃ were mixed. The prepared solutions were added to a titanium piston-cylinder. The piston cylinder was removed from the glovebox and pressurized to 10 bar. The cylinder was placed in an oven at 130 °C for 24 h.

After 24 h the cylinder was cooled to room temperature and transferred to the glovebox. Here solution was filtered and the solid FeCO₃ product was washed several times and let to dry. The product was confirmed by x-ray powder diffraction (XRPD) to be FeCO₃, see Figure 1.

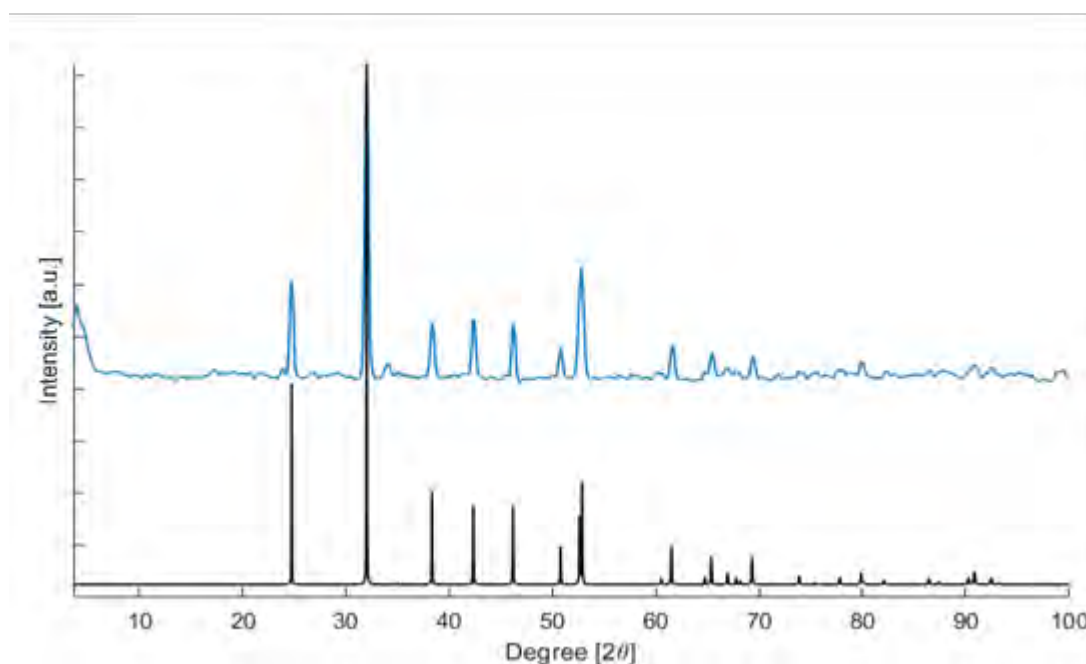


Figure 1. XRPD of FeCO₃

2.3 FeCO₃ solubility

All samples were prepared in the glovebox.

The solubility of FeCO₃ in water was conducted at ambient pressure in the temperature range 25 to 80 °C. The experiments were performed on the setup equivalent to the setup previously described by Fosbøl et al. [17]. The setup consists of an equilibrium unit with up to 5 cells connected parallel to a heating/cooling circulation bath (Julabo).

15 mg of FeCO₃ and 22 g of degassed Milli-Q water were added to a 25 mL blue-cap bottle. Silicon oil was transferred to the blue-cap bottle to prevent oxygen contamination and evaporation of the sample. Each sample solution was submerged in the cell and set to equilibrate for up to 35 days.

To determine the impact of CO₂ on the FeCO₃ solubility, pressure reaction vessels (Andrews Glass) were used. Approximately 15 g of FeCO₃ and 22 g degassed water were added to the glass reaction vessel together with a magnet. The vessel was closed and removed from the glovebox. All vessels were pressurized with CO₂ and left to equilibrate for 14 days.

All samples were filtrated using 0.22 µm PVDF membrane (Merck Millipore Ltd.).

Iron content was determined spectrophotometrically (Hach Lange, DR 3900) using iron test kits from Hach Lange (LCK321, LCK320).

3. Results and Discussion

3.1 FeCO₃-H₂O

The solubility of FeCO₃ in water as a function of equilibrium time is presented in Figure 2 at temperatures 25, 40, 60, and 80 °C. Equilibrium was reached when the Fe concentration did not significantly change over time.

Equilibrium was obtained between 3 to 5 days, as shown in Figure 2b, Figure 2c, and Figure 2d. The kinetics of reaching equilibrium was affected by temperature. This

is seen as the sample held at 25 °C reached an almost constant Fe concentration after more than ten days.

Comparing the equilibrium Fe concentrations at 25-80 °C reveal that the FeCO₃ solubility is constant with

temperature. This phenomenon is also seen in the CaCO₃ system when no CO₂ is present [12].

The results give an initial impact of the influence of temperature on the FeCO₃ solubility.

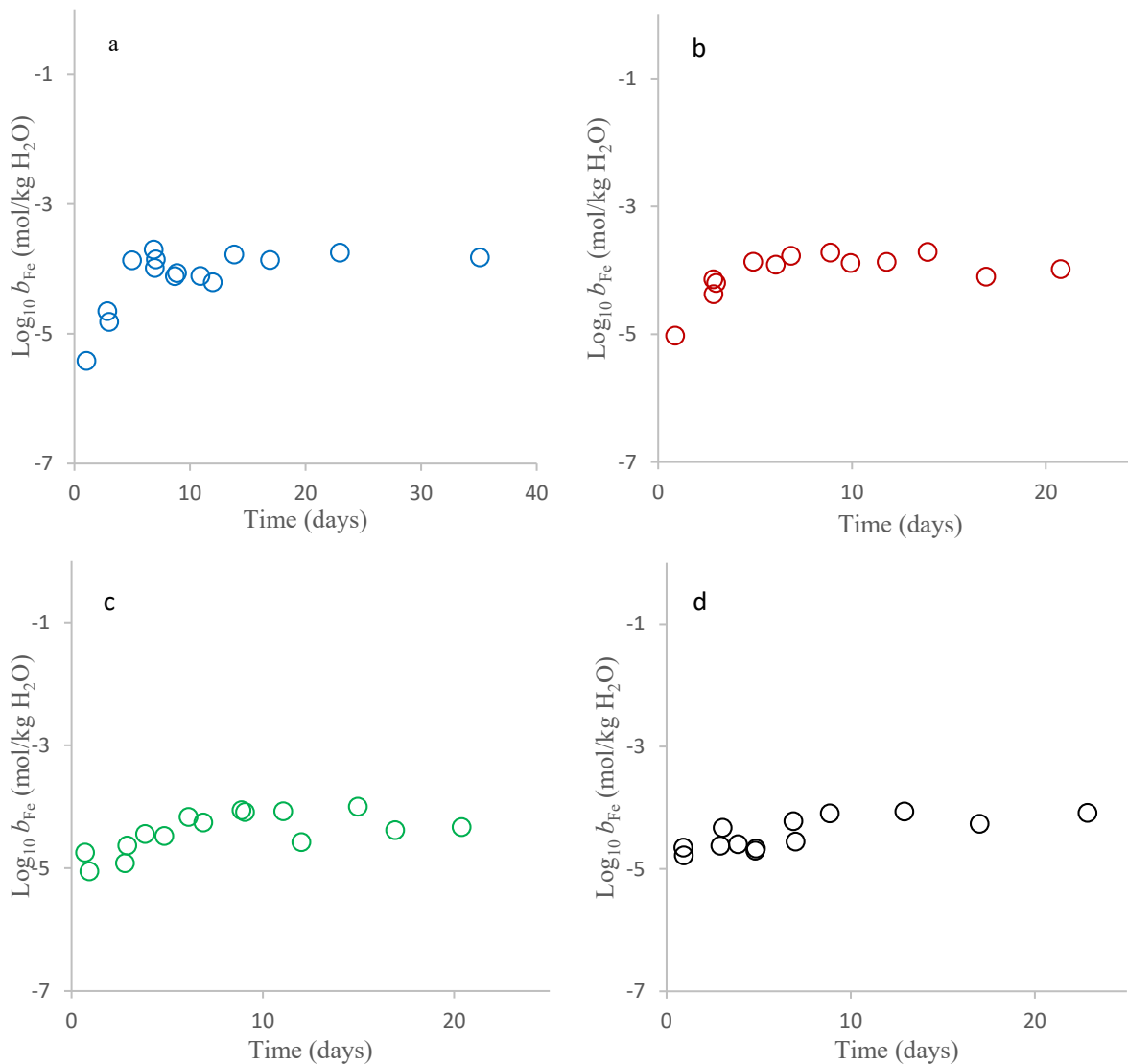


Figure 2. FeCO₃ solubility in water as a function of equilibrium time. (a) 5 °C, (b) 25 °C, (c) 40 °C, (d) 60 °C, and (d) 80 °C.

3.2 FeCO₃-CO₂-H₂O

The impact of CO₂ on the FeCO₃ solubility at 25 and 40 °C is shown in Figure 3. The full circles are the Fe²⁺ concentration, and the circles without is the Fe³⁺ concentration.

The temperature ranging from 25 to 40 °C has little impact on the solubility. However, the partial pressure of CO₂ affects solubility. A global maximum of the solubility of FeCO₃ was measured at 1.5 bar of CO₂. Hereafter the solubility curves are decreasing, increasing the pressure. There was not found a global minimum in the conditions investigated in this study.

The initial results of the impact of CO₂ on the FeCO₃ solubility gives some initial knowledge on how the CO₂ affects the solubility. The results at 40 °C mimic at rich loaded solvent after leaving the absorption column. This is a stage where corrosion would be expected as the CO₂ content is high in the liquid solvent.

The impact of CO₂ on the FeCO₃ solubility is not comparable to the trends in other carbonate systems [13], [14], and therefore the FeCO₃-CO₂-H₂O system needs to be studied further.

The oxidation of FeCO₃ is, with minor outliers, relatively stable around -4.5 mol/kg.

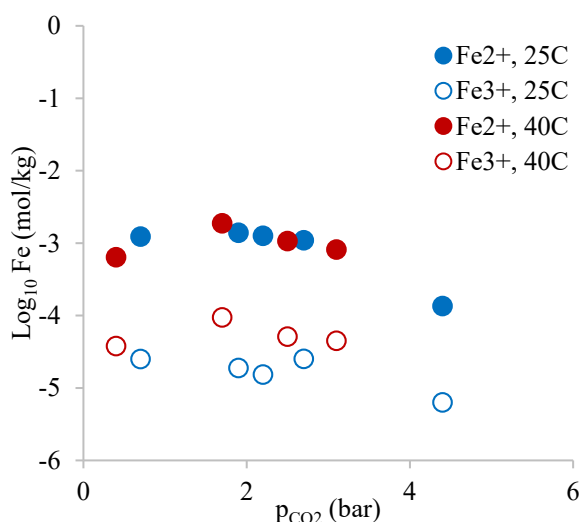


Figure 3. CO₂ impact on FeCO₃ solubility.

4. Conclusion

The solubility of FeCO₃ in water with and without the impact of CO₂ was measured in this study.

The results show that the FeCO₃ solubility is constant with temperature, which is also seen CaCO₃ system with no air present.

The impact of CO₂ was also studied. The preliminary results showed that the CO₂ pressure influences solubility. The solubility increases up to a CO₂ pressure of 1.5 bar, and increasing the pressure above 1.5 bar, the solubility decreases. This is contrary to typical carbonate solubility phenomena.

There is a need for more experiments investigating the mechanism and the impact of CO₂ on solubility.

Acknowledgements

This work received funding from the Danish Hydrocarbon Research and Technology Centre (DHRTC) through the on-going project "CO₂ impact on corrosion product (FeCO₃) solubility" (CTR.2 D.15, LR_21).

References

- [1] V. A. Glezakou, L. X. Dang, and B. P. McGrail, "Spontaneous activation of CO₂ and possible corrosion pathways on the low-index iron surface Fe(100)," *J. Phys. Chem. C*, vol. 113, no. 9, pp. 3691–3696, 2009.
- [2] P. Fosbøl, E. Stenby, and K. Thomsen, *Carbon Dioxide Corrosion: Modelling and Experimental Work Applied to Natural Gas Pipelines*. 2007.
- [3] W. Stumm and G. F. Lee, "Oxygenation of Ferrous Iron," *Ind. Eng. Chem.*, vol. 53, pp. 143–146, 1961.
- [4] S. Garg, A. L. Rose, A. Godrant, and T. D. Waite, "Iron uptake by the ichthyotoxic *Chattonella marina* (Raphidophyceae): Impact of superoxide generation," *J. Phycol.*, vol. 43, no. 5, pp. 978–991, 2007.
- [5] T. P. Salmon, A. L. Rose, B. A. Neilan, and T. D. Waite, "The FeL model of iron acquisition: Nondissociative reduction of ferric complexes in the marine environment," *Limnol. Oceanogr.*, vol. 51, no. 4, pp. 1744–1754, 2006.
- [6] S. Kakooei, M. C. Ismail, B. Raja, H. Mohebbi, S. S. Emamian, and M. Moayedfar, "Formation of nano-scale FeCO₃ protective corrosion product in carbon dioxide-saturated 3% sodium chloride solution," *Key Eng. Mater.*, vol. 740 KEM, no. June, pp. 3–8, 2017.
- [7] J. Hernandez, A. Munoz, and J. Genesca, "Formation of iron-carbonate scale-layer and corrosion mechanism of API X70 pipeline steel in carbon dioxide-saturated 3% sodium chloride," *AFINIDAD LXXIX*, vol. 560, pp. 251–258, 2012.
- [8] W. Farida, T. Hemmingsen, T. Berntsen, and P. Rabindran, "Effect of Precorrosion and Temperature on the Formation Rate of Iron Carbonate Film," *Pipeline Technol. Conf.*, 2012.
- [9] A. Kahyarian, M. Achour, and S. Nestic, *CO₂ corrosion of mild steel*. Elsevier Ltd, 2017.
- [10] G. Schmitt and Michaela Hörstmeier, "Fundamental aspects of CO₂ metal loss corrosion - Part II: Influence of different parameters on CO₂ corrosion mechanisms," *Corrosion*, vol. 06112, pp. 1–26, 2006.
- [11] P. L. Fosbøl, K. Thomsen, and E. H. Stenby, "Review and recommended thermodynamic properties of FeCO₃," *Corros. Eng. Sci. Technol.*, vol. 45, no. 2, pp. 115–135, 2010.
- [12] J. Kendall and V. Dunlop, "The solubility of calcium carbonate in water," *Philos. Mag.*, vol. 23, pp. 958–976, 1912.
- [13] D. C. De Andrade *et al.*, "Strontium carbonate solubility data in aqueous mixtures of monoethyleneglycol under a carbon dioxide atmosphere," *Brazilian J. Chem. Eng.*, vol. 35, no. 2, pp. 395–402, 2018.
- [14] J. Li, R. Ahmed, and X. Li, "Thermodynamic modeling of CO₂-N₂-O₂-brine-carbonates in conditions from surface to high temperature and pressure," *Energies*, vol. 11, no. 10, 2018.

CO₂ CAPTURE WITH STRUCTURED SORBENTS CONTAINING MULTIWALLED CARBON NANO TUBES AND POLYETHYLENEIMINE (PEI)

Shreenath Krishnamurthy¹, Richard Blom¹, Kari Anne Andreassen¹, Carlos Grande¹, Vesna Middelkoop², Marleen Rombouts² and Adolfo Benedito Borrás³, (1) SINTEF Industry, Oslo, Norway, (2) Vito, Mol, Belgium, (3) AIMPLAS, Valencia, Spain

Corresponding author's email: Shreenath.Krishnamurthy@sintef.no

Abstract

In this work monolithic adsorbents containing polyethyleneimine (PEI) and multiwalled carbon nanotubes obtained by 3D printing. CO₂ and N₂ isotherms were measured using a commercial volumetric apparatus. Breakthrough experiments were carried out with a synthetic flue gas containing 15% CO₂ and the rest N₂. The information was used to simulate and optimize a 6-step Vacuum swing Adsorption (VSA) cycle for post-combustion CO₂ capture from a flue gas stream containing 15% CO₂ and 85% N₂. Detailed process optimization revealed that it was indeed possible to achieve 95% CO₂ purity and 90% CO₂ recovery targets.

Keywords: 3D Printing, Vacuum swing adsorption, PEI

1. Introduction

Processes that utilize solid adsorbents to capture CO₂ are promising alternatives to state-of-art technologies using water-based amine solutions as absorbents for capturing CO₂ from large point sources such as power plants. Although the energy needs of solid sorbent-based processes are low, the process footprint and consequently the capital cost connected to its implementation can be large due to the relatively long cycle times needed to get the required capture rate and purity of the CO₂ product. To overcome this challenge, processes having structured adsorbents like laminates, monoliths etc. are needed owing to their low pressure drop and better mass transfer characteristics [1, 2]. In recent times, 3D printing of structured adsorbents has been gaining significant attention due the versatility in shapes of the adsorbents and good control over the channel dimensions.

Even though there are several published studies in the context of structured adsorbents, they are mostly restricted to characterization of the adsorbents with respect to equilibrium and mass transfer[3-5]. Very few published studies exist on a process level demonstrating an improvement in the process performance in comparison with pellets[6, 7]. It has been shown that, the true potential of any adsorbent only be obtained through rigorous optimization of a cyclic adsorption process [8].

The aim of this work is to study a 3D printed sorbent for its suitability to post-combustion CO₂ capture. These adsorbents were then printed in the form of monoliths by the 3D printing technique called robocasting. First pure component CO₂ and N₂ isotherms were measured using a commercial volumetric apparatus. Breakthrough experiments were then carried out with a dry mixture of CO₂ and N₂. The information from the adsorbent characterization was then used to simulate and optimize a vacuum swing adsorption process in order to identify the operating conditions corresponding to 95% CO₂ purity and 90% CO₂ capture rate targets to capture CO₂ from a coal fired power plant containing 15% CO₂, 85% N₂.

2. Materials and Methods

2.1 3D Printing

CNT-PEI based pastes were prepared by AIMPLAS. These pastes were then printed by VITO using a technique called robocasting and the methodology is shown in Figure 1. The printing process is a computer-controlled extrusion of the paste. Once a structure with desired dimensions is printed, it is then dried in a furnace at 40°C overnight. Each structure was 2 cm in height and 2.1 cm in diameter. The average diameter of the channels in the middle of the monolith was 2 mm with a wall thickness of 0.7 mm.

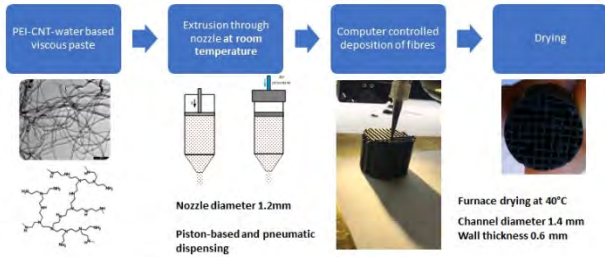


Figure 1: Schematic of the printing process

2.2 Adsorbent characterization

2.2.1. Volumetric apparatus

First, CO₂ and N₂ adsorption isotherms were obtained using a commercial volumetric apparatus. One of the printed structures was crushed and packed into the volumetric cell and regenerated overnight at 100°C. After regeneration, experiments were carried out with pure CO₂ and N₂ for pressures up to 1 bar. The CO₂ adsorption isotherms were measured for 4 different temperatures (70, 80, 90 and 100°C) and the nitrogen adsorption was carried out for 70 °C.

2.2.2. Breakthrough experiments

In the breakthrough apparatus, 2 structures weighing 4 g in total were packed in a column that was about 4 cm in length. Experiments were then carried out using a feed containing 15% CO₂ and 85% N₂ and this was followed by desorption using nitrogen purge. The adsorption part of the breakthrough experiment was analyzed using a 1D adsorption process model by fitting the adsorption rate equation co-efficient (Linear driving force co-efficient) and the heat transfer parameters. The analysis was done for multiple temperatures to obtain a meaningful set of parameters.

2.3. Process simulation and optimization

For the process simulations we chose a flue gas stream containing 15% CO₂ and 85% N₂ which is typical of a coal-fired power plant. In this work a 6-step vacuum swing adsorption cycle was simulated. The schematic of the 6-step cycle is shown in Figure 4 [9]. The steps in the cycle are as follows, adsorption with feed, rinse, co-current evacuation, counter-current evacuation, light reflux, and light product pressurization. A 1-D non-isothermal, non-isobaric model was used to simulate the 6-step VSA cycle. The model equations were discretized in the spatial domain by finite volume method and the resultant system of differential algebraic equations (DAEs) were solved in MATLAB. The simulations were performed up to cyclic steady state (CSS) and this was ensured the mass balance error was less than 0.5% for 5 consecutive cycles.

The next step was to optimize the cycle to identify operating conditions with minimum specific energy and maximum productivity for target CO₂ purity and recoveries of 95% and 90% respectively. The optimization was carried out using MATLAB's inbuilt multi objective genetic algorithm function gamultiobj. The use of genetic algorithm for optimization of VSA cycles is well-documented in literature [8, 10, 11].

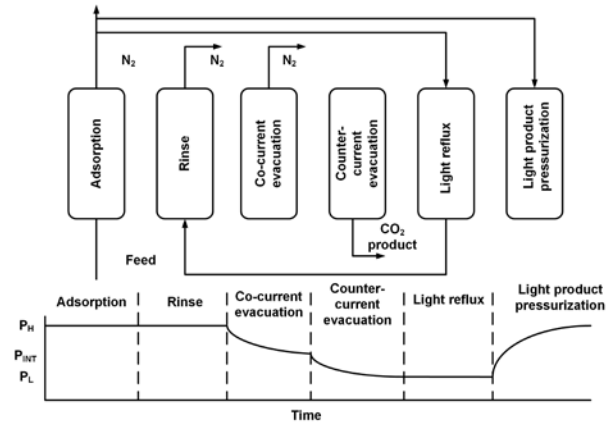


Figure 2: Schematic of the 6-step VSA cycle simulated in this study.

The performance indicators like CO₂ purity, recovery, specific energy consumption and productivity are defined in the following manner:

$$\text{Purity} = \frac{\text{Moles}_{CO_2, \text{Cn-ovac}}}{\text{Moles}_{\text{total}, \text{cn-ovac}}} \quad (1)$$

$$\text{Recovery} = \frac{\text{Moles}_{CO_2, \text{Cn-ovac}}}{\text{Moles}_{CO_2, \text{adsorption}}} \quad (2)$$

$$\text{Productivity} = \frac{\text{Moles}_{CO_2, \text{Cn-ovac}}}{V_{\text{Adsorbent}} t_{\text{cycle}}} \quad (3)$$

$$\text{Specific energy} = \frac{E_{\text{compression}} + E_{\text{vacuum}}}{\text{Moles}_{CO_2, \text{Cn-ovac}}} \quad (4)$$

3. Results and Discussion

3.1 Adsorbent characterization

3.1.1. Volumetric apparatus

The adsorption isotherms of CO₂ and N₂ are shown in Figure 3. From Figure 3, one can see that the nitrogen adsorption is negligible, and the CO₂ is much more strongly adsorbed. The CO₂ data was fitted to a dual-site Langmuir model [12] and the heat of adsorption value obtained from the fitting was around 100 kJ/mol, typical of chemisorption mechanism. The adsorption isotherms of CO₂ on the structured sorbent and that of the pristine paste are shown in Figure 2b. The loss in capacity compared to the pristine paste could be due to the printing and drying processes. The adsorption isotherm parameters of CO₂ are shown in Table 1.

Table 1: Dual site Langmuir isotherm parameters

Parameter	Value
q _{s1} (mol/kg)	0.23
b _{0,1} (bar ⁻¹)	3.9 × 10 ⁻¹⁷
ΔH ₁ (kJ/mol)	-109.4
q _{s2} (mol/kg)	0.58
b _{0,2} (bar ⁻¹)	7.4 × 10 ⁻¹¹
ΔH ₂ (kJ/mol)	-58.7

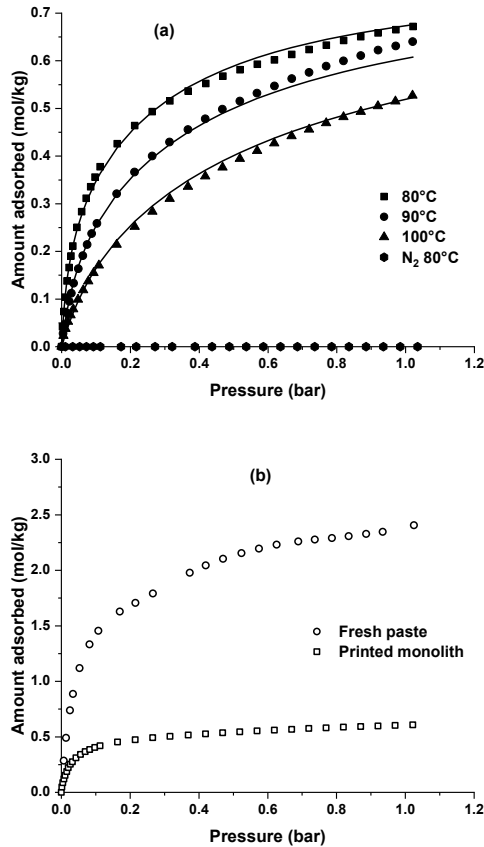


Figure 3: (a) CO₂ and N₂ adsorption isotherms in the 3D printed adsorbent and (b) comparison of capacities in the fresh paste and 3D printed monolith.

3.1.1. Breakthrough experiments

Breakthrough experiments were carried out at 4 different temperatures namely 70, 80, 90 and 100°C. As mentioned earlier, the residual between the experimental and simulated breakthrough curves by fitting the adsorption rate (LDF) coefficient and the heat transfer parameters

From the breakthrough curves shown in Figure 3, one can observe a good match between the simulated curves from the 1D model and experimental breakthrough curves. One can see a small kink in the CO₂ breakthrough curve and this kink could be due to the cracks present in the monolith which were formed during the drying. The other possibility could be due to the differences in the channel sizes i.e., the channels in the corners are smaller than those in the middle of the monolith. Further studies either by experiments or by computational fluid dynamics modelling may help us to understand this phenomenon better.

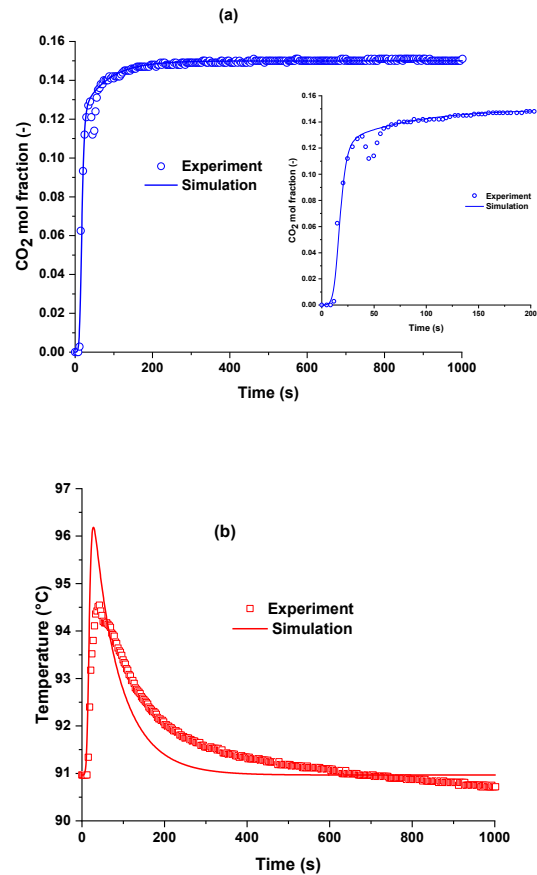


Figure 4: (a) concentration and (b) temperature breakthrough curves.

3.2. Process simulation and optimization

The 6-step VSA cycle was first validate using parameters and simulated profiles from literature [9]. Then detailed process optimization was carried out using MATLAB's in built non-dominated sorting genetic algorithm (NSGA-II) function for multi-objective optimization. In total 4200 simulations were performed.

Figure 5 shows the specific energy vs productivity pareto fronts and these points satisfy purity values of > 95% and recovery values are > 90%. The minimum specific energy was 0.67 MJ/kg, and the maximum productivity was 0.89 mol/m³ ads/s. The average cycle time for points on the pareto front were approximately 2 minutes. The adsorption step time varied from 27 s to 49 s for the different conditions. It should be noted that the energy consumption reported is on an electricity basis.

Figure 6 shows the bed profiles at the end of the simulation and at cyclic steady state (CSS) conditions. Cyclic steady state means that the conditions in the column at a given cycle are the same as that of the previous cycle. Moreover, as mentioned earlier, the mass balance error is less than 0.5% for 5 consecutive cycles. Looking at the CO₂ concentration profile, one can understand what happens in very step. The inlet concentration at the adsorption step is the feed concentration. During the rinse step, the CO₂ concentration in the bed is enhanced by the stream coming from the light reflux step and nitrogen is

collected at the product. The co-current evacuation step removes the remaining nitrogen in the column so that high purity CO₂ product can be obtained from the counter-current evacuation step. The light product pressurization step uses nitrogen from the adsorption step and hence the concentration is lower.

As mentioned earlier, the adsorbent has a high heat of adsorption. This high heat of adsorption has high temperature swings inside the column. This also explains the spread in the CO₂ concentration profile i.e., the presence of considerable CO₂ close to the exit of the column.

In our simulations, we have not considered the presence of oxygen or water in the flue gas stream. The presence of oxygen is known to cause irreversible loss of capacity of these structured sorbents[13]. Secondly, the presence of moisture is known to enhance the CO₂ adsorption which could further reduce the CO₂ capacity. Depending on the amine group used, it is also possible that these amines get leached with repeated use in a cyclic process. All these factors must be considered when we use these amine containing sorbents for cyclic adsorption processes.

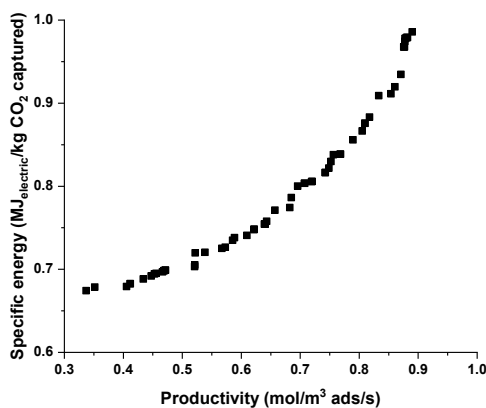


Figure 5: Specific energy vs productivity Pareto curve. All points on the Pareto curve satisfy >95% purity and >90% recovery.

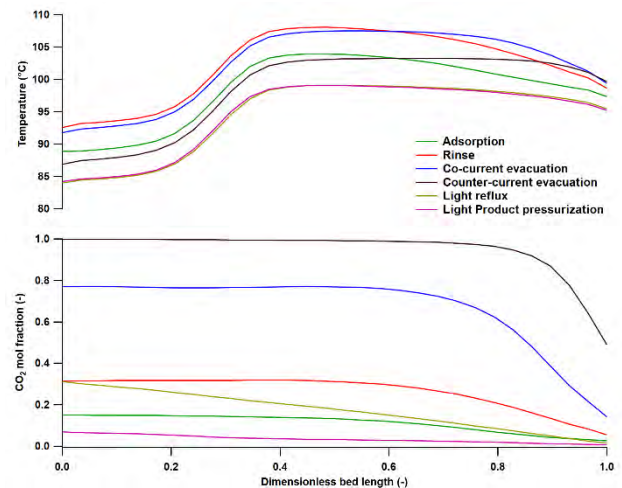


Figure 6: CO₂ concentration and temperature profiles in the column at CSS for maximum productivity.

4. Conclusions

In this work a structured sorbent made by 3D printing methods was characterized for adsorption equilibrium and kinetics. The information was fed to a process simulator and detailed process optimization of 6-step VSA cycle showed that it was indeed possible to achieve 95% purity and 90% recovery from a 15% CO₂ stream.

While it is possible to produce structures with moderate CO₂ capacity values, still issues remain with respect to printing CNT-PEI pastes. First and foremost, the printing process was not stable, and this necessitated the use of additives. This affected the capacity of the structured sorbent. Secondly, the presence of water in the paste resulted in a large shrinkage of the final structure. While this is probably not a challenge in lab scale systems, it may pose a challenge when printing large structures on a pilot scale. Moreover, the printed structure also had cracks due to local gradients in drying rates and stress build up as well as the resistance to shrinkage due to the presence of a base plate. Therefore, further work is necessary for the optimization of pastes and the drying process to print structures with good capacity and mechanical stability.

Acknowledgement

This work is a part of the CARMOF project. This project has received funding from the European Union's Horizon 2020 research and innovation programme under grant agreement No 760884

For more information on this project visit the project web page <https://carmof.eu/>

References

1. Ruthven, D.M. and C. Thaeron, *Performance of a parallel passage adsorbent contactor*. Separation and Purification Technology, 1997. **12**(1): p. 43-60.
2. Rezaei, F., et al., *Comparison of Traditional and Structured Adsorbents for CO₂ Separation by Vacuum-Swing Adsorption*. Industrial & Engineering Chemistry Research, 2010. **49**(10): p. 4832-4841.
3. Couck, S., et al., *3D-printed SAPO-34 monoliths for gas separation*. Microporous and Mesoporous Materials, 2018. **255**: p. 185-191.
4. Middelkoop, V., et al., *3D printed versus spherical adsorbents for gas sweetening*. Chemical Engineering Journal, 2019. **357**: p. 309-319.
5. Grande, C.A., et al., *Multiscale investigation of adsorption properties of novel 3D printed UTSA-16 structures*. Chemical Engineering Journal, 2020. **402**: p. 126166.
6. Mohammadi, N., *CO₂ Capture From Flue Gas By A PSA Process Using A Novel Structured Adsorbent*, in *College of Engineering and Computing*. 2017, University of South Carolina.
7. Sharma, I., et al., *Monolithic Adsorbent-Based Rapid-Cycle Vacuum Pressure Swing Adsorption Process for Carbon Capture from Small-Scale Steam Methane Reforming*. Industrial & Engineering Chemistry Research, 2020. **59**(15): p. 7109-7120.
8. Rajagopalan, A.K., A.M. Avila, and A. Rajendran, *Do adsorbent screening metrics predict process performance? A process optimisation based study for post-combustion capture of CO₂*. International Journal of Greenhouse Gas Control, 2016. **46**: p. 76-85.
9. Khurana, M. and S. Farooq, *Simulation and optimization of a 6-step dual-reflux VSA cycle for post-combustion CO₂ capture*. Chemical Engineering Science, 2016. **152**: p. 507-515.
10. Haghpanah, R., et al., *Cycle synthesis and optimization of a VSA process for postcombustion CO₂ capture*. AIChE Journal, 2013. **59**(12): p. 4735-4748.
11. Maruyama, R.T., et al., *Improving the performance of vacuum swing adsorption based CO₂ capture under reduced recovery requirements*. International Journal of Greenhouse Gas Control, 2020. **93**: p. 102902.
12. Krishnamurthy, S., et al., *Post combustion carbon capture with supported amine sorbents: From adsorbent characterization to process simulation and optimization*. Chemical Engineering Journal, 2021. **406**: p. 127121.
13. Sonnleitner, E., G. Schöny, and H. Hofbauer, *Assessment of zeolite 13X and Lewatit® VP OC 1065 for application in a continuous temperature swing adsorption process for biogas upgrading*. Biomass Conversion and Biorefinery, 2018. **8**(2): p. 379-395.
14. Sutanto, S., et al., *CO₂ removal from biogas with supported amine sorbents: First technical evaluation based on experimental data*. Separation and Purification Technology, 2017. **184**: p. 12-25.
15. Gelles, T., et al., *Recent advances in development of amine functionalized adsorbents for CO₂ capture*. Adsorption, 2020. **26**(1): p. 5-50.

A MULTISCALE APPROACH FOR EVALUATING UTSA-16 ADSORBENT FOR POST COMBUSTION CARBON CAPTURE

Shreenath Krishnamurthy¹, Enzo Mangano², Maria-Chiara Ferrari², Richard Blom¹, Carlos Grande¹, Daniel Friedrich², Lev Sarkisov³ and Stefano Brandani^{2*}

1. SINTEF Industry, Oslo, Norway 2. University of Edinburgh, Edinburgh, United Kingdom 3. University of Manchester, Manchester, United Kingdom

Presenting author's contacts: Shreenath.Krishnamurthy@sintef.no

Corresponding author's contacts: s.brandani@ed.ac.uk

Abstract

UTSA-16 is considered as one of most promising Metal-Organic Frameworks (MOFs) for post combustion carbon capture in a vacuum swing adsorption (VSA) process. Current studies base their predictions on the equilibrium information for the crystalline material and assuming that the mass transfer is dominated by macropore diffusion. Performance of the real process depends not only on the equilibrium adsorption characteristics, but also on the morphology and mass transfer characteristics of the pellet. In this study, we use a series of complementary techniques to first characterize UTSA-16 pellets and develop a detailed understanding of the mass-transfer mechanisms in these pellets. Using the obtained data, we performed process simulations and optimization to explore performance of real UTSA-16 pellets in carbon capture VSA cycle. We have optimized a 4-step cycle with light product pressurization to identify operating conditions with minimum energy and maximum productivity subject to purity-recovery targets. Further, the performance of UTSA-16 was compared with that of the reference material Zeolite 13X.

Keywords: UTSA-16; vacuum swing adsorption (VSA), energy penalty, Zero length column (ZLC)

1. Introduction

Anthropogenic CO₂ emissions have been established as the major cause for global warming. Therefore significant efforts are currently being pursued to limit the global temperature rise to below 2°C and carbon capture and storage (CCS) is being advocated as a possible solution to meet this challenge [1]. Adsorption processes using solid sorbents like Zeolites [2], Carbons [3] Metal organic frameworks (MOFs) [4], supported amine sorbents [5] and zeolitic imidazolate frameworks (ZIFs) [6] are currently being explored as potential candidates for carbon capture.

A typical post-combustion flue gas contains about 4-5% CO₂ for a natural gas combustion cycle and about 10-15% CO₂ in case of a pulverized coal combustion cycle along with a large amount of nitrogen. The adsorbent chosen must have a good CO₂ capacity and lower affinity to nitrogen to achieve high purity and recovery targets.

UTSA-16 is a metal organic framework that has been found promising for post-combustion carbon capture application by means of rigorous process optimization [7,8]. However, the process optimization was based only on the equilibrium information of a crystalline material and assuming that the mass transfer is dominated by macropore molecular diffusion. The morphology of the pellet and mass-transfer mechanisms also play an important role in the overall performance of the process. An adsorbent pellet basically consists of microporous crystals bound together and intracrystalline macropores. Adsorption of a gas is governed either by the diffusion in the macropores, or micropores or both. In case of a

macropore controlled diffusion process, the uptake is generally governed by the pellet size, i.e. small pellets have a faster uptake than larger pellets. Moreover, smaller pellets also mean larger pressure drop and in case of a macropore diffusion-controlled process, the pellet size is a decision variable, which affects the performance of the adsorption process [9]. In case of a micropore controlled diffusion process, the uptake of CO₂ is not governed by the size of the adsorbent pellets. It is therefore important to establish the right mass transfer mechanism and the time constants to obtain the true performance of the adsorption process.

The aim of this work is to characterize UTSA-16 adsorbent (Figure 1) for obtaining information on adsorption equilibrium and kinetics and establish the mass transfer mechanism. Using this information detailed optimization of a 4-step vacuum swing adsorption (VSA) cycle was performed to identify operating conditions with minimum energy consumption and maximum productivity subject to 95% purity and 90% CO₂ recovery targets. The performance of UTSA-16 was compared with Zeolite 13X, the current benchmark sorbent for post-combustion carbon capture.



Figure 1: UTSA-16 extrudates used in this study.

2. Materials and methods

2.1. Volumetric apparatus

Single component CO₂ and N₂ adsorption isotherms were obtained using a commercial volumetric apparatus AUTOSORB IQ purchased from Quantachrome instruments. The volumetric apparatus was also used to study the diffusional time constant for pure CO₂ adsorption by recording the transient pressure response at different pressure steps. About 0.5 g of sample was used for the isotherm measurements and 11 mg of sample was used for the kinetic measurements

2.2. Zero length column (ZLC) apparatus

The zero-length column apparatus (ZLC) has been traditionally used for measuring diffusion in zeolites and other microporous sorbents [10,11] by providing a step input in concentration (CO₂+Carrier gas) and desorption is carried out by purging the column with the carrier gas. The advantage of this apparatus is that it uses relatively small amounts of sample thereby eliminating external mass and heat transfer resistances. Furthermore, it is possible to obtain both the equilibrium and kinetic parameters by simply varying the flowrate to carry out experiments in the equilibrium and kinetic regimes. For this work, a single UTSA-16 pellet weighing 11 mg was packed into a 1/8" Swagelok union. Experiments were done at different flowrates (7.5 cc/min to 30 cc/min) with a 10% CO₂-He mixture first to establish the kinetic regime. Once the kinetic regime was established, the carrier gas was switched to nitrogen. The volumetric experiments and the zero length column experiments were complemented with independent mercury intrusion experiments.

2.3. Process simulation

Next, a 4-step cycle with light product pressurization (LPP) [7,8] shown in Figure 2 was simulated using CySim software using the equilibrium and kinetic information obtained from the lab-scale experiments. The four steps are Adsorption with feed, co-current evacuation to an intermediate pressure, counter-current evacuation to low pressure and pressurization with light product. The cycle was optimized using NSGA-II to identify operating conditions with minimum specific energy consumption and maximum productivity subject to 95% CO₂ purity and 90% recovery.

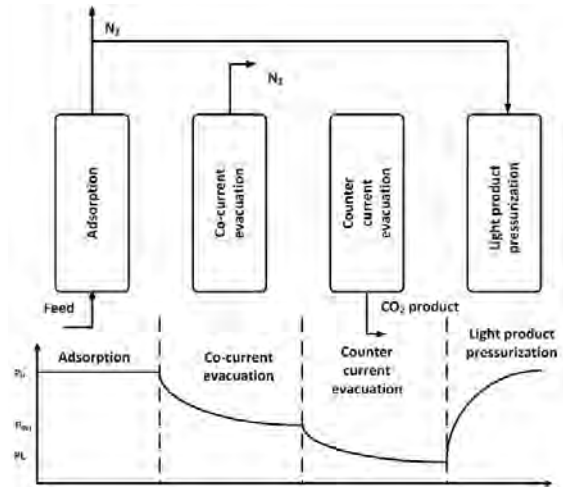


Figure 2: Schematic of the 4-step cycle with LPP

3. Results and discussion

3.1. Volumetric apparatus

The adsorption isotherms of CO₂ and N₂ are shown in Figure 3 and the experimental data was fitted to a Langmuir isotherm. It can be seen that the adsorption of CO₂ is stronger and the equilibrium loading corresponding to a pressure of 0.1 bar and 308 K is 1.2 mmol/g and these values are similar to the ones reported by Agueda et al., who observed 1.05 mmol/g at 313K [12].

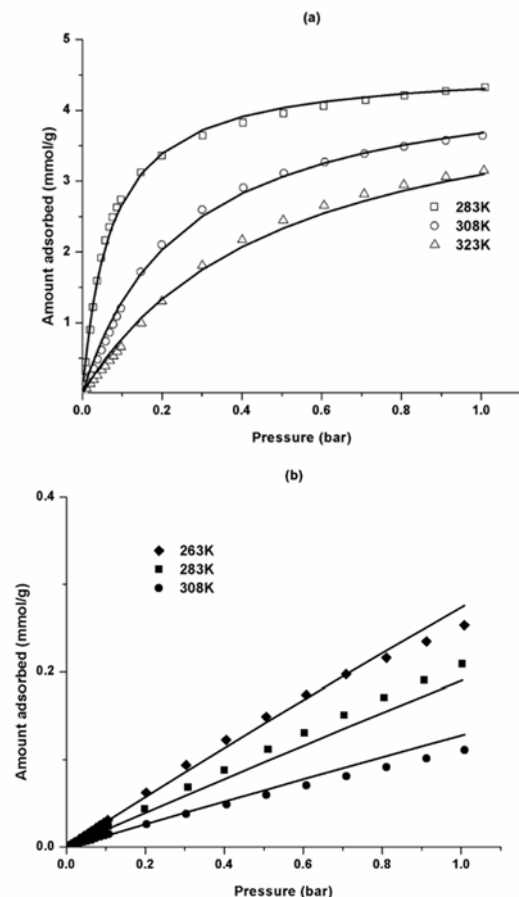


Figure 3: (a) CO₂ and N₂ adsorption isotherms in UTSA-16.

The transient pressure responses at 308 K for different pressure steps were analysed by a piezometric model developed by Brandani [13]. This involves analysing the normalized experimental curve with the piezometric model by fitting the valve co-efficient and the diffusional time constant for different pressure steps. More details about this method are given in earlier publications [14,15]. Figure 4a shows the comparison of the experimental pressure profile and the piezometric model. Figure 4b shows the diffusional time constant as a function of the pressure and one can see that the adsorption becomes faster

From the diffusional time constant, the effective diffusivity was calculated using the slope of the isotherm obtained from the initial and final pressure of the dosing and the particle porosity which was obtained from high pressure mercury intrusion experiments. Assuming macropore diffusion controlled

$$D_p^e = \frac{\epsilon_p \frac{D_{macro}}{\tau}}{\epsilon_p + (1 - \epsilon_p)K} \quad (1)$$

The experiments correspond to a pure gas adsorption and therefore the macropore diffusion is governed by Knudsen, viscous and surface diffusion components. Neglecting surface diffusion, the macropore diffusivity is given by

$$D_{macro} = D_{viscous} + D_{Knudsen} \quad (2)$$

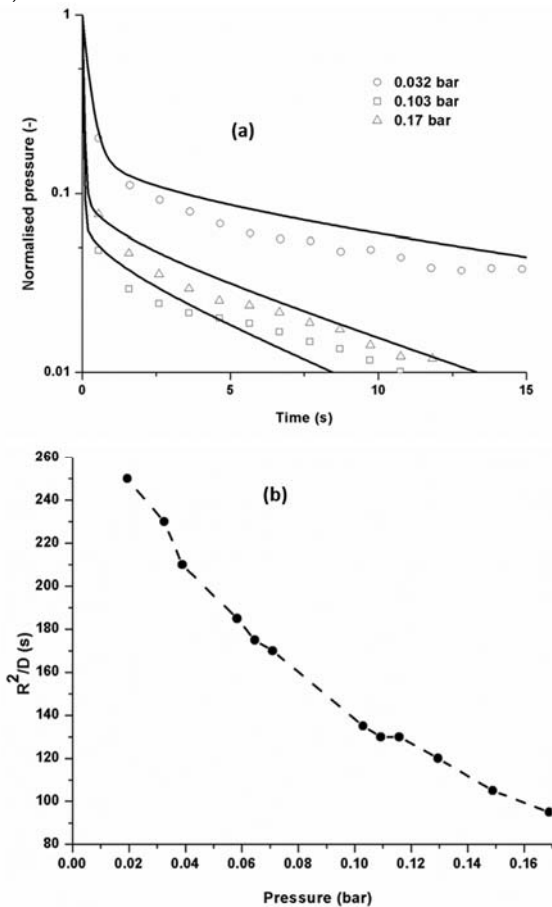


Figure 4: (a) Pressure response from experiments and (b) diffusional time constants with respect to pressure.

Using the effective diffusivity shown in Figure 4b and the macropore diffusivity calculated from the average pore size, which was obtained from the mercury intrusion, the average tortuosity was found to be 3.59 ± 0.1 and in Figure 5, the agreement between the measured and the predicted diffusivities are shown. From this analysis, it can be seen that there is a good agreement suggesting that the system is macropore diffusion controlled.

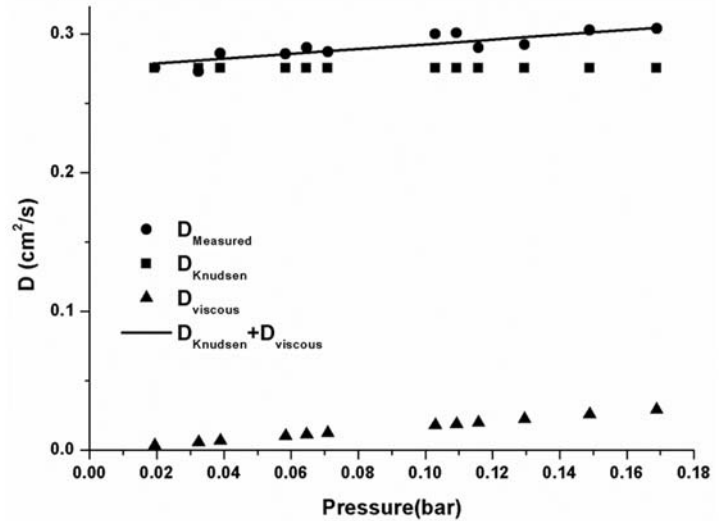


Figure 5: Summary of volumetric experiments for CO₂ adsorption at 308 K.

3.2. Zero length column (ZLC) apparatus

After the zero-length column experiments, the normalized concentration C/C_0 was plotted a function of flow rate \times time. In Figure 6, the curves corresponding to two higher flowrates cross the lower flow rate curves indicating the kinetic regime. At this point, the carrier gas is switched to N₂ and experiments are repeated. One can see from Figure 7a that the slope of the long-time region (between 10^{-1} and 10^{-2}) is different for the two carrier gases. This clearly established the system was indeed governed by diffusion through macropores. If the adsorption was governed by micropore diffusion, then there would not have been any differences in the slope, i.e., the curves with two carrier gases would have overlapped one another. The curves were fitted using an automated ZLC tool (Figure 7b) to estimate the diffusional time constants and correspondingly the tortuosity [16]. The tortuosity values were estimated to be 3.57. This is in good agreement with the values obtained from the single component volumetric experiments.

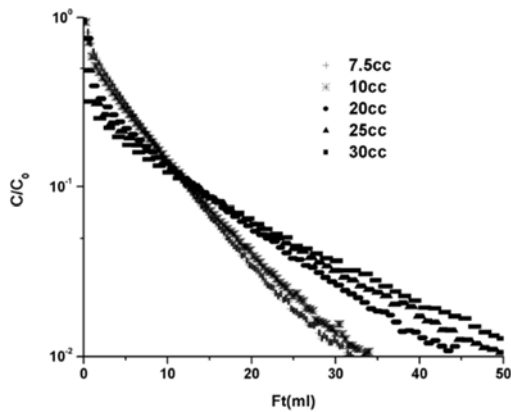


Figure 6: ZLC curves for 10% CO₂-He mixture

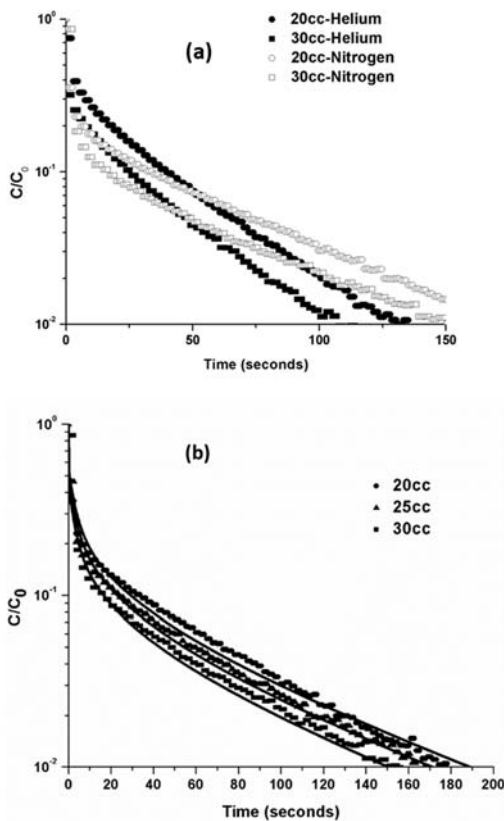


Figure 7: (a) ZLC curves with different carrier gases and (b) comparison of the experimental and simulated ZLC curves.

3.3. Process simulation

Figure 8 shows the pareto fronts for the UTSA-16 sorbent with the measured and assumed kinetic constants. The results are compared with that of Zeolite 13X, the current benchmark sorbent for CO₂ capture. UTSA-16 performed better than zeolite 13X both with respect to specific energy consumption and productivity. The minimum energy consumption and maximum productivity values for Zeolite 13X were 26.6 kJ/kg and 1.1 mol/m³ ads/s. In comparison, UTSA-16 had minimum specific energy value of 22.5 kJ/kg and a maximum productivity value of 1.25 mol/m³ ads/s,

respectively. The improvement in performance can be attributed to the fact that UTSA-16 had a lower affinity to nitrogen in comparison with Zeolite 13X. This meant that coarser vacuum was needed to remove the nitrogen in the co-current evacuation step for UTSA-16 than Zeolite 13X. The values of the co-current evacuation step pressure were 0.08-0.11 bar. In case of zeolite 13X, these values were 0.055-0.082 bar.

With a higher effective diffusivity (2.2×10^{-6} m²/s) a better performance in terms of productivity and specific energy. The minimum specific energy in two cases were 22.5 and 23.3 kJ/mol respectively. The maximum productivity values were 1.25 and 1.98 mol/m³ ads/s. The improvement in performance can be attributed to faster cycles (110 to 232 s vs. 180 to 280 s) and higher co-current evacuation pressure (0.1 to 0.15 bar vs 0.08 to 0.11 bar) chosen by the optimizer as seen from the figure 9.

Further, the energy penalty was calculated based on the maximum productivity values for 13X and UTSA-16 based on equations 3 and 4. We have considered a 600 MW power plant emitting 11690 kg-mole/hr CO₂ captured [17]. This translated into 95.5 MW power required to capture 90% of the CO₂ emitted by the power plant. Therefore, the energy penalty was 15.9%. For zeolite 13X, these values were 105.9 MW and 17.7% respectively. Therefore, a VSA process with UTSA-16 will be 10% more efficient than the one with Zeolite 13X adsorbent.

The power required for capture is calculated as

$$\text{Power}_{\text{capture}} =$$

$$\text{CO}_2 \text{ emission} \times \text{Recovery} \times \text{Specific energy consumption} \quad (3)$$

$$\text{Energy penalty} = \frac{\text{Power}_{\text{capture}}}{\text{Power}_{\text{no capture}}} \times 100 \quad (4)$$

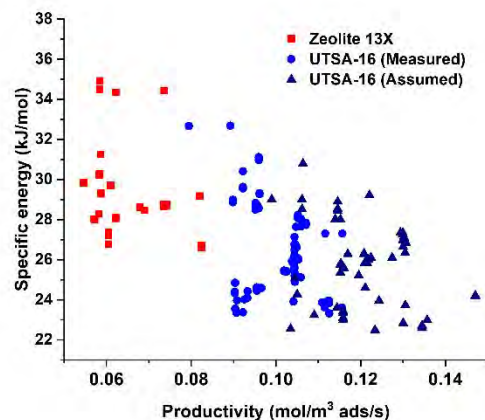


Figure 8: Specific Energy vs Productivity pareto fronts for Zeolite 13X and UTSA-16.

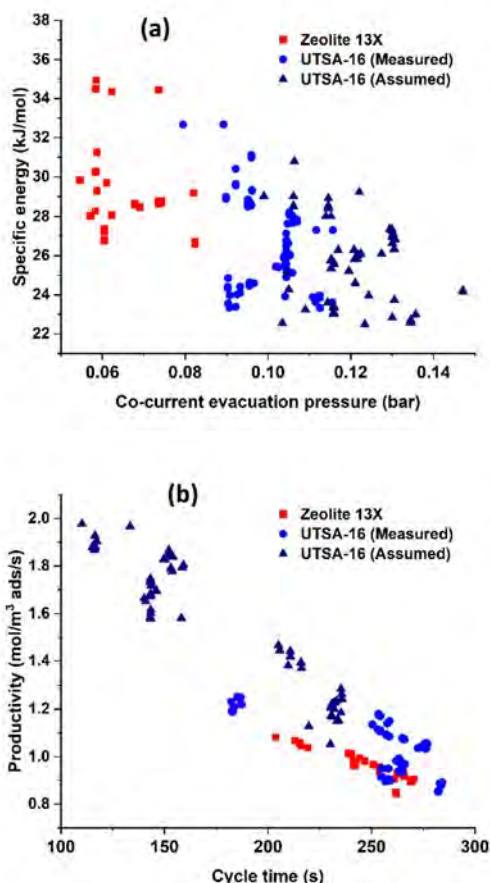


Figure 9: (a) Specific energy vs co-current evacuation pressure and (b) productivity vs cycle time.

Conclusions

UTSA-16 extrudates were synthesized by SINTEF up to 200g and these were characterized for adsorption equilibrium and kinetics at the University of Edinburgh. Using the information from the characterization, process optimization study was carried out and these results showed that UTSA-16 sorbent showed better performance than Zeolite 13X. This work also established the importance of establishing the mass transfer mechanism and the obtaining the right kinetic constants to obtain the true potential of an adsorbent.

Acknowledgements

This work has been supported by the UK Engineering and Physical Sciences Research Council (EPSRC), grants EP/L021064/1 EP/N007859/1.

References

1. IPCC, 2014: Climate Change 2014: Synthesis Report. Contribution of Working Groups I, II and III to the Fifth Assessment Report of the Intergovernmental Panel on Climate Change. IPCC, Geneva, Switzerland.
2. Krishnamurthy S, Rao VR, Guntuka S, Sharratt P, Haghpanah R, Rajendran A, et al. CO₂ capture from dry flue gas by vacuum swing

- adsorption: A pilot plant study. *AIChE J.* 2014;60:1830-42.
3. Shen, C., Liu, Z., Li, P., Yu, J., *Two-Stage VPSA Process for CO₂ Capture from Flue Gas Using Activated Carbon Beads.* *Industrial & Engineering Chemistry Research*, 2012. 51(13): p. 5011-5021.
4. Yang H, Li J-R. Metal-Organic Frameworks (MOFs) for CO₂ Capture. In: Lu A-H, Dai S, editors. *Porous Materials for Carbon Dioxide Capture.* Berlin, Heidelberg: Springer Berlin Heidelberg; 2014. p. 79-113
5. S. Krishnamurthy, A. Lind, A. Bouzga, J. Pierchala, R. Blom, *Chem Eng J* 2021, 406, 127121.
6. Phan A, Doonan CJ, Uribe-Romo FJ, Knobler CB, O'Keeffe M, Yaghi OM. Synthesis, Structure, and Carbon Dioxide Capture Properties of Zeolitic Imidazolate Frameworks. *Accounts ChemRes.* 2010;43:58-67.
7. Rajagopalan AK, Avila AM, Rajendran A. Do adsorbent screening metrics predict process performance? A process optimisation based study for post-combustion capture of CO₂. *Int J Greenh Gas Con.* 2016;46:76-85.
8. Khurana M, Farooq S. Adsorbent Screening for Postcombustion CO₂ Capture: A Method Relating Equilibrium Isotherm Characteristics to an Optimum Vacuum Swing Adsorption Process Performance. *Ind Eng Chem Res.* 2016;55:2447-60.
9. Farmahini AH, Krishnamurthy S, Friedrich D, Brandani S, Sarkisov L. From Crystal to Adsorption Column: Challenges in Multiscale Computational Screening of Materials for Adsorption Separation Processes. *Ind Eng Chem Res* 2018;57:15491-511
10. Ruthven DM, Brandani S. Measurement of diffusion in porous solids by zero length column (ZLC) methods. *Mem Sci Tech* 2000. 187-212.
11. Hu X, Brandani S, Benin AI, Willis RR. Development of a Semiautomated Zero Length Column Technique for Carbon Capture Applications: Study of Diffusion Behavior of CO₂ in MOFs. *Ind Eng Chem Res.* 2015;54:5777-83.
12. Agueda VI, Delgado JA, Uguina MA, Brea P, Spjelkavik AI, Blom R, et al. Adsorption and diffusion of H₂, N₂, CO, CH₄ and CO₂ in UTSA-16 metal-organic framework extrudates. *Chem Eng Sci.* 2015;124:159-69
13. Brandani, S.. "Analysis of the Piezometric Method for the Study of Diffusion in Microporous Solids: Isothermal Case." *Adsorption* 1998 4(1): 17-24.
14. Krishnamurthy S, Blom R, Ferrari MC, Brandani S. Adsorption and diffusion of CO₂ in CPO-27-Ni beads. *Adsorption* 2020; 26(1): 711-721
15. Brandani S, Brandani F, Mangano E, Pullumbi P. Using a volumetric apparatus to identify and measure the mass transfer resistance in

- commercial adsorbents. Micropor Mesopor
Mat. 2020, 304, 109277
16. Friedrich D, Mangano E, Brandani S. Automatic estimation of kinetic and isotherm parameters from ZLC experiments. Chem Eng Sci. 2015;126:616-24.
 17. Khurana M, Farooq S. Integrated Adsorbent Process Optimization for Minimum Cost of Electricity Including Carbon Capture by a VSA Process. AIChE J. 2019;65:184-95.

PHASE EQUILIBRIUM MEASUREMENTS OF AMMONIA BASED CO₂ CAPTURE SOLVENTS WITH FTIR FOR GAS PHASE ANALYSIS

Inna Kim*, Actor Chikukwa, Hanne Kvamsdal, Karl Anders Hoff, Thor Mejdell, Geir Haugen
SINTEF Industry, Trondheim, Norway

* Corresponding author e-mail: inna.kim@sintef.no

Abstract

Vapor-liquid-solid equilibrium (VLSE) was measured for four solvents (blends A-D) at atmospheric pressure in a low-temperature setup at 20 °C and at 20, 35, and 55 °C for blend E. The blends are ammonia-based aqueous solutions selected to evaluate the potential for CO₂ capture at post-combustion conditions with high pressure solvent regeneration. The set-up was modified to enable analysis of ammonia and CO₂ in the vapor phase using FTIR®. Solid formation in the liquid phase was monitored using optical probes FBRM® and PVM® to determine maximum CO₂ loadings for the precipitation-free range.

Keywords: vapor-liquid equilibrium, solvent, carbon dioxide, ammonia

1. Introduction

Solvent technology for CO₂ capture has been demonstrated at different scales and several processes are now commercially available from a few suppliers. However, to mitigate climate changes, more cost-effective technologies and technology provider are necessary. Research on the development of more energy efficient and low-cost solutions is ongoing in many different projects around the world. Water-lean solvents and solvents allowing to strip the CO₂ at higher pressure are considered promising as having potential to reduce CO₂ capture cost significantly. Cost reduction potential for CO₂ capture due to lower heat capacity and high reaction kinetics are reported for some non-aqueous solvents [1], while the solvents that can be regenerated at higher pressure allow savings in the cost (both OPEX and CAPEX) of CO₂ compression.

Several solvent formulations were tested in the present work to evaluate their performance in terms of CO₂ solubility and absorption capacity and explore a potential for high pressure stripping. Ammonia-based solvents for CO₂ capture have several advantages compared to monoethanolamine (MEA) which is often used as a reference solvent [2]-[3]. The main advantages are low cost, no degradation and potential for high-pressure high-temperature stripping. The main disadvantages of this type of solvents are very high volatility of the ammonia and operational challenges due to formation of solid ammonia bicarbonate from vapor phase on cold surfaces.

Only a few work report measurements of the ammonia in the vapor phase over aqueous ammonia solutions using gas chromatography (GC), see for example [4]-[6]. No experimental data are found for ammonia-based mixtures.

In the CLIMIT Demo project IMPRESS (2019-2021) candidate solvents were evaluated for high-pressure stripping applications aiming at the demonstration of the best performing candidate at SINTEF's Tiller CO₂Lab, which will be equipped with a high-pressure stripper in

2021 in the MPSolv project funded through the ECCSEL ERIC program.

In the IMPRESS project absorption performance was evaluated for several solvent blends containing 5 mole ammonia per kg water (molal concentration) mixed with an amine and potassium carbonate, or only with amines. The objective was to evaluate the effect of solvent composition on ammonia volatility and absorption capacity for CO₂, and to estimate potential for high pressure stripping for a blend with the most promising absorption performance.

Absorption performance (phase equilibrium) was measured at 20 °C in a low-pressure set-up with in-situ analysis of the gas phase. Potential for high pressure stripping was assessed by extrapolating the low temperature data to a higher temperature using an inhouse empirical model [7]. Additionally, Aspen Plus simulation was also utilized in this performance assessment.

2. Experimental

2.1. Chemicals

Chemicals were used as received without additional purification. Aqueous solutions were prepared using distilled de-ionized water. All solvent blends consisted of 5 mole ammonia (NH₃) per kg water, 0 or 2 mole K₂CO₃, and 2-2.5 mole amine according Table 1.

Table 1. IMPRESS blends tested in this work

Coded name	Composition, molal basis		
	NH ₃	K ₂ CO ₃	Amine
Blend A	5	2	2 amine A
Blend B	5	2	2 amine B
Blend C	5	2	2 amine C
Blend D	5	0	2 amine D
Blend E	5	0	2 amine A + 0.5 amine D

2.2. Experimental set-up and procedure

Partial pressure of CO₂ and NH₃ over loaded solutions at absorber conditions was measured using the LabMax® (Mettler Toledo) reactor setup connected to an analytical instrument for the analysis of the vapor in the head space.

The setup consists of a mechanically agitated jacketed glass reactor of 1 L volume, equipped with Pt100 temperature sensor (uncertainty 0.1 °C), Leo3 pressure transducer (0-30 bar, uncertainty 0.1 % FS), and probes for online Particle Vision and Measurement (PVM) and Focused Beam Reflectance Measurement (FBRM) for characterization of phase change systems (liquid-liquid or liquid-solid).

For the head space analysis in the present study, the setup was connected to the ABB Fourier Transform infrared spectroscopy (FTIR) gas analyzer via a heated transfer line. The vapor phase is circulated using an inline micropump (RS PRO Diaphragm Electric Operated Positive Displacement Pump). To avoid condensation/precipitation of the ammonium salts, the reactor lid and tubing are heat traced and kept at the same temperature as the reactor. Vapor sample is transferred to the FTIR via a transfer line kept at 180°C, same temperature as in the FTIR cell. Any degradation of amines due to high temperature was assumed negligible due to short residence time at high temperature and relatively short experimental time. Liquid samples (5-7 ml) are taken at each equilibrium point and analyzed for CO₂ (Apollo 9000 Combustion TOC Analyzer) and total alkalinity (acid-base titration).

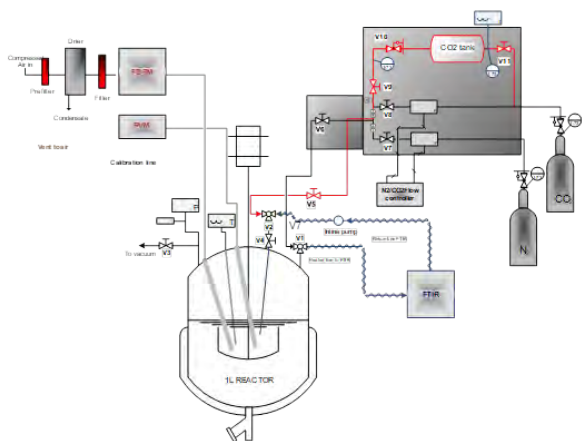


Figure 1: Experimental setup for VLSE measurements with FTIR for head space analysis, and PVM and FBRM for solid phase monitoring.

The experiments were terminated when precipitation took place. Precipitate formation was monitored using FBRM and PVM optical probes.

Precipitation-free operation was selected as one of the criteria for solvent optimization. To determine the saturation loading, at which no more CO₂ is solvable in the liquid phase, the experiment was stopped when precipitation was observed. At this point, the stirrer was stopped to allow the precipitate to settle (Figure 2) and a liquid sample of clear liquid without precipitate was taken. An example of the precipitate images taken with

PVM is shown in Figure 3. No analysis of the precipitate was done, however, based on the earlier work, we can say from the crystals shape that the solids are most probably potassium bicarbonate crystals.



Figure 2: Images of the reactor with solvent (522 DPD) at the last loading point when precipitation took place (above, left), and after precipitate was left to settle (above, right).

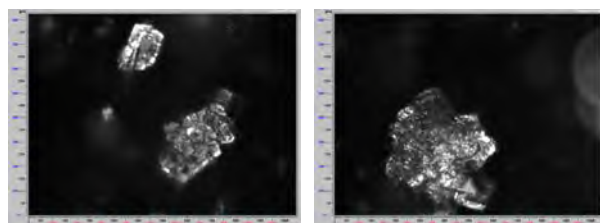


Figure 3: Images of the formed crystals taken with PVM®.

2.3 Calibration of FTIR

The FTIR was used for the analysis of CO₂ and NH₃ in the gas phase. The instrument was calibrated with the premixed calibration gases, supplied by a gas provider together with the certificate of analysis. Calibration for CO₂ was done using 1000 ppm, 2.5, 5, 10, and 40 vol% CO₂ in nitrogen. Calibration for ammonia was done using 1, 5, and 15 vol% ammonia in nitrogen.

The premixed gases were used to acquire calibration spectra, which in turn were used for the development of component models. The FTIR model performance vs calibration gas composition is shown in Table 1.

Table 2: FTIR model performance vs. calibration gas

	FTIR (vol %)	Calibration Gas (vol %)	Absolute relative deviation (%)
CO ₂ (vol%)	0.09	0.10	7.72
	2.53	2.50	1.32
	4.94	5.00	1.24
	9.32	10.00	6.84
	14.29	15.00	4.72
	39.76	40.00	0.59
NH ₃ (vol%)	1.08	1.00	8.04
	5.29	5.00	5.74
	15.92	15.00	6.10

As maybe seen from Table 2, there is a room for improvement of the FTIR models, i.e., more calibration data points are needed to tweak the component models. This will be done in future work.

2.4 Validation of the experimental procedure

For the validation of the experimental procedure for measuring partial pressure of CO₂ using FTIR, VLE measurements with 30 wt% MEA solution was done and data compared with literature data [8]. Partial pressure of CO₂ measured in this work using FTIR agrees well with the data reported by Aronu et al. [8] (see Figure 4). A major advantage is that FTIR allows analysis of the ammonia in the vapor phase in addition to CO₂.

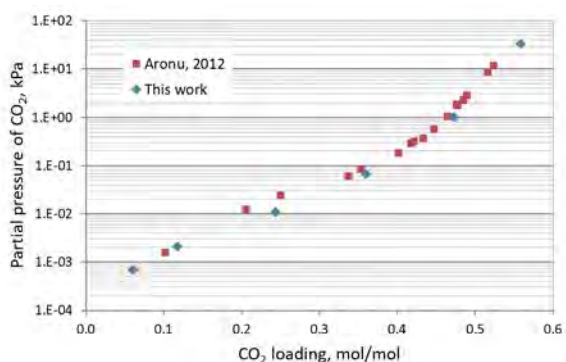


Figure 4: Partial pressure of CO₂ over 30 wt% MEA solution at 40°C as function of CO₂ loading: comparison with literature data.

To validate ammonia pressure measurements, partial pressure of ammonia for Blend A is compared with predictions from AspenPlus. As seen in Figure 5b the measured results agree very well with the simulation results.

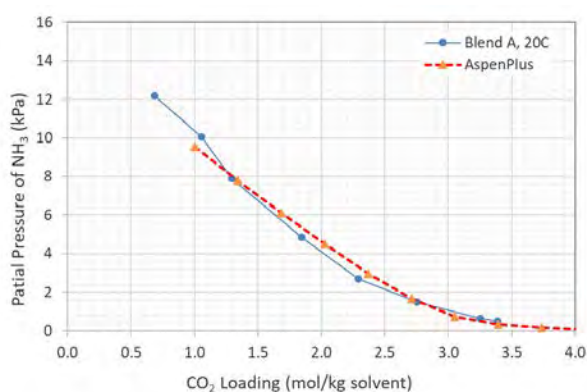


Figure 5. Equilibrium partial pressure of ammonia for Blend A measured at 20 °C using FTIR compared with AspenPlus predictions.

3. Results and Discussion

Experimental partial pressure of CO₂ in the gas phase tested at 20 °C is compared with data for 30 wt% MEA at 40 °C (reference solvent at its optimal absorption

temperature) as shown in Figure 6a. Lower partial pressure of CO₂ after CO₂ loading of about 2.5 mol/kg for all blends presently studied indicates that all of them have higher CO₂ absorption capacity. Partial pressure of ammonia in the gas phase above the same blends at 20°C is compared as shown in Figure 6b. It should be noted that CO₂ loading in these plots includes CO₂ introduced to the solvent with K₂CO₃. (1 mol/kg). As may be seen from the figure, partial pressure of ammonia above the blend E is the lowest. This solvent was therefore selected for further testing to evaluate its potential for high pressure stripping.

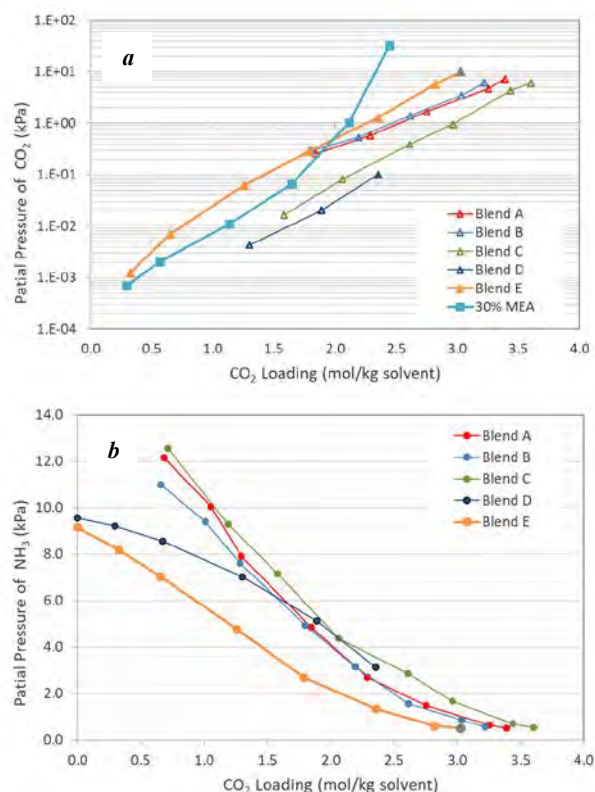


Figure 6. Experimental partial pressure of CO₂ (a) and NH₃ (b) for tested solvent blends at 20 °C.

Equilibrium partial pressure of CO₂ and ammonia for the blend E was also measured at 35 and 55 °C. Tests at higher temperature is not possible in the same setup using the same procedure because total pressure is higher than atmospheric. To compensate for the lack of experimental data at stripper conditions (120 °C), the experimental data for this solvent blend measured at 20, 35 and 55 °C, were used to develop a vapor-liquid equilibrium (VLE) model for predicting equilibrium at 120 °C, thus allowing assessment of the cyclic capacity and potential for high pressure stripping with this solvent. The model is based on the assumption of constant heat of absorption for a specific loading. This assumption is embedded in the derivation of the Gibbs Helmholtz equation (see [7] for further details). This assumption on constant heat of absorption is reasonable for data with moderate span in temperatures and has been applied to a lot of solvent systems studied by SINTEF. This is seen, also from experimental data, as an almost equal distance between VLE isotherms when plotted on logarithmic or semi-

logarithmic scale. Thus, it is believed that the extrapolation to 120 °C is reasonable for the present study, but obviously this should be validated at a later stage.

The model fit for the P_{CO₂} data is shown in Figure 7a also including the VLE curve for 120 °C predicted by the model. Experimental and modelled partial pressure of NH₃ for the same blend is shown in Figure 7b.

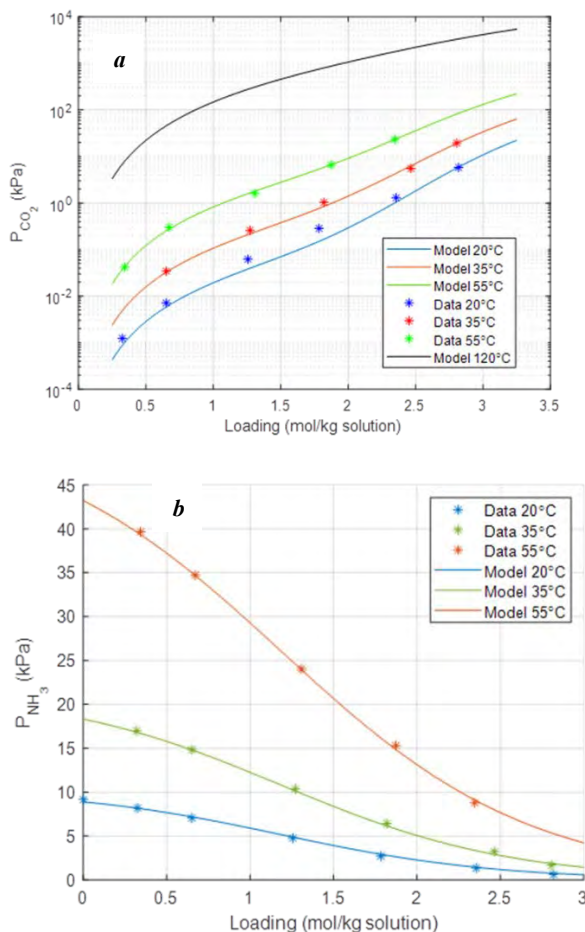


Figure 7. Partial pressure of CO₂ (a) and NH₃ (b) for the blend E at 20, 35, and 55 °C: experimental and modelling results.

To estimate partial pressure of ammonia for this blend at stripper conditions 120°C, extrapolation was also done.

Results for solvent blend E at 20 and 120 °C compared with data for 30 wt% MEA at 40 and 120 °C, shown that blend E has much higher absorption capacity and higher partial pressure of CO₂ at stripper conditions. The improved capacity is clearly shown in Figure 8 as the distance between the equilibrium isotherms at absorber conditions (40 °C) and stripper conditions (120 °C) for both solvents systems.

Furthermore, total pressure in the stripper will be very high due to ammonia vapor pressure making it possible to strip the CO₂ at higher pressure.

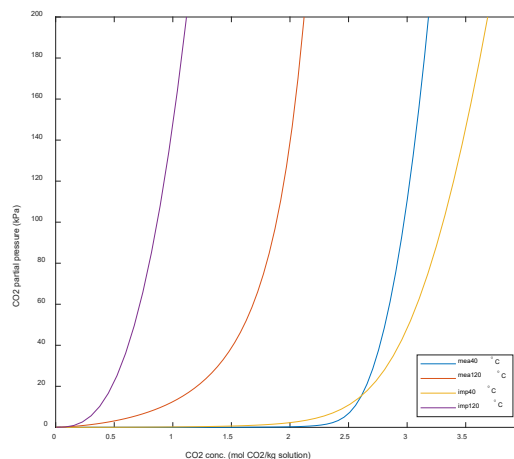


Figure 8: CO₂ equilibrium based on an equilibrium model for 30 wt% MEA at 40 and 120 °C compared to the solvent E (imp in the figure) in the present study.

4. Conclusions

A low-pressure set-up available at SINTEF was connected to FTIR to enable measurements of both CO₂ and ammonia in the vapor phase and VLE for the selected solvent blends measured at 20 °C. The experimental procedure was validated and good agreement with literature data or with simulations in AspenPlus was observed.

One of the tested blends was selected for further characterization to evaluate the potential for high pressure stripping and testing at Tiller CO₂Lab.

Even though it was concluded that stripping will be possible at high pressure (7-10 bar), some considerations are necessary before this solvent can be tested in the Tiller pilot.

During VLE measurements it was observed that even though the reaction rate is high in the beginning, it is decreased quickly, and considerable time is needed to reach the equilibrium at higher CO₂ loadings. This means that higher residence time may be needed for this solvent in the absorption column, or a higher column may be needed.

Partial pressure of ammonia is still very high at the absorber conditions requires implementation of a system to capture and return ammonia to the process, as well as preventing emissions. The existing water configurations at Tiller CO₂Lab are very efficient with amines but will not be sufficient with an NH₃-rich solvent. The acid wash system will capture emissions but will imply a loss of NH₃ that should be returned to the process.

At stripper conditions, operational challenges are foreseen due to possibility of solids formation from vapor phase on the cold surfaces. For testing at pilot scale, the stripper section of the pilot has to be carefully heat traced to avoid any cold spots. This seems to be challenging in the condenser, where water and ammonia should be separated from CO₂ leaving the desorber column. A

solution for this issue needs to be prepared and implemented at Tiller before this solvent can be tested.

Acknowledgements

The presented work forms part of the IMPRESS project funded by CLIMIT-DEMO program under grant number 618158.

References

- [1] Report of the Mission Innovation Carbon Capture, Utilization, and Storage Experts' Workshop. Mission Innovation, September 2017
- [2] Jayaweera, I.; Jayaweera, P.; Elmore, R.; Bao, J.; Bhamidi, S., 2014. Update on mixed-salt technology development for CO₂ capture from post-combustion power stations. *Energy Procedia* 63, 640-650
- [3] Yu, H. 2018. Recent developments in aqueous ammonia-based post-combustion CO₂ capture technologies. *Chinese Journal of Chemical Engineering* 26, 2255-2265
- [4] Göppert, U. and Maurer, G., 1988. Vapor-liquid equilibria in aqueous solutions of ammonia and carbon dioxide at temperatures between 333 and 393 K and pressures up to 7 MPa. *Fluid Phase Equilibria*, 41, 153-185
- [5] Maurer, G., 1987. Vapor-liquid equilibrium in the ternary system ammonia-carbon dioxide-water. *Int. Conf. on Thermodynamics of Aqueous Systems with Industrial Applications*, May 10-14, Warrenton, VA, USA.
- [6] Kurz, F., et al., 1995. Vapor-liquid-solid equilibria in the system NH₃-CO₂-H₂O from around 310 to 470 K: New experimental data and modelling. *Fluid Phase Equilibria* 104, 261-275
- [7] Mejdell et al., 2008. Simplified solvent equilibrium modelling using both equilibrium and calorimetric measurements for post combustion capture. *GHGT-9*, 16-20 November 2008, Washington DC.
- [8] Aronu, U.E. et al., 2011. Solubility of CO₂ in 15, 30, 45 and 60 mass % MEA from 40 to 120°C and model representation using the extended UNIQUAC framework. *Chemical Engineering Science* 66, 6393-6406

PROCESS INTEGRATION OF INDIRECTLY HEATED CARBONATE LOOPING IN LIME PLANT FOR ENHANCED CO₂ CAPTURE

Peloriadi Konstantina^{1*}, Atsonios Konstantinos¹, Nikolopoulos Aristeidis¹, Intzes Konstantinos², Dimitriadis Giorgos², Nikolopoulos Nikos¹

¹ Centre for Research and Technology Hellas, Athens, Gr-15310, Greece

² CaO Hellas, Thessaloniki, Gr-57013, Greece

* Corresponding author e-mail: peloriadi@certh.gr

Abstract

Lime (CaO) production emits significant amounts of CO₂ through both the calcination reactions and the fuel combustion process. In order for the lime industries to reduce their mainly non-avoidable CO₂ emissions, the deployment of carbon capture and storage (CCS) technologies appears as a necessity. One very promising carbon capture method is the indirectly heated carbonate looping (IHCaL). This paper aims to investigate two novel IHCaL concepts, the tail-end and the fully integrated process in order to provide a better understanding of their integration in the lime sector. The concepts are developed and simulated in Aspen PlusTM, heat and mass balance equations are established and a detailed sensitivity analysis is performed. The tail-end process is ideal for retrofitting of existing lime plant, whereas a newly-build lime plant could use the fully integrated IHCaL concept in order to achieve higher CO₂-capture and lower energy consumption. The numerical results for the aforementioned scenarios, revealed that high carbon capture efficiency, 92% and 94% respectively, can be achieved at both concepts. Moreover, the power generation from the heat recovery steam cycle is calculated. Key parameters for effective integration of the concepts are the preheating of the combustion air, the efficiency of the sorbent solid-solid heat exchanger and the utilization of the sorbent purge as lime product.

Keywords: Calcium looping, CO₂ capture, lime production, indirect heating, process model

1. Introduction

Lime (CaO) is a key product for various sectors and plays an essential role for downstream industries. As an important element for soil treatment, it is traditionally used in agriculture, but it has also multiple applications in the manufacturing industry [1].

However, the production of lime remains a carbon-intensive process, since carbon dioxide (CO₂) is released from both the calcination of the raw material, limestone (CaCO₃), and the combustion of the required fuel. It is important to underline that the CO₂ emissions from the calcination process are non-avoidable and cannot be tackled using renewable energy sources. Many carbon capture technologies are being developed with the view for the lime industry to become more CO₂-efficient and maintain its competitiveness [2].

A very promising carbon capture technology is the Indirectly Heated Carbonate Looping (IHCaL), which is considered a very competitive option in comparison to MEA scrubbing and oxy-fuel technology [3].

In calcium looping process, a continuous recirculation of calcium-based sorbents takes place between two main reactors, the carbonator and the calciner. In the fluidized

bed carbonator, the carbon dioxide (CO₂) is captured, as it reacts exothermically, typically at 600°C with lime particles (CaO) and forms limestone (CaCO₃). The sorbents regeneration and release of CO₂ takes place typically at 900°C in the second fluidized bed, the calciner. Since the calcination reaction is strongly endothermic in high temperatures, an amount of thermal energy is needed. In conventional Carbonate Looping (CaL) process, the heat is provided from simultaneous fuel combustion inside the calciner. Moreover, an Air Separation Unit (ASU) is used to provide pure oxygen and a nitrogen-free environment, resulting to a high-purity CO₂ stream at the exit of the calciner. In the case of the IHCaL, the heat for the calcination is transferred indirectly from an external combustor to the calciner with heat pipes, a fact that reduces the efficiency penalty considerably compared to the direct firing inside the reactor.

The main objective of this study is to investigate the integration of Indirectly Heated Carbonate Looping (IHCaL) in a lime plant, by simulating two novel IHCaL concepts, the tail-end and the integrated process.

2. Process Concepts

The reference unit studied in the present paper is a lime plant from CaO Hellas located in Thessaloniki, Greece. The plant comprises a double-shaft kiln, which burns limestone into lime with a production capacity of 150 tonnes per day in normal operating conditions. The raw material of the process is rich in limestone (98%) and the fuel used to provide the necessary heat is petcoke.

The steady-state process models are developed in ASPEN Plus™ to calculate the balances of the existing plant and of the integration scenarios. Two IHCaL scenarios are studied based on the specific lime plant, the first one is the retrofitting of the CO₂ capture unit in the existing lime plant (tail-end process) and the second one is the fully integrated process.

2.1 Tail-end process

In the tail-end solution, the IHCaL facility is located downstream the lime process line as shown schematically in Fig.1. This concept entails a low amount of integration, which makes it suitable for retrofitting. The reference lime plant facility from CaO Hellas is depicted on the left within the dotted area. The raw material stream consisting mainly of limestone and the required fuel for the combustion, petcoke, enter the double shaft kiln. The calcination of limestone takes place and the produced lime exits the kiln and is cooled down. In addition, the flue gases leave from the upper part of the kiln and an amount of their heat is recovered and used in the calcination process for the raw material preheating.

In the IHCaL unit, the flue gases from the lime plant of CaO Hellas, together with the flue gases produced from the combustion of fuel for IHCaL, insert the carbonator

with the aid of a blower. In the carbonator, the CO₂ reacts with the CaO that comes from the calciner forming CaCO₃. The resulting multiphase solid-gas stream exits through the top of the carbonator and is separated in Cyclone 1. The gas which consists of the CO₂-lean flue gas, exits the cyclone through the top and the solids leave through the bottom.

The solids from the carbonator flow into the second reactor and undergo full calcination at high temperature, releasing CO₂. A high purity CO₂-stream is separated then from the solid particles of CaO in Cyclone 2. Part of the CaO stream returns back to the carbonator and the remaining part is extracted as a purge stream through a sorbent extraction point. The purged CaO has high lime concentration (>98%) and therefore, it can be considered as lime product output. Thus, the implementation of the tail-end solution expands the lime production capacity of the plant, while allowing the carbon capture from its flue gases.

Regarding the energy optimization of the process, a solid-solid heat exchanger is installed to transfer heat between the circulating sorbent streams that exit the cyclones, reducing the energy requirement in the calciner to heat up the entering solids. Another parameter that reduces the IHCaL fuel consumption in the combustor is the preheating of the air from the combustion flue gases. Finally, the excess heat from the CO₂-lean flue gases, the CO₂-rich flow cooling and the regulation of the carbonator temperature is exploited to produce electricity power through a heat recovery steam generator [4].

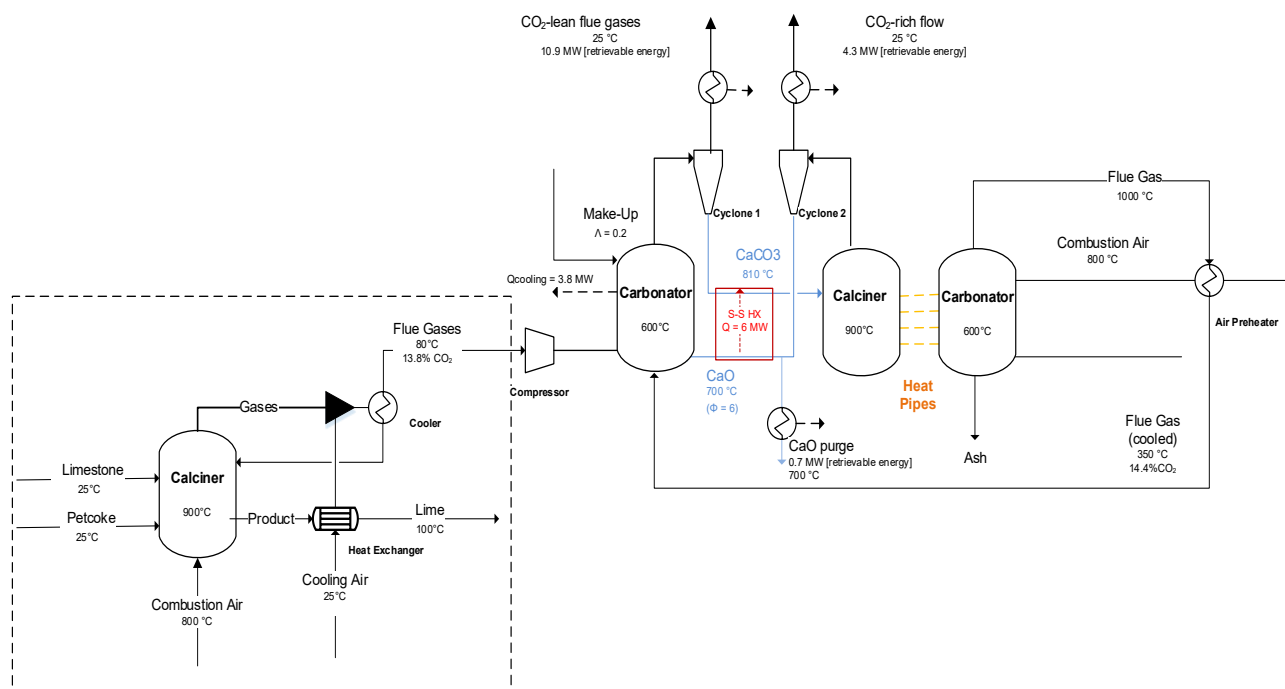


Figure 1: Flowsheet diagram of the tail-end integration of the IHCaL downstream to the lime plant of CaO Hellas

2.2 Fully integrated process

The second concept is the full integration of the process. The lime production kiln is holistically replaced by the IHCaL process, which serves both as a calcination unit and as a carbon capture facility, as it is illustrated in Fig.2. The same operation parameters as in the tail-end process are used.

The raw material, limestone, is fed directly to the carbonator, where it is mixed with the circulating lime solids. Similarly, the flue gases from the IHCaL combustor enter the carbonator, where the CO₂ they contain reacts with the lime particles forming CaCO₃. The solids and the gases exiting the carbonator are separated by Cyclone 1. The solid CaCO₃ stream is calcined producing a high purity CO₂-stream and a solid CaO stream which are separated in Cyclone 2. One part of the solid CaO reenters the carbonator, while the other part exits as purge product of the process.

Similar to the tail-end process, a steam cycle that recovers the excess heat for power generation is considered.

The particularity of this solution is that the CO₂ from the limestone calcination is produced entirely in the calciner, avoiding the need for an extensive downstream separation for mainly particle matter removal. Because of this, the only CO₂ emissions to be captured in the carbonator are the ones related to the burning of the fuel in the combustor to generate the heat for the calciner. This poses a huge advantage with respect to the tail-end scheme as much lower heat penalties and recirculation rates for the same conditions are happening.

Additionally, since in the integrated solution the calcination is carried out with indirectly added heat, there is no contamination of the lime with fuel-related particles like ash or sulfur, thus, a purer product than in the conventional way is to be expected.

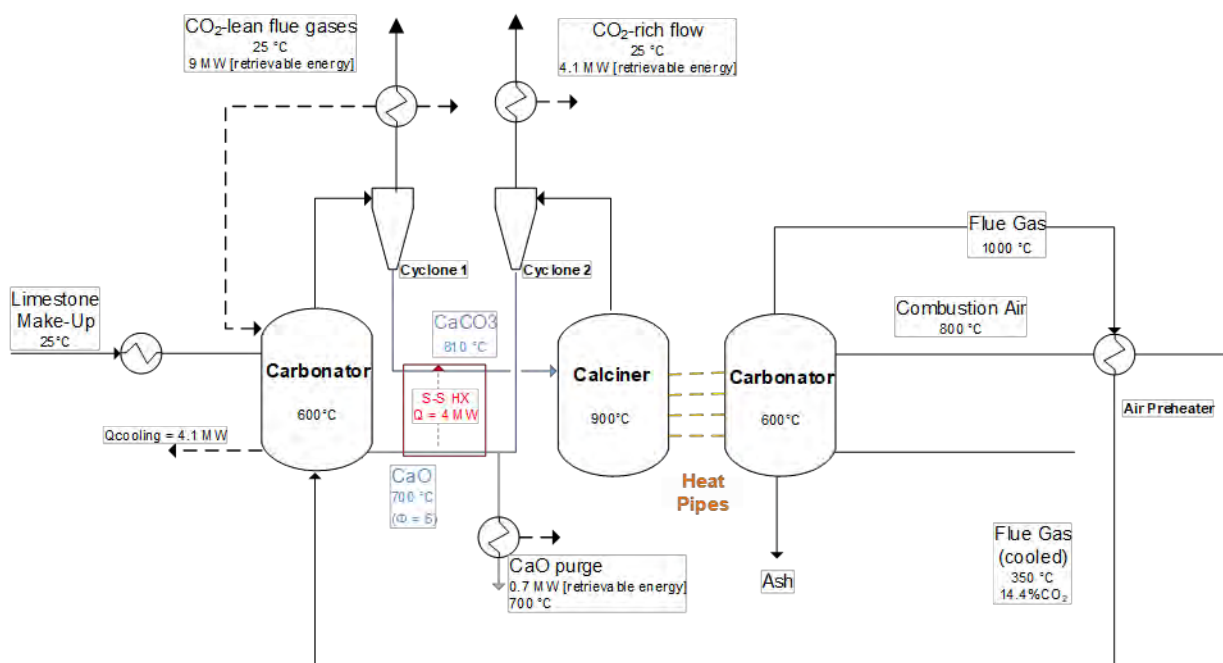


Figure 2. Flowsheet diagram of the fully integrated process

3. Methods

3.1 Process modeling

In this paper, the software ASPEN Plus™, version V11, was used to perform the mass and energy balances calculations. ASPEN Plus™ is a process simulation software, which has a powerful database of properties for various substances [5]. For the process, all simulations were developed in steady-state condition and the calculation of the properties of the substances were based on the Redlich-Kwong-Soave model [6]. The solid-gas separation in the cyclones was assumed to be ideal. The system pressure was set to 1.013 bar, while pressure drops were neglected.

To model the fuel combustion in ASPEN Plus™, the fuel was inserted into a yield reactor that decomposes the stream into its elementary molecules and heat. The resulting stream is burned with air in a Gibbs reactor, which minimizes the Gibbs' free energy, assuming chemical equilibrium. The temperature of the IHCaL combustor is set to 1000°C to allow for 100°C temperature difference between the combustor and the calciner. The calcination and carbonation process in the IHCaL reactors are modelled also with a Gibbs reactor, assuming chemical equilibrium.

However, since in the carbonator only the active solids take part in the reactions, in order to account for the limitations of the kinetics the $X_{max,ave}$ is used. $X_{max,ave}$ is the turning point from the fast to the slow carbonation

regime, which shows the average maximum carbonation conversion of the solids and represents their CO₂ carrying capacity. In the simulation, a fraction ($X_{max,ave}$) of CaO enters the carbonator to react with CO₂ and the rest ($1 - X_{max,ave}$) by-passes the carbonator and is introduced back to the calciner unreacted.

$X_{max,ave}$ is influenced by the specific sorbent circulation as well by the make-up flow and is calculated based on the following equation of the model of Abanades [7]:

$$X_{max,ave} = \frac{f_m(1 - f_w) * F_o}{F_o + F_R(1 - f_m)} + f_w \quad (1)$$

The f_m and f_w are constants which depend on sorbent's physical and chemical characteristics. F_o and F_R represent the make-up flow and the circulation flow respectively.

Moreover, another important parameter is the molar conversion of CaO into CaCO₃ (X), which is defined as the ratio of moles of CaCO₃ to the moles of Ca (Eq. (2)).

$$X = \frac{n_{CaCO_3}}{n_{Ca}} \quad (2)$$

In particular, there are two characteristic X -values that are used in the analysis of CaL processes, the molar conversion of the sorbent exiting the carbonator (X_{carb}) and the molar conversion of the sorbent exiting the calciner (X_{calc}) [8]. The upper limit for the former molar ratio is the $X_{max,ave}$.

The fuel and raw material composition is defined according to the reference plant. Petcoke (NHV=8287 kcal/kg) is implemented as fuel for the combustor in the reference lime plant of CaO Hellas and in the IHCaL. Similarly, the limestone composition from the reference plant (98 wt% CaCO₃) was used for all the limestone inputs in the model.

3.2 Key Performance Indicators

The following key performance indicators were identified in order for a detailed evaluation of the concepts to be achieved. Many key components of the study are based on previous work developed by Charitos et al. [9].

The carbon capture efficiency, E , is defined as the ratio of the captured CO₂ to the generated CO₂, in terms of molar flow rate. There values considered in Eq.3 for the calculation of E , are the output mole flows of CO₂ from the calciner ($F_{CO_2}^{calc,out}$) and from the carbonator ($F_{CO_2}^{carb,out}$).

$$E = \frac{F_{CO_2}^{calc,out}}{F_{CO_2}^{calc,out} + F_{CO_2}^{carb,out}} \quad (3)$$

An important indicator for this study is the product ratio (PR), i.e., the ratio of the production capacity of the new process ($\dot{m}_{CaO,prod}^1$) to the original production ($\dot{m}_{CaO,prod}^0$) as defined in Eq. 4.

$$PR = \frac{\dot{m}_{CaO,prod}^1}{\dot{m}_{CaO,prod}^0} \quad (4)$$

The heat ratio, HR, Eq.(5), is used to present the heat requirement for CO₂ capture and lime production. It is calculated considering the lime produced and the heat requirement in the original process, (Q_{in}^0) and in the entire process including CO₂ capture solution (Q_{in}^1).

$$HR = \frac{Q^1 / \dot{m}_{CaO,prod}^1}{Q^0 / \dot{m}_{CaO,prod}^0} \quad (5)$$

3.3 Operational Parameters

One dimensionless parameter is the specific make-up ratio (Λ), which is defined in Eq. (4) as the ratio between the molar flow of make-up calcium species into the IHCaL (F_o) and the total CO₂ molar flow. In order to sustain the continuous carbonate looping process for the capture of CO₂, it is necessary to purge the solid inventory and replace it with fresh limestone (make-up flow). This refreshing of the sorbent is necessary to (i) avoid the build-up of inert species such as ash and calcium sulfate (CaSO₄), and to (ii) ensure the proper activity of the sorbent.

$$\Lambda = \frac{F_o}{F_{CO_2}} \quad (6)$$

Another important dimensionless parameter is the specific sorbent circulation rate (Φ), which considers the molar flow rate of calcium species that are fed back to the carbonator from the calciner, F_R , as defined in Eq.(5).

$$\Phi = \frac{F_R}{F_{CO_2}} \quad (7)$$

Moreover, a base case was defined and its key parameters are shown in Table 1. In the sensitivity analyses that follow, the base case values undergo a range of variation, where each base case parameter changed leaving the others constant in order to study their influence on the process.

Parameter	Description	Value
Λ	Specific make up rate	0.2
Φ	Specific sorbent circulation rate	6
$T_{Preheated\ Air}$	Preheated air temperature[°C]	800
$T_{CaCO_3\ in}$	Sorbent temperature at calciner inlet[°C]	810
$T_{Calciner}$	Calciner operating temperature[°C]	900
$T_{Carbonator}$	Carbonator operating temperature[°C]	650
$T_{Combustor}$	Combustor operating temperature[°C]	1000
$E_{Cyclone}$	Cyclone separation efficiency[%]	100

Table 1. Main IHCaL parameters with their base case values

4. Results and discussion

4.1 Results of the reference plant

In the present work, a steady-state process model was developed of the reference lime plant of CaO Hellas without the IHCaL process. The heat and mass balances of the facility were calculated with less than 2% deviation from the reference values provided and therefore, the model is assumed validated.

Parameter	CaO Hellas Data	Simulation Data	Relative Error
CO ₂ in flue gases [v/v% _{wet}]	13.8	13.7	+0.7%
Direct fuel consumption [MJ/t _{CaO}]	5620	5575	-0.8%
Production [t/h]	150	148	-1.4%

Table 2. Validation of the lime plant simulation of CaO Hellas

4.2 Results of the IHCaL models with the base case parameters

A summary of the results of the IHCaL simulations is presented in Table 3. For the calculations the base case parameters were assumed for both concepts.

In the tail-end concept, the product ratio is as high as 2.66, which means that more lime is being produced in the IHCaL facility than in the reference lime plant. Additionally, in the integrated concept the product ratio is 0.98. It was expected that for the same raw material input as in the reference plant the amount of produced lime in the integrated process would be similar. The purge lime extracted from IHCaL showed a high purity (98 wt% CaO). Consequently, it can be sold as product of the lime production, which makes both IHCaL concepts especially suitable and profitable for application to lime plants.

The direct fuel consumption of the reference plant is 5575 MJ/t_{CaO}. In the tail-end process there is a 265% increase of the fuel consumption with respect to the reference plant. For the fully integrated process, the increase in fuel consumption is 239%. The electricity generated through heat recovery amounts to 67.6% and 65.3% respectively of the total thermal energy input. This implies a strong reduction in the net CO₂ emissions, considering the avoidance of the CO₂ produced from the grid's power generation.

Parameters	Tail- end solution	Integrated solution
System Parameters		
Heat Ratio (HR)	2.66	1.57
Product Ratio (PR)	1.63	0.98
CO ₂ capture efficiency(E)	92%	94%
Specific sorbent circulation rate (Φ)	6	6
Specific Make-up ratio (Λ)	0.20	0.48
Carbonator		
Operating Temperature [°C]	650	650
Flue gas from lime plant molar flow [kmol/s]	0.31	-
Flue gas from IHCaL combustion [kmol/s]	0.32	0.21
Total Flue gas flow to the carbonator [kmol/s]	0.63	0.21
Total CO ₂ molar concentration in the flue gas [kmol/s]	0.14	0.14
Flue gas inlet temperature [°C]	114	336
Sorbent temperature at carbonator inlet [°C]	700	700
Molar conversion of the sorbent exiting the carbonator, X_{carb} [mol _{CaCO3} / mol _{Ca}]	0.18	0.14
Max. average carbonation conversion, X_{max} [mol _{CaCO3} /mol _{Ca}]	0.25	0.33
Calciner		
Operating Temperature[°C]	900	900
Sorbent mole flow at calciner inlet[kmol/s]	2020	1427
Sorbent temperature at calciner inlet[°C]	810	810
Purge CaO flow[t/day]	93.9	145
Heat Input[MW]	20.2	11.9
Combustor		
Operating Temperature [°C]	1.000	1.000
Total fuel Consumption IHCaL[kg/s]	0.64	0.41

Table 3. Results of the tail-end and the integrated solution with the parameters of the base case

	Tail-End	Integrated
CO₂ balance		
CO ₂ Molar flow rate from kiln [kmol/h]	156	-
Molar flow rate of CO ₂ from IHCaL combustor [kmol/h]	169	107
Molar flow rate of CO ₂ from calcined make-up in IHCaL [kmol/h]	65	106
Total CO ₂ output [kmol/h]	390	226
Direct CO ₂ emissions [kmol/h]	358	213
Captured CO ₂ flow rate [kgco ₂ /t _{CaO}]	1573	1562
Energy balance		
Total Heat Input [MW]	29.1	15
Direct fuel consumption [MJ/t _{CaO}]	14787	13352
Power generation (P_{el}) [MW _{el}]	19.7	9.8

Table 4. Model results: CO₂ and energy balances

4.3 Sensitivity Analysis

4.3.1. Tail-end process

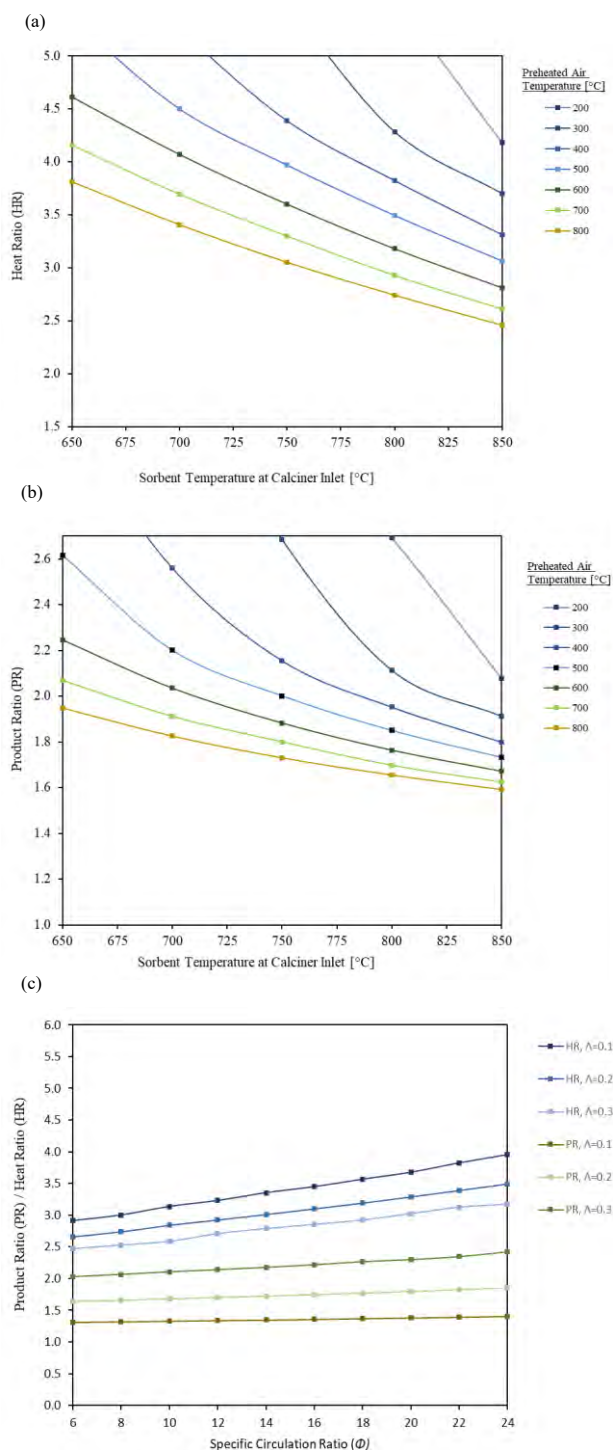


Figure 3: Sensitivity analysis for the tail-end integration concept. In (a),(b) the influence of $T_{PreheatedAir}$ and T_{CaCO_3in} on heat ratio (HR) and product ratio (PR) respectively is shown.

In (c) the variation of HR and PR for different specific circulation ratio (Φ) and make-up ratio (Λ) is depicted.

In Fig. 3 (a) HR is shown as a function of the sorbent temperature at the calciner inlet (T_{CaCO_3in}) for different values of preheated air temperature ($T_{PreheatedAir}$) under the assumption of constant circulation rate (Φ) and make-up ratio (Λ). An increase in the temperature of the

combustion air and the temperature of the sorbent stream at the calciner inlet, leads to lower HR. This means that the heat requirement is influenced by the heat exchange at the preheater and at the solid-solid heat exchanger. The process becomes more efficient as the required amount of energy decreases and the value of HR drops accordingly for a fewer fuel consumption. The preheating of the air appears to be a very important factor of the IHCaL simulation as not only is less fuel needed in the combustor to raise the temperature at the desirable levels, but also the subsequent smaller CO₂-emissions from this unit decrease the heat needs of the carbonation/calcination loops. Additionally, in Fig. 3 (b) it is seen that in this case the PR decreases similarly. This fact is expected, because as the CO₂ emissions decrease due to smaller fuel consumption, less make-flow enters the calciner and the purge stream decreases proportionally.

Fig.3(c) presents the relation of heat ratio (HR) and product ratio (PR) to specific circulation ratio (Φ) for different values of make-up ratio (Λ). A rise in Φ results in an increase of HR, because higher circulation requires higher consumption of fuel, due to the sensible heat needed to balance the temperature difference of the two reactors, i.e. the carbonator (650 °C) and the calciner (900 °C). The product rate remains almost constant, because the circulation has an insignificant effect on purge production. Additionally, the influence of Φ on Λ is illustrated. The limestone make-up flow has a proportional relationship to purge lime flow, since inside the calciner it is decomposed to carbon dioxide and lime, therefore the amount of produced purge lime rises. Moreover, the HR value reduces for higher Λ . Hence, if HR decreases and PR increases for higher Λ , it is evident that it is more efficient to add extra limestone in the IHCaL process to be calcined than to calcine it in the traditional lime plant process. As every additional limestone particle added in the lime plant energy is needed to both calcine it and capture the respective CO₂ in the IHCaL plant. In contrast, the direct calcination of the limestone in the calciner of the IHCaL plant inherently creates a high purity CO₂ stream.

4.3.2. Fully Integrated process

For the fully integrated solution, the make-up stream is the main raw material input, limestone, for the calcination process. Consequently, the make-up ratio can only be controlled indirectly and is considered a dependent variable in the sensitivity analysis.

In comparison to the tail-end solution, there is no variation in the production flow due to changes in the temperatures. This is expected because the make-up flow rate is a constant value. Thus, there is no variation of the PR at different temperatures.

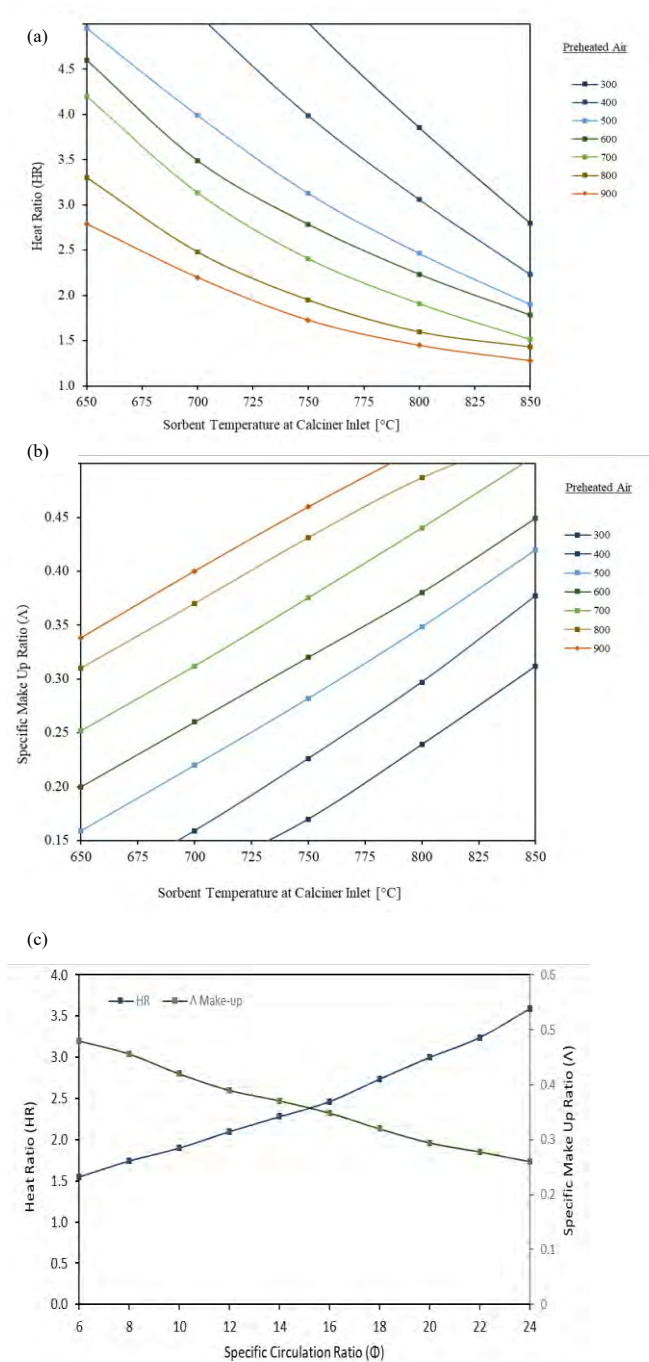


Figure 4: Sensitivity analysis for the full integration concept. In (a),(b) the influence of $T_{\text{PreheatedAir}}$ and $T_{\text{CaCO}_3\text{in}}$ on heat ratio (HR) and specific make up ratio (PR) respectively is shown. In (c) the variation of HR and Λ for different Φ is shown.

In Fig.4 (a) the value of HR decreases for higher $T_{\text{CaCO}_3\text{in}}$ and higher $T_{\text{PreheatedAir}}$ under the assumption of constant circulation rate (Φ). It is remarkable that, compared to the results from the tail-end solution, the values of HR are much lower for the same temperature values. Furthermore, towards the limit of the maximum theoretical integration, the HR tends towards 1.0, whereas in the tail-end solution, the minimum achievable HR is around 2.5.

The impact of higher $T_{\text{CaCO}_3\text{in}}$ and $T_{\text{PreheatedAir}}$ on Λ is shown in Fig.4 (b). The value of Λ will rise, because the process becomes more efficient and the CO₂ decreases.

Fig.4 (c) presents the relation of heat ratio (HR) and make-up ratio (Λ) to specific circulation ratio (Φ). A rise in Φ results in an increase of HR, because higher circulation requires more fuel consumption, due to the required sensible heat to balance the temperature difference of the carbonator and the calciner in the process. The make-up ratio has a negative correlation to the CO₂-flow, which increases for higher circulation and therefore Λ decreases accordingly.

5. Conclusions

This study presents two approaches for the integration of the IHCaL process into a lime plant using as process simulation tool the software of ASPEN PLUS™, version V11.

The tail-end solution is suitable for retrofitting to the existing lime plants since the CO₂ emissions were captured with an efficiency of 92% with an increase of 166% in the total direct fuel consumption. Additionally, the high product output mass flow from the tail-end process proves that a great increase in the production takes place, of 65%, and therefore, this concept appears to be a good option for existing lime production facilities that opt to minimize their carbon footprint by capturing CO₂ and expand their production capacity.

In the fully integrated solution, where the lime production is integrated into the IHCaL process, decreased CO₂ emissions can be achieved. It is worth noting that the CO₂ capture efficiency reaches 94% with an increase of 57% in the direct fuel consumption. Therefore, it can be proposed that a new lime plant could be constructed with a fully integrated process to achieve very high CO₂ capture at smaller cost.

From the sensitivity analyses, it is concluded that a low energy penalty in the IHCaL process can be opted with the maximization of the preheating temperature of the combustion air and with the best possible heat exchange in the solid-solid heat exchanger. Furthermore, the utilization of the produced lime in the IHCaL process is important for the viability of the tail-end solutions.

The developed models and results will be further used to establish boundary conditions for upcoming test campaigns at a pilot plant within the ANICA project framework, as well as to execute economic, environmental, and risk analyses on the integration of the IHCaL into the lime production process.

Acknowledgements

This study has been carried out in the framework of the ANICA project. This project ANICA is funded through the ACT programme (Accelerating CCS Technologies, Horizon2020 Project No 294766).

Financial contributions were made from the German Federal Ministry of Economic Affairs and Energy, the Department for Business, Energy and Industrial Strategy of the United Kingdom and the Greek General Secretariat for Research and Technology.

References

- [1] Vladimir V. Lukin, Francis M. Epplin. Optimal frequency and quantity of agricultural lime applications Agricultural systems 76 (2003) 949–967
- [2] T.P. Hills, M. Sceats, Daniel Rennie, P.S. Fennel. LEILAC: low cost CO₂ capture for the cement and lime industries, Energy Procedia, 114 (2017), pp. 6166-6170
- [3] C.J. Abanades, G. Grasa, M. Alonso, N. Rodriguez, E.J. Anthony, L.M. Romeo. Cost Structure of a Postcombustion CO₂ Capture System Using CaO. Environmental Science & Technology 41(15) (2007) 5523-5527.
- [4] Lasheras A, Ströhle J, Galloy A, Eppl B. Carbonate looping process simulation using a 1D fluidized bed model for the carbonator. International Journal of Greenhouse Gas Control 2011;5(4):686–93.
- [5] Zhang Y, Cao S-X, Shao S, Chen Y, Liu S-L, Zhang S-S. Aspen Plus-based simulation of a cement calciner and optimization analysis of air pollutants emission. Clean Techn Environ Policy 2011;13(3):459–68.
- [6] Tilak P, El-Halwagi MM. Process integration of Calcium Looping with industrial plants for monetizing CO₂ into value-added products. Carbon Resources Conversion 2018;1(2):191–9.
- [7] Abanades, J.C., Anthony, E.J., Wang, J., Oakey, J.E.: ‘Fluidized bed combustion systems integrating CO₂ capture with CaO’, Environmental science & technology, 2005, 39, (8), pp. 2861–2866
- [8] Vorrias, I., Atsonios, K., Nikolopoulos, A., Nikolopoulos, N., Grammelis, P., Kakaras, E.: ‘Calcium looping for CO₂ capture from a lignite fired power plant’, Fuel, 2013, 113, pp. 826–836
- [9] A. Charitos, N. Rodríguez, C. Hawthorne, M. Alonso, M. Zieba, B. Arias, G. Kopanakis, G. Scheffknech, and J.C. Abanades. Experimental Validation of the Calcium Looping CO₂ Capture Process with Two Circulating Fluidized Bed Carbonator Reactors. Industrial Engineering Chemical Research 50 (2011)

Nomenclature

CaL	Calcium Looping
Calc	Calciner
Carb	Carbonator
IHCaL	Indirectly Heated Carbonate Looping
CH	CaO Hellas
E	CO ₂ Capture Efficiency
F_0	Molar Flow of Make-up CaCO ₃
F_{CO_2}	Total Mole Flow of Produced CO ₂
F_R	Molar Flow of CaO fed to Carbonator
HMB	Heat and Mass Balance
HR	Heat Ratio
KPI	Key Performance Indicator
NHV	Net Heating Value of Fuel
PR	Product Ratio
\dot{Q}_{IHCaL}	Heat requirement IHCaL
$\dot{Q}_{Lime\ Process}$	Heat requirement for lime production
$T_{CaCO_3\ in}$	Sorbent temperature at calciner inlet
$T_{Preheated\ Air}$	Preheated air temperature
X	Molar Conversion of CaO to CaCO ₃
Λ	Specific Make-up Ratio
Φ	Specific Sorbent Circulation Ratio

HIGH LEVEL ANALYSIS OF CO₂ CAPTURE IN THE WASTE-TO-ENERGY SECTOR

J.A. Ros^{1*}, J.G.M-S. Monteiro¹, E.L.V. Goetheer¹

¹ TNO, Leeghwaterstraat 44, 2628 CA, Delft, The Netherlands

* Corresponding author e-mail: jasper.ros@tno.nl

Abstract

There is currently a large amount of interest from the Waste-to-Energy (WtE) sector in Europe towards implementation of post-combustion carbon capture technology. This study gives a high level analysis of the implementation of a CO₂ capture plant (no post-treatment of the captured CO₂ is considered) for three generic WtE plants that process 60, 200 and 500 kton of waste per year respectively. The heat and electricity demand of the plants are analysed and compared to the energy generation of the reference WtE plant. It is shown that regardless of the size of the plant, approximately 53% of the steam for district heating and 5% of the electricity generation of the reference WtE plant is needed to run the CO₂ capture plant. Additionally, a techno-economic analysis has been conducted that shows that the expected costs for a CO₂ capture plant are 30 to 55 €/ton CO₂ captured, depending on the considered scale. Additionally, it is shown that for smaller WtE plants, CAPEX is the dominant factor, while for larger WtE plants, the variable OPEX is dominating.

Keywords: CO₂ capture, Waste-to-Energy, process modelling, TEA

1. CO₂ capture in the Waste-to-energy sector

Waste incineration is used as a means to reduce the volume of non-recyclable waste and capturing or destroying of hazardous substances, as compared to landfilling of waste. Additionally, incineration enables the recovery of the energy released by the oxidation of the organic waste and high pressure steam is generated, which is often used in a combined heat and power (CHP) system. Often, the generated electricity is transferred to the grid, and the heat is used for district heating. The gross efficiency (useable energy versus total energy input) of the CHP system is much higher than systems with electricity generation only.

Waste-to-Energy (WtE) plants are generally one or two orders of magnitude smaller than full-scale power plants. The average WtE plant in Europe has an incineration capacity of ca. 200 kton/year [1]. In 2019, AVR (Duiven, The Netherlands) has commissioned the first commercial full-scale CO₂ capture plant in the WtE sector. The captured CO₂ is liquefied and transported for direct use in the horticulture sector. The capture plant of AVR is shown in Figure 1.

The main advantages of implementing CO₂ capture in the WtE sector is that a large part of the waste (ca. 50%) is biogenic of nature, and thereby, the same percentage of CO₂ has a biogenic origin. Negative emissions can be achieved when capturing and storing the majority of the CO₂ in the flue gas. Additionally, the business model for the WtE plant is generally based on incineration of the waste, and therefore, energy (in the form of low pressure steam) is often available at relatively low prices. This is

especially relevant in the summer, when the need for district heating is low or null.



Figure 1, the commercial AVR CO₂ capture plant in Duiven, The Netherlands [2].

To illustrate the implications of CO₂ capture in the WtE sector, this chapter discusses three case studies. The three case studies are based on different scales, representative for the WtE sector: 60 kton/year (Norwegian average), 200 kton/year (European average), and 500 kton/year (Dutch average). The case study of the 200 kton/year WtE plant was developed and reported in the ALIGN-CCUS project (<https://www.alignccus.eu/>). In that project, both the first generation MEA solvent and the second generation CESAR1 solvent (a mix of AMP and Piperazine) have been evaluated, and it was found that

MEA is the preferred solvent when energy/heat is relatively cheap. Therefore, the cases in this study use MEA (30 wt%) as the solvent of choice. A detailed description of the capture plant modelling can be found in the ALIGN-CCUS work [3].

2. Reference WtE and CO₂ capture plant description

The simplified reference WtE plant used in this study can be found in Figure 2. The energy content of the waste is estimated at 11.2 MJ/kg (wet basis, 20 wt% moisture). Simple mass and energy balance calculations are used to calculate the flue gas composition and temperature, before entering the waste heat recovery unit (WHRU), where high pressure steam is produced at 40 bar and 400 °C. After the WHRU, the flue gas continues to the flue gas pre-treatment and finally to the CO₂ capture plant. The produced steam is used for electricity generation, and the low pressure steam (at 3 bar) is used for district heating and/or CO₂ capture. The main results of the WtE plant modelling without CO₂ capture can be found in Table 1.

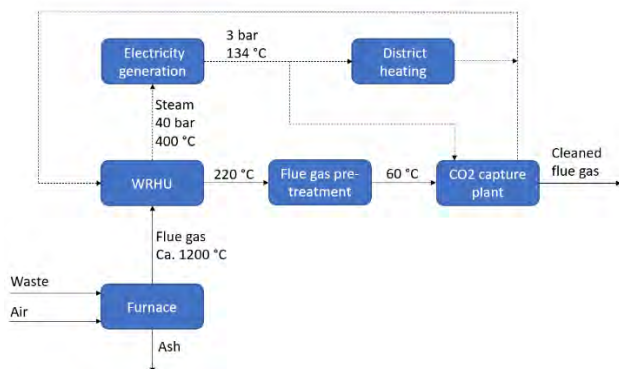


Figure 2, schematic overview of the simplified WtE plant. Flue gas streams are represented by a continuous line, while the steam cycle is represented by a dotted line.

Table 1, Main results from the WtE plant modelling

Parameter	Units	60 kton/year	200 kton/year	500 kton/year
Electricity generation	MW _e	3.01	10.24	25.74
District heating generation	MW _{th}	13.89	47.22	118.65
Flue gas flow rate	kg/hr	57000	190000	475000
CO ₂ concentration in flue gas	vol% (wet)	8.94	8.94	8.94

Figure 3 shows a schematic representation of the CO₂ capture plant simulated in this study. The simulation tool used in this work is ProTreat. The MEA model in ProTreat has been validated against VLE data [4], and pilot plant operation [3].

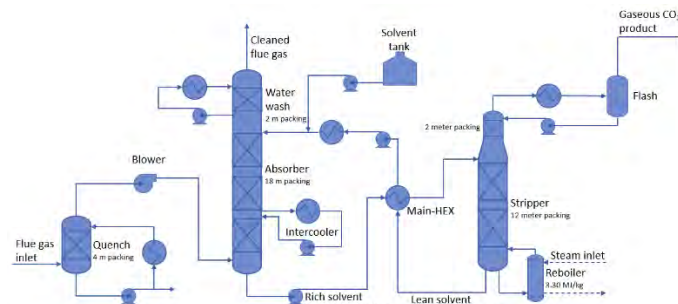


Figure 3, schematic representation of the CO₂ capture plant used in this study, including modelling parameters that are constant for all three cases.

The CO₂ capture plant is modelled assuming a 70% flooding parameter in all columns, and is further optimized by varying the solvent flow rate to minimize the reboiler duty. The main results can be found in Table 2. 47.9% of the steam for district heating and 4.4% of the electricity generated by the reference plant are used in the CO₂ capture plant (regardless of scale). Note that CO₂ conditioning (e.g. liquefaction) is not included in this study, which would have a significant impact on the electricity demand. Also note that there is a possibility for generating additional heat for the district heating system with the returned cooling water of the capture plant. This is especially relevant for the stripper condenser heat exchanger, which has a cooling duty of 31% of the reboiler duty in the simulations. This option has not been taken into account in our analysis, but should be explored in future research.

Table 2, main operational results of the CO₂ capture plant

Parameter	Units	60 kton/year	200 kton/year	500 kton/year
CO ₂ capture percentage	%	90	90	90
Reboiler duty	MW _{th}	6.66	22.2	55.5
Electricity demand	kW _e	133	443	1109
Solvent flow rate	kg/hr	100500	335000	837500

3. Techno-economic analysis

The techno-economic analysis has been performed using the Aspen Capital Cost Estimator V10 (ACCE). The total direct cost of material is taken from ACCE for all equipment, together with the engineering, procurement and construction costs, and the cost methodology shown in Table 3 is followed.

Table 3, main assumptions for the techno-economic analysis. TPC = Total process costs

Parameter	Units	Value
Cost year (Europe)	-	2019
Discount factor	%	8
Depreciation of plant	Years	15
Plant availability	%	90
Maintenance costs	% of TPC	2.5
Labour percentage of maintenance	% of maintenance	40
Operators costs (6 operators)	k€/year	360
Technologist costs	k€/year	100
Insurance costs	% of TPC	2
Administrative and overhead labour costs	% of total labour costs	30
Heat costs	€/GJ	4

Electricity costs	€/kWh	0.1
Cooling water costs*	€/m ³	0.3

* Cooling water make-up is estimated at 1 m³/GJ cooling

The total process costs of installing the CO₂ capture plant at the existing reference WtE plants is estimated at 9.3, 16.5 and 31.4 M€ for the 60, 200 and 500 kton WtE plants respectively. The corresponding total cost of CO₂ capture for the three cases is evaluated between 30 and 55 €/ton CO₂ captured, and is shown in Figure 4. The higher cost for the small scale can be fully accounted to the higher specific CAPEX (economy of scale) and fixed OPEX (as the same amount of operators and technologist costs are expected for the different scales). At the larger scales, the variable OPEX becomes the cost-dominating factor.

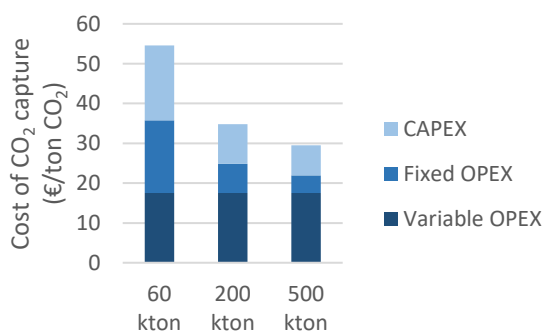


Figure 4, cost of CO₂ capture for the three WtE plant sizes considered in this study.

A breakdown of the variable OPEX costs are shown in Figure 5 (specific costs per ton of CO₂ are identical for all three cases). The heat/steam costs dominate the variable OPEX, as is common for post-combustion CO₂ capture. In this study, the assumption is made that heat is available at 4 €/GJ. In reality, this value is variable, and could be much lower for WtE plants with a CHP system, especially when the demand for district heating is low. This could decrease the total cost of CO₂ capture further below 30 €/ton for large scale plants.

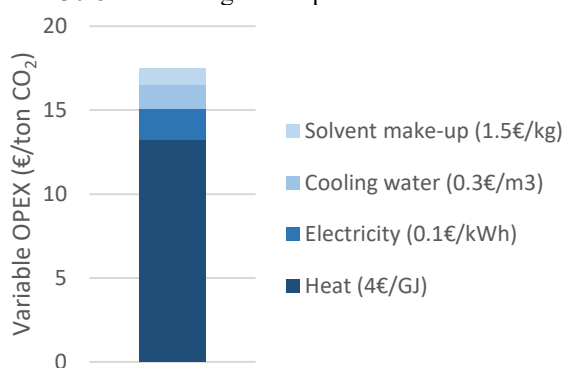


Figure 5, Variable OPEX costs

In all three cases, the columns (absorber, stripper and quench) dominate the equipment costs (60 to 65%), followed by the heat exchangers including the reboiler (15 to 20%), as shown in Figure 6. The other equipment combined accounts to approximately 20 to 25 % of the costs. It is also shown that the columns experience a lower economy of scale effect than the other units, as the percentage of column costs increases with scale.

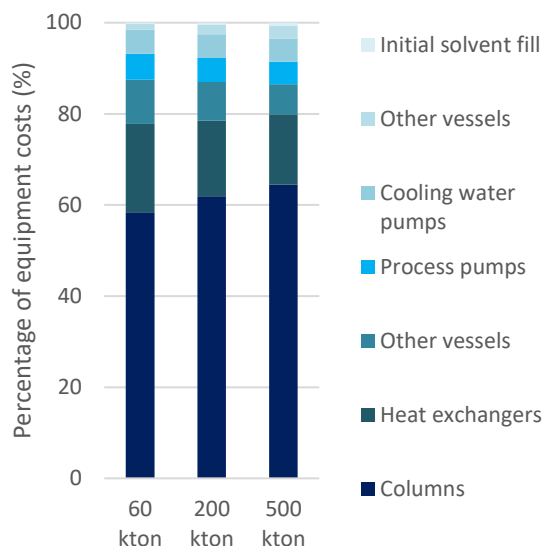


Figure 6, impact of different equipment on the total cost

4. Conclusions

This paper evaluates the cost of CO₂ capture in the WtE sector, focusing on the effect of the plant scale. The results indicate that the cost of CO₂ capture for a 60 kton/year scale plants (Norwegian average) is 55 €/ton CO₂ captured, which is significantly higher than for a 500 kton/year scale plant (Dutch average), evaluated at 30 €/ton CO₂ captured. Additionally, for smaller WtE plants where energy is relatively cheap, cost optimization could be achieved by optimizing the design of the plant and reducing the CAPEX, rather than minimizing the energy demand of the plant. Considering that most of the CO₂ in the flue gas of WtE plants is biogenic, CCS in this sector offers a very cost competitive negative emissions option.

References

- [1] European Commission, "Best Available Techniques (BAT) Reference Document for Waste Incineration," *Jrc Sci. Policy Rep.*, no. 9781461457510, p. 851, 2019.
- [2] AVR, "First tons of CO₂ captured from residual waste supplied to greenhouse horticulture," 2019. [Online]. Available: <https://www.avr.nl/en/press/first-tonnes-of-co2-captured-from-residual-waste-supplied-to-greenhouse-horticulture>.
- [3] S. Garcia *et al.*, "ALIGN D1.4.3: Guidelines and Cost-drivers of capture plants operating with advanced solvents," 2021.
- [4] P. H. M. Feron, A. Cousins, K. Jiang, R. Zhai, and M. Garcia, "An update of the benchmark post-combustion CO₂-capture technology," *Fuel*, vol. 273, 2020.

HIGH LEVEL ANALYSIS OF CO₂ CAPTURE ON LNG FUELLED SHIPS

J.A. Ros^{1*}, J.G.M-S. Monteiro¹, E.L.V. Goetheer¹

¹ TNO, Leeghwaterstraat 44, 2628 CA, Delft, The Netherlands

* Corresponding author e-mail: jasper.ros@tno.nl

Abstract

Recently, there has been an increased level of interest from the maritime sector towards ship based carbon capture (SBCC) as a way to achieve at least 50% emission reduction by 2050. The SBCC technology works especially well when integrated on LNG fuelled ships, which drastically reduces the variable OPEX of the system. This study considers the integration of a CO₂ capture, liquefaction and temporary on-board storage plant on a hypothetical LNG fuelled ship. It is found that by heat integration of the exhaust gas with the capture plant, and the LNG vaporization with CO₂ liquefaction, a capture percentage of ca. 80% can be achieved, using the available utilities. Additionally, a techno-economic analysis has been conducted which has shown that for the hypothetical vessel discussed in this work, the cost of CO₂ capture is 168 €/ton CO₂. For the future perspective, considering higher average loads of the engine/ship, and standardization of the technology, the cost of CO₂ capture could theoretically drop to 45 €/ton CO₂.

Keywords: CO₂ capture, LNG, SBCC, process modelling, TEA

1. Introduction to carbon capture and storage in the maritime sector

The maritime sector has set the goal to reduce their carbon emissions by at least 50% by 2050 [1]. To this extend, a lot of research is conducted towards the deployment of zero emission fuels (ZEF's). However, these fuels are still at a relatively low TRL, and are expected to remain expensive in the coming decades [2]. Ship-based carbon capture (SBCC) on existing or new-built vessels could play a large role in decarbonizing the maritime sector before 2050. At the moment of writing, there are several number of papers available that discuss the conceptual designs of SBCC technology on board of LNG and diesel fuelled vessels [3]–[6], but no piloting or demonstration campaigns have been reported so far. The SBCC technology consists of a CO₂ capture, liquefaction and temporary on-board storage plant. In this study, a techno-economic analysis for the SBCC technology, using the first generation 30wt% MEA capture solvent, is performed for a hypothetical LNG fuelled ship, and recommendations for successful large-scale implementation of the technology are given.

2. Reference vessel and CO₂ capture plant description

The case study discusses a hypothetical vessel with an LNG fuelled electric propulsion (single) engine with a maximum continuous rating (MCR) of 9.2 MW [7]. The hypothetical sailing profile of the considered ship is shown in Figure 1, assuming that 20% of the total time the ship is in harbor with the main engine off. The total single voyage time (for which the CO₂ storage tanks are designed), is assumed at 14 days.

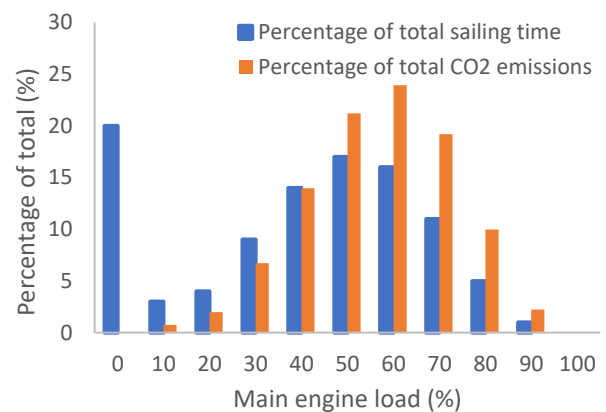


Figure 1, sailing profile and percentage of CO₂ emissions for the reference vessel.

The synergy of implementing CO₂ capture on an LNG fuelled ship comes mainly from the heat integration between the exhaust gas and the CO₂ capture plant, and the heat integration between the LNG evaporation and CO₂ liquefaction, as shown in Figure 2. This drastically reduces the variable OPEX, and only electricity is needed as utility (cooling water is relatively inexpensive at sea), and the total cost will be CAPEX dominated.

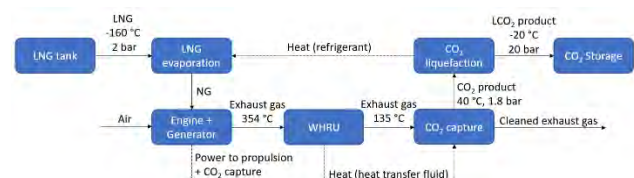


Figure 2, simplified schematic overview of the LNG fuelled vessel integrated with a CO₂ capture plant.

The CO₂ capture plant is designed at 75% engine load of the main engine. The main results from the reference vessel (which serve as input for the SBCC design) can be found in Table 1. The electricity demand of the CO₂

capture plant is estimated (before modelling) at 2.5% of the power generation of the vessel, and this is added to the propulsion system power demand.

Table 1, main results from the reference vessel.

Parameter	Units	Value
Propulsion power demand	kW	6900
SBCC power demand (estimation)	kW	175
Total main engine power demand	kW	7075
WHRU heat recovery	kW _{th}	3163
Cooling capacity of LNG	kW _{th}	232.1
Flue gas flow rate	kg/hr	47592
CO ₂ concentration in flue gas	Vol% (wet)	4.17

A schematic representation of the CO₂ capture and liquefaction plant can be found in Figure 3. The main restriction for the capture plant design is the maximum height of equipment on the ship, assumed to be 15 meters in this study. This leads to an maximum packing height of approximately seven meters for each column. The water wash is designed as a separate column, as opposed to being placed on top of the absorber. For the heat transfer fluid (HTF) between the flue gas and the capture plant, oil is assumed, while for the refrigerant, to transfer the heat from the CO₂ to the LNG, ammonia is assumed. The CO₂ capture plant is modelled with ProTreat, while the CO₂ liquefaction plant is modelled with Aspen.

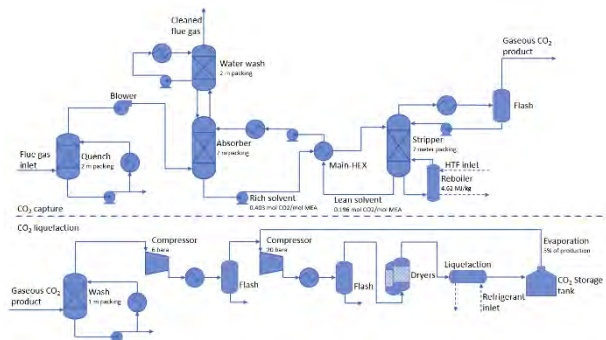


Figure 3, CO₂ capture, liquefaction and storage plant for the SBCC case study.

The main results from the capture, liquefaction and storage plant can be found in Table 2. The CO₂ capture rate can be limited either by the heat availability in the flue gas, or the cooling capacity of the LNG for the CO₂ liquefaction. In this specific case, both limitations give a similar capture rate, which is 80.2%. For simplification of the analysis in this study, it is assumed that all parameters are constant at different engine loads, and 80.2% of the CO₂ in the exhaust gas at a specific engine load can be liquefied. For engine loads higher than 75%, it is assumed that part of the exhaust gas is vented, so that no flooding occurs in the quench and absorber columns.

Table 2, main results of the CO₂ capture and liquefaction plant

Parameter	Units	75% engine load (design)
CO ₂ capture percentage	%	80.2
CO ₂ capture flow rate	kg/hr	2467
Solvent flow rate	kg/hr	55000
Hot-oil flow rate	kg/hr	230000
Ammonia flow rate	kg/hr	4000
Reboiler duty	kW _{th}	3163
Total electricity demand of plant	kWe	201.6
Total cooling duty of plant	kW _{th}	4939
CO ₂ liquefaction duty	kW _{th}	232.1

3. Techno-economic analysis

The techno-economic analysis is performed using the Aspen Capital Cost Estimator V10 (ACCE). The main assumptions for this study can be found in Table 3 and Table 4.

Table 3, main cost assumptions for the TEA. TPC = total process costs.

Parameter	Units	Value
Cost year (Europe)	-	2019
Discount factor	%	8
Depreciation of plant	Years	15
Maintenance costs	% of TPC	2.5
Operators costs	k€/year	0
Technologist costs	k€/year	100
Insurance costs	% of TPC	2
Administrative and overhead labour costs	% of O&M labour	30
LNG costs	€/ton	400
Solvent costs	€/ton	1500

Table 4, specific assumptions per case study. Case 1 is the base case; Case 2 discusses constant high engine load of the engine; Case 3 discusses standardization of the SBCC concept, and Case 4 is a combination of Case 2 and 3.

Parameter	Units	Case 1	Case 2	Case 3	Case 4
Average engine load	%	40	75	40	75
CO ₂ Capture rate	ton/yr	11675	22387	11675	22387
EPC costs	-	Aspen	Aspen	10% of Aspen	10% of Aspen
Process contingency	%	30	30	10	10
Maintenance costs	% of TPC	2.5	2.5	1	1
Installation factor	-	Aspen	Aspen	50% of material	50% of material

The main results for the base case (case 1) can be found in Figure 4. The calculated total cost of CO₂ capture is estimated at 168 €/ton CO₂ and is fully CAPEX dominated (as fixed OPEX is mostly a function of CAPEX). The CAPEX division shows that the capture

plant accounts for 40%, the liquefaction plant for 20%, the storage tanks for 10% and the engineering, procurement and construction (EPC) for 30% of the total capture costs. Note that in this study, for the EPC costs, the results from the ACCE software are used, which will not take all relevant costs associated to ship based installation into account (e.g. costs associated to docking and downtime of ship).

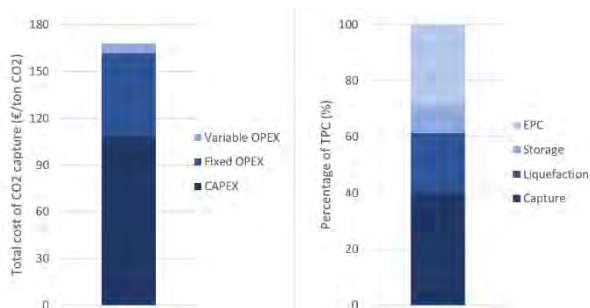


Figure 4, (left) division of CAPEX into capture, liquefaction, storage and EPC costs, (right) division of CAPEX, fixed OPEX and variable OPEX of the total CO₂ capture costs.

Lowering the specific CAPEX (€/ton CO₂) of the SBCC technology could lead to drastic reduction of the total CO₂ capture costs. This can be achieved by increasing the CO₂ capture flowrate for a given plant size and/or lowering the plant costs. Increasing the total CO₂ capture flowrate without changing the equipment design can be achieved by avoiding to run the engine at low engine loads (see Table 2). To illustrate this, case 2 is defined in which the engine operates constantly at 75% engine load, opposed to the average engine load based on the sailing profile shown in Figure 1, which approximately doubles the CO₂ capture rate with the same installation. Standardization of CO₂ capture plants for SBCC is proposed as a strategy to lower the plant costs, assuming a drastic reduction of equipment and EPC costs (case 3). Case 4 is the combination of both strategies: running the engine at high engine loads and standardizing the CO₂ capture plant. The assumptions per case are given in Table 4, and the resulting CO₂ capture costs are found in Figure 5.

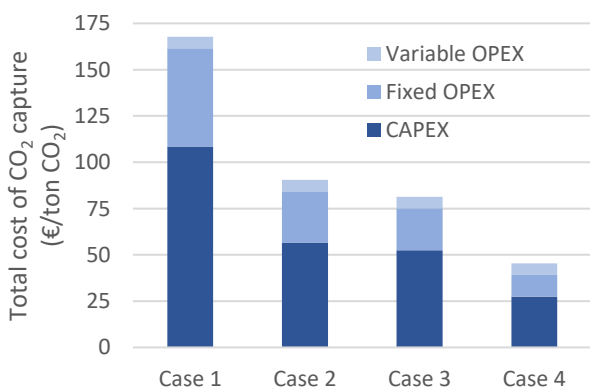


Figure 5, results of the four case studies considered in this study.

Figure 5 suggests that the total capture costs of SBCC can be drastically reduced, with the strategies for lowering the specific CAPEX. The total capture costs could drop anywhere between the 45 and 80 €/ton CO₂. Moreover, sailing more often at higher engine loads will have

additional economic and environmental benefits (e.g. competitive advantage; lowering CH₄ slip).

4. Conclusions

In this study, the SBCC technology on LNG fuelled vessels is evaluated. Because of the high synergy between the LNG fuelled vessel and the CO₂ capture plant, variable OPEX is reduced drastically as compared to CO₂ capture in power and industry. This means that for SBCC on LNG fuelled vessels, the CO₂ capture costs are dominated by the CAPEX. In the design proposed in the current study, a height restriction was imposed to the capture equipment, leading to a specific reboiler duty (SDR) of 4.62 MJ/kgCO₂, which is considerably above the optimal range obtained using 30wt% MEA in gas-fired power plants, with similar CO₂ content in the flue gas. This illustrates clearly that the optimization for the SBCC technology should not be centred on the SRD, and attention should be given to mass transfer rates.

For the base SBCC case investigated in this study, the capture costs are estimated at 168 €/ton CO₂. To lower these costs, sailing at more constant high engine loads, and standardization of the capture equipment should be considered, which could drop the total cost of CO₂ capture anywhere between 45 and 80 €/ton CO₂.

References

- [1] IMO, "Adoption of the Initial Imo Strategy on Reduction of Ghg Emissions From Ships and Existing Imo Activity Related To Reducing Ghg Emissions in the Shipping Sector," p. 27, 2018.
- [2] IMO, "Fourth IMO GHG Study 2020," *Int. Marit. Organ.*, vol. 53, no. 9, pp. 1689–1699, 2020.
- [3] M. Feenstra, J. Monteiro, J. T. van den Akker, M. R. M. Abu-Zahra, E. Gilling, and E. Goetheer, "Ship-based carbon capture onboard of diesel or LNG-fuelled ships," *Int. J. Greenh. Gas Control*, vol. 85, pp. 1–10, 2019.
- [4] J. Monteiro, "CO₂ASTS – carbon capture, storage and transfer in shipping, a technical and economic feasibility study: Public Concise Report," 2020.
- [5] X. Luo and M. Wang, "Study of solvent-based carbon capture for cargo ships through process modelling and simulation," *Appl. Energy*, vol. 195, pp. 402–413, 2017.
- [6] J. A. Ros *et al.*, "Post-combustion Carbon Capture and Storage on LNG Fuelled Ships," *Int. Nav. Eng. Conf. Exhib.*, 2020.
- [7] MAN, *Project Guide – Marine Four-stroke dual fuel engine compliant with IMO Tier III (MAN 51/60DF)*. 2018.

CO₂ CAPTURE FROM LIME AND CEMENT PLANTS USING AN INDIRECTLY HEATED CARBONATE LOOPING PROCESS – THE ANICA PROJECT

Jochen Ströhle^{1*}, Carina Hofmann¹, Martin Greco-Coppi¹, Bernd Epple¹

¹ Technical University of Darmstadt, Energy Systems and Technology, Darmstadt, Germany

* Corresponding author e-mail: jochen.stroehle@est.tu-darmstadt.de

Abstract

The overall aim of the ANICA project is to develop concepts of the indirectly heated carbonate looping (IHCaL) process for CO₂ capture from lime and cement plants. CO₂ avoidance costs of the IHCaL process for lime and cement production plants are expected to be in a well below 25 €/t, which is close to current CO₂ prices and significantly lower than competing CO₂ capture solutions for lime/cement plants. The novel process concepts are developed with the aid of advanced process simulations. The technology is demonstrated in a 300 kW_{th} pilot plant at industrially relevant conditions using the same fuels, sorbents, and operating conditions as can be expected in large-scale commercial IHCaL plants for lime and cement applications. A detailed techno-economic assessment and a life-cycle-analysis is performed for both lime and cement applications. The basic design of a 20 MW_{th} IHCaL demonstration plant is developed using two different technologies, i.e. fluidized bed reactors and Direct Separation technology, and costs of these plants are estimated. The paper presents an overview of the project as well as first results related to process simulations and design of the pilot plant.

Keywords: CO₂ capture; Lime plant; Cement plant; Calcium looping; Pilot plant

1. Introduction

Several different CO₂ capture processes are currently being developed, but most of them have the consequence of high energy consumption leading to lower plant efficiencies and increased costs [1]. Pre-combustion capture is not suitable for lime and cement processes since it is not possible to capture CO₂ that is released by calcination of raw material within the industrial process. These so-called process emissions amount to around 65 % of total CO₂ emissions of a cement plant. Oxyfuel combustion has the potential to capture the CO₂ from both the process emissions and the combustion emissions. In that case, a complete redesign of the cement production process is required, as well as the need for oxygen production. In order to avoid oxygen production, the process CO₂ can be captured using indirect heating of the cement calciner in a process called Direct Separation. However, the CO₂ from combustion of fuels is not captured, so that this process is limited to about 65% capture. Post-combustion capture using amine based solvents is a rather mature technology that can be used to retrofit lime and cement plant, but is associated with rather high energy requirements for regeneration of the solvent leading to high CO₂ avoidance costs [2]. The carbonate looping process (also named calcium looping) is another post-combustion capture technology using lime-based materials such as natural limestone as a solid sorbent. It offers synergies with the lime and cement industry through the possibility to use purged CaO for lime or cement production. Based on techno-economic assessment, CO₂ avoidance costs were determined for MEA absorption (80 €/tCO₂), oxyfuel process (44 €/tCO₂), chilled-ammonia process (66 €/tCO₂), membrane-assisted

CO₂ liquefaction (84 €/tCO₂), and calcium looping (52-55 €/tCO₂) [2]. Although CO₂ avoidance costs are lowest for oxyfuel technology, the calcium looping process can more easily be retrofitted to existing cement plants, since it has a lower impact on the cement production process.

The carbonate looping (CaL) process has the potential to significantly reduce the efficiency penalty compared to solvent-based technologies, since the process operates at high temperatures, which allows the utilization of heat for power production in a highly efficient steam cycle [3-5]. The CO₂ contained in the flue gas of an industrial plant is absorbed by CaO in the carbonator at around 650 °C [3, 6]. The CaCO₃ formed hereby is transferred to the calciner, where the CO₂ is released by an increase of temperature to around 900 °C. The stream of highly concentrated CO₂ is ready for further processing and storage/usage, and the regenerated CaO is transferred back to the calciner closing the solid loop. As the calcination reaction is endothermic, the calciner needs to be supplied with heat. The most straightforward heat supply is the direct combustion of fuel with oxygen in the calciner. For power applications, the efficiency penalty related to the oxygen demand of the directly fired calciner is around 3 %-points [3].

The efficiency penalty of the process can be further decreased when the need for technical oxygen in the plant can be avoided. This can be achieved by indirect heating of the calciner, e.g. through metallic walls, by solids circulation [3], or via heat pipes [7, 8]. Heat pipes offer an excellent heat transfer performance based on evaporation and condensation of a liquid (i.e. sodium for temperatures >800 °C) inside a closed pipe and have been successfully applied to an indirectly heated

gasification process. For CO₂ capture from coal-fired power plants, the net efficiency of the IHCaL process is around 1.5 % points higher than that of the standard CaL, [7, 9]. The CO₂ avoidance costs have been calculated to 22.6 €/t_{CO2} excluding CO₂ storage [9].

The feasibility of the IHCaL process using heat pipes was demonstrated in a 300 kW_{th} pilot plant during more than 300 hours of stable CO₂ capture at various operating points [10, 11]. Furthermore, a large-scale heat pipe with a length of 6 m and an outer diameter of 48.3 mm demonstrated the possibility of an up-scale during long-term performance tests for a total run-time of more than 1500 hours at University of Erlangen-Nürnberg.

Concepts of the IHCaL process for CO₂ capture from lime and cement plants are currently being investigated in the ACT project ANICA (Advanced Indirectly Heated Carbonate Looping Process). This paper will present the process concept, an overview of the ANICA project as well as first results related to process simulations and design of the pilot plant.

2. Process Concept

The main innovation of the IHCaL process is the use of an indirectly heated calciner for regeneration of the CaL sorbent. The heat for the calcination is produced by the combustion of fuel with air in an additional external combustion chamber and transferred to the calciner by means of heat pipes. The flue gas of the external combustion chamber is directed to the carbonator, where most of the CO₂ contained in this flue gas is absorbed by CaO. The main advantages of the IHCaL process compared to the standard CaL process are summarized as follows:

- No air separation unit is needed to produce technical pure oxygen, which leads to lower investment costs and to a lower energy consumption.
- Fewer impurities (sulphur, ash) from a supplementary firing are brought into the Ca-loop, so that spent sorbent will be of higher purity and therefore be better suited for further utilization.
- Lower CaO deactivation rates are expected due to “mild” calcination around the heat pipe surfaces compared to rather harsh conditions in an oxy-fired calciner, so that sorbent remains more reactive.
- Lower attrition rates are expected due to a low fluidization velocity in the calciner, which improves the operability of the fluidized bed system.
- An almost pure CO₂ stream leaves the calciner, which allows for technically easy and cost-effective CO₂ purification process for compression and storage/utilization of CO₂.

So far, the IHCaL process has solely been evaluated with respect to CO₂ capture from power plants. This section discusses novel technical concepts for integrating the IHCaL process into lime and cement production plants.

2.1 Integration of IHCaL into a lime plant

The integration of the IHCaL concept into the lime production process can be realized either as a tail-end solution in an existing lime plant (placed after the kiln and capturing the CO₂ of the flue gas) or as an integrated solution, as illustrated in Figure 1.

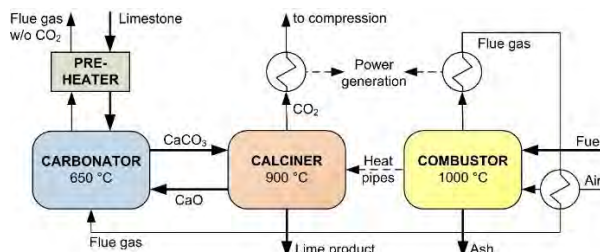


Figure 1: Concept of an IHCaL process integrated into a lime plant

Raw material (limestone) is used as sorbent for the IHCaL process, and the purge from the IHCaL process consists of CaO, which is the main product. The heat of the flue gas leaving the carbonator or calciner could be used to pre-heat the raw material. The heat of the remaining flue gases can be extracted in heat recovery steam generators for power generation using a highly efficient steam cycle as well as for pre-heating the combustion air. The produced electricity can be partially used on site for various consumers (such as fans, pumps, mills, electrolysis for CO₂ utilization) and partially sent to the grid, generating additional value/income for the plant operator. This concept results in a completely new lime production process that has various advantages compared to conventional lime kilns (such as shaft furnaces or rotary kilns):

- The fuel is no longer in direct contact with the lime, which improves the purity of the lime and allows the utilization of “dirty” but cheap fuels, such as waste-derived fuels.
- The temperature in the calciner is uniform and well-controlled, which enables to meet precise product specifications.
- A smaller particle size is used (0.1 – 0.5 mm) compared to shaft furnaces, which reduces the calcination time, intensifying production and minimizing inhomogeneities within the particle mixture.

2.2 Integration of IHCaL into a cement plant

The integration of IHCaL into the cement process can be realized either as a tail-end solution or as an integrated solution using the raw meal as sorbent. A tail-end solution is placed at the back-end of the cement plant capturing CO₂ from the fuel gas before sending it to the stack. This option could easily be retrofitted to existing cement plants. However, a drawback of the tail-end solution is that the process CO₂ is released twice, and the solids mass flows in the IHCaL reactor exceed that of the cement plant, leading to rather huge plant sizes. Although the energy penalty is low since the additional fuel introduced into the combustor is efficiently converted to power, the economical performance is questionable due

to the rather high investment and high additional fuel consumption considering the strongly varying revenues of the electricity market.

The integrated solution could offer significant benefits compared to the tail-end variant, as calcium carbonate is a main constituent of cement clinker raw materials, and the kiln system already includes a calciner. One possibility for such an integrated solution is illustrated in Figure 2. Raw materials for clinker production (mainly limestone) are used as sorbent for the IHCaL process, and the purge from the IHCaL process (mainly CaO and other oxides from silica, alumina, and iron) is fed to the cement kiln. Hence, the calciner of the IHCaL unit replaces the pre-calciner of a conventional cement plant. The flue gas leaving the carbonator (and/or calciner) is used to pre-heat the raw materials, potentially using existing cyclone arrangement of the cement plant. Excess heat of the calciner/combustor is extracted in heat recovery steam generators for power generation in a highly efficient steam cycle (potentially utilizing parts of an already existing power plant on the cement production site) and for pre-heating the combustion air. The produced electricity can be partially used on site for various consumers (such as fans, pumps, mills, electrolysis for CO₂ utilization) and partially sent to the grid, generating additional value/income for the plant operator.

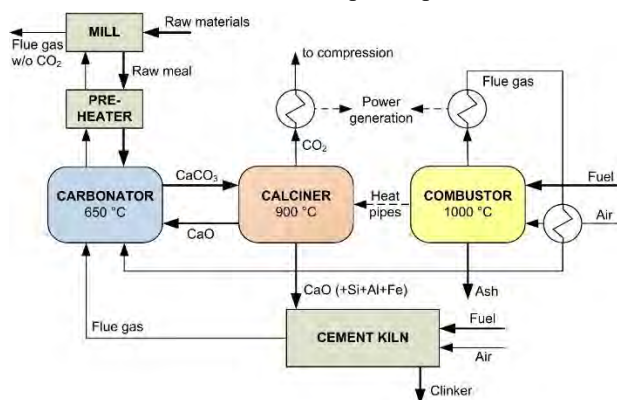


Figure 2: Concept of an IHCaL process integrated into a cement plant

However, there are some technical challenges related to the integrated solution. The use of cement raw meal instead of limestone as sorbent may cause difficulties, as these contain other components like silica, alumina and iron to form the mineral clinker phases, which may have a negative impact on the activity of the sorbent for CO₂ absorption. Furthermore, the rather small particle size and stickiness of the raw meal may impose challenges regarding fluidization characteristics (Geldart A/C particles) and fouling of heat pipes in a bubbling fluidized bed. The risks related to fluidization and fouling could be reduced by various means. One option is to replace the bubbling bed calciner by an entrained flow calciner. However, an entrained flow reactor is much larger than a fluidized bed, and heat transfer rates to heat pipes are much lower due to the low solids loading.

Fluidized beds are generally well suited for conversion of fuels that are difficult to exploit as an energy source and complicated in terms of handling and logistics, such as

solid waste. Although fluidized beds are used in IHCaL technology, using such fuels has never been tested with immersed heat pipes. The ANICA project will address this issue by pilot tests using waste derived fuels to provide proof of concept prior to commercial application.

2.3 Novel concepts of the IHCaL reactor system

One major challenge of the IHCaL process is the high heat duty of the calciner since the flue gases from the external air-fired combustor are additionally fed to the carbonator. Furthermore, the large number of required heat pipes may lead to a rather large size of the calciner. The following options are investigated in the ANICA project to counterbalance these effects in terms of CAPEX and OPEX:

- An improved heat pipe performance reducing the number and/or size of the heat pipes
- A solid/solid heat exchanger transferring heat from the “hot” solids leaving the calciner to the “cold” solids coming from the carbonator, so that less heat is required in the calciner to heat up the incoming solids to 900 °C
- A two-stage calciner that lowers the temperature of the solids exiting the calciner by a dilution with steam in the 2nd stage, aiming at reduced heat demand of the calciner.

3. The ANICA project

The ANICA (Advanced Indirectly Heated Carbonate Looping Process) project is a collaboration between various academic and industrial partners from Germany, the United Kingdom, and Greece, funded by national authorities within the funding program ACT (Accelerating CCS Technologies). It started in October 2019 and lasts for three years. This section gives a brief overview of the objectives and the work program of the ANICA project.

3.1 Objectives

The overall aim of the project is to develop a novel technology with very low energy penalty and costs using lime-based sorbents – namely the indirectly heated carbonate looping (IHCaL) process – for CO₂ capture from lime and cement plants. The specific objectives of the project are:

- 1) To decrease the costs for CO₂ capture from lime and cement plants below 25 €/t_{CO2} by developing novel IHCaL process concepts with > 90 % CO₂ capture efficiency, > 95 % CO₂ purity, and > 45 % net electrical efficiency for heat utilization.
- 2) To aim at net negative CO₂ emissions by utilizing waste derived fuels with a high biogenic fraction.
- 3) To achieve more than 90 % utilization of sorbent as raw material for lime and cement production employing a high level of integration of heat and material streams.

- 4) To reduce energy requirements and equipment costs by 30 % compared with current design through development of new reactor concepts.
- 5) To demonstrate IHCaL technology in relevant environment (i.e. TRL 6) by long-term pilot tests at 300 kW_{th} scale under realistic conditions (i.e. fuels, sorbents, and operating conditions) for lime and cement applications, thereby proving the long-term performance/stability of sorbent and heat pipes.
- 6) To enable fast and reliable scale-up of the technology by developing accurate 1D and 3D models of the dual fluidized bed reactor system with an uncertainty of less than 10 %.
- 7) To provide a basis for comparing the IHCaL process with competitive CO₂ capture solutions (amine wash, oxyfuel combustion) for lime and cement plants by evaluating risks, economic performance, and environmental impact of the full-scale IHCaL process.
- 8) To accelerate the deployment of IHCaL technology by providing the basic design, plant layout and a cost estimation of a semi-industrial IHCaL demonstration plant at 20 MW_{th} scale on a cement production site, which could bring the technology to the next level of maturity (i.e. TRL 7) in a follow-up project.

3.2 Work program

This section briefly summarizes the work program of the ANICA project. Concepts for integrating IHCaL into lime and cement plants (see Sections 2.1 and 2.2) are developed in two steps. In a 1st step, these process concepts are based on existing knowledge/models and are used to define the operating conditions for pilot tests. The experimental data of these pilot tests are used for validation of 1D and 3D models for the IHCaL reactors. The validated models and novel concepts for optimising the IHCaL reactor systems (see Section 2.3) are used to further update the process concepts for integrating IHCaL in a 2nd step. The updated heat & mass balances are used for the assessment of these process concepts with respect to risks, techno-economics, environmental impact, and societal readiness. The process and reactor concepts are further used for the design of a 20 MW_{th} demonstration plant using two different technologies, i.e. fluidized bed technology and Direct Separation Technology.

4. Results and Discussion

Around one year after the start of the ANICA project, most of the tasks are still on-going or have not started yet. This section presents selected preliminary results related to simulations of integrating the IHCaL process into lime plants and preparations for pilot testing.

4.1 Process simulations

Two concepts for integrating the IHCaL process into an existing lime plant in Germany, which uses a preheated rotary kiln (PRK) to burn limestone, have been

investigated by means of process simulations. With the PRK, more than 600 tons of lime are produced per day in normal operating conditions. One concept is a tail-end solution in an existing lime plant placed after the kiln and capturing the CO₂ of the flue gas. The other is an integrated solution in which the lime production and the carbon capture are realized within the IHCaL facility.

A steady state model in ASPEN PLUS™ has been developed for the process simulations. The rotary kiln is modelled using three reactor blocks. To model coal combustion, the fuel is first inserted into a yield reactor that decomposes it into the elementary molecules and heat. Afterwards, the resulting stream is burned with the combustion air in a Gibbs reactor, which minimizes the Gibbs' free energy in order to calculate the heat production and the yield of products. For all combustion processes, an air-fuel equivalence ratio (λ) of 1.2 is considered according to the reference plant. The temperature of the IHCaL combustor is set to 1000 °C to allow for 100 K temperature difference to the calciner. The calcination and carbonation reactions in the IHCaL reactors are modelled with conversion reactor blocks, where the reactions take place at specified conversion rates according to previous models of the research group. The solid-gas separation in the cyclones is considered ideal. The fuel and raw material composition is defined according to the reference plant. The same lignite (LHV=21,500 kJ/kg) used to fire the PRK is implemented as fuel for the combustor in the IHCaL. Similarly, the limestone's composition from the reference plant (98.3 wt% CaCO₃) is used for all the limestone inputs in the model.

In order to evaluate the solutions proposed, the following key performance indicators are considered. The CO₂ capture efficiency, defined as the ratio of the captured CO₂ to the generated CO₂, is kept constant at 90 %. The product ratio, *PR*, considers the production of the entire process including the IHCaL unit in relation to the production in the reference plant. The heat ratio, *HR*, is used as the indicator of the heat requirement for CO₂ capture and lime production. It is calculated considering the lime produced, the heat requirement in the original process as well as in the entire process including CO₂ capture. For the power generation from the high temperature heat of the IHCaL, a heat-to-power efficiency of 45 % is assumed in this work, according to values of thermal power plants. For the CO₂ balance, the direct CO₂ emissions are calculated by the amount of CO₂ directly emitted into the atmosphere from the complete process per unit of lime produced.

With respect to the boundary conditions, the operating temperature of the calciner is set at 900 °C to enable a full calcination at nearly pure CO₂ atmosphere. The operation temperature of the carbonator is set to 650°C in order to achieve a maximum capture efficiency of around 90 %. The make-up flow, which is needed to avoid the build-up of inert species and to maintain the proper activity of the sorbent, is characterized with the make-up ratio, *A*, i.e. the ratio of the molar flow rate of make-up calcium species to the total molar flow rate of CO₂. For the tail-end concept, the make-up ratio was set to 0.2. For

the fully integrated solution, the make-up flow is determined by the raw material input that is considered the same as for the reference plant to have the same production. The specific sorbent circulation rate considering the molar flow rate of calcium species that are transferred from the calciner to the carbonator was set

the integrated concept is very similar to the reference plant because the raw material input is the same for both.

The direct fuel consumption of the reference PRK is 5090 MJ/t_{CaO}. The tail-end solution leads to a 154 % increase of the direct fuel consumption and a 70.5 % reduction of the direct CO₂ emissions with respect to the

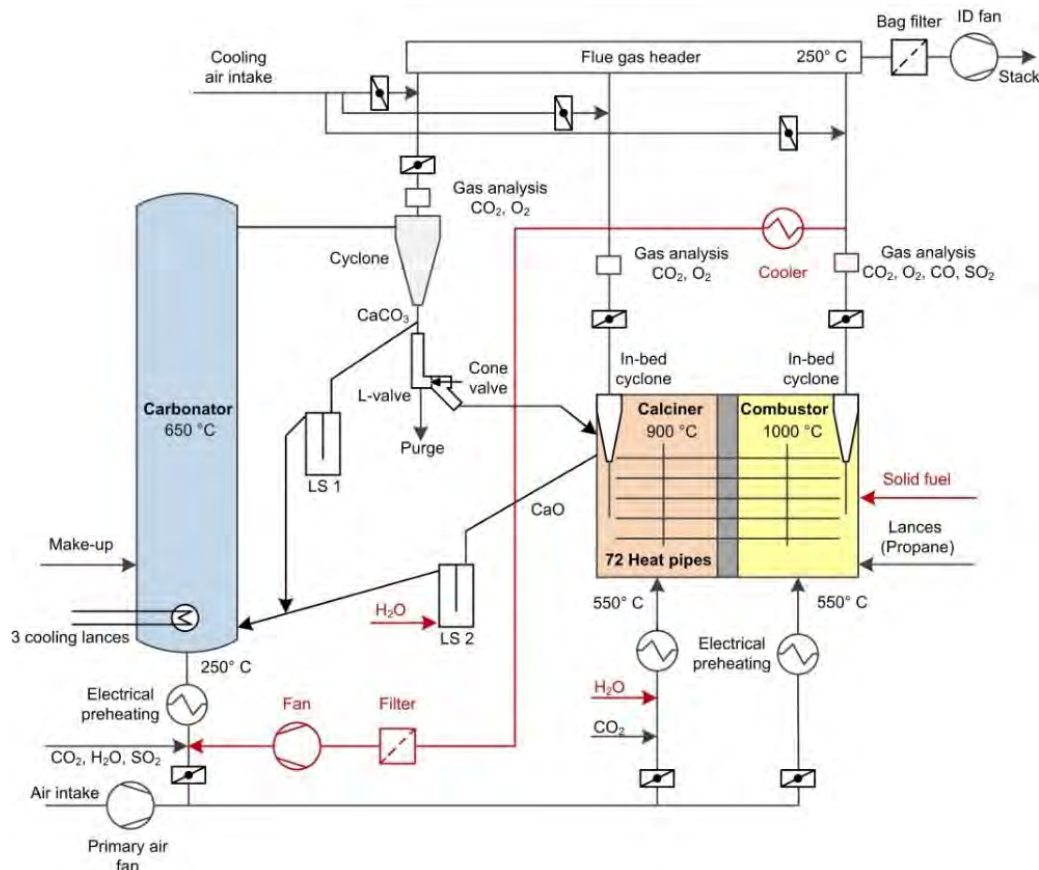


Figure 3: Process scheme of the 300 kW_{th} pilot plant with adaptions marked in red color.

to 6.

The main results of the base case process simulations are summarized in Table 1. The specific make-up ratio controls the production from the IHCaL facility in the case of the tail-end solution. While it may be more reasonable to keep this production low, it is necessary to maintain a certain make-up. Due to the high value of A for the integration solution, a highly reactive solid inventory can be expected, which could allow for a reduction of the solid circulation rate and/or solid inventory in the carbonator.

Table 1: Results of base case simulations

	Tail-end concept	Integrated concept
Specific make-up ratio (A)	0.20	0.47
Product ratio (PR)	2.26	1.01
Heat ratio (HR)	2.54	1.63

The product ratio is as high as 2.26 in the tail-end concept, which means that more lime is being produced in the IHCaL facility than in the PRK. The production of

reference plant. For the fully-integrated case, the increase in fuel consumption is only 63 %, and the reduction in direct CO₂ emissions is 87.4 %. For this case, the electricity generated through heat recovery amounts to 29.6 % of the total thermal energy input. This implies a further reduction in the net CO₂ emissions, considering the avoidance of the CO₂ from the grid's power generation. Furthermore, the combustor can be adapted to burn waste-derived fuels with a high biogenic content, which would allow for negative CO₂ emissions.

A more detailed assessment of the results and a sensitivity study is included in a publication of Greco-Coppi et al. [12].

4.2 Pilot plant design

One aim of the ANICA project is the demonstration of the IHCaL process for integration into lime and cement plants by pilot tests in a 300 kW_{th} pilot plant under real conditions, with the same fuels, sorbents, and operating conditions as specified in the process concepts for these plants. Coal and solid recovered fuel (SRF) are used as fuels, while limestone and cement raw meal are used as sorbents. This section describes the existing pilot plant and the adaptions that are currently being installed.

The design and experimental results of the existing 300 kW_{th} pilot plant (see Figure 3) were published by Reitz et al. [11]. The plant consists of the heat-pipe heat exchanger connecting the calciner and the combustor, a carbonator with a cyclone separator, loop seals, and a combination of a L-valve and a cone-valve for the coupling of the carbonator with the calciner. The pilot plant contains 72 heat pipes with an outer diameter of 33.7 mm and a length of 2.18 m. The carbonator operates as a circulating-fluidized bed (CFB) reactor. The combustor and calciner are bubbling fluidized bed (BFB) reactors. The dimensions of the three reactors are listed in Table 2.

Table 2: Dimensions of the pilot plant

	Unit	Height	Length x Depth
Carbonator (CFB)	m	8	0.25 (diameter)
Calciner (BFB)	m	2.3	1.05 x 0.3
Combustor (BFB)	m	2.3	1.05 x 0.3

The plant has previously been operated using an artificial flue gas (i.e. air mixed with CO₂, water seam, SO₂) entering the carbonator and propane as fuel in the combustor. Hence, the existing pilot plant has to be upgraded to enable realistic conditions for lime and cement applications. This includes the design and installation of a solid fuel feeding system for the combustor as well as a flue gas path (ducts, heat exchanger, filter, fan, and flow control) from combustor to carbonator. A flow sheet of the process is shown in the Figure 3, with the main upgrades depicted in red.

In order to feed the combustor with solid fuel such as SRF or coal, the pilot plant is expanded by a complete solid feeding and dosing system. The solid fuel is filled into a receiver tank. A gas-sealed flap ensures that no hot gases are leaving the system. Another container is connected to a loss-in-weight feeder to control the mass flow. A rotary valve has the function of a pressure seal. The solids are fed into the dense bed of the combustor by a screw feeder. For ash discharge, a discontinuous sluice system at the bottom of the combustor will be installed.

The flue gas from the combustor needs to be cooled and dedusted before entering the carbonator. After leaving the cyclone of the combustor, the flue gas passes an existing control valve, aiming to control the pressure in the combustor. The gas passes a sensor that analyses the gas composition in terms of CO, O₂, CO₂, SO₂, H₂O, and HCl. Afterwards, the flue gas is divided into a portion leaving the reactor system via the air quench through the chimney and a portion transferred to the carbonator. This flow is controlled by an additional control valve. Then, the flue gas is cooled down in the flue gas heat exchanger to around 200 °C, located vertically in the flue gas path behind the combustor. After the cooler, a bag filter is installed in order to separate the fine dust particles from the flue gas flow and protect the downstream equipment. Finally, a fan is required to compensate the pressure difference between combustor outlet and carbonator inlet as well as the pressure losses in the flue gas path.

Besides the above-mentioned major upgrades, some minor modifications are integrated in order to improve

the operability of the test rig. The existing make-up dosing is modified in order to feed a higher amount of solid material into the carbonator. A solid sampling system consisting of a conveyor is installed in the loop seal between carbonator and calciner in order to deliver enough solid samples for the investigation related to usage in cement or lime plants. All adaptations of the pilot plant are expected to be finalized in summer 2021, so that the pilot tests can be performed in the same year.

The pilot tests will be used to evaluate various key performance indicators of the IHCaL process. The CO₂ capture efficiency will be determined by measurements of the CO₂ concentrations and volume flows leaving the reactor system. The CO₂ product quality will be assessed by measuring the gas composition of the gas leaving the calciner. Furthermore, the purged sorbent will be analysed to evaluate the quality of the solid with respect to its usage in the clinker burning process for cement production or as lime product. Process models will be validated by the pilot data and then scaled to industrial size in order to calculate the key performance indicators of a real industrial process.

5. Conclusions

In the ANICA project, novel concepts for integrating the IHCaL process into lime and cement plants for CO₂ capture are being developed. These concepts have a high potential for reducing the energy penalty and costs compared to competing CO₂ capture technologies. Preliminary results of process simulations show that a highly integrated IHCaL process for lime production has significantly less heat requirements compared to a tail-end solution. The feasibility of the IHCaL process for lime and cement applications will be tested in a 300 kW_{th} pilot plant that has been redesigned to enable realistic conditions close to commercial applications. The experimental results of these pilot tests will be used to validate models that will then be applied to design demonstration and industrial plants. Based on the heat and mass balances of the industrial plants, a techno-economic evaluation will be performed to determine the lime/cement production and CO₂ avoidance costs of this technology. Assuming that the construction of a demonstrator will start after this project in 2023, the first commercial plant could go into operation around the year 2028.

Acknowledgements

The work leading to these results has received funding through the ACT program (Accelerating CCS Technologies, Horizon 2020 Project N° 294766) within the ANICA project. Financial contributions were made from the German Federal Ministry of Economic Affairs and Energy, the Department for Business, Energy and Industrial Strategy of the United Kingdom, and the Greek General Secretariat for Research and Technology.

References

- [1] IEAGHG. CO₂ Capture at Coal Based Power and Hydrogen Plants. 2014/3. 2014.
- [2] Voldsund M, Gardarsdottir SO, Roussanaly S, Anantharaman R, Fu C, Berstad D, et al. CEMCAP techno-economic and retrofitability analysis. *ECRA/CEMCAP/CLEANER Workshop*. 2018.
- [3] Abanades JC, Anthony EJ, Wang J, Oakey JE. Fluidized bed combustion systems integrating CO₂ capture with CaO. *Environm Sci Technol* 2005;39(8):2861-6.
- [4] Ströhle J, Galloy A, Epple B. Feasibility study on the carbonate looping process for post-combustion CO₂ capture from coal-fired power plants. *Energy Procedia* 2009;1(1):1313-20.
- [5] Shimizu T, Hiramata T, Hosoda H, Kitano K, Inagaki M, Tejima K. A twin fluid-bed reactor for removal of CO₂ from combustion processes. *Chemical Engineering Research Design* 1999;77(1):62-8.
- [6] Bhatia SK, Perlmutter DD. Effect of the product layer on the kinetics of the CO₂-lime reaction. *AIChE Journal* 1983;29(1):79-86.
- [7] Junk M, Reitz M, Ströhle J, Epple B. Thermodynamic evaluation and cold flow model testing of an indirectly heated carbonate looping process. *Chem Eng Technol* 2013;36:in press.
- [8] Hoeffberger D, Karl J. The indirectly heated carbonate looping process for CO₂ capture - A concept with heat pipe heat exchanger. *Journal of Energy Resources Technology* 2016;138(4):042211-.
- [9] Junk M, Reitz M, Ströhle J, Epple B. Technical and economical assessment of the indirectly heated carbonate looping process. *Journal of Energy Resources Technology* 2016;138(4):042210-.
- [10] Reitz M, Junk M, Ströhle J, Epple B. Design and Erection of a 300 kW_{th} Indirectly Heated Carbonate Looping Test Facility. *Energy Procedia* 2014;63:2170-7.
- [11] Reitz M, Junk M, Ströhle J, Epple B. Design and operation of a 300 kW_{th} indirectly heated carbonate looping pilot plant. *Int J Greenhouse Gas Control* 2016;54(1):272-81.
- [12] Greco-Coppi M, Hofmann C, Ströhle J, Walter D, Epple B. Efficient CO₂ capture from lime production by an indirectly heated carbonate looping process. *15th International Conference on Greenhouse Gas Control Technologies*. Abu Dhabi, UAE; 2021.

HEURISTIC METHODS FOR PIPELINE NETWORK DESIGN

Christopher Yeates^{1*}, Cornelia Schmidt-Hattenberger¹, David Bruhn^{1,2}

¹Geoenergy Department, Geoforschungszentrum (GFZ), Potsdam, Germany

² Faculty of Civil Engineering and Geosciences, Delft University of Technology, Netherlands

*cyeates91@gmail.com

Abstract

We showcase geospatial heuristic methods for network design and optimization. We propose and adapt graph algorithms to achieve optimal (or close to optimal) fluid transportation networks meeting quantifiable criteria (such as minimizing cost for example). Typically, these are used on pipeline infrastructure design, for CO₂ collection or H₂ distribution for example. The pipeline cost functions involved in the optimization depend on both pipeline length and a concave function of pipeline capacity. As such, discrete optimization methods are required. We have extended the tool to integrate other known aspects of network design. A sink placement algorithm can identify the minimum-cost storage location (and in parallel construct the rest of the a priori unknown network structure). The tools have finally been adapted to allow the inclusion of pre-existing pipeline infrastructure at a lower cost. They can then propose networks that prioritize planning along pre-existing pipeline routes.

Keywords: Pipelines, transportation, optimization, graphs

1. Introduction

German net-zero carbon emission targets of 2050 still require a variety of new technologies as many key sectors of industry currently don't have decarbonization pathways. To meet this challenge, carbon capture and storage of CO₂ originating from industrial sources represents a technologically mature and achievable solution and its potential warrants a reevaluation in the wider German climate discussion [1]. The German case for Underground Carbon Storage is not only assisted by the large potential storage capacity identified on- and off-shore [2,3].

While finding a capable, safe and acceptable storage sites is often the foremost subject of investigation in planning a large-scale storage operation, a key aspect of its success involves the judicious clustering of sources and transportation network design in a way that meets all the constraints (geological, social, technical) but also does so with the lowest cost possible.

For large, long-term CO₂ sources, pipeline transport is understood to be both safest and most economical method [4].

Due to specific technical pipeline requirements for CO₂ transport, the case for "from scratch" (i.e. new pipelines) networks is reasonable. This further opens the possibilities of network designs available.

To find minimum-cost networks with a broad range of system constraints, heuristic graph methods can be considered due to their intuitiveness, transparency, and adjustability. Heuristic methods try to make improvements by applying calculated small changes to the current best solution. They do not always result in optimal solutions but usually perform well and within reasonable time. Furthermore, exact methods (such as

Branch & Bound [5]) often rely on having the best possible starter solution, usually obtained from a heuristic method.

We provide an overview of our contributions to the topic, through descriptions and rudimentary pseudo-code where possible. These include a new network topology (i.e., structure) optimization algorithm based on transferring edges of high valency nodes, that achieves (as far as we know) above state-of-the-art performance for finding minimum-cost pipeline networks. In particular for larger networks, it overcomes local minima and achieves optimal solutions in a significant number of cases within reasonable time.

In addition, we provide an optimal storage location algorithm, which attempts to identify the minimum-cost location to place a sink in a series of sources with an undefined network structure. While we use the example of a storage node, in a distribution network, this may take the role of a supply node. In a multi-level network, the algorithm could equivalently place an intermediate relay node optimally.

Finally, we provide adapted versions of our methods that integrate prior pipeline infrastructure or planning routes. In this way, priority is given to pipelines built on pre-existing pipeline routes, as a means of acknowledging the legal or social complexities of planning new pipeline routes.

Some overall examples are provided of real-world potential CO₂ collection networks. The point source emission volumes were established from taking the average of large emitters from the European Carbon Trading scheme registry for 2015-2018 [6]. Industrial CO₂ sources shown in Figure 1 are clustered in an infrastructure-aware way (detailed further down), and

minimum-cost networks are calculated that place sink nodes optimally.

2. Technical contributions

2.1 A new topology optimization heuristic

Local network design heuristics make small modifications to initial solutions in order to find lower-cost configurations. Such methods are required as exhaustive solutions rapidly become impractical for large graphs. Indeed, Calvey's formula states that there exists n^{n-2} distinct spanning trees for n nodes. These heuristic methods often (but not exclusively) involve creating a cycle within the network and breaking the cycle in a different location. This simple transformation is named a local transformation. Heuristics then repeat such a procedure as soon as a better overall solution is found (for the case of first-descent heuristics). Sometimes, local network design heuristics get stuck in local minima. In this way, step-by-step local modifications of the network structure, in which one pipeline is replaced by another, do not lead to lower-cost solutions. Instead, multiple successive higher-cost jumps are required to find a lower-cost solution. These jumps are usually not permitted by local heuristics and require either random [7] or calculated moves [7] to other solutions. We describe a new metaheuristic, the High Valency Shuffle Metaheuristic, to guide local heuristics out of local minima by placing the edges of high valency nodes on their immediate neighbors and attempting a local heuristic on this tentative solution. Pseudocode is provided in Table 1:

Table 1: High Valency Shuffle Metaheuristic algorithm

Step 0:	Start from an initial local minimum
Step 1:	Initiate empty solution list
Step 2:	Identify all the nodes n_{HV} with high valency (3 and above edges)
Step 3a:	For each node n_{HVi} of these n_{HV} : - Identify closest nodes n_C
Step 3b:	For each node n_{Ci} of these n_C : - Transfer edges from n_{HVi} to n_{Ci} - Connect n_{HVi} to n_{Ci} if not already done
Step 3c:	If a cycle is detected in the graph: For each of the edges in the cycle: - Tentatively remove edge from cycle - Run a lower-level local heuristic - Add the solution to the solution list Else: - Run a lower-level local heuristic - Add the solution to the solution list
Step 4:	Find minimal-cost solution from solution list
Step 5:	If this solution is better than current incumbent solution: - Set this new solution as incumbent - Restart algorithm from Step 1 Else: - End algorithm and return incumbent

Detailed performance calculations and comparison to other literature solutions can be found elsewhere [8].

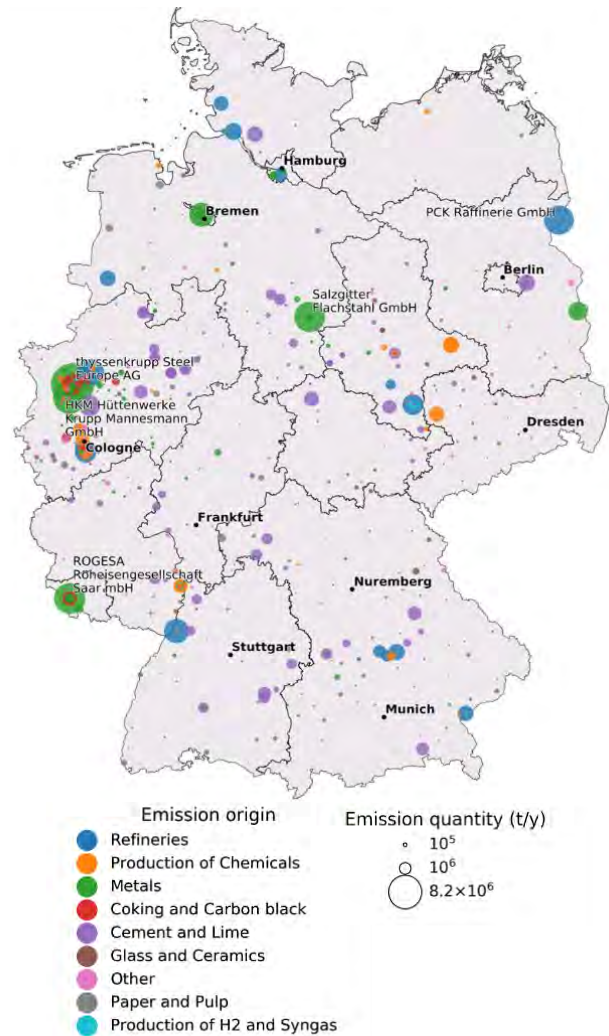


Figure 1: Map of Germany with emission origin, color-coded according to industrial category. The size of the circles displays the emission quantity.

2.2 A sink location algorithm

Locating the lowest cost potential sink location in an undefined network adds significant complexity to the network design problem. Starting from the observation that a sink node will only be connected to a certain subset of nodes (named the “housing nodes”, forming a polygon P) of the graph, we can then place the sink optimally for the given subset via the weighted geometric median. Indeed, for a given set of node weights (here given by pipeline costs per unit length for the given pipeline widths of pipelines flowing towards the sink), there exists a unique location for the placement of a new node that minimizes the total cost of the new pipelines. The difficulty here lies in the fact that the weights upon the housing nodes are yet undefined as they depend on the specific network topology of the remaining network. A combined process of simultaneous topology optimization and minimal-cost sink location is the algorithmic solution we propose. Starting from an initial guess of housing polygon, the algorithm is based around a back-and-forth between optimizing the topology of the network (allowing edges to change, while the sink node location is fixed), then optimizing the placement of the sink node (allowing only the sink node placement to change, while

the edges do not change). In this way, an initial bad guess of housing nodes can potentially lead to a final good solution as the algorithm can “drift” gradually through the network to a better configuration, finding lower-cost solutions at each step. Despite permitting the drift, local minima can still be reached, and the choice of initial guess determines to a reasonable degree the extent of the drift. Further research is currently underway to establish a model for good initial guesses for varying cost functions. Within the scope of this paper, we take a Delaunay triangulation of the network, and use the 10 triangles with the largest total amount of node capacity as initial input guesses.

Table 2: Optimal Sink Placement with drift algorithm

Step 1:	Make initial guess of nodes P connected to sink
Step 2:	Initialize network around P (without changing edges to sink) – with an adapted topology optimization heuristic
Step 3:	Place sink optimally for initialized weights
Step 4a:	While a better solution is found (drift loop):
Step 4b:	Use topology heuristic (allowing all edges to change) – e.g. the algorithm given in 2.1
Step 4c:	Reposition sink optimally for new weights on sink (potentially new set of nodes P')

2.3 Integrating established pipeline routes

Planning new pipeline routes is suspected to be highly dependent on land use due to technical or legal obstacles to creating pipeline routes on new areas. In this way, it is supposed that greater priority should be given to stretches of land with pre-existing pipeline channels in proposing a network design. As mentioned previously, due to CO₂ pipeline specificities, this does not necessarily entail recycling pre-existing pipelines themselves (although the methods could permit it with case-specific cost functions) but instead globally lowering the cost of individual pipelines along known pipeline corridors by a given amount. Some further modifications are made to local topology optimization heuristics and to the optimal sink placement algorithm. To integrate known pipeline routes to a new local network of CO₂ sources, a considerable portion of the pre-existing pipeline network is considered for potential use. Nodes of the preexisting network are also added to the new network graph object, despite not carrying any supplementary capacity. The combined network graph is therefore a single entity composed of 3 different types of edges:

1. Pre-existing routes which carry no flow. These have no cost but can still be part of the combined network and be considered to re-route flow.
2. Pre-existing routes which carry flow. These have reduced cost.
3. New routes which carry flow. These have full cost.

Topology optimization heuristics are therefore simplified if the breaking and recombining of the network is done in a way that flow carrying routes only are considered for re-routing (edges 2 and 3), as other modifications have no effect on cost.

The sink placement algorithm can be modified to accommodate for the reduced cost of pre-existing pipeline routes. The calculation of the geometric median presupposes that all potential sink locations will require pipelines to a given housing node following the same cost function. The reduced cost function for pre-existing pipeline routes then invalidates this assumption. Indeed, the geometric median often places the sink node on the highest flow-carrying node of the housing polygon. The geometric median calculation of a later step might then have to choose between replacing the sink node via constructing new pipelines from each housing node or leaving its current “sub-optimal” configuration with a reduced cost along a preexisting pipeline route. In this scenario, replacing the node may be denied if it leads to a lower-cost solution. This therefore results in a local minimum which terminates the algorithm.

3. Results

In this section we give an example of a simple network constructed from combining a CO₂ source emission cluster from the South of Germany with a preexisting pipeline network and placing sinks in a minimum-cost configuration. The sources whose primary function is energy production (essentially coal plants) were omitted due to their planned phase out as well as sources that emit less than 50000 tons per year to decrease network complexity. The cost of a new pipeline is given by the function $LC^{0.6}$ where L is the pipeline length and C is the required pipeline capacity. A concave dependence of the capacity integrates the economy of scale of larger pipelines (0.6 is a typical exponent for CO₂ networks [9]). The pipeline network data was obtained from a recent data supplement that carefully aggregates multiple decentralized sources for the German national pipeline grid [10]. Source clustering was performed in a “network-aware” manner. A DBSCAN clustering algorithm was used and input with a precalculated distance matrix, whose values correspond to the pairwise shortest path along the pre-existing network between the sources considered. As the CO₂ sources are not connected to the pre-existing pipeline network, direct links are added between each source and its 2 closest network nodes. In our network design procedure, the relative cost factor of building a pipeline on a pre-existing route, C_{eq} , was set to 75%, 50%, 25% and 0% of the equivalent cost of constructing an identical pipeline elsewhere. In the 0% scenario, utilizing established pipeline routes then adds no cost to the network. This simple choice led to final networks that vary greatly in structure and give distinct minimum-cost sink locations. The scenario with no reduction in cost for routing on pre-existing pipelines (i.e., $C_{eq} = 100\%$) is also provided for comparison.

To fasten the optimization process, we decrease the complexity of the pre-existing pipeline network by only selecting pipelines within the convex hull of the sources, further extended by 30 km.

We show the sources with the considered established pipeline routes in Figure 2.

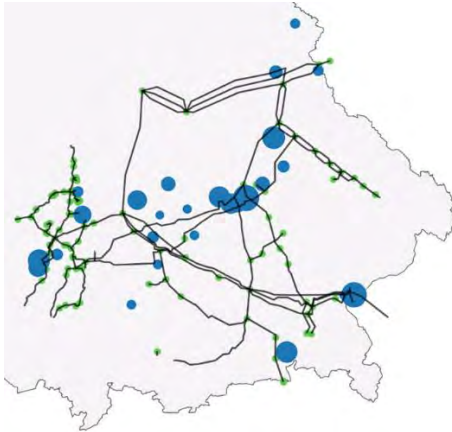


Figure 2: Considered CO₂ sources (blue) and pre-existing pipeline infrastructure (black lines) and network nodes (green) for the South of Germany.

The final optimized networks for values of C_{eq} of 0%, 25%, 50%, 75% and 100% are given in Figure 3 and 4. Calculation time was fast for all examples, taking roughly an hour to repeat the entire algorithm for the 10 different initial guesses of housing polygons. The intermediate topology optimization heuristic used in step 4b of the algorithm described in Table 2 was the metaheuristic described in Table 1.

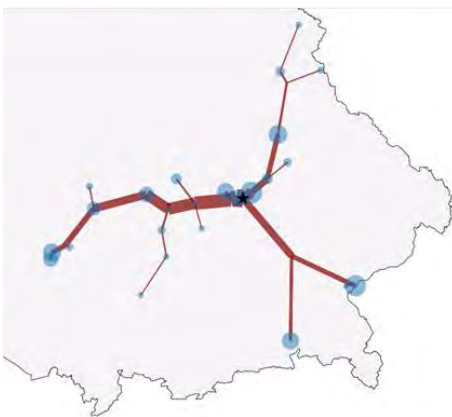
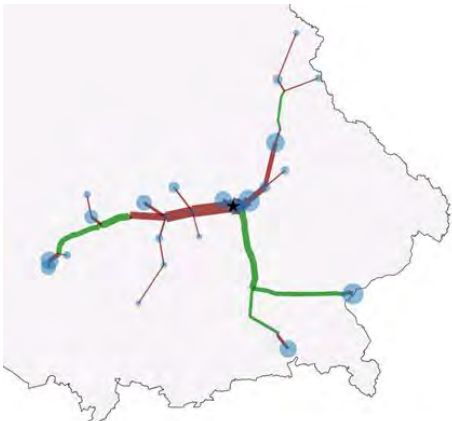


Figure 3: Minimum-cost networks and sink location utilizing pre-existing pipeline routes for C_{eq} of 75% (top) and 100% (bottom), the 100% case being the reference case without cost reduction for pipelines over pre-existing routes.

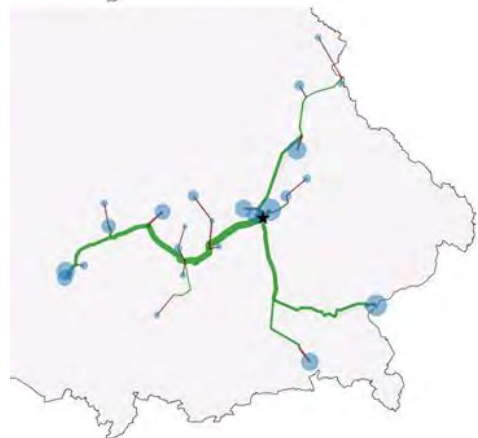
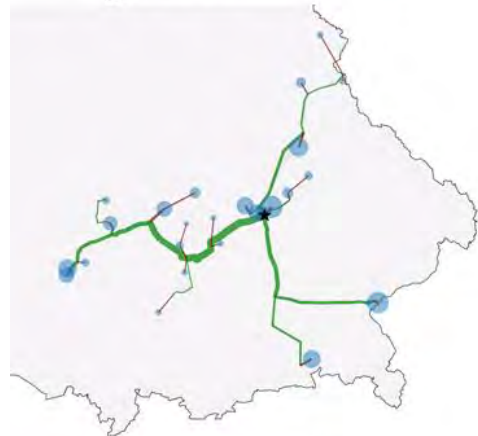
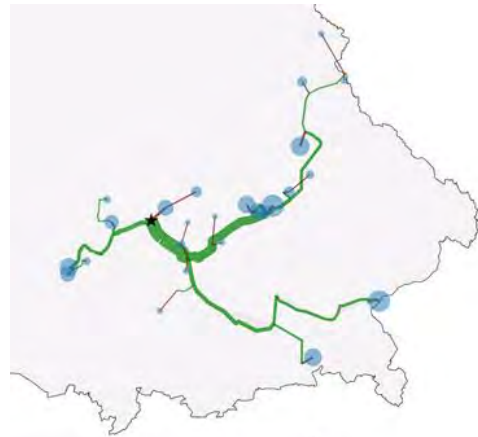


Figure 4: Minimum-cost networks and sink location utilizing pre-existing pipeline routes for C_{eq} of 0% (top) and 25% (middle) and 50% (bottom). The optimal sink location is shown as a black star in both plots.

In these figures, solution pipelines constructed upon pre-existing pipeline routes are shown in green whilst new routes are given in red. CO₂ sources are shown as blue circles with a size proportional to the emission volume. The pipeline thickness is proportional to the capacity required for flow material balance, which is furthermore unique if there is a match between total source and sink capacity.

We notably observe that as C_{eq} increases, overall length of the networks decreases as sinuous detours utilizing pre-existing routes no longer become economical. For lower values of C_{eq} seen in Fig. 4, the minimum-cost

networks naturally tend to be built on a larger amount of pre-existing pipeline routes, whereas at the opposite extreme of full cost (Fig. 3, bottom), the minimum-cost network is constructed exclusively upon new routes (all pipelines shown in red).

The optimal locations of the sink (shown as black stars) appear also appear to change in each scenario, although chosen the locations are remarkably similar for the 25%, 50%, 75% and 100% C_{eq} parameters, situated within a dense cluster of 4 emitters and 4 preexisting network nodes. The chosen locations are identical for the $C_{eq} = 25\%$ and $C_{eq} = 50\%$. The similarity of final optimal sink locations is observed despite a series of distinct initial guesses of housing nodes. The same final solution is often obtained for different initial guesses via the algorithm drift.

Details of the algorithm progression for each final lowest cost solution are given in Figure 5. We show how the overall network cost is decreased at each step of the algorithm, including notably multiple rounds of the drift loop for $C_{eq} = 75\%$ and $C_{eq} = 25\%$ scenarios.

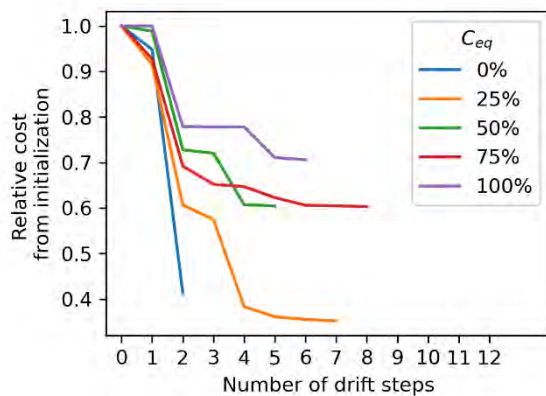


Figure 3: Algorithm progression (post-initialisation) for the final lowest-cost networks for each pre-existing pipeline route cost parameter.

4. Conclusion

Throughout this paper we explore a combination of methods enabling the design of minimum-cost pipeline networks considering features such as optimal sink placement or integration of prior pipeline routes. We give distinct network solutions established from clustering large industrial CO₂ sources of the South German region and utilize the prior regional gas pipeline network routes with varying cost of inclusion. While the networks shown here may not take into account other regional complexities, either geographical or geological (subsurface storage potential has nonetheless been established in the Southern region), the example demonstrates the functionality of the methods.

References

[1] Speech by Federal Chancellor Dr Angela Merkel at the Xth Petersberg Climate Dialogue, Berlin, 14 May 2019: <https://www.bundesregierung.de/breg-en/news/speech-by-federal-chancellor-dr-angela-merkel-at-the-xth-petersberg-climate-dialogue-berlin-14-may-2019-1612592>

[2] Müller, C & Reinhold, K (2011). Geologische Charakterisierung tiefliegender Speicher- und Barrierehorizonte in Deutschland – Speicher-Kataster Deutschland. – Schriftenr. dt. Ges. Geowiss., Vol. 74; Hannover. (ISSN 1860-1782)

[3] Höller, S, & Viebahn, P (2011). Assessment of CO₂ storage capacity in geological formations of Germany and Northern Europe. *Energy Procedia*, 4:4897-4904.

[4] Peletiri, SP; Rahmanian, N; Mujtaba, IM (2018). CO₂ Pipeline Design: A Review. *Energies*, 11, 2184. <https://doi.org/10.3390/en11092184>

[5] Lawler EL, Wood, DE (1966). "Branch-and-Bound Methods: A Survey," *Operations Research*, INFORMS, vol. 14(4):699-719

[6] German Environment Federal Office (2019). Installations covered by ETS Germany in 2018, Deutsche Emissionshandelsstelle. Available at: https://www.dehst.de/SharedDocs/downloads/EN/installation_lists/2018.pdf (Accessed: 2 September 2020)

[7] Brimberg J, Hansen P, Lin K, Mladenovi N, Breton M, Brimberg, J (2003). An oil pipeline design problem. *Operations Research*, 51(2):228–239. <https://doi.org/10.1287/opre.51.2.228.12786>

[8] Yeates, C., Schmidt-Hattenberger, C, Weinzierl, W, & Bruhn, D (2020, December 17). Comparison of heuristic methods for achieving minimum-cost capacitated networks with a new metaheuristic based on node valency. <https://doi.org/10.31224/osf.io/eqcqzh>

[9] Kazmierczak T, Brandsma R, Neele F, Hendriks C (2009). Algorithm to create a CCS low-cost pipeline network. *Energy Procedia*. 1(1):1617–1623. <https://doi.org/10.1016/j.egypro.2009.01.212>

[10] Kunz, F, Kendzioriski, M, Schill, W, Weibezahn, J, Zepter, JM, Hirschhausen, C, Hauser, P, Zech, M, Möst, D, Heidari, S, Felten, B, & Weber, C (2017). Electricity, heat, and gas sector data for modeling the German system.

IMPACT OF INNOVATIONS FROM THE NORWEGIAN CCS RESEARCH CENTRE (NCCS)

Grethe Tangen^{1*}, Inna Kim¹, Amy Brunsvold², Mona J. Mølnevik², Solrun J. Vevelstad¹, Elin Skurtveit³, Simon Roussanaly², Svend T. Munkejord², Pierre Cerasi¹, and Peder Eliasson¹

¹ SINTEF AS, Trondheim, Norway

² SINTEF Energy Research, Trondheim, Norway

³ Norges Geotekniske Institutt (NGI), Oslo, Norway

* Corresponding author e-mail: grethe.tangen@sintef.no

Abstract

We have evaluated the potential impact of the research and innovation performed in the Norwegian CCS Research Centre (NCCS). In this context, impact was evaluated along several axes. Examples include reduced emissions, economic impact (increased value creation, saved cost), improved decision making, saved energy, and industrial potential. The reference system is the envisaged CCS network in Europe by 2030. The study illustrates how the research and expected innovations can impact CCS chains and society when applied.

Keywords: CCS, innovations, impact

1. Introduction

NCCS' main goal is to fast-track CCS deployment by timely delivery of safe and cost-efficient CCS technologies. This is facilitated by promoting an innovative environment through concrete collaboration between scientists and industry partners. As an international CCS research hub, NCCS is built to stimulate open innovation processes where companies involved in the Centre will be able to commercialize ideas and emerging technologies from outside their company borders, building on others' ideas and even bringing ideas from NCCS into new and emerging markets. This model optimizes innovation and technology output across company boundaries and increases the potential gain for each company involved, as the pool of ideas and concepts emerging from NCCS will be larger than that of each company.

Research within CO₂ capture, transport and storage is multi-disciplinary and covers a wide range of topics. Consequently, the outcomes have different characteristics with respect to type of innovation, maturity, and applicability in the CCS chain.

Building on the methodology from the Research Council impact study [1]-[2], NCCS has assessed the potential impact of selected innovations from the 12 NCCS research tasks covering the whole CCS chain, including CO₂ capture, transport, storage, and value chain. The innovations in this study mainly fall under four categories: 1) new technology, 2) models and simulation tools, 3) new methods, and 4) new standards and guidelines. The NCCS deployment cases serve as basis for the quantitative illustration of impact made for each innovation to indicate the order of the potential gains.

1.1 NCCS Deployment Cases – directing research for maximum impact

NCCS originally defined two CCS deployment cases (DCs) to help structure and align the research, and support NCCS in fulfilling its ambition to overcome critical barriers and accelerate CCS deployment. **NCCS DC2025 - CCS for Norwegian Industry** is similar to the Norwegian full-scale project and includes CO₂ capture from industry sources and transport with ship to ensure a flexible solution for CO₂ storage on the Norwegian Continental Shelf (NCS). One storage site in offshore aquifers is anticipated, with a capacity of 1-1.5 Mt/year in 2025 (**Figure 1**).

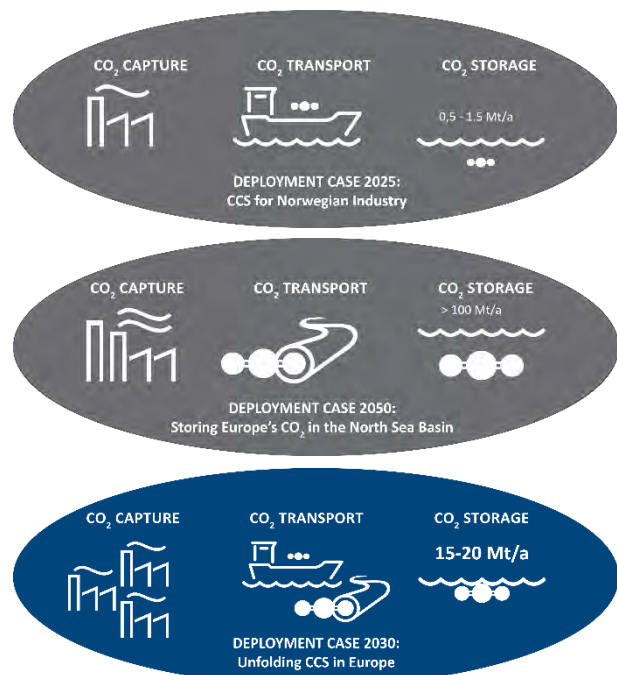


Figure 1. NCCS deployment cases: DC2025, DC2050, and DC2030

The second deployment case, **NCCS DC2050 – Storing Europe's CO₂**, comprises captured CO₂ from numerous sources in Europe and transport via a pipeline network to Norwegian storage sites in the North Sea. Several major storage sites are foreseen, some with an opportunity for EOR, with a storage capacity of ~100 Mt/year by 2050.

For this NCCS impact study a third deployment case is defined to serve as basis for analysis: **NCCS DC2030 -**

Unfolding CCS in Europe. DC2030 incorporates all European CCS projects implemented, under construction and those planned to be in operation within 2030. It includes industry sources, power generation, natural gas processing and H₂ production. A combination of ship and pipeline transport of CO₂ to aquifers and depleted gas fields ensures flexibility. Capacity in 2030 is estimated to be 15-20 Mt/year, with the ambition to increase it to more than 40 Mt/year after 2030 (**Figure 2**).

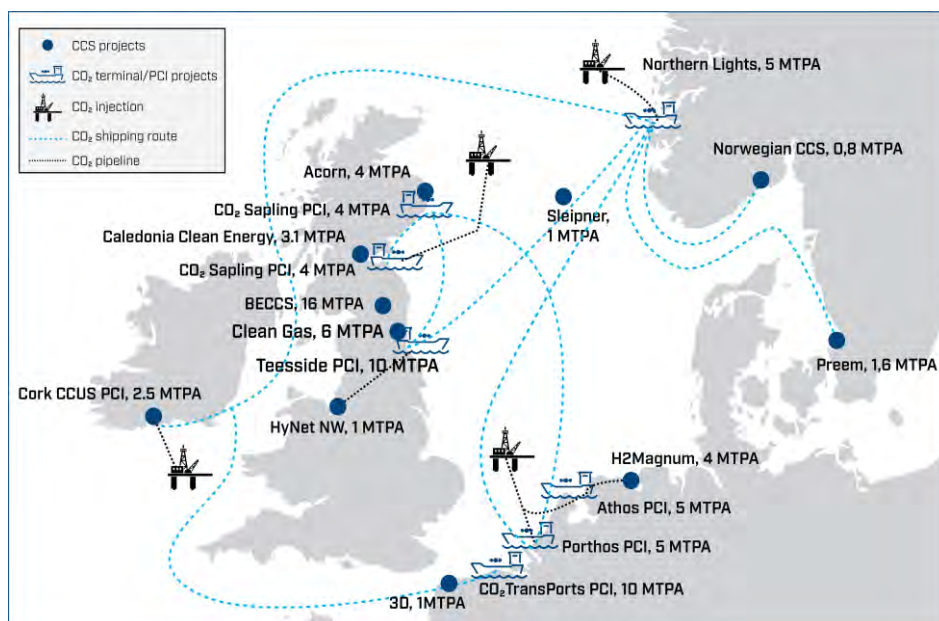


Figure 2. Projects included in NCCS DC2030 - Unfolding CCS in Europe (data source: [3], [4], project's webpages).

2. Expected impact from selected cases

2.1 Methodology

The case studies were conducted by the researchers within the 12 NCCS tasks in an iterative process, including dialogue with industry partners. For each case,

the addressed challenge was documented before describing the innovation and its potential impacts if successfully implemented in a CCS project. To indicate the order of magnitude of potential economic impact, simplified illustrative examples were made for all cases. In the following, 6 of the case studies are summarized.

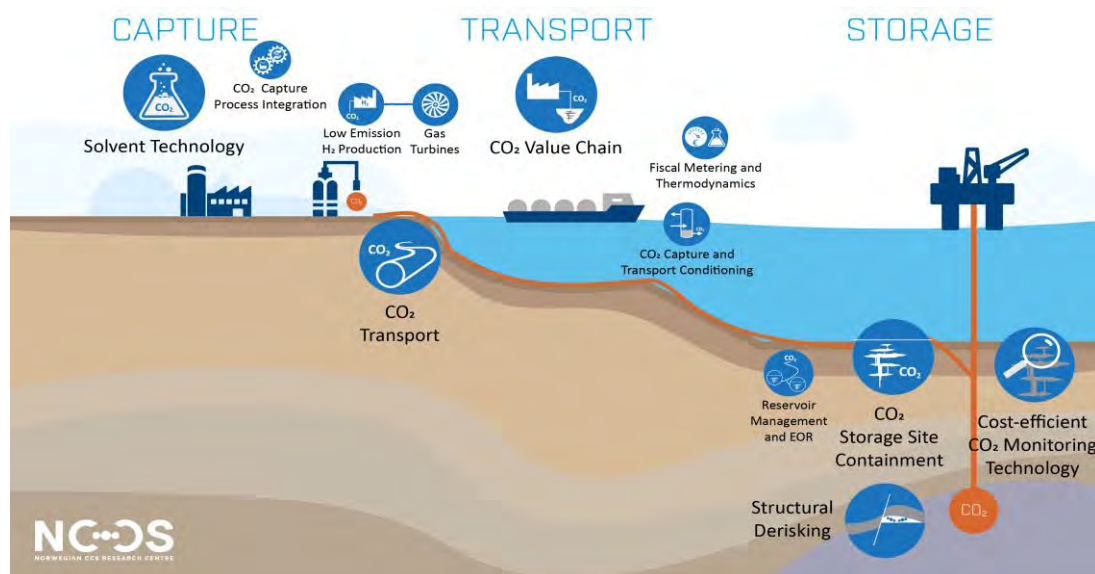


Figure 3: The 12 research tasks in NCCS cover the whole CCS value chain. 6 tasks (larger circles) contributed with the case studies presented in this paper.

2.2 Impact evaluation for selected case studies

Case 1 – Solvent loss reduction in amine-based CO₂ capture

Main impact:

Reduced OPEX and improved safety in operation and operational environment

The challenge:

During chemical absorption, CO₂ present in a flue gas is absorbed and chemically bound to a solvent. The reaction is reversed during solvent regeneration and the solvent is reused to absorb CO₂. A part of the solvent will react with other compounds in the flue gas forming compounds that cannot be regenerated. Formation of unwanted compounds depends on the composition of the flue gas, the solvent used and the operation of the pilot plant. Over time, these reactions lead to loss of capture efficiency, and could cause problems such as corrosion, fouling, foaming, and increased emissions.

The innovations:

- Technologies for removal of oxygen and iron from the solvent to reduce degradation.
- Methodology for identification of solvents with higher chemical stability

Potential impact:

Base case for illustration: 2 Mt/yr CO₂ captured from two power plants using 30% MEA-based solvent technology in DC2030. With MEA cost of 2 €/kg and solvent degradation rate of 2 kg MEA/ton CO₂, the cost of solvent loss is 8 M€/year.

Estimated effect from implementing NCCS innovations for oxygen and iron removal is up to 50% lower degradation of MEA based solvent. This would give potential savings up to 4 M€/year in replacement cost of the active solvent components.

Besides, the methodology for predicting chemical stability based on structure - degradation relationship for various amines would enable selecting a stable solvent at early stage of the solvent development.

Case 2 – Increased storage capacity with improved geological fault models

Main impact:

Reduced uncertainty resulting in improved safety for storage sites and increased storage capacity.

The challenge:

Implementation of large-scale CO₂ storage will require utilization of a wide range of storage reservoirs including faulted reservoirs with structural traps. The sealing properties of faults are challenging to predict, and conservative estimates and high uncertainty may limit the total injection volume or even disqualify a storage site. Existing industrial models have limitations when addressing fault risk related to CO₂ injection in faulted aquifers.

The innovations:

An improved fault de-risking framework that includes dynamic pressure changes related to CO₂ injection and addressing along-fault fluid migration. Such a framework would:

- Reduce uncertainty related to fault properties
- Increase confidence in site integrity and confinement
- Enable qualification of increased storage capacity

Potential impact:

The development of the Horda Platform area for CO₂ injection showed that high uncertainty in existing fault seal prediction models for shallow, fault-bound aquifers like Smeaheia (**Figure 4**), limits the capacity and provides major obstacle for site qualification. The Norwegian CO₂ storage atlas [5] indicates around 40 Gt storage capacity in Norwegian North Sea aquifers. The effective volumes found suitable for safe and long-term storage during technical maturation may be as low as 10% of the estimated capacity.

For the Norwegian North Sea this gives a suitable safe capacity around 4 Gt. Assuming this volume could be increased with roughly 10% if risk related to fault sealing is reduced, a total increase in storage capacity of 400 Mt can be estimated, enabling 20 years of storing 20 Mt CO₂/year (NCCS DC2030). Improved fault seal models and reduced uncertainty is a necessary, although not sufficient, step towards qualification of additional storage capacity.

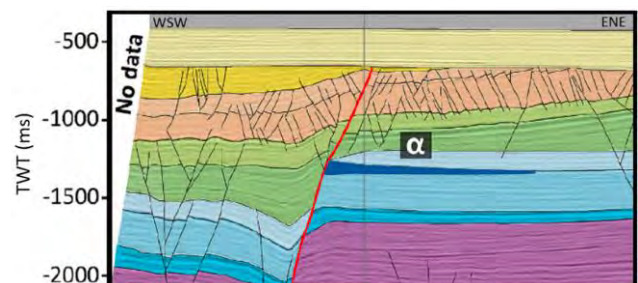


Figure 4. Seismic section with fault interpretation for Smeaheia [6], modified from M. Mulrooney.

Case 3 – Models for identifying optimal conditions for transport of CO₂ via ship

Main impact:

Showing potential reduction in CAPEX and OPEX in future projects with lower pressure-based CO₂ transport.

The challenge:

CO₂ shipping is expected to play an important role in early CCS development, for "small" capacities, and/ or "long" distance transport. Over the last few years, questions on optimal transport conditions (T and P) have been raised. Although the density of liquid CO₂ decreases, and the costs of storage tank and ship increase, with increasing pressure, the cost of liquefaction is higher for the lower transport pressure. 15 bar is currently considered the best option for the Norwegian full-scale project, based on maturity and safety. However, work in NCCS has shown that in the future, lower pressure-based

transport could be a better solution due to its potentially lower cost.

The innovations:

A tool for identification of optimal conditions (pressure, temperature) for transport of CO₂ by ship that would lead to significant reduction in the costs of CO₂ liquefaction and transport. The transport conditions of interest are especially the low-pressure option (7 bar) and the medium-pressure option (15 bar).

Potential impact:

Base case for illustration: A possible case within DC2030 is transport of 5Mt/yr CO₂ from Netherlands to Norway (1000km distance to Northern Lights).

The NCCS work demonstrates that enabling 7 bar instead of 15 bar based shipping can significantly lower costs (Figure 5):

- Investment could be reduced by nearly 50%.
- Reduction in operating cost of 15%.
- Overall liquefaction and shipping cost would be reduced by 30%.

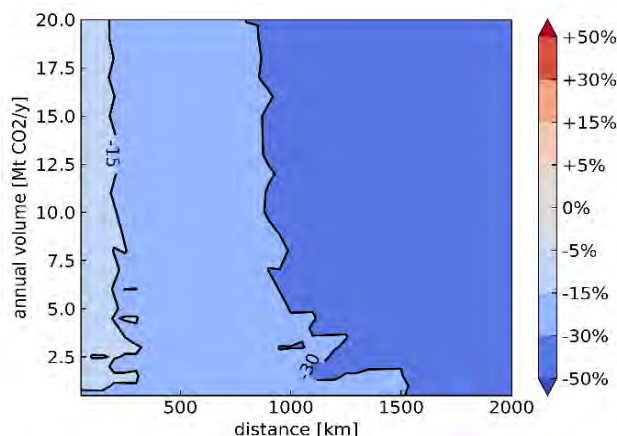


Figure 5. CO₂ conditioning and transport cost reduction achievable by 7 bar ship option compared to the 15 bar ship option (color code indicates cost reduction) [7]-[8].

Case 4 – Model enabling qualification of natural gas pipelines for CO₂ transportation

Main impact:

Reduced uncertainties in the design of new pipelines and re-qualification of existing ones improves safety, lower the costs and accelerates deployment of CCS.

The challenge:

CCS deployment requires a pipeline network for CO₂ transportation. Some natural gas (NG) pipelines are scheduled for decommissioning. Re-use of the NG pipelines for CO₂ transport requires qualification. One of the issues that need consideration is fracture propagation control, i.e., that a crack does not develop into a long, running ductile fracture (RDF). Existing engineering tools (Battelle two-curve method, BTCM) are not developed for CO₂ or modern steels.

The innovations:

The coupled FE-CFD model for assessment or running-ductile fracture (RDF), see [9]-[10], can significantly contribute, among other methods and measures, to re-qualifying existing NG pipelines for CO₂ transportation (Figure 6). The model is flexible and has a wider range of use than existing tools and would be expected to approve more reuse cases. It could lead to reduction of safety margins and hence reduced costs. It could contribute to a larger operational window.

The FE-CFD model can be used to develop a simpler-to-use RDF engineering tool.

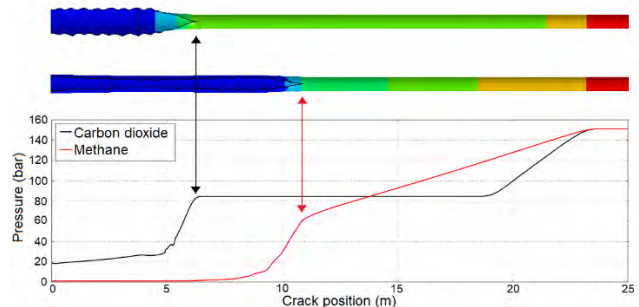


Figure 6. Example calculation showing that CO₂ gives a higher load on the opening pipe flaps compared to methane. Figure by G. Gruben.

Potential impact:

Base case for illustration: 200 km (offshore) pipeline is requalified for transporting 2.5 Mt/yr CO₂, assumptions relevant for DC2030.

Avoided costs and CO₂ emissions due-to re-qualification of existing natural gas pipeline to transportation of CO₂:

- Avoided investment cost according to Sepra et al [11] for a 200 km 12" offshore pipeline: 1.18 M€/km*200 km = 236 M€.
- Avoided CO₂ emissions by not having to produce and install the pipeline, calculated using iCCS [12]: 460 t/km * 200 km = 92 kt.

Case 5 – Innovative laboratory testing of cement to rock bonding in CO₂ injection wells

Main impact:

Innovative laboratory methodology for testing of cement to rock bonding, giving access to all needed strength values for correctly assessing a well integrity barrier.

The challenge:

Satisfactory sealing of the abandoned wells is mandatory and may limit the total injection volume or even disqualify a storage site, if not proven. Existing well construction and sealing (P&A) methods rely on Portland cement with additives or alternative materials, which are difficult to qualify and test. On average, primary cementing services constitute around 5% of well cost. Secondary cementing can result in an incremental increase of up to 20% of well cost [13]. In order to assess experimentally the performance of a well sealant, bulk as well as interface properties need to be correctly measured

[14]. Similarly, for predictive modelling purposes, strength values, both in shear and tension mode, are needed for cement bulk as well as interface with steel and with rock. These last properties were until now difficult to assess and seldom taken correctly into account in numerical models.

The innovations:

The testing method, developed in the laboratory, addresses several aspects needed to fully assess how a cement or other sealing material will perform at realistic down-hole conditions by performing thorough testing of the basic mechanical parameters needed for modelling purposes at field-relevant conditions. Several test methodologies have been developed, targeting both shear and tensile properties of cement bonding to rock. In addition, an ECCSEL rig is developed allowing to assess loss of cement bond in a field-relevant radial concentric geometry, including steel casing and surrounding rock (Figure 7).

Potential impact:

Less conservative models for cement integrity will reduce construction and maintenance costs and reduce demand for materials, and by this also reduce the CO₂ footprint. Testing at field relevant conditions also increases confidence in CO₂ storage.

Base case for illustration: 15-20 Mt/yr CO₂ is to be stored in NCCS DC-2030. The cost per ton of Portland cement is around 40 €/t. Additive pricing goes from 80 €/t for gypsum to 4000 €/t for fluid loss additives. Cementing corresponds to between 2-8 M€ per well. Assuming average optimal injection rate of 0.2 – 1 Mt/year per well, with optimized placement, one would need up to 100 wells to reach the DC 2030 scenario, with cement costs reaching up to 800 M€.

- 10 % less cement per well would lead to an economy of up to 80 M€.
- Additional 10 % cost reduction could be obtained by not having to use special cement additives.
- Plug and abandonment (P&A) needs for existing wells: 400 k€ per day * 30 days up = 12 M€ per well to plug (www.fourphase.com). Halving the required plug length compared to current regulation results in 1 day less per well, this sums up to 40 to 1200 M€ savings depending on number of wells, on top of the well construction cost reduction.

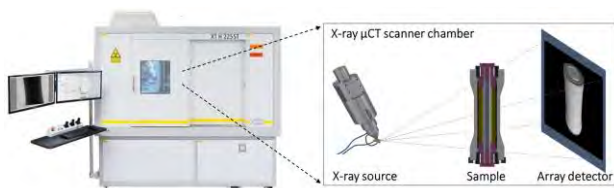


Figure 7. The ECCSEL well integrity research infrastructure. This mini-wellbore simulator is used for in-situ investigation of cement integrity under CT imaging. Sketch by A. Ghaderi.

Case 6 – Novel methodology based on two-step Bayesian approach for quantitative CO₂ monitoring

Main impact:

Reduced monitoring costs, more predictable operation, improved safety, and support for communication with regulators and the public.

The challenge:

CO₂ monitoring is a regulatory requirement and an essential tool for predictable operation and safe CO₂ storage. While conventional monitoring focus mainly on determining the location and extent of the CO₂ plume, a more quantitative monitoring approach is useful for detailed conformance (agreement between observations and predictions) assessment and reliable operational decision making. A quantitative approach could also be used during the characterization phase to give more accurate assessment of storage capacity.

The innovations:

The Bayesian Rock Physics Inversion method developed and investigated in NCCS, in collaboration with the Pre-ACT project [15], is a two-step approach consisting of geophysical inversion followed by rock physics inversion with uncertainty propagation (Figure 8) [16]. The method allows quantification of the most relevant rock physics parameters including their uncertainties. It is, in particular, useful for discrimination between pressure and saturation changes in the reservoir. The method handles multiple types of geophysical input data and can take prior information (e.g., well logs or down-hole measurements) into account for reliable assessment of site performance.

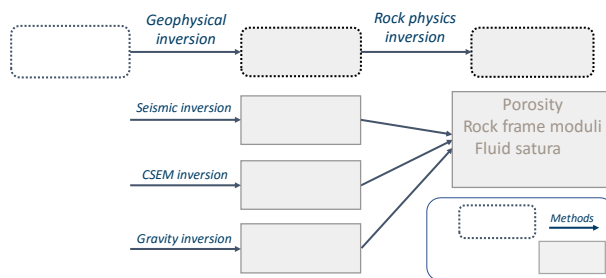


Figure 8. Two-step workflow combining geophysical and rock physics inversion. Figure by B. Dupuy, SINTEF.

Potential impact:

The two-step Bayesian approach for quantitative CO₂ monitoring contributes directly to more informed operational decisions, safer storage, and at the same time fewer costly interventions during CO₂ injection. In addition, the approach uses available data in an efficient way, which can help to reduce the need for frequent (costly) geophysical surveys. Any operator could profit from adapting such a workflow as part of their Measurement, Monitoring, and Verification (MMV) plans, for updates of their reservoir models, better forecasts, and improved decision making. The quantitative information, and especially the uncertainty assessments, may also be helpful for communication with other stakeholders and with the public.

Illustrative example: With more efficient use of acquired data, we assume that the interval between geophysical surveys can be increased by up to 25% and that every second or third survey can be sparser and more targeted. This could result in around 30% overall reduction of monitoring costs. For a storage project of Sleipner to Aurora size (DC2025) and 20 geophysical surveys at 10 M€ per survey, this means a potential cost reduction of around 60 M€. In addition, we foresee a reduction in risk of, and costs related to, unexpected events like temporary interruption of operation, unplanned well intervention, need for additional wells, or even early abandonment of the storage project.

3. Discussion and conclusions

Assessment of the possible impact of innovations which are currently at low TRL, is not an easy task and is typically based on different assumptions.

During the NCCS impact study, the following reflections were made:

- It is important to communicate that the quantitative estimates are not socio economic or business economic studies, but simplified calculations to demonstrate order of magnitudes.
- Transparent assumptions are essential to enable discussion of premises for the examples.
- Dialogue with industry is valuable to create realistic quantitative examples of potential impact.
- Mapping of qualitative and indirect effects is also useful but may be overlooked when quantitative examples are made.
- Many innovations build on outcomes from several research projects over many years.
- Innovations often represent one critical part of the CCS chain, and deployment will depend on implementation of the whole chain.

Nevertheless, this exercise helps to build a larger picture for the technology developers and show possible application and potential gains that industrial partners may have from implementing these innovations.

To contribute to the mitigation of climate change and limit temperature increase to 1.5°C per year, about 10 Gt CO₂ needs to be captured and stored annually. The NCCS impact study illustrates that novel methodologies and even incremental improvements in the technologies can contribute to significant cost reduction, improved safety opportunities for upscaling, thus accelerating full-scale CCS deployment.

Acknowledgements

This publication has been produced with support from the NCCS Research Centre, performed under the Norwegian research program Centres for Environment-friendly Energy Research (FME). The authors acknowledge the following partners for their contributions: Aker Carbon Capture, Allton, Ansaldo Energia, Baker Hughes,

CoorsTek Membrane Sciences, Equinor, Fortum Oslo Varme, Gassco, KROHNE, Larvik Shipping, Lundin Norway, Norcem, Norwegian Oil and Gas, Quad Geometrics, Stratum Reservoir, Total, Vår Energi, Wintershall DEA and the Research Council of Norway (257579/E20).

References

- [1] Effekter av energiforskningen. Impello Management AS. Trondheim, 28. desember 2018.
- [2] Størset et al, 2019. Profiting from CCS innovations: A study to measure potential value creation from CCS research and development. *International Journal of Greenhouse Gas Control*, vol. 83, p. 208-215. <https://doi.org/10.1016/j.ijggc.2019.02.015>
- [3] <https://co2re.co/>
- [4] https://ec.europa.eu/energy/infrastructure/transparency_platform/map-viewer/main.html
- [5] <https://www.npd.no/en/facts/publications/co2-atlases/co2-storage-atlas-norwegian-north-sea/>
- [6] Mulrooney et al, 2020. Structural analysis of the Smeaheia fault block, a potential CO₂ storage site, northern Horda Platform, North Sea. *Marine and Petroleum Geology*, 121, November 2020, 104598.
- [7] Roussanaly S, Deng H, Skaugen G, 2021. Cost-optimal conditions for transport of CO₂ by ship. 15th International virtual conference on Greenhouse Gas Control Technologies. 15th-18th of March 2021, virtual.
- [8] Roussanaly S, Deng H, Skaugen G, Gundersen T., 2021. What are the cost-optimal conditions for transporting CO₂ by ship? An in-depth comparison of 7 and 15 bar shipping. Submitted to *Energies*.
- [9] Nordhagen HO, Munkejord ST, Hammer M, Gruben G, Formeau M, Dumoulin S, 2017. A fracture-propagation-control model for pipelines transporting CO₂-rich mixtures including a new method for material-model calibration. *Engineering Structures* vol. 143, pp. 245—260, [10.1016/j.engstruct.2017.04.015](https://doi.org/10.1016/j.engstruct.2017.04.015).
- [10] Gruben G, Macdonald K, Munkejord ST, Skarsvåg HL, Dumoulin S, 2020. Pipeline fracture control concepts for Norwegian offshore carbon capture and storage. In: *13th International Pipeline Conference, IPC2020*, virtual. [10.1115/IPC2020-9766](https://doi.org/10.1115/IPC2020-9766).
- [11] Sepra et al., 2011. Technical and economic characteristics of a CO₂ transmission pipeline infrastructure. EUR – Scientific and Technical Research Report. DOI: 10.2790/30861
- [12] Roussanaly S, Brunsvold AL, Hognes ES, 2014. Benchmarking of CO₂ transport technologies: Part II – Offshore pipeline and shipping to an offshore site. *International Journal of Greenhouse Gas Control* vol. 28, pp. 283–299. [10.1016/j.ijggc.2014.06.019](https://doi.org/10.1016/j.ijggc.2014.06.019).
- [13] www.scmdaleel.com.
- [14] Opedal, N., Cerasi, P. & Vrålstad, T. in *International Conference on Offshore Mechanics and Arctic Engineering*. V008T011A039 (American Society of Mechanical Engineers).
- [15] www.sintef.no/pre-act
- [16] Dupuy et al., 2021. Combined geophysical and rock physics workflow for quantitative CO₂ monitoring. *International Journal of Greenhouse Gas Control*, vol. 106, <https://doi.org/10.1016/j.ijggc.2020.103217>.

FAST WATER-LEAN SOLVENT SCREENING USING FTIR SPECTROSCOPY: IN-SITU (IN-LINE) MONITORING USING AN ATR REACTION CELL INTEGRATED WITH ON-LINE MONITORING ATTACHED TO A LIQUID-FLOWCELL

Jayangi D. Wagaarachchige¹, Zulkifli Idris², Maths Halstensen¹, Klaus-J. Jens^{2*}

¹ Department of Electrical, IT and Cybernetics, University of South – Eastern Norway, Kjølnes Ring 56, 3918 Porsgrunn, Norway

² Department of Process, Energy and Environmental Technology, University of South – Eastern Norway, Kjølnes Ring 56, 3918 Porsgrunn, Norway

* Corresponding author e-mail: Klaus.J.Jens@usn.no

Abstract

This study presents a fast and precise solvent characterizing method for the screening of novel CO₂ capture systems. In this method, time-base Attenuated Total Reflectance-Fourier Transform Infrared (ATR-FTIR) spectroscopy was used for in-situ monitoring of CO₂ absorption and desorption processes of non-aqueous amine systems. Different equal mole amines were used to qualify and quantify changes of the IR vibrations. The method enables identification of reaction mechanism along with full speciation. In order to confirm repeatability and representability of the screening test, a replication experiment using liquid-flow cell FTIR analysis is also presented.

Keywords: FTIR-ATR, fast solvent screening, representative sampling, non-aqueous solvents, speciation

1. Introduction

The annual increase in CO₂ emissions is the main contributor to the increase in the greenhouse gas (GHG) level causing climate changes and global warming [1]. Fossil-fuel combustion and industrial processes are the dominant triggers of anthropogenic CO₂ emissions [2]. Integration of the post-combustion CO₂ capture (PCC) to industrial point sources is an essential attempt to alleviate this phenomenon [3, 4].

Different processes are employed for CO₂ capture and separation such as distillation, absorption, adsorption, and advanced membrane filtration [5]. Aqueous amine based gas-liquid chemical absorption is the most common method currently being used in industrial plants [4, 6]. Aqueous 30% MEA solvent is the benchmark capture system and the first patented amine-based solvent system [7-9]. MEA-based solvents are most popular due to MEA's high reactivity and low cost.

However, main concerns of aqueous MEA systems are energy intensiveness, solvent corrosivity and degradation in addition to solvent emissions. Although amine based solvent development has been in focus for several decades to identify appropriate solvent systems, it is still challenging to overcome the aforementioned drawbacks. A method enabling fast screening of solvent systems is thus essential to identify promising CO₂ capture systems.

Amines are widely used for chemical absorption of CO₂. During this reaction, reversible carbonaceous products are formed. In this context, amines are an interesting group of chemical compounds which can be classified into three main groups of primary, secondary, or tertiary amines. Furthermore, amines may react differently due to

steric hindrance, cyclic structures or multiple amine functions present in one amine molecule. Aqueous, non-aqueous, water-lean, by-phasic, and ionic/eutectic amine based solvents systems are being investigated to identify the most promising capture systems.

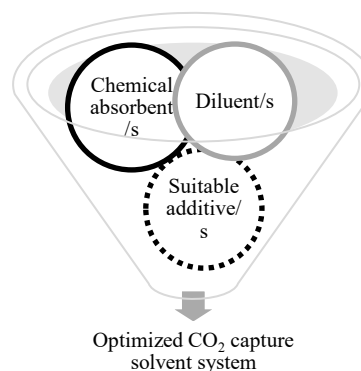


Figure 1: Amine based CO₂ capture system interpretation

Generally, an amine based CO₂ capture system is a blend of several components as shown in Figure 1. It may consist of an amine or a blend of amines to act as a chemical absorbent of CO₂. Moreover, this part is diluted with suitable diluents like water or organic solvents. Furthermore, this system may be optimized by addition of suitable additives to enhance the solvent's chemical and physical properties. Since all components may interact with each other, identifying a novel and promising CO₂ capture system is a challenging task. Therefore, combination of fast and precise chemical analytics with chemical mechanistic insight is paramount.

There are several methods currently being employed to characterize potential solvent. The wetted wall column (WWC) is a well-known apparatus for CO₂ absorption rate measurements also used in a modified version for solvent screening [10]. An atmospheric solvent screening apparatus has been developed to mimic the CO₂ absorption and desorption processes [11-13]. Solvent performance can be determined versus reference solvents by continuous monitoring of the CO₂ capture rate using non-dispersive infrared (ND-IR) CO₂ sensor [14]. The same method was used to screen strong bicarbonate-forming solvents gathering at the same time information on solvent foaming, solid precipitation, and discoloration [15]. Furthermore, Luo et.al. introduced a rapid screening apparatus for improved analysis of single and blended amine solvent systems [16]. Molecular simulations [17] or different modeling tools like soft SAFT[18], COSMO-RS [19, 20] are also used to predict reactive absorption properties of novel solvents without doing laborious experiments.

FT-IR spectroscopy is a versatile method for the analysis of chemical structures used in a wide range of applications. In FT-IR spectrum analysis, the bands of the functional groups and the molecular fingerprint of a chemical mixture are analyzed to give qualitative and quantitative chemical data. This is a fast and precise analysis method for efficient screening of chemicals at small sample volume. Furthermore, vibrational spectroscopy is well suited to application of multivariate calibration models to extract chemical data of species, especially for online monitoring of dynamic systems [21-23].

Chemical speciation of aqueous DEA [24] and heterocyclic amine [25] solvent systems has been performed by ATR-FTIR spectroscopic in situ monitoring. This method can be used for online monitoring of several chemical components simultaneously using Partial Least Regression (PLS-R) models [25-27].

We recently reported a novel sulfolane based non-aqueous solvent system for CO₂ capture [28]: a mixture of diisopropylamine (DIPA), sulfolane (SULF), and methanol (MeOH). Herein we report development and representativity[29]of a fast solvent screening method applied for analysis of the above-mentioned DIPA-MeOH-SULF study. The FTIR-based bulk liquid analysis was performed to confirm the fast-screening result are representative and reproducible.

2. Materials and Methods

All chemicals used in the experiments are tabulated in table 1.

Table 1 Chemical information: Name, CAS number, mole fraction purity, role, and supplier of chemicals.

Chemical name	CAS number	Mole fraction purity	Role	Supplier
Diisopropylamine (DIPA)	108-18-9	≥0.99	Amine	Sigma-Aldrich
Sulfolane (SULF)	126-33-0	≥0.99	Diluent	Sigma-Aldrich
Methanol (MeOH)	67-56-1	≥0.99	Diluent	VWR
Carbon dioxide (CO ₂)	124-38-9	0.9999	Gas	AGA Norge AS

2.1 Fast solvent screening method including solvent speciation

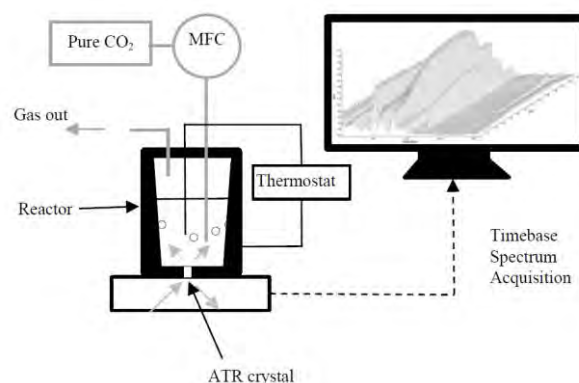


Figure 2: Schematic diagram of the experimental set-up used for the fast-screening of the non-aqueous DIPA system.

The schematic diagram of the fast-screening method is shown in Figure 2. A detailed description of the experimental procedure is given in an earlier publication [28]. The set-up (figure2) was used for screening a set of non-aqueous solvent systems as well as performance evaluation based on the spectroscopic information gathered by in-situ FTIR monitoring.

2.2 Bulk flow analysis for verifying the representativity of the screening results.

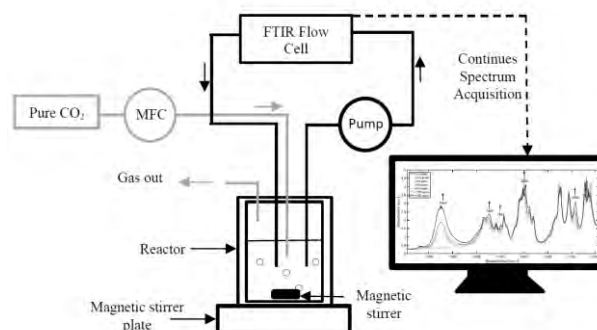


Figure 3: Schematic diagram of the experimental set-up2 for the acquisition of liquid flow cell FTIR spectra.

Since the FTIR-ATR method provides solvent composition on the surface of the ATR crystal, the representativeness of the fast-screening results for the

bulk solvent liquid needs to be assured. Hence, CO₂ absorption tests were performed using set-up2 i.e. bulk liquid-flow analysis. The schematic diagram of the set-up2 is shown in Figure 3. The reactor is a double-jacketed glass vessel with 4 inlet-outlet ports on the top. 50 ml of unloaded solution was placed inside the reactor and the solvent was mixed using a magnetic stirrer with a stirring rate of 250 rpm. Two ports were connected to the gas inlet and outlet while the other two ports were connected to the liquid flow cell inlet and outlet. To analyse the reaction liquid, the solvent was passed through a liquid-flow cell connected to a FTIR liquid sampling accessory. The liquid sampling accessory was attached to the Perkin Elmer Spectrum One FT-IR Spectrometer and the liquid passing through the sampling device was scanned at pre-determined set time. The sampling accessory is equipped with a programmable, variable-speed peristaltic pump to pass the liquid through the flow cell. The waste liquid end of the sampler was sent back to the reactor to recycle the liquid flow through the flow cell.

Prior to each experiment, a background scan of the empty flow cell was recorded. Then the sampler was turned on and unloaded CO₂ solvent started to flow through the cell. Several scans of unloaded liquid were recorded. Then, CO₂ gas was introduced into the glass reactor at a flow rate of 0.10 NL/min using a mass flow controller (MFC) from Sierra Instruments. Scans of the reaction liquid were performed timely during the CO₂ absorption reaction.

FTIR spectra were baseline corrected by Automatic Whittaker Filter method using a chemometrics software, PLS-toolbox with MATLAB® (R2019b).

3. Results and Discussion

3.1 In-situ monitoring and fast screening of a non-aqueous solvent system

In the experimental set-up1, in-situ monitoring was used to observe reaction changes during CO₂ absorption-desorption of the solvent system. The tests were performed in a reaction cell containing a diamond crystal top plate (P/N GS10507) with Golden Gate™ single reflection diamond ATR system. An inherent advantage of this system is that only small mass of solvent is needed (approx. 5g) for one screening experiment. An example of ATR-FTIR raw spectra obtained from time-based in-situ monitoring is shown in Figure 4 (a).

According to Figure 4(a), in-situ monitoring of the chemical changes in the reaction aliquot was performed in four stages. A time gap of each stage was decided during the experiment along with the appeared stack of spectra. The chemical reaction changes can be observed as ATR-FTIR spectra variations. This is a benefit of set-up1 since we can do the experiment without prior information about the time gaps of each step. It is possible to control the parameters accordingly during the experiment while observing the spectra.

Initially, a few FTIR scans were performed to check the unloaded solution. There was no evidence of premature CO₂ capture species formation or water contamination in the sample. Representative FTIR bands of mixture components were also identified.

Then CO₂ was introduced into the solvent. During this second stage, several peaks were seen to increase, decrease and shift. At the same time, several new peaks appeared according to the developing carbonaceous products. The second stage absorption step continues until the increasing band intensity is seen constant.

In the third step, the loaded solvent was observed after further CO₂ pumping. During this time all bands stayed stagnant, implying the capture products to be stable at this condition. This stage was completed after approximately 25 minutes.

In the fourth step, the temperature of the reaction cell was increased to observe the desorption reactions of the system. The reaction cell was heated up gradually and reduction of peaks were seen. Temperature for this step was kept at 58°C. At this stage, in-situ reaction monitoring is important to determine the proper desorption temperature of the new system through observation of spectra changes.

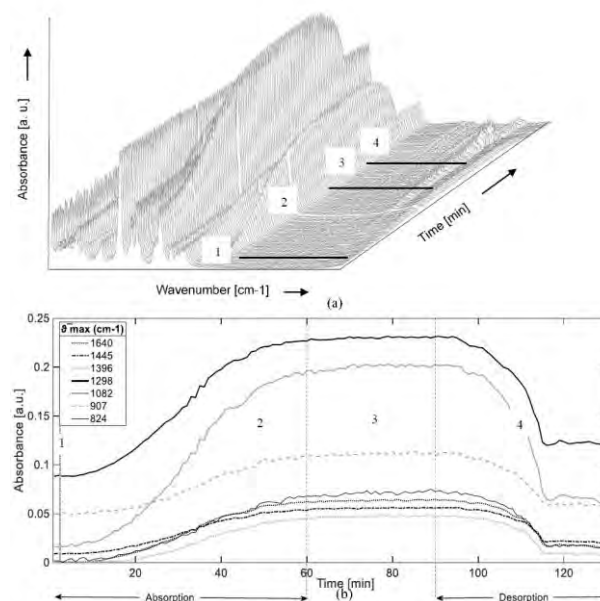


Figure 4: (a) Time-based ATR-FTIR scans (b) IR absorbance variation with time from changing IR vibrational bands; non-aqueous DIPA solvent system during the CO₂ absorption and desorption.

3.2 Full chemical speciation using time-based ATR-FTIR spectra of non-aqueous solvents

From in-situ monitoring of a reaction, plenty of chemical information about the reaction can be acquired. However, this information is available as the vibrational bands of the FTIR spectra. Vibrational band assignment of the

spectra was performed to identify the chemical species of the novel solvent system.

Spectroscopic spectra can be considered to be a multivariate output of a sample that consists of an abundance of hidden chemical information. Extracting the spectrum data would be an inexpensive method of chemical speciation. Data preprocessing tools are needed to extract qualitative and quantitative information from a specific spectrum. In this contribution, qualitative information extraction will be discussed.

Vibrational peak assignment was carried out for the changing peaks of the baseline-corrected spectra. The baseline corrected fingerprint region of the IR spectra of unloaded, loaded, and desorbed solvent are shown in Figure 5. Wavenumbers of all the increasing peaks were recognized and assigned to the relevant vibrational groups according to literature. Tabulated peak assignment information is given in Table 2. According to the peak assignment for increasing peaks, we identified the CO₂ capture product of the non-aqueous solvent system to be monomethyl carbonate (MMC) species. A proposed reaction mechanism according to the vibrational assignments has been published [28].

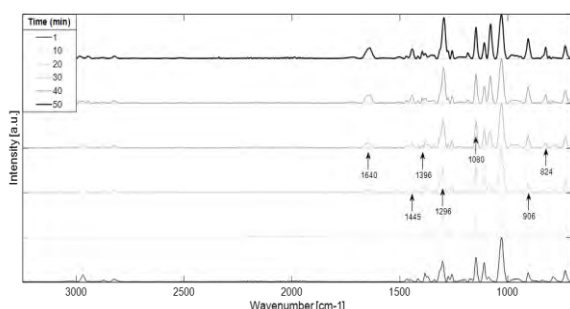


Figure 5: Increasing of the specific peak's intensities with the time during the CO₂ absorption reaction of the non-aqueous DIPA solvent system.

Therefore, in-situ monitoring by ATR-FTIR spectroscopy is a fast-screening method which is able to observe the CO₂ absorption-desorption reaction with full speciation.

Table 3. Monomethyl carbonate (MMC) peak identification of the non-aqueous DIPA system

Characteristic IR vibrational bands ν_{max} (cm ⁻¹)	MMC Peak Assignment	Reference
1640	C=O Stretching vibration	[30] [31]
1443	CH ₃ asymmetric deformation	[30] [31]
1396	CH ₃ symmetric deformation	[30] [31]
1296	O-C-O asymmetric stretching vibration	[30] [31]

1080	O-C-O symmetric stretching vibration	[30] [31]
906	CH ₃ -O stretching	[31]
824	CO ₃ deformation	[31]

However, concluding full chemical reaction speciation by in-situ monitoring in a closed system might have some uncertainties. The concerns on the non-aqueous systems could be two-fold.

1. If the system becomes heterogeneous during the absorption (e.g. phase change) the spectroscopic results will not be accurate
2. If precipitation happens on the ATR crystal the observed spectra may not represent the liquid CO₂ capture solvent.

To address the above-mentioned concerns, bulk analysis of the reaction system was conducted by using the same FTIR instrument with a different reactor set-up.

3.3 On-line bulk liquid flow monitoring of the non-aqueous solvent system to verify the fast-screening results

This experiment was conducted to check the representability of the results of the fast-screening method.

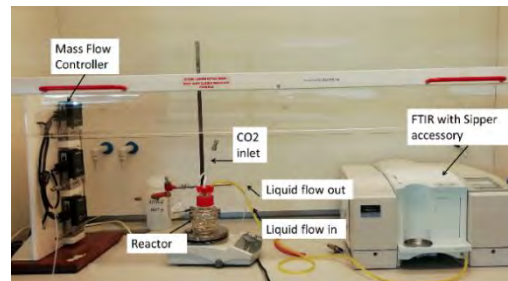


Figure 6: Laboratory arrangement of Set-up2 with a glass reactor

Precipitation on the ATR crystal may lead to analysis error, since the solvent penetration depth of the ATR measurement is very narrow, and the analysis happens at the bottom of the reaction volume. In set-up2 (shown in Figure 6), a glass reactor without an ATR crystal was used to perform the CO₂ absorption reaction. The solvent was continuously circulated through a FTIR flow cell. Therefore, the solvent system bulk was identified thus enabling verification that not solidification or precipitation occurred during the CO₂ absorption reactions.

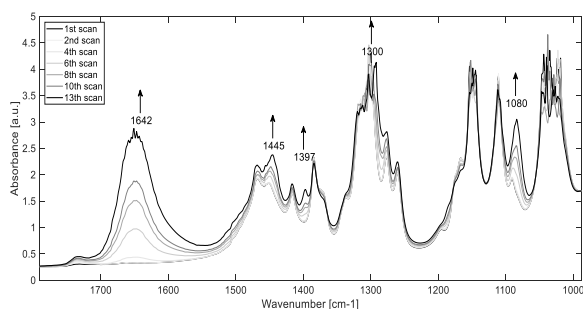


Figure 7: IR spectra obtained from liquid-flow cell measurements during CO₂ absorption experiments

All relevant MMC bands from 1000 cm⁻¹ to 1800 cm⁻¹ were identified by the liquid stream analysis using the liquid-flow cell. However, the band at 824 cm⁻¹ (MMC O-CO₂ deformation) was invisible due to the CaF₂ window material cut-off of the liquid-flow-cell. The obtained results confirmed the fast-screening speciation and showed the representativeness of the fast-screening results of the non-aqueous DIPA CO₂ absorption system.

Conclusion

From in-situ reaction monitoring using set-up1, it is shown that it was possible to obtain a fast and easy chemical characterization of non-aqueous CO₂ capture solvents. The instant observability of the reaction changes at running conditions and the possibility of inexpensive reaction mechanism identification are the main benefits of the set-up1. Furthermore, it is connected to qualitative and quantitative comparability of several solvent systems according to the IR vibrational changes.

The replication experiments using set-up2 confirm the results by addressing some concerns of set-up1. The qualitative results from set-up1 are repeatable and independent of the way of performing the FTIR analysis and the level of solvent mixing. This confirms the capture products are not a solid, gel, or high viscous liquid since the same results were obtained from liquid-flow cell measurements.

Therefore, screening set-up1 is a fast, reliable approach for identification of unknown solvent systems requiring less volume, less time, and less money as compared to traditional solvent analysis methods. Furthermore, representativeness and repeatability of the results was ensured. For non-aqueous amine systems use of an enhanced method like set-up2 is recommended.

Acknowledgements

This work was supported by the Ministry of Education and Research of the Norwegian Government.

References

[1] IPCC, IPCC Special Report on Carbon Dioxide Capture and Storage, Prepared by Working Group III of the

Intergovernmental Panel on Climate Change, in, Cambridge, 2005.

[2] IPCC, Based on Global Emissions From 2010. Details About the Sources Included in These Estimates Can Be Found in the Contribution of Working Group III to the Fifth Assessment Report (AR5) of the Intergovernmental Panel on Climate Change, in, 2014.

[3] IEA, World energy outlook special report on energy and climate change. International Energy Agency (IEA), in, 2015.

[4] G.T. Rochelle, Amine Scrubbing for CO₂ Capture, Science, 325 (2009) 1652-1654.

[5] N. MacDowell, N. Florin, A. Buchard, J. Hallett, A. Galindo, G. Jackson, C.S. Adjiman, C.K. Williams, N. Shah, P. Fennell, An overview of CO₂ capture technologies, Energy & Environmental Science, 3 (2010) 1645-1669.

[6] Y. Wang, L. Zhao, A. Otto, M. Robinius, D. Stolten, A Review of Post-combustion CO₂ Capture Technologies from Coal-fired Power Plants, Energy Procedia, 114 (2017) 650-665.

[7] P. Luis, Use of monoethanolamine (MEA) for CO₂ capture in a global scenario: Consequences and alternatives, Desalination, 380 (2016) 93-99.

[8] R.B. Roberts, U. S. Patent No. 1,783,901, in: D. Washington (Ed.) U. S. Patent and Trademark Office, 1930.

[9] H. Lepaumier, E.F. da Silva, A. Einbu, A. Grimstvedt, J.N. Knudsen, K. Zahlsten, H.F. Svendsen, Comparison of MEA degradation in pilot-scale with lab-scale experiments, Energy Procedia, 4 (2011) 1652-1659.

[10] J. Kim, H. Kim, J. Kim, S.J. Hwang, K.S. Lee, Experimental method for simultaneous and continuous measurement of absorption rate, viscosity and heat of reaction of carbon dioxide capture solvents, Journal of Industrial and Engineering Chemistry, 61 (2018) 152-160.

[11] U.E. Aronu, H.F. Svendsen, K.A. Hoff, Investigation of amine amino acid salts for carbon dioxide absorption, International Journal of Greenhouse Gas Control, 4 (2010) 771-775.

[12] P. Brüder, A. Grimstvedt, T. Mejdell, H.F. Svendsen, CO₂ capture into aqueous solutions of piperazine activated 2-amino-2-methyl-1-propanol, Chemical Engineering Science, 66 (2011) 6193-6198.

[13] A. Hartono, A.F. Ciftja, P. Brüder, H.F. Svendsen, Characterization of Amine-impregnated Adsorbent for CCS Post Combustion, Energy Procedia, 63 (2014) 2138-2143.

[14] F.A. Chowdhury, K. Goto, H. Yamada, Y. Matsuzaki, A screening study of alcohol solvents for alkanolamine-based CO₂ capture, International Journal of Greenhouse Gas Control, 99 (2020) 103081.

[15] A. Hartono, S.J. Vevelstad, A. Ciftja, H.K. Knuutila, Screening of strong bicarbonate forming solvents for CO₂ capture, International Journal of Greenhouse Gas Control, 58 (2017) 201-211.

[16] X. Luo, S. Liu, H. Gao, H. Liao, P. Tontiwachwuthikul, Z. Liang, An improved fast screening method for single and blended amine-based solvents for post-combustion CO₂ capture, Separation and Purification Technology, 169 (2016) 279-288.

[17] J. Noroozi, W.R. Smith, Accurately Predicting CO₂ Reactive Absorption Properties in Aqueous Alkanolamine Solutions by Molecular Simulation Requiring No Solvent Experimental Data, Industrial & Engineering Chemistry Research, 59 (2020) 18254-18268.

[18] I.I.I. Alkhatib, M.L. Ferreira, C.G. Alba, D. Bahamon, F. Llovel, A.B. Pereiro, J.M.M. Araújo, M.R.M. Abu-Zahra, L.F. Vega, Screening of Ionic Liquids and Deep Eutectic Solvents for Physical CO₂ Absorption by Soft-SAFT Using Key Performance Indicators, Journal of Chemical & Engineering Data, 65 (2020) 5844-5861.

- [19] Z. Song, X. Hu, H. Wu, M. Mei, S. Linke, T. Zhou, Z. Qi, K. Sundmacher, Systematic Screening of Deep Eutectic Solvents as Sustainable Separation Media Exemplified by the CO₂ Capture Process, *ACS Sustainable Chemistry & Engineering*, 8 (2020) 8741-8751.
- [20] M. Nakaoka, K.V.B. Tran, K. Yanase, H. Machida, K. Norinaga, Prediction of Phase Behavior of CO₂ Absorbents Using Conductor-like Screening Model for Real Solvents (COSMO-RS): An Approach to Identify Phase Separation Solvents of Amine/Ether/Water Systems upon CO₂ Absorption, *Industrial & Engineering Chemistry Research*, 59 (2020) 19020-19029.
- [21] M.H.W.N. Jinadasa, K.-J. Jens, L.E. Øi, M. Halstensen, Raman Spectroscopy as an Online Monitoring Tool for CO₂ Capture Process: Demonstration Using a Laboratory Rig, *Energy Procedia*, 114 (2017) 1179-1194.
- [22] M. Akram, M.H.W.N. Jinadasa, P. Tait, M. Lucquiaud, K. Milkowski, J. Szuhanski, K.-J. Jens, M. Halstensen, M. Pourkashanian, Application of Raman spectroscopy to real-time monitoring of CO₂ capture at PACT pilot plant; Part 1: Plant operational data, *International Journal of Greenhouse Gas Control*, 95 (2020) 102969.
- [23] M. Halstensen, H. Jilvero, W.N. Jinadasa, K.-J. Jens, Equilibrium Measurements of the NH₃-CO₂-H₂O System: Speciation Based on Raman Spectroscopy and Multivariate Modeling, *Journal of Chemistry*, 2017 (2017) 7590506.
- [24] F. Diab, E. Provost, N. Laloué, P. Alix, V. Souchon, O. Delpoux, W. Fürst, Quantitative analysis of the liquid phase by FT-IR spectroscopy in the system CO₂/diethanolamine (DEA)/H₂O, *Fluid Phase Equilibria*, 325 (2012) 90-99.
- [25] A. Einbu, A.F. Ciftja, A. Grimstvedt, A. Zakeri, H.F. Svendsen, Online Analysis of Amine Concentration and CO₂ Loading in MEA Solutions by ATR-FTIR Spectroscopy, *Energy Procedia*, 23 (2012) 55-63.
- [26] A. Grimstvedt, M. Wiig, A. Einbu, S.J. Vevelstad, Multi-component analysis of monoethanolamine solvent samples by FTIR, *International Journal of Greenhouse Gas Control*, 83 (2019) 293-307.
- [27] G. Richner, G. Puxty, Assessing the Chemical Speciation during CO₂ Absorption by Aqueous Amines Using in Situ FTIR, *Industrial & Engineering Chemistry Research*, 51 (2012) 14317-14324.
- [28] J.D. Wagaarachchige, Z. Idris, N.B. Kummamuru, K.A.S. Sætre, M. Halstensen, K.-J. Jens, A new sulfolane based solvent for CO₂ capture, in: 15th International Conference on Greenhouse Gas Control Technologies, GHGT-15, 15th 18th March 2021 Abu Dhabi, UAE, 2021.
- [29] C. Wagner, K.H. Esbensen, Theory of Sampling: Four Critical Success Factors Before Analysis, *Journal of AOAC INTERNATIONAL*, 98 (2019) 275-281.
- [30] G. Socrates, *Infrared and Raman Characteristic Group Frequencies: Tables and Charts*, 3rd ed., Wiley, 2004.
- [31] W. Behrendt, G. Gattow, M. Dräger, Über Chalkogenolate. LXI. Untersuchungen über Halbester der Kohlensäure. 1. Darstellung und Eigenschaften von Monomethyl- und Monoäthylcarbonaten, *Zeitschrift für anorganische und allgemeine Chemie*, 397 (1973) 237-246.

CCS IN THE EUROPEAN ENERGY TRANSITION TO CLIMATE NEUTRALITY

Reigstad, G. A.^{1*}, Straus, J.¹, Wolfgang, O.¹, Ouassou, J. A.¹, Seck, G.S.², Hache, E.², Villavicencio, M.³

¹ SINTEF Energy Research, Trondheim, Norway

² IFP Energies Nouvelles, Paris, France

³ Chaire European Electricity Markets, PSL Research University, LEDa [CGEMP], Paris, France

* Corresponding author e-mail: Gunhild.reigstad@sintef.no

Abstract

The transition of the European energy system to reach climate neutrality by 2050 will require a development and deployment of technologies capable of decarbonizing the energy system in an unprecedented scale. Increased sector integration through electrification and system-wide application of hydrogen necessitates the coherent consideration of all energy sectors for transition planning and facilitation through an improved policy framework. The *Hydrogen for Europe* study has applied energy system models to analyse the potential role of hydrogen in all sectors, and in co-existence with electricity and other energy carriers. The current work focuses on the role of CCS as it emerged from this analysis, and how limitations in deployment rate of CCS impacts the energy transition. It was shown that limits on both the annual CO₂ injection rate and minimum usage of renewable energy significantly affects the chosen route for hydrogen production.

Keywords: CCS, Energy transition, Energy system models, Electrolyser

1. Introduction

The *Hydrogen for Europe* study was initiated in 2020 to provide new knowledge on the role of hydrogen in reaching the EU Green Deal aim of climate neutrality by 2050. EU policies have been in a rapid development from stating that "for Europe to lead the world towards climate neutrality means achieving it by 2050" [1] in 2018, to launching the EU Green Deal a year later and in 2020 submitting to the European Parliament the legislative proposal for an EU Climate Law that enshrines the 2050 climate neutrality target in EU legislation. An EU hydrogen strategy [2] was also released in 2020. In the strategy, hydrogen was acknowledged for its ability to complement electrification in decarbonizing all the sectors of the European energy system. The strategy emphasises hydrogen's role as provider of seasonal storage and as energy carrier that can be distributed to remote demands. The strategy concludes that hydrogen is an important part of the energy transition Europe must undergo to meet the 2050 climate neutrality goal of the European Green Deal.

Several studies have investigated the potential role of hydrogen in the sectors of the European energy system. One of the most comprehensive analyses to date is "A Clean Planet for All" [3], the vision paper launched by the EU commission in 2018. The Hydrogen Roadmap Europe (2019) [4], published by Fuel Cells and Hydrogen Joint Undertaking also provides a comprehensive overview of the potential use of hydrogen to cover the European energy demands. Still, there are significant knowledge gaps in terms of how to optimally foster and support a hydrogen market optimized for minimum transition costs for the society. These questions are related to in which sectors hydrogen will play the most significant role in

decarbonizing and how hydrogen should be produced over the entire timespan from today and until 2050.

As part of the *Hydrogen for Europe* study we have shown that the assumptions related to deployment of CO₂ storage has a significant influence on the development of carbon capture and storage (CCS) and the hydrogen market in Europe. We will hence present in the current paper an overview of the role of CCS in the transition of the European energy system to carbon-neutrality and how annual storage constraints impact the production of hydrogen from natural gas reforming with CCS. To this end, Section 2 will elaborate the demand for CCS in Europe while Section 3 will present recent research on potential annual CO₂ injection rate. Section 4 will present the methodology in the *Hydrogen for Europe* study and Section 5 will present the impact of modelling assumptions on CCS.

2. The need for CCS in the transition to climate neutrality in Europe

Analyses by the IEA identified a clear need for CCS if we are to reach the Paris agreement at a global level [5]. The demand for CCS however differs between the continents due to the current state of the energy system. As an example, CCS could be a vital option for the power sector in Asia due to the possibility of retrofitting coal power generation plants with a long remaining lifetime, the situation is quite different in Europe where a large share of the coal power capacities are near end of lifetime. Some European countries have also decided a general phasing out of coal power, which adds to the reduced capacity. Hence, the role and level of CCS in Europe is uncertain.

Looking at the European energy system from a high-level, the demand for storage of CO₂ stems from four needs in decarbonizing the energy system:

- Capture of CO₂ emissions from the industry sector; certain industries such as cement production have no other decarbonization options than CO₂-capture due to inherent process emissions.
- Decarbonization of the power system; a sharp increase of variable renewable power is expected in the power sector. This increases the demand for power capacities with the ability to stabilize the power supply and to bridge seasonal variations. Part of this demand could be covered by power production with integrated CCS.
- Carbon Dioxide Removal (CDR) technologies that can compensate for hard to abate CO₂ emissions. Power and hydrogen production from biomass with integrated CO₂ capture (BECCS) and direct air capture (DACs) of CO₂ have the CDR capability and all rely on the possibility to store the captured CO₂ permanently.
- Production of hydrogen from natural gas with integrated capture of CO₂; these technologies allow producing large quantities of hydrogen within the next decades with accompanying low emission rates of CO₂ based on existing technology and independent of a decarbonised power system. This can give a head start to the development of a European hydrogen market and can facilitate the introduction of increasing production of hydrogen from variable renewables.

The deployment of CCS within the industry, power and hydrogen sectors, as well as for CDR, depends upon several factors including (i) growth rates for industries depending on CCS for CO₂ mitigation, (ii) the need for compensating remaining emissions by CDR, (iii) the competitiveness of CCS relative to other mitigation options, and (iv) limitations in the utilization of CCS due to constraints on the up-scaling of annual injection rates or total storage potential. In particular, the latter limitations could, if present, cause a competition between the sectors for access to storage of CO₂.

3. Limitations for CO₂ storage deployment in Europe

For CO₂ storage in Europe, there are two main physical limitations: the total storage volumes available and the accessible injection rate in terms of CO₂ injected per year. The potential for CO₂ storage is to some degree known in Europe, for example through the establishment of the JRC CO₂ storage database. Geological storage atlases for Norway and the UK conclude that they have the possibility to store 70 Gt each on their continental shelves. The storage potential on the Dutch continental shelf is estimated to be 1.7 Gt.

The main limiting factor for CCS deployment is thus how fast potential sites for CO₂ storage and corresponding infrastructure can be made available. This has to a very small degree been assessed. As part of the review of the EU SET-Plan, the current European plans for CO₂ storage by 2030 has been assessed to 50 Mt/a. Ringrose and Meckel [6] estimated the potential for scale-up of CO₂

storage in three offshore regions including the Norwegian continental shelf. Figure 1 shows the results of Ringrose and Meckel for the Norwegian continental shelf, which form the basis for the chosen injection rate in the *Hydrogen for Europe* study.

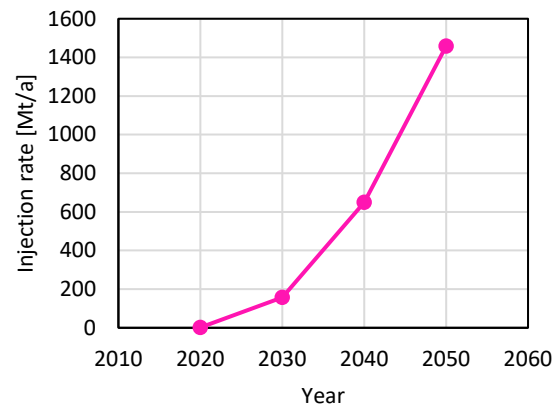


Figure 1: Injection rate on the Norwegian continental shelf (adapted from Ringrose and Meckel [6]).

4. The Hydrogen for Europe study

The *Hydrogen for Europe* study [7] is based upon a framework consisting of two state-of-the-art energy system models: A detailed European energy system model (MIRET-EU), and a more aggregated model to include endogenous learning (Integrate Europe). Technical assumptions as well as baseline assumptions such as demand growth and fossil fuel prices are heavily based upon the databases provided by the Joint Research Centre. The chosen set of policy assumptions is aligned with the existing EU policies and the Green Deal. Hydrogen production technologies such as water electrolysis, natural gas reforming with integrated capture of the produced CO₂ and pyrolysis are all under rapid development. Hence, it has been of high importance in the *Hydrogen for Europe* study to include the most recent performance and cost data for these technologies as well as expectations for future cost reductions to ensure a technology neutral approach.

The model framework includes all aspects of the European energy system, including energy supply, conversion and end-use demand. The coverage of each of the demands and the production of energy carriers such as electricity and hydrogen are not pre-determined, but rather a result of the optimization. The optimization objective is minimizing the total costs for the entire energy system over the considered period from 2020 to 2050. In total 27 European countries are included in the study, of which 3 countries are non-EU members.

Two different scenarios have been established within the study to assess different potential transition paths to climate-neutrality. The *Technology Diversification (TD)* scenario is characterised by its policy framework that consists of the existing policy framework together with a climate law that binds the considered countries to a reduction in greenhouse gas emissions of 55 % compared to 1990 level in 2030 and net-zero emissions by 2050. In the second scenario, the *Renewables Push (RP)* scenario, the renewable energy directive is renewed and set targets

for shares of renewables in gross final energy consumption to 40 %, 60 %, and 80 % in 2030, 2040, and 2050, respectively. In both scenarios, annual CO₂ injection to permanent storage is restricted to 1 Gt until 2040, with a subsequent increase to 1.4 Gt by 2050.

In the current analysis, we will consider results from the *TD* and *RP* scenarios, in addition to results from a sensitivity analysis of the *TD* scenario where the CO₂ injection rate is unrestricted (*TD-S*). We will show how the CO₂ deployment varies between these scenarios, and how this affects the markets for electricity and hydrogen.

5. Results

Figure 2 shows the different annual injection rates of CO₂ to permanent storage. We can draw two important conclusions from this figure:

1. The *TD* scenario is constrained in both 2040 and 2050. This can be deduced from the sensitivity (*TD-S*), where the injection rate is increased by 20 % and 30 % respectively as the relevant constraint is removed.
2. Requiring an increased share of renewable energy in the gross final energy (*RP*) leads to non-binding CO₂ injection rate constraints.

Hence, considerable differences in the captured CO₂ from the individual sectors is expected. It should also be noted that the cost optimal injection rates are higher in 2030 and 2040 compared to the study by Ringrose and Meckel [6], highlighting the importance of a fast increase in the annual injection rate.

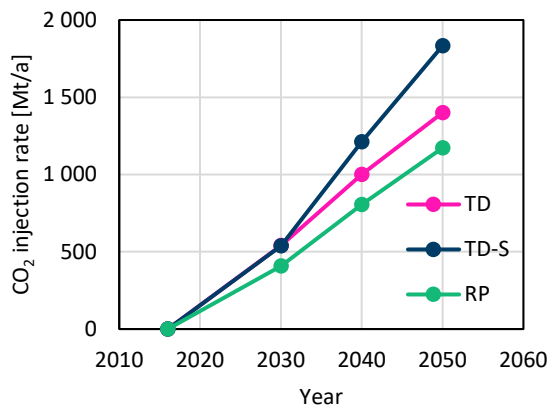


Figure 2: Annual injection of CO₂ to permanent storage.

Figure 3 illustrates the on-grid power generation for each scenario. On-grid power generation in *TD* and *TD-S* scenarios are almost identical. However, total power generation in the *RP* scenario is approximately 7 % higher for 2030, which corresponds to the extra renewable energy needed in that scenario for that year. The alternative to extra renewable power generation would be increased utilization of biomass, but the available biomass resources are limited. Hence, extra renewable power generation from solar PV and wind power is required for achieving the 40 % share. For 2040 and onwards the on-grid power generation is near equal for the three scenarios.

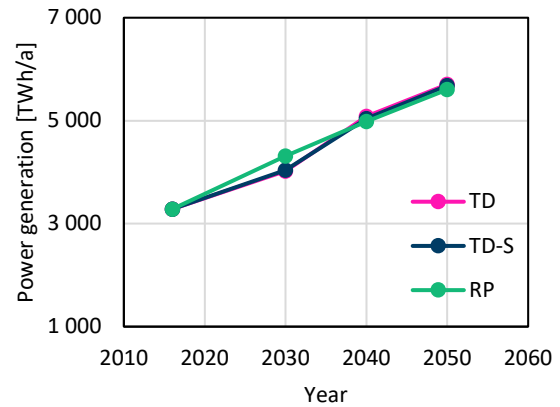


Figure 3: On-grid power generation in Europe excluding power for hydrogen production.

Until 2040, total hydrogen production is largely unaffected by the chosen scenario as shown in Figure 4. By 2050 the differences are more pronounced and partly stem from an increased usage of hydrogen in e-fuels in the *RP* scenario. The cause for this behavior is most likely again the target for renewable share in final energy demand, as e-fuels are considered as renewable, if the hydrogen is produced from renewable energy sources. Increased availability of injection capacity for CO₂ also increases the hydrogen production.

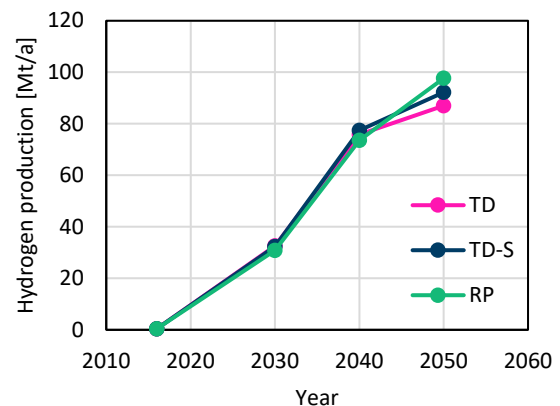


Figure 4: Hydrogen production in Europe.

Figure 5 illustrates the CO₂ captured from the industry sector. Although there are differences between the scenarios, it is not straight-forward to explain them. It is not unexpected, that the *TD-S* scenario results in the highest amount of CO₂ captured, as it also corresponds to the unconstrained CO₂ injection rate. However, less CO₂ is captured in the industry sector in the *TD* scenario than the *RP* scenario although the total CO₂ injection is higher. The constraint related to a higher share of renewables in gross final energy consumption in the *RP* scenario gives the possibility to the industry to keep using fossil-fuel based technologies, thus higher amounts of CO₂ emissions than in *TD*. A small decrease is observed in 2050 in all scenarios due to the increase of renewables with the carbon neutrality constraint. The past investments are at the end of their lifetime by 2040-2050, and that new investments are not based on fossil-fuel consumption, and hence, do not require CCS.

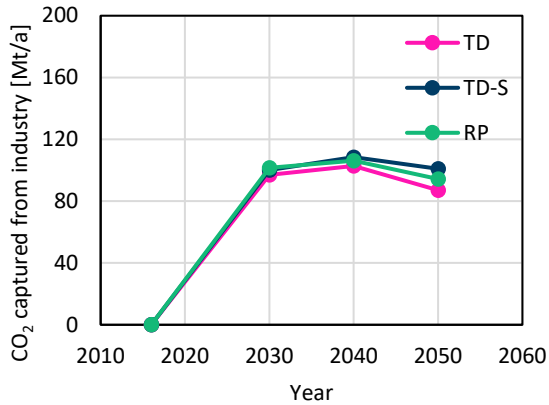


Figure 5: Captured CO₂ in the industry sector.

Figure 6 illustrates the CO₂ captured in the power sector. This includes both CO₂ captured from biomass (BECCS) and from fossil fuels. While there is no significant difference in 2030 between the *TD* scenario and its sensitivity, we see a major difference in both 2040 and 2050. This difference corresponds to 166 Mt/a and is mostly caused by a significant investment in BECCS and natural gas + CCS in the sensitivity due to the unconstrained CO₂ injection rate. The *TD* scenarios compensate the reduced investments in carbon capture technologies through increased investments in nuclear and variable renewable power. The *RP* scenario requires higher CO₂ capture from the power sector than the *TD* scenario, specifically due to the requirement of flexible power generation which is mostly provided through electricity generation via BECCS. The CO₂ intensity of BECCS is higher than for NG+CCS. Hence, the amount of captured CO₂ is higher per generated electricity.

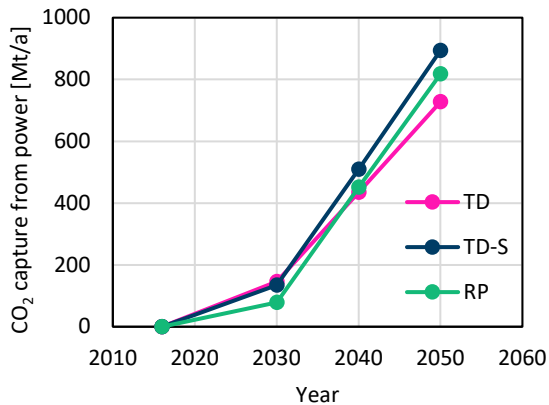


Figure 6: Captured CO₂ in the power sector.

Figure 7 illustrates the captured CO₂ from carbon dioxide removal technologies via CDR deemed necessary to compensate emissions on hard-to-abate sectors. This includes both CO₂ captured from biomass in the power sector and in hydrogen production. As we can see in this figure, CO₂ captured from CDR is comparable in both main scenarios in 2040 and 2050, while the unconstrained CO₂ injection rate sensitivity has significantly more CO₂ captured in 2040 and 2050 using CDR.

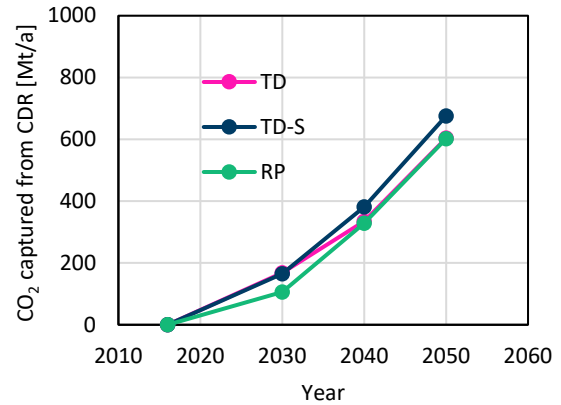


Figure 7: Captured CO₂ from CDR technologies.

This increase is mostly due to an increased usage of DAC. The total CO₂ captured from biomass is similar in all scenarios, although the distribution between hydrogen production and power generation differs. Seen together with the level of DACs, it can be concluded that the carbon removal technologies are required in all scenarios for achieving a zero-emission energy system. However, the total system costs may be affected by the chosen CO₂ injection rate and renewable energy constraints, as *TD-S* captured significantly more CO₂ from DAC compared to the two main scenarios. Hence, it may be beneficial to continue using oil and compensate the emissions with DAC.

Figure 8 highlights the captured CO₂ from hydrogen production. Compared to the other sectors, we can directly see that the amount of captured CO₂ varies significantly between the scenarios. While the captured CO₂ is similar in 2030 in both the *TD* scenario and its sensitivity, it is already significantly higher than in the *RP* scenario. This corresponds to 50 % of the CO₂ injection rate difference in Figure 2. The picture is even more pronounced in 2040 and 2050 where CO₂ captured from hydrogen production differs significantly between all scenarios. The small value in the *RP* scenario can be explained by the high share of renewables in the gross energy consumption. The difference between the *TD* scenario and its sensitivity *TD-S* is affected by the CO₂ injection as it corresponds to 37 % and 39 % of the increase in the CO₂ injection rate in 2040 and 2050, respectively.

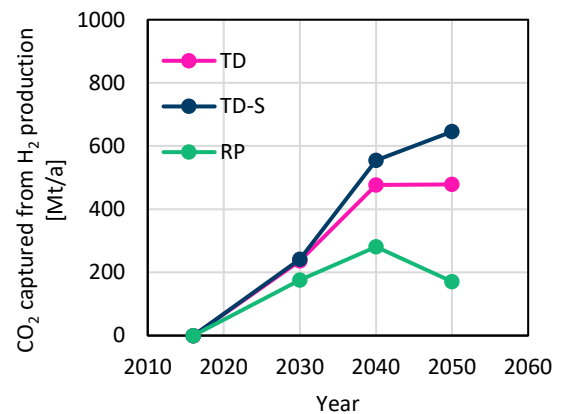


Figure 8: Captured CO₂ from hydrogen production.

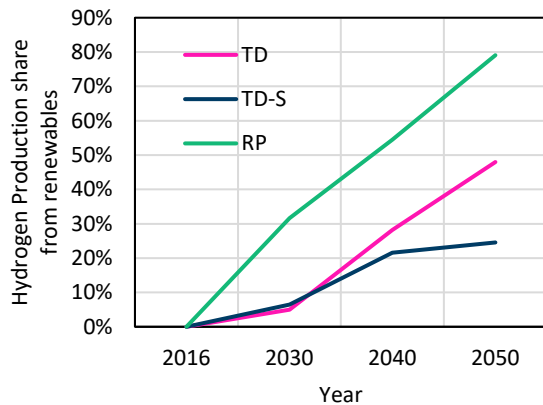


Figure 9: Share of hydrogen produced from renewable sources (wind, solar, biomass *via* electrolysers and gasification of biomass).

The total hydrogen production is however similar in all scenarios, as shown in Figure 4. Correspondingly, the share of hydrogen produced from electrolyser and renewable power is increased especially in the *RP* scenario, as shown in Figure 9. Note that this increase correlates with the increased share of renewable energy in the gross final energy consumption.

CCU was also implemented in the models. The e-Fuels are then mostly used for decarbonizing the aviation sector. However, the difference in CO₂ used for power-to-liquid is rather small (31 Mt) between *TD-S* and *RP*. Hence, CCU does not affect the hydrogen market significantly in terms of production routes.

6. Conclusion

The pace at which CO₂ injection rates unfold has a major impact on the deployment of carbon capture in particular and on the decarbonization pathways in general. The implications are however very different across sectors. The industry sector is almost not affected by this due to the lack of alternatives for decarbonisation. The differences in the power sector are more pronounced, although it is surprising that the *Renewable Push* scenario with the lowest overall CO₂ injection rate captures more CO₂ from the power sector. The major difference occurs in the breakdown of hydrogen production technologies. A limit in the CO₂ injection rates significantly disfavour hydrogen production *via* reforming with integrated CCS.

In the case of the *RP* scenario, the required CO₂ injection rate is lower than for the other scenarios since CO₂

abatement is achieved through the use of renewables which is brought about by the requirement for renewable energy in the gross final energy demand.

Acknowledgements

The authors acknowledge the *Hydrogen for Europe* study for funding the scientific work which the current publication is based on.

References

- [1] 'The Commission calls for a climate neutral Europe by 2050*', *European Commission - European Commission*. https://ec.europa.eu/commission/presscorner/detail/en/IP_18_6543 (accessed May 21, 2021).
- [2] 'A hydrogen strategy for a climate-neutral Europe'. COMMUNICATION FROM THE COMMISSION TO THE EUROPEAN PARLIAMENT, THE COUNCIL, THE EUROPEAN ECONOMIC AND SOCIAL COMMITTEE AND THE COMMITTEE OF THE REGIONS. Accessed: Dec. 16, 2020. [Online]. Available: https://ec.europa.eu/energy/sites/ener/files/hydrogen_strategy.pdf
- [3] EU Commission, 'A Clean Planet for all A European strategic long-term vision for a prosperous, modern, competitive and climate neutral economy', Nov. 2018. Accessed: May 21, 2021. [Online]. Available: <https://eur-lex.europa.eu/legal-content/EN/TXT/PDF/?uri=CELEX:52018DC0773&from=EN>
- [4] Fuel Cells and Hydrogen 2 Joint Undertaking., *Hydrogen roadmap Europe: a sustainable pathway for the European energy transition*. LU: Publications Office, 2019. Accessed: Apr. 23, 2021. [Online]. Available: <https://data.europa.eu/doi/10.2843/341510>
- [5] IEA, 'World Energy Outlook 2020, IEA, Paris', 2020. [Online]. Available: <https://www.iea.org/reports/world-energy-outlook-2020>
- [6] P. S. Ringrose and T. A. Meckel, 'Maturing global CO₂ storage resources on offshore continental margins to achieve 2DS emissions reductions', *Sci. Rep.*, vol. 9, no. 1, p. 17944, Nov. 2019, doi: 10.1038/s41598-019-54363-z.
- [7] Deloitte Finance, IFPEN, and SINTEF, 'Hydrogen4EU - Charting pathways to net zero', 2021.

SHORT PAPERS FROM THE 11TH INTERNATIONAL TRONDHEIM CCS CONFERENCE

These proceedings contain the Short Papers from the 11th International Trondheim CCS Conference (TCCS-11), which was organised as a virtual event owing to the pandemic on June 22nd – 23rd, 2021.

The bi-annual Trondheim CCS Conference is one of the leading scientific CCS technology conferences. Since its inception in 2003, the conference has become a globally important meeting place for CCS experts. In summer 2021, around 350 people joined the conference to listen to world-leading keynote speakers, scientific presentations and panel discussions.

The conference is hosted jointly by SINTEF and NTNU and is organized by the Norwegian CCS Research Centre (NCCS).